75TH HIGHWAY GEOLOGY SYMPOSIUM

2026 HGS PROCEEDINGS

RENO NEVADA

BETTER HIGHWAYS THROUGH APPLIED GEOLOGY

SEPTEMBER 28 – OCTOBER 1, 2026
RENO, NEVADA

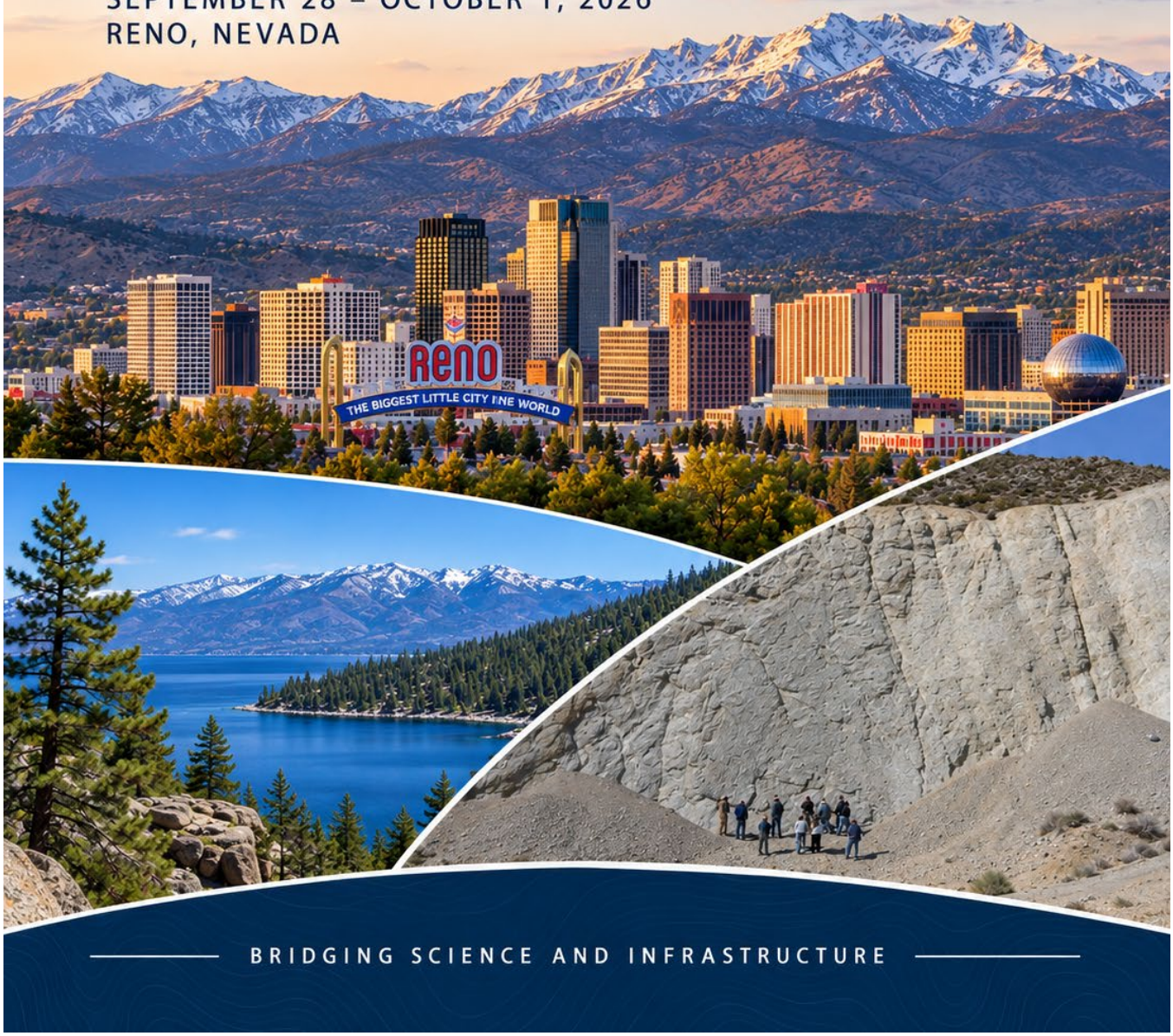

BRIDGING SCIENCE AND INFRASTRUCTURE

ABOUT THE COVER

Reno and the Sierra Nevada
The central image highlights Reno, Nevada, host city of the 75th Highway Geology Symposium, set against the eastern front of the Sierra Nevada. The setting reflects the close relationship between geology, topography, transportation, and the growth of communities throughout northern Nevada.

Lake Tahoe and the Sierra Nevada
Lake Tahoe represents one of the region's most recognizable landscapes. The Tahoe Basin and surrounding Sierra Nevada reflect a complex geologic history shaped by faulting, uplift, volcanism, and glaciation. The landscape provides a dramatic regional setting for transportation corridors that must contend with steep terrain, rock slopes, seismic hazards, snow, and other geologic constraints.

Genoa Fault
The lower right photograph shows an exposure associated with the Genoa Fault, one of the major active faults along the eastern front of the Carson Range. The exposure provides a striking illustration of the active tectonic setting of western Nevada and the importance of understanding faulting and seismic hazards in the planning and design of transportation infrastructure.

Disclaimer

Statements and views presented in the abstracts are strictly those of the author(s), and do not necessarily reflect positions held by their affiliations, the Highway Geology Symposium (HGS), or others acknowledged. The mention of trade names for commercial products does not imply approval or endorsement by HGS.

Copyright Notice

Copyright © 2026 Highway Geology Symposium (HGS)

All Rights Reserved. Printed in the United States of America. No part of this publication may be reproduced or copied in any form or by any means – graphic, electronic, or mechanical, including photocopying, taping, or information storage and retrieval systems – without prior written permission of the HGS. This excludes the original author(s).

TABLE OF CONTENTS

Acknowledgements	4
Welcome to the 75th Highway Geology Symposium	5
75 Years of Impact: The Highway Geology Symposium	6
Hotel Map	7
Schedule at a Glance	8
Highway Geology Symposium History Organization and Function	9
HGS National Steering Committee Officers	16
HGS National Steering Committee Members	16
Past, Present, and Future Symposium Contacts	18
Emeritus Steering Committee Members	19
Medallion Award	20
Young Author Award	21
Field Trip Schedule	22
Sponsors	23
Exhibitors	27
Highway Geology Symposium 2026, Mini-Sessions	33
Technical Session Schedule	34
Papers	38

75th Highway Geology Symposium

September 28- October 1, 2026
Whitney Peak Hotel
Reno, NV

Grateful Acknowledgments

The Highway Geology Symposium National Steering Committee would like to acknowledge and extend a sincere appreciation for their efforts to make the 75th HGS a success.

75th Local Steering Committee:

Gary Norris
Sherif Elfass
John Pilipchuk
John Louie
Sajid Sulahria
Emerson Loisel
Chris Ruppen
Erik Rorem
Kyle Halverson
Saeedeh Naziri
Sarah McInnes
Jesse Ruzicka
Cheryl Youngblood
Delaney Event Management

Welcome to the 75th Highway Geology Symposium

On behalf of the Local Steering Committee, it is our great pleasure to welcome you to the 75th Highway Geology Symposium in Reno, Nevada.

This year's symposium represents an important milestone in more than one way. Not only are we celebrating the 75th gathering of the Highway Geology Symposium, but this is also the first time the symposium has been hosted in Reno. We are proud to welcome you to Northern Nevada, a region where geology has played an important role in shaping our transportation systems, communities, and infrastructure.

We are also pleased to introduce a stronger seismic component to this year's symposium. Nevada and the surrounding western states provide an ideal setting for expanding the discussion of how earthquakes and seismic hazards affect transportation infrastructure. By incorporating seismic topics into the technical program, we hope to broaden the exchange between engineering geology, geotechnical engineering, earthquake engineering, and transportation professionals while remaining true to the practical focus that has defined the Highway Geology Symposium for many years.

Our Local Steering Committee has worked diligently to develop a program that combines technical presentations, field experiences, professional exchange, and opportunities to reconnect with longtime colleagues and build new relationships. We hope the symposium provides an environment where practical experience and new ideas come together, leading to discussions and collaborations that continue well beyond our time in Reno.

We also encourage you to enjoy Reno and the surrounding region while you are here. From the unique geology and landscapes of Northern Nevada to the nearby Sierra Nevada and Lake Tahoe, this area provides an especially fitting setting for the Highway Geology Symposium.

Organizing an event of this scale requires the efforts of many people. We extend our sincere appreciation to the members of the Local Steering Committee, symposium leadership, speakers, sponsors, exhibitors, volunteers, and everyone who contributed their time and expertise to making this event possible.

Most importantly, thank you for joining us and for being part of the 75th Highway Geology Symposium. Your participation, knowledge, and professional engagement are what have sustained this symposium for 75 gatherings and will carry its legacy forward.

Welcome to Reno. We hope you have a productive, enjoyable, and memorable symposium.

Gary Norris and Sherif Elfass

75 Years of Impact: The Highway Geology Symposium

This year we celebrate the 75th gathering of the Highway Geology Symposium. Seventy-five gatherings over 77 years is no small accomplishment. Since that first meeting in Richmond in 1950, there have been wars and more wars, 13 presidents, two new states, trips to the moon, a global pandemic, and an extraordinary expansion of technology. In our own professions, we have gone from slide rules to artificial intelligence, surveying transits to satellite imagery, and blueprints to digital point clouds. Plate tectonics itself would not become broadly accepted until well after the first Symposium. The changes have been staggering.

Yet, for all that has changed, the basic idea behind HGS has changed remarkably little. The stated purpose of that first gathering was "to foster the exchange of ideas between highway engineers and geologists on problems relating to highway construction." The early proceedings make clear that this exchange was intended to be practical, informal and personal. A 1956 foreword emphasized practical subjects over involved scientific treatises, diversity over a central theme, and considerable latitude for the local sponsors. Those principles remain recognizable today.

Perhaps even more important is the personal interaction that has always been at the heart of the Symposium. The 1956 program arrangements observed that a one-day technical program left too little time for the personal contacts and acquaintanceships that frequently form the most profitable part of a meeting. Their solution was a social gathering the evening before the program. That same spirit has endured through banquets, field trips, informal conversations and friendships that have crossed agencies, disciplines, states and generations. The field trip, now central to HGS, takes us to places many of us might otherwise never visit and lets us stand together at an outcrop, a landslide, a bridge or a rock cut and learn from one another.

That ethos was tested during the COVID-19 pandemic. Rather than simply substitute a virtual meeting for the gathering, HGS accepted a hiatus. In doing so, it affirmed something our predecessors understood early: HGS is more than a collection of papers. The face-to-face exchange is part of the event itself. In an era of remote work and artificial intelligence, that may become more important, not less.

The resiliency of HGS also owes much to its deliberately simple structure. There is no large central organization. There are bylaws, officers and a National Steering Committee, but each year considerable responsibility and flexibility pass to a local host committee. That balance has allowed the Symposium to adapt without losing its character. Technical tools and practices have evolved continuously - controlled blasting, rock reinforcement, remote sensing, numerical modeling, LiDAR, point clouds and much more - while the emphasis on practical solutions and open exchange has remained.

We benefit today from the foresight and leadership of the many people who preceded us, beginning with the chair of the 1st HGS, W. T. Parrott from the VA Department of Highways, A.

C. Dodson from the NC State Highway and Public Works Commission for the 7th HGS, and continuing through generations of organizers, authors, speakers, field-trip leaders and attendees. The proceedings they left behind are a remarkable record of both the development of highway geology and the people who made that development possible.

Seventy-five gatherings later, better highways are one result. Just as important are the relationships, shared experience and willingness to learn from one another that have sustained the Symposium. Technology will continue to change. The geology will continue to challenge us. It is the spirit behind HGS that has kept it going, and it is that spirit we carry forward.

75th Highway Geology Symposium

September 28- October 1, 2026
Whitney Peak Hotel
Reno, NV

Whitney Peak Hotel, The Third Floor

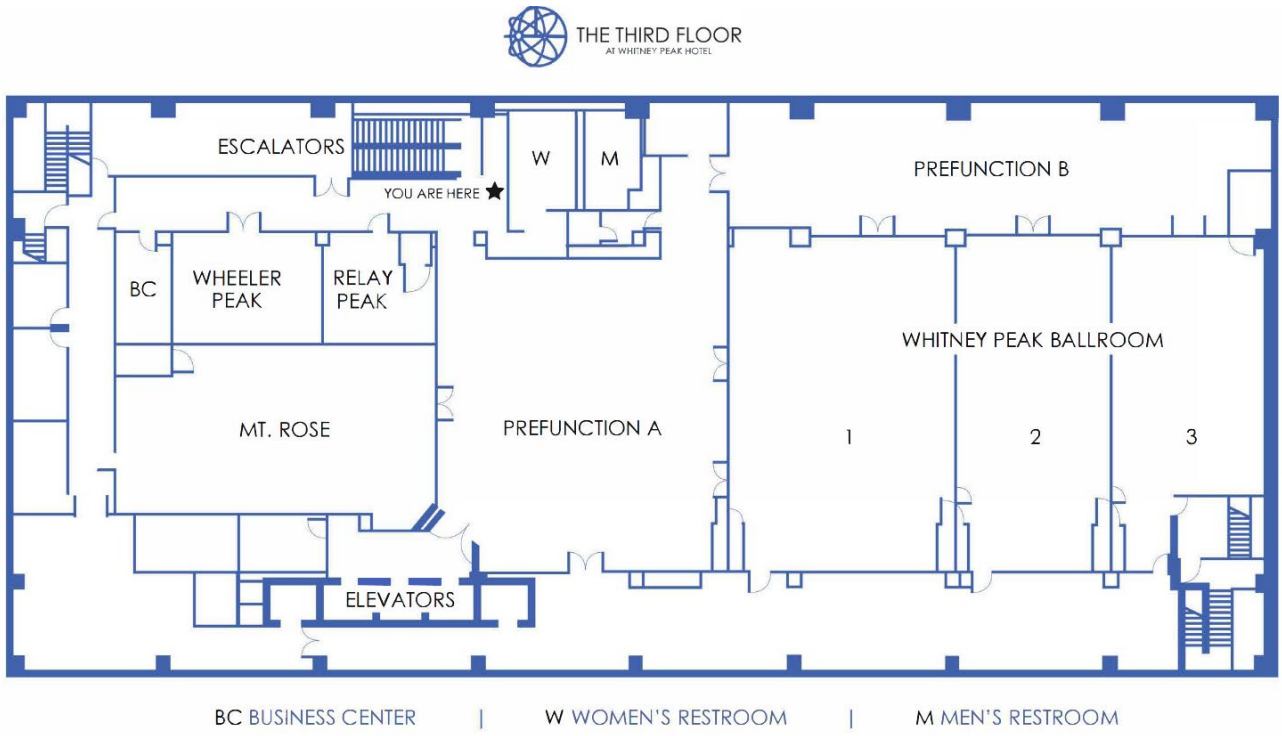

75th Highway Geology Symposium **Schedule at a Glance**		
	Monday, September 28, 2026	**Location**
9:00 AM - 5:00 PM	Exhibitor Move-in & Setup	Prefunction A
9:00 AM - 6:00 PM	Registration Open	Prefunction A
10:00 AM - 5:00 PM	Offsite Sessions (Pre-Registration Required)	University of Nevada, Reno - Transportation departs from Hotel
10:00 AM - 11:30 AM	Shear-Wave Surveying	
1:00 PM - 2:30 PM	Slope Stabilization Based on Soil-Pile Interaction	
3:00 PM - 4:30 PM	Improving Infrastructure Resilience Through Experimental Seismic Engineering	
5:00 PM - 6:30 PM	HGS National Steering Committee Meeting	Whitney Peak 1
6:00 PM - 8:00 PM	Icebreaker Reception ***Sponsored by GeoStabilization International***	Prefunction AB
	Tuesday, September 29, 2026	**Location**
7:00 AM - 8:00 AM	Breakfast	Boundary Peak
7:00 AM - 4:30 PM	Registration Open	Prefunction A
7:00 AM - 4:30 PM	Exhibits Open	Prefunction A
8:00 AM - 9:30 AM	Welcome to Nevada!	Whitney Peak Ballroom
9:00 AM - 4:00 PM	Guest Trip to Virginia City (Pre-Registration Required)	Offsite
9:30 AM - 10:00 AM	Morning Break - ***Sponsored by DOWL***	Prefunction AB
10:00 AM - 12:00 PM	Technical Session 1: Young Authors	Whitney Peak Ballroom
12:00 PM - 1:00 PM	Lunch	Boundary Peak
1:00 - 2:20 PM	Technical Session 2: Young Authors and Others	Whitney Peak Ballroom
2:20 PM - 2:50 PM	Afternoon Break - ***Sponsored by GFT***	Prefunction AB
2:50 PM - 4:10 PM	Technical Session 3	Whitney Peak Ballroom

	Wednesday, September 30, 2026	**Location**
7:00 AM - 8:00 AM	Breakfast	Boundary Peak
7:00 AM - 4:00 PM	Registration	Prefunction AB
7:00 AM - 5:00 PM	Exhibits open	Prefunction AB
8:00 AM - 10:00 AM	Technical Session 4A	Whitney Peak Ballroom
8:00 AM - 10:00 AM	Technical Session 4B	Boundary Peak
10:00 AM - 10:30 AM	Morning Break ***Sponsored by Hager-Richter Geoscience, Inc.***	Prefunction AB
10:30 AM - 11:50 PM	Technical Session 5A	Whitney Peak Ballroom
10:30 AM - 11:50 PM	Technical Session 5B	Boundary Peak
11:50 PM - 1:00 PM	Lunch	Boundary Peak
1:00 PM - 2:20 PM	Technical Session 6	Whitney Peak Ballroom
2:20 PM - 2:50 PM	Afternoon Break - ***Sponsored by Fragmentation***	Prefunction AB

	Efficiency Services, Inc./KESCO, Inc.	
2:50 PM - 4:00 PM	Technical Session 7	Whitney Peak Ballroom
3:00 PM	Exhibitor Tear-down	Prefunction AB
3:30 PM - 4:00 PM	Field Trip preview	Whitney Peak Ballroom
6:00 PM - 7:00 PM	Banquet social	Prefunction AB
7:00 PM - 10:00 PM	HGS Banquet & Awards ***Sponsored by GeoStabilization International***	Whitney Peak Ballroom

	Thursday, October 1, 2026	**Location**
6:30 AM - 7:00 AM	Grab & Go breakfast	Whitney Peak Ballroom
7:00 AM	HGS Field Trip Departs **Transportation sponsored by Maccaferri, Inc.** **Snacks/soft drinks sponsored by Ameritech Slope Constructors** **Adult Beverages sponsored by Scarptec**	Offsite
12:00 PM	Lunch-***Sponsored by Geobrugg***	Genoa Golf Club
6:00 PM	Return to Whitney Peak	Hotel Lobby

Highway Geology Symposium History Organization, and Function

Inaugural Meeting and Beginnings

Established to foster a better understanding and closer cooperation between geologists and civil engineers in the highway industry, the Highway Geology Symposium (HGS) was organized and held its first meeting on March 14, 1950, in Richmond Virginia. Attending the inaugural meeting were representatives from state highway departments (as referred to at that time) from Georgia, South Carolina, North Carolina, Virginia, Kentucky, West Virginia, Maryland, and Pennsylvania. In addition, a number of federal agencies and universities were represented. A total of nine technical papers were presented. W.T. Parrott, an engineering geologist with the Virginia Department of Highways, chaired the first meeting. It was Mr. Parrott who originated the Highway Geology Symposium. It was at the 1956 meeting that future HGS leader, A.C. Dodson, began his active role in participating in the Symposium. Mr. Dodson was the Chief Geologist for the North Carolina State Highway and Public Works Commission, which sponsored the 7th HGS meeting.

Organization

Unlike most groups and organizations that meet on a regular basis, the Highway Geology Symposium has no central headquarters, no annual dues and no formal membership

requirements. The governing body of the Symposium is the National Steering Committee composed of approximately 20 – 25 geologist and geotechnical engineers from state and federal agencies, colleges and universities, as well as private service companies and consulting firms throughout the country. Steering committee members are elected for three-year terms, with their elections and re-elections being determined principally by their interests and participation in and contribution to the Symposium. The officers include a chairman, vice chairman, secretary, and treasurer. all of whom are elected for a two-year term. Officers, except for the treasurer, may only succeed themselves for one additional term. A number of three-member standing committees conduct the affairs of the organization. The lack of rigid requirements, routing and relatively relaxed overall functioning of the organization is what attracts many participants. The symposia are generally run for 3 days, with 2 days for technical papers and a full day field trip. The Symposium is often preceded with a special session or workshop and an opens with an evening Ice-Breaker. Occasionally, an optional workshop or field trip may follow the Symposium

Symposium Locations

Since the initial meeting, 73 annual (2 years missed for COVID) Symposiums have been held in 36 different states. Between 1950 and 1962, the meetings were east of the Mississippi River, with Virginia, West Virginia, Ohio, Maryland, North Carolina, Pennsylvania, Georgia, Florida, Tennessee, and Nevada serving as host state. In 1962, the symposium moved west for the first time to Phoenix, Arizona where the 13th annual HGS meeting was held. Since then, it has alternated, for the most part, back and forth from the east to the west.

1st	1950	Richmond, VA	39th	1988	Park City, UT
2nd	1951	Richmond, VA	40th	1989	Birmingham, AL
3rd	1952	Lexington, KY	41st	1990	Albuquerque, NM
4th	1953	Charleston, WV	42nd	1991	Albany, NY
5th	1954	Columbus, OH	43rd	1992	Fayetteville, AR
6th	1955	Baltimore, MD	44th	1993	Tampa, FL
7th	1956	Raleigh, NC	45th	1994	Portland, OR
8th	1957	State College, PA	46th	1995	Charleston, WV
9th	1958	Charlottesville, VA	47th	1996	Cody, WY
10th	1959	Atlanta, GA	48th	1997	Knoxville, TN
11th	1960	Tallahassee, FL	49th	1998	Prescott, AZ
12th	1961	Knoxville, TN	50th	1999	Roanoke, VA
13th	1962	Phoenix, AX	51st	2000	Seattle, WA
14th	1963	College Station, TX	52nd	2001	Cumberland, MD
15th	1964	Rolla, MO	53rd	2002	San Luis Obispo, CA
16th	1965	Lexington, KY	54th	2003	Burlington, VT
17th	1966	Ames, IA	55th	2004	Kansas City, MO
18th	1967	Lafayette, IN	56th	2005	Wilmington, DE
19th	1968	Morgantown, WV	57th	2006	Breckinridge, CO

20th	1969	Urbana, IL	58th	2007	Pocono Manor, PA
21st	1970	Lawrence, KS	59th	2008	Santa Fe, NM
22nd	1971	Norman, OK	60th	2009	Buffalo, NY
23rd	1972	Old Point Comfort, VA	61st	2010	Oklahoma City, OK
24th	1973	Sheridan, Wy	62nd	2011	Lexington, KY
25th	1974	Raleigh, NC	63rd	2012	Redding, CA
26th	1975	Coeur d'Alene, ID	64th	2013	North Conway, NH
27th	1976	Orlando, FL	65th	2014	Laramie, WY
28th	1977	Rapid City, SD	66th	2015	Sturbridge, MA
29th	1978	Annapolis, MD	67th	2016	Colorado Springs, CO
30th	1979	Portland, OR	68th	2017	Marietta, GA
31st	1980	Austin, TX	69th	2018	Portland, ME
32nd	1981	Gatlinburg, TN	70th	2019	Portland, OR
33rd	1982	Vail, Co	71st	2022	Asheville, NC
34th	1983	Stone Mountain, GA	72nd	2023	Tacoma, WA
35th	1984	San Jose, CA	73rd	2024	Lawrence, KS
36th	1985	Clarksville, TN	74th	2025	Morgantown, WV
37th	1986	Helena, MT	75th	2026	Reno, NV
38th	1987	Pittsburgh, PA			

Symposium Format

The symposia are scheduled for three days, with two days of technical papers and a full day for the field trip. The Symposium is often preceded with a special session and/or workshops and opens with evening Ice-Breaker, followed by two days of technical presentations and a full day field trip.

Highway Geology Symposium Field Trip

The field trip is the focus of the meeting. In most cases, the trips cover approximately 150 to 200 miles, with stops visiting geological, geotechnical, and cultural points of interests in the host state or nearby.

Some highlights of past Symposium field trips: In Wyoming (1973), the group viewed landslides in the Big Horn Mountains; Florida's trip (1976) included a tour of Cape Canaveral and the NASA space installation; the Idaho and South Dakota trips dealt principally with mining activities; North Carolina provided stops at a quarry site, a dam construction site, and a nuclear generation site; in Maryland (1978), the group visited the Chesapeake Bay hydraulic model and the Goddard Space Center. The Oregon trip included visits to the Columbia River Gorge and Mount Hood; the Central mine region was visited in Texas.

The Tennessee meeting in 1981 provided stops at several repaired landslide in Appalachia

regions of East Tennessee. In Utah (1988) the field trip visited sites in Provo Canyon and stopped at the famous Thistle Landslide. In New Mexico (1990), the emphasis was on rockfall treatments in the Rio Grande River canyon and included a stop at the Brugg Wire Rope headquarters in Santa Fe. Mount St, Helens was visited by the field trip in 1994 when the meeting was in Portland, Oregon.

1995 the West Virginia meeting took us to the New River Gorge Bridge that has a deck elevation of 876 feet above the water, and at the time, was the longest single arch span in the world. In Cody Wyoming, the 1996 field trip visited the Chief Joseph Scenic Highway and the Beartooth Uplift in northwest Wyoming. In 1997 the meeting in Tennessee visited the newly constructed future I-26 highway in the Blue Ridge of East Tennessee.

New River Gorge Bridge

The Arizona meeting in 1998 visited the Oak Creek Canyon near Sedona and a mining ghost town at Jerome, Arizona. The Virginia meeting in 1999 visited the "Smart Road"Project that was under construction. This was a joint research project of the Virginia Department of Transportation and Virginia Tech University. The Seattle Washington meeting in 2000 visited an ancient lahar in the Mount Rainier area. A highlight of the Maryland symposium in 2001 was visiting the Sideling Hill road cut for I-68, which beautifully exposes a tightly folded syncline, common in the Valley and Ridge physiographic province of the Appalachians. The California field trip in 2002 provided a field demonstration of the effectiveness of rock netting against rock falls along the Pacific Coast Highway. The Kansas City meeting in 2004 visited the Hunt Subtropolis which is said to be the "world's largest underground business complex". It was created through the mining of limestone by way of the room and pillar method. The Rocky Point Quarry provided an opportunity to search for fossils at the North Carolina meeting in 2005. The group also visited the US-17 Wilmington Bypass Bridge which was under construction. Among the stops at the Pennsylvania meeting were the Hickory Run Boulder Field, the No.9 Mine and Wash Shanty Museum, and the Lehigh Tunnel. The New Mexico field trip in 2008 included stops at a soil nailed wall along US-285/84 north of Santa Fe and a road cut through the Bandelier Tuff on highway 502 near Los Alamos where rockfall mesh was used to protect against rockfalls. The New York field trip in 2009 included the Niagara Falls Gorge

and the Devil's Hole Trail.

In Oklahoma (2010) the trip saw the complex geology of the Arbuckle Mountains in the southern part of the state along with stops at Tucker's Tower and Turner Falls. In the bluegrass state of Kentucky (2011) the trip included stops at Camp Nelson, the site of the oldest exposed rocks in Kentucky, near the Lexington and Kentucky River Fault Zones.

Sidling Hill Syncline

Additional stops at the Darby Dan Farm and the Woodford Reserve Distillery illustrated how the local geology has played such a large part in the success of breeding prized thoroughbred horses and made Kentucky the "Birthplace of Bourbon". In Redding, California, the 2012 field trip included stops at the Whiskeytown Lake, which is one in a series of lakes that provide water and power to northern California. Additional stops included Rocky Point, a roadway construction site containing Naturally Occurring Asbestos (NOA), and Oregon Mountain where the geology and high rainfall amounts have caused Hwy 299 to experience local and global instabilities since first constructed in 1920.

The 2013 field trip in New Hampshire highlighted the topography and geologic remnants left by the Pleistocene glaciation that fully retreated approximately 12,000 years ago. The field trip included stops at various overlooks of glacially carved valleys and ranges; the Old Man of the Mountain Memorial Plaza, which is a tribute to the famous cantilevered rock mass in the Franconia Notch that collapsed on May 3, 2003; the lacustrine deposits and features of the Glacial Lake Ammonoosuc; views of the Presidential Range; bridges damaged during Tropical Storm Irene in August 2011; and the Willey Slide, located in the Crawford Notch where all members of the Willey family were buried by a landslide in 1826. The 2014 (Wyoming) field trip presented a breathtaking tour of the geology and history of southeast Wyoming, ascending from the high plains surrounding Laramie at 7000 feet to the Medicine Bow Mountains along the Snowy Range Scenic Byway. Visible along the way were a Precambrian shear zone, and glacial deposits and features. From the glacially carved Mirror Lake and the Snowy Range Ski Area, the path wound east to the Laramie Mountains and the Vedauwoo Recreational Area, a popular rock climbing and hiking area. The 2015 field trip in Sturbridge, Massachusetts, focused on the Connecticut Valley, a Mesozoic rift basin that signaled the breakup of Pangea, and the Berkshires, which represents the collision and amalgamation of an island arc system with the North American Laurentian margin.

The field trip in Colorado (2016) was an urban setting along the western edge of Colorado Springs and around Manitou Springs. Stops included the Pikeview Quarry, Garden of the Gods Visitor Center, and several other locations where rockfall and debris flow mitigation, post-flooding highway embankment repair, and a nonconformity in the rock records that spans 1.3 billion years were observed.

Garden of the Gods

Penobscot Narrows Bridge

The Georgia (2017) field trip provided an opportunity to view the geology of northern Georgia. Stops included the Bellwood Quarry, which, at one time was run by the City of Atlanta and served as a prison labor camp. Upon completion of a tunnel to connect the quarry to two water treatment plants and three pump stations, It will serve as a 2.4 billion-gallon water storage facility for the City of Atlanta. Additional stops included the Buzzi Unicem Cement Plant to get a close up view of the Clairmont Melange, The Cooper Furnace near the Allatoona Dam, and the New Riverside Ochre-Emerson Barite mine.

The 2018 field trip of the Portland, Maine Symposium presented a good overview of the geology of coastal Maine. Field trip stops included the Sherman Salt Marsh near Newcastle which was recently restored to its natural state after the dam that carried US Highway 1 washed out during a 2005 storm, the site of the 1996 landslide near Rockland Harbor that consumed several homes, and the rock slope remediation project at the Penobscot Narrows Bridge near Prospect Maine. A lobster lunch along the shore of Penobscot Bay was one of several highlights of the field trip.

The 2019 field trip in Portland, Oregon travelled the Columbia River Gorge west. Starting at the Crown Point Vista House and Portland Women's Forum State Scenic Viewpoint above the gorge to learn about the river highway. Descending into the gorge, we stopped at scenic Multnomah Falls and Benson Bridge, and saw flexible rockfall fence installed to protect the lodge and historic Columbia River Highway. Other stops included lunch at Cascade Locks, Bonneville Landslide and rockfall areas along the highway. There was no symposium in 2020 and 2021 due to Covid-19 restrictions.

In 2022, we got back together again in Asheville, North Carolina. The field trip took us through Ordovician (500 my) to Precambrian (1.2 by) migmatized ortho and paragneisses, metamorphosed intrusives, thrust faults and contacts representing three orogenies and

complex sequences of basement and terranes. We crossed the Brevard Fault zone several times, which is a structure that has been studied and interpreted for 100 years. Various attempts to define the structure have been made, especially in the pre-plate tectonic era. It has been theorized that these structures were as high, or higher than the Rockies at formation. 200 million years of rifted erosion leave us with an exposed look at deep orogenic roots of multiple thrust events. Precipitation in the areas is between 60-100” per year. There are deep ancient colluvial deposits, complex mineralization and weathering profiles, and non- linear/planar discontinuities. We traveled over I-26 and the Blue Ridge Escarpment where the highway is being widened. Stops included the I-26 Old Howard Gap Slide Area, the US 74 Gerton Slide, a shallow landslide barrier on I-40 W, and the Buckner Gap Cut.

The 2023 Field trip in Tacoma, Washington traveled to Mt Rainer where HGS goers were able to take various hikes around the park. Additional highlights included driving down into the Ohop Valley outwash channel, a drive by of Alder Lake, a drive along Copper Creek Forest Road 59, a view of Nisqually Glacier from Nisqually River and a final stop at Ricksecker Point.

The Lawrence Kansas (2024) symposium field trip took us to the Tallgrass Prairie National Preserve, lunch on the Dakota Formation sandstone bluff at Coronado Heights, and saw the unique differential weathering of the Dakota Formation at Mushroom Rock State Park.

Mushroom Rock State Park

The 74th HGS field trip took us into the mountains of West Virginia. Morning stops showcased the complex folding and geology of the Valley and Ridge physiographic province along recently a recently completed section of US-48 (Appalachian Highway System Corridor H). We then head down the South Branch of the Potomac River to Seneca Rocks, a 1000’ vertical outcrop of Silurian Tuscarora sandstone. After lunch at Blackwater Falls State Park, we accessed a new and yet unopened section of corridor H, with a stop looking at the Cheat River bridge consisting of 9 spans, one of which will be longest steel plate girder span in the U.S. The last stop examined the challenges of highway construction through massive (and moving) slump blocks of the Devonian Foreknobs Formation.

Seneca Rocks

HGS National Steering Committee
Officers

Bill Webster, Chairman

Bill Webster – (CHAIR) CalTrans (Retired)
7645 Woodborough Drive Granite Bay, CA
95746 Phone: 916-257-1146
Email: mtnbiker@wavecable.com

Kyle Halverson, Vice-Chairman

Kansas DOT
Bureau of Structures and Geotechnical Svc.
700 SW Harrison Street
Topeka, KS 66603
785-291-3860
Kyle.halverson@ks.gov

Marc Fish, Secretary

WSDOT Geotechnical Office
1655 S. 2nd Ave.
Tumwater, WA 98512
360-709-5898
fishm@wsdot.wa.gov

John Pilipchuk, Treasurer

NCDOT Geotech Engineering Unit (Retired)
1512 US Highway 70 East
Hillsborough, NC 27278
919-622-3381
johnpilipchuk@yahoo.com

HGS National Steering Committee Members

Ken Ashton
West Virginia Geological Survey
1 Mont Chateau Road
Morgantown, WV 26508
304-594-2331
ashton@wvgs.wvnet.edu

Vanessa Bateman
Geotechnical, Geology, & Materials CoP Leader
Eng. & Construction HQ
U.S. Army Corp of Engineers 202-761-7423
Vanessa.c.bateman@usace.army.mil

Simon Boone
Geostabilization International
10225 Westmoor Drive
Westminster, CO 80021

540 420-2678
simon@alcinc.com

James Dahill
Wyoming DOT
5300 Bishop Boulevard
Cheyenne, WY 82009
307-777-4205
james.dahill@wyo.gov

Bob Henthorne
PEC
400 S. Kansas Ave. Topeka, KS 66603
785-233-8300
Bob.henthorne@pec1.om

Jody Kuhne
NCDOT (Retired)
778 Flint Street
Asheville, NC 28801
828-779-9482
jodykuhne@gmail.com

Sarah McInnes
PA DOT
Engineering
District 6-0
7000 Geerdes Blvd.
King of Prussia, PA
19406 610-205-6544
smcinnes@pa.gov

Krystle Pelham
New Hampshire DOT
Bureau of Materials and Research
P. O. Box 483
5 Hazen Drive
Concord, NH 03302-0483
603-271-1657
Krystle.j.pelham@dot.state.nh.us

Victoria Porto
PA DOT (Retired)
10 Oine Lake
Drive Carlisle, PA
17015

717-805-5941
vamporto@aol.com

Eric Rorem
Ameritech Slope Constructors
21 Overland Industrial Blvd. Asheville, NC 28806
505 690-7144
erorem@ameritech.pro

Christopher Ruppen
Geostabilization International
3808 Sunflower Road
New Brighton, PA
15066 727-272-7532
Christopher.ruppen@gsi.us

Tim Shevlin
Geobrugg North America LLC
Salem, OR 97302

503-423-7258
Tim.shevlin.@geobrugg.com

Jay Smerekanicz
Scarptec, Inc.
P. O. Box 326
Monument Beach, MA
02553 603-493-6274
jay@scarptec.com

Deana Sneyd
Petrologic Solutions, Inc.
3997 Oak Hill Road
Douglasville, GA 30135
678-313-4147
dsneyd@gmail.com

John Szturo
HNTB
Corporation 715
Kirk Drive
Kansas City, MO
64105 816-525-2275
jszturo@hntb.com

Cheryl Youngblood
NC Dept. of Transportation
1020 Birch Ridge Drive
Raleigh, NC 27610
919-707-6873
cyoungblood@ncdot.gov

Past, Present, and Future Symposium Contact List

2017	Georgia	Deana Sneyd	678-313--4147	dsneyd@gmail.com
2018	Maine	Krystle Pelham	603-271-1657	krystle.j.pelham@dot.state.nh.us
2019	Oregon	Tim Shevlin	503-423-7258	tim.shevlin@geobrugg.com
2022	North Carolina	John Pilipchuk	919-622-3381	johnpilipchuk@yahoo.com
		Jody Kuhne	828-779-9482	jodykuhne@gmail.com
2023	Washington	Marc Fish	360-709-5898	fishm@wsdot.wa.gov
2024	Kansas	Kyle Halverson	785-600-8165	Kyle.halverson@ks.dot
2025	West Virginia	Ken Ashton	304-594-2331	ashton@wvgs.wvnet.edu
2026	Nevada	Gary Norris	775-331-5582	norris@unr.edu
		Sherif Elfass	775-784-6664	elfass@unr.edu
2027	Pennsylvania	Sarah Mclnnes	724-272-7532	smcinnes@pa.gov
		Chris Ruppen	724-272-7532	christopher.ruppen@gsi.us

Emeritus Members of the Steering Committee

A number of past members of the national steering committee have been granted Emeritus status. These individuals, usually retired, resigned from the HGS Steering Committee, or are deceased, have made significant contributions to the Highway Geology Symposium. A total of 46 people have been granted Emeritus status by the Steering Committee.

R.F. Baker
John Baldwin
David Bingham
Vernon Bump
Virgil E. Burgat
Robert G. Charboneau
Hugh Chase
Jim Coffin
Dick Cross
Jeff Dean
A.C. Dodson
John Duffy
Walter F. Fredricksen
Brandy Gilmore
Russell Glass
Robert Goddard
Joseph Gutierrez
Mike Hager
Rich Humphries
Peter Ingraham
Charles T. Janik
Richard Lane
John Lemish
Bill Lovell
Henry Mathis
William McCasland
George S. Meadors, Jr.
David Mitchell
Harry Moore
W.T. Parrot
Paul H. Price
Nicholas Priznar
David L. Royster
Bill Sherman
Willard L. Sitz
Mitchell Smith
Jim Stroud
Steve Sweeney
Sam Thornton
Berke Thompson
Mike Vierling
Burrell Whitlow
W.A. “Bill” Wisner
Earl Wright
Ed J. Zeigler

Medallion Award

The Medallion Award was instituted in 1969 to recognize individuals who have made significant contributions to the Highway Geology Symposium over many years. The award is a 3.5” medallion mounted on a walnut shield and appropriately inscribed. The Medallion Award is presented during the banquet at the annual symposium.

Medallion Award recipient	Year		Medallion Award recipient	Year
Hugh Chase	1970		Russell Glass	1998
Tom Parrott	1970		Harry Ludowise	2000
Paul Price	1970		Bob Henthorne	2004
K. B. Woods	1970		Michael Hagar	2005
R. J. Edmonson	1972		Joseph A. Fischer	2007
C. S. Mullin	1974		Ken Ashton	2008
A. C. Dodson	1975		David Martin	2008
Burrell Whitlow	1978		Richard Cross	2009
Bill Sherman	1980		Mike Vierling	2009
Virgil Burgat	1981		John Szturo	2009
Henry Mathis	1982		Jeff Dean	2012
David Royster	1982		Chris Ruppen	2012
Terry West	1983		Eric Rorem	2014
Dave Bingham	1984		John Pilipchuk	2015
Vernon Bump	1986		Pete Ingraham	2016
C. W. “Bill” Lovell	1989		Richard Lane	2017
Joseph A. Gutierrez	1990		Steve Sweeney	2018
Willard McCasland	1990		John Duffy	2018
W. A. “Bill” Wisner	1991		Krystle Pelham	2018
David Mitchell	1993		Vanessa Bateman	2019
Harry Moore	1996		Marc Fish	2023
Earl Wright	1997		Victoria Porto	2025

Young Author Award

The Highway Geology Symposium has always encouraged participation of young professionals knowing that they are the future of the organization. To recognize and promote participation of young professionals, an annual National Young Author Competition was established in 2014. To qualify, participants may be up to 35 years old or younger, must be the principal author, and the sole presenter of the paper at the Symposium. Papers are reviewed and judged based on technical presentation of the paper (including geology), Originality of the Work, Applicability of the Work to Others and Paper Layout. One recipient is selected each year to receive the coveted Young Author Award, consisting of a plaque and cash prize to be presented at the annual Symposium banquet.

Young Author Award winners:

2014 - **Simon Boone**, "Performance of Flexible Debris Flow Barriers in a Narrow Canyon"

2015 - **Cory Rinehart**, "High Quality H20: Utilizing Horizontal Drains for Landslide Stabilization"

2016 - **Todd Hansen**, "Geologic Exploration for Ground Classification: Widening of the I-70 Veterans Memorial Tunnels"

2017 - **James Arthurs**, "Construction of Transportation Infrastructure in Weathered Volcanic Ash Soils"

2018 - **Brian Felber**, "Geotechnical Challenges for Bridge Foundations & Roadway Embankment Design in Peats and Deep Glacial Lake Deposits"

2019 - **Anya Brose**, "The Assessment and Remediation of Wabasha St. Rock Fall"

2022 - **Christopher Mayer** "Using Geophysics to Evaluate the Results of a Grouting Program in Karstic Geology

2023 - **Cody Chaussee**, "Bolt Creek Fire: Post-Wildfire Debris Flow Risk Assessment and Barrier Design on US 2, Near Grotto, WA

2024 - **Katelyn Card**, "Post Wildfire Effects on Geotechnical Assets".

2025- **Christina Comuso**, "Rockfall Mitigation and Slope Stability Solutions for Interstate 78 in Bethlehem, New Jersey"

75th Highway Geology Symposium Field Trip

October 1, 2026

Departing the Whitney Peak Hotel at the Reno Arch at 7:30 AM, and returning at 6:00 PM, The 75th HGS Field Trip will be an all-day extravaganza covering globally notable interactions between key highways and both the urban and rural geological environments. In HGS tradition, the buses will be fully provisioned thanks to generous sponsors, and we will enjoy a lunch at an exclusive country club. Among the features we will view, with history and descriptions by local experts:

- An Interstate viaduct over an operating casino
- A fuel tank farm in active cleanup
- A gravel pit filled by a flood 30 years ago that is now a public beach and marina
- An urban basin with soft sediments amplifying and extending earthquake shaking
- The world's longest concrete cathedral arch bridge span
- A huge landslide that ripped across a highway in 1983
- The western margin of the expanding Basin and Range
- The interplay between Pluvial lakes and <1 Ma volcanics
- An inverted water-supply siphon built in 1873 with a drop of 1,870 ft
- Granite bodies on the footwall and on the hanging wall of normal faults
- One of the world's top 10 most spectacular earthquake fault scarps
- North America's largest, 2nd deepest, and most blue alpine lake, Tahoe
- Sources and deposits of titanic Pluvial jökulhlaups
- A lakeside bike trail constructed with zero sediment input to the lake
- An alluvial fan cut by dozens of fault traces
- An Interstate bridge built directly over a 100 MW geothermal field

Photographer: Kyle House

Photographer: Josiah Hassler

Photographer: Terri Garside

SPONSORS

The 2026 Highway Geology Symposium extends a huge "Thank You" to the sponsors for their contributions.
The Symposium wouldn't be possible without their generous support!

PLATINUM LEVEL SPONSORS

Geobrugg

Tim Shevlin
Email: tim.shevlin@geobrugg.com
Phone: 503-423-7258
www.geobrugg.com

Field Trip Lunch- Thursday

BRUGG Geobrugg
Safety is our nature

True to this guiding principle, we have been developing and manufacturing protection solutions since 1951. High-tensile steel wire nets and matching services monitor and protect against natural hazards such as rockfall, landslides, debris flows, avalanches or coastal erosion. They ensure safety in mining and tunneling as well as on motor sports tracks, in industry and in test facilities. With experience, a spirit of research, continuous internal training and close cooperation with research institutes, we drive innovation and industry standards.

GeoStabilization International

Rachel Jackson
Email: rachel.jackson@gsi.us
Phone: 855-687-4157
www.geostabilization.com

Wednesday Banquet and Awards

GSI GeoStabilization International®

GeoStabilization International is a geohazard mitigation firm operating throughout the USA and Canada. We specialize in emergency landslide repairs, rockfall mitigation, and grouting using design/build and design/build/warranty contracting.

Maccaferri, Inc.

Mike Koutsourais
Email: m.koutsourais@maccaferri.com
Phone: 301-641-8072
www.maccaferri.com/us

Field Trip Transportation - Thursday

MACCAFERRI

Established in 1879, Maccaferri operates in more than 130 companies worldwide and has become a global technical reference in the research, design and implementation of innovative

solutions within civil, geotechnical and environmental engineering. The company operates within numerous market sectors including infrastructure, mining, river control and environmental protection. In addition to geohazard mitigations, solutions offered to these markets include soil reinforcement, hydraulic works, ground stabilization, retaining structures and erosion protection. Maccaferri does not simply supply products but works in partnership with clients, offering technical expertise to deliver versatile, cost-effective and environmentally friendly solutions.

SILVER LEVEL SPONSORS

Ameritech Slope Constructors

Field Trip Snacks -Thursday

Erik Rorem
Email: erorem@ameritech.pro
Phone: 505-690-7144
www.ameritech.pro

Ameritech Slope Constructors, Inc. is a geohazard mitigation contractor providing rockfall and debris flow mitigation, anchor drilling and mesh installation, shotcrete application, and related rope access services for stabilizing soil and rock slopes. Safely, correctly, and on time. Your geohazard specialists.

BGC Engineering

Melissa Murray
Email: marcom@bgcengineering.ca
Phone: 604-684-5900
www.bgcengineering.com

BGC Engineering is a globally recognized consulting firm specializing in geotechnical, environmental, and applied earth sciences. Established in 1990, BGC delivers innovative and sustainable solutions for complex engineering and environmental challenges worldwide. Our dedicated team of over 900 professionals—engineers, geoscientists, technicians, software professionals and corporate support staff—provides comprehensive investigation, design, and construction review services across more than 20 offices in North and South America, Australia, Europe, and the Caribbean. We combine technical excellence with a deep understanding of our clients' needs to provide tailored solutions across various industries including mining, pipelines, transportation, energy, and community sectors. BGC operates as one team with a focus on connection between our people, sectors, disciplines, and offices across the globe to provide clients with innovative, common-sense solutions partnered with exceptional service.

BoreDM

Louis Aaron
Email: louis@boredm.com
Phone: 773-609-3854
www.boredm.com

BoreDM is the modern geotechnical and geoenvironmental data management platform. Manage borehole logs, lab data, and subsurface reports.

DOWL

Tuesday AM Break

Keri Nutter
Email: knutter@dowl.com
Phone: 907-562-2000
www.dowl.com

DOWL is a multidisciplinary consulting firm with more than 60 years of experience delivering civil engineering and related services throughout the western United States. With offices in Alaska, Arizona, Montana, Nevada, Oregon, Washington, and Wyoming, DOWL provides comprehensive in-house expertise in public involvement, planning and permitting, geoscience, environmental services, civil and structural engineering, landscape architecture, surveying, hydrology, GIS, transportation and airfield engineering, construction administration, and inspection services. A cornerstone of DOWL's capabilities is its geotechnical and geoscience expertise, supported by a dedicated team of geotechnical professionals and technical staff. DOWL's geotechnical engineers and geologists deliver a thorough understanding of subsurface conditions, including geohazards, soil, rock, and groundwater, providing the foundation for safe, reliable, and cost-effective project delivery. Their experience spans a wide range of infrastructure projects, including roads, bridges, utilities, dams, rockfall mitigation, and construction inspection services in both remote and urban environments. Backed by advanced training, local knowledge, strong client relationships, and proven project delivery experience, DOWL provides high-quality geotechnical evaluations, materials testing, and engineering solutions that help clients successfully address complex project challenges.

Fragmentation Efficiency Services, Inc. /KESCO, Inc.

Wednesday PM Break

Daniel Conn
Email: dconn@kesco-fes.com
Phone: 724-548-2811
www.fesconsult.com

Designing precise, innovative, and safe explosive engineering solutions that address complex geological environments.

GFT

Tuesday PM Break

Amy Meadows
Email: ameadows@gftinc.om
Phone: 717-886-5367
www.gftinc.com

GFT is a recognized leader in geotechnical and geological engineering. We provide consultation for dams, deep foundations, ground improvement, geohazard mitigation, and risk management, offering innovative solutions to safeguard infrastructure and communities. Our team of geoprofessionals specializes in landslide stabilization, rockfall mitigation, debris flow management, and seismic hazard evaluation. Using cutting-edge technology, including LiDAR, remote sensing, and predictive modeling, we assess and address complex geotechnical challenges for transportation, water, energy, and public sector clients. With decades of experience, we develop customized, cost-effective strategies to enhance resilience and protect critical assets from natural hazards, ensuring safety, sustainability, and long-term performance in diverse and challenging environments.

Hager-Richter Geoscience, Inc.

Wednesday AM Break

Jeff Reid
Email: jeff.reid@hager-richter.com
Phone: 603-893-9944
www.hager-richter.com

HAGER-RICHTER GEOSCIENCE, INC. (HRGS) is an established small business that specializes in surface and borehole geophysics services for engineering and environmental applications. The firm has been in business since 1984, has grown to be one of the largest full service geophysical specialty firms in the eastern United States, and has earned a national reputation for quality geophysical services. HRGS has fully staffed and equipped offices in Derry, New Hampshire and Fords, New Jersey, and satellite offices in Nashville, Tennessee and Ashland, Oregon allowing rapid response to projects anywhere in the United States.

Lumos & Associates

Emma Condon
Email: econdon@lumosinc.com
Phone: 775-827-6111
www.lumosinc.com

Founded in 1978, Lumos & Associates is a multidisciplinary engineering and consulting firm headquartered in Reno, Nevada. They provide comprehensive civil and structural engineering, surveying and mapping, geotechnical services, and construction management to communities across the Western United States.

TabLogs
David Adcock
Email: david@tablogs.com.au
Phone: 0402 333 783
www.tablogs.com

TabLogs makes geotechnical investigations simple. As a company founded by a geotechnical engineer, we understand the pain points of the people on the ground. We also understand what is needed to ensure client satisfaction, meaning we're always open to making enhancements to our software. It's our dedication and willingness to listen to our users that has helped us become one of the most trusted tools used by geotechs, drillers, environmental consultants and more - right across the globe.

CONTRIBUTING SPONSORS

Scarptec, Inc.
Peter Ingraham
Email: peter@scarptec.com
www.scarptec.com

Field Trip Beverages - Thursday

Voss Signs
Tom Tenerovicz
Email: tom@vosssigns.com
Phone: 315-682-6418
www.vosssigns.com

Since 1965, Voss Signs, LLC has produced custom and stock signs for various customers that include: Forestry Professionals, Land Owners, State and Federal Government Agencies.

EXHIBITORS

Central Mine Equipment Company
Bill White
Email: whiteb@cmeco.com
Phone: 800-325-8827
www.cmeco.com

CME manufactures auger, core and rotary drilling rigs mounted on trucks, skids, tracks, and rubber-tire all-terrain carriers. We also manufacture hollow stem augers, conventional flight augers, sampling and drilling tools to support our machines.

Delve Underground

Amãna Bowman
Email: abowman@delveunderground.com
Phone: 925-300-5774
www.delveunderground.com

Delve Underground is a leader in heavy civil engineering, serving the transportation, water, wastewater, and energy industries. Specializing in tunnel design, we provide innovative solutions to the most challenging underground problems. We offer comprehensive design, construction management, and dispute resolution capabilities. Our expertise includes civil, structural, and geotechnical engineering. Founded in 1954, as Jacobs Associates, Delve Underground is an employee-owned firm with 25 offices and 350 team members throughout the United States, Canada, Australia, and New Zealand.

The Delve Underground Geohazards Group includes a team of highly skilled engineering geologists and geotechnical engineers that specialize in the characterization and mitigation of a wide variety or geological hazards. Our teams of geoprofessionals are well versed in evaluating complex hazards impacting civil facilities including highways, pipelines, hydropower facilities, dams, and civil structures.

Geotechnical & Environmental Services

Kylara Jane Miller
Email: clientrelations@ges-west.com
Phone: 775-622-3844
www.ges-west.com

GES is a multi-disciplined firm providing geotechnical engineering, materials testing and inspection, and environmental consulting services. GES has succeeded for 34 years in building a strong reputation for providing personalized high-end services to our clients which include governmental (federal, state, and local), private sectors, commercial developers, contractors, architects, and civil engineers.

Gilson Company Inc.

Abbi Smith
Email: asmith@gilsonco.com
Phone: 740-548-7298
www.globalgilson.com

For over 85 years, Gilson has been committed to providing safe, rugged, efficient materials testing equipment that delivers accurate and reliable results. We offer one of the largest selections of equipment for concrete, asphalt, aggregates, and soils in addition to our core products. We regularly update and expand our inventory to meet customer needs and industry demands, and we continue to establish ourselves as a worldwide authority and trusted source for quality equipment.

Harrison Western Construction

Robert Group
Email: rgroup@harwest.com
Phone: 720-990-7377
www.harrisonwestern.com

Harrison Western is an American-owned and operated civil, geotechnical, and tunneling contractor in operation since 1968. Our work takes us from coast to coast and encompasses all phases of geo-construction, including earth retention, micropiles, slope stabilization, rockfall mitigation, retaining wall construction, drill/blast, and specialty grouting.

Our PMs, engineers, and teams of jobsite managers are all well-versed in the scopes we offer, bringing extensive experience, knowledge, skill and professionalism to each engagement. We work closely with owners, designers and engineers to deliver quality outcomes and value-engineer the best possible solution for each project.

Jean Lutz North America

Michel Lariau
Email: contact@jeanlutzna.com
Phone: 330-702-1476
www.jeanlutzna.com

Manufacturer of advanced instrumentation applied to foundations and Geotechnical Construction.

KANE GeoTech, Inc.

Holly Butler
Email: holly.butler@kanegeotech.com
Phone: 209-472-1822
www.kanegeotech.com

America's Leader in Geohazard Engineering - KANE GeoTech, Inc specializes in difficult civil and geotechnical engineering problems. Our services include rockfall, debris flow and shallow landslide mitigation, as well as geotechnical instrumentation, and geotechnical analysis and design. We build partnerships with our clients and affiliates, taking time to learn project needs and how we can deliver the best solutions, most effective products and fastest service.

Keller

Lila Scott
Email: lila.scott@keller-na.com
Phone: 410-551-8200
www.keller-na.com

Keller develops innovative, practical, and cost-effective solutions for geotechnical challenges across the entire construction industry, including deep foundations, environmental

remediation, ground improvement, groundwater control and dewatering, liquefaction mitigation, releveling structures, slope stabilization, support of excavation, underpinning, and instrumentation and monitoring. Keller is the largest geotechnical specialty contractor in the world with over 65 offices throughout the US and Canada.

MetaField

Mara Zimmerman
Email: mzimmerman@agileframeworks.com
Phone: 651-767-2799
www.metafield.com

MetaField is industry-leading, modern software that automates field, lab, and reporting workflows for geotechnical engineering, construction materials testing, and inspection firms of all sizes. It replaces manual processes and disconnected systems with a single platform, enabling teams to capture data once and use it across every stage of work—improving accuracy, speed, and visibility. Built for the complexity of real-world operations, MetaField is trusted by 175+ firms across North America to streamline workflows and deliver consistent results. Learn more at https://www.metafield.com/.

Mobile Drill International

Charles Orzeske
Email: charlie.orzeske@mobiledrill.net
Phone: 317-787-6371
www.mobiledrill.net

Mobile Drill International has been a trusted name in the drilling industry for over seven decades. We specialize in manufacturing and refurbishing high-performance drill rigs and tooling for geotechnical, environmental, water well, and mineral exploration applications. Our commitment to quality, innovation, and customer success sets us apart.

NewFields

Jesse Ruzicka
Email: jruzicka@newfields.com
Phone: 775-741-0755
www.newfields.com

NewFields provides geotechnical engineering services in support of transportation related improvements, such as bridge foundations, cut and fill slope design, and retaining wall design. NewFields services the mining industry with environmental permitting as well as engineering design and technical services.

RE-MONITOR INC

Tony Simmonds
Email: t.simmonds@re-monitor.com
Phone: 472-244-8575

www.re-monitor.com

RE-MONITOR, established in the United States as a subsidiary of NHAZCA S.r.l., brings state-of-the-art monitoring solutions to the North American market. Our core mission is to transform remote sensing practices by integrating advanced technologies, including Satellite and Terrestrial InSAR, and our proprietary Photo monitoring system, to address the growing need for reliable, scalable, and effective monitoring.

SIMCO Drilling Equipment

Ryan Gross
Email: Rgross@simcodrill.com
Phone: 800-338-9925
www.simcodrill.com

Drill Rig Manufacturer

Terēan, Inc.

John Louie
Email: jlouie@terean.com
Phone: 775-674-9525
www.terean.com

Terēan provides subsurface investigation solutions to the engineering, construction, mining, water resources, and security industries, and for research. Terēan AI-powered technologies are used around the world to image subsurface activities, soil, and rock at depths from 10 feet to 25 miles.

Trumer Schutzbauten Americas

Ahren Bichler
Email: a.bichler@trumer.cc
Phone: 604-732-0325
www.trumer.us

Trumer is your competent partner for design and manufacturing of geohazard mitigation systems involving unstable slopes, rockfall, debris flows and avalanches. They have been bringing an Austrian approach of high quality, robust solutions to the industry for more than 30 years. More recently, Trumer is producing American-Made, high-tensile steel netting for your anchored mesh and drape mesh applications.

Williams Form Engineering Corp.

Ryan Williams
Email: ryan@williamsform.com
Phone: 616-866-0815
www.williamsform.com

Williams Form Engineering Corporation, a family owned American company, was started in the garage of our founder Mr. Cl Williams in 1922. WFEC has evolved over the decades, becoming the most trusted name in the geotechnical support industry.

Along with our original product line of Concrete Form Hardware, our Rock, Soil and Concrete Anchors, Micropiles, Post Tensioning and Wind Turbine Foundation Systems featuring our fully threaded steel bars are the trusted industry standard. Excellent customer service and extensive technical know-how are what you can expect from our next 100 years!

Highway Geology Symposium 2026, Mini-Sessions

Reno, NV - September 28

Location: Auditorium, Earthquake Engineering Laboratory, University of Nevada, Reno. Transportation is provided to and from the hotel before, between, and after sessions. Continental breakfast and breakout coffee service will be provided, generously sponsored by Terēan.

Program	Time
Transportation from the hotel	9:30 am
Continental breakfast	9:45 am
Session 1 — Terēan Shear-Wave Surveying	10:00 – 11:30 am
Lunch (not provided)	11:30 am – 1:00 pm
Transportation from the hotel	12:30 pm
Session 2 — Slope Stabilization Based on Soil-Pile Interaction	1:00 – 2:30 pm
Transportation from the hotel	2:30 pm
Break	2:30 – 3:00 pm
Session 3 — Advancing Infrastructure Resilience Through Research and Testing	3:00 – 4:30 pm
Transportation to the hotel	4:45 pm

Session 1: Terēan Shear-Wave Surveying

Prof. John Louie & Alison Starr • 40 min classroom demo + 45 min outdoor demo

Terēan® ReMi solutions help engineers and geologists measure ASCE 7-22 Site Class, find depth to bedrock, map liquefaction potential, image faults, and locate voids. Terēan's Chief Scientist and Lead Geophysicist will demonstrate VsSurf ReMi® software with client case histories, then move outdoors for a live ēDAQ™ data-acquisition demo determining site class in under 30 minutes.

Session 2: Slope Stabilization Based on Soil-Pile Interaction

Prof. Mohamed Ashour • 45 min seminar + 45 min software demo

An examination of driven piles as a technique for stabilizing active slopes and embankments, covering shallow and deep failure surfaces and the transition between plastic-flow and intermediate soil-pile interaction modes. A hands-on demonstration of Dr. Ashour's design software (developed for WVDOT and ALDOT) follows the seminar; trial copies will be available.

Session 3: Advancing Infrastructure Resilience Through Research and Testing

Prof. Sherif Elfass • 45 min classroom presentation + 45 min facility tour

A look at UNR's earthquake engineering program, from evolving shake-table capabilities to landmark tests on straw bale wall systems, multi-span steel girder bridges, nonstructural systems, accelerated bridge construction, and rocking-column bridges. The session also covers the nation's largest laminar soil box, used to study soil-structure interaction, liquefaction, and lateral spreading under seismic loading.

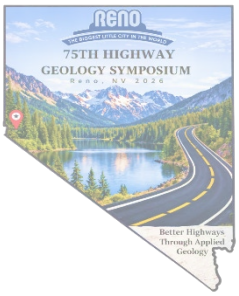

75th Highway Geology Symposium

September 28 – October 1, 2026

Reno, Nevada

TECHNICAL SESSION SCHEDULE

Tuesday, September 29			
8:00-8:10		**Welcome, Opening Remarks & Announcements**	
8:10 - 8:30		**Tracey Larkin Thomason, Director of Nevada DOT**	
8:30 - 9:30		**Why Nevada Geology is So Exciting** - *Jonathan Price, Nevada State Geologist Emeritus*	
9:30-10:00		**BREAK**	
Technical Session 1			Page
1	10:00-10:20 Young Author	**Distributed Monitoring of Rock Slope Performance in Colorado Using Time- Lapse Photography and Vision-Language Models** - *Luke Weidner, BGC Engineering*	57
2	10:20-10:40 Young Author	**Uphill Without a Drill – HVSR as a flexible seismic method for inaccessible sites** - *Mishak Boshoff, Hager-Richter Geoscience*	77
3	10:40-11:00 Young Author	**Mapping What We Can't Touch: LiDAR-Driven Rock Structure Modeling for Safer Highways** - *Will Brandenberger, HDR Engineering, Inc.*	97
4	11:00-11:20 Young Author	**Enhanced Monitoring of High-Risk Unstable Slopes Using Remote Sensing and AI-Assisted Change Detection** - *Katelyn Card, WSDOT*	115
5	11:20-11:40 Young Author	**Bridge or Blast? Sub-title: A Look Into US19W South/ Little Creek Road Design For Repair After Hurricane Helene Damages Under Progressive Design-Build Project Delivery Method** - *Callan Swafford, HDR Engineering, Inc. of the Carolinas*	131
6	11:40-12:00 Young Author	**Integrating UAS Remote Sensing and In-Situ Instrumentation for Landslide Hazard Monitoring to Support Highway Infrastructure Resilience** - *Ashley Butterworth, Idaho State University and BGC Engineering Inc; Donna Delparte, James Mahar, Matthew Belt, Betty Brown, Idaho State University; Shawn Enright, Idaho Transportation Department*	151
12:00-1:00		**LUNCH**	

Technical Session 2			
7	1:00-1:20 Young Author	**Design Considerations for Attenuators and Hybrid Barriers** - *Lucas Martins, Mike Koutsourais & Leticia Genelhu, Maccaferri, Inc*	171
8	1:20-1:40	**Glaciolacustrine Deposits On The SR 3002 Landslide Remediation Project** -*Jason M. Gardner, GFT*	187
9	1:40-2:00	**Emergency Landslide Response and Integrated Field-Design Approaches: US-95 MP 146.5, Idaho** - *Brittany Dayley & Malcolm Perkins, Delve Underground*	205
10	2:00-2:20	**Hidden Elements: A Context Sensitive Application of Rock Anchors for Slope Stabilizaation** - *Brian Collins, Seamus Millett, Cole Christiansen, Scott Anderson, BGC Engineering; Nicholas Farny, Western Federal Lands Highway Division*	223
2:20-2:50		**BREAK**	
Technical Session 3			
11	2:50-3:10	**The Advantages of Hybrid Barriers Over Attenuators** - *Takeshi Arita & Kiyoshi Takmori, Tokyo Rope*	240
12	3:10-3:30	**Take 2 - Rock Fall Mitigation System Replacement At Fairlee, Vermont** - *Jay R. Smerekanicz & David J. Scarpato, Scarptec, Inc; Ethan J. Thomas & Christopher W. Case , Vermont Agency of Transportation*	253
13	3:30-3:50	**Dynamic Performance Monitoring of a Rockfall Attenuator System** - *Darren Beckstrand, Rachel Hunt & Evan Beyer, Landslide Technology*	275
14	3:50-4:10	**Rockfall Wall Catchment Systems in Colorado** - *Ben Arndt, RJ Engineering and Consulting, Inc*	295

Wednesday, September 30			
Concurrent Technical Session 4A			
15	8:00-8:20	**Recent Advances in Rockfall Mitigation Technologies in Japan** - *Yoichi Nishita & Hiroshi Masuya, PROTEC ENGINEERING Co., Ltd.*	311
16	8:20-8:40	**Floyd Hill West Cut: Navigating the Investigation, Design, and Construction of a Major Rock Cut along I-70** - *Todd Schlittenhart & Melissa Boyd, Yeh and Associates, Inc.*	331
17	8:40-9:00	**From Risk Inventory To Real World Failure: Hurricane Helene Validation Of USMP Geohazard Prioritization** - *Jason A. Holland, Schnabel Engineering*	348
18	9:00-9:20	**Comprehensive Load Test Program for Steel H-Piles Driven in Intermediate Geomaterials** - Nafis Masud, Schnabel Engineering; *Kam Ng & Shaun Wulff, University of Wyoming*	361
19	9:20-9:40	**Evaluation of Drag Load and Downdrag on Axially Loaded Piles** - *Mohamed Ashour, Alabama A&M University & Aser Abbas, University of Rhode Island*	381
20	9:40-10:00	**NCDOT Measurement While Drilling (MWD) Implementation and Testing Program** - *Nick Moore, North Carolina DOT*	398

Concurrent Technical Session 4B			
21	8:00-8:20	**Advancing Geotechnical Site Characterization With 3D SPT-Seismic Testing** - *Khiem T. Tran & Bingkun Yang, University of Florida*	418
22	8:20-8:40	**Integrated Geotechnical and Geophysical Interpretation of Sterling Highway Milepost 45 to 60 Project** - *Keri Nutter & David Barrick, DOWL*	428
23	8:40-9:00	**The Chilkat Connector Feasibility Study in Southeast Alaska** - *Rachel Hunt, Paige Stuhlmuller & Benjamin A. George, Cornforth Consultants Inc. - Landslide Technology*	448
24	9:00-9:20	**Improving Williamsport Road – Overcoming Geological and Geographical Challenges in Remote Alaska** - *Kyle Brennan & Katarah Glashan, Shannon & Wilson, Inc.*	468
25	9:20-9:40	**The Famous "Billings Rims" and the Stagecoach Trail – Integrating 3D Geologic Modeling, Limit Equilibrium Slope Stability, and Discrete Element Rockfall Analyses** - *David Crotsley & Bret Watkins, HDR Engineering, Inc.*	483
10:00 - 10:30		**BREAK**	
Concurrent Technical Session 5A			
26	10:30-10:50	**Photomonitoring for Transportation Infrastructure in Geohazard Environments: Operational and Economic Advantages for Asset Owners** - *Tony Simmonds, Re-Monitor Inc.; Michele Gaeta, Marco Fiorio & Paolo Mazzanti, Nhazca Srl*	499
27	10:50-11:10	**ReMi® Seismic Surveys for Non-Intrusive ASCE 7-22 Compliant Site Class, Rippability, Fault Location, and Design** - *John Louie, Alison Starr & Bill Honjas, Terēan*	517
28	11:10-11:30	**Combined Geotechnical and Geophysical Data Collection for Pile Design at the Ankau Bridge in Yakutat, Alaska** - *Chloe Bjerklie & Matt Blakeslee, DOWL*	532
29	11:30-11:50	**Monitoring While Drilling Glacial Deposits** - *Bruma Souza, Weston & Sampson; Jean Benoît, University of New Hampshire*	547

Concurrent Technical Session 5B			
30	10:30-10:50	**Risk-Based Blasting Specifications for Highway Rock Excavation: Mitigating Project Risk Through Proper Specification Development** - *Anthony Konya & Juliette Oke, DetX*	569
31	10:50-11:10	**Developing a Database of Rockfall-Vehicle Impacts to Evaluate Human Vulnerability Along Transportation Routes** - *Autumn L Helfrich & Brian D. Collins,U.S. Geological Survey, Landslide Hazards Program*	588
32	11:10-11:30	**The Interrelationships of the Characteristic and Dilatant Friction Angles and Tangent Poisson's Ratio** - *Gary Norris, University of Nevada Reno*	606
33	11:30-11:50	**Developing the Triaxial Test Responses of Soil from Available Correlations and a Nonlinear Exponential Equation** - *Sherif Elfass & Gary Norris, University of Nevada, Reno; Horng-Jyh Yang (Tigra), Geo-Environmental Branch Naval Facilities Engineering Systems Command (Mid-Atlantic)*	621
11:50 - 1:00		**LUNCH**	
Technical Session 6			
34	1:00-1:20	**I-80 Mine Subsidence: Geologic Characterization and Emergency Stabilization, Wharton, New Jersey** - *Christina M. Comuso, New Jersey DOT; Matthew D. Riegel & Brian T. Felber, HNTB*	640
35	1:20-1:40	**Overview of Landslide Management Programs for Linear Pipeline Infrastructure Corridors** - *Chris Markley & Bailey Theriault, Geosyntec Consultants*	661
36	1:40-2:00	**Two Dimensional Seismic Site Response Analysis for a New Bridge in a Subduction Zone Environment** -*Zia Zafir, Kleinfelder*	676
37	2:00-2:20	**LiDAR-Based Delineation of Alluvial and High-Angle Fan Landforms for Hazard Recognition, Land Use Planning, and Transportation Corridor Resilience**-*Jonathan R. Lovekin & Amy Crandall, Co. Geological Survey*	691
2:20-2:50		**BREAK**	
Technical Session 7			
38	2:50-3:10	**A Framework for Corrosion and Asset Prioritization in Reinforced Soil Systems** *Nelson Pearson, University of Nevada, Reno*	712
39	3:10-3:30	**Applications of the Smart Rock Technology to Evaluate Rockfall Hazards** - *Bruma Souza, Weston & Sampson; Jean Benoît, University of New Hampshire; Marion Bost, Cerema*	734
	3:30-4:00	**Field Trip Preview**	

Why Nevada Geology is So Exciting

Jonathan G. Price, PhD, CPG
State Geologist Emeritus
Nevada Bureau of Mines and Geology
University of Nevada, Reno
2175 Raggio Parkway
Reno, Nevada 89512
(775)-200-8077
jprice@unr.edu

Prepared for the 75th Highway Geology Symposium, September 2026

Acknowledgements

Many thanks to Beth Price, who served as Reviewer of the manuscript, Chemist checking mineral formulas, Bridge Partner, and Scale in one of the photos in the presentation.

Disclaimer

Statements and views presented in this paper are strictly those of the author(s), and do not necessarily reflect positions held by their affiliations, the Highway Geology Symposium (HGS), or others acknowledged above. The mention of trade names for commercial products does not imply the approval or endorsement by HGS.

Copyright

Copyright © 2026 Highway Geology Symposium (HGS)

All Rights Reserved. Printed in the United States of America. No part of this publication may be reproduced or copied in any form or by any means – graphic, electronic, or mechanical, including photocopying, taping, or information storage and retrieval systems – without prior written permission of the HGS. This excludes the original author(s).

* *

ABSTRACT

The excitement of Nevada geology arises from a combination of the rocks and resources in them, geological hazards, environmental issues, and the geos* who live and work here. Nevada leads the country in the production of gold, barite, and lithium; is a leader in silver; and has abundant geothermal resources for producing electricity and heating buildings. Hazards include floods, landslides, avalanches, swelling clays, earthquakes, and volcanoes. Environmental issues include subsidence due to groundwater withdrawal, radon (mostly associated with granites and rhyolites), arsenic (in volcanic rocks and with gold, silver, and copper deposits), mercury (found alone and with gold and silver), endangered species (found near some mineral deposits), social concerns (encountered nearly everywhere), including those of Indigenous people, drought, concerns about CO_2 and the siting of solar- and wind-energy facilities, and disposal of nuclear waste. Geos have many opportunities to gather at meetings of the Geological Society of Nevada, Nevada Petroleum & Geothermal Society, Nevada Water Resources Association, and local chapters of the Association of Environmental & Engineering Geologists and Society for Mining, Metallurgy & Exploration, and American Institute of Professional Geologists. For the general public, the Nevada Bureau of Mines and Geology writes books and leads field trips on local geology (during Earth Science Week, the second full week in October).

*Geos is a term that includes all sorts of geologists and related folks: engineering geologists, economic geologists, geological engineers, geotechnical engineers, geotechnicians, geochemists, geophysicists, geostatisticians, geoarchaeologists, hydrogeologists, hydrologists, paleontologists, geobiologists, geodesists, and the geologically interested public.

INTRODUCTION

There are four main reasons why Nevada geology is so exciting:

1. The rocks and the resources in them (Fig. 1 & 2).
2. The hazards (Fig. 3).
3. The environmental issues (Fig. 4)
4. The geos, including the geologically interested public (Fig. 5 & 6)

Figure 1. Clayton Valley lithium-brine pond, with Quaternary volcano in the background.

Figure 2. Gold sample from the Round Mountain mine (approximately 3 cm long).

Figure 3. Unreinforced masonry building that collapsed during the magnitude 6.0 earthquake in Wells, Nevada on 21 February 2008, photo by C. dePolo (*1*).

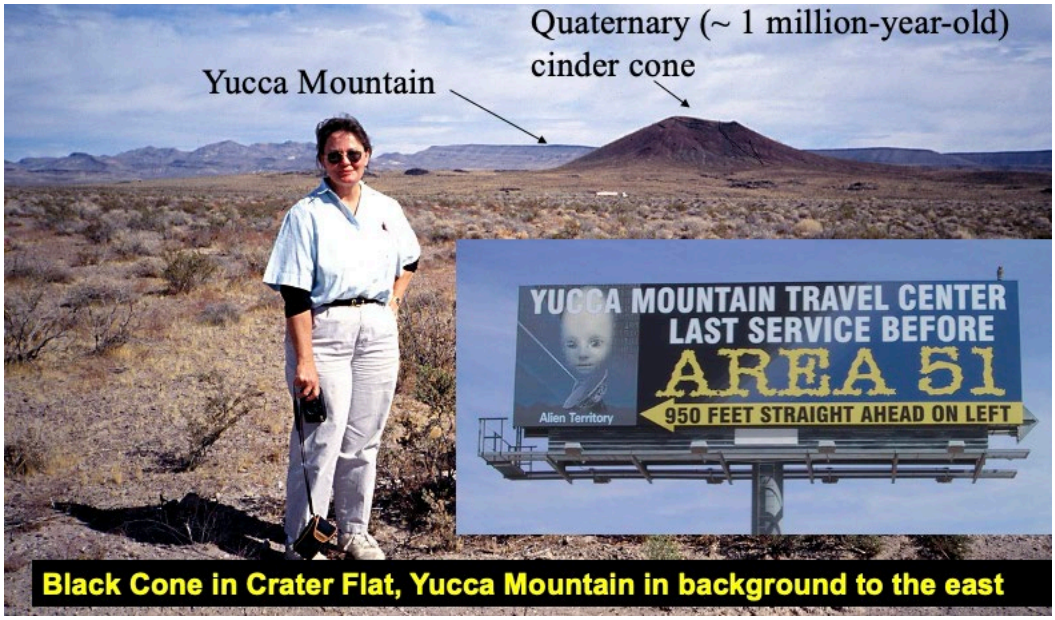

Figure 4. Yucca Mountain, site of a proposed nuclear waste storage facility (variously termed a repository, suppository, or dump).

Figure 5. Some geo-organizations active in Nevada.

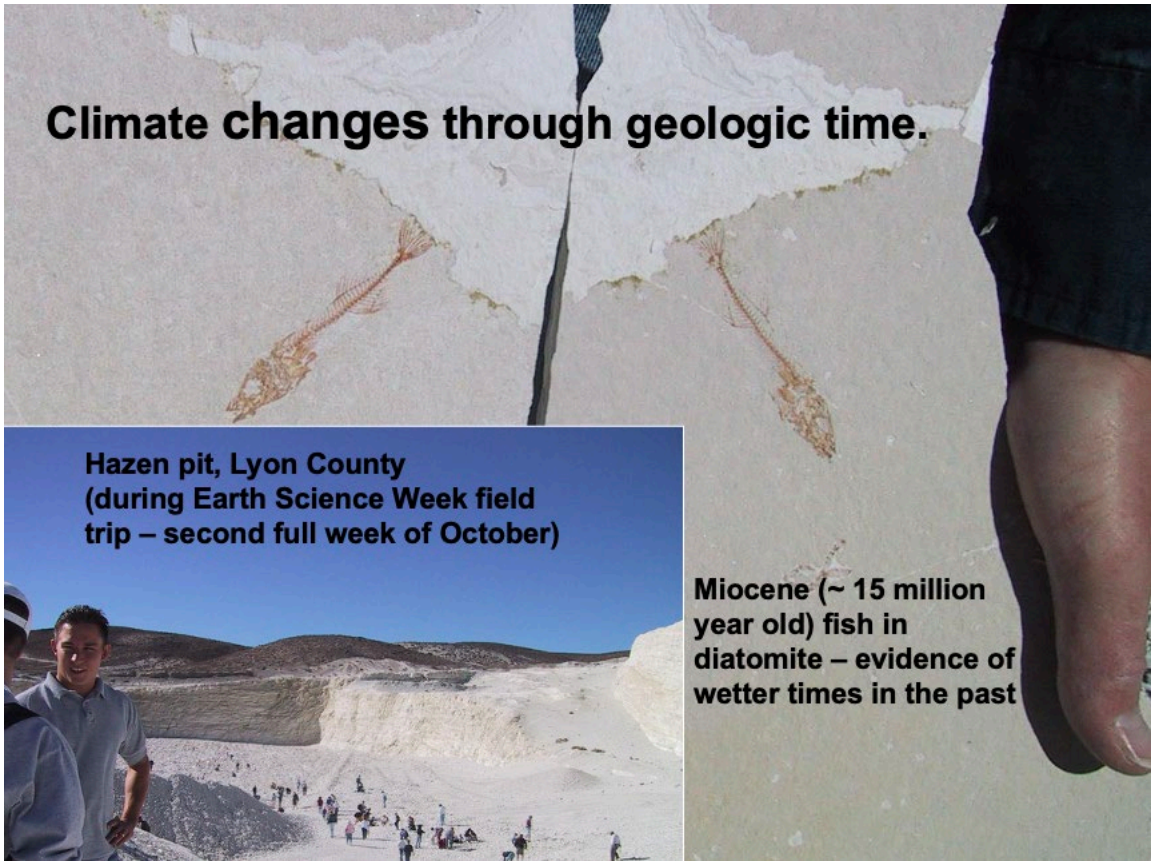

Figure 6. Miocene fish fossils found on an Earth Science Week field trip.

THE ROCKS AND THE RESOURCES IN THEM

The geological history of Nevada (Table 1) is punctuated by magmatic events (Fig. 7), many of which are linked to mineral resources, particularly gold, silver, and copper. Although Nevada is the Silver State (named for the silver-gold mines on the Comstock Lode in Virginia City, which helped the Union during the Civil War), it produces more gold than any other state (Fig. 8). Nevada leads the nation in non-fuel mineral production (*2*). In terms of value, gold dominates, followed by copper, geothermal energy, aggregate, and silver (Fig. 9). Nevada leads the U.S. in the production of gold, lithium, and barite. Exploration is active across the state (Fig. 10).

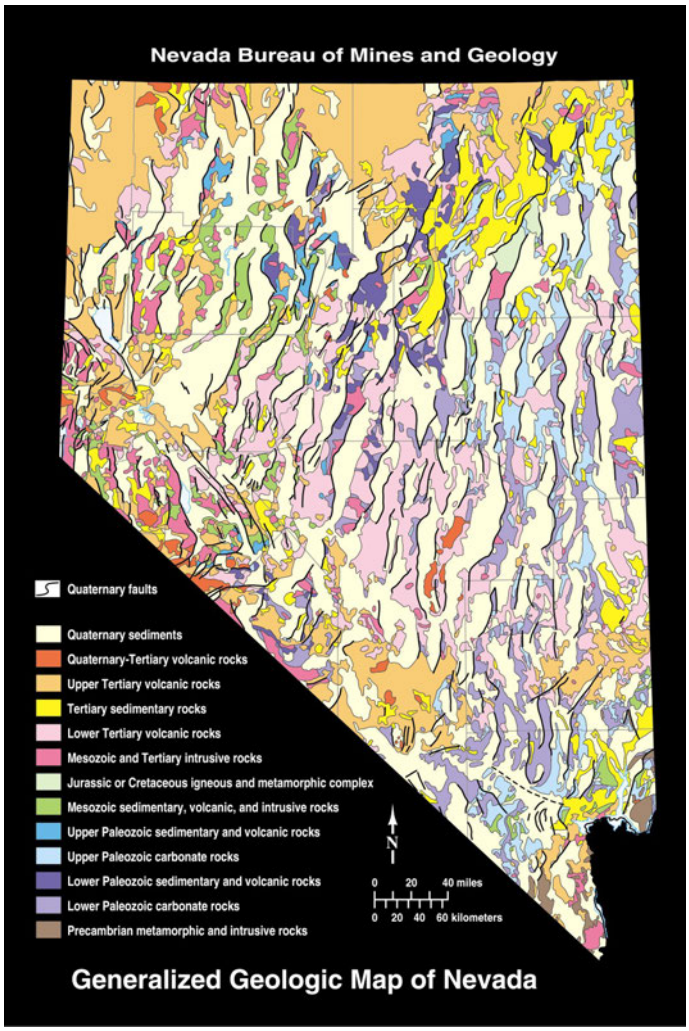

Figure 7. Geologic map of Nevada (*3*).

Precambrian events included thrusting, folding, metamorphism, intrusion, and sedimentation. Paleozoic thrusting, folding, oceanic crust formation, and sedimentation was followed by Mesozoic thrusting, folding, intrusion and volcanism. Cenozoic compression was followed by volcanism and intrusion, crustal extension with north-trending mountain ranges, and faulting, including right-lateral strike-slip faulting.

Table 1. Geologic time scale with major events in Nevada history.

Million years before present		
	CENOZOIC	
	Quaternary	Modern earthquakes, mountain building, volcanism, and geothermal activity are expressions of Basin and Range extension that began in the Tertiary Period. The crust is being pulled apart in Nevada, causing valleys to drop relative to mountains. Prior to 10,000 years ago, ice ages caused glaciers to form in the higher mountains and large lakes to develop, in places connecting today's valleys.
2.58		
	Tertiary	Basin and Range extension began about 30 to 40 million years ago. Igneous activity during the Tertiary Period was caused not only by extension but also by subduction (descent of oceanic crust into the Earth's mantle) of oceanic plates beneath the North American Plate and, in northern Nevada, by motion of the crust over the Yellowstone hot spot in the mantle. Numerous Nevada ore deposits, including most major gold and silver deposits and the copper ores near Battle Mountain, formed during this time. Gypsum deposits formed from evaporating lakes in southern Nevada.
66		
	MESOZOIC	
	Cretaceous	The Cretaceous Period and Mesozoic Era ended abruptly with the extinction of dinosaurs and many marine species; chemical, mineralogical, and other geological evidence suggests that these extinctions were caused by a large meteorite striking the Earth. Numerous granitic igneous intrusions, scattered throughout Nevada, originated from subduction along the west coast of North America. Much of the granite in the Sierra Nevada formed at this time. The igneous activity caused many metallic mineral deposits to form, including the copper-gold-silver-lead-zinc ores at Ruth, near Ely in White Pine County, copper-molybdenum ores north of Tonopah in Nye County, and tungsten ores in several mining districts. In southern and eastern Nevada, sheets of rocks were folded and thrust from the west to the east during the Sevier Orogeny (mountain building), which began in Middle Jurassic time and ended at or beyond the end of the Cretaceous Period.
145		
	Jurassic	A subduction zone to the west caused igneous intrusions, volcanism, and associated ore deposits, including copper deposits near Yerington. Sandstones, including those in the Valley of Fire, were deposited in southeastern Nevada, and sedimentary gypsum deposits formed in northwestern Nevada.
201		
	Triassic	The general geography of Nevada during the Triassic Period was similar to that during the Jurassic Period—igneous activity in the west and deposition of sedimentary rocks in continental to shallow marine environments to the east. Explosive volcanism produced thick ash-flow tuffs in west-central Nevada. Economically important limestone, gypsum, and silica-sand deposits formed in southern Nevada. The Sonoma Orogeny, which began during Late Permian time and ended in Early Triassic time, moved rocks from the west to the east along the Golconda Thrust in central Nevada. The large marine reptiles at Berlin-Ichthyosaur State Park lived during the Triassic Period.
252		
	PALEOZOIC	
	Permian	Volcanism to the west and deposition of thick limestones to the east were characteristics of much of the Paleozoic Era in the Great Basin. Some marine gypsum deposits formed in southern Nevada.
299		
	Pennsylvanian	The Antler highland, formed earlier, was eroded and shed sediments into the basins to the east. Carbonate rocks were deposited in eastern and southern Nevada.
323		
	Mississippian	During the Antler Orogeny, from Late Devonian to Early Mississippian time, rocks were folded and thrust from the west to the east. The Roberts Mountains Thrust, below which many of the gold deposits in north-central Nevada occur, formed at this time. Conglomerate, sandstone, siltstone, and shale were deposited in the thick basin of sediments derived from the Antler highland, and carbonate rocks were deposited further east.
359		
	Devonian	Limestone was deposited in eastern Nevada, and shale, chert, and economically important barite were deposited in northeastern and central parts of the state. No record of middle to lower Paleozoic rocks exists in the western part of the state. The quiet, shallow-marine tectonic setting that persisted earlier in the Paleozoic Era began to change, as small land masses from the Pacific Ocean collided with western North America.
419		
	Silurian	Carbonate rocks (dolomite and limestone) in the eastern part of the state and silica-rich rocks (shale, sandstone, and chert) in the central part of the state record similar deposition to that during the rest of the middle to early Paleozoic Era.
444		
	Ordovician	Marine deposition during the Ordovician Period was similar to that during the rest of the early Paleozoic Era, with the exception of basalts (metamorphosed to greenstones) locally interbedded with sedimentary rocks found today in the central part of the state. Some sedimentary barite deposits and copper-zinc-silver ores formed in sea-floor sediments during this time.
485		
	Cambrian	Middle and Upper Cambrian deposition resembled that during much of the Paleozoic Era, with carbonate rocks to the east and shale plus sandstone to the west. Lower Cambrian and uppermost Precambrian rocks are characterized by quartzite and metamorphosed siltstone throughout much of Nevada.
541		
	PRECAMBRIAN	
		The oldest rocks in Nevada (at least 2,500 million years old in the East Humboldt Range in northeastern Nevada and at least 1,700 million years old in southern Nevada) are metamorphic rocks (including gneiss, schist, marble, and metamorphosed granite, pyroxenite, hornblendite, and pegmatite). Precambrian rocks also include granites (about 1,450 million years old) and younger sedimentary rocks. Beginning approximately 750 million years ago, Antarctica and Australia may have rifted away from western North America, setting the stage for the development of a western continental margin that is similar to the Atlantic coast of today. A shallow marine, tectonically quiet setting persisted in eastern Nevada for the next 700 million years.

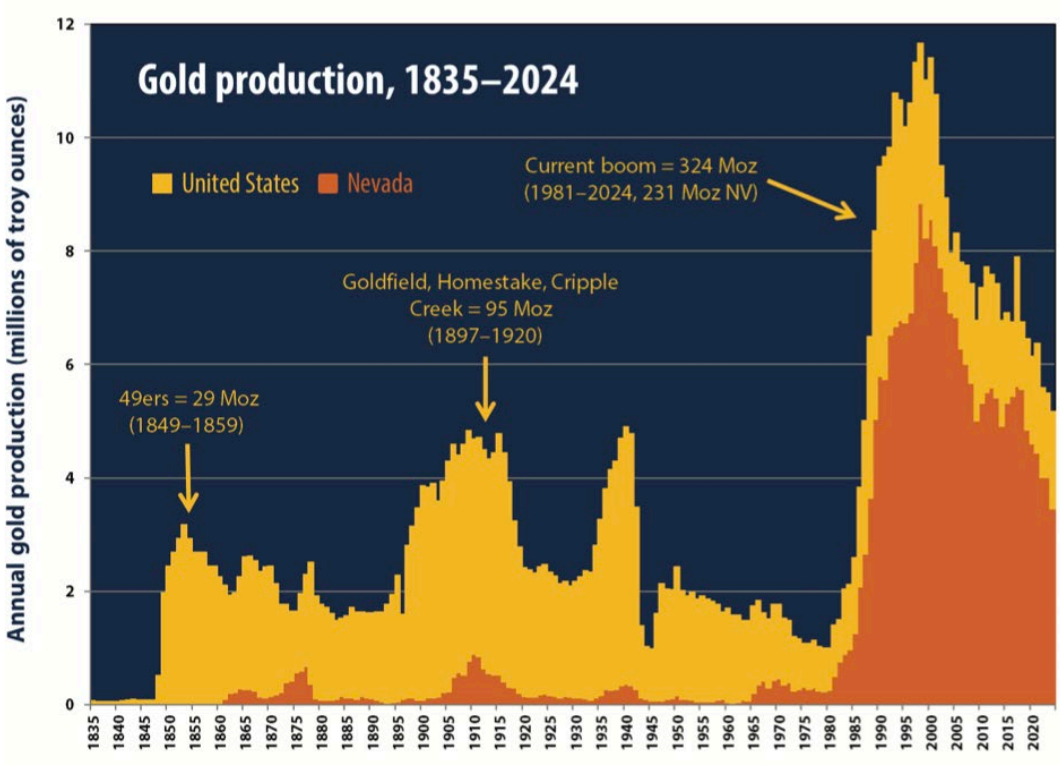

Figure 8. Gold production in the United States and Nevada, 1835 to 2024 (*4*).

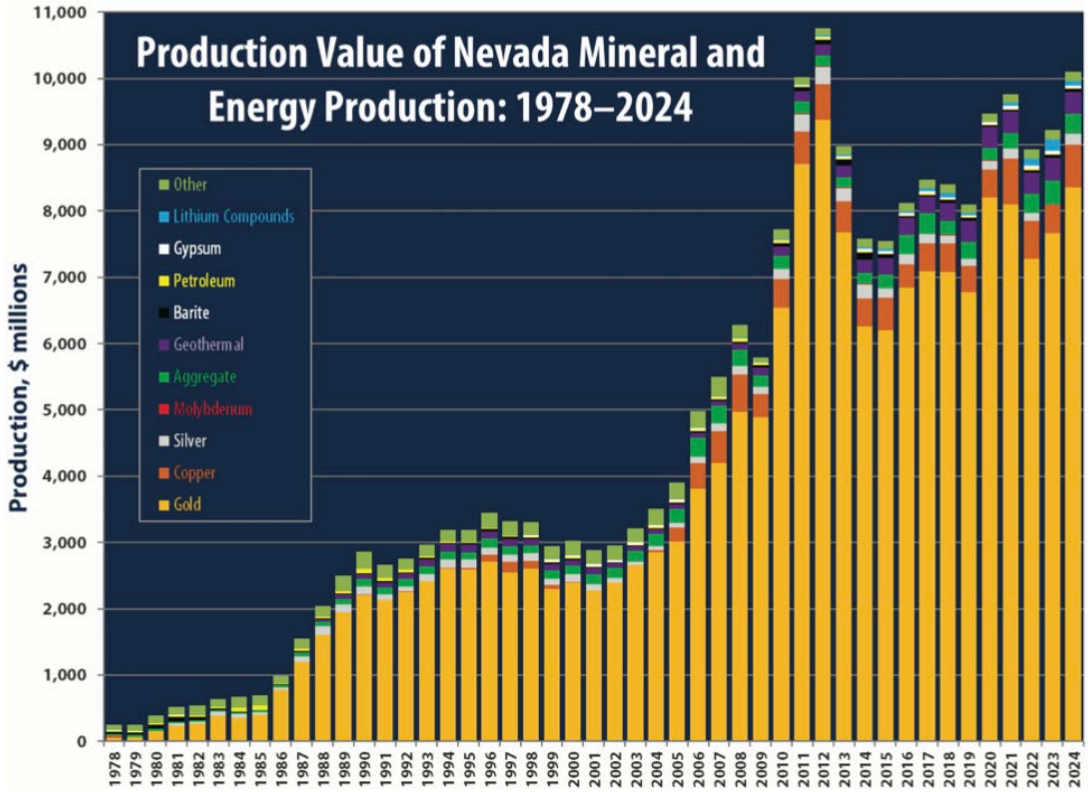

Figure 9. Mineral-resource production in Nevada (*4*).

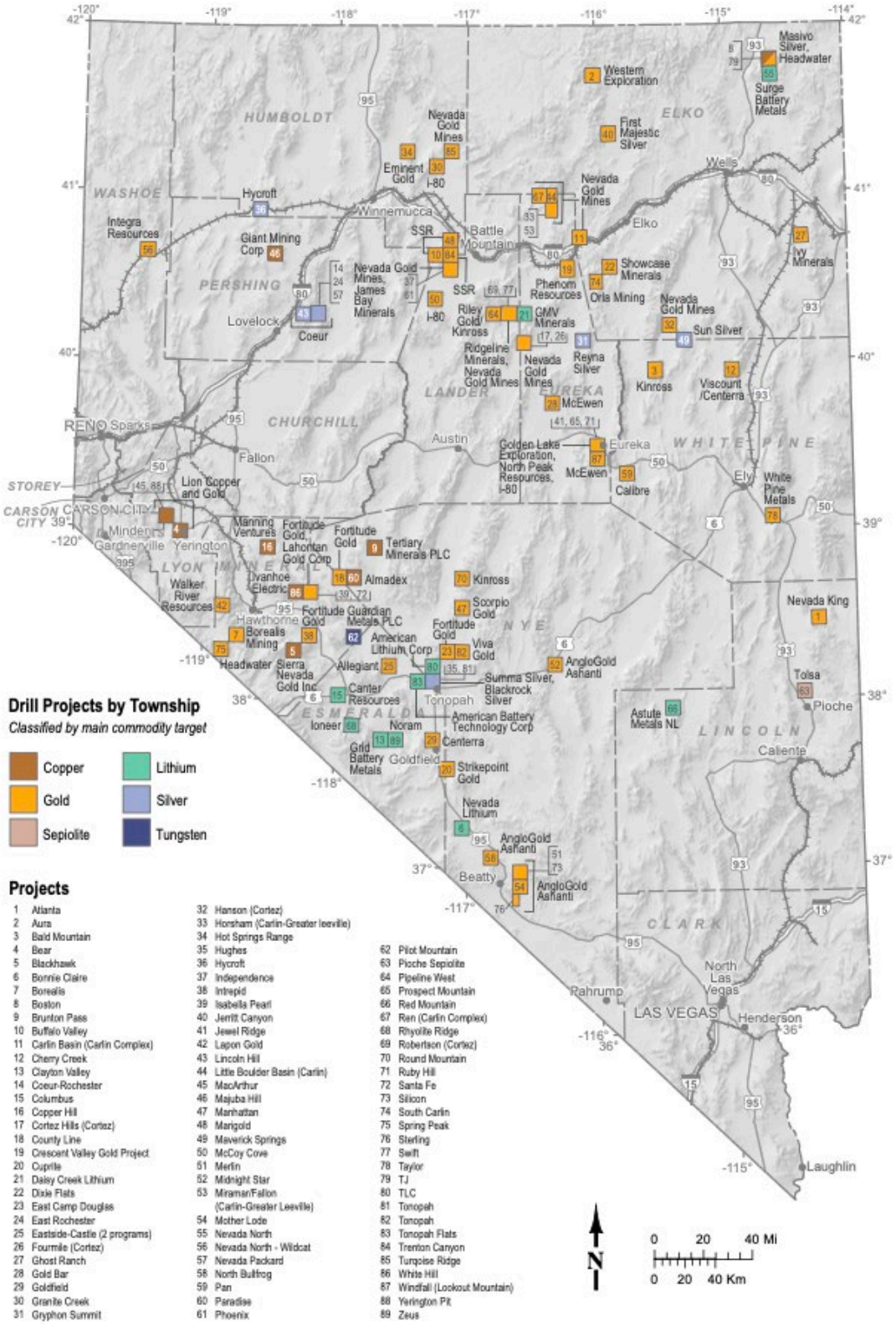

Figure 10. Exploration projects in Nevada (*4*).

THE HAZARDS

Major geologic hazards in Nevada include earthquakes and floods. Historical earthquakes have been as high as magnitude 7.3 (Figs. 11 & 12), and Quaternary faults occur throughout the state (Fig. 13). The Walker Lane (Fig. 11) accommodates approximately 20% of the motion between the Pacific and North American plates, most of which occurs along the San Andreas fault. Floods occur throughout the state as well (Fig. 14). Landslides and avalanches are locally significant in mountainous regions. All these hazards have impacts on our highways.

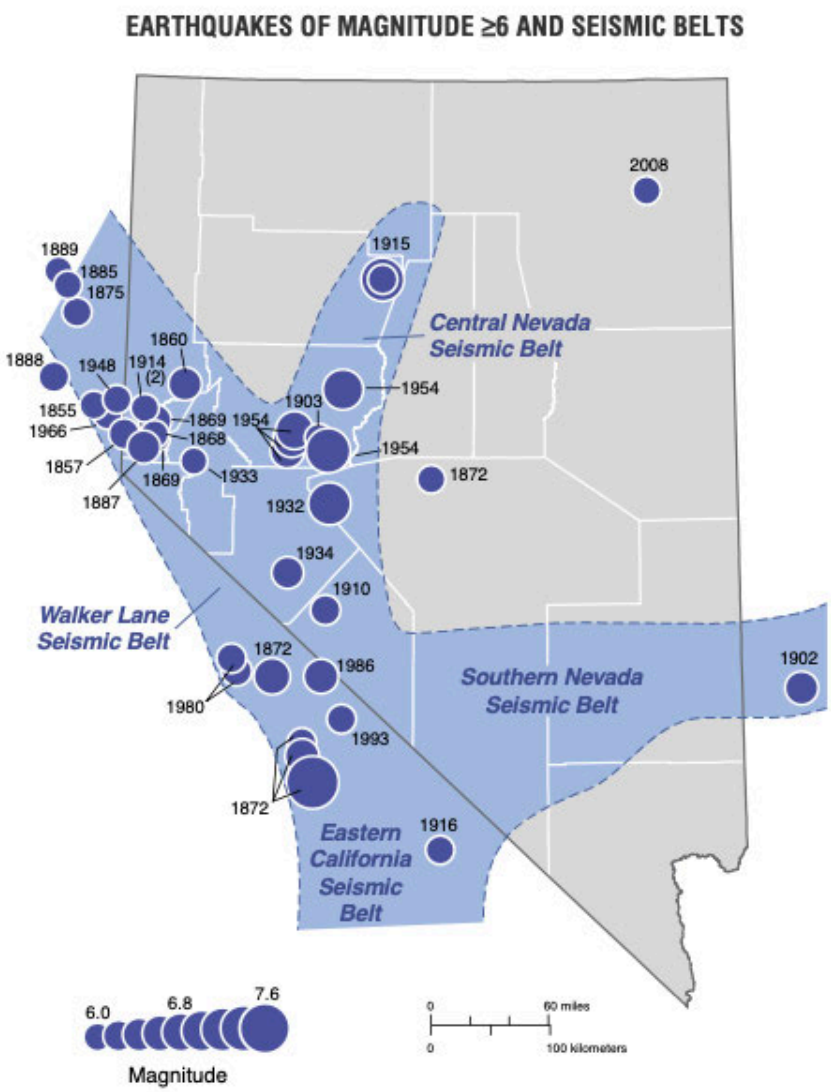

Figure 11. Historical earthquake of magnitude 6 or greater (*5*)

Nevada also has volcanoes (Fig. 14). The most recent eruption occurred approximately 5,500 year ago at Soda Lake near Fallon in Churchill County (*6*). Seismic and geodetic data indicate that magma resides in the lower crust (*7*), and future eruptions are likely, although the hazard are low to moderate.

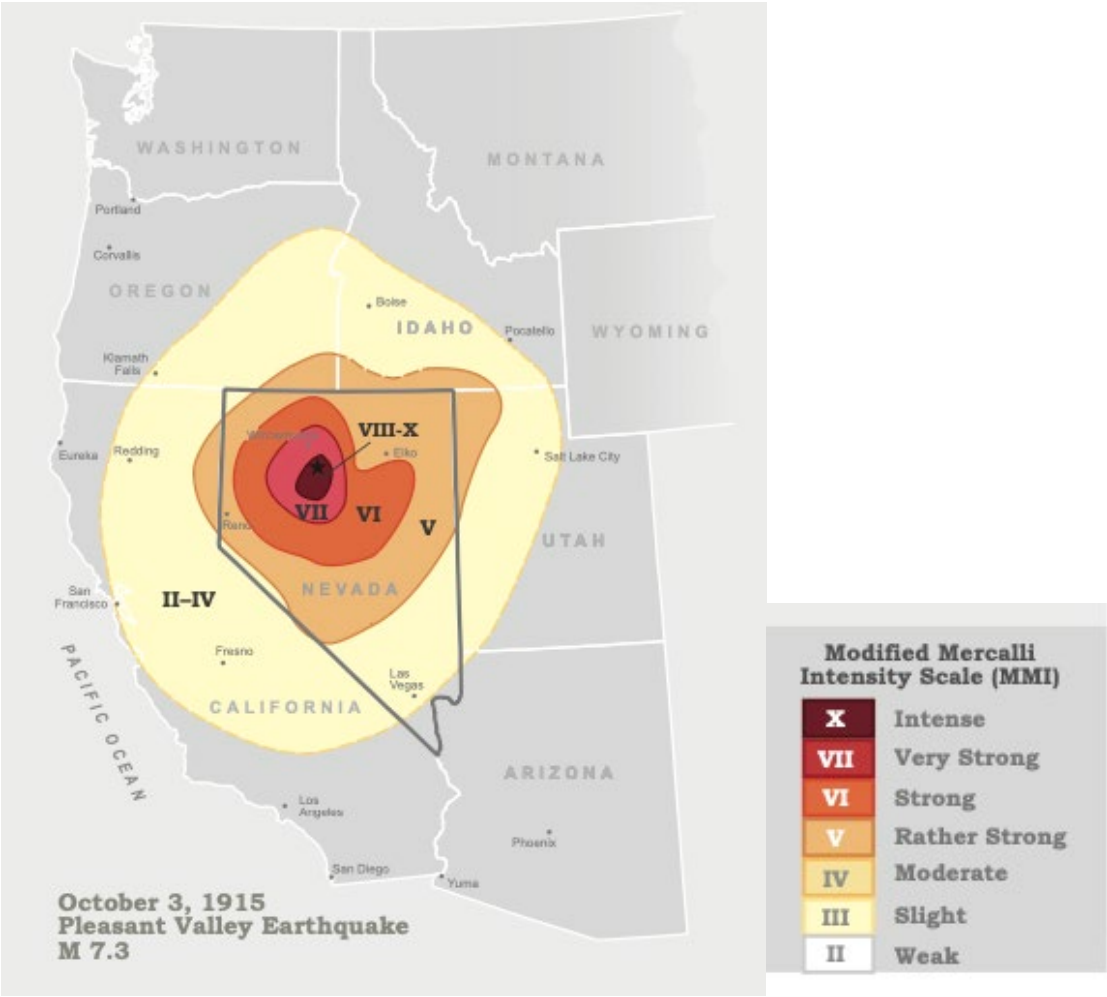

Figure 12. Intensity map of the Pleasant Valley earthquake in 1915 (*8*).

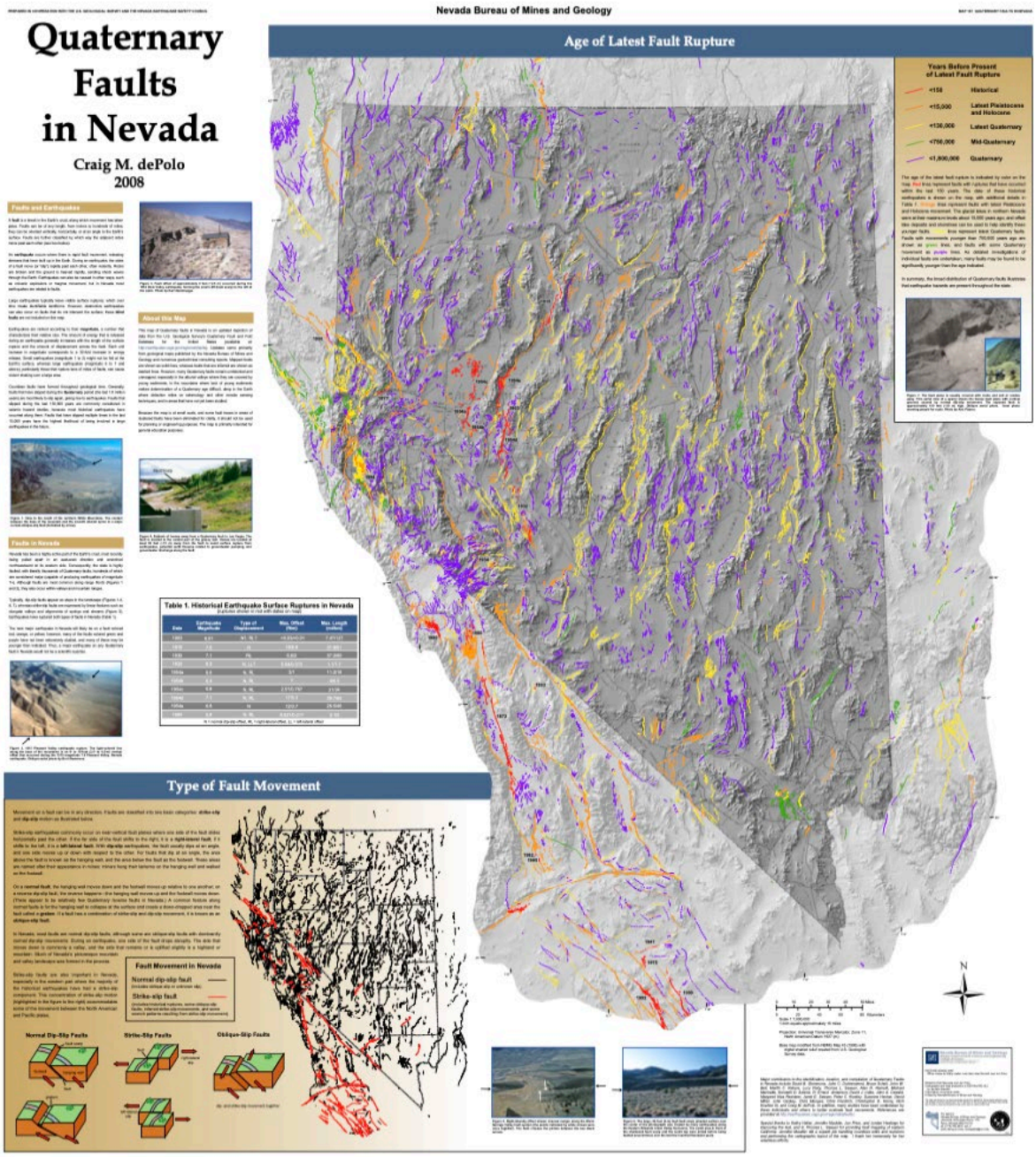

Figure 13. Quaternary faults in Nevada (9).

Figure 14. Flood in Meadow Valley Wash, Clark County, January 2005 (photo courtesy of Gale Fraser, Clark County Regional Flood Control District).

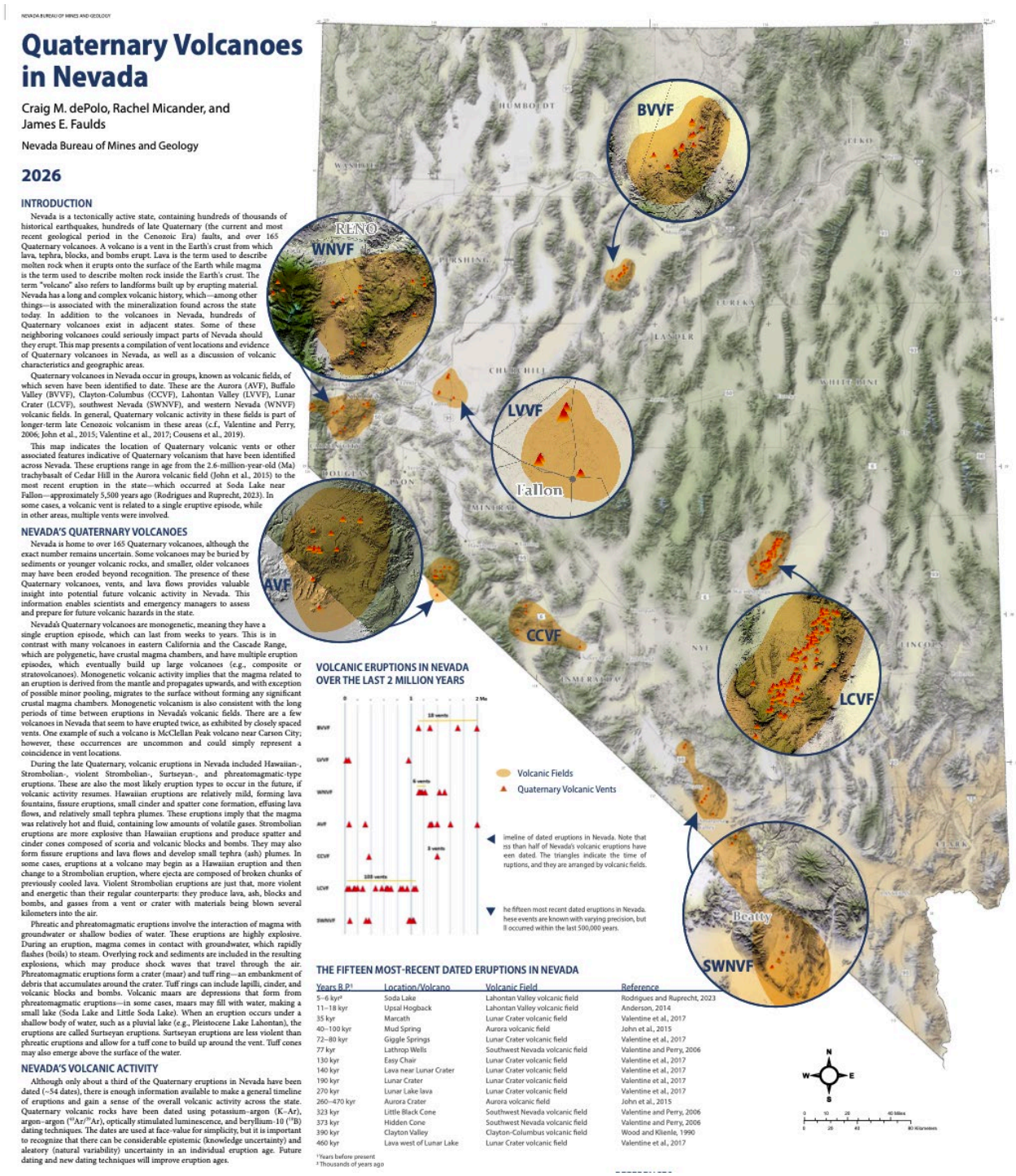

NEVADA BUREAU OF MINES AND GEOLOGY

Quaternary Volcanoes in Nevada

Craig M. dePolo, Rachel Micander, and James E. Faulds

Nevada Bureau of Mines and Geology

2026

INTRODUCTION

Nevada is a tectonically active state, containing hundreds of thousands of historical earthquakes, hundreds of late Quaternary (the current and most recent geological period in the Cenozoic Era) faults, and over 165 Quaternary volcanoes. A volcano is a vent in the Earth's crust from which lava, tephra, blocks, and bombs erupt. Lava is the term used to describe molten rock when it erupts onto the surface of the Earth while magma is the term used to describe molten rock inside the Earth's crust. The term "volcano" also refers to landforms built up by erupting material. Nevada has a long and complex volcanic history, which—among other things—is associated with the mineralization found across the state today. In addition to the volcanoes in Nevada, hundreds of Quaternary volcanoes exist in adjacent states. Some of these neighboring volcanoes could seriously impact parts of Nevada should they erupt. This map presents a compilation of vent locations and evidence of Quaternary volcanoes in Nevada, as well as a discussion of volcanic characteristics and geographic areas.

Quaternary volcanoes in Nevada occur in groups, known as volcanic fields, of which seven have been identified to date. These are the Aurora (AVF), Buffalo Valley (BVVF), Clayton-Columbus (CCVF), Lahontan Valley (LVVF), Lunar Crater (LCVF), southwest Nevada (SWNVF), and western Nevada (WNVF) volcanic fields. In general, Quaternary volcanic activity in these fields is part of longer-term late Cenozoic volcanism in these areas (c.f., Valentine and Perry, 2006; John et al., 2015; Valentine et al., 2017; Cousens et al., 2019).

This map indicates the location of Quaternary volcanic vents or other associated features indicative of Quaternary volcanism that have been identified across Nevada. These eruptions range in age from the 2.6-million-year-old (Ma) trachybasalt of Cedar Hill in the Aurora volcanic field (John et al., 2015) to the most recent eruption in the state—which occurred at Soda Lake near Fallon—approximately 5,500 years ago (Rodrigues and Ruprecht, 2023). In some cases, a volcanic vent is related to a single eruptive episode, while in other areas, multiple vents were involved.

NEVADA'S QUATERNARY VOLCANOES

Nevada is home to over 165 Quaternary volcanoes, although the exact number remains uncertain. Some volcanoes may be buried by sediments or younger volcanic rocks, and smaller, older volcanoes may have been eroded beyond recognition. The presence of these Quaternary volcanoes, vents, and lava flows provides valuable insight into potential future volcanic activity in Nevada. This information enables scientists and emergency managers to assess and prepare for future volcanic hazards in the state.

Nevada's Quaternary volcanoes are monogenetic, meaning they have a single eruption episode, which can last from weeks to years. This is in contrast with many volcanoes in eastern California and the Cascade Range, which are polygenetic, have crustal magma chambers, and have multiple eruption episodes, which eventually build up large volcanoes (e.g., composite or stratovolcanoes). Monogenetic volcanic activity implies that the magma related to an eruption is derived from the mantle and propagates upwards, and with exception of possible minor pooling, migrates to the surface without forming any significant crustal magma chambers. Monogenetic volcanism is also consistent with the long periods of time between eruptions in Nevada's volcanic fields. There are a few volcanoes in Nevada that seem to have erupted twice, as exhibited by closely spaced vents. One example of such a volcano is McClellan Peak volcano near Carson City; however, these occurrences are uncommon and could simply represent a coincidence in vent locations.

During the late Quaternary, volcanic eruptions in Nevada included Hawaiian-, Strombolian-, violent Strombolian-, Surtseyan-, and phreatomagmatic-type eruptions. These are also the most likely eruption types to occur in the future, if volcanic activity resumes. Hawaiian eruptions are relatively mild, forming lava fountains, fissure eruptions, small cinder and spatter cone formation, effusing lava flows, and relatively small tephra plumes. These eruptions imply that the magma was relatively hot and fluid, containing low amounts of volatile gases. Strombolian eruptions are more explosive than Hawaiian eruptions and produce spatter and cinder cones composed of scoria and volcanic blocks and bombs. They may also form fissure eruptions and lava flows and develop small tephra (ash) plumes. In some cases, eruptions at a volcano may begin as a Hawaiian eruption and then change to a Strombolian eruption, where ejecta are composed of broken chunks of previously cooled lava. Violent Strombolian eruptions are just that, more violent and energetic than their regular counterparts: they produce lava, ash, blocks and bombs, and gasses from a vent or crater with materials being blown several kilometers into the air.

Phreatic and phreatomagmatic eruptions involve the interaction of magma with groundwater or shallow bodies of water. These eruptions are highly explosive. During an eruption, magma comes in contact with groundwater, which rapidly flashes (boils) to steam. Overlying rock and sediments are included in the resulting explosions, which may produce shock waves that travel through the air. Phreatomagmatic eruptions form a crater (maar) and tuff ring—an embankment of debris that accumulates around the crater. Tuff rings can include lapilli, cinder, and volcanic blocks and bombs. Volcanic maars are depressions that form from phreatomagmatic eruptions—in some cases, maars may fill with water, making a small lake (Soda Lake and Little Soda Lake). When an eruption occurs under a shallow body of water, such as a pluvial lake (e.g., Pleistocene Lake Lahontan), the eruptions are called Surtseyan eruptions. Surtseyan eruptions are less violent than phreatic eruptions and allow for a tuff cone to build up around the vent. Tuff cones may also emerge above the surface of the water.

NEVADA'S VOLCANIC ACTIVITY

Although only about a third of the Quaternary eruptions in Nevada have been dated (~54 dates), there is enough information available to make a general timeline of eruptions and gain a sense of the overall volcanic activity across the state. Quaternary volcanic rocks have been dated using potassium-argon (K-Ar), argon-argon ($^{40}Ar/^{39}Ar$), optically stimulated luminescence, and beryllium-10 (^{10}B) dating techniques. The dates are used at face-value for simplicity, but it is important to recognize that there can be considerable epistemic (knowledge uncertainty) and aleatory (natural variability) uncertainty in an individual eruption age. Future dating and new dating techniques will improve eruption ages.

Figure 15. Quaternary volcanoes in Nevada (*10*).

THE ENVIRONMENTAL ISSUES

Nevada has its issues:

- Radon, mostly associated with granites and rhyolites
- Arsenic, commonly found with gold, silver, and copper deposits
- Mercury, often found alone and with gold and silver deposits
- Endangered species, found near some mineral deposits
- Waste disposal, including low- and high-level nuclear waste
- Drought, a major concern regarding wildfires
- CO_2, and siting of solar & wind energy facilities and data centers
- Social concerns, encountered nearly everywhere, including those of Indigenous people.

THE GEOS, INCLUDING THE GEOLOGICALLY INTERESTED PUBLIC

Nevada is a great place for geology and geologists. Most geos in Nevada work in industry (mining and mineral exploration, geothermal, environmental, engineering, water resources). We have monthly meetings of the Geological Society of Nevada (in Reno, Elko, Winnemucca, and Las Vegas), Nevada Petroleum and Geothermal Society, Nevada Water Resources Association, and local sections of the Society for Mining, Metallurgy, and Exploration and Association of Environmental and Engineering Geologists. The Nevada System of Higher Education includes geos at universities and colleges in Reno, Las Vegas, Carson City, and Elko, including the Nevada Bureau of Mines and Geology (state geological survey), Nevada Seismology Laboratory, and the Desert Research Institute. Geos are also employed in local and state government (Department of Transportation, Department of Conservation and Natural Resources, Commission on Mineral Resources – Division of Minerals).

The public is invited to participate in activities like geo-society and university lectures and Earth Science Week field trips for the public during the second full week of October. Nevada provides excellent opportunities for collecting interesting fossils, minerals, rocks (Figs. 6, 16, and 17).

Figure 16. Minerals of Nevada (*11*, photos by J. Scovil):

a. Opalized wood, Virgin Valley, Humboldt County, 2.5 cm diameter. Opal, $SiO_2 \cdot nH_2O$, is the State Gemstone.

b. Gypsum, Robinson District, White Pine County, 12 cm long.

c. Gold, Round Mountain, Nye County, 3.3 cm high.

d. Stibnite, Sb_2S_3, Betze-Post Mine, Eureka County, 6.7 cm,

e. Clinoclase (blue), $Cu_3(AsO_4)(OH)$, and cornubite (green), $Cu_5(AsO_4)_2(OH)_4$, Majuba Hill mine, Pershing County, 1.0 cm field of view.

f. Barite, $BaSO_4$, Northumberland Mine, Nye County, 7.3 cm wide.

g. Realgar, AsS, and fluorite, CaF_2, Getchell Mine, Humboldt County, 6.5 cm wide.

h. Azurite, $Cu_3(CO_3)_2(OH)_2$, 4.6 cm field, Robinson district, White Pine County.

Figure 16. Samples from Easy Chair crater, 140,000-year-old volcano, Nye County. Upper photos of an unusual clinopyroxene [$Ca(Mg,Fe)Si_2O_6$] crystal with holes, 3 cm long; lower photo of a volcanic bomb, 7 cm long.

REFERENCES

1. dePolo, C.M., and LaPointe, D.D., Eds., 2011, An introduction to the 21 February 2008 M_w 6.0 Wells, Nevada earthquake, A compendium of earthquake-related investigations prepared by the University of Nevada, Reno: Nevada Bureau of Mines and Geology Special Publication 36 , https://data.nbmg.unr.edu/Public/freedownloads/sp/sp036/.
2. U.S. Geological Survey, 2026, Mineral commodity summaries, 226 p., https://pubs.usgs.gov/periodicals/mcs2026/mcs2026.pdf.
3. Tingley, S.L., 1999, Generalized geology map of Nevada: Nevada Bureau of Mines and Geology, https://pubs.nbmg.unr.edu/Generalized-geologic-map-of-Nev-p/e030.htm.
4. Jowitt, S.M., Fisher, T., Micander, R., Lindsey, C., Lu, C., and Reynolds, D., 2025, The Nevada mineral industry - 2024: Nevada Bureau of Mines and Geology Special Publication MI-2024, 105 p., https://pubs.nbmg.unr.edu/The-Nevada-Mineral-Industry-2024-p/mi2024.htm.
5. dePolo, D.M., and dePolo, C.M., 2012, Earthquakes in Nevada: 1840s to 2010: Nevada Bureau of Mines and Geology Map 179, 1:1,000,000 scale, https://pubs.nbmg.unr.edu/Earthquakes-in-NV-1840s-to-2010-p/m179.htm.
6. Rodrigues, K., and Ruprecht, P., 2023, Luminescence-based methods for dating phreatomagmatic eruptions: a case study from Soda Lake, NV: Geological Society of America Abstracts with Programs, v. 55, no. 4.
7. Smith, K.D., von Seggern, D., Blewitt, G., Preston, L., Anderson, J.G., Wernicke, B.P., and Davis, J.L., 2004, Evidence for deep magma injection beneath Lake Tahoe, Nevada-California: Science, p. 1277-1280.
8. dePolo, C.M., 2012, Damaging earthquakes in Nevada, 1840s to 2008: Nevada Bureau of Mines and Geology Special Publication 37, 1:1,000,000-scale, with text, 4 p., https://pubs.nbmg.unr.edu/Damaging-earthquakes-in-NV-p/sp037.htm.
9. dePolo, C.M., 2008, Quaternary faults in Nevada: Nevada Bureua of Mines and Geology Map 167, 1:1,00,000 scale, https://pubs.nbmg.unr.edu/Quaternary-faults-in-Nevada-p/m167.htm.
10. dePolo, C.M., Micander, R., and Faulds, J.E., 2026, Quaternary volcanoes in Nevada: Nevada Bureau of Mines and Geology Open-File Report 2026-1, 1:1,000,000-scale, https://pubs.nbmg.unr.edu/Quaternary-volcanoes-in-Nevada-p/of2026-01.htm.
11. Castor, S.B. and Ferdock, G.C., 2004, Minerals of Nevada: Nevada Bureau of Mines and Geology Special Publication 31, 512 p.

01. Distributed Monitoring of Rock Slope Performance in Colorado Using Time-Lapse Photography and Vision-Language Models

Luke Weidner
BGC Engineering Inc.
600 12th St. #300
Golden, CO, 80401
+1 720-598-5982
lweidner@bgcengineering.ca

Prepared for the 75th Highway Geology Symposium, September, 2026

Acknowledgements

The authors would like to acknowledge funding support from BGC Engineering Inc. and logistical support from the Colorado Department of Transportation. We would also like to thank Mark Vessely and Gabriel Walton for reviewing an early draft of this manuscript.

Disclaimer

Statements and views presented in this paper are strictly those of the author(s), and do not necessarily reflect positions held by their affiliations, the Highway Geology Symposium (HGS), or others acknowledged above. The mention of trade names for commercial products does not imply the approval or endorsement by HGS.

Copyright Notice

Copyright © 2026 Highway Geology Symposium (HGS)

All Rights Reserved. Printed in the United States of America. No part of this publication may be reproduced or copied in any form or by any means – graphic, electronic, or mechanical, including photocopying, taping, or information storage and retrieval systems – without prior written permission of the HGS. This excludes the original author(s).

ABSTRACT

The proper design and maintenance of rock slopes is essential to ensure the safety of road users, but performance information for existing rock slopes is often lacking. Distributed rock slope monitoring using time-lapse single-camera photography has the potential to provide valuable information for a fraction of the cost of lidar or photogrammetry. This study presents a framework for low-cost automated rock slope monitoring using time-lapse photography and computer vision-based image analysis. Camera system hardware is assembled from off-the-shelf components (total cost approximately $370 USD per unit). The hardware is freestanding, solar-powered, and can be installed in a few minutes.

A change detection workflow is developed using a combination of alignment, structural similarity, image differencing, and deep-learning-based interpretation. We experimented with two vision-language models (GPT-5 and Qwen3) for automated rockfall identification. The models are prompted with sets of images and change masks to provide general descriptions of the changes and classify whether new rockfall is visible in the ditch.

The overall workflow is demonstrated on three rock slope sites along highways in Colorado. Results show that the image change detection successfully resolved rockfall events as small as approximately 30-40 pixels in diameter, although the vision-language models did not reliably interpret rockfalls at this scale and sometimes mischaracterized the cause of larger changes. While further work is needed to improve the reliability of automated image interpretation using VLMs, the overall framework shows promise as a low-cost method for distributed rock slope monitoring.

INTRODUCTION

Proper design, maintenance, and monitoring of rock slopes is essential for safety, and this is often guided by observations of past slope failures and performance (*1*). Slope performance data come from a variety of sources, ranging from field-based ratings and inventorying of photographs (*2*) to remote sensing techniques using laser scanning or photogrammetry to measure millimeter-scale deformations (*3*), (*4*). Understanding where and when slope failures are most common enables more targeted, effective planning and prevention strategies. Consistent site-scale monitoring can also enable early warning of failures (*5*). Rock slope monitoring is therefore an important part of maintaining the safety of mountain infrastructure.

3D remote sensing using laser scanning and photogrammetry is an increasingly standard approach for understanding rock slope behavior. However, they are also relatively expensive and time consuming to install, which severely limits the number of sites it is practical to instrument (*6*). Fixed photogrammetry systems also require appropriate line of sight locations to place multiple cameras for parallax (*7*). An alternative method which has gained recent interest in literature is monitoring based on a single fixed camera per site (i.e., no overlap between adjacent photos). Instead of capturing the slope in 3D and deriving changes from the volumetric differences, single-camera (monocular) monitoring relies on image processing techniques to infer rock slope changes based on changes in pixel intensities (*8*).

While this method does not provide direct 3D measurements of slope changes, it can still provide useful information on the timing and approximate size of rockfall events at a fraction of the cost and complexity of 3D methods. Recent research has aimed to use analysis of visual or thermal video to detect rockfalls and map their trajectories essentially immediately as they occur (*9*), (*10*). An additional potential benefit is that single time-lapse cameras are inexpensive and simple to install. However, previous research has focused on relatively specialized hardware, which can still incur significant costs for installation.

Various techniques are available to automatically identify changes in images, with a common algorithm being the structural similarity index method (SSIM) (*11*) and other similar classical image processing methods. Recently, deep learning has been explored for interpretation of geohazards in single images, such as for general detection of landslides (*12*) or extraction of slope movement vectors (*13*). Whereas image processing algorithms employ manually-crafted rules, deep learning methods derive rules through training based on a large set of examples.

A vision-language model (VLM) is a deep neural network trained on both images and text, allowing it to understand and generate descriptions of images (*14*). Whereas other machine learning models are trained for specific tasks and require task-specific training data, such as many examples of rockfall images, currently available VLMs are trained on general datasets to learn broad patterns. These types of models, referred to as foundation models, show potential in generalizing to a wide range of tasking in earth sciences without expensive retraining (*15*). VLMs have the potential to provide an additional layer of automated image interpretation for rock slope monitoring, potentially reducing the need for manual inspection of images. Recent work has demonstrated expert-level interpretation of single landslide images using multimodal

large language models (*16*). However, to our knowledge, VLMs have not been applied to change detection in ground-based time-lapse monitoring imagery, where the relevant changes are small, repeated, and embedded within an otherwise fixed scene, and their performance in this context is therefore unknown.

Study Objectives

The current study has two main goals: first, to build a low-cost remote time-lapse system capable of capturing and transmitting photos automatically; and second, to investigate the feasibility of employing VLMs for automated image change detection, in combination with standard image change detection methods. Specifically, we hypothesize that the current generation of foundational VLMs, with its possible relative lack of earth-science focused input data, may struggle to effectively identify rockfalls to an acceptable level of accuracy.

The specific contributions of this work are as follows:

- A fully specified low-cost camera system design, assembled entirely from off-the-shelf components for approximately $370 USD per unit, which is freestanding, solar-powered, and installable in a few minutes.
- An automated change detection workflow implemented entirely with freely available Python libraries.
- The first evaluation, to our knowledge, of general-purpose VLMs applied to rockfall change detection in terrestrial time-lapse imagery, covering both a commercial cloud-hosted model (GPT-5) and an open-weights model run offline on consumer-grade hardware (Qwen3).
- Demonstration of the complete framework at three operational highway rock slopes in Colorado, spanning approximately 340 camera-days and 1,700 images and including both real and synthetic rockfall events.

METHODS

Camera System Hardware

The camera system used in this study consists of several off-the-shelf components, as listed in Table 1 and illustrated in Figure 1. This section describes each component in detail. While there are a few similar commercial systems available for time-lapse photography, we found that they did not meet all of our requirements for low cost, remote deployment, and customizability, hence our decision to build our own. The system is controlled by the Raspberry Pi Zero 2W, one of the smaller Raspberry Pi models. The Zero 2W was chosen for its small footprint and low power consumption. The computer runs a version of the Linux operating system, and Python scripts can be used for camera control and image processing. The Raspberry Pi Camera V3 is connected to the Zero 2W via a ribbon cable. The Camera V3 has a 12-megapixel sensor and auto-focus capabilities, which tends to result in sharper images under a variety of lighting conditions in our experience.

A Voltaic Systems "Always-On" 24 Watt-hour battery is used, which is designed for continuous charging from a solar panel while powering a load. Minimizing power consumption is important, as the battery has limited capacity and can sustain a running Raspberry Pi continuously for only a few hours. An external power management and real-time clock board (Witty Pi 4 Mini) is used to schedule power on/off times at certain times of day, meaning that the system is powered off when not in use. The WittyPi 4 Mini is a power management add-on designed specifically for Raspberry Pi computers. It can be configured to power on the Raspberry Pi at specific times of day. We set the schedule to power on the system five times per day, at two-hour intervals starting at 8:00 AM. When powered on, a Python script is executed to capture an image using the Raspberry Pi Camera, save it to local storage, and upload it to a remote FTP server via a 4G cellular modem.

Components are mounted inside a plastic enclosure and secured with brackets and adhesives. The enclosure is mounted inside a landscaping fake rock, which is used as a cover mainly to provide structure and elevate the camera above ground level. The fake rock also provides some protection from rain and a small amount of camouflage. The fake rock is placed over a stack of concrete blocks, preventing it from blowing away in wind.

Table 1 – List of camera system components and general costs in USD

Component	Description	Cost
Raspberry Pi Camera 3	12MP camera designed for Raspberry Pi	$30
Raspberry Pi Zero 2W	Single-board computer	$15
Real-Time Clock and Power Management	WittyPi 4 Mini	$20
Power Supply	Voltaic Systems, "Always-On", 24 Wh	$45
Solar Panel	Voltaic Systems, 5W	$35
4G Modem	Verizon/Novatel USB Modem U620L	$100
Storage	SD card, 32GB	<$5
Enclosure	Plastic container	$0
Cover	Landscaping fake rock	$100
Mounting Hardware	Various brackets, bolts, adhesives	$20
Total		**$370**

Figure 1 – (Left) Overview photos of the camera installation locations. (Right) Inside view of the camera system enclosure, showing the main components.

Installation Locations and Monitoring

Three camera systems were installed at rock slope sites along highways in Colorado, USA (Figure 2, Table 2). The sites were selected based on known history of rockfall activity through other monitoring methods (terrestrial lidar and fixed photogrammetry).

- Camera 1 was placed in the ditch at a south-facing interbedded sedimentary rock cut on US Highway 24 in Manitou Springs. This rock cut has been monitored daily using a fixed photogrammetry system since 2020 and has detected several significant rockfalls during that time (*17*). The ditch near the camera location is generally clear of vegetation.

- Camera 2 is located at the base of an east-facing rock slope on a county road near Dillon in Summit County. The Camera 2 rock slope has three main rock units: the lower and uppermost units are alternating layers of sandstone and shale, while the middle unit is a

massive igneous intrusion (*3*). The rock slope has a relatively narrow ditch which is bare of vegetation.

- Camera 3 is located at a south-facing gneiss rock cut on Colorado Highway 74 west of Morrison. This slope was the subject of a mitigation program including scaling, bolting, and removing a traffic lane to widen the ditch (*3*). As a result of the wider ditch, vegetation growth is more prevalent.

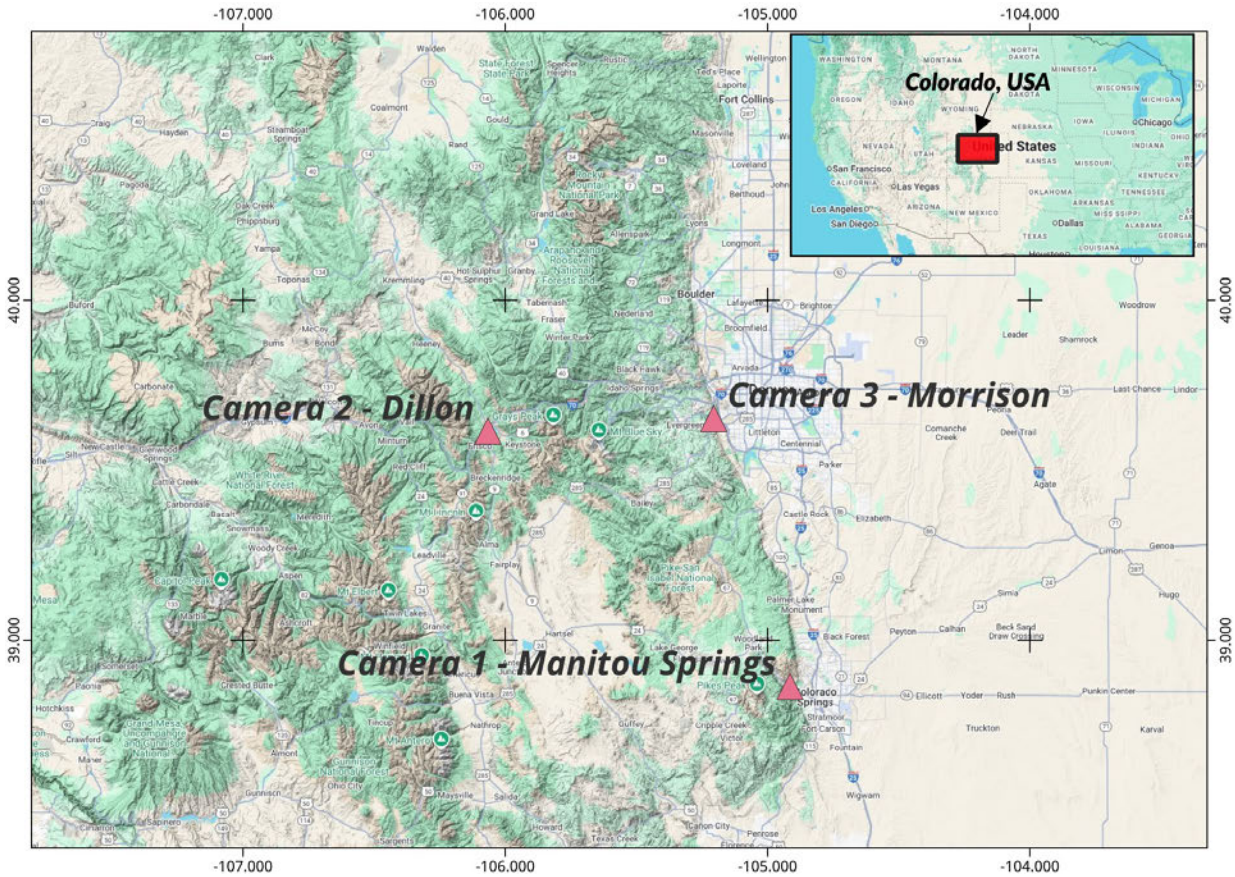

Figure 2 – Locations of the three camera installations in Colorado, USA.

Table 2 – Camera installation locations and monitoring dates			
Camera	Location	Rock Type	Dates
Camera 1	US Highway 24, Manitou Springs	Interbedded sedimentary rock	March 18, 2025 – October 1, 2025
Camera 2	County road near Dillon, Summit County	Sandstone, shale, igneous intrusion	August 26, 2025 – December 15, 2025
Camera 3	Colorado Highway 74, Morrison	Gneiss	November 30, 2025 – January 1, 2026

Image Analysis Workflow

The image analysis workflow is designed to automatically identify rockfall events soon after they occur. It consists of two main parts, each with several steps. The software is built using open-source Python libraries including OpenCV, scikit-image, NumPy, and Matplotlib. The first part is classical image processing and differencing, and the second component is automated image interpretation using VLMs. In the first part, images are aligned and corrected for lighting differences. Then, image differencing and structural similarity analysis are used to identify areas of change between images. The detailed steps of the workflow are as follows (and illustrated in Figure 3):

1. **Image Alignment**: Align images to account for shifts in the camera position using feature matching and homography. Before alignment, we apply Contrast Limited Adaptive Histogram Equalization (CLAHE) to improve feature detection and account for lighting differences caused by cloud cover. We used ORB descriptors and RANSAC to estimate the homography matrix. The reader is referred to the OpenCV documentation for more details on these methods (*18*).

2. **Structural Similarity**: Compute the Structural Similarity Index (SSIM) between aligned images to identify regions with significant changes in texture and structure. The original SSIM is defined as the product of three components: luminance, contrast, and structure (*11*), weighted by parameters α, β, and γ. In our case, we set both α and β to zero, focusing solely on the structure component to detect changes in texture and structure while ignoring lighting variations. This is equivalent to computing the normalized cross-correlation between image patches. The SSIM is computed using a sliding window approach across the image, and the window size was tuned to balance sensitivity to small changes and noise reduction (currently set to 20 pixels).

3. **Image Differencing**: Compute the mean absolute difference between aligned images to identify pixel-level changes, then apply a mean filter to suppress noise.

4. **Combination and Masking**: In initial testing, we observed that image differencing was generally more sensitive to small changes compared to SSIM but was influenced by lighting variations, so we combined the two methods according to the following rule:

$$Combination(x,y) = (1 - Corr(x,y)) \cdot Diff(x,y)$$

   Where $Corr(x,y)$ is the SSIM value at pixel (x,y), and $Diff(x,y)$ is the image difference value at pixel (x,y). This results in an overall change map where larger values indicate more significant changes in both texture and pixel intensity. The combination map is then thresholded to create a binary change mask.

5. **Multi-Day Comparison**: To improve robustness, we compare each image to multiple previous images (e.g., the last seven days at the same time of day) and sum the binary change masks. A change object is recorded if it appears in at least three comparisons, preventing a transient change from being recorded.

6. **Overall Change Metrics**: For each detected change object, we compute the total number of pixels changed and use this as an indication of the overall amount of activity on the slope and in the ditch.

Automation with Vision-Language Models

The change detection workflow described above is designed to identify regions of change between images, but it does not provide any information on the nature of the changes. This means that interpretation is still required to determine if the changes are due to rockfall events, weather effects, lighting changes, or other factors. This is where vision-language models (VLMs) can potentially provide automation. There are a wide variety of VLMs available for general use, both open-source and low-cost commercial, with varying capabilities and performance. In this study, we experimented with using two VLMs: GPT-5 (commercial, cloud-hosted) and Qwen3 (open-weights, run offline) to inspect flagged change regions and provide descriptions of the changes, such as if the changes can be attributed to weather conditions or if new rocks are clearly visible in the ditch.

GPT-5 is a multimodal large language model developed by OpenAI and released in August 2025 (*19*). It natively supports both images and text inputs at the same time (e.g., uploading two images and asking "What are the differences between these images?"). The testing involved with creating the current study ran hundreds of images through the OpenAI API at a total cost of less than $5 USD. Qwen3 is a large language model funded by Alibaba Cloud, also released in 2025 (*20*). As an open-weights model, Qwen3 is distributed in a number of different formats and sizes, some of which support image inputs, and many of which can be run on consumer-grade hardware. For this study, we used the Qwen3 VLM with 8 billion parameters with an NVIDIA RTX 4000 Ada Generation GPU. The model is run using the LM Studio python API.

The workflow for using the VLM follows three main steps:

1. If the total area of detected change for a given day using image analysis exceeds a user-defined threshold, the comparison is flagged for VLM analysis. This prevents unnecessary model calls for minor changes that are unlikely to be of interest.

2. All images and the change mask associated with the flagged comparison are passed to the VLM along with a prompt requesting a short description of the changes observed in the images, along with a True/False classification of whether new rockfall is visible in the ditch.

3. Regardless of whether the VLM identifies new rockfall, the output descriptions and classifications are stored for further analysis. For example, the description can be used to indicate the cause of the changes (e.g., weather-related vs. rockfall).

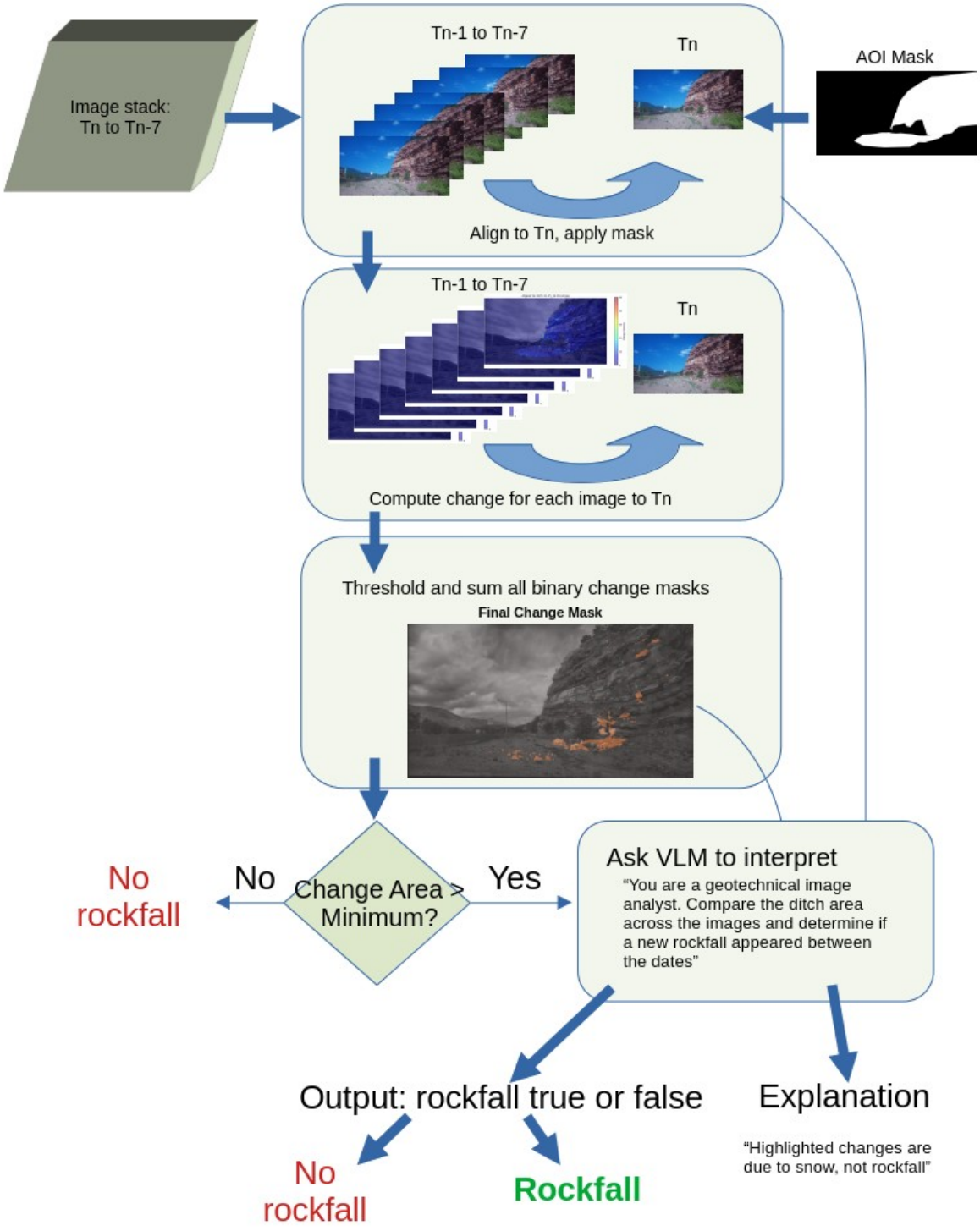

Figure 3 – Overview of the image analysis workflow.

Note that while we ran both GPT-5 and Qwen3 for all experiments, a detailed comparison of their performance is outside the scope of this initial study and will be the subject of future work. Preliminary results indicate similar performance between the two models, and for brevity we only present Qwen3 results in the following sections, highlighting the capabilities of open-weights models.

Synthetic Rockfall Experiment Design

As shown in Table 2, at the time of writing, the three cameras have been collecting data for varying lengths of time, with Camera 1 having the longest monitoring period of about eight months. During this time, several notable rockfalls were detected, primarily at the Camera 1 slope. However, overall the number of rockfalls captured has been limited. As a result, we conducted a synthetic rockfall experiment by digitally altering images to appear to have new rockfalls in the ditch. This was done by selecting images from the monitoring dataset and overlaying cutouts of rocks from other parts of the images onto the ditch area, simulating new rockfall events. Filters were applied to the cutouts to blend them into the background and ensure they appear at least superficially realistic. The image analysis workflow, including VLM interpretation, was then run on both the altered images and unaltered images to evaluate detection performance.

RESULTS

Synthetic Rockfall Experiment

Synthetic rockfall experiments were conducted using images from Cameras 2 and 3, as these cameras had not yet recorded any real rockfall events at the time of writing. For Camera 2, a pile of several large blocks was added to the ditch area in one image, while for Camera 3, two small rockfalls were added in one image and one large rockfall in another image.

A rock slope failure at the Camera 2 slope was created near the center of the visible scene, which crosses the full width of the ditch and hits the concrete barrier (Figure 4). In this example, the contrast of the rock slope is relatively poor due to the lighting conditions at the time. Despite this, the image analysis workflow is able to detect a large anomaly in the ditch area. The Qwen3 VLM in this example also correctly identifies the changes as a rockfall, but we noted that the VLM will incorrectly report no rockfalls if only the raw images (without the change map) are provided.

For Camera 3, neither GPT-5 or Qwen3 correctly identified the two small synthetic rockfalls, despite both rockfalls being highlighted in the image analysis change results (Figure 5, left panels). It was also noted that in the results for Camera 3, vegetation in the foreground of the scene is often highlighted as a change region due to movement in the wind, meaning that the changes caused by the small synthetic rockfalls are relatively minor compared to the overall amount of change detected. In contrast to the small synthetic rockfalls, both GPT-5 and Qwen3 correctly identified the large synthetic rockfall (Figure 5, right panel), which was clearly highlighted in the change detection results as the largest change region. In the unaltered images

for both cameras (i.e., without any synthetic rockfalls added), both VLMs correctly identified that no new rockfalls were present.

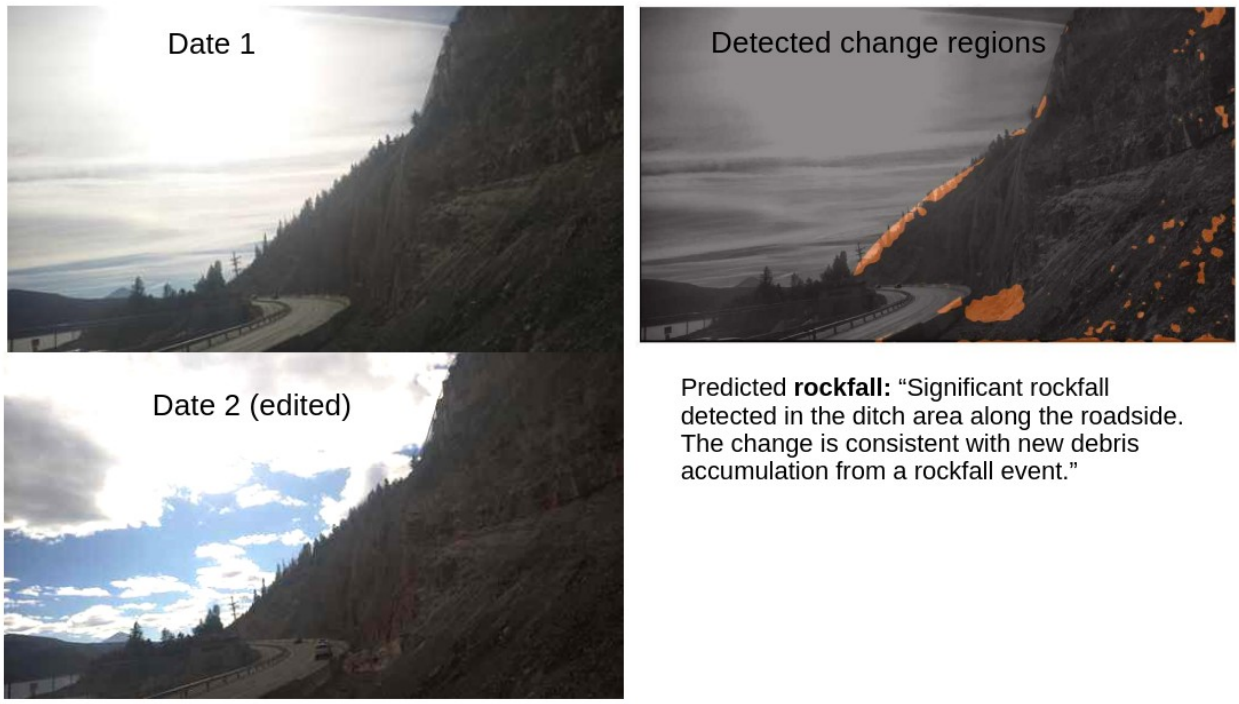

Figure 4 – Synthetic rockfall experiment for Dillon slope (Camera 2). (Left) Before and after images, where the bottom image is edited to include a synthetic rockfall. (Right) The detected changes region using the image analysis workflow, along with the classification output of the Qwen3 model.

Through-Time Evaluation

We applied the full analysis workflow to the entire monitoring dataset for all three cameras. Camera 1 detected several real rockfalls during the monitoring period as illustrated in Figure 6. All rockfalls occurred during or shortly after heavy rain or snowmelt events and were resolved in image change detection results within one day. The image change detection results successfully highlighted all rockfalls, with the smallest detected rockfall being approximately 30-40 pixels in diameter. Figure 7 shows the time series of daily detected change area at Camera 1 location between May and October 2025. The largest peaks in detected change area correspond to known rockfall events and major snow and rain storms. Note that at Camera 1, snow accumulation was minimal such that while there were some snow storms, they were never substantial enough to be flagged as such by the VLM. For dates with larger than 300,000 pixels of detected change area, the VLM analysis was triggered. Each of the three real rockfall events were followed 1-3 days later by a classification of rockfall by the VLM. No false positives were observed in the 2025 summer period, however we have some preliminary indication that the false negative rate (the rate of real rockfalls being missed), at least for the smallest rockfalls, is significant. This is illustrated by the smallest rockfall occurring on May 6, in which the VLM did not immediately classify the change as rockfall until four days after the event happened. In other

words, it failed to identify the rockfall in three out of four days in which it was clearly visible in image change results.

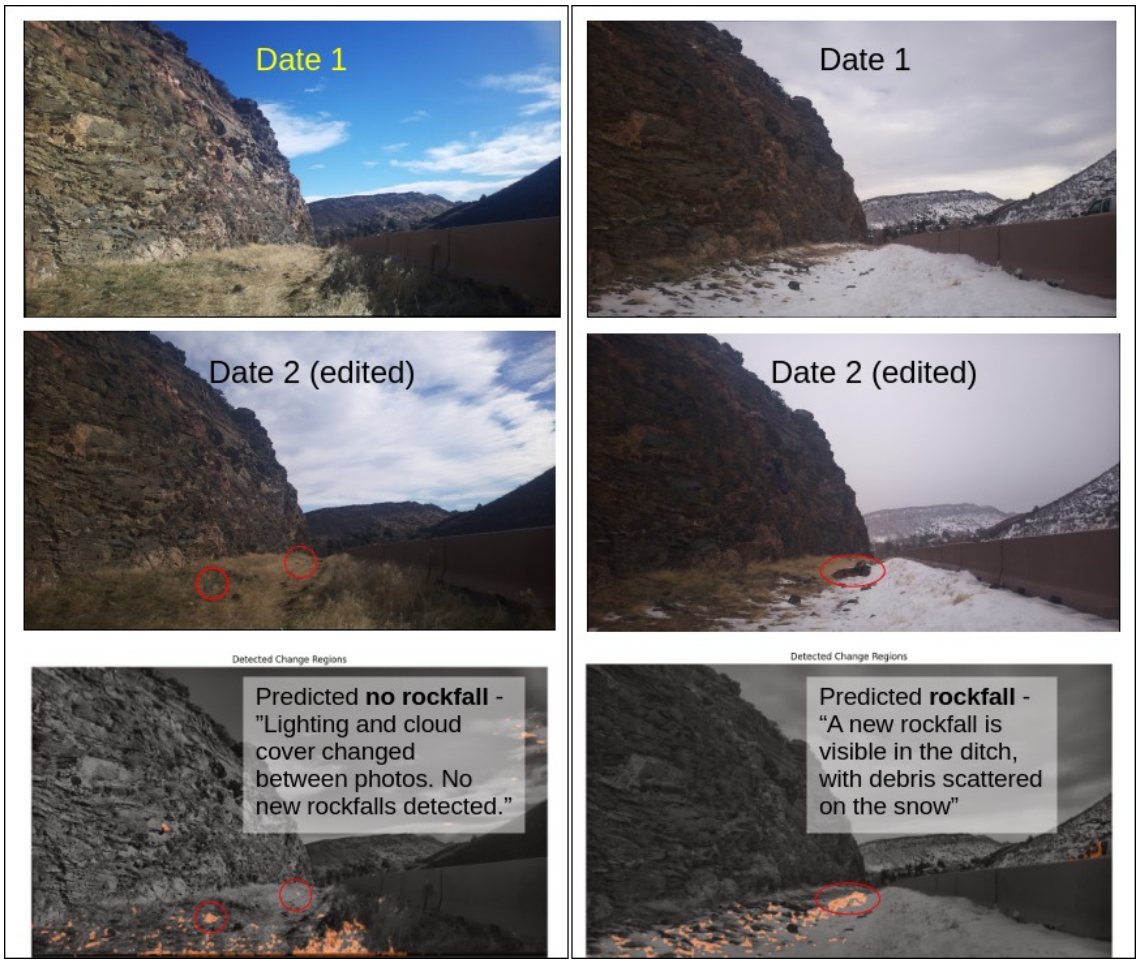

Figure 5 – Example of synthetic rockfall experiment for Camera 3. (Left) Experiment with two small rockfalls added to the ditch. (Right) One large rockfall added. The bottom panel on both sides shows the detected change regions along with the classification output of the Qwen3 model.

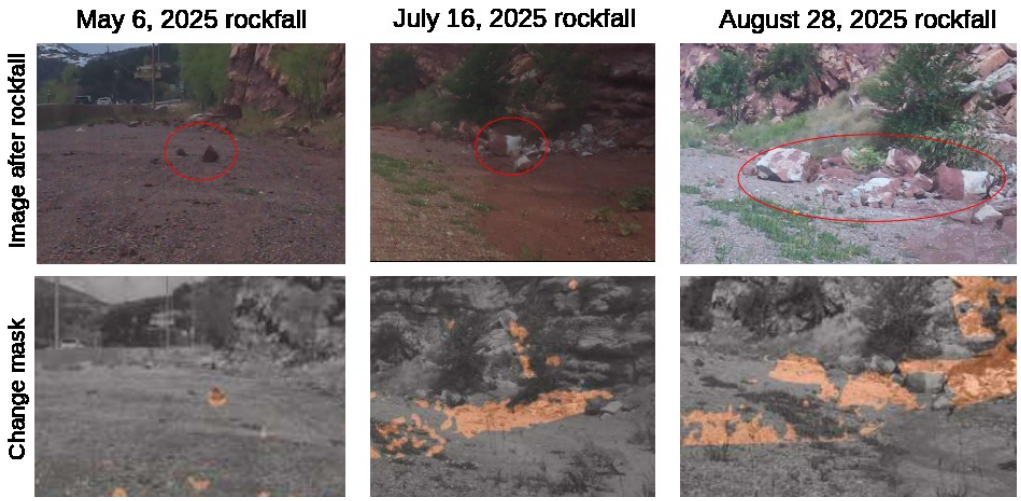

Figure 6 – Photos of real rockfalls detected at Camera 1 location during the monitoring period. (Bottom right) Change detection results for the August 28 rockfall, with pink areas representing significant changes.

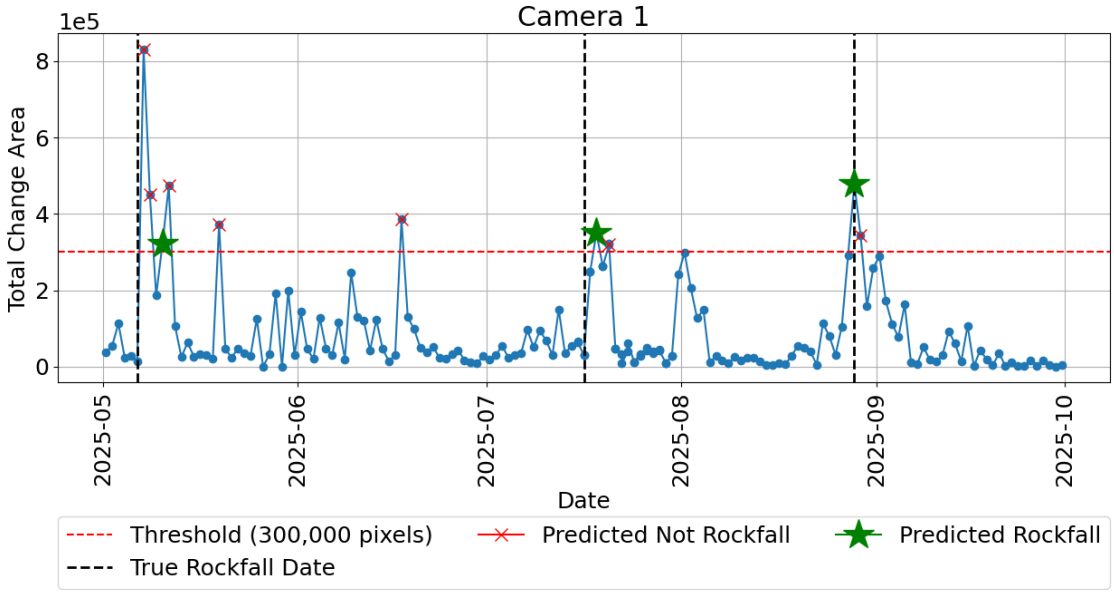

Figure 7 – Time series of daily detected change area at Camera 1 location over a 5-month period. Dates of real rockfalls are indicated by vertical black lines. Horizontal red line indicates the change area threshold used to trigger VLM analysis.

The Camera 2 slope change detection time series is presented in Figure 8. Camera 2 is focused on a ditch where the majority of the right side of the frame is filled with a talus slope which experiences regular slope wash in response to rain. This activity is readily picked up by the image change detection as broad changed areas, but these are not intended to be classified as rockfalls. In all but one instance, the VLM correctly identifies that these types of change are not rockfalls, but the justifications/explanations of the changes are usually incorrect. The model typically cites "lighting/shadow variations" or "vegetation movement" which are not present. In

two cases of snow events which caused large image changes, the VLM correctly identifies the source of the changes as "significant snow accumulation".

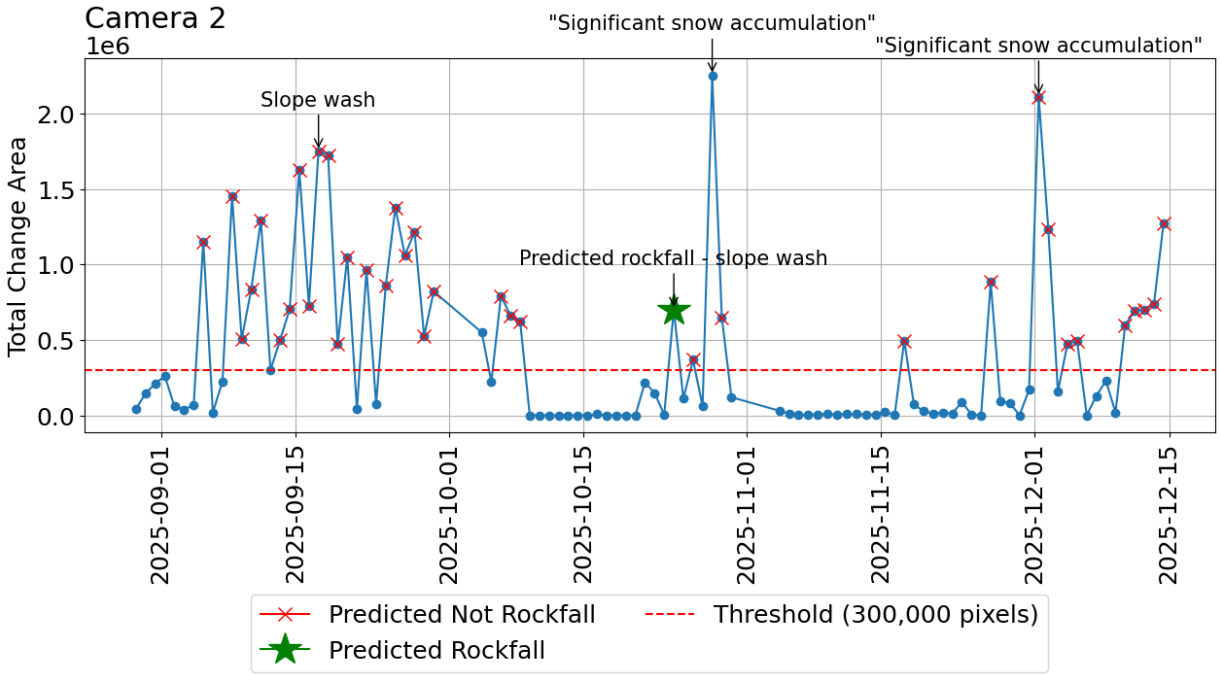

Figure 8 – Time series of daily detected change area at Camera 2 location over a 3-month period.

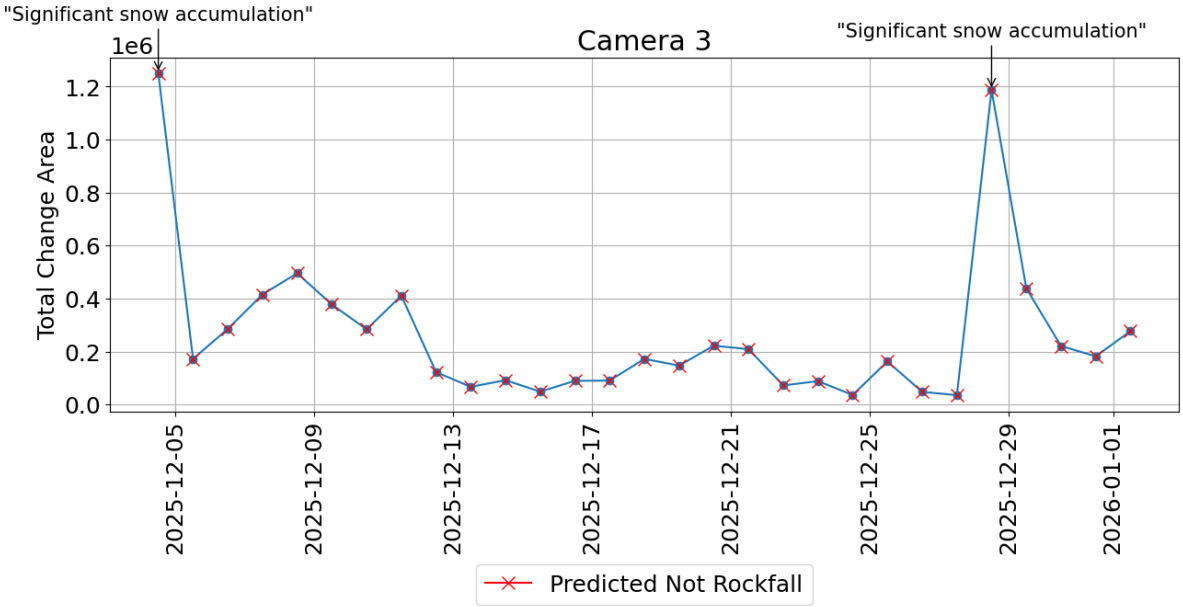

Figure 9 – Time series of daily detected change area at Camera 3 location over a 2-month period. Note that no threshold was used to limit VLM analysis. The VLM was applied to each image date.

The Camera 3 slope had the shortest time series of data available at the time of writing (Figure 9). However, it still is useful to illustrate the ability of the VLM to identify major snow events when they result in large change areas.

DISCUSSION AND CONCLUSIONS

Low-Cost Camera System Hardware

The camera system hardware developed in this study provides a low-cost solution for distributed rock slope monitoring. The total cost of materials is approximately $370 USD per unit, which is comparable to or lower than many commercial time-lapse camera systems. The system is designed to be freestanding and solar-powered, allowing for remote deployment without the need for external power sources. Installation is relatively simple and can be completed in a few minutes, making it feasible to deploy multiple units across a wide area. The use of off-the-shelf components also allows for easy replacement and maintenance of the system. One limitation of the current design is the reliance on 4G cellular connectivity for image transmission, which may not be available in all remote locations. However, satellite-based internet could be used instead.

Image Analysis and VLM Performance

The image-based change detection routine developed in this study shows high sensitivity to slope changes and has adjustable parameters to improve performance at specific sites. However, the high sensitivity has a downside in that the method is also sensitive to vegetation and slope wash, if present. Rain and snow storms also cause major slope changes. While adjustable, this sensitivity means that the image change detection alone will likely have a relatively high false positive rate and a low false negative rate.

The goal of applying a VLM to automatically interpret the images and change results is to filter out obviously non-interesting results and reduce the false positive rate. To this end, our results show that general purpose VLMs show promise at doing this effectively, although they clearly have not reached human levels of image understanding. We find that while the image change detection resolves small rockfalls, the VLMs did not reliably interpret rockfalls approximately 40 pixels across and smaller (e.g., Figure 5). In other cases, we find that the VLMs made different interpretations depending on what input data it was provided: in several cases the model would classify no rockfalls if the change map was removed, even if the rockfall in question was obvious to a human.

The existence of these major interpretation errors indicates that VLMs cannot be relied on to make critical decision. However, we find that generally larger changes are more accurately interpreted than smaller ones, and in a practical sense these changes are the ones we are most interested in.

Implications for Rock Slope Monitoring

The low-cost workflow developed in this study provides a tool with both research and practical applications for rock slope monitoring. The ease of installation enables rapid deployment of multiple camera units across a region or at specific sites of concern, and the automated image analysis reduces the need for manual inspection of potentially hundreds of images. The developed system has been automated such that the operator will receive an email notification within 15 minutes when a change is detected, and otherwise the system can run unattended. This approach could be particularly useful if budget constraints limit the number of systems that can be deployed. A high-resolution photogrammetric monitoring system, such as has been deployed at a site in Manitou Springs, Colorado (*17*) could cost on the order of approximately $30,000 USD. If our system was used instead, a transportation agency could deploy two monitoring units at each of 25 different slopes, albeit with lower resolution and accuracy, for the same cost. Such a distributed monitoring network would represent a step change over current practices, where some regions or agencies may not have a single instrumented site.

The main limitations of the current framework are related to the performance of the VLMs in accurately interpreting small changes in the images. Future work could focus on fine-tuning VLMs or developing models specifically for rockfall detection tasks. Additionally, longer-term monitoring at the current sites will provide more data to evaluate the performance of the framework under real-world conditions. Overall, the combined system has the potential to significantly enhance rock slope monitoring practices.

Conclusions

The main conclusions of this study are as follows:

1. A freestanding, solar-powered rock slope monitoring unit can be assembled from off-the-shelf components for approximately $370 USD and installed in a few minutes, much lower than the cost of a typical fixed photogrammetric installation at a comparable site.

2. The combined structural similarity and image differencing workflow resolved every real rockfall observed at the Camera 1 slope within one day of occurrence, including events as small as approximately 30-40 pixels in diameter.

3. General-purpose vision-language models (VLMs) correctly classified large rockfalls and major snow accumulation events without any task-specific training, but did not reliably interpret smaller rockfalls, and frequently supplied incorrect justifications. Overall, performance of VLMs was inconsistent.

4. On this evidence, general-purpose VLMs are currently best deployed as a triage filter to reduce the volume of imagery requiring manual inspection, rather than as an autonomous decision-maker. However, this conclusion should be re-evaluated as model capabilities change in the future.

REFERENCES:

1. Macciotta, R., C. Gräpel, T. Keegan, J. Duxbury, and R. Skirrow. Quantitative risk assessment of rock slope instabilities that threaten a highway near Canmore, Alberta, Canada: Managing risk calculation uncertainty in practice. *Canadian Geotechnical Journal*, vol. 57 (3), March 2020, pp. 337–353. doi: 10.1139/cgj-2018-0739.

2. Santi, P. M., C. P. Russell, J. D. Higgins, and J. I. Spriet. Modification and statistical analysis of the Colorado Rockfall Hazard Rating System. *Engineering Geology*, vol. 104 (1), February 2009, pp. 55–65. doi: 10.1016/j.enggeo.2008.08.009.

3. Weidner, L., and G. Walton. Monitoring the Effects of Slope Hazard Mitigation and Weather on Rockfall along a Colorado Highway Using Terrestrial Laser Scanning. *Remote Sensing*, vol. 13 (22), November 2021, p. 4584. doi: 10.3390/rs13224584.

4. Jaboyedoff, M., A. Abellán, D. Carrea, M.-H. Derron, B. Matasci, and C. Michoud. Mapping and Monitoring of Landslides Using LIDAR. In *Natural Hazards: Earthquakes, Volcanoes, and Landslides*, CRC Press, Boca Raton, Fla., 2018, pp. 397–402. doi: 10.1201/9781315166841.

5. Walton, G., A. Malsam, N. Oester Mapes, and B. Arpin. Forecasting and Mitigating Rockfall based on Lidar Monitoring: A Case Study from Colorado. *Transportation Research Record*, May 2023, Article 03611981231169530. doi: 10.1177/03611981231169530.

6. Mastrantoni, G., G. Santicchia, A. Cosentino, A. Molinari, G. M. Marmoni, and P. Mazzanti. Automatic photomonitoring analysis for spatiotemporal evaluation of rockfall failure hazard. *Engineering Geology*, vol. 339, September 2024, Article 107662. doi: 10.1016/j.enggeo.2024.107662.

7. Blanch, X., M. Guinau, A. Eltner, and A. Abellan. Fixed photogrammetric systems for natural hazard monitoring with high spatio-temporal resolution. *Natural Hazards and Earth System Sciences*, vol. 23 (10), October 2023, pp. 3285–3303. doi: 10.5194/nhess-23-3285-2023.

8. Cosentino, A., A. Brunetti, and P. Mazzanti. Photomonitoring as a Tool for Monitoring Landslides: A Technology within Everyone's Reach. *Transportation Research Record: Journal of the Transportation Research Board*, vol. 2679 (2), February 2025, pp. 1667–1675. doi: 10.1177/03611981241270173.

9. Su, G., W. Huang, C. Li, and X. Huang. Rockfall-YOLO Deep Learning Model for Rockfall Motion Object Detection. *Journal of Computing in Civil Engineering*, vol. 39 (6), November 2025, Article 04025104. doi: 10.1061/JCCEE5.CPENG-6268.

10. Wellman, E. C., *et al.* Observation of Rockfall in the Thermal Infrared. *Rock Mechanics and Rock Engineering*, December 2024. doi: 10.1007/s00603-024-04254-1.

11. Wang, Z., A. C. Bovik, H. R. Sheikh, and E. P. Simoncelli. Image quality assessment: From error visibility to structural similarity. *IEEE Transactions on Image Processing*, vol. 13 (4), 2004, pp. 600–612.

12. Catani, F. Landslide detection by deep learning of non-nadiral and crowdsourced optical images. *Landslides*, September 2020. doi: 10.1007/s10346-020-01513-4.

13. Hendrickx, H., M. Elias, X. Blanch, R. Delaloye, and A. Eltner. AI-based tracking of fast-moving alpine landforms using high-frequency monoscopic time-lapse imagery. *Earth Surface Dynamics*, vol. 13 (4), August 2025, pp. 705–721. doi: 10.5194/esurf-13-705-2025.

14. Zhang, J., J. Huang, S. Jin, and S. Lu. Vision-Language Models for Vision Tasks: A Survey. *IEEE Transactions on Pattern Analysis and Machine Intelligence*, vol. 46 (8), August 2024, pp. 5625–5644. doi: 10.1109/TPAMI.2024.3369699.

15. Zhang, H., *et al.* When Geoscience Meets Foundation Models: Toward a general geoscience artificial intelligence system. *IEEE Geoscience and Remote Sensing Magazine*, vol. 13 (4), December 2025, pp. 79–118. doi: 10.1109/MGRS.2024.3496478.

16. Areerob, K., *et al.* Multimodal artificial intelligence approaches using large language models for expert-level landslide image analysis. *Computer-Aided Civil and Infrastructure Engineering*, vol. 40 (19), August 2025, pp. 2900–2921. doi: 10.1111/mice.13482.

17. Walton, G., C. Christiansen, R. Kromer, and A. Silaev. Evaluation of rockfall trends at a sedimentary rock cut near Manitou Springs, Colorado, using daily photogrammetric monitoring. *Landslides*, August 2023. doi: 10.1007/s10346-023-02121-8.

18. Bradski, G. The OpenCV Library. *Dr. Dobb's Journal of Software Tools*, 2000.

19. OpenAI. Introducing GPT-5. OpenAI, San Francisco, Calif., August 2025. https://openai.com/index/introducing-gpt-5/. Accessed July 27, 2026.

20. Yang, A., *et al.* Qwen3 Technical Report. Report arXiv:2505.09388. arXiv, May 2025. doi: 10.48550/arXiv.2505.09388.

02. Uphill Without a Drill – HVSR as a flexible seismic method for inaccessible sites

Mishak Boshoff

Hager-Richter Geoscience

26 Kendall Pond Road, Derry, New Hampshire

603-458-8502

Mishak.Boshoff@Hager-Richter.com

Prepared for the 75th Highway Geology Symposium, September 2026

Acknowledgements

The author thanks Jeffrey Reid, P.G., José Carlos Cambero Calzada, P.G., and all my colleagues and friends at Hager-Richter Geoscience for their input and tutelage.

Disclaimer

Statements and views presented in this paper are strictly those of the author(s), and do not necessarily reflect positions held by their affiliations, the Highway Geology Symposium (HGS), or others acknowledged above. The mention of trade names for commercial products does not imply the approval or endorsement by HGS.

Copyright

Copyright © 2026 Highway Geology Symposium (HGS)

All Rights Reserved. Printed in the United States of America. No part of this publication may be reproduced or copied in any form or by any means – graphic, electronic, or mechanical, including photocopying, taping, or information storage and retrieval systems – without prior written permission of the HGS. This excludes the original author(s).

ABSTRACT

Highway geo-engineering investigations can occur in steep terrain and cramped urban environments. Bedrock information is often required at locations inaccessible to drill rigs. Where drilling is not feasible, geophysics can fill the data gaps. Seismic refraction, considered to be the industry standard geophysical method for determining depth and configuration of bedrock, is also subject to access limitations, as well as seismic noise constraints. Without reliable bedrock data, engineers may be forced to make decisions without critical subsurface information.

Horizontal to vertical spectral ratio (HVSR or H/V) is a seismic method which can be used to estimate bedrock depth at locations not suitable for seismic refraction or drilling. HVSR uses an ultra-portable seismograph to record ambient seismic noise. A mathematical relationship between the HVSR peak resonance frequency and bedrock depth is established for the site using measurements at locations with known bedrock depths. That relationship is then used to determine rock depths at other locations across the site. HVSR records can be acquired singly or along transects to develop bedrock profiles and/or contour plots.

Borehole data improves the precision of HVSR results, though the method still provides actionable depth estimates and clear topographic trends when boring data is scarce or absent. Bedrock depth information, based on HVSR data, facilitates geo-engineering decisions where there are gaps in critical subsurface information. In this paper we discuss three projects in which HVSR was used as the primary method or in concert with other geophysical methods to gather bedrock information.

At the first site we predicted bedrock depth in an approximately 1050-foot by 120-foot area of interest, at 42 individual stations. HVSR data were calibrated using 6 boreholes, and models of bedrock depth were generated on a station-by-station basis. Bedrock depth ranged from 90 to 120 feet with an estimated error of 6.1% (n = 4, SD = 8.5%).

At the second site we used a subset 31 of 56 stations positioned on boreholes to generate a linear regression model ($p = 2.2x10^{-16}$, $R^2 = 0.91$, SE = 3.63ft) describing the relationship between bedrock depth and HVSR peak frequency. Using the regression model, we predicted bedrock depth for a subset of 52 of 301 HVSR stations at the 95% Prediction Interval and Confidence Interval levels. Bedrock depth ranged from 48 to 70 feet.

At the third site we performed a reconnaissance survey of bedrock depth and topography using transects of HVSR stations spaced approximately 70 feet apart over five transects for a total of 11,000 feet, as well as nine passive shear wave velocity transects for calibration of the HVSR data. Bedrock depth and topography were visually represented in synthetic contour plots. Bedrock depth ranged from 20 to 300 feet and errors in estimates of bedrock depth were estimated at 10% - 20%.

1. INTRODUCTION

Highway projects are required in a variety of settings, each with their own challenges. In an increasingly developed world, and with travel in higher demand than ever [1], work must often be conducted under spatial constraints which can greatly inhibit geotechnical investigations [2]. Such constraints span from the anthropogenic to the biological and geological, from buildings and infrastructure to slopes and bluffs. Examples of natural impediments to subsurface investigations include wetlands, dense forests, environmentally sensitive sites, steep terrain, deep ravines, dunes, river crossings, floodplains, coastal bluffs with erosion hazard, active landslides, and loose sediments. Anthropogenic barriers to subsurface investigation include built up areas, airports, tunnels, cultural heritage sites, contaminated sites, and right of way constraints [2].

When engineers need bedrock information, a variety of tools are available: drill rigs can determine bedrock depth pointwise, and seismic or electrical methods can generate profiles showing depth and topography of subsurface layers. What options are available to an engineer when bedrock information is required in areas unavailable to the methods mentioned above?

A method that would allow for markedly better-informed decision making and more efficient progress on highway projects with access limitation would have the following characteristics:

- ultra-portable
- non-destructive
- operated by a single individual
- capable of providing relatively accurate estimates of bedrock depth in situations where no other method is feasible

In this paper we present the Horizontal to Vertical Spectral Ratio (HVSR or H/V) Method, as an effective tool to fill the niche described above [3]. The HVSR Method, also known as the Single Station Passive Seismic Stratigraphy Survey, uses seismic noise to estimate properties of unconsolidated overburden. By recording the Horizontal and Vertical components of the ambient vibrations at a single station, the fundamental resonance frequency (f_0) of the overburden at that point is determined. The mathematical relationship (Equation 1) between f_0, shear-wave velocity (V_s), and layer thickness (h) is constrained using observed variables to predict unknown variables [4]. Shear-wave velocity tends to be site-specific and once it is determined at one point it may be used to constrain Equation 1 at other on-site HVSR recording locations to predict sediment thickness.

Equation 1. relationship between resonance frequency, shear wave velocity, and bedrock depth

$$f_0 = Vs / (4h)$$

f_0	resonance frequency
Vs	shear-wave velocity

h layer thickness

Eq. 1

The system uses a seismometer capable of recording seismic motion on three main orthogonal directions, (North-South, East-West and Up-Down), and allows for the identification of resonance frequencies of subsoils in a passive, non-intrusive way. Ambient seismic noise, or microtremors, in the subsoil are generated by sources such as traffic, industrial activity, wind, and ocean waves. Microtremors recorded at a given site can vary greatly with respect to source and characteristics. However, it has been shown that the spectral division of the HVSR components has an effective normalization power: it cancels the source and enhances the subsoil response, so the HVSR remains unchanged with time [5].

The HVSR curves acquired along 2D profiles can be synthetically reproduced as contour plots, where colors indicate HVSR amplitude. Since high amplitude values of the HVSR peaks indicate high impedance contrasts in the subsoil (reflectors), a contour plot image can help identify the lateral continuity of the seismic reflectors. In this type of plot, the horizontal axis indicates the distance along the transect (on the ground surface) while the vertical axis indicates frequency.

There is error in the estimation of thickness/velocity using the HVSR spectral method introduced by certain geological conditions. General estimates of error for the calculation of bedrock depth range from under 10% for optimum conditions, increasing to as much as 50% where several complicating geologic factors are present.

2. GENERAL EQUIPMENT AND METHODOLOGY

The Horizontal to Vertical Spectral Ratio (HVSR) method consists of estimating the ratio between the Fourier amplitude spectra of the Horizontal to Vertical components of the ambient noise vibrations recorded at a single station. The ratio of the average HVSR frequency spectrum is used to determine the fundamental site resonance frequency, from which the bedrock depth can be estimated.

The HVSR data are acquired using a recording time of 10 - 30 minutes per station with the instrument axis pointed toward a common fixed direction to avoid potential directional effects from morphologic structures. The quality of the HVSR data depends largely on the coupling between the measurement unit and the ground surface. To optimize data acquisition several field procedures were followed. The recording unit was leveled and set on natural ground, avoiding loose soil and rocks, concrete, asphalt, etc. where possible. Also, wind may adversely affect the measurements, so the unit was sheltered in windy conditions by placing an inverted, weighted bucket over the instrument during recording.

We used a Tromino Zero system developed by Moho Science & Technology (Moho), located in Venice, Italy. The system is a seismometer capable of recording seismic noise motion on three main orthogonal directions, (North-South, East-West and Up-Down), and allows for the identification of resonance frequencies of subsoils in a passive, non-intrusive way. Microtremors generated by ambient noise, such as traffic, ocean waves, and wind, recorded at a given site vary over time. It has been shown that the spectral division of the HVSR components has an effective normalization power: that is it cancels the source and enhances the subsoil response, so the ratio of horizontal to vertical spectra remain unchanged with time [5].

The seismic data were analyzed using Grilla® 8.0 software, a commercially licensed software package developed by Moho. The processing involves selecting the most stable portions of the entire recording of HVSR at a given station. The selected portions are then averaged, producing a single HVSR curve for the station. The processing from this point can follow three different paths, each of which is discussed in further detail, using case studies, in the following sections.

As with all geophysical measurements, there is error in the estimation of thickness/velocity using the HVSR spectral method. In general, geologic conditions that may increase error in the determination of bedrock depth include the edges of sedimentary basins, narrow basins, areas with gradual transitions from weathered bedrock to competent bedrock, and areas of highly variable bedrock topography.

3. CASE STUDY 1

Scattered Points with Bedrock Depth Predicted Pointwise

3.1 Study design

At a confidential site in the northeast USA an HVSR survey was conducted as part of a geotechnical investigation in support of a tunnel project. The stratigraphy was reported to be fill at the surface, followed by a layer of organic deposits, estuarine deposits (clay and silt with sand lenses), glacial till, a layer of weathered rock, and finally bedrock at approximately 90 – 120 feet below ground surface. The terrain was level, though access for drilling was limited by swamps and built features. These same features, as well as seismic noise generated by highly active railways, roadways and industries excluded seismic refraction for subsurface characterization.

The chosen stations for HVSR recording were planned to be interpreted individually, as scattered points, though they were arranged in a coarse line to follow the area of interest for the investigation (Figure 1).

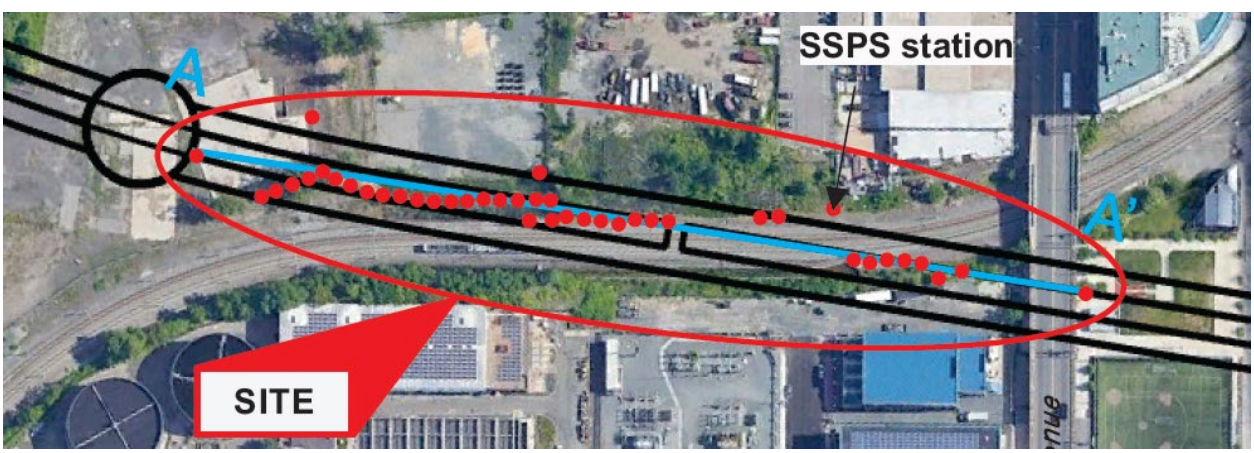

Figure 1. Site plan showing HVSR stations as red dots (SSPS refers to "single-station passive seismic" – another term for HVSR).

3.2 Data collection procedures

The fieldwork was conducted over two days, by a crew of two. The area of interest was the proposed path of the tunnel. 42 HVSR stations were located where site conditions were favorable

and arranged roughly linearly. Stations were spaced approximately 20 feet apart and installed in a matrix of fine gravel and fine-grained soil, using a recording time of 16 minutes per station. The positions of the stations were surveyed using a Trimble Geo 7X CM GPS system. Of the 42 data stations, 6 were positioned at boreholes where bedrock depth was known.

3.3 Data analysis

The shear-wave velocity was determined at each of the six borehole locations using the relationships described by Equation 1. This was done by generating a synthetic HVSR curve using the observed, borehole-derived bedrock depth and an assumed shear-wave velocity value as inputs into the model. The synthetic model was then compared to the observed average HVSR curve for the given station (Figure 2). The assumed shear-wave velocity was iteratively adjusted to minimize discrepancy between the synthetic and observed models, until an optimal shear-wave velocity was found. This process was repeated for each of the six borehole locations. Note that the peak frequency is linked to the fundamental resonance frequency of the soil, and the peak amplitude indicates the degree of impedance contrast between the overburden and bedrock, such that higher amplitude indicates higher contrast.

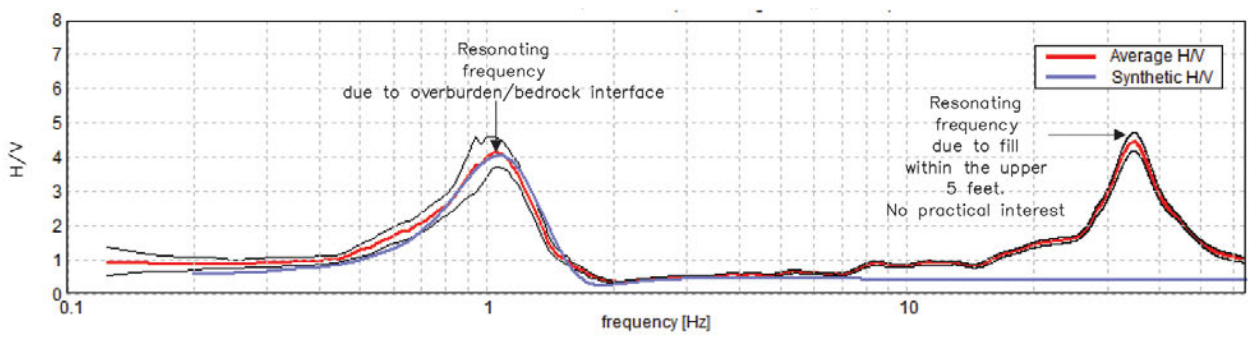

Figure 2. Synthetic and average observed curves of HVSR (H/V) vs. microtremor frequency at station #31.

For the remaining 36 HVSR recording stations an average HVSR frequency peak was determined, and Equation 1 was constrained with said peak frequency, as well as with the previously derived shear-wave velocities to determine bedrock depth on a station-by-station basis.

A few of the recording locations had sub-optimal natural ground for instrument emplacement, and this may have resulted in imperfect coupling between the instrument and the soil, adding noise and uncertainty to the predicted bedrock depth at those locations.

3.4 Results

Clearly defined frequency peaks were identified for all of the 42 recording stations in the study. An example HVSR peak is shown in Figure 2. A subset of the results was presented in tabular form (Appendix 1) showing station ID, coordinates (redacted), predicted bedrock depth, surface elevation, and bedrock elevation.

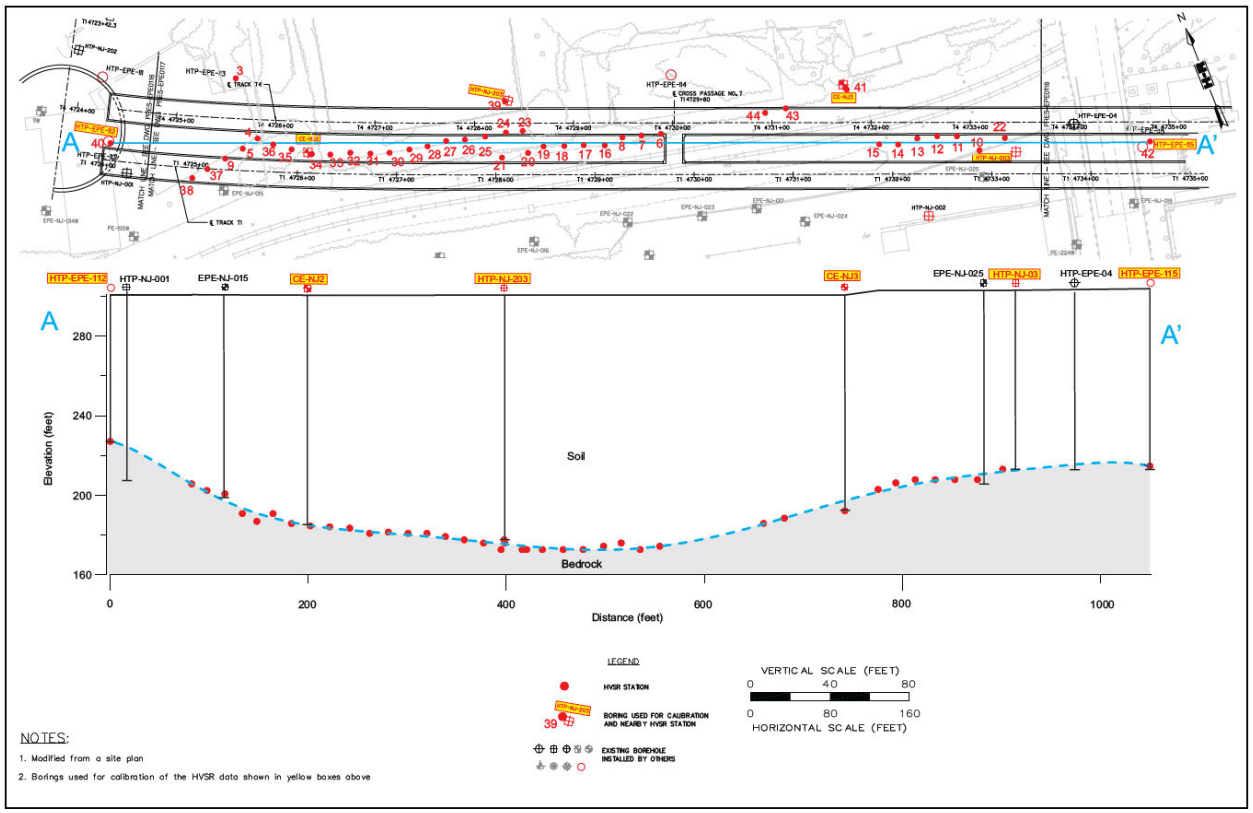

Figure 3. Schematic of HVSR recording stations and bedrock profile.

The results were also represented as a profile, beneath a schematic of recording locations to provide an intuitive model of bedrock depth (Figure 4). Note that the HVSR stations were not arranged truly linearly, so the profile shown in Figure 4 involves lateral extrapolation of the HVSR data, as well as interpolation between stations, introducing error into the model. Figure 4 also shows the discrepancy between observed and predicted bedrock depth at four locations where borehole data was available but not used as calibration points for the HVSR survey. The average difference between the depth of bedrock based on the borings versus the HVSR model was 6.1% with a standard deviation of 8.5%.

4. CASE STUDY 2

Scattered Points – Bedrock Depth Predicted by Regression

4.1 Study design

At a confidential site in the northeast USA a large HVSR investigation was performed as part of a geotechnical study supporting the design of a confidential infrastructure project. Boreholes on the site sampled overburden consisting of layers of fill, mud, sand, clay, and gravel over bedrock. The HVSR investigation was aimed at determining the depth and configuration of the bedrock surface in the many areas of the site where drill rig access was not feasible due to dense urban development. Seismic refraction was not possible on this site due to access limitation and the seismic noise generated by the residential and urban surroundings.

4.2 Data collection procedures

The fieldwork was conducted over six days, by a crew of one. The area of interest followed the alignment of the proposed structure, and included public park walkways, sidewalks, and landscaped areas. Data were acquired at 301 HVSR recording stations, including 56 stations positioned at borehole locations. Stations where bedrock depth was unknown were positioned along 20 separate straight-line transects and spaced approximately 20 feet apart, using a recording time of 10 minutes per station. The positions of the stations were tied to permanent features shown on site plans of the area of interest. For brevity only a subset of these data were used in the present paper, specifically 31 HVSR stations positioned on borehole locations and 52 HVSR stations where bedrock depth was to be predicted.

The instrument was placed and leveled on pavement or soil, avoiding loose material, cracks in the pavement, and other features deemed by the field personnel to be possibly detrimental to the HVSR recording quality.

4.3 Data analysis

The HVSR peak frequency was determined at each of the 31 borehole locations where bedrock depth was known, using the relationships described by Equation 1, and following the procedures described in section 2.1 above. These values were used to calculate a site-specific linear regression (Equation 2) based on the relationship between the bedrock depth (y) and the HVSR peak resonance frequency (f_r) of the main peak in the HVSR spectra. The fit of the data to polynomial regression functions was evaluated, and linear regression was determined as the best fit based on visual interpretation of the residual plot [6].

Equation 2. linear function used to predict bedrock depth based on HVSR peak frequency

$$y = b*(f_r) + c$$

where:

b, and c are empirically derived coefficients [7].

The regression model was significant, with a p-value of $2.2x10^{-16}$ at the 95% confidence level. The standard error was 3.63 feet. The residual plot for the HVSR recording locations with known bedrock depth from associated boreholes (training data) indicated a linear relationship between bedrock depth and HVSR peak frequency, with unbiased and homoscedastic residuals. The R^2 for the regression model was 0.91, suggesting the model explains 91% of the variability in bedrock depth [6].

Due to the HVSR recordings being performed sequentially, we performed a Durbin-Watson test for autocorrelation using the car package in R [8], and found no statistically significant evidence of autocorrelation. The Durbin-Watson statistic was 2.06, suggesting no autocorrelation. The p-value was 0.96, thus we failed to reject the null hypothesis that the residuals are not autocorrelated.

Prediction Intervals and Confidence Intervals were calculated for each of the 52 HVSR recording stations where bedrock depth was not known using a fitted regression model. For each HVSR peak frequency value, the predicted depth value was assigned uncertainty arising from both the estimation of the regression coefficients and the inherent scatter of the data about the model. The resulting 95% Prediction Intervals represent the range within which a new observation is expected to fall with 95% probability, assuming the model assumptions hold [6].

Confidence Intervals provide information about confidence in the regression model that generates the predicted bedrock depth. The Confidence Intervals indicate precision of mean estimated values of bedrock depth at particular HVSR peak frequencies; thus the 95% Confidence Intervals are narrower than the Prediction Intervals.

Prediction Intervals and Confidence Intervals widen away from the center of the observed bedrock depth data (boreholes) and during extrapolation, reflecting increasing uncertainty. These intervals were computed using standard regression theory and provide a realistic measure of uncertainty for predicted depths [6]. Statistical modeling and uncertainty analysis were performed in R [9].

Using a regression model to predict bedrock depth assumes the relationship between bedrock depth and HVSR peak frequency is linear in nature, and that the regression model captures the systemic variation in bedrock depth. It is also assumed that HVSR peak frequency values were accurately measured.

4.4 Results

Clearly defined frequency peaks were identified for 50 of the 52 recording stations in the study. The other 2 had vague but identifiable frequency peaks. Figure 5 shows the regression model with observed bedrock depths (training data), predicted bedrock depths, 95% Confidence Interval limits, and 95% Prediction Interval limits.

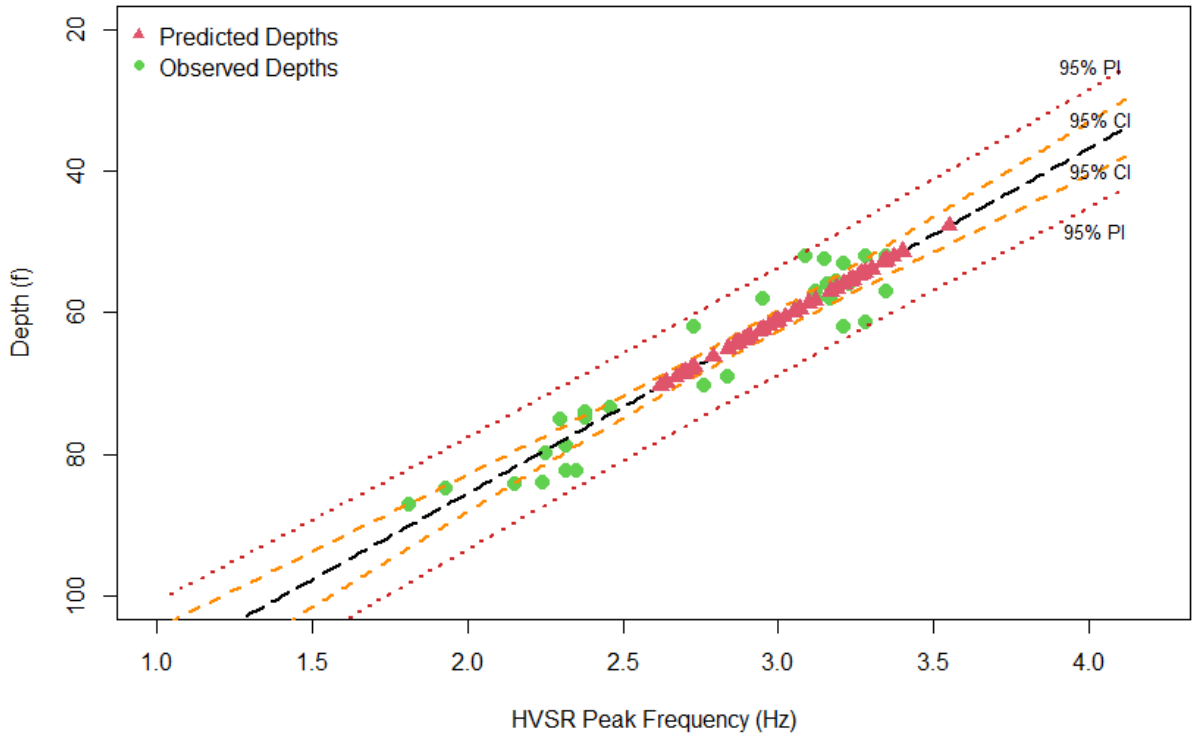

Figure 4. Linear regression model of bedrock depth predicted by HVSR peak frequency, with 95% Confidence Intervals and 95% Prediction Intervals

Figure 6 shows an example site plan, one of 20, with HVSR data stations shown in red along with the estimated bedrock elevations. Stations where boreholes were used to train the regression model are shown in purple with their reported bedrock elevation, based on coring. We note that some of the boreholes were completed after the HVSR survey and their final locations were different than the originally proposed locations at the time of the survey.

A small subset of the results were presented in tabular form (Appendix 2) showing station ID, coordinates, predicted bedrock depth, surface elevation, and bedrock elevation.

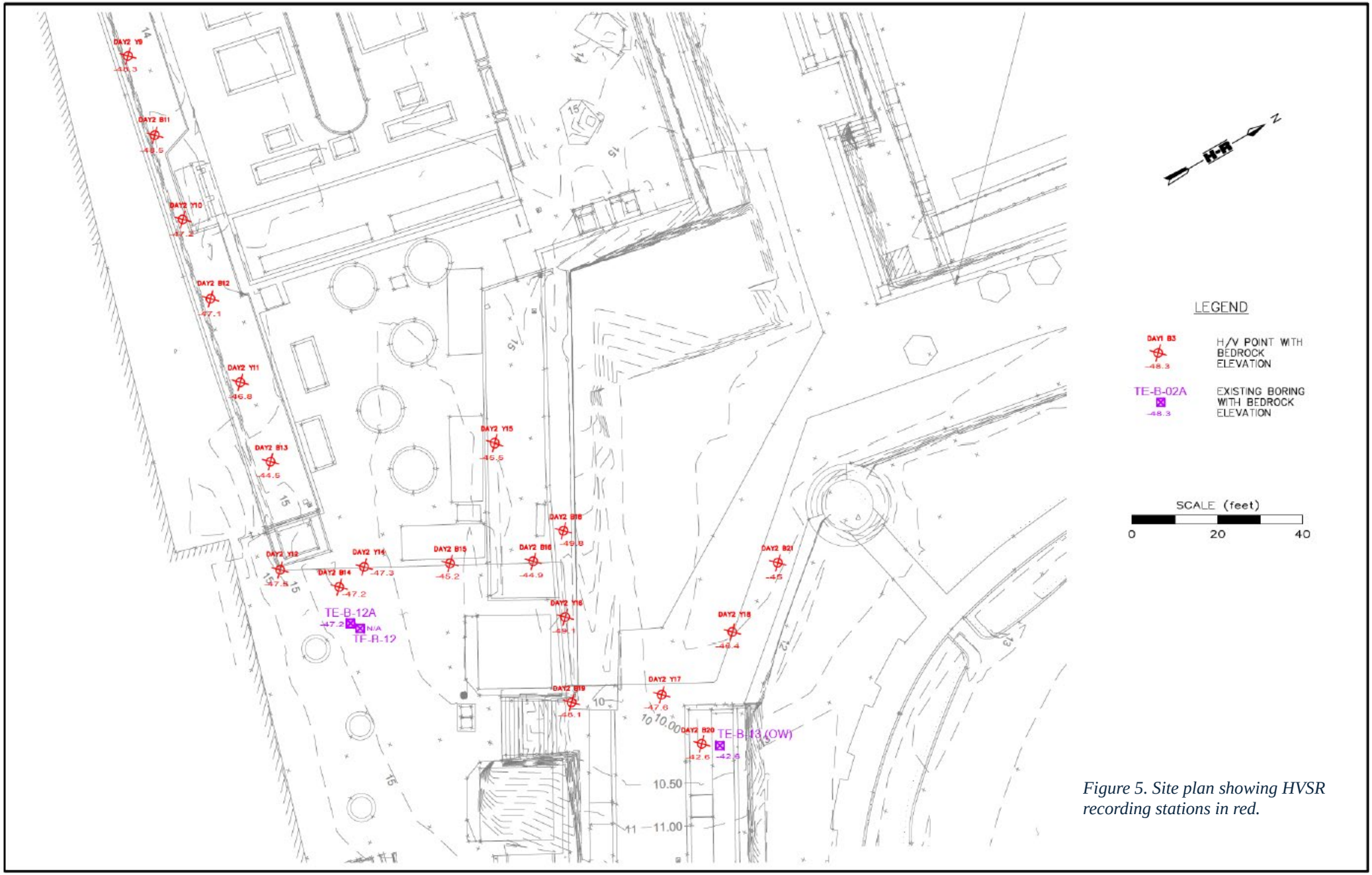

Figure 5. Site plan showing HVSR recording stations in red.

5. CASE STUDY 3

HVSR Profiles without Boring Calibration

5.1 Study design

The site was an undeveloped area in the southwest USA. The local geology consisted of early Proterozoic granitic rock underlying Quaternary and Holocene surficial deposits. The depths of the lithologic units were not known, though bedrock outcrops were visible at the site. The HVSR survey was aimed at providing reconnaissance, cost-effective estimates of bedrock depth and detection of coarse changes in geology to guide future investigations at the site. The remoteness, size of the site, and the low resolution requirements excluded drilling and seismic refraction as cost-effective options for this reconnaissance project.

Five transects were specified around the site, allowing HVSR data to be combined into profiles. To calibrate the HVSR data in the absence of boreholes, Passive Shear-wave Velocity testing (pVs), was conducted, distributed along the HVSR transects.

The (pVs) method produces a vertical shear-wave velocity profile at a single location by analyzing a particular type of seismic wave recorded on a multichannel record. The pVs method uses Rayleigh waves which are dispersive (meaning that the velocity is a function of the wavelength), and the amplitude of such waves decreases with depth. The Rayleigh wave velocity depends primarily on the shear wave velocities and layering of the subsurface material.

Rayleigh waves are a significant part of the ambient subsurface noise at most sites. Such noise includes wind, pedestrian and vehicular traffic, surface and subway trains, and construction activities. Although such noise can be troublesome for most seismic methods, it is the source of signals for the pVs method, and the higher the noise level, the better the results for this method.

5.2 Data collection procedures

The fieldwork was performed by a team of two personnel over five days. HVSR recording stations were spaced 50-70 feet apart, and transect length ranged from 840 feet to 3,660 feet, for a total length of 11,000 feet. Nine pVs transects were positioned over the HVSR transects at approximately even spacing. The positions of the transects are shown in Figure 3.

For acquisition of the pVs data low frequency (4.5 Hz) geophones were installed 10 ft apart along a straight line and connected to a seismograph. We used a 48-channel digital seismograph (Geometrics Geode) coupled to 24 geophones to acquire the pVs data.

The ambient noise was recorded for 30 seconds two or three times and examined to be sure that noise of sufficiently low frequency was present. If the noise was sufficient, then 10 to 15 such records were acquired. When the noise spectrum did not reach sufficiently low frequencies, then one person walked or ran along the test line during data acquisition to add low frequency noise to

the ambient noise.

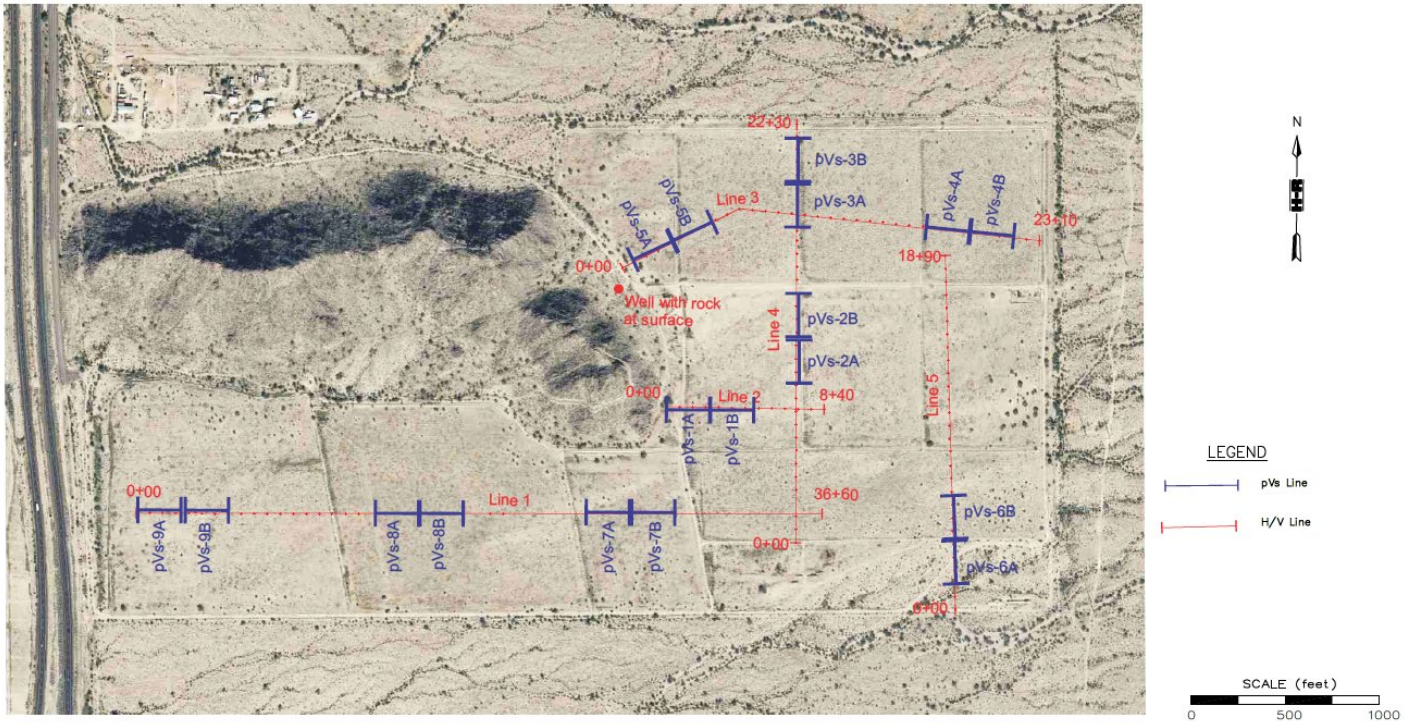

Figure 6. Transect locations for HVSR and pVs surveys at a confidential site in the southwest USA

5.3 Data analysis

The pVs data were analyzed using SeisOpt® ReMi™, a commercially licensed software package developed by Optim, Inc. located at the University of Nevada at Reno. Results consisted of tables showing shear wave velocity as a function of depth at the center of the transect.

The procedures described in section 2.1. above were followed to produce stable HVSR curves for each recording station. All the HVSR curves for a given transect were then combined longitudinally into a synthetic contour plot of distance versus depth (a profile), with HVSR on the z axis. The shear-wave velocity was determined at each of the 9 pVs transects and used as inputs when generating contour plots. The contour plots were adjusted for elevation.

When representing frequency versus depth, the HVSR curve is shown exactly as processed from the spectral analysis. The conversion from HVSR-frequency domain to HVSR-depth domain is achieved based on the user's defined assumptions about the V_s profile with depth. In the simplest cases, the V_s profiles with depth have the shape of an exponential law with different V_s gradients that vary with depth:

Equation 3. Relationship between shear wave velocity and depth

$$V_s(Z)=V_o(1+Z)^{\alpha}$$

Where:

$V_s(Z)$ = V_s at a given Z depth
V_o=V_s at the surface
Z= Depth
α= (alpha) V_s gradient with depth. The gradients for fine alluvial plains are better represented by small α values, commonly 0.25.

Site specific shear-wave velocity information was used to constrain the formula and determine the V_o and α coefficients that are applied to determine the 2D plots of depth versus distance shown in Figure 7.

Without boreholes to calibrate the HVSR data there is increased uncertainty associated with the bedrock depths determined this way. There is also experimental error in the velocities that are determined using the passive shear wave velocity seismic method. For the pVs method, the accuracy of V_{avg} is stated by Optim, Inc. to be 5-15%.

5.4 Results

The data quality for the survey was good, and clearly defined frequency peaks were identified for most of the data stations. The V_o (V_s at the surface) and alpha (α) were determined using the pVs data. V_o varied between 1,000 and 1,500 ft/s for α between 0.25 and 0.38.

In the synthetic contour plots shown in Figure 7, the color shades represent HVSR amplitude, and a consistent color scheme is used for all plots. Since high amplitude values of the HVSR (the so-called peaks) indicate high impedance contrasts in the subsoil (reflectors), a contour plot image can help identify the lateral continuity of the seismic reflectors. In this type of plot, the horizontal axis indicates the ground surface while the vertical axis indicates frequency.

Resonance occurs at interfaces where acoustic impedance changes. Acoustic impedance is a measure of resistance of acoustic energy to transfer from one layer to another and depends upon seismic velocity and density. A sufficient contrast must exist at the interface for it to be identified by the HVSR method. The stronger the contrast in impedance, the higher the amplitude of the relative spectral response (brighter colors on the profiles in Figure 7).

The peak of the frequency response spectrum (red and yellow in Figure 7) represents the estimated bedrock surface. Where the interface is strong and consistent (high impedance contrast), it is shown as a solid yellow line. Where the amplitude of the response drops (lower impedance contrast), but is still relatively consistent, it is shown as a solid white line. The combination of solid white and solid yellow lines represents the inferred bedrock surface.

For some of the profiles, additional resonating layers are present below the inferred bedrock surface. The interfaces between these layers occur at amplitude peaks and are shown as dashed white lines in Figure 3. Whether these interfaces represent a change in geology or a change in rock quality cannot be determined without ground truth from boreholes.

Based on the HVSR survey, the depth of competent bedrock varies between about 20 and 300 feet along Line 1. Rock is deepest at the west end, shallowing significantly to the east. The bedrock surface along Lines 2 and 3 varies from outcropping at the west ends of the lines to about 100 feet deep to the east. Lines 4 and 5 generally exhibit shallow bedrock at their south and north ends and deepen slightly in their centers to about 100 feet or so.

The only way to truly assess the accuracy of the derived model is to ground-truth the model against boreholes with known depths of bedrock. As indicated in the limitations section, the accuracy of depths determined is estimated to be in general about +/-10 – 20 %, based on having limited borings available for calibration.

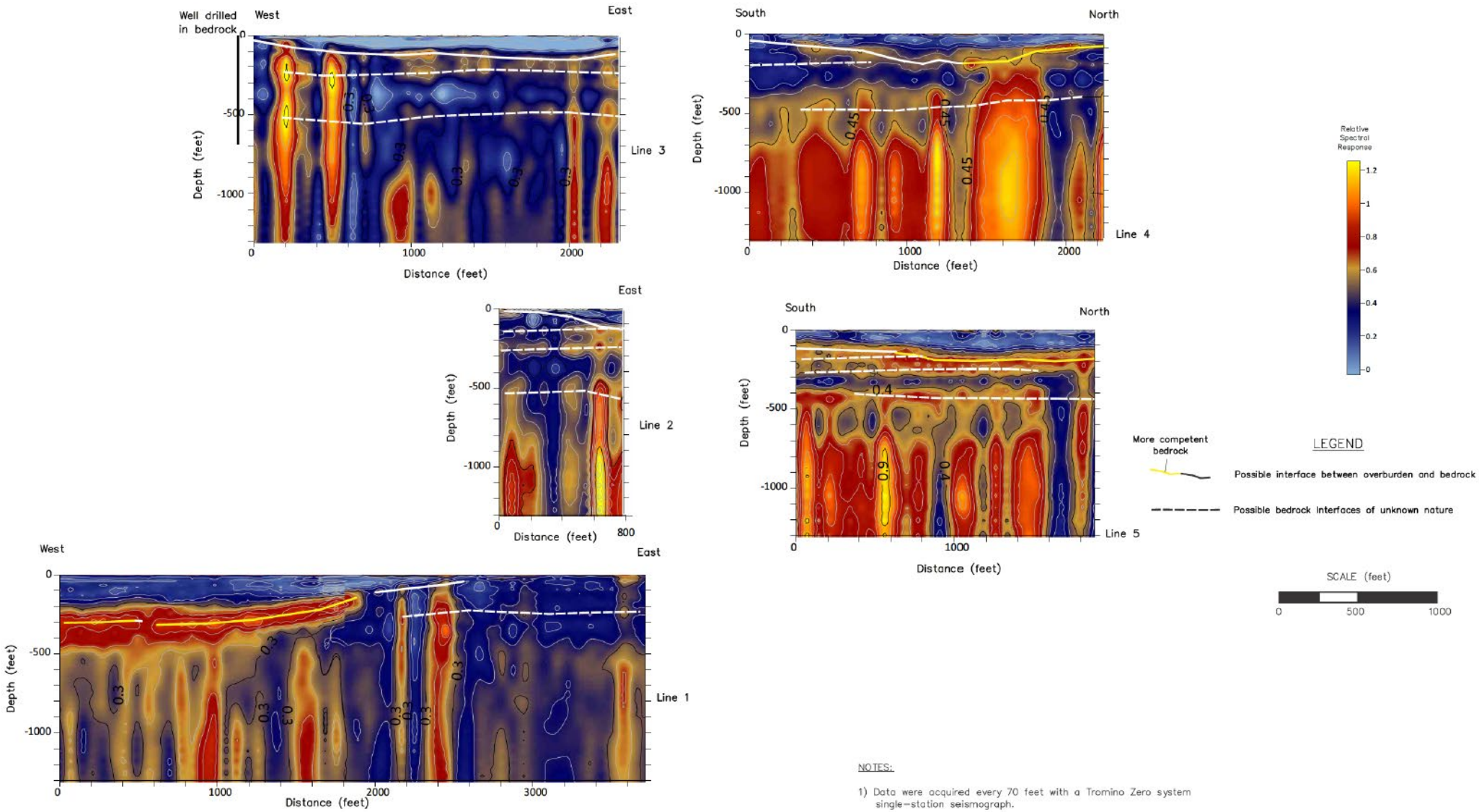

Figure 7. Synthetic contour plots of HVSR for five transects recorded at a confidential site

6. DISCUSSION

In section 3.1 we demonstrated how the product of the simplest HVSR survey type provides both intuitive visualization of trends in bedrock topography, especially when arranged roughly linearly (Figure 4), and specific estimates of bedrock depth at scattered locations accessible to a field operative on foot. The coarse measure of uncertainty used in this approach – comparing predicted bedrock depth to the nearest borehole-derived borehole depth – revealed an error of 6.15% (n = 4, SD = 8.5%). This translates to an error of around 7 feet for most of the study area, given that bedrock is around 100 feet deep on the site. Filling the data gaps between borings allowed engineers greater confidence than the alternative, which would have entailed interpolating depths across hundreds of feet between boreholes.

Although the particular study presented in Section 3.1 does not feature coarse changes in bedrock topography revealed by the HVSR survey but invisible to the borehole data, the HVSR survey does indicate the absence of such features, enabling engineers to proceed with confidence that they have not missed major bedrock features.

In Section 3.2 we examined how a more statistically sophisticated approach to processing HVSR data can allow powerful bedrock depth predictions with statistically robust ranges of predicted bedrock depth, when sufficient borehole data is available to train a regression model. In the example used in section 3.2 there were 31 data points with both borehole-derived bedrock depth and HVSR peak frequency information, however the method can function effectively with far fewer boreholes.

In Section 3.2, the margin of error at the 95% Prediction Interval level was around 7.6 feet for the subset of data presented in Appendix 2, which is an error of approximately 13% when taken as a percentage error. However, percentage error, being a function of bedrock depths, inflates errors at shallower bedrock depths. Furthermore, the borehole data at the site does indicate relatively heterogeneous bedrock depths (Figure 5). The statistical methods used to derive 95% Prediction Intervals take into account the natural scatter in the data – unlike the simpler percentage error method used in Section 3.1. This statistically rigorous method prevents overconfidence in predictions.

Finally, we described a third use-case of HVSR in section 3.3, where reconnaissance level bedrock depth and topography information was required over a large site. Other methods would have required far greater field effort and subsequent expense to provide the same coverage, and other methods may have provided higher resolution not necessary for the stage of the proposed project. With no borehole data for calibration, confidence in the HVSR data and resultant bedrock depth predictions is subjective and based solely on theory and prior experience with the method.

Interpretation of the contour plots produced by this survey (Figure 7) relies on the experience and prior knowledge of the geophysicist performing the interpretation and is thus non-repeatable. The geophysicist in question can provide a subjective assessment of confidence in the interpretations, in terms of the goals of the survey.

7. CONCLUSION

In this paper we discussed the results of three separate investigations where HVSR provided detailed and useful results in situations where site conditions precluded other methods, namely: comprehensive borehole programs and seismic refraction. We found that HVSR offered the highest confidence results when used in conjunction with borehole programs, and that the design of the survey can be tailored to efficiently match the necessary resolution requirements of the particular project.

We conclude that HVSR is an effective geophysical method for providing information on bedrock depth and topography when site conditions or project goals render other methods unfeasible, inefficient, or otherwise impractical.

REFERENCES

[1] S. H. &. T. H. Rashid, "Summer Driving Season Is Here, and More Americans Than Ever Are Hitting the Road," The Wall Street Journal, 3 July 2026. [Online]. Available: https://www.wsj.com/economy/consumers/summer-driving-season-is-here-and-more-americans-than-ever-are-hitting-the-road-80ba059c. [Accessed 22 July 2026].

[2] Federal Highway Administration, Geotechnical aspects of pavements: Chapter 4 - Subsurface investigation., U.S. Department of Transportation, 2006.

[3] Molnar, S., Cassidy, J. F., Castellaro, S., Cornou, C., Crow, H., Hunter, J. A., Matsushima, S., Sánchez-Sesma, F. J., & Yong, A., "Application of microtremor horizontal-to-vertical spectral ratio (MHVSR) analysis for site characterization: State of the art," *USGS Publication Warehouse,* 2018.

[4] U.S. Environmental Protection Agency, "Passive seismic (HVSR)," 16 December 2025. [Online]. Available: https://www.epa.gov/environmental-geophysics/passive-seismic-hvsr. [Accessed 20 July 2026].

[5] Y. Nakamura, "A method for dynamic characteristics estimation of subsurface using microtremor on the ground surface.," *Quarterly Report of Railway Technical Research Institute,* vol. 1, no. 30, pp. 25-33, 1989.

[6] R. Christensen, Plane Answers to Complex Questions: The Theory of Linear Models (5th ed.), Springer Nature Switzerland AG, 2020.

[7] I.-V. Seht. A. Wohlenberg, "Microtremor measurements used to map thickness of soft sediments," *Bulletin of the Seismological Society of America,* vol. 89, no. 1, 1999.

[8] J. Fox, A. Weisberg, "An R Companion to Applied Regression, 3rd Edition," Sage, 2019.

[9] R Core Team, "R: A Language and Environment for Statistical Computing," R Foundation for Statistical Computing, Vienna, Austria, 2023. [Online]. Available: https://www.R-project.org/. [Accessed 20 July 2026].

APPENDIX

Appendix 1. Table with subset of HVSR results from an investigation at a confidential site

Station ID / Borehole	Distance Along Profile (feet)	Easting (feet)	Northing (feet)	Overburden Thickness (feet)	Surface Elevation (feet)	Bedrock Elevation (feet)
40 HTP-EPE-112	0	[redacted]	[redacted]	73.8	300.9	227.1
38	82.3	[redacted]	[redacted]	95.1	300.9	205.7
37	97.7	[redacted]	[redacted]	98.4	300.8	202.4
9	115.8	[redacted]	[redacted]	100.1	300.8	200.7
5	133.4	[redacted]	[redacted]	109.9	300.7	190.8
4	148.1	[redacted]	[redacted]	113.8	300.7	186.9
36	164.4	[redacted]	[redacted]	109.9	300.7	190.8
35	183	[redacted]	[redacted]	114.8	300.7	185.8
34 CE-NJ2	202	[redacted]	[redacted]	116.0	300.6	184.6

Appendix 2. Table with subset of bedrock depths predicted suing regression model HVSR peak frequency as a function of bedrock depth from an investigation at a confidential site

Station ID	HVSR Peak Frequency (Hz)	Predicted Bedrock Depth (feet)	Lower 95% PI (feet)	Upper 95% PI (feet)	Margin of error (95%) (feet)
Day 1 B9	3.2	55.5	47.9	63.2	7.7
Day 1 B10	3.3	54.8	47.1	62.5	7.7
Day 1 B14	3.0	60.6	53.1	68.2	7.6
Day 1 B15	3.0	61.9	54.3	69.4	7.6
Day 1 B16	2.9	63.3	55.8	70.9	7.6
Day 1 B17	3.0	61.4	53.8	69.0	7.6
Day 1 B18	3.0	62.4	54.8	69.9	7.6
Day 1 Y9	3.4	52.1	44.4	59.9	7.7
Day 1 Y10	3.3	52.9	45.1	60.6	7.7

03. Mapping What We Can't Touch: LiDAR-Driven Rock Structure Modelling for Safer Highways

Will N. Brandenberger, PE, PG

HDR Inc.
1670 Broadway, Suite 3400
Denver, CO 80202
will.brandenberger@hdrinc.com

Prepared for the 75th Highway Geology Symposium, September 2026

Acknowledgements

The author thanks the technical and field teams at HDR Inc. and the transportation and water-development partners whose projects provided the case histories discussed in this paper. The author also thanks the geologists, rope-access personnel, surveyors, drilling crews, geophysics specialists, and software users who collected, reviewed, and reconciled the field, point-cloud, borehole, and three-dimensional modeling datasets. Special thanks are given to David Crotsley, the fearless leader of the Denver Geotechnical Group at HDR.

Disclaimer

Statements and views presented in this paper are strictly those of the author(s), and do not necessarily reflect positions held by their affiliations, the Highway Geology Symposium (HGS), or others acknowledged above. The mention of trade names for commercial products does not imply the approval or endorsement by HGS.

Copyright

Copyright © 2026 Highway Geology Symposium (HGS)

All Rights Reserved. Printed in the United States of America. No part of this publication may be reproduced or copied in any form or by any means - graphic, electronic, or mechanical, including photocopying, taping, or information storage and retrieval systems - without prior written permission of the HGS. This excludes the original author(s).

ABSTRACT

High-resolution terrestrial and unmanned-aerial LiDAR was used on three infrastructure projects to collect supplemental rock discontinuity data where direct measurement was limited by traffic exposure, height, tunnel geometry, or rope-access constraints. This paper evaluates LiDAR-based discontinuity mapping as a supplemental field data collection method by comparing LiDAR-derived orientations and mapped structural sets with conventional hand mapping, rope-access scanline mapping, tunnel observations, and other geologic data. The case histories include the Elephant Butte Tunnel in California, the Stagecoach Trail highwalls in Montana, and the left abutment of the LaPrele Dam Replacement Project in Wyoming. The evaluation indicates that LiDAR can increase mapped coverage and reduce direct exposure to difficult or hazardous terrain; however, LiDAR measures exposed surfaces only and can be affected by line-of-sight geometry, occlusion, vegetation, resolution, weathering, and surface conditions. The LiDAR datasets were primarily used to evaluate discontinuity orientation and structural-set classification. Where sufficient exposed surface was available, mapped plane size, trace length, and apparent spacing provided additional context, but these values were reviewed as exposed-surface measurements rather than direct measurements of subsurface persistence. Reviewed datasets were used for stereonet comparison and, where supported by other observations, can inform structural surfaces in three-dimensional geologic models. The results support a combined workflow in which LiDAR is used to improve spatial coverage, field mapping is used to check geologic meaning, and three-dimensional models are used only where the structural interpretation is supported by sufficient observations.

INTRODUCTION

Rock mass characterization for highway and infrastructure projects commonly requires measurement of bedding, foliation, joints, and other discontinuities that control rock mass behavior. These measurements are often needed on steep cuts, tunnel crowns, canyon walls, and abutments where direct access is limited. Conventional field mapping remains necessary, but the resulting dataset can be biased toward accessible parts of the exposure.

Terrestrial laser scanning (TLS) and unmanned-aerial vehicle (UAV) LiDAR provide an additional means of collecting structural data from exposed rock surfaces. After a point cloud is processed into a triangulated mesh, discontinuity orientations and other exposed-surface measurements can be extracted from areas that are difficult or impractical to measure directly. These measurements are useful only after geologic review because the point cloud records surface geometry and does not, by itself, identify geologic origin or persistence.

The objective of this paper is to evaluate LiDAR-based discontinuity mapping as a supplemental field data collection method. The evaluation focuses on where LiDAR improves mapping coverage, where the LiDAR-derived structural data agree or disagree with conventional field observations, and what limitations should be considered before using LiDAR-derived structural data in stereonet analysis or three-dimensional geologic modeling. Three case histories are used: the Elephant Butte Tunnel on State Route 70 in Plumas County, California; the Stagecoach Trail project in Billings, Montana; and the left abutment mapping for the LaPrele Dam Replacement Project in Converse County, Wyoming. The paper does not present independent stability analyses or design recommendations for these projects.

Table 1. Case Study Roles in the Data-Collection Evaluation

Case Study	Primary Geometry	Data Sources Used in Paper	Evaluation Focus
Elephant Butte Tunnel, California	Unlined granitic highway tunnel with inaccessible crown	TLS point cloud, tunnel mesh, stereonets, inspection observations	TLS documented crown and wall structures that were difficult to measure directly from the roadway.
Stagecoach Trail, Montana	South- to southwest-facing sandstone highwalls along proposed trail infrastructure	UAV LiDAR, hand measurements, stereonet comparison, top-of-rock model	UAV mapping increased highwall coverage; hand mapping provided checks on smaller features and surface conditions.
LaPrele Dam Replacement Project, Wyoming	Left-abutment canyon wall and foundation excavation in sedimentary rock	Rope-access scanlines, left-abutment rock-wall LiDAR, televiewer/core data	Left-abutment wall scans required comparison with rope-access and subsurface data to evaluate bedding and joint representation.

METHODOLOGY

Data Acquisition and Point-Cloud Preparation

The projects used high-density TLS for tunnel and canyon-wall exposures and UAV-derived data for broader topographic and highwall mapping. The raw point clouds were registered to project coordinate systems and processed to remove vegetation, vehicles, utilities, loose anthropogenic features, and other non-rock returns where practical. Where pointcloud data

is poor or heavily vegetated, cleaning and meshing of the 3D datasets can improve resolution for discontinuity extraction. Deciding upon if discontinuity extraction should be done on the pointcloud or a mesh is a project by project decision. This process is visualized in Figure 1.

Figure 1. Point-Cloud Processing Workflow Used to Develop a Three-Dimensional Mesh (2)

Discontinuity Extraction and Field Comparison

The discontinuity extraction process used geologist-guided point-cloud review. Representative planes or structural sets were selected in the point cloud or mesh, and Maptek Pointstudio software were used to search for surfaces within user-defined angular and size tolerances. At Stagecoach Trail, discontinuity data were selected from the UAV-derived dataset and compared with hand measurements collected during the field visit. At LaPrele, rope-access scanline mapping and the left-abutment rock-wall scan were reviewed together to evaluate which structural sets were represented by each data source.

Field comparison focused on three questions. First, do the LiDAR-derived structural sets agree with physically measured orientations where both are available? Second, does LiDAR document exposed structures that could not be reached safely by field personnel? Third, what structures are underrepresented or missed because of scan geometry, occlusion, weathering, vegetation, or point-cloud resolution?

Three-Dimensional Model Integration

After field comparison and geologic review, the structural data were used to develop reviewed mapping datasets. Stereonets provided a compact way to compare LiDAR-derived and physically measured orientations. Three-dimensional models were used, where appropriate, to evaluate how reviewed discontinuity measurements could inform structural surfaces in Leapfrog

Works. These surfaces should be treated as interpretive model inputs and not as independent confirmation of discontinuity persistence.

The workflow followed a repeatable sequence: collect point-cloud and field data; extract candidate discontinuity planes; compare the results against hand mapping, televiewer, core, geophysical, and field observations; remove false or non-geologic features; and use the reviewed dataset for stereonet comparison and, where supported, structural-surface modeling.

CASE STUDY 1: ELEPHANT BUTTE TUNNEL REMOTE MAPPING

Project Setting

The Elephant Butte Tunnel is an unlined horseshoe-shaped highway tunnel on State Route 70 in Plumas County, California. The tunnel is approximately 1,200 feet long and carries two lanes of traffic with narrow shoulders. Historical records indicate that rockfall has occurred since the tunnel was constructed in 1937, and the frequency and size of rockfalls have increased in recent years (2).

The tunnel is excavated in the Grizzly Creek Pluton, described as a coarse-grained hornblende-biotite-quartz-plagioclase monzotonalite that locally grades into diorite. The rock mass has a strong exfoliation structural trend that produces sheets and slabs roughly parallel to the modern topographic surface. In the tunnel crown, exfoliation surfaces combine with cross-cutting joints to form detachable roof blocks (1, 2). A view of the rock bedding and cross-cutting joint relationship within the tunnel is provided as Figure 2.

Figure 2. View of exposed rock within the Elephant Butte Tunnel

Data Collection

The tunnel case provides an example of TLS mapping where the primary exposed surfaces were difficult to access directly. The crown and upper walls would require lane closures, manlift access, or other controls for conventional measurements. LiDAR imagery collected in July 2024 provided point clouds of the left and right halves of the tunnel along the crown centerline. The data was collected by a truck-mounted TLS scanner manned and operated by CalTRANS. The point clouds were processed in PointStudio and Leapfrog to create triangulated mesh models of the tunnel interior, following the general workflow shown in Figure 1. Field measurements by HDR geologists were taken over two days of lane closures along the tunnel walls and at several perpendicular tunnel outlets.

The 3D mesh model of the tunnel can be colorized for dip direction, which can help in visually selecting discontinuities. It also provides a clear image of how discontinuities are presented in the 3D model. A view of this is provided as Figure 3.

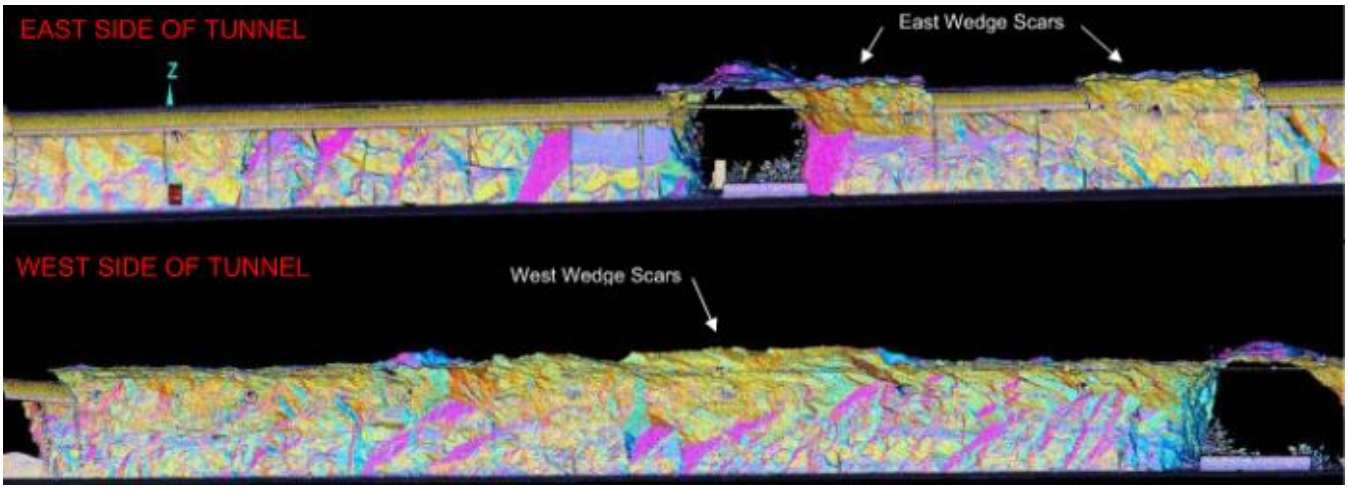

Figure 3. View of Elephant Butte Mesh, Colorized for Dip Direction of Surfaces

Six structural sets were identified from the tunnel mesh and plotted against measurements taken in the field by experienced geologists using the RocScience DIPS software. The mean orientations from the project report are summarized in Table 2, and the LiDAR-derived stereonet outputs are shown in Figure 2.

Table 2. Elephant Butte Tunnel Rock Mass Joint Set Orientations

Joint Set	Mean Dip (degrees)	Mean Dip Direction (degrees)	Interpretive Note
1	28	297	Low- to moderate-angle structural surface associated with exfoliation/topographic release.
2	69	130	Steep joint set identified from the tunnel mesh.
3	62	252	Steep joint set identified from the tunnel mesh.
4	85	013	Near-vertical set identified on the crown and walls.
5	63	112	Steep joint set identified from the tunnel mesh.
6*	36	292	Foliation plane measurement.

** Foliation plane measurements. Values from the Elephant Butte Tunnel stabilization evaluation report (2).*

Data-Collection Evaluation

For the tunnel, TLS increased the mapped area by allowing the crown and upper walls to be reviewed from the point cloud. These surfaces are difficult to map directly and consistently from the roadway. The mesh allowed the same exposed surfaces to be reviewed after the field visit and provided a reproducible basis for assigning discontinuity sets. The principal limitation was that LiDAR measured exposed geometry, not internal persistence. In general, it can be gleaned from Figure 3 that field and LiDAR derived measurements match aside from with regard

to Set 1. Set 1 was particularly prominent along the tunnel crown where physical access by HDR geologists was not feasible. In this case, it was necessary to carefully check the discontinuity set on the 3D mesh and validate that the measurements were accurate and not false readings.

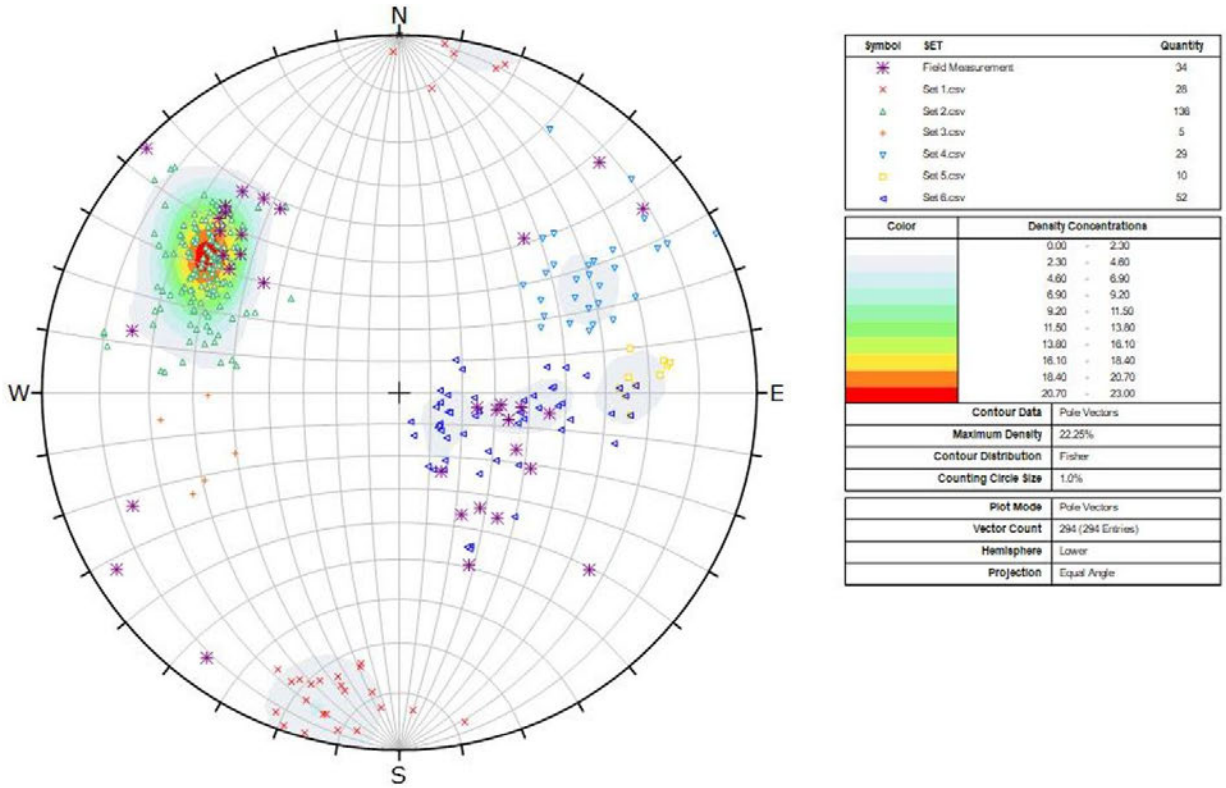

Figure 3. Elephant Butte Tunnel Stereonet Output Used to Compare Joint-Set Orientations of Field and LiDAR-Derived Datasets (2)

CASE STUDY 2: STAGECOACH TRAIL FIELD-MAPPING COMPARISON

Project Setting

The Stagecoach Trail project is located along the sandstone bluffs of the Rimrocks in Billings, Montana. The site includes south- to southwest-facing highwalls near Zimmerman Trail Road and proposed trail infrastructure. The competent sandstone cliffs are associated with the Eagle Formation, while the lower slope-forming material includes colluvium and shale bedrock associated with the Telegraph Creek Formation (3).

The April 7, 2025 field visit documented changes in rock mass character from east to west, including differences in block size, bedding expression, weathering, calcite-rich sandstone, dissolution features, and local raveling. Measurements of rock bedding and discontinuity orientation were collected by experienced HDR geologists. Separately, a UAV drone mapping program was performed at the project site which focused on the cliffs above and at the project area. A view of the project area with some notable points of interest is provided as Figure 4.

Figure 4. View of the Stagecoach Project Area with Notable Areas of Interest (3)

Data Collection

The Stagecoach Trail provided a comparison between UAV-based structural mapping and conventional field measurements. Digital discontinuity data were interpreted from high-resolution UAV data and plotted on stereonets in Dips. Field measurements collected at accessible portions of the highwall were added to the stereonet to compare against the digital data and to document smaller features that were not readily resolvable in the point cloud.

The two datasets provided different types of information. UAV mapping provided broader coverage of steep and elevated surfaces that could not be mapped efficiently from the ground. Field mapping provided direct confirmation of bedding, smaller-scale joints, weathering characteristics, calcite-rich zones, and observed surface conditions. The comparison supports use of a combined workflow in which the point cloud expands mapped coverage and field mapping provides geologic confirmation. A sample view of the extracted discontinuities on the 3D LiDAR dataset is provided as Figure 5 to visually show how the extraction presents on the model.

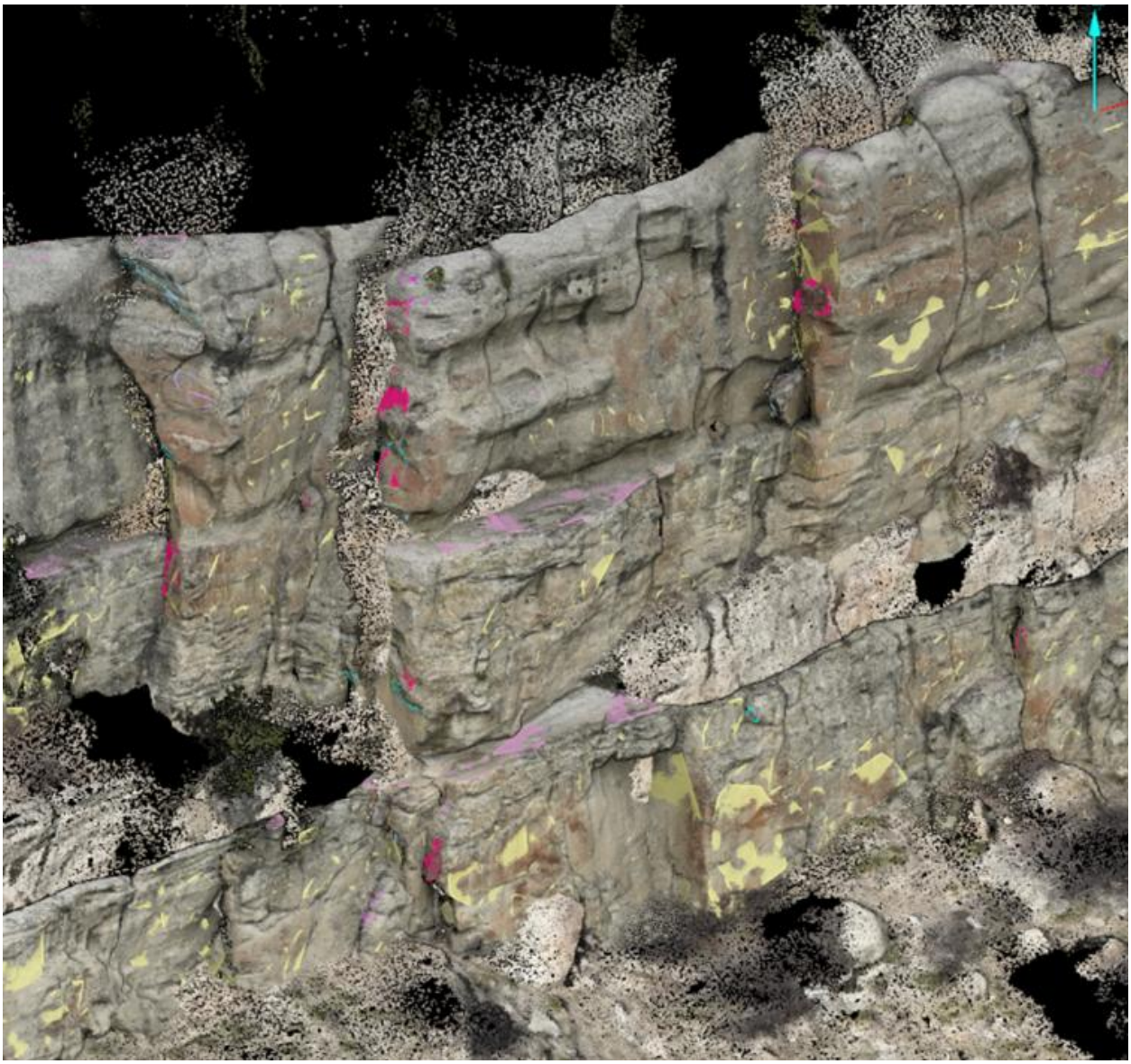

Figure 5. View of Discontinuity Sets As-Measured on the 3D Pointcloud

Data-Collection Evaluation

The stereonet comparison in Figure 6 indicates that the LiDAR-derived dataset and the smaller hand-measured dataset captured similar principal discontinuity trends. The LiDAR-derived dataset also provided a larger number of measurements and better coverage of elevated highwall exposures.

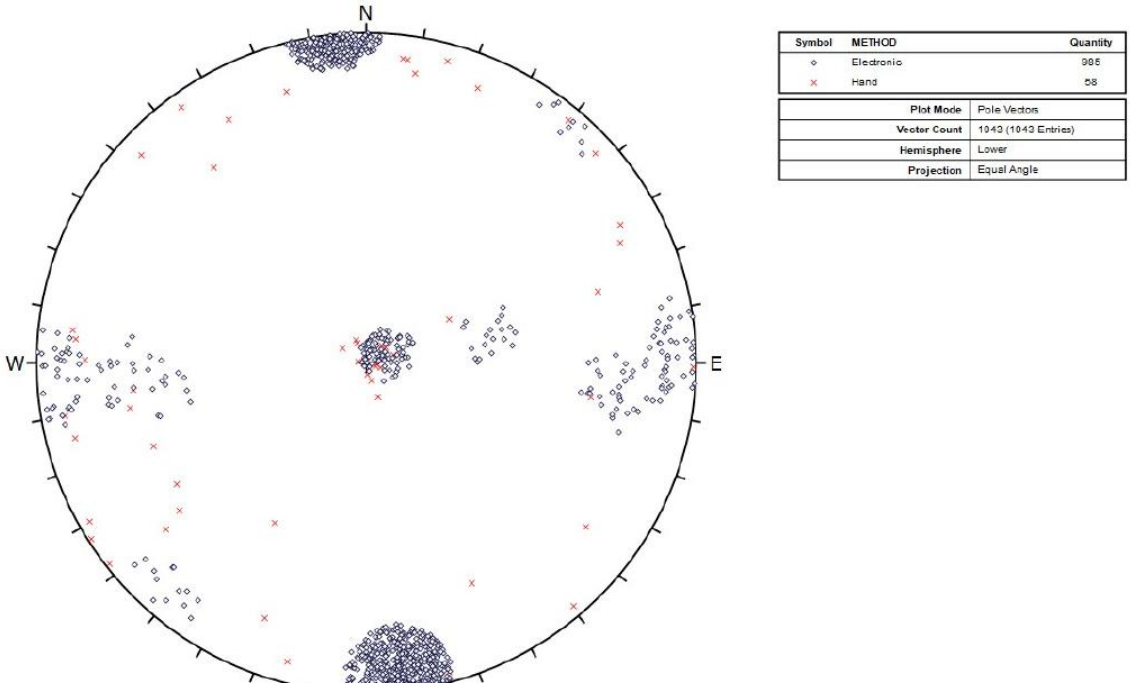

Figure 6. Stagecoach Trail Stereonet Comparing LiDAR-Derived and Hand-Measured Discontinuities (3)

The Stagecoach Trail data indicate that measurement count alone is not sufficient to evaluate a structural dataset. The UAV-derived dataset provided more measurements and captured elevated discontinuity surfaces that were not practical to reach from the ground. The smaller hand-measured dataset provided a check on surface origin, weathering, joint condition, and smaller discontinuities. Both datasets were needed to evaluate the reliability of the discontinuity mapping. It is also particularly helpful to determine frequency of orthogonal joint sets within sandstone bedrock. Field measurements encountered many near-vertical orthogonal measurements, but electronic measurement confirmed which orthogonal joint sets were most prevalent along the cliff band.

CASE STUDY 3: LAPRELE DAM LEFT-ABUTMENT HIGHWALL MAPPING

Project Setting

The LaPrele Dam Replacement Project is located in Converse County, Wyoming, where the proposed roller-compacted concrete dam foundation and left abutment are sited in a canyon cut into Paleozoic sedimentary rock. The local foundation units include limestone, dolomite, sandstone, siltstone, and claystone intervals, and the geologic interpretation evolved through multiple investigation phases. The proposed design includes large cut slopes into the existing canyon to form the footprint of the proposed dam and surrounding areas.

For this paper, the relevant data-collection question is how the left-abutment LiDAR scan characterized exposed discontinuities and how that dataset compared with rope-access scanline

mapping and downhole televiewer observations. The LiDAR scan was not used as a stand-alone site interpretation. It was evaluated as one component of the left-abutment structural dataset.

Data Collection

Rope-access vertical scanline mapping collected 73 structural data points, and the three-dimensional rock-wall scan produced 817 data points for the left abutment. The data report notes that the rock-wall scan confirmed bedding orientations recorded during the scanline survey and provided additional measurements of near-vertical joints that are difficult to obtain from vertical borings or limited-access scanlines.

The LaPrele investigation also shows that data density alone is not sufficient for structural interpretation. Televiewer and wall-scan interpretations required review to remove extraneous or erroneous discontinuities and to reinterpret features caused by bedding, partial fractures, mottled color changes, breccia, or mechanical drilling effects. The design report states that the downhole survey dataset was reduced from 7,430 identified features before re-evaluation to 3,783 after re-evaluation. This review affected the model basis. Removing non-geologic or non-persistent features reduced the potential to over-predict fracture density and helped focus the Leapfrog structural-surface interpretation on features that could reasonably persist between observations.

Table 3. LaPrele Structural Data Types and Use in Data-Collection Evaluation

Data Type	Approximate Scale or Count	Primary Use	Primary Limitation or Required Check
Rope-access scanlines	73 data points	Direct observations of wall structure; used to check bedding and joint measurements.	Limited spatial coverage and access constraints.
3D rock-wall scan	817 data points	Remote measurements of exposed wall surfaces and near-vertical joint sets.	Orientation bias where bedding is visible mainly as traces.
Televiewer surveys	7,430 raw features reduced to 3,783 after re-evaluation	Borehole observations; used to check consistency with subsurface data.	Requires review against core photos and drilling/mechanical-break evidence.
Leapfrog geologic model	Project-scale 3D interpretation	Visualization of reviewed structural surfaces between observations.	Dependent on reviewed inputs and construction-stage confirmation.

Counts and interpretations summarized from the LaPrele data and design reports (5, 6).

Data-Collection Evaluation

The LaPrele workflow illustrates a targeted use of LiDAR in engineering geology. LiDAR characterized exposed left-abutment canyon-wall structure, but the interpretation still required integration with televiewer data, core photos, water pressure testing, and field mapping. The resulting dataset was a reviewed interpretation of exposed structures and potential structural surfaces.

The left-abutment stereonet in Figure 7 shows how LiDAR-derived measurements were compared with conventional structural observations. Figure 8 shows the left-abutment rock-wall scan and rope-access scanline locations used to compare the mapping methods. Televiewer data was performed at various borehole locations across the project site.

In general, good agreement was found between wall scan data measurements and those taken via rope access or downhole televiewer.

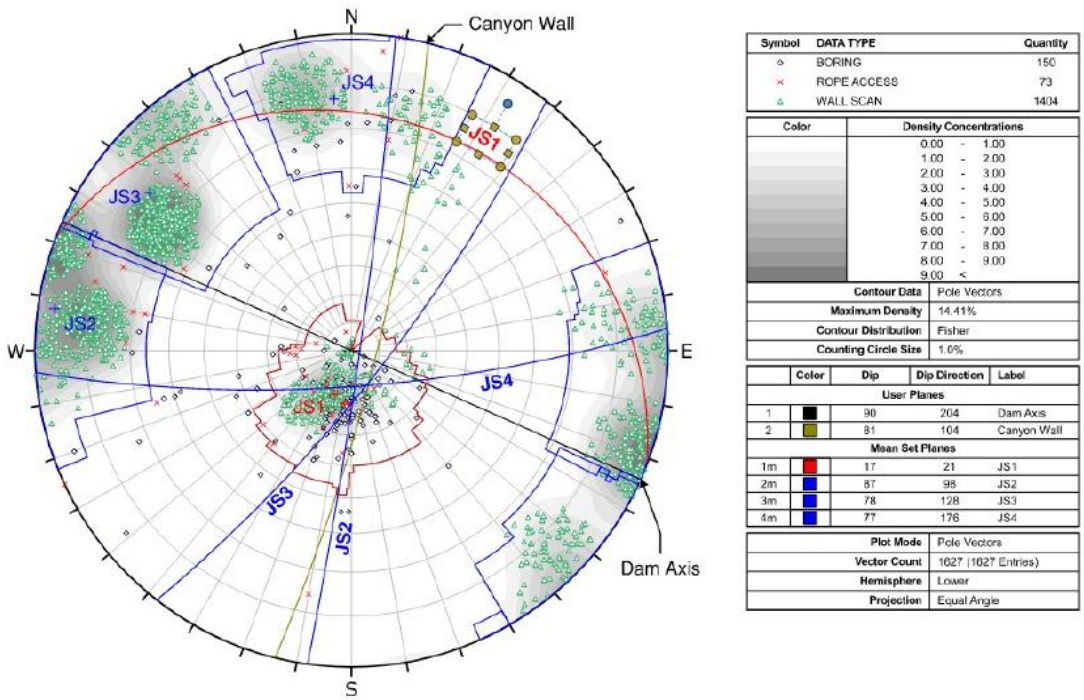

Figure 7. LaPrele Dam Left Abutment Stereonet Showing Boring, Rope-Access, and Wall-Scan Measurements (6)

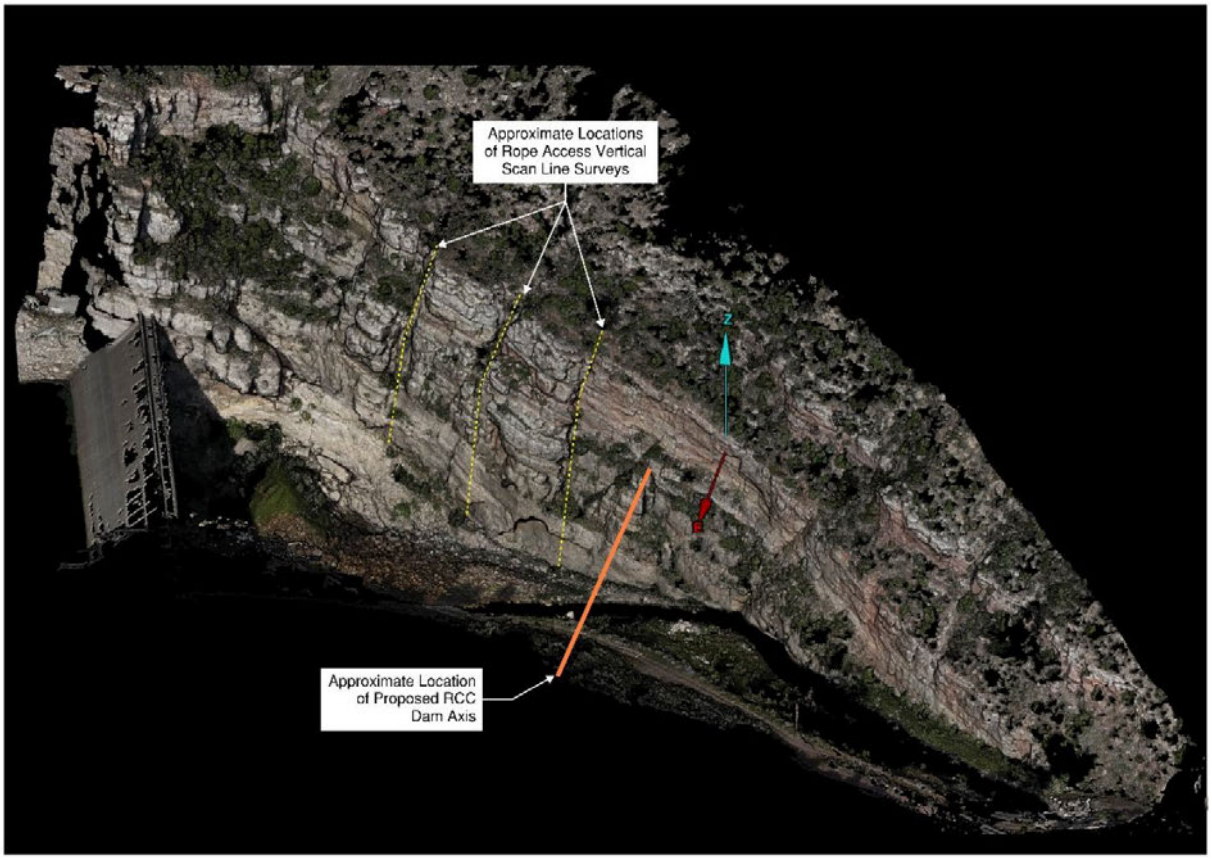

Figure 8. LaPrele Dam Left Abutment Rock-Wall Scan and Rope-Access Scanline Locations (6)

DISCUSSION

Role of LiDAR in Spatial Coverage

The three case studies show that LiDAR increased the mapped area where direct access was limited. At Elephant Butte, TLS allowed the tunnel crown and upper walls to be reviewed from the mesh. At Stagecoach Trail, UAV mapping increased coverage of steep sandstone highwalls. At LaPrele, the left-abutment scan provided a dense surface dataset that could be compared with rope-access scanline mapping and subsurface observations. In each case, LiDAR reduced access limitations but did not eliminate the need for field verification.

The limiting factor was interpretation, not point count. A high-density point cloud can identify many planar surfaces, but it cannot independently determine origin, persistence, infilling, weathering state, or relevance to the design volume. A useful workflow therefore treats digital extraction as a first pass that must be reviewed by an engineering geologist.

Common Sources of Discrepancy

Table 4. Common Differences Between LiDAR-Derived and Field-Mapped Structural Data

Difference	Typical Cause	Observed Consequence	Recommended Control
Line-of-sight/orientation bias	Plane is parallel or sub-parallel to scan direction; bedding exposed only as traces.	Automated extraction under-represents bedding or other low-angle structures.	Use hand mapping, trace mapping, alternate scan positions, and borehole/televiewer checks.
Access bias in hand mapping	Field geologists can measure only reachable portions of outcrop.	Hand dataset under-represents highwall, crown, or crest structures.	Use TLS/UAV LiDAR to capture inaccessible surfaces and compare with field data where overlap exists.
Scale and resolution bias	Small joints, rough surfaces, or narrow apertures fall below point-cloud or mesh-search thresholds.	Small-scale features may be missed or smoothed.	Set search parameters deliberately and supplement with close field observations.
Surface texture and weathering	Weathered rinds, calcite coatings, vegetation, or rounded edges alter surface normals.	Extracted orientation may differ from the mapped structural plane.	Clean/inspect field surfaces where accessible and filter rugged or vegetated surfaces.
Excavation or drilling artifacts	Blast half-casts, mechanical scaling scars, drilling-induced breaks, or color/breccia textures.	False joint sets or inflated fracture density.	Review against core photos, televiewer images, construction history, and geologic continuity.

Limitations of LiDAR-Based Discontinuity Mapping

The following limitations should be considered when interpreting LiDAR-derived discontinuity data:

• LiDAR measures exposed surfaces only and does not establish subsurface persistence.

• Substantial cleaning of constructed surfaces (concrete, roads, etc.) and vegetation is required to effectively search for similar discontinuities in a pointcloud or mesh. Additional filtering and removal of false discontinuities within the 3D dataset is also required to ensure false measurements do not matriculate into the final discontinuity sets.

• Mapped plane size, trace length, and apparent spacing are influenced by exposure, scan position, and point-cloud density.

• Bedding or other low-angle structures may be underrepresented where the surface is parallel or sub-parallel to the scanner line of sight.

• Vegetation, staining, blasting, weathering, surface roughness, and non-geologic color changes can affect plane selection.

• Field review is needed to assign geologic meaning to mapped planes and to identify features that should not be used as structural data.

Recommended Combined Workflow

Based on these case histories, the recommended workflow is to use LiDAR to expand the observation window and traditional geologic mapping to check the interpretation. First, collect point-cloud data appropriate for the geometry of interest, including multiple scanner positions if bedding or other critical planes are likely to be occluded. Second, extract candidate discontinuities using documented tolerances for angular variance, minimum area, and surface roughness. Third, compare candidate sets with field measurements, televiewer data, core, photographs, and observed rock mass conditions. Fourth, remove false or non-persistent features before using the dataset in engineering evaluations. Finally, integrate the reviewed dataset into stereonet plots and, where justified by supporting observations, three-dimensional geologic models that address the project question directly.

The workflow should also document uncertainty. Reports should state where the LiDAR dataset is reliable, where the point cloud is limited by geometry or resolution, and how those limitations were addressed. Remote mapping can improve safety and coverage, but the engineering geologist remains responsible for determining what the mapped planes represent.

CONCLUSIONS

1. LiDAR-based rock structure mapping can improve worker safety and mapped coverage for tunnel crowns, steep highwalls, and abutment exposures where direct access is limited.

2. LiDAR products used for engineering interpretation should be geologist-reviewed structural datasets derived from triangulated meshes or pointclouds and checked against field, borehole, televiewer, photographic, and geophysical data where available.

3. Orientation bias is a limitation of remote structural mapping. Structures that are parallel or sub-parallel to the scanner line of sight, including bedding on vertical walls, may be under-represented in automated or semi-automated plane extraction.

4. False discontinuities can be introduced by blasting, mechanical excavation, drilling damage, brecciation, color changes, weathering, and surface coatings. These features should be reviewed and removed before using the dataset for stereonet comparison or model input.

5. Three-dimensional geologic models provide a way to compile and evaluate reviewed structural measurements between observations. At LaPrele, Leapfrog model integration was used as an interpretive tool for left-abutment structural surfaces, not as independent confirmation of discontinuity persistence.

6. The recommended practice is a combined workflow: use LiDAR to increase coverage of exposed rock surfaces, use field geology to check the measurements, and use three-

dimensional models only where the structural interpretation is supported by sufficient observations.

REFERENCES

(1) Hiatanen, A. Geology of the Pulga and Bucks Lake Quadrangles, Butte and Plumas Counties, California. Geological Survey Professional Paper 731, U.S. Geological Survey, Washington, D.C., 1973.

(2) HDR. Elephant Butte Tunnel Stabilization Evaluation Final Report. Prepared for Caltrans Project ID 02-PLU-070-0.99, Highway 70, Plumas County, California, November 15, 2024.

(3) HDR. Geotechnical Engineering Report: Stagecoach Trail, Billings, Montana. Yellowstone County, Montana, May 2026.

(4) Terracon Consultants, Inc. Geotechnical and Materials Engineering Report: Zimmerman Trail Road Phase II Improvements. Billings, Montana, 2017.

(5) HDR. LaPrele Dam Combined Geotechnical Data Report. LaPrele Dam Replacement Project, Converse County, Wyoming, February 2026.

(6) HDR. Geotechnical Design Summary Report. LaPrele Dam Replacement Project, Converse County, Wyoming, February 2026.

(7) U.S. Bureau of Reclamation. Engineering Geology Field Manual, Vol. I, 2nd Ed., 1998.

(8) Maptek. PointStudio Geotechnical Module User Guide. Maptek Pty Ltd, Adelaide, South Australia, 2024.

(9) Rocscience Inc. Dips: Graphical and Statistical Analysis of Orientation Data. Toronto, Ontario, 2024.

(10) Seequent. Leapfrog Works Software, Version 2024.1.3. Bentley Systems, March 2025.

04. Enhanced Monitoring of High-Risk Unstable Slopes Using Remote Sensing and AI-Assisted Change Detection

Katelyn Card
Washington State Department of Transportation
310 Maple Park, Transportation Building
Olympia, Washington 98504
(360) 789-8334
katelyncard@wsdot.wa.gov

Prepared for the 75th Highway Geology Symposium, September, 2026

Acknowledgements

The author would like to thank the individuals/entities for their contributions in the work described:

Samuel Johnston – Washington State Department of Transportation
Marc Fish – Washington State Department of Transportation
Cody Chaussee – Washington State Department of Transportation
Tracy Trople – Washington State Department of Transportation
Veronica Raub – Washington State Department of Transportation

Disclaimer

Statements and views presented in this paper are strictly those of the author(s), and do not necessarily reflect positions held by their affiliations, the Highway Geology Symposium (HGS), or others acknowledged above. The mention of trade names for commercial products does not imply the approval or endorsement by HGS.

Copyright Notice

Copyright © 2026 Highway Geology Symposium (HGS)

All Rights Reserved. Printed in the United States of America. No part of this publication may be reproduced or copied in any form or by any means – graphic, electronic, or mechanical, including photocopying, taping, or information storage and retrieval systems – without prior written permission of the HGS. This excludes the original author(s).

ABSTRACT

Transportation agencies across mountainous regions face a growing challenge: many high-risk unstable slopes threaten highways, yet the cost to fully mitigate these hazards can exceed available funding by tens of millions of dollars. In Washington State, mitigation of several high-risk slopes and repair of damaged geotechnical assets is estimated to exceed $100 million, making immediate stabilization impractical for many sites. As a result, transportation agencies increasingly rely on enhanced monitoring programs to manage risk and detect early signs of slope instability.

To address this challenge, the Washington State Department of Transportation (WSDOT) State Geotechnical Office has initiated an expanded monitoring program focused on high-risk slopes identified through the agency's Geotechnical Asset Management Plan (GAMP). These slopes were prioritized using likelihood and consequence factors including rockfall frequency, roadway exposure, traffic volumes, and maintenance records. The monitoring program integrates remote sensing techniques including terrestrial lidar scanning, unmanned aerial systems (UAS), fixed camera monitoring, and satellite observations to collect high-resolution point clouds and imagery of slope conditions.

A key objective of this effort is evaluating automated and AI-assisted change detection techniques to process large monitoring datasets. Algorithms compare repeat lidar scans, analyze pixel-level changes in imagery, and identify potential movement or rockfall source areas indicating developing instability.

This paper presents the framework for WSDOT's enhanced monitoring program and applications of remote sensing and change detection techniques. The work explores how automated analysis can improve interpretation of monitoring data, support earlier hazard detection, and guide mitigation strategies where full stabilization is not immediately feasible.

INTRODUCTION

Unstable slopes pose an ongoing risk to highway infrastructure and the traveling public, particularly along transportation corridors through steep and mountainous terrain. Transportation agencies are tasked with managing large inventories of known unstable slopes while balancing limited resources among competing infrastructure needs. Although many high-risk slopes have been identified through established inspection and asset management programs, comprehensive mitigation is not always feasible. Within Washington State, the combined cost of mitigating several known high-risk unstable slopes and repairing damaged geotechnical assets is estimated to exceed $100 million. As a result, additional risk-management strategies are needed to bridge the gap between routine inspection and eventual mitigation.

The Washington State Department of Transportation (WSDOT) manages over 3,000 known unstable slopes through its Unstable Slopes Management System (USMS) and Geotechnical Asset Management Plan (GAMP), which provide a risk-based framework for identifying and prioritizing unstable slopes. However, limited program funding and increasing construction costs mean that comprehensive mitigation of some high-risk slopes may be deferred for an extended period. To better manage risk during this period, WSDOT has proposed an enhanced monitoring program that supplements existing inspections with repeat remote sensing and automated change detection.

The enhanced monitoring program has two primary objectives: (1) improve early detection of potentially hazardous slope movement, and (2) support more targeted and cost-effective mitigation by identifying the most active portions of large unstable slopes. The program will use terrestrial lidar, unmanned aerial systems (UAS), and fixed-camera monitoring to collect repeat observations that can be evaluated through change detection and subsequent geotechnical review.

The purpose of this paper is to present WSDOT’s enhanced monitoring program, including the framework for monitoring high-risk unstable slopes, the remote sensing and change-detection technologies being evaluated, and the anticipated implementation and future development of the program.

BACKGROUND

WSDOT has a long history of identifying, evaluating, and managing unstable slopes along the state highway system. The agency's approach has evolved from primarily responding to slope failures as they occur to proactively assessing and prioritizing known hazards based on their potential risk to the highway and traveling public. Through the USMS and GAMP, WSDOT maintains an inventory of known unstable slopes and uses risk-based criteria to prioritize sites for investigation and mitigation. This existing asset-management framework provides the foundation for identifying the high-risk slopes considered for enhanced monitoring.

WSDOT Unstable Slope Management System (USMS)

WSDOT began development of the USMS in 1993 to establish a systematic approach for managing unstable slopes along the state highway system (*1*). The program provided a consistent process for evaluating and prioritizing known unstable slopes, developing preliminary project scopes and cost estimates, and evaluating potential mitigation projects. The State Geotechnical Office is responsible for the technical management of the statewide program.

Initial development of the USMS included compiling a statewide inventory of known unstable slopes using information provided by WSDOT regional maintenance, including slope locations, types and frequency of instability, and associated maintenance impacts (*1*). Consistent criteria were established to document and evaluate these sites, creating the foundation for WSDOT's statewide unstable slope inventory.

Since its initial development, the USMS rating system has evolved into a risk-based approach that considers both the likelihood of slope failure and the potential consequence to the highway and the traveling public. This approach allows WSDOT to compare various unstable slope hazards across the highway network and identify those presenting the greatest risk. The USMS inventory and rating methodology have subsequently been incorporated into WSDOT's broader GAMP and are used to prioritize high-risk unstable slopes.

Geotechnical Asset Management Plan (GAMP) and High-Risk Slope Prioritization

Through the GAMP, WSDOT works to maintain and preserve geotechnical assets while reducing risk and increasing the resiliency of the state highway system. The GAMP includes both known unstable slopes and constructed geotechnical assets, which are managed through routine inspection, condition assessment, and risk-based prioritization (*2*). For unstable slopes, these inspections provide updated information on site conditions and documented slope activity, allowing changes in risk to be tracked over time.

Unstable slopes are assigned a risk level based on the likelihood of failure and potential consequences to the highway and traveling public. The evaluation considers factors including the frequency and magnitude of documented slope activity, roadway impacts, available catchment, traffic impedance, sight distance, pavement damage, and previous incidents (*2*). Maintenance records, including roadway rockfall removal documented through WSDOT's Highway Activity Tracking System (HATS), provide an additional record of historical slope activity. Slopes classified as high or very high risk are considered to be in poor condition and receive the highest priority for mitigation.

Through this risk-based prioritization process, WSDOT has identified high- and very high-risk unstable slopes throughout the state highway system. The slopes currently considered for enhanced monitoring are distributed across several regions of Washington and include both rock slopes and landslides. Figure 1 shows the statewide distribution of the high-risk unstable slopes included in the proposed enhanced monitoring program.

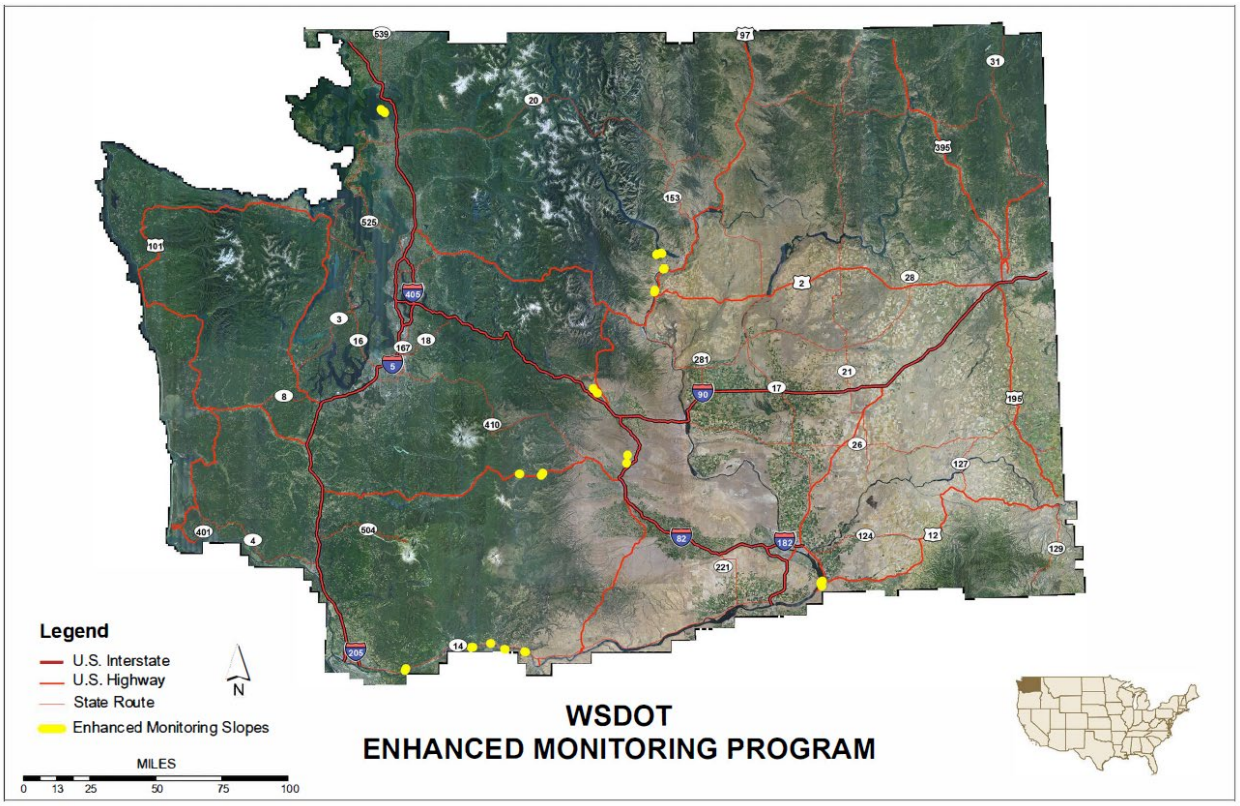

Figure 1 – Map of High-Risk Slopes in Washington State for Enhanced Monitoring Program

Funding and Mitigation Constraints

Funding for WSDOT's Unstable Slope Program has decreased substantially since the program was established in the mid-1990s. Program funding has been reduced by nearly 50 percent, while inflation and increasing construction costs have made proactive mitigation of large-scale unstable slopes increasingly difficult. The program currently receives approximately $8 million per year for proactive slope work. Full mitigation of some large rock slopes is currently estimated to cost approximately $10 million per site, while mitigation of large deep-seated landslides can approach $25 million per site. As a result, comprehensive stabilization of every identified high-risk slope is not feasible within available funding, requiring WSDOT to increasingly consider partial or targeted mitigation approaches.

The high- and very high-risk unstable slopes currently considered for enhanced monitoring are summarized in Table 1 below. Several have previously advanced toward design or mitigation but were deferred because of funding limitations and competing priorities, while others require additional investigation to better identify the most active or hazardous portions of the slope. The estimated cost to mitigate or partially mitigate the high-risk slopes identified in Table 1 is approximately $77 million.

Table 1 – High-Risk Unstable Slopes				
High-Risk Unstable Slopes – USMS Slope Number(s)	Slope Locations			Estimated Mitigation Cost
	Region	State Route	Milepost Limits	
1350, 3140, 3141	North Central	97A	224.30 – 224.70	$6,000,000
11, 13, 14	North Central	97A	213.30 – 214.20	$8,550,000
3518, 3519, 3520, 3521	North Central	971	6.90 – 7.30	$2,000,000
2887, 3301	North Central	971	10.30 – 11.50	$6,000,000
518, 519, 2917, 2918, 2919, 2920, 2575	Northwest	11	11.30 – 13.50	$13,700,000
229	South Central	10	95.90 – 96.20	$1,000,000
1875	South Central	10	98.20 – 98.55	$1,500,000
2778, 2780, 2839, 2840	South Central	12	155.60 to 155.90	$6,000,000
183, 2790, 2793, 2794, 1762	South Central	12	164.50 – 165.80	$8,000,000
546, 548, 549, 551	South Central	730	4.00 – 5.00	$3,500,000
1972	South Central	821	2.90 – 3.20	$1,200,000
2942, 3152	South Central	821	6.80 – 7.00	$2,000,000
1600, 2352	Southwest	14	24.90 – 25.90	$4,000,000
1701, 2122	Southwest	14	55.00 – 56.00	$4,000,000
1305	Southwest	14	63.00 – 63.20	$1,600,000
3091	Southwest	14	68.80 – 69.10	$3,000,000
1662	Southwest	14	77.30 – 77.80	$5,000,000
			Total	**$77,050,000**

Given these limitations, WSDOT is increasingly considering targeted mitigation strategies for large unstable slopes. Enhanced monitoring provides a means of identifying active rockfall source areas, zones of deformation, and other locations where measurable change is occurring over time. This information can support partial mitigation strategies that direct available resources towards areas where they can provide the greatest reduction in risk, rather than immediately mitigating the entire slope.

Together, the increasing cost of slope mitigation, limited program funding, and need to manage risk at high-priority sites provide the basis for WSDOT's proposed enhanced monitoring program.

PURPOSE AND OBJECTIVES OF ENHANCED MONITORING

WSDOT's enhanced monitoring program is intended to provide an additional risk-management tool for high-risk unstable slopes. The program has two primary objectives: (1)

improve public safety through early warning of potentially hazardous slope movement, and (2) support targeted mitigation to make more effective use of available funds. These objectives are described in the following sections.

Objective 1 – Early Warning and Operational Decision Support

The first objective focuses on public safety. Repeat monitoring and automated change detection may identify movement or changes in slope conditions that indicate increasing instability. When significant changes are detected, WSDOT may conduct additional engineering review or field inspection, increase monitoring frequency, or implement temporary protective measures, including highway closures when warranted. Enhanced monitoring is not intended to predict slope failures with certainty or replace engineering judgment; rather, it provides additional information for recognizing changing conditions and supporting timely risk-management decisions.

Objective 2 – Targeted Mitigation and Better Use of Limited Funding

The second objective is to make more effective use of limited mitigation funding by providing objective data to support mitigation design. Repeat remote sensing and change detection can identify active rockfall source areas, zones of deformation, and other locations where measurable change is concentrated. For example, if monitoring indicates that approximately 90 percent of rockfall activity originates from one area of a large rock slope, mitigation could be focused on that area and potentially reduce a substantial portion of the rockfall hazard at a fraction of the cost of mitigating the entire slope.

PROPOSED ENHANCED MONITORING FRAMEWORK

The proposed enhanced monitoring framework provides a systematic approach for monitoring high-risk unstable slopes. The framework consists of four primary components: (1) site selection and monitoring approach, (2) remote sensing data collection, (3) change detection and quality assurance, and (4) interpretation and risk-management decisions.

Site Selection and Monitoring Approach

The enhanced monitoring program will initially focus on the high- and very high-risk unstable slopes identified in Table 1. Several of these sites are large and complex, with slopes exceeding 300 feet in height and extending for thousands of feet along the highway. Some require additional investigation before an appropriate partial mitigation strategy can be developed, while others have previously advanced into design but were deferred because of funding limitations and competing priorities. Enhanced monitoring at these locations is intended to better define the portions of each slope, contributing most significantly to risk and support development of more focused mitigation strategies.

Monitoring may also be used to better target subsequent site investigations. Subsurface exploration, including test borings, can be costly, particularly for large or complex landslides where boring locations are critical to obtaining representative subsurface information. Monitoring surface deformation over time may help delineate active portions of a landslide and better target subsequent subsurface investigations to obtain the most relevant geotechnical information.

The monitoring approach at each site will be selected based on site-specific conditions and the type of information needed. No single monitoring technology is expected to be suitable for all locations. Individual or complementary monitoring methods will therefore be selected based on their ability to provide appropriate coverage and reliably detect the anticipated slope movement. The capabilities and limitations of individual technologies are discussed in a later section.

Remote Sensing Data Collection

Baseline datasets will be collected at each site to establish existing slope conditions for subsequent change analysis. Depending on the selected method, these datasets may include terrestrial lidar, UAS-derived point clouds or imagery, and fixed-camera imagery. Repeat datasets will then be collected at intervals appropriate for the monitoring objective and selected technology. At selected sites, multiple monitoring technologies will be used concurrently to compare change-detection results and evaluate the ability of each method to detect slope movement.

WSDOT regional UAS pilots have begun collecting baseline and repeat aerial imagery and point-cloud data at selected high-risk slopes. Additional surveys will be collected using consistent methods to support reliable change detection.

At selected locations, fixed monitoring cameras will provide more frequent observations between periodic remote sensing surveys. Camera locations and fields of view will be selected in coordination with WSDOT geotechnical staff to adequately capture areas of interest. Installation will require consideration of site access, visibility, power, data transmission, and long-term equipment maintenance. Once established, repeat imagery can be evaluated using automated image-based change detection.

Change Detection and Quality Assurance

Change detection analyses will identify and quantify changes in slope conditions over time. Analyses will use both three-dimensional point-cloud data and repeat imagery, with parameters adjusted according to the geohazard and anticipated scale of displacement. For three-dimensional datasets, repeat surveys will be aligned to a common reference and compared to identify areas of material movement or loss, while repeat imagery may be evaluated using pixel-based change detection. The analytical methods are discussed further in a later section..

Change detection results will be reviewed through quality assurance and quality control (QA/QC) before being used for slope-management decisions. The proposed process includes algorithmic validation followed by engineering review to determine whether identified changes are geotechnically significant. False-positive and false-negative detections will also be evaluated as the program progresses. This process is intended to distinguish actual slope movement from noise, vegetation, processing effects, and other sources of apparent change.

Interpretation and Risk-Management Decisions

Following QA/QC, identified changes will be interpreted within the geologic and geotechnical context of each site to evaluate their significance. The location, magnitude, and pattern of detected movement, together with knowledge of slope conditions and anticipated

failure mechanisms, can be used to determine whether additional investigation, monitoring, or other action is warranted.

Over time, monitoring results may identify recurring rockfall source areas, zones of deformation, or other patterns of movement that can inform subsequent investigation and targeted mitigation.

MONITORING TECHNOLOGIES

The proposed enhanced monitoring program will utilize terrestrial lidar, UAS, and fixed-camera monitoring to collect repeat observations of unstable slope conditions. Each technology has advantages and limitations that influence its applicability for unstable slope monitoring. WSDOT has previously applied several of these technologies on a limited scale, providing early examples of their potential use for rockfall and landslide monitoring. The capabilities, limitations, and previous applications of each method are discussed below.

Terrestrial Lidar

Terrestrial lidar uses laser-based distance measurements to generate high-resolution three-dimensional representations of a slope surface (*3*). Individual measurements are processed into a point cloud. Repeat point clouds can then be compared to identify and quantify areas where material has moved or been removed. WSDOT has previously used terrestrial lidar at several high-risk rock slopes.

Terrestrial lidar is particularly effective for exposed rock cuts, where high-resolution measurements of the slope face can be obtained from accessible locations along the highway. Repeat datasets can be used to identify the location and extent of rockfall activity. Figure 2 shows an example of lidar change detection along SR 971.

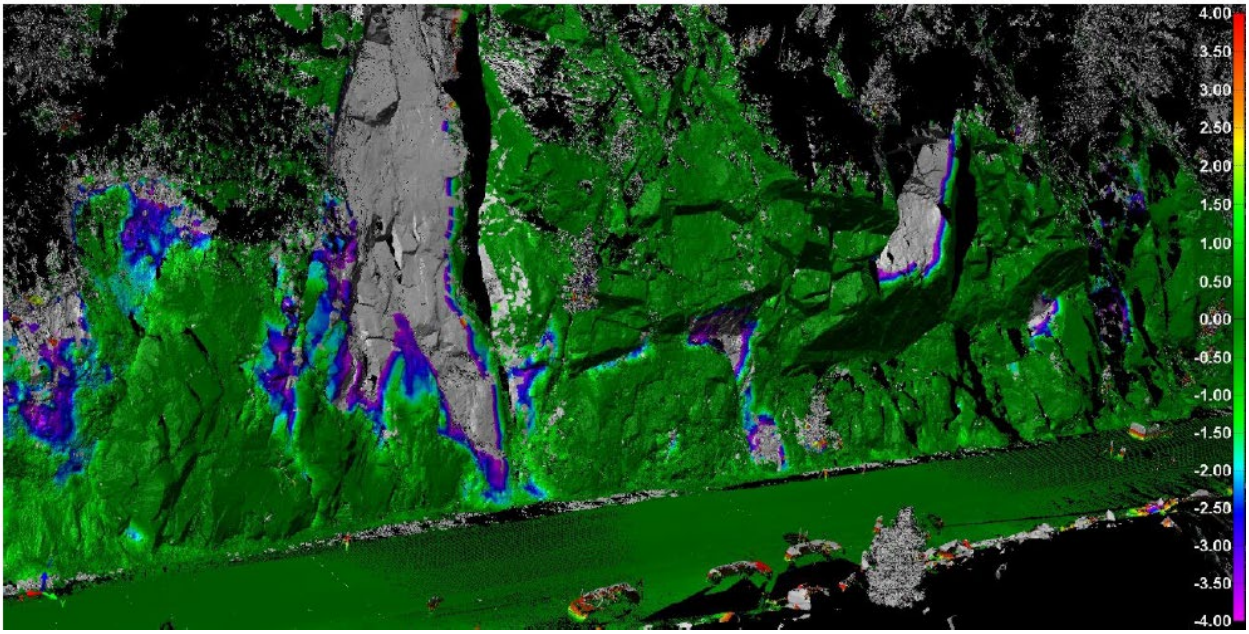

Figure 2 – Example of lidar change detection analysis along SR 971, gray, blue, and purple areas indicate areas where rockfall has occurred.

The primary limitations of terrestrial lidar are line-of-sight and slope coverage. Tall slopes may not be completely visible from highway scanning locations, and poor viewing angles can reduce data quality. Vegetation may also obscure portions of the slope and create gaps within the resulting point cloud. Where adequate coverage cannot be obtained from the ground, terrestrial lidar may be supplemented by UAS-based data collection.

Unmanned Aerial Systems (UAS)

UAS provides an aerial perspective for data collection. High-resolution imagery can be used directly or processed using photogrammetry to generate three-dimensional point clouds, while UAS-mounted lidar can provide an alternative method for collecting three-dimensional data.

A primary advantage of UAS surveys is the ability to collect data from portions of a slope that may be difficult to observe using ground-based methods. This is particularly useful for tall or extensive slopes where terrestrial lidar or fixed cameras may have limited coverage. UAS surveys can provide multiple viewing perspectives and broader slope coverage and may be used independently or to supplement terrestrial lidar.

WSDOT previously evaluated UAS-based change detection along SR 14 as an early application of this approach. High-resolution imagery collected during repeat surveys was compared using pixel-based change detection, successfully identifying the source location of a small rockfall that occurred between surveys. This application demonstrated the potential for UAS monitoring to identify localized rockfall activity that may be difficult to document through routine inspections alone. Figure 3 presents an example of the SR 14 change detection results.

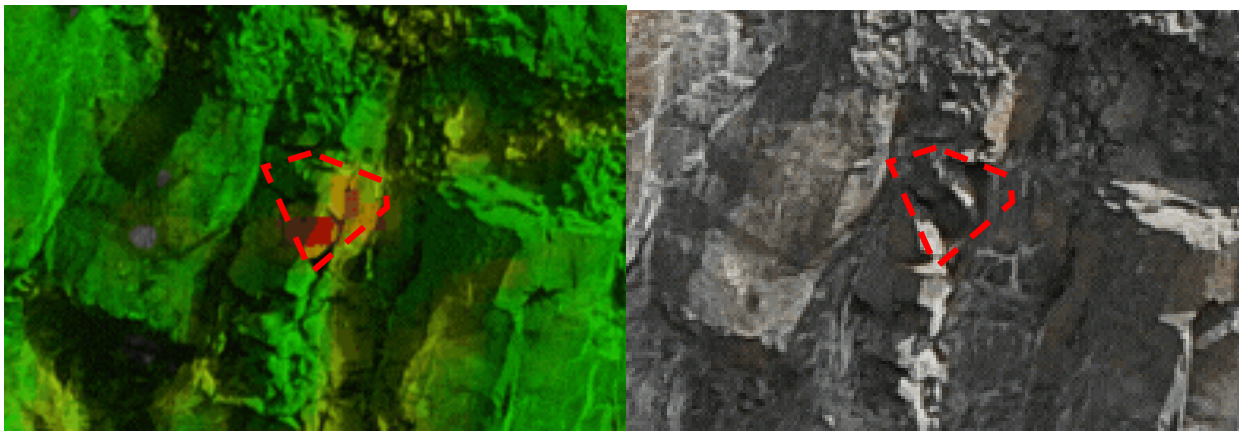

Figure 3 – UAS Change Detection Analysis Example from SR 14 (Figure Courtesy of Re-Monitor/Nhazca)

Similar to terrestrial lidar, UAS monitoring has limitations that may affect data coverage and quality. Vegetation can obscure the slope surface in both aerial imagery and photogrammetrically derived point clouds. Despite this limitation, the ability to efficiently collect repeat data over large or inaccessible slopes makes UAS an important component of the enhanced monitoring program.

Fixed-Camera Monitoring

Fixed-camera monitoring provides frequent, repeat imagery of unstable slopes from a consistent viewing location. Cameras can be programmed to capture multiple images each day, allowing changes to be observed at a higher temporal frequency than is typically practical with periodic lidar or UAS surveys. Where cellular service is available, imagery may also be transmitted remotely for automated change detection.

WSDOT previously evaluated fixed-camera monitoring and image-based change detection at the SR 112 Clallam Bay landslide. Repeat imagery was analyzed using pixel-level change detection to identify movement within the landslide. This early application demonstrated the potential for fixed-camera imagery to monitor an active landslide and helped inform its proposed use within the broader enhanced monitoring program. Figure 4 presents an example of the SR 112 change detection results.

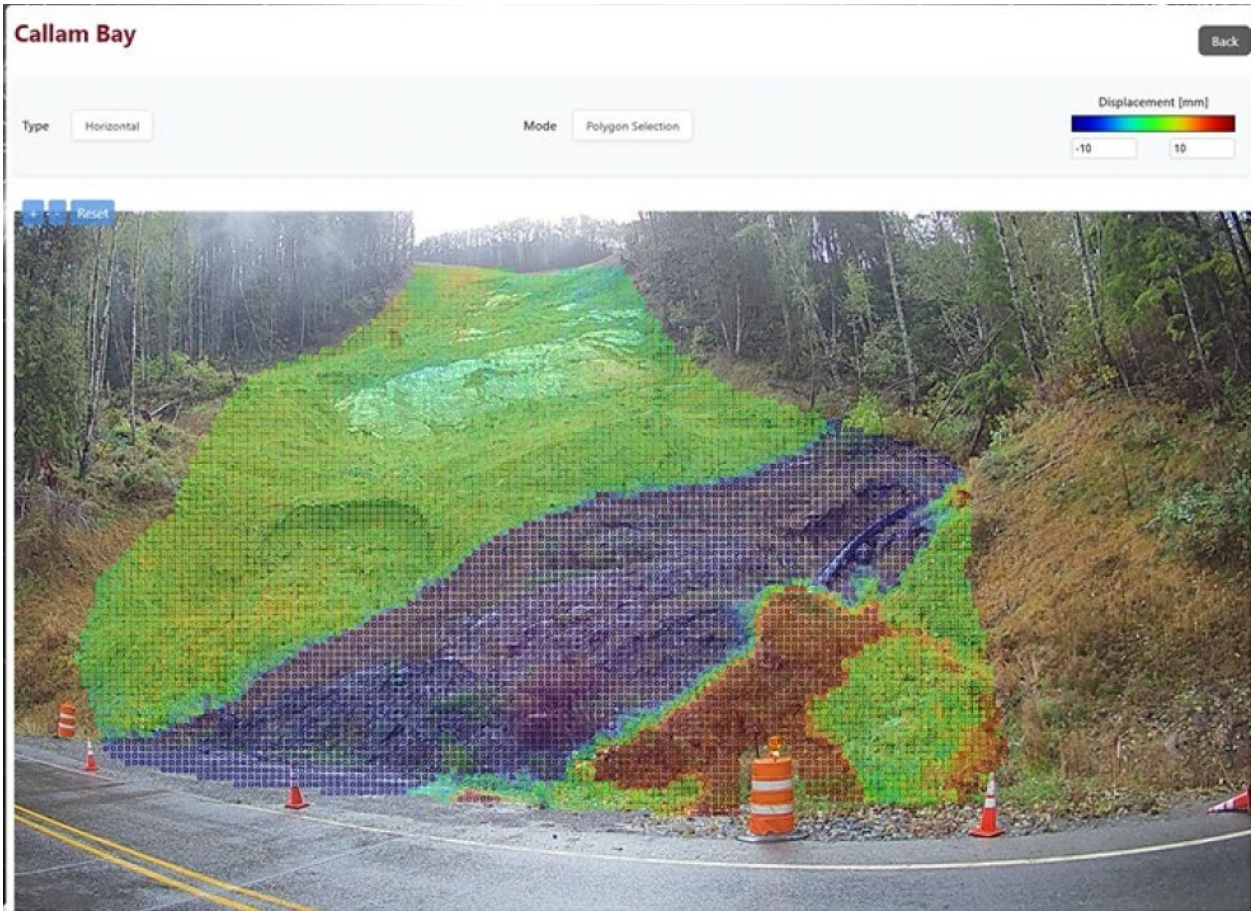

Figure 4 – Example of change detection analysis using fixed camera imagery for the Clallam Bay Landslide. This was completed using propriety software.

Fixed-camera monitoring is primarily limited by camera placement and visibility. Vegetation can obstruct portions of the slope, while large or tall slopes may be difficult to capture adequately from a single location. Installation may also be constrained by highway right-of-way, surrounding terrain, and the availability of a stable location without an unobstructed view. Fixed cameras are therefore expected to be most effective where areas of interest can be clearly viewed and may be supplemented by periodic UAS or lidar surveys where additional coverage is needed.

Integrated Monitoring Approach

The monitoring technologies described above are intended to be complementary rather than standardized across all sites. Depending on monitoring needs, a site may use a single technology or a combination of monitoring methods. For example, terrestrial lidar or UAS surveys may provide detailed periodic measurements of slope conditions, while fixed cameras provide more frequent observations between surveys. As the program is implemented, WSDOT will evaluate these technologies individually and in combination to determine effective monitoring approaches for different unstable slopes.

AUTOMATED CHANGE DETECTION AND FUTURE AI APPLICATIONS

Implementation of the enhanced monitoring program will generate large volumes of repeat lidar, UAS, and fixed-camera data that must be efficiently processed to identify significant changes in slope conditions. Manual comparison alone would be time intensive and could limit the number of slopes and frequency of observations that can be practically evaluated. Automated change detection provides a way to systematically screen repeat datasets and identify potentially significant changes. As the program develops and a larger library of validated monitoring data becomes available, WSDOT also intends to evaluate opportunities for future AI-assisted analysis.

Automated Change Detection

Automated change detection will be used to compare repeat remote sensing datasets and identify areas where measurable changes in slope conditions occur. The specific processing methodology will depend on whether the monitoring data consists of three-dimensional point clouds or repeat imagery.

For point-cloud datasets, repeat surveys must first be accurately aligned or registered before changes can be measured. The proposed methodology uses algorithm-based alignment and terrain-informed segmentation, with procedures designed to prevent areas of actual slope movement from adversely influencing the registration. Following alignment, noise-reduction techniques are applied, and datasets are compared using parameters appropriate for the geohazard and anticipated magnitude of movement. For image-based monitoring, automated comparison of baseline and subsequent imagery can identify pixel-level changes and highlight areas for additional review. WSDOT will use a third-party web-based platform to review change detection results and evaluate identified areas of change.

An important consideration in both approaches is the limit of detection, or the minimum magnitude of change that can be reliably distinguished from noise and measurement uncertainty (*4*). Establishing these limitations will be particularly important for slowly moving landslides or small-scale changes where the magnitude of movement may approach the resolution of the monitoring method.

Geotechnical Interpretation of Automated Results

Automated change detection provides an initial screening of monitoring data, but geotechnical interpretation is needed to evaluate the significance of the detected changes. Interpretations will consider the location, magnitude, and spatial pattern of changes detected in the context of known slope conditions and behavior. For rock slopes, this may include evaluating

recurring rockfall source areas, while landslide monitoring may identify the distribution and progression of surface deformation over time.

FUTURE WORK AND PROGRAM DEVELOPMENT

Initial implementation of WSDOT's enhanced monitoring program will serve as a trial period to evaluate the effectiveness and practical application of the proposed monitoring framework. Lessons learned will be used to refine monitoring and analytical methods, evaluate future AI-assisted applications, and identify the resources needed to expand WSDOT's in-house monitoring capabilities. The long-term objective is to develop a repeatable and sustainable program that can be adapted to individual unstable slopes and expanded as resources allow.

Initial Program Implementation and Evaluation

Initial implementation of the enhanced monitoring program is underway, with funding currently available through June 30, 2027. Baseline terrestrial lidar scans have been completed at the selected monitoring sites, and WSDOT regional UAS programs have begun collecting baseline data. Fixed-camera installation at selected sites is planned for September 2026. Repeat lidar scans and UAS surveys are anticipated to occur monthly or bi-monthly through the winter of 2026-2027, depending on weather and staff availability.

Monitoring through the winter of 2026–2027 will serve as the initial evaluation period for the expanded program. WSDOT will evaluate the quality and completeness of collected data, the ability of the selected methods to reliably detect relevant slope changes, the performance of automated change detection and QA/QC procedures, and the practicality of monitoring results for geotechnical decision making. Findings will be used to refine monitoring methods and analytical workflows as the program progresses.

WSDOT plans to summarize findings from the initial monitoring period in a report prior to June 2027. Continued monitoring beyond June 30, 2027, will depend on additional funding anticipated to be requested for the 2027–2029 biennium. Extending the program would allow longer records of slope behavior to be developed and provide additional opportunities to evaluate and refine the monitoring approach.

Future AI-Assisted Analysis

As the enhanced monitoring program progresses, the accumulation of repeat monitoring data and validated change detection results will provide an opportunity to evaluate potential applications of AI within the monitoring workflow. The initial program will focus on automated change detection and geotechnical review; however, future AI-assisted methods may help distinguish actual slope movement from vegetation, environmental effects, or other false detections, classify detected changes, and prioritize areas for further evaluation.

As additional monitoring records are collected, datasets of confirmed rockfalls, landslide movement, and other validated changes may also provide opportunities to evaluate recurring spatial or temporal patterns. The objective is to determine whether AI-assisted methods can improve the efficiency of data screening and interpretation while maintaining engineering judgement and risk-management decisions.

Development of Long-Term In-House Capabilities

A long-term goal of the enhanced monitoring program is to develop greater in-house capability for collecting, processing, and interpreting unstable slope monitoring data. WSDOT already has internal capabilities for portions of the workflow, including UAS data collection and geotechnical interpretation. The initial implementation period will help determine which additional methods can be effectively performed using WSDOT staff and resources and where specialized expertise may continue to be needed.

Knowledge transfer during initial implementation will be important to achieving this goal. The proposed change detection work includes delivery of analysis results, metadata, configuration files, and processing parameters, allowing WSDOT to understand and reproduce the analytical workflows developed during the monitoring effort. Experience gained through implementation will help identify data processing, change detection, QA/QC, and data-management procedures that can be standardized for routine WSDOT use.

CONCLUSIONS

Managing high-risk unstable slopes remains a challenge where the number and scale of known hazards exceed the funding available for comprehensive mitigation. WSDOT's existing USMS and GAMP provide a systematic approach for identifying and prioritizing these hazards; however, some high-risk slopes may remain unstable for extended periods before mitigation can be implemented. Enhanced monitoring provides an additional risk-management tool for addressing this gap by improving WSDOT's understanding of how slope conditions change over time.

The proposed program uses terrestrial lidar, UAS surveys, fixed-camera monitoring, and automated change detection to support two primary objectives: improving early warning systems and identifying the most active or hazardous portions of unstable slopes for targeted mitigation. Initial implementation through the winter of 2026–2027 will provide an opportunity to evaluate the effectiveness and practical application of these methods and refine the monitoring framework based on lessons learned.

Enhanced monitoring is not intended to replace routine inspection, engineering judgment, or permanent slope mitigation. Rather, it provides additional information to support risk-management decisions while mitigation is being developed, or funding is unavailable and to help focus future investigations and mitigation where they can provide the greatest reduction in risk. As the program develops, lessons learned from the initial implementation will also support evaluation of AI-assisted analysis and development of more in-house monitoring capabilities.

REFERENCES:

1. Lowell, S. and P. Morin. *Unstable Slope Management Washington State*. TR News, No. 207, March-April 2000, pp. 11-15.
2. Washington State Department of Transportation. *Geotechnical Asset Management Plan*. WSDOT, 2024. Washington State Department of Transportation, State Geotechnical Office, Olympia, WA, 2024.
3. Wasser, L.A. *The Basic of LiDAR – Light Detection and Ranging – Remote Sensing.* National Ecological Observatory Network (NEON), 2026. Accessed Aug. 20, 2026.
4. Winiwarter, L., K. Anders, B. Hofle. M3C2-EP: Pushing the limits of 3D topographic point cloud change detection by error propagation. *ISPRS Journal of Photogrammetry and Remote Sensing* vol. 178, August 2021, pp. 240-258.

05. Title: Bridge or Blast?

Sub-title: A Look Into US19W South/ Little Creek Road Design For Repair After Hurricane Helene Damages Under Progressive Design-Build Project Delivery Method

Callan Swafford, P.G.
Geologist
555 Fayetteville St. Suite 900
Raleigh, NC 27601
(984)-325-0512
Callan.Swafford@hdrinc.com

Prepared for the 75th Highway Geology Symposium, September, 2026

Acknowledgements

The author would like to acknowledge the residents, families, and communities of Western North Carolina who were affected by Hurricane Helene. The devastation caused by the storm resulted in significant loss, hardship, and disruption throughout the region. The resilience, perseverance, and determination demonstrated by these communities during the recovery effort have been both inspiring and humbling. This paper is dedicated to recognizing the challenges Western Carolina and surrounding areas have faced and highlights the ongoing work required to restore the infrastructure, homes, and livelihoods impacted by the disaster. The author would like to also thank NCDOT for its commitment to restoring roadways and building for resilience across North Carolina.

Disclaimer

Statements and views presented in this paper are strictly those of the author(s), and do not necessarily reflect positions held by their affiliations, the Highway Geology Symposium (HGS), or others acknowledged above. The mention of trade names for commercial products does not imply the approval or endorsement by HGS.

Copyright Notice

Copyright © 2026 Highway Geology Symposium (HGS)

All Rights Reserved. Printed in the United States of America. No part of this publication may be reproduced or copied in any form or by any means – graphic, electronic, or mechanical, including photocopying, taping, or information storage and retrieval systems – without prior written permission of the HGS. This excludes the original author(s).

ABSTRACT

HDR Engineering, Inc. of the Carolinas (HDR) is working with Branch Civil, Inc., for NCDOT, on approximately 12 miles of roadway along US19W in Yancey County, North Carolina. The overall scope of this project is to evaluate, design, and reconstruct the US19W roadway and associated infrastructure along the alignment that was damaged during Hurricane Helene under a progressive design build (PDB) project delivery method. Little Creek Road (LCR), a 0.4-mile, secondary road off US19W, was destroyed during Helene when the Cane River scoured away the existing embankment. The road has remained closed since the storm, and the public crosses over Cane River on a temporary railcar bridge. The original design option, Option 1, was to construct a new bridge over Cane River and permanently close LCR. Due to borrow source demands across the region, obtaining sufficient material for project-wide repairs within reasonable hauling distances also became a concern. To address this concern, while still providing permanent road solutions, Design Option 2A was introduced. Design Option 2A included cutting into the hillside to produce sufficient volume of borrow material and rebuilding LCR. A phased investigation approach to support the geotechnical feasibility analysis of Option 2A was utilized. The Geotechnical investigation included eighteen borings with wireline coring, geologic mapping of readily accessible outcrops and road cuts, as well as seismic refraction surveys at the top of the ridge. Data along the existing slope face was limited due to project schedule and site accessibility. Analyses included kinematics, rockfall modeling of various rock cut scenarios, and global slope stability. Preliminary findings support that sufficient borrow, in terms of both quantity and quality, can be obtained by cutting into the slope. However, due to constructability, schedule, and rock production risk concerns, Design Option 2A has been replaced by Design Option 2B. Design Option 2B includes embankment rebuilding of LCR using engineered stabilization measures. Geotechnical recommendations are ongoing for Option 2B, and close coordination with NCDOT and the Contractor has been critical for design progression.

INTRODUCTION

Hurricane Helene devastated Western North Carolina's communities on September 24th, 2024. Damages were severe along the US19W South corridor, where roads, bridges, and even homes were decimated along the Cane River. Emergency repairs, including embankment reconstruction and a temporary rail-car bridge installation, were made shortly after the storm to reestablish access for the community and public passing through the corridor. These repairs were successful for temporary purposes, but long-term repairs are necessary.

Due to the size, complexity, and schedule needs of the project, the contract delivery method of Progressive Design Build (PDB) was selected by NCDOT. The project was awarded to Branch Civil, Inc. (Branch) as the General Contractor (GC) and HDR Engineering, Inc. of the Carolinas (HDR) as the Designer. The project consists of 12 miles of roadway repairs and ten bridge repairs or replacements.

The LCR design is significant to the project because it served as the only access route to the community upslope. When the road was destroyed during the storm, people were cutoff from surrounding areas until a temporary railcar was installed to facilitate traffic over Cane River to US19W South highway. Throughout the design of Little Creek Road rebuild, the contractor and client required preliminary design and quantities for three options before deciding on a final design. HDR's geotechnical team worked alongside roadway, hydraulics, structures, stream restoration, right of way, and environmental teams to support the design progress for each option. Three preliminary design options for permanent repairs on Little Creek Road were geotechnically investigated:

- Design Option 1
  - A new bridge over Cane River from US19W South to Little Creek Road and Phillips Road intersection. This would permanently close Little Creek Road.
- Design Option 2A
  - Repair and realign portions of Little Creek Road by cutting into the hillside. Design cut limits to supply borrow material for this project and an adjacent project construction.
- Design Option 2B
  - Repair Little Creek Road by rebuilding the road on the existing alignment or shifting towards Cane River. Engineered fill embankments to meet roadway standard typical sections will be designed throughout this alignment.

The focus of this paper is to describe the geotechnical investigation, analysis, and recommendations of design Option 2A, cut slope with Little Creek Road rebuild, while working within the constraints, and benefits of, of the PDB project delivery method.

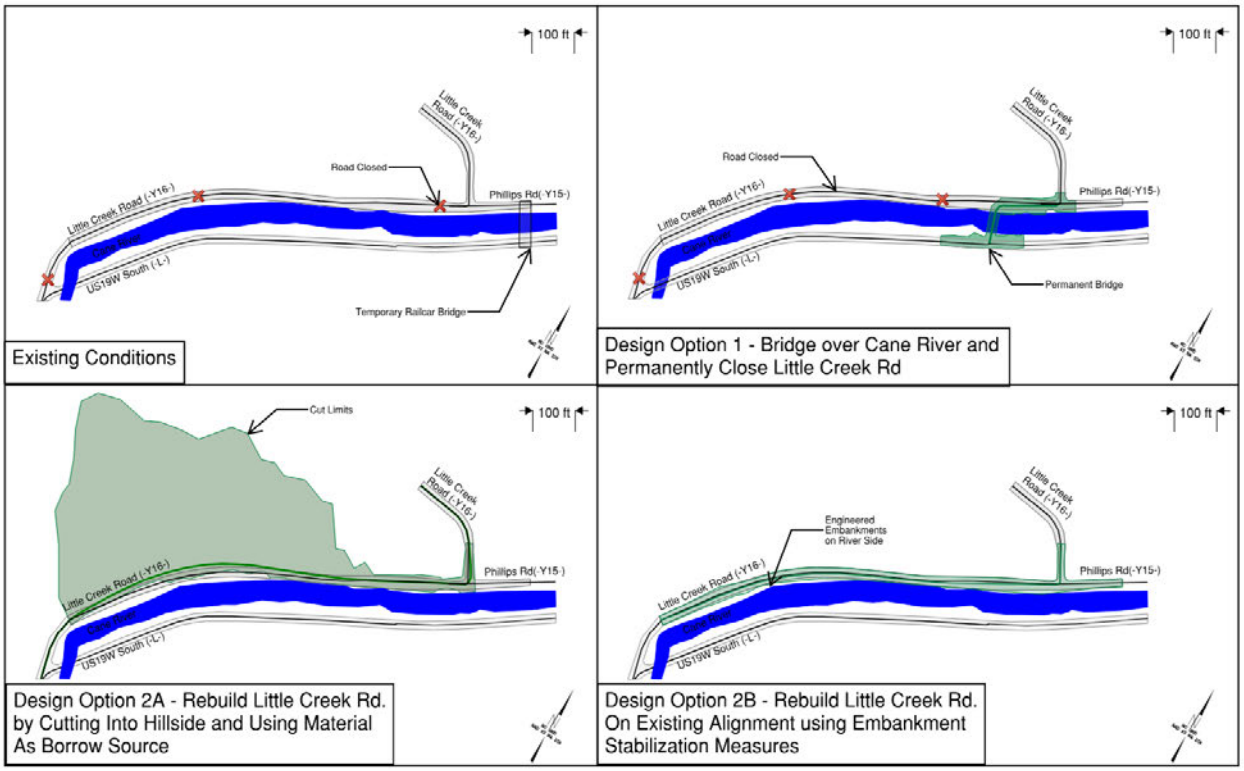

Figure 1. Design Options for Little Creek Road

Timeline

Hurricane Helene struck in September 2024, and emergency repairs began immediately after. The US19W South permanent repairs project was awarded to Branch and HDR in April 2025. When the project first initiated, the plan for permanent access was to construct a new bridge from US19W South over Cane River to Little Creek Rd/ Phillips Rd intersection (Design Option 1). The concern for rock borrow material sources arose, as twelve miles of embankment repair would require a significant amount of rock fill, and available material in the region is difficult or costly to acquire and transport due to post-storm demand. Thus, to resolve the problem of borrow material, design Option 2A was developed in October 2025. The design concept of Option 2A is to rebuild Little Creek Road by re-aligning portions of the roadway left of existing, into the hillside, and using the hillside as a borrow source to meet project needs.

Geotechnical recommendations for Option 2A heavily influenced the overall geometry of Little Creek Road rebuild. The design of the cut slope considered geotechnical recommendations and the volume of material needed for construction. Option 2A geotechnical investigations began in November 2025, and HDR and Branch prepared a cost estimate for Option 1 vs Option 2A in January 2026. Due to time constraints, subsurface investigations and geotechnical recommendations were issued with only preliminary borehole data and outcrop/rock cut mapping. In January, NCDOT decided based on the preliminary cost comparison and the long-term maintenance concerns of maintaining an additional structure that the preference was to pursue rebuilding Little Creek Rd (Option 2A).

Additional borehole data and geophysical survey testing was performed, and reports were updated in June 2026. Roadway designs were revised to reflect new geotechnical information and the concept moved forward to constructability considerations.

By July 2026, concern for constructability and risk began outweighing the pros of Option 2A. However, instead of resorting back to Option 1, an alternative design, Option 2B, was proposed. Design Option 2B, to rebuild Little Creek Road through engineered embankments, was selected over Option 2A in July 2026. Additional investigations are ongoing to support final plan design of Option 2B, with construction scheduled to be completed by Summer 2027.

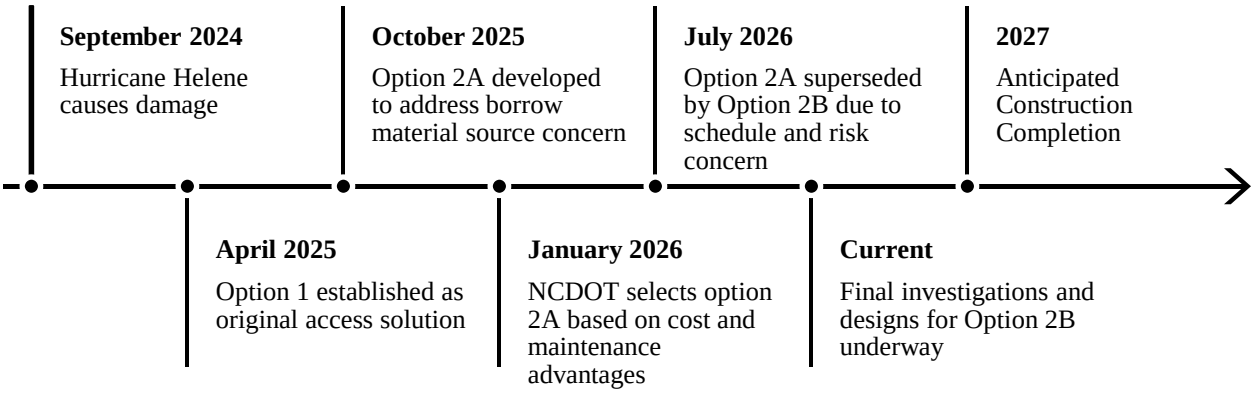

Figure 2. Little Creek Road Design Evolution Timeline

Project Delivery Method (PDB)

Progressive Design Build (PDB) is a project delivery method where the Owner (NCDOT) selects a design-build team (Branch and HDR) to progressively develop design and construction plans with the owner's input before a final construction price is established. Once the final price is agreed upon, the project moves into construction. PDB allows the team to develop the project and understand the risks before finalizing a cost. Utilizing a PDB delivery method can be particularly beneficial when accelerated delivery is required despite evolving project scope, site conditions, and risk profiles. Other benefits include greater owner and contractor involvement throughout design, improved cost certainty before construction begins, and enhanced collaboration between the owner, designer, and contractor.

Project Location

The project is located in Yancey County, North Carolina outside of the town of Burnsville. The project is along 10 miles of U.S. 19W from Cane River School Road (S.R. 1454) to Piney Hill Road (S.R. 1386), 1 mile of Little Creek Road (S.R. 1411) from U.S. 19W to Copperhead Drive, and 1 mile of Phillips Road (S.R. 1425) from Little Creek Road to the end of state maintenance limits.

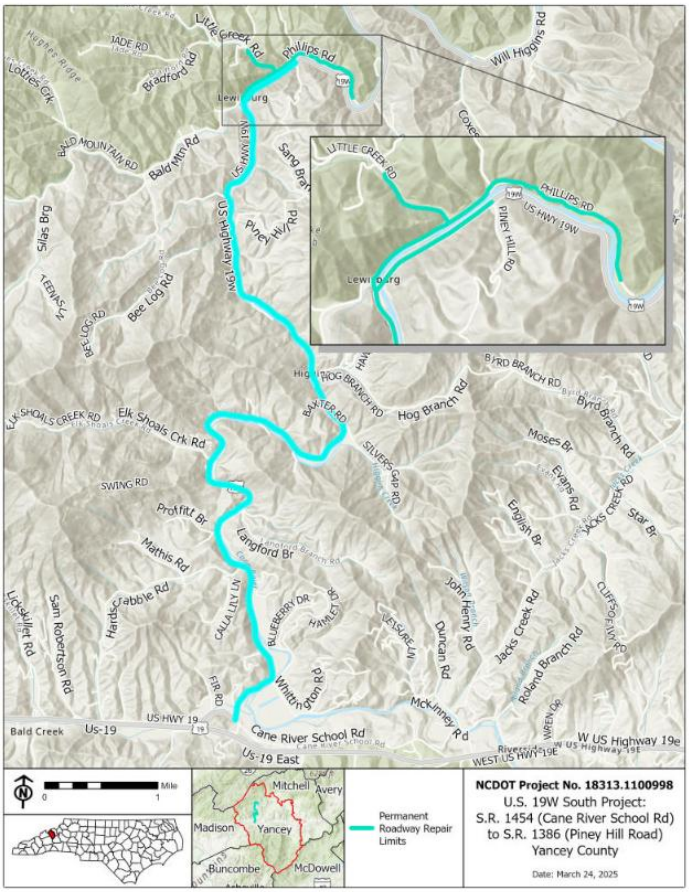

Figure 3. Project Location

Regional Geology

The project site area is physiographically located in the Blue Ridge Mountain Province of North Carolina. Topography consists of moderately high, highly weathered mountain ranges with scattered high elevation peaks and deeply dissected to gently rolling valleys. The pre-Cambrian to Cambrian bedrock geology is mostly metamorphosed gneisses and schists; soils are typically deep, well-drained, acidic sandy and gravelly loams (McNab, et al. 2007). Bedrock geologic quadrangle maps indicate the project area is underlain with mid-Proterozoic layered biotite granitic gneiss and is described as a thick repetitive sequence of layered biotite granitic gneiss to quartz dioritic gneiss; intergraded and interlayered with amphibolite, biotite, schist, and protomylonite. Layered biotite granitic gneiss to quartz dioritic gneiss is very light gray to pale orange to medium light gray; equigranular to inequigranular; granoblastic to lepidoblastic; and locally mylonitic (Merschat, 2003).

GEOLOGIC INVESTIGATION

Design Option 1 was not geotechnically investigated prior to abandoning the new bridge crossing in favor of Option 2A. Due to the geotechnical sensitivity and schedule of Design Option 2A, investigations were separated into three phases and were performed from November 2025 to May 2026. The design decision between Option 1 and 2A was made after Phase 1 investigations were completed in January 2026. Phase 1 included surficial geologic mapping and seven (7) vertical standard penetration test (SPT) and rock core borings. Six (6) of the Phase 1 borings were located along Little Creek Road, and one (1) at the crest of the mountain. Phase 2 included an additional twelve (12) vertical borings along Little Creek Road. Phase 3 included geophysical survey testing. The geotechnical feasibility report was re-issued at each phase of investigations as more data and testing became available. Additional borehole data on the existing rock and soil slope was not collected due to site access and permitting delays. Investigations to support the design of Option 2B are ongoing and not included in the investigation summaries below.

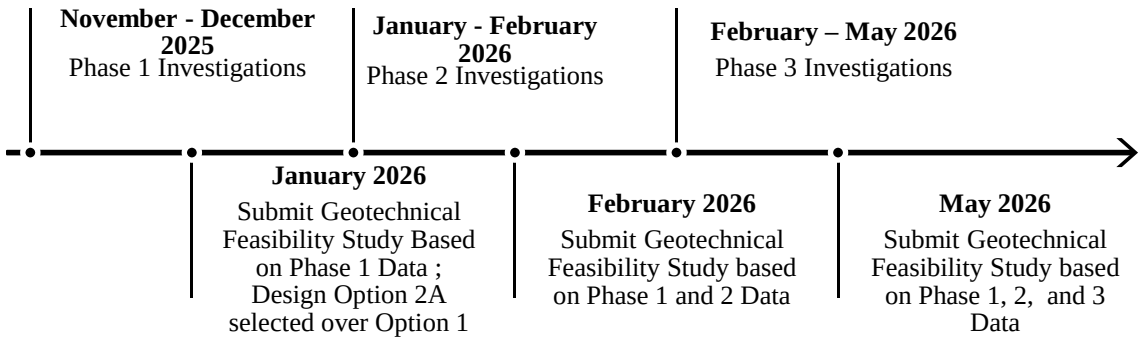

Figure 4. Evolution of Design Phase 2A Geotechnical Feasibility Report

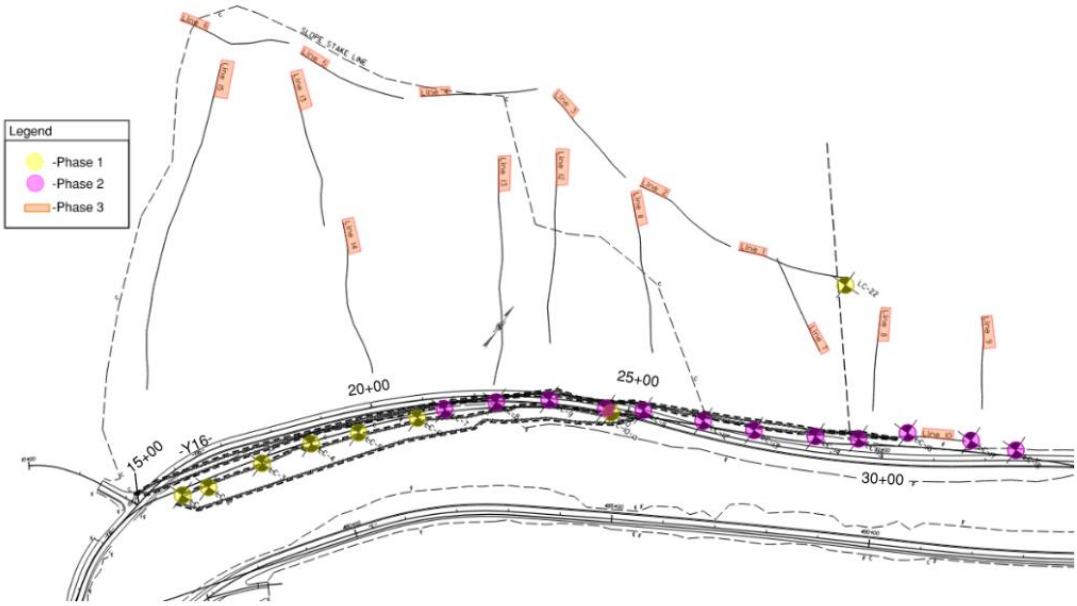

Figure 5. Design Phase 2A Geotechnical Investigation Plan

Geologic Mapping

HDR personnel performed geologic mapping of existing outcrops along Little Creek Road on December 2-3, 2025. Significant portions of the slope were obscured by vegetation at the time of the mapping effort but mapping was performed in general conformance to procedures outlined in ISRM, 1978. Outcrops consisted of predominantly hornblende gneiss, with lesser exposures of amphibolite, quartz-biotite gneiss, and mica schist layers. Few rocks were observed in the existing roadway catchment; however multiple rock clasts were observed on the upper vegetated slopes. Schmidt hammer testing was performed on competent exposed planar surfaces of gneiss and amphibolite outcrops. Generally, foliation was observed to be moderately dipping to the east/southeast, with multiple low and high-angle joint planes dipping to the west/northwest, cross-cutting the foliation planes within the exposed rock mass. Generally, the eastern third of the rock slope appears to decrease in rock competency closer to the Little Creek Road / Phillips Road intersection, corresponding to greater occurrences of softer mica schist and biotite gneiss deposits along the existing road cut, at approximately -Y16- STA. 29+00. There is an existing residence at the top of this section of the -Y16- alignment. Conversations with the property owner indicate that the slope down- gradient from the residence has been historically susceptible to landslides. This information was confirmed after a desktop review of the digital elevation model (DEM), which indicates the presence of failure scarps. Discontinuity characteristics such as weathering, aperture, spacing, persistence, joint roughness, and infilling were documented. No significant water seeps were observed emanating from the existing cuts and the weather was partly cloudy with no recorded precipitation during the mapping effort.

SPT/ Rock Core Borings

HDR subcontracted Universal Engineering Services, Inc. (UES) and Froehling & Robertson (F&R) to perform a geotechnical drilling investigation of the proposed cut. Nineteen (19) test borings were advanced using hollow-stem auger and NQ wireline coring methods – eighteen (18) borings were drilled along Little Creek Road below the proposed cut, and one (1) boring was drilled at the top of the slope near the existing house near -Y16- STA. 29+30. Borings were drilled in accordance with NCDOT Geotechnical Engineering Unit standards. Borings were drilled in two phases to accommodate report delivery schedule needs. Borings drilled at the toe of slope were advanced to below the bottom of Cane River, and the boring at the top of the slope was advanced to 200 ft.

Geophysical Survey

To obtain additional subsurface information, HDR subcontracted Collier Geophysics, Inc. to perform seismic refraction tomography (SRT) survey lines across sixteen (16) individual transects totaling 5,110 linear feet. SRT seismic surveys estimate compressional Primary wave (P-Wave) velocities through subsurface materials using a line of geophones and a trigger source. P-Wave velocities are measured in feet per second (ft/s) and can provide an indication of subsurface material layering. Line locations were determined by topographical access and were performed by certified rope access technicians rappeling down from the top of the slope.

SUBSURFACE INTERPRETATION

Subsurface Layers

Geologic mapping, borehole, and geophysical survey data was used to interpret the subsurface into three layers: Overburden (Ob), Rippable Rock (RR), and Nonrippable Rock (NRR). Overburden soils were identified in borings when SPT N-values were less than 100 blows per foot (<100 BPF), based on NCDOT logging criteria. Minimal overburden soil was encountered in borings drilled along Little Creek Road due to rock outcropping up to station 29+00. The boring located at the top of the slope (B-22) was used to represent overburden soil characteristics. Overburden soils consisted of loose to very dense, silty sand and silt, with trace to little mica. For Phase 1 and 2 reporting, overburden thickness was assumed to be 30 ft, based on B-22, unless rock was identified as outcropping. Geophysical data collected in Phase 3 supported further refinement of overburden soil's geometric extents, and was identified by velocities less than 3,000 ft/s.

Both RR and NRR were identified to be interlayered gneiss and amphibolite from stations 15+00 to 29+00, and mica schist with gneiss and amphibolite from stations 29+00 to 35+00. The delineation between the two layers is to represent material strength and weathering degrees, rather than two unique geologic stratums with differing origins or mineralogy. RR was identified in borings when SPT-N values were greater than 100 blows per foot (100/<1.0'). NRR was identified in borings when SPT-N values were 60 over less than one tenth of a foot (60/<0.1'). In addition, the Caterpillar Handbook of Ripping was reviewed, which assigns rock rippability indices based on seismic velocities. According to the handbook, a velocity of 3,000 ft/s corresponds to rippable metamorphic rocks. Rippability is defined as being excavatable with a D8-sized dozer with a single or multiple ripping shanks. Conversely, non-rippable metamorphic rock velocities range from 5,800 to 7,500 ft/s. A velocity of 6,000 ft/s was selected to represent the transition from RR to NRR. Data validation between borehole and geophysical test results is below. Note that depth was measured to nearest whole foot, P-wave velocities are inferred from SRT profiles, and GSI was derived by quantification methods per Hoek Diederichs (2013).

Non-Rippable Rock				
Boring ID	**Depth**	**RQD (%)**	**GSI**	**P-wave Velocity (ft/s)**
LC-15	>19	44	50-55	7,000
LC-16	>8	41	35-40	5,000
LC-17	>14	57	40-45	6,000
LC-22	>48	79	65-70	6,000

Table 1. Non-Rippable Data Validation

Rippable Rock				
Boring ID	**Depth (ft)**	**RQD (%)**	**GSI**	**P-Wave Velocity (ft/s)**
LC-15	7-19	19	20-25	3,500
LC-16	3-8	WR	WR	3,000
LC-17	9-14	WR	WR	4,000
LC-22	28-48	35	15-20	3,000

Table 2. Rippable Rock Data Validation

3D Geologic Modeling

Geologic cross-sections and profiles are historically drafted in 2-D using Microstation GEOPAK software for NCDOT projects, but the use of 3-D modeling software for this site was crucial for developing geometric extents of layers due to the variability in type of data, phased data collection methods, and due to the mountainous, steep topography. Using Seequent's Leapfrog Works program, a 3-D geologic model was developed using a site-specific DEM as the primary model topography. The SRT seismic velocity profiles for all 16 lines, borehole data, and surface mapping results were incorporated into the model to establish estimated 3-D volumes for the three (3) generalized material layer types. Once the model was completed, the 3-D surfaces for each layer boundary were provided to HDR's Roadway designers and incorporated into Microstation for use in 2-D design. The roadway engineers can use the model and apply it to not only Design Option 2A, but also future (Option 2B) designs, without any additional effort from the geotechnical team. Below are example figures of the 2-D subsurface model produced in Leapfrog and import results in Microstation.

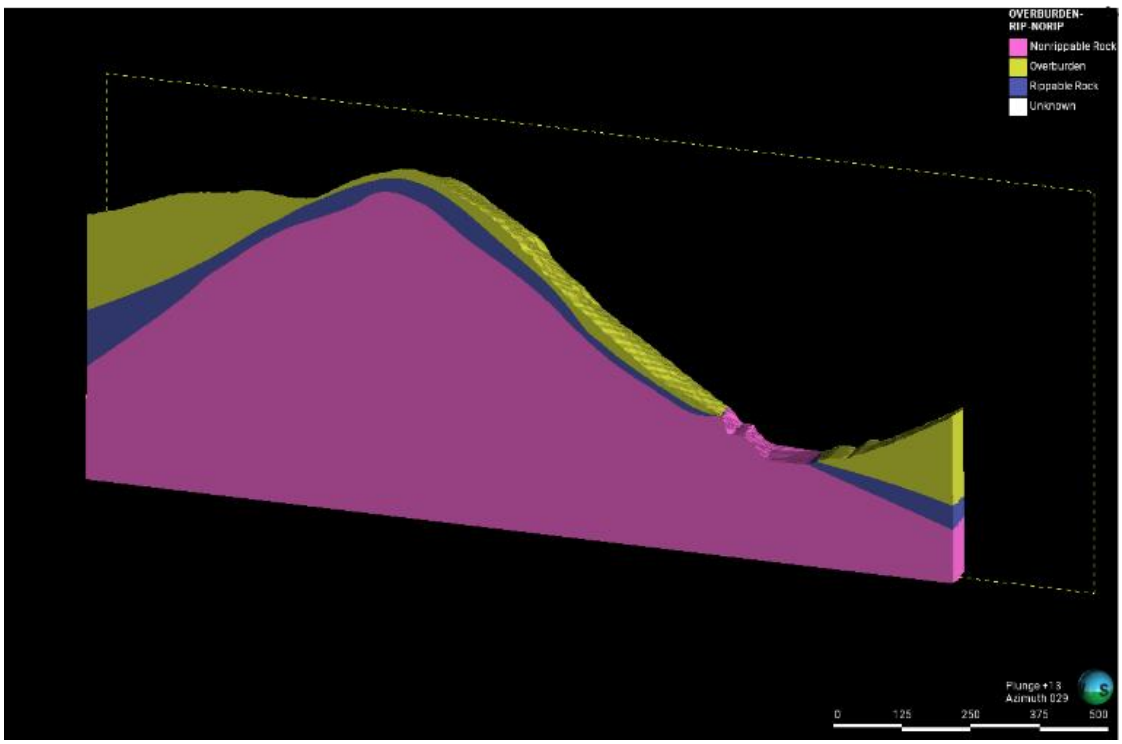

Figure 6. Leapfrog Works Subsurface Model

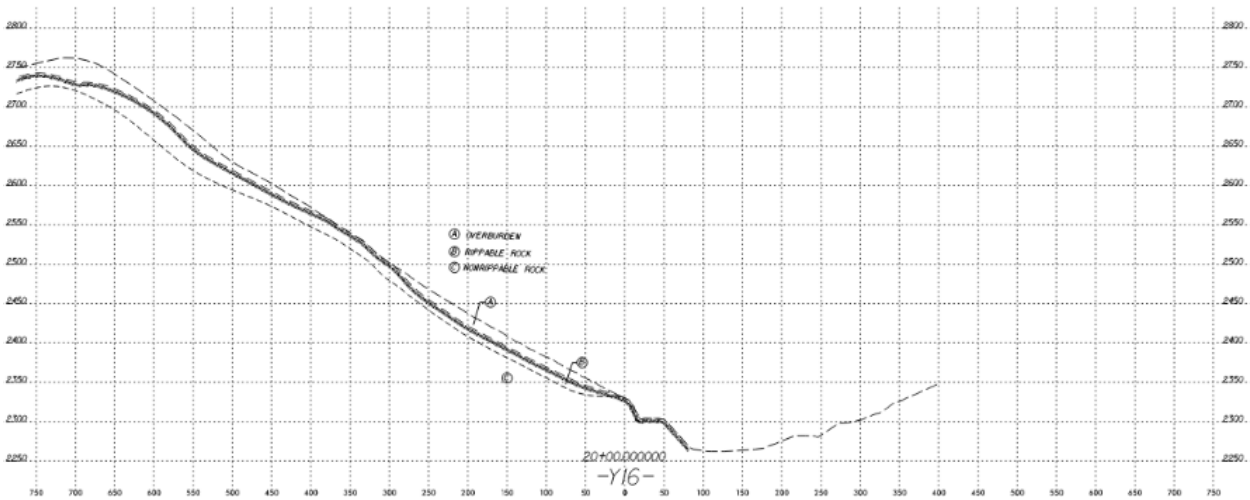

Figure 7. 2D Cross-Section of Subsurface Model from Microstation

GEOTECHNICAL ANALYSIS

Rock Mass Stability

Kinematic Analysis

Foliation and joint measurements derived from rock face mapping were kinematically analyzed by comparing the proposed cut slope orientations against the mapped discontinuity orientations. The stability of the overall competent crystalline rock mass exposed in outcrops appears to be discontinuity-controlled; however, stability of the eastern third (-Y16- STA. 29+00 +/-) of the slope where mica schist deposits are more prominent may be more susceptible to shear failure. Kinematic analyses assess the potential likelihood for rock slope failures and are categorized into planar, wedge, and flexural/direct toppling. The criteria for planar, wedge, and toppling failures is based on methods developed by Hoek and Bray (1981) and Goodman (1989). The major rock mass discontinuities observed are primarily SE-dipping foliation planes with cross-cutting low to high-angle joint faces associated with tectonic stress relief.

Kinematic analyses were performed based on the proposed cut wall orientations derived from Roadway layout sheets. Two wall cut dip directions were used: 125° and 152°. For these downslope directions, two proposed slope cut angles were analyzed = 1.0H:1.0V (45°) and 0.67H:1.0V (56°). Rocscience® Dips™ (v. 8.0) was used to perform the kinematic runs. Cluster analysis provided the statistical mean values for four subsets of the 121 total measured discontinuities, as indicated below:

- Set 1m – Foliation – (Dip Direction 119° / Dip 40°)
- Set 2m – Joint Trends – (Dip Direction 068° / Dip 73°)
- Set 3m – Joint Trends – (Dip Direction 264° / Dip 40°)
- Set 4m – Joint Trends – (Dip Direction 356° / Dip 85°)

Analysis inputs include the joint and foliation measurements, proposed cut slope orientations, friction angle of the discontinuities (set at 30°), and 20° lateral limits (for planar, flexural/direct toppling). The analysis for each type of failure provides an estimate for likelihood of failure

related to all critical discontinuity intersections in the data set. Findings from the kinematic analysis results are as follows:

Station 15+00 – 22+00 0.67H:1.0V (N = 121)	
Dip; Dip Direction: 56°; 125°	
Type of Failure	%
Planar Sliding	
All	33.1
Set 1 (Foliation)	78.4
Wedge Sliding	
All	38.9
Flexural Toppling	
All	2.5
Set 4 (Joint)	3.8
Direct Toppling	
Direct Toppling (Int.)	2.5
Oblique Toppling (Int.)	1.3
Base Plane (All)	38.8
Base Plane (Set 1-Foliation)	90.2

Station 15+00 – 22+00: 1.0H:1.0V (N = 121)	
Dip; Dip Direction: 45°; 125°	
Type of Failure	%
Planar Sliding	
All	18.2
Set 1 (Foliation)	43.1
Wedge Sliding	
All	19.4
Flexural Toppling	
All	0.8
Set 4 (Joint)	-
Direct Toppling	
Direct Toppling (Int.)	1.7
Oblique Toppling (Int.)	1.3
Base Plane (All)	26.5
Base Plane (Set 1-Foliation)	60.8

Station 22+00 – 28+50: 0.67H:1.0V (N = 121)	
Dip; Dip Direction: 56°; 152°	
Type of Failure	%
Planar Sliding	
All	5.0
Set 1 (Foliation)	11.8
Wedge Sliding	
All	17.7
Flexural Toppling	
All	0.8
Set 4 (Joint)	7.1
Direct Toppling	
Direct Toppling (Int.)	1.8
Oblique Toppling (Int.)	2.2
Base Plane (All)	11.6
Base Plane (Set 1-Foliation)	23.5

Station 22+00 – 28+50: 1.0H:1.0V (N = 121)	
Dip; Dip Direction: 45°; 152°	
Type of Failure	%
Planar Sliding	
All	0.8
Set 1 (Foliation)	2.0
Wedge Sliding	
All	7.6
Flexural Toppling	
All	0.8
Set 5 (Joint)	7.1
Direct Toppling	
Direct Toppling (Int.)	1.1
Oblique Toppling (Int.)	2.2
Base Plane (All)	7.4
Base Plane (Set 1-Foliation)	13.7

Table 3. Kinematic Analysis Summary

Based on the kinematic analysis results, the dominant failure modes are planar sliding along foliation planes and wedge sliding along foliation and high-angle joint surfaces, with moderate to higher likelihood of planar and wedge failures occurring along slope lengths from Station 15+00 to Station 22+00. It should be emphasized that kinematic analyses do not consider specific characteristics of these discontinuity surfaces.

Intact Rock Strength

Compressive strength of the discontinuity surfaces is an important component of estimating shear strength. A quantitative method for determining discontinuity compressive strength is the Schmidt rebound hammer test (ISRM 1978). Schmidt hammer testing was performed on competent exposed planar surfaces of gneiss and amphibolite outcrops. Per the method, each surface is tested 10 times, with the lowest five readings of each test group being discarded and the mean rebound value is calculated by averaging the five highest readings of each test group. The hammer angle and direction of each test is recorded in the field and a correction factor is applied. Uniaxial compressive strength is then estimated using the mean rebound number (r) and the applicable rock density value (γ in pcf) using the following equation (Deere & Miller, 1966):

$$\log_{10}(\sigma_c) = 0.00014*\gamma*r+3.16$$

Where σ_c is the uniaxial compressive strength, in pounds per square inch (psi). A density value of 176 pcf was used for calculation purposes. Overall, nine (9) test groups were attempted, subdivided by foliation and joint surfaces; however, only eight (8) were completed as one of the

test groups was from incompetent mica schist rock. In general, significantly higher compressive strength values were observed on joint surfaces versus foliation surfaces. A summary of rebound hammer test results is provided in Table 4.

Estimated Uniaxial Compressive Strength		
	Foliation	**Joint**
	Qu (psi)	**Qu (psi)**
Count (N) =	5	4
Mean =	10,596	24,403
Median =	10,328	23,603
SD =	6,411	13,403
Minimum =	1,445	10,235
Maximum =	18,101	40,170

Table 4. Rebound Hammer Testing Results

Laboratory tests were performed on ten (10) intact, fresh core samples collected from wireline corehole borings. Intact rock samples were tested for uniaxial compressive strength using ASTM D-7012 Method C, with a summary of test results presented on the following table. These samples should be considered representative of the Non-Rippable rock layer.

	Qu (psi)	**ρ (pcf)**
Count (N) =	10	10
Mean =	10,424	175
Median =	10,514	176
SD =	3,318	11
Minimum =	6,167	162
Maximum =	17,687	191

Table 5. Uniaxial Compressive Strength Summary Results

The average values derived from the rock laboratory test results are similar to rebound hammer-derived estimates of foliation plane surfaces; however joint surface rebound hammer strength estimates were significantly higher. A review of the UC break test photos reveals most tested samples failed in shear (not compression), with breaking surfaces cross-cutting foliation planes. Average strength values for amphibolite samples were significantly lower than gneiss samples.

Discontinuity Strength

Given the relatively high intact rock strengths exhibited from uniaxial compression testing of the crystalline rock present at the site, the stability of the majority of the rock slope is discontinuity-controlled. To ascertain the rock mass strength, the Geological Strength Index (GSI) correlation method developed by Hoek-Diederichs (2013) was used, according to the following equation:

$$GSI = 1.5\ JCond_{89} + RQD/2$$

Where the joint condition rating ($JCond_{89}$) method is determined as defined by Bieniawski (1989) and the rock quality designation (RQD) method is estimated from drillhole data as defined by Deere (1963). Using the referenced method, scores were assigned for each category based on borehole logs and later combined and evaluated for trends. Two (2) generalized comparable rock types with similar characteristics were observed (varying types of gneiss and

amphibolite). A summary table showing GSI and RQD ranges as percents of total rock cored is below in Table 6. A summary table showing GSI and RQD ranges as percents of total rock within the recommended cut limits (-Y16- STA. 15+00-28+50) is below in Table 7.

GSI and RQD Range	GSI as Percent of Total Rock Cored	RQD as Percent of Total Rock Cored
0-10	6%	3%
10-20	1%	2%
20-30	2%	1%
30-40	6%	4%
40-50	8%	13%
50-60	13%	24%
60-70	18%	1%
70-80	14%	10%
80-90	18%	11%
90-100	13%	31%

Table 6. GSI and RQD vs Total Rock Cored

GSI and RQD Range	GSI as Percent of Rock Cored STA. 15+00-28+50	RQD as Percent of Rock Cored STA. 15+00-28+50
0-10	8%	4%
10-20	1%	0%
20-30	0%	1%
30-40	0%	5%
40-50	0%	4%
50-60	5%	14%
60-70	24%	1%
70-80	19%	14%
80-90	25%	15%
90-100	17%	42%

Table 7. GSI and RQD vs Rock Core within Proposed Cut Limits

Shear strength parameters have been developed to estimate the degree of sliding failure along foliation and joint planes. Three potential modes of failure along a sliding discontinuity exist:

- Asperity override at low normal stress
- A combination of asperity override and failure through asperities at intermediate normal stresses
- Failure through asperities at high normal stresses

Undulations and asperities of rock mass discontinuities have a significant influence on the shear strength of the interface surface. A way of quantifying the effect of discontinuity undulation and surface roughness is through the Joint Roughness Coefficient (JRC) by measuring amplitude over a given discontinuity length. Studies have shown that surface roughness significantly increases shear strength along the surface planes (Patton 1966; Barton 1973, 1976; Barton and Choubey 1977). Failure through rock asperities is not anticipated due to low normal stresses and relatively high intact rock mass strengths as compared with the kinematic analysis results.

Site-specific data is not available for the basic friction angle, ϕ_b, of the discontinuities. Wylie and Norrish (1996) give values of the basic friction angle for gneiss of 27° to 34°. Barton (1973, 1976) gives values of the basic friction of amphibolite of 31° to 33° degrees. A value of 27° (lower third of the range) is used to estimate the shear strength of rock on rock along the foliation planes and 30° along joint planes (mid-point between the values of schistose gneiss and amphibolite).

Based on the kinematic analysis of combined discontinuity orientations, planar failure occurs along foliation planes with an average dip direction of 145° and dip of 51°. Wedge failures occur along the intersection of foliation and two cross-cutting high-angle joint planes with mean dip directions / dips of 068° / 73° and 356° / 85°. These intersecting planes produce lines with trend and plunge values of 144° / 37° and 082° / 34°, respectively.

For Joint Compressive Strength (JCS), the mean amphibolite uniaxial compressive strength value of 6,865 psi is recommended as an initial value, with a reduction factor of 2.5 to estimate the scaling effect of JCS with increasing sliding plane lengths (block sizes) as recommended by Barton & Choubey (1977) and Barton (1990) for unweathered surfaces. The following values used to estimate shear strength along foliation and joints are summarized in Table 8.

Parameter	Foliation Surface Values	Joint (High-Angle) Surface Values
JRC*	6.1	7.8
JCS**	395 kips/ft^2	
Base Friction Angle	27°	30°
Rock Unit Weight	0.176 kips/ft^3	
* - Joint Roughness Coefficient – Derived from geologic mapping of exposure surfaces. ** - Joint Compressive Strength		

Table 6. Discontinuity Shear Strength Parameters

Rockfall Catchment

Rockfall impact includes the detachment of individual or multiple clasts from a rock slope face, typically less than 6 feet in the largest dimension. Sub-global (rockfall) stability was analyzed using a Roadway Cross Section from -Y16- STA. 19+00 and 24+50 using the statistical probability analysis program RocFall™ 2D (v. 8.0) developed by Rocscience, Inc®. This critical cross-section was selected based on existing groundline geometry and estimated rocklines. Optimal cut slope orientations derived from the global stability analysis were used in developing the slope geometries for each critical section. The following conditions were used in formulating rockfall scenarios:

- Maintain a minimum 5’ wide, 4:1 foreslope catchment geometry. A rockfall catchment design with a minimum of 90% retainment is typically required by NCDOT; however, due to the minimal anticipated traffic volumes along this section of Little Creek Road, NCDOT allowed a waiver of this requirement.
- Assumed a production blast rock face on slopes.
- No benching of the finished rock faces.
- NCDOT standards typically direct a rockfall catchment design with 90% retainment.

Observations and vertical extents of each material unit on the slope were estimated and given a representative name that correlated to a range of values for surface roughness, the normal coefficient (Rn) and tangential coefficient (Rt). Surface roughness is defined as the perpendicular variation of the slope within the slope distance equal to the radius of a potential falling rock. A surface roughness of 0.0 was used for conservative purposes. Rn is a measure of the degree of elasticity in a collision normal to the slope, and Rt is a measure of frictional resistance to movement parallel to the slope. Model input values for each slope material type simulated are provided on Table 9.

Slope Material Properties	Normal Restitution (Rn)	Tangential Restitution (Rt)
Nonrippable Rock	0.35	0.85
Talus Cover	0.32	0.80
Overburden	0.30	0.81
Catchment floor	0.35	0.85
Pavement (asphalt)	0.40	0.90
Rippable Rock	0.32	0.71
* Parameters selected based on HDR experience with similar slope conditions. ** 3x normalized standard deviation of most parameters was used.		

Table 7. Slope Input Parameter Values

For analysis purposes, a rockfall generator (point seed) elevation was set at the top of the rippable proposed rock cut (Seeder 1) and at the top of the 1:1 nonrippable slope crest (Seeder 2), as determined from interpretation of available subsurface data obtained through SPT / wireline borings and geophysical survey data. Two rock types were modeled: gneiss and amphibolite. Assumed density values of 171 lb/ft3 and 190 lb/ft3 were used for each rock type, with varying ellipsoidal and sphere block sizes of 1'x2', 2'x3', and 5'x6' dimensions. Horizontal and vertical starting velocities for each seeder of 1 ft/sec at the top of each crystalline rock cut with a 3x normalized standard deviation were used and 1,000 rockfall events were modeled.
Using these criteria, catchment and slope geometry was modeled based on the following scenarios:

- Station 19+00LT & 24+58 – Maximum 1.0H:1.0V cut slope with 12-ft wide 4:1 rock-lined catchment

Table 10 provides a summary of rockfall analysis results regarding data collected at the proposed edge of pavement for the current alignment.

Critical Section Station		19+00LT
Applicable Sections		15+00 – 22+50
Crystalline Rock Cut		1.0H:1.0V
Rock Cut Height (Max, ft)		520
4H:1V Catchment Width (ft)		12
Edge of Pavement Metrics	Percent Retained (%) Total	33
	Bounce Height (Mean, ft)	9.9
	Total Kinetic Energy (Mean, kJ)	122

Table 8. Rockfall Analysis Summary STA. 19+00 to 22+50

Critical Section Station		24+50LT
Applicable Sections		22+50 –26+50
Crystalline Rock Cut		1.0H:1.0V
Rock Cut Height (Max, ft)		230
4H:1V Catchment Width (ft)		12
Edge of Pavement Metrics	Percent Retained (%) Total	40
	Bounce Height (Mean, ft)	4.5
	Total Kinetic Energy (Mean, kJ)	58

Table 9. Rockfall analysis summary STA. 22+40 to 26+50

GEOTECHNICAL RECOMMENDATIONS

Slope Recommendations

Slope kinematics indicate that a rock cut slope steeper than 1.0H:1.0V in NRR may pose a higher likelihood of failure due to the orientation of average planar and wedge surfaces. 2:1(H:V) slopes are recommended in both OB and RR layers. The feasibility recommendations note that if slopes need to be steepened to accommodate design needs, additional geotechnical

data and analyses would be required. Steepening of slopes may include stabilization measures, including but not limited to, soil nail wall, rock plating, or turn reinforcement mat (TRM) with pinned mesh. Based on derived parameters, rockfall simulations performed at the critical section at -Y16- STA. 19+00 and 24+50 indicate that a 12-ft wide 4.0H:1.0V catchment will only retain approximately 33% and 40%, respectively, of future rockfall with a 1.0H:1.0V slope cut orientation. The NCDOT 90% rockfall catchment design criteria has been waived on this project by NCDOT. The criteria was waived due to the secondary road status of LCR, and the consideration of rockfall to be a future maintenance responsibility. Based on these preliminary findings, recommendations included the following:

- Station 15+00 +/- to Station 28+50 +/-:
    - A 1.0H:1.0V cut within NRR using production blasting techniques with a minimum 10’ wide overburden bench at the top of the 1.0H:1.0V crystalline rock cut. A spot bolting and rock cut scaling contingency should be included to stabilize any potentially adverse planar and wedge features revealed during blasting and excavation activities.
    - Above the 1.0H:1.0V NRR cut, the overlying RR and OB material should be cut back at a minimum 2.0H:1.0V orientation. A steeper residuum cut may require on-slope reinforcement that should be confirmed and designed using slope stability analyses.
    - Create a minimum 5 feet wide 4.0H:1.0V catchment at the base of the 1.0H:1.0V crystalline rock cut to facilitate drainage and maintenance. The catchment surface should be lined per NCDOT’s discretion.
- Station 28+50 +/- to Station 34+81 +/-:
    - Interpreted rock quality is estimated to degrade to softer mica schist and residuum at STA. 29+00. Cut slope excavations shall also have no impact to the residence at the top of the slope beginning at approximately STA. 28+50; therefore, the proposed roadway alignment could shift back to the original alignment, with no excavation to the LT side of LCR ahead STA. 28+50. Construction disturbance (i.e. blasting) activities should consider the presence of the residence at the top of the slope and this section's susceptibility to landslides.

Roadway Volume Quantities

Utilizing the geotechnical slope recommendations listed above, HDR’s roadway design team progressed with the design of 1:1 cut in NR rock and 2:1 in RR and OB. The 3-D geologic model provided to roadway was projected into MicroStation design files for estimation only purposes. The contractor estimated a need of 300,000 CY of NR material and 250,000 CY for RR and OB materials. With the intent to satisfy material fill needs, while adhering to geotechnical and other discipline’s recommendations, roadway developed slope geometries in the preliminary plans. These updated slope geometries could produce an estimated 306,000 CY of NR material and 335,000 CY RR and OB material.

CONCLUSION

The Little Creek Road rebuild demonstrates the challenges and benefits of progressive design build (PDB) project delivery method in the wake of natural disaster repairs. Three

permanent access solutions, Design Option 1, 2A, and 2B, were evaluated. Design Option 1 included a new bridge crossing over Cane River and the permanent abandonment of Little Creek Road. Design Option 2A was favored over Design Option 1 due to the potential to produce borrow source material for the project. Design Option 2A included geotechnical feasibility analysis of a hillside cut adjacent to Little Creek Road. The investigations and analyses, detailed in this report, indicate that a cut can be constructed to be geotechnically stable and also produce sufficient material volumes. However, through continued collaboration with NCDOT, HDR, and Branch Civil, constructability, schedule, and rock production risk considerations led to the decision to abandon Design Option 2A and instead progress further with Design Option 2B. Design Option 2B includes Little Creek Road rebuild by repairing embankment slopes toward Cane River and stabilizing using engineered solutions. Borrow material for the project will be sourced from regional quarries. Geotechnical investigations and recommendations for Design Option 2B are ongoing. The progression from Option 1 to Option 2A to Option 2B highlights the value of PDB methods, where design concepts can be refined as the scope, risk, and schedule become further understood. This project also demonstrates that successful geotechnical engineering on emergency recovery projects requires flexibility, rapid data collection, and close coordination with other engineering disciplines. The use of phased reporting to meet projected decision schedules and the use of 3-D modeling software proved to be critical for the geotechnical team to produce quality subsurface interpretations and engineering design within the confinement of project demands and schedule. Although Option 2A was not selected for final design, the geotechnical investigation and analyses provided critical information to inform project decision making, reduce uncertainty, and support development of the design option.

REFERENCES:

1. Barton, N. 1973. Review of a new shear strength criterion for rock joints. Engineering Geology, Vol. 7, p. 287-332.
2. Barton, N. 1976. The shear strength of rock and rock joints. International Journal of Rock Mechanics, Mining Science and Geomechanical Abstracts, Vol. 13, p. 255-279.
3. Barton, N. 1990. Scale effects or sampling bias?, in Pinto da Cunha, A., ed., Scale Effects in Rock Masses, Proceedings of the First International Workshop on Scale Effects in Rock Masses. A. A. Balkema/Rotterdam/Brookfield, pp. 31-35.
4. Barton, N. and S. Bandis. 1982. Effects of block size on the shear behavior of jointed rock, in, Goodman, R. E. and F. E. Heuze, eds., Proceedings of the Twenty-Third Symposium on Rock Mechanics, The University of California, Berkeley, California, August 25-27, 1982. p. 739-760
5. Barton, N. and B. Choubey. 1977. The shear strength of rock joints in theory and practice. Rock Mechanics, Vol. 10, p. 1-54.
6. Bieniawski, Z.T. 1989. "Engineering rock mass classification." New York: Wiley Interscience.
7. Deere, D.U. 1963. "Technical description of rock cores for engineering purposes." Rock Mechanics and Engineering Geology. 1 (1), 16-22.
8. Goodman, Richard. 1989. Introduction to Rock Mechanics: 2nd Edition. University of California,
   Berkeley. Wiley Publishing. 1989.
9. Hoek, E., Carter, T.G., and Diederichs, M.S. 2013. "Quantification of the Geological Strength Index Chart". American Rock Mechanics Association. ARMA 13-672. June 23-26, 2013.
10. Hoek, E., and Bray, J.W. "Rock Slope Engineering". 3rd Edition. Institution of Mining and Metallurgy. 1981.
11. ISRM (International Society for Rock Mechanics). 1978. "Suggested Methods for the Quantitative Description of Discontinuities in Rock Masses. International Journal of Rock Mechanics and Mining Sciences & Geomechanical Abstracts, Vol. 15 pp 319-368.
12. McNab, W.H., Cleland, D.T., Freeouf, J.A., Keys, Jr., J.E., Nowacki, G.J., and Carpenter, C.A. 2007. "Ecological Subregions: Sections of the Conterminous United States." US Department of Agriculture, Forest Service. General Technical Report WO-76B. January 2007. Map and Text.
13. Merschat, C.E. 2003. "Bedrock Geologic Map of the Bald Creek 7.5-Minute Quadrangle, North Carolina & Tennessee." North Carolina Geological Survey. Open File Report 97-05. 2003. Map Scaled 1:24,000.
14. North Carolina Department of Transportation Geotechnical Engineering Unit 2021. Geotechnical Investigation and Recommendations Manual.
15. Patton, F. D. 1966. Multiple modes of shear failure in rock. Proceedings of the 1st Congress, International Society for Rock Mechanics. Lisbon. 1, p. 509-513.
16. Wyllie, D. C. and N. I. Norrish. 1996. Rock strength properties and their measurement, p. 372-390, in, Turner, A. K. and R. L. Schuster, eds., Landslides: Investigation and Mitigation: Transportation Research Board, Special Report 247, National Academy Press, Washington, D.C., 673p.

06. Integrating UAS Remote Sensing and In-Situ Instrumentation for Landslide Hazard Monitoring to Support Highway Infrastructure Resilience

Ashley Butterworth, G.I.T.
BGC Engineering Inc.
600 12th St, #300
Golden, CO 80401
303-874-8398
ButterworthA@bgcengineering.ca

Donna Delparte, Ph.D.
Idaho State University, Department of Geosciences
921 S 8th Ave, Stop 8072
Pocatello, ID 83209
(208) 282-4419
delparte@isu.edu

James Mahar, Ph.D., L.P.G, P.G., P.H.G.
Idaho State University, Department of Civil Engineering
921 S 8th Ave, Stop 8060
Pocatello, ID 83209
(208) 282-5287
mahajames@isu.edu

Matthew Belt
Idaho State University, Department of Geosciences
921 S 8th Ave, Stop 8072
Pocatello, ID 83209
beltmatt@isu.edu

Betty Brown
Idaho State University, Department of Geosciences
921 S 8th Ave, Stop 8072
Pocatello, ID 83209
bettybrown@isu.edu

Shawn Enright, P.G.
Idaho Transportation Department, District 6
206 N Yellowstone Hwy
Rigby, ID 83442
Shawn.enright@itd.idaho.gov

Prepared for the 75th Highway Geology Symposium, September, 2026

Acknowledgements

The authors would like to thank the Idaho Transportation Department Research Program and Technical Advisory Committee for their contributions in the work described:

Chad Clawson, P.E. – Idaho Transportation Department
Shawn Enright, P.G. – Idaho Transportation Department, District Six
Greydon Wright, P.E. – Idaho Transportation Department, District Five
Nikolas Stevens, P.G. – Idaho Transportation Department, District One
Anne Rector – Idaho Transportation Department, District Six
Jet Johnstone – Idaho Transportation Department, District HQ
Mark Hayes, P.E. – Idaho Transportation Department, District Six
Tyler Coy, P.E. – Idaho Transportation Department, District HQ
Amanda Laib – Idaho Transportation Department, Research Program
Darrell Hanners, P.L.S. – Idaho Transportation Department, District Five
Garrett Speeter, P.G. – Idaho Transportation Department, District Two
Zach Lifton, Ph.D., P.G. – Idaho Geological Survey
Ed Miltner, P.E. – FHWA, Idaho Division

Disclaimer

Statements and views presented in this paper are strictly those of the author(s), and do not necessarily reflect positions held by their affiliations, the Highway Geology Symposium (HGS), or others acknowledged above. The mention of trade names for commercial products does not imply the approval or endorsement by HGS.

Copyright Notice

Copyright © 2026 Highway Geology Symposium (HGS)

All Rights Reserved. Printed in the United States of America. No part of this publication may be reproduced or copied in any form or by any means – graphic, electronic, or mechanical, including photocopying, taping, or information storage and retrieval systems – without prior written permission of the HGS. This excludes the original author(s).

ABSTRACT

Highways, especially those constructed along steep terrain, are susceptible to landslide impacts, including public safety risks and economic disruptions. Early detection of potential landslides is essential for informed decision-making in highway infrastructure planning. Traditional landslide monitoring through in-situ instrumentation provides precise subsurface measurements but is spatially limited and resource-intensive. The Idaho Transportation Department, in partnership with Idaho State University, Department of Geosciences, is developing cost-effective monitoring strategies that improve spatial coverage while maintaining reliable displacement measurements. Unmanned Aerial System (UAS) surveys are a cost-effective approach to landslide hazard monitoring along transportation networks, offering repeatable high-resolution terrain models that can facilitate early detection of mass movements. This study utilized repeat UAS LiDAR and photogrammetry surveys to perform change detection along landslide-susceptible state highway US-26, which were synthesized with inclinometer measurements and bore logs to produce a comprehensive slope stability assessment. Surface displacement was quantified using the Cloud-to-Cloud Comparison (C2C) change detection method. Pairing UAS-derived products with inclinometer measurements provided a validation framework for linking surface change to subsurface movement. Bore logs further identified lithologic controls and potential slip surfaces. Repeat UAS monitoring successfully identified an unstable slope threatening a state highway, demonstrating the capability of UAS-based surveys in assessing landslide hazards along Idaho Transportation Department highway assets and reinforcing the need for continuous monitoring.

INTRODUCTION

Landslides are one of the most persistent and costly hazards facing transportation infrastructure, capable of damaging pavement, blocking roadways, and endangering motorists. Managing this risk often depends on the ability to detect slope movement early and to reliably monitor susceptible areas over time, yet conventional ground-based instrumentation methods alone are often cost-intensive and spatially limited. Unmanned Aircraft Systems (UAS) equipped with red-green-blue (RGB) and light detection and ranging (LiDAR) sensors have emerged as a practical complement to traditional monitoring, offering safer access to hazardous terrain and the ability to capture high-resolution topographic data at a relatively low cost (*1*). When paired with in-situ geotechnical instrumentation, UAS-derived data can help bridge the gap between discrete point measurements and continuous spatial coverage, improving the detection of landslide activity across a site. Despite the growing use of UAS for landslide monitoring, no standardized approach exists for selecting platforms, sensors, or processing methods for monitoring landslide hazards, and few studies have examined how to effectively pair remote sensing data with in-situ instrumentation.

This paper presents findings from a research study conducted between 2023 and 2024 by Idaho State University (ISU) in collaboration with the Idaho Transportation Department (ITD) to evaluate the integration between remotely sensed data and in-situ instrumentation. Repeat UAS surveys derived from LiDAR and photogrammetry were paired with inclinometer data to assess slope movement over time, applying change detection to quantify surface displacement. This study also establishes and develops a workflow for UAS-based infrastructure surveys to support more standardized, cost-effective landslide monitoring along transportation corridors.

Study Site

Located in southeastern Idaho, the Swan Valley site along U.S. Highway 26 (US-26) contains a major landslide area (Figure 1). Historic landslide activity is observed both above and below the highway alignment, including scarps near the base of the slopes above the highway. The site extends between mile markers 373.85 and 374.6 and is bounded by longitudes 111°23'53"W and 111°23'10"W and latitudes 43°27'33"N and 43°26'51"N. Study site elevations range from 5265 to 5742 ft (1605 to 1750 m). Uplands are characterized by agricultural fields that transition to steeper terrain covered by sagebrush, grass, and forb vegetation. Below US-26 is the South Fork of the Snake River. All observed slide activity during the investigation period occurred on the hillside north of US-26. No evidence of pavement damage or roadway surface deformation was observed.

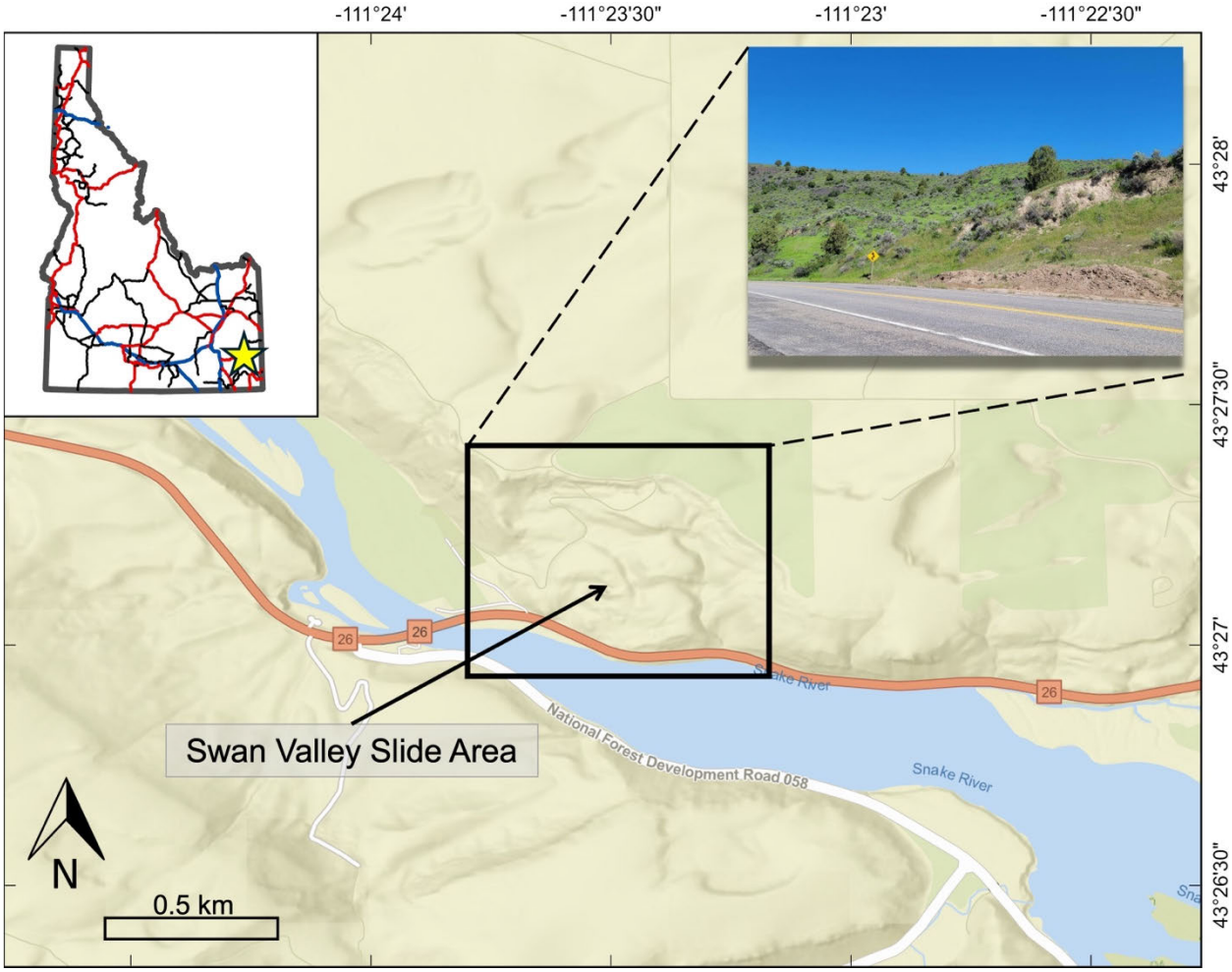

Figure 1 – Swan Valley Study Area in Southeastern Idaho

Site Geology

The Swan Valley site is underlain by a sequence of Tertiary and Quaternary volcanic, eolian, and alluvial deposits that control the site's history of slope instability (Figure 2). Five principal soil and rock units are identified within the complex: loess (Ql), alluvium (Qal), landslide debris (Qls), basalt (Qbar/Tbs), and tuff (Qyh) (*2*). The uplands overlying the slide-prone slopes are mantled by a structureless, silt-dominated loess (Ql) that reaches thicknesses of up to 80 ft (24 m). This eolian cap unconformably overlies a volcanic sequence comprising the Quaternary-age Antelope Flat Basalt, the regionally extensive Huckleberry Ridge Tuff, and the older Tertiary-age Swan Valley Basalt. Where exposed, these units are expressed as black, columnar, vesicular basalt interbedded with devitrified rhyolitic ash-flow tuff with columnar jointing (*2*). Available literature suggests the majority of landslides within the highland areas of the study are not presently active, with observed movement generally limited to slow incremental creep. Landslides post-dating the loess deposits are, in most cases, now dormant; however, localized reactivation, as documented during the investigation, demonstrates these features retain the potential for renewed movement (*2,3,4,5*).

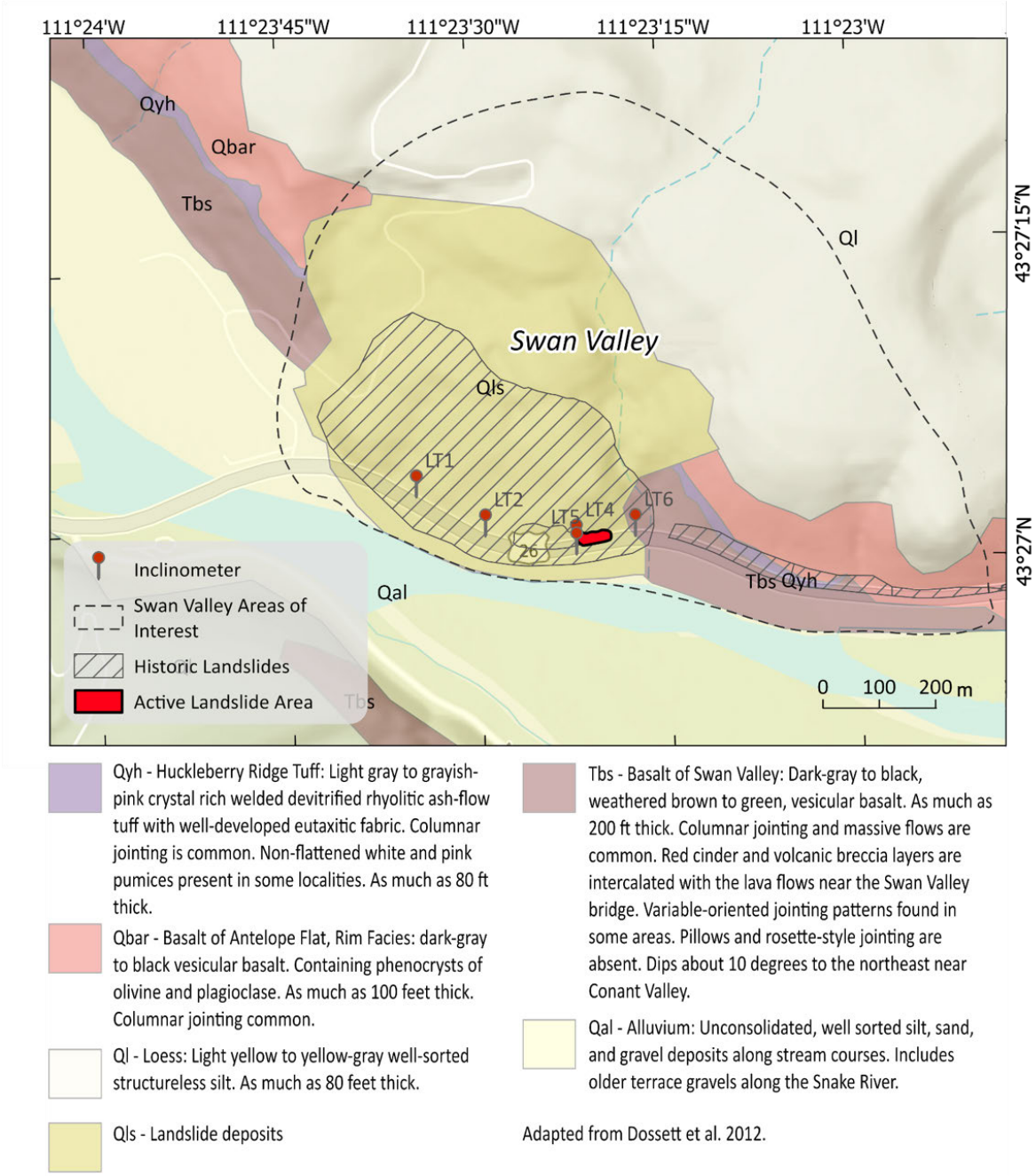

Figure 2 – Swan Valley Geologic Map

Regional volcanism, together with associated uplift and normal faulting, is interpreted to have initiated in the Swan Valley area approximately 16 million years ago, with paleomagnetic and volcanic stratigraphic data suggesting eruptive recurrence intervals every 100,000 years (*3*). Geologic mapping of the study area reveals a pattern of episodic uplift along northwest-trending fault structures, which has, in turn, driven successive cycles of fluvial incision, hillslope erosion, and sediment deposition. These processes are evident in the modern and paleo-channel deposits of the South Fork of the Snake River, where sand, silt, and gravel containing basalt clasts mantle the valley floor. The greater Swan Valley area is bound by two normal faults: the Grand Valley

Fault to the northeast and the Snake River Fault to the southwest, consistent with the basin and range extensional setting of this region (*4*).

GEOTECHNICAL INVESTIGATION

Borings

Geotechnical boring logs were prepared by Landslide Technology of Portland, Oregon, for inclinometer installations authorized by ITD. Standard Penetration Testing (SPT) and split-spoon sampling were performed in compliance with ASTM D1586, and samples were described in accordance with ASTM D2488. HQ3 triple tube core barrel was used for rock coring.

Inclinometers

A total of 5 inclinometers (LT1, LT2, LT4, LT5, and LT6) were installed by ITD at the Swan Valley site in 2017 (Table 1). Most of the inclinometers were placed along US-26 adjacent to areas of active movement (Figure 3). Casings were installed to depths of 38 to 49 ft (11.6 to 14.9 m) below the ground surface and were grouted from the end caps to the surface. Initial baseline readings were recorded by ITD personnel on 25 and 26 September 2017 and on the following dates during the active ITD-ISU field investigation period: 06 July 2023, 24 April 2024, 30 May 2024, and 07 November 2024.

Table 1 – In-Situ Instrumentation Description

Inclinometer	Location (Lat/Long)	Ground Surface Elevation	Total Depth	Status
LT-1	43.450493 / -111.39301	5287 ft / 1611 m	48 ft / 14.6 m	Operational
LT-2	43.449854 / -111.391592	5297 ft / 1614 m	48 ft / 14.6 m	Operational
LT-4	43.449635 / -111.389541	5301 ft / 1615 m	48 ft / 14.6 m	Operational
LT-5	43.449493 / -111.389541	5294 ft / 1613 m	49 ft / 14.9 m	Operational
LT-6	43.449805 / -111.388246	5297 ft / 1614 m	38 ft / 11.6 m	Operational

UAS SURVEY

Ground Control

Ground control points (GCPs) are used to georeference remotely sensed data, ensuring that imagery can be accurately aligned spatially. High-contrast mesh targets with clearly defined centroids were placed throughout the survey site, providing known coordinates distinguishable within the RGB and LiDAR UAS surveys. Mesh target GCPs were positioned outside of potential viewing angle obstructions throughout the topographic highs and lows of the study area (*6*). GCP coordinates were recorded with paired base-and-rover survey-grade GPS units (Emlid RS2) and processed using PPK (post-processing kinematics) workflows. Poorly situated targets hidden from the flight path, on unstable ground, or visible in fewer than four images have been found to degrade survey accuracy (*7*). Given this variability, 6 GCPs were placed at the Swan Valley site to ensure adequate visibility (Figure 3).

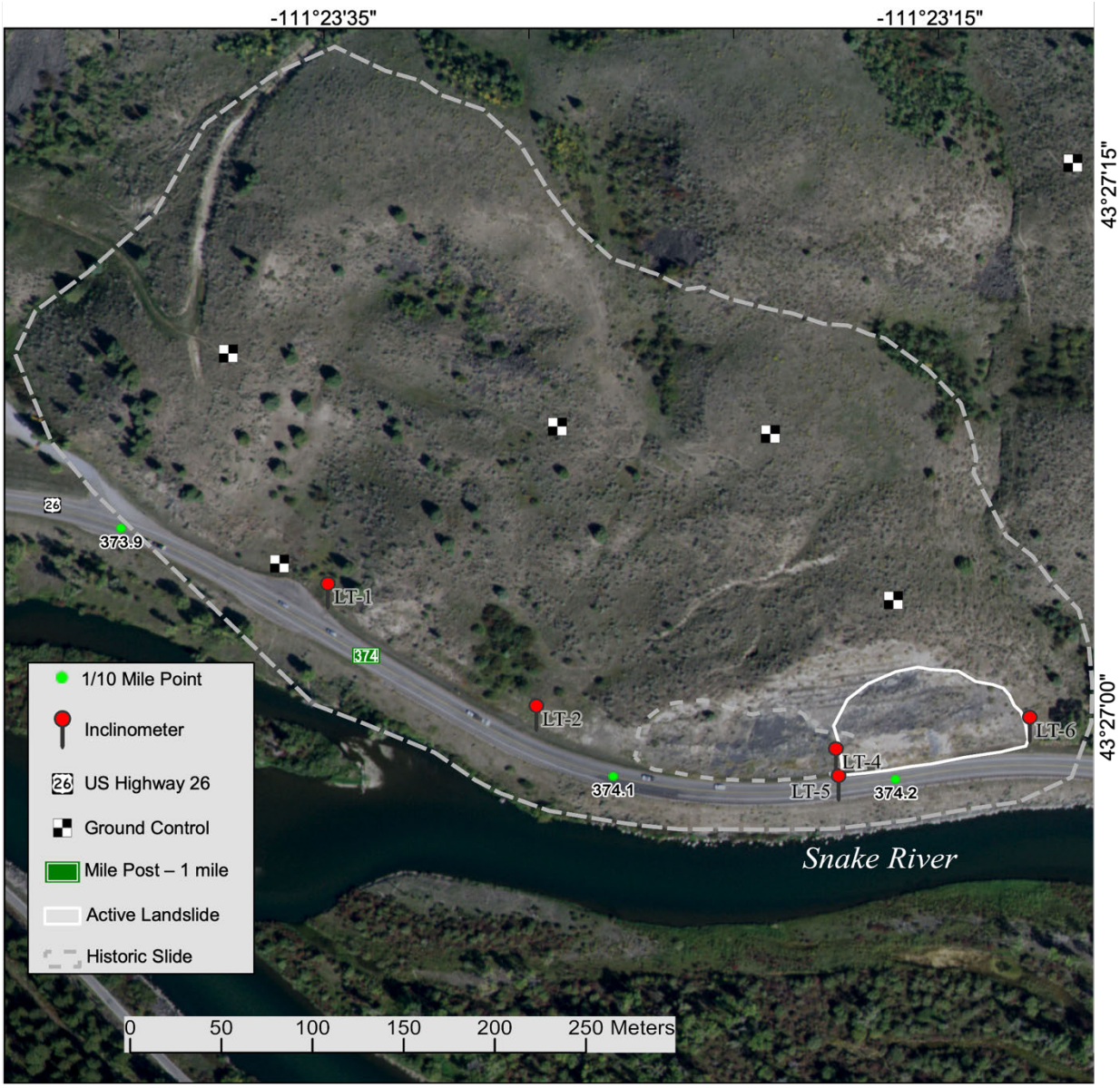

Figure 3 – Ground Control and Inclinometer Locations

Platforms and Sensors

A vertical take-off and landing (VTOL) fixed-wing UAS surveyed the Swan Valley site. UAS platforms included both the Trinity F90+ and the Trinity™ Pro manufactured by Quantum Systems GMBH (Figure 4). The Trinity platforms offer a maximum flight time of 90 minutes, a cruising speed of 38 mph (61 km/h), and a coverage area of up to 2.5 mi^2 (6.5 km^2). The VTOL capability allows users to take off and land in limited spaces such as tight highway corridors.

For this study, the YellowScan Q240 LiDAR system was utilized (Figure 4). The Q240 facilitated data collection at 50-100 points per square meter. The sensor is equipped with a geomatics-grade GPS with an estimated precision of 0.7–1.0 in (1.8–2.5 cm). This sensor

provided LiDAR coverage of the Swan Valley site in 2024. Due to a delay in Q240 delivery, 2023 flights instead used a D2M Oblique sensor payload, equipped with one nadir and four oblique 26-megapixel cameras (Figure 4). While unable to penetrate forest canopy like the Q240, this sensor excels at capturing detailed imagery of sloped and rugged terrain, providing a resolution of 1.8 cm/px at 120 m (394 ft) above ground level (AGL).

Figure 4 –Trinity F90+ platform, Yellowscan Qube 240 LiDAR sensor, and D2M Oblique camera

Mission Planning

UAS mission planning was conducted using Quantum Systems' Qbase software, which allows users to define a flight area by drawing a polygon over satellite imagery of the site. Within Qbase, users can pre-program flight-line overlap, flight altitude, sensor payload, and terrain-following settings, while the remote pilot monitors aircraft status and progress in real time during flight. Qbase software also accommodated a uAvioni pingUSB device to monitor local air traffic and potential conflicts with manned aircraft.

Flights using the D2M Oblique payload were flown at 328–394 ft (100–120 m) AGL with 70–75% overlap between flight paths, using advanced terrain following to maintain consistent height above ground. For the Q240 LiDAR sensor, Qbase incorporates pre- and post-flight calibration maneuvers to align inertial measurement unit (IMU) data with LiDAR point cloud output. The IMU records aircraft motion and orientation, which, combined with the onboard geomatics-grade GPS, establishes precise aircraft position throughout the flight. Following calibration, data acquisition was conducted at 328–394 ft (100–120 m) AGL with

terrain following and 50–65% overlap between flight paths, concluding with a final calibration pattern.

Before beginning flight operations, a geomatics-grade Trimble R10 base station was established to collect GPS data for a minimum of 2 hours during the flight operation for post-processing. The baseline between the base station and the onboard GPS/IMU system within the Q240 LiDAR improves spatial accuracy. After completing all inspections and safety checks, the flight plans were uploaded to the UAS. An FAA-certified remote pilot and at least one visual observer were present during all flight operations. Post-flight, maintenance checks were performed, and then the UAS was disassembled.

The ISU Department of Geosciences conducted UAS flights at the Swan Valley site area three times during the two-year investigation period (Table 2). The initial UAS survey was performed on 19 July 2023 and the last survey on 20 June 2024.

Table 2 – Swan Valley UAS Surveys

Sensor	Date
D2M - Oblique	07-19-2023
Q240 - LiDAR	06-20-2024

DATA PROCESSING

Photogrammetry

To process RGB imagery from the D2M Oblique camera, Agisoft Metashape v. 2.1.4 software was used to create point clouds in LAS 1.4 format, digital elevation models (DEM), and orthomosaics (Figure 5). Agisoft Metashape is a structure from motion (SfM) software package that combines photogrammetry principles with computer vision to process UAS images into seamless models. Prior to importing individual cameras into Agisoft, camera positions were post-processed using Qbase software. Using corrected GPS base station data and recorded flight logs from the Trinity platform, PPK processing corrected the GPS locations more precisely for each camera position. The recommended processing steps provided by Agisoft were utilized to stitch together the images with ground control point coordinate locations to produce an RGB point cloud (*8*).

LiDAR

To address common repeat LiDAR issues, the following workflow was applied (Figure 5). Four software packages supported LiDAR post-processing: CloudStation v. 2403.0.1, Applanix POSPac UAV v. 8.4, BayesStripAlign v. 2.25, and LAStools. The workflow began with extraction of flight data from the Q240 LiDAR sensor and the Trimble R10 base station. The Q240 generated point cloud data and a T04 file containing IMU and GPS information in Applanix (Trimble) binary format, while the Trimble R10 recorded position in T02 file format. POSPac UAV combined the T02 and T04 files to create a georeferenced Smoothed Best Estimated Trajectory (SBET) file. Because the R10 Trimble base station occupied an unknown reference location for a minimum of two hours, Trimble's CenterPoint RTX Post-Processing

service accurately established the base station position. After processing the Q240 data and correcting the base station position, the GNSS-Inertial Processor in POSPac computed SBETs from the raw data. Yellowscan's proprietary CloudStation software used the SBETs to generate LAS point clouds, incorporate ground control points, colorize point clouds with the D2M Oblique sensor orthomosaics, and automatically classify noise, ground, vegetation, and other features. The final point clouds were exported in LAS 1.4 format.

Strip Alignment and Point Cloud Classification

Although CloudStation runs a LiDAR strip alignment processing step, BayesStripAlign was used to further refine alignment by applying a Bayesian inference workflow to correct the absolute and relative geometric errors in individual flight lines (Figure 5). The software uses timestamped LAS files and SBET trajectories to register overlapping flight lines and correct errors associated with IMU drift, boresight misalignment, lever-arm errors, and internal geometry miscalibration. The study area was divided into individual flight lines before realignment using the applied corrections to generate new point clouds with improved accuracy. The flight lines were then realigned and exported as a new point cloud, resulting in alignment accuracy values with an XY RMS error of 0.14–0.36 m and a Z RMS error of 0.034 m.

The newly aligned point clouds were processed with LAStools to correct ground and vegetation classification errors. The LASindex tool first generated spatial indexing information for each point cloud. To facilitate easier processing, the point clouds were divided into 100 m^2 tiles with 10 m buffers using the LAStile tool. The LASnoise tool classified noise, followed by manual correction of misclassified points with the LASview tool. Tiles were saved as LAY files and converted into LAZ files using the LASlayers tool. All tiles were then merged into one point cloud using the LASmerge tool and exported in WGS84 UTM Zone 12N.

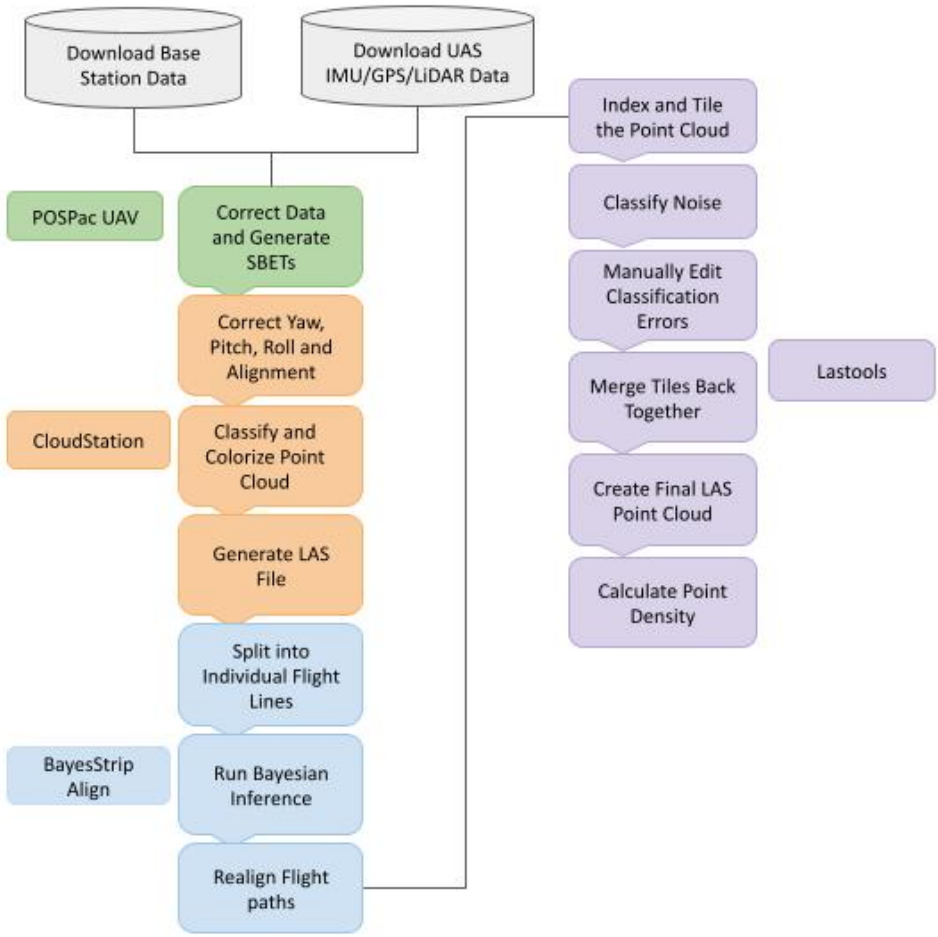

Figure 5 – LiDAR and RGB Processing Workflow

ANALYSIS

Change Detection

After point clouds were aligned, the Cloud-to-Cloud (C2C) method was used to quantify geomorphic change. C2C is a direct comparison between two dense point clouds collected at different times, using an algorithm that calculates distances between closest points (*9*). The overall surface changes in Swan Valley determined in the ISU Photogrammetry/LiDAR surveys between July 2023 and October 2024 are shown in Figures 6 and 7. Areas in red indicate upward or positive movement, and in blue downward displacement. Magnitudes of movement are indicated by the color intensity scale bar on the right side of the figure. The areas in white are trees that inhibited measurements.

An active landslide was detected between the July 2023 and June 2024 UAS surveys (Figure 7). Based on the movement pattern, the affected area is approximately 150 ft (46 m) wide and 105 ft (32 m) upslope. A scarp is noticeable at the top of the slide, and hummocky ground is present in and near the toe. The scarp at the top of the slide has a maximum downward

displacement of 8 ft (2.4 m). The corresponding maximum heave near the toe of the slope is approximately 4.5 ft (1.4 m).

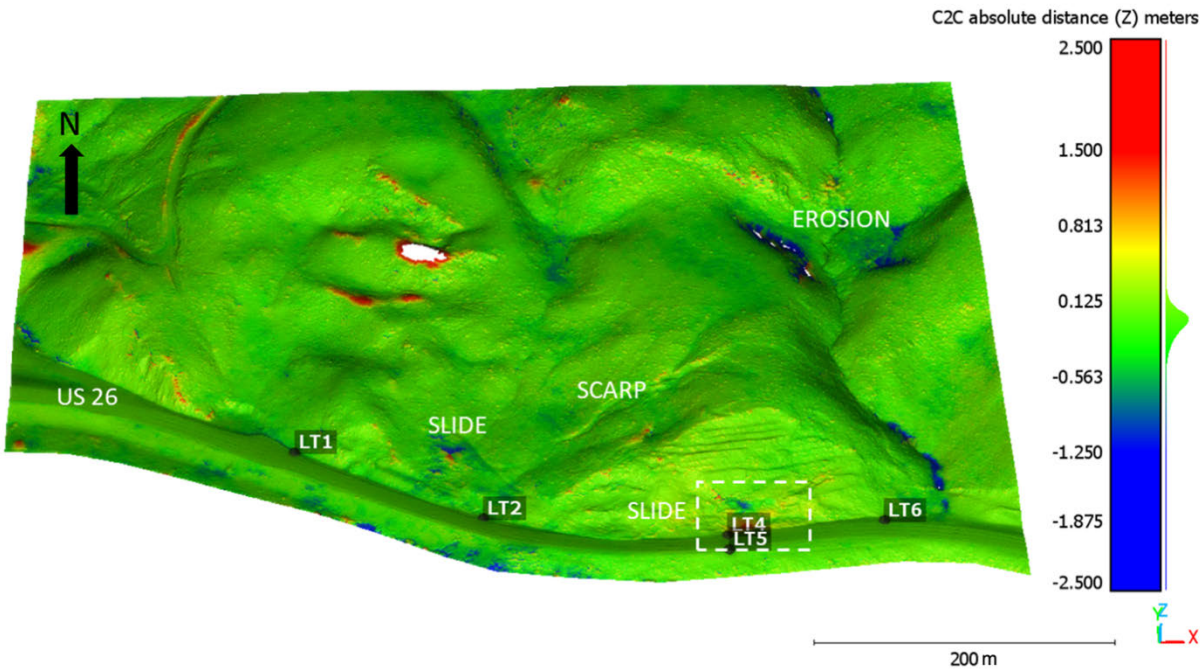

Figure 6 – Swan Valley Change Detection July 2023 to June 2024

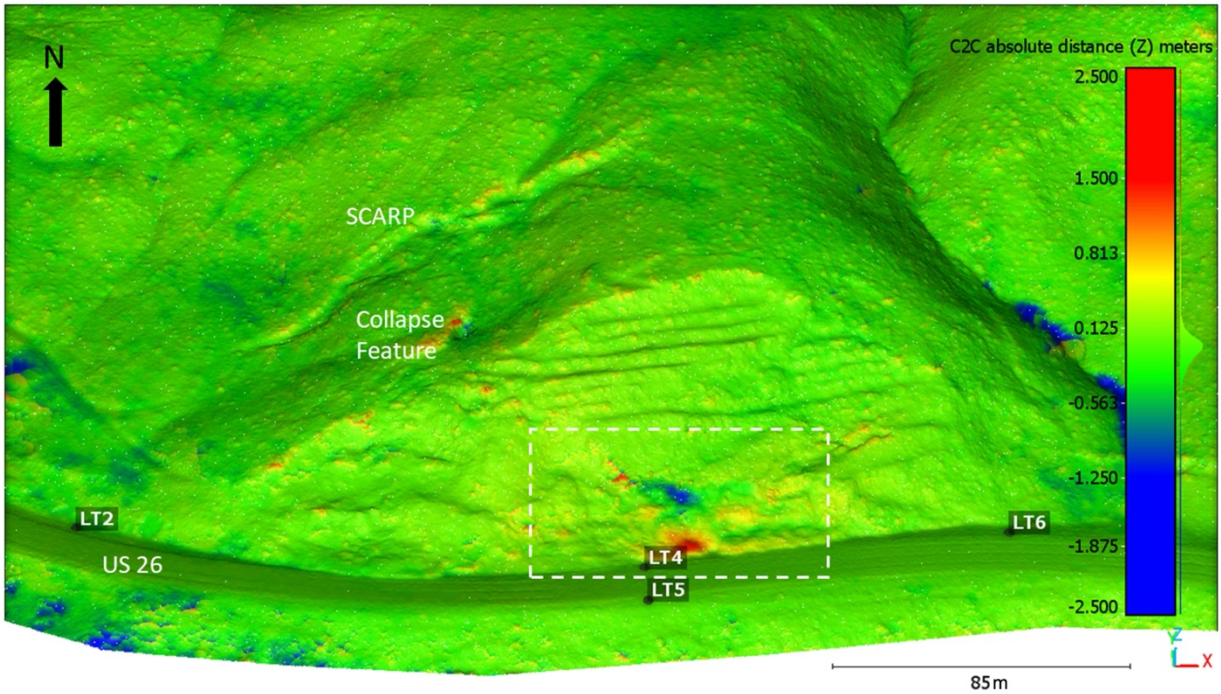

Figure 7 – Swan Valley Change Detection Landslide Features July 2023 to June 2024

A discontinuous linear feature is noted in the change detection approximately 400 ft (121 m) above the active slide area and is a positive indicator of a much larger future slide that could impact the highway (Figure 7). The UAS survey also revealed a major collapse feature along an intermediate scarp 265 ft (81 m) above the road. The depression serves as an active infiltration zone where surface water collects on the slope, flows underground, and saturates the downslope portion of the slide area, potentially leading to slope failure.

Inclinometer Measurements

The active landslide in Swan Valley is located between inclinometers LT4 and LT6. The A-axis, upslope-downslope axial displacement at depth, is plotted against the corresponding boring log. The inclinometer data in the B-axis direction is not included in the diagrams because the measured displacement is parallel to the slope. The absence of inclinometer movement in the LT4 is consistent with the displacement pattern obtained in the 2023-2024 LiDAR surveys, given that LT4 is situated outside the zone of movement (Figure 8).

Lateral displacement at depth was recorded in LT2 adjacent to the active slide area before and during the study period. The displacement-depth plot shows rigid body rotation movement of approximately 0.3 in (0.7 cm) to a depth of 24 ft during the 6 July 2023 to 7 November 2024 measurement period (Figure 9). The displacement continues downward in shear to a depth of 30 ft. The LT2 boring log shows the failure zone in the lower colluvium described as brown silty CLAY(CL) with trace sand. In December 2017, the groundwater table was at and just above the base of the movement zone in the lower colluvial formation. The colluvium, in which the movement is taking place, is resting on a sandy GRAVEL (GW) with trace clay described in the boring log as LANDSLIDE/SLIDE DEBRIS. The LiDAR data indicated no measurable movement during the study period, even though the inclinometer showed a total displacement of 0.3 in (0.7 cm) at and below the ground surface. The incremental slope movement of 0.3 in (0.9 cm) has not reached the 2 cm (0.8 in) horizontal and 3 cm (1.2 in) vertical thresholds for measurable displacement in the LiDAR survey.

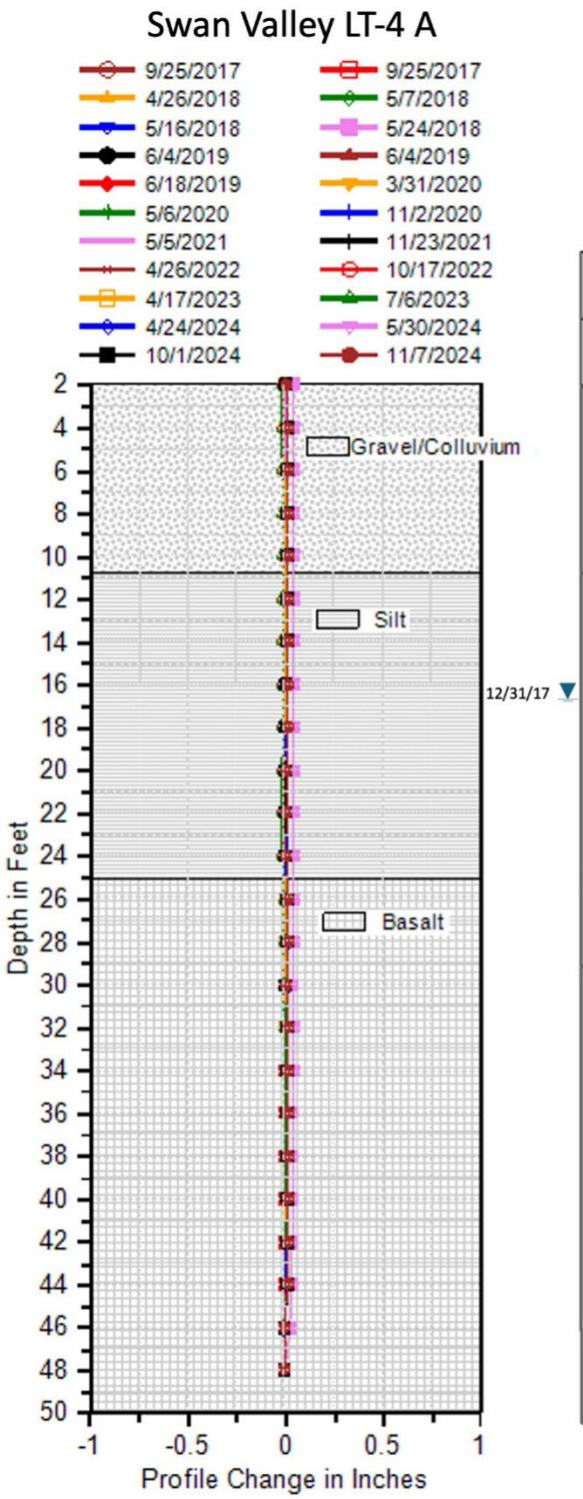

LT-4
09/08/2017

Elevation (ft)	Material Description	N(B/FT)
5275.0	VERY DENSE, orange to brown, silty, sandy GRAVEL (GW); trace clay, fine to coarse sand, gravel up to 1-inch; relict rock texture, dry (COLLUVIUM)	57
5264.2		50/3 in
	HARD, black, sandy, slightly clayey to clayey SILT (ML); numerous rock fragments up to 1-inch, relict rock fragments up to 1-inch, relict rock texture (DECOMPOSED BASALT)	50/2 in
		50/1 in
5249.9	HARD (R4), dark gray, slightly weathered, BASALT; very highly to highly fractured fractures (45-60°), rough to smooth planar joints, clean, dominant, vesicular, occasional healed joint surface, minor white secondary mineralization (SWAN VALLEY BASALT)	CR/RQD 100/50
		100/89
	Becomes highly to moderately fractured below 30.0 feet	100/89
		100/89
		100/91
	Bottom of Boring: 50.0 ft	

Figure 8 – Inclinometer Displacements and Corresponding Log of Boring LT-4.

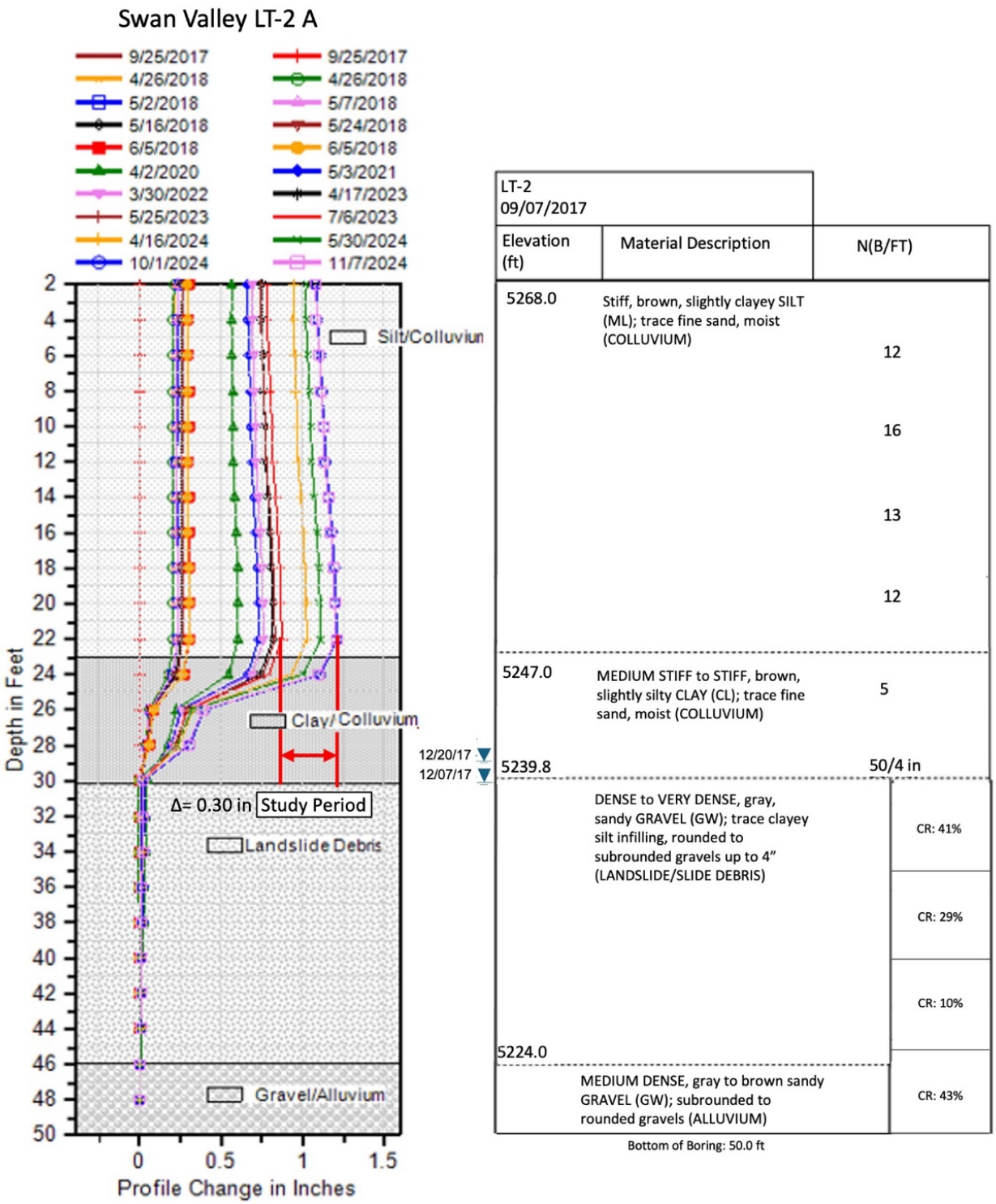

Figure 9 – Inclinometer Displacements and Corresponding Log of Boring LT-2.

Precipitation

Daily precipitation records for the Swan Valley area were obtained from the NOAA Swan Valley, ID weather station, located 5 miles from the study area (Figure 10). Based on the precipitation data, the slope movements east of inclinometers LT4/LT5 most likely occurred during the February to early March 2024 time period. The total precipitation during this period at the gauge location was approximately 3.3 in., with a 1.86 in. rainfall event in the first week of March. The displacement-time plot of the upslope-downslope A-axis in LT2 also shows a significant increase in the magnitude and rate of ground surface movement during the same time period (Figure 9). A combination of weaker lithologies and heavy rainfall during this period was the likely cause of the slope movement event.

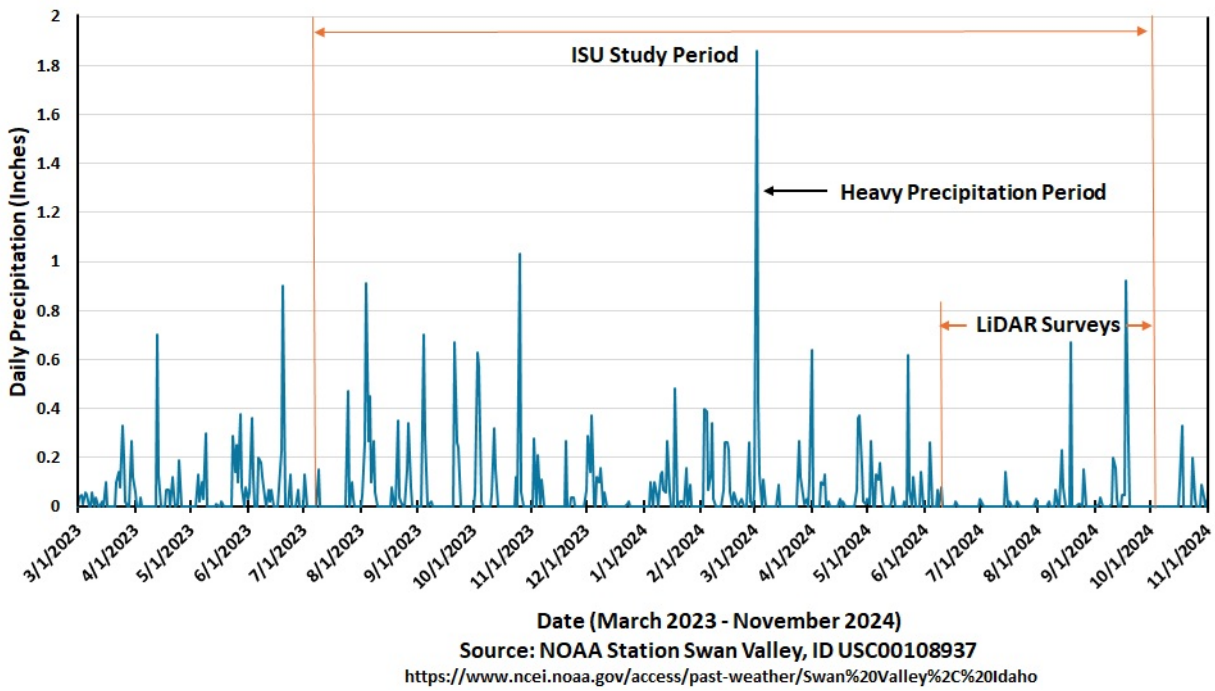

Figure 10 – Swan Valley Precipitation Record

Historical Comparison

ITD provided ISU researchers with aerial imagery captured on 05 November 1987. These large-scale (1:3600) aerial images were scanned, georeferenced, and processed into 3D models using Agisoft Metashape (Figure 11). The 1987 dataset was aligned to the 2024 models for comparative analysis. Review of the models shows a collapse feature present in 2024, but the depression is absent in 1987. A cross-sectional view of the depression shows vertical displacement of up to 2.56 m, indicating that the feature developed in the intervening period (Figure 12).

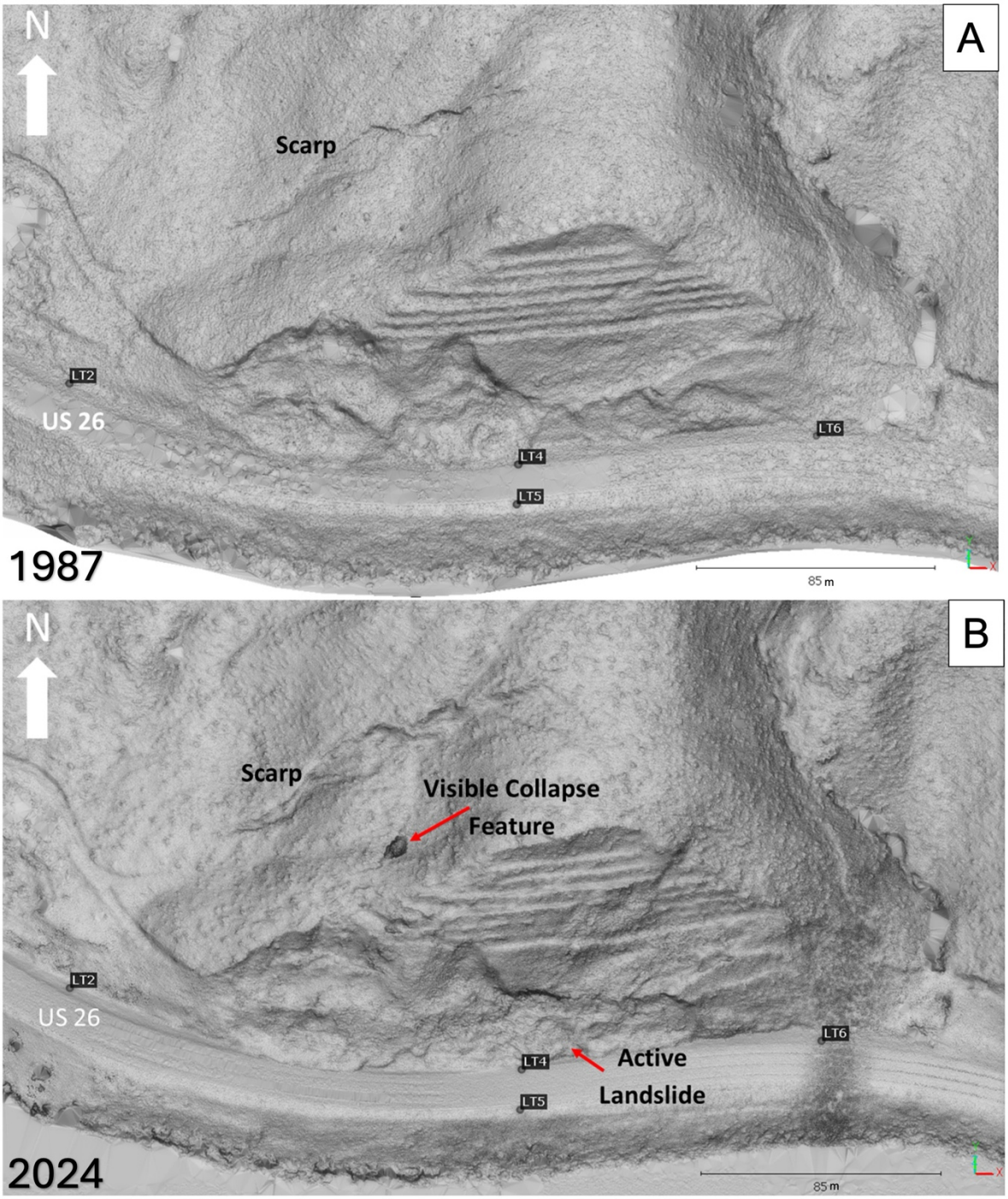

Figure 11 – A) 1987 Swan Valley Terrain Model and B) 2024 Swan Valley Terrain Model

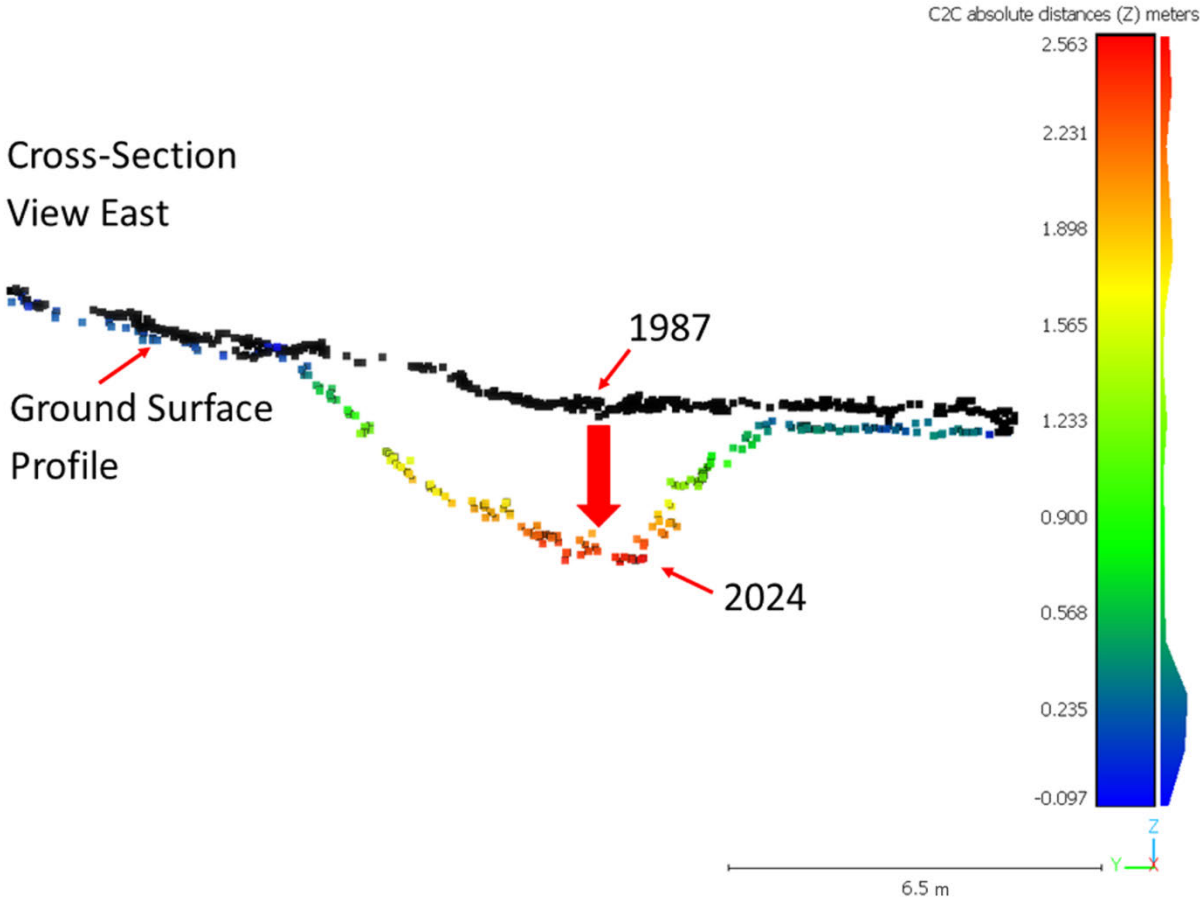

Figure 12 – Swan Valley Collapse Feature Growth between 1987 and 2024.

CONCLUSIONS AND RECOMMENDATIONS

A significant area of potential instability in the Swan Valley study area has been identified in the ISU LiDAR surveys. The area contains progressive scarps upslope above the road. The breadth of the potentially unstable area extends between the east and west drainages and more than 1000 ft laterally along the slope. At this time, the upper scarp is discontinuous but is intermittent and can easily coalesce with further downslope displacement. Further, the depression in the intermediate scarp serves as a source of groundwater infiltration, which increases pore water pressures acting along the surface of sliding. At present, there are no dewatering wells in the slope to dissipate the excess pressures. The infiltration is responsible for the landslide, which stopped short of the roadway between the 2023 and 2024 measurement periods. It is apparent in this study that the LT-inclinometer measurements in Swan Valley alone did not provide the necessary data on the active landslide which developed between 2023 and 2024. The situation not only shows the benefits of UAS LiDAR/photogrammetry surveys but also identifies a potential public safety hazard. Yearly UAS LiDAR and photogrammetry monitoring is recommended.

REFERENCES:

1. Sun, J., Yuan, G., Song, L., and Zhang, H. Unmanned Aerial Vehicles (UAVs) in Landslide Investigation and Monitoring: A Review. *Drones* vol. 8 (1), 2024, p. 30.

2. Dossett, T.S., Reed, T.H., McILrath, S.L., Moore, D.K., and Embree, G.F. *Geologic Map of the South Fork of the Snake River Between Swan Valley and Ririe, Idaho.* Brigham Young University-Idaho, Rigby, 2012.

3. Morgan, L.A., McIntosh, W.C. Timing and development of the Heise volcanic field, Snake River Plain, Idaho, western USA. *Geological Society of America Bulletin* vol. 117 (3-4), 2005, pp. 288–306.

4. Henderson, S., Rivera, T., Lippert, P., Jicha, B. Geomorphic and tectonic development of Swan Valley, southeast Idaho, since the eruption of the Basalt of Antelope Flat—new 40Ar/39Ar, geochemical, and paleomagnetic data. *Geology of the Intermountain West* vol. 9, 2022, pp. 115–130.

5. Jobin, D., and Schroeder, M., 1964, *Geology of the Conant Valley quadrangle, Bonneville County, Idaho*. Miscellaneous Field Studies Map 277, U.S. Geological Survey, 1964.

6. James, M.R., Robson, S., d'Oleire-Oltmanns, S., and Niethammer, U. Optimising UAV Topographic Surveys Processed with Structure-from-Motion: Ground Control Quality, Quantity and Bundle Adjustment. *Geomorphology* vol. 280, 2017, pp. 51–66.

7. Zimmerman, T., Jansen, K., and Miller. J. Analysis of UAS Flight Altitude and Ground Control Point Parameters on DEM Accuracy along a Complex, Developed Coastline. *Remote Sensing* vol. 12 (14), 2020, p. 2305.

8. Agisoft. *Aerial Data Processing (with GCPs) - Orthomosaic & DEM Generation*. Agisoft Helpdesk Portal. https://agisoft.freshdesk.com/support/solutions/articles/31000153696-aerial-data-processing-with-gcps-orthomosaic-dem-generation. Accessed Jan. 3, 2024.

9. Girardeau-Montaut, D., M. Roux, R Marc, and G Thibault. 2005. "Change Detection on Points Cloud Data Acquired with a Ground Laser Scanner. *International Archives of Photogrammetry, Remote Sensing and Spatial Information Sciences* vol. 36 (3), 2005, pp. 30-35.

07. Design Considerations for Attenuators and Hybrid Barriers

Lucas Martins
Maccaferri, Inc
825 Commonwealth Ave.
Hagerstown, MD 21740
Ph: 240-707-0633
l.martins@maccaferri.com

Mike Koutsourais, PE
Maccaferri, Inc
825 Commonwealth Ave.
Hagerstown, MD 21740
Ph: 301-641-8072
m.koutsourais@maccaferri.com

Leticia Genelhu
Maccaferri, Inc.
825 Commonwealth Ave.
Hagerstown, MD 21740
l.genelhu@maccaferri.com

Prepared for the 75th Highway Geology Symposium, September 2026

Disclaimer

Statements and views presented in this paper are strictly those of the authors, and do not necessarily reflect positions held by their affiliations, the Highway Geology Symposium (HGS), or others acknowledged above. The mention of trade names for commercial products does not imply approval or endorsement by HGS.

Copyright

Copyright © 2026 Highway Geology Symposium (HGS)

All Rights Reserved. Printed in the United States of America. No part of this publication may be reproduced or copied in any form or by any means – graphic, electronic, or mechanical, including photocopying, taping, or information storage and retrieval systems – without prior written permission of the HGS. This excludes the original authors.

ABSTRACT

The capabilities of traditional rockfall barrier systems are measured according to the magnitude of their tested impact energies, and the testing and design of these systems are well established. However, as attenuators and hybrid barriers have become increasingly used in North America, their application and design are often not well understood, and no standard test and design method are available. Therefore, misapplication and a general misunderstanding of the system itself and its purpose are often the result. From terminology to design principles and system application, there is a basic need to dissect these systems and understand their purpose and limitations and how to design the various components of the system.

This paper will first discuss how to identify the application and purpose of the system based on site-specific conditions. A further discussion will be provided to explain how the various components of each system are affected by the forces acting on those components and how to design for them.

INTRODUCTION

Alternative systems to rockfall draperies and barriers, that incorporate characteristics of each, have grown in popularity and are more routinely being used to mitigate against rockfall events. These alternative systems are “hybrids” of conventional draperies and barriers which combine the energy absorption capabilities of a dynamic rockfall barrier with the reduced-maintenance advantages of a rockfall drapery.

A hybrid system may offer lower installation and maintenance costs compared to traditional drapery and barrier solutions. For instance, rather than draping a long slope, a hybrid system may be installed below the source zone of the rockfall, covering only a portion of the slope. They can be designed either as a “catch and release” system (i.e. open toe) to progressively slow the rocks beneath the mesh, bringing them safely into a catchment at the toe of the slope, or as a full catchment (i.e. closed toe) that can withstand repeated impacts without requiring repair and is easier to maintain versus a standard rockfall barrier installed high on the slope.

There are various applications of hybrid systems. Duffy, John D. (2023) makes the distinction between applications based on whether the mesh has ground contact or not. He states that combining key elements of a flexible rockfall barrier and an unsecured drapery creates a hybrid design whose purpose is to reduce rockfall energy and trajectory. Duffy summarized that different entities have developed and carried out tests, studies and model experiments on various systems, however, there is currently no testing and design guidelines or certifications for these systems in the applications intended. As Duffy explains the need to standardize nomenclature, design guidelines and testing procedures, this paper will attempt to move this discussion forward by offering the authors’ views of these important aspects of “hybrid” systems in the various applications that these systems are being used.

APPLICATIONS

Unlike a rockfall drapery, a ‘hybrid system’ (hybrid) is installed below the source zone of the rockfall and is meant to intercept the rockfall bounce and energy. The system can be designed to either 1) deflect, 2) reduce, or 3) fully arrest the rockfall velocity and energy. As implied, the system may or may not fully arrest the impact energy of the rock as a conventional rockfall barrier is designed to do, and therefore, system design must consider the energy exiting the system and how that energy will eventually be brought to rest, either within the system or beyond it. The desired end-result will affect the forces and loads acting on the individual components of the system. Therefore, the authors believe that the nomenclature of these hybrid systems should be representative of what the system is designed to achieve, as that determination governs the forces acting on the system components and design considerations applied to each unique application.

Bichler, A., et.al. (2012) made distinctions between drapes, attenuators, hybrid barriers and conventional catchment barriers based on the energy absorption of the structure. Figure 1 is a modified version taken from Bichler, A., et. al. (2012) to include the application of a hybrid system that can be more accurately referred to as a “Deflector”. Progressing from left to right,

Deflectors, shown on the far left, absorb the least energy, and conventional rockfall catchment barriers, shown on the far right, absorb the most energy. These hybrid systems – Deflectors, Attenuators, and Hybrid Barriers – will be discussed in more detail in the following sections.

LOW >>>>>>>>>>>> Energy Absorption by Structure >>>>>>>>>>>>>> HIGH

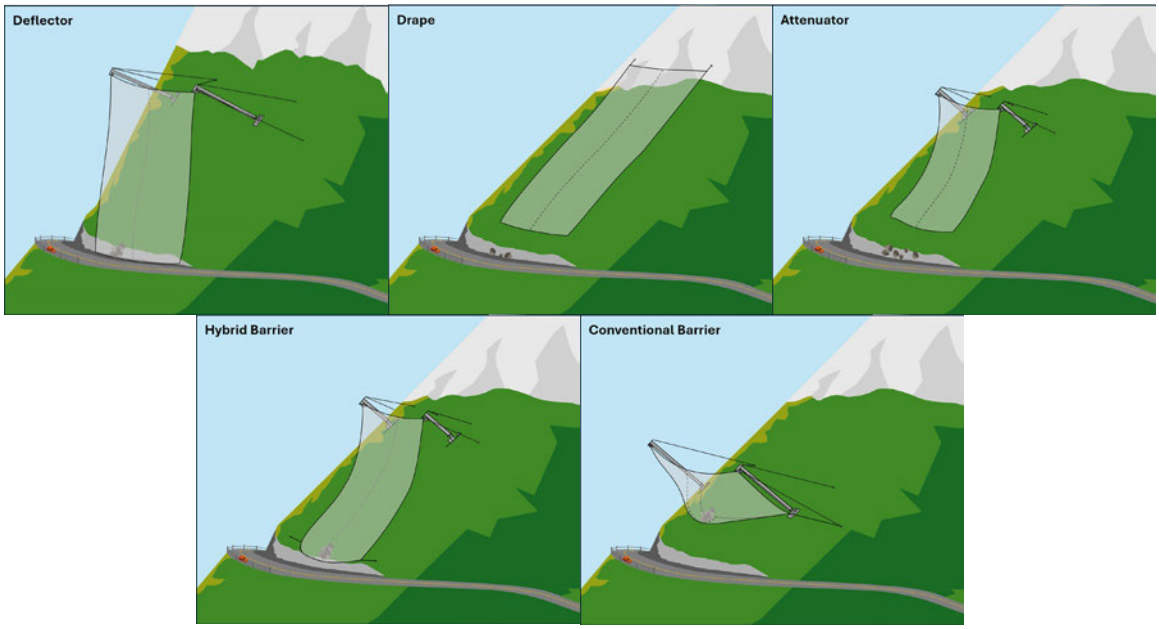

Figure 1. Energy absorption by structure (modified from Bichler, A. et.al. 2012)

Deflectors

A Deflector can best be described as a vertically hanging drape with little to no ground contact. It is a hybrid structure that only absorbs a portion of the impact energy as the netting is primarily designed to deflect the rock into the ground, where a major portion of the energy is absorbed. This contrasts with conventional rockfall barriers where all the impact energy is absorbed and contained within the system itself. The Deflector may alternatively be secured at the toe, in which case it is absorbing a greater impact energy and containing the rockfall within the system.

Figure 2 shows a schematic of a Deflector, comprising of a freely hanging steel wire mesh suspended from steel posts bolted to the rock face and may be designed with either an open or closed toe.

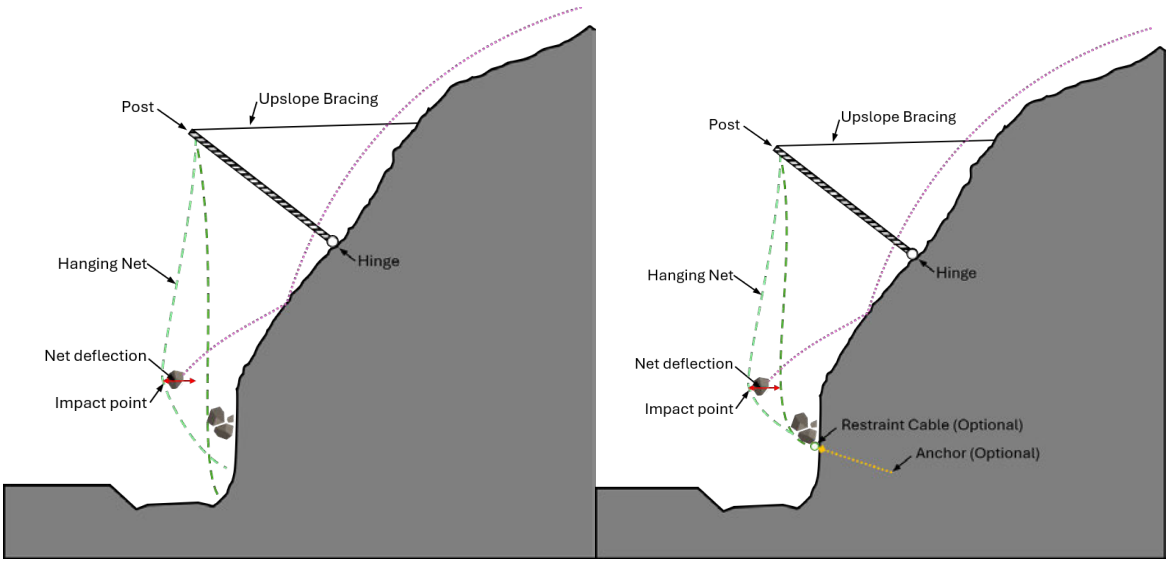

(a) **(b)**

Figure 2. Schematic of a Deflector, re-directing the energy into the ground (a) Open-Toe, and (b) Closed-Toe

Wyllie et. al., (2017) describes a full-scale testing program carried out to verify the detailed mechanics and behavior during impact into a freely hanging net with no toe anchorage. The testing was performed by dropping rocks down a natural slope, impacting the rock face with both translational and rotational forces. Documentation was gained with respect to such factors as net impact, load transfer into the support cables, and net deflection. Specifically, the authors found that an appropriate ratio between the mass of the rockfall and the mass of the net must be considered in the system design.

The results of this testing showed that the translational speed can be decreased by about 50 percent, and the speed remained approximately constant until impact with the ground occurred. The testing also showed that the rotational speed reduced to zero upon impact, then reversed and ***increased*** to more than the impact rotational velocity until it impacted the ground. This reversal of the rotational velocity during impact with the net helps to re-direct (i.e. deflect) the rocks into the ditch. Because the velocity of the blocks is only reduced by their impact with the net, only a portion of the impact momentum (and energy) must be absorbed by the net and support system, and the performance of this hybrid system can be measured by the net's ability to absorb the initial impact and redirect the rock into the catchment area at the base of the slope.

Attenuators

An Attenuator (i.e. raised drapery) is more akin to a drape regarding energy absorption capabilities, since both are a 'catch and release' system. However, there are significant differences in the forces that the attenuator system must resist compared to a drapery system. The main difference between an attenuator and a conventional drapery system is that the attenuator netting is installed below the source zone of the rockfall and, therefore, must resist an initial kinetic energy impact comprising of both translational and rotational forces. Where large

initial impact energies are present, the ability for the netting to first absorb the initial impact and subsequently reduce the rock's energy and velocity into a controlled location is determined by the netting's tensile and punch strength, which resists the initial impact, and its weight (i.e. mass per unit area) and runout length, which provides the necessary dampening effect that "attenuates" the rockfall energy into a controlled location. Attenuators may be installed as a single structure, for low to medium impact energies, or in a series of multiple structures to attenuate larger impact energies. Alternatively, an attenuator may be combined with a more traditional rockfall barrier at the base of the slope to fully arrest the energy.

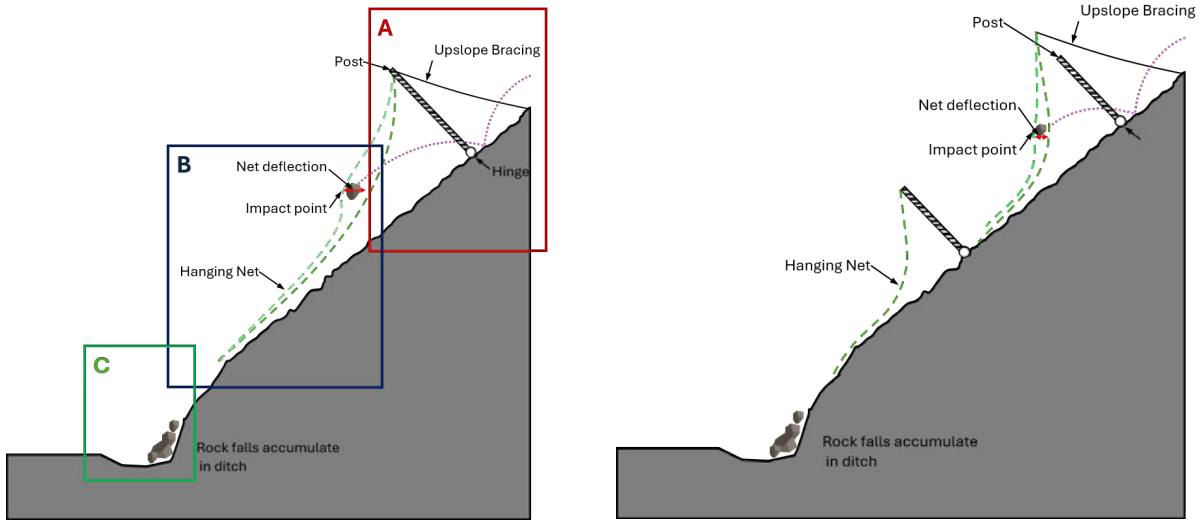

(a) **(b)**

Figure 3. Schematic of an Attenuator, reducing the rockfall energy into a catchment (a) Single Attenuator, and (b) Multiple Attenuators

Figure 3 shows the various zones and components of an attenuator system designed to reduce the rockfall energy into a controlled location. Zone A at the top is where the structure intercepts the rock. The netting is designed to first intercept the falling rock, as a standard flexible rockfall barrier would. In this Interception Zone, the greatest dissipation of energy will occur. Zone B is the Transition Zone where the drape section of the barrier drives rocks and debris toward the toe of the slope, slowing the speed and reducing the energy. Zone C is the Catch Area which may include either a catchment ditch sized to accept the volume of debris leaving the system or a conventional rockfall barrier designed to fully arrest the rockfall energy exiting the system. It is important to note that an attenuator system itself does not fully arrest the rockfall energy as the draped tail is left open at its bottom to allow the rocks and debris to exit the system.

The most prominent attenuator testing to date was sponsored by the Colorado Department of Transportation at Georgetown Pike in Georgetown, CO (Arndt, B., et.al. (2009). This full-scale field-testing program was conducted to better understand the durability and performance of available mesh products used to construct rockfall attenuators. The goal of the evaluation was to subject these systems and materials to realistic loading and impact conditions to better

understand their effectiveness in dissipating rockfall energy and mitigating rockfall hazards. To provide a controlled testing program with consistent results, CDOT conducted the tests using manufactured concrete blocks with a standard and consistent shape, size and mass to reduce the inherent variability of natural rocks. A crane was then used to drop the manufactured concrete block onto a ramp simulating energy impacts up to 500kJ on a series of different mesh materials.

In addition to assessing mesh performance to rock impacts, other important objectives of the program were to assess the effects of rotational energies on the attenuator mesh, and the energy dampening effect of the attenuator tail length, both of which are design-critical elements. The testing found that rotational kinetic energies were as much as 30% of total kinetic energy. For reference, standard rockfall barrier testing will have 100 % translational energy with 0% rotational energy. The testing showed that rotational energies can impart a significant frictional force underneath the mesh which may cause tearing. Other observations from the testing found that the combination of panel weight, tail length, and aperture size are critical elements to the function of the attenuator system.

A heavier mesh in the draped section will require a shorter tail, while a lighter mesh may be applied for lower energies (<150kJ) and/or with longer tails. However, the added tail length can result in greater rigidity of the interception panel, acting as though the mesh were secured as in the case of a traditional rockfall barrier, making it more vulnerable to puncture damage.

Hybrid Barrier

Both Attenuators and Hybrid Barriers can be described as a raised rockfall drapery that is hung from the top of a barrier post and extending down the slope a specific distance. To fully arrest the rockfall energy within the attenuator, the toe of the drape must be fully secured; this application is referred to as a Hybrid Barrier. As previously mentioned, an attenuator is a ‘catch and release’ system that dampens the initial impact of the rockfall energy, controls its movement down the slope and allows the rock to exit the system and enter a catchment area. While attenuators are designed to absorb only a significant portion of the energy of the rocks traveling down the slope, hybrid barriers are designed to absorb the total energy of the rockfall.

Therefore, a hybrid barrier has a closer relationship to a traditional rockfall barrier, since the toe of the drapery section is secured, and the rock is brought to a stop, rather than released through the toe of slope. Figure 4 is a schematic of a typical hybrid barrier system with the tail-end of the drapery section anchored to secure the rock and not allow it to exit the system. This application is often used when the slope length and/or catchment area are insufficient to fully arrest the rock’s energy and volume of debris.

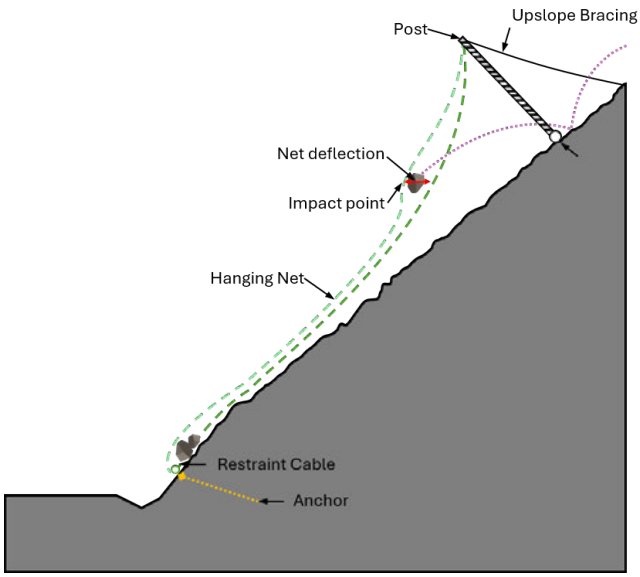

Figure 4. Schematic of a Hybrid Barrier, fully arresting the rockfall energy

DESIGN

Hybrid systems can be designed to: 1) deflect, 2) attenuate, or 3) fully arrest the rockfall velocity and kinetic energy of a falling rock. Compared to conventional rockfall barrier, a hybrid system may not always fully arrest a block during a rockfall event. Therefore, the design must also consider the energy absorbed by the system, the residual energy of the block exiting the system, and how that energy will eventually be ultimately dissipated, either within the system or beyond it. The magnitude of the energy reduction provided by the hybrid system is directly proportional to the forces acting on the individual components of the system. For this reason, each component must be designed according to its purpose. The design approach should consider the system's primary function and mechanism of action to achieve the desired benefit of the mitigation; the authors will address the key design considerations that should be addressed for each application. To facilitate the design and selection of these systems, a summary table has been developed (Table 1) that outlines the primary design philosophies and key design considerations for each mitigation approach.

Deflectors

The primary function of a rockfall deflector is to redirect falling rock blocks by intercepting a block moving from upslope of the structure and modifying its trajectory to channel its fall in between the slope and the deflector. Upon impact, the rock undergoes a reversal in rotational direction which does not necessarily result in a change in the translational direction of the block. Although there is a reduction in kinetic energy during the impact, most of the energy dissipation provided by the deflector system is attributed to the impact of the block into the ground, being the primary and sole function of the structure to redirect the blocks towards the ground within a specified deflection limit.

With this mechanism of action in mind, the design considerations of the structure are clear. The hanging net should have enough mass and stiffness to create enough resistance to maintain the exit trajectory of the block within the specified design limits. The rock impact creates a risk of perforation of the net which requires appropriate measures such as using a net type with appropriate resistance or in some cases doubling of the net within the interception zone. It is important to note that very long geometrical configurations will accentuate this risk, and impact will cause increased stress in the net due to pre-tensioning of the net by its own weight.

The system must also be designed to resist static loads. Although these systems have little to no ground contact, post, support cables and anchors should be designed considering the effect of the self-weight of the structure, as well as possible environmental loads such as ice accumulation in wet locations.

When considering the geometry of rockfall deflectors, it is very import to consider the entering and exiting trajectory of the rock. The system should have enough height and inclination to intercept the rocks accounting for the bounce height of the rock. Different approach angles of the rock will also interact with the net differently. The redirected trajectory of rocks exiting the system must be controlled so that the blocks fall within a designated catchment zone capable of safely dissipating the remaining kinetic energy.

Attenuators

Although the design philosophy for a rockfall attenuator is related to the one described for a deflector, the ground contact between the net and slope, and the general geometry of the system introduces additional design considerations. As an attenuator intercepts a block from upslope, it continually dissipates the kinetic energy of the rock mass through repeated impacts on the ground and mesh tail until it exits the system. To fully address a rockfall hazard, attenuator systems will require a separate structure to address the exiting rock block such as a series of attenuators, a rockfall fence, a rock catchment ditch with appropriate geometry.

It is evident then that the weight of the mesh tail is a key design parameter for attenuators, since it must possess enough mass to counter the momentum of the impacting rock mass while reducing the uplift on the tail, while also allowing the block to travel beneath the net in a controlled manner and exiting the system within the design specifications. A lightweight mesh can be lifted on impact, which limits its ability to control the rock trajectory and channel its energy. In this case, the structure must be supplemented with a device for limiting the uplift movement of the mesh tail. The weight of the tail can be calculated by multiplying the tail length by the mesh unit weight. This creates a relationship where an attenuator tail length is inversely correlated to the mesh mass per unit area.

In addition to the tail weight, the interaction of the tail with the ground has an interface behavior like a rockfall drape where the undulations and roughness of the surface will increase the friction coefficient between the mesh and slope. This is important because it creates a resistance on the tail against the upslope pull resulting from an impacting rock. Therefore, there

will be an increased risk of perforation of the net within the interception zone during rockfall impacts. The requirements of punch and tensile resistance of the mesh will increase as the weight of the tail, length of the tail and possible snow load increases. These effects become increasingly significant when considering attenuator systems with long mesh tail lengths. Increasing the tail length generally improves the dampening effect of the rock's energy, but the increased tail length will result in greater forces acting on the mesh and a reduced available deformation during impact. Therefore, attenuators with long tail lengths may behave similar to a hybrid barrier system with an anchored tail.

The mesh mass per unit area used for an attenuator system will determine the length of tail necessary to reduce the energy of a block from an initial energy to a design exiting energy specification and must be strong and heavy enough to resist the deceleration momentum created by the block. Figure 5 illustrates the relationship between a specific energy level and the mesh mass per unit area and tail length. For a given energy level, a mesh with a lighter mass per unit area will require a longer tail length to dissipate the energy. Whereas a shorter tail length would be required for a heavier mesh to dissipate the same level of energy. For example, Maccaferri SteelGrid (Type 1), with a mass per unit area of 0.50 lbs/sf, requires a longer tail length than RockMesh (Type 2), with a mass per unit area of 0.70 lbs/sf. And the HEA panel (Type 3), with a mass per unit area of 1.0 lbs/sf, requires the least length of tail.

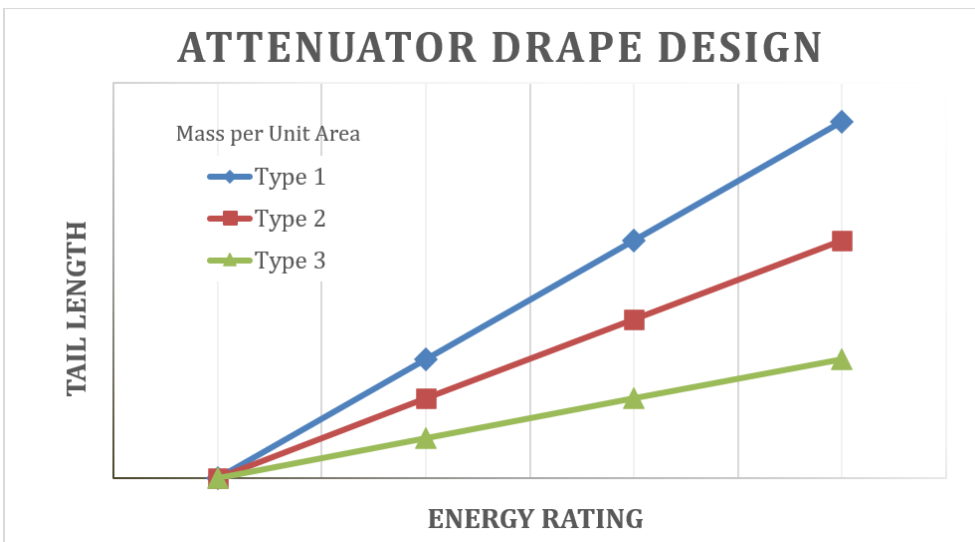

Figure 5. Relationship between a mesh's mass per unit area and tail length required to dissipate a specific energy level

The structure of an attenuator is also of crucial importance. When comparing the design of these systems to a widely accepted design of open-toe simple draperies, the anchor points of an attenuator's support cables are typically spaced wider, with post spacing typically varying from 25 – 40 ft (8 - 12m) making the behavior of the support cables and anchors an important design consideration. The distance between anchor points influences the cable tension and load-carrying capacities. Cables are tension-only elements which produce only axial tension due to a load configuration. For a given cable load system and span, increasing sag reduces the horizontal tension at the supports, while reducing sag increases tension. Using the catenary

theory and a sag-tension relationship, it is possible to dimension the wire rope cable specification and determine the loads at the posts and anchors while maintaining the minimum system height necessary to intercept the rockfall trajectories. Typical rockfall attenuators have tight sag allowance that significantly impacts the load on the posts and anchors.

The posts and foundations should be designed for the combined effects of both a static load and a dynamic load. Meaning that the perpendicular force exerted by a dynamic impact will act in addition to the self-weight and environmental loads. These systems are not designed to fully arrest a block. Consequently, the dynamic demand on the posts and anchors will be less than the dynamic demands of a traditional rockfall barrier. This relationship of impacting forces comes from the deceleration time and distance, and the amount of energy dissipated by the system compared to the rock's initial impact energy. For a traditional rockfall fence you expect deceleration times of 0.5 secs and an energy delta of 100%. However, for attenuators the deceleration time is about 2.5-3 secs without fully arresting its energy.

The layout of an attenuator system is directly related to the rockfall trajectory. The attenuator must intercept the trajectory of the hazard. The closer you can position the system to the rockfall source, the less bounce, lateral dispersion, translational and rotational kinetic energy a block will develop. It is important to note that the rotational velocity of a rockfall impact significantly affects the overall behavior of the impact on which the shape of the rock and the slope morphology play an important role in developing.

Overall, attenuator systems should be designed combining the principles of the static loading of an open-toe simple drapery and the dynamic design principle of a traditional rockfall barrier. The resulting attenuator solution should be capable of withstanding multiple impacts without requiring maintenance while maintaining the specified capacity in dampening rockfall energy.

Hybrid Barriers

Hybrid barriers combine the same functionality provided by attenuators or deflectors with the catch-and-contain capability of a closed-toe simple drapery. Unlike the previously discussed systems which allow rock blocks to continue downslope after dissipating a portion of their kinetic energy, the objective of a hybrid barrier is to fully arrest the rockfall within the system. Consequently, the dynamic demands imposed on the impacted structure are consistent with those of conventional rockfall barriers, while the static loading conditions closely relate to those of closed-toe drapery systems.

Where the site layout does not allow the installation of an additional downstream interception structure required for attenuator systems, it is common practice to incorporate a lower retention cable anchored to the ground to stop the blocks before they leave the structure. Although this principle has proven effective, it fundamentally changes the main mode of operation and introduces two consequences on the design considerations of the system: 1) the rock is suddenly stopped at the toe which results in peak loads that are very difficult to calculate, and 2) the accumulation of rock debris at the toe will impart a static load on the system. It is therefore necessary to account for both additional loading conditions when designing the support

structure of a hybrid barrier system. Furthermore, maintenance becomes an integral part of system design. As the accumulation of debris reaches its design capacity, it should be cleared. Failure to comply with system maintenance requirements can lead to a premature failure of the structure.

The standard practice to determine the static debris load affecting hybrid systems is to account for a homogeneous expected accumulation pocket defined by a debris accumulation height (H_d) and width (W_d) as shown in Figure 6. The corresponding debris volume per linear width is multiplied by the debris density of the accumulated material to correctly dimension the debris load.

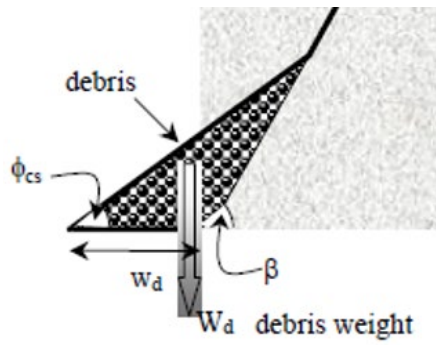

Figure 6. Loading due to debris accumulation at the toe of a hybrid barrier

This debris load should then be combined with the snow load, ice load and mesh weight to determine the total static load affecting the system. This total distributed static load in lbs/ft (kN/m) will also be used to verify the net tensile capacity and to dimension the support cables, anchors and posts to be used for the system.

As with attenuator systems, both a static load and a dynamic load should be considered when designing the elements of the system. However, because the mesh is restrained by the anchorage system designed to fully arrest the rock, the dynamic demand on the intercepting elements of the system is similar to a conventional rockfall barrier. The resulting impact forces are associated with a shorter deceleration time, a smaller stopping distance and a greater amount of energy being absorbed by the structure. It is evident that the supporting structure of a hybrid barrier system must be generally more robust than an attenuator system. Where appropriate, hybrid systems may use energy dissipator devices connected to cable to reduce the peak impact loads transmitted to the post and anchors.

The geometric configuration of the hybrid system and rockfall trajectory also play a critical role in its performance. Anchor spacing, support cable elevations, post spacing, and the length of the tail portion of the mesh influence both the dynamic impact capacity and the mechanisms of energy dissipation of the system. Consequently, the design should consider both localized loading within the impact zone and the global redistribution of forces throughout the system.

Hybrid barrier solutions should also be capable of withstanding multiple impacts at service energy levels without requiring immediate maintenance apart from the removal of the accumulated material at the toe. However, these systems are designed to safely withstand one maximum energy impact consistent with a traditional rockfall catchment fence. In conclusion, because hybrid barrier systems perform multiple functions simultaneously, it is critical that their design is verified through an integrated analysis of both the static and dynamic demands to ensure satisfactory long-term performance.

SOLUTION	OPEN TOE SIMPLE DRAPERY	DEFLECTOR	ATTENUATOR	CLOSED TOE DRAPERY	HYBRID BARRIER	ROCKFALL BARRIER
DESIGN PHILOSOPHY	CONTROLLED GUIDANCE	TRAJECTORY MODIFICATION	CONTROLLED ENERGY DISSIPATION	CONTROLLED GUIDANCE + CONTAINMENT	CONTROLLED ENERGY DISSIPATION + CONTAINMENT	IMPACT ARREST
PRIMARY FUNCTION	DIRECTION	DIRECTION	DAMPENING + DIRECTION	DAMPENING + CATCHMENT	DAMPENING + CATCHMENT	CATCHMENT
DYNAMIC IMPACT	NO	YES	YES	NO	YES	YES
ROCK ENERGY ABSORPTION	<100%	<100%	<100%	100%	100%	100%
REQUIRES EXTERNAL CATCHMENT	YES	YES	YES	NO*	NO*	NO*
MESH GROUND CONTACT	MAXIMUM	MINIMUM	MEDIUM	MEDIUM	MEDIUM	NONE
INCORPORRATED RETENTION DEVICES	NO	NO	NO	YES	YES	YES
RETAINED DEBRIS LOAD	NO	NO	NO	YES	YES	NO
SNOW LOAD	YES	NO	YES	YES	YES	NO
ICE LOAD (WET SLOPES IN WINTER WEATHER)	YES	YES	YES	YES	YES	NO
RELATIVE COST	$	$$	$$	$$	$$$	$$$

***** While no external catchment is required, the deflection of the mitigation upon being loaded or impacted should be considered

TABLE 1: Design Considerations for Deflectors, Attenuators and Hybrid barriers

SUMMARY

Alternative systems to rockall draperies and barriers, that incorporate characteristics of each, have grown in popularity and are more routinely being used to mitigate against rockfall events. These alternative systems are “hybrids” of conventional draperies and barriers which combine the energy absorption capabilities of a dynamic rockfall barrier with the reduced-maintenance advantages of a rockfall drapery. A ‘hybrid system’ is installed below the source zone of the rockfall and is meant to intercept the rockfall bounce and energy. The system can be designed to either 1) deflect, 2) reduce, or 3) fully arrest the rockfall velocity and energy.

A Deflector is a freely hanging steel wire mesh that only absorbs a portion of the impact energy as the netting is primarily designed to deflect the rock into the ground, where a major portion of the energy is absorbed. The performance of this hybrid system is measured by the net’s ability to absorb the initial impact and redirect the rock into the catchment area at the base of the slope.

An Attenuator is a ‘catch and release’ system that may be installed as a single structure, or in a series of multiple structures to attenuate very large impact energies. An Attenuator must resist an initial kinetic energy impact comprising of both translational and rotational forces. Where large initial impact energies are present, the ability for the netting to first absorb the initial impact and subsequently reduce the rock’s energy and velocity into a controlled location is determined by the netting’s tensile and punch strength, which resists the initial impact, and its weight (i.e. mass per unit area) and runout length, which provides the necessary dampening effect that “attenuates” the rockfall energy into a controlled location.

A Hybrid Barrier can be described as a raised rockfall drapery that is hung from the top of a barrier post, extending down the slope a specific distance, and anchored at the tail-end of the drapery section to fully arrest the rockfall energy. A hybrid barrier has a closer relationship to a traditional rockfall barrier, since the toe of the drapery section is secured, and the rock is brought to a stop, rather than released through the toe of slope. While attenuators are designed to absorb only a significant portion of the energy of the rocks traveling down the slope, hybrid barriers are designed to absorb the total energy of the rockfall. This application is often used when the slope length and/or catchment area are insufficient to fully arrest the rock’s energy and volume of debris.

Hybrid systems may or may not fully arrest the impact energy of the rock, and therefore, system design must consider the energy exiting the system and how that energy will eventually be brought to rest, either within the system or beyond it. The desired end-result will affect the forces and loads acting on the individual components of the system.

While similarities exist, each of these hybrid systems are unique, as their application is defined by their final objective. As such, the forces acting on the system components must be considered separately for each application. There are clear and unique design considerations that must be addressed for each system. Therefore, testing and design must be conducted and applied based on the specific system and application being considered. The authors caution against applying research testing and design of one hybrid system to another without thoroughly

understanding and considering the differences in the forces acting on the components of each hybrid system before offering it as a solution to a rockfall hazard.

REFERENCES

Arndt, B., Ortiz, T., Turner, K., Colorado's Full-Scale Field Testing of Rockfall Attenuator Systems. Transportation Research Circular E-C141, Transportation Research Board, Washington, D.C., October 2009.

Bichler, A., et.al. 2012. A Fresh Approach to the Hybrid/Attenuator Rockfall Fence.

Duffy, John D., P.G., C.E.G., Raised Draperies: Defininig Hybrid Barriers and Attenuators by Application, 72nd Highway Geology Symposium, Tacoma, Washington, August 2023.

Wyllie, Duncan, Shevlin, Tim, Glover, James, Wendeler, Corinna. Development of design method for rockfall Attenuators. Prepared for the 68th Highway Geology Symposium, Marietta, Georgia, May 2017.

08. GLACIOLACUSTRINE DEPOSITS ON THE SR 3002 LANDSLIDE REMEDIATION PROJECT

Jason M. Gardner, P.E.
GFT Infrastructure, Inc.
300 Sterling Parkway,
Suite 200
Mechanicsburg PA 17050
(717)-886-5429
jgardner@gftinc.com

Prepared for the 75th Highway Geology Symposium, September 2026

Acknowledgements

The author would like to thank the following individuals/entities for their contributions in the work described:

Isaac R. Bragunier, P.E. – PENNDOT 3-0, District Geotechnical Engineer

Disclaimer

Statements and views presented in this paper are strictly those of the author(s), and do not necessarily reflect positions held by their affiliations, the Highway Geology Symposium (HGS), or others acknowledged above. The mention of trade names for commercial products does not imply the approval or endorsement by HGS.

Copyright Notice

Copyright © 2026 Highway Geology Symposium (HGS)

All Rights Reserved. Printed in the United States of America. No part of this publication may be reproduced or copied in any form or by any means – graphic, electronic, or mechanical, including photocopying, taping, or information storage and retrieval systems – without prior written permission of the HGS. This excludes the original author(s).

ABSTRACT

In mid-August 2018, a 2-day storm system dumped approximately 6-8 inches of rain on the northern tier of Pennsylvania resulting in extreme flooding in the Region. The flooding induced erosion of roadway slopes causing many landslides that affected roadways owned and maintained by PennDOT, District 3-0. Two distinct landslides were identified within a ½ mile stretch of the SR 3002 roadway in southern Bradford County. The slope movement required the SR 3002 roadway to be closed to traffic in this area; however, one lane remained in service to allow local residents access to their homes.

An initial subsurface exploration program was performed in Fall 2018 at each of the 2 slide locations, and unusually thick glaciolacustrine deposits were encountered. In addition, laboratory testing was performed on representative glaciolacustrine samples to estimate the engineering properties of these soils, and the results indicated the glaciolacustrine soils exhibited extremely low peak and residual shear strength. During a site visit in June 2019, two additional landslides were observed between the original 2 landslide locations. The initial preferred remediation alternative was to realign the SR 3002 roadway to avoid the glaciolacustrine deposits and minimize risk of future landslide activity negatively impacting the SR 3002 roadway. An additional subsurface exploration program was performed for the proposed realignment and these borings also encountered thick glaciolacustrine deposits that were expected to be problematic. Based on the additional subsurface information, the preferred remediation alternative was to stay on the existing SR 3002 alignment and stabilize the 4 landslides using tangent pile walls.

INTRODUCTION

SR 3002, locally referred to as Overton Road, is a two-lane roadway that is a southwest/northeast corridor through the Endless Mountains Region of Bradford County in northeast Pennsylvania. The SR 3002 corridor is situated in the southern portion of Bradford County and carries traffic between SR 87 at the southwest end of the corridor to SR 220 in the town of New Albany at the northeast end of the corridor.

A massive storm event dumped approximately 6-8 inches of rain on Bradford County, Pennsylvania between August 14-15, 2018. The excessive rain resulted in flooding along many local waterways. Erosion that resulted from the flooding triggered a significant number of landslides in the region that impacted many roadways owned and operated by the Pennsylvania Department of Transportation (PennDOT). The SR 3002 corridor in south central Bradford County was one of the hardest hit areas of the region, as 2 distinct areas of the roadway, denoted as Sites 1 and 2, were impacted by landslides within an approximately 0.5-mile stretch of SR 3002 to the southwest of the Borough of New Albany, Pennsylvania. The landslides caused roadway displacements, which resulted in closure of this portion of SR 3002 in August 2018.

A map showing the general location of the project is provided in Figure 1 and the location of the 2 landslide sites observed in August 2018 are shown on the map presented as Figure 2.

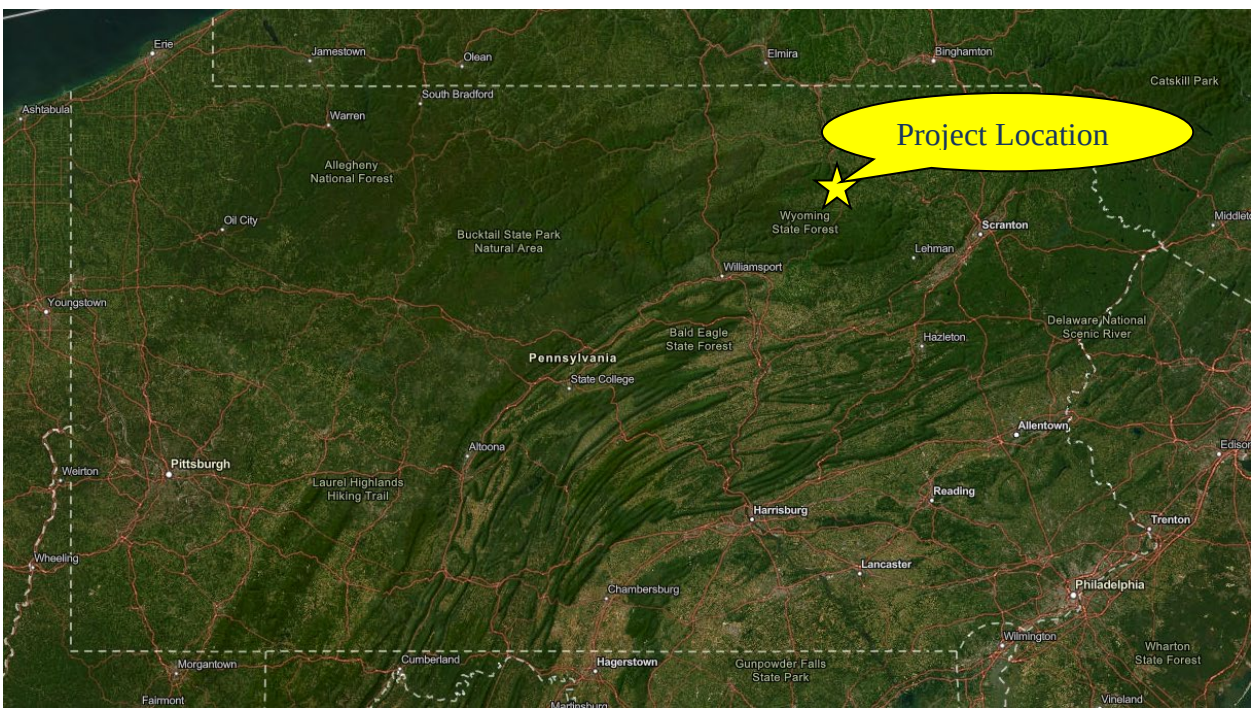

Figure 1: Project Location Map

Figure 2: Landslide Sites Location Map – August 2018

The impacted portion of SR 3002 is situated adjacent to Ladd's Creek. Ladd's Creek is a tributary to the South Branch Towanda Creek that ultimately empties into Towanda Creek and the Susquehanna River. PennDOT engaged Gannett Fleming, now GFT, in August 2018 to assist with the landslide remediations that were ultimately advertised for construction in 2024, construction began in Spring 2025, and is currently scheduled to be complete by the end of 2026.

PROJECT HISTORY

The following chronological timeline presents the significant events that were part of this project and will be discussed in detail in subsequent sections of this paper:

- August 2018 – GFT engaged by PennDOT to remediate Sites 1 and 2.
- Fall 2018 – Preliminary subsurface exploration performed at Sites 1 and 2.
- Winter 2018/Spring 2019 – Developed preliminary landslide remediation alternatives.
- June 2019 – Site visit revealed 2 additional landslides denoted as Sites 3 and 4.
- Summer 2020 – Emergency repair contract to restore access for local residents.
- Fall 2020 – Preferred remediation was SR 3002 realignment alternative.
- April 2021 – Performed subsurface exploration for realignment alternative.
- May 2021 – Emergency repair from Summer 2020 begins to fail.
- July 2021 to Spring 2022: Design for the SR 3002 realignment proceeds.

- September 2021 – Emergency repair from Summer 2020 completely fails.
- February 2022 – SR 3002 realignment alternative cost estimate grows.
- March 2022 – Preferred alternative is to remediate the 4 landslides observed along the existing SR 3002 alignment.
- March/April 2022 – Performed additional subsurface exploration program at Sites 1, 2, 3, & 4.
- Summer 2022/Spring 2024 – Complete final design of the project, prepare PS&E.
- July 2024 – Contract awarded.
- Spring 2025 – Landslide remediation construction began.

SITE GEOLOGY

Physiographical Conditions

The entire project site is located in the Glaciated Low Plateau Section of the Appalachian Plateaus Province based on the mapping provided by the Pennsylvania Department of Conservation and Natural Resources (PaDCNR), Map 13 – Physiographic Provinces of Pennsylvania. In general, the section consists of rounded hills and valleys with low to moderate relief (*1)*.

Surficial Geology

The soils in the area of the project sites are Valley Bottom Sand and Gravel (VSG) and Lake Sediments – Varves (L) along SR 3002 according to the Surficial Geology of the Towanda 30x60-mintue Quadrangle mapping. The VSG consists of a heterogeneous mixture of stratified sand and gravel with some beds of silt and clay. Clasts are dominantly sandstone. Deposits underlie flat surface of valley bottoms. Thickness is variable and ranges from more than 100 feet in the Susquehanna River valley to only a few feet in Towanda Creek valley. The Lake Sediments are composed of silt-clay couplets each a fraction of an inch to several inches in thickness. Sediments may contain some clasts up to boulder size. Thickness is generally only a few 10's of feet but may be more than 100 feet in some valleys (*2*).

Bedrock Geology

Based on the Pennsylvania Department of Conservation and Natural Resources, the entire project site is underlain by the Devonian aged Catskill Formation (Dck) (*3*). The Catskill Formation consists of a succession of grayish-red sandstone, siltstone, shale, and some conglomerate and mudstone, generally in fining-upward cycles. The top of the unit is defined as the uppermost red bed. Bedding is well developed in most places. Thicknesses range from less than 1 foot to 10 to 16 feet in coarser beds. Crossbedding is common. The maximum thickness is about 6,200 feet, thinning to the west. (*4*).

FIELD RECONNAISSANCE - 2018

Field reconnaissance of Sites 1 and 2 was performed on September 7, 2018 by GFT personnel. The following observations were made during the site visit.

Site 1

- The slide area is approximately 200 feet in length, approximately 20 feet high and is characterized as a translational failure occurring along exposed medium to highly plastic, varved, glaciolacustrine deposits as shown in Photos 1 & 2.
- Heavy rainfall and flooding caused Ladds Creek to further erode the slope resulting in loss of material beneath the pavement section on the south side of SR 3002, impacting the eastbound lane. SR 3002 is currently closed in this area .
- Varved glaciolacustrine deposits were also observed at the ground surface on the north side of Ladds Creek.
- Large blocks of asphalt (~4 to 5 feet thick) are evident within the slide material, indicating that paving operations have been performed in this area for a prolonged time in order to restore rideability due to displacement of the roadway.
- Reddish brown sandstone outcrops are present along the south side of Ladds Creek. No glacial lake clay was observed on the south bank of Ladds Creek at Site 1.
- Bedrock was not observed within the slide area (i.e., north side of Ladd's Creek).
- Rockfill wrapped with geotextile was observed within the slide area, indicating evidence of prior slope stabilization measures.
- A corrugated metal pipe was visible within the slide area.

Photo 1: Site 1 Landslide

Photo 2: Site 1 Exposed Varved Glaciolacustrine Deposit

Site 2

- The slide area is approximately 150 feet in length and is characterized as a circular or rotational failure with the crown of the slide crossing both lanes of SR 3002, which requires the roadway to be closed at this location as shown in Photo 3.
- Medium to highly plastic, varved, glacial lake clay deposits were observed at the toe of the landslide, just upslope of Ladds Creek.
- Approximately 0.10 to 0.70 feet of displacement has been measured on the roadway, along the headscarp of the slide.
- The slide extends to the stream level at the base of the slope. A toe bulge was observed impacting the course of the stream along with hummocky ground conditions with overturned trees within the slide mass.
- A corrugated plastic pipe located along the westbound shoulder was uplifted and exposed to the right of a private driveway during a recent flooding event.
- The contact between the glacial lake clay and bedrock was observed in the stormwater ditch adjacent to the shoulder, to the north of SR 3002 and west of the private driveway.
- Bedrock was observed near the creek elevation at the western limits of the slide mass.

Photo 3: Site 2 Landslide

SUBSURFACE EXPLORATION – FALL 2018

A preliminary subsurface exploration program was conducted at Sites 1 and 2 between September and October 2018. Two borings, designated RB-01 and RB-03, were drilled at Site 1 and two borings, designated RB-05 and RB-06 were drilled at Site 2. The purpose of the borings was to determine the subsurface conditions at each Site and collect soil and rock samples for laboratory testing to substantiate the geotechnical design of each landslide remediation. A brief summary of the subsurface exploration program performed at each Site is summarized below.

Site 1 Results

Borings RB-01 and RB-03 encountered approximately 5 feet of material at the surface that was identified as fill and colluvium. Underlying the fill/colluvium material, an extremely thick layer of glaciolacustrine material was encountered at Site 1. The glaciolacustrine deposit consisted of silt and clay and was 25.5-feet to 33.5-feet thick in the borings. Previous projects in this region of Pennsylvania have typically encountered glaciolacustrine deposits on the order of 10-feet thick or less. A thin layer of very dense residuum was encountered below the glaciolacustrine material and siltstone bedrock was encountered at 38.5 feet below adjacent ground surface at both boring locations.

Two undisturbed soil samples were collected at Site 1 and were laboratory tested using consolidated-drained direct shear with residual shear measurements. The samples were collected in Boring RB-01U, located a few feet from Boring RB-01, between 12 and 16 feet below ground surface within the glaciolacustrine deposit. The results indicate that the peak friction angle ranged

from 14.5 to 18.3 degrees with cohesion values ranging from 0 to 577.9 pounds per square foot (psf), while the residual friction angle ranged from 9 to 12.5 degrees.

Site 2 Results

Borings RB-05 and RB-06 encountered approximately 10-12 feet of material at the surface that was identified as fill and glacial outwash. Underlying the fill/glacial outwash material, an extremely thick layer of glaciolacustrine material was encountered at Site 1. The glaciolacustrine deposit consisted of silt and clay and was approximately 5-feet thick in Boring RB-05 to 26.5-feet thick in Boring RB-06. A thin layer of very dense residuum was encountered below the glaciolacustrine material and sandstone and siltstone bedrock was encountered at depths ranging between 19.2 feet in Boring RB-05 to 38.5 feet in Boring RB-06 below adjacent ground surface.

Three undisturbed soil samples were collected at Site 2 and were laboratory tested using consolidated-drained direct shear with residual shear measurements. The samples were collected from Borings RB-05B and RB-06U (i.e., borings offset a few feet from Borings RB-05 and RB-06) between 12 and 22 feet below ground surface within the glaciolacustrine deposit. The results indicate that the peak friction angle ranged from 17.5 to 22.4 degrees with cohesion values ranging from 0 to 110 psf, while the residual friction angle ranged from 5.8 to 10.6 degrees.

PRELIMINARY LANDSLIDE REMEDIATION ALTERNATIVES

Based on the information obtained from the subsurface exploration program and experience working with PennDOT on landslide repair projects, the following landslide remediation alternatives were considered during Winter 2018/Spring 2019 for Sites 1 and 2:

- Overexcavation and replacement with rock embankment
- Soil nails
- Cantilever sheet piles
- Anchored sheet piles
- Overexcavation and replacement with lightweight fill
- Battered micropile wall

Further evaluation of these remediation alternatives was performed and based on the thickness and extremely low shear strength values of the glaciolacustrine deposit, none of the preliminary remediation alternatives were deemed practical. Therefore, a continuous, rigid retaining structure was believed to be the best alternative to remediate these landslides. Accordingly, a tangent caisson wall alternative was evaluated, and was determined to be feasible from and engineering perspective; however, the cost to construct this remediation alternative far exceeded the funds available to repair this section of SR 3002 in rural Bradford County.

LANDSLIDE SITES 3 & 4

A utility coordination meeting was held at the project site with PennDOT and GFT personnel on June 20, 2019. During the site visit, 2 additional landslides were observed between Sites 1 and 2. These 2 additional landslides were referred to as Sites 3 and 4 and these locations are shown on the map provided as Figure 3

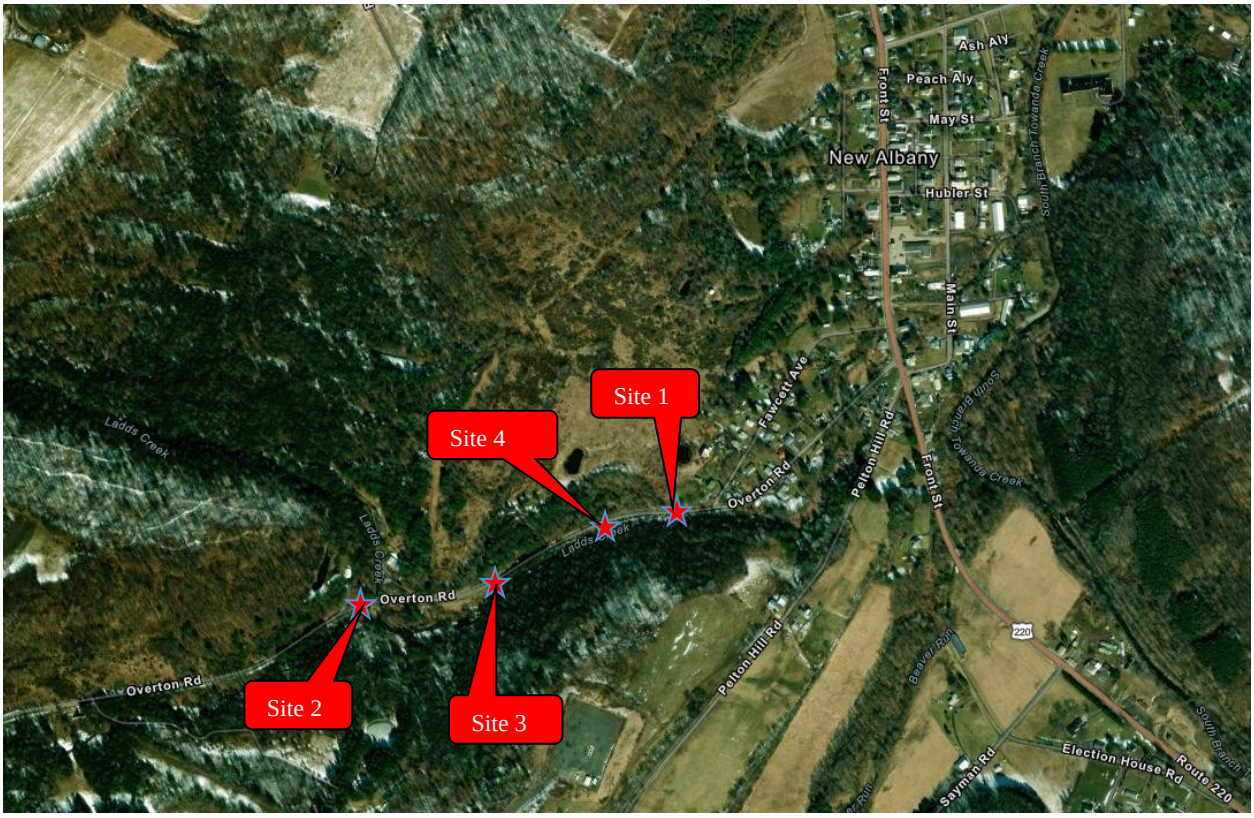

Figure 3: Landslide Sites Location Map – June 2019

The following observations were made during the site visit.

<u>Site 3</u>

- The slide area is directly adjacent to Ladd's Creek, was approximately 120 feet in length, approximately 15 feet in height, and was characterized as a circular or rotational failure with the headscarp of the landslide located at the shoulder of the SR 3002 eastbound lane as shown in Photo 4.

Photo 4: Site 3 Landslide

Site 4

- The slide area was located immediately adjacent to Ladd's Creek, was approximately 100 feet in length, approximately 15 feet in height, and was characterized as a circular or rotational failure with the headscarp of the landslide located downslope of the shoulder of the SR 3002 eastbound lane.

FINAL LANDSLIDE REMEDIATION ALTERNATIVES

The discovery of the landslides at Sites 3 and 4 in June 2020 made it clear that the entire stretch of SR 3002 between Sites 1 and 2 was likely near equilibrium and could be subject to slope instability issues if the existing slopes were impacted due to future flood events, grading operations, etc. Furthermore, the additional landslides reinforced the results of the preliminary analyses that conventional landslide remediation alternatives utilized by PennDOT were not feasible for this project. Although the tangent caisson walls were feasible, they were not considered the preferred alternative due to the cost associated with constructing tangent caisson walls. Therefore, the preferred remediation alternative in June 2020 was to realign the SR 3002 roadway to avoid the landslide prone areas.

EMERGENCY REPAIR CONTRACT

The condition of the SR 3002 roadway had deteriorated significantly by early 2020 at Sites 1 and 2, and with the discovery of Sites 3 and 4 and final design of the remediation strategy not yet started, it was determined that if the existing SR 3002 roadway in the areas of Sites 1 and 2 was left untreated, access to the 3 residences within the project area could be jeopardized. Therefore, PennDOT awarded an emergency repair project in the Summer of 2020 to restore the SR 3002 roadway at Sites 1 and 2 to ensure local residents could access their property until a permanent solution could be provided. The repairs included a rock buttress and a 14-foot travel lane at Site 1 and restoring the pavement at Site 2 and the repairs were completed by Fall 2020. By May 2021, movement was observed within the rock buttress repair performed at Site 1 and by the end of September 2021, the repair at Site 1 had failed as shown below in Photo 5.

Photo 5: Failure of Repairs at Site 1

SUBSURFACE EXPLORATION – SPRING 2021

A subsurface exploration program was conducted for an SR 3002 realignment alternative, which consisted of moving SR 3002 upslope of the existing alignment by approximately 300 feet in an attempt to move the roadway to a more stable location. Seventeen borings, designated as RB-21 to RB-37, were drilled in April and May of 2021 for the proposed realignment. The purpose of the borings was to determine the subsurface conditions underlying the proposed SR 3002 realignment and to collect soil and rock samples for laboratory testing to substantiate the geotechnical design of the roadway. A brief summary of the subsurface exploration program is summarized below. The SR 3002 relocation alternative and boring locations are shown in Figure 4.

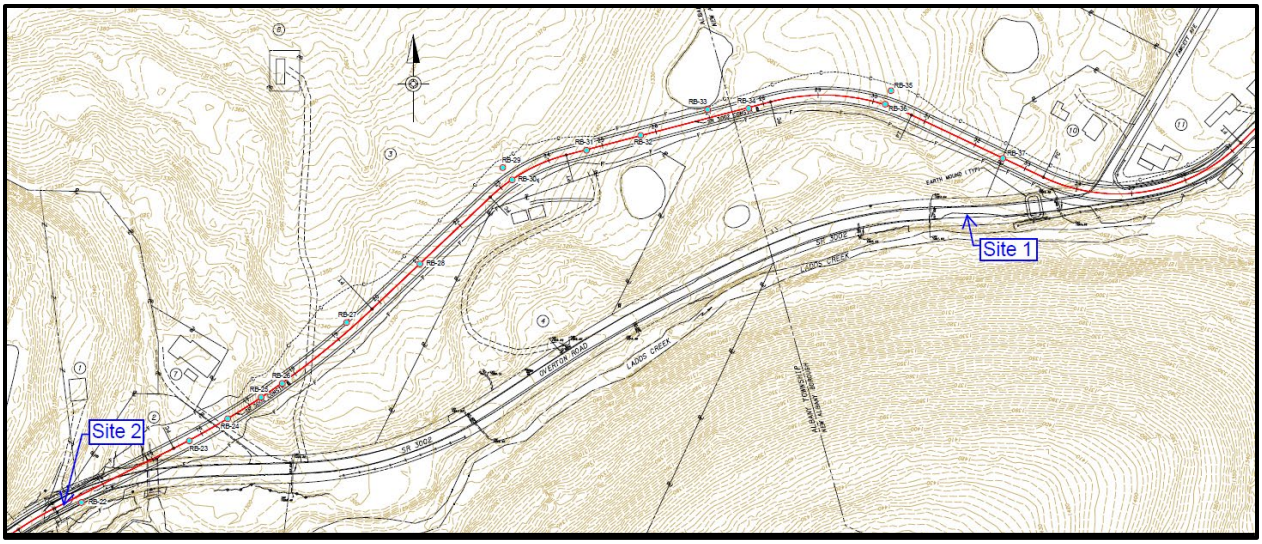

Figure 4: SR 3002 Realignment Location and Boring Locations

The borings generally encountered sand and gravel that was described as glacial till at the surface that extended to depths ranging between 7.5 feet and 33 feet below ground surface. Underlying the glacial till material, the glaciolacustrine silt and clay was encountered in the majority of the borings and ranged in thickness from approximately 13 feet to 50 feet. The groundwater table encountered in the borings was generally less than 5 feet below existing grade throughout the proposed realignment of SR 3002.

LANDSLIDE REMEDIATION DESIGN

Geotechnical design was completed for the SR 3002 relocation and the design required cut slopes to be rock lined and at 3H:1V to satisfy stability requirements due to the high groundwater levels encountered throughout the proposed realigned corridor. In addition, tangent caisson walls were required at the tie-in points to existing SR 3002 (i.e., one wall at Site 1 and one wall at Site 2) to repair the existing landslide areas in order to satisfy stability requirements. Since the borings showed the SR 3002 realignment was also underlain by thick glaciolacustrine deposits, there was still a risk of future landslide activity, regardless if SR 3002 alignment was maintained as-is or relocated. Furthermore, the SR 3002 realignment alternative would impact wetlands, created stormwater management issues that required significant basins to mitigate, required right-of-way acquisition since it was not located within existing PennDOT right-of-way, and was more difficult to permit than staying on the existing alignment,

Due to the estimated cost and risk of future landslide activity associated with the SR 3002 realignment alternative that was similar to remediating the landslide with tangent caisson walls on the existing alignment, it was determined in March 2022 that the length of each wall should be verified. Furthermore, additional borings were performed at each of the 4 landslide sites to obtain subsurface information for design of the tangent walls at Sites 3 and 4 and to obtain additional subsurface information at Sites 1 and 2. A site visit with GFT and PennDOT's District Geotechnical Engineer was conducted on March 10, 2022 to verify the required wall lengths at each of the 4 sites and layout ten additional borings. The final wall lengths were determined to range from 165 feet at Sites 3 and 4 to 285 feet at Sites 1 and 2. The ten additional borings, one at Site 2 and three at Sites 1, 3 and 4, were performed to assist with design of the tangent caissons. The main goal of the borings

was to verify the type/quality of the bedrock therefore, at least 20 feet of bedrock was cored in each of the 10 borings. The borings indicated that the bedrock at Sites 1 and 2 is Siltstone and the bedrock at Sites 3 and 4 is Sandstone.

Geotechnical design was performed for the tangent caisson walls. The design was based on an assumed loss of soil material in front of the wall that was substantially more than what was depicted on the cross sections developed by the GFT design team. The caissons were designed for the design heights shown in Table 1 below.

Site No.	Design Height (ft)
1	16.0
2	15.5
3	9.0
4	15.5

Table 1: Summary of Design Heights

The tangent caisson walls were designed in accordance with PennDOT design guidelines and AASHTO LRFD Bridge Design Specifications. Each of the tangent caisson walls designed by GFT required a caisson diameter of 5 feet in soil and 4.5 feet in rock, and the minimum rock socket length to satisfy wall stability requirements is provided below in Table 2. The deflection of the walls was estimated to be less than 0.25-inches for each wall.

Site No.	Min. Rock Socket Length (ft)
1	17.5
2	16.3
3	9.6
4	12.3

Table 2: Summary of Minimum Rock Socket Lengths

The tangent caisson walls were designed to promote drainage by including a 24-inch diameter perforated pipe that would extend to top of bedrock and be backfilled with AASHTO No. 57 Coarse Aggregate between every pair of caissons. In addition, a curb was placed on the top of the wall to not allow sheet flow over the caisson walls. A typical wall plan view is provided below as Figure 5.

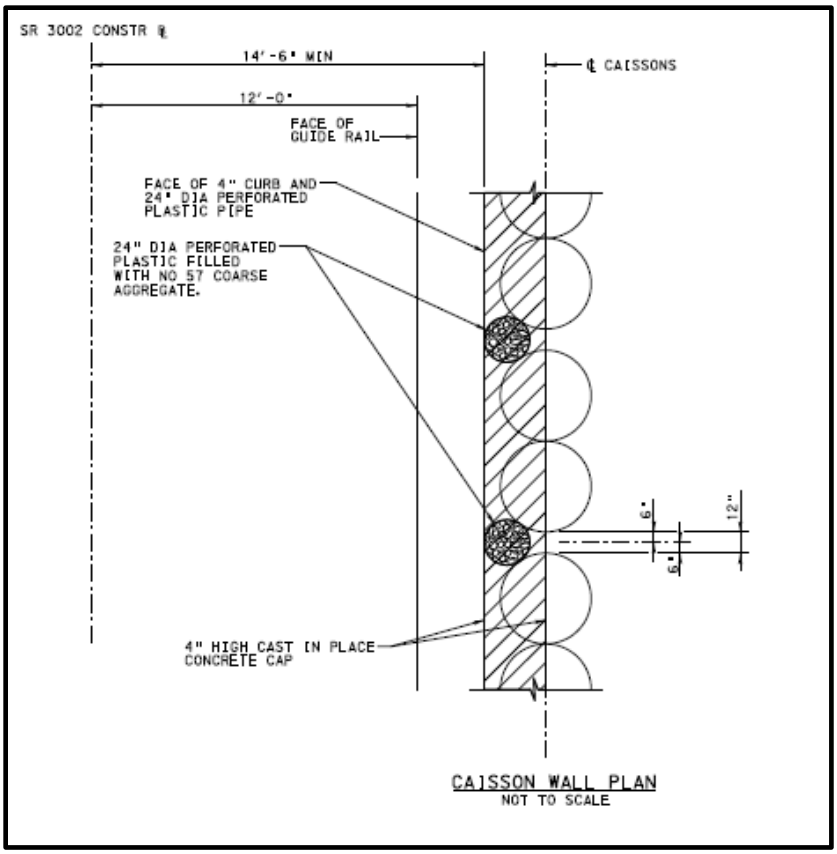

Figure 5: Typical Caisson Wall

A cost estimate was prepared for the SR 3002 realignment described above, as well as for 4 distinct tangent caisson walls and a continuous tangent caisson wall from Site 1 to Site 4. The cost comparison between these 3 remediation alternatives is provided in Table 3 below.

Alternative	Cost Estimate
SR 3002 Relocation	$17,864,000
4 Caisson Walls	$15,480,000
Continuous Caisson Walls	$38,800,000

Table 3: Cost Estimates of Remediation Alternatives

Based on the cost estimate that was performed it was determined that the most economical alternative for this project was to construct 4 distinct tangent caisson walls to remediate the existing landslides observed at Sites 1-4 along the SR 3002 corridor. It was determined by PennDOT that the project would be Design-Build and GFT would be responsible for preparing a Foundation Design Guidance Report with special provisions for design and construction of the caisson walls for the Design-Build team to use in designing each of the 4 tangent caisson walls.

CONSTRUCTION

A Design-Build contract was awarded in July of 2024 to the low bidder at a cost to the Department of $12,432,722.60, which was less than the Engineer's estimate. The final designer of the caisson walls was able to use slightly smaller caisson diameters/rock sockets as summarized below in Table 4.

Site No.	Caisson Diameter in Soil (ft)	Caisson Diameter in Rock (ft)	Min. Rock Socket Length (ft)
1	5.0	4.5	5.0
2	5.0 to 5.5	4.5 to 5.0	14.5
3	5.0	4.5	5.0
4	5.0	4.5	8.0

Table 4: Summary of Caissons Used by Design-Build Team

Based on discussions with District 3-0 Construction staff, construction of the tangent caisson walls has progressed well, and Photo 6 was taken during construction of the landslide remediation at Site 2.

Photo 6: Completed Tangent Caisson Wall at Site 2

REFERENCES

(1) Sevon, W.D. (Compiler). Pennsylvania Geological Survey, *Physiographic Provinces of Pennsylvania.* 4th Ed. , Map 13, 2000.

(2) Sevon, William D. and Braun, Duane D., Pennsylvania Bureau of Topographic and Geologic Survey, *Surficial Geology of the Wellsboro and Towanda 30x60-Minute Quadrangles, Pennsylvania.* Open File Reports 97-02 and 97-03, 1997.

(3) Pennsylvania Department of Conservation and Natural Resources, Bureau of Topographic and Geologic Survey, *PAGEODE,* September 2018.

(4) Geyer, S.R. and Wilshusen, J.P., Pennsylvania Bureau of Topographic and Geologic Survey, *Engineering Characteristics of the Rock of Pennsylvania,* Revised 1982.

09. Emergency Landslide Response and Integrated Field-Design Approaches: US-95 MP 146.5, Idaho

Brittany Dayley, LEG/CEG, PG
Delve Underground
2000 SW First Ave., Suite 410
Portland, OR 97201
360-233-7166
dayley@delveunderground.com

Malcolm Perkins, PE
Delve Underground
1011 Western Ave., Suite 706
Seattle, WA 98104
978-987-2006
perkins@delveunderground.com

Prepared for the 75th Highway Geology Symposium, September, 2026

Acknowledgements

The authors would like to thank the following individuals and organizations for their contributions to the work described in this paper:

Idaho Transportation Department (ITD) – Project Owner and Maintenance Crews
Delve Underground – Emergency Response, Design and Construction Oversight
Haz-Tech Drilling, Inc. – Drilling and Exploration Contractors
Braun-Jensen, Inc. – Field Construction and General Contractors

Disclaimer

Statements and views presented in this paper are strictly those of the author(s), and do not necessarily reflect positions held by their affiliations, the Highway Geology Symposium (HGS), or others acknowledged above. The mention of trade names for commercial products does not imply the approval or endorsement by HGS.

Copyright

Copyright © 2026 Highway Geology Symposium (HGS)

All Rights Reserved. Printed in the United States of America. No part of this publication may be reproduced or copied in any form or by any means – graphic, electronic, or mechanical, including photocopying, taping, or information storage and retrieval systems – without prior written permission of the HGS. This excludes the original author(s).

ABSTRACT

US-95 is the sole north-south corridor serving many communities in northern Idaho. In March 2025, a landslide occurred at US-95 MP 146.5 along the western slopes of the Weiser River, between the residential communities of Pine Ridge and Tamarack, Idaho, approximately 19 miles (31 km) west of the tourism hub of McCall. A portion of the northbound lane collapsed during spring snowmelt, prompting a full roadway closure and implementation of lengthy detours, resulting in significant regional economic impacts and potential constraints on emergency response.

An exploration program was initiated within approximately 48 hours of the failure and included geotechnical borings, drone reconnaissance, and detailed geologic mapping. The rapid response was enabled in part by proactive reconnaissance performed in October 2024 and by a drill crew that had already been mobilized for a previously scheduled investigation. Repair design began within one week and addressed challenges associated with an accelerated schedule, limited material availability, and steep, constrained terrain. The selected repair consisted of an anchored soldier pile retaining wall with drilled-shaft deadmen and extensive surface drainage improvements.

Construction encountered additional challenges, including large boulder obstructions, groundwater inflow, hole instability, and equipment limitations. Continuous field-based engineering geology support facilitated real-time communication with the design team regarding subsurface variability, modification to pile installation procedures, and development of alternative construction sequences. The roadway reopened to the public by April 30, 2025, 45 days after the initial failure was reported.

This case study highlights the value of flexible exploration strategies; parallel field-design coordination; and collaboration between the owner, designer, and contractor during all stages of the design and construction process in emergency highway response environments.

INTRODUCTION

U.S. Route 95 (US-95) is the only continuous north-south highway in Idaho and runs through much of the northern half of the state. It serves as the sole practical corridor that connects communities, freight routes, and emergency services. Where US-95 crosses mountainous terrain, there are few parallel roadways capable of carrying highway traffic, so even a localized closure of US-95 can sever regional connectivity and force detours that add several hours of travel time. The reliability of US-95 is therefore critically important to the communities it serves, both economically and from a public safety standpoint.

The site discussed in this paper is located at approximately Milepost (MP) 146.5, on the western slopes of the north-south trending Weiser River Valley, between the residential communities of Pine Ridge and Tamarack, Idaho, and roughly 19 miles (31 km) west of the tourism hub of McCall. At this location, the highway is cut into a moderately steep hillside, with the roadway prism supported in part by fill placed over native colluvial and residual soils.

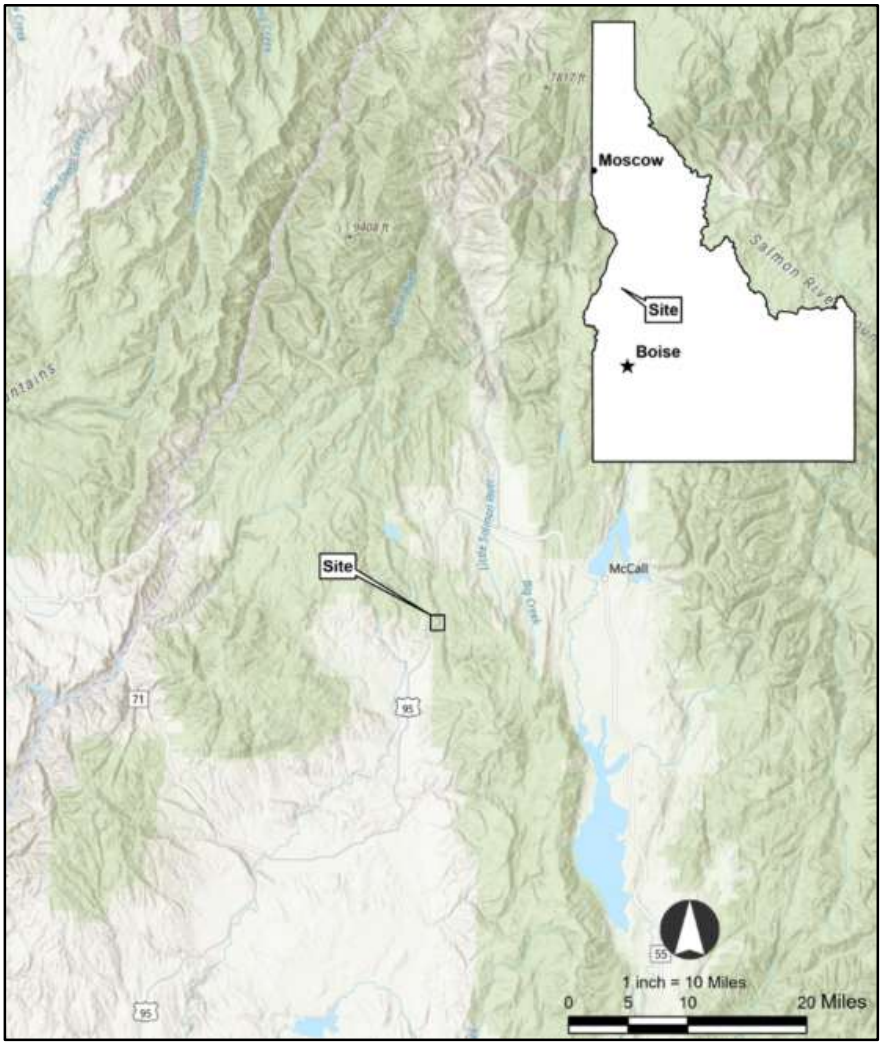

Figure 1 – Vicinity Map of US-95 MP 146.5, Adams County, Idaho

Geologic and Landslide History

Landslides have been documented historically in and around the site. Published mapping and the statewide landslide inventory record numerous slope failures along this reach of the Weiser River Valley (*1*, *2*). These failures are commonly associated with movement along irregular bedrock contacts and with the local slope morphology, and they are frequently triggered by periods of intense rainfall or by rapid snowmelt. Regionally, the site is underlain by Miocene-age basalt flows of the Columbia River Basalt Group (CRBG) (*1*). At and below the roadway elevation, the CRBG is represented by the Imnaha Basalt, a medium- to coarse-grained, plagioclause-phyric unit with olivine phenocrysts up to 3 centimeters (cm) long; and reach thickness of approximately 400 feet and is commonly deeply weathered. Upslope of the roadcut, the Imnaha Basalt is overlain by the younger, more resistant Grande Ronde Basalt, a fine-grained unit composed of six to eight individual flows within a combined thickness of 500 to 600 feet. The contact between these two basalt formations is irregular and represents a preferential pathway for groundwater movement and slope instability. At the site, the combination of clay-rich soils overlying a variable bedrock surface creates conditions in which elevated groundwater can reduce effective stress along potential failure surfaces, particularly during the spring melt season.

Pre-Failure Reconnaissance

In October 2024, Delve Underground conducted a preliminary site reconnaissance in the vicinity of MP 146.5 in response to settlement in the area that Idaho Transportation Department (ITD) maintenance crews had observed. Of particular note, the maintenance crews had identified field indicators of developing instability, including localized sagging of the roadway surface and new cracks forming in the northbound (NB) lane. The maintenance personnel had recognized how important these subtle distress features were, signaling an early warning, which allowed ITD to begin planning for a subsurface investigation before any major failure would occur.

Figure 2 – NB Lane Showing Cracking Prior to Failure, Photo Taken March 3, 2025

Based on the findings of the reconnaissance, two geotechnical boreholes were marked in the field, and drilling was scheduled to take place on March 18, 2025. The site was also flown with an unmanned aerial vehicle (drone) as part of this initial reconnaissance, which recorded pre-failure site conditions and slope geometry. A drilling crew was secured for the scheduled investigation; this coincidental timing allowed the crew to respond rapidly to the landslide emergency.

THE FAILURE EVENT

On the evening of Sunday, March 16, 2025, a landslide occurred that took out a portion of the NB lane of US-95 at MP 146.5. The failure developed during the spring snowmelt period, consistent with the historical pattern of slope instability in the area. The next morning, Monday, March 17, 2025, Delve Underground was notified of the failure, coincidentally, as the project geologist was preparing to drive to the site for the investigation that had already been scheduled.

The failure closed US-95 to through traffic between Council and New Meadows, Idaho, until the roadway could be repaired. The closure forced a detour of several hours for local residents and commercial traffic, and it carried significant economic consequences for the surrounding towns, which rely heavily on trucking for the movement of goods. The closure also had the potential to constrain emergency response throughout the affected region. These impacts propelled the repair to a high-priority emergency project and set the tone for the accelerated schedule that followed.

Figure 3 – Overhead View of Failure, Taken with Drone on March 19, 2025

EMERGENCY EXPLORATION PROGRAM

Because a drill crew had already been secured for the previously planned March 18 investigation, Delve Underground and ITD were positioned to react rapidly once the failure was reported. The pre-positioning of this resource allowed the exploration program to begin within approximately 48 hours of the failure, rather than days or weeks that emergency mobilization can otherwise require.

Mobilization and Drilling

The exploration program was expanded from the two boreholes that were originally planned to four boreholes located at key positions in and around the head scarp of the slide. With the roadway already closed to through traffic, the drill rig could be positioned more freely than would have been possible under traffic control, improving access to the most informative locations.

Drilling was performed using hollow-stem auger (HSA) methods. Depth to refusal was variable, and boulder obstructions were considered likely based on the drilling response, as presented in Table 1 below. The accelerated schedule did not allow time for laboratory testing of soil or rock-core samples; characterization therefore relied on field observation and the experience of the field team. HSA methods were selected partly because they allowed direct observation of groundwater conditions during drilling, which was critical given the role of groundwater in the failure. The four borings (BH-01 through BH-04) were advanced around the head scarp of the slide, with each hole terminated at auger refusal. Standard penetration testing was performed at regular intervals, and groundwater was encountered only in the southernmost boring, BH-04, at approximately 39.5 feet (12 m) below ground surface where the drill met refusal.

Figure 4 – Hollow-Stem Auger Drilling During the Field Investigation

Subsurface conditions encountered in borings BH-01 through BH-04 were generally consistent across the site, though bedrock depth and groundwater conditions were variable. From the ground surface elevation downward, a consistent sequence was identified, as follows:

Pavement: All four borings encountered asphalt pavement ranging from 5 to 12 inches below ground surface (bgs).

Road Base/Fill: Coarse-grained fill consisting of dense to very dense sandy GRAVEL with silt (GP-GM/GM) or silty to clayey SAND with gravel (SM/SC), typically dark gray to brown with angular, basaltic gravel clasts. This unit ranged from approximately 2 to 8 feet bgs.

Residual Soil: Reddish-brown, sandy CLAY with gravel (CL), locally grading to clayey SAND (SC) with clayey GRAVEL (GP-GC) near the base of the unit. Consistency was variable both within and between borings, ranging from hard to very stiff near the surface, to medium stiff to very soft with depth (BH-04). Iron-oxide mottling and staining were common throughout. Scattered cobbles and boulders were noted within this unit.

Decomposed/Weathered Basalt (Saprolite): In BH-04, a translational saprolitic zone of medium dense to dense clayey GRAVEL with sand (GP-GC) was identified from 22 to 38 feet bgs. A similar but thinner transition zone into clayey residual soils/saprolite was also identified in BH-02 at 11 feet bgs, immediately above the bedrock contact.

Columbia River Basalt Bedrock: All four borings terminated at auger refusal on dark-gray to black, fine-grained, massive BASALT, slightly to moderately weathered and medium strong to strong (R3-R4). Initial interpreted bedrock elevations varied based on auger refusal depths, ranging in elevations of approximately 3,408 feet at BH-02 (northern scarp) to approximately 3,380 feet at BH-04 (southern scarp), a difference of roughly 28 feet over a lateral distance of approximately 80 feet. This variability in rock-surface geometry is consistent with the boulder obstructions encountered during subsequent pile installation.

Groundwater: Boreholes BH-01, BH-02, and BH-03 were observed to be dry both during and after drilling. Groundwater was encountered in BH-04, at approximately 39.5 feet bgs (measured after a 10-minute stabilization period), near the contact between the residual soil and bedrock transition zone, which was consistent with groundwater observed during construction and the subsequent pile installation.

Table 1 – Borehole Summary

Borehole ID	Location	Surface Elevation (ft, amsl)	Total/Refusal Depth (ft, bgs)	Interpreted Bedrock Elevation (ft, amsl)	Groundwater (ft, bgs)	Notes
BH-01	Northernmost, NB lane	3,421.9	33.1	3,388.8	Dry	-
BH-02	Northern side scarp	3,421.7	13.7	3,408.0	Dry	Shallowest bedrock contact
BH-03	Head scarp Vertex	3,422.5	19.3	3,403.3	Dry	Cobbles/boulders noted in CL/SC unit
BH-04	Southern side scarp	3,421.8	41.4	3,380.4	39.5	Deepest boring with thick saprolite zone, groundwater observed following drilling at bedrock contact

Geologic Mapping and Drone Reconnaissance

In addition to drilling, geologic mapping of the slide area was performed to characterize the head scarp, the extent of ground disruption, and the relationship between the failure and the underlying slope morphology. The site was flown again with the drone after the failure, allowing direct comparison with the pre-failure imagery to quantify changes in slope morphology. The availability of both pre- and post-failure aerial data was atypical and valuable; in most emergency response settings, only the post-failure condition can be documented.

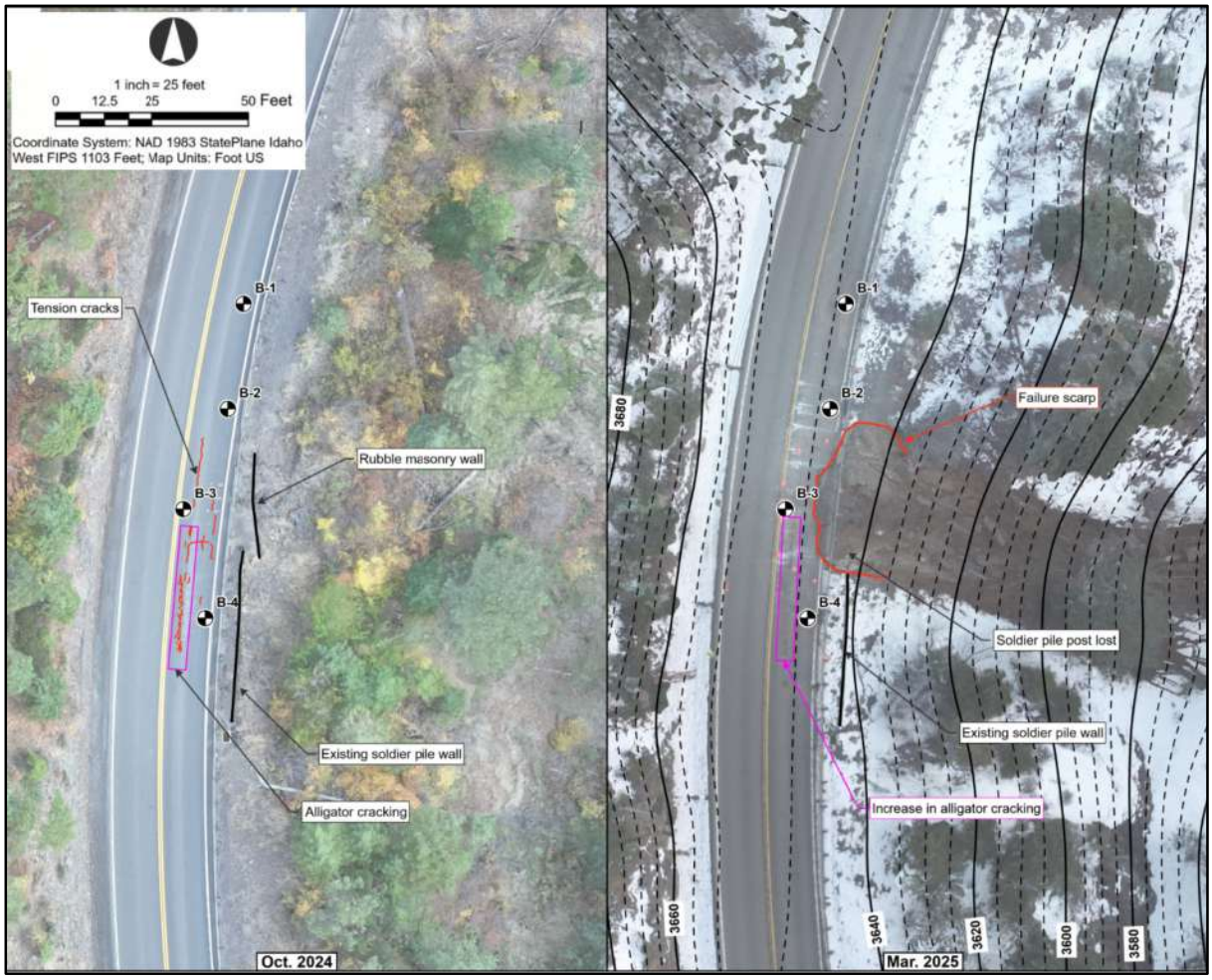

Figure 5 – Pre- and Post-Failure Aerial Imagery Comparison

REPAIR DESIGN

Preliminary repair designs were completed within two weeks following the completion of drilling. The compressed design schedule required close coordination between the field and design teams and an approach that could accommodate the uncertainty inherent in a site that is characterized rapidly. Daily coordination meetings that brought together the client, all members of the design team, and the contractors as a single working group were essential to the repair design process. Having every stakeholder meet on a daily basis created a real-time feedback loop in which design concepts could be proposed, tested against field realities, and refined within a single day rather than over the course of a conventional multi-week submittal-and-review cycle. This structure proved especially valuable given the compressed emergency schedule.

Having the contractor present in these discussions was particularly beneficial to the design effort. The contractor was able to advise the design team directly on which equipment was available and could be mobilized quickly, and which materials were in stock or readily obtainable, including steel member sizes, tie-rod sizes, and corrosion protection options. This

information allowed the designers to make selections that were constructible without incurring procurement delays. Rather than specifying components that might have to be sourced on a long lead time, the team could design around materials and methods that were immediately available, keeping the work on its accelerated timeline.

The daily meetings also allowed the team to jointly manage the critical path for both design and construction. By understanding the contractor's mobilization schedule and material availability, the design team could prioritize its efforts on the elements that most directly governed the construction sequence, focusing design attention where it was most needed and deferring lower-priority details. This alignment of design and construction priorities minimized idle time and prevented design bottlenecks from delaying field progress.

Finally, the continuous involvement of the client kept its staff fully informed of design and construction progress at all times. This awareness enabled the client to communicate accurate and timely updates through its own external channels, keeping the traveling public and the surrounding community informed regarding the status of the closure and the anticipated reopening of US-95.

Design Concept

Five mitigation alternatives were evaluated: (1) a rock buttress, (2) a mechanically stabilized earth (MSE) wall, (3) a cantilevered soldier pile wall, (4) a tieback soldier pile wall, and (5) a deadman-restrained soldier pile wall. The buttress and MSE options were eliminated because a stable foundation could not be established on the steep, clay-rich slope below the roadway, and the fully cantilevered option could not develop sufficient passive resistance at the required wall height. The deadman-restrained wall was selected because it avoided mobilizing a specialty anchor-drilling subcontractor, could be constructed more quickly, and posed less risk to the anchorage during backfill and roadway restoration.

The selected repair consisted of excavating a working pad into the slope and constructing an exterior anchored soldier pile retaining wall, supported by an inboard deadman pile retaining wall installed as drilled shafts. The wall system was complemented by runoff and surface drainage improvements intended to reduce future infiltration and groundwater buildup behind the wall. Because boulder obstructions and the depth to bedrock could not be precisely defined within the available schedule, the design was intentionally conservative to account for this subsurface uncertainty.

Deadman Design

The anchored portions of the soldier pile wall required a deadman system to develop the lateral restraint necessary to resist the retained earth loads, as the steep slope in front of the retaining wall did not provide sufficient passive resistance. At this site, the steep slope on the opposite side of the roadway sharply limited the distance available behind the wall face. A conventional deadman could not be set back far enough to clear the active zone without extending beyond the buildable footprint, rendering the typical approach unworkable within the confined roadway geometry.

To resolve this, the design substituted drilled shafts for the conventional buried deadman. Rather than depending on the passive resistance of the surrounding soil, the drilled-shaft deadman developed its capacity through the embedment depth and flexural stiffness of the shaft itself, behaving as a laterally loaded pile. Each front-wall waler was connected to the corresponding deadman shaft by a steel tie rod, transferring the wall load to the shaft, which in turn mobilized lateral resistance along its embedded length. Because this mechanism did not rely on placement outside the active wedge, the deadman shafts could be located much closer to the wall, fitting within the narrow confines of the slope. The approach carried an additional practical advantage: the drilled-shaft rig was already mobilized on site for installation of the soldier piles, so the deadman shafts could be constructed using equipment and crews already in place, without mobilizing a separate operation or specialized deadman-installation methods.

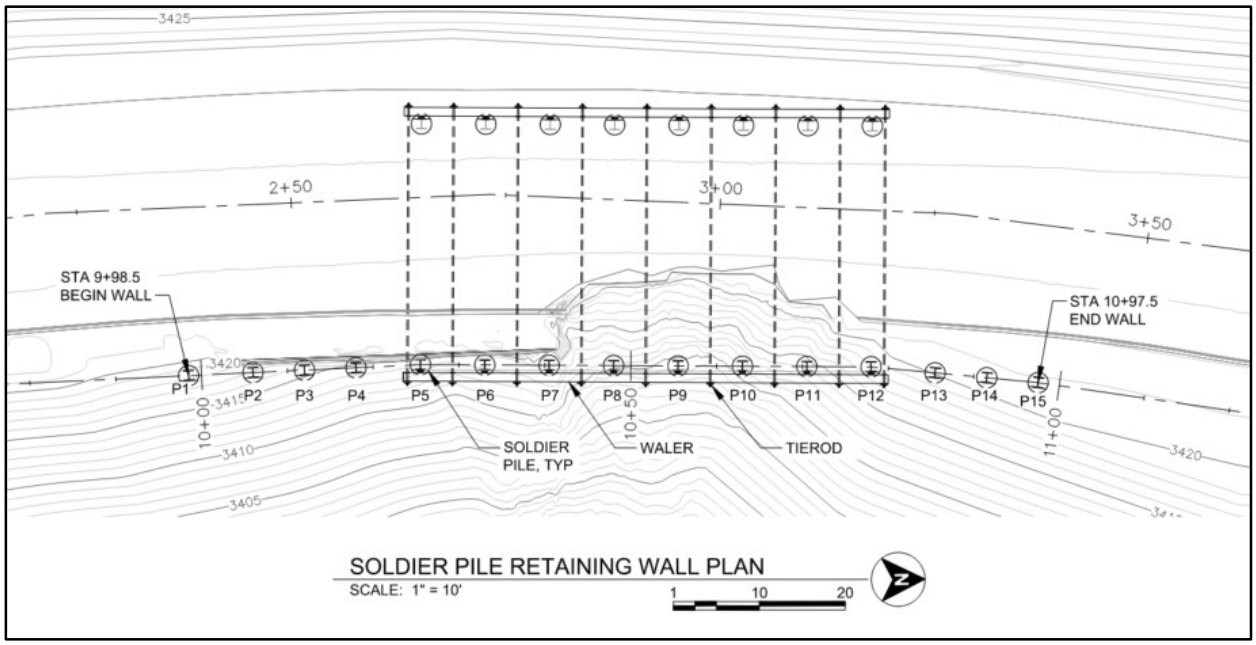

Figure 6 – Repair Design: Soldier Pile Wall, Deadman Configuration, and Drainage Plan

Accelerated Schedule

Working pad excavation began on Monday, March 31, 2025, and the first pile installation was scheduled to begin on Wednesday, April 2, 2025. The project goal was to complete construction and reopen US-95 to the public by April 30, 2025. Through traffic remained prohibited during the construction period, which both protected the work zone and allowed construction to proceed without the constraints of staged traffic control.

CONSTRUCTION AND FIELD ENGINEERING SUPPORT

A central element of the project approach was the continuous presence of an engineering geologist on site during excavation and the initial pile installations. The goal was to ensure successful pile installation with little or no downtime by allowing design decisions to be made in the field, in real time, as actual subsurface conditions were revealed.

If bedrock was encountered shallower or deeper than anticipated at a given pile location, the wall height could be shortened or lengthened accordingly without waiting for an off-site design cycle. This capability was especially important because there was no cellular signal at the site; the nearest reliable signal was located approximately 15 minutes north. Having a qualified geologist on site, rather than reachable only by telephone, removed a potential bottleneck in communicating and resolving design changes.

Two additional field concerns shaped the construction approach. First, minimizing ground vibration was a priority, because vibratory removal of the temporary casing posed a potential risk to slope stability. Second, groundwater, seepage, and overall slope stability were monitored throughout construction, as continued snowmelt was expected to increase groundwater levels during the work.

Construction Challenges

Construction encountered a series of challenges that tested the project team's ability to adapt. In each case, the integrated field-design approach allowed the team to develop and implement a solution without halting the overall effort or compromising the reopening schedule.

Narrow Project Site

The confined nature of the site imposed significant constraints on construction means and methods. US-95 is a two-lane highway at this location, and the failure had removed a substantial portion of the road prism severely limiting through-access for the duration of the work. Because equipment and material could not easily pass the failure, the work area functioned as a single dead-end corridor: hauling was limited to one direction, and all excavation spoil, casing, steel, and concrete had to be staged and sequenced from the same approach to avoid stranding equipment or double-handling material. The narrow drill pad excavated along the alignment further restricted the drill rig's mobility, allowing it to advance in only one working direction along the wall. As a result, the drilled soldier piles could not be installed in an arbitrary order; instead, they were sequenced progressively along the pad so that the rig, crane, and concrete truck could maintain access to each successive pile location without being boxed in by completed work or by adjacent staged materials.

Boulder Obstructions

Basalt boulders, some up to approximately 4 feet (1.2 m) in diameter, were confirmed within the clay-rich soils during construction. Their presence was consistent with the obstructions inferred from the drilling observations. The surrounding soils were generally moist but well-drained, despite the ongoing increase in snowmelt. The boulders complicated both drilling and pile placement and became a recurring factor in the installation difficulties described below.

Hole Collapse and Groundwater

Advancing and casing the boreholes to depth was generally successful; however, initial attempts to drill the upper portion of a hole without full casing led to hole collapse, driven by groundwater at the bedrock contact at approximately 40 feet (12 m) below ground surface (bgs).

The team responded by casing each hole to its full depth. Groundwater encountered at the bedrock contact also produced several feet of standing water within the hole. To address this, the standing water was pumped out and the remaining water was displaced from the bottom of the hole using a tremie.

Installation Complications

During concrete placement, two equipment limitations emerged simultaneously. The cement truck did not carry enough tremie pipe to reach the bottom of the hole, and the pump that was provided was not powerful enough to remove the several feet of standing water remaining downhole. Work was stopped to develop a revised installation procedure.

The first revised approach was a cold-pour pile installation, in which the casing would be backfilled and pulled in lifts, and a crane would be used to install the pile after backfilling. This approach failed when a boulder obstruction prevented placement of the pile at approximately 20 feet (6 m) bgs.

Casing Removal in Lifts

The second approach refined the cold-pour method for the lower portion of the hole. The casing would be backfilled and pulled in lifts for the lower 15 feet (4.6 m) of the borehole, and all standing water would be pumped out or displaced via tremie in every boring before placement. Before fully setting each pile, the crane was first used to confirm that the casing could be extracted easily. If extraction was straightforward, the team continued to backfill and pull the casing in lifts using the crane; if not, the contingency plan would be invoked. Plan 2 proved successful and became the production method for the remaining piles.

Figure 7 – Pile Installation

Splice Contingency

A third approach was developed as a last resort in case the crane could not easily extract the casing during backfilling after the lower portion of a pile had been poured. Under this contingency, the pile would be installed in segments and spliced. Working overnight, the structural engineering group developed updated splicing plans by the following morning so that the option would be available if needed. Splicing was always intended as a last resort, but having a vetted plan in hand provided the team with an additional tool and reduced schedule risk. Ultimately, splicing was not required.

OUTCOME AND US-95 REOPENING

Pile installation was completed successfully using the casing removal methods, and no splicing was required. Avoiding the need to splice piles in stages provided additional flexibility in the final design. Because the piles did not have to be installed and spliced in separate stages, the final road grade and runoff design could be refined, and the piles could be completed on a more efficient schedule. The successful method also allowed two rigs to operate simultaneously on the drill pad: one rig could advance casing and drill while the other installed a pile using the crane and cement truck.

The roadway reopened to the public by April 30, 2025, 45 days after the initial failure was reported and consistent with the original project goal. The combination of rapid exploration, parallel design, and adaptive construction enabled the corridor to be restored within a remarkably short timeframe for a repair of this complexity.

Figure 8 – Completed Repair and Reopened Roadway, Looking Southward

CONCLUSIONS

The emergency response at US-95 MP 146.5 illustrates several practices that contributed to a successful outcome and that may be transferable to other emergency highway response settings:

- Proactive observation. The early identification of sagging and cracking by ITD maintenance crews, followed by reconnaissance in October 2024, allowed planning and resources to be in motion before the failure occurred.
- Pre-positioned resources. A drill crew secured for a previously scheduled investigation allowed the exploration program to begin within approximately 48 hours of the failure.
- Parallel field-design coordination. Conducting exploration, mapping, and design largely in parallel, rather than in strict sequence, made the 45-day reopening achievable.

- On-site engineering geology support during construction. Continuous field presence allowed real-time design adjustments and development of alternative construction sequences, which was essential at a site with no cellular signal.

- Collaboration among owner, designer, and contractor throughout the design process. Close cooperation throughout design and construction allowed the team to adapt to boulders, groundwater, hole instability, and equipment limitations without losing the reopening schedule.

Taken together, these factors demonstrate the value of flexible exploration strategies, integrated field-design approaches, and strong collaboration in restoring a critical transportation corridor under emergency conditions.

REFERENCES

1. Garwood, D. L., and Othberg, K. L. *Geologic Map of the Fruitvale Quadrangle, Adams County, Idaho*. Digital Web Map 106, 1:24,000-scale. Idaho Geological Survey, Moscow, Idaho, 2009.

2. Idaho Geological Survey. *Landslide Inventory Database for Idaho (DD-10)*. Digital Database DD-10. University of Idaho, Moscow, Idaho, 2010. Available at: https://idahogeology.org/pub/Digital_Data/Digital_Databases/DD-10_report.pdf. Accessed June 2026.

10. Hidden Elements: A Context Sensitive Application of Rock Anchors for Slope Stabilization

Brian Collins, PE
BGC Engineering
Suite 300 – 600 12th Street
Golden, CO 80401
360-597-8211
bcollins@bgcengineering.ca

Seamus Millett, PE
BGC Engineering
Suite 300 – 600 12th Street
Golden, CO 80401
720-657-3009
smillett@bgcengineering.ca

Cole Christiansen, PE
BGC Engineering
Suite 300 – 600 12th Street
Golden, CO 80401
720-617-1848
cchristiansen@bgcengineering.ca

Scott Anderson, PhD, PE
BGC Engineering
Suite 300 – 600 12th Street
Golden, CO 80401
720-617-1873
scanderson@bgcengineering.ca

Nicholas Farny, LEG, LG
Western Federal Lands Highway Division
610 East Fifth Street
Vancouver, WA, 98660
360-619-7670
nicholas.farny@dot.gov

Prepared for the 75th Highway Geology Symposium, September 2026

Acknowledgements

The BGC project team included many of our geologists, engineers, geophysicists, Cambio Earth, and our remote sensing and instrumentation teams with support from our partners at Western Federal Lands Highway Division and National Park Service. Special thanks to Heather Brooks, PhD, PE, Kris Hornsby, PG, Jamey Turner, PG, Evan Garich, PE, and Denny Capps, for their key contributions in the site investigation, modeling, design and construction.

Disclaimer

Statements and views presented in this paper are strictly those of the author(s), and do not necessarily reflect positions held by their affiliations, the Highway Geology Symposium (HGS), or others acknowledged above. The mention of trade names for commercial products does not imply the approval or endorsement by HGS.

Copyright

Copyright © 2026 Highway Geology Symposium (HGS)

All Rights Reserved. Printed in the United States of America. No part of this publication may be reproduced or copied in any form or by any means – graphic, electronic, or mechanical, including photocopying, taping, or information storage and retrieval systems – without prior written permission of the HGS. This excludes the original author(s).

ABSTRACT

Construction of a new bridge over the Pretty Rocks Landslide in Denali National Park required 67,000 cubic yards of excavation and a rock cut up to 160 feet tall to construct the approach to the west abutment. The rock mass and overburden were characterized through field geologic mapping of outcrops, drilling investigations with downhole televiewer logging of drill holes, laboratory testing, and geophysical surveys. Three-dimensional (3D) geologic modeling and kinematic analysis of the rock mass revealed potential rock slope failure mechanisms for the proposed cut slope orientations. The new cut is in a highly visited area along Denali Park Road that required a context-sensitive design solution to develop a natural appearance for the new cut slope. This limited possible methods of stabilization. Tensioned rock anchors, commonly known as rock bolts, were used to mitigate potential failures in the rock cut during each lift of the excavation. After the rock bolts were constructed and the grout reached design strengths, the protruding ends were cut flush with the rock surface and covered with grout matching the surrounding native rock. The rock cut was constructed without overruns in quantities or impacts to schedule and constructability, reducing geotechnical risks to the adjacent bridge and roadway. The findings demonstrate the effectiveness of a kinematic analysis and use of rock bolts as a context-sensitive solution for stabilizing new cut slopes.

INTRODUCTION

Infrastructure construction within sensitive national park settings presents unique challenges, particularly in complex geological conditions. Construction of a new bridge over the Pretty Rocks Landslide in Denali National Park exemplifies this complexity. The project site is located on Polychrome Pass, one of the most picturesque locations along Denali Park Road, and special consideration was given to all of the proposed improvements to preserve the natural appearance of the area. The west approach to the new bridge is on a new alignment that required 67,000 cubic yards of excavation to form an approximately 160-foot-tall soil and rock cut slope (Figure 1). The design of the cut slope required consideration of long-term stability, rockfall potential, aesthetics, and constructability. This paper will detail the methods employed in evaluating the rock mass of a proposed cut slope and implementing stabilization strategies, showcasing how a context-sensitive approach can effectively address the geotechnical challenges encountered in such projects.

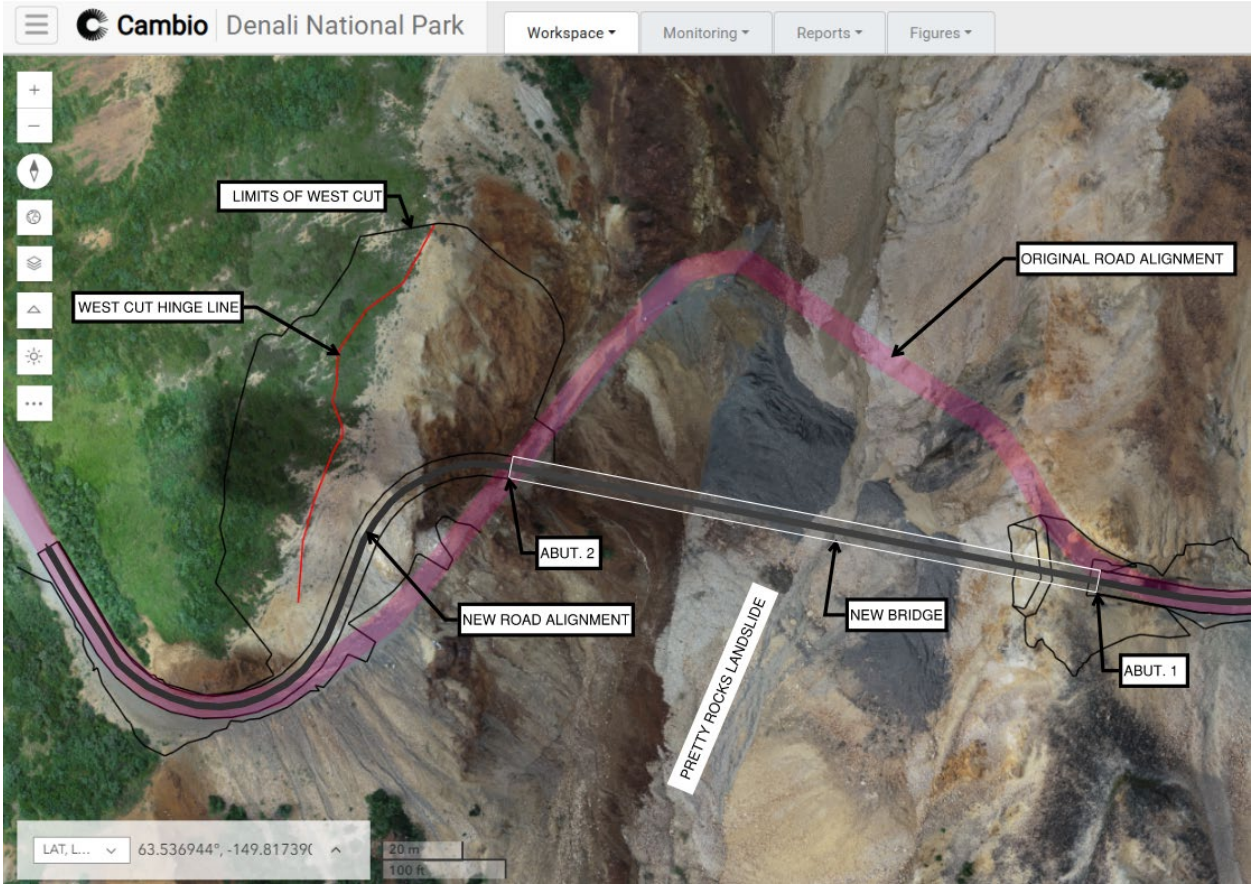

Figure 1 - Project Site Map with Aerial Imagery (August 2, 2023), Original Road Alignment, New Alignment, and Limits of the West Cut.

PROJECT BACKGROUND

The Denali Park Road is a 92-mile-long scenic roadway that provides the only road access extending deep into Denali National Park. With over 500,000 visitors entering the park each year, the road is a major piece of infrastructure for the National Park Service (NPS). In

September 2021, the road was closed due to accelerated movement of the Pretty Rocks Landslide located at approximately Mile Post 45 on Polychrome Pass. Following a risk assessment and alternative analysis process, the NPS, in conjunction with the Western Federal Lands Highway Division (WFLHD) of the Federal Highway Administration (FHWA), selected a new bridge to re-establish the roadway at the Pretty Rocks Landslide. The bridge consists of a 475-foot single-span steel truss. To avoid future landslide movement and minimize the bridge length, the west abutment needed to be located on an outcrop of competent material on a new alignment that is on a bearing tangent to the original roadway alignment. This required a large cut for the west bridge approach, which was named the West Cut (Figure 2).

Figure 2 - Pre-Construction Photograph of West Cut (August 20, 2022) Looking from Approximately Abutment 1 Location towards Abutment 2 and West Cut.

The project was delivered using the Construction Manager General Contractor (CMGC) method. WFLHD is delivering the CMGC project for the NPS. Jacobs Engineering and BGC Engineering are the designers of record contracted to WFLHD. A preliminary design package was developed in 2022. WFLHD awarded the CMGC contract to Granite Construction based on the preliminary design package. Design collaboration between the contractor and design team began in January 2023. Issued for Construction plans were delivered in July 2023, and construction began in August 2023. The west cut was constructed during the 2023 and 2024 construction seasons. The bridge superstructure was launched during the 2025 construction season. The bridge is mostly

completed at the time of this paper and is expected to be open to the public during the 2027 season.

DESIGN CRITERIA

Geotechnical design guidance for rock cut slopes is provided in the Federal Lands Highway Project Development and Design Manual (PDDM) (*1*) and the Geotechnical Technical Guidance Manual (TGM) (*2*). Consistent with these manuals, project design criteria were selected to balance the desire to provide an acceptable relative measure of safety from rockfall and cost for maintenance with the desire to minimize excavation and maintain the visual characteristics of the site.

Chapter 6 of the PDDM (*1*) requires geologic structure mapping, kinematic and limit equilibrium analysis for rock cuts when the consequences of failure are especially critical. The PDDM (*1*) specifies a minimum factor of safety in the range of 1.3 to 1.5, depending on the consequence of failure and how representative the analysis is of actual conditions. The analysis for the West Cut considered both inter-slope and overall slope failures. Overall failure surfaces originate behind the crest of the cut and exit at or below the toe of the cut. Inter-slope failures are categorized as failures that originate at or below the crest of the cut slope and exit above the toe of the slope. For this project, inter-slope failures were evaluated against a static factor of safety criteria of 1.3, and overall slope failures were evaluated against a static factor of safety criteria of 1.5.

The TGM (*2*) recognizes that rockfall ditch catchment design criteria may vary from 60 percent catchment for low volume roads to 95 percent catchment for interstate highways. For this project, FHWA established a rockfall catchment criterion for rockfall impact of 99% and rockfall rollout of 75% for the West Cut, except slopes with a height greater than 80 feet tall were assigned a design criterion of 90% rockfall impact and 75% rockfall rollout. The lesser criterion for slopes greater than 80 feet was established to address concerns by NPS that large ditches for rockfall catchment are not within the current character of the Park Road. These criteria were established based on the assumption of 1/2H:1V rock cut slopes up to 110 feet high. The final design implemented a 1:1 rock cut slope up to 160 feet high, so the design criteria were revisited during final design.

Aesthetic criteria were not specifically quantified; however, the NPS desires to have the West Cut blend with other natural slopes and historic man-made cuts along Polychrome Pass. Exposed rock slope stabilization mesh or other reinforcement elements are undesirable. Half-casts from blast holes must be removed from the final slope face. The aesthetics of the new cut will be considered successful if the cut does not look like a constructed feature when completed.

In addition to the above design criteria, the contractor collaborated with designers on the West Cut design. The contractor's key design constraint was that any elements had to be installed as the cut was constructed from the top down. The contractor also provided input on readily available rock bolt materials since the lead time from design to construction was a couple of months, and the West Cut was in the first stages of the contractor's schedule.

SITE CHARACTERIZATION

A variety of innovative site investigations and remote sensing tools were applied to this project (*3*). Site investigations of the West Cut included structural geologic mapping, helicopter-access drilling investigations, surface and downhole geophysical surveys, a weather station, and installation of remote monitoring units to transmit near-real-time weather, photo, and borehole instrumentation data. Instrumentation installed at the site included vibrating wire piezometers, inclinometer casing, shapeaccelarrays, thermistor strings, and temperature sensors. Remote sensing at the site included terrestrial and airborne lidar, InSAR, photogrammetry, and time-lapse cameras. The site investigation data was loaded into an interactive GIS software platform with a live link to active instrumentation. These tools were used to inform decisions on the West Cut alignment and cut slope design. Details of the site characterization are described in Collins et al (*3*).

The stratigraphy encountered in the West Cut, from top down, consists of colluvium, Lower Rhyolite, an airfall ash and bentonite clay bed approximately 6 feet thick, and Upper Basalt (Figure 3). These units are dipping south to southwest at approximately 50 degrees. The geophysical surveys indicate seismic P-wave velocities range between approximately 2000 ft/sec and 10,000 ft/sec within the limits of the proposed West Cut (*4*). An ice-rich frozen colluvium permafrost layer was encountered in boreholes and consists of poorly sorted gravel, sand, and clay with some cobbles and boulders with up to 50% ice by volume.

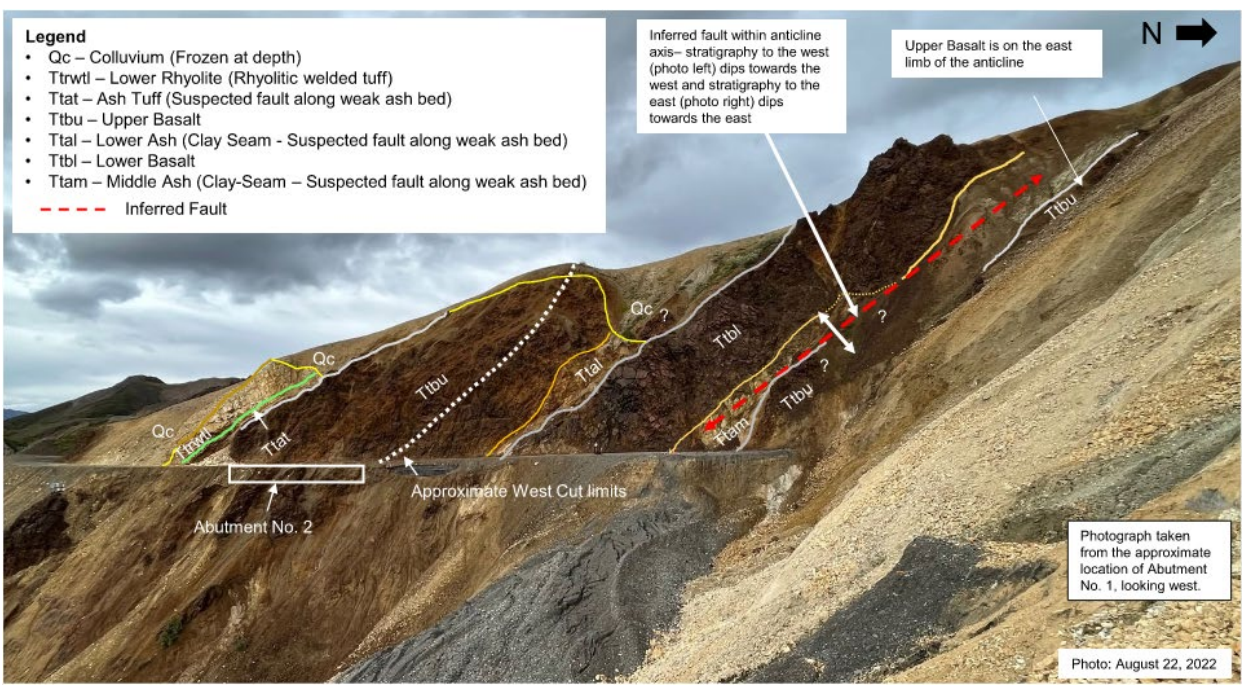

Figure 3 - Pre-Construction Interpreted Geology at Proposed West Cut Location. Photograph is Looking West from Abutment No. 1 Down the New Bridge Alignment Towards Abutment No. 2 and the West Cut.

SUBSURFACE MODELING

Because of the site's complex geologic structure, a geologic model consisting of 3D triangular mesh surfaces was created using Leapfrog Works (*5*) to support interpretation and design of the West Cut. The surfaces represent geotechnical unit boundaries that were created using the following data:

- Borehole logs (unit contacts)
- Televiewer surveys (unit contact orientations)
- Structural mapping (unit contact orientations and regional trends)
- Geologic mapping (unit contacts)
- Geophysics (frozen colluvium/bedrock contact)

Surfaces were fit through the contact points identified in borehole logs and geologic mapping and given orientations based on the televiewer and structural mapping data collected from the existing rock cut (Figure 4). In areas where the location or orientation of the contacts was poorly constrained, a regional orientation determined from structural mapping was applied to the surface. The base of the frozen colluvium surface along the west ridge was also defined using borehole logs and electrical resistivity geophysical data (*4*). The geophysical survey results highlight the approximate extent of the ice-rich deposit spatially, as regions of high electrical resistivity greater than about 2200 ohm-m (Figure 4).

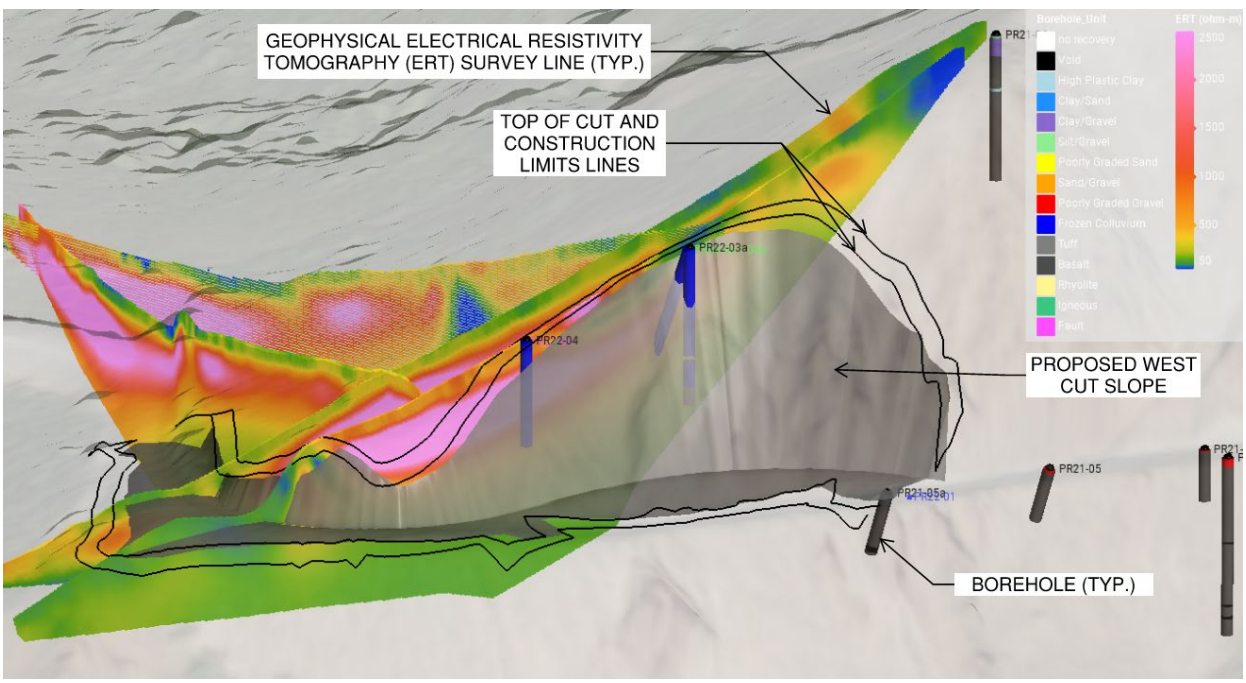

Figure 4 - Leapfrog Subsurface Model (after 3).

ANALYSIS AND DESIGN

The West Cut slope was on a curved alignment and had a variable height, which helps limit the cut volume and helps the cut to blend with other native rock and soil slopes along Polychrome Pass. The material in the West Cut consists mostly of ice-rich permafrost colluvium and basalt bedrock. Therefore, a compound cut was designed using a flatter 2H:1V cut slope in the colluvium portion of the cut overlying a 1H:1V rock cut slope down to the ditch line (Figure 5). The Leapfrog subsurface model was used to develop the 3D hinge line where the slope transitioned from colluvium to rock. The 3D hinge line was specified in the plans using a series of points with coordinates and elevations.

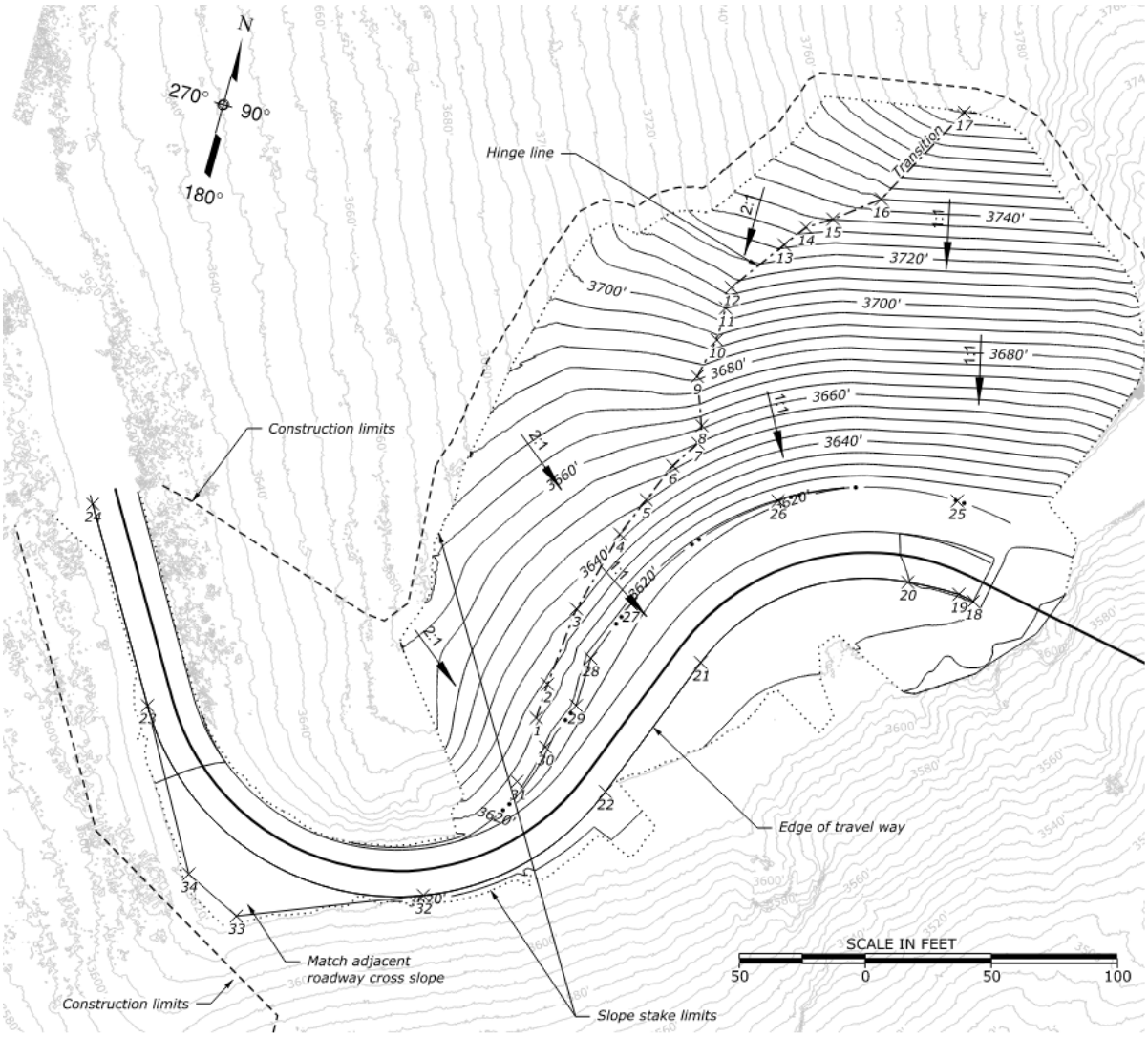

Figure 5 - West Cut Grading Plan (*6*).

Road Alignment

The West Cut design was an iterative process between roadway designers and geotechnical designers, consisting of developing a preliminary cut slope model, performing geotechnical design and updating the cut slope model, and repeating the process until the alignment satisfied roadway design criteria and the cut slope satisfied the geotechnical design criteria. The limits of the West Cut were shortened through design iteration and feedback from NPS to maintain an existing rock outcrop located just after the new alignment rejoined the existing alignment.

Kinematics

The design included kinematic analysis of the rock mass to identify potential rock slope failure mechanisms (planar, wedge, and toppling), and to identify slope orientations (slope inclination and slope azimuth) for which each failure mechanism is possible (Figure 6). Review of discontinuity data from downhole geophysical surveys and surface mapping and the associated

kinematics of the rock slope indicate that at a slope azimuth of about 180 degrees, planar and wedge failure in the rock mass are possible at slope inclinations greater than 40 degrees from horizontal. Therefore, the rock cut slope was designed at 1H:1V inclination and on an alignment to avoid slope azimuth where the adversely dipping joint set would impact slope stability of the cut. Additionally, the slope was designed to have slope azimuths no greater than 170 degrees, which required some adjustment to the cut as it approached the bridge abutment – the cut was skewed from the alignment as it approached the abutment to maintain the slope azimuth of 170 degrees (Figure 5). This design balanced the desire to provide an acceptable relative measure of safety from rockfall and cost for maintenance with the desire to minimize excavation and maintain the visual characteristics of the site.

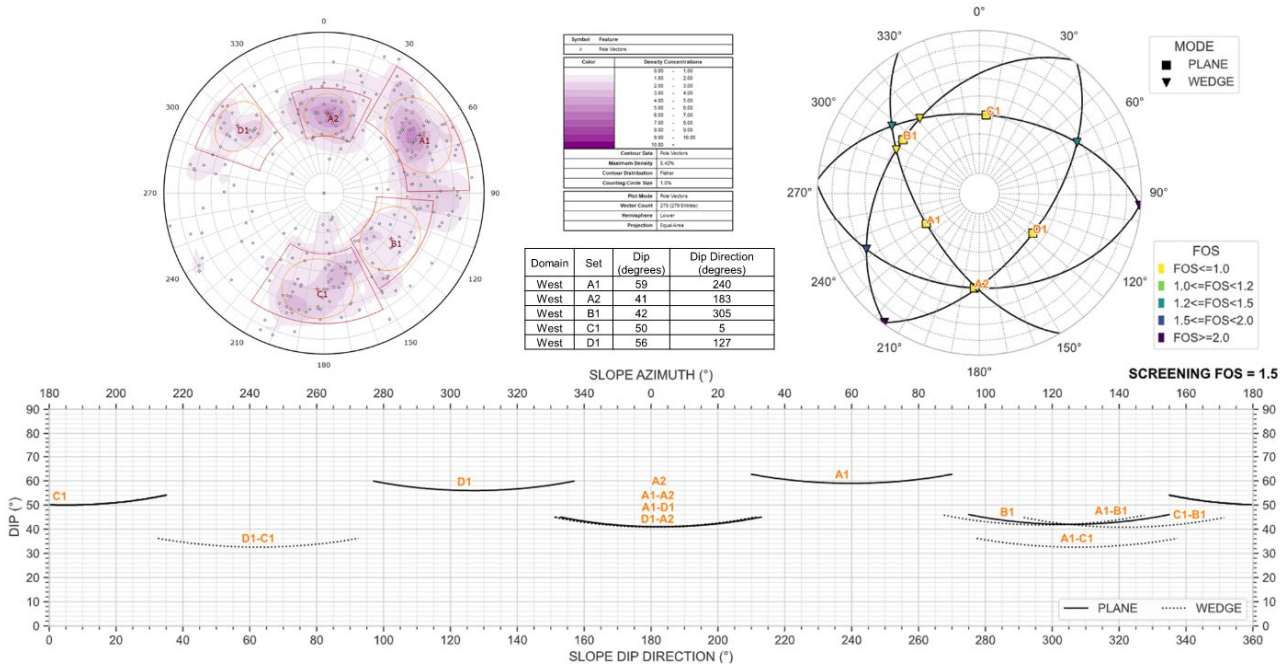

Domain	Set	Dip (degrees)	Dip Direction (degrees)
West	A1	59	240
West	A2	41	183
West	B1	42	305
West	C1	50	5
West	D1	56	127

Figure 6 - Discontinuity Data and Kinematic Analysis for the West Cut.

Limit Equilibrium

Limit equilibrium analyses were completed to analyze global stability using Slide2 (*7*). Stability analyses were completed along the fall line of the highest and steepest portions of the proposed rock cut and through the thickest area of frozen colluvium. The stability of the frozen colluvium layer will change as the active layer is re-established following cut construction. The long-term conditions limit equilibrium analysis was completed assuming the frozen colluvium is in an unfrozen state.

The stability analysis considered potential failures that occur both through intact rock and along potential discontinuities. Despite the efforts adjusting slope geometries to minimize potential failure modes, the limit-equilibrium analysis without slope reinforcement that included considerations for discontinuity sets resulted in factor of safety values below the design criteria. Rock bolts were added to the design, which resulted in acceptable long-term factor of safety values.

The geometry of the cross sections and subsurface stratigraphy were developed from the 3D geological model. Material strengths for the stability assessments were interpreted from data obtained in the field investigation programs, laboratory testing, back analysis, and engineering judgment. Geotechnical units were initially divided into soil-like materials and rock materials based on the expected shear strength behavior. These materials were further subdivided based on geologic unit and overall rock mass characterization.

Mohr-Coulomb failure criterion parameters were used to model the strength of the soil-like geotechnical units. The values for the unit weight, cohesion, and effective friction angle of the soil-like layers were selected based on the information available for each unit and empirical relationships found in the literature.

The strength of the rock geotechnical units was derived using the Hoek-Brown failure criterion (*8*). Rock mass anisotropy is incorporated into the stability assessments to represent discontinuities (e.g., joints, faults, shears, foliation) observed in the boreholes and surface mapping. In these cases, the strength of the rock mass along these weaknesses was estimated using Mohr-Coulomb failure criterion.

Rockfall Catchment

The rock cut slope has a maximum height of approximately 165 feet, but only for a relatively short length. Illustrating this, the rock slope varies in heights ranging from 50 feet to 165 feet within 100 feet of the end of bridge location. Rock cut slopes with heights up to 80 feet were analyzed using the Rockfall Catchment Area Design Guide (*9*) and slopes greater than 80 feet using RocFall2 (*10*). The design rockfall catchment is a maximum of 19 feet wide. The proposed cut slope that is taller than 154 feet does not achieve the 75% rollout catchment criteria with a 19-foot ditch. Higher retention from rollout could have been achieved through additional stabilization measures, but it would have required a 24-foot-wide ditch, draped mesh, or a rockfall barrier, all of which are out of character with other parts of the road, and therefore not desired by NPS.

Rock Bolt Design and Limitations

Through the different analyses and design iterations, it was concluded that tensioned rock anchors (rock bolts) were necessary to increase the long-term stability of the cut slope (Figure 7). The rock bolts were designed to manage larger instabilities associated with wedge and planar failures. Due to the desire for the cut slope to resemble a natural slope, the rock bolts were not designed to a set pattern, instead, they were specified to be installed during construction at locations identified by the project engineering geologist/geotechnical engineer. One hundred (100) 30-foot long galvanized #10 Grade 75 or Grade 80 all-thread bars were specified for the rock bolts. The contractor used an 8-foot minimum bond zone length and 3- to 4-inch diameter drill holes. The rock bolt design load is 60 kips. All rock bolts were tested to 125% of the design load during construction.

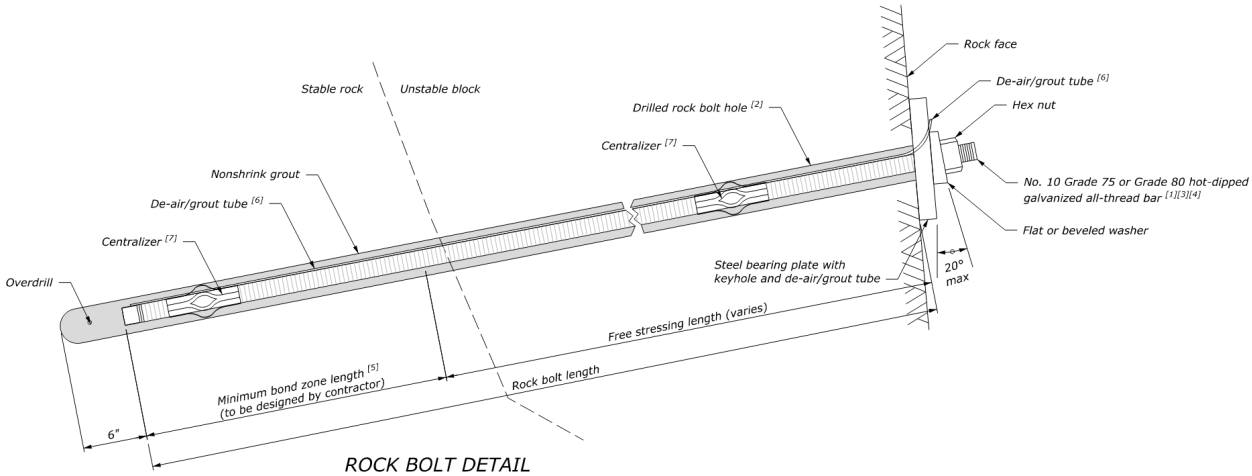

Figure 7- Rock Bolt Detail.

FHWA has context-sensitive practice on NPS projects to remove the plate, washer, and hex nut from rock bolts after grouting is completed. The bar is then cut off at the rock surface, and the annular space is filled with a colored grout matching the surrounding native rock. Any exposed bar ends are galvanized and treated with a weathering agent (Figure 8).

Figure 8 - Photograph of Completed West Cut and Close-Up of a Completed Rock Bolt Location (June 16, 2026).

CONSTRUCTION

Construction began in August 2023, and excavation of the West Cut began by mid-August 2023 with a pioneer road up the cut to provide access for equipment and materials to the top of the cut (Figure 9). Winter shutdown was from October 2023 to April 2024. The West Cut was completed to design grade in June 2024. The cut was generally constructed using drilling and

blasting techniques in the basalt (Figure 10) and excavators with ripper shanks and digging buckets in the frozen colluvium (Figure 11). The excavation was brought down in eleven 15-foot-high lifts. After each blast, excavators removed the shot rock from the cut slope. Scaling of the final face was carried out using pry bars and compressed air concurrent with excavation of each lift.

Figure 9 - Photograph of the Pioneer Access to the Top of the West Cut (August 23, 2023).

Figure 10 - Photograph of West Cut Excavation (May 31, 2024).

Figure 11 – Photograph of Frozen Colluvium Excavation (May 30, 2024).

Once scaling was finished, the geotechnical engineer/engineering geologist identified and painted locations for rock bolts, which were then drilled and installed in two stages. Due to the drilling methods used for the rock bolts, it was not feasible to revisit previous lifts for additional bolting after the blast for the next lift. Therefore, onsite structural mapping and identification of potential wedge features were crucial for making informed decisions throughout the construction phases. This process required careful judgment to assess how each lift interacted with one another and to strategically determine where to place bolts based on potential areas of instability that could arise in the subsequent lift. The contractor drilled the blast holes for the next lift during the time that the rock bolts were grouted (two stages), stressed and tested, and locked off at the design load.

Additionally, the remote location of the project meant that additional quantities of materials could not be acquired within the proposed construction timeline. The team diligently tracked progress during construction, balancing the estimated number of bolts needed against the surface area of each lift to forecast the burn rate for rock bolt installation. The contractor's surveyor collected as-built locations for rock bolts after each lift was completed. BGC tabulated and plotted rock bolt quantities on each lift in Leapfrog Works (*5*) (Figure 12). This strategic approach allowed real-time adjustments and ensured that stabilization measures were adequately addressed without compromising the overall timeline and safety of the project. The West Cut was completed in June 2024, and the slope is performing well with limited rockfall being observed since the cut was completed (Figure 13).

Figure 12 - Perspective View in Leapfrog Works (*5*) Looking North at Installed Rock Bolt Locations (Black Dots) as Surveyed in the West Cut (imagery and topography collected October 6, 2024, and provided by Granite Construction Inc.).

Figure 13 - Photograph of Completed West Cut (June 16, 2026).

SUMMARY AND CONCLUSIONS

Construction of the 160-foot-tall West Cut on the Pretty Rocks Bridge project required excavation of 67,000 cubic yards of material in complex geology that included highly fractured rock and ice-rich frozen colluvium. A 3D geologic model with input from drill holes, geophysical surveys, and surface mapping was used to determine the 3D location of the cutslope hinge point where the slope laid back from a 1:1 rock cut to a 2H:1V soil cut. The modeled location proved to be accurate within a few feet during construction.

The success of the West Cut construction can be attributed to collaboration between the contractor and the design team. Besides the rock bolts in the west cut, the project included ground anchors and micropiles to support bridge foundations and rock dowels and soil nails for slope reinforcement. The main input from the contractor was to use equipment and materials that would not cause project delays. This was done by: 1) using borehole, casing, and bar diameters compatible with the contractors equipment; 2) using consistent materials when possible (e.g., the soil nails, rock bolts, and rock dowels were all #10 Grade 75 or 80 bars), 3) including a contingency in material quantities (approximately a 10% contingency was included in the rock bolt quantity and all the contingency quantities were installed), 4) high-early strength grout was specified for the rock bolts, enabling the contractor to install the bond zone one day and tension and grout the second stage on the following day, 5) monitoring quantities of rock bolts installed

on each lift, and 6) having a full-time engineer or engineering geologist on site so that the rock cut could be immediately reviewed after the contractor completed scaling for selection of rock bolt locations. The collaboration between contractors and designers continued through construction during planning and startup phase meetings, submittal reviews, blasting, excavation, and rock bolt installation.

REFERENCES

1. Federal Highway Administration, 2012. *Federal Lands Highway Project Development and Design Manual, Chapter 6 – Geotechnical*. 73p.
2. Federal Highway Administration, 2006. *Geotechnical Technical Guidance Manual*, 335p.
3. Collins, B., Christiansen, C., Anderson, S., Brooks, H., Capps, D., and Garich, E., 2023. *Using State-of-the-Art Technologies and Tools for Geotechnical Investigation and Design*, Proceedings of the 72nd Highway Geology Symposium, 753p.
4. BGC Engineering USA Inc., 2022. Geotechnical Report 01-22, AK NPS DENA 10(49), *Polychrome Area Improvements – Geotechnical Data Report*, Prepared for Western Federal Lands Highway Division, Federal Highway Administration, FHWA.
5. Seequent Limited, 2022. *Leapfrog Works Software.* (v.2021.2). Bentley Systems.
6. Jacobs, 2024. *Polychrome Area Improvements, Plans for Proposed Project*, AK NPS DENA 10(49), NPS PMIS No. 251978, U.S. Department of the Interior, National Park Service, Denali National Park and Preserve.
7. Rocscience, 2023. *Slide2.* (v5.0).
8. Hoek, E., Kaiser, P.K. and Barden, W.F. (1995). *Support of underground excavations in hard rock.* Rotterdam: Balkema.
9. Pierson, L.A., Gullixson, C.R., and Chassie, R.G., 2001. *Rockfall Catchment Area Design Guide*, Oregon Department of Transportation, Salem, Oregon, 92p.
10. Rocscience, 2023. *RockFall2. Statistical Analysis of Rockfalls*. (v8.022) [64 bit].

11. The Advantages of Hybrid barriers over Attenuators

Takeshi Arita
Tokyo Rope USA, Inc.
8301 Ronda Drive, Canton, MI 48187
+1-734-664-7891
takeshi.arita@tokyoropeusa.com

Kiyoshi Takamori
TOKYO ROPE MFG. CO., LTD.
2-37-28 Eitai
Koto-ku, Tokyo
135-8306
takamori.kiyoshi@tokyorope.jp

Prepared for the 75th Highway Geology Symposium, September, 2026

Acknowledgements

The authors would like to thank the individuals/entities for their contributions in the work described:

Hiroshi Hashiguchi – TOKYO ROPE MFG. CO., LTD.
Hideaki Kabe – TOKO TECHNO CO., LTD.
Kazuhito Kawano – TOKYO ROPE MFG. CO., LTD.

Disclaimer

Statements and views presented in this paper are strictly those of the author(s), and do not necessarily reflect positions held by their affiliations, the Highway Geology Symposium (HGS), or others acknowledged above. The mention of trade names for commercial products does not imply the approval or endorsement by HGS.

Copyright Notice

Copyright © 2026 Highway Geology Symposium (HGS)

All Rights Reserved. Printed in the United States of America. No part of this publication may be reproduced or copied in any form or by any means – graphic, electronic, or mechanical, including photocopying, taping, or information storage and retrieval systems – without prior written permission of the HGS. This excludes the original author(s).

ABSTRACT

In Japan, rockfall prevention measures in narrow areas that occur in steep and complex terrain are a serious challenge. Rockfall prevention measures are broadly classified as preventive measures (active method) and protective measures (passive method), with protective measures (passive method) further divided into protective fences and protective nettings. There are two types of protective nettings: attenuators, which are a construction method designed to attenuate rockfall energy within the protective netting. Hybrid barriers, on the other hand, are designed to reliably capture falling rocks, limit damage to protected objects, and safely guide them to the bottom of the protective netting.

It is generally known that protective nettings require a wide area to capture large rockfall energy (high energy).

In this study, a full-scale test was conducted using two hybrid barrier test barriers with a limited area, measuring 33 ft (10 m) in effective length and 30 ft (9 m), and 50 ft (15 m) in effective length and 30 ft (9 m) in effective height. The test test barrier was constructed by combining a buffer device with a high-strength wire netting that has high resistance to destruction. As a result, it was confirmed that both test barriers could capture a block impact energy of 1,400 kJ and 2,800 kJ, respectively, and safely guide the block simulating a falling rock to the bottom of the protective netting.

INTRODUCTION

We distinguish between attenuators and hybrid barriers as follows: Attenuators change the trajectory of rockfalls rather than stop them and moderate the velocity to varying degrees, while hybrid barriers stop and guide them to the toe of the slope and reduce the velocity to zero (1, 2, 3, 4).

One of the rockfall protection measures employed in Japan is the conventional pocket-type rockfall protection net as described in Figure 1-(a), which belongs to hybrid barriers. This method involves installing wire netting extending from the roadside up to the mid-slope and using posts to keep the upper edge of the wire netting open; this allows the system to intercept and capture falling rocks before guiding them down the slope. It is well-suited to Japan's terrain, which features many steep slopes, and has a proven record of accomplishment nationwide thanks to its cost-effectiveness and ease of construction.

However, its capacity of the conventional pocket-type rockfall protection net to withstand rockfall energy is limited to 150 kJ, so it is generally used in conjunction with preventive measures (active method). On the other hand, as mitigation projects often require considerable time, such as land acquisition, there has been a recent increase in the adoption of high-energy-absorption systems capable of capturing rocks with higher energy levels at the slope toe as described in Figure 1-(b).

This study details full-scale tests conducted on a high-energy-absorption hybrid barrier, utilizing actual ground conditions and a compact test barrier (featuring a lower effective net height and narrower post spacing) to simulate sites with limited available space.

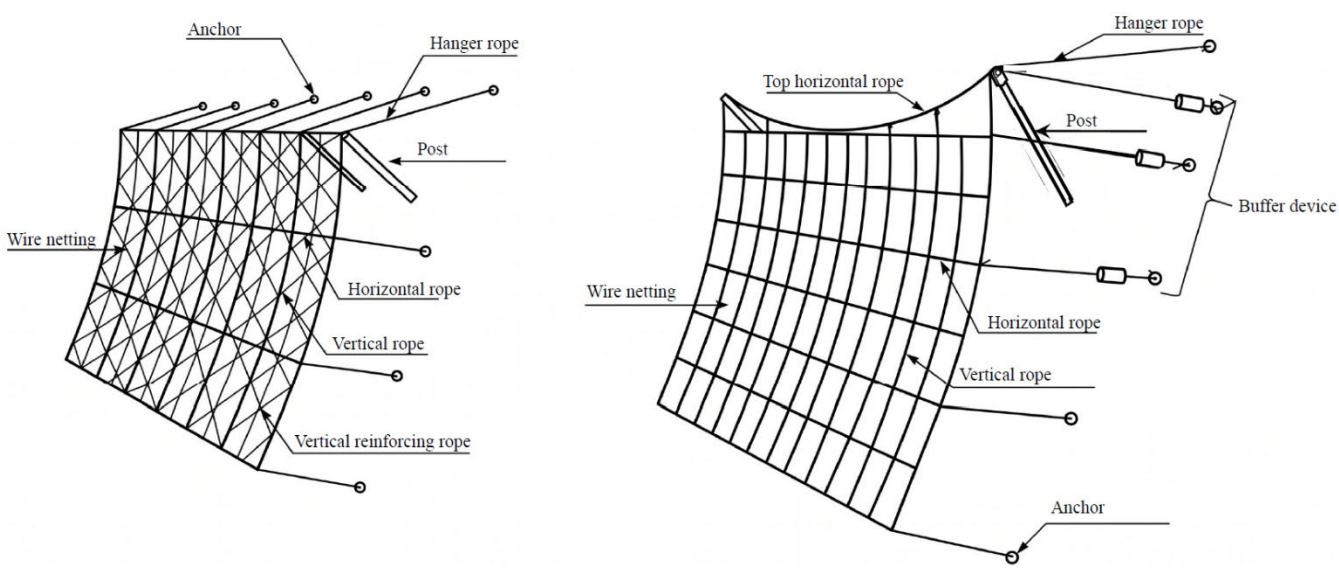

(a) conventional type (b) high-energy-absorption type

Figure 1: Sketch of a conventional pocket-type rockfall protection net (a) and a high-energy-absorption pocket-type rockfall protection net (b)

Full-scale tests

1,400kJ

TOKYO ROPE conducted the full-scale test in accordance with *Guide on Rockfall Countermeasures* (5). In the tests, a block is released at a predetermined height on a runway installed in a quarry and collides with a test barrier installed in front of the lower end of the runway as shown in Figure 2. The release height was 180 ft (55 m), and the gradient was 55 degrees. The test barrier has 33 ft (10 m) in spacing between posts and 30 ft (9m) in effective height as shown in Figure 3.

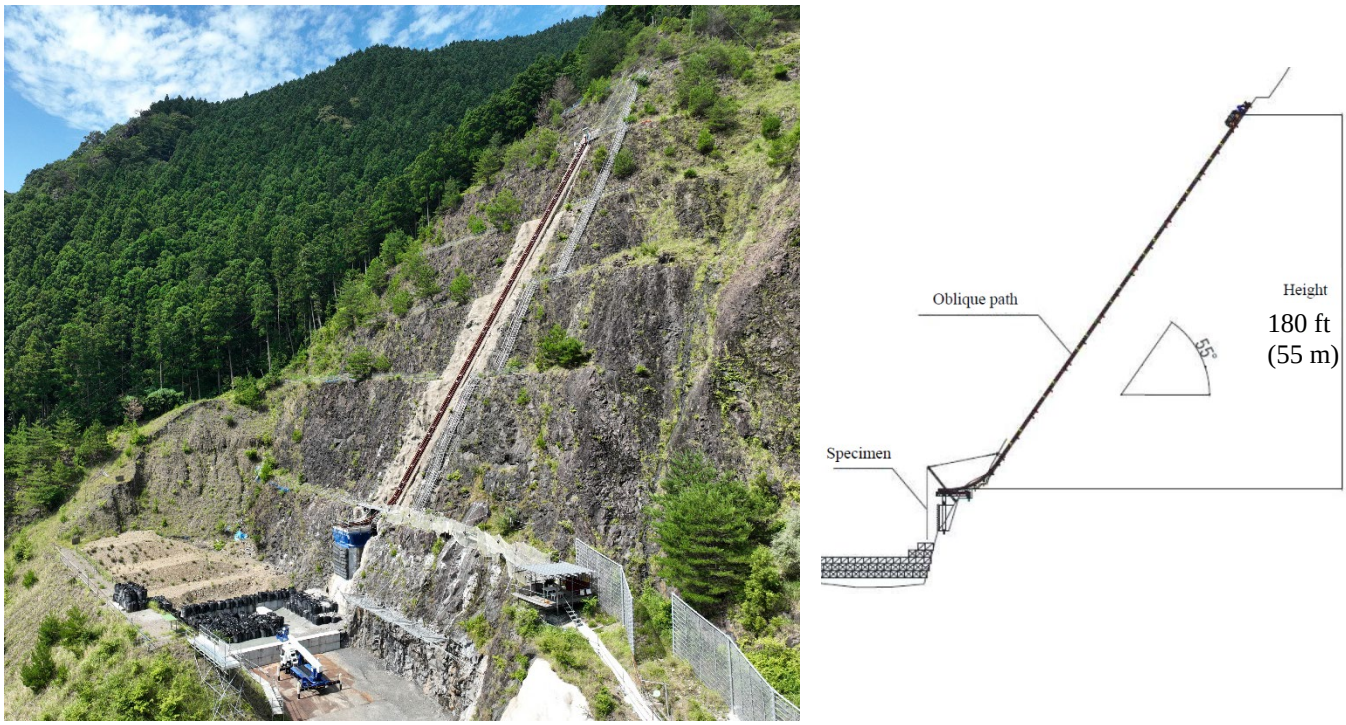

Figure 2: Test facility

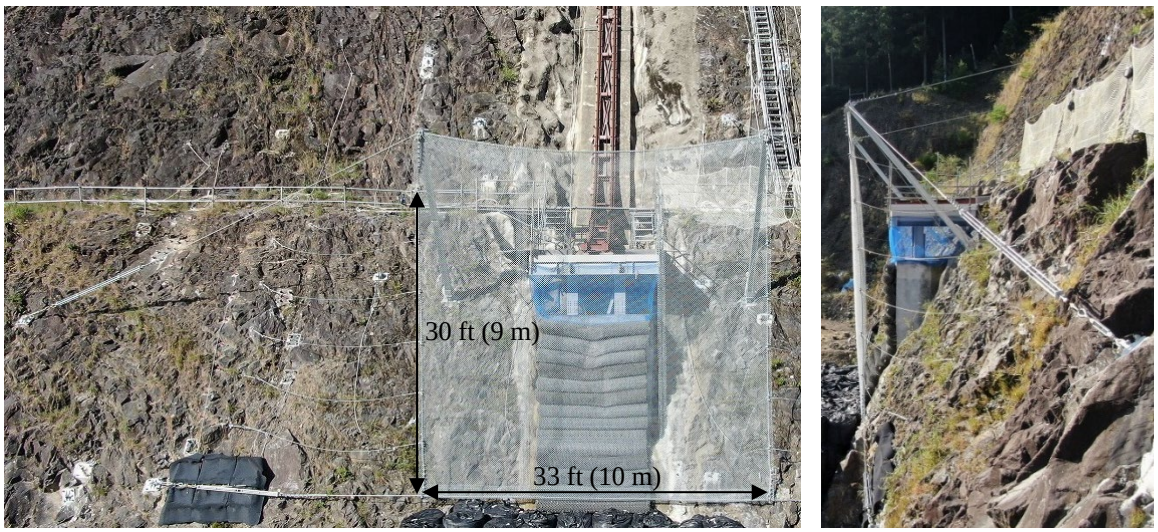

Figure 3: Test barrier of 1,400 kJ

The block used in the full-scale test was a concrete block (mass: 2.9 ton) as shown in Figure 4. Based on *Guide on Rockfall Countermeasures*, the density was 2,300 kg/m^3.

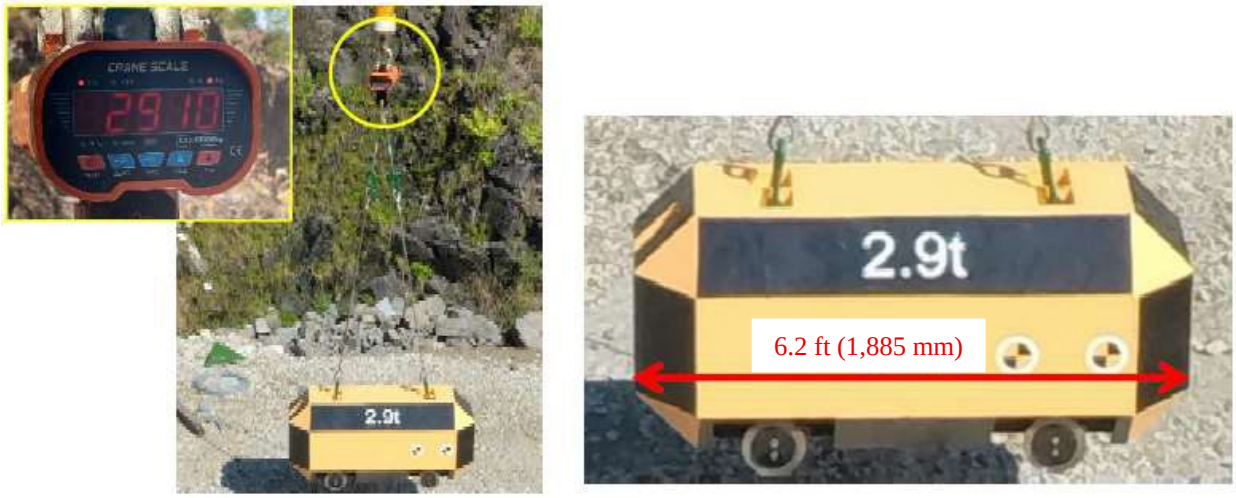

Figure 4. Block details

In the full-scale test, the block velocity was measured by a high-speed camera. It can photograph 960 frames per second. The block passed the barrier during 58 frames as shown in Figure 5 (a) and (b).

(a) Velocity measurement start

(b) Velocity measurement end

Figure 5: Velocity measurement

58 frames correspond to 0.06 seconds (58/960). The length of the block is 6.2 ft (1.885 m), and thus its velocity was 1.885m / (58/960) s= 31.2 m/s. This value satisfies the conditions described in *Guide on Rockfall Countermeasures*, which is that the velocity is no less than 25 m/s. The impact energy was as follows;

$E=1/2 \times m \times V^2= 1/2 \times 2.9 \times (31.2)^2 = 1{,}411$ kJ.

The test barrier after the full-scale test is shown in Figure 6 and 7. The test barrier could capture the block and effectively guide it to the toe of the slope.

Figure 6: Behavior of test barrier (bird's-eye view)

Figure 7: Behavior of test barrier (side view)

In this full-scale test, we measured the generated tension on wire ropes by a data acquisition system and load cells. Figure 8 shows the time-history response waveforms of the loads on the top horizontal rope (CH3, 4) and the bottom horizontal rope (CH17, 18) equipped with buffer devices. The effect of these devices is evident: once the load exceeds approximately 80–90 kN, the rapid increase in load is suppressed as the waveforms exhibit small-amplitude oscillations.

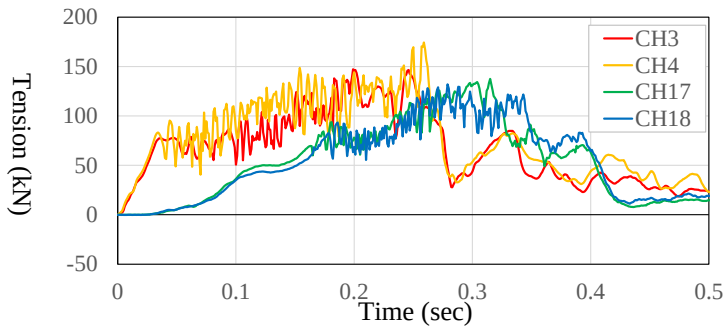

Figure 8: Time-history response of tension on horizontal ropes

Although the rupture of wire netting near the point of impact was observed, it was caused by rotating wheels of the block and the block was seen to rebound after being caught; therefore, we determined that the structure's overall containment performance was satisfactory.

Furthermore, no significant tilting of the posts was observed between the moment of maximum deflection and the time following the impact. After the full-scale test, we could easily dismantle the test barrier and remove it. This means that, even after the actual events of rockfalls, administrators can easily maintain this hybrid barrier.

2,800kJ

TOKYO ROPE conducted the full-scale test of 2,800 kJ in the same manner as that of 1,400 kJ. The test barrier has a 50-ft (15 m) spacing between posts and 30 ft (9 m) in effective barrier height as shown in Figure 9.

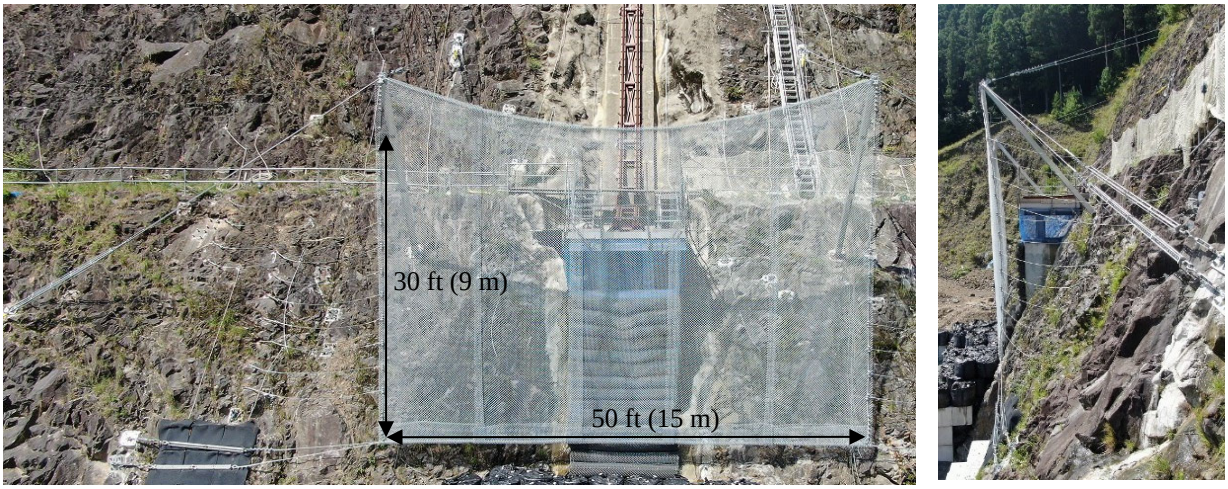

Figure 9: Test barrier of 2,800 kJ

We increased the number of wire netting layers (from 1 layer to 2 layers), upslope ropes (from 1 to 2 ropes), top horizontal ropes (from 1 to 2 ropes), and bottom horizontal ropes (from 1 to 2 ropes), respectively.

The block used in the full-scale test was again a concrete block (mass: 6.4 ton) as shown in Figure 10. Based on the *Guide on Rockfall Countermeasures*, the density was 2,300 kg/m^3.

Figure 10: Block details

In the full-scale test, the block velocity was measured by a high-speed camera. It can photograph 960 frames per one second. The block passed by during 80 frames as shown in Figure 11 (a) and (b).

(a) Velocity measurement start

(b) Velocity measurement end

Figure 11: Velocity measurement

80 frames correspond to 0.08 second (80/960). The length of the block is 8.2 ft (2.495 m), and thus its velocity was 2.495m / (80/960) s= 29.9 m/s. This value satisfies the conditions described in the *Guide on Rockfall Countermeasures*, which is that the velocity is no less than 25 m/s. The impact energy was as follows;
$E=1/2 \times m \times V^2 = 1/2 \times 6.4 \times (29.9)^2 = 2{,}868$ kJ.

The test barrier after the full-scale test is shown in Figure 12 and 13. The test barrier could capture the block and effectively guide it to the toe of the slope.

Figure 12: Behavior of test barrier (bird's-eye view)

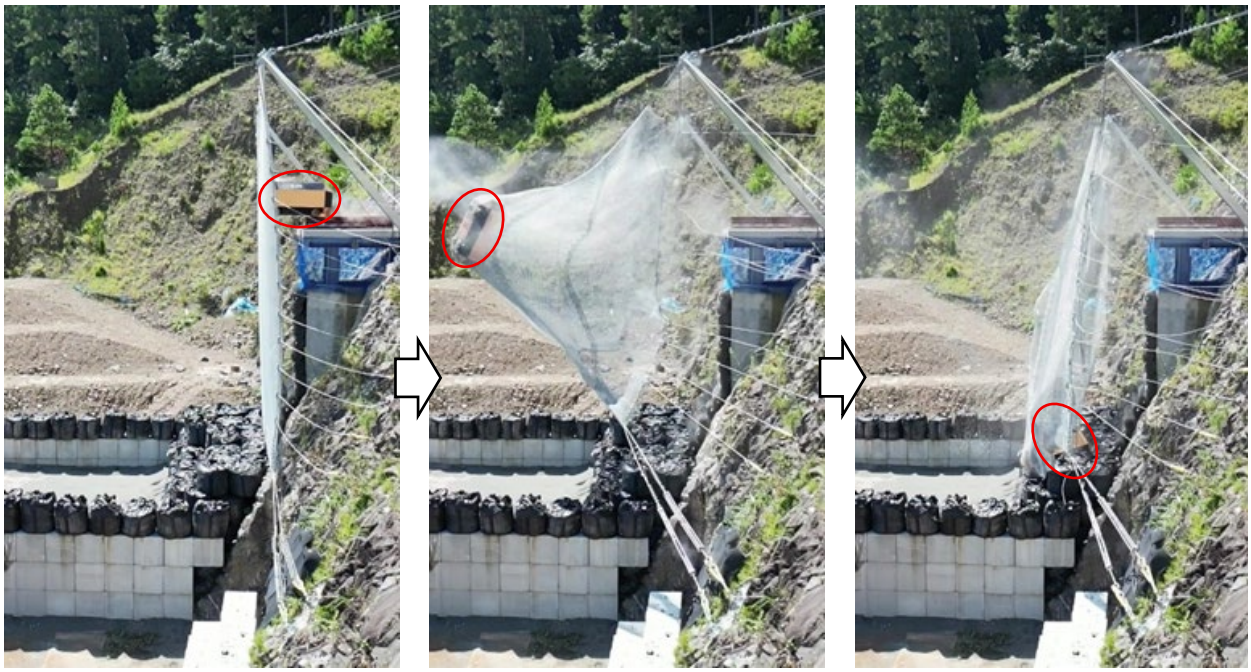

Figure 13: Behavior of test barrier (side view)

In this full-scale test, we measured the generated tension on wire ropes by a data acquisition system and load cells. Figure 14 shows the time-history response waveforms of the average loads on the top horizontal ropes (CH5, 6 and CH7, 8) and the bottom horizontal ropes (CH31, 32 and CH33, 34) equipped with buffer devices. The effect of these devices is evident: once the load exceeds approximately 70 kN, the rapid increase in load is suppressed as the waveforms exhibit small-amplitude oscillations.

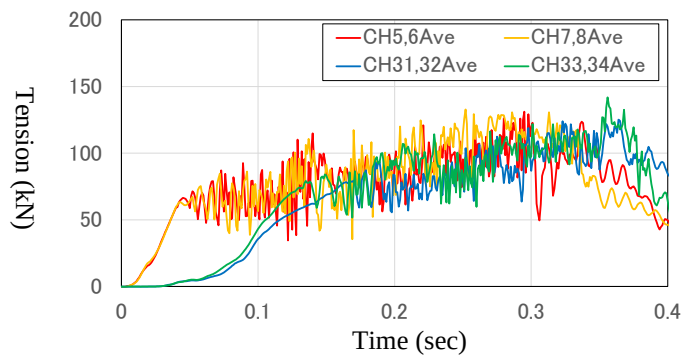

Figure 14: Time-history response of tension on horizontal ropes

Although a deformation of the wire netting near the point of impact was observed, it was caused by rotating wheels of the block and the block was seen to rebound after being caught; therefore, we determined that the structure's overall containment performance was satisfactory.

Furthermore, no significant tilting of the posts was observed between the moment of maximum deflection and the time following the impact. After the full-scale test, we could easily dismantle the test barrier and remove the structure components while leaving posts in place. This means that, even after the actual events of rockfalls, administrators can easily maintain this hybrid barrier.

CONCLUSIONS

Protective nettings require a wide area to capture large rockfall energy (high energy). However, in this study, full-scale tests proved that a limited area of hybrid barrier could capture high energy. The test barrier with 33 ft (10 m) in spacing between posts and 30 ft (9m) could capture 1,400 kJ. The one with 50 ft (15 m) in spacing between posts and 30 ft (9m) could capture 2,800 kJ. In both cases, the block velocity was reduced to zero, and the block was effectively guided to the toe of the slope.

This result shows that hybrid barriers can reduce the velocity to zero. While attenuators allow the rock blocks to continue down the slope for collection at the toe of the slope, hybrid barriers can collect rockfall at the bottom of the system.

Let’s take a look from the viewpoint of installation. One mitigation scheme was shown in *Colorado’s Full-Scale Field Testing of Rockfall Attenuator Systems* (1). Attenuator is installed at a higher place of the slope, Fence or Attenuator at a middle place, and Catchment Fence along

the road as described in Figure 15. In this scheme, 3 systems are installed. From the viewpoint of installation, this is not cost effective.

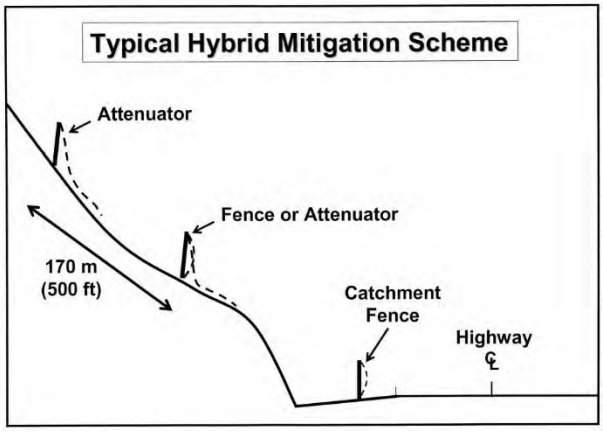

Figure 15: Conceptual diagram showing installation of attenuator sequence extracted from *Colorado's Full-Scale Field Testing of Rockfall Attenuator Systems*

On the other hand, if we utilize hybrid barrier, secondary catchment along the road is not required in the best case as shown in Figure 16. We can shorten the installation time and utilize the cost effectively.

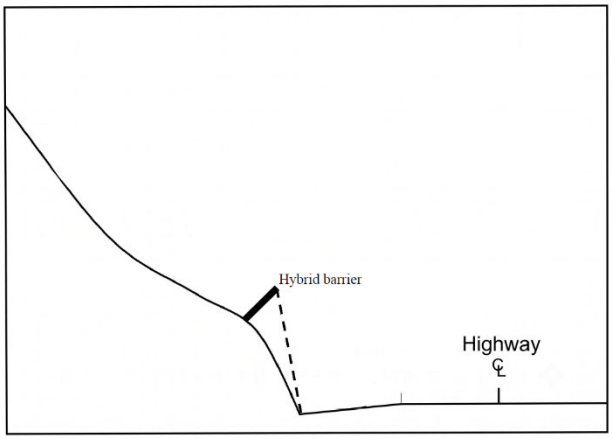

Figure 16: Conceptual diagram showing installation of hybrid barrier

REFERENCES:

1. Arndt, B., T. Ortiz, and K, Turner, *Colorado's Full-Scale Field Testing of Rockfall Attenuator Systems*, Transportation Research Circular E-C141, Transportation Research Board, October 2009

2. Tim Shevlin and Remo Dudler ATTERO: A New Design Tool for Rockfall Attenuator Performance. *In 2025 HGS Proceedings: 74th HIGHWAY GEOLOGY SYMPOSIUM*, Morgantown, WV, 2025. pp. 383-394.

3. Hybrids are not attenuators. An Austrian Perspective https://aghp.shorthandstories.com/aghp-annual/featured-stories/hybrids-are-not-attenuators-an-austrian-perspective/index.html Accessed May 31, 2026

4. Bichler, A. and Stelzer, G., A fresh approach to the hybrid/attenuator rockfall fence, *Landslides and Engineered Slopes: Protecting Society through Improved Understanding* edited by Eberhardt et al. Proceedings of the 11th Annual Symposium on Landslides and Engineered Slopes, Banff, Canada, 3-8 June 2012, Taylor and Francis Group, London, 2012, pp. 1209-1214.

5. Inagaki et al. *Guide on Rockfall Countermeasures.* JAPAN ROAD ASSOCIATION, TOKYO, edited on 27th December 2017, pp. 160.

12. Take 2 – Rock Fall Mitigation System Replacement at Fairlee, Vermont

Jay R. Smerekanicz, P.G., C.P.G.
Scarptec, Inc.
P.O. Box 326
Monument Beach, MA 02553
(603) 493-6274
jay@scarptec.com

David J. Scarpato, P.E.
Scarptec, Inc.
P.O. Box 326
Monument Beach, MA 02553
(603) 361-0397
pingraham@golder.com

Ethan J. Thomas
AOT Geologist III
Construction & Materials Bureau, Geotechnical Engineering Section
Vermont Agency of Transportation
Dill Building Unit B, 2178 Airport Road
Berlin, VT 05641-8628
(802) 595-6752
Ethan.Thomas@vermont.gov

Christopher W. Case
AOT Geologist II
Construction & Materials Bureau, Geotechnical Engineering Section
Vermont Agency of Transportation
Dill Building Unit B, 2178 Airport Road
Berlin, VT 05641-8628
(802) 595-9359
Chris.W.Case@vermont.gov

Prepared for the 75th Highway Geology Symposium, September 28 - October 1, 2026

Acknowledgements

The author(s) would like to thank the individuals / entities for their contributions in the work described:

Kevin Nesnow – Climb Aloha (aka rope access "force multiplier")
Tom Eliassen – Peters Construction Consultants, Inc.
Chris Eddy and Chris Koteas, Ph.D. – Haley & Aldrich, Inc.
Nick Newland – Vermont Agency of Transportation
Jason Gaudette, P.E. – GEODesign, Inc.
Apex Rockfall & Access Limited Construction

Disclaimer

Statements and views presented in this paper are strictly those of the author(s) and do not necessarily reflect positions held by their affiliations, the Highway Geology Symposium (HGS), or others acknowledged above. The mention of trade names for commercial products does not imply the approval or endorsement by HGS.

Copyright Notice

Copyright © 2026 Highway Geology Symposium (HGS)

All Rights Reserved. Printed in the United States of America. No part of this publication may be reproduced or copied in any form or by any means – graphic, electronic, or mechanical, including photocopying, taping, or information storage and retrieval systems – without prior written permission of the HGS. This excludes the original author(s).

ABSTRACT

The Palisades rock slope on Interstate 91 in Fairlee, Vermont was a highlight of the 2003 Highway Geology Symposium field trip, featuring a large, draped mesh rockfall mitigation project (197,000 ft^2) constructed in 1996. The rock slope is composed of a relatively young and resistant quartz monzonite pluton (Devonian) that was later sheared by Acadian-aged thrust faulting, forming brittle structures prone to toppling failure, and is the tallest rock slope requiring mitigation in the Vermont Agency of Transportation's asset management system. Later continental glaciation "plucked" the leeward side of the pluton, forming a roche mountonnée having a very steep slope with heights approaching 400 feet above roadway grade. Long-term weathering includes joint infilling with soil/talus, ice riving, and a progressive increase in the size and frequency of rockfalls.

The draped mesh system performed well until 2020-2021, with occasional toppling angular rockfalls that tore holes in the aging mesh, but was no match for a large rockfall toppling event that occurred on February 27, 2024. The estimated 200 cubic yards of rockfall debris ripped the mesh open and spilled out onto the southbound lanes of the interstate, fortunately without injury or damage to the public.

Vermont, like much of the northeast, is experiencing more extreme weather events, such as more frequent freeze/thaw cycling that likely exacerbated conditions leading to the rock fall. As the drape system was nearing its 30th year in service and was no longer effectively preventing rockfall from reaching the roadway, the Vermont Agency of Transportation (VTrans) conducted a phased approach to mitigate the source area, address other potential risks, reopen the roadway and redesign mitigation for the entire slope. This consisted of an initial emergency mitigation phase to remove or secure additional immediate rockfall hazards in late winter/early spring 2024, followed by a temporary mitigation phase during the remainder of 2024 to address potential longer-term rockfall hazards.

The second phase bought more time for a third phase to develop and construct an effective, long-term rock slope mitigation design. This improved design utilized extensive scaling, rock dowels, shotcrete, drains, and both pinned and draped mesh, and was constructed in the latter half of 2025. This project highlights the challenges associated with an initial emergency response that evolved into a mitigation redesign project, constructed using fast-paced methods during highly variable New England weather conditions.

INTRODUCTION

The project site is located along Interstate 91 (I-91) in the Connecticut River Valley, between Vermont and New Hampshire (see Figure 1). The interstate is a 4-lane limited access roadway, with an annual average daily traffic count of 4,200, and is a critical transportation corridor linking southern New England and northern Vermont and Québec. Major highways such as I-91 run north-south due to the dominant structural geology of western New England, where through tectonic and glacial processes, long valleys and mountain ranges are oriented north-south.

VTrans cut the lower half of the natural, very steep rock slope to place the new interstate highway between the recut rock slope and a preexisting two-lane highway (U.S. Route 5) and an adjacent railroad. Detailed project history is provided below.

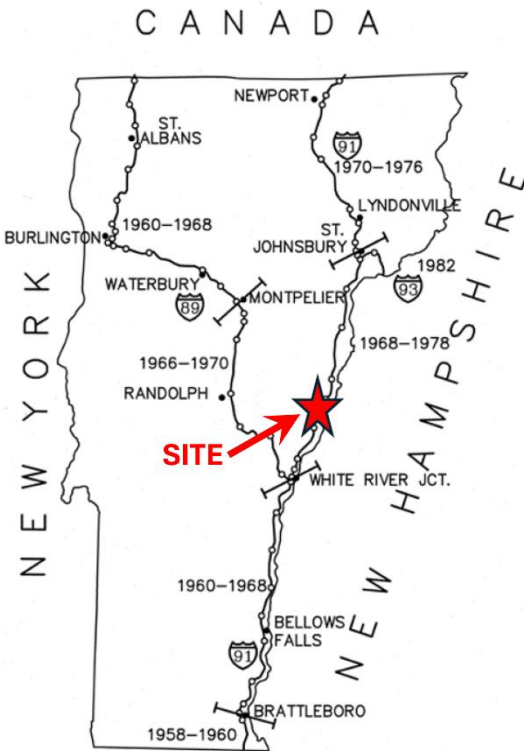

Figure 1 - Site Location Map. Dates indicate when sections of interstate were constructed (Eliassen & Ingrahm, 2000)

REGIONAL AND SITE GEOLOGY

Initial regional geologic mapping identified the bedrock as Late Ordovician Fairlee Quartz Monzonite, an igneous pluton assigned to the Late Ordovician Highlandcroft plutonic suite of western New Hampshire (Hadley, 1951). That mapping described the lithology consisting of crushed and foliated, greenish gray, with local pink tinges, coarse-grained granitic rock, containing bluish-gray quartz, perthitic microcline and oligoclase or andesine, with secondary chlorite, sericite and green biotite. Later mapping correlated the Fairlee Quartz Monzonite with similar rocks of the Devonian Bethlehem Gneiss to the east in New Hampshire (Indian Pond Pluton), transported to the west on the upper block of the Ammonoosuc Fault in a post-Taconian extensional tectonic regime (Hadley, 1951; Moench, 1990). Updated regional geologic mapping assigns the Fairlee Quartz Monzonite an Early Devonian age (410 ± 5 Ma), with a lithology described as greenish-gray, pink-tinged, weakly foliated, coarse-grained to porphyritic biotite granite (Ratcliffe et al., 2011; see Figure 2). Numerous xenoliths and felsic dikes occur within the rock mass.

The Fairlee Pluton has been extensively impacted by shearing and fault movement, as evident at the site by a prominent subhorizontal to northwest-dipping fault daylighting on the rock slope face, which drains groundwater. Drag folds on the upper block initially suggested a normal sense of movement counter to recent regional tectonic interpretations; however detailed field mapping by Haley and Aldrich, Inc. (H&A) and Scarptec in 2024 indicates that the fault surface dips steeply to the northwest and is likely a high-angle reverse transpressional fault. Several splays off this fault occur with similar suspected relative movement. This is consistent with a reverse fault mapped as bounding the eastern portion of the pluton roughly adjacent to the west

bank of the Connecticut River (Moench, 2007). This complex faulting, along with orogenic events has resulted in the formation of at least six (6) prominent joint discontinuity sets crosscutting the rock mass.

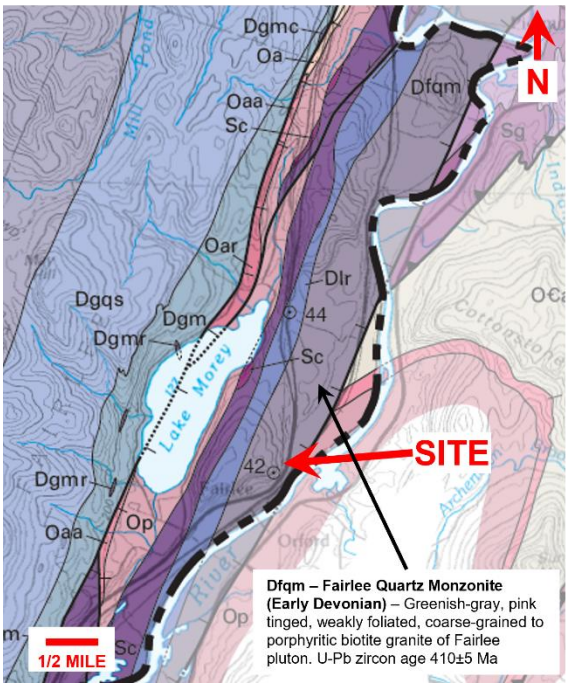

Figure 2 - Geology (Ratcliffe et al. 2011)

Overburden materials above the rock slope crest, inclusive of soils, generally appeared to be 2 to 5 feet thick with angular quartz monzonite rock blocks (talus) contained within a matrix of modified ablation till and slope wash (colluvium). Low outcrops and subcrops of quartz monzonite occur above the slope crest. The Laurentide Ice Sheet flowed generally southeasterly, forming the Palisades (as a roche mountonnée), and likely "plucked" rock blocks from the southeast face, contributing to the fractured nature of the slope. Glacial erratic cobbles and boulders up to 12 feet in longest dimension are present above the crest of the slope. Small talus aprons, estimated to be less than a few feet thick, were noted on the upper portions of the slope at the southwest end, where the slope angle is roughly 45 to 50 degrees. The overburden materials are generally covered with grassy and brushy vegetation, with locally large diameter hard wood tree varieties and white pine trees.

PROJECT HISTORY

Original Construction

VTrans completed the original I-91 construction in Fairlee by 1971 (Eliassen, 1997; Westerman et al., 2003). To create the corridor for four lane traffic for the new highway, VTrans excavated lower sections of the rock slope using perimeter control blasting (i.e., presplitting) to construct four (4) presplit benches along the slope, each less than about 2 feet wide and about 30 feet high, for a total height of 120 feet above roadway elevation. These benches were cut at a 4 vertical to 1 horizontal angle (4V:1H; ~76 degrees), with the half-barrel casts spaced at about 3 feet. The drilling was splayed out at the end of at least one bench to match the existing natural rock slope angle. The rock slope/cut is about 600 feet long and up to about 400 feet high. Excessive drill hole wander occurred between presplit holes, producing spacings significantly greater and less than the nominal 3-foot spacing. Overbreak and underbreak also occurred despite utilizing presplit methods. VTrans also conducted trim blasting above the presplit face to remove overhanging and unstable rock masses, based on a few vertical half-barrel casts near the top of the slope, abandoned in place drill rods, and the presence of some rusty winching cables adjacent to the crest access road.

1996 Mitigation

Recurring rockfall events occurred in 1973, 1985, 1987 and 1990 emanating from above the presplit benches that involved vehicle strikes and southbound roadway closures (Baskerville et al., 1993; Westerman et al. 2003). In summer and fall of 1996 VTrans designed and constructed the first rockfall drape system used in the State as part of a regional interstate safety program (Eliassen, 1997). During this work, southbound traffic on I-91 was detoured onto adjacent U.S. Route 5 between Exits 16 and 15 to accommodate construction, including a large crawler crane with about 250 feet of boom length (see Figure 3). Prior to drape placement, the rock slope was cleared of vegetation, hand scaled (over three weeks), and subject to trim blasting. During scaling activities, some rock struck the slope face and ramped over I-91 southbound into I-91 northbound, and then rolled into the adjacent U.S. Route 5 and into the railroad tracks, a distance of over 200 lateral feet. Four large rock blocks that appeared potentially unstable and would exceed the capacity of the drape were secured with ten (10) rock bolts. These consisted of #8 (1-inch diameter) galvanized, 30 foot long, Grade (GR) 150 threadbars, installed in 1-5/8-inch diameter drill holes using a drill on a platform suspended from the large crane, and grouted using fast and slow epoxy setting resin. The threadbars were then tensioned to a proof load of 90,000 pounds (90 kips) and locked off on a bearing plate at 75 kips.

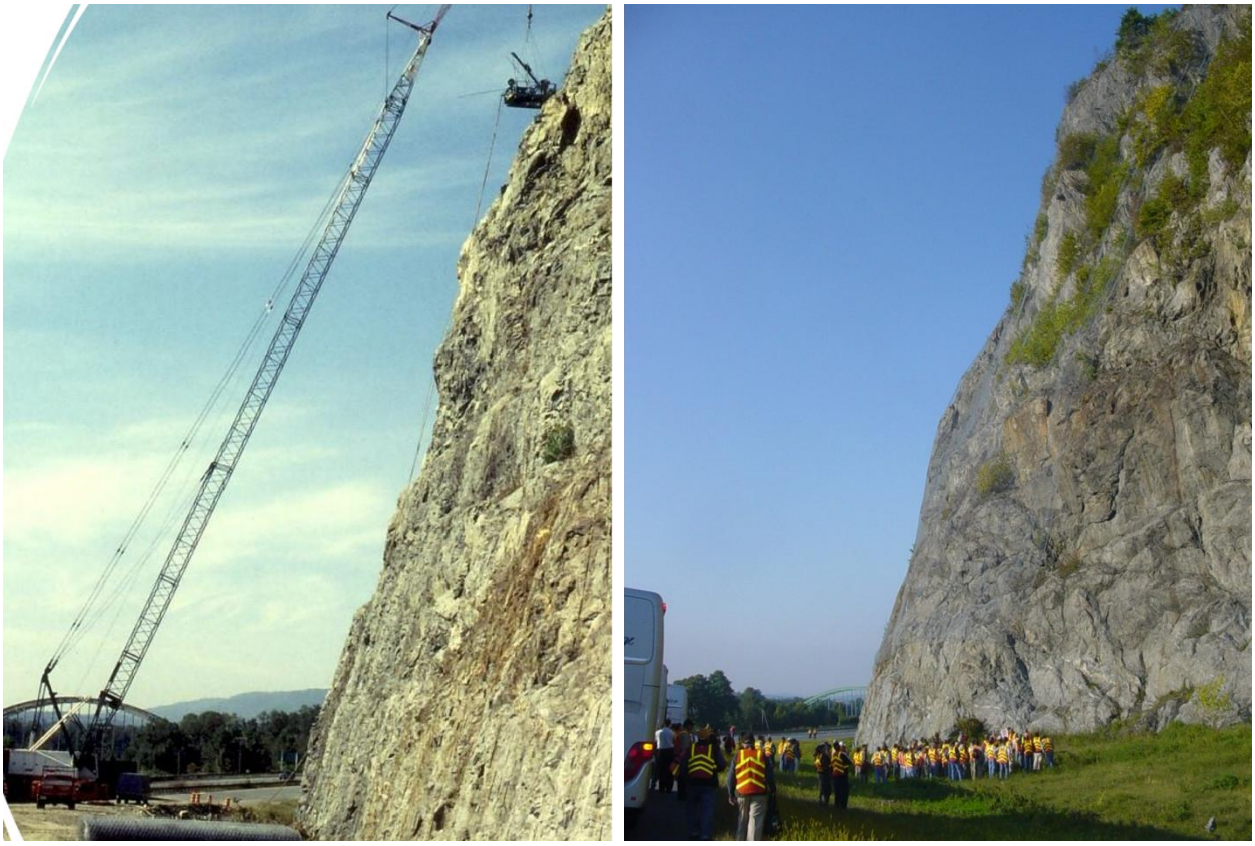

Figure 3 - 1996 Construction with crawler crane (left; VTrans); 2003 HGS field trip site visit (right, J. Smerekanicz 2003)

The drape material consisted of Maccaferri No. 11 gauge, galvanized double-twist mesh made of steel wire with a tensile strength of 70,000 pounds per square inch (70 ksi). The mesh was suspended by ¾ (0.75)-inch diameter galvanized wire ropes attached to vertical GR 60 galvanized #8 threadbars above the crest of slope and grouted using resin cartridges (in rock) and cementitious grout (in overburden). The drape was extended to about 30 feet above the slope toe. Two cranes were used to install the drape: the large crawler crane staged on the southbound lanes, and a smaller one located above the crest of the slope on an excavated crane pad. The installed draped mesh quantity was 196,146 square feet (ft^2).

Due to occasional rock falls damaging the double-twist material, including rock falls emanating from the presplit portion of the slope, VTrans performed localized repairs in 2022 consisting of placement of Maccaferri double-twist mesh patches attached to the damaged mesh. The drape remained in-place until the entire system was deemed as needing repair after the February 2024 rockfall event.

Rock Fall Hazard Rating

In 2007, VTrans rated the rock slope with a preliminary ranking of "A", meaning that rockfall is expected to occur and reach the roadway, i.e., it has a high hazard potential despite the drape installation (VTrans, 2007). This high rating was due to the northern portion of the slope not included during the 1997 construction and the continued rockfall activity requiring occasional maintenance and repairs to the drape. The Rockfall Hazard Rating Score (RHR) for this site was 828 making it the highest scored rock slope in the State's inventory requiring mitigation.

February 27, 2024 Rock Fall Event

At approximately 11:00 p.m. on February 27, 2024, a rockfall occurred at approximately mile marker 92.55 on I-91, consisting of an estimated 100 to 200 cubic yards (CY) of rock debris, some of which impacted the southbound (SB) lanes with boulders exceeding 4 feet in maximum dimension (see Figure 4). No injuries or significant vehicular damage were reported. The rock fall originated from the upper reaches of the 300-foot-high slope, and ripped through existing rockfall drape netting (Figure 5). The rock fall caused full closure of the north and southbound highway lanes for emergency response and assessment. Northbound traffic was allowed to resume the following day, and one lane of southbound traffic was opened after deployment of temporary concrete barriers and other traffic control.

In the days following the rock fall event, VTrans commissioned Haley & Aldrich, Inc. (H&A) to conduct emergency geotechnical services to assess the existing conditions and determine the cause of the rock fall. VTrans attributed the rockfall mechanism to toppling pillars and slabs of rock, loosened by freeze/thaw effects in nearly vertical, dilated joints oriented parallel with the roadway. The rockfall mechanism appears similar to a smaller rockfall event that occurred in 2018, located approximately 600 feet northeast (Golder Associates Inc., 2019).

Figure 4 – Drone image of scalers beginning emergency response on March 5, 2024, following the February 27, 2024 rock fall (VTrans)

Figure 5 – Drone images of rock fall source area prior to rock fall (left) on April 5, 2022, and scar following rock fall (right) March 5, 2024 (VTrans)

MITIGATION APPROACH

VTrans divided the rockfall mitigation project into three phases: emergency response, interim mitigation, and long-term rock fall mitigation design and construction.

Phase I – Emergency Response

This initial phase consisted of installing temporary rockfall barrier and protection of traffic, removal of damaged draped mesh, scaling of loose rock remaining in the failure area, design and installation of 28 rock dowels, and removal of associated debris. This phase was conducted from early March to early April 2024.

Phase II – Interim Mitigation

This second phase consisted of removal of the existing draped mesh, clearing/removal of vegetation, scaling of remaining loose rock previously covered by the drape, an additional 168 rock dowels, and temporary cable lashing. Due to the potential for scaled rock and other debris affecting I-91 and U.S. Route 5, southbound traffic was detoured onto U.S. Route 5 from Exit 16 to Exit 15 until November 23, 2024. Two temporary, portable rockfall catchment barriers were employed to protect northbound traffic (a primary 1,000 kJ barrier on the right side of the travel lane, and a secondary 35 kJ barrier on the left shoulder of the passing lane), along with temporary rolling roadblocks. This phase started in mid-April 2024 and was completed in early January 2025.

During the fall of 2024, it became apparent that the Phase II work would not be completed by the onset of winter at the end of 2024 due to an extensive amount of hand scaling and rock dowels being required. As such, the southwestern 200 linear feet of the existing double-twist mesh was left in place, with its removal, hand scaling and permanent mitigation to be included during Phase III. Several rock masses and blocks that were potentially unstable and could present rockfall hazards that could overwhelm the mesh during the 2024-2025 winter season were secured using temporary mitigation methods. This consisted of removing one small rock block, cable lashing two rock masses and one rock block, and securing the northeastern edge of the cut mesh with wire rope cable anchors, completed by mid-December 2024.

Phase III – Long-Term Rock Fall Mitigation Design and Construction

This phase consisted of developing, evaluating and designing a “permanent” (i.e., long-term) rock slope mitigation in summer 2024 through winter 2025, followed by construction in summer 2025 through winter 2026, both the subject of this paper. The recommended design and mitigation approach consisted of a more robust rockfall protection system including a “pinned mesh” for the higher section of the rock slope and a “wire mesh drape” for the lower. A summary of the elements involved is included below:

- Temporary rockfall mitigation and traffic protection during construction (designed by the contractor)
- Removal of remaining mesh and temporary rockfall mitigation elements
- Clearing and Grubbing
- Wire Mesh Panels with Wire Mesh Dowels (“Pinned Mesh”)
- Glacial erratic boulder removal
- Wire Mesh Dowel, Rock Slope Stabilization Dowel, and Wire Rope Anchor Testing
- Wire Mesh Dowels (for the Pinned Mesh)
- Rock Slope Stabilization Shotcrete
- Rock Slope Stabilization Nails (for shotcrete support)
- Cable Lashing

- Hand Scaling
- Wire Mesh Panels ("Draped Mesh")
- Rock Slope Stabilization Dowels ("Rock Dowels")
- Rock Slope Stabilization Drains
- Wire Rope Anchors

VTrans advertised the Phase III project on April 2, 2025, awarded it on May 13, 2025, and issued a conditional notice to proceed with construction on July 7, 2025, followed by the notice to proceed with construction on July 17, 2025.

PROJECT CHALLENGES

A key project challenge was that the local populace in the Fairlee area along with regional transportation have suffered major impacts due to the Phase I and II mitigation activities during most of 2024 due to the extensive I-91 southbound closure. To reduce those impacts, VTrans elected to start the Phase III design during construction of Phase II. This led to tight time schedules to develop the design and prepare for bidding of Phase III. To further reduce transportation impacts during Phase III, VTrans instituted an incentive/disincentive period, allowing the contractor to have a full southbound closure for up to 35 days, along with using rolling road blocks on the northbound side as needed. For time outside the incentive/disincentive period, the contractor was allowed to maintain a single southbound travel lane closure. Additionally, to shorten the construction schedule, VTrans allowed provisions for night and full weekend work. To improve access and staging areas above the crest of the slope, in winter 2025, VTrans cleared large trees that surrounded the crane pad developed for the 1996 mitigation. Further, to reduce schedule impacts, the design approach and contracts allowed for the use of helicopter deployment of mitigation elements, specifically wire mesh panels, along with a large staging area north of the site for helicopter operations and storage of the large amount of materials needed for the project.

A significant amount of the old mesh was located on the upper portion of the slope, but on relatively low angles ranging from 50 to 60°. In this area, extensive vegetative growth of bushes and trees, coupled with being 300 to 400 feet above the toe of the slope, would have made removal difficult and time consuming. As the old mesh in this area provides protection against raveling and soil loss, along with promoting vegetative growth, the design approach incorporated leaving this portion of the old mesh in place, with new pinned mesh placed over it.

PHASE III MITIGATION DESIGN

As in all rock slope mitigation projects that require scaling, the final rock slope condition is not known until the scaling is complete. Therefore, the design must be adaptable to the encountered conditions, and the Fairlee Phase III design was no different. A variety of likely-needed mitigation elements were included in the design, such that the contractor could prepare the means, methods and materials that may be needed.

Discontinuity Data

Rock slope mitigation design requires a three-dimensional understanding of rock mass discontinuities. Geologic and geotechnical data collected in 2024 of 159 discontinuities (joints,

faults and mineral veins), including location, discontinuity type, dip angle, dip angle direction, persistence, aperture, infilling, shear strength, surface roughness, shape, water, and spacing. After plotting dip/dip direction on stereonets, we assigned six (6) joint sets based on a minimum concentration density of 2.7% (see Table 1 and Figure 6). The orientation of these joint sets aided in evaluating and designing mitigation elements and measures.

Table 1 – Discontinuity Set Summary

Set Identification	Discontinuity Type	Dip/Dip Direction [°]
J1 m	Joint Set 1	75/264
J2 m	Joint Set 2	46/137
J3 m	Joint Set 3	46/093
J4 m	Joint Set 4	83/095
J5 m	Joint Set 5	79/025
J6 m	Joint Set 6	87/355

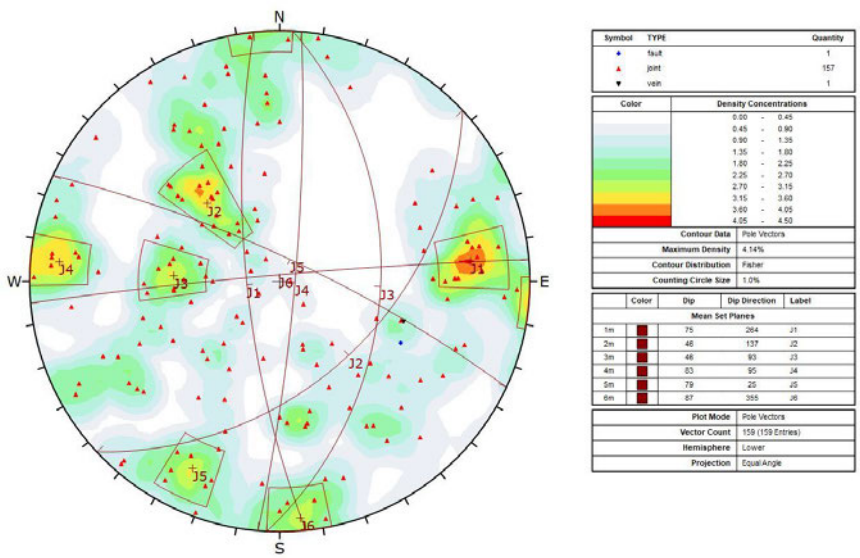

Figure 6 – Stereonet of discontinuity sets (equal angle projection; 0.45% contour interval)

Rock Strength Data

To also aid in mitigation element design, we conducted shallow core drilling at the toe of the slope to obtain NQ-size core for unconfined strength testing (UCS) and unit weight analysis per ASTM D7012-10, Method C. Table 2 provides a summary of the index testing results.

Table 2 - Geotechnical Laboratory Index Testing Results Summary

Sample ID	#1A	#1B	#2	#3	#4	#6	#7	Average
Station	89+49	89+49	89+77	90+04	90+05	89+48	89+06	n/a
Depth [in.]	0-4	6-10	0.5-4.5	3-7	2-6	0.5-4.5	1.5-5.5	n/a
Unit Weight [pcf]	167.2	168.4	166.8	168.7	169.2	167.3	167.9	**167.9**
UCS [psi]	8,770	10,100	4,750	5,150	5,320	6,100	11,150	**7,334**

Notes:
pcf = pounds per cubic foot
psi = pounds per square inch
Core sample #5 was excluded as it did not have intact core lengths > 4-in. per ASTM requirements.

Rock Slope Stabilization Dowels

Due to the potential of large rock blocks (exceeding 16 cubic yards) overwhelming the protection systems, the design included untensioned spot rock dowels for internal reinforcement, incorporating hydrostatic and seismic loads. The dowels were designed using the methods outlined by Wyllie (2018) and Spang and Egger (1990), which utilize the steel and encapsulating grout strength to increase the shear resistance across the underlying weak joint plane. The dowels design consists of #10 (1.25-inch) diameter galvanized GR75 threadbars, with a minimum embedment length of 15 feet, a minimum bond length of 10 feet in intact rock and installed in a borehole with a minimum diameter of 3.5-inches. The design includes a 6-inch by 6-inch galvanized face plate and nut.

Wire Rope Anchors

The mitigation design includes incorporating wire rope anchors to support both the pinned and draped mesh systems. These anchors consist of double-legged, ¾-inch diameter galvanized wire rope, with a minimum 10-foot embedment length in intact rock, installed in a minimum diameter 3.5-inch borehole.

Pinned Mesh

The mitigation approach included a tensioned pinned mesh design applied to the upper half of the rock slope, up to about 160 vertical feet, where potential rock fall energy is greatest. This is an important improvement over the 1996 mitigation design, where the mesh provides containment of loosened rock blocks, and the stagger pattern of pins (essentially rock dowels) provides additional internal reinforcement to the rock mass. To ease construction, the pin design is identical to the rock dowel design. The mesh design consisted of GeoBrugg Tecco® G65/4mm high tensile strength mesh, secured using pins placed on a stagger pattern varying from 8 feet by 8 feet to 12 feet by 12 feet, depending on the slope installation angle, which varied from about 80° to 50°. The mesh design utilized GeoBrugg's Ruvolum dimensioning software for both talus/overburden and rock conditions. The mesh design includes galvanized spike plates,

torqued to 11 kips for rock and 6.7 kips for soil conditions. The perimeter design includes 5/8-inch galvanized wire ropes connected to wire rope anchors. The pinned mesh design included two non-contiguous rock outcrops above the limits of the old (and new) pinned mesh to retain rock blocks that might migrate further down slope.

Draped Mesh

The lower half of the slope is generally very steep, ranging from 75 to 90°, including several overhanging areas. The vertical height of the lower half ranges from about 180 feet to 120 feet, and the top of this zone roughly corresponds with the top of the old presplit benches. This area of the slope is relatively more intact, with less potential rock fall energy that may impact the roadway. As such, a separate draped mesh system was designed to be placed below the upper pinned mesh system. The draped mesh system design utilizes its own wire rope anchors and cabling system and acts independently from the pinned mesh system, and was designed with anticipated snow and ice buildup loads. To facilitate occasional cleanout of accumulated rock fall debris, the system includes “pig tails” attached to vertical cables within the mesh. The draped mesh design extends to within 15 to 20 feet above the toe of slope.

Shotcrete

Due to the presence of potential overhangs, loose rock masses and partially detached rock masses, the design included shotcrete for both buttressing and dental purposes. Shotcrete design incorporated steel fiber reinforcement, along with internal welded wire fabric rebar and short rock nails (similar to the rock dowel design) for support, and a minimum 6-inch thickness. The design also included geocomposite drainage boards for drainage.

Cable Lashing

Due to the potential for large rock masses that cannot be removed using hand scaling methods alone, such as trim blasting, the design approach incorporating using cable lashing to provide additional support to pinned or draped mesh and rock dowels. The lashing design incorporated using wire rope anchors and cabling identical to those used for the mesh systems.

Drains

Jointing in several areas of the slope, mainly in the lower half of the slope below the large transpressional fault discussed above, provide conduits for perennial groundwater drainage onto the slope. In winter, these areas typically freeze, and thawing causes minor rock falls and degradation to the slope. To drive the saturated groundwater front into the slope, behind the freezing front, drilled drains with a minimum length of 20 feet and a PVC stub-out pipe at the collar were included in the design, and were targeted below shotcrete areas and the persistently seeping segments of the fault.

Sacrificial Pull Testing

To verify design assumptions regarding the minimum rock-to-grout bond strength of 125 psi, along with checking the contractor's installation methods and materials, the design included pull testing of sacrificial rock dowels, pinned mesh anchors and wire rope anchors.

CONSTRUCTION

Temporary Rock Fall Barrier

Figure 7 - Temporary rock fall barrier arrangement and sand cushion (Scarptec, 2025)

Following temporary closure of the southbound travel lane on July 2, 2025, the contractor setup a temporary rockfall barrier in the travel lane to provide traffic protection during clearing and grubbing activities above the crest of the slope. The temporary barrier, an internal contractor design, was based on GeoBrugg's GBE-500A system with a capacity of 500 kilojoules (kJ), and a height of 20 feet. The barrier used concrete-filled "water buffaloes" weighing approx. 4,000 lbs. as foundation bases for the vertical I-beam posts, and concrete Jersey barriers as anchors for the tie-back cables and braking systems (Figure 7). The passing lane was closed on July 26, 2025 as part of the incentive/disincentive period, and the rockfall barrier was moved into the passing lane on July 30, 2025 to protect traffic during scaling and remaining draped mesh removal. The contractor placed cushion sand in the catchment ditch and on the right shoulder and travel lane to absorb rockfall energy and reduce potential pavement damage.

Clearing and Grubbing

Prior to hand scaling and remaining old mesh removal, the contractor conducted clearing and grubbing of vegetation between the crest of the slope and the clearing and grubbing limit.

Hand Scaling & Remaining Mesh Removal

Between July 30 and August 18, 2025, the contractor conducted hand scaling of the entire rock slope, moving generally from northeast to southwest (see Figure 8). The contractor successfully completed the scaling work within the incentive/disincentive period, which extended by contract from July 26 through August 30, 2025, with the southbound passing lane reopened on August 26, 2025. This included removal of most of the old double-twist mesh remaining from the 2024

Figure 8 - Hand scaling operations (Scarptec 2025)

Phase 2 interim mitigation. Per the design described above, the contractor left an area of the old mesh about 150 feet wide by 300 feet long on the upper southeastern face of the slope, where the grade was approximately 45 to 50°. The contractor used pneumatic jacks (i.e., air bags) to aid in removal of larger interlocked rock blocks. Due to potential detrimental effects to the transportation infrastructure, trim blasting was not allowed. As a precaution, the contractor used rolling roadblocks on the northbound lanes during scaling of areas where rock falls could have overwhelmed or bounced over the temporary rockfall barrier.

As scaling progressed and segments of the slope were completed, Scarptec rappelled the slope with the contractor to check the thoroughness of scaling, check rock blocks for tightness or need for additional scaling, and identified tree roots that required removal. After cleanup and "check" scaling was completed, mitigation element layout, drilling and installation commenced.

Glacial Erratic Boulder Removal

The hand scaling portion of the project plans included the demolition of a large glacial erratic boulder (approximately 7 feet high by 12 feet wide by 9 feet long) sitting about 20 feet upslope of the crest. The contractor used a hydraulic rock breaker to break up the boulder, and used the rock fragments to build a staging area for one of the grout plants.

Sacrificial Element Installation and Testing

To verify the design pullout strength values used for the design of the rock dowels, pinned mesh anchors and wire rope anchors, five (5) sacrificial wire mesh/rock slope stabilization dowels and three (3) sacrificial wire rope anchors were marked out at the slope crest and toe. Between August 25 and 26 2025, the contractor conducted pull testing of the sacrificial wire mesh/rock slope stabilization dowels and wire rope anchors.
For each test, after the jack alignment load of 5% was set, the contractor stressed the sacrificial element at 25% increments from 25% to 125% of the specified design load (DL), which was 33 thousand pounds (33 kips) for 2 feet of grout bonded length. Each load increment was held for 1- to 2 minutes, with no obvious signs of grout bond pullout failure observed. After the 125% DL increment was completed, the test load was increased to 133% and held for 10 minutes to measure total creep elongation. Each anchor held the maximum load, and the measured creep

for each anchor was below the maximum of 0.04 inch prescribed by the Post-Tensioning Institute (PTI, 2014).

We note that for the design, we assumed an allowable bond stress (between rock and cementitious grout) of 125 psi. Back calculation analysis of the testing results indicates that the minimum bond strength achieved (without failure) was approximately 166 psi,

Table 3 below provides a summary of the test anchor results.

Table 3 – Sacrificial Element Testing Summary

Test Anchor ID	Location	Station [feet]	Element Type	Bonded Length [feet]	Test Result
MTA-1	crest	87+45	threadbar	2.50	passed creep at 133% DL
MTA-2	crest	83+75	threadbar	2.67	passed creep at 133% DL
MTA-3	toe	89+30	threadbar	2.40	passed creep at 133% DL
TD-1	toe	88+05	threadbar	2.80	passed creep at 133% DL
TD-2	toe	85+44	threadbar	2.40	passed creep at 133% DL
WTA-1	crest	85+45	wire rope anchor	2.00	passed creep at 115% DL
WTA-2	toe	84+80	wire rope anchor	2.00	passed creep at 133% DL
WTA-3	crest	87+75	wire rope anchor	2.50	passed creep at 133% DL

Note: DL designates the design load, which was 33,000 pounds (33 kips)

Layout

Between July 29 and September 18, 2025, Scarptec laid out locations for wire mesh dowels, rock slope stabilization dowels, wire rope anchors, cable lashing, rock slope stabilization nails, rock slope stabilization shotcrete, and drains on the slope. We conducted most of the mark out using rope access methods, with the aid of our subconsultant Climb Aloha (see Figure 9). When available, the contractor also provided use of manlifts to aid layout in the lower portions of the slope. We used a combination of pin flags, surveyor flagging and spray paint to mark out the drilling and shotcrete locations. When possible, a unique identification designation (ID) was written on the pin flags and/or surveyor flagging for anchors, dowels, nail and cable lashing locations. Scarptec then used the weekly drone flight photographs to add the IDs to the anchor locations and submitted these to the project team for planning and tracking.

Drilling & Element Installation

Between August 18 and November 25, 2025, the contractor drilled and installed 2,103 rock slope mitigation elements, consisting of pull testing elements, wire rope anchors, wire mesh dowels, rock slope stabilization dowels, shotcrete rock nails, and drains, with a total drilling length of 33,106.67 linear feet, based on VTrans' field tracking information. Table 4 below provides a summary of the mitigation elements installed.

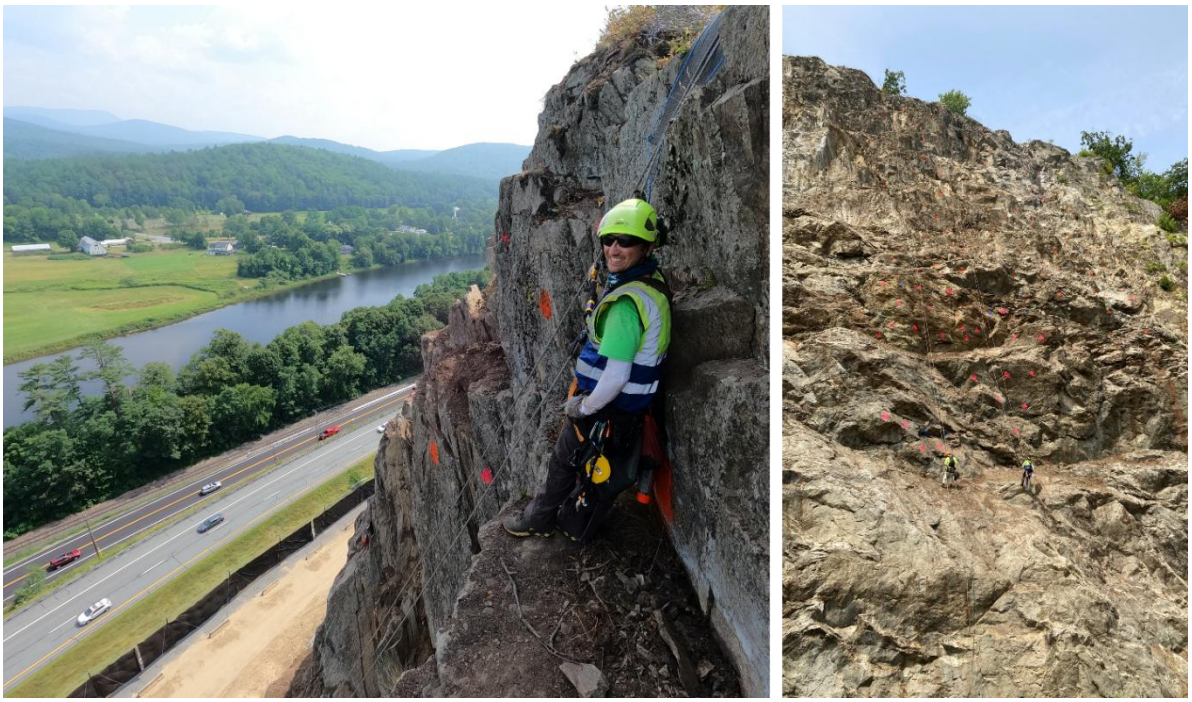

Figure 9 - Layout of mitigation elements using rope access methods (Scarptec 2025)

Table 4 – Mitigation Element Summary

Mitigation Element	Count	Pay Length [feet]
Test Elements	8	105.5
Wire Rope Anchors (OC-8 & OC-10 areas [WRA])	14	140.0
Wire Rope Anchors (Above Crest [WC])	34	363.0
Wire Rope Anchors (On Slope [WS])	115	1,453.5
Wire Mesh Dowels (Above Crest [MC])	153	2,346.0
Wire Mesh Dowels (On Slope [MS])	1,414	21,917.0
Slope Stabilization Dowels (On Slope [SS])	267	5,675.0
Rock Nails [RN]	60	311.67
Drains [DR]	38	795.0
Totals:	**2,103**	**33,106.67**

The contractor used several wagon drills for most of the drilling, each using a down hole hammer with a 3.5-inch diameter carbide button drill bit. The wagon drills were powered by air compressors staged at the top and bottom of the slope, and maneuvered on the slope using an air-powered winch on the drills and operated by a driller and helper on separate rope rappel. The contractor also used a hydraulically powered drill with a 20-foot stroke, mounted on a Magni telescopic telehandler. This drill was operated remotely, typically by one driller on rope rappel, operating both the Magni and the hydraulic drill. This drill also used compressed air to operate the hammer drill, which also had a 3.5-inch diameter carbide button bit. The contractor also

subcontracted a 175-ton, 5-axle wheeled crane to move wagon drills in the lower general 2/3 of the slope, as well as to provide other support.

Shotcrete

Prior to mesh installation, the contractor installed shotcrete in three areas, locally known as "Coffin Rock," consisting of a large column of fractured rock bound by two prominent soil infilled joints located in the upper slope; and the "School Bus" and "The Whale," consisting of moderate sized overhangs in the lower slope. The contractor installed production shotcrete on both sides of "Coffin Rock" to fill the dilated joint with dental shotcrete. ALC installed production dental/buttress shotcrete at the "School Bus" and at "The Whale."

The shotcrete consisted of Quickcrete Shotcrete MS #1229, reinforced with a blend of polypropylene and steel fibers. Prior to production, the contractor shot a preproduction test panel, and drilled core samples for unconfined compressive strength and boiled absorption testing by the VTrans materials laboratory in Berlin, VT. Prior to production shotcrete installation, the contractor installed geotextile composite drainage board. At "Coffin Rock," the contractor placed the drainage board in the lowermost/deepest portions of the dilated joints and then installed galvanized welded wire fabric (WWF; size 4-inch by 4-inch by W8.0/W8.0 [0.16-inch diameter]), using the previously installed rock nails for attachment points. The WWF served to provide additional reinforcement in portions of the shotcrete that had a thickness exceeding 6-inches. At the "School Bus" and at "The Whale," the contractor placed the drainage boards vertically at 8-foot centers across the generally horizontal dilated joints at these locations and a row of rock nails spaced at equivalent 4-foot centers. A total of 55.8 cubic yards (CY) of shotcrete was used in the project.

Pinned Mesh

The wire mesh panels used for both pinned and draped application consisted of GeoBrugg's Tecco® G65/4mm mesh, delivered to the site in 218 rolls, having a width of 3.5 meters (approx. 10.4 feet), and a length of 30 meters (approx. 98.4 feet.) The contractor installed the upper pinned mesh in two general phases, as further described below:

OC-8 & OC-10: These two outcrop areas lie in the southwest end of the upper backslope, and the mesh was designed to contain loose rock blocks that could be dislodged and slide down the lower slope onto the newly installed mesh.

Main Upper Slope: Prior to main upper slope pinned mesh installation, the contractor ran 0.625-inch diameter galvanized perimeter wire rope around the entire area, threading the rope through the eyelets of the wire rope anchors, spaced generally at 20 feet. Additionally, the contractor installed rolled erosion control matting (ECM) in areas of the pinned mesh over soil/talus areas to further limit erosion until vegetation becomes established. The contractor then installed the main slope upper mesh in two phases, between November 11 to 15, and December 3 to 9, 2025 using two different helicopter operators. The contractor prepared each panel lift at the northern staging area, seaming rolls of mesh together for each panel. The helicopter used a custom spreader bar to lift the panels and fly them to the slope. The contractor's technicians used rope

access methods to first attach the top of the panels with galvanized pin-screw shackles to the top 0.625-inch diameter galvanized perimeter cable (installed prior to the lifts), and then the helicopter slowly lowered the panel, with technicians following to pull the mesh into place and attach it to adjacent panels using the T3 seaming clips. Once most of the panel was placed, the pilot activated a remote release mechanism "flop" the spreader bar down and thus release the panel (see Figure 10).

Figure 10 - Pinned mesh installation using helicopter (Scarptec 2025)

The panels were cut about 10 feet longer than needed such that the bottoms were folded up and temporarily tied so that once the lower drape mesh was installed, the folded portion then was extended to cover the gap between the lower portion of the pinned mesh section and the top of the draped mesh. As the mesh was installed, the contractor installed T3 clips at the vertical seams and 0.75-inch galvanized screw-pin shackles on the perimeter wire ropes using rope access methods or from a man basket of the wheeled crane to complete the attachment of the mesh. The contractor also attached galvanized GeoBrugg P33 diamond spike plates and nuts to the bar anchors, with the long axis of the spike plates generally oriented horizontally. Where local surface irregularities in the slope prevented one of the two spikes on the plates from contacting the rock surface, galvanized beveled washers were recommended to be placed below the nut to help improve contact. The contractor used an air impact wrench to tighten the nuts to the plates, and then a hand-operated torque wrench to apply the design load of 6.7 kips for soil and 11 kips for bearing on rock. For tracking purposes, the contractor painted a green dot on spike plates that had been torqued.

Cable Lashing

During layout, Scarptec recommended that two rock masses within the pinned mesh limits be reinforced using cable lashing given the irregular shape of the constituent rock blocks. The intent of the lashing was to reduce localized punching stresses on the mesh surface. The cable lashing design utilized limit equilibrium methods, incorporating hydrostatic and seismic loads. The ¾-in. diameter galvanized cable lashing segments were installed underneath (i.e., before) the wire mesh panels and connected to ¾-in. diameter galvanized wire rope anchors installed around the perimeter of both loose rock masses.

Draped Mesh

Between October 11 and December 23, 2025, the contractor installed the lower slope draped mesh, which also consisted of GeoBrugg Tecco G65/4mm mesh. This mesh was attached to a

horizontal galvanized ¾-inch upper support wire rope, threaded through wire rope anchors spaced generally 15 feet. This rope was "broken" at roughly 75 foot intervals, where three (3) wire rope anchors (WRAs) were drilled. Two (2) of these anchors were used to support overlapping ends of the horizontal cable. One (1) WRA, located between the two (2) end WRAs at every 75-foot interval, was used to attach a vertical galvanized 5/8-inch diameter wire cable for "pigtails" to allow lifting of the mesh for periodic cleanout. The contractor used a combination of the wheeled crane, Magni telescopic telehandler, and manlifts to hang the mesh (see Figure 11). The contractor attached the mesh on the horizontal cable using galvanized 0.75-inch screw pin shackles, and adjacent panels were seamed using T3 clips. The contractor then extended the 5/8-inch diameter cables below the bottom of the drape and constructed the pigtail loop for future mesh cleanout maintenance from below. Additionally, per the design, a bottom horizontal 0.625-inch diameter galvanized wire rope was added, attached to WRAs at the lower ends, and wrapped the mesh over the rope to create a hem.

Figure 11 - Installation of draped mesh using a crane and telehandlers (Scarptec 2025)

After installation of both the upper pinned and lower draped mesh, the additional lower 10 feet of the pinned mesh that had been temporarily folded up was folded down over the gap between the two wire mesh systems. The wire mesh over the gap was secured using T3 clips to the lower draped mesh.

Based on VTrans and ALC records, approximately 244,600 ft^2 of pinned and draped mesh was installed on the upper slope, including the OC-8 and OC-10 outcrop areas. We note at the time of publication, this amount has not been finalized and is approximate pending confirmation. Additionally, due to the roughness of the slope, approximately 48,500 ft^2 of additional mesh were placed compared with the 1996 mitigation.

CONCLUSIONS

This project highlights that rock slopes, especially those that include rock slope excavation to expose rock masses to natural weathering, will require monitoring and maintenance throughout their lifetime. The relatively geologically-young, resistant but fractured rock mass forming the Fairlee Palisades is an excellent example. Rock slopes are valuable assets, and should be treated as such, like bridges, embankments and other vital elements of transportation systems. Installation of mitigation such as mesh often "hides" the need for continual attention; mitigation only slows down the effects of erosion, and needs to be maintained and eventually redesigned and replaced once it no longer becomes effective. We recommend agencies and private institutions anticipate and program long-term capital budgets to include both monitoring & maintenance, and replacement costs.

REFERENCES

Baskerville, C.A., Lee, F.T. and Ratté, C.A., 1993. Landslide Hazards in Vermont. U.S. Geological Survey Bulletin 2043, 23 p. https://pubs.usgs.gov/bul/2043/report.pdf

Eliassen, T.D., 1997. Wire Mesh Netting of the Palisades, Interstate 91, Fairlee, Vermont. NESGE September/October Meeting, 13 p.

Eliassen, T.D., and Ingraham, P., 2000. Review, Rockfall Hazard Rating and Repair of Aging Interstate Rock Cuts in Northeastern Vermont. Proceedings: 51st Highway Geology Symposium, Seattle, Washington, p. 233-244 https://highwaygeologysymposium.org/wp-content/uploads/hgs_51-OPT.pdf.

Golder Associates Inc., May 5, 2019. Preliminary Rockfall Mitigation Design, Fairlee Escarpment Southbound Interstate 91, Milepost 92.7, Fairlee, Vermont, 33 p. https://vtrans.vermont.gov/sites/aot/files/FairleeRockfallMitigationDesign%20dated%205-10-19%20LINK.pdf

Hadley, J.B., 1951. Geology of the Bradford-Thetford Area, Orange County, Vermont. Vermont Geologic Survey, Bulletin No. 1, 36 p., 2 plates. https://anrweb.vt.gov/PubDocs/DEC/GEO/Bulletins/Hadley_1950.pdf

Moench, R.H., 1990. The Piermont Allochthon, Northern Connecticut Valley Area, New England – Preliminary Description and Resource Implications. Chapter J, U.S. Geological Survey Bulletin 1887, Summary Results of the Glens Falls CUSMAP Project, New York, Vermont and New Hampshire, p. J1-J23. https://pubs.usgs.gov/bul/1887/report.pdf

Moench, R.H., 2007. The Piermont allochthon revisited and redefined at its type locality: Discussion. Geological Society of America Bulletin, March/April 2007, v. 119, no. ¾, p. 493-499.

Post-Tensioning Institute, 2014. Recommendations for Prestressed Rock and Soil Anchors. PTI DC35.1-14, 110 p.

Spang, K. and Egger, P., 1990. Action of Fully Grouted Bolts in Jointed Rock. Rock Mechanics and Rock Engineering, vol. 23, no. 3, p. 201-229.

Ratcliffe, N.M., Stanley, R.S., Gale, M.H., Thompson, P.J., and Walsh, G.J., 2011. Bedrock Geologic Map of Vermont. U.S. Geological Survey Scientific Investigations Map 3184, 3 sheets, scale 1:100,000. https://dec.vermont.gov/geological-survey/publication-gis/VTrock

Vermont Agency of Transportation, November 13, 2007. Rockfall Hazard Rating of Rock Cuts on U.S. and State Highways in Vermont. Research Project RSCH010-974, 134 p. https://resources.vtrans.vermont.gov/documents/archivedresearch/2007%20-%2016%20(OCR)%20Rockfall%20Hazard%20Rating%20of%20Rock%20Cuts%20on%20US%20and%20State%20Highways%20in%20Vermont.pdf

Westerman, D.S., Eliassen, T.D., Finucane, R., and Wright, S.F., 2003. Highway Geology Symposium Field Trip Guide for Central Vermont, 54th Highway Geology Symposium, Burlington, Vermont, September 25, 2003, p. 3-7.

Wyllie, D.C., 2018. Rock Slope Engineering – Civil Applications, 5th ed., CRC Press, Boca Raton, Florida, 568 p.

13. Dynamic Performance Monitoring of a Rockfall Attenuator System

Darren Beckstrand, C.E.G.
Landslide Technology
9000 SW Gemini Drive
Beaverton, OR 97008
(503) 452-1200
darren.beckstrand@ccilt.com

Rachel Hunt, R.G.
Landslide Technology
9000 SW Gemini Drive
Beaverton, OR 97008
(503) 452-1200
rachel.hunt@ccilt.com

Evan Beyer, P.E.
Landslide Technology
9000 SW Gemini Drive
Beaverton, OR 97008
(503) 452-1200
evan.beyer@ccilt.com

Prepared for the 75th Highway Geology Symposium, September, 2026

Acknowledgements

The author(s) would like to thank the following individuals/entities for their contributions in the work described:

Nicholas Farney – Western Federal Lands
Douglas Anderston -Western Federal Lands (Retired)

Disclaimer

Statements and views presented in this paper are strictly those of the author(s), and do not necessarily reflect positions held by their affiliations, the Highway Geology Symposium (HGS), or others acknowledged above. The mention of trade names for commercial products does not imply the approval or endorsement by HGS.

Copyright Notice

Copyright © 2026 Highway Geology Symposium (HGS)

All Rights Reserved. Printed in the United States of America. No part of this publication may be reproduced or copied in any form or by any means – graphic, electronic, or mechanical, including photocopying, taping, or information storage and retrieval systems – without prior written permission of the HGS. This excludes the original author(s).

ABSTRACT

The Western Federal Lands Highway Division (WFLHD) commissioned an advanced dynamic instrumentation system to monitor two mid-slope rockfall attenuator systems along the Ketchum–Challis Highway corridor in central Idaho. These systems have experienced structural distress from heavy snow loads, rockfall, and avalanche impacts, resulting in bent posts, deformed base plates, broken wire ropes, and mesh panel failures. To quantify the loading mechanisms responsible and support future design optimization, WFLHD prioritized a high-resolution dynamic monitoring system capable of 20 Hz data acquisition.

Landslide Technology designed and installed the instrumentation system, equipping each attenuator's three to four posts with strandmeters on wire ropes, load cells on post anchors, and strain gauges near post bases to capture axial loads and bending strains under snow and avalanche loading. Campbell Scientific CR1000xe dataloggers and VWIRE 305 vibrating-wire analyzers enable capture of rapid load cycles from impact events. Each system is supported by 300 AmpHr of battery capacity and 800 W of solar input to sustain continuous high-frequency measurements.

Data transmits via 900 MHz radios to a base station within cellular coverage, then forwards to cloud-based platforms for near-real-time visualization of snow depth, wire rope loads, post strains, and site imagery. Threshold-exceedance rules trigger dynamic event recording in response to abrupt changes in measurements.

Landslide Technology completed installation in summer 2025, deploying a three-person SPRAT-qualified team with rope hauling systems to access the steep terrain. Monitoring is now underway, and the data collected will enable WFLHD to drive design improvements and develop more resilient rockfall and avalanche attenuation infrastructure.

INTRODUCTION

Rockfall hazards present a persistent challenge along mountainous highway corridors, where steep slopes, fractured rock masses, and seasonal environmental processes create ongoing risks to roadway users and infrastructure. Transportation agencies employ a range of mitigation measures to reduce these risks, including stabilization systems, draped mesh, rockfall barriers, and midslope rockfall attenuators. Among these, midslope rockfall attenuators serve as a flexible risk-reduction strategy that intercepts and dissipates rockfall energy while allowing controlled passage of debris downslope, reducing the likelihood of hazardous impacts reaching the roadway.

Despite their widespread use in the western US over the past 15 to 20 years, the performance of attenuator systems under real-world loading conditions remains poorly understood. Existing designs are generally based on engineering judgment, application of approaches for similar systems (draped mesh, flexible rockfall barrier), post-event observations, and design guidance from select DOT-sponsored research. Field measurements of actual loads generated by rockfall impacts, snow accumulation, and avalanche activity are limited. As a result, critical questions remain regarding the magnitude, distribution, and interaction of static and dynamic loads acting on attenuator components, particularly in environments subject to combined rockfall and snow-related hazards.

To address this knowledge gap, the Western Federal Lands Highway Division (WFLHD) initiated a field monitoring program along the Ketchum–Challis Highway (SH-75) corridor in central Idaho (Figure 1). The objective of this effort is to directly measure the structural response of midslope rockfall attenuators under operational conditions and develop a better understanding of the loading mechanisms that govern system performance. This paper presents the design and implementation of a high-frequency instrumentation system capable of capturing both static and dynamic loading events, and outlines the monitoring program, instrumentation approach, and anticipated applications of the resulting data for future attenuator design and resilience improvements.

Corridor Rockfall Assessment

WFLHD studied the geotechnical and geometric deficiencies on SH-75 between Stanley and Clayton. The narrow, two-lane highway experiences significant seasonal recreational traffic as one of the three routes into the Stanley basin. Like many of the interior Idaho highways, the route followed historical routes into the basin with minor improvements with each iteration from horse trail, to wagon road, to eventual highway. This existing highway does not feature modern ditches, shoulders, or clear zones. WFLHD’s process to focus on critical improvements identified a critical segment that exhibited high rockfall activity, suboptimal shoulders and ditches, and marginally stable embankments.

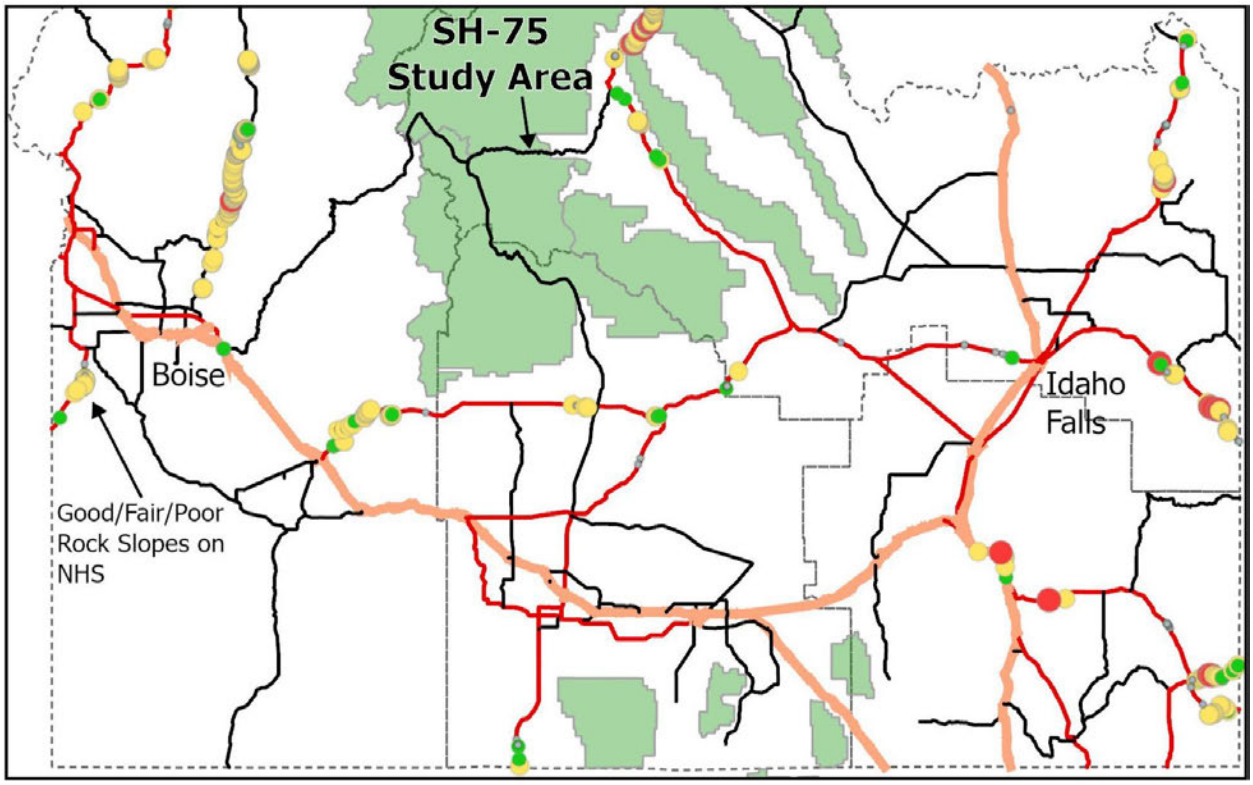

Figure 1 – Map of Southern Idaho with the Study Area Indicated.

The identified project corridor occupies a 1.3-mile segment of SH-75 (Forest Highway 26) in Custer County running between approximately Milepost 205.72 and 206.53 along the Salmon River canyon (Figure 2). Known locally as "The Narrows," the site is doubly constrained: the Salmon River, federally designated as a National Wild and Scenic River, borders the roadway on its downhill side, while steep rock slopes rise immediately from the uphill shoulder, leaving essentially no room to widen the fallout area or shift the alignment without incurring major river impacts or excavation. The corridor lies entirely within the Sawtooth National Recreation Area (SNRA), placing it under Forest Service jurisdiction and imposing visual quality objectives that restrict the range of mitigation options available and the aesthetic character of any installed systems.

The regional geology is dominated by the Idaho Batholith, a large intrusive complex composed principally of granodiorite. At the project site, the road cuts expose this granitic rock with highly variable jointing, with joint spacing ranging from a few inches to more than ten feet, and joints that vary from tight and closed to open and soil-filled. The combination of adverse joint orientations, weathering along discontinuities, and loss of soil matrix support in fractured zones creates persistent conditions for block instability and release. Overburden materials, where present above the cuts, consist of unconsolidated talus: angular rock fragments of variable size in a fine-grained soil matrix. As weathering and erosion progressively remove the binding soil, talus blocks are freed and can mobilize as rockfall. At the northern and southern ends of the project, glacial till containing large to very large boulders in a soil matrix presents a structurally distinct but equally active hazard, with boulders released as the supporting till is eroded by rain, snowmelt, and wind action. The regional seismic environment adds a further destabilizing

influence; the 1983 Borah Peak earthquake, magnitude 6.9, had its epicenter approximately 40 miles east of the project and the 2020 Stanley earthquake, magnitude 6.5, with its epicenter approximately 20 miles northwest of the project site; and is a reminder that episodic strong ground motion can mobilize otherwise stable blocks throughout the corridor.

The site is located within recognized avalanche terrain. Natural drainage and debris chutes bisect the rock cuts at multiple locations along the corridor, concentrating both rockfall and occasional snow avalanche runout onto the roadway. These chutes are a defining geomorphic feature of the site: they provide high-volume, channelized pathways for material from upslope source areas, including large outcrops with evidence of historical rockfall activity, focusing debris directly towards the roadway below (Figure 3).

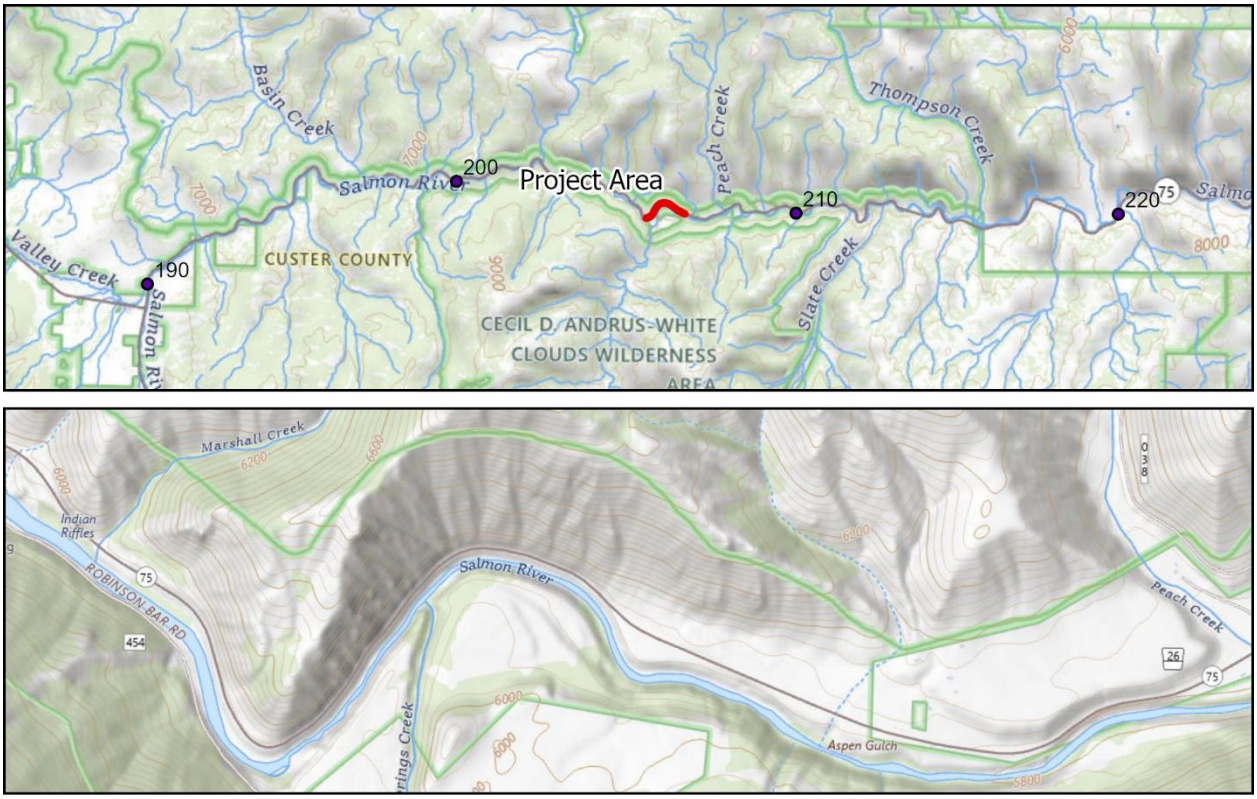

Figure 2 – Project Vicinity and General Site Map

Rockfall Mitigation Design and Construction

To facilitate design and construction, ‘The Narrows’ was subdivided into 15 individual slope management areas. This segmentation allowed site-specific characterization of rockfall source zones, slope geometry, geologic conditions, and hazard mechanisms along the corridor. Each slope was evaluated independently to determine the most appropriate combination of mitigation measures while maintaining continuity of protection along the highway.

The selected rockfall mitigation strategy employed a combination of active and passive measures tailored to the conditions present within each slope segment. Stabilization measures included rock scaling to remove unstable material and rock bolts to reinforce potentially unstable

rock masses. Passive containment measures included draped mesh systems, pinned mesh installations, and midslope rockfall attenuators designed to intercept and reduce the energy of falling rock before it could reach the roadway. The distribution and extent of these systems varied between slopes based on rockfall modeling, geologic mapping, and constructability considerations.

Figure 3 – 2011 Aerial Oblique of Debris and Avalanche Chutes Pre-Mitigation

In addition to the rockfall mitigation work, the project incorporated several roadway improvements intended to enhance safety and operational performance through the corridor. These improvements included roadway grade and geometric modifications to improve sight distance and vehicle maneuverability, as well as the construction of short retaining walls where space constraints limited the available roadway prism.

Mid-slope attenuator systems for the Ketchum–Challis project were designed following WSDOT design guidance, with their location and size based on the site investigation and rockfall trajectory modeling. Rockfall simulations were conducted using Rocfall v4.0 software at representative cross sections. The attenuator heights were short, with 5-foot posts, to both reduce the visual impacts in the Sawtooth National Recreation Area and to reduce the potential load from potential snow avalanches.

The project was constructed between 2013 and 2015. The initial phase of the project constructed two attenuator systems with the goal of understanding their performance in high

snow loads. The first winter was a very low snow year and the systems did not experience high loads. The second phase of the project installed the remaining attenuator systems.

AVALANCHE DAMAGE EVENT AND REPAIRS

The winter of 2016–2017 was characterized by an extended sequence of heavy snowfalls followed by rapid warming events that produced widespread natural avalanche activity throughout central Idaho. The snowpack set the 30-year trend curve for the region (Figure 4). Snow depth on site was estimated to be 6 to 8 feet. Idaho Transportation Department records document repeated closures of SH-75 beginning on January 9, 2017, with additional closures on January 11, February 8, and February 9 as unstable snow conditions persisted. By mid-February, a regional avalanche cycle forced prolonged closures between Stanley and Clayton after multiple large natural avalanches reached the roadway, with national news reports describing residents stranded for several days by deep avalanche deposits. These events damaged several mid-slope attenuators; damage included broken support ropes, bent posts, and complete loss of several attenuator installations (Figure 5). Wildlife activity is suspected to have been a potential trigger, evidenced by animal carcasses tied up in the rockfall mitigation.

Overall, the static and dynamic load damage to the attenuators resulted in four destroyed nets and eight more systems significantly damaged. Emergency funding for repairs was sought and provided via FHWA and the Idaho Transportation Department. Repairs were designed and implemented in the years that followed.

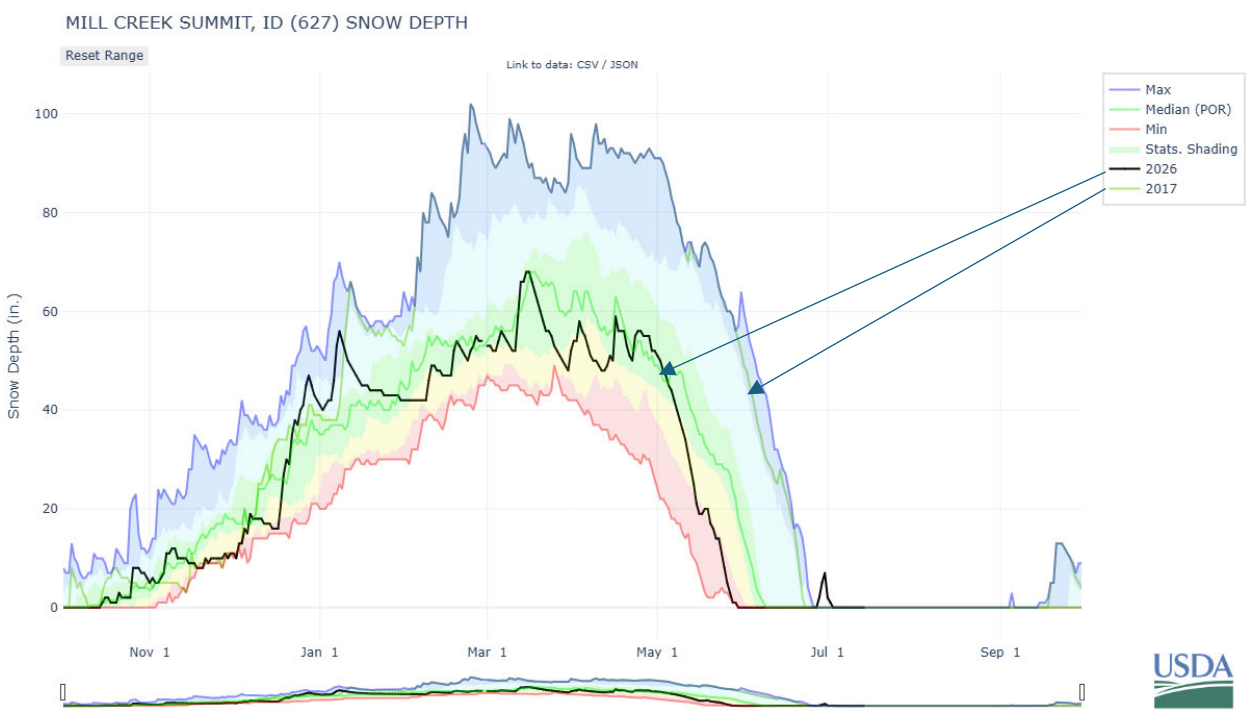

Figure 4 – Snowpack Depth at the Nearest Snotel Site 17 miles NNE of The Narrows. Note that Snowpack Depth in 2026 at the Attenuator Site was Under One Foot All Winter.

a

b

c

d

e

f

g

h

Figure 5 – Photographs of Typical Avalanche Damage, February 15, 2017 (a, b, c, & d) and from Later Detailed Repair Design Reconnaissance (e, f, g, & h). All Photos from WFL.

Damage patterns varied according to slope geometry and vegetation conditions. Attenuators located below steep, sparsely vegetated chutes ranging from approximately 45 to 55 degrees experienced the most severe impacts. In these locations, large snow avalanches activated substantial portions of the systems simultaneously, resulting in the complete removal of attenuator nets, broken support ropes, and permanent deformation of posts and connection hardware. This more severe damage may be attributed to the avalanche impacts. In contrast, systems installed on shallower slopes with limited vegetation cover generally remained in place but exhibited a distinct "shower curtaining" failure mode. These failures were characterized by localized detachment and downslope sagging of the attenuator mesh, accompanied by bent posts and damaged hardware. These less severe damages may be attributed to static snow loading.

Field investigations of the damaged systems identified several recurring component-level failure mechanisms. One common mode involved failure or detachment of the support rope at the post connection, resulting in loss of support for the attenuator mesh and rapid degradation of the system's load-carrying capacity. Another frequently observed mechanism was failure of the lacing rope connecting the attenuator mesh to the support rope. Once the lacing rope severed, the mesh progressively detached from the support structure, producing the characteristic "shower curtaining" configuration. Continued loading after this initial failure often led to redistribution of forces to adjacent components, accelerating damage and, in some cases, culminating in partial or complete loss of the attenuator net.

Damage Repairs

Repairs implemented following the February 2017 avalanche damage focused on strengthening components that exhibited the most severe distress during post-event inspections. Observations of broken support ropes, failed anchor connections, and deformed hardware indicated that critical load paths within the attenuator systems had been overloaded during large avalanche and snow-loading events. To increase system resilience, the attenuator net support rope was upsized from 3/4 in. to 1 in. diameter, increasing the ultimate capacity of the wire rope from 58 kips to 103 kips. Connection hardware was similarly strengthened throughout the system. Intermediate post connection plates were enlarged from 1/2 in. thick to 1 in. thick. Swivel diameters were increased from 7/8 in. to 1 in. In addition, intermediate post plates and swivels were standardized to match the larger end-post specifications, eliminating weaker components within the load path and with the goal of providing more uniform load transfer throughout the attenuator system.

Additional modifications addressed failure mechanisms associated with mesh detachment and post-damage. Because lacing rope failures were frequently observed as a precursor to the "shower curtaining" failure mode, the lacing rope diameter was increased from 5/16 in. to 9/16 in., and the connection details were redesigned to provide a more robust loop attachment between the mesh, support rope, and end posts. New corner cables were also incorporated to improve load distribution and reduce stress concentrations near system boundaries. Where damaged posts required replacement, oversized post anchorage plates were developed to allow upgraded post assemblies to be retrofitted onto the existing concrete foundations without complete foundation reconstruction. Collectively, these repairs represented a performance-based redesign effort that used field observations from the avalanche-damaged systems to target the

components most susceptible to overload and improve the overall robustness of the attenuator installations.

Actual loads experienced by the systems were not measured and are not available from the manufacturers. This performance methodology has been effective in the years since reconstruction in 2019 and 2020; however the lack of actual static and dynamic load data and a heavy snow year highlights the need for real-world observations that can inform design.

STUDY MOTIVATION AND PROJECT OBJECTIVES

The extensive damage sustained by the attenuator systems highlighted a significant knowledge gap regarding the actual loads imposed on mid-slope rockfall attenuators under real-world conditions. While design methodologies and manufacturer guidance provide a basis for evaluating rockfall performance, little empirical information exists regarding the magnitude and distribution of loads generated by sustained snow accumulation, dynamic rockfall impacts, or the combination of static and dynamic loading acting simultaneously. Following the avalanche-related failures, repairs and component upgrades were necessarily based on engineering judgment and observed performance because no field data were available to quantify the forces responsible for the observed damage. Consequently, the relationship between loading mechanisms and system response remained poorly understood, limiting the ability to optimize future attenuator designs or confidently assess the adequacy of proposed repairs.

Note that it is likely that each system will experience variable loads and react in a complex manner, with mesh-ground surface interface friction, slope angle, snow density, and frozen and non-frozen interfaces, being variables that will change system to system and winter to winter. These variables cannot be controlled nor fully defined or accounted for during system design.

To help address these uncertainties, WFLHD initiated a study focused on quantifying the real-world loads experienced by a system. The primary objectives were to establish an understanding of static snow loading, capture the magnitude and characteristics of dynamic loading events associated with rockfall and avalanches, and evaluate how combined loading conditions influence system behavior. Ultimately, the collected data are intended to support the development of improved design guidance, more resilient component specifications, and performance-based approaches for attenuator systems installed in demanding mountain environments. The project was structured in two phases. Phase 1 focused on identifying critical performance parameters, evaluating instrumentation technologies, and developing a monitoring strategy capable of capturing both static and dynamic responses. Phase 2 involved field reconnaissance, final instrumentation design, installation of the monitoring systems, and long-term data collection to document attenuator performance under actual environmental loading conditions.

PHASE 1: INSTRUMENTATION SYSTEM DESIGN

Phase 1 focused on developing a monitoring framework capable of quantifying the loads and structural responses associated with static snow accumulation, dynamic avalanche loading,

and dynamic rockfall impacts. The primary objective of Phase 1 was therefore to identify the important structural and environmental parameters to monitor, evaluate available instrumentation technologies, understand sensor and datalogging limitations, power requirements, and communication requirements, and develop cost estimates for a variety of monitoring approaches capable of operating in the challenging conditions of the corridor.

A key outcome of the Phase 1 effort was the identification of measurement targets necessary to characterize both the loads applied to the attenuator systems and the resulting structural response. The monitoring program was designed to capture wire rope loads through the installation of strandmeters on the primary support ropes, designated as the B, C, and F ropes within the attenuator system (Figure 6a). Structural response was to be measured through strain monitoring at critical locations near the base of the posts, including both the post flanges and base plates where significant bending stresses had been observed following previous avalanche events. Anchor loads were identified as another critical parameter because post-anchor connections represented one of the primary load-transfer mechanisms within the attenuator structure (Figure 6b). In addition to structural measurements, environmental monitoring was incorporated to provide context for loading events. Snow depth and temperature measurements were included to establish relationships between seasonal snow accumulation and system response, while site imagery was recognized as essential for correlating instrument readings with visible deformation, avalanche activity, and rockfall events (Figure 6c and 6d). Manufacturer-supplied notification systems were considered but were not installed either due to lack of cellular signals or a lack of compatibility between attenuators (meant to redirect rock) and the design intent of flexible rockfall barriers (meant to stop rock). Layout of the sensors on one of the systems is shown on Figure 7.

Figure 6 – Images of Strandmeters (a), Load Cells (b), the Camera (c), and Snow Depth Sensor (d).

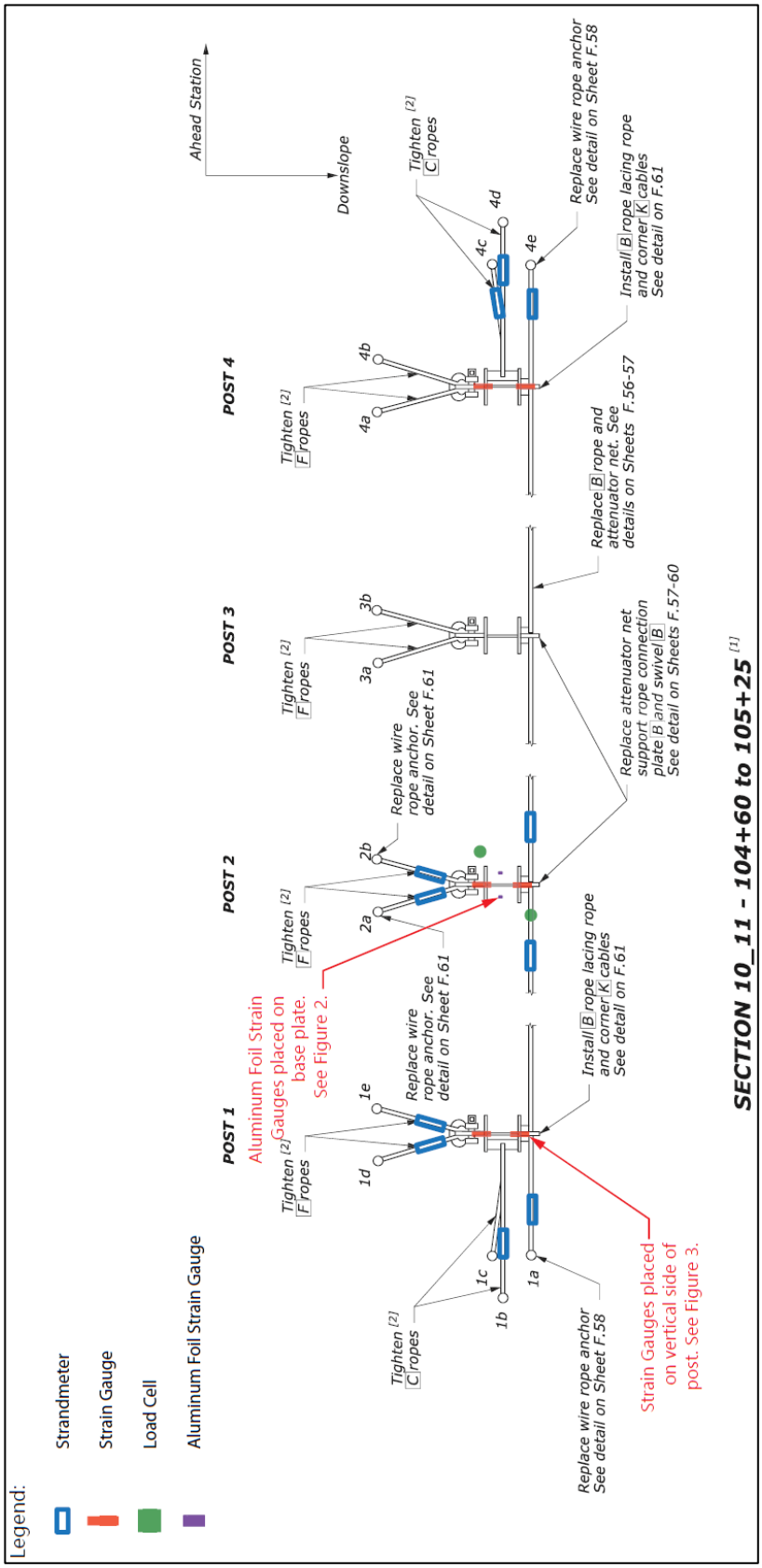

Figure 7 – Sensor Layout on one of the Attenuator Systems.

A component of the study involved evaluating the requirements of the static and dynamic monitoring approaches and determining the level of data acquisition required to satisfy project objectives. The static approach relied on measurements collected at intervals ranging from approximately one to thirty minutes and was intended primarily to document gradual changes associated with snow accumulation and seasonal loading. While relatively simple to implement, the passive system lacked the ability to capture short-duration loading events such as rockfall impacts or avalanche strikes. The active monitoring approach incorporated high-frequency sampling at rates up to 20 Hz, enabling direct measurement of transient loading events and rapid structural responses. Although the dynamic system imposed substantially greater demands on power supply, data storage, communications, and programming complexity, Phase 1 concluded that dynamic monitoring would be required to address the response from the damage event's primary cause.

Phase 1 also established the framework for data acquisition, communications, and data management. A Campbell Scientific, Inc. (CSI) datalogger platform was selected as the foundation of the monitoring system because of its compatibility with vibrating-wire instrumentation and its ability to support both static and dynamic measurements via various peripherals. Dynamic vibrating wire measurements require specialized interface, the system incorporated CSI's VWIRE 305 vibrating-wire analyzers, which continually 'pluck' the vibrating wire allowing data collection at a 20Hz cadence. CSI's CR1000xe datalogger was capable of reading the resistance-based load cells and strain gauges at 20Hz.

The project corridor lacked reliable cellular service. Therefore, a radio telemetry network was required to transmit data from the attenuator sites 9.5 miles east to reliable cellular service. The communications system was designed to upload data hourly during daylight hours while transmitting site photographs twice daily to provide visual confirmation of site conditions.

The study concluded with a list of options to facilitate budgeting and decision-making for WFL, including various options for static, dynamic, or a combination of monitoring approaches.

PHASE 2: SITE SELECTION AND INSTALLATION

Following completion of the Phase 1 planning effort, two attenuator systems were selected by WFL for dynamic instrumentation based on their history of snow loading, avalanche exposure, and observed structural distress. The selected monitoring locations included Sections 5–6 and 10–11, both of which experienced damage during the winter of 2016–2017 and represented different combinations of slope geometry, avalanche exposure, and rockfall activity. An initial site reconnaissance was conducted in October 2024 to evaluate installation logistics, identify suitable sensor locations, establish datalogger and solar panel locations, and assess communications feasibility.

Radio testing demonstrated that direct communication between the instrumented attenuators and cellular service locations within the valley was possible, but vulnerable to signal deterioration due to terrain shielding and the narrow geometry of the Salmon River canyon (Figure 8). The testing demonstrated that high-power, 1-watt radios and Yagi directional

antennas were required in all configurations. The project team tested a repeater-based telemetry strategy that utilized a ridge-top relay station positioned above the corridor, but the repeater position was not available due to permitting issues. This direct configuration provided nearly line-of-sight communication between the attenuator systems and the base station while allowing the repeater to communicate with a lower-elevation base station located within cellular coverage. The resulting communications configuration ensured that high-frequency monitoring data could likely be transmitted reliably from the remote attenuator sites while designing power supplies for the higher power consumption. Note that the selected option provided reliable, but slow, remote communications.

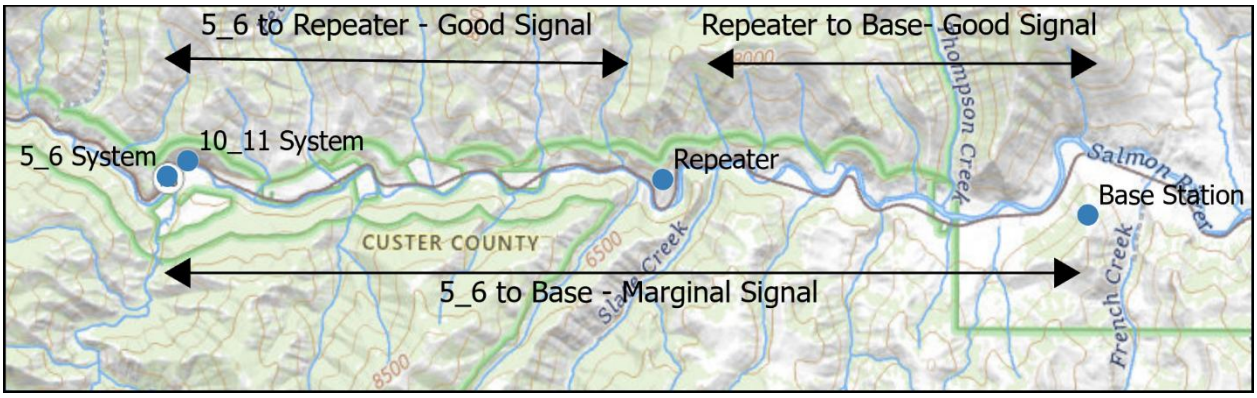

Figure 8 – Radio Path Testing Results

Installation

Installation of the monitoring system presented significant logistical challenges that ultimately became one of the defining aspects of the project. Phase 1 estimated that helicopter support would be required for installation. However, helicopter availability in the intermountain west during summer fire season proved to be difficult to secure. During Phase 2 planning, the use of a boom lift to facilitate transportation of equipment and installation of instrumentation on the attenuator structures was anticipated. However, the steep terrain, limited roadway geometry, required lift height, and restricted access conditions prevented practical deployment of lift equipment at the selected locations, with the boom lift topping out about 20 feet from the minimum required height and offset. Once field operations began, it became clear that virtually all equipment, tools, and construction materials would need to be transported manually from the roadway to the instrument locations using rope-haul systems. This dramatically increased the complexity and difficulty of the installation effort and required quick adaptation to safely move heavy equipment through the steep and exposed work areas (Figure 9). Additional traffic control and personnel were required for this adapted operation.

The materials required for the instrumentation system were substantial. Each attenuator installation included large-capacity battery banks, weatherproof instrumentation enclosures, solar power systems, dataloggers, radio equipment, and hundreds of feet of instrumentation cable. Individual battery assemblies weighed approximately 130 lb (59 kg), instrumentation enclosures approached 75 lb (34 kg), and numerous 60-lb (27 kg) bags of concrete were required for equipment foundations and support structures. Solar panels, steel mounting hardware, and more than 1,000 ft (300 m) of instrumentation cable also had to be transported to locations situated

well above the roadway on steep, loose slopes. Moving these materials required the use of the mechanical rope-haul systems, multiple hauling stages, and coordinated effort among the installation team. In many cases, equipment was raised incrementally up the slope using anchored hauling systems before being repositioned and hauled again to reach its final installation location. All rope access was supervised by our SPRAT-qualified geotechnical personnel.

a b

Figure 9 – Boom Lift Proving Insufficient (a) and Rope Haul System Implementation with a 130 lb. Battery (b)

Following equipment mobilization, sensors were installed and datalogger enclosure posts prepared. Strandmeters were mounted directly to selected support ropes and configured to measure elongation associated with changes in rope strain. Installation required fabrication of custom attachment assemblies and careful positioning to avoid lacing wire conflicts. Vibrating-wire and resistance strain gauges were bonded to post flanges and base plates at locations selected to capture bending strains generated by snow loading and impact events. Surface preparation, gauge alignment, strain gauge shields, and cable routing were critical to minimal potential damage in the rockfall-prone chutes. Sensor cables were installed on the downhill side of the attenuator top ropes to minimize rock strike chances. Sensor cables were secured to the mitigation elements when possible.

Each monitoring station was supported by a dedicated 800-watt solar array and a 12V battery system with 400 ampHr capacity designed to sustain continuous operation throughout the winter months. Each system installation incorporated two weatherproof equipment enclosures housing dataloggers, vibrating-wire analyzers, radios, and power management components. Solar arrays were sized to maintain battery charge during periods of reduced winter sunlight while supporting continuous monitoring, cameras, high-power radios, and continuous high-frequency sensor interrogation (Figure 11). Given the project's location within the Sawtooth National Recreation Area, special attention was paid to the visual appearance of the installations. Equipment locations, mounting configurations, and enclosure finishes were selected to minimize visual impacts and maintain compliance with environmental and aesthetic requirements established for the corridor.

Figure 10 – Anchor Load Cell (left), Top Rope Strandmeter (middle), VW Strain Gauge (right)

The remote base station was installed on a ridgeline outside of the SNRA to manage communications and data transmission from the remote monitoring sites. Data transmitted from the attenuator sites were routed to a ridgeline base station equipped with a cellular modem, enabling automated upload of monitoring data to cloud-based servers. This architecture allowed near-real-time access to instrumentation data while maintaining reliable operation in an area with limited communications infrastructure. Upon completion of installation, the system provided continuous monitoring of attenuator loads, structural response, environmental conditions, and site imagery, establishing one of the first high-frequency monitoring programs dedicated to understanding the real-world performance of midslope rockfall attenuators.

Figure 11 – Wiring on System 10_11 (left) and Solar Array on 5_6 (right)

DATA AND EVENT OBSERVATIONS

Hourly and dynamic data are available to WFL on an interactive website, with data uploaded hourly during daylight hours (Figure 12). Dynamic data is stored and written to tables when an event is sensed; any reading change that surpasses 10% of the sensor's full scale range. Roughly, this is about a 6,000 lb load change in the strandmeters and load cells. When a dynamic is detected, the dynamic 20 Hz data are stored from 30 seconds before the event and then 180 seconds thereafter. The plots are automatically updated and plotting in the website once data are uploaded to the cloud server. Emails with the current weekly readings are sent each Monday morning. Photos are obtained at 8am and 4pm and updated on the website automatically.

Annual Trends

The winter of 2025-2026 showed exceptionally low snow, thus moderate or major static snow loading was not experienced or measured by the monitoring systems. However, when snowfall was experienced with a visual build-up on the draped mesh portions, the system did exhibit clear reactions that quickly dissipated as snow melted (Figure 12).

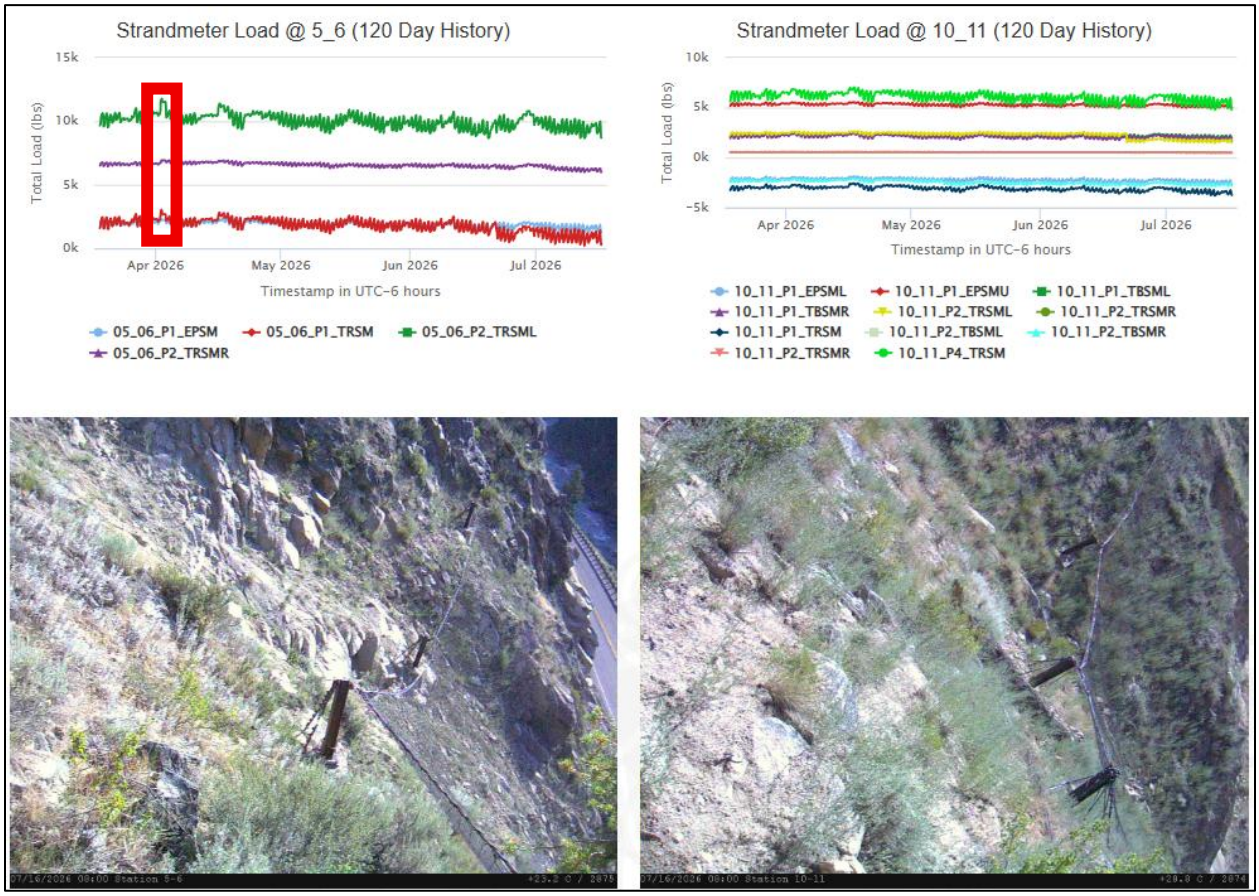

Figure 12 – Snippet of the Website and Twice-Daily Site Photographs. Red Box on the Left Highlights a System Reaction to a Slight (<2-inches) Snowfall.

Dynamic Events

Several dynamic events have been recorded at System 10_11, primarily at the onset of cold winter weather and repeat freeze-thaw cycles. A noteworthy one occurred October 24, 2025 at 11:39 AM. This event is interpreted to consist of a sequence of six to seven distinguishable sub-events occurring over approximately three minutes. The event was recorded at the 20 Hz sampling rate following threshold exceedance in a strandmeter installed on the right tieback of the system's second post. The triggering response corresponded to an instantaneous load increase of approximately 6,000 lbs at Event 2, with a smaller Event 1 recorded before the trigger event. Load changes in the tieback wire ropes were maintained for brief periods while load changes in the top ropes reverberated through the rope before returning to near its base load. Base plate strain gauge only slightly changed during the first four events. Event 5 reduced loads on the tieback and increased loads on the base plate on the right, uphill side of the base plate while reducing load on its downhill left side. Events 4 through 6 reduced tieback loads with some reverberation on the top rope, with 5 and 7 seeing load increases and drops on the baseplate, suggesting a debris release between events 4 through 7.

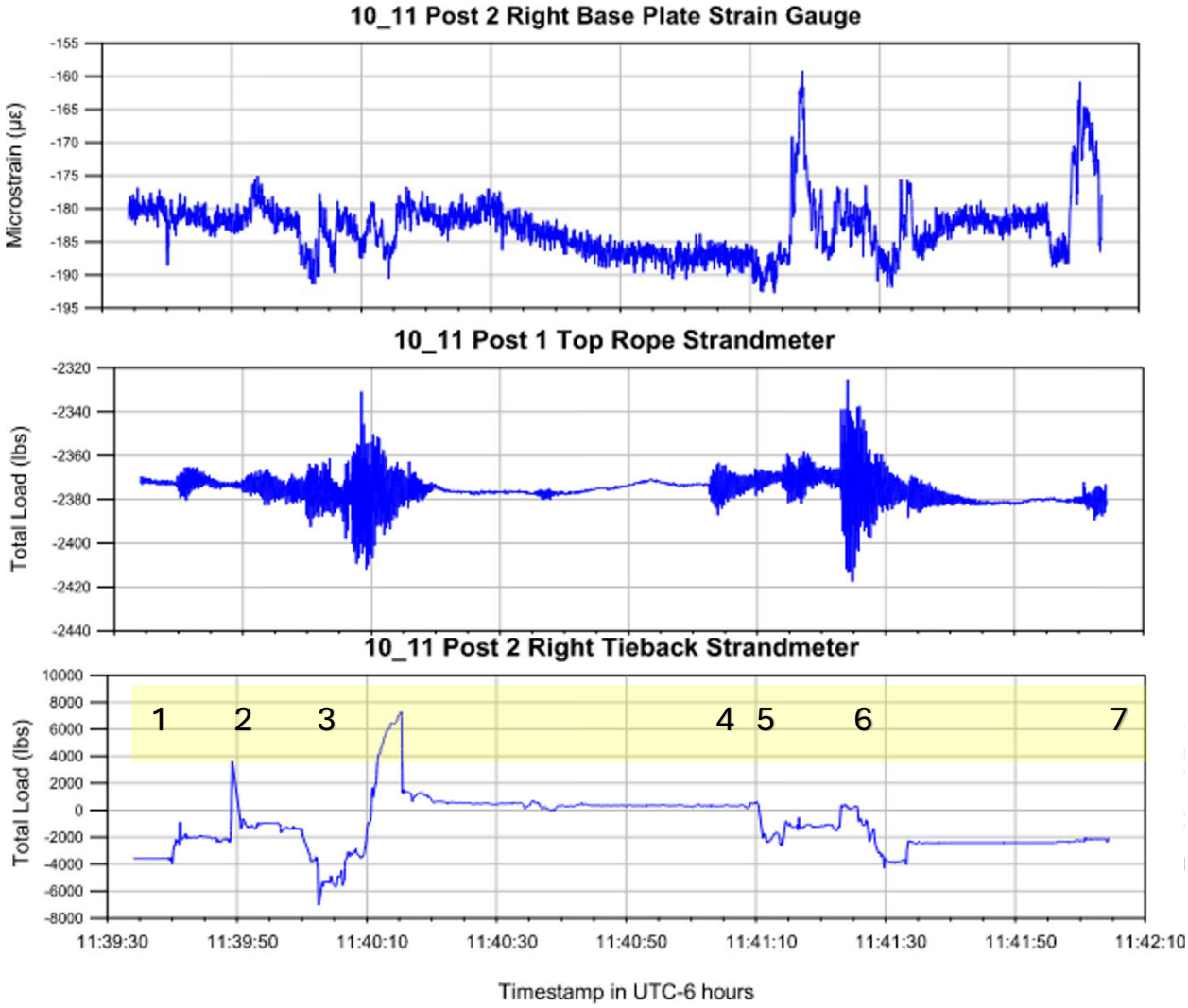

Figure 13 – Example of a Dynamic Event on a Base Plate (top), a Reverberation Response on the Top Rope (middle), and a Large (~12,000 lbs) Load Increase on a Tie Back (bottom).

DISCUSSION & NEXT STEPS

The monitoring data collected to date demonstrates that the instrumented attenuator systems are capable of capturing and differentiating dynamic loading events that would otherwise go unobserved. Even relatively small, sub-threshold rockfall events produce measurable responses throughout the system, with distinct load patterns observed between support ropes, tieback ropes, and post elements. Individual impact events have generated instantaneous load changes exceeding 10,000 lb in single components, providing direct measurements of dynamic load transfer within an operational attenuator. The data also suggest that, despite very low snowfall in the first winter, seasonal snow accumulation imposes a measurable static preload on the system, indicating that the most critical loading condition may involve dynamic impacts occurring while structural components are already subjected to significant static forces.

Although the monitoring program has already provided valuable insights into attenuator behavior, several important questions remain. The instrumentation system does not directly measure rock size, impact velocity, or trajectory, limiting the ability to correlate measured loads with specific rockfall characteristics. Likewise, the system has not yet experienced a major winter avalanche event nor significant static loading, preventing evaluation of the loading conditions believed to have caused the 2016–2017 failures. The two-winter monitoring program currently underway will continue to expand the dataset, supporting future analysis. If the upcoming winter season doesn’t produce large snowpacks, the monitoring period may be extended.

Following completion of data collection and analysis, a potential Phase 3 would focus on translating the monitoring results into practical design improvements. This phase would use the measured static and dynamic load data to evaluate existing design assumptions, identify vulnerable components, and develop recommendations for revised component capacities, connection details, anchorage requirements, and system configurations. The ultimate objective would be to incorporate field-validated performance data into future attenuator design guidance, resulting in more resilient systems capable of accommodating the combined effects of rockfall, snow loading, and avalanche activity in mountainous transportation corridors.

14. Rockfall Wall Catchment Systems in Colorado

Ben Arndt, PE, PG
ben@rj-eng.net
RJ Engineering and Consulting, Inc
3082 Evergreen Parkway, Suite E
Evergreen, CO

Prepared for the 75th Highway Geology Symposium, September 2026

Acknowledgements

The author would like to acknowledge Nicole Oster-Mapes at the Colorado Department of Transportation (CDOT) and Andrew Knapp (formerly at CDOT) for providing opportunities to mitigate rockfall sites with different ideas and methods.

Disclaimer

Statements and views presented in this paper are strictly those of the author(s), and do not necessarily reflect positions held by their affiliations, the Highway Geology Symposium (HGS), or others acknowledged above. The mention of trade names for commercial products does not imply the approval or endorsement by HGS.

Copyright

Copyright © 2026 Highway Geology Symposium (HGS)

All Rights Reserved. Printed in the United States of America. No part of this publication may be reproduced or copied in any form or by any means – graphic, electronic, or mechanical, including photocopying, taping, or information storage and retrieval systems – without prior written permission of the HGS. This excludes the original author(s).

ABSTRACT

For many rockfall prone sites next to roadway corridors, a typical rockfall fence or attenuator may not be practical or efficient for containing or mitigating rockfall. Additionally, rockfall fences and attenuators may require extensive repair or maintenance after repeated impacts.

In certain instances, rockfall wall containment systems have been used in Colorado where a higher impact energy system may be needed, or the roadway ditch width is limited (but wide enough to accommodate vertical faced systems). The intent is to have a more resilient rockfall system than may partially or fully restore the raveling slope to a stable angle over time and are slender enough to fit within the roadway width requirements.

This presentation illustrates multiple case histories of rockfall wall containment systems in Colorado. These systems function to absorb energy impacts, fit within the catchment shoulder of the roadway, and are designed to restore raveling rockfall prone slopes to more resilient stable angles.

INTRODUCTION

The paper is an overview of a basic concept for mitigating rockfall along roadway corridors that were originally constructed before the slope geology was considered and how slope cuts would erode and become long term maintenance issues. In the years between 1940 and 1980, cut slopes along steep mountainous roadway corridors have experienced long-term maintenance and realignment issues where the slope cut was steeper than the angle of repose and/or have eroded significantly with ever present rockfall.

One factor in evaluating cut slopes is to look at natural slopes within these mountainous roadway corridors and, at least in Colorado, many of these corridors have talus slopes that are reasonably stable. This is typically illustrated where lichens are evident of the surfaces of the talus rocks indicating these rocks have not moved for decades or even centuries. Figure 1 is an example where the left side of the talus slope is intact, but the right side of the talus slope has displaced downward. This is evident by the talus slope color differences. The left side has various lichens that are darker, but the right side is lighter colored rock that has moved in recent times. This was an example where the toe of the talus slope was removed and/or disturbed on the right and the entire talus mass began to move downward into the roadway. These slope angles are typically between 33 to 36 degrees and if they are changed even by 1 degree steeper, they begin to move and are no longer stable.

Figure 2 is an example where a small-scale talus slope is supported by a wall feature to stabilize the slope to the angle of repose and match the original slope prior to construction of the roadway. Figure 2 essentially captures the concept of attempting to re-establish the natural slopes to the pre-highway angle of repose and make the rockfall mitigation system more resilient and less of the constant maintenance issue to clean and maintain a system.

Figure 1 – Existing Talus Slope in Colorado. Left (darker colored) side is non-displaced talus. Right (lighter colored) side is an example where the toe was disturbed and triggered the entire slope to move downhill to re-establish the existing angle of repose.

Figure 2 – Talus Slopes in Colorado where a small rockery wall is stabilizing the natural slope.

CASE HISTORY PROJECTS

Interstate I-70 – Glenwood Canyon – Glenwood Springs, CO

Interstate I-70, which is a major roadway system that bisects Colorado east to west, and has various cut sections that are examples of not considering the geologic effects of cutting a slope to fit a four-lane interstate highway widening during the 1960's and 1970's. This eventually created long-term erosional and stability issues. Figure 3 is an example just west of Glenwood Springs Colorado in which gabion baskets were stacked in an effort to stabilize a natural talus type slope in the late 1960's. The resulting tiered gabion baskets have subsequently failed and become long-term maintenance issues shortly after construction.

Figure 3 – I -70 near Glenwood Springs, CO with tiered gabion system to stabilize the cut slope.

Figure 4 depicts the original design plans that illustrate the natural slope that was at the angle of repose and the tiered gabion system that was placed.

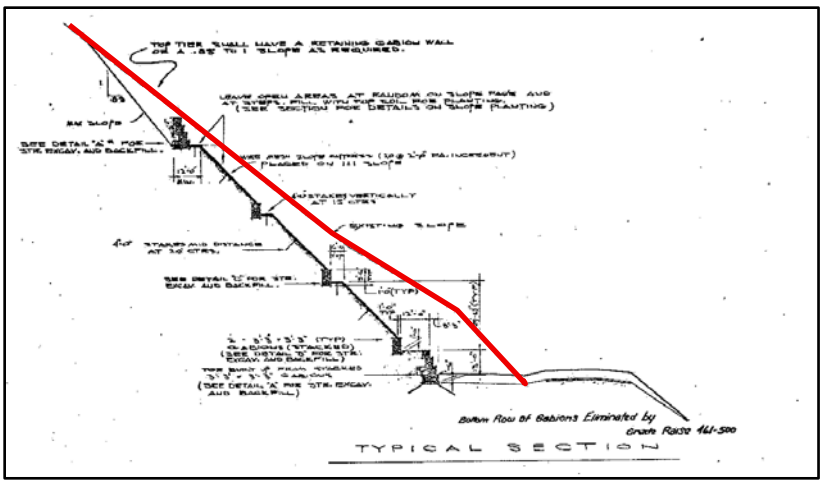

Figure 4 – I -70 near Glenwood Springs, CO original Project Plans with tiered gabion system in an effort to stabilize the cut slope. The red line was the original slope at the angle of repose, and the tiered gabion system is much steeper.

We were provided the opportunity to evaluate and mitigate one smaller section of the raveling and unstable cut slope in this section of I-70 that was prone to rockfall rolling out over a bike path and into the lanes of I-70. The evaluation and design eventually used a double-sided vertically faced wire wall system that was designed to mitigate rockfall and eventually fill in and mimic the natural slope angle that was in place prior to the slope cut.

Figure 5 depicts a generalized rockfall section that illustrates the location of the tiered gabion baskets, some of which at the lower section were completely buried. Rockfall modeling and field evidence suggested significant rockfall on the bike path and out into I-70. Figure 6 is an example of modeling the slope in filling with talus materials, to recreate the natural slope before the I-70 widening.

Figures 7 and 8 depict the construction using a shoring wall to support the existing slope and the completed vertically faced rockfall containment system that will eventually fill in creating a slope slightly less than the angle of repose.

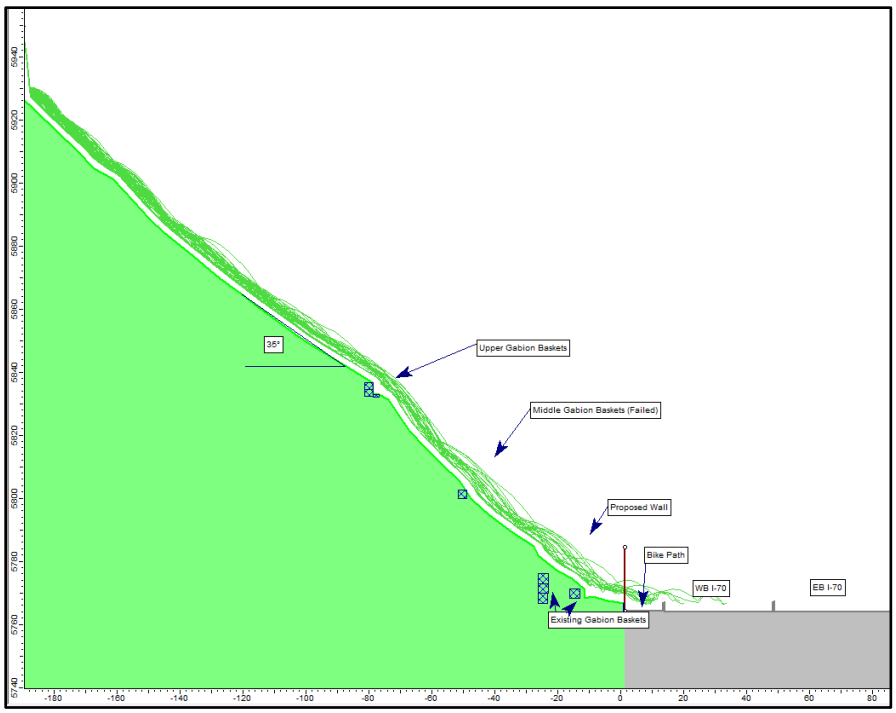

Figure 5 – I -70 near Glenwood Springs, CO. Rockfall model of the tiered gabion system that was filling in and not effective at slope stabilization or rockfall containment.

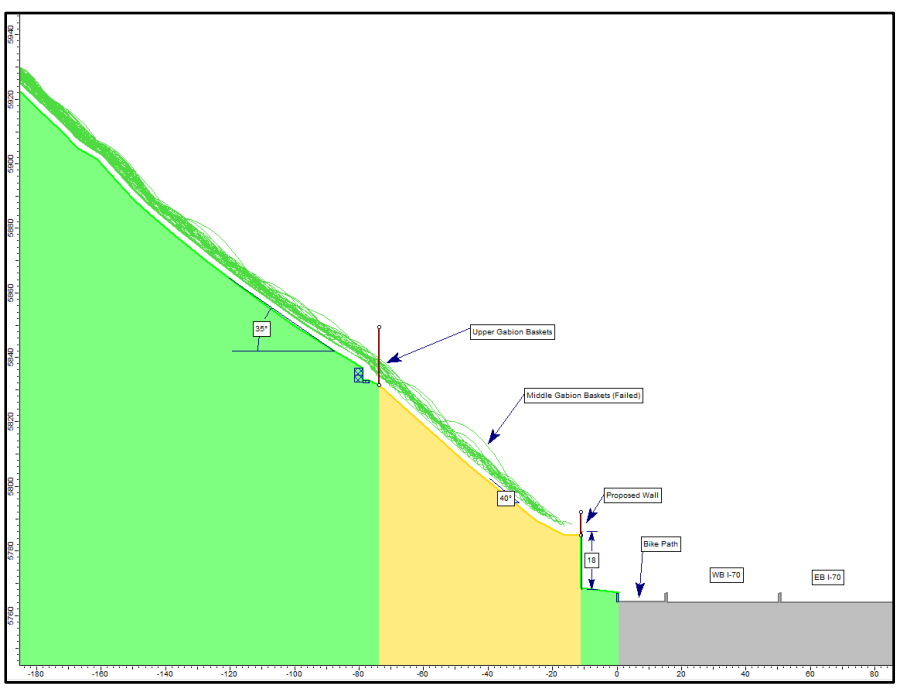

Figure 6 – I -70 near Glenwood Springs, CO. Rockfall model of vertical wall system at base of slope in the process of filling in to create a slope at the angle of repose.

Figure 7 – I -70 near Glenwood Springs, CO. Construction of the double-sided wire vertical faced rockfall containment wall. Soil nail wall is located behind and out of view.

Figure 8 – I -70 near Glenwood Springs, CO. Final construction of the double-sided wire vertical faced rockfall containment wall.

CO 133 – Penny Hot Springs – Redstone, CO

CO 133 is another example of the slope being cut steeper than the angle of repose to accommodate a roadway. Figures 9 and 10 are examples of the slope that the toe was cut out of an existing talus slope to accommodate the roadway alignment prior to the 1970's. Since then, the cut slope has been a constant erosional and maintenance problem for CDOT.

Figure 11 is an example of a talus slope that was located across the river valley that was in a natural slope condition at the angle of repose that is relatively stable and has lichen growing on the individual boulders.

Figure 9 – CO 133 slope cut into talus slope forming a long term erosional and maintenance issue.

Figure 10 – CO 133 slope cut into talus slope forming a long term erosional and maintenance issue.

Figure 11 - CO 133 is an example of a talus slope that was located across the river valley that was in a natural slope condition at the angle of repose.

Figure 12 depicts the vertically faced rockfall concrete block system that was constructed at the site. The characteristics of the rockfall at the site resulted in lower rockfall energy levels and overall smaller rockfall diameters making it possible to use a rigid concrete block in lieu of a flexible deformable facing. The use of the concrete elements also expedited construction and provided for a safer construction timeline in which larger equipment was used to place the blocks

limiting exposure of workers to rockfall. The intent of the concrete block wall is to allow the back (cut) side of the wall to fill in over time, to eventually create a talus slope that will mimic the natural slope that was in place prior to the roadway construction.

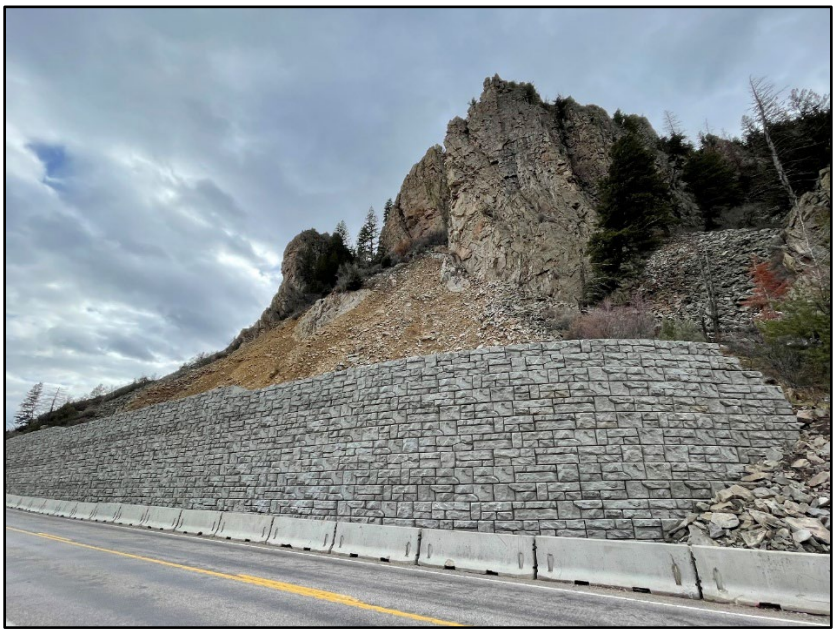

Figure 12 – CO 133 slope cut with block wall that will eventually fill in to mimic the natural talus slope.

US 550 –Deer Creek – Silverton, CO

US 550 at Deer Creek is yet another example of cutting the slope of a proposed roadway into an existing slope that was at the angle of repose. Figures 13 and 14 are examples of the slope that was completely removed from an existing talus slope which resulted in a constant erosional and maintenance problem for CDOT.

Figure 13 –US 550 Deer Creek. Slope that was cut to accommodate roadway leaving an over steepened erosional rockfall prone slope.

Figure 14 –US 550 Deer Creek. Side view of slope that was cut to accommodate roadway leaving an over steepened erosional rockfall prone slope.

US 550 was like other slopes except that it was excavated so far back into the original slope that it required the very top (which formed an almost vertical slope face) to be flattened as part of the mitigation. The mitigation for the slope also consisted of a vertical wire faced deformable wall.

Figure 15 is a general depiction of the slope with a typical rockfall from the source area. Figure 16 is the proposed vertical faced wire system which will fill in over time. Figure 17 depicts the generalized rockfall impacts to the wall system using a finite element model to estimate deformation and outward deflection. Figure 18 depicts the completed wall system.

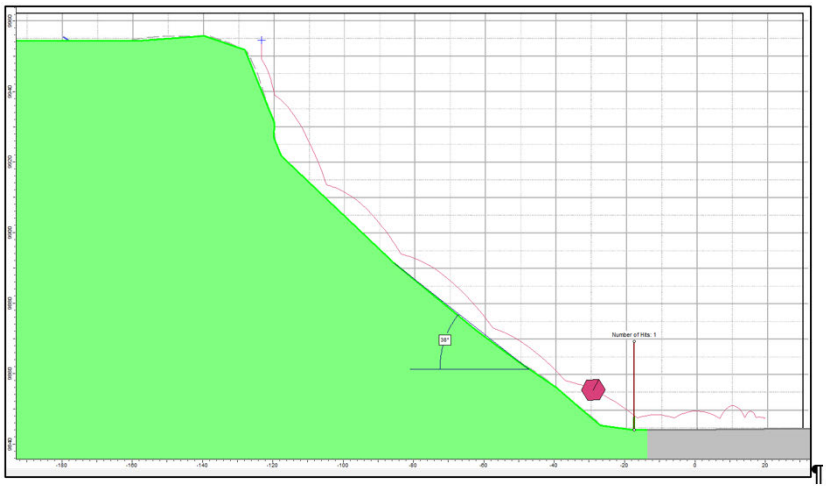

Figure·9.·Maximum·energy·roll·for·a·Group·1·rock·at·Sta.·245+60·of·1387·kJ.¶

Figure 15 is a general depiction of the slope with a typical rockfall from the source area.

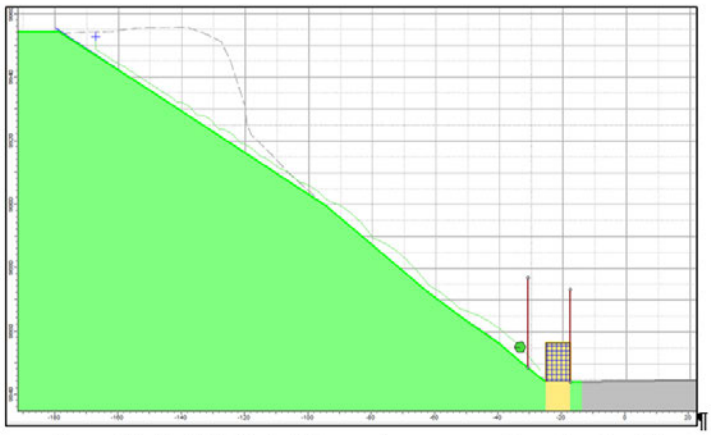

Figure·13.··Sta.·245+60·depicting·maximum·energy·Group·1·rock·roll.¶

Figure 16 is the proposed vertically faced wire system which will fill in over time.

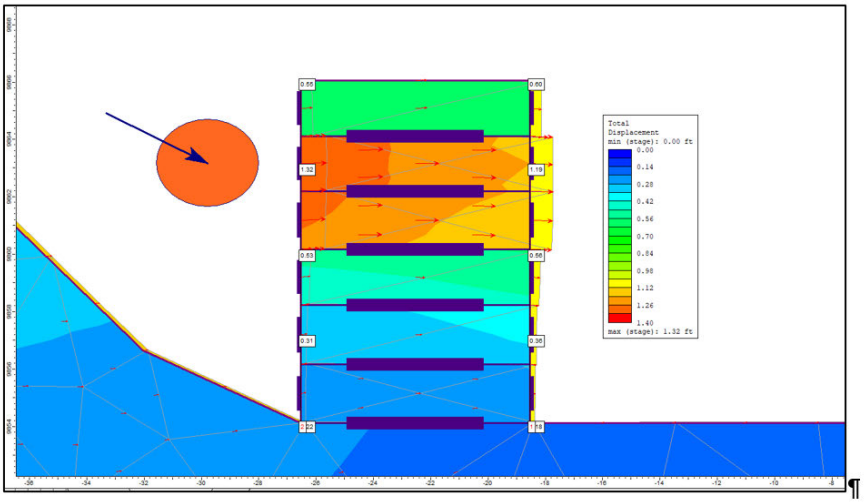

Figure·14.··Resulting·deformation·from·a·Group·1·rock·roll·into·the·rockfall·wall·system.·· (Greater·than·one·(1)·foot·of·face·deformation).¶

Figure 17 depicts the generalized rockfall impacts to the wall system using a finite element model to estimate deformation and outward deflection.

Figure 18. US 550 completed rockfall containment system.

SUMMARY

Evaluating and designing of the described rockfall containment wall systems shared common traits and characteristics that include:

- The existing cut slopes were at the angle of repose prior to roadway widening.
- The design intent is to re-establish the angle of repose and reduce the required maintenance and increase the resilience and longevity of the rockfall containment systems.
- Rockfall containment design required many facets that included internal, external, global stability, overturing, impact resistance and final earth pressure loadings of the walls using a variety of rockfall modeling programs, global stability programs and finite element analysis.
- We also have experienced that if the rockfall containment structure is not vertically faced, rapidly rotating angular rocks can get traction on a slightly battered (ramped) wall face and easily climb/roll up and over the wall. It is also possible to model and show such events.
- Additionally for roadway width constraints a vertically faced front and back facing provides the smallest footprint for the space and lane width requirements along roadways.

15. Recent Advances in Rockfall Mitigation Technologies in Japan

Yoichi Nishita, Ph.D.
PROTEC ENGINEERING, INC.
5322-26 Hasugata, Seiro-machi, Kitakanbara-gun, Niigata, Japan
+81-25-278-1551
nishita@proteng.co.jp

Hiroshi Masuya, Ph.D.
PROTEC ENGINEERING, INC.
3F, Benefit Stage, 1-442 Takaodai, Kanazawa, Ishikawa, Japan
+81-76-227-9305
masuya@proteng.co.jp

Alisa Yokota
PROTEC ENGINEERING, INC.
6F, Sumitomo Fudosan Shiba Building No.2, 1-5-9 Shiba, Minato-ku, Tokyo, Japan
+81-3-6435-2680
yokota@proteng.co.jp

Prepared for the 75th Highway Geology Symposium, September 2026

Disclaimer

Statements and views presented in this paper are strictly those of the authors, and do not necessarily reflect positions held by their affiliations, the Highway Geology Symposium (HGS), or others acknowledged above. The mention of trade names for commercial products does not imply the approval or endorsement by HGS.

Copyright Notice

Copyright © 2026 Highway Geology Symposium (HGS)

All Rights Reserved. Printed in the United States of America. No part of this publication may be reproduced or copied in any form or by any means – graphic, electronic, or mechanical, including photocopying, taping, or information storage and retrieval systems – without prior written permission of the HGS. This excludes the original author(s)

ABSTRACT

Rockfall hazards along mountainous roads have long posed significant risks to road users in Japan. Since the tragic Hida River bus accident in 1968, which was triggered by a sediment disaster, research and technological development in rockfall mitigation have progressed significantly. In addition, the collapse of a rock shed along the Echizen Coast in 1989 led to revisions in the design of approaches for rock slope failures and protective structures.

While rock sheds were historically the primary countermeasure, high-energy-absorption rockfall protection fences have increasingly been adopted because of their structural efficiency, constructability, and cost-effectiveness. Among these countermeasures, pile-supported vertical rockfall protection fences installed at the toe of slopes have become widely used in Japan, particularly in locations where installation space is limited, such as along roadways and behind residential areas.

This paper focuses on vertical rockfall protection fences installed at the toe of slopes. The study reviews the background behind their increasing adoption in Japan and examines their structural performance, including impact energy absorption capacity and deformation behavior during rockfall impact. Representative installation of case studies along highways and behind residential areas are also presented to demonstrate the effectiveness and practical applicability of these systems.

INTRODUCTION

Rockfall mitigation in Japan has evolved since the Hida River bus accident on August 18, 1968, in which 104 people were killed or went missing after a bus plunged into the river. Following this accident, rockfalls came to be recognized not merely as unavoidable natural events but as hazards for which road administrators could be held liable. Consequently, the demand for rockfall protection structures increased.[1]

Research on rockfall protection structures in Japan is generally considered to have begun with rockfall barrier experiments conducted at Kobe University in 1967.[2] Studies on rockfall fences, now widely installed along roads in Japan, were subsequently carried out by the Japan Highway Public Corporation beginning around 1973 and formed the basis of modern rockfall fence design.[3] **Figure 1** shows a conventional Japanese rockfall fence, and **Figure 2** shows a conventional pocket-type rockfall net.

Research on rock sheds was active from the 1970s to the 1990s. Following the catastrophic rock slope failure along the Echizen Coast in July 1989, in which a rock shed collapsed and 15 people were killed, the current rock shed design methodology was established. **Figure 3** shows the Echizen Coast rock slope failure, and **Figure 4** shows a prestressed concrete (PC) rock shed.

Figure 1 - Standard-Type Rockfall barrier

Figure 2 - Standard-Type Rockfall net

(a) Before the rockfall

(b) After the rockfall

Figure 3 - Rock slope failure at the Echizen Coast

Since the 1980s, many rock sheds have been constructed in Japan as a major rockfall countermeasure. However, declining public infrastructure investment in the late 1990s led to changes in rockfall protection strategies and the development of alternative protection systems.

One such system is the high-energy absorption rockfall barrier equipped with energy dissipation devices (brake systems). These barriers absorb impact energy through friction and plastic deformation of the devices. Originally developed in Europe and North America, they were introduced to Japan in the mid-1990s.

The history of rockfall countermeasures in Japan can be divided into four stages. The first extends from the 1968 Hida River bus accident to the first edition of the *Rockfall Countermeasure Manual* in 1983. The second covers the period until the 1989 Echizen Coast rock slope failure in Fukui Prefecture. The third continues until the revised *Rockfall Countermeasure Manual* was published in 2000.

Since 2000, the fourth stage has been marked by the development of domestic high-energy absorption barriers and the rapid adoption of overseas systems. Although performance-based design was introduced, performance verification methods were not fully established. The 2017 revision of the *Rockfall Countermeasure Manual* addressed this issue by introducing performance-based design procedures for rockfall protection structures. **Figure 5** shows a high-energy absorption rockfall barrier.

This paper presents the development of a post-reinforced rockfall barrier, one of the most widely used rockfall protection systems in Japan.

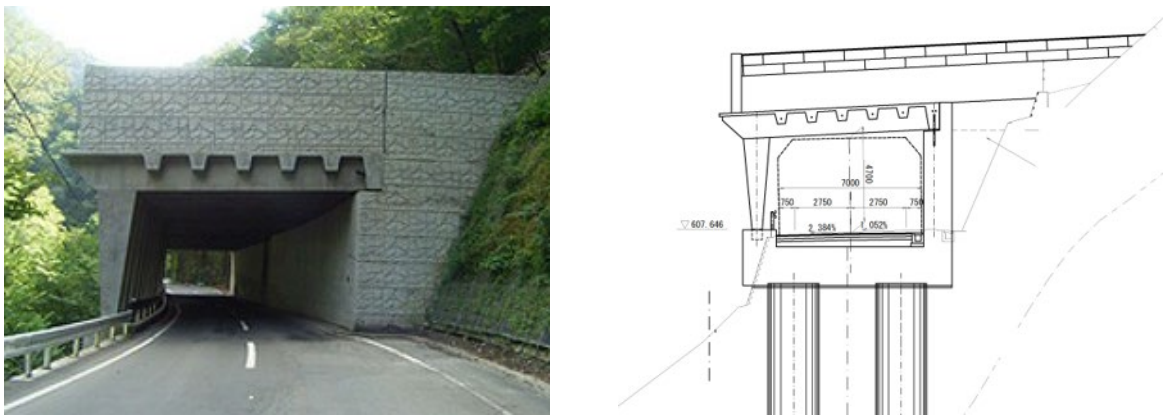

Figure 4 - Example of a Prestressed Concrete (PC) Rock Shed

(a) Net-Reinforced Type (b) Post-Reinforced Type

Figure 5 - Example of a High-Energy Absorption Rockfall Barrier

PERFORMANCE REQUIREMENTS FOR ROCKFALL BARRIERS IN JAPAN

The performance requirements for rockfall protection structures in Japan are defined as follows:[3]

Performance Level 1:
The structure remains intact or, if damaged, does not impair the function of the road section.
Performance Level 2:
Structural damage is limited, and although the road function is partially impaired, it can be restored promptly.
Performance Level 3:
Structural damage impairs the road function but does not result in catastrophic failure.
For rockfall barriers, Performance Level 2 is the required limit state. Performance may be verified by conventional, experimental, or analytical methods. For new structural systems, verification is primarily based on full-scale testing.

DEVELOPMENT CASE STUDY OF A POST-REINFORCED ROCKFALL BARRIER

Structural Overview

Many post-reinforced rockfall barriers are designed to undergo large deformations while maintaining the bending resistance of their structural members. **Figure 6** shows an example of a post-reinforced rockfall barrier.

In this type of structure, the steel posts and pile foundations are integrated into a single structural system, resulting in relatively small overall deformation. In addition, because no anchor ropes are required, this type of barrier is widely used at sites where available installation space is limited.

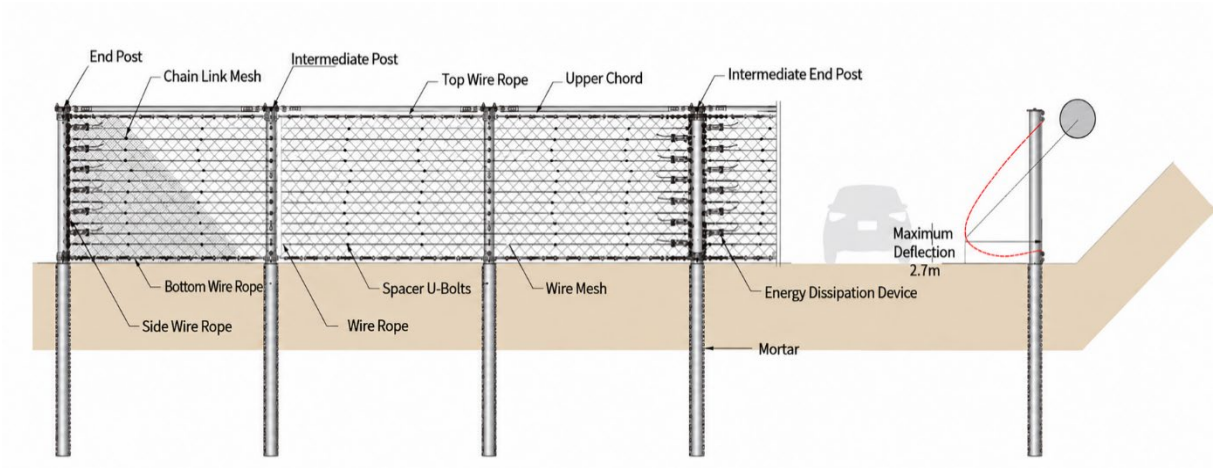

Figure 6 - Example of a Post-Reinforced Rockfall Barrier (Slope Guard Fence)

Test Specimen

The test specimens had a barrier height of 3.5 m and a total length of 15 m, with a post spacing of 5 m. The specifications of the test specimens are summarized in **Table 1**. Three specimen types, designated Type A, Type B, and Type C, were tested. Type A and Type B were designed for an impact energy level of 500 kJ, whereas Type C was designed for an impact energy level of 1,200 kJ.

Table 1. Test Specimen Types

Type	Schematic Diagram	Specifications
A	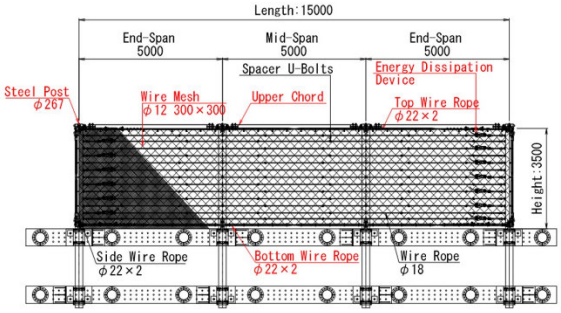	• 500-kJ class • Steel posts (Ø267 mm) • Upper chord installed over the entire barrier length • Wire mesh (Ø12 mm, 300 mm × 300 mm) • Energy dissipation device installed on one end of each wire rope • No energy dissipation device on the top wire rope • No energy dissipation device on the bottom wire rope • No spacer plates
B	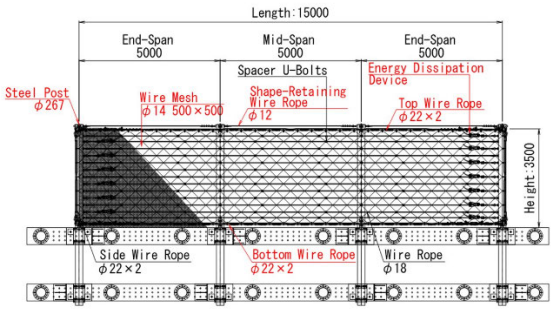	• 500-kJ class • Steel posts (Ø267 mm) • No upper chord • Wire mesh (Ø14 mm, 500 mm × 500 mm) • One energy dissipation device installed at one end of each wire rope • No energy dissipation device on the top wire rope • No energy dissipation device on the bottom wire rope • No spacer plates
C	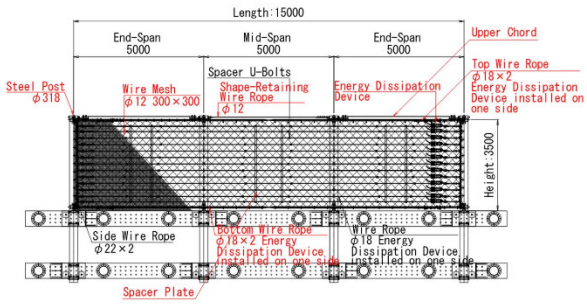	• 1,200-kJ class • Steel posts (Ø318 mm) • Upper chord installed only in the end spans • Wire mesh (Ø12 mm, 300 mm × 300 mm) • Energy dissipation devices installed at both ends of each wire rope • One energy dissipation device installed at one end of the top wire rope • One energy dissipation device installed at one end of the bottom wire rope • Spacer plates provided

The principal structural components of the barrier consisted of steel posts (STK400), upper chords (STK400), wire ropes (FC6×24, Ø22 mm or 3×7, Ø18 mm), wire mesh (FC6×24, Ø12 mm), chain link mesh (Z-GS7, Ø4.0 mm, 50 mm × 50 mm), and energy dissipation devices.

The steel posts consisted of Lotus Root Steel Tube (LST) members, in which seven small-diameter steel tubes and six high-strength reinforcing bars were arranged inside an outer steel tube, as shown in **Figure 6**, and the voids were filled with mortar. Two post diameters, Ø267 mm and Ø318 mm, were adopted. The upper chord was installed between adjacent post heads and served to distribute the longitudinal loads transmitted from the end posts through the interception system to multiple posts, thereby controlling the overall deformation behavior of the barrier. When no upper chord was provided, adjacent post heads were connected by a shape-retaining wire rope. Type A employed upper chords over the entire barrier length, whereas Type B employed shape-retaining wire ropes over the entire barrier length. In Type C, upper chords were installed only in the end spans, while shape-retaining wire ropes were installed in the middle span.

The interception system consisted of wire ropes, wire mesh, and chain link mesh, arranged in this order from the valley side. A total of thirteen wire ropes were installed at 250-mm intervals in the vertical direction. The wire mesh was fabricated by weaving wire ropes into a lattice pattern and was connected to the top wire rope, bottom wire rope, and side wire ropes using shackles.

As shown in **Figure 7**, the energy dissipation device consisted of two steel plates clamping a wire rope, which were tightened using high-strength bolts. The energy absorption mechanism was based on a frictional slip system, in which the excess length of the rope slipped through the device once a predetermined tensile force was reached. In Types A and B, one energy dissipation device was installed at one end of each wire rope, whereas in Type C, energy dissipation devices were installed at both ends of each wire rope. In addition, Type C incorporated energy dissipation devices on both the top wire rope and the bottom wire rope.

The wire mesh, shown in **Figure 8**, was fabricated by weaving wire ropes into a lattice pattern. Types A and C used Ø12-mm wire ropes with a mesh opening of 300 mm × 300 mm, whereas Type B used Ø14-mm wire ropes with a mesh opening of 500 mm × 500 mm. The mesh was connected to the top wire rope, bottom wire rope, and side wire ropes using shackles.

The spacer U-bolts were installed at the intersections of the wire ropes and the wire mesh to maintain the spacing between them. The spacer plates were used to maintain the vertical spacing of the wire ropes and were provided only in Type C.

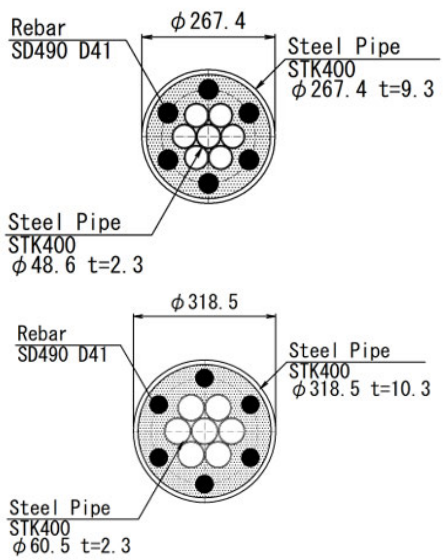

Figure 7 - Cross Section of the Steel Post

Figure 8 - Friction-Slip Energy Dissipation Device

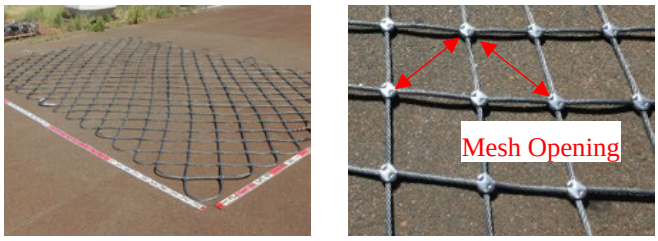

Figure 9 - Wire Mesh

Test Cases and Experimental Methods

The test cases are summarized in **Table 2**, and the experimental setup is shown in **Figures 10** and **11**. The test specimens were installed on a cantilever-type test frame so that the interception system was maintained in a horizontal position. A test weight was lifted to a predetermined height using a crane and released by a release mechanism to produce a free-fall impact.

The impact weights used in the tests had masses of 1,513 kg (density: 2.6 t/m³) and 3,479 kg (density: 2.5 t/m³). Each weight consisted of a polyhedral steel shell filled with concrete. The impact location was set at the center of either the middle span or the end span in the horizontal direction and at a height of 2.5 m above the base. After the impact test on the middle span, damaged members were repaired or replaced before conducting the impact test on the end span.

The measured parameters included the drop height, impact velocity, acceleration of the impact weight, residual barrier height, deformation of the interception system, and wire rope tension.

Figure 10 - Experimental Setup

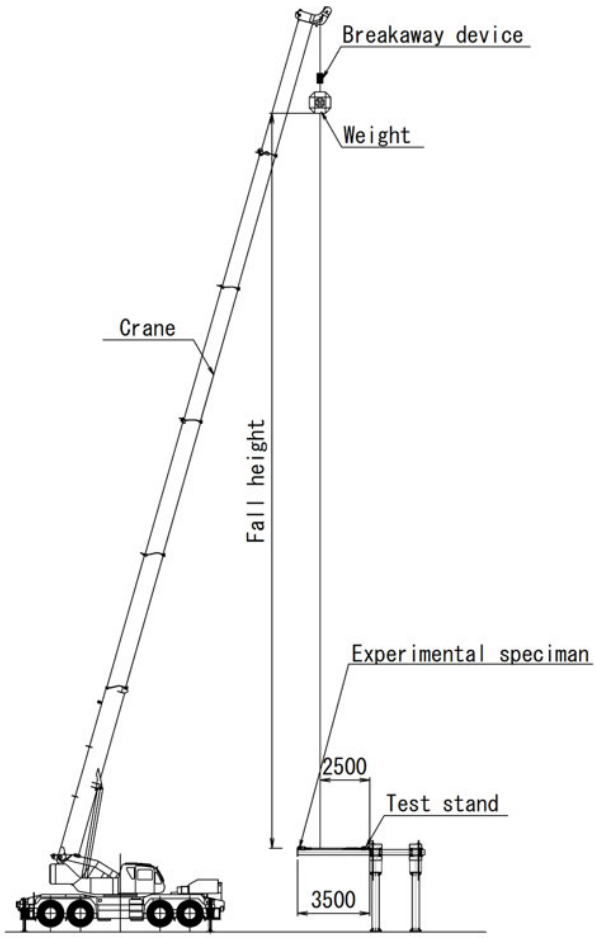

Figure 11 - Schematic of the Experimental Setup

Table 2. Test Cases

Case	Specimen Type	Impact Weight (kg)	Drop Height (m)	Impact Velocity (m/s)	Impact Energy (kJ)	Impact Location
Case1	A	1513	35.0	26.2	519	Middle Span
Case2	A	1513	33.9	25.8	503	End Span
Case3	B	1513	34.4	26.0	510	Middle Span
Case4	B	1513	34.3	25.9	509	End Span
Case5	C	3479	35.2	26.3	1200	Middle Span
Case6	C	3479	35.3	26.3	1204	End Span

Test Results

Test Results and Damage Assessment

The test results and damage assessment are summarized in **Table 3**.

The results of Cases 1–4 confirmed that the 500-kJ-class barrier successfully intercepted the impact weight using either Ø12-mm wire mesh with a 300 mm × 300 mm mesh opening in combination with upper chords or Ø14-mm wire mesh with a 500 mm × 500 mm mesh opening without upper chords. Although local denting of the chain link mesh was observed after impact, its primary function is to prevent small rocks from passing through the wire mesh. Therefore, unless severe rupture occurs, its effect on interception performance is considered negligible.

All wire ropes remained intact. Because the energy dissipation devices were worn by rope slippage, replacement of the devices and re-tensioning of the wire ropes were required. Partial rupture of the wire mesh was observed, requiring replacement. Although the steel posts exhibited residual deformation after impact, previous studies confirmed that the LST posts used in this study retained their load-carrying capacity up to a deformation angle of 15°. Therefore, post reuse was considered feasible in Cases 1–3. In Case 4, however, the residual deformation reached 15°, indicating that post replacement was required. Comparison of Cases 1 and 3, and Cases 2 and 4, showed that installing upper chords reduced the residual post deformation to approximately 40% of that without upper chords.

The results of Cases 5 and 6 showed that the 1,200-kJ-class barrier, which employed stronger posts and additional energy dissipation devices, exhibited damage to the interception system comparable to that of the 500-kJ-class barrier. Plastic deformation of the spacer plates was observed, requiring replacement. The residual post deformation was 1° for the middle-span impact and 10° for the end-span impact. Post replacement was required after the end-span impact.

These results indicate that both the 500-kJ-class and 1,200-kJ-class barriers satisfy the requirements of Performance Level 2.

Table 3. Test Cases

Case	Specimen Type	Impact Energy (kJ)	Result	Damage Assessment		Performance Evaluation
				Interception System	Steel Post	
Case1	A	519	Intercept	Chain link mesh: Dented Top, bottom, and side wire ropes: Intact Wire ropes: Intact Energy dissipation devices: Wear; rope slippage Wire mesh: Partial rupture	Reusable (Residual deformation: 2°)	Performance Level 2
Case2	A	503	Intercept	Chain link mesh: Dented Top, bottom, and side wire ropes: Intact Wire ropes: Intact Energy dissipation devices: Wear; rope slippage Wire mesh: Partial rupture	Reusable (Residual deformation: 7°)	Performance Level 2
Case3	B	510	Intercept	Chain link mesh: Dented Top, bottom, and side wire ropes: Intact Energy dissipation devices: Wear; rope slippage Wire mesh: Partial rupture	Reusable (Residual deformation: 5°)	Performance Level 2
Case4	B	509	Intercept	Chain link mesh: Dented Top, bottom, and side wire ropes: Intact Wire ropes: Intact Energy dissipation devices: Wear; rope slippage Wire mesh: Partial rupture	End post replacement required (Residual deformation: 15°)	Performance Level 2
Case5	C	1200	Intercept	Chain link mesh: Dented Top, bottom, and side wire ropes: Intact Wire ropes: Intact Energy dissipation devices: Wear; rope slippage Wire mesh: Partial rupture Spacer plates: Plastic deformation	Reusable (Residual deformation: 1°)	Performance Level 2
Case6	C	1204	Intercept	Chain link mesh: Dented Top, bottom, and side wire ropes: Intact Wire ropes: Intact Energy dissipation devices: Wear; rope slippage Wire mesh: Partial rupture Spacer plates: Plastic deformation	End post replacement required (Residual deformation: 10°)	Performance Level 2

Residual Barrier Height and Maximum Deflection

The measured residual barrier height and maximum deflection are summarized in Table 4, and the residual barrier height is shown in **Figure 12**. Each maximum deflection of barrier is also shown in **Figure 13**.

The residual barrier height after impact ranged from 2.9 to 3.2 m, corresponding to 80–90% of the original barrier height (3.5 m). Cases 1 and 3 showed little influence of the upper chord or wire mesh type on the residual barrier height under middle-span impact. Under end-span impact (Cases 2 and 4), the residual barrier height was slightly lower without the upper chord.

The maximum deflection was also similar in Cases 1 and 3. However, under end-span impact (Cases 2 and 4), the maximum deflection increased by approximately 10% without the upper chord, mainly due to greater deformation of the end post. In Cases 5 and 6, the maximum deflection was approximately 40% larger than that in Cases 1–4, because the energy dissipation devices on the top and bottom wire ropes allowed additional rope slippage.

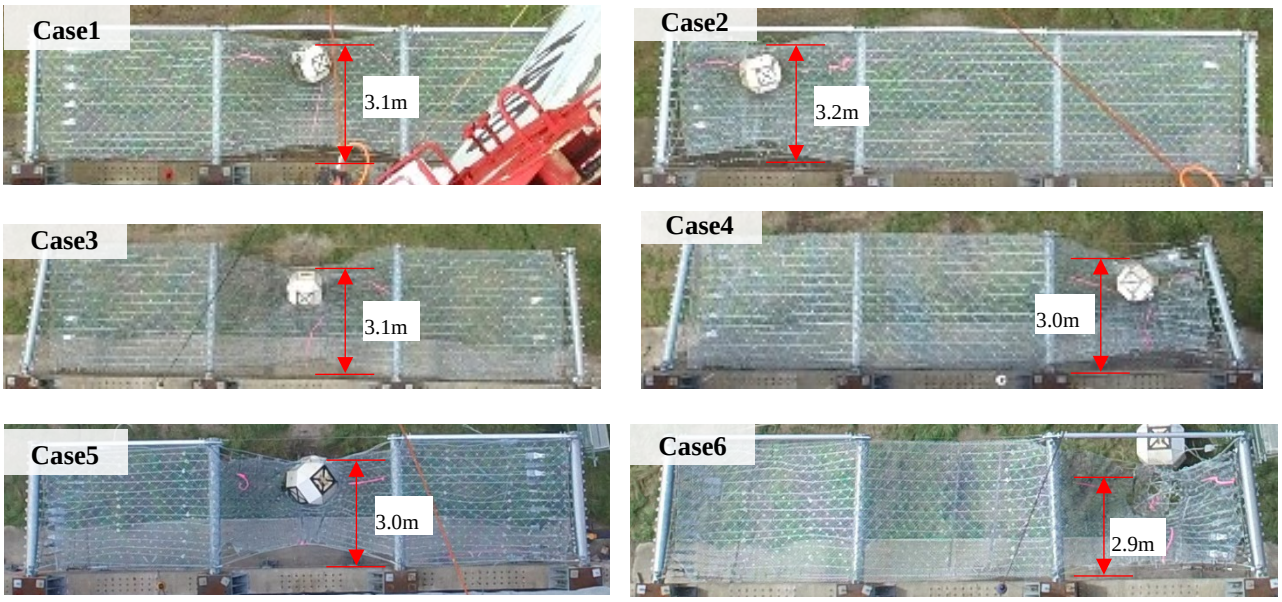

Note: The impact weight rebounded and fell onto the end span.

Figure 12 - Residual Barrier Height

Table 4. Residual Barrier Height and Maximum Deflection

Case	Residual Barrier Height (m)	Maximum Deflection (m)
Case1	3.1	2.7
Case2	3.2	2.4
Case3	3.1	2.7
Case4	3.0	2.7
Case5	3.0	3.7
Case6	2.9	3.4

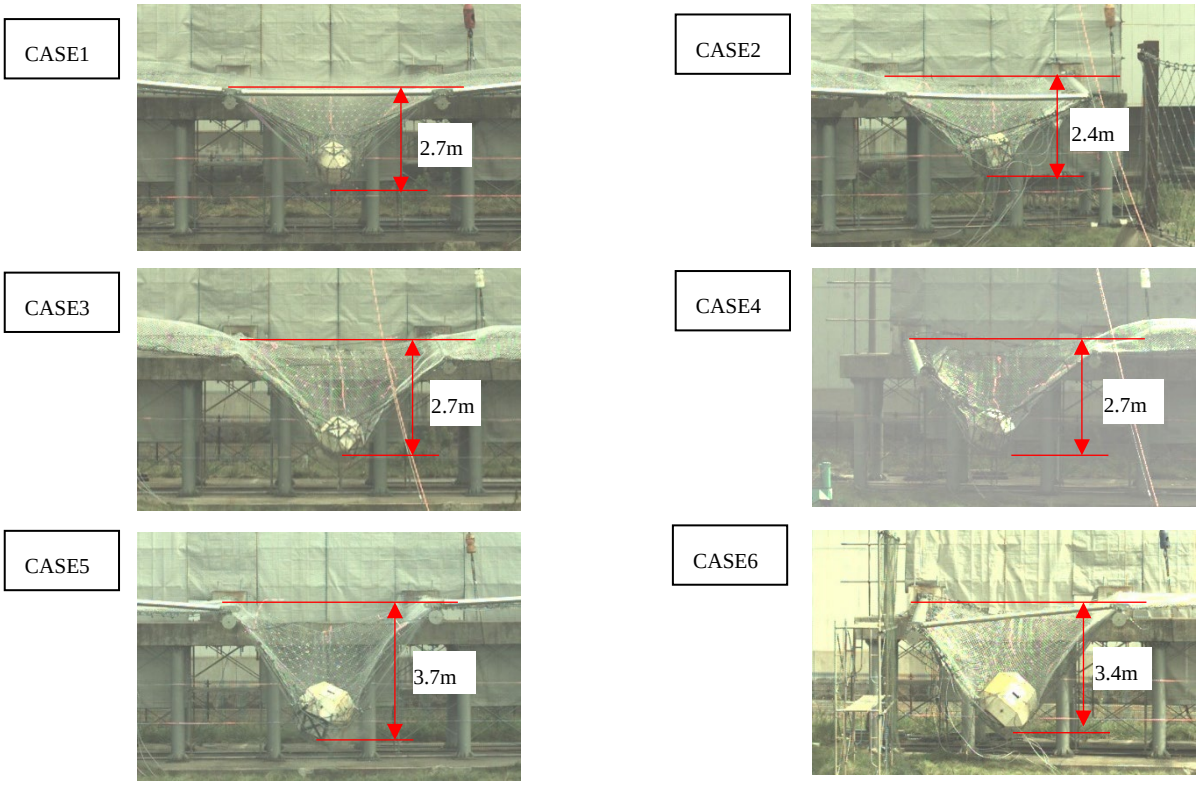

Figure 13 - Maximum Deflection

PERFORMANCE EVALUATION BY LARGE-DEFORMATION FEA

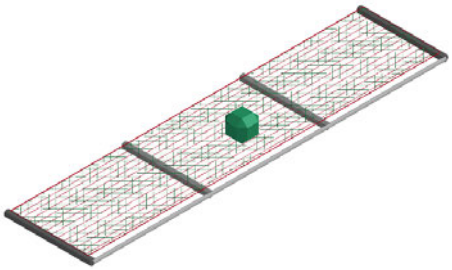

Figure 14 - Analysis Model

Analysis Overview

The LS-DYNA analysis model is shown in **Figure 14**. The model consisted of steel posts, upper chords, wire ropes, wire mesh, and energy dissipation devices. To simplify the analysis, the Chain link mesh was not modeled. The analysis reproduced the middle-span impact tests for each specimen type (Cases 1, 3, and 5).

Beam elements were used for the steel posts, cable elements for the wire ropes and wire mesh, and spring elements for the energy dissipation devices. The steel posts were modeled using the measured material properties and a moment-curvature relationship obtained by the fiber-section method, with fixed supports at the base. The FC6×24 wire ropes were modeled using stress-strain relationships obtained from previous tensile tests, while the 3×7 wire ropes were defined according to the Rockfall Countermeasure Manual. The energy dissipation devices were modeled as tension-only springs. Their spring force was defined as the average rope tension during slippage, based on the measured rope tension histories. Spacer U-bolts were modeled using cable elements connecting the wire ropes and wire mesh, while the spacer plates were modeled as elastoplastic SS400 beam elements.

The analysis results were compared with the measured impact weight displacement, top wire rope tension, and bottom wire rope tension from the full-scale tests. The measured impact weight displacement was obtained by double integration of the measured acceleration. The displacement was defined as X = 0 m when the impact weight first contacted the interception system. The maximum top and bottom wire rope tensions were compared. The impact weight displacement for Case 1 was not compared because the acceleration data were unavailable due to a broken cable connected to the triaxial accelerometer.

Analysis Results

Impact Weight Displacement

The time histories of the impact weight displacements for Case3 and 5 are shown in **Figures 15(a)** and **15(b)**. The analytical and experimental results showed good agreement in both the maximum displacement and the displacement history up to the peak response. The calculated maximum displacement was 0.9–1.0 times the measured value. These results indicate that the LS-DYNA large-deformation finite element analysis can accurately reproduce the deformation behavior of the barrier and is an effective tool for predicting interception system deformation under conditions different from those examined in the full-scale tests.

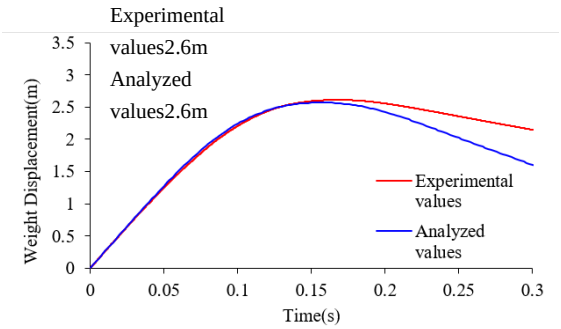

Figure 15(a) - Impact Weight Displacement (Case 3)

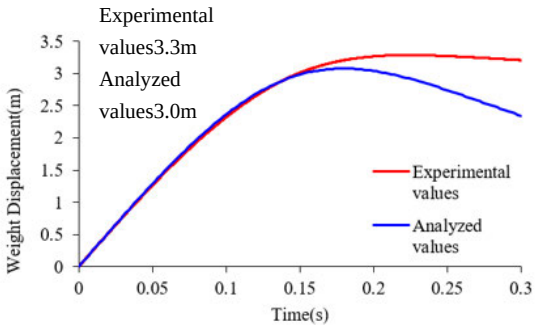

Figure 15(b) - Impact Weight Displacement (Case 5)

Top and Bottom Wire Rope Tension

The time histories of the wire rope tension are shown in **Figures 16(a)–(f)**. For Cases 1 and 3, in which no energy dissipation devices were installed on the top or bottom wire ropes, the analytical results agreed well with the experimental results in both the peak rope tension and its duration.

For Case 5, the analytical peak rope tension differed from the experimental value. This difference is attributed to the treatment of the energy dissipation device. In the experiment, the rope tension increased momentarily when rope slippage began, whereas the analysis used the average rope tension during slippage to define the spring force. Nevertheless, the duration of the rope tension agreed well between the analysis and the experiment.

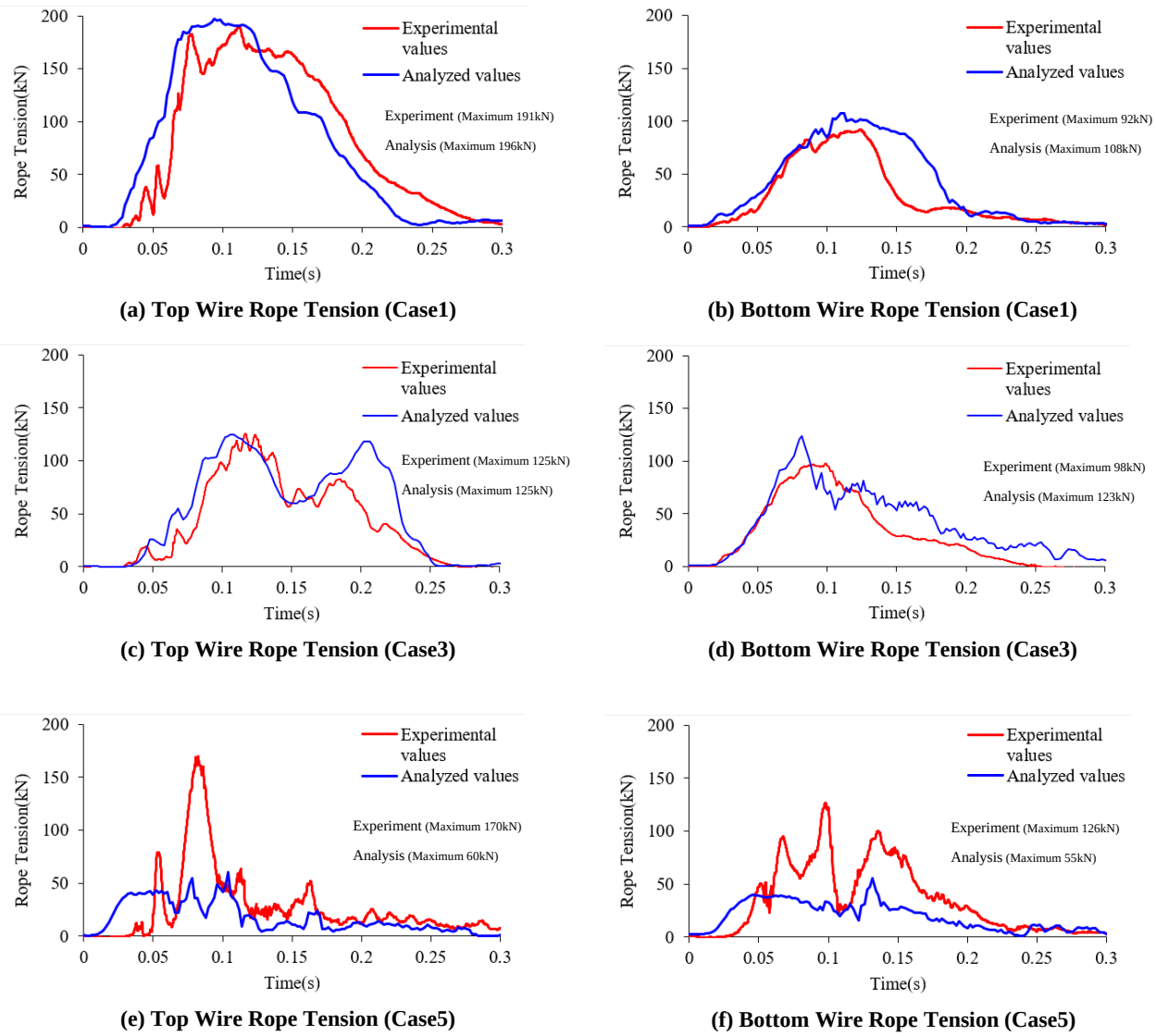

(a) Top Wire Rope Tension (Case1)

(b) Bottom Wire Rope Tension (Case1)

(c) Top Wire Rope Tension (Case3)

(d) Bottom Wire Rope Tension (Case3)

(e) Top Wire Rope Tension (Case5)

(f) Bottom Wire Rope Tension (Case5)

Figure 16 - Top and Bottom Wire Rope Tension

APPLICATION EXAMPLE

Application examples are shown in **Figure 17**. The site required a rockfall barrier capable of intercepting a 50-kN rock with an impact energy of approximately 1,000 kJ. Although a conventional rockfall barrier and a gravity retaining wall with a spread foundation had already been installed, neither system was capable of resisting the required impact energy, necessitating the investigation of alternative rockfall protection measures.

Because the allowable maximum deflection toward the roadway was limited to 3.5 m, a slope-installed high-energy-absorption barrier with anchor foundations and a pile-supported rockfall barrier were compared. Compared with the pile-supported system, the anchor-supported barrier required installation on the slope, resulting in larger deformation, additional land acquisition, and a temporary working platform for anchor installation. In contrast, the pile-supported barrier could be constructed from the roadside using a down-the-hole hammer without large temporary working platforms or scaffolding, substantially reducing temporary works and shortening the construction period by approximately 50%.

Based on these considerations, the pile-supported rockfall barrier was adopted because it could be installed within the site boundary while providing superior constructability and cost-effectiveness.

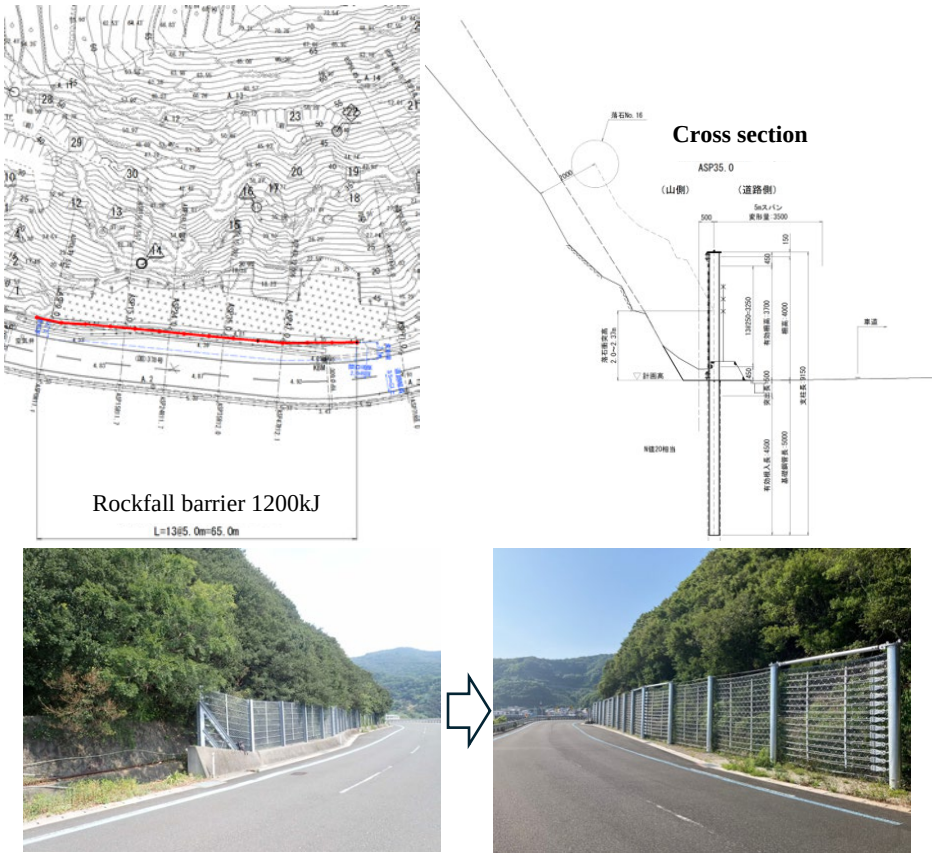

(a) Existing Rockfall Barrier (50 kJ) (b) Post-Reinforced Rockfall Barrier (1200 kJ)

Figure 17 - Application Examples

CONCLUSIONS

The main findings from the full-scale tests, numerical analysis, and field application of the 3.5-m-high, 15-m-long rockfall barrier are summarized as follows:

1. In Japan, both net-reinforced high-energy absorption barriers and post-reinforced rockfall barriers are widely used for rockfall protection.

2. After rockfall impact, the barrier performance can be restored by replacing the energy dissipation devices, wire mesh, and spacer plates, and by readjusting the wire ropes. For the 500-kJ barrier without an upper chord and the 1,200-kJ barrier, replacement of the end post is required after end-span impact.

3. Installing an upper chord reduced the residual deformation of the 500-kJ steel posts by approximately 40%.

4. The residual barrier height remained 80–90% of the original height. For the 500-kJ barrier, the upper chord and wire mesh type had little influence under middle-span impact, whereas the residual barrier height was slightly lower under end-span impact without the upper chord.

5. For the 500-kJ barrier, the maximum deflection was almost unaffected by the upper chord or wire mesh type under middle-span impact. Under end-span impact, the maximum deflection increased by approximately 10% without the upper chord. The maximum deflection of the 1,200-kJ barrier was approximately 40% greater than that of the 500-kJ barrier.

6. The impact weight displacement obtained from the LS-DYNA analysis ranged from 0.9 to 1.0 times the experimental values, indicating good agreement with the experimental results. Therefore, the present analytical approach is considered to be an effective tool for evaluating the deformation behavior under conditions that are difficult to investigate experimentally, provided that the analysis is applied within the range of conditions for which its validity has been confirmed through full-scale testing.

7. The field application demonstrated that the post-reinforced high-energy absorption barrier is an effective solution for sites with limited installation space because of its relatively small deformation.

REFERENCES

1. Committee on Structural Engineering, Japan Society of Civil Engineers: Impact Behavior and Design Methods for Structures: Design Manual for Rockfall Protection Galleries, April 1995. (in Japanese)

2. Department of Civil Engineering, Kobe University, and Kobe Steel, Ltd.: Field Test Report on the Shinko-Type Rockfall Barrier, April 1967. (in Japanese)

3. Japan Road Association: Rockfall Countermeasure Manual, December 2017. (in Japanese)

4. Sakai, K., Okuda, T., Tanabe, R., Kishi, N., and Komuro, M.: "Numerical Study on the Protective Performance of a High-Energy Absorption Rockfall Barrier with Reinforced Posts," Journal of Structural Engineering, Vol. 65A, pp. 946-954, 2019. (in Japanese)

5. Komuro, M., Umezawa, H., Okuda, T., Kawarai, T., and Kishi, N.: "Performance Verification of a Post-Reinforced High-Energy Absorption Rockfall Barrier by Full-Scale Impact Tests," Journal of Structural Engineering, Vol. 65A, pp. 955-963, 2019. (in Japanese)

6. Fukunaga, K., Teshima, R., Futami, G., and Matsumoto, S.: "Full-Scale Impact Performance Test of a High-Energy Absorption Rockfall Barrier with Reinforced Posts and Energy Dissipation Devices," Proceedings of the 12th Symposium on Impact Problems in Civil Engineering Structures, Japan Society of Civil Engineers, 2019. (in Japanese)

7. Ishii, T., Nishita, Y., and Masuya, H.: "Full-Scale Testing and Numerical Analysis of a Rockfall Barrier with a Hybrid Interception System," Proceedings of the 12th Symposium on Impact Problems in Civil Engineering Structures, Japan Society of Civil Engineers, 2019. (in Japanese)

16. Floyd Hill West Cut:

Navigating the Investigation, Design, and Construction of a Major Rock Cut along I-70

Todd Schlittenhart, P.E.
Yeh and Associates, Inc.
2000 Clay Street, Suite 200
Denver, CO 80211
(303) 781-9590
tschlittenhart@yeh-eng.com

Melissa Boyd, P.G.
Yeh and Associates, Inc.
2000 Clay Street, Suite 200
Denver, CO 80211
(303) 781-9590
mboyd@yeh-eng.com

Prepared for the 75th Highway Geology Symposium, September, 2026

Acknowledgements

The author(s) would like to thank the individuals/entities for their contributions in the work described:

Kurt Kionka, P.E. – Colorado Department of Transportation
Matt Aguirre, P.E. – AtkinsRéalis
David Thomas, P.E. – Colorado Department of Transportation
Noah Patterson – Salisbury & Associates
Nathan Davis – COLOG
Jon Altschuld, RLA, ASLA – Chinook Landscaping Architecture
Nicole Pendrigh – Collier Geophysics
Dennis Sack, P.E. – Olson Engineering
Matt Hogan – Kraemer North America

Disclaimer

Statements and views presented in this paper are strictly those of the author(s), and do not necessarily reflect positions held by their affiliations, the Highway Geology Symposium (HGS), or others acknowledged above. The mention of trade names for commercial products does not imply the approval or endorsement by HGS.

Copyright Notice

Copyright © 2026 Highway Geology Symposium (HGS)

All Rights Reserved. Printed in the United States of America. No part of this publication may be reproduced or copied in any form or by any means – graphic, electronic, or mechanical, including photocopying, taping, or information storage and retrieval systems – without prior written permission of the HGS. This excludes the original author(s).

ABSTRACT

The I-70 Floyd Hill project is a major expansion and realignment of an 8-mile stretch of the Interstate 70 Mountain Corridor in the foothills of the Colorado Rocky Mountains. Serving as the primary access for Coloradans and its visitors to visit the mountains, I-70 is the lifeline for commerce and tourism that support the mountain town economies. The goals of the Floyd Hill project are to improve travel time reliability, safety, and mobility by adding additional lanes, reducing steep grades, eliminating sharp curves, and addressing deficient infrastructure. The project is subdivided into three segments; East, Central, and West, to aid in the design and delivery of the overall project.

A large rock cut within the West Section of the project serves to widen and realign the highway by eliminating a tight curve, allowing increased design speeds through this segment. The rock cut, informally named the “West Cut” reaches a maximum cut height of approximately 210 feet and includes removal of over 350,000 cubic yards of highly metamorphosed gneiss. Investigation, design, and construction of the West Cut faces the challenges of working within a steep, narrow mountainous canyon, variable degrees of metamorphism, strong foliation, designing a rock cut within a curved alignment, and assessing impacts of the rock cut on a high-voltage electrical transmission tower situated at the top of the cut. Within the framework of a CM/GC contract, multiple surface and subsurface investigative techniques were utilized during the design phase to achieve the rock cut design that is now under construction.

INTRODUCTION

Colorado's interstate system primarily consists of two highways, the north-south running Interstate 25 (I-25) and the east-west running Interstate 70 (I-70). With the major population growth in Colorado over the past few decades, these Interstates have seen increasing volumes and stress to their aging infrastructure. I-25 runs along the Colorado Front Range, where the majority of population growth has occurred and I-70 is the major highway that takes this population west to the premier recreation area in Colorado, the Rocky Mountains. Along with transporting Coloradans to the mountains, I-70 also serves as a major conduit for the commercial and tourism industries. Every weekend and holiday, summer or winter, I-70 fills with vehicles carrying locals and tourists who are eager to enjoy the skiing, camping, hiking, biking, and sightseeing the mountains have to offer. Added hours of travel time are not uncommon during the weekend traffic jams and any accident on I-70 only increases these delays due to a lack of viable detours. The need to improve safety and sight lines to lessen the stress on the highway has been at the forefront of the Colorado Department of Transportation (CDOT) planners for decades.

Widening and improving I-70 faces the unique challenges of highway construction in the Rocky Mountains; steep terrain, narrow and winding canyons, and the absence of viable alternative routes. One section of I-70 that epitomizes these challenges is the Floyd Hill area. This stretch of I-70, which was originally constructed in the 1950's for lower volumes and slower speeds than current standards, starts the highway transition from the Front Range to the Rocky Mountains. The Floyd Hill section begins on the east end near the Homestead Road interchange (mile marker 247) where the highway transitions from a six-lane configuration to five lanes (two lanes in each direction plus a climbing lane for eastbound traffic). I-70 then traverses a steep (>6%) grade for three miles to the interchange with US Highway 6 (MM 244). This interchange only allows three out of the four possible movements between I-70 and US 6 and is the location of a sharp curve at the base of the steep grade over a poorly-rated bridge constructed in 1959. From the US 6 interchange, I-70 winds for one mile through a narrow canyon bound by steep rock cuts on one side and the Clear Creek river on the other. A brief canyon opening occurs at the interchange with Hidden Valley (MM 243) before the highway winds again for another mile through steep rock cuts and Clear Creek until it meets the Veterans Memorial Tunnels (VMT) near MM 242. Figure 1 shows a generalized location map of Floyd Hill.

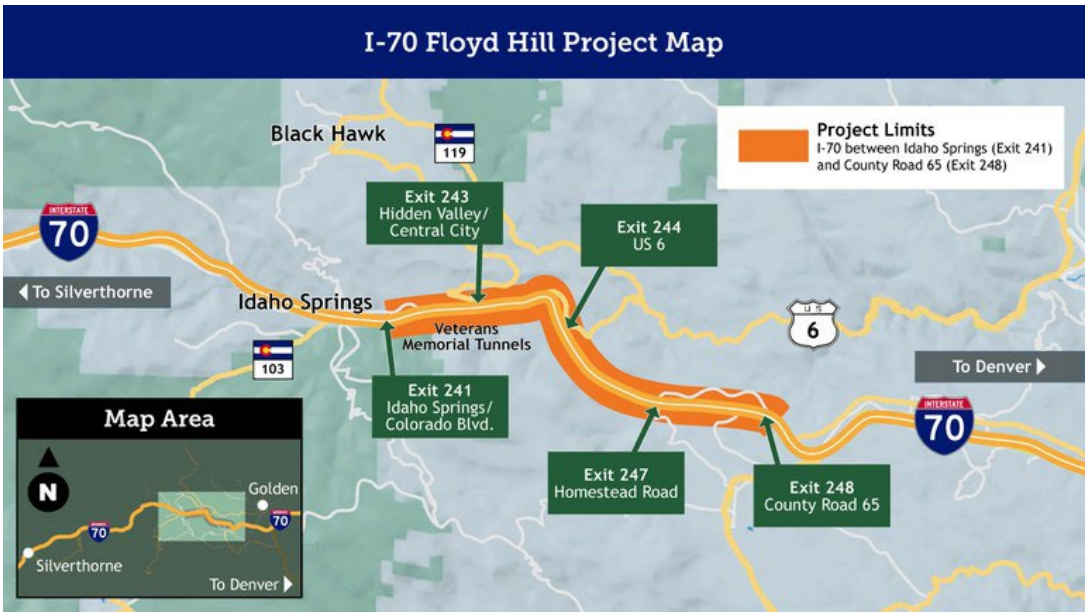

Figure 1 – I-70 Floyd Hill Location Map (courtesy of CDOT)

Improving this steep, functionally obsolete stretch of highway has been under consideration since the completion of the 2014 VMT widening project to the west of Floyd Hill. The conceptual study began in 2018 with the goal of removing steep grades, straightening sharp curves, replacing aging infrastructure, improving capacity, adding tolled Express Lanes, and adding climbing lanes to tie into the widened VMT to the west and previously widened roadway to the east.

Two primary concepts were developed through the 2018 study; a tunnel option and a bridge viaduct option. Both concepts would allow construction to occur while I-70 remained open to traffic. The bridge viaduct option was selected as the preferred alternative, primarily due to lower costs of construction. This option provides a six-lane roadway section throughout an eight-mile stretch of improvements and a climbing lane for eastbound I-70 through the steep Floyd Hill grade. It includes a greater than one-mile-long viaduct bridge for westbound traffic that starts halfway down the steep grade of Floyd Hill and eliminates the sharp curve at the US 6 interchange. Eastbound and westbound traffic cross alignments at the US 6 interchange and remain that way through a curve straightening section that includes a major realignment within a new rock cut area informally known as the Saddle Cut. The old alignment of I-70 is converted into an extension of US 6 to allow a full movement interchange to coincide with the Hidden Valley interchange. More curve straightening occurs between Hidden Valley and the VMT, requiring a major rock cut informally known as the West Cut.

The estimated cost of construction for the I-70 Floyd Hill Project in 2018 was approximately $750 million. Due to steep rises in construction costs, this estimate rose to approximately $905 million when construction began in July 2023 and currently sits closer to $950 million.

The preferred delivery method of a CM/GC (Construction Manager/General Contractor) was selected based on the complexity of the project, the need for innovation, a compressed

design and construction schedule, and the identified project risks (*1*). The CM/GC team was selected in January of 2022 at the 30% level to collaborate with designers and deliver the project.

GEOLOGY

The geology of the Floyd Hill area is mapped on the USGS 1:24,000-scale geologic map of the Squaw Pass quadrangle (*2*). Mapped geologic bedrock formations in this area include various Precambrian-aged gneissic rock units, which are generally characterized by alternating dark and light mineral layers exhibiting strong foliations. The foliation in the metamorphic rocks reflect the regional Precambrian anticline that plunges to the northeast and the more local complex folds and faults seen in the bedrock structure (*3*). Two branches of the northwest trending Floyd Hill fault cross the project area, dissecting I-70 in multiple locations and dividing the bedrock units. In some locations, the fault contributes to slope instabilities, such as the Floyd Hill Landslide located near MM 244 at the base of Floyd Hill. The bedrock units form the basement of the Front Range uplift and lie within the Colorado Mineral Belt. The Colorado Mineral Belt, as shown in Figure 2, is a narrow belt extending from Boulder to Breckenridge characterized by productive mineral deposits associated with intrusive porphyritic rocks (*3*). Local to Floyd Hill, these porphyries are commonly coarse-grained white, pink, and light gray granite pegmatites.

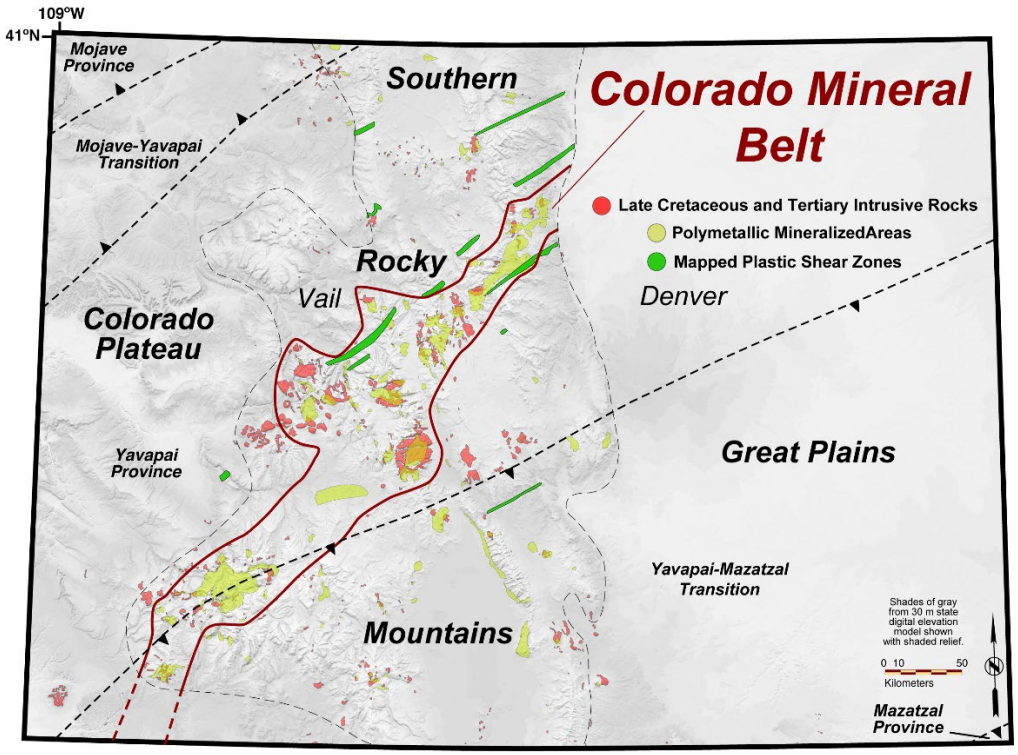

Figure 2 – Colorado Mineral Belt Map (courtesy of USGS)

ROCK CUTS

Multiple rock cuts are required as part of the I-70 Floyd Hill Project, varying in size and volume. The majority of materials excavated from the rock cuts can be processed and used for

roadway base, wall backfill, and riprap. As planned, over 500,000 cubic yards of rock will be excavated as part of the project. This paper focuses on the largest of those rock cuts, the West Cut, which will aid in roadway curve straightening through a narrow canyon section.

The West Cut reaches a maximum cut height of approximately 210 feet and includes removal of over 350,000 cubic yards of highly metamorphosed gneiss. It was identified as an ideal location for a rock cut due to a relatively flat bench area in the upper portion of the slope that provides a bench for pioneering to the top of the cut, thereby eliminating extensive pioneer blasts. Investigation, design, and construction of the West Cut faced the challenges of working within a steep, narrow mountainous canyon, varying depths and amounts of overburden and weathered rock, variable degrees of metamorphism, strong foliation, designing a rock cut within a curved alignment, and assessing the impacts of the rock cut to a high-voltage electrical transmission tower situated directly above the top of the cut (see Figure 3).

Figure 3 – Photo of the West Cut Showing the Curved Roadway, Flat Bench, Variable Jointing and Foliation, and Electrical Tower

Drilling Investigation

Investigation of the West Cut began with six borings; two drilled horizontally at the base of the cut and four borings drilled vertically from the top of the cut. The horizontal borings served the purpose of quantifying the depth of colluvial materials at the base of the West Cut on its westernmost end. At this end of the cut, removal of the gravity-deposited colluvial slope facilitated the designed roadway template. The horizontal borings were drilled by CDOT's geotechnical drill crew; one of the few local drilling crews with rigs capable of horizontal wireline coring methods. The two borings were drilled to depths of 43 and 55 feet using HQ core equipment with a standard core barrel assembly from the surface to the total depth of exploration. The rock face was encountered at a depth of 23 feet in the 43-foot deep boring but was not encountered in the 55-foot deep boring, providing confidence that removal of the colluvium back to the rock face would allow the planned roadway design template to fit within the widened area.

Access to the top of the West Cut proved a unique challenge due to the high-voltage electrical transmission tower situated at the top of the cut and its associated power lines. The presence of the tower and power lines precluded using a helicopter to transport a drill rig to the top of the cut. A rugged access road, presumably used to access the tower through private property, was discovered during early site reconnaissance trips. Fortunately, the selected CM/GC for the project was actively working with the private property owner on a nearby aggregate quarry and facilitated permission to use and improve the access road. Through coordination with Salisbury and Associates, a difficult access drilling company based out of Spokane, Washington, a winch and pulley system was set up to allow drill rig access from the terminal point of the access road to the top of the proposed cut line. Four rock cut borings were drilled vertically near the proposed top of cut by Salisbury with their custom, portable, difficult-access drill rig using NQ wireline coring methods with a triple tube core barrel assembly to advance the borings to total depths between 155 and 200 feet.

The bedrock encountered in the borings varied from strongly banded gneiss to massive amphibolite to medium-to coarse-grained granite and pegmatite. The encountered bedrock was generally moderately to highly fractured with closely to widely spaced fractures. The rock varied from fresh to decomposed, with the encountered amphibolite generally more decomposed than other rock types encountered. Rock Quality Designation (RQD) was measured in each run of recovered core. As shown in Figure 2, the increase of RQD values over depth was not as expected, with only a slight trend of increasing values with depth, indicative of the high metamorphism within the Colorado Mineral Belt. The low (less than 40) RQD values seen in Figure 4 at the lower elevations caused concern during design of the West Cut.

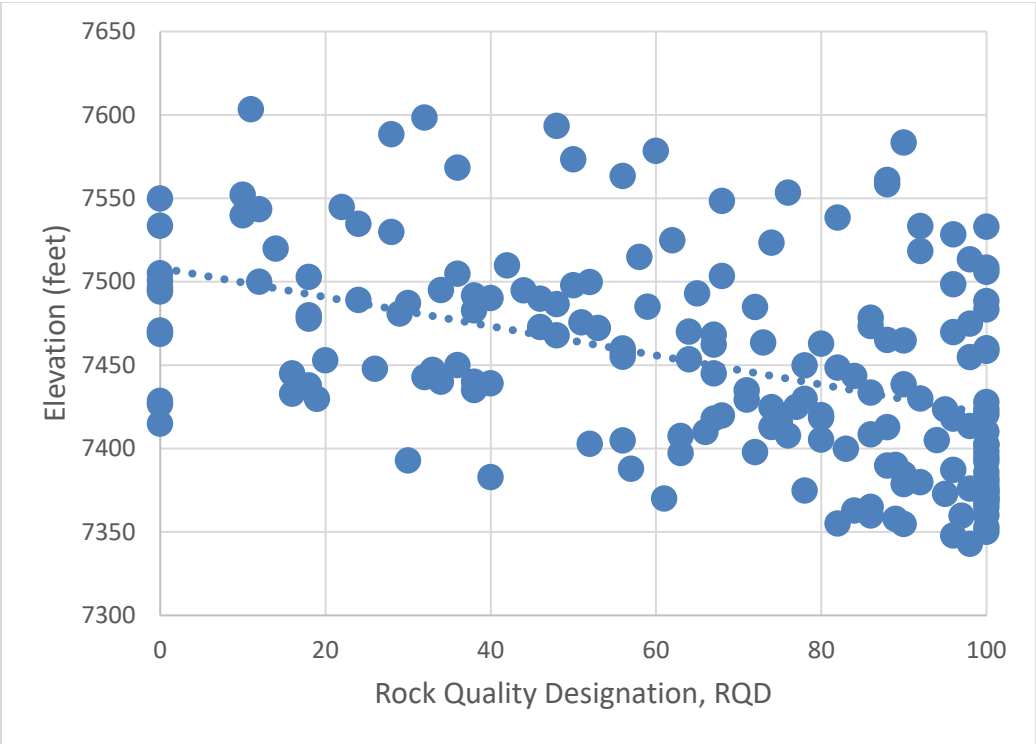

Figure 4 – RQD Measurements in Vertical Borings (Trendline Added)

Laboratory testing for the West Cut borings included selecting rock core samples from the borings to evaluate the intact rock strength. The tested samples generally consisted of fresh to slightly weathered metamorphic bedrock. The peak strengths from Unconfined Compressive Strength (UCS) testing are shown in Figure 5. Similar to the RQD results, the UCS testing showed little to no trend of increasing rock strength with depth.

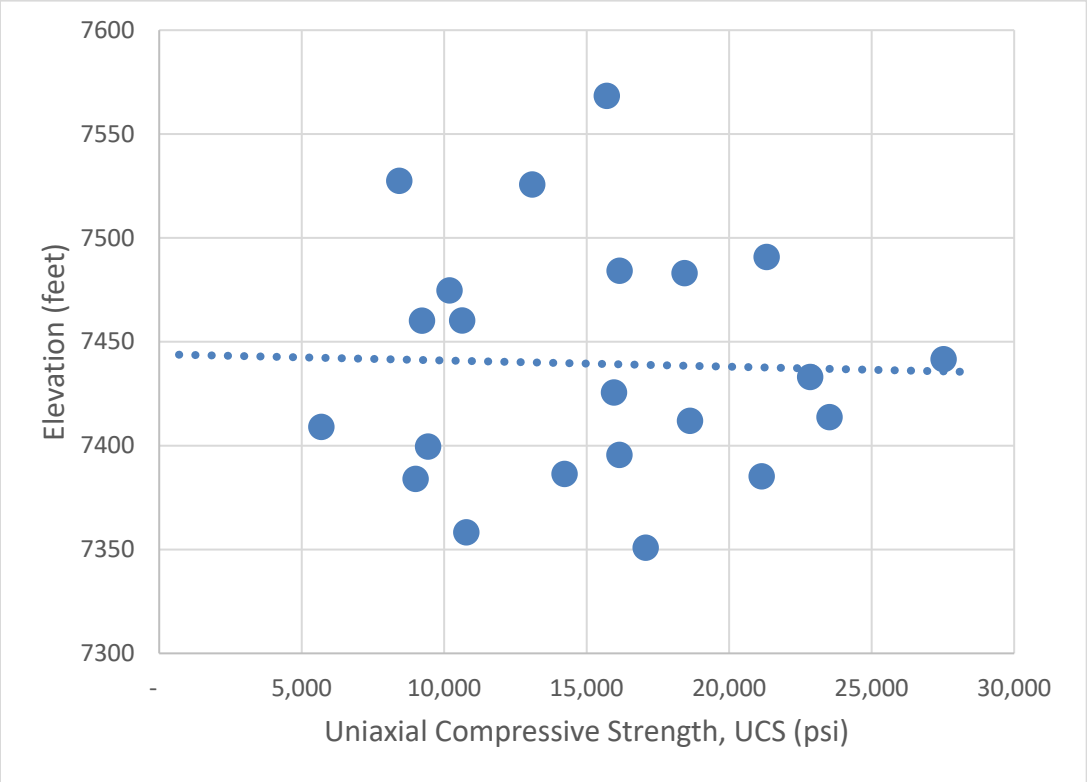

Figure 5 – West Cut UCS Test Results (Trendline Added)

Rock Structure Mapping

Determining the orientation of the jointing and foliation within the rockmass is essential for rock slope kinematic analysis and global stability analysis. Rock structure data was obtained through downhole borehole televiewer, photogrammetry-based surface mapping, and field mapping.

A borehole televiewer was used to image the vertical borings using optical and acoustic methods, as appropriate when considering water-filled holes due to the selected drilling method. Borehole televiewer services were provided by Colog, Inc. of Lakewood, Colorado. The borehole televiewer provided a continuous, orientated, high-resolution representation of the boring wall, providing depth-controlled structure data about the fracture and stress orientations, which was especially useful where core recovery was incomplete. The data was imported into DIPS (developed by Rocscience) to produce stereonet plots of the discontinuity orientations for kinematic and global stability analyses. The televiewer was limited by occasional obstructions in the boreholes, preventing the instrument from advancing the full depth in several of the borings.

Overburden soils and weathered bedrock at the top of each boring required that the drill casing be left in the hole until imaging was complete, which also limited the data collected. Despite these limitations, over 2500 discontinuity orientation points were collected from the four vertical borings.

A detailed surface mapping investigation of the existing rock cut at the West Cut location helped to characterize the geological conditions and assess the potential stability of the proposed rock cut slope in the same location. The investigation of the existing rock cut included rock slope mapping using an unmanned aerial system (UAS) and field mapping using “window” mapping techniques.

Rock slope mapping using an unmanned aerial system (UAS) was performed in the project area by Chinook Landscape Architecture of Centennial, Colorado. Multiple UAS flights collected images and videos for photogrammetric processing, covering the existing rock cut slope face. Ground control points were chosen by Chinook within the area of UAS mapping then surveyed into project survey coordinates by the design team surveyor. These ground control points were marked in the field, and the points were included in the photos taken during the slope mapping. The images collected were processed by Chinook into geo-located three-dimensional (3D) point cloud data in the software program Pix4Dmapper, using tie points and ground control points. Data provided from Chinook included 3D point cloud files in .las format, Pix4D project files and processing reports, and raw photographs.

These data files were used in Maptek PointStudio to evaluate the geometry of rockmass discontinuities, including joints and fractures, for use in the rock slope design and evaluation for constructability. The data processing in PointStudio involved removing most of the vegetation from the point cloud data and breaking the rock slope into smaller sections that could be processed for rock structure data more quickly.

Discontinuity sets were identified visually within the colorized point cloud, and PointStudio was used to find 3D planes from the point cloud that were within ±20° of the same orientation of each set. This process resulted in five discontinuity sets for the rock slope, with the average orientation (dip and dip direction) for each set of planar discontinuities shown in Table 1.

Table 1 – Summary of Rockmass Discontinuity Data from UAS Mapping, Window Mapping, and Borehole Televiewer

Discontinuity Type	Dip Direction (degrees)	Dip (degrees)
Joint	95	86
Joint	200	34
Joint	190	83
Joint	346	87
Foliation	9	46

To verify and supplement the discontinuity data from the 3D point cloud, orientations (dip and dip direction) were measured within representative sections, or “windows” selected along the cut face using the FieldMove Clino mobile app and a Brunton geological compass.

Discontinuity orientations obtained from the televiewer imaging were also compared to the field and 3D point cloud measurements to verify that discontinuity measurements recorded on the ground surface were representative of subsurface discontinuity orientations.

ROCK SLOPE DESIGN

Kinematic analysis was used to identify potential rock slope failure modes based on the presence of discontinuities in the rockmass, considering the discontinuity orientations relative to the proposed slope orientation. Since the West Cut occurs within a curve of the roadway, cut slope orientations were analyzed in 15° increments. Using the discontinuity orientations shown in Table 1 and the four cut slope orientation sections shown in Table 2, kinematic analyses were performed using DIPS within each section to evaluate whether planar failure, wedge failure, or direct toppling are kinematically possible. Kinematic analysis assumes that discontinuities are highly persistent and cohesionless. A conservative lower-bound discontinuity friction angle of 26° was assumed for the analyses based on the observed rock type, degree of weathering and alteration, and surface roughness of discontinuities.

For planar sliding failure to occur, the dip direction of a discontinuity surface must be within 20° of the slope dip direction. Additionally, to permit sliding, the dip angle of the discontinuity must be shallower than the slope angle (i.e., the discontinuity must daylight onto the slope face) but steeper than the discontinuity friction angle. Critical zones in which planar sliding are kinematically possible are then highlighted in red by DIPS.

For wedge sliding failure to occur, the line of intersection between two discontinuities must daylight on the slope face, and its plunge (angle from horizontal) must be steeper than the discontinuity friction angle.

For direct toppling to occur, intersections of discontinuities must dip into the slope, forming slabs or blocks that are prone to toppling onto or out of the slope. There must also be a basal discontinuity plane that is oblique or perpendicular to the intersecting discontinuities, which allows detachment of the slabs or blocks. The orientation of the intersection lines must be within approximately 10° of the slope dip direction. Oblique toppling is a special case in which the intersection lines are not within 10° of the slope dip direction but are at least as steep as the slope angle so that blocks may topple out of the slope at some other angle if permitted by the topography of the slope. In general, the potential for blocks to topple increases as their intersection lines approach vertical.

A cut slope gradient of 0.25H:1V (Horizontal:Vertical) was selected as the preferred cut slope gradient for the kinematic analysis. This preferred cut slope gradient was based on observations of the existing cut slope, which was also at a 0.25H:1V gradient and showed no signs of instability. The kinematic analyses considered cut slope gradients of 0.75H:1V (about 53°), 0.5H:1V (about 63°), as well as the preferred 0.25H:1V (about 76°). The results of the kinematic analyses for the 0.25H:1V gradient are summarized in Table 2, indicating if each of the failure modes as determined by DIPS are critical (feasible) or not critical (not feasible) at each of the four different slope orientation sections.

Table 2 – Summary of Kinematic Analyses						
Analyzed Cut Slope Gradient		Cut Slope Dip Direction (degrees)	Critical Poles/Intersections			
H:V	Degrees		Planar Sliding	Wedge Sliding	Direct Toppling	Oblique Toppling
0.25:1	76	185	Critical	Critical	Critical	Critical
0.25:1	76	170	Not Critical	Critical	Not Critical	Critical
0.25:1	76	155	Not Critical	Critical	Not Critical	Critical
0.25:1	76	140	Not Critical	Critical	Not Critical	Critical

The analysis for the preferred 0.25H:1V slope showed possible planar sliding failures in one of the sections and possible wedge failures throughout the cut slope. However, based on field observations of the existing cut slope, the possible sliding and wedge failures were not persistently unstable and were able to be mitigated through localized slope stabilization with rock dowels and rock bolts. The analysis also showed possible direct toppling failures in one of the sections and possible oblique toppling failures throughout the cut. However, the analyses did not indicate a basal discontinuity plane to allow detachment of the toppling slabs or blocks.

Based on the kinematic analyses, the rock structure at the West Cut was determined to be relatively stable, with large-scale, structurally controlled slope failures considered relatively unlikely. However, measured and observed discontinuity orientations vary widely from localized discontinuities within the Colorado Mineral Belt, causing concern over localized planar sliding, wedge sliding, and toppling failures. Although these localized failures were not expected to influence the global stability of the slope, they were expected to release relatively small rock blocks contributing to rockfall throughout the West Cut. This rockfall was considered to be especially common in sections where wedge sliding and oblique toppling were shown to be kinematically feasible. Additionally, there were observed zones of highly fractured, weathered, and/or altered rock within the borings, which tend to ravel and erode, especially during periods of precipitation and snowmelt.

DEPTH OF OVERBURDEN AND WEATHERED BEDROCK EVALUATION

Determining the depth of the overburden soils and the thickness of the weathered bedrock portion along the top of the cut allowed the designers to account for necessary laid-back gradients at the top of the slope. Since the rock cut progressed in a top-down construction method, defining the top of cut line based on the overburden and weathered rock gradients was essential. The depth of overburden and thickness of weathered bedrock was measured in each boring and connected between borings through a geophysical survey along the top of the cut line.

Collier Geophysics (*4*) performed a geophysical survey using Seismic Refraction Tomography (SRT) along the proposed top of cut line with the primary purpose of evaluating depth to bedrock where overburden soils were observed at the surface and to characterize excavatability of the geologic materials encountered in the proposed rock cut. Due to access limitations, the geophysical survey was unable to provide continuous data along the cut line. In

these locations, the estimated thicknesses of weathered bedrock and overburden soils were based on visual field observations.

P-wave velocities from seismic refraction surveys are useful for evaluating the excavatability of geologic materials that will be encountered in proposed excavations. Rippability charts published in the Caterpillar Performance Handbook (*5*) summarize the ability of Caterpillar D-8 through D-11 dozers (or equivalent) to rip various geologic materials based on the P-wave velocities of the materials. The Collier report provided P-wave velocity profiles along the proposed top of cut line to be used in the excavatability evaluation. In general, P-wave velocities less than 6,000 feet per second (fps) were considered rippable by a D-9 dozer. This velocity was set as the limit between the weathered rock slope and the 0.25H:1V rock cut slope and correlated well with the logged contact between weathered and intact rock in the four vertical borings. A P-wave velocity of 2,000 fps was selected as the contact between overburden soils and the weathered bedrock. Based on the results of the geophysical investigation, the proposed excavation appeared to contain rippable material consisting of soil, colluvium, and weathered bedrock at depths generally between 0 and 30 feet. A slope gradient of 1H:1V was set for the weathered rock and a slope gradient of 2H:1V was established for the overburden soils.

ROCK CUT SLOPE DESIGN

Preliminary rock cut slope recommendations were presented to the design and CM/GC team to discuss constructability, right-of-way impacts, and construction costs. Multiple revisions to the rock cut slopes were made based on required aesthetic slope rounding, anticipated overburden and weathered rock, and constructability reviews. Constructability reviews primarily focused on pioneering access along the top of cut line and the ability to establish working benches at least 20 feet wide.

Design of the preferred cut slope gradient of 0.25H:1V was reliant on the blasting contractor using presplitting as the controlled blasting technique for the final face. Presplitting is a perimeter control blasting technique involving a single row of closely spaced holes drilled along the neat excavation line that are loaded and fired before any adjoining excavation area is blasted. Presplitting creates a clean fracture plane between holes, reducing overbreak and improving rock face stability.

The slopes on the west end of the West Cut were identified through the horizontal subsurface drilling and geophysical surveys to consist of talus soils derived from the adjacent rock slopes to the full height of the planned cut. The design in this section called for the talus soils to be excavated back to the approximated rock face, providing additional roadside rockfall catchment beyond that required by the roadway design.

TOWER FOUNDATION INVESTIGATION

Since the proposed cut line for the West Cut was adjacent to the rock face supporting a high-voltage electrical transmission tower, concern arose over the rock supporting the tower. The concern was that the West Cut excavation may undermine the rock face and vibrations from

blasting and hammering on the rock slope may destabilize the rock face causing damage to the tower foundation.

Unfortunately, the foundation type for the tower was unknown. When contacting the utility owners about the as-built condition of the tower foundation, the only available plan drawings from 1965 were typical plans for multiple tower locations and showed a 48-inch diameter drilled shaft with a 66-inch diameter bell bottom extending 16 feet below grade supporting each corner of the tower. A drilled shaft with a bell bottom seemed unlikely due to the rock directly beneath the tower and the difficult access to the tower. To further investigate the tower foundation a non-destructive testing (NDT) survey was conducted.

Olson Engineering (*6*) performed Impact Echo (IE) on all four foundations for depth determination and attempted Sonic Echo/Impulse Response (SE/IR) testing on one foundation. Two randomly selected anchor bolts were tested with Ultrasonic Testing (UT) for length and integrity on each of the four foundation legs (eight bolts total).

The IE test was conducted on exposed top of concrete areas near the edge of each foundation block to measure the depth of concrete. The IE method involved hitting the concrete surface with a small hammer and identifying the reflected wave energy with a displacement or accelerometer receiver mounted on the surface. The impact force was used to excite the concrete, and the resulting displacement response was received by the built-in displacement transducer. In the case of concrete thicker than approximately six feet or where the concrete was well-bonded to the underlying rock, true concrete thickness was not be discernable by the IE method. On the first foundation tested, testing was also attempted with the SE/IR method to measure depth in case the foundation was deeper than about six feet. The SE/IR results indicated the foundation block to be less than five feet deep, so the IE method was used on all four blocks to measure depth. The IE results showed the depth of the concrete foundations to be from 24.8 to 42.2 inches.

The UT testing of the anchor bolts involved a high frequency echo test designed to determine the thickness of metal plates or the lengths of metal bolts and rods. The equipment used for the test was an ultrasonic transducer, a hand-held data acquisition system, and ultrasonic couplant gel. For UT, the ultrasonic transducer acted as both the emitter and receiver for the ultrasonic waves. The test was performed by placing the ultrasonic transducer on the top of the anchor bolt to be tested. An ultrasonic pulse was sent into the test piece. The pulse continued through the material until it contacted a different medium, or a discontinuity in the material, such as a defect or the end of the piece. When the wave contacted these discontinuities, the waves were reflected back towards the transducer. The time between when the pulse was emitted and received, as well as the material velocity, was used to calculate the distance traveled by the sound wave. A total of eight anchor bolts were tested, with two per tower leg. All measured bolt lengths were consistently within 0.3 inches of each other, and showed an overall length of about 132 inches. There were no shallow breaks or discontinuities apparent in the data records.

Based on the IE and UT results taken together, it appeared that the tower leg foundations consisted of 11-foot long steel anchor bolts set into bedrock, with relatively short concrete

cubical blocks placed around the anchor bolts at the top. The concrete blocks had grout pads in place between the concrete and the tower leg steel.

TOWER FOUNDATION DESIGN

The results of the NDT of the tower foundation indicated that the shallow rock anchors supporting the tower directly interacted with and relied upon the surrounding rock face for support. Loss of material from the rock face or further fracturing would be detrimental to the tower foundation. Therefore, an extensive rock bolting plan was designed to support the face and was specified to be installed and pre-tensioned prior to excavation and blasting operations at the West Cut. The rock bolts needed to avoid the tower foundation anchors while stabilizing a rock face with multiple fracture and foliation lines. The 3D point cloud created through photogrammetry proved to be an invaluable tool in identifying fractures and foliation. The point cloud also assisted in planning rock bolts to avoid the tower foundation anchors and each other. Figure 6 is the schematic from the plan set showing the rock bolt locations at the tower.

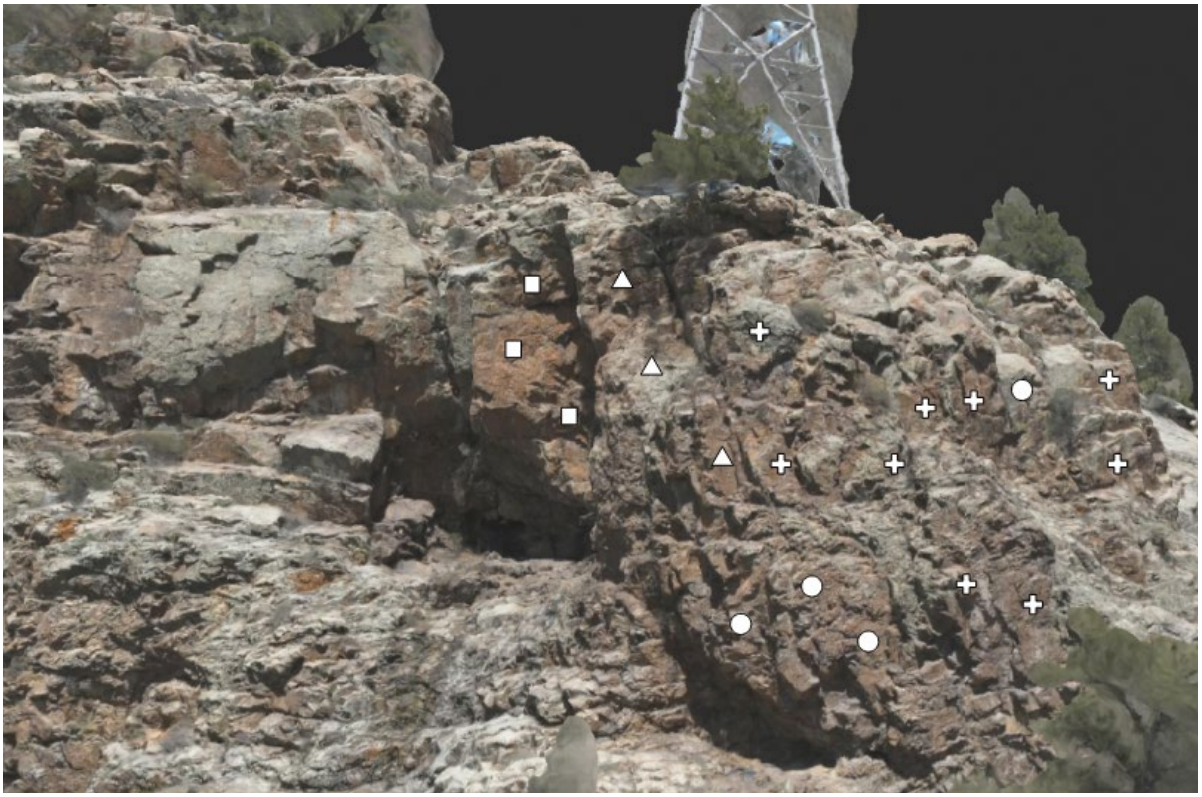

Figure 6 – Tower Rock Bolting from Plan Set (Symbols Represent Different Lengths and Loading of Bolts)

CONCLUSION

The West Cut presented a challenging rock cut within the I-70 Floyd Hill Project, with the combination of steep terrain, complex metamorphic geology, variable rock quality, limited

site access, and the presence of a high-voltage transmission tower. By combining data from multiple investigative techniques, the design effort was able to characterize the rock mass and evaluate potential hazards. The use of multiple techniques improved confidence in design assumptions and supported the use of a 0.25H:1V final rock slope with localized rock stabilization measures.

The collaborative CM/GC delivery process that enabled constructability feedback during design will continue into the construction and excavation of the West Cut. Concerns over the localized complex folding, highly variable rock types, and low RQD values near the base of the rock cut will be addressed during construction as the cut progresses.

REFERENCES:

1. Keleman, M. and Ogden, N. *Construction Manager/General Contractor Delivery Method and Procurement Schedule Concurrence – Floyd Hill to Veterans Memorial Tunnel Project*, Colorado Department of Transportation, 2020.
2. Sheridan, D.M. and Marsh, S.P. *Geologic map of the Squaw Pass quadrangle, Clear Creek, Jefferson, and Gilpin Counties, Colorado*. U.S. Geological Survey, Map GQ-1337, scale 1:24,000, 1976,
3. Lovering, T.S. and Goddard, E.N. *Geology and Ore Deposits of the Front Range Colorado*, US Geological Survey Professional Paper 223, 1950.
4. Collier Geophysics. *Geophysical Letter Report | Project # 230096, Floyd Hill West Cut Project, Idaho Springs, CO*, 2023.
5. Caterpillar. *Caterpillar Performance Handbook*, Version 48, 2018.
6. Olson Engineering. *Nondestructive Testing Investigation Report, Concrete Foundation Investigation – SE/IR, IE, UT Testing, Floyd Hill Xcel Tower Foundation, Idaho Springs, CO*, Olson Job No. 7330A, 2023.

17. From Risk Inventory to Real-World Failure: Hurricane Helene Validation of USMP Geohazard Prioritization

Jason A. Holland, PG
Schnabel Engineering
3902 Market Street
Wilmington, NC 28403
910-512-5622
jholland@schnabel-eng.com

Prepared for the 75th Highway Geology Symposium, September 2026

ACKNOWLEDGEMENTS

Schnabel would like to thank the Federal Highway Administration, Eastern Federal Lands Highway Division, National Park Service Blue Ridge Parkway staff, WSP USA, Inc., Appalachian Landslide Consultants, PLLC, and Schnabel Engineering team members who supported the Blue Ridge Parkway USMP inventories and the post-Hurricane Helene geotechnical investigation. These efforts depended on coordinated field assessment, agency and maintenance input, subsurface exploration, data management, quality control, and photographic documentation.

DISCLAIMER

Statements and views presented in this paper are strictly those of the author(s), and do not necessarily reflect positions held by their affiliations, the Highway Geology Symposium (HGS), or others acknowledged above. The mention of trade names for commercial products does not imply the approval or endorsement by HGS.

Copyright

Copyright © 2026 Highway Geology Symposium (HGS)

All Rights Reserved. Printed in the United States of America. No part of this publication may be reproduced or copied in any form or by any means – graphic, electronic, or mechanical, including photocopying, taping, or information storage and retrieval systems – without prior written permission of the HGS. This excludes the original author(s).

ABSTRACT

The Unstable Slope Management Program (USMP) provides a systematic framework for identifying and prioritizing unstable slopes along transportation corridors. In late September 2024, Hurricane Helene produced record setting rainfall across western North Carolina, triggering multiple landslides along segments of the Blue Ridge Parkway previously inventoried under the USMP. This extreme event provided a rare opportunity to evaluate how well USMP risk ratings correlate with real world slope failures.

This presentation compares USMP inventory results with documented landslides that occurred following Hurricane Helene, focusing on eight failure sites between Mileposts 336 and 349 investigated as part of post storm geotechnical exploration efforts. USMP risk ratings, hazard classifications, and slope characteristics were evaluated alongside post hurricane field observations, subsurface exploration data, and repair documentation. Spatial comparisons were performed between pre storm high risk USMP locations and confirmed landslide occurrences.

Results indicate that several Hurricane Helene landslides occurred at or immediately adjacent to slopes previously identified as unstable or high risk within the USMP framework. Contributing factors commonly included steep terrain, adverse geologic structure, drainage conditions, and rainfall driven groundwater response. These findings demonstrate that USMP ratings provide meaningful insight into slope vulnerability during extreme precipitation events, supporting their use as a proactive risk management and prioritization tool for transportation agencies.

INTRODUCTION

Mountain transportation corridors commonly cross steep slopes, residual soil, engineered fill, weathered rock, drainage crossings, and older geomorphic features that may remain marginally stable for years. Roadways along ridge flanks and narrow benches also modify natural drainage and slope geometry. Under extreme rainfall, these pre-existing vulnerabilities can develop into pavement distress, slope movement, roadway washout, debris accumulation, or complete loss of the travel way. *(1)*

This paper compares two related Blue Ridge Parkway efforts: pre-storm corridor-scale USMP inventories and a post-Hurricane Helene geotechnical investigation of eight landslide sites. The intent is not to claim that USMP predicted the timing, limits, or mechanism of individual failures. Rather, the comparison evaluates whether systematic field inventory and risk-based ratings established a useful baseline of slope vulnerability before the storm.

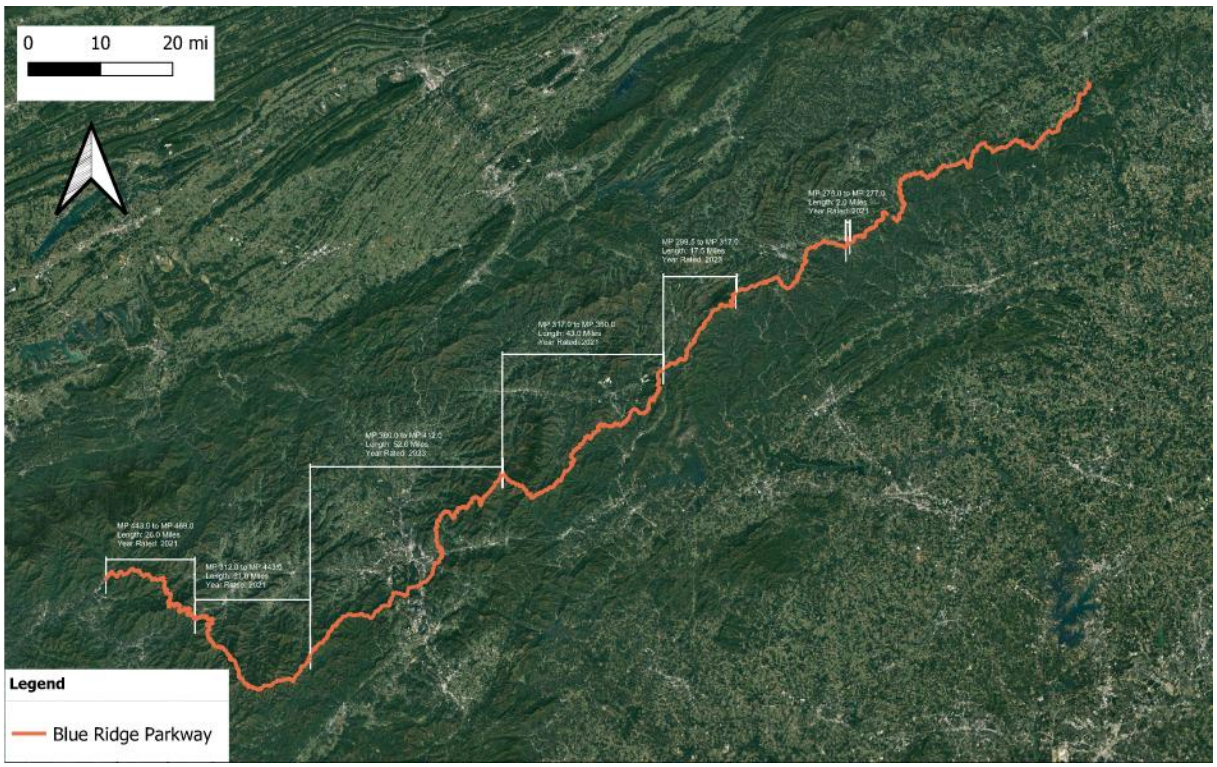

Figure 1. Blue Ridge Parkway sections mapped during the 2021 USMP inventory. The 2021 program covered Sections A through D: MP 275–277, MP 317–360, MP 443–469, and MP 412–443.

LOCAL GEOLOGIC SETTING

The study reach lies within the Blue Ridge physiographic province of North Carolina and crosses several metamorphic and intrusive units. The southwestern part of the corridor includes the Ashe Metamorphic Suite and Tallulah Falls Formation; the middle and northeastern portions

include the Alligator Back Formation; and localized intrusive bodies occur toward the northern end. The Ashe and Tallulah Falls rocks commonly include foliated to massive metagraywacke interbedded with mica schist, muscovite-biotite gneiss, and graphitic schist. The Alligator Back Formation includes gneiss, phyllite, schist, amphibolite, and locally metasedimentary rocks. Intrusive rocks in the area include quartz diorite and granodiorite.

From an engineering-geology standpoint, the mapped contacts provide only the regional framework. Slope behavior is controlled at the site scale by orientation, persistence, spacing, and condition of foliation, joints, fractures, faults, and folds, the depth and character of weathering, residual-soil thickness, and the relationship between those materials and roadway drainage. The post-storm borings encountered fill, coarse and fine-grained residual soils, partially weathered rock, and bedrock including metagraywacke, phyllitic schist, and quartzite. Rock quality varied from very poor to good in the cored intervals. That heterogeneity explains why nearby slopes subjected to the same storm did not respond uniformly. *(2)*

BLUE RIDGE PARKWAY USMP INVENTORY

The 2021 inventory covered approximately 102 miles of the Blue Ridge Parkway and evaluated both rock slopes and landslides using the Federal Lands Highway USMP methodology. Field teams evaluated 1,228 slopes and entered 454 unstable slopes into USMP, including 277 rock slopes and 177 landslides. Ratings ranged from 113 to 904, with an average of 347, and 57 slopes were rated above 500. *(3) (4)*

USMP separates the evaluation into site information, preliminary screening, detailed hazard ratings, and detailed risk ratings. The field form applies the standard 3, 9, 27, and 81 scoring progression to categorical observations and uses calculated scores, capped at 100 points, for directly measured variables. Landslide screening considers roadway width affected, slide or erosion effects, and roadway length affected, while rockfall screening considers ditch effectiveness, rockfall history, and representative block size or event volume. Common risk categories include impact on use and traffic or recreational importance. Detailed ratings add slope drainage, annual rainfall, slope height or landslide axial length, maintenance and movement history, geologic character, roadway width, human exposure, sight distance, right-of-way and environmental consequences, maintenance complexity, and event cost. *(5)*

The total USMP score combines the applicable hazard total with the common risk total. Total scores below 200 are categorized as Good, scores from 200 through 400 are Fair, and scores above 400 are Poor. Those descriptors are useful for portfolio-level comparison, but they should not be interpreted as failure probabilities. The score is a prioritization index that integrates observed condition, geologic hazard, exposure, and consequence. The reliability of the rating therefore depends on consistent measurements, defensible field observations, maintenance input, and the judgment of experienced geotechnical personnel.

POST-HURRICANE HELENE LANDSLIDE INVESTIGATION

The post-storm investigation evaluated eight landslide sites between MP 336.7 and MP 348.9. Seventeen test borings were advanced between August 21 and September 3, 2025, generally with one boring on each flank of each failure and an additional offset boring at MP

348.9. Standard Penetration Testing, selected rock coring, laboratory testing, groundwater observations, and photographic documentation were used to characterize conditions. *(2)*

CORRELATION METHOD

Each post-storm landslide milepost was compared with the nearest pre-storm USMP site. A correlation was accepted where the milepost, recorded failure type, rating, and photographic record consistently represented the same roadway-slope setting. Five post-storm sites met that standard. No pre-storm USMP match was identified for MP 342.7, MP 343.7, or MP 343.8.

Table 1 - Correlation between the eight post-Hurricane Helene landslide sites and available pre-storm USMP records.

Post-storm Landslide MP Location	Correlated USMP Rated Slope MP	Pre-storm Failure Mode Identified (USMP)	USMP Rating Score
336.7	336.6	Translational slide	414
338.2	338.2	Translational slide	305
342.7	None identified	—	—
343.7	None identified	—	—
343.8	None identified	—	—
345.7	345.7	Rotational / Translational	310
346.8	346.7	Rotational	626
348.9	348.8	Rotational	549

PRE-STORM (USMP) / POST-STORM SITE CORRELATIONS

USMP MP 336.6 / MP 336.7

The post-storm failure at MP 336.7 removed the roadway on the southeastern fill slope. The correlated pre-storm USMP site is MP 336.6, classified as a translational slide with a rating of 414. The pre-storm photograph documents a broad vegetated downslope area immediately beyond the roadway shoulder. The correlation demonstrates that the inventory had already identified translational movement susceptibility at essentially the same milepost before the complete roadway washout.

Figure 2. Pre- and Post-Storm Conditions at MP 336.7. Left: pre-storm USMP photograph at MP 336.6. Right: post-Hurricane Helene roadway washout at MP 336.7.

USMP MP 338.2 / MP 338.2

The MP 338.2 post-storm landslide affected the north side of the roadway and produced asphalt stress cracking and slope creep in the outside lane. The USMP record is a direct milepost match and classified the site as a translational slide with a rating of 305. The pre-storm photograph shows a longitudinal pavement crack near the roadway edge. This is the clearest photographic example in the dataset of roadway distress being documented before and after the storm-related movement was investigated.

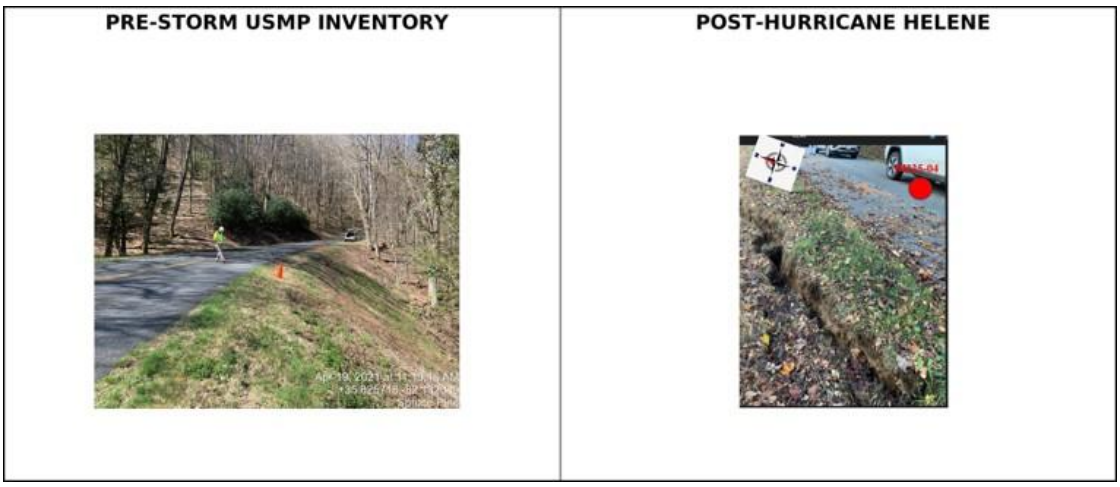

Figure 3. Pre- and Post-Storm Conditions at MP 338.2. Left: pre-storm pavement cracking. Right: post-storm outside-shoulder deformation near MP 338.2.

USMP MP 345.7 / MP 345.7

The MP 345.7 post-storm site is a landslide complex with two distinct features. The pre-storm USMP record is a direct milepost match, classified as rotational/translational with a rating of 310. The photograph shows an open roadway curve with a steep wooded downslope side and no obvious large fresh scarp visible from the camera position. The significance of this correlation is not that the photograph alone predicts the later failure; rather, the USMP field assessment and rating preserved a record of instability at the same location before the storm.

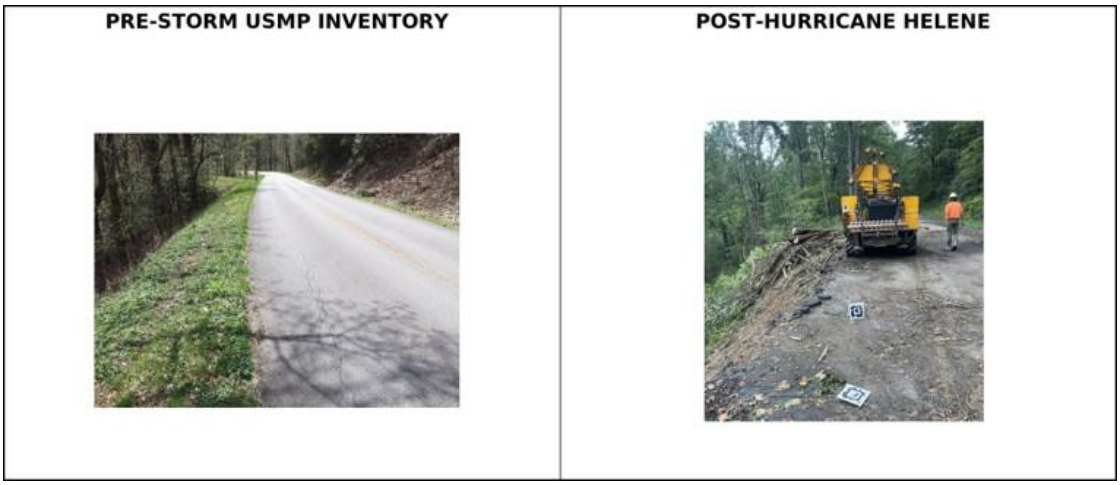

Figure 4. Pre- and Post-Storm Conditions at MP 345.7. Left: pre-storm USMP view. Right: post-storm roadway-edge failure and debris.

USMP MP 346.7 / MP 346.8

The post-storm landslide at MP 346.8 affected the western fill slope. The correlated USMP site is MP 346.7, classified as rotational with a rating of 626. The photograph shows a curved roadway section with a steep wooded downslope side beyond the outside edge. This is the highest-rated of the five correlated sites and provides a strong example of a pre-storm high-risk location later experiencing storm-related instability.

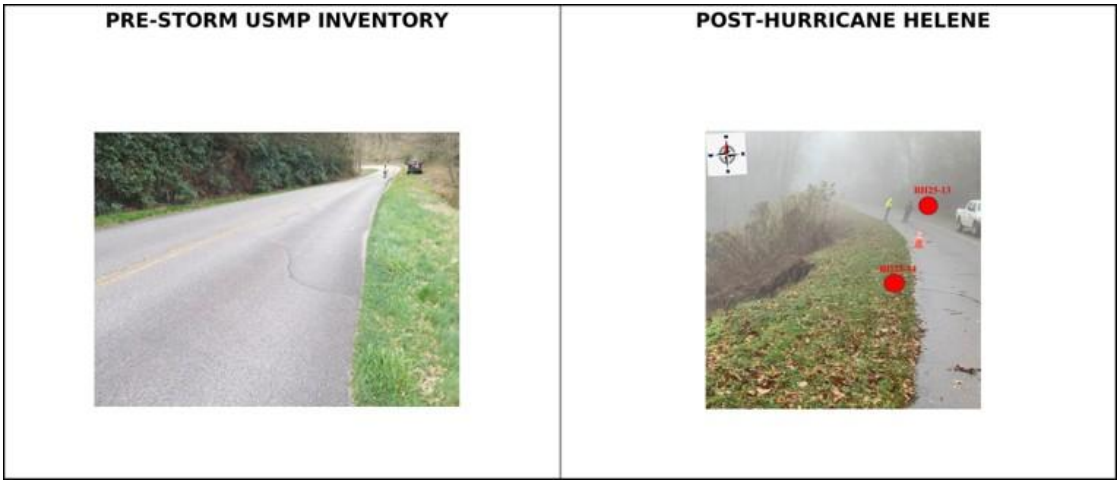

Figure 5. Pre- and Post-Storm Conditions at MP 346.8. Left: pre-storm USMP view at MP 346.7. Right: post-storm fill-slope failure and boring locations BH25-13 and BH25-14.

MP 348.9 / USMP MP 348.8

The post-storm MP 348.9 site includes two landslides, pavement cracking, grade separation, slope creep, and exposed bedrock. The correlated pre-storm USMP site is MP 348.8, classified as rotational with a rating of 549. The photograph shows a forested roadway bend with a steep outside slope. The high pre-storm rating and near identical milepost support a meaningful spatial correlation, while the post-storm investigation supplies the additional detail on roadway and slope deformation.

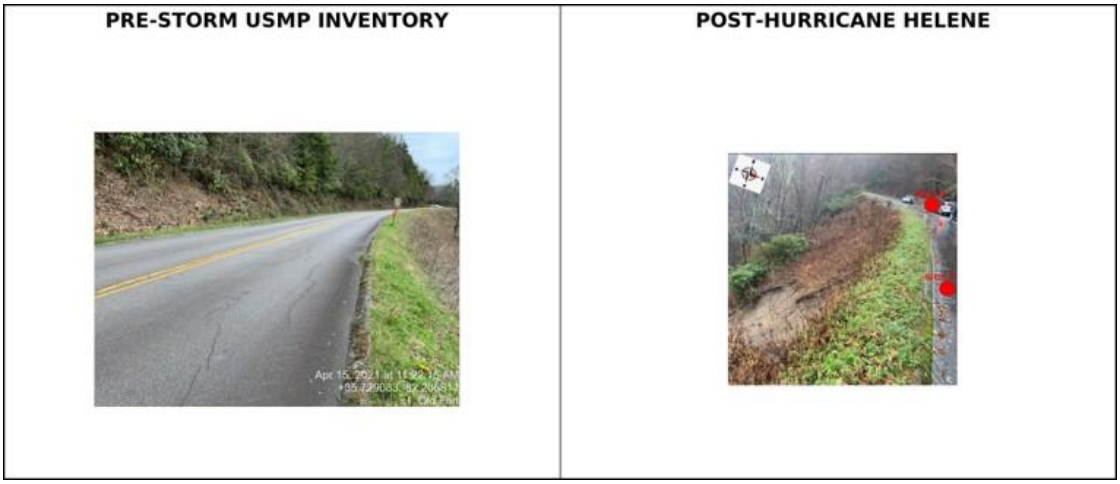

Figure 6. Pre- and Post-Storm Conditions at MP 348.9. Left: pre-storm USMP view at MP 348.8. Right: post-storm slope failure and boring locations BH25-15 and BH25-16.

DISCUSSION

Five of the eight post-storm sites have a documented pre-storm USMP match. The ratings span Fair and Poor condition categories and range from 305 to 626. Two correlated sites MP 346.8 and MP 348.9 had ratings above 500. Three correlated sites had ratings from 305 to 414. The outcome therefore supports corridor vulnerability screening but does not support use of a single score threshold as a failure predictor.

The photographs improve the comparison because they preserve what the field team could see before the storm. At MP 338.2, the pavement crack is direct evidence of roadway distress. At the other matched sites, the photos document roadway geometry, slope position, vegetation, and the visible terrain context. The rating record, not the photograph by itself, provides the formal pre-storm classification and score.

Correlation Between Inventory and Observed Failure

The study goal was to test whether USMP ratings, hazard classifications, and documented slope characteristics provided meaningful insight into actual slope performance during an extreme precipitation event. Five of the eight post-storm sites were spatially correlated with pre-storm USMP locations. The matches include translational, rotational, and combined rotational/translational settings and span scores from 305 to 626. The result is not a perfect one-to-one validation, nor should it be. USMP is a corridor-scale prioritization framework, while a landslide is the site-specific response of a particular soil-rock-groundwater system which correlates to a particular loading history. The meaningful finding is that the inventory repeatedly placed attention on the same slope settings that later experienced damaging movement.

The side-by-side photographs strengthen that finding because they connect database entries and numerical scores to visible changes in the transportation asset. At MP 336.7, the pre-storm corridor setting progressed to complete loss of the roadway prism. At MP 338.2, pavement cracking visible before the storm was followed by outside shoulder deformation. At MP 345.7, MP 346.8, and MP 348.9, the post-storm images show roadway edge or fill slope damage at locations previously rated for instability. These photographs do not establish the timing or rate of movement, but they demonstrate that the USMP records represented real geomorphic and roadway conditions rather than abstract points in a database.

Meaning of the Rating Range

The matched sites include Fair and Poor condition categories. Two matched sites were rated above 500, while three were rated between 305 and 414. This range is important to interpret the results. The higher-scoring sites support use of USMP to focus attention on locations with a strong combination of hazard and consequence. The intermediate scoring failures show that a lower relative priority does not mean a slope is stable or immune to extreme rainfall. A USMP score ranks observed vulnerability within a portfolio; the score does not define a rainfall threshold, calculate a factor of safety, or predict the probability of failure during a specific storm.

Accordingly, the post-storm Helene comparison supports the rating system without overstating the rating system. The inventory successfully differentiated slopes that warranted documentation and management attention. The storm then imposed a level of hydrologic loading that activated some of those slopes and also produced failures at three locations with no identified pre-storm match. The non matches are not merely exceptions to be explained away. The non matches identify where inventory coverage, visibility, selection criteria, drainage recognition, spatial accuracy, or subsequent slope evolution may have limited the pre-storm record. A defensible validation includes those limitations because the limitations help define how the next inventory can be improved.

Geology, Drainage, and Groundwater Response

The correlations are best understood in the context of the Blue Ridge geologic and topographic setting. The corridor crosses foliated metamorphic rock, intrusive rock, residual soil, partially weathered rock, and constructed fill. Weathering depth and material character vary over short distances, and discontinuities can provide preferred seepage paths or kinematic release surfaces. Roadway cuts and fills modify the natural slope profile, while ditches, culverts, and shoulder grades redistribute runoff. During extreme rainfall, these controls act together: infiltration reduces effective stress, concentrated flow erodes support, perched water develops above lower-permeability horizons, and discontinuities transmit water into weathered rock and soil masses.

This integrated interpretation explains why rainfall alone is not a sufficient indicator of the failures. Hurricane Helene supplied the trigger, but slope response depended on preexisting susceptibility. Steep terrain, adverse structure, fill geometry, residual soil development, drainage concentration, and groundwater response determined where the rainfall produced deformation severe enough to damage the roadway. That distinction directly supports the abstract. USMP ratings provide meaningful insight because the ratings organize observable evidence of susceptibility before an extreme event exposes the consequences of that susceptibility.

Implications for Geohazard Prioritization

For transportation agencies, the practical value of USMP is the ability to move from isolated observations to corridor level decisions. A systematic inventory provides a repeatable basis for comparing slopes, preserving pre-event evidence, communicating uncertainty, and directing limited resources toward inspection, monitoring, drainage improvement, subsurface exploration, or mitigation. The Helene case study shows that this information remains useful after a disaster as well. Pre-storm records can guide reconnaissance, help distinguish newly developed damage from chronic distress, and provide context for emergency repair and capital programming.

The study also indicates that prioritization should remain dynamic. Ratings should be revisited when pavement distress progresses, drainage changes, maintenance history accumulates, repairs alter geometry, or extreme events reveal new behavior. High scoring sites warrant attention, but intermediate scoring slopes with active distress, adverse drainage, or significant closure consequences should not be dismissed. The most defensible program couples

the numerical rating with experienced engineering geologic review and updates the record as the slope and transportation asset evolve.

CONCLUSIONS

Hurricane Helene provided a rare field scale test of a pre-storm unstable slope inventory. Five of the eight investigated landslide sites between MP 336.7 and MP 348.9 correlate with pre-storm USMP locations. Those correlations include translational, rotational, and combined rotational/translational settings with ratings from 305 to 626. The spatial correlations observed hazard types, and paired photographs collectively support the central premise of the study. USMP ratings and inventory observations provide meaningful insight into where slope vulnerability exists before extreme precipitation converts that vulnerability into roadway damage.

The results do not demonstrate that USMP predicts the precise location, timing, boundaries, or magnitude of a future landslide. Such a conclusion would exceed the purpose of the method and the available evidence. Instead, the results show that a systematic field inventory can identify vulnerable slope settings at a scale useful for transportation management. The matched sites demonstrate successful recognition of susceptibility. The three sites without an identified pre-storm match demonstrate the complementary lesson that no corridor inventory is complete or static, particularly in steep, vegetated terrain where drainage, weathering, and geomorphic expression can be difficult to observe.

The range of scores among the matched sites is equally instructive. The higher rated MP 346.8 and MP 348.9 sites show the value of identifying slopes with substantial combined hazard and consequences. The intermediate rated MP 336.7, MP 338.2, and MP 345.7 sites show that damaging failure during an exceptional storm is not confined to the highest numerical tier. Condition categories should therefore be used to structure relative priorities, not as binary statements of stability. Numerical scores are most effective when combined with field evidence of movement, drainage sensitivity, geologic setting, roadway consequence, and professional judgment.

The photographic comparisons provide the clearest visual expression of the study outcome. The post-storm damage did not occur in a geologic vacuum. The damage developed where the roadway crossed steep slopes, weathered materials, constructed fills, and drainage-sensitive terrain that had already warranted inventory. At MP 338.2, pre-storm pavement cracking is particularly important because the cracking documents progressive roadway response before the storm. At MP 336.7, the complete roadway washout illustrates the consequence when an already vulnerable fill slope setting is subjected to extreme hydrologic loading.

From an engineering geology perspective, the broader conclusion is that effective geohazard management requires integration. Surface indicators, geologic structure, weathering profile, residual soil and fill conditions, groundwater, drainage, maintenance history, and consequence cannot be evaluated independently. USMP provides the organizational framework for assembling those observations into a consistent corridor record. Site-specific exploration and analysis then provide the additional resolution required for design and stabilization decisions.

For transportation agencies, the recommended use of USMP is proactive and iterative. Inventory data should inform pre-storm planning, inspection priorities, monitoring, drainage maintenance, emergency response, and capital programming. Ratings should be updated when conditions change or when major events reveal new behavior. Used in this manner, USMP does not promise prediction, it provides something more practical and a defensible repeatable basis for recognizing vulnerability, comparing risk, preserving institutional knowledge, and directing limited resources before the next extreme event.

REFERENCES

1. Federal Highway Administration. Geohazards, Extreme Weather Events, and Climate Change Resilience Manual. Report FHWA-HIF-23-008. Washington, D.C., February 2023.
2. Schnabel Engineering. Geotechnical Subsurface Exploration – NC NP BLRI 2M31, MP 336 to MP 352. 2025.
3. WSP USA, Inc. and Schnabel Engineering. Blue Ridge Parkway USMP Inventory Close-Out Meeting. December 3, 2021.
4. Schnabel Engineering. USMP Assessment Report, Blue Ridge Parkway. December 8, 2023.
5. Federal Highway Administration. Unstable Slope Management Program for Federal Land Management Agencies. Report FHWA-FLH-19-002. Washington, D.C., January 2019.

18. Comprehensive Load Test Program for Steel H-Piles Driven in Intermediate Geomaterials

Nafis Bin Masud, Ph.D. M. ASCE
Senior Staff Engineer, Schnabel Engineering
3902 Market St.
Wilmington, NC 28403
(910)-769-1621
nmasud@schnabel-eng.com

Kam Ng, P.E., Ph.D., M. ASCE
Professor
Department of Civil and Architectural Engineering and Construction Management,
University of Wyoming
1000 E. University Ave
Laramie, WY 82072
(307)-766-1121
kng1@uwyo.edu
(Corresponding Author)

Shaun S. Wulff, Ph.D.
Professor
Department of Mathematics and Statistics
University of Wyoming
1000 E. University Ave
Laramie, WY 82072
(307)-766-1121
wulff@uwyo.edu

Prepared for the 75th Highway Geology Symposium, September, 2026

Acknowledgements

The authors express their gratitude to the research supports from the Wyoming Department of Transportation as the lead agency, Colorado Department of Transportation, Iowa Department of Transportation, Kansas Department of Transportation, North Dakota Department of Transportation, Idaho Transportation Department and Montana Department of Transportation under the Grant RS05219. Additional support from Mountain Plains Consortium is also acknowledged.

Disclaimer

Statements and views presented in this paper are strictly those of the author(s), and do not necessarily reflect positions held by their affiliations, the Highway Geology Symposium (HGS), or others acknowledged above. The mention of trade names for commercial products does not imply the approval or endorsement by HGS.

Copyright Notice

Copyright © 2026 Highway Geology Symposium (HGS)

All Rights Reserved. Printed in the United States of America. No part of this publication may be reproduced or copied in any form or by any means – graphic, electronic, or mechanical, including photocopying, taping, or information storage and retrieval systems – without prior written permission of the HGS. The State of Wyoming, WYDOT and University of Wyoming reserve a royalty-free, nonexclusive, unlimited, and irrevocable license to reproduce, published, or otherwise use, and to authorize others to use the copyright in any work that is generated from the research project entitled Wyoming, Comprehensive Field Load Test and Geotechnical Investigation Program for Development of LRFD Recommendations of Driven Piles on Intermediate Geomaterials, TPF 5-391.

ABSTRACT

Full-scale static and dynamic load tests were conducted on eleven steel H-piles driven into intermediate geomaterials (IGMs) in Colorado, Iowa, Kansas, North Dkota, and Wyoming. Three static load test (SLT) systems were developed to address the construction scenarios encountered across the study sites. The first SLT system was an Independent Static Pile Load System (IndeSPLS), which was conducted on test piles (TP) 1 to TP5 driven into shale and claystone in Iowa, Kansas, and North Dakota. The second system was an Integrated Static Pile Load System (InteSPLS) designed for TP6 and TP7, which were driven into siltstone in Wyoming. The third system was an Innovative Static Pile Load System (InnoSPLS), which was designed for TP8 to TP11 driven into shale, siltstone, and claystone in Colorado. Dynamic load tests (DLTs) were conducted using Pile Driving Analyzer (PDA) with the Case Pile Wave Analysis Program (CAPWAP). This paper presents site and subsurface conditions, test pile instrumentation and protection, data collection, load distribution from SLTs, and the comparison of load test results. Six failure criteria were used to determine the ultimate failure resistances from the SLT. The ultimate resistances of TP1, TP3, TP4 and TP10 based on all failure criteria were lower than that from CAPWAP at the 24-hour restrike. For TP7 and TP6, the ultimate resistances based on the Davisson, De Beer YL, Fuller & Hoy, 10% pile size, and 1-in displacement criteria were higher than that from CAPWAP. The ultimate resistances of TP8 and TP9 based on all failure criteria were higher than those from CAPWAP. Comparison with CAPWAP showed that the agreement between static and dynamic resistance estimates varied depending on the test pile and failure criterion. The findings provide practical guidance for selecting appropriate SLT systems for driven piles in IGMs under different bridge construction conditions.

INTRODUCTION

Due to the shallow bedrock, especially in the Rocky Mountain and Appalachian regions of the United States and Canada, driven pile foundations are commonly used to support transportation infrastructure such as bridges. These piles often gain their resistance from Intermediate Geomaterial (IGM) layers, which exhibit properties between soils and hard rock. IGM has been defined as fine-grained geomaterials (e.g., clay shale and mudstone) with undrained shear strength (s_u) of 5–50 ksf or coarse-grained geomaterials (e.g., glacial till and sandstone) with corrected SPT N-values between 50 and 100 blows/ft (*1-2*). However, definitions of IGM vary widely because of its heterogeneity and differing engineering applications (*3*). Many studies define IGM based on unconfined compressive strength (q_u) (*4-7*), while others classify IGM using corrected SPT N-values, rock mass rating (RMR), q_u (*8*), or s_u > 2.7 ksf for fine-grained materials (*9*).

AASHTO LRFD Bridge Design Specifications (*10*) define IGM as a transitional material between soil and rock and recommend treating it as soil when estimating driven pile resistance. Consequently, driven pile design in IGMs commonly relies on static analysis (SA) methods developed for soils. However, this approach may lead to construction challenges, such as premature pile refusal and pile damage due to the lack of appropriate design methods and sufficient load-test data (*11*). Studies have shown that soil-based SA methods often provide inconsistent and conservative resistance predictions compared with DLT results (*3, 9-10*).

Research on driven piles in IGMs remains limited, particularly regarding SLT. Mokwa and Brooks (*3*) evaluated piles from nine Montana bridge projects using several prediction methods and found little comparison with CAPWAP-estimated resistances. Long (*12*) conducted seven SLTs and 77 DLTs in Wisconsin and reported that predictions from CAPWAP based on beginning-of-restrike data underestimated measured pile capacities by about 15%. The study also proposed empirical SA methods for estimating shaft and end-bearing resistance in fine and coarse-grained IGM. However, these methods are based on modified SPT values, which are not widely available in historical geotechnical records, and corresponding LRFD resistance factors have not been developed.

Because pile behavior in IGM is not well understood without SLT measurements, SLT remains essential for evaluating load-displacement behavior and load-transfer mechanisms, despite the practical advantages of DLT. To address these limitations, a comprehensive field-testing program was conducted across multiple states representing a range of IGM conditions. This paper presents eleven full-scale load tests on steel H-piles driven into IGMs at bridge sites in Kansas, North Dakota, Iowa, Wyoming, and Colorado. Three SLT systems were developed: IndeSPLS for TP1–TP5 in shale and claystone, InteSPLS for TP6–TP7 in siltstone, and InnoSPLS for TP8–TP11 in shale, siltstone, and claystone. The paper describes pile instrumentation and protection, data acquisition, SLT systems, and load test results. The findings provide guidance for selecting suitable SLT systems for driven piles in IGMs and for validating DLT-based assessments. The field test results presented in this paper were part of the recently completed Federal Highway Administration (FHWA) Pooled Fund Study TPF-5(391) reported in Ng et al. (*13*). The final report included classification for IGMs, new SA methods for piles in IGMs (*14-15*), field test results, improved Wave Equation Analysis program (WEAP)

procedures, machine learning methods for pile weight prediction, variability analysis, and overall LRFD recommendations.

SITE DESCRIPTION AND SUBSURFACE CONDITION

Subsurface investigations consisting of 2 to 6 boreholes were completed at each bridge site to characterize soil and bedrock conditions. The test piles consisted of HP steel sections installed in varying geologic conditions, including clay, silty clay, sand, gravel, glacial till, and sedimentary bedrock formations such as shale, sandstone, claystone, lignite, and siltstone. TP1 and TP2 were located in Iowa, where piles were driven through overburden soils into shale bedrock at depths of approximately 34 to 50 ft. TP3 in North Dakota encountered clay, silty sand, and sand deposits overlying sandstone, claystone, and lignite bedrock at about 42 ft. TP4 and TP5 in Kansas were installed within the Wellington Formation, consisting primarily of soft to moderately hard shale. TP6 and TP7 in Wyoming were driven through sand, gravel, silt, and sandy clay deposits into siltstone bedrock at depths of approximately 48 ft. TP8–TP11 in Colorado were founded in sedimentary bedrock formations including shale, siltstone, sandstone, and claystone with pile penetration lengths ranging from approximately 18 to 41 ft. Groundwater conditions varied across the sites, with groundwater encountered at TP2 and TP6, but not observed during exploration at most other locations. Figures 1a–1k present the groundwater conditions, SPT N-values, and subsurface profiles for all eleven test pile sites. The test pile and bearing layer properties are summarized in Table 1.

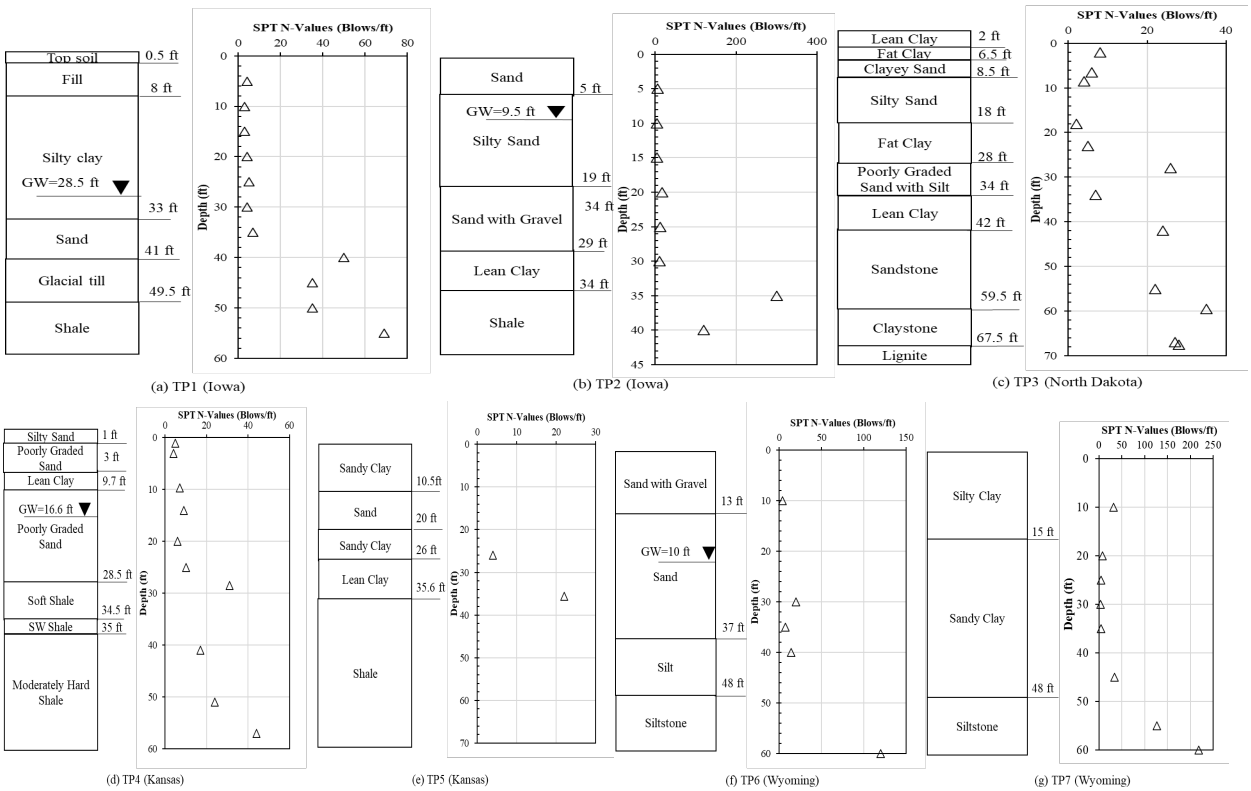

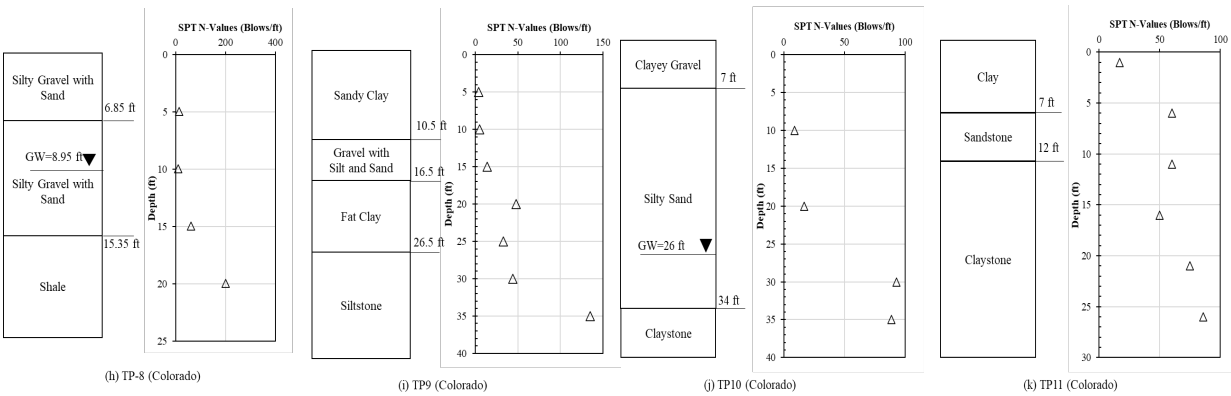

Figure 1. Subsurface profiles and SPT N-values of a) TP1 in Adair County, IA, b) TP2 in Wapello County, IA, c) TP3 in McKenzie County, ND, d) TP4 in Sumner County, KS, e) TP5 in Sedgwick County, KS, f) TP6 in Laramie County, WY, g) TP7 in Sweetwater County, WY, h) TP8 in Delta County, CO, i) TP9 in Arapahoe County CO, j) TP10 in EL Paso County, CO, and k) TP11 in Jefferson and Denver Counties, CO.

Table 1. Test Pile and Bearing Layer Properties of Different SLT Systems.

Test Pile	State	SLT System	Test Pile Size	Pile Length (ft)	Pile Penetration (ft)	Bearing Layer	q_u of Bearing Layer (ksf)
TP1	IA	IndeSPLS	HP10×57	60	56.1	Shale	9.4
TP2	IA		HP10×42	42	36.0	Shale	-
TP3	ND		HP12×53	80	67.5	Claystone	14.4
TP4	KS		HP12×53	55	51.0	Shale	6.1
TP5	KS		HP12×53	75	66.5	Shale	9.0
TP6	WY	InteSPLS	HP10×42	60	57.2	Siltstone	22.0
TP7	WY		HP12×53	60	59.1	Siltstone	9.5
TP8	CO	InnoSPLS	HP14×89	21	18.2	Shale	720.0
TP9	CO		HP12×74	35	28.5	Siltstone	117.0
TP10	CO		HP14×89	60	41.0	Claystone	16.0
TP11	CO		HP14×89	40	24.5	Claystone	5.7

THREE STATIC LOAD TEST SYSTEMS

Independent Static Pile Load System (IndeSPLS)

The IndeSPLS system shown in Figure 2a consisted of a test pile centered within a reaction frame supported by four HP14×89 reaction piles spaced 7 ft from the test pile, exceeding the ASTM D1143 (*16*) minimum spacing requirement. The reaction system included two 10-ft hold-down spreader beams and an 18-ft W40×183 main reaction beam connected with steel rods, plates, nuts, and C-clamps. Axial load was applied using a hydraulic jack and measured with a load cell, while uplift resistance was provided by the reaction piles through shaft resistance. The system was designed for a maximum load of approximately 1,000 kips with a safety factor of 2. SLT was performed in accordance with the ASTM D1143 (*16*) quick load test procedure A using 20 equal load increments followed by 10 load decrements until either geotechnical failure or structural capacity was reached. The IndeSPLS was designed as an independent loading and reaction system that was not part of the bridge foundation. Hence, it

was not a critical path of bridge construction. This SLT system is conventionally conducted to load a pile to failure (Table 2).

Integrated Static Pile Load System (InteSPLS)

InteSPLS, which is shown in Figure 2b, was developed using four HP12×53 production piles (P1–P4) as reaction piles and a TP at the center. The nearest production piles (P2 and P3) were located about 9 ft 3 in from the TP, exceeding the ASTM minimum spacing of 5 ft. The system included a main reaction beam assembly of W36×150 sections and four hold-down spreader beams made from C10×25 channels reinforced with 0.5-in steel plates. Each spreader beam was secured with 1.75-in diameter high-strength bars anchored to the production piles. Axial load was applied to the TP using a hydraulic jack and measured with a load cell. As for IndeSPLS, the load was transferred through the reaction beam, spreader beams, bars, and reaction piles. With a safety factor of 2, the design load was 775 kips. Testing continued until the maximum structural or geotechnical capacity was reached. Compared with IndeSPLS, InteSPLS is more economical because production piles serve as reaction piles, although the SLT remains a critical activity in the bridge construction schedule (Table 2).

Innovative Static Pile Load System (InnoSPLS)

InnoSPLS, as shown in Figures 2c and 2d, was adopted in Colorado without using a temporary loading frame nor reaction piles, thereby reducing labor and setup costs (Table 2). The TP was part of the permanent bridge foundation and was loaded by the bridge with dead loads (abutment cap, wing walls, girders, deck, barriers, utilities, etc.), and eventually traffic loads. Steel pile hats were installed on four adjacent production piles to create a 1-in gap between the pile tops and abutment cap, allowing loads to be transferred primarily to the TP. The pile hats were integrated into the abutment cap using welded rebars and later filled with non-shrink grout after testing to restore full load sharing among all piles. Strain gauges (SGs) were installed on the TP to measure pile strains and settlements throughout construction stages. The axial loads and displacements of the TP were calculated from the SGs readings induced by these progressive construction loads.

Table 2. Summary of primary features and advantages of three static load test systems

SLT System	Primary Feature	Main Advantage
IndeSPLS	Independent reaction frame	Conventional full-scale testing
InteSPLS	Production piles as reaction piles	Reduced testing cost
InnoSPLS	Permanent bridge structures	Eliminate reaction frame

Figure 2. Photos of three static load test systems: (a) IndeSPLS for TP1 to TP5, (b) InteSPLS for TP6 and TP7, and (c) InnoSPLS for TP8 to TP11.

TEST PILE AND LOAD TEST PREPARATION

Strain Gauge Installation

Each TP was instrumented with eight pairs of Geokon® VW 4000A SGs on both web faces along the pile length to determine load distribution and pile bending during the SLT. These SGs were selected for their long-term stability, resistance to water and lightning damage, and reliable signal transmission over long cable lengths. Before installation, the pile surface was cleaned to remove rust and dirt. Mounting blocks were positioned using a spacing jig and welded to the pile web, after which the SGs were secured between the blocks with hose clamps and protective coils (Figure 3). The change in SG readings (ΔR) was converted to microstrain (ε) using a gauge factor (G = 4.062) and batch factor (B = 0.96) by Equation (1).

$$\epsilon = G \times B \times \Delta R \tag{1}$$

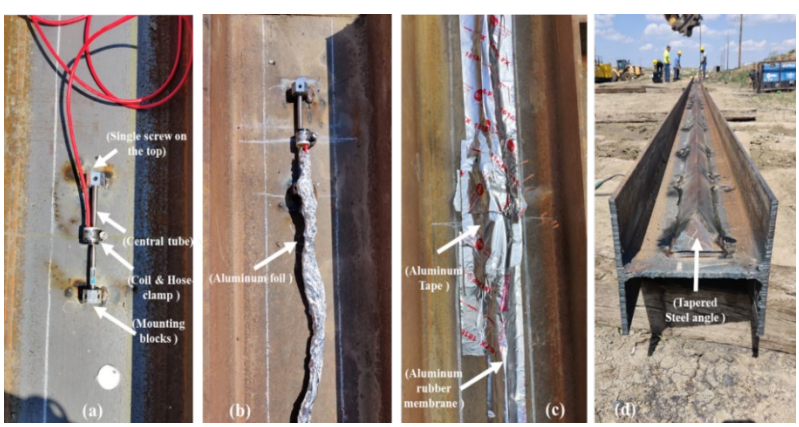

Figure 3. Test pile instrumentation: a) SG welded on the web face of the TP, b) protection of cables with aluminum foils, c) protection of SGs and cables with aluminum tapes and membranes, and d) protection using steel angles with tapered steel angles near the pile tip.

Strain Gauge Protection

The SGs and cables were protected from welding heat and sparks using aluminum foil, aluminum tape, and aluminum-laminated rubber membrane. To prevent damage during pile driving, the SGs and cables were enclosed in 3-in steel angles welded to the TP. The steel angles were attached using continuous 6-in fillet welds at 24-in intervals and tapered at the pile tip to minimize soil disturbance during installation (Figure 3) and ensure reliable measurements throughout pile driving and SLT. Following installation and protection, the SG measurements were converted to microstrain and subsequently to pile stress (σ). Pile stress was calculated from the microstrain and the pile modulus of elasticity (E) using Equation (2) before and after end of driving (EOD), beginning of restrike (BOR), and during SLT.

$$\sigma = \epsilon E = G \times B \times \Delta R \times E \tag{2}$$

Static Load Test Setup

A 355-ton Power Team™ hydraulic jack, with a 10-in stroke, was used to apply axial loads to the TP in the InteSPLS and IndeSPLS systems. The jack was powered by a double-acting gasoline-driven hydraulic pump capable of producing pressures up to 10,000 psi, with a digital pressure gauge used for accurate pressure monitoring. A 500-ton Honeywell load cell measured the applied load, and its readings were calibrated using the hydraulic pump pressure before testing. Pile-top displacements were measured using four UniMeasure JX-P420 linear position transducers mounted on independent wooden reference beams. In addition, two string potentiometers mounted on separate wooden beams were used to monitor the upward movement of the reaction or production piles during the SLT (Figure 4).

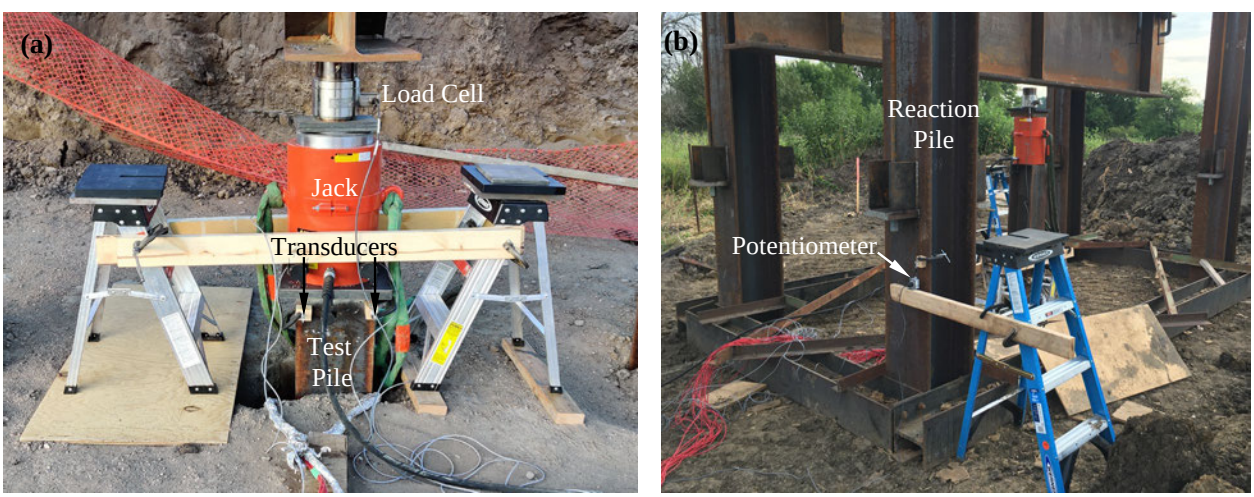

Figure 4. Static load test setup at the a) test pile, and b) reaction or production Pile.

Data Acquisition System

A 16-channel Geokon Model 8032 multiplexer was used to collect readings from all vibrating-wire SGs (Figure 5). LabVIEW software synchronized measurement times and organized the data for processing. The multiplexer sequentially reads each sensor through a programmed relay system. A Model 8020-59 VW-analog converter excited the sensors,

measured the frequencies, and converted the readings into voltage outputs proportional to strain and stress values. The data acquisition system (DAS) included a power supply, hard drive, and control switch, and stored all measurements via USB. Load cell data and readings from six displacement sensors were continuously monitored and recorded on a connected PC.

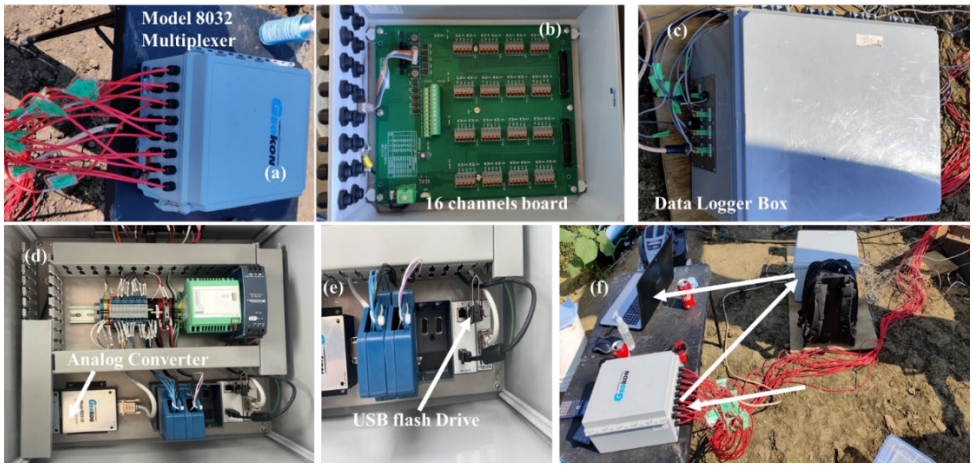

Figure 5. a) multiplexer, b) 16-channels in the multiplexer, c) data logger box, d) vw analog converter, e) usb flash drive, and f) computer system to collect the readings during SLT.

STATIC LOAD TEST RESULTS

SLTs were performed between 1 and 61 days after EOD, and the pile head load–displacement responses are presented in Figures 6a–6g. For TP1–TP7, the applied load increased approximately linearly with displacement, indicating elastic pile behavior within the monitored load range. TP8–TP11 were monitored using the InnoSPLS system in Colorado. Loads were induced by sequential construction of structural components, including the abutment cap, wing walls, girders, deck panels, haunch, and concrete deck with live load. The load–displacement responses (Figures 6h–6k) remained linear, with pile head displacements ranging from 0.08 to 0.13 in., indicating that the piles remained in the elastic range and ultimate resistance was not mobilized. To estimate the full load–displacement response of TP8–TP11, the extrapolation method was used (*17*). The measured and extrapolated responses are plotted in Figures 6l–6o. Ultimate resistances were evaluated using the Davisson (*18*), De Beer (*19*) Yield Load (YL), Fuller and Hoy (*20*), 10%B, 5%B, and 1-in. displacement criteria (*21*). For the 10%B and 5%B criteria, equivalent pile diameters were calculated (*22*).

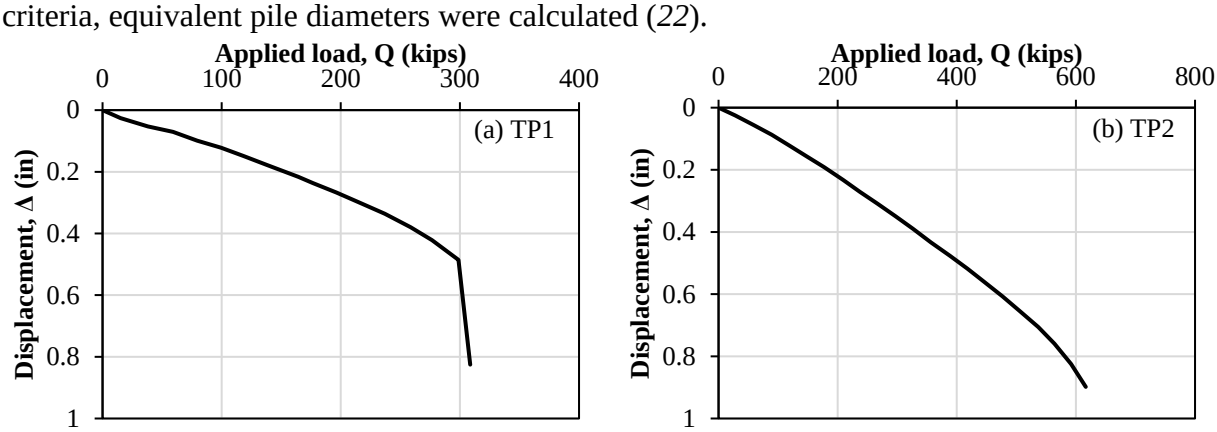

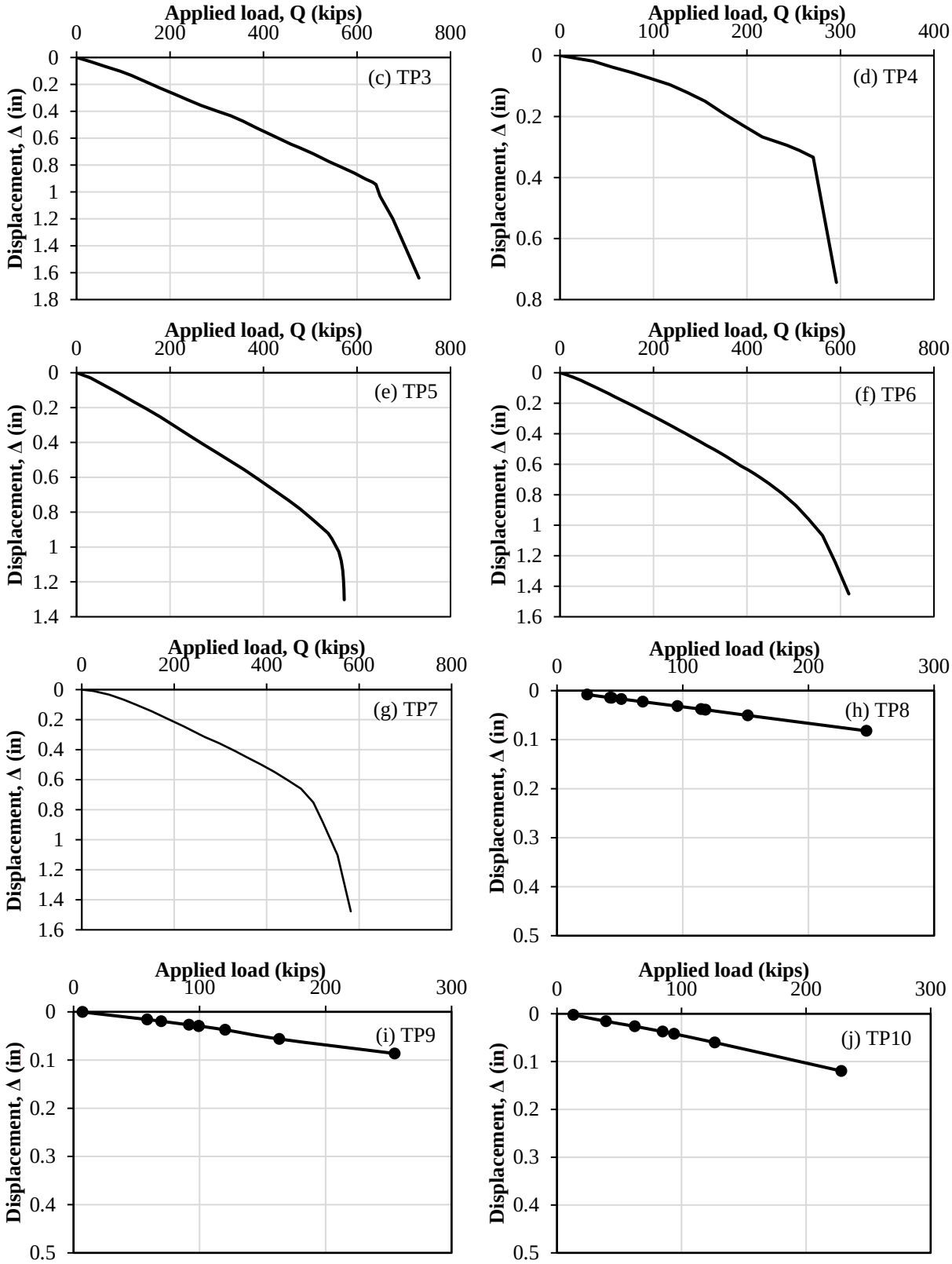
(c) TP3
(d) TP4
(e) TP5
(f) TP6
(g) TP7
(h) TP8
(i) TP9
(j) TP10
Applied load, Q (kips)
Applied load (kips)
Displacement, Δ (in)

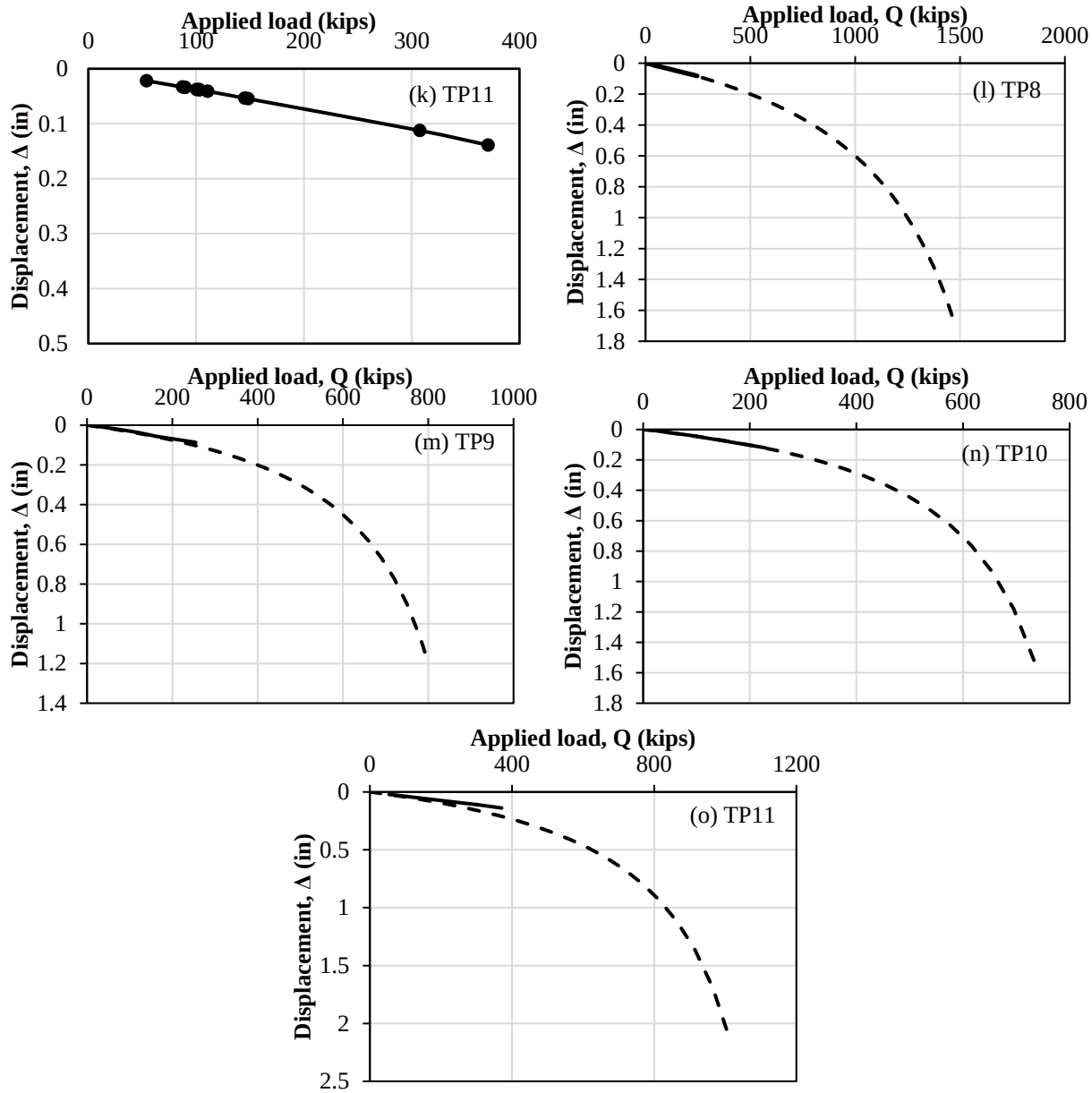

Figure 6. Load displacement response of a) TP1, b) TP2 , c) TP3, d) TP4, e) TP5, f) TP6, g) TP7, h) TP8, i) TP9, j) TP10, k) TP11, and extrapolated load displacement response of l) TP8, m) TP9, n) TP10, and o) TP11.

Figure 7 presents axial load distributions along the pile length. Shaft resistance was calculated as the difference between pile head and pile toe loads, while end bearing was taken as the load measured at the pile toe. Based on Davisson's criterion, maximum ultimate resistances of 305, 732.5, 292, 571, 602, and 561 kips were obtained for TP1, TP3, TP4, TP5, TP6, and TP7, respectively. The highest ultimate resistances for TP8–TP11were obtained using the 10%B criterion. For TP2, geotechnical failure was not reached before structural yielding occurred, indicating that pile yield strength governed. Except for TP2 and TP8, end bearing contributed less than 50% of the total ultimate resistance, while shaft resistance contributed more than 50%,

indicating that shaft resistance was the primary load-transfer mechanism for most piles that were tested.

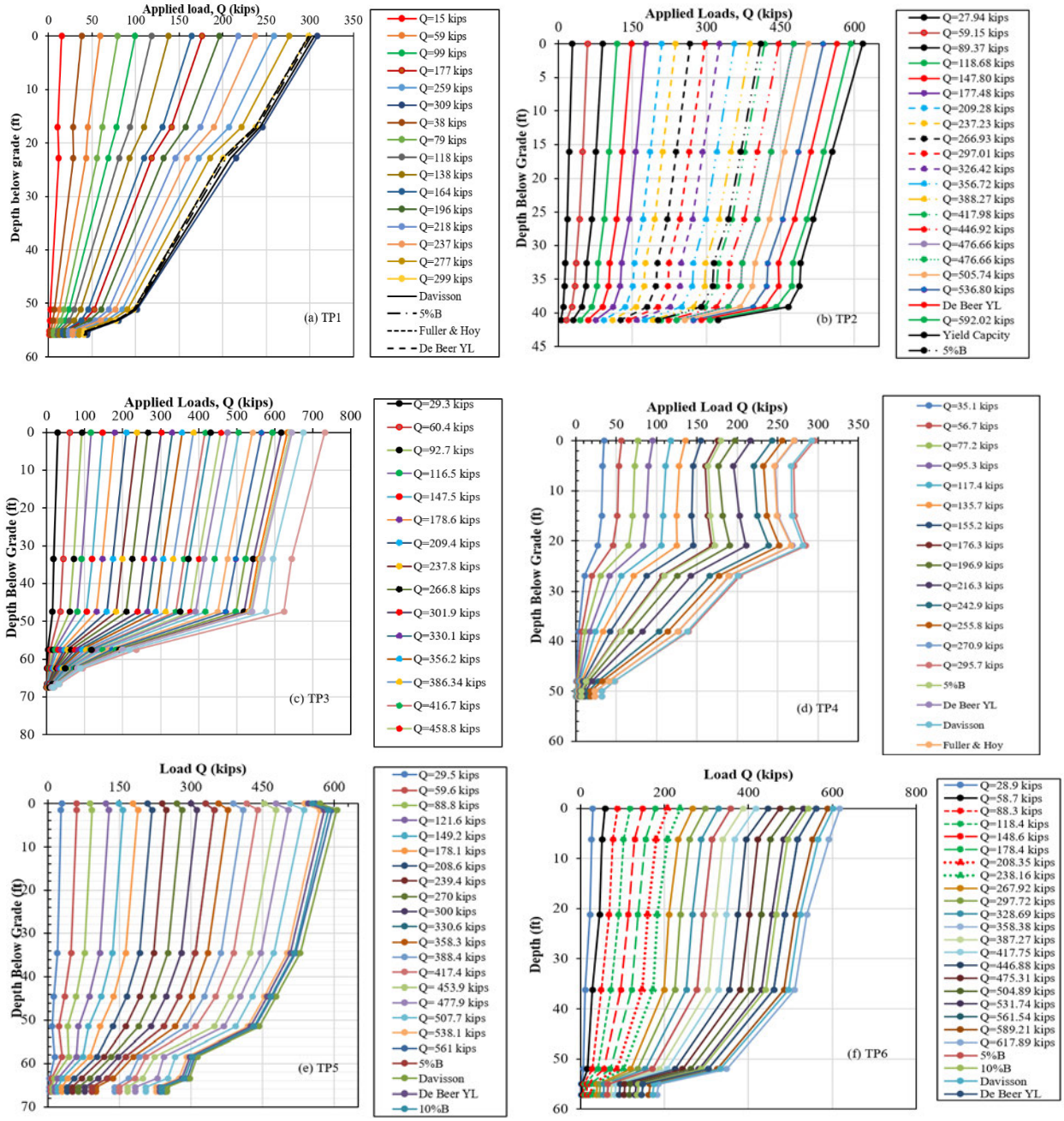

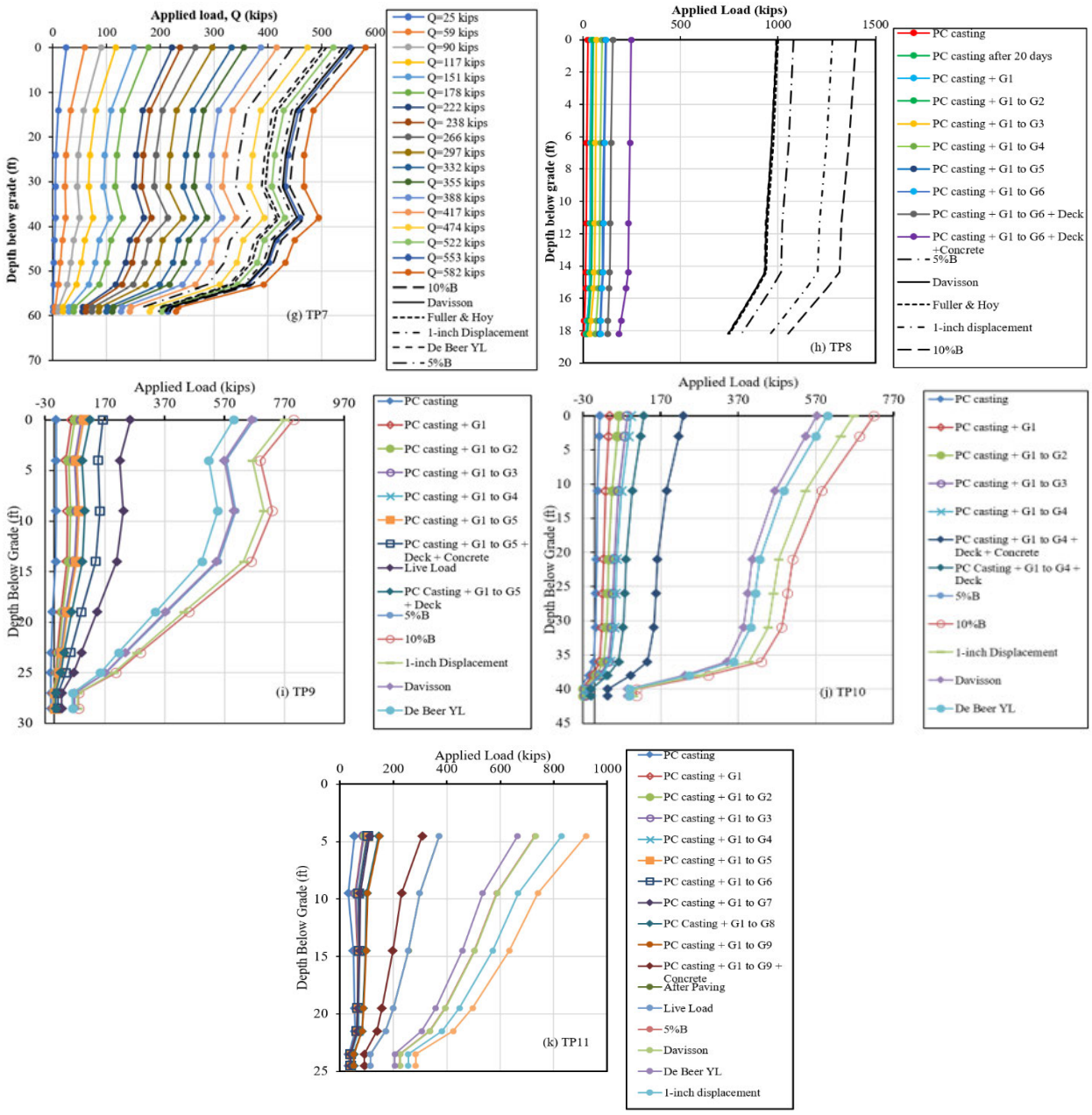

Figure 7 Axial load distribution along the pile length of a) TP1, b) TP2 c) TP3, d) TP4, e) TP5, f) TP6, g) TP7, h) TP8, i) TP9, j) TP10, and k) TP11.

PILE RESISTANCES FROM DYNAMIC LOAD TEST ANALYSIS

PDA was used to monitor all test piles during driving and subsequent restrikes. Restrikes were performed 24 hours after the EOD for all test piles except TP7, which was restruck 61 days after EOD. PDA measurements were analyzed using CAPWAP to estimate shaft resistance and end bearing. The CAPWAP-estimated resistances at EOD and BOR are presented in Figure 8. The total pile resistance of TP1increased from 274 kips at EOD to 337 kips at BOR or by 23% (Figure 8a). For TP2, only a marginal increase of 0.3% was observed from 506 kips to 507 kips (Figure 8b). TP3 exhibited the largest increase of 93% from 429 kips at EOD to 820 kips at BOR

(Figure 8c). Overall, all test piles showed an increase in total resistance at BOR. Both shaft resistance and end bearing contributed to the increase in total resistance. The highest shaft resistance contribution of 69% was observed in TP3, while TP8 exhibited the highest contribution of 86% from end bearing.

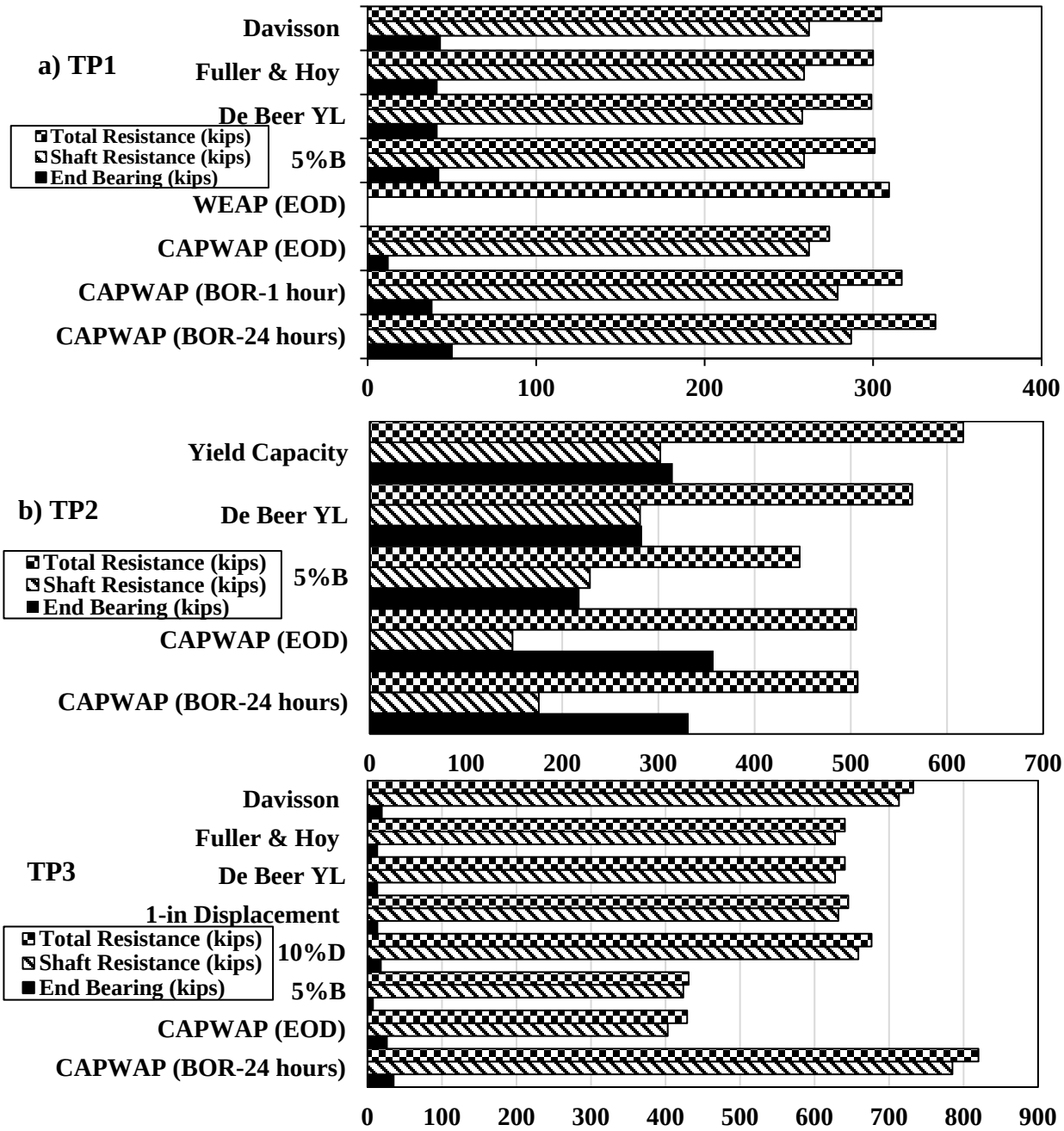

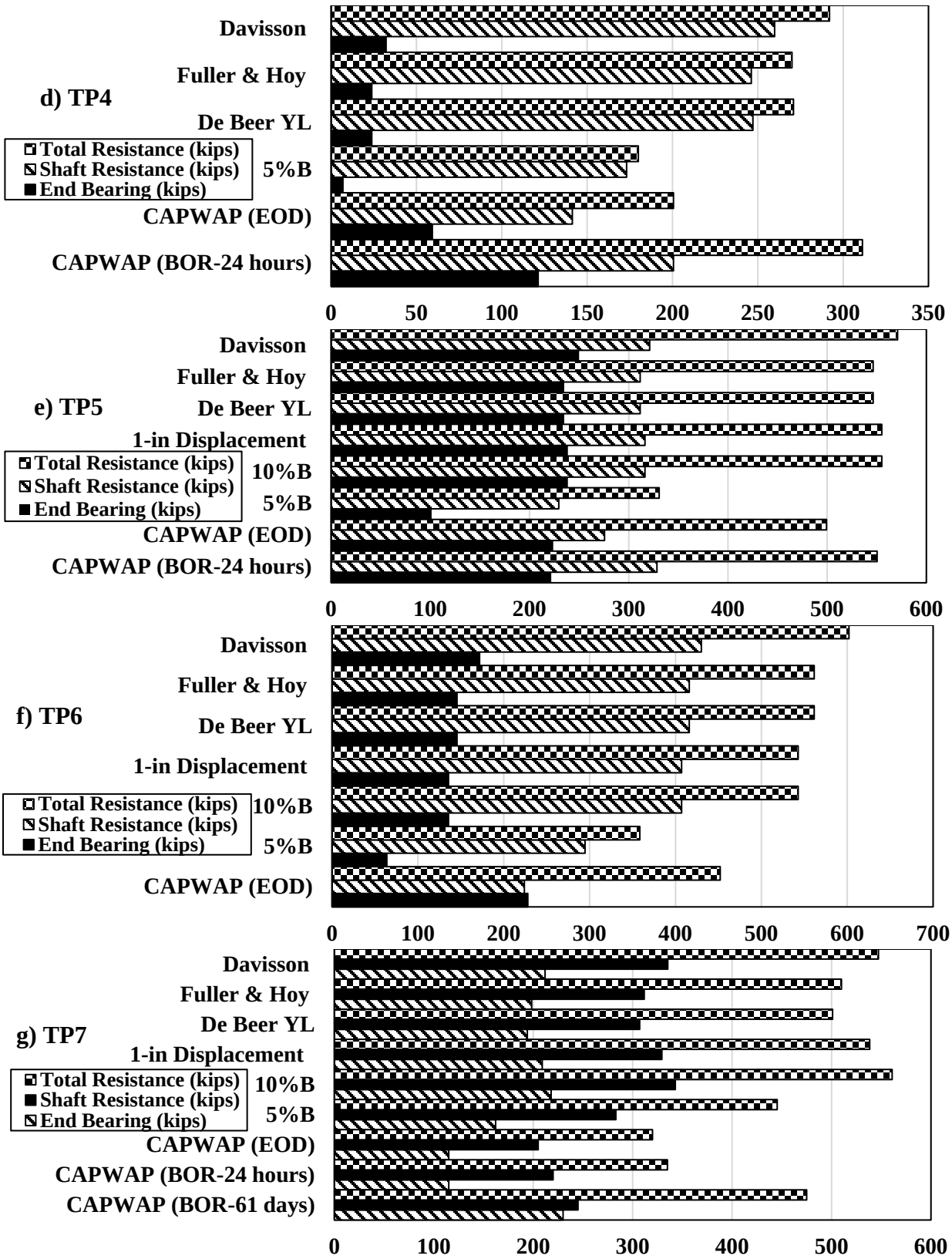
d) TP4
Davisson
Fuller & Hoy
De Beer YL
5%B
CAPWAP (EOD)
CAPWAP (BOR-24 hours)
Total Resistance (kips)
Shaft Resistance (kips)
End Bearing (kips)
0 50 100 150 200 250 300 350
e) TP5
Davisson
Fuller & Hoy
De Beer YL
1-in Displacement
10%B
5%B
CAPWAP (EOD)
CAPWAP (BOR-24 hours)
Total Resistance (kips)
Shaft Resistance (kips)
End Bearing (kips)
0 100 200 300 400 500 600
f) TP6
Davisson
Fuller & Hoy
De Beer YL
1-in Displacement
10%B
5%B
CAPWAP (EOD)
Total Resistance (kips)
Shaft Resistance (kips)
End Bearing (kips)
0 100 200 300 400 500 600 700
g) TP7
Davisson
Fuller & Hoy
De Beer YL
1-in Displacement
10%B
5%B
CAPWAP (EOD)
CAPWAP (BOR-24 hours)
CAPWAP (BOR-61 days)
Total Resistance (kips)
Shaft Resistance (kips)
End Bearing (kips)
0 100 200 300 400 500 600

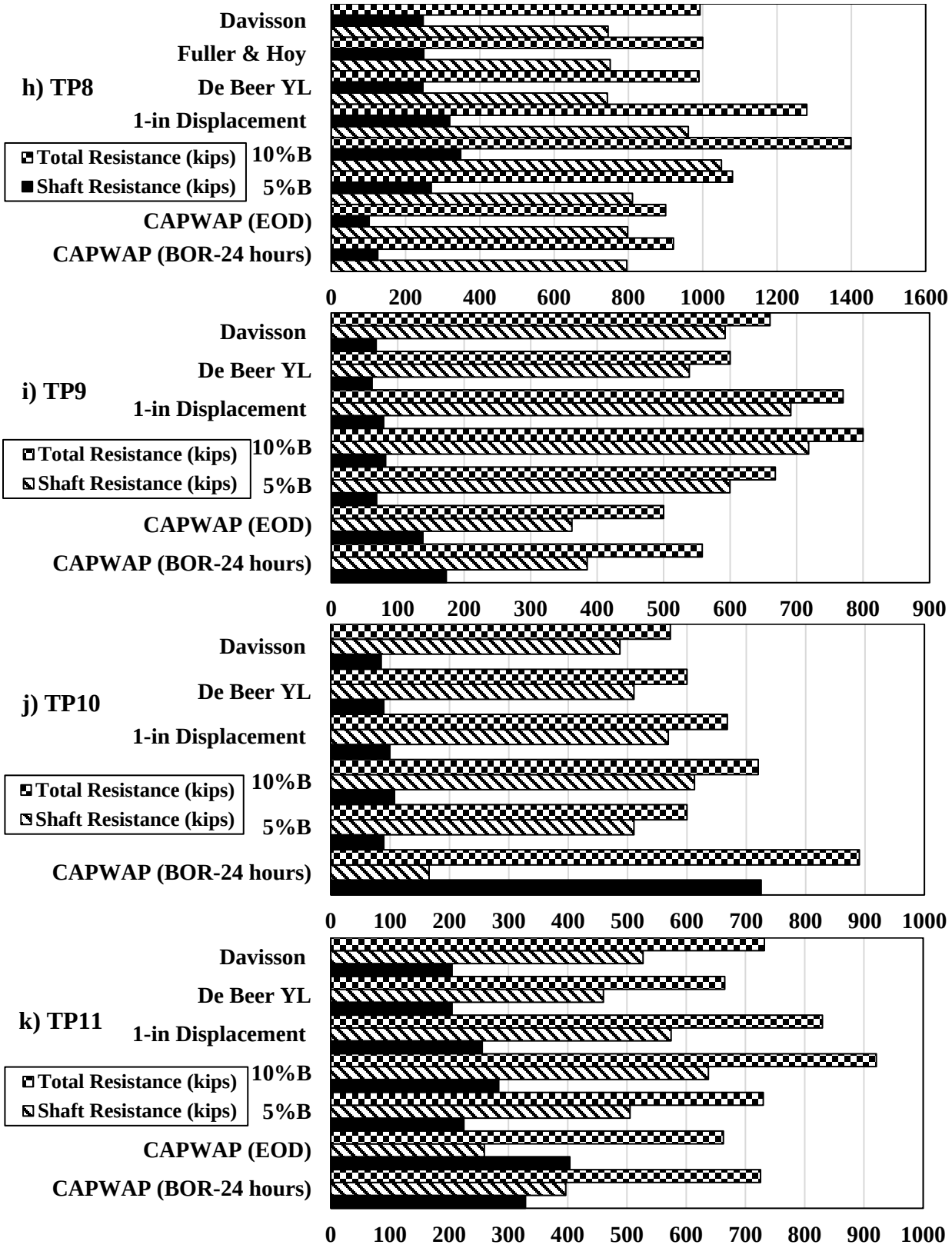

Figure 8. Comparison of total resistance, shaft resistance, and end bearing: a) TP1, b) TP2 c) TP3, d) TP4, e) TP5, f) TP6, g) TP7, h) TP8, i) TP9, j) TP10, and k) TP11.

COMPARISON OF DYNAMIC AND STATIC LOAD TEST RESULTS

Figure 8 compares pile resistances obtained from SLT with those predicted by CAPWAP and WEAP. For TP1–TP4, the ultimate resistances by the Davisson's criterion were 6–11% lower than that by CAPWAP, where CAPWAP generally overpredicted both shaft resistance and end bearing. For TP5, the total resistance by Davisson was 8% higher than that by CAPWAP, although CAPWAP still overpredicted shaft resistance and slightly underpredicted end bearing. For TP6–TP11, SLT-based resistances generally exceeded that by CAPWAP and WEAP. CAPWAP underpredicted shaft resistance and, in many cases, end bearing, with the largest differences observed in TP8–TP10. For TP7, both CAPWAP and WEAP underestimated the total resistance compared with those from all SLT failure criteria. For TP2, structural yielding occurred before geotechnical failure, resulting in substantial differences between measured and predicted resistance components. Overall, CAPWAP tended to overpredict resistance components for TP1–TP5, but underpredicted shaft resistance and end bearing for TP6–TP11 in several cases. The greatest underestimation occurred at TP8–TP10, where dynamic analyses substantially underestimated the resistances measured or extrapolated from the SLT. The findings provide practical recommendations for selecting SLT systems under different bridge construction scenarios while improving confidence in evaluating driven pile resistance in IGMs.

CONCLUSIONS

Three proposed SLT systems and DLT were conducted on steel H-piles driven in IGMs in five states. Vibrating-wire SGs were used to monitor load distribution along the piles. The main conclusions are as follows:

- IndeSPLS was applied on TP1–TP5, where neither the test pile nor the reaction piles were part of the bridge foundation system. InteSPLS was used on TP6 and TP7, where production piles served as reaction piles, although the test pile was not part of the bridge foundation. Both systems follow the ASTM D1143 quick-load procedure and can load piles to geotechnical or structural failure. While these systems provide direct measurements of pile capacity, they are more costly and labor-intensive. InteSPLS may extend bridge construction duration, whereas IndeSPLS does not affect the construction schedule.
- InnoSPLS was implemented on TP8–TP11 using production piles of the bridge foundation system. No loading frame nor reaction piles were required, as loads were generated by superstructure dead and live loads. InnoSPLS is more cost-effective, does not impact construction duration, and enables long-term monitoring throughout bridge construction. Although ASTM loading and unloading procedures cannot be strictly followed and pile failure may not be reached.
- Ultimate resistances were evaluated using six failure criteria: Davisson, De Beer Yield Load (YL), Fuller and Hoy, 5%B, 10%B, and 1-in. displacement. The highest ultimate resistances for TP1, TP3, TP4, TP5, and TP6 were 305, 732.5, 292, 571, and 602 kips, respectively, based on Davisson's criterion. For TP7–TP11, the highest ultimate resistances were 561, 1,399, 800, 720, and 931 kips, respectively, based on the 10%B criterion. For TP8, the predicted ultimate resistance of 1,399 kips exceeded the structural capacity of the HP14×89 pile (1,305 kips) by approximately 7%. For TP2, the resistances determined using the De Beer YL and 5%B criteria were 9% and 28% below the pile

yield strength of 617 kips, indicating that structural strength governed the pile capacity rather than geotechnical resistance.

- Comparison with dynamic analyses showed mixed agreement. For TP1, TP3, TP4, and TP10, CAPWAP at the 24-hour BOR predicted higher resistances than those determined by SLTs. For TP6 and TP7, the ultimate resistances determined using the Davisson, De Beer YL, Fuller and Hoy, 10%B, and 1-in. displacement criteria were higher than those from the CAPWAP. For TP8 and TP9, ultimate resistances determined from all six failure criteria were higher than those predicted by both CAPWAP and WEAP.

REFERENCES

1. Martin, D., and P. Stacey. *Guidelines for Open Pit Slope Design in Weak Rocks*. CSIRO Publishing, Australia, 2018.

2. O'Neill, M. W., and L. C. Reese. *Drilled Shafts: Construction Procedures and Design Methods*. Report No. FHWA-IF-99-025. Department of Transportation, Federal Highway Administration, Office of Implementation, McLean, VA, 1999.

3. Mokwa, R. L., and H. Brooks. *Axial Capacity of Piles Supported on Intermediate Geomaterials*. Report No. FHWA/MT-08-008/8117-32. Montana Department of Transportation, Research Programs, Helena, 2008.

4. Clarke, B. G., and A. Smith. Self-Boring Pressuremeter Tests in Weak Rocks. *Construction and Building Materials* vol. 6 (2), 1992, pp. 91–96.

5. Marinos, P. G. *Hard Soils-Soft Rocks: Geological Features with Special Emphasis to Soft Rocks*. In Geotechnical Engineering of Hard Soils Soft Rocks (A. Anagnostopoulos, F. Schlosser, N. Kalteziotis, and R. Frank, eds.), Balkema, Rotterdam, Netherlands, 1997.

6. Akai, K. *Testing Methods for Indurated Soils and Soft Rocks-Interim Report*. Balkema, Rotterdam, Netherlands, 1997.

7. De Freitas, M. H. *Introduction to Session 1.2: Weak Arenaceous Rock*. Proc., 26th Annual Conference of the Engineering Group of the Geological Society, Leeds, UK, A.A. Balkema, Rotterdam, 1993.

8. Adhikari, P., K. W. Ng, Y. Z. Gebreslasie, S. S. Wulff, and T. A. Sullivan. Geomaterial Classification Criteria for Design and Construction of Driven Steel H-Piles. *Canadian Geotechnical Journal* vol. 57 (4), 2020, pp. 616–621.

9. Masud N. B., K. W. Ng, S. S. Wulff, and T. Johnson. Driven piles in fine-grained soil-based intermediate geomaterials. *Journal of Bridge Engineering* vol. 27(6), 2022, 04022037.

10. AASHTO. *AASHTO LRFD Bridge Design Specifications*. 10th Ed. U.S. Customary Units. American Association of State Highway and Transportation Officials (AASHTO), Washington, D.C., 2024.

11. Ng, K. W., S. Y. Yasrobi, and T. A. Sullivan. *Current Limitations and Challenges of Driven Piles in Rock as Demonstrated Using Three Case Studies in Wyoming*. In IFCEE, San Antonio, TX, ASCE, Reston, VA, 2015, pp. 500–517.

12. Long, J. H. *Static Pile Load Tests on Driven Piles into Intermediate GeoMaterials*. Report No. WHRP 0092-12-08. University of Illinois at Urbana-Champaign, Department of Civil Engineering, Urbana, 2016.

13. Ng, K.W., N. Masud, O. Oluwatuyi, and S. S. Wulff. *Comprehensive Field Test and Geotechnical Investigation Program for Development of LRFD Recommendations of Driven Piles on Intermediate Geomaterials*. Final Report WY-2501F to Wyoming Department of Transportation, Cheyenne, WY, 2025. (https://rosap.ntl.bts.gov/view/dot/84984)

14. Masud N. B., K. W. Ng, and S. S. Wulff. Resistance responses and design recommendations for driven piles in coarse-grained soil-based intermediate geomaterials. *Soils and Foundations* vol. 63(6), 2023, 101381.

15. Masud N.B., K. W. Ng, H. K. Kalauni, and S. S. Wulff. Reliability-based design improvement and prediction of steel driven pile resistances in rock-based intermediate geomaterials. *Acta Geotechnica* vol. 19(2), 2024, pp. 1083-1105.

16. ASTM. *Standard Test Methods for Deep Foundations Under Static Axial Compressive Load*. D 1143/D 1143M-07. Annual Book of ASTM Standards, West Conshohocken, PA, 2007.

17. Paikowsky, S. G., and T. A. Tolosko. *Extrapolation of Pile Capacity from Non-Failed Load Tests*. Report No. FHWA-RD-99-170. Federal Highway Administration, McLean, VA, 1999.

18. Davisson, M. T. *High Capacity Piles*. In Proceedings of the Innovations in Foundation Construction (M. T. Davisson, ed.), Soil Mechanics Division, Chicago, IL, ASCE, NY, Vol. 52, 1972, pp. 81–112.

19. De Beer, E. E. Proefondervindelijke Bijdrage Tot de Studievan Het Grensdraagvermogen van Zand Onder Funderin-genOpStaal (Deel 2–3). *Annalesdestravaux publics deBel-gique* (2nd series) vol. 69 (1), 1968, pp. 44–88.

20. Fuller, F. M., and H. E. Hoy. Pile Load Tests Including Quick-Load Test Method, Conventional Methods, and Interpretations. *Highway Research Record* vol. 333, 1970, pp. 74–86.

21. Bica, A. V. D., M. Prezzi, H. Seo, R. Salgado, and D. Kim. Instrumentation and Axial Load Testing of Displacement Piles. Proceedings of the Institution of Civil Engineers, *Geotechnical Engineering* vol. 167 (3), 2014, pp. 238–252.

22. Seo, H., I. Z. Yildirim, and M. Prezzi. Assessment of the Axial Load Response of an H Pile Driven in Multilayered Soil. *Journal of Geotechnical and Geoenvironmental Engineering* vol. 135 (12), 2009, pp. 1789–1804.

19. Evaluation of Drag Load and Downdrag on Axially Loaded Piles

Mohamed Ashour
Department of Mechanical and Civil Engineering
Alabama A&M University
4900 Meridian Street, Room 305A
Normal, AL 35762
Mohamed.Ashour@aamu.edu

Aser Abbas
Assistant Professor, Department of Civil and Environmental Engineering University of Rhode Island
Fascitelli Center for Advanced Engineering, Room 209
2 East Alumni Avenue
Kingston, RI 02881
aser.abbas@uri.edu

Prepared for the 75th Highway Geology Symposium, September 2026

Acknowledgements

This research was sponsored by the Alabama Department of Transportation (ALDOT) and the National Center for Transportation Infrastructure Durability & Life-Extension (TriDurLE). The authors acknowledge and thank Mr. Scott George, Ms. Kaye Chancellor Davis, Ms. Kidada Dixon and Mr. Calvin Smith at ALDOT, and Professor Xianming Shi at TriDurLE for their support and encouragement.

Disclaimer

Statements and views presented in this paper are strictly those of the author(s), and do not necessarily reflect positions held by their affiliations, the Highway Geology Symposium (HGS), or others acknowledged above. The mention of trade names for commercial products does not imply the approval or endorsement by HGS.

Copyright Notice

Copyright © 2026 Highway Geology Symposium (HGS)

All Rights Reserved. Printed in the United States of America. No part of this publication may be reproduced or copied in any form or by any means – graphic, electronic, or mechanical, including photocopying, taping, or information storage and retrieval systems – without prior written permission of the HGS. This excludes the original author(s).

Evaluation of Drag Load and Downdrag on Axially Loaded Piles

ABSTRACT

Piles installed through soil that settles after construction of the piles can develop negative skin friction along the upper part of the shaft or along its full length, that increases the axial force carried by the pile and can add to its settlement. The soil settlement may be produced by consolidation under fill or dewatering, by reconsolidation following liquefaction, or by collapse of a metastable deposit upon wetting. Common force-equilibrium procedures locate the neutral plane by balancing driving and resisting forces, treat the shaft resistance as fully mobilized, and evaluate the pile settlement separately from the force calculation. This paper presents a soil-pile model that couples the soil and pile settlement profiles with the mobilized skin friction and tip resistance in an iterative analysis. The load transfer (t-z and q-z) relationships are constructed from soil properties, pile properties, soil-pile interaction, and a single constitutive soil model rather than prescribed empirically, so the shear mobilized at each depth follows from the relative soil-pile displacement computed at that depth. For a given permanent pile-head load, the analysis returns the axial load distribution, the maximum drag load, the location of the neutral plane, the extent of the transition zone from negative to positive skin friction, the mobilized tip resistance, and the pile-head settlement. The procedure is extended to long piles in which the pile-head load and the drag load are fully resisted above the pile tip. Comparisons are presented with two full-scale field tests: one at Bangkok, where the downdrag was induced by soil consolidation settlement, and one at Nikopol, where the downdrag was triggered by the inundation of collapsible soil.

Keywords: downdrag; drag load; negative skin friction; neutral plane; load transfer; soil-pile interaction

INTRODUCTION

Piles installed through settling ground can develop axial forces greater than the permanent load applied at the pile head. Where the surrounding soil settles more than the pile, the relative movement mobilizes downward shear along the pile shaft, referred to as negative skin friction. The accumulated downward shear produces a drag load that increases the compressive force in the pile. Downdrag refers to the pile settlement associated with this interaction. At greater depth, the direction of relative movement may reverse, causing the shaft resistance to act upward. The depth at which the soil and pile settlements are equal defines the neutral plane and generally corresponds to the maximum axial force in the pile. The combined permanent load and drag load governs the structural strength check of the pile section, whereas the resulting pile settlement governs serviceability (*1, 2*).

The ground settlement that initiates negative skin friction can result from several mechanisms. Consolidation may follow placement of an embankment or surcharge, dewatering, or another increase in vertical effective stress (*3, 4, 5, 6*). Reconsolidation following liquefaction can also produce ground settlement (*7, 8*). In metastable sandy and silty deposits, wetting can cause collapse under the existing vertical stress, even without an increase in external load. Potential sources of wetting include a rising groundwater table, irrigation, leakage from utilities, and surface impoundment (*9, 10, 11, 12*). Although the mechanisms and rates of settlement differ, their effects on the pile are governed by the resulting soil settlement profile and its movement relative to the pile.

Long-term instrumented field tests have established the features that an analysis should reproduce. Endo et al. (*4*) monitored four steel pipe piles in Tokyo for more than two years and identified the neutral point at which the axial force reaches its maximum, with drag load transmitted to the pile above it and positive shaft resistance and tip resistance developing below it. Fellenius (*13*) showed that the change from negative to positive shaft resistance may occur over a transition zone rather than at a sharp boundary. The length of this zone depends on the relative movement available to mobilize shaft resistance. Centrifuge tests reported by Leung (*14*) further indicate that negative skin friction depends primarily on the magnitude of soil movement rather than on the mechanism producing that movement. Field and numerical studies also show that the neutral plane can migrate upward as the permanent pile-head load increases (*15, 16*). These observations require an analysis that enforces compatibility between the soil settlement, pile settlement, and mobilized shaft and tip resistances.

A common design approach locates the neutral plane by satisfying force equilibrium. The permanent pile-head load and drag load above the neutral plane are balanced by the positive shaft resistance and mobilized tip resistance below it (*1, 2, 17*). The pile settlement is then evaluated separately using the soil settlement at the neutral plane and the elastic compression of the pile. This approach is practical for design, but equilibrium alone does not determine how much shaft or tip resistance is mobilized. Simplified implementations commonly assign ultimate shaft resistance to the negative and positive friction zones and represent the change in direction at a single depth. Consequently, the soil settlement profile does not directly control the calculated mobilization of resistance, and the extent of the transition zone is not resolved. Analytical methods based on hyperbolic load-transfer curves provide a displacement-dependent treatment of

the interface response (*18, 19*), but the adopted curves are empirical and assume full mobilization at a prescribed relative displacement of approximately 0.08 in. (2 mm). The elastic-plastic solution of Matyas and Santamarina (*20*) estimates the neutral-plane location and transition-zone length, but idealizes the pile as rigid and assumes that shaft resistance increases linearly with depth. The force-equilibrium approach also does not explicitly address long piles for which the permanent load and drag load are fully resisted by positive shaft resistance before reaching the pile tip (*21*).

This paper presents a coupled soil-pile model for evaluating drag load and downdrag caused by soil settlement (*21*). The subsequent sections are organized as follows. The load-transfer relationships section establishes the mechanical basis for the shaft and tip responses used in the analysis. The downdrag and load-distribution section then describes how these responses are coupled with the soil and pile settlement profiles, including the treatment of long piles. The comparison section evaluates the calculated response against two full-scale field tests selected to represent different settlement mechanisms: consolidation of soft marine clay beneath an embankment in Bangkok and inundation-induced collapse at Nikopol. The concluding section summarizes what these comparisons support.

LOAD-TRANSFER RELATIONSHIPS

The coupled downdrag framework of Ashour and Abbas *(21)* discretizes the pile and surrounding soil profile into pile segments and soil sublayers of equal thickness. Each pile segment is connected to the adjacent soil sublayer through a nonlinear t-z spring, the pile tip is connected to the bearing sublayer through a nonlinear q-z spring, and the elastic compression of each pile segment is represented by a linear spring. The t-z relationships for sandy and clayey soils follow the models developed by Ashour and Helal *(22)* and Ashour and Abbas *(23)*, respectively. The q-z relationships for sandy and clayey soils follow Elfass *(24)* and Elfass et al. *(25)*, respectively. For inundated collapsible soils, both relationships are constructed using the post-inundation soil properties and stress-strain response developed by Ashour and Abbas *(26)*. The t-z relationships connect soil-pile relative displacement to mobilized shaft shear, which acts as positive shaft resistance or negative skin friction depending on the direction of relative movement. The q-z relationships connect relative tip movement to mobilized tip resistance. The stiffness and limiting values of these relationships follow from the soil properties, pile geometry, and soil-pile interaction rather than from prescribed curve shapes. The complete formulations are provided in the cited studies.

Shaft Load Transfer

The adopted t-z models differ in their treatment of soil type and drainage condition, so only their common framework is summarized here. They combine the soil stress-strain relationship introduced by Norris *(27)* and adjusted by Ashour et al. *(28)* with the applicable Mohr-Coulomb failure relationship. For a given soil-pile relative displacement and current confining pressure, each model iteratively determines compatible values of shear strain and mobilized interface shear stress that satisfy the soil displacement field observed by Robinsky and Morrison (*29*) and the constitutive response. Repeating this calculation over increasing relative displacement defines the nonlinear t-z relationship. Clay undergoing consolidation is treated using the drained formulation, since field measurements indicate that the mobilized adhesion is governed by

effective stress rather than by the undrained shear strength *(3, 4)*. The use of drained shear strength represents this long-term interface response. The detailed formulations are provided in the cited studies *(22, 23, 26)*.

Tip Load Transfer

The q-z models for sand and clay differ in how they idealize the failure mass beneath the pile tip. The sand model represents four interacting failure zones using a system equivalent to 3.75 overlapping Mohr circles connected by a curvilinear failure envelope. The clay model represents the failure mass using 4.5 Mohr circles bounded by the undrained Mohr-Coulomb failure envelope (*24, 25, 30*). At each loading increment, the stress state within the zones determines the mobilized tip resistance and the stress level immediately below the pile tip. The constitutive soil model provides the corresponding vertical strain, and the pile-tip displacement is calculated from the area beneath the triangular strain distribution defined by the Schmertmann influence factor (*31, 32*). Repeating the calculation over increasing stress levels defines the nonlinear q-z relationship. For an inundated collapsible bearing layer, the procedure uses the post-inundation soil properties and stress-strain response (*26*). The detailed formulations are given in the sources cited above.

DOWNDRAG AND LOAD-DISTRIBUTION ANALYSIS

The downdrag analysis couples the soil settlement profile with the pile response through the t-z and q-z relationships described above. The soil settlement at each sublayer is prescribed as an input and may be calculated using the method appropriate for the settlement mechanism. Negative skin friction develops where the soil settles more than the pile, whereas positive shaft resistance develops where the pile moves more than the soil. The magnitude of the mobilized shaft shear is obtained from the t-z relationship for the corresponding sublayer. The calculation begins at the pile tip, where the q-z relationship provides the tip resistance corresponding to an assumed relative tip movement. The force and displacement at the top of each segment provide the conditions at the bottom of the segment above, allowing the calculation to proceed upward to the pile head. Within each segment, the shaft shear, axial force, elastic compression, and pile displacement are updated iteratively until they are compatible. Figure 1 illustrates the coupling among the soil and pile settlement profiles, the shaft and tip responses, and the resulting axial-load distribution *(21)*.

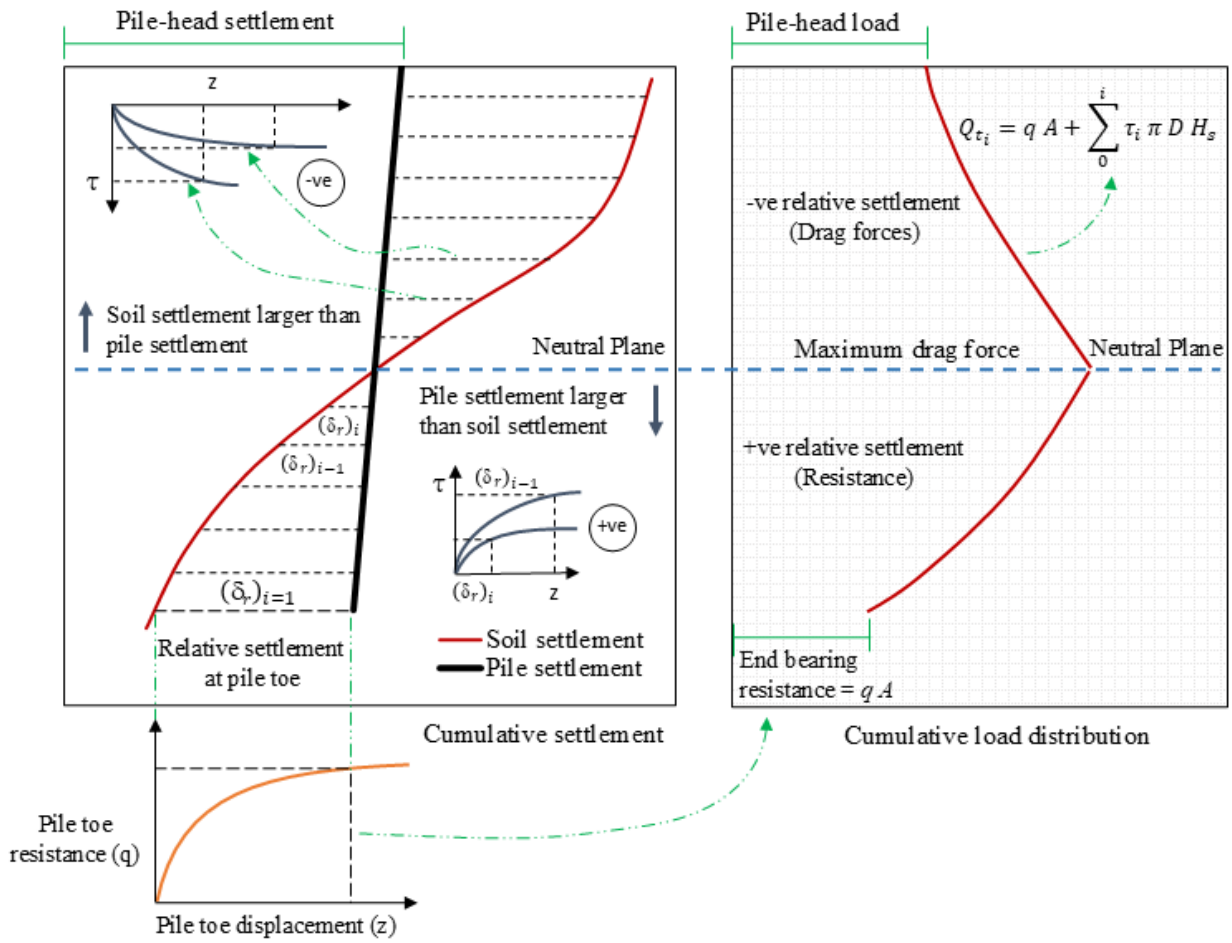

Figure 1 – Pile and soil settlement profiles coupled with the pile side and tip load-displacement relationships to capture the mobilized response of a pile subjected to negative skin friction. After Ashour and Abbas (*21*)

Coupled Analysis Procedure

The pile segments and soil sublayers are numbered from the pile tip upward, with i = 1 denoting the lowest segment and i = n denoting the uppermost segment. Downward displacement is taken as positive. The soil settlement at the midpoint of each sublayer, $S_{mid,i}$, and at the pile tip, S_1, are obtained from the prescribed soil settlement profile. For the case in which the axial load reaches the pile tip, the calculation begins by assuming a trial relative pile-tip displacement, $Z_{b,1,rel}$. The corresponding mobilized tip load, $Q_{b,1}$, is obtained from the q-z relationship assigned to the bearing sublayer. Because the q-z relationship is expressed in terms of relative movement, the actual pile-tip displacement is

$$Z_{b,1,\text{actual}} = Z_{b,1,\text{rel}} + S_1 \tag{1}$$

The effective pile-tip area can be adjusted to represent plugged, partially plugged, or unplugged behavior for open-ended piles.

For pile segment i, the elastic compression of the lower half of the segment, Z'_i, is initially set to zero. The displacement at the midpoint of the segment is calculated from

$$Z_{\text{mid},i} = Z_{b,i} + Z'_i \tag{2}$$

where $Z_{b,i}$ is the displacement at the bottom of the segment. The signed relative displacement between the pile segment and the adjacent soil sublayer is

$$\delta_i = Z_{\text{mid},i} - S_{\text{mid},i} \tag{3}$$

A positive value of δ_i indicates that the pile segment moves downward more than the adjacent soil, resulting in positive shaft resistance. A negative value indicates that the soil settles more than the pile segment, resulting in negative skin friction. The magnitude $|\delta_i|$ is used with the applicable t-z relationship to determine the magnitude of the mobilized interface shear stress, τ_i. The corresponding shaft force magnitude is

$$T_i = \tau_i p_i H_s \tag{4}$$

where p_i is the pile perimeter and H_s is the segment height. The axial force at the top of the segment is then obtained from equilibrium:

$$Q_{t,i} = \begin{cases} Q_{b,i} + T_i & \text{for } \delta_i > 0 \\ Q_{b,i} - T_i & \text{for } \delta_i < 0 \end{cases} \tag{5}$$

where $Q_{b,i}$ and $Q_{t,i}$ are the axial forces at the bottom and top of the segment, respectively. The updated compression of the lower half of the segment is calculated as

$$Z'_i = \frac{(3Q_{b,i} + Q_{t,i})H_s}{8A_p E_p} \tag{6}$$

where A_p and E_p are the cross-sectional area and Young's modulus of the pile, respectively. Equations 2 through 6 are repeated until the midpoint displacement, relative displacement, mobilized shaft force, and axial forces are compatible. After convergence, the elastic compression of the entire segment is

$$Z''_i = \frac{(Q_{b,i} + Q_{t,i})H_s}{2A_p E_p} \tag{7}$$

and the displacement at the top of the segment is

$$Z_{t,i} = Z_{b,i} + Z''_i \tag{8}$$

The calculated top force and displacement become the bottom force and displacement of the next segment:

$$Q_{b,i+1} = Q_{t,i} \text{ and } Z_{b,i+1} = Z_{t,i} \tag{9}$$

The procedure is repeated upward until the pile head is reached. The force and displacement calculated at the top of the uppermost segment define one point on the pile-head load-settlement relationship. If a negative axial force is calculated within the pile, the assumed relative pile-tip displacement is increased and the analysis is repeated. Progressively larger trial tip displacements generate a spectrum of permanent pile-head loads and their corresponding settlements. The response associated with the specified permanent pile-head load is then selected.

The neutral plane occurs where the soil-pile relative displacement changes direction and generally corresponds to the maximum axial force in the pile. Where the relative displacement remains small over a finite depth interval, the model produces a transition zone in which the shaft shear changes gradually from negative to positive. The analysis therefore provides the pile-head settlement, axial-load distribution, drag load, neutral-plane location, transition-zone extent, and mobilized tip resistance for the specified permanent load. The calculated pile-head load is unfactored, and the resulting load-settlement relationship represents the response to permanent loading rather than cyclic or transient loading *(21)*.

Long-Pile Case

For a sufficiently long pile, the permanent pile-head load and drag load may be fully transferred to the surrounding soil before the axial force reaches the pile tip, as shown in Figure 2. The lower portion of the pile then remains outside the active load-transfer length, and no tip resistance is mobilized. Applying the standard procedure over the full pile length would not represent this condition because it begins with an assumed pile-tip displacement.

The long-pile analysis begins by assuming an active length extending from the pile head to a lower segment m. Because no axial load is transferred below this active length, the force and displacement at the bottom of segment m are set to zero:

$$Q_{b,m} = 0 \text{ and } Z_{b,m} = 0 \tag{10}$$

To initiate the calculation, a small trial value is assigned to the elastic compression, Z'_m, of the lower half of segment m. Because the displacement at the bottom of the segment is zero, this trial compression produces an equal displacement at the midpoint of the segment. The trial value only initializes the iteration, and the converged solution is insensitive to its magnitude. Comparing the midpoint displacement with the settlement of the adjacent soil provides the relative displacement required to obtain the mobilized shaft shear from the t-z relationship. The mobilized shaft shear is then used to calculate the axial force at the top of the segment. The elastic compression, midpoint displacement, shaft shear, and axial force are updated iteratively until they are compatible. After convergence, the force and displacement at the top of segment m become the conditions at the bottom of the segment above, and the calculation proceeds upward to the pile head.

If the calculated pile-head load is smaller than the specified permanent load, the active length is extended downward by one segment and the calculation is repeated using the same initialization. This process continues until the calculated pile-head load equals or slightly exceeds the specified load. If this condition is reached before the active length extends to the pile tip, the load is fully transferred through shaft resistance and no tip resistance is mobilized. If the active length reaches the pile tip first, the analysis continues using the standard tip-supported procedure. Repeating the calculation for increasing permanent loads defines how the active pile length expands as additional shaft resistance is mobilized *(21)*.

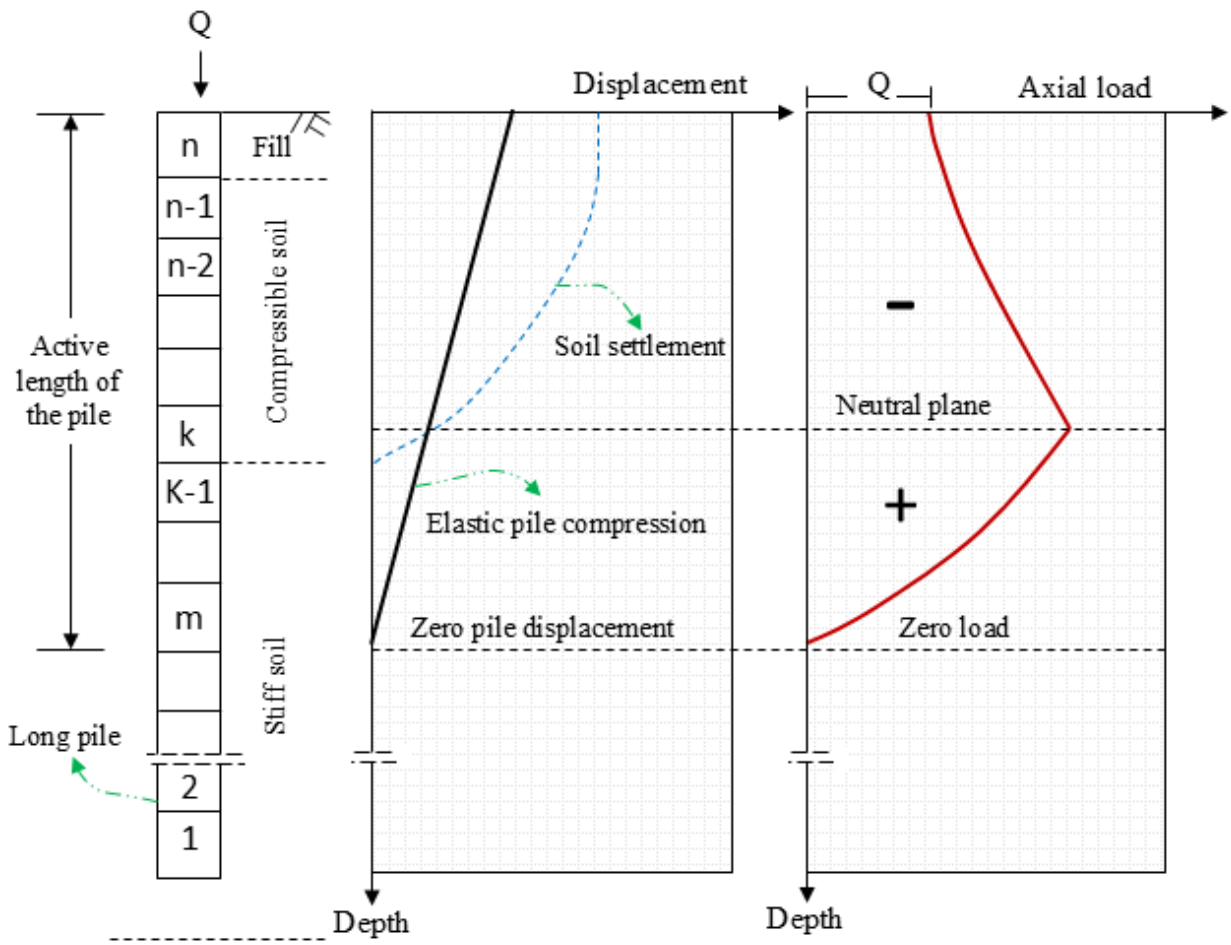

Figure 2 – Modeling the behavior of long piles subjected to downdrag. After Ashour and Abbas (*21*)

COMPARISON WITH FULL-SCALE TESTS

The model is evaluated against two full-scale field tests selected to represent different causes of soil settlement. The Bangkok test examines negative skin friction caused by consolidation of soft marine clay beneath an embankment. Because the measured soil settlement profile is supplied directly to the analysis, this comparison primarily evaluates the calculated load transfer and pile response. The Nikopol test examines negative skin friction caused by inundation-induced collapse. For this case, the settlement profile is calculated from the collapse model before it is

coupled with the pile response. The two cases therefore examine the application of the same downdrag framework to different settlement mechanisms, although the field measurements available for comparison differ between the sites *(21)*.

Bangkok, Thailand

Indraratna et al. *(6)* reported long-term measurements from two prestressed concrete piles driven 82.0 ft (25 m) below the natural ground surface, with 6.6 ft (2 m) extending above the surface. The piles had an outside diameter of 15.7 in. (0.40 m) and an inside diameter of 9.8 in. (0.25 m). Negative skin friction was induced by constructing a 6.6-ft (2-m) embankment over highly plastic soft marine clay. The groundwater table was located between 4.9 and 6.6 ft (1.5 and 2.0 m) below the ground surface. One pile was coated with bitumen, whereas the other was left uncoated. Only the uncoated pile is considered in this comparison. The last reported measurements were obtained 256 days after construction of the embankment, before primary consolidation was complete. The measured soil settlement profile at that time was therefore supplied directly to the analysis rather than calculated. The reported pile and soil properties used in the analysis are summarized in Table 1.

Figure 3 compares the measured cumulative load distribution along the uncoated pile with the distributions calculated by the coupled model and the finite-element analysis reported by Indraratna et al. *(6)*. Both analyses reproduce the increase in axial force through the negative skin friction zone, the maximum axial force, and the subsequent decrease toward the pile tip. Through much of the upper portion of the pile, the coupled-model result lies closer to the measured distribution, whereas the finite-element analysis predicts larger axial forces. Between depths of 56.8 and 72.5 ft (17.3 and 22.1 m), the coupled-model distribution is nearly vertical because the relative displacement between the soil and pile is small. This interval corresponds to the transition zone described by Fellenius *(13)* and emerges from the analysis rather than being assigned in advance. The finite-element result provides an additional numerical benchmark, although it depends on the selected soil stiffness and soil-pile interface parameters. Because the measured soil settlement profile was used as input, the comparison evaluates how the model converts soil settlement into mobilized load transfer and axial-load distribution. It does not evaluate the calculation of consolidation settlement *(21)*.

Table 1 – Input soil parameters used for the Bangkok, Thailand test (*6, 21*)

Thickness, ft (m)	Soil type	Unit weight, lb/ft³ (kN/m³)	ε_{50}	Friction angle, deg	S_u, lb/ft² (kN/m²)
6.6 (2)	Fill	99.9 (15.7)	0.008	30	N/A
13.1 (4)	Weathered clay	99.9 (15.7)	0.02	18	N/A
26.2 (8)	Soft clay	93.6 (14.7)	0.15	20	N/A
26.2 (8)	Soft clay	99.9 (15.7)	0.15	22	N/A
13.1 (4)	Medium stiff clay	121.0 (19.0)	0.01	23	N/A
328 (100)	Stiff clay	124.8 (19.6)	0.005	N/A	2,089 (100)

Note: values are reported in U.S. customary units with SI values in parentheses. Conversions used: 1 m = 3.28 ft; 1 kN/m³ = 6.37 lb/ft³; 1 kN/m² = 20.9 lb/ft².

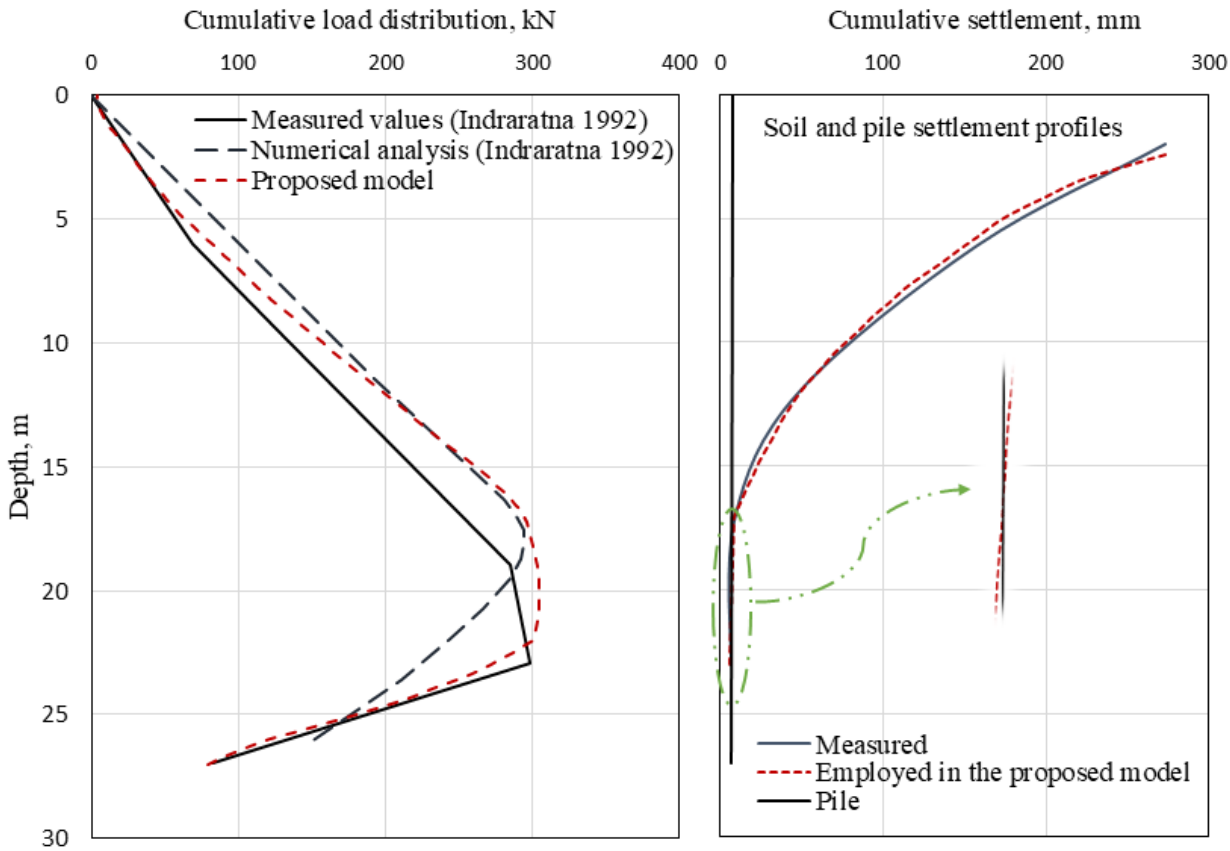

Figure 3 – Measured and predicted pile response for the Bangkok, Thailand test. Measured and finite-element results from Indraratna et al. (*6*). After Ashour and Abbas (*21*)

Nikopol, Ukraine

Grigorian *(33)* reported a full-scale test on an instrumented bored, cast-in-place pile subjected to prolonged wetting at the Nikopol experimental site. The pile was 72.2 ft (22 m) long and 19.7 in. (0.50 m) in diameter and carried a sustained pile-head load of 146 kips (650 kN). A 65.6 by 65.6 ft (20 by 20 m) test pit surrounding the pile was flooded to a depth of 1.6 ft (0.50 m) for 2.5 months. The conditions adopted in the analysis follow the interpretation of the test records by Noor et al. *(11)*. According to that interpretation, the upper 19.7 ft (6 m) of the collapsible stratum was inundated, the initial degree of saturation was approximately 20 percent, the collapse potential was approximately 7 percent, and the measured drag load was 42 kips (186 kN). The soil properties used in the analysis are summarized in Table 2. The soil settlement profile was calculated using the collapse-potential model of Ashour et al. *(34)*, which uses the pre-inundation void ratio, degree of saturation, applied pressure at wetting, and coefficient of uniformity. The predicted collapse potential increased from approximately 7.5 percent near the ground surface to 10.7 percent at the base of the inundated zone. The near-surface prediction is close to the reported collapse potential of approximately 7 percent. The calculated settlement profile and post-inundation soil properties were then used with the load-transfer and downdrag procedures described above *(21, 26)*.

Figure 4 presents the calculated response of the Nikopol test pile. Figure 4(a) compares the soil and pile settlement profiles, and Figure 4(b) presents the corresponding axial-load distribution. For the sustained pile-head load of 146 kips (650 kN), the analysis predicted a maximum drag load of 46 kips (205 kN), approximately 10 percent greater than the measured value of 42 kips (186 kN). The drag load increased the maximum axial force in the pile to approximately 192 kips (855 kN) at a depth of 19.4 ft (5.9 m), near the base of the inundated zone. The predicted pile-head settlement was 0.33 in. (8.5 mm). The neutral plane occurs at the intersection of the soil and pile settlement profiles in Figure 4(a) and at the depth of maximum axial force in Figure 4(b). The soil settlement at the ground surface exceeds 19.7 in. (500 mm), whereas the pile-head settlement is only 0.33 in. (8.5 mm). This difference fully mobilizes negative skin friction throughout the inundated depth and places the neutral plane near its base. Unlike the Bangkok comparison, this case includes calculation of the soil settlement profile before evaluating the pile response.

Table 2 – Input soil parameters used for the Nikopol, Ukraine test (*11, 33*)

Depth, ft (m)	Water content, %	Void ratio	Saturated water content, %	Unit weight, lb/ft³ (kN/m³)	Cohesion, lb/ft² (kPa)	Friction angle, deg
0 to 26.2 (0 to 8)	7.0	0.91	28.70	111.8 (17.57)	104 (5)	20
26.2 to 75.5 (8 to 23)	4.3	0.86	30.82	116.8 (18.34)	125 (6)	16
75.5 to 98.4 (23 to 30)	11.3	0.71	21.20	117.1 (18.40)	104 (5)	18

Note: values are reported in U.S. customary units with SI values in parentheses. Conversions used: 1 m = 3.28 ft; 1 kN/m³ = 6.37 lb/ft³; 1 kPa = 20.9 lb/ft².

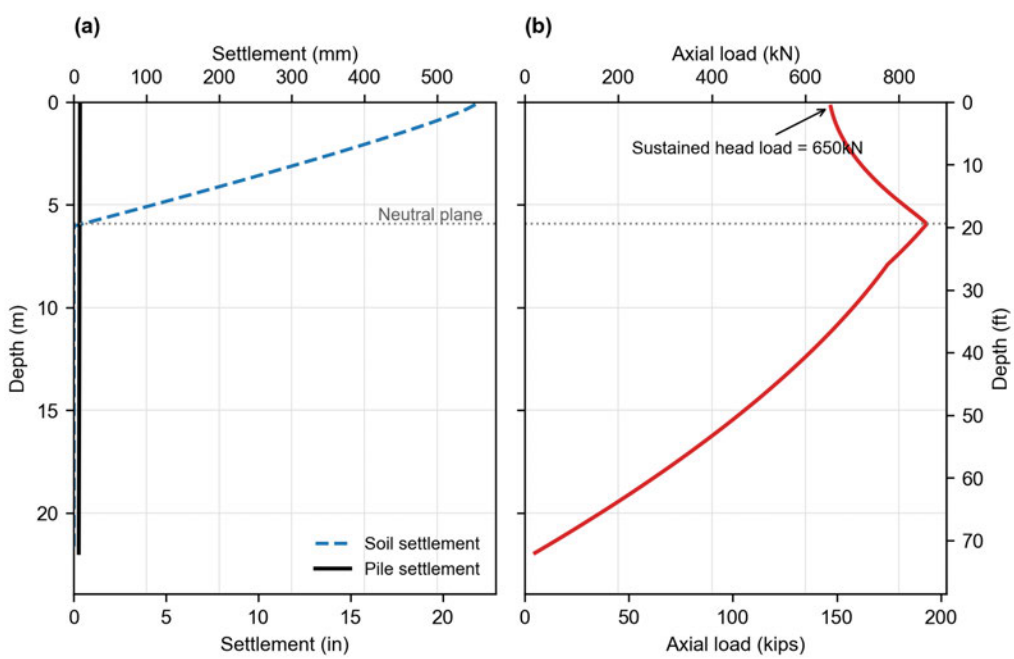

Figure 4 – Predicted response of the Nikopol test pile: (a) soil and pile settlement profiles; and (b) axial load distribution along the pile

SUMMARY AND CONCLUSIONS

This paper presents a coupled soil-pile model for evaluating drag load and downdrag. The analysis combines soil settlement with pile displacement through nonlinear t-z and q-z relationships constructed from soil properties, pile properties, soil-pile interaction, and the soil constitutive response. Because soil settlement is supplied as input, the same calculation procedure applies whether settlement results from consolidation, reconsolidation following liquefaction, or collapse of a metastable deposit upon wetting.

For a specified permanent pile-head load, the analysis provides the axial-load distribution, maximum drag load, neutral-plane location, extent of the transition zone, mobilized tip resistance, and pile-head settlement. The relative displacement calculated at each pile segment determines the direction and degree of shaft-shear mobilization. Consequently, the transition from negative skin friction to positive shaft resistance may extend over a finite interval rather than occur at a single depth. The procedure also treats long piles for which the permanent pile-head load and drag load are fully transferred through shaft resistance before reaching the pile tip, a condition not explicitly addressed by common force-equilibrium procedures.

Two comparisons with full-scale tests support the procedure. At Bangkok, where settlement was produced by consolidation of soft marine clay under an embankment, the predicted load distribution follows the measured response. At Nikopol, where settlement was produced by collapse of a metastable deposit upon prolonged wetting, the predicted maximum drag load was 10 percent greater than the measured value. The agreement obtained for these distinct settlement mechanisms indicates the potential of the coupled approach for evaluating drag load and downdrag under different settling-ground conditions.

REFERENCES

1. Fellenius, B. H. Unified Design of Piles and Pile Groups. Transportation Research Record 1169, 1989, pp. 75-82.

2. Hannigan, P. J., F. Rausche, G. E. Likins, B. R. Robinson, and M. L. Becker. Geotechnical Engineering Circular No. 12, Volume 1, Design and Construction of Driven Pile Foundations. Report FHWA-NHI-16-009. Federal Highway Administration, U.S. Department of Transportation, Washington, D.C., 2016.

3. Johannessen, I. J., and L. Bjerrum. Measurements of the Compression of a Steel Pile to Rock Due to Settlement of the Surrounding Clay. Proc., 6th International Conference on Soil Mechanics and Foundation Engineering, Vol. 2, University of Toronto Press, Toronto, 1965, pp. 261-264.

4. Endo, M., A. Minou, T. Kawasaki, and T. Shibata. Negative Skin Friction Acting on Steel Piles in Clay. Proc., 8th International Conference on Soil Mechanics and Foundation Engineering, Vol. 2, Mexico Geotechnical Society, Mexico, 1969, pp. 85-92.

5. Fellenius, B. H. Downdrag on Piles in Clay Due to Negative Skin Friction. Canadian Geotechnical Journal, Vol. 9 (4), 1972, pp. 323-337.

6. Indraratna, B., A. Balasubramaniam, P. Phamvan, and Y. Wong. Development of Negative Skin Friction on Driven Piles in Soft Bangkok Clay. Canadian Geotechnical Journal, Vol. 29 (3), 1992, pp. 393-404.

7. Tokimatsu, K., and H. B. Seed. Evaluation of Settlements in Sands Due to Earthquake Shaking. Journal of Geotechnical Engineering, Vol. 113 (8), 1987, pp. 861-878.

8. Ishihara, K., and M. Yoshimine. Evaluation of Settlements in Sand Deposits Following Liquefaction During Earthquakes. Soils and Foundations, Vol. 32 (1), 1992, pp. 173-188.

9. Lawton, E. C., R. J. Fragaszy, and J. H. Hardcastle. Collapse of Compacted Clayey Sand. Journal of Geotechnical Engineering, Vol. 115 (9), 1989, pp. 1252-1267.

10. Houston, S. L., W. N. Houston, C. E. Zapata, and C. Lawrence. Geotechnical Engineering Practice for Collapsible Soils. Geotechnical and Geological Engineering, Vol. 19 (3-4), 2001, pp. 333-355.

11. Noor, S. T., A. Hanna, and I. Mashhour. Numerical Modeling of Piles in Collapsible Soil Subjected to Inundation. International Journal of Geomechanics, Vol. 13 (5), 2013, pp. 514-526.

12. Mashhour, I., and A. Hanna. Drag Load on End-Bearing Piles in Collapsible Soil Due to Inundation. Canadian Geotechnical Journal, Vol. 53 (12), 2016, pp. 2030-2038.

13. Fellenius, B. H. Results from Long-Term Measurement in Piles of Drag Load and Downdrag. Canadian Geotechnical Journal, Vol. 43 (4), 2006, pp. 409-430.

14. Leung, C. Negative Skin Friction on Piles. Proc., Indian Geotechnical Conference, Indian Geotechnical Society, Guntur, India, 2009, pp. 827-836.

15. Xia, L., H. Hu, S. Zhou, and J. Huang. Test Research on the Development of Negative Skin Friction on Piles Under Vertical Loads and Surcharges. Proc., Geo-Hubei 2014 International Conference on Sustainable Civil Infrastructure, American Society of Civil Engineers, Reston, Va., 2014, pp. 87-96.

16. Sun, T., W. Yan, and D. Su. Fully Coupled Consolidation Analysis of Shear Strength Mobilization and Dragload of a Pile Subject to Negative Skin Friction. International Journal of Geomechanics, Vol. 15 (3), 2015, 04014057.

17. Siegel, T. C., R. Lamb, D. Dasenbrock, and P. J. Axtell. Alternative Design Approach for Drag Load and Downdrag with the LRFD Framework. Proc., 38th Annual Conference on Deep Foundations, Deep Foundations Institute, Phoenix, Ariz., 2013, pp. 23-39.

18. Zhou, W., R. Chen, and Y. Chen. Development of Negative Skin Friction of Piles on Soft Grounds. Proc., GeoShanghai International Conference 2006, American Society of Civil Engineers, Reston, Va., 2006, pp. 277-284.

19. Cao, W., Y. Chen, and W. E. Wolfe. New Load Transfer Hyperbolic Model for Pile-Soil Interface and Negative Skin Friction on Single Piles Embedded in Soft Soils. International Journal of Geomechanics, Vol. 14 (1), 2014, pp. 92-100.

20. Matyas, E., and J. Santamarina. Negative Skin Friction and the Neutral Plane. Canadian Geotechnical Journal, Vol. 31 (4), 1994, pp. 591-597.

21. Ashour, M., and A. Abbas. Mobilized Response of Piles Subjected to Downdrag. International Journal of Geomechanics, Vol. 21 (8), 2021, 06021019.

22. Ashour, M., and A. Helal. Pre-Liquefaction and Post-Liquefaction Responses of Axially Loaded Piles in Sands. International Journal of Geomechanics, Vol. 17 (9), 2017, 04017073.

23. Ashour, M., and A. Abbas. Response of Piles in Multilayers of Soil Under Uplift Forces. International Journal of Geomechanics, Vol. 20 (6), 2020, 04020056.

24. Elfass, S. A New Approach for Estimating the Axial Capacity of Driven Piles in Sand Up to True Soil Failure. PhD thesis. Department of Civil and Environmental Engineering, University of Nevada, Reno, 2001.

25. Elfass, M., J. Pooranampillai, A. Elsayed, and G. Norris. Undrained Point Load Point Displacement Response of Piles/Drilled Shafts in Clay and Sand. Proc., International Foundation Congress and Equipment Expo, American Society of Civil Engineers, Reston, Va., 2009, pp. 175-182.

26. Ashour, M., and A. Abbas. Axially Loaded Piles in Inundated Collapsible Soils Under Compression and Tension Forces. Canadian Journal of Civil Engineering, Vol. 48 (2), 2021, pp. 144-158.

27. Norris, G. M. Theoretically Based BEF Laterally Loaded Pile Analysis. Proc., Numerical Methods in Offshore Piling: 3rd International Conference, Editions Technip, Paris, France, 1986, pp. 361-386.

28. Ashour, M., A. Abbas, and S. Boskovic. Pile Cap Interaction with Bridge Pile Foundations Under Lateral Loads. Journal of Bridge Engineering, Vol. 24 (6), 2019, 04019053.

29. Robinsky, E. I., and C. F. Morrison. Sand Displacement and Compaction Around Model Friction Piles. Canadian Geotechnical Journal, Vol. 1 (2), 1964, pp. 81-93.

30. Elfass, S., and G. Norris. A New Look into the Pile Tip Resistance in Sand. Proc., 36th Annual Symposium on Engineering Geology and Geotechnical Engineering, University of Nevada, Las Vegas, 2001, pp. 629-637.

31. Schmertmann, J. H. Static Cone to Compute Static Settlement over Sand. Journal of the Soil Mechanics and Foundations Division, Vol. 96 (3), 1970, pp. 1011-1043.

32. Schmertmann, J. H., J. P. Hartman, and P. R. Brown. Improved Strain Influence Factor Diagram. Journal of the Geotechnical Engineering Division, Vol. 105 (6), 1978, pp. 715-726.

33. Grigorian, A. A. Pile Foundations for Buildings and Structures in Collapsible Soil. A.A. Balkema, Brookfield, Vt., 1997.

34. Ashour, M., A. Abbas, A. Altahrany, and A. Alaaeldin. Modelling the Behavior of Inundated Collapsible Soils. Engineering Reports, Vol. 2 (4), 2020, e12156.

20. NCDOT Measurement While Drilling (MWD) Implementation and Testing Program

Nick Moore, LG
North Carolina Department of Transportation
3301 Jones Sausage Road, Suite 100
Garner, NC 27529
984-920-8914
nomoore1@ncdot.gov

Prepared for the 75th Highway Geology Symposium, September, 2026

Acknowledgements

The author would like to thank the individuals for their contributions in the work described:

John Pilipchuk, PE, LG – North Carolina Department of Transportation (Retired)
Neil Roberson, LG – North Carolina Department of Transportation
Michelle Morency, LG – North Carolina Department of Transportation
Nick Zimarino, LG – North Carolina Department of Transportation
Thomas Miller, LG – North Carolina Department of Transportation (Retired)
Chris Walker – North Carolina Department of Transportation
Jordan Edmondson – North Carolina Department of Transportation (Retired)
Cheryl Youngblood, LG – North Carolina Department of Transportation
Dr. Mo Gabr, Ph.D, PE – North Carolina State University
Ali Sheikhmiri, Ph.D Candidate – North Carolina State University
Greg Lucier, North Carolina State University
Dr. Mike Rodgers, Ph.D, PE – University of Florida, Sandhill Engineering
Michel Lariau- Jean Lutz
Ben Rivers, PE – GeoEvolutions, LLC
Catlin Engineers and Scientists (CES), LLC
Infrastructure Consulting and Engineering (ICE), LLC
Terracon Consultants, INC
DFI MWD Users Group

Disclaimer

Statements and views presented in this paper are strictly those of the authors, and do not necessarily reflect positions held by their affiliations, the Highway Geology Symposium (HGS), or others acknowledged above. The mention of trade names for commercial products does not imply the approval or endorsement of HGS.

Copyright Notice

Copyright © 2026 Highway Geology Symposium (HGS)

All Rights Reserved. Printed in the United States of America. No part of the publication may be reproduced or copied in any form or by any means – graphic, electronic, or mechanical, including photocopying, taping, or information storage, and retrieval systems – without prior written permission of the HGS. This excludes the original author(s).

ABSTRACT

The North Carolina Department of Transportation (NCDOT) partnered with North Carolina State University (NCSU) in 2024 to conduct a research project on the establishment of correlations between Measurement While Drilling (MWD) data and strength properties of soils in North Carolina. The project led to the procurement of an MWD console and multiple sensors which were installed by a certified technician on a CME-55 track drill owned by NCDOT in December of 2024.

The general thesis of this program is to gather statistically significant datasets that include MWD data as well as SPT, CPT and soil test data within the same geologic units at the same depths and locations allowing for comparison and correlation of these datasets. To this end, NCDOT is also working with multiple consultants to install and operate MWD equipment during the initial subsurface site investigation for the Cape Fear Memorial Bridge in New Hanover County.

While the primary objective of this program is to correlate MWD data to soil strength properties, it also hopes to prove that MWD testing provides more thorough subsurface data than traditional methods alone. MWD testing offers advantages over SPT and CPT since it can be performed in material too dense for CPT testing and can record data in soils too soft for traditional undisturbed sampling techniques. MWD testing also provides a continuous data profile in SPT borings where traditional SPT alone typically leaves gaps in the logs between tests.

Current research of correlations between MWD data and strength properties of soils in eastern NC shows promise. Opportunities for further study exist in the utilization of MWD in rock coring at drilled pier locations, inclusion of SPT-seismic data collection and in the characterization of weak sedimentary deposits of the Triassic Basins in NC.

INTRODUCTION

North Carolina maintains the 2nd most highway miles (80,000) and over 13,500 bridges. North Carolina is also the 9th most populated state with about 11.2 million people and is projected to reach 15 million people by 2050. NCDOT Geotechnical Engineering Unit has started to look to emerging technology to reduce field and office costs, reduce material and construction costs, record more data, produce more complete subsurface investigation data sets, and, overall, work on innovative solutions with very talented and intelligent professionals across the world to keep up with the traffic demands in our state.

North Carolina's varied and complex geology allows field geologists and geotechnical engineers the opportunity to overcome several foundation design challenges. To accomplish this, we must use multiple tools in our geotechnical toolbox such as Standard Penetration Test (SPT) mud-rotary drilling, SPT Hollow Stem Auger drilling, rock coring, Cone Penetration Test (CPT) drilling, hand auger drilling, Vane Shear Test, Dynamic Cone Penetration (DCP) test, etc; however, limitations in some of these common tools can lead to many unreliable field interpretations and conservative design calculations which cause higher project costs. SPT drilling leaves data gaps between test runs and CPT cannot penetrate dense soils which renders the test useless in about 2/3 of North Carolina. Alternatively, Measurement While Drilling (MWD) is a promising geotechnical tool candidate to record continuous, in-situ data in every geologic environment, regardless of soil density.

NCDOT partnered with North Carolina State University (NSCU) to begin our MWD research. First, we needed to procure and install the MWD sensors. Then, we tested the MWD equipment on test projects before we began drilling with MWD to use the data for interpretations. NCDOT also collected MWD data on projects with CPT borings to compare the data sets. Finally, NCDOT also worked with private engineering firms (PEFs) to install MWD sensors on their drill rigs and assist us with collecting more field data on a large coastal bridge replacement project.

BACKGROUND

Measurement While Drilling (MWD)

MWD monitors and records the mechanical and hydraulic response of a drill rig while advancing a borehole, generating real-time and continuous, high-resolution data about subsurface strata. MWD was initially developed in the 1960's for the oil and gas industry to control boreholes and hit subsurface target depths. Europe and Japan adapted MWD (originally known as Drilling Parameter Recording or DPR) for geotechnical applications to monitor drilling operations and assess subsurface conditions in the 1970s (*1*). These early MWD systems relied on analog equipment with limited sensors and produced low precision data with limited interpretations.

Digital recording systems were introduced in the 1980s and significantly improved data accuracy and enabled the collection of reliable and comprehensive subsurface information during drilling operations (*2*). MWD has since been utilized in other industries, such as mining, and

continues to emerge as a tool for enhancing the drilling process and providing valuable rock and soil data during subsurface investigations.

The International Organization for Standardization (ISO) recognized the potential of MWD for geotechnical site characterization and released ISO 22476-15 (Geotechnical Investigation and Testing – Field Testing – Part 15: Measuring While Drilling) in 2016 . This standard has mainly been used in Europe and established guidelines for using MWD in geotechnical investigations to detect voids and cavities, optimize drilling operations, and identify stratigraphy changes.

The Federal Highway Administration (FHWA) and other researchers began to take notice of MWD for geotechnical instigation purposes in the early- to mid-2010s from various publications and presentations on MWD. The University of Florida in Gainesville began researching shear-strength assessments using MWD for drilled shaft drilling (*3*). Initial research analyzing MWD for geotechnical site characterization is less than a decade old in North America (*4, 5, 6*).

FHWA created the Advanced Geotechnical Methods in Exploration (A-GaME) initiative to focus on geotechnical site characterization practices in early 2019 with MWD noted as a crucial and underutilized technology. The A-GaME initiative included workshops, peer exchanges, webinars, and development of educational media to promote MWD to government agencies and private firms. The Deep Foundations Institute (DFI) created an MWD Users Group in 2021 and holds meetings every month. Attendees hear presentations followed by an open discussion from state DOTs, researchers, equipment manufacturers, and software developers.

North Carolina Geology

North Carolina has a 1.8 Ga. (Ga. stands for “giga annum” and represents one billion years) complex geologic history characterized by the Grenville orogeny (1.8 Ga.-980 Ma. Ma. stands for “mega annum” and represents one million years), Taconic orogeny (470 Ma.-440 Ma.), Acadian orogeny (375 Ma.-325 Ma.), and Alleghenian orogeny (325 Ma.-260 Ma.), rifting of Pangea (235 Ma.-200 Ma.), mountain erosion, sediment deposition, and creation of the Atlantic coastal plain (66 Ma.-present day; Fig. 1; *7*). North Carolina has numerous folds, thrust faults, reverse faults, normal faults, unconformities, accreted volcanic arcs, plutons, rift basins, and fluvial to marine sedimentary formations.

North Carolina has numerous geologic environments across the state and this presents different civil engineering challenges to overcome. North Carolina is divided into three physiographical provinces (Fig. 2). The Blue Ridge province is the mountainous region in the western North Carolina and contains Proterozoic-aged sedimentary, volcanic, igneous, and metamorphic rocks. The Blue Ridge province contains the Blue Ridge Mountains which are part of the eastern Appalachian Mountains chain. The Blue Ridge and western Piedmont province contain multiple shear zones and compressional/tensional deformation leading to folding, faulting, and jointing features in the bedrock. The North Carolina Geological Society (NCGS) has mapped more than 4,500 historical landslides.

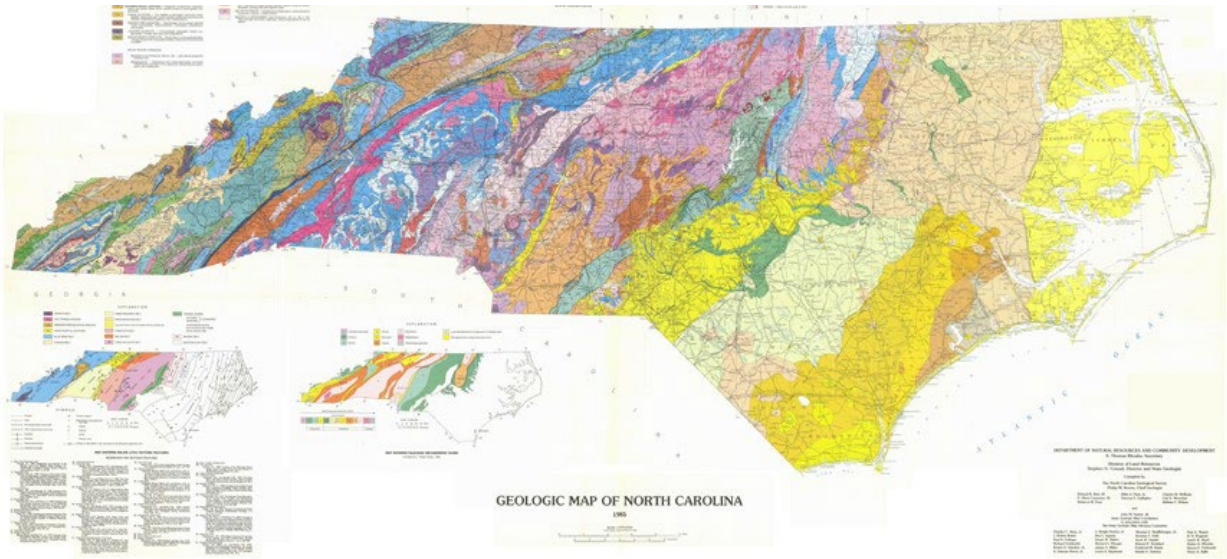

Fig. 1 - Generalized Geologic Map of North Carolina.

In 2024, Hurricane Helene triggered an additional 2,000 to 3,000 landslides in western North Carolina. NCDOT is forced to build roadways and bridges through highly unstable historical landslide zones and colluvium deposits due to topographic constraints.

The Piedmont province is a region in central North Carolina which contains mainly igneous and metamorphic rocks. Evidence of volcanic activity during the Alleghenian orogeny is observed in the Carolina Slate Belt. Triassic rift basins from the breakup of Pangea are also found in the Piedmont. Differential weathering is also widely observed leading to the presence of weathered rock and vastly different bedrock elevations over short horizontal distances. The Triassic rift basins contain sedimentary deposits that cause significant engineering problems. The soil and sedimentary mudstone can produce high SPT N-values and high recovery and Rock Quality Designation (RQD) values of rock cores; however, the very dense soil and sedimentary rock disintegrate when exposed to water. Diabase dikes and sills are also present in the rift basins and knowing their physical limits is key for roadway recommendations and structure foundation support.

The Coastal Plain province is North Carolina's largest geologic region and covers about 45% of the state and is comprised of sediments and sedimentary rocks. The western Coastal Plain province creates a unique geotechnical problem due to the thin layers of marine and fluvial sediment deposited on residual soil and bedrock of the Piedmont. This leads to rapid origin changes vertically and sometimes horizontally. A field professional unfamiliar with this part of North Carolina can easily misidentify the correct origin and formation of the soil. The eastern part of the Coastal Plain province is generally comprised of very deep, low SPT N-value sediment deposits with thin intermittent layers of limestone. Cemented sands are also present in southeastern North Carolina and can easily be missed by novice field professionals. These cemented sand layers can lead to punching shear failure if they are not accurately recorded by the field professional. The punching shear failure caused by the pile punching through the cemented sand layer decreases the lateral shear strength of the column because the broken brittle pieces of

cemented sands do not adhere to the column. Finally, low SPT N-value overburdened soils are also present throughout the eastern Coastal Plain province. These soils appear weak, highly compressible, and unsuitable to meet bearing capacity for large loads; however, these deep soils were compressed by immense pressure of past geologic forces. This causes the soil particles to be packed tightly together creating a dense, strong soil that has limited settlement.

Figure 2 – Physiographic Province Map of North Carolina with a Generalized Geologic Cross Section of the state from A-A'.

METHODS

MWD Installation and Testing

The NCDOT Geotechnical Engineering Unit (GEU) selected its 2010 CME-55 track-mounted drill rig to be retrofitted with the MWD monitoring sensors (Fig. 3). The CME-55 track-mounted rig was chosen for its off-road mobility allowing drilling in virtually all land-based environments for maximum MWD data collection. MWD monitoring sensors were purchased from Jean Lutz including a data recording monitor, connection box, RPM sensor, depth-sensor, multi-process variable flowmeter with flow pressure sensor, vibration sensor,

crowd pressure sensor, and data reporting software. Two torque sensors were also purchased from MWD One including a NWJ wireless torque transducer, a hollow stem auger (HSA) 3-1/4" wireless torque transducer, and a wireless interface box for integration with the Jean Lutz Dialog system (FIG. 3J-L).

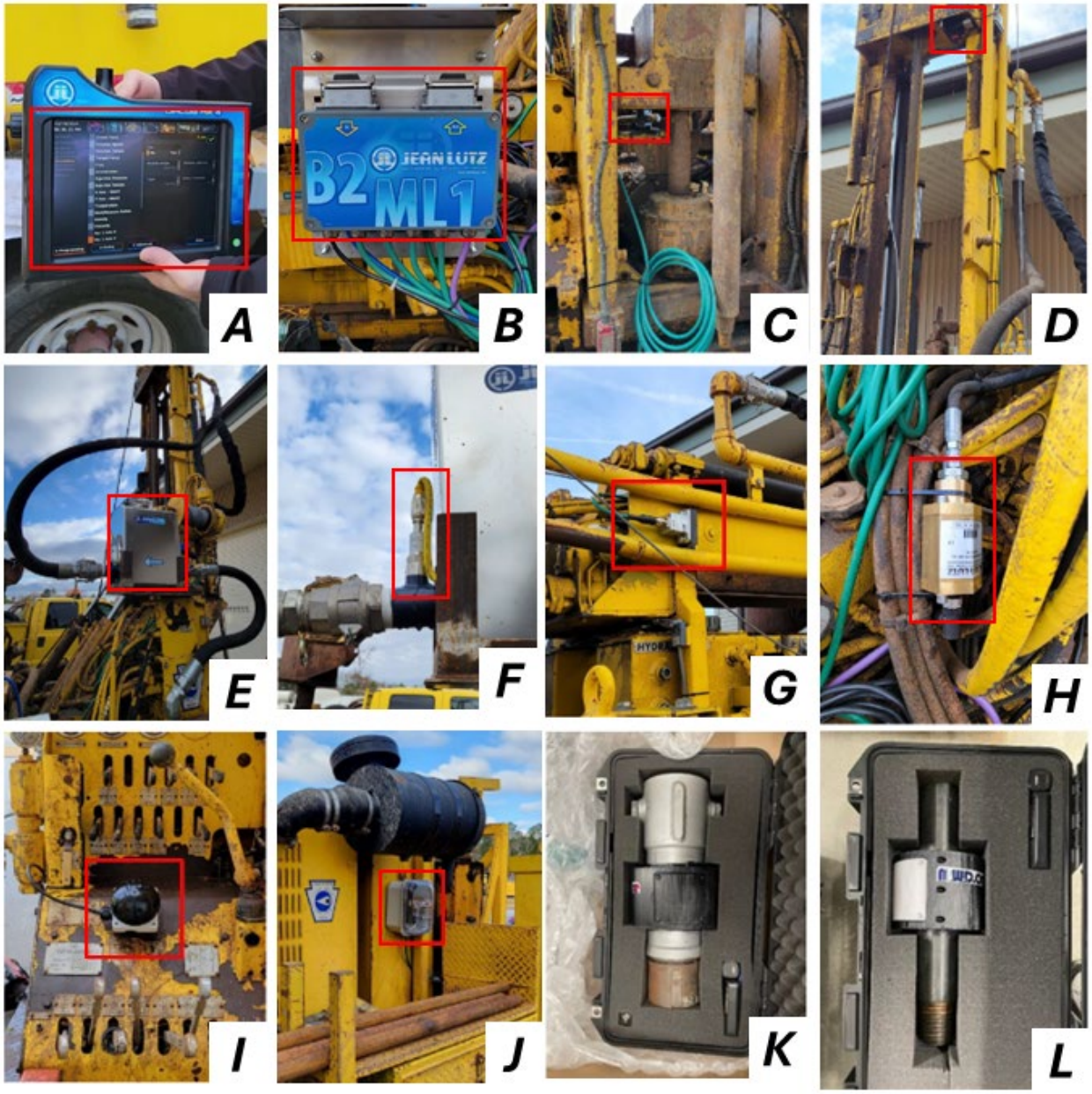

Fig. 3 – MWD equipement and installed sensors on NCDOT CME-55 Track-rig. A – Jean Lutz Dialog Box; B – Connection Box; C – RPM Sensor; D – Depth Sensor; E – Flow Meter; F – Flow Pressure Sensor; G – Vibration Sensor; H – Crowd Pressure Sensor; I – Driller Button; J – MWD One Wireless Torque Sensor Interface Box; K – Hollow Stem Auger 3 ¼" Torque Transducer; L – NWJ Torque Sensor Transducer.

A Jean Lutz technician installed the MWD sensors on the CME-55 track-mounted rig between December 17-19, 2024. NCDOT engineering geologists, drill rig operators, welders, mechanics, and NCSU researchers were also present to collaborate and assist with the installation. Initial MWD sensor functionality testing was conducted after installation to ensure all sensor cables were properly connected to the connection box and properly displaying the data on the recording monitor.

Initial field testing was conducted in January 2025 on a roadway realignment project with shallow bedrock. The main purpose of this project was to ensure the drillers and field geologists were comfortable setting up and using the MWD Dialog box. Most of the borings on the project were less than 12' deep due to bedrock refusal. Thirty borings were performed and allowed our field crew to acclimate to using the Jean Lutz Dialog box to start and terminate boring data, calibrate the sensors, and download the data to a USB drive. Major issues were not encountered during this field testing phase.

We immediately began collecting MWD data on NCDOT production projects once the initial field test project concluded. We have collected data on 15 in-house projects for a total of 60 borings to date of this publication (Table 1). The majority of this data has been collected from projects in the eastern Piedmont and Coastal Plain provinces. One thing to note on Table 1 is the 'MWD Missed Parameter' column indicating unrecorded or partially recorded (indicated by *) MWD data due to sensor failures. We had several sensors stop working for an entire project or stop working intermittently during the project. The RPM sensor was damaged by a mechanic while the drill rig was in the shop for repairs unrelated to MWD sensors. We had an issue where the voltage from the flow meter was too high and caused the MWD dialog box to not receive power. This was corrected by installing a 24v-12v adapter to lower the voltage output to the correct level; however this adapter malfunctioned and had to be replaced on the next field project. The depth sensor also stopped working and had to be replaced. Overall, replacing some the sensors caused the majority of the projects to not have a complete MWD dataset.

Table 1 - NCDOT MWD Projects List

Row No.	County	Project WBS	Boring No.	Total Depth (ft)	Drill Method	Drill Bit Type	MWD Missed Parameter
1	FRANKLIN	17BP.5.PE.33	B26	33.5	H.S. Augers	Hollow Auger Head	Torque
2			B27	43.6	H.S. Augers	Hollow Auger Head	Torque
3			B17	2.9	H.S. Augers	Hollow Auger Head	Torque
4			B2	1.3	H.S. Augers	Hollow Auger Head	Torque
5			B3	5.0	H.S. Augers	Hollow Auger Head	Torque
6			B18	8.1	H.S. Augers	Hollow Auger Head	Torque
7			B4	7.9	H.S. Augers	Hollow Auger Head	Torque
8			B19	13.2	H.S. Augers	Hollow Auger Head	Torque
9			B20	22.3	H.S. Augers	Hollow Auger Head	Torque
10			B21	34.9	H.S. Augers	Hollow Auger Head	Torque
11			B7	20.0	H.S. Augers	Hollow Auger Head	Torque
12			B8	20.3	H.S. Augers	Hollow Auger Head	Torque
13			B9	20.3	H.S. Augers	Hollow Auger Head	Torque
14			B23	14.9	H.S. Augers	Hollow Auger Head	Torque
15			B22	20.1	H.S. Augers	Hollow Auger Head	Torque

Table 1 - NCDOT MWD Projects List Continued

Row No.	County	Project WBS	Boring No.	Total Depth (ft)	Drill Method	Drill Bit Type	MWD Missed Parameter
16			B11	15.1	H.S. Augers	Hollow Auger Head	Torque
17			B10	7.1	H.S. Augers	Hollow Auger Head	Torque
18			B6	8.5	H.S. Augers	Hollow Auger Head	Torque
19			B5	18.9	H.S. Augers	Hollow Auger Head	Torque
20			B25	8.0	H.S. Augers	Hollow Auger Head	Torque
21			B24	0.5	H.S. Augers	Hollow Auger Head	Torque
22			B13	2.0	H.S. Augers	Hollow Auger Head	Torque
23			B14	5.2	H.S. Augers	Hollow Auger Head	Torque
24			B15	1.6	H.S. Augers	Hollow Auger Head	Torque
25			B16	6.7	H.S. Augers	Hollow Auger Head	Torque
26			B1	2.6	H.S. Augers	Hollow Auger Head	Torque
27			B28	5.6	H.S. Augers	Hollow Auger Head	Torque
28			B29	8.7	H.S. Augers	Hollow Auger Head	Torque
29			B30	1.0	H.S. Augers	Hollow Auger Head	Torque
30			B12	1.7	H.S. Augers	Hollow Auger Head	Torque
31	DUPLIN	BP3.R007.1	EB1-B	108.9	Mud Rotary	Drag Bit	Torque*
32			EB2-B	109.1	Mud Rotary	Drag Bit	Torque*
33	WAKE	BP5.C001	C-2	11.2	H.S. Augers	Hollow Auger Head	
34			L1832LT	14.1	H.S. Augers	Hollow Auger Head	Torque*
35			C-1	14.3	H.S. Augers	Hollow Auger Head	
36	PASQUOTANK	1B.207011	B1-B	50.5	Mud Rotary	Drag bit	Torque
37	DARE, TYRRELL	HB-0001+	E1-A	174.3	Mud Rotary	Drag bit	Rotational Speed
38			W1-A	159.7	Mud Rotary	Drag bit	Rotational Speed, Torque*
39	CURRITUCK	34470.1.TA1	90-00	150.0	Mud Rotary	Drag bit	
40			60-00	200.0	Mud Rotary	Drag bit	
41			98-00	150.0	Mud Rotary	Drag bit	
42	CAMDEN	BP1.R027.1+	EB2-A	124.5	Mud Rotary	Drag bit	
43			EB1-A	124.0	Mud Rotary	Drag bit	
44	MARTIN	BP1.R021.1	EB2-B	119.6	Mud Rotary	Drag bit	
45			EB1-B	119.5	Mud Rotary	Drag bit	
46	BERTIE	BP1.R024.1+	EB1-A	114.8	Mud Rotary	Drag bit	
47			EB2-B	114.5	Mud Rotary	Drag bit	
48	CAMDEN	BP1.R001.1+	EB1-B	139.7	Mud Rotary	Drag bit	
49			EB2-B	124.8	Mud Rotary	Drag bit	
50	GATES	BP1.R016.1+	EB1-B	129.3	Mud Rotary	Drag bit	Crowd
51			EB2-B	129.4	Mud Rotary	Drag bit	Crowd
52	BERTIE	BP1.R025.1+	EB1-B	114.7	Mud Rotary	Drag bit	
53			EB2-A	114.7	Mud Rotary	Drag bit	
54	CRAVEN	BP2.R022.1+	EB2-A	109.4	Mud Rotary	Drag bit	
55	EDGECOMBE	BP4.R020.1+	EB1-B	103.7	Mud Rotary	Drag bit	
56			EB2-B	108.8	Mud Rotary	Drag bit	
57	WAKE	50138.1.155	B1	36.4	H.S. Augers	Hollow Auger Head	
58			B1(MWD1)	36.4	H.S. Augers	Hollow Auger Head	
59			B2	35.2	H.S. Augers	Hollow Auger Head	
60			B2(MWD1)	35.2	H.S. Augers	Hollow Auger Head	

Mid-Currituck Testing

The Mid-Currituck Bridge project is located in Currituck County in northeastern North Carolina and will consist of a newly constructed, 4.7 mile-long, two-lane toll bridge across the

Currituck Sound between the communities of Aydlett (mainland) and Corolla (Outer Banks), an interchange between US-158 and the mainland approach to the bridge, a bridge across Maple Swamp as part of the mainland approach, and limited improvements to existing NC-12 and US-158 (Fig. 4). Catlin Engineering and Scientists, LLC (CES) was the private engineering firm (PEF) for the project and conducted SPT and CPT borings along the proposed alignments. NCDOT developed a boring plan and coordinated with CES to mobilize our CME-55 track rig and drill MWD borings at select locations to verify the MWD data with the well-established CPT and SPT data.

Fig. 4 – Map view of Mid-Currituck Bridge Study Area.

NCDOT chose to mud-rotary drill three MWD borings at three different locations in proximity to the previously drilled CPT and SPT borings in Maple Swamp (Fig. 5). Water was mixed with powdered bentonite to achieve the desired slurry consistency. A three-year old minimally worn drag bit (Fig 6A-B) was used to drill through the alternating sand and clay layers encountered. Access mats were placed for ease of access of the heavy equipment on site for the duration of drilling in Maple Swamp (Fig. 7); however, the access mats were scheduled to be pulled up right after we demobilized from the site. This meant our field crew had just a few days to drill the MWD borings and the accelerated schedule did not allow for further MWD or SPT testing at this site.

In addition to collecting MWD data, a field geologist recorded drill rig behavior such as “rig chatter” and depths of noticeably harder and softer drilling. The field geologist also recorded mud slurry behavior such as thickening or thinning and recorded if mud slurry was lost in the boring during drilling operations.

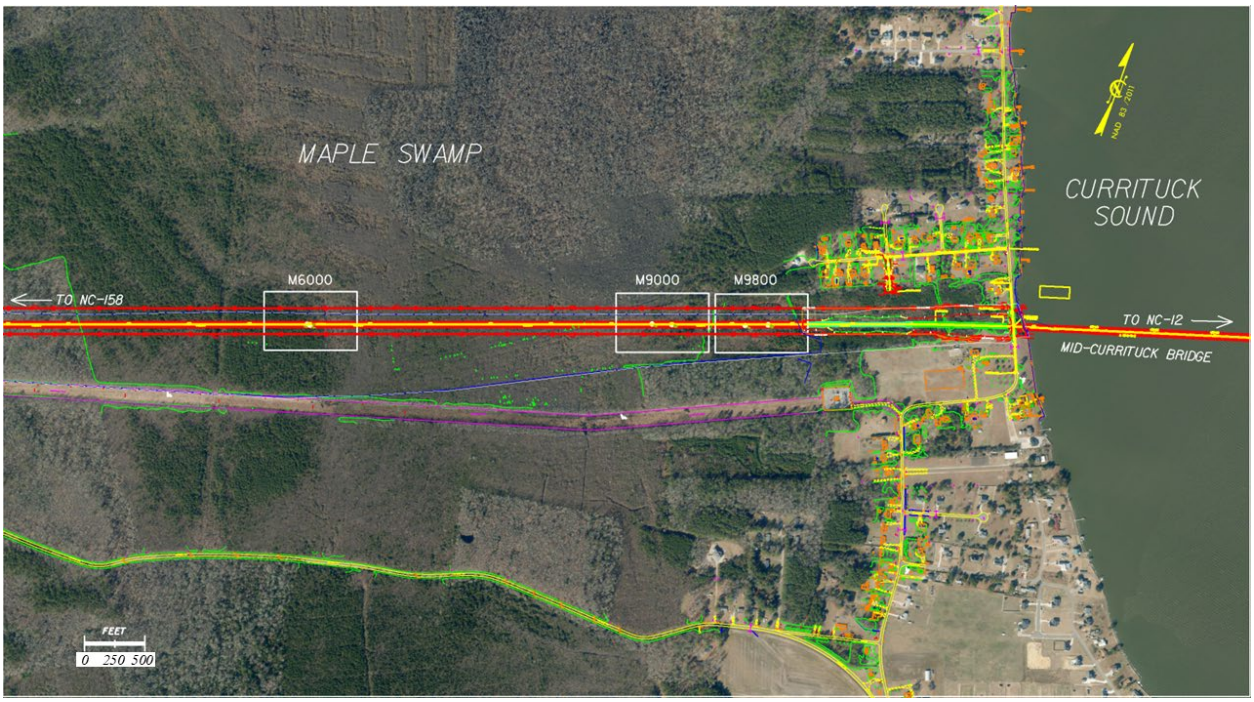

Fig. 5 – Map view of Maple Swamp showing the three MWD boring location study sites highlighted by the white boxes.

Fig. 6 – Drag bit used by NCDOT for MWD borings showing minimal wear

Fig. 7 – Timber mats to access the borings in Maple Swamp

Cape Fear Memorial Bridge Testing

The Cape Fear Memorial Bridge project is located in New Hanover County in southeastern North Carolina and will consist of replacing the bridge number 13 on US-74/76/17/421 over the Cape Fear River and interchange improvements on the west and east side of the river (Fig. 8). NCDOT hired Infrastructre Consulting and Engineering, LCC (ICE) and Catlin Engineers and Scientists, LLC (CES) to complete the geotechnical field investigations for this project. The same MWD sensors that were installed on NCDOT's CME-55 track rig were also installed on the engineering firms Diedrich D-50 drill rig and a CME 45C drill rig for this project. Pre-fieldwork MWD meetings were conducted to confirm everyone involved on the project was aware of the best drilling procedures for collecting the most accurate MWD data. MWD borings were drilled within a five-foot offset of select SPT borings for analysis. A total of 23 MWD borings were completed by the mud rotary drilling method. Several more MWD borings were planned but could not be completed due to sensor failures and subsequent repair time, schedule deadline, or traffic control conflicts. This paper focuses on eleven MWD bridge borings drilled on the west side of the Cape Fear River (Fig. 9).

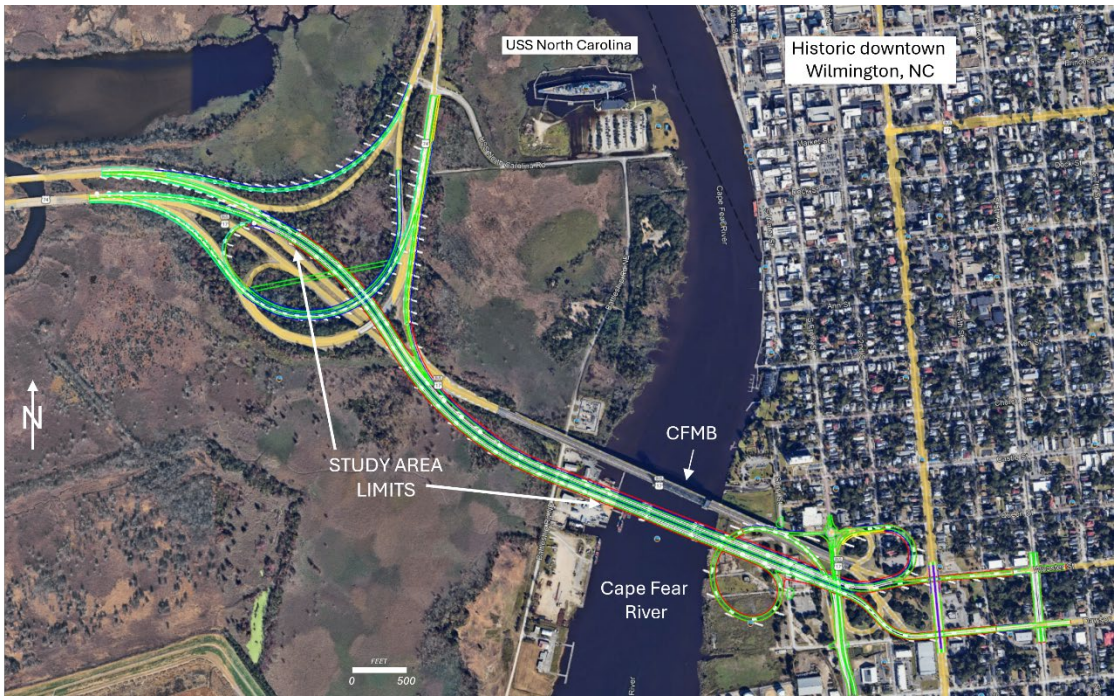

Fig. 8 – Map view of the Overall Cape Fear Memorial Bridge Replacement Study Area. CFMB = Cape Fear Memorial Bridge.

Fig. 9 – Map View Showing the MWD Boring Locations (Yellow Circle) on the West Side of the Cape Fear River. CFMB = Cape Fear Memorial Bridge.

RESULTS

Mid-Currituck Bridge Results

The MWD data collected from this study are plotted with the CPT and SPT data collected from CES at location M9000 (Fig. 8). More CPT, SPT, and MWD data was collected at this site but not presented in this paper. The MWD parameters displayed in this paper are penetration rate, torque force, rotation speed, water flow, water pressure, and crowd force. The CPT parameters displayed in this paper are cone resistance, friction ratio, pore pressure, Soil Behavior Type Index, and soil behavior type (Robertson, 2010). The SPT parameters displayed in this paper are SPT N-Values and observed stratigraphy.

The general stratigraphy in Maple Swamp is mainly composed of 2-10 feet of alluvial muck overlying at least 200 feet of Coastal Plain Yorktown Formation interbedded fine-coarse sands and silty clays with shell fragments.

MWD boring M9000 was drilled to a depth of 150 feet in 2 hours and 30 minutes (Fig. 8). The SPT boring was drilled 164 feet away from the MWD and CPT borings. Overall, the distance should not be a problem because the Coastal Plain stratigraphy is virtually flat and uniform. The data trends between MWD, CPT, and SPT also match up well (Fig. 10). The MWD data show an anomoly between 98-102 feet that is not recorded in the CPT and SPT data.

Cape Fear Memorial Bridge Results

A full suite of MWD and CPT data were collected for this project. CPT data for this project was not included in this report because all the CPT borings were terminated around 30-40 feet due to encountering a hard, coarse sand layer present at that depth throughout the entire project area. The majority of the MWD and SPT borings were drilled to depths of 150-200 feetThe MWD torque data (light blue graphs) collected from eleven bridge borings on the west side of the Cape Fear River are plotted along a profile view of the prosposed alignment for the new bridge (Fig. 11). MWD torque data was the chosen parameter to display along the profile to highlight several interesting findings discussed in the conclusion.

The general stratigraphy of this field area is 15-20 feet of dark brown and gray, highly organic, alluvial, silty sands and sandy silts (muck/peat). All SPT drives in the alluvial layer produced blow counts of less than 10 blows per foot and are depicted by the light green bars placed over the torque graphs indicating the depth range of these blow counts (Fig. 11). Underlying the alluvial layer is 7-17 feet of Coastal Plain Peedee Formation coarse sand. The torque values are generally high in this layer but there are some borings where the torque value is dramatically lower (B15-B17). Underlying the Coastal Plain Peedee Formation coarse sand layer is 8-20 feet of Coastal Plain Peedee Formation sandy limestone interbedded with calcareous sandstone. Underlying the sandy limestone layer is 100+ feet of Coastal Plain Peedee Formation calcareous silty sand interbedded with very hard, thinly bedded, sandstone ledges and cemented concretions. The torque values are generally low with periodic high spikes. A key observation in this layer is the layers where SPT blow counts are greater than 75 which is depicted by light purple bars placed over the torque graphs (Fig. 11).

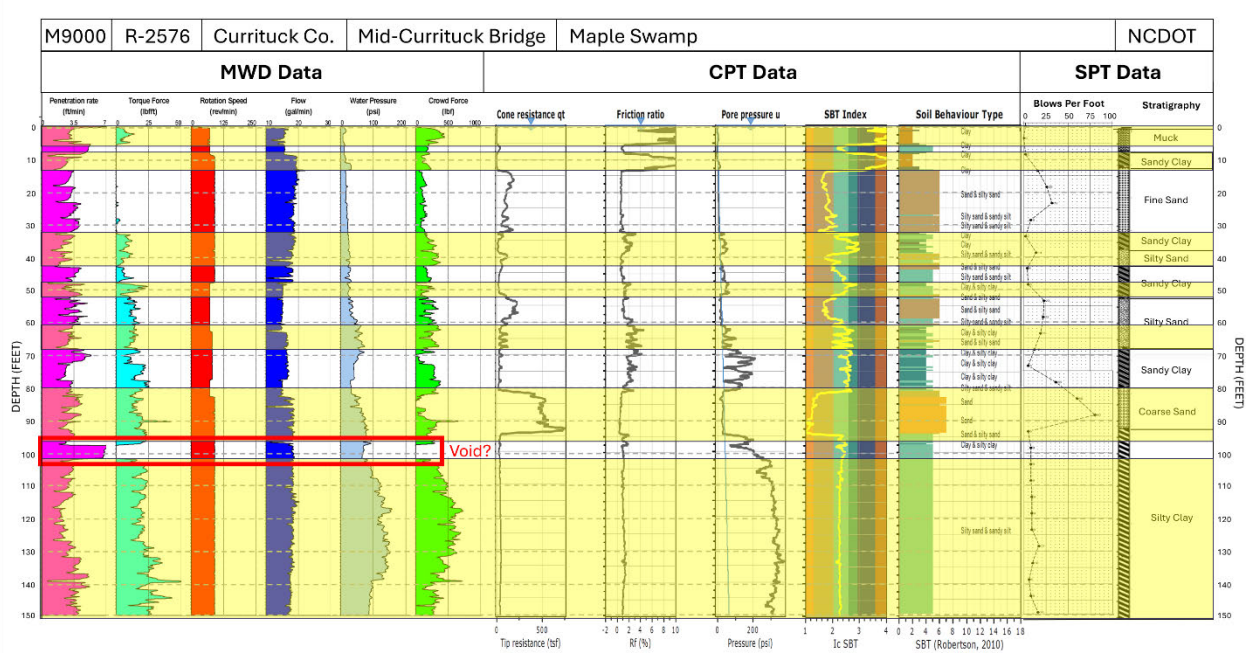

Fig. 10 – Mid-Currituck MWD, CPT, and SPT Graph for Boring M9000 in Maple Swamp. The Red Box Highlights a Possible Void Shown in the MWD Dataset.

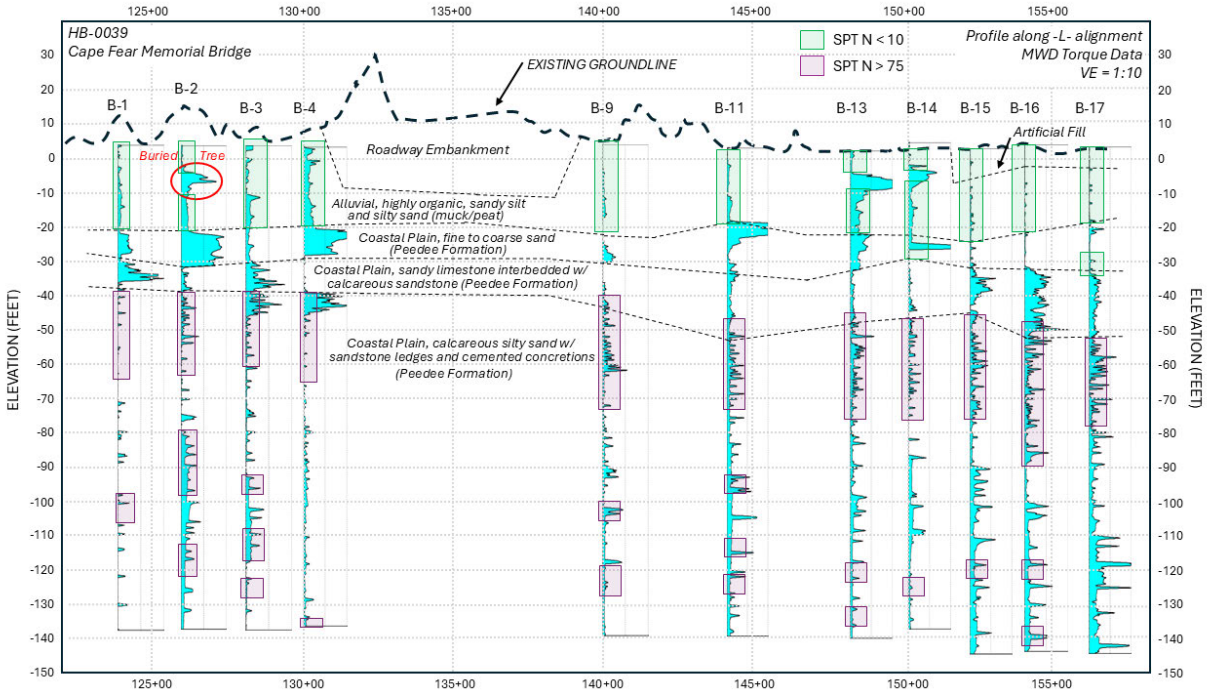

Fig. 11 – MWD Torque Data (blue graphs) Plotted Along the -L- Profile for the Cape Fear Memorial Bridge Project with General Observed Stratigraphy and SPT Blow Count Data Green Boxes Have N Values Less Than 10 Blows. Purple Boxes Have N Values Greater Than 75 Blows.

DISCUSSION

Mid-Currituck Bridge Discussion

Boring M9000 has a couple of layers that show obvious correlations between the MWD, CPT, and SPT data. The MWD crowd force and CPT pore pressure follow similar trends; however, the MWD crowd force data has a similar trend to the CPT friction ratio in the alluvial muck layer (Fig. 10). Generally when crowd force is high, water pressure is high, and torque force is low the observed stratigraphy is a cohesive soil such as a silty or sandy clay; however, if the crowd force is low or neutral, water pressure is low, and torque force is high then the inferred stratigraphy is a granular soil such as a fine to coarse sand. These MWD guidelines are also shown to not always be correct and one explanation is there is a range of physical soil parameters that affect the MWD data. A future study will throughly test and examine physical soil properties such as grain-size distribution, liquid limit values, and plastic index values.

There is an anomaly where the penetration rate significantly increases, the torque force decreases to virtually 0, and the crowd force decreases to virtually 0 between 98-102 feet below ground surface (Fig. 10). The SPT N-values are constant above and below this depth range and the CPT test values are also constant at this elevation. One interpretation is this is a local void in this borehole between 98-102 feet. An emerging technology that could help validate this interpretation is SPT-Seismic data. NCDOT is currently committed to a Pooled-Fund study with Dr. Khiem Tran of University of Florida to integrate and test SPT-Seismic on future NCDOT projects.

Cape Fear Memorial Bridge Discussion

MWD collects a plethora of data and it can be challenging to display the data in a useful way for a DOT production project. Several NCDOT colleagues have been interested in our MWD research project and have questioned the usefullness of the technology. Numerous industry professionals, researchers, graduate students, and technicians are working on understanding and interpreting the MWD datasets and verifying repeatability of reliable field testing so we can establish correlations to soil properties and, ultimately, use MWD data for engineering design on projects. This project presented the opportunity of collecting MWD data from several deep borings drilled along an alignment every 200 feet. Initally plotting the torque data along the -L- alignment profile with the observed stratigraphy and the very low (N<10) and very high (N>75) SPT N-value data can allow a strong visual for the types of general graphs that can be produced for production projects (Fig. 11).

The torque data values are relatively low with low SPT N-values in the alluvial muck layer; however, the torque data show a spike in B-2, B-13, and B-14 with SPT N-values increasing from 0 to 12-14 blows per foot. The field geologist noted an observed buried tree in the SPT field log for B-2. A different field geologist logged borings B-13 and B-14 and did not indicate a buried tree as the reason for the the torque and SPT N-value increases at those depths in those borings. The alluvial layer is highly organic as noted by the callout of muck/peat and a reasonable interpretation could more buried logs were encountered in those borings at those depths.

The torque values for the fine to coarse sand of the Coastal Plain Peedee Formation are much higher than relative to the overlying alluvial muck layer and can be easily interpreted as a strata change; however, borings B-3, B-15, B-16, and B-17 have similar low torque values as the overlying alluvial muck layer.

The torque data begins to look different in the sandy limstone layer of the Peedee Formation. First, there are zones of relatively low and high torque in this layer. Second, the torque data shows more eratic values. This is consistent with how variable the limestone is within the Peedee formation (Fig. 12). Figure 12 shows a core photograph of this variable limstone collected from a core just on the east side of the Cape Fear River. There are some sections with higher strength limestone yielding a high rock quality designation value and other sections with lower strength limestone yielding a lower rock quality designation value. Core L_20-A also contains the interbedded calcareous sandstone layers which are typically harder than the surround limestone. The CPT could not penetrate through the top of this limestone layer which, ultimately, prevents the collection of about 120 more feet of continuous data that we collected with the MWD boring.

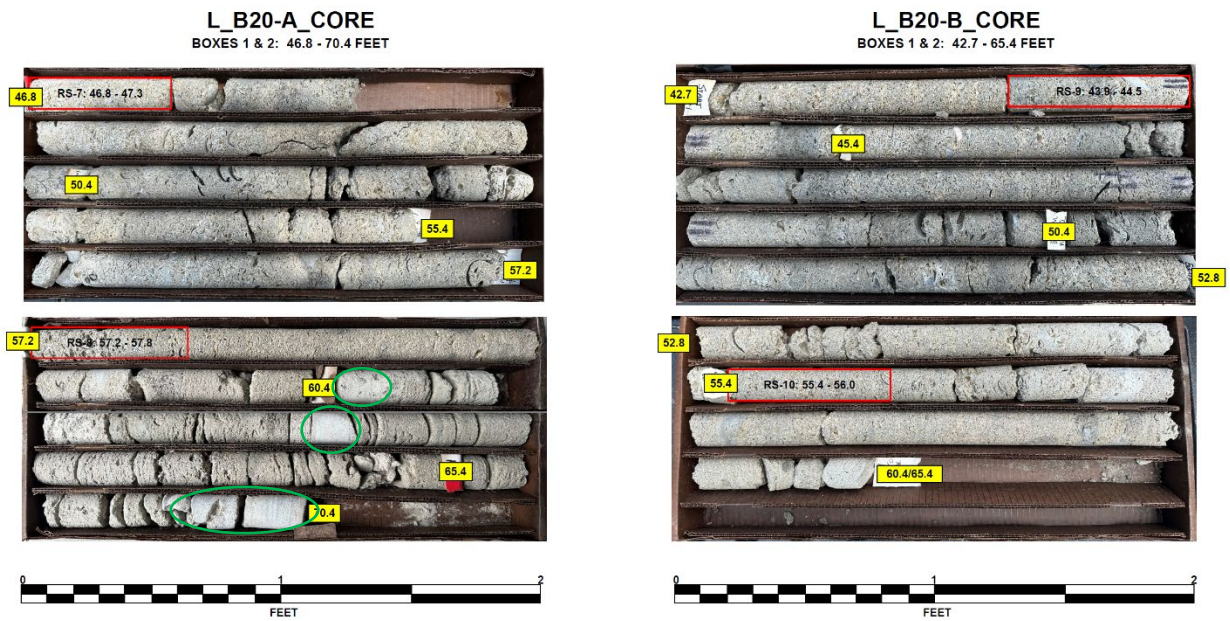

Fig. 12 – Coastal Plain Peedee Formation Sandy Foraminiferal Biomicrite (Limestone) and Quartz Sandstone with Abundant Marine Fossil Molds. Core Collected From the East Side of the Cape Fear River. Interbedded Calcareous Sandstone Indicated by Green Circles.

The torque data of the calcareous silty sand layer of the Peedee Formation is also highly variable and has a similar eratic profile to the overlying sandy limestone especially towards the top of the layer. Generally, the contact between these two layers is indicated by the high SPT N-values which are greater than 75 blows per foot with majority of the drives advancing less than 1 foot by 100 blows. This bottom of this continuous hard layer extends from -60 feet below mean sea level (BMSL) to -90 feet BMSL towards the Cape Fear River. The torque values stay

relatively low below -90 BMSL to -150 BMSL except for periodic spikes. Several of these torque data spikes have SPT N-values greater than 75 blows per foot. These are likely the sandstone ledges and cemented concretions present within this layer. The sandstone ledges are also not a continuous layer that can be easily followed along a profile. They are variable thicknesses vertically and they pinch in and out horizontally down the profile. It would be virtually impossible for a seasoned field geologist to record all these sandstone ledges and cemented concretions, much less a less-experienced field geologist. This nuanced stratigraphy adds to the complexity of the Coastal Plain field logging in North Carolina. Plotting the MWD torque data, stratigraphy, and SPT-N value data along an alignment profile elucidates a much deeper and complete subsurface story.

CONCLUSIONS

MWD has the potential to enhance our understanding of the subsurface conditions on projects especially as we continue to refine our drilling methods and research correlations to soil properties. Raw MWD data parameters match general CPT data trends and MWD torque data is useful to understand a more complete subsurface story. NCDOT is still collecting MWD data and working with NCSU on correlating MWD data to SPT N-values. We have more MWD research planned with NCSU in the future. NCSU is also using AI and machine-learning to correlate and interpret data quicker. While this paper focused on North Carolina Coastal Plain MWD data, we have Blue Ridge MWD data sets provided by Terracon, LLC that NCSU is using in their analysis. We are also continuing to work with and help train our consultants on MWD data collection processes. I am constantly talking with other DOTs and MWD researchers about current issues and future projects. The main goal is to keep collecting as much MWD data from as many different geological environments as we can so we build a robust MWD data repository.

REFERENCES

1. Benoit, J., Souza, B., and Regan, J. *Use of Drilling Parameters for Enhancing Geotechnical Site Investigations with Applications to Rock Assessment.* Report FHWA-NH-RD-42372F. FHWA, U.S. Department of Transportation, 2024.

2. Reiffsteck, P. *Standardization of MWD Through ISO 22476-15*. GeoStrata Magazine Archive, Geo-Institute of ASCE, 2023/2024, pp. 48-53.

3. Rodgers, M., McVay, M., Ferraro, C., Horhota, D., Tibbetts, C., and Crawford, S. Measuring Rock Strength While Drilling Shafts Socketed into Florida Limestone. *Journal of Geotechnical and Geoenvionmental Engineering*, vol. 144 (3), 2018.

4. Reiffsteck, P., Benoit, J., Bourdeau, C., and Desanneaux, G. Enhancing Geotechnical Investigations Using Drilling Parameters. *Journal of Geotechnical and Geoenvionmental Engineering*, vol. 144 (3), 2018.

5. Rodgers, M., McVay, M., Horhota, D., Hernando, J., and Paris, J. Measuring While Drilling in Florida Limestone for Geotechnical Site Investigation. *Canadian Geotechnical Journal*, vol. 57 (11), pp. 1733-1744.

6. Rodgers, M., McVay, M., Horhota, D., Hernando, J., and Paris, J. Operational Limits of Measuring While Drilling in Florida Limestone for Geotechnical Site Investigation. *Journal of Geotechnical and Geoenvionmental Engineering*, vol. 14 (12), 2021.

7. Horton, J.W. and Zullo, V.A., *The Geology of the Carolinas*. Carolina Geological Society Fiftieth Anniversary Volume, , University of Tennessee Press, Knoxville, 1991, pp. 1-10.

21. Advancing Geotechnical Site Characterization with 3D SPT-Seismic Testing

Khiem T. Tran
University of Florida
Gainesville, FL 32611
ttk@ufl.edu

Bingkun Yang
University of Florida
Gainesville, FL 32611
bingkunyang@ufl.edu

Prepared for the 75th Highway Geology Symposium, September, 2026

Acknowledgements

This study was supported by Florida Department of Transportation (FDOT): grant BED31-977-01. We thank the FDOT state material office for assisting in conducting the SPT-seismic data.

Disclaimer

Statements and views presented in this paper are strictly those of the author(s), and do not necessarily reflect positions held by their affiliations, the Highway Geology Symposium (HGS), or others acknowledged above. The mention of trade names for commercial products does not imply the approval or endorsement by HGS.

Copyright Notice

Copyright © 2026 Highway Geology Symposium (HGS)

All Rights Reserved. Printed in the United States of America. No part of this publication may be reproduced or copied in any form or by any means – graphic, electronic, or mechanical, including photocopying, taping, or information storage and retrieval systems – without prior written permission of the HGS. This excludes the original author (s)

ABSTRACT

Recent advancements in seismic testing have led to the development of the 3D SPT-seismic method, an innovative approach that integrates seismic wave analysis with conventional standard penetration test (SPT) measurements to enable volumetric imaging around boreholes. Unlike traditional geotechnical characterization methods that rely on discrete measurements at borehole locations, this approach utilizes the seismic energy generated during routine SPT hammer blows. These impacts act as repeatable seismic sources that produce body and surface waves propagating through the surrounding ground. The resulting wavefields are recorded at the surface using a dense 2D array of geophones, capturing detailed waveform information that can be used to reconstruct subsurface properties.

The recorded seismic data are processed using 3D full-waveform inversion (3D FWI), a physics-based imaging technique that iteratively updates subsurface models until the simulated waveforms closely match the observed data. By utilizing the full waveform information, including amplitude, phase, and scattering effects, FWI provides significantly higher resolution than conventional seismic methods that rely primarily on travel-time analysis. In the 3D SPT-seismic framework, hammer blows at multiple depths along the borehole serve as vertically distributed seismic sources, enabling the inversion to illuminate the surrounding subsurface from multiple directions and improving the stability and resolution of the reconstructed models.

This paper presents a comprehensive validation of the method at three geologically complex sites in Florida. Results demonstrate that subsurface properties can be imaged at sub-meter resolution within a 3D volume extending up to approximately 18 m laterally from the borehole and to the full depth reached by SPT. Multiple voids at various depths (5 to 15 m) were detected and confirmed by SPT data. A strong correlation between the shear-wave velocity (Vs) profiles derived from FWI and measured SPT blow counts (N-values) is observed across all sites. This relationship enables reliable 3D estimation of SPT-equivalent N-values, providing continuous volumetric characterization that can significantly enhance geotechnical site investigation and foundation design.

INTRODUCTION

Current practice in site investigation relies heavily on invasive point-based methods such as Standard Penetration Test (SPT), Cone Penetration Test (CPT), and rock coring. While these methods provide high-quality measurements, they sample only a very small volume of material within individual boreholes. As a result, large portions of the subsurface remain uncharacterized, and critical features (such as voids, soft zones, or irregular bedrock surfaces) remain undetected between boreholes. Surface-based geophysical methods can provide broader spatial coverage; however, their resolution typically decreases rapidly with depth due to signal attenuation, limiting their effectiveness for deeper subsurface imaging.

To overcome these limitations, recent advances in seismic testing have enabled the development of the three-dimensional SPT-seismic method, which integrates conventional SPT operations with seismic wavefield analysis to provide volumetric imaging of the subsurface. This approach utilizes byproduct seismic waves generated during SPT hammer impacts, recorded by a surface geophone array, and processed using three-dimensional full-waveform inversion (3D FWI) to reconstruct high-resolution Vs distributions around the borehole. Compared to traditional surface-wave methods, the 3D SPT-seismic approach offers improved spatial resolution, while avoiding the logistical complexity of cross-borehole testing.

Building upon prior developments, this study presents validation of the 3D SPT-seismic method at three geologically complex coastal sites in Florida. The results demonstrate sub-meter resolution imaging within a three-dimensional volume extending up to approximately 18 m laterally from the borehole and covering the full SPT depth interval. In addition, a strong and consistent relationship between FWI-derived Vs and SPT N-values is established, enabling reliable three-dimensional estimation of SPT resistance for engineering design and hazard assessment.

METHODOLOGY

The SPT-seismic data are analyzed by the 3D FWI method (Tran et al., 2019) based on elastic-wave propagation and Gauss-Newton inversion optimization. The method consists of the two following steps.

Step 1: simulate wave propagation using 3D elastic wave equations as:

$$\rho \dot{v}_i = \sigma_{i1,1} + \sigma_{i2,2} + \sigma_{i3,3} \quad (1)$$

$$\rho \dot{\sigma}_{ij} = \lambda(v_{1,1} + v_{2,2} + v_{3,3}) + 2\mu v_{i,j} \quad \text{if } i = j \quad (2)$$

$$\rho \dot{\sigma}_{ij} = \mu(v_{i,j} + v_{j,i}) \quad \text{if } i \neq j \quad (3)$$

where indices *i* and *j* correspond to spatial directions (*x*, *y*, *z*). The stress tensor components are denoted by σ_{ij}, particle velocity by v_i, density by ρ, and Lamé parameters by λ and μ. Time derivatives are indicated by dots, while spatial derivatives are represented by commas.

The equations are solved numerically using a finite-difference scheme (Virieux, 1986), with perfectly matched layers (PML) implemented for boundary absorption (Komatitsch and Martin, 2007). Additional implementation details can be found in Nguyen and Tran (2018).

Step 2: update material properties (Vs and Vp) by minimizing the misfit function E(**m**) via Gauss-Newton optimization as:

$$E(\mathbf{m})=\frac{1}{2}[\mathbf{F}(\mathbf{m})-\mathbf{d}]^t[\mathbf{F}(\mathbf{m})-\mathbf{d}], \quad (4)$$

$$\mathbf{m}^{n+1}=\mathbf{m}^n - \alpha^n\left[\mathbf{J}^t\mathbf{J} + \lambda_1\mathbf{P}^t\mathbf{P} + \lambda_2\mathbf{I}^t\mathbf{I}\right]^{-1}\mathbf{J}^t[\mathbf{F}(\mathbf{m})-\mathbf{d}]. \quad (5)$$

where observed data **d** and simulated **F(m)** wavefields are compared. The forward response is computed by solving the governing equations for the current model parameters. The model is updated iteratively using the Gauss–Newton scheme until convergence is achieved. The Jacobian matrix **J** represents the sensitivity of the wavefield to model parameters, while regularization terms stabilize the inversion. A constant step length of 0.5 is used in this study. Details on efficient Jacobian computation and parameter selection are provided in Tran et al. (2019).

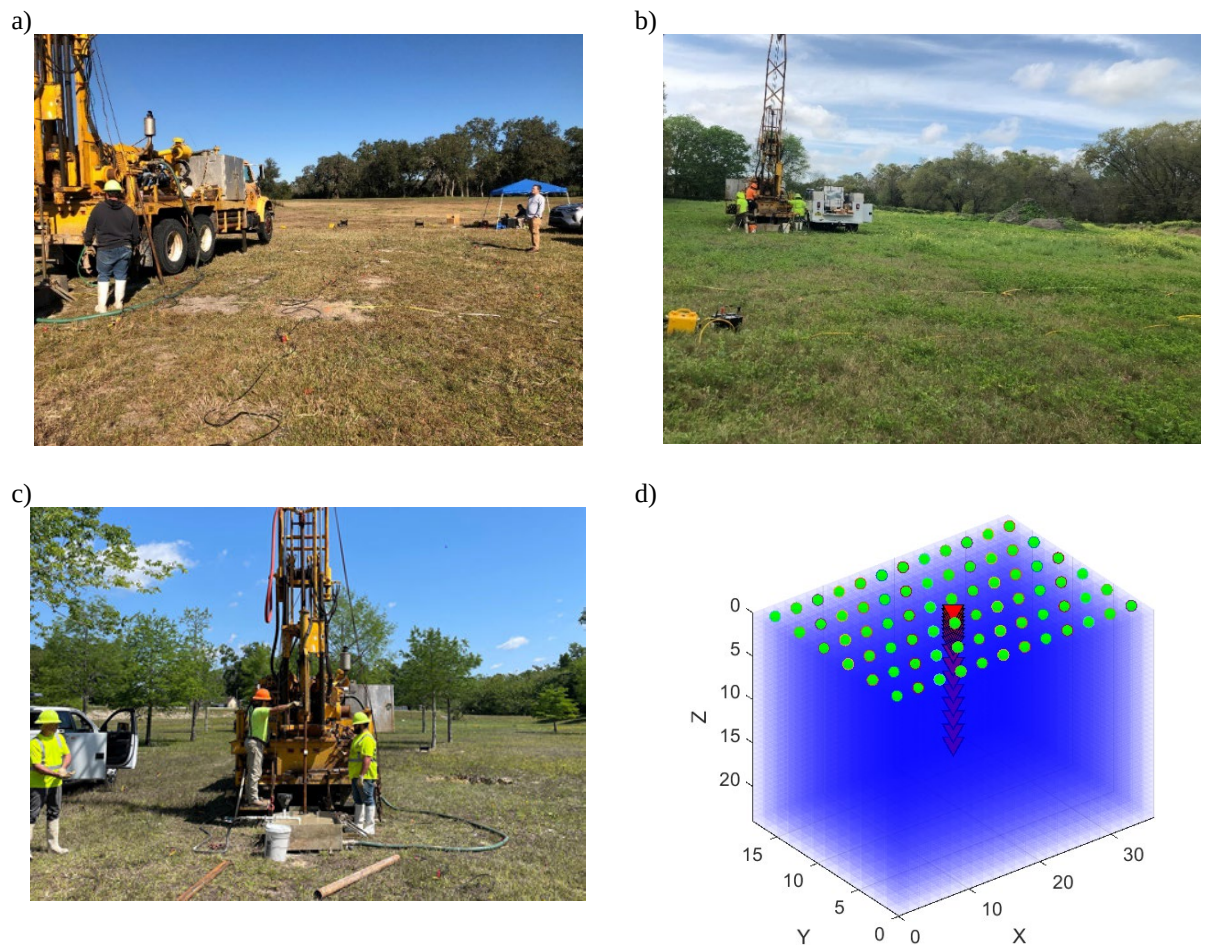

Figure 1. Field experiments at three test sites: a) Bell site, b) Kanapaha site, c) Newberry site, and (d) test configuration with sources (red triangle) and receivers (cyan circle). The 72 geophones (6 × 12 grid) were placed over a test area of 18 × 36 m. The SPT location is at the center of the test area.

FIELD EXPERIMENT

The presented method was validated at three sites in Florida (Bell, Kanapaha, and Newberry), selected for their complex subsurface conditions and presence of karst features. At each location, a surface geophone array recorded seismic waves generated by SPT hammer blows at successive depths. The recorded data were processed using the 3D FWI algorithm to obtain volumetric Vs and Vp models, which were subsequently compared with SPT N-values.

Data acquisition

At the Bell site (Fig. 1a), 72 vertical geophones (4.5 Hz) were deployed in a 6 × 12 grid with 3 m spacing, covering an area of 18 × 36 m. A single SPT was conducted at the center of the array. The SPT hammer (140 lb) was dropped from a height of 0.76 m, generating 116 impacts between depths of 0 and 15.24 m. Data acquisition terminated at this depth due to loss of drilling fluid circulation.

At the Kanapaha site (Fig. 1b), an identical acquisition setup was used. A total of 100 hammer blows were recorded down to 17.4 m depth. A sudden drop in resistance at approximately 11 m (N = 0) suggested the presence of a void or very weak material.

At the Newberry site (Fig. 1c), located in a dry retention pond with karstic limestone geology, the SPT reached a depth of 18.9 m. A total of 146 hammer blows were recorded. Between 13 m and 17 m depth, the hammer advanced under its own weight, indicating a significant void zone. Due to the lack of resistance, minimal seismic energy was generated at these depths, resulting in limited usable signals.

Data analysis

A consistent inversion workflow was applied to all datasets. The computational domain measured 24 × 36 × 18 m and was discretized into cells of 0.60 × 0.75 × 0.75 m. Source locations were assigned based on SPT depths and mapped to the nearest grid nodes. Signals from repeated blows at the same depth were stacked to improve signal-to-noise ratio.

An initial velocity model (Fig. 2) was constructed using a one-dimensional gradient, with Vs increasing from 200 m/s near the surface to 400 m/s at depth. The initial Vp was assumed to be twice Vs. Inversion was performed over a range of 10–40 Hz. Iterations were terminated after either 100 iterations or when misfit reduction became negligible. Comparison between observed and simulated waveforms shows strong agreement (Fig. 3), indicating accurate modeling and successful convergence without cycle skipping.

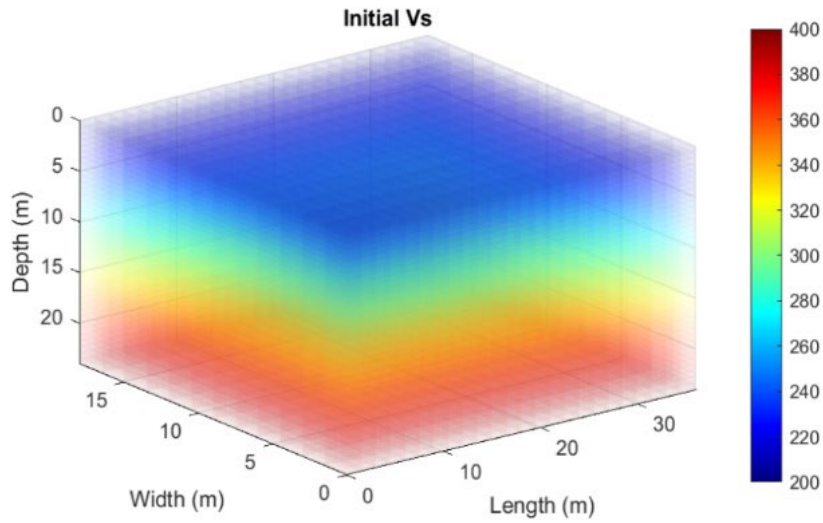

Figure 2. Initial Vs model used for inversion of all three test sites (Vp = 2×Vs)

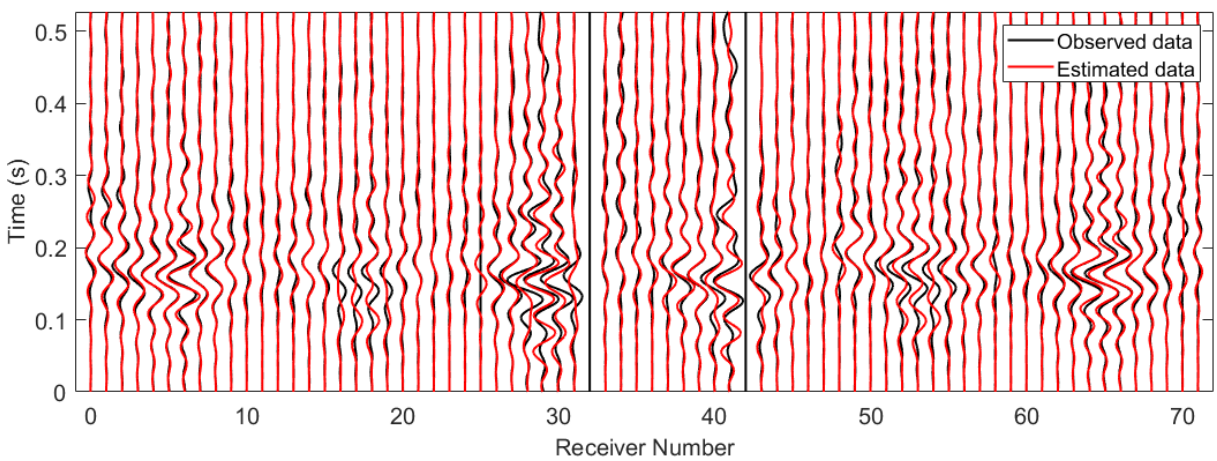

Figure 3. Comparison of observed (measured) and synthetic waveforms at Bell site for a sample source at 10.2 m depth, two noisy channels excluded from analysis.

SPT-seismic results

The inverted 3D Vs models reveal detailed subsurface features at all sites as shown in Fig. 4. At the Bell site (Fig. 4a), a soft soil layer overlies limestone, with the bedrock depth varying from 6 to 15 m. A localized low-velocity anomaly at approximately 15 m suggests a void connected to the borehole. At the Kanapaha site (Fig. 4b), the limestone surface varies between 10 and 13 m depth. A distinct low-velocity zone at approximately 11 m corresponds to the void indicated by SPT data. At the Newberry site (Fig. 4c), both soil and limestone layers are clearly imaged. Two separate voids are identified near 15 m depth, one intersecting the borehole and another located nearby, demonstrating the ability of the method to detect off-hole anomalies. Compared to conventional borehole logs, these 3D results provide significantly enhanced spatial information, including the extent and geometry of subsurface features.

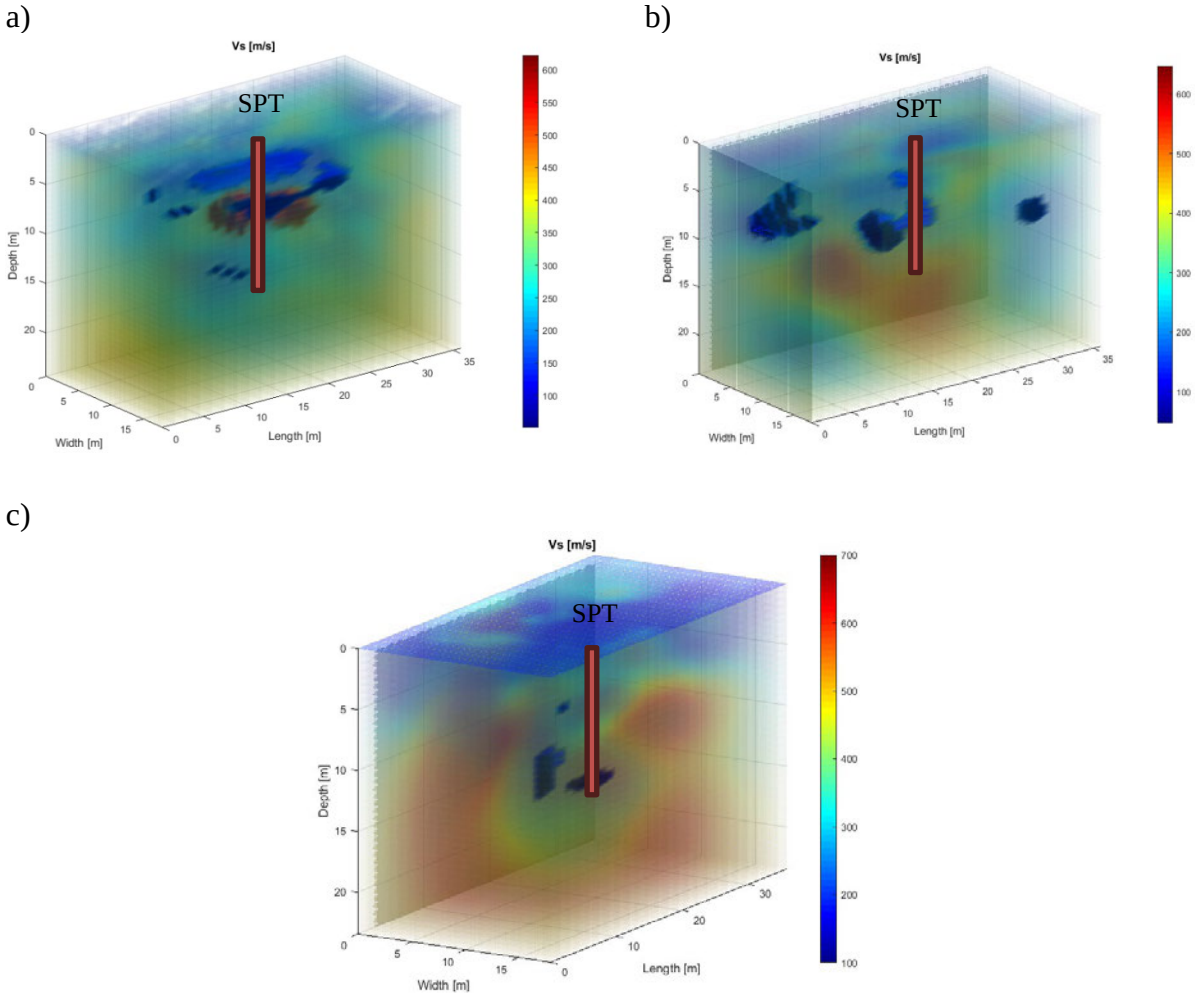

Figure 4. The 3D rendering of inverted shear wave velocities at three test sites: a) Bell site, b) Kanapaha site, c) Newberry site.

Comparison between inverted Vs profiles and SPT N-values shows strong agreement across all sites. Low Vs zones correspond to low blow counts, while high Vs values align with dense or competent materials. At Bell, the inversion captures both stiff limestone and underlying soft zones. At Kanapaha, the void and stratigraphy are clearly resolved. At Newberry, the general trend matches SPT data, although the Vs profile is smoother due to spatial averaging and regularization in the inversion process. Overall, the results confirm the reliability of the SPT-seismic approach in characterizing subsurface conditions.

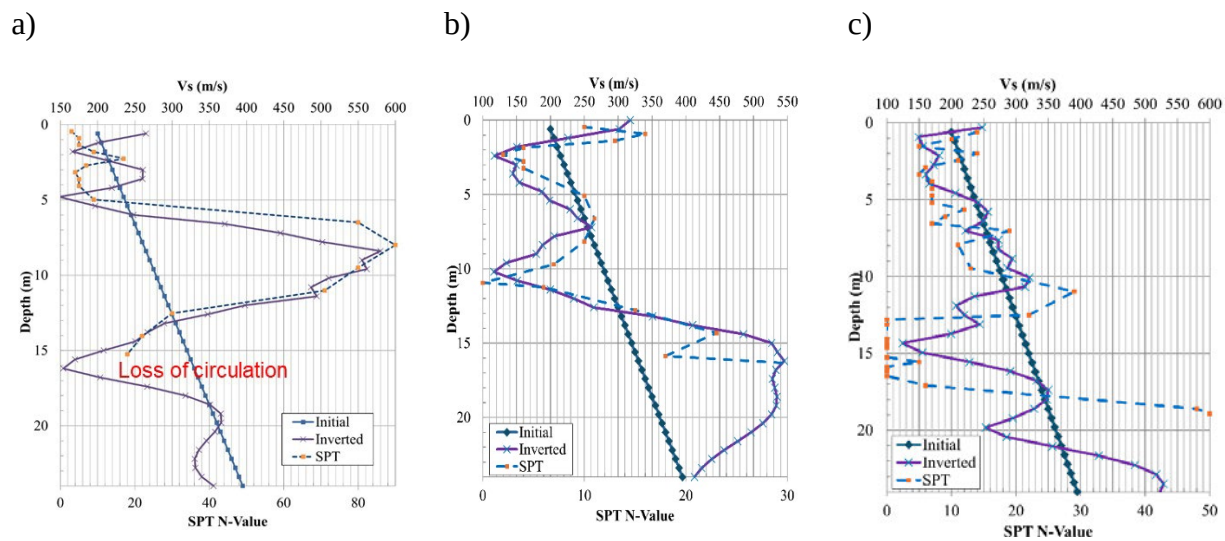

Figure 5. Comparison of inverted V_s with SPT N-values for three test sites: a) Bell site, b) Kanapaha site, c) Newberry site

Correlation of SPT N-value and Vs across sites

The Vs values obtained from inversion were correlated with SPT N_{60} values to develop empirical relationships. The combined dataset from all sites spans a wide range of soil and rock conditions. Regression analysis indicates that a power-law relationship provides the best fit, consistent with previous studies (Rahimi et al., 2020).

$$V_s = 110.54(N_{60})^{0.3094} \quad (6)$$

The resulting model explains approximately 58% of the variability in Vs, demonstrating a reasonably strong correlation given the heterogeneous conditions.

CONCLUSION

This study demonstrates that the 3D SPT-seismic full-waveform inversion method is an effective tool for high-resolution geotechnical site characterization, particularly in complex karst environments. Field validation at three Florida sites shows that the method can resolve subsurface features at sub-meter scale within a radius of approximately 18 m from a borehole. The resulting 3D velocity models successfully identify key features such as stratigraphic boundaries, bedrock topography, and subsurface voids. Strong agreement with SPT-N data further confirms the accuracy of the method. By integrating seismic imaging with conventional SPT operations, the 3D SPT-seismic method provides a practical and efficient tool for geotechnical site investigation, particularly for foundation design and hazard assessment.

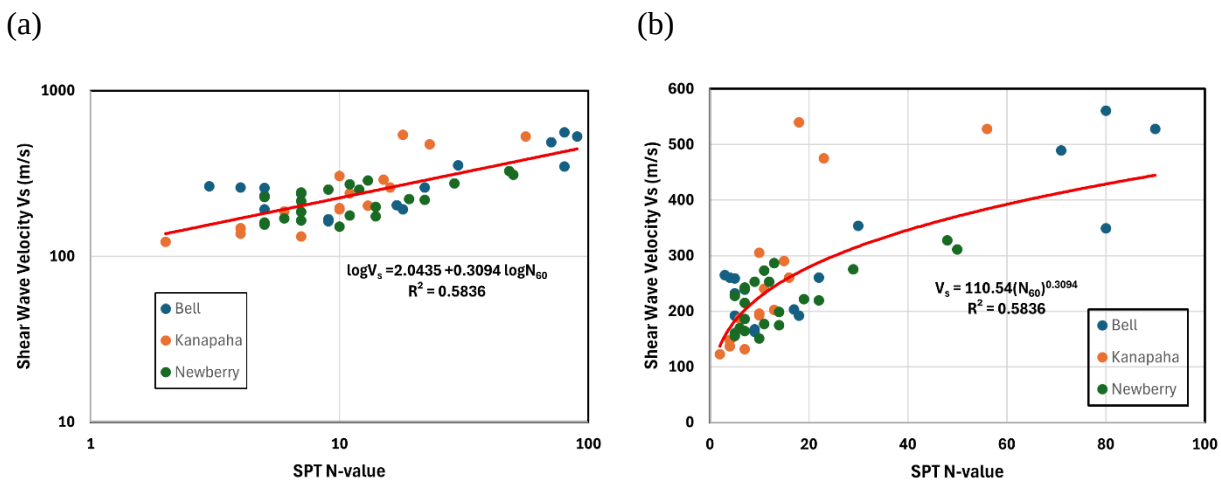

Figure 6. Correlation between SPT-N values and V_s for all three sites: (a) Linear regression in logarithmic scale, (b) Power-law fit in regular scale

REFERENCES

Komatitsch, D. and R. Martin, 2007, An unsplit convolutional perfectly matched layer improved at grazing incidence for the seismic wave equation: Geophysics, **72**, no. 5, SM155-SM167.

Mirzanejad, M., Tran, K.T., McVay, M., Horhota, D., Wasman, S., 2020, Sinkhole detection with 3D full seismic waveform tomography: Geophysics, 85 (5), pp. B147–B157.

Mirzanejad, M., Tran, K.T., McVay, M., Horhota, D., Wasman, S.J.: Coupling of SPT and 3D full waveform inversion for deep site characterization. Soil Dynamics and Earthquake Engineering. 136, (2020).

Nguyen, T.D., and Tran, K.T., 2018, Site characterization with 3D elastic full-waveform tomography: Geophysics, 83(5), R389-R400.

Rahimi, S., Wood, C.M., Wotherspoon, L.M.: Influence of soil aging on SPT-Vs correlation and seismic site classification. Eng Geol. 272, (2020).

Tran, K.T., Mirzanejad, M., McVay, M. and Horhota, D., 2019, 3-D time-domain Gauss–Newton full waveform inversion for near-surface site characterization: Geophysical Journal International, 217, 206-218.

Tran, K.T., Mirzanejad, M., Horhota, D., Wasman, S.J.: 3D Full-Waveform Tomography of Standard Penetration Test-Seismic Wavefields in Karst Florida Limestone. Transportation Research Record, 2678, 248–256 (2024).

Virieux, J., 1986, P-SV wave propagation in heterogeneous media: Velocity-stress finite-difference method: Geophysics, 51, 889-901.

22. Integrated Geotechnical and Geophysical Interpretation of Sterling Highway Milepost 45 to 60 Project

Keri Nutter, CPG
DOWL
5015 Business Park Boulevard, Suite 4000
Anchorage AK, 99503
(907)-865-1317
knutter@dowl.com

David Barrick, PE
DOWL
1300 Cedar Street
Helena, MT 59601
406-324-7403
dbarrick@dowl.com

Prepared for the 75th Highway Geology Symposium, September, 2026

Acknowledgements

The author(s) would like to thank the individuals/entities for their contributions to the work described:

Julia Hanson, P.E. – Construction Project Manager, Alaska DOT&PF
Jonathan Tymick, P.E. – Construction Project Manager, Alaska DOT&PF
Derek Duncan, PG, CPG – Engineering Geologist - DOWL

Disclaimer

Statements and views presented in this paper are strictly those of the author(s), and do not necessarily reflect positions held by their affiliations, the Highway Geology Symposium (HGS), or others acknowledged above. The mention of trade names for commercial products does not imply the approval or endorsement by HGS.

Copyright Notice

Copyright © 2026 Highway Geology Symposium (HGS)

All Rights Reserved. Printed in the United States of America. No part of this publication may be reproduced or copied in any form or by any means – graphic, electronic, or mechanical, including photocopying, taping, or information storage and retrieval systems – without prior written permission of the HGS. This excludes the original author(s).

ABSTRACT

The Sterling Highway Milepost 45 to 60 project consists of 15 miles of new highway cutting across the steep topography north of Cooper Landing on the Kenai Peninsula in Alaska. To date, field investigations include more than 200 test holes, 160 test pits, mapping of geological features, dozens of near-surface geophysics transects, and the collection of groundwater and inclinometer data.

The geology of the project alignment varies across the project corridor; significant portions of the corridor consist of glacial till overlying schist bedrock of the Valdez Group. The schist is generally highly fractured, with zones of steeply dipping foliation, and has a mylonitic to migmatitic texture.

DOWL and its project partner, Landslide Technology, in collaboration with the Alaska Department of Transportation & Public Facilities, investigated the section of the project where the new highway alignment intersects the existing Sterling Highway. This area is characterized by very steep topography, dense vegetation, and culturally sensitive sites, which limit access with traditional drilling equipment.

To address these investigative challenges, the project team combined test hole data with multiple geophysical methods, including seismic refraction tomography (SRT), multichannel analysis of surface waves (MASW), and electrical resistivity tomography (ERT), to estimate stratigraphic coefficient of variation, which is a parameter in Reliability Based Design (RBD). The geophysical and limited borehole data were then integrated into Leapfrog Geo®, a 3D geological modeling software, to support the interpretation of the subsurface conditions to evaluate options for steep slopes and retaining walls.

Results demonstrate that integrated geophysical and geotechnical characterization reduces stratigraphic uncertainty and improves confidence in subsurface interpretation for the design of steep cuts and retaining walls.

INTRODUCTION

The Sterling Highway is a critical access route connecting the western Kenai Peninsula in southcentral Alaska to Anchorage. Several segments of this highway feature narrow, winding roads with little to no shoulder, posing hazards to vehicle traffic on a busy recreational and truck route. The Sterling Highway between Mileposts 45 and 60 encompasses the community of Cooper Landing and multiple public access points to world-class salmon fishing. Seasonal vehicle traffic, uncontrolled driveways, and a lack of pedestrian facilities were all drivers of the need to construct 15 miles of new highway to reduce traffic congestion, improve safety, and bring the Sterling Highway into compliance with current design standards. The new highway realignment (the 'Juneau Creek Alternative') cuts across steep topography with thick vegetation and dense forest undergrowth, with the significant feature being the Juneau Creek Canyon at the approximate project midpoint. The project corridor is divided into five project phases, with the Stage 5 portion, where the western end of the new alignment intersects with the existing Sterling Highway, the focus of this paper. Figures 1 and 2 illustrate the project corridor and the Stage 5 area of focus.

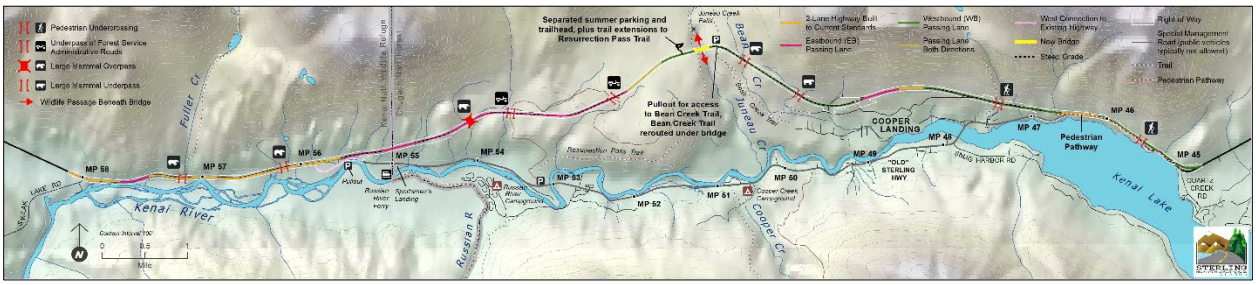

Figure 1 - Sterling Highway MP 45-60 Project Corridor

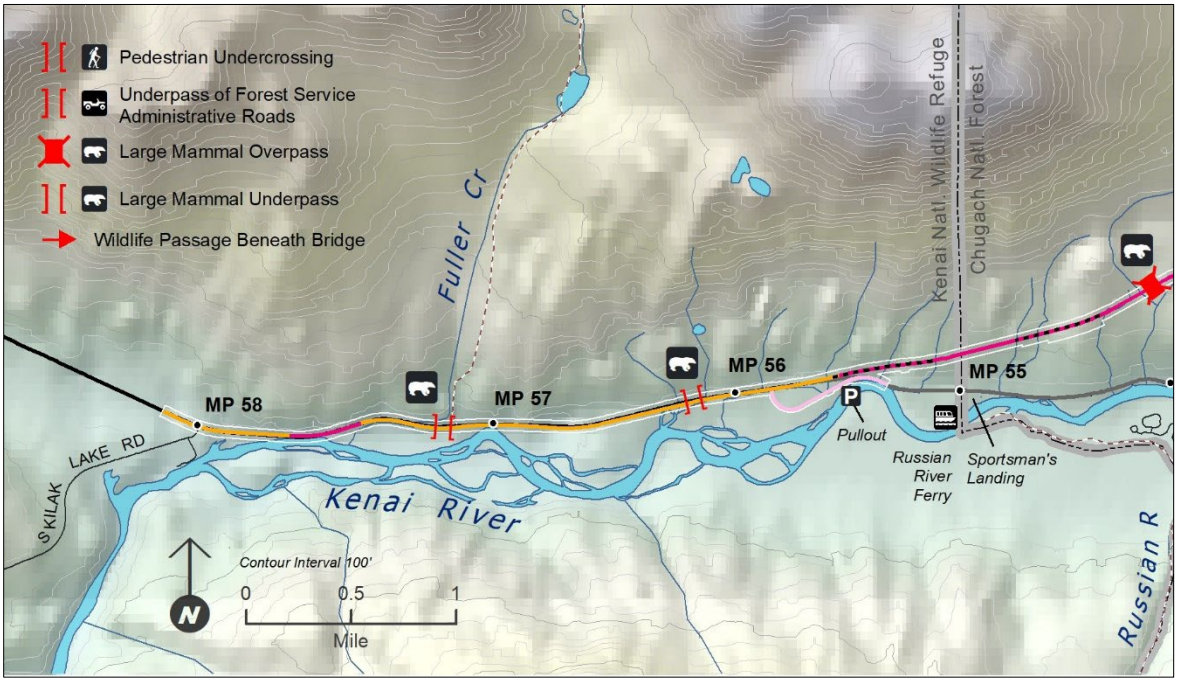

Figure 2 - Sterling Highway MP 45-60, Stage 5

The Stage 5 portion of the project area is characterized by near-vertical schist bedrock outcropping along the northern side of the existing Sterling Highway and the Kenai River channel along the south side. The project design for Stage 5 access to the site was provided by Alaska DOT&PF (DOT&PF) and the CM/GC contractor. During the geotechnical and near-surface geophysical investigation, the area was mostly cleared, with some areas protected for archaeological preservation. The near-surface geophysical investigation was performed before the geotechnical investigation to aid in borehole site selection and to develop a two-dimensional understanding of the site subsurface conditions. The intent of the site characterization is to aid in understanding stratigraphic uncertainty and geomaterial engineering properties for the analysis of proposed slope modifications or retaining wall designs. The project consists of a combination of rock and soil cuts. The rock cut is approximately 30 feet tall and above the rock cut, an approximate 10-foot-tall soil cut is proposed. Because of the steepness of the underlying schist bedrock, a retaining wall design has been proposed but the design team is seeking alternative slope stabilization options.

The focus is on this portion of Stage 5 because the geometry of the proposed highway includes the proposed tight-diamond interchange is pushing road cuts on the north side of the highway in close proximity to several environmentally sensitive areas (ESAs). This is forcing some cut areas to be steeper than the planned 2:1 for assumed soil slopes, pushing design in the direction of retaining walls, unless bedrock is present. Limited access to drill test borings in the area has resulted in limited test boring data indicating that bedrock is at depths ranging from 9 to 27 feet below existing grade; however, as the depth to bedrock is inconsistent and overlain by glacial till and outwash overburden, the depth to bedrock along this area was of detailed interest to confirm the intersection of cut daylights and bedrock surface.

This paper discusses the combined use of applied geophysics and limited geotechnical borehole data, and their incorporation into the coefficient of variation, which is a parameter of Reliability-Based Design (RBD). The broader spatial coverage afforded by geophysical methods reduces uncertainty when interpreting stratigraphic thicknesses, while boreholes provide critical ground-truth calibration.

LITHOLOGY and GEOLOGY

Atop the proposed road cut from Station 1202+50 to 1208+50, the lithology of the project area consists of lodgement till deposits, varying in boulders, cobbles, gravel, and sand, supported in a matrix typically comprised of overconsolidated, low-plasticity silt and clay. The lodgemont till is a dense, unsorted glacial sediment deposited directly beneath a moving glacier. During the geotechnical investigation, the upper 5 feet of the lodgement till exhibit loose to medium-dense relative density but quickly transitions to very dense properties. Because of the steepness of the project area, unconsolidated colluvial deposits resembling the gradation of the lodgment till were also observed.

Below the lodgement till and consistently outcropping in the Stage 5 project area are highly jointed and foliated metasediments of the Valdez Group. The schist bedrock of the Valdez Group generally has joints and other discontinuities that tend to be steeply dipping, with

fractures along the foliations. The schist bedrock forms naturally steeper, higher-elevation slopes across the project alignment, with colluvial slopes at the base of some of the larger slopes.

GEOTECHNICAL INVESTIGATION

A geotechnical investigation was performed in the fall of 2025, consisting of the drilling of four geotechnical test borings (TH-7-W-059 to TH-7-W-062) within the limits of interest for this paper. The geotechnical drilling was performed using HWT-size casing advance methods in the lodgement till with sampling performed using a 3-inch outside-diameter split sampler during standard penetration tests (SPT) Upon refusal the drilling method switched to HQ triple-tube rock coring for core recovery and rock quality designation (RQD) data. Figure 3 illustrates the locations of the four geotechnical test borings, as well as the location of six geophysical transects. Test borings TH-7-W-062 and TH-7-W-061 consist of hybrid or directional drilling of a vertical and angled borehole (Landslide Technology, 2026).

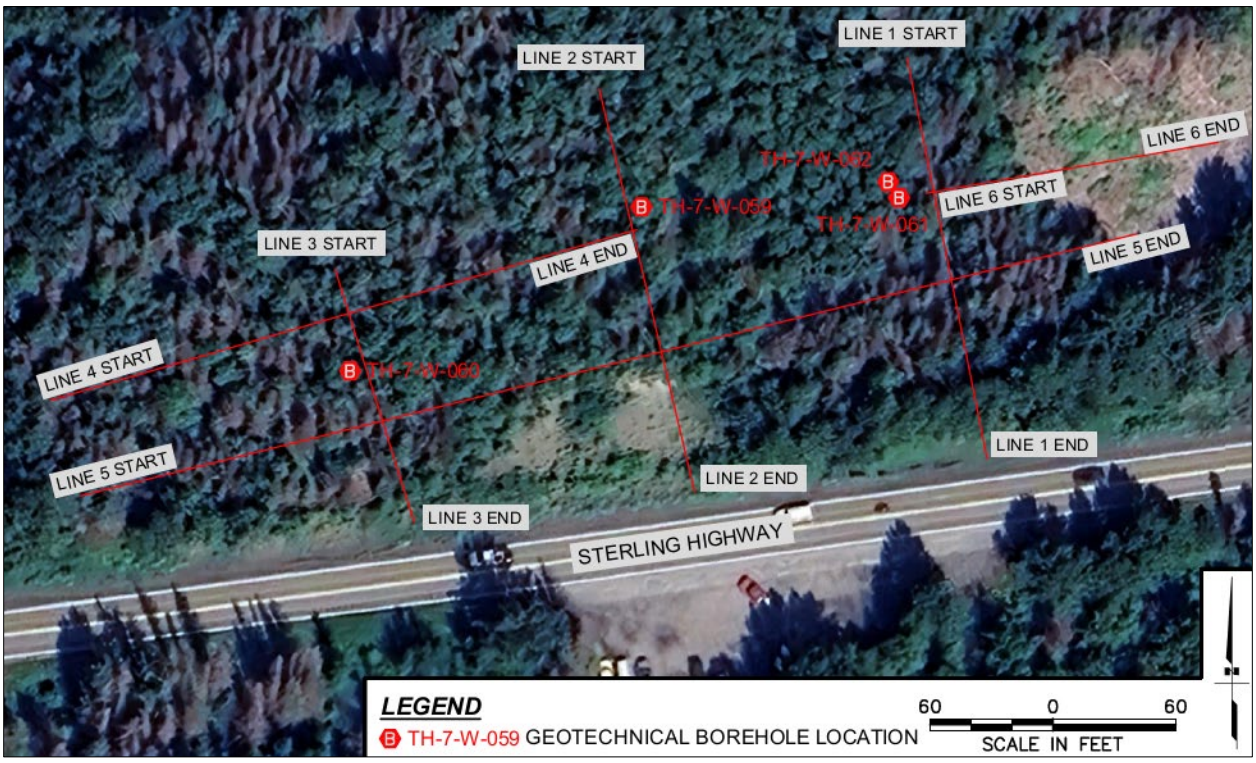

Figure 3 – Test Boring and Geophysical Transect Location Map – Station 1202+50 to 1208+50

NEAR-SURFACE GEOPHYSICAL SURVEY

To develop a deeper understanding of the steep project area for the proposed road cut and slope stabilization design, DOWL and Landslide Technology conducted a near-surface geophysical survey. Because each geophysical method measures a different physical property, relying on a single technique provides only a partial picture. Per the United States Environmental Protection Agency (EPA.gov) and the Transportation Research Board (Transportation Research Circular, 2008), at least two geophysical methods should be selected for a single objective. The

two geophysical methods provide converging evidence supporting a single interpretation. For this project, three methods were deployed, consisting of seismic refraction tomography (SRT), multichannel analysis of surface waves (MASW), and electrical resistivity, along the same alignments (transects) to supplement each other. The geophysical alignments were “field-fit” to maximum data collection and subsurface resolution while considering the efficiency of equipment, cable, and geophone or electrode placement. Because of the steep topography, significant elevation changes affect the mathematical inversion process. Elevation data used for the profiles was collected with a Bad Elf® GPS and converted to DOWL’s LiDAR survey datum to ensure it matches the project’s design drawings. Regarding this paper, geophysical data from Line 1 and Line 4 were extracted to compare with geotechnical boreholes and to evaluate subsurface uncertainty.

Seismic Refraction Tomography

The seismic refraction tomography (SRT) method calculates subsurface compressional wave velocity (Vp). Using the same first-arrival times, a tomographic solution can be computed by discretizing the subsurface into a grid cell structure rather than layers. The seismic velocities of each grid cell are adjusted to reduce the misfit between the observed and calculated travel times. Iterations are repeated until the user is confident with the fit between the calculated and observed times (Schuster et al., 1993). The tomography approach thus lends itself to characterizing laterally variable subsurface media. Specifically, tomography methods can image gradients and lateral velocity variations, which are common in shallow site investigations due to weathering transition zones or compaction (Sheehan et al., 2004). Rayfract® refraction tomography software was used to produce the 2D p-wave velocity tomograms.

Multichannel Analysis of Surface Waves

The seismic data recorded for SRT purposes were used for Multichannel Analysis of Surface Waves (MASW), thereby eliminating the need for separate data collection. This efficiency is enabled by the SeisImagerSW™ (Geometrics, Inc.) software, which uses a common-midpoint stacking approach rather than the standard off-end analysis. The two-dimensional (2D) MASW uses Common-Mid-Point (CMP) gathers between source and receiver pairs to generate shear wave velocities from Rayleigh surface waves. Rayleigh surface waves are approximately 90% of the velocity of shear waves (Burger, Sheehan, and Jones, 2006). Although the 2D s-wave-velocity profiles resemble discretized velocity models, they are formed from 1D s-wave-velocity profiles calculated at twice the geophone spacing. The starting model was set to 15 layers for the calculations. Thus, the resolution of the MASW 2D model is twice the geophone spacing horizontally and 15 layers vertically, resulting in a coarser resolution than SRTs. The figures show the gridded and contoured results from the individual 1D shear-wave depth-velocity profiles. The wavefield transformation used is a slant stack (τp) first introduced by McMechan and Yedlin (1981).

Bedrock depth interpretation is based on experience and site-specific subsurface data, such as borehole data along Sterling Highway. Additionally, published correlations of seismic velocities for bedrock and dense sediments (Press, 1966) and the spacing of seismic tomogram contours were factored into the interpretation, as shown in Table 1. The sound bedrock ranges in

Table 1 are performed in a laboratory setting. Because intact rock core does not typically represent the properties of a rock mass, compressional seismic velocities are typically measured in the field. Shear wave velocities were calculated and tabulated based on the following rule-of-thumb relationships (Burger, Sheehan, and Jones, 2006):

- Vs = 0.6Vp for crystalline rocks
- Vs = 0.5Vp for sedimentary rocks
- Vs = 0.4Vp for soils and unconsolidated sediment materials.

Table 1 – Range of Compressional Seismic Velocities (feet per second)

Unconsolidated Materials			**Sound Bedrock (no groundwater)**		
Material Type	P-wave Velocities	S-wave Velocities	Material Type	P-wave Velocities	S-wave Velocities
Alluvium	1,640-6,560	660-2620	Granite	16,400-19,680	9,840-11,810
Clay	3,610-8,200	1,440-3,280	Basalt	17,710-20,990	10,630-12,600
Unsaturated Sand	660-3,280	262-1,310	Metamorphic Rocks	11,480-22,960	6,980-13,780
Saturated Sand	2,620-7,220	262-1,310	Sandstone & Shale	6,560-14,760	3,280-7,380
Unsaturated Sand and Gravel	1,310-1,640	525-660	Limestone	6,560-19,680	3,280-7,380
Saturated Sand and Gravel	1,640-4,920	525-660	**Non-geomaterials**		
Unsaturated Glacial Till	1,310-3,280	525-1,310	Material Type	P-wave Velocities	S-wave Velocities
Saturated Glacial Till	2,620-6,550	525-1,310	Water	4,592-5,248	N/A
Very Dense Glacial Till	3,940-6,890	1,574-2,760	Groundwater	4,200-6,600	N/A

Using SRT, the compressional wave velocity in weathered and/or fractured schist bedrock or geomaterials with standard penetration tests greater than 50 blows per foot is typically greater than 3,000 feet per second above the groundwater table. For the Sterling Highway project, we estimate that weathered bedrock and/or fractured schist have compressional wave velocities of approximately 4,000 to 5,000 feet per second, based on four geotechnical boreholes (TH-7-W-059 to TH-7-W-062) in the project area from Station 1202+50 to 1208+50. As the profile deepens into the schist bedrock, the rock mass rating increases as less weathering and fracturing are observed. From experience, sound schist bedrock is estimated to be 7,000 feet per second. A compressional wave profile for Line 1 with interpreted 4,000 and 7,000 feet per second p-wave velocities with two concurrent boreholes (TH-7-W-061 and TH-7-W-062) is shown in Figure 4.

From the interpretation of published data and DOWL's experience comparing seismic velocities to known ground truths, DOWL interpreted a shear-wave velocity of 1,500 feet per second for weathered and/or fractured schist bedrock or geomaterials with standard penetration tests greater than 50 blows per foot and a shear-wave velocity of 2,500 feet per second as the threshold for what is interpreted to be sound schist bedrock. A shear wave profile for Line 1 is shown in Figure 5.

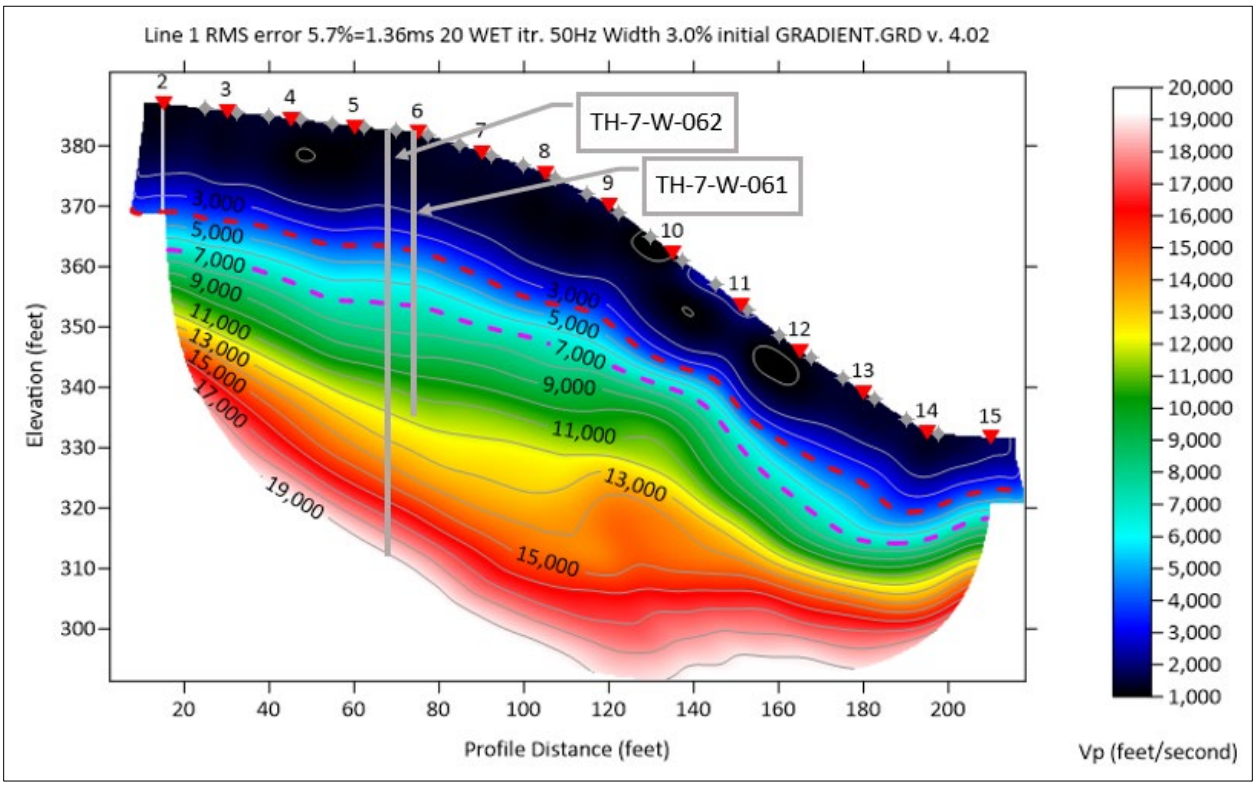

Figure 4 – Sterling Highway – Compressional Wave Profile – Line 1

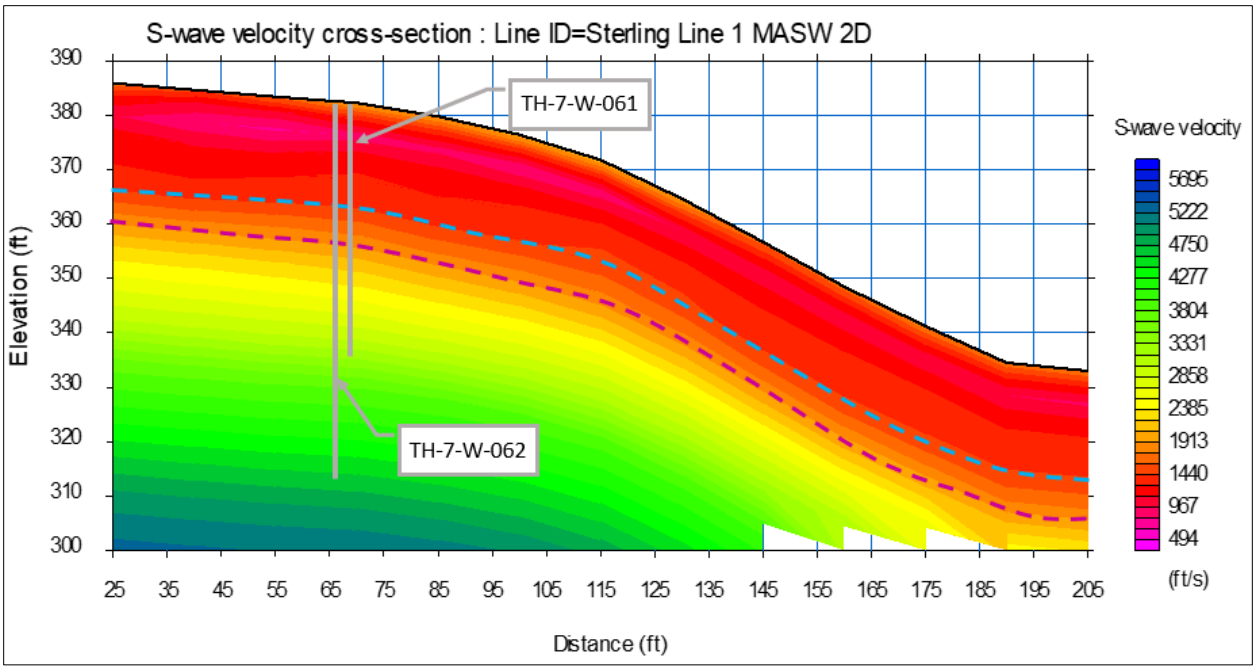

Figure 5 – Sterling Highway – Shear Wave Profile – Line 1

Electrical Resistivity Tomography

The electrical resistivity tomography (ERT) method utilizes differences and contrasts in electrical resistivity to identify the subsurface materials, depth to water, and subsurface structures. The project team collected the ERT data in general accordance with ASTM D6431-18, Standard Guide for Using the Direct Current Resistivity Method for Subsurface Site Characterization. In this method, the subsurface bulk electrical resistivity is measured, providing information on changes in subsurface lithology and groundwater saturation. The measured apparent resistivity is a function of different parameters, such as porosity, salinity concentration, clay content (especially within unconsolidated sediments), and water saturation. The measured apparent resistivity would be the same as the earth's true resistivity if the earth were isotropic and homogeneous. To compute the true resistivity, a mathematical inversion method is used. The 2D resistivity data were inverted using Res2DInv® (Seequent Software). The inversion code is based on the smoothness-constrained least squares method. The range of resistivity values is logarithmic and varies significantly per type of soil and rock, as illustrated in Figure 6.

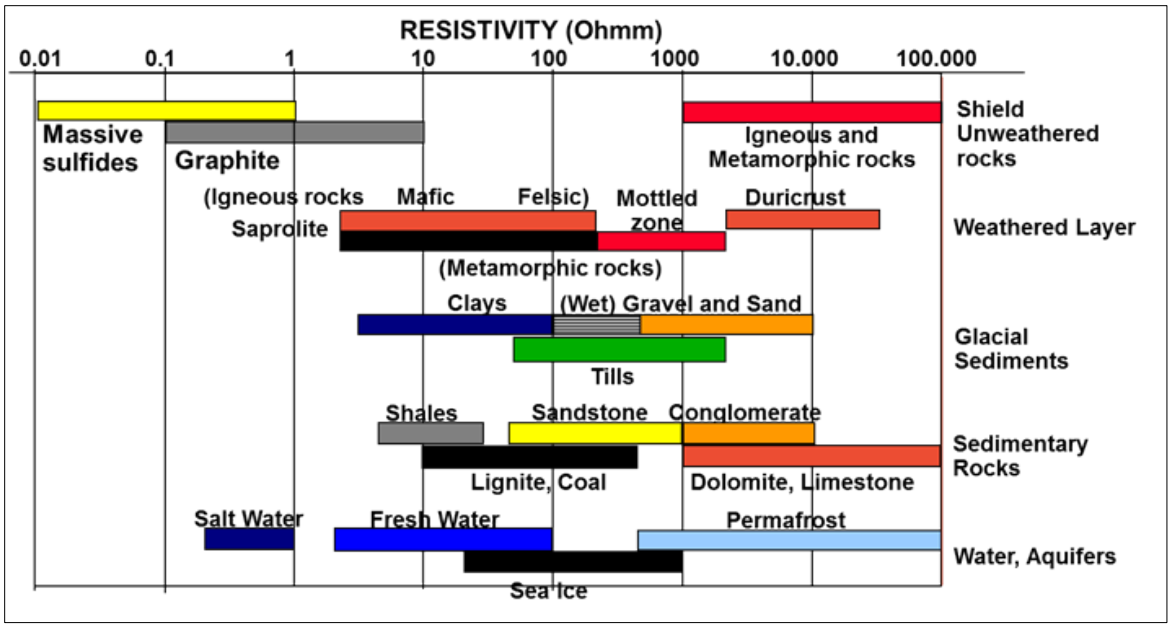

Figure 6 – Resistivity Ranges of Different Geomaterials (Palacky, 1987)

The lithology in the project area consists of lodgement till overlying schist metasedimentary bedrock. As shown in Figure 7, the lodgement till exhibits very high electrical resistivity, typically greater than 500 ohm-meters. The underlying schist bedrock exhibits much lower electrical resistivity values, typically less than 500 ohm-meters. Two concurrent boreholes (TH-7-W-061 and TH-7-W-062) are shown as gray vertical lines in Figure 7 to identify their location along the electrical resistivity profile.

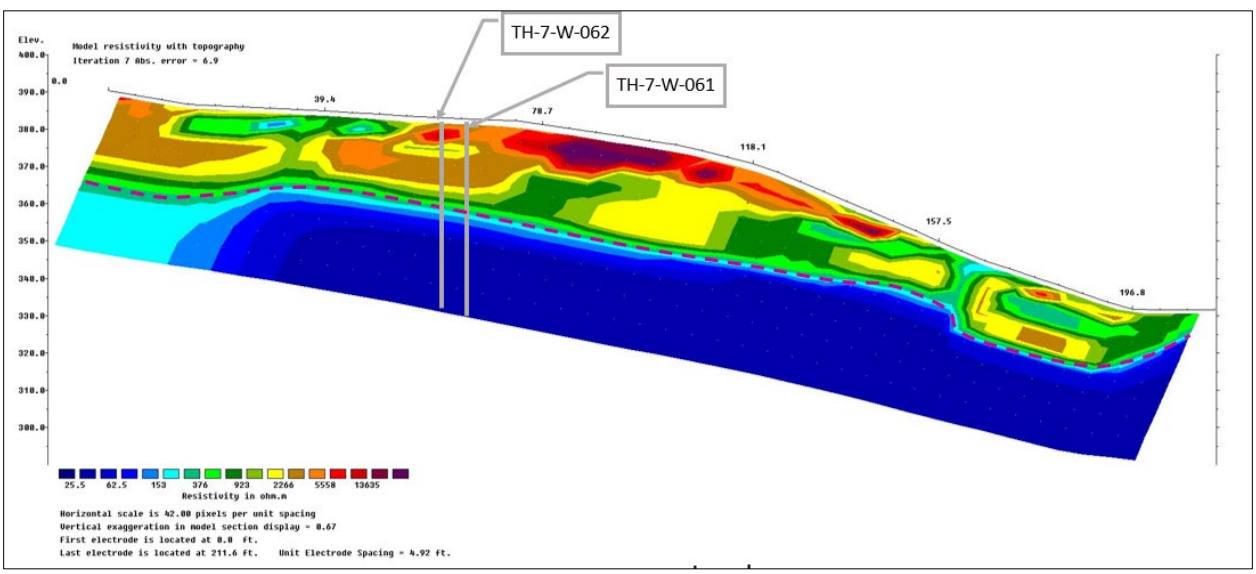

Figure 7 – Sterling Highway – Electrical Resistivity Profile – Line 1

TRADITIONAL COMPARISON OF GEOTECHNICAL & GEOPHYSICAL PROFILES

Traditionally, geotechnical borehole data is compared with geophysical profiles by matching the borehole location along the transect, as shown in Figure 7. Seismic velocities and resistivity values can be compared with lithology on borehole logs to develop a best-fit model of transitions between geological layers. However, there is nuance to this method, as there is uncertainty in layer transitions in geotechnical boreholes and in geophysical methods. Table 2 summarizes the interpretive depth to schist between boreholes and SRT/ERT profiles.

Table 2 – Comparison of Depth to Schist Bedrock Boreholes and SRT/ERT

Borehole	Depth to Schist Bedrock in Borehole (feet)	Approximate Depth to Schist in SRT (feet)	Approximate Depth to Schist in ERT (feet)
TH-7-W-059	22.7	21	21
TH-7-W-060	9.0	13	11
TH-7-W-061	27.0	22	18
TH-7-W-062	25.0	23	22

Using the 4,000-foot-per-second compressional wave contour, SRT could predict the schist bedrock with a mean of 3.2 feet and a standard deviation of 1.3 feet. Using a 500 ohm-meter contour, ERT could predict the schist bedrock with a mean of 3.9 feet and a standard deviation of 3.0 feet. Since MASW is more difficult to compare with boreholes because of the lower profile resolution, it was not compared in Table 2.

DISCUSSION

Geological Uncertainty

Subsurface uncertainty is a major risk factor in geotechnical site characterization and design. Recent years have seen a trend toward treating uncertainty more formally, particularly by applying the results of reliability theory to geotechnical engineering and by making it common in government geotechnical manuals (United Facilities Criteria, 2025). Reliability theory itself evolved from the structural, aerospace, and manufacturing industries; it has required special adaptation to deal with the geological environment (Baecher and Christian, 2013). Soil stratification (or geological) uncertainty heavily governs Reliability-Based Design (RBD). Accurate predictions of soil stratification remain challenging for engineers and geologists because of inherent variability in subsurface conditions (Tang and Phoon, 2021). To develop a deeper understanding of the steep project area for the proposed road cut and/or retaining walls, the soil and rock property uncertainty may be quantified using the coefficient of variation (COV). The COV is defined as the ratio of the standard deviation to the mean, as shown in Equation 1. It provides a second-moment characterization of the data scatter (Phoon et al., 2022). COV measures data dispersion relative to the mean and is unitless, making it ideal for comparing datasets with different units.

$$Coefficient\ of\ Variation\ (COV) = \frac{Standard\ Deviation}{Mean}$$

One of the goals of this paper is to evaluate the site's borehole stratigraphic uncertainties and compare them with geophysical uncertainties. The first step is to define the reliability-uncertainty per COV stratigraphic uncertainty, as shown in Table 2.

Table 3 – Stratigraphic Uncertainty Classification

Stratigraphic Uncertainty Class	Range of COV
Low	COV Thickness < 0.20 & Presence Frequency ≥ 0.80
Moderate	COV Thickness ≤ 0.50 & Presence Frequency ≥ 0.50
High	Anything worse than Moderate

The stratigraphic uncertainty for both the geotechnical boreholes and the three geophysical methods is estimated from layer thickness and frequency. The presence frequency is the frequency with which the layer appears in the borehole or geophysical profile. The following equations break down the stratigraphic uncertainty:

$$COV_{Layer\ Thickness} = \frac{\sigma_H}{\mu_H}$$

Where: σ_H = standard deviation of layer thickness
μ_H = mean layer thickness

$$Presence\ Frequency = \frac{Number\ of\ Boreholes\ Where\ Layer\ is\ Pressent}{Total\ Number\ of\ Boreholes}$$

For other projects, other factors may be calculated to estimate stratigraphic uncertainty. Other factors may include the apparent slope of the layer boundary, uncertainty in continuity, and boundary confidence. Because the geology is a simple two-layer lithology with continuous layers, a simple method of layer thickness and frequency of occurrence was applied in this paper.

RESULTS

The following sections provide summaries of geotechnical borehole and geophysical uncertainties and compare the parameters. The use of Leapfrog software is also discussed.

Geotechnical Borehole – Stratigraphic Uncertainty

Table 4 summarizes the stratigraphic uncertainty estimated from the four geotechnical boreholes illustrated in Figure 3. From the variability of layer thicknesses and presence frequency of the lodgemont till and schist layers, the geotechnical boreholes indicated a moderate stratigraphic uncertainty classification.

Table 4 – Stratigraphic Uncertainty from Four Geotechnical Boreholes	
	Lodgment Till Layer
Total Number of Boreholes	4
Number of Boreholes Where Layer is Present	4
Presence Frequency	1
Mean Thickness (feet)	20.9
Standard Deviation Thickness (feet)	8.1
Coefficient of Variation of Till Thickness	0.39
Stratigraphic Uncertainty Classification	Moderate

When the number of observations is less than 8, all methods for calculating COV should be used with caution (Lofman, 2016). The lack of geotechnical data supports the coupling with near-surface geophysics parameters. The small sample size of geotechnical boreholes produces unstable COV estimates and therefore requires support from geophysical investigation.

Geophysical Stratigraphic Uncertainty

To assess geophysical uncertainty at the project site, data were obtained from two 2D profiles, yielding five 1D profiles from each. The five 1D profiles are equally spaced, with the center profile in the middle. Since Line 1 is 225 feet long, the 1D profiles were extracted at Station 62.5, 87.5, 112.5, 137.5, and 162.5 feet. Line 4 is 300 feet long with 1D profiles at 90, 112.5, 150, 187.5, and 225 feet. The authors used Surfer® mapping software (Golden Software) and MATLAB (MathWorks, Inc.) to extract geophysical data. The data from both geophysical lines were combined to evaluate subsurface uncertainty. The extracted geophysical profiles should not be interpreted as statistically independent observations; rather, they provide a measure of spatial continuity along the investigated transects. Figure 8 shows examples of the extracted 1D geophysical profiles along Line 4.

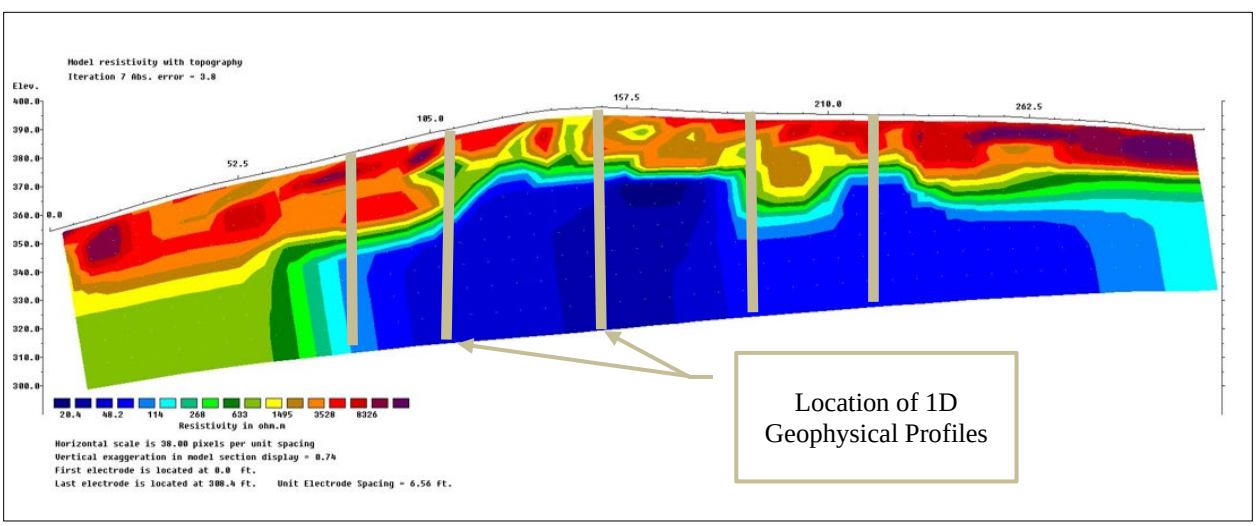

Figure 8 – Sterling Highway – Electrical Resistivity Profile – Line 4

From the five 1D geophysical profiles shown in Figure 8, the geophysical data were extracted for the lodgment till and schist bedrock. The 2D geophysical profiles illustrate stratigraphy, with

layering roughly parallel to the topography and moderate undulations at the lodgment till-schist bedrock contact. The moderate undulations of the schist bedrock reflect variable weathering conditions and highly fractured zones within the substrate. Table 5 summarizes the geophysical stratigraphic uncertainty from two geophysical transects (Lines 1 and 4).

Table 5 – Stratigraphic Uncertainty from Two Geophysical Transects

	Lodgement Till Layer
Total Number of 1D Geophysical Profiles	10
Number of Locations Where 1D Profiles are Present	10
Presence Frequency	1
Mean Thickness (feet)	26.9
Standard Deviation Thickness (feet)	3.7
Coefficient of Variation of Till Thickness	0.14
Stratigraphic Uncertainty Classification	Low

The stratigraphic uncertainty classification of the lodgement till from geotechnical boreholes is 0.39, which equates to a moderate uncertainty classification, as shown in Table 4. The geophysical stratigraphy uncertainty is 0.14 (low stratigraphic uncertainty), as shown in Table 5. The higher stratigraphic uncertainty in the boreholes reflects a much smaller data set, whereas the geophysics is more representative of the entire subsurface.

Stratigraphic uncertainty, quantified by layer geophysical thickness changes and presence frequencies, is an objective measure of the reliability of subsurface geological models and the risk associated with interpolated borehole data. If borehole data were used independently in the site evaluation, the limited data most likely would have promoted a more conservative design. This paper presents a case study showing that, intuitively, more subsurface data from geophysics would lead to greater uncertainty. However, the opposite is true: the lack of geotechnical borehole data results in greater scatter in the plot. The methodology of quantifying stratigraphic uncertainty can support future RBD implementation.

Integrated Geophysical Methods

As previously mentioned, it is recommended that at least two geophysical methods to complement each other to approach a single interpretation. SRT, MASW, and ERT methods have strengths and weaknesses. ERT can reveal low-resistivity anomalies associated with water-filled voids, or high-resistivity areas associated with air-filled voids. However, various environmental factors, such as heterogeneous conditions with variable water saturation, may result in misleading outcomes (Martinez-Moren et al., 2015). SRT using p-waves provides high-resolution profiles, but low-velocity air-filled regions may prevent effective wave propagation (Grandjean and Leparoux, 2004). MASW can identify low-velocity zones but typically provides poorer resolution than SRT.

Currently, the authors only import SRT profiles into Leapfrog Geo® for 3D depth-to-bedrock evaluation. To evaluate the quality of the SRT profiles, the authors compared the SRT interpretive depth to the 4,000 feet per second bedrock contour, the 1,500 feet per second MASW contour, and the 500 ohm-meter ERT contour for geophysical Lines 1 and 4. Figures 9

and 10, respectively, illustrate the Interpretive Bedrock Contours for the three geophysical methods.

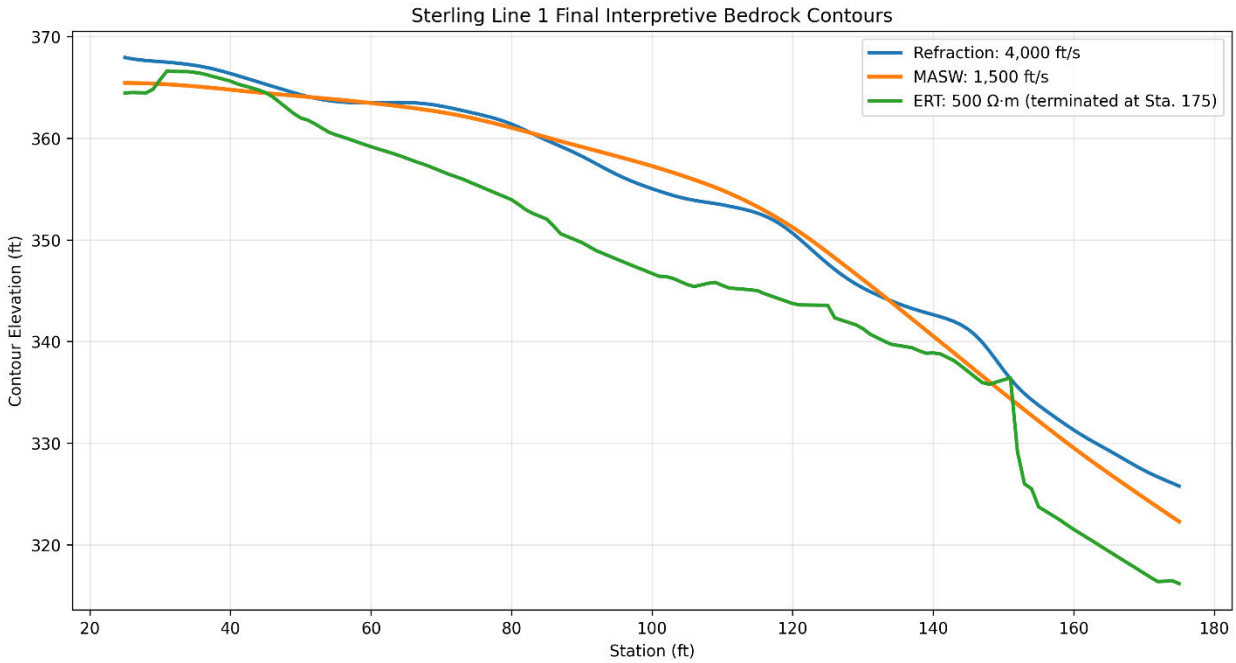

Figure 9 – Comparison of Interpretive Bedrock Contours of Three Methods for Line 1

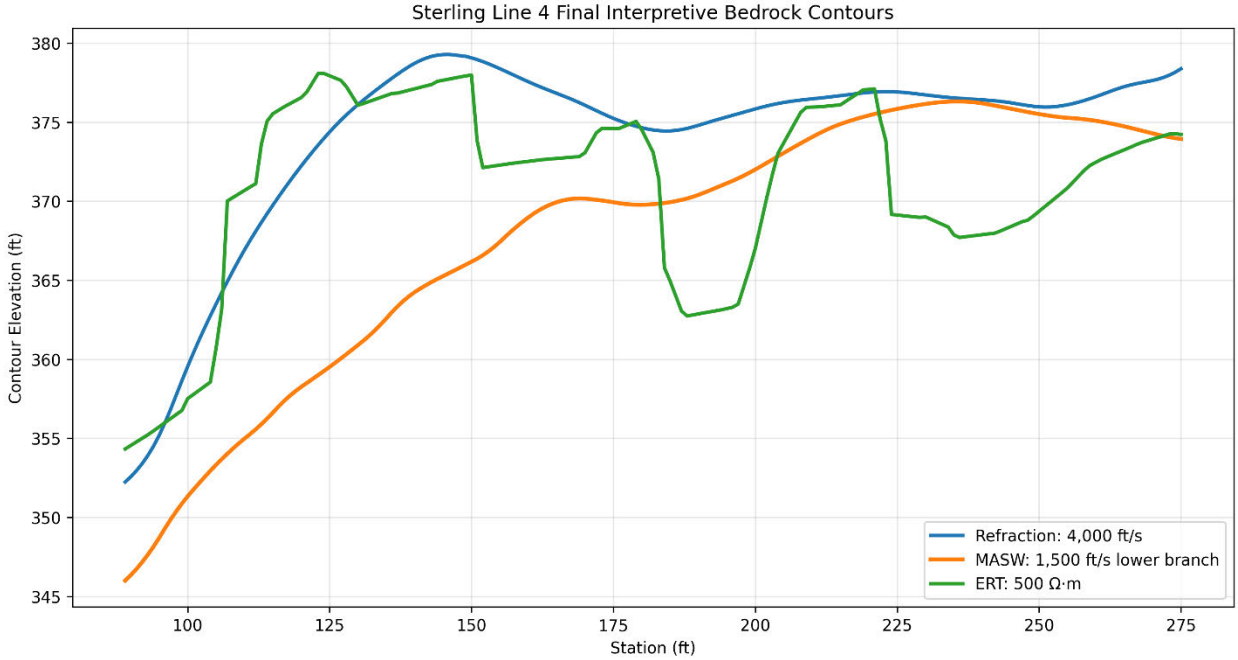

Figure 10 – Comparison of Interpretive Bedrock Contours of Three Methods for Line 4

Table 6 – Three Geophysical Methods Depth to Schist Bedrock Misfit Summary			
Comparison of Methods	Mean Absolute Misfit (ft)	RMSE (ft)	Maximum Misfit (ft)
Line 1			
Refraction to MASW	1.36	1.65	3.49
Refraction to ERT	5.79	6.51	10.30
MASW to ERT	5.48	6.38	10.63
Line 4			
Refraction to MASW	5.95	7.93	15.23
Refraction to ERT	4.99	6.11	12.59
MASW to ERT	7.02	8.74	18.66

When comparing the interpretive bedrock contours for SRT, MASW, and ERT (Table 6), Line 1 showed better results than Line 4 for Mean Absolute Misfit, Root Mean Squared Error, and Maximum Misfit. For Line 1, the refraction (SRT) and MASW are very closely aligned with a mean absolute misfit of only 1.36 feet. The higher misfits for Line 4 are most likely due to variable topography and more severely undulating schist bedrock, as shown in the ERT profiles. MASW also typically performs worse in steep topography.

The comparison of interpretive depth to bedrock using three geophysical methods, coupled with a measurement of stratigraphic uncertainty, gave the authors confidence in the validity of the SRT contour of 4,000 feet per second for Leapfrog Geo® analysis. SRT was chosen for the Leapfrog Geo® because of the ease of use to apply to the software, strong borehole correlation, and high resolution.

COMBINED RESULTS OF COLLECTED DATA – LEAPFROG GEO®

The results of the geotechnical test boring logs, geophysical surveys, and geological mapping were compiled into Leapfrog to model the bedrock surface, with the primary focus of providing the design team with a bedrock surface to determine if road cut daylights will intersect rock or soil and inform the need for slope stabilization. The benefits of using a three-dimensional geological program to build CAD compatible surfaces were realized in the multiple iterations the design team had to run to adjust the road alignment to accommodate ESAs. The modeling (Figure 11) facilitated a greater level of certainty of the bedrock surface in areas where borings could not be drilled than traditional geological interpolation, incorporating multiple data points from field investigations.

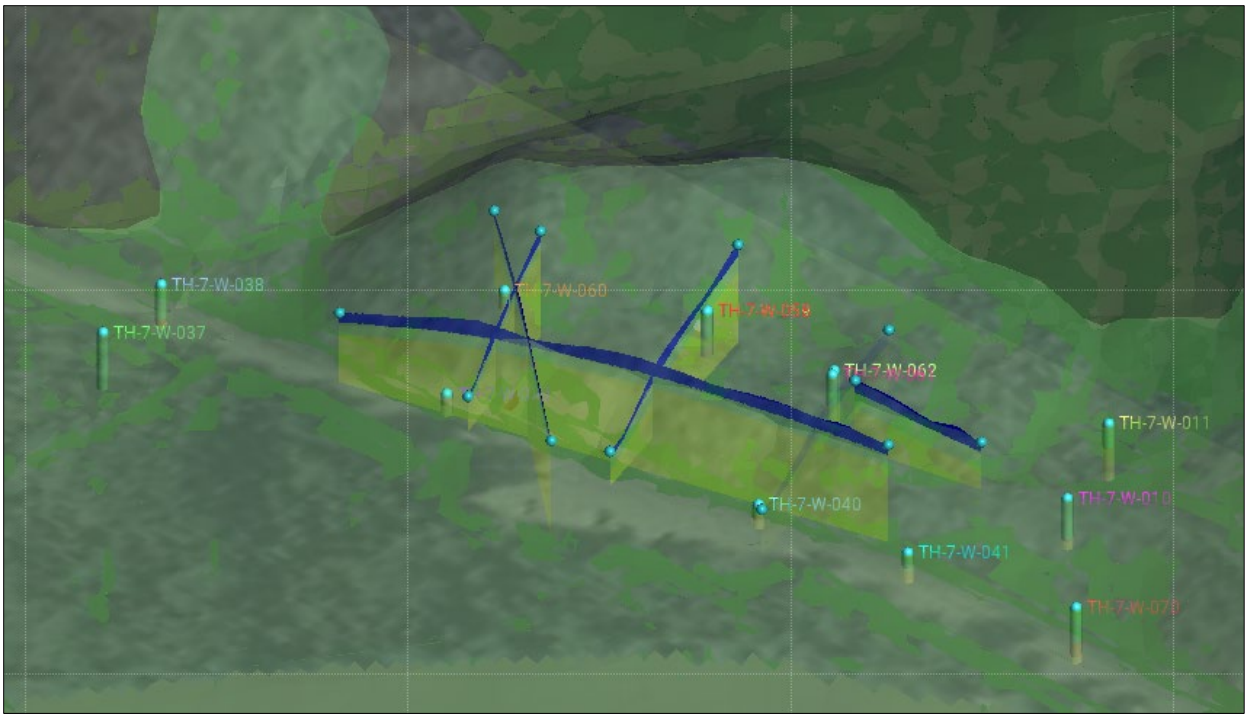

Figure 11 – Leapfrog Model with Test Boring and Geophysical Transects - Station 1202+50 to 1208+50

The streamlined interface between CAD and Leapfrog allowed for real time model refinement as the area of potential effect to the ESAs changed and value engineering by the contractor adjusting the design. For example, after the initial modeling of the test boring and geophysical survey data was provided, the contractor was able to focus additional potholes in specific areas and provide the observed bedrock surface, which was in turn used to further refine the model. As the project geotechnical program is being performed in phases as ESAs are cleared for access, the design team can quickly update the road cut daylights and adjust cut slopes for soil or rock materials, further refining areas where slope stabilization may be required and therefore better refining the project costs with the project contractor.

FUTURE GEOTECHNICAL DATA COLLECTION AND ANALYSIS

To continue refining the 3D geologic model in Leapfrog and support design, additional test pits are planned to be excavated at regular intervals at the top of the proposed rock cut later this summer. This will further define the top of bedrock to confirm the geophysical profile and where the bedrock surface intersects the road cut daylights. The future geotechnical data collection will further reduce the site's geological uncertainty.

The evaluation of geophysical, geomaterial, and stratigraphic uncertainty was a simple task at the Sterling Highway site because of the high contrast in seismic velocities and resistivity values between the lodgemont till and schist bedrock. Further research is needed to evaluate sites with ambiguous boundaries, pinch-outs, and gradual transition zones between geological substrates.

REFERENCES:

1. Landslide Technology, *Sterling Highway MO 45-60, Sunrise to Skilak Lake Rd. Phase 5 (1178+00 to 1259+50) Geotechnical Data Report Addendum (draft),* Landslide Technology, 2026, 52p.

2. United States Environmental Protection Agency. Surface Geophysical Methods. Environmental Geophysics Resources. https://www.epa.gov/environmental-geophysics/surface-geophysical-methods. Accessed July 12, 2026.

3. Burger, H.R., Sheehan, A.F., and Jones, C.H. Introduction to Applied Geophysics. W.W. Norton and Company, Inc., New York, NY, 2006, pp. 20-21.

4. Press, F. Seismic Velocities. In Handbook of Physical Constants, Geological Society of America Memoir 97, Geological Society of America, Boulder, CO, 1966, pp. 195-218.

5. Schuster, G.T., and Quintus-Bosz, A. Wavepath Eikonal Traveltime Inversion. Geophysics, Vol. 58, 1993, pp. 1314-1323.

6. Sheehan, J.R., Doll, W.E., and Mandell, W. Comparison of MASW and Refraction Tomography. In Proc., 17th Symposium on the Application of Geophysics to Engineering and Environmental Problems (SAGEEP), Environmental and Engineering Geophysical Society, Colorado Springs, CO, 2004.

7. McMechan, G.A., and Yedlin, M.J. Analysis of Dispersive Waves by Wave Field Transformations. Geophysics, Vol. 46, 1981, pp. 869-874.

8. Palacky, G. Resistivity Characteristics of Geologic Targets. Geological Survey of Canada, Ottawa, Ontario, Canada, 1987.

9. Anderson, N., and Hoover, R. Geophysical Methods Commonly Employed for Geotechnical Site Characterization. Transportation Research Circular E-C130, Transportation Research Board of the National Academies, Washington, D.C., 2008, pp. 21-22.

10. ASTM International. ASTM D5777-18, Standard Guide for Using Seismic Refraction Method for Subsurface Investigation. ASTM International, West Conshohocken, PA, 2018.

11. ASTM International. ASTM D6431-18, Standard Guide for Using the Direct Current Resistivity Method for Subsurface Site Characterization. ASTM International, West Conshohocken, PA, 2018.

12. Grandjean, G., and Leparoux, D. The Potential of Seismic Methods for Detecting Cavities and Buried Objects: Experimentation at a Test Site. Journal of Applied Geophysics, Vol. 56, 2004, pp. 93-105.

13. Martinez-Moreno, F.J., Galindo-Zaldívar, J., Pedrera, A., González-Castillo, L., Ruano, P., Calaforra, J.M., and Guirado, E. Detecting Gypsum Caves with Microgravity and ERT Under Soil Water Content Variations. Engineering Geology, Vol. 193, 2015, pp. 38-48.

14. Baecher, G.B., and Christian, J.T. Reliability and Statistics in Geotechnical Engineering. John Wiley & Sons, Hoboken, NJ, 2013.

15. Tang, C., and Phoon, K.-K. Model Uncertainties in Foundation Design. CRC Press, Boca Raton, FL, 2021, pp. 18-19.

16. Phoon, K.-K., Cao, Z., Ji, J., Leung, Y.F., Najjar, S., Shuku, T., Tang, C., Yin, Z.-Y., Ikumasa, Y., and Ching, J. Geotechnical Uncertainty, Modeling, and Decision Making. Soils and Foundations, Vol. 62, No. 5, 2022.

17. Lofman, M. Determination of Characteristic Values of Geotechnical Parameters. In Proc., 25th European Young Geotechnical Engineers Conference, Sibiu, Romania, 2016.

18. Kulhawy, F.H., and Chen, J. Evaluation of Penetration Tests and Their Correlations in Gravelly Soils. In Proc., 16th International Conference on Soil Mechanics and Geotechnical Engineering, Osaka, Japan, 2005.

19. Daniel, C.R., Howie, J.A., and Sy, A. Method for Correlating Large Penetration Test (LPT) to Standard Penetration Test (SPT) Blow Counts. Canadian Geotechnical Journal, Vol. 40, No. 1, 2003, pp. 66-77.

20. Harder, L.F., Jr. Application of Becker Penetration Test for Evaluating Liquefaction Potential of Gravelly Soils. In Proc., NCEER Workshop Evaluation of Liquefaction Resistance of Soils, Salt Lake City, UT, 1997, pp. 129-148.

21. VandenBerge, D., Brandon, T., Martin, R., and McGuire, M. Unified Facilities Criteria (UFC): Foundations and Earth Structures (UFC 3-220-01). Naval Facilities Engineering Systems Command, U.S. Department of Defense, Washington, D.C., 2025.

23. The Chilkat Connector Feasibility Study in Southeast Alaska

Rachel Hunt
Cornforth Consultants Inc. - Landslide Technology
5725 W Randolph Dr.
Boise, Idaho 83705
720-384-6851
Rachel.Hunt@CCILT.com

Paige Stuhlmuller
Cornforth Consultants Inc. - Landslide Technology
9000 SW Gemini Drive
Beaverton, Oregon 97008
Paige.Stuhlmuller@CCILT.com

Benjamin George
Cornforth Consultants Inc. - Landslide Technology
9000 SW Gemini Drive
Beaverton, Oregon 97008
Ben.George@CCILT.com

Prepared for the 75th Highway Geology Symposium, September, 2026

Acknowledgements

The author(s) would like to thank the individuals for their contributions in the work described:

Mitch McDonald – Alaska Department of Transportation & Public Facilities
Keri Nutter, CPG; Matthew Blakeslee, CPG; and Team – DOWL

Disclaimer

Statements and views presented in this paper are strictly those of the author(s), and do not necessarily reflect positions held by their affiliations, the Highway Geology Symposium (HGS), or others acknowledged above. The mention of trade names for commercial products does not imply the approval or endorsement by HGS.

Copyright Notice

Copyright © 2026 Highway Geology Symposium (HGS)

All Rights Reserved. Printed in the United States of America. No part of this publication may be reproduced or copied in any form or by any means – graphic, electronic, or mechanical, including photocopying, taping, or information storage and retrieval systems – without prior written permission of the HGS. This excludes the original author(s).

ABSTRACT

The Alaska Department of Transportation & Public Facilities (DOT&PF) initiated a new feasibility study focused on the west side of Lynn Canal with the goal of connecting Juneau to the Haines Highway. The proposed corridor, named the Chilkat Connector, is roughly 65 miles long, and represents one of the few remaining opportunities to provide overland access to Alaska's capital city. This feasibility study evaluated the geotechnical and geological aspects related to the long-term viability of developing a combination of new roadway, bridge structures, and associated ferry terminals that would link Juneau with northern communities and the broader highway network.

As part of this effort, a high-level geotechnical reconnaissance of the project corridor was conducted by Landslide Technology (LT) and DOWL to identify major geologic and terrain considerations that may influence corridor feasibility, construction methods, and potential costs. The reconnaissance focused on non-invasive field methods, including geologic mapping, collection of surface samples, broad evaluation of soil and rock conditions, and preliminary assessment of geologic hazards such as landslides, rockfall, glacial deposits, karst terrain, and steep coastal terrain.

After the field reconnaissance, LT created a geohazard inventory with 69 individual landslides, 19 landslide complexes, 34 debris flows, and 47 karst features within the project study area. LT also completed shallow landslide and debris flow susceptibility mapping. The results from the susceptibility mapping highlight that most of the project corridor is susceptible to shallow landslides and debris flows, common for the overstepped terrain observed along most of the corridor. Findings from this feasibility study will be used to narrow potential alignments, identify locations where more detailed surface and subsurface exploration may be needed, and highlight areas of significant engineering concern.

This paper will describe the geohazard findings for the feasibility study. It summarizes the observations and interpretations from the 2025 reconnaissance, identifies key geotechnical considerations related to geohazards along the proposed corridor, and provides baseline information that will inform subsequent engineering evaluations, environmental review, and future project development phases.

INTRODUCTION

The Alaska Department of Transportation and Public Facilities (DOT&PF) conducted a feasibility study to evaluate improving transportation between Haines and Juneau by means of new road/ferry infrastructure along the west side of Lynn Canal. The study assessed potential corridors, engineering and constructability challenges, environmental considerations, and cost implications, with the goal of identifying a viable option for improving access between Juneau and northern destinations. The study area is shown in Figures 1.

A high-level geotechnical reconnaissance of the project corridor was conducted by Landslide Technology (LT) and DOWL in August 2025. The purpose of the investigation was to identify major geologic and terrain considerations that may influence corridor feasibility, construction methods, and potential costs. LT's reconnaissance focused on non-invasive field methods, broad evaluation of soil and rock conditions, and preliminary assessment of geologic hazards such as landslides, rockfall, and karst features. This information was mapped and described to support the identification of a feasible alignment, identify data gaps, and quantify potential mitigation.

This paper summarizes LT's observations and interpretations of geohazards from the 2025 reconnaissance, identifies key considerations for geohazards along the proposed corridor, and provides baseline information that will inform subsequent engineering evaluations, environmental review, and future project development.

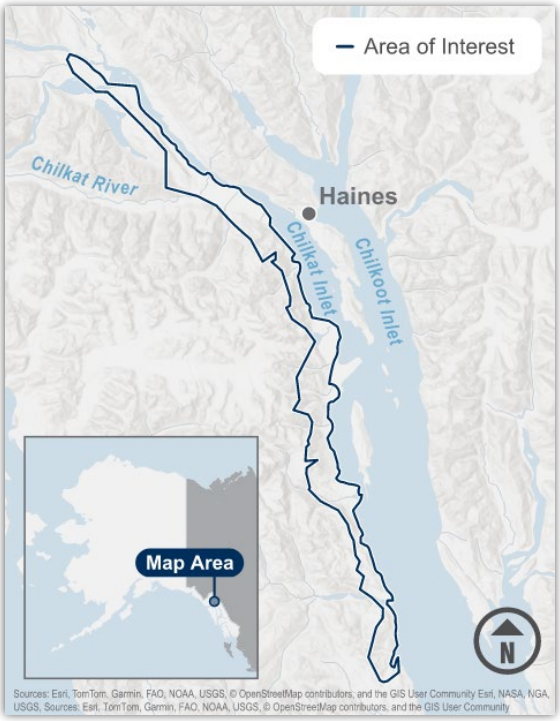

Figure 1 – Chilkat Connector Study Area

PROJECT SETTING

The project area runs along the steep, glacially carved mountainous terrain of West Lynn Canal. The proposed alignment spans roughly 35 miles of West Lynn Canal from William Henry Bay to Glacier Point. This section is characterized by a steep, fjord-influenced coastal margin with benched topography, U-shaped valleys, kettle lakes, and drowned forests associated with glacial activity, erosion, and slope instability. From Glacier Point, the proposed alignment spans roughly 30 miles from the Chilkat Inlet to the delta of the Klehini River. This section is characterized as an inland valley shaped by the fluvial processes of a large, braded river system. Lynn Canal averages about 6 miles wide and reaches depths up to 240 feet. Over 80 drainages of varying size and type exist throughout the project area, including waterfalls, fluvial and alluvial fans, braided rivers, and glacial streams. Several rock units in this region contain carbonate-rich lithologies,

such as marble and limestone, making them susceptible to karst development and complex subsurface drainage systems. Steep slopes with shallow soils are susceptible to landslides and debris flows, while near vertical rock slopes have risk of rockfall and rockslides.

GENERAL GEOLOGY

Geology

Dominant rock types mapped along the proposed alignment include Ordovician to Devonian aged calcareous, metasedimentary, and volcanic rock formations including limestones, dolomitic marble interlayered with greenschist of the Gambier Bay Formation (Dgbm); black phyllite, marble, meta-chert, argillite, and amphibolite of the Four Winds complex (SZfw); and cherty graywacke, argillite, limestone, and locally metamorphosed volcanics, phyllite, marble, greenstone, and hornfels of the Cannery Formation and Porcupine Slate unit (PDcf) ([1]Wilson, 2015). Less frequent rocks mapped along the proposed alignment include Cambrian to Permian intermediate volcanic breccia, agglomerate, flows, conglomerates, turbidites, and greenschist of the Point Augusta Formation (Sv); and actinolite schist, semi-schist, dark-green garnet amphibolite and some marble of the Gambier Bay Formation (Dgb) that exhibit varying degrees of metamorphism and structural folding and faulting. Confined units of plutonic rocks such as Early Permian to Pennsylvanian granodiorite (PPgi) and Oligocene to Eocene granodiorite and quartz diorite (Tod) are mapped in the northern quarter of project study area. A geologic map is shown in Figure 2.

The Lynn Canal region lies within a complex tectonic boundary zone influenced by the continental margin of the Pacific and North American plates. Most of the relative plate motion is accommodated offshore by the right-lateral Queen Charlotte–Fairweather Fault (QCFF) System ([2]USGS, 2025). The Queen Charlotte Fault splays into the Fairweather Fault to the north-northwest and the Chatham Strait Fault (CSF) to the east. There are no known records of other constrained or inferred, active faults that intersect or impact the project corridor along the proposed alignment.

Geohazards

Geohazards were inventoried along the proposed project corridor to assess feasible alignments, identify data gaps, and quantify possible mitigation. Lynn Canal is characterized by steep terrain adjacent to marine waterways, often susceptible to landslides, landslide complexes, debris flows, rockfall, snow avalanches, flooding, avulsion processes, glacial outburst floods, and erosion adjacent, as documented during field reconnaissance.

Calcium carbonate limestones and marbles of the Gambier Bay Formation (Dgbm) ([1]Wilson, 2015) mapped along the project alignment are susceptible to karst formation. Highly acidic drainage from peatlands and other forest vegetation is directed by zones of weakness in bedrock, forming solution cavities and channels along the surface and subsurface. Within areas mapped as marble, evidence of well-defined karst surface features, such as coastal spires, crevasse-like dissolved fissures, sinkholes and caves were documented during field reconnaissance.

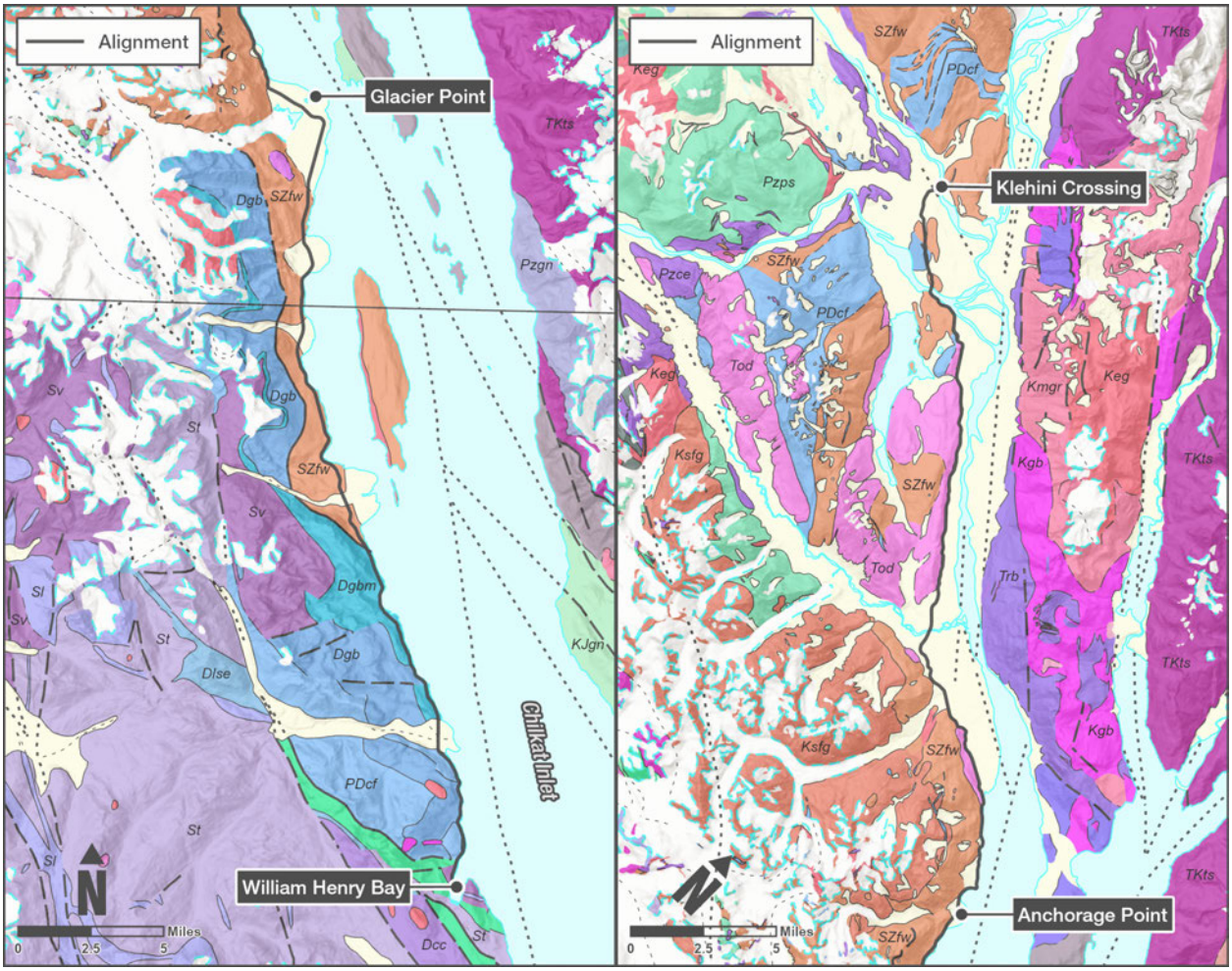

Figure 2 – Geologic Map of West Lynn Canal

GEOLOHAZARD MAPPING

Geomagnetic Data Collection

A limited geophysical survey was conducted to collect magnetic data across mapped marble deposits along the proposed alignment. Data collection focused on acquiring high-resolution magnetic field measurements to support field evaluation of potential karst features. An Unoccupied Aerial System (UAV) equipped with a magnetometer and GPS positioning systems were deployed to collect data across marble deposits. Processed data highlighted low magnetic field strength areas, indicating potential karst features. These low-magnetic zones were targeted during reconnaissance to further evaluate their significance and confirm geologic anomalies.

Geohazard Inventory Mapping

LT created a geohazard inventory geodatabase for about 60 miles of proposed alignment from William Henry Bay to Covenant Life. The inventory includes landslides, landslide complexes,

debris flows, rockfall at proposed rock cuts, and karst. Hazards associated with snow avalanches, alluvial channels, avulsion processes, erosion, and marine environments were evaluated by others. Imagery used for mapping included publicly available aerial imagery, 2012 USGS Interferometric Synthetic Aperture Radar (IFSAR[1]) data with 5-meter resolution, 2018 Alaska Division of Geological & Geophysical Surveys (DGGS) LiDAR with 1-meter resolution, and August 2025 project-specific LiDAR collected by NV5 with 0.5-meter resolution. The landslide and debris flow inventory database was modeled after Oregon Department of Geology and Mineral Industries' (DOGAMI) Special Paper 42 ([3]Burns and Madin, 2009). Landslides, debris flows, rock slopes, and karst mapping were supplemented by field observations from helicopter reconnaissance and ground confirmation of select geohazard features. Geohazard inventory maps are presented in Figure 3.

Geohazards inventoried during this study that required mitigation to protect the proposed alignment received a qualitative assessment of impact severity if left unmitigated. The impact ratings were categorized as no impact, low, moderate, or high severity of impact based on our review of the geohazard inventory, proximity to the alignment, and our professional judgment. Rough order of magnitude costs were assigned to possible mitigation methods for features with moderate or high severity of impact to understand feasibility of the proposed alignment. A summary of mapped geohazards and impact to the proposed alignment is presented in Table 1.

Table 1 – Summary of Geohazard Inventory

Geohazard	Description	Total Inventoried	No. of Geohazards with Moderate to High Impact Severity to Alignment
Landslides and Landslide Complexes	Landslides and landslide complexes were mapped using distinguishing features observed in topography such as hummocks, scarps, and grabens. Field observations of landslide terrain included tilted or pistol-butted trees, sag ponds, debris chutes, ground cracks, and scarps. Minor changes in slide conditions due to natural processes (i.e. heavy precipitation), seismic activity, or earthwork activities such as cuts, fills, or changes to groundwater and surface runoff patterns may activate marginally stable landslides.	88	37
Debris Flows	Debris flows were mapped using distinguishing features such as oversized boulders, scour, scars, exposed soil in source areas or along drainage channels, debris accumulations/ tree throw within and at the base of drainage channels, raised ridges of sediment along channels, and lobes of poorly sorted soil near base of drainages.	34	11
Rockfall	Rockfall hazards considered include only proposed constructed rock cuts. Areas of potential rockfall hazard were identified based on locations where the alignment and grade design required excavation and where bedrock outcrops are adjacent / upslope of the alignment.	81	71
Karst	Areas of potential karst topography were initially mapped using published geologic maps and geophysical surveys. Areas of calcareous rock were delineated using an overlay of the 2018 DGGS GIS data on a shaded relief basemap	47	7

[1]While both IfSAR and InSAR stand for Interferometric Synthetic Aperture Radar, they are different. IfSAR is topographic data (DEM) derived from satellite radar. InSAR uses change detection from satellite radar. IfSAR was used for Alaska imagery because there was a large area to cover and LiDAR was not considered cost effective at the time of data collection Additionally, IfSAR penetrates cloud cover to provide imagery for ground surfaces.

Table 1 – Summary of Geohazard Inventory			
Geohazard	Description	Total Inventoried	No. of Geohazards with Moderate to High Impact Severity to Alignment
	derived from LiDAR. Subsequent field reconnaissance efforts verified the presence of mapped karst terrain such as coastal spires, crevasse-like dissolved fissures, sinkholes, and caves. Specific landforms were then identified through higher-resolution, project-specific LiDAR datasets.		
Jökulhlaups	Glacial outburst floods, commonly referred to as jökulhlaups, are the rapid and sometimes catastrophic releases of water stored beneath glacial ice or behind ice or moraine-dammed glacial lakes that can risk pose to downstream communities and infrastructure. Jökulhlaups were identified at two stream crossings (Glacier Point and Anchorage Point); however, the overland flood paths, sediment transport potential, and foundation disturbance risk were not analyzed at this level of study	2	NA

Susceptibility Mapping

The susceptibility maps developed for this study are intended to provide a screening level tool for informing future work on the corridor, if pursued. These maps serve as a regional snapshot of conditions as understood with available data at the time of this study. The susceptibility maps highlight areas that may be more susceptible to slope movements and channelized debris flows, providing a basis for feasibility-level planning. The maps help to identify areas where more detailed landslide and debris flow mapping is warranted for design; the maps do not predict landslide or debris flow probability or frequency.

Limitations of input data and modeling methods restrict the use of the maps. They are not suitable for answering site-specific questions regarding alignment development, land-use regulation, or building-code development. Susceptibility results presented here are a preliminary product based on available published data (i.e., bedrock geology and geohazard inventory mapping) and do not reflect finalized products.

Shallow Landslide Susceptibility Mapping

LT conducted shallow landslide susceptibility mapping throughout the project corridor, shown in Figure 4. This was conducted in general accordance with DOGAMI's Special Paper 45 ([4]Burns, 2012). LT used project specific LiDAR data from NV5 with a 0.5 meters resolution for landslide mapping and resampled the data to 1.8-m DEM for susceptibility modeling. The coarser DEM better represents slope gradients at the study scale and avoids overestimating slope inclination. Mapping procedures combined two GIS datasets: 1) landslide inventory mapping, as described above and 2) factor of safety (FS) class maps.

FS maps were developed by considering geologic material properties, slope angle, an assumed 15-foot failure depth, and saturated groundwater conditions. Due to the preliminary nature of this

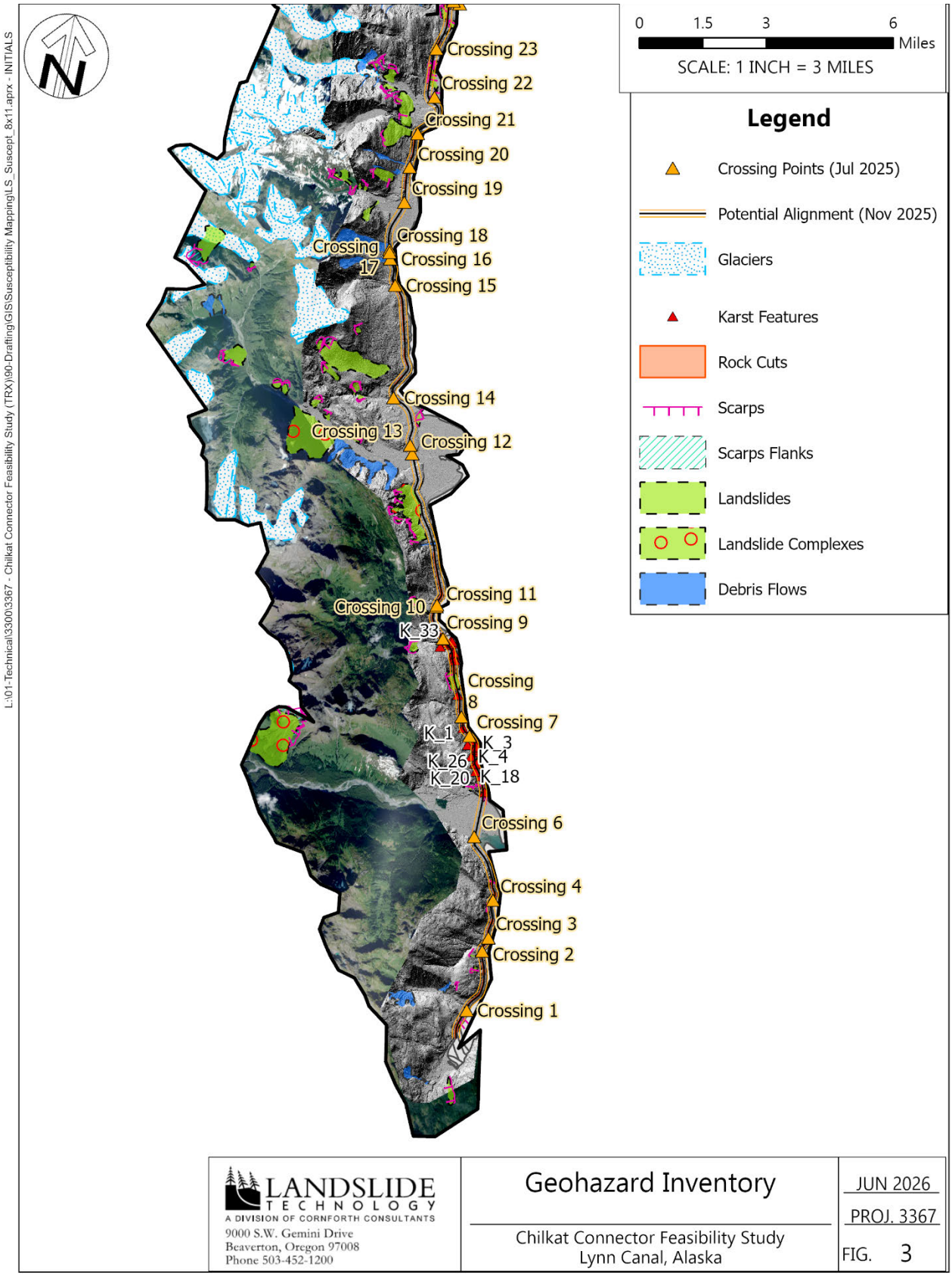

Figure 3 – Geohazard Inventory

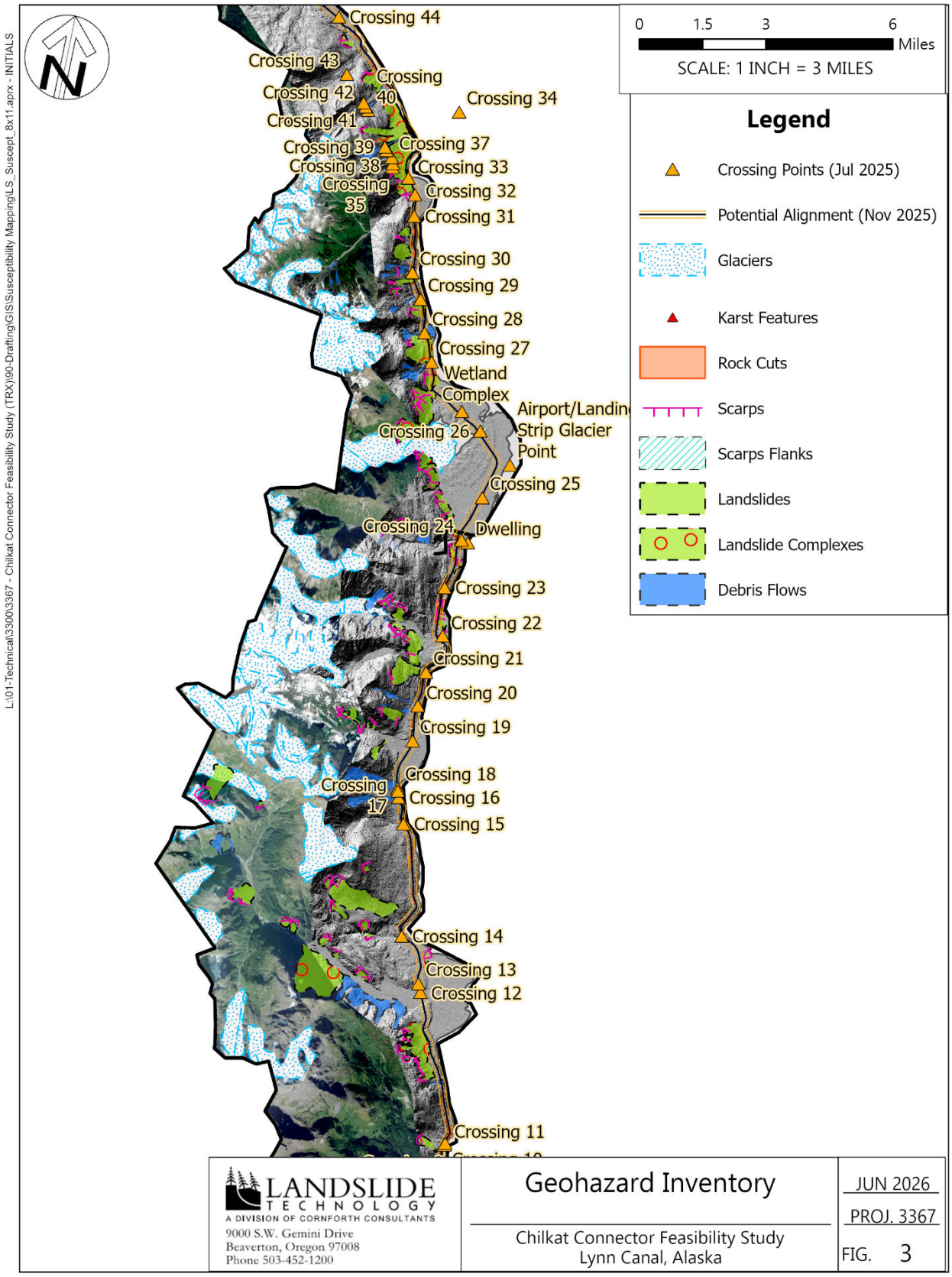

Figure 3 (continued) – Geohazard Inventory

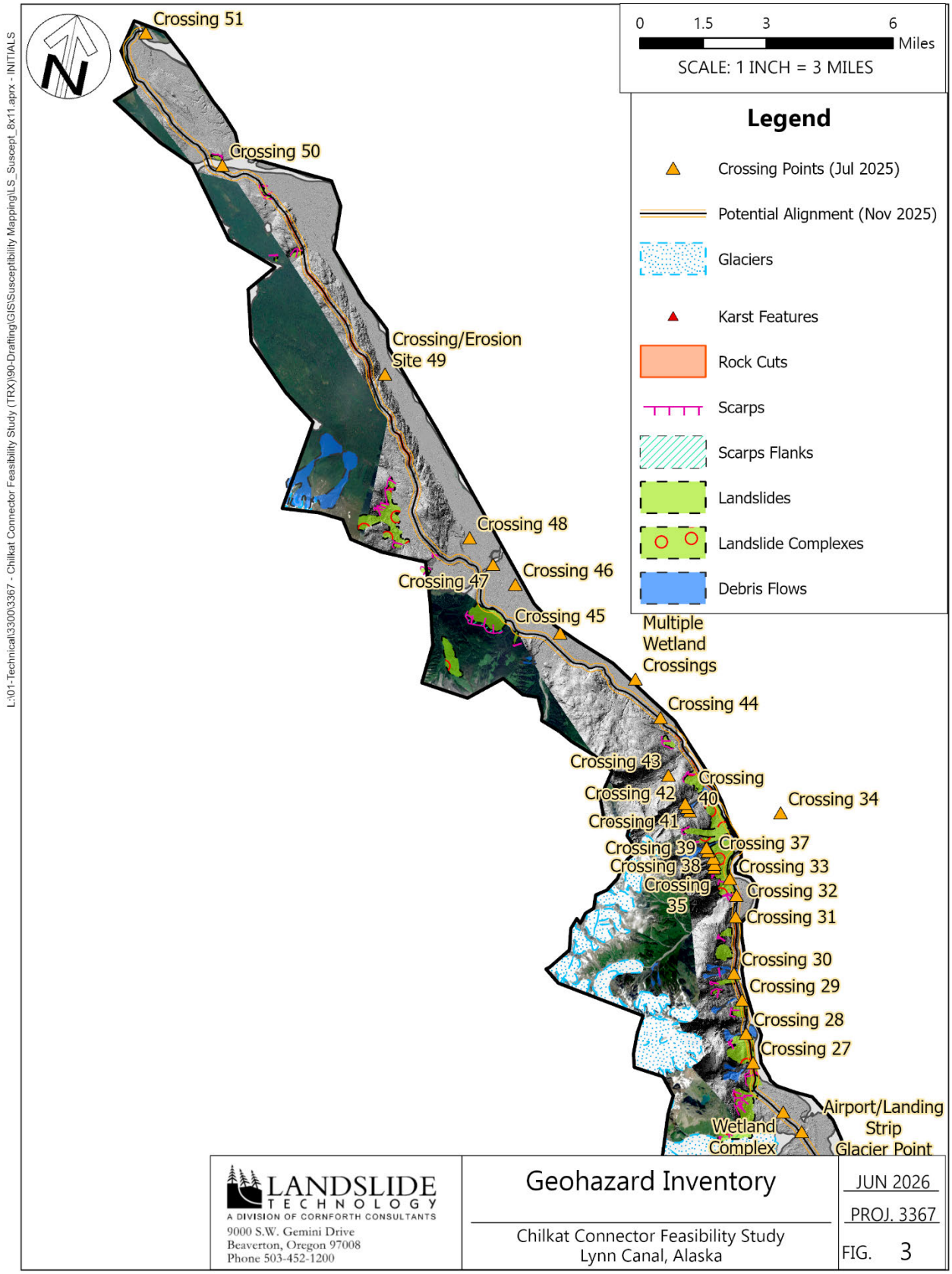

Figure 3 (continued) – Geohazard Inventory

study, surficial material mapping to refine strength, geometry, and groundwater assumptions was not conducted during reconnaissance. Therefore, required material properties, were based on available bedrock mapping within the project area ([1]Wilson, 2015). Material properties are based on professional judgement and are in general accordance with published literature ([5]Goodman, 1989; [6]West, 1995). Cohesion was not considered for material strength parameters as a conservative approach based on professional judgment, lack of published values for rock materials, and lack of site-specific surficial mapping.

Figure 4 indicates high susceptibility for shallow landslides cross much of the corridor, particularly on steep slopes (>15°), within incised drainage channels, and where the Four Winds complex (SFfw) is mapped. In general, steeper slopes and those comprised of lower strength materials are more susceptible to shallow landslides.

The southern end of the proposed alignment between Crossing 1 and 6 is shown to have slopes with relatively high shallow landslide susceptibility. During limited field reconnaissance conducted in this area and observations from imagery, there was little evidence that slope movements have occurred, and thus the high susceptibly presented in these maps may be misleading. This area warrants further investigation to understand surficial conditions.

Areas dominated by marble bedrock (Dgb and Dgbm) between Crossing 6 and 12 and igneous plutonic materials (Tod) from Crossing 44 to 49 contain near vertical bedrock cliffs and benches observed during field reconnaissance. The model likely overestimates shallow landslide susceptibility in these areas because steep bedrock slopes produce high slope values in the DEM despite having relatively low shallow landslide potential.

Debris Flow Susceptibility Mapping

LT conducted Debris Flow Susceptibility mapping throughout the project corridor. Debris flow susceptibility maps are shown in Figure 5. This mapping was conducted using Grfin Tools ([7]Reid et al., 2025; [8]Burns et al., 2022), a DEM based software package that applies empirical mobility relationships to delineate areas potentially affected by landslides, debris flows, or other related mass movements. It analyzes channel topography downslope of a debris flow initiation point to identify possible initiation locations, inundation extents, and estimates an approximate volume of debris entrainment along the channel if triggering conditions are met. Analyses on the project corridor were conducted using a 2025 LiDAR survey-based DEM and a user-defined parameter file. Where possible, parameters were selected based on previous modeling performed by DOGAMI ([8]Burns et al., 2022) and DGGS ([9]Nicolazzo and Larsen, 2024).

In general, the debris flow susceptibility maps show that most drainages within the project corridor are susceptible to debris flows, and that areas with multiple intersecting drainages are generally capable of producing larger runout zones than those with single-channel drainages.

Similar to the shallow landslide susceptibility results, higher concentrations of modeled debris flow events tend to correlate with areas where the Four Winds complex (SFfw) is mapped, on over steepened slopes (>15°), and within over steeped drainage channels (>15°), which matches field reconnaissance observations.

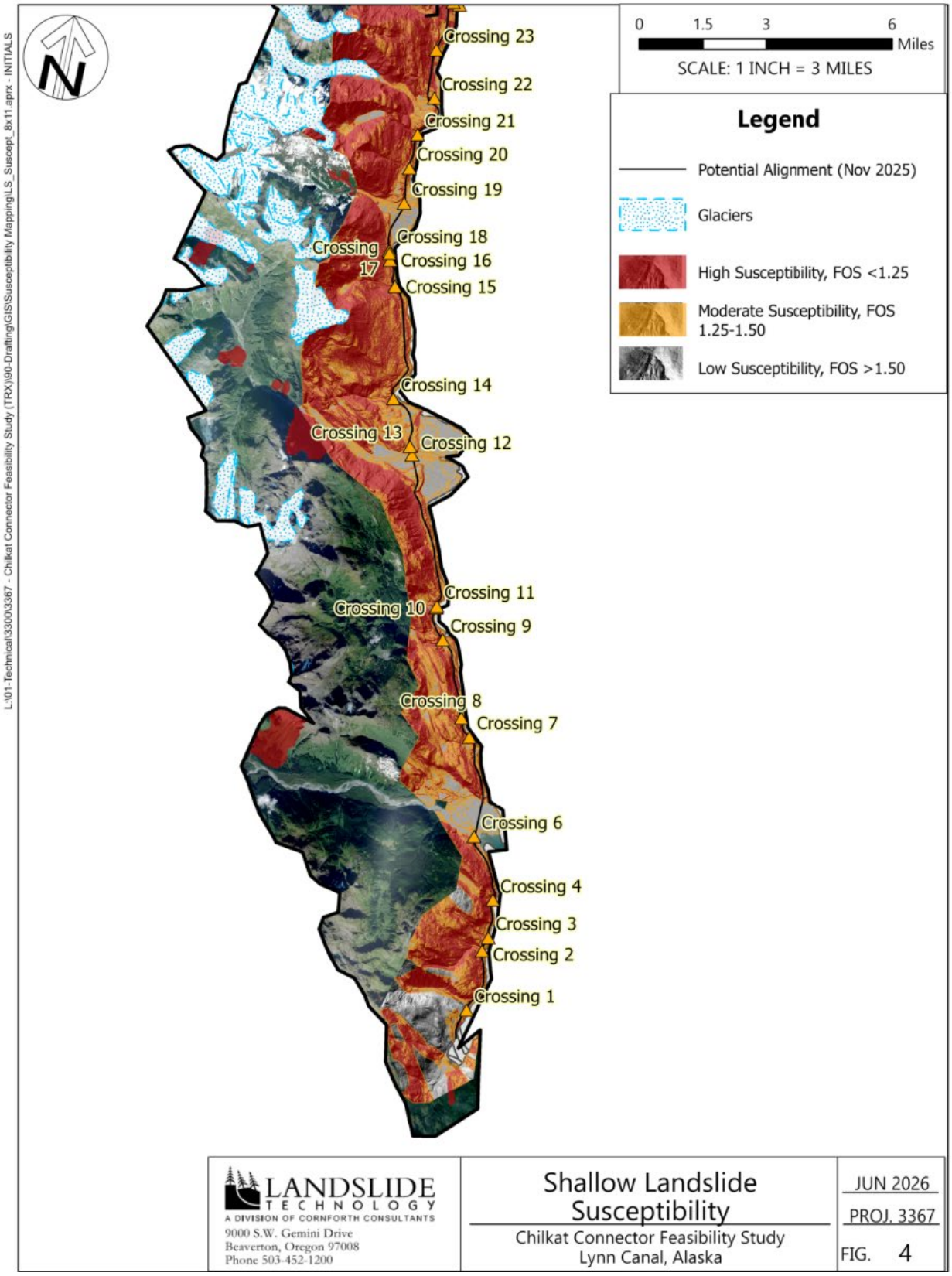

Figure 4– Shallow Landslide Susceptibility

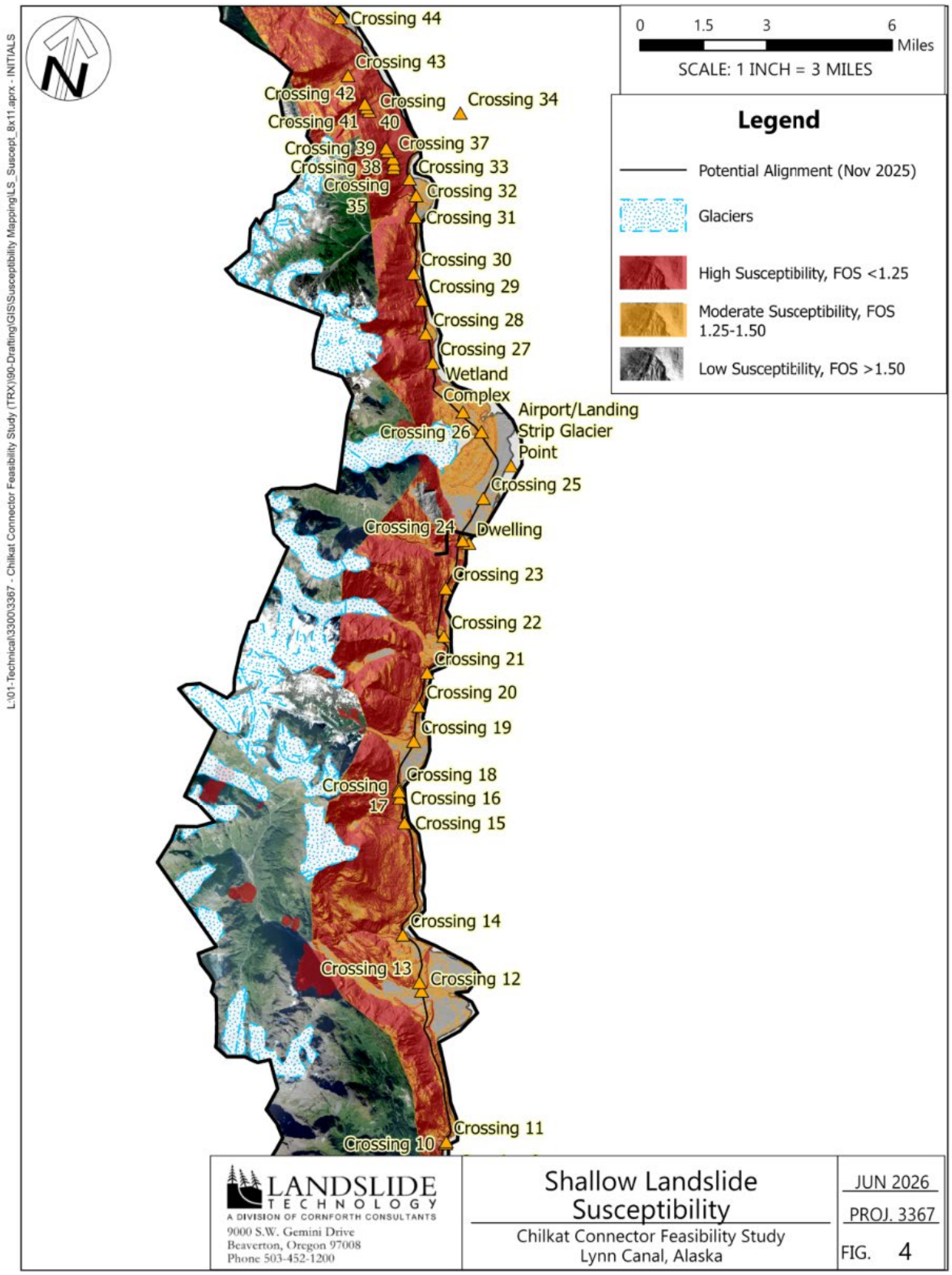

Figure 4 (continued) – Shallow Landslide Susceptibility

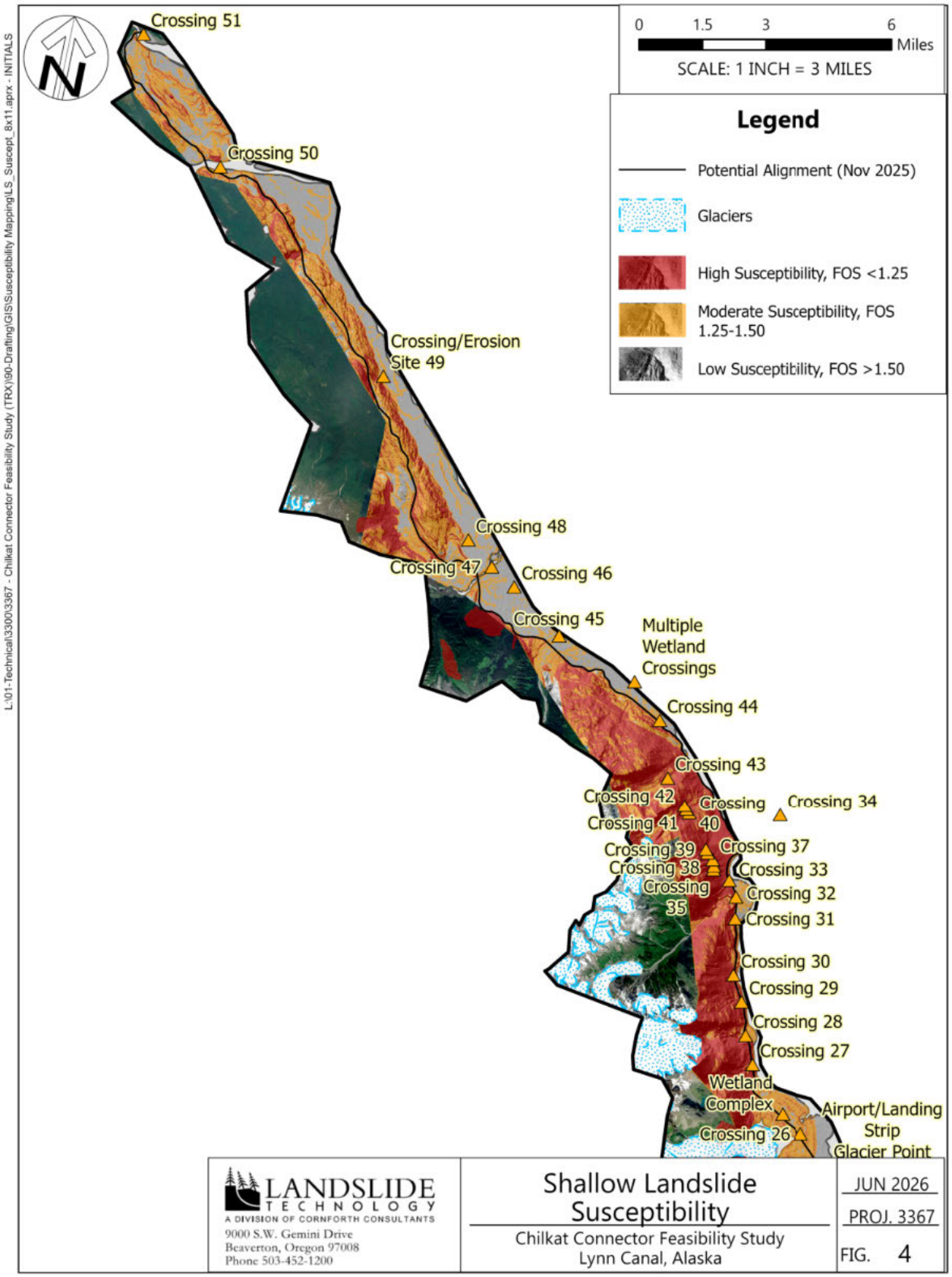

Figure 4 (continued) – Shallow Landslide Susceptibility

Although the susceptibility models show that most drainages are susceptible to debris flow mass movements, deposits of debris flow materials were not commonly observed within drainages outside of the areas mapped as the Four Winds complex (SFfw) during our field reconnaissance, This is interpreted to reflect that, although possible, high-volume and/or high-frequency debris flow events are not typical at these locations. Consequently, observable debris flow deposits were limited during our limited field reconnaissance.

Areas dominated by marble bedrock (Dgb and Dgbm) between Crossing 6 and 12 and igneous plutonic materials (Tod) from Crossing 44 to 49 were observed to have hear vertical bedrock cliffs and bedrock benches throughout these sections during the field reconnaissance. Typical and moderate to extreme debris flow susceptibility shown in these areas is interpreted to be due to steep elevation change in high-resolution slope raster for these drainages. The exposed bedrock slopes and drainages are likely to have lower debris flow hazards than represented in these maps, highlighting a limitation in the Grifn tools methodology where geologic materials and surficial conditions are not included within the model.

GEOTECHNICAL CONSIDERATIONS FOR GEOHAZARDS

Selection of mitigation should account for project design goals, project limitations (i.e., ROW, environmental, permitting), and cost-benefit analyses. When identifying geohazard mitigation measures, consequences of the hazards and cost of maintenance and/or temporary loss of an asset are weighed against cost of constructing mitigation measures. Multiple approaches are incorporated into a preferred combination of elements that balance project requirements.

For all geohazards, one risk reduction approach considered for the proposed alignment is avoidance, which includes realigning the roadway or adjusting the proposed alignment away from/over/around the geohazard. Other risk reduction considerations are summarized in Table 2.

Table 2 – Risk Reduction Considerations

Hazard	Mitigation Alternative
Landslides and Debris Flow	(1) Maintenance techniques for landslide/debris flow management typically result in minimal to no improvement in stability and are conducted on an as-needed basis to reduce hazardous conditions. (2) Partial stabilization may improve portions of landslides or reduce rate/frequency of slide movement. (3) Full stabilization includes mitigation designed fully stabilize the landslide or debris flow. Partial and full stabilization mitigation can include earthwork (e.g., berms, buttresses), structural (e.g., MSE walls), or drainage type (e.g., dewatering). (4) Protection entails containment areas/structures or diversion berms/structures.
Rockfall	(1) Stabilization measures can be used to prevent rockfall (i.e. removal via scaling/excavation or rock bolt/dowel reinforcement). (2) Protection measures are used to limit rockfall energy and restrict falling rocks from reaching the roadway (i.e., enlarged ditches, barriers, draped meshes, attenuators).
Karst	(1) Drainage control can improve and reduce infiltration, reducing risk of solution features from forming or worsening. (2) Excavation and engineered backfill/grouting replacement in voids can reduce the risk of sink hole formation. It is likely that solution processes will continue throughout the life of the roadway likely requiring on-going maintenance and/or subsequent mitigation measures.

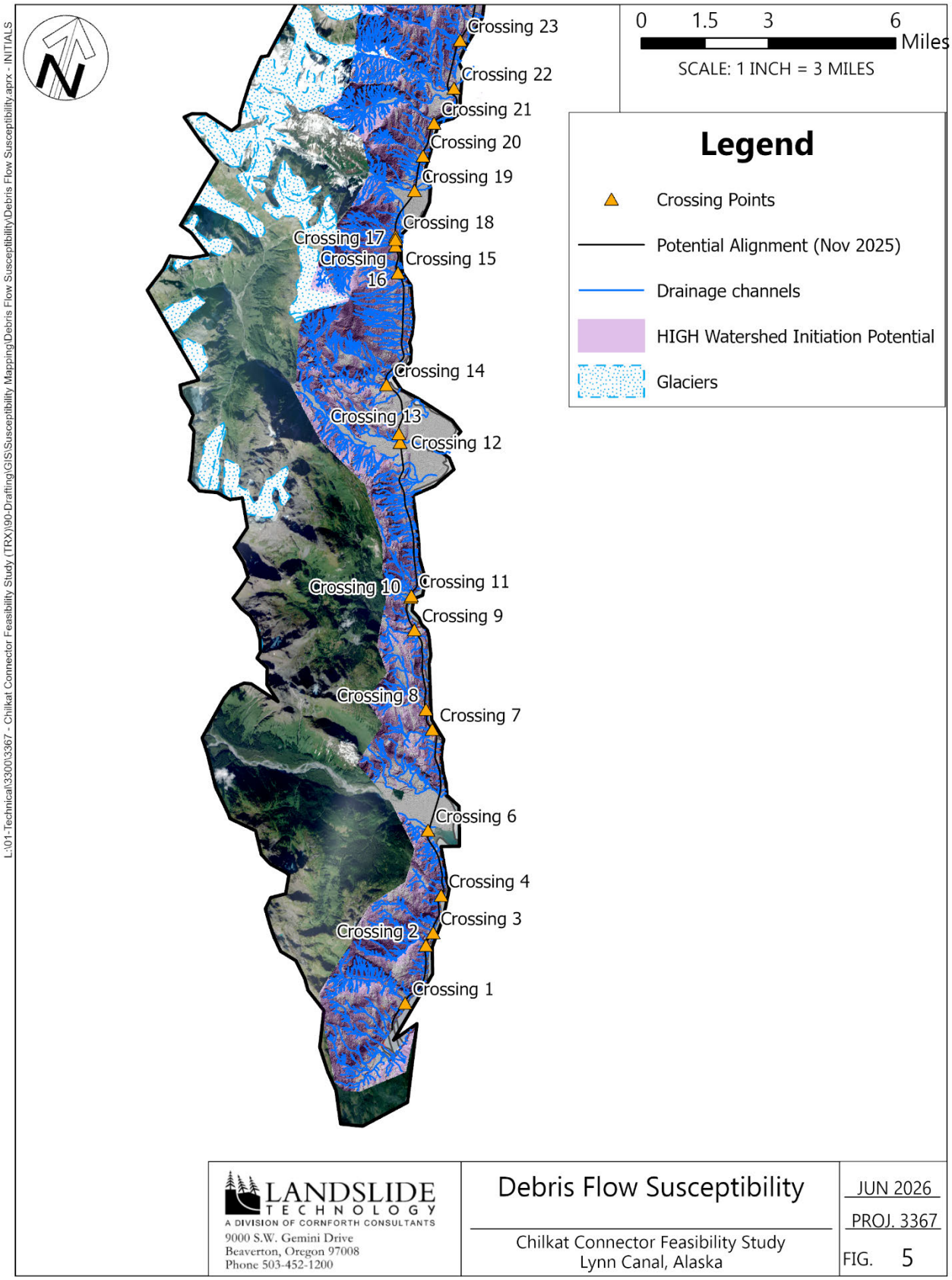

Figure 5 – Debris Flow Susceptibility

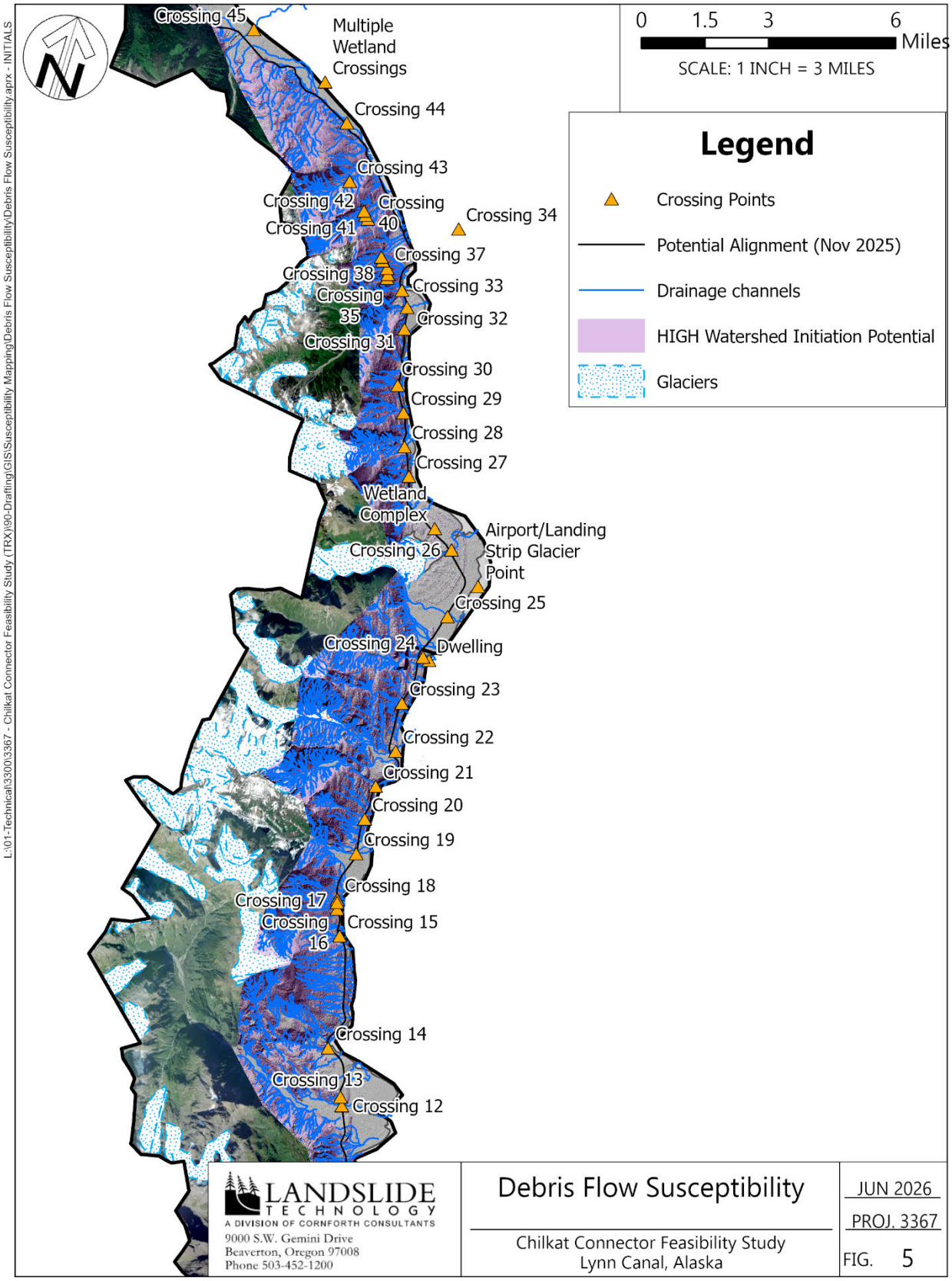

Figure 5 (continued) – Debris Flow Susceptibility

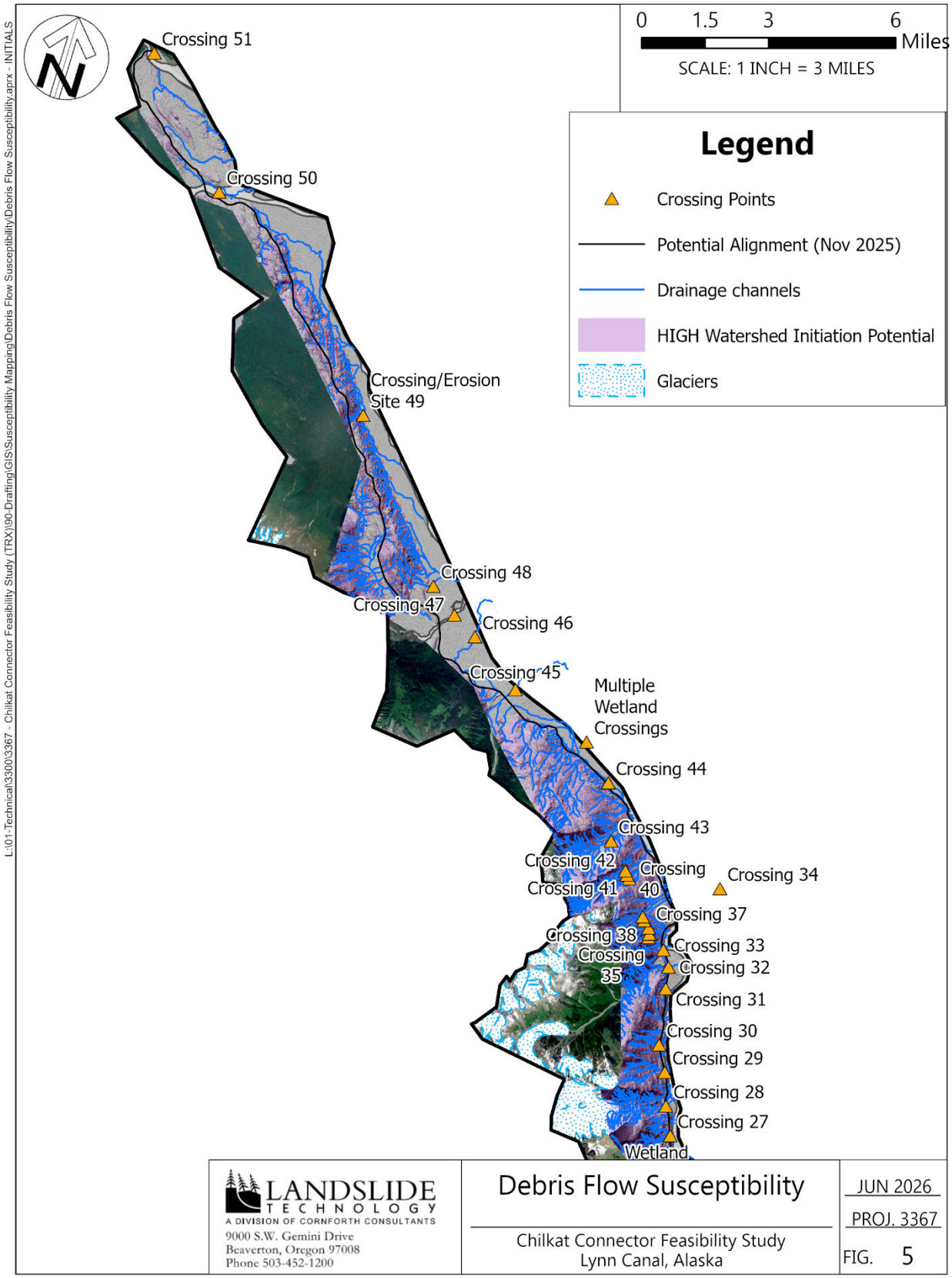

Figure 5 (continued) – Debris Flow Susceptibility

LIMITATIONS

Two DEMs collected in 2018 were available for the project site for field reconnaissance. These data had misrepresentative terrain throughout the project corridor and had limited extents compared to the study area. The timeline for collecting and processing project specific LiDAR did not facilitate use of updated DEMs for field reconnaissance. Due to the expedited project schedule, there was limited imagery data and time available to conduct a thorough desktop study to identify geohazards for field verification and execute detailed field reconnaissance. Therefore, reconnaissance was focused on geohazards that had low confidence from the desktop study. Detailed site characterization of each geohazard, mapping and characterization of surficial materials, and erosion were not completed for the scope of this feasibility study.

FUTURE STUDIES

There are several areas where future studies could be completed to optimize alignment location, understand subsurface conditions for detailed geotechnical recommendations, and improve cost estimates for feasibility. Additional studies include detailed surficial and geohazard mapping, instrumentation and monitoring to refine understanding of slope stability, bedrock geometry, structural features, and material variability along the alignment, and subsurface exploration to understand subsurface conditions for bridge foundations and road section recommendations.

REFERENCES:

1. Wilson, F. *Geologic Map of Alaska*, U.S. Geological Survey. Scientific Investigations Map 3340, pp. 197, 2 sheets, 2015. Scale 1:1,584,000.
2. U.S. Geological Survey. *M 3.0 - 5 km WSW of Haines, Alaska: Region Info*, U.S. Geological Survey Earthquake Event Page, accessed July 23, 2025, https://earthquake.usgs.gov/earthquakes/eventpage/ak0251ab5vi0/region-info.
3. Burns, W. and Madin, I. *Protocol for Inventory Mapping of Landslide Deposits from LiDAR Imagery*, Oregon Department of Geology and Mineral Industries, Special Paper 42. 2009.
4. Burns, W., Madin, I., and Mickelsen, K. *Protocol for Shallow-Landslide Susceptibility Mapping.* Oregon Department of Geology and Mineral Industries, Special Paper 45. 2012.
5. Goodman, R. *Introduction to Rock Mechanics*. 2nd Edition, John Wiley & Sons Ltd., New York. 1989.
6. West, T. *Geology Applied to Engineering,* 1st Edition, Prentice-Hall, Upper Saddle River, 560. 1995.
7. Reid, M., Brien, D., Cronkite-Radcliff, C., and Perkins, J. *Grfin Tools – User guide and methods for modeling landslide runout and debris-flow growth and inundation*; U.S. Geological Survey Techniques and Methods, book 14, chap. A3, 2025. pp. 105.
8. Burns, W., Franczyk, J., and Calhoun, N. *Protocol for channelized debris flow susceptibility mapping.* Oregon Department of Geology and Mineral Industries. Special Paper 53. 2022.
9. Nicolazzo, J., and Larsen, M. *Landslide hazard susceptibility mapping in Haines, Alaska.* Alaska Division of Geological & Geophysical Surveys Report of Investigation 2024-8, 16 p., 3 sheets. 2025. scale 1:25,000.

24. Improving Williamsport Road – Overcoming Geological and Geographical Challenges in Remote Alaska

Kyle Brennan, PE
Shannon & Wilson, Inc.
5430 Fairbanks Street, Suite 3
Anchorage, Alaska 99518
(907)561-2120
kyle.brennan@shanwil.com

Katarah Glashan
Shannon & Wilson, Inc.
5430 Fairbanks Street, Suite 3
Anchorage, Alaska 99518
(907)561-2120
katarah.glashan@shanwil.com

Prepared for the 75th Highway Geology Symposium, September 2026

Disclaimer

Statements and views presented in this paper are strictly those of the author(s), and do not necessarily reflect positions held by their affiliations, the Highway Geology Symposium (HGS), or others acknowledged above. The mention of trade names for commercial products does not imply the approval or endorsement by HGS.

Copyright

Copyright © 2026 Highway Geology Symposium (HGS)

All Rights Reserved. Printed in the United States of America. No part of this publication may be reproduced or copied in any form or by any means – graphic, electronic, or mechanical, including photocopying, taping, or information storage and retrieval systems – without prior written permission of the HGS. This excludes the original author(s).

ABSTRACT

Williamsport Road, constructed in the late 1930s, traverses wild and undeveloped terrain between Iliamna Bay in Cook Inlet and Pile Bay on Lake Iliamna. The road follows a historic Native Alaskan portage route approximately 14 miles long and is owned and operated by the Alaska Department of Transportation & Public Facilities (DOT&PF). It serves as a vital route for hauling supplies and fuel to Lake Iliamna communities and is also used to haul fishing vessels of the Bristol Bay Fishery. The southern end of the road rises from extensive mud flats on Iliamna Bay and traverses up three miles over steep mountainous terrain. The mud flats present access and boat staging challenges and the road is a treacherous, single lane roadway that experiences significant rockfall, erosion, and slope instabilities that often limit road serviceability for weeks at a time. To improve resiliency of the transportation corridor, the DOT&PF is improving the roadway and adjacent facilities. This paper includes an overview of the project and a description of the challenging geologic, seismic, and geographical conditions in which it exists. It includes a review of our data collection approaches including aerial imagery evaluation, drone-based photogrammetry and processing, hand-collected measurements, and remote-operations challenges encountered. The paper incudes a description of our engineering analyses, additional data needs, and how the collected data will support design of road improvements in an extremely challenging environment, focusing on overcoming rock and soil slope instability and development over tidal mud flats.

INTRODUCTION

Williamsport Road is a 14-mile road traversing the Chigmit Mountains, and provides an overland route connecting Iliamna Bay in Lower Cook Inlet to Pile Bay on Iliamna Lake. The road is used to haul equipment, fuel, goods, and other resources from ocean-going vessels to rural communities on Lake Iliamna. In addition, the road is used to portage over 120 boats every summer to access salmon fisheries in Bristol Bay (via Lake Iliamna and the Kvichak River) from Cook Inlet.

Since its construction was completed nearly 100 years ago, the roadway has required frequent maintenance and has experienced long closures related to geologic events such as rockfall, flooding, slope failure, erosion, etc. The reliability of the transportation corridor is of high importance to the viability of the communities it serves and the surrounding region. The State of Alaska Department of Transportation & Public Facilities (DOT&PF) is undertaking efforts to improve this transportation asset for increased safety and resilience of the roadway.

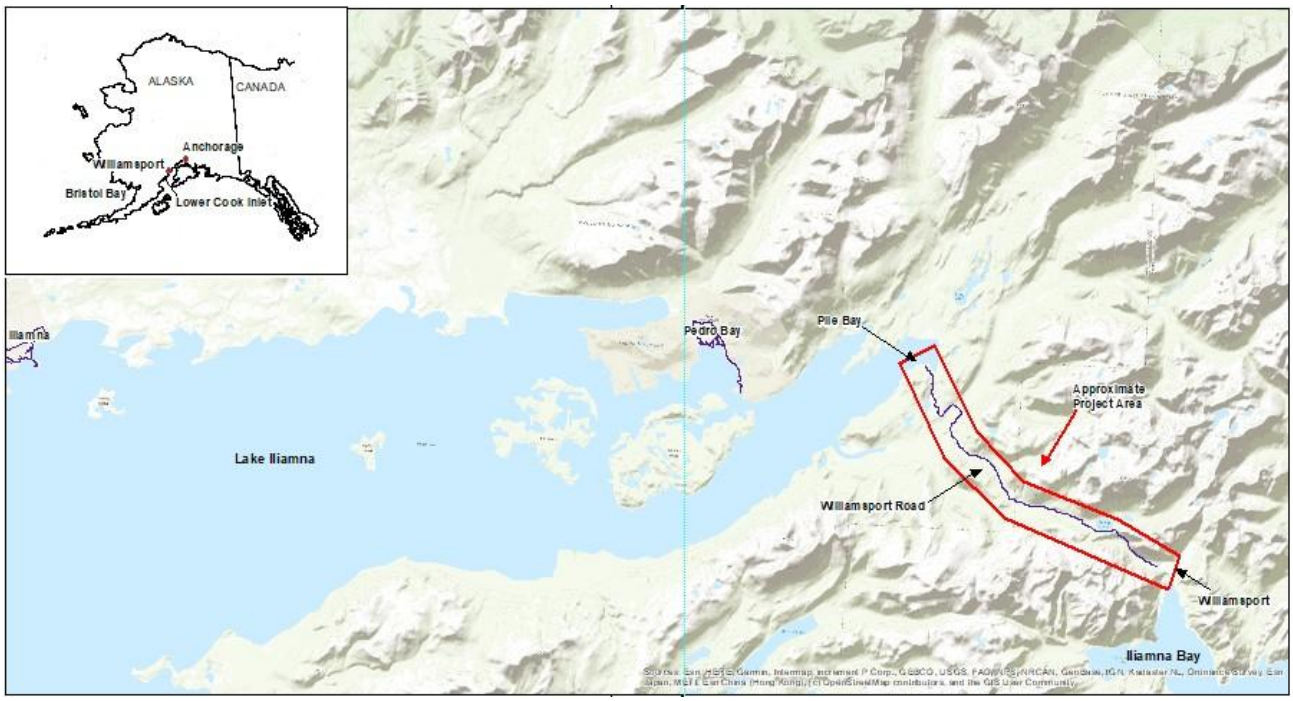

Figure 1. Site and vicinity map showing project area (annotated ESRI basemap).

Existing Facilities

The existing road is a single lane with minimal to no shoulders and several passing pull-outs. The roadway follows the natural ground surface with minimal embankments and cut sections with the exception of the eastern 3 miles that traverse mountainous terrain. The average gradient in profile is relatively moderate with isolated areas of steep grades and sharp, winding curves. Several locations along the road have been developed as borrow sources representing a mix of alluvial soil materials and bedrock. The roadway crosses several stream and drainage features, most notably Iliamna Creek and Chinkleyes Creek on major structures. The bridge over Iliamna

Creek is a pile supported steel structure that was constructed in the mid 2010s to replace the original bridge. The bridge over Chinkleyes Creek is a retrofitted Bailey Bridge that has been in place since at least the mid 1950s. Several other smaller stream crossings exist on single span timber and steel cribbing structures that are typically less than approximately 30 to 40 feet wide.

The upland facilities at both ends of the roadway consist of staging pads for equipment, trucks, and trailers that are used to haul materials over the road and load/unload barges in Lake Iliamna and Iliamna Bay. The Lake Iliamna side in Pile Bay has a barge landing and a fuel and camp facility that is used by one of the contractors that hauls materials over the roadway and maintains the road. A similar barge landing is present on the Iliamna Bay side of the road, however the tidal flats at this location are flat and expansive, making the barge landing only accessible at very high tides. A small basin has been excavated adjacent to the barge landing to allow smaller boats to stage without going dry throughout the tide cycle.

Area History

The approximate alignment of Williamsport Road was an established portage used by indigenous peoples of the area and was subsequently used by fur traders after the turn of the 18th Century with the arrival of the Russian-American Company in Cook Inlet. At the turn of the 20th Century, there was an effort to build a short line railroad from Cook Inlet to Nome that would have included the current Williamsport Road alignment, but only minor grading and survey work was performed. In 1917, the Alaska Road Commission (ARC) began construction and after several iterations of attempts to build and then re-build sections piecemeal, construction of what is essentially the existing road was completed in 1938. Final construction efforts were funded by the ARC and largely performed by Carl Williams, who purchased approximately 25 acres of land on the Williamsport end of the road. After construction was completed, the ARC and later the DOT&PF, overtook maintenance of the road and Carl Williams and his family operated hauling operations over the road. To this day, descendants of Williams still operate a hauling operation on the road and perform road maintenance activities under contract to the DOT&PF.

Geographic Setting

The western terminus of Williamsport Road on the far east end of Lake Iliamna in Pile Bay is accessible via an approximately 2-hour boat ride or 30-minute helicopter ride from the town of Iliamna and the nearest paved runway. The eastern terminus in Iliamna Bay is accessible via barge or fishing boat from Cook Inlet, roughly 80 miles over water from Homer, Alaska. The only fixed wing landing strip along the road is a derelict and unmaintained runway approximately 4 miles from the east end of the road that is not usable in its current condition. Digital communications from the entire alignment is only achievable through satellite phones or Starlink as there is no cell phone service in the area.

Williamsport Road experiences a subarctic climate characterized by long, cold winters and short, cool summers. The climate is transitional between continental and maritime regimes. The North Pacific Ocean and the large surface area of Iliamna Lake create moderate seasonal temperature extremes relative to interior Alaska. Mean temperatures are typically below 32°F from November through April, and mean temperatures from May to October range from 38 and 58 °F.

Annual precipitation is moderate with the largest amount recorded during late summer and autumn. Winter precipitation falls primarily as snow, resulting in persistent seasonal snow cover and lake ice that commonly extends from late November into April.

GEOLOGIC CONDITIONS

The geologic conditions within the project area can be described in general terms through relatively sparse existing information. The mountainous areas are dominated by shallow bedrock with thicker soil deposits accumulating at lower elevations along the toes of the mountain slopes and in riverbeds. Thicker soils exist in the expansive mud flats and estuaries within Iliamna Bay on the east end of the road.

Geology

Based on existing geologic mapping and our on-site observations, the bedrock geology in the area is dominated by intrusive igneous rocks, consisting mostly of blocky and massive granitic and dioritic rocks. The roadway traverses areas mapped to be within the Jurassic Phase of the Alaska-Aleutian Range Batholith (Mapped as Jgr in the geologic map below). The larger Alaska-Aleutian Range batholith ranges from granite and granodiorite to quartz diorite and tonalite and includes some quartz monzonite. The Jurassic phase, in general, is exposed on the east side of the batholith. The most extensive area of exposure is in the Aleutian Range on the west side of Cook Inlet, where the plutons lie to the southeast of the Castle Mountain and Lake Clark Fault Systems and are bounded on the east by the Bruin Bay Fault.

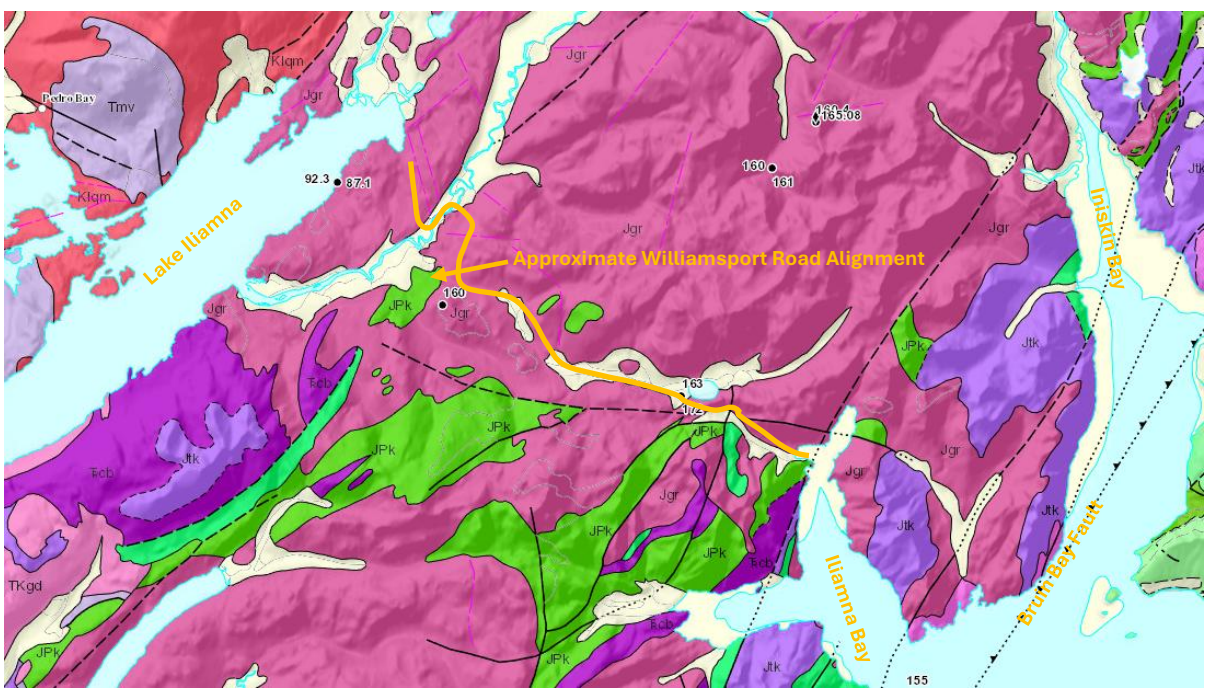

Figure 2. Geologic Map of Project Vicinity
https://alaska.usgs.gov/science/geology/state_map/interactive_map/AKgeologic_map.html

Soil deposits within the project corridor consist of a wide range of soil types and depositional mechanisms. Upland areas typically include a surface layer of organic soils that are largely less than several feet thick with the thickest organic soils associated with low-elevation, poorly drained areas. Well graded, clean sands and gravels are present in alluvial deposits associated with Iliamna River, Chinkleyes Creek, and Williams Creek. Poorly graded coarse-grained deposits are present in many locations along the road at the base of steep mountain slopes and in runout zones associated with channelized rockfall and debris flows. The soils exposed on the tidal flats in Iliamna Bay are fine sand and silt of glacial origin. Glacial drift deposits exist along the alignment in upland and offshore areas, however they are typically isolated and buried by the more recent alluvial, colluvial, and marine/tidal deposits.

Tectonics and Seismicity

The regional seismic conditions in the project area are dominated by the Aleutian Megathrust (forming the Aleutian Subduction Zone) which is responsible for generating large earthquakes throughout southcentral and southwestern Alaska. The subduction of the Pacific Plate under the North American Plate in this area is capable of producing earthquakes of Magnitude (M) 9.0 and greater, resulting in widely felt consequences such as long period ground motions, upland and submarine slope failures, liquefaction, tsunamis, etc. The site is also adjacent to the Bruin Bay Fault trending through Iniskin Bay. The Bruin Bay Fault is a high angle thrust fault, and includes associated minor crustal fault traces to the west of the primary rupture expression closer to Williamsport and Iliamna Bay.

PROJECT

Though improvements to Williamsport Road have been considered for approximately the last 20 years, there is renewed interest in improving the road conditions with anticipation of resource development in the difficult to reach portions of Alaska north of Lake Iliamna. More resilient and reliable use of the road is also essential to the viability of existing communities and industries around Lake Iliamna. Currently, the project is in its early stages consisting of early planning, data collection, characterization, and identification of individual projects that can be undertaken to incrementally improve the asset. The current project vision, formed through an early-stage site visit with the design team and the DOT&PF includes three primary focus areas of work to address the chief issues associated with its reliability:

- Improving the existing road, specifically the eastern-most three miles through the mountain pass;
- Identification of material sources along the road that can be used to support construction of improvement projects; and
- Establishing a causeway and barge landing in deeper waters of Iliamna Bay to ease tidally influenced access conditions for barges and fishing vessels.

In coordination with the design team and DOT&PF, we identified projects that could be undertaken to advance early understanding of geologic conditions within the project limits and begin the preliminary design process. Existing data within the project limits is sparse and site access/seasons are limited so new data collection activities need to be efficient with site time.

Road Improvements

Improvements to Williamsport Road include widening the roadway to two lanes, realigning tight curves, reducing steep grades, and mitigating slope hazards in mountainous terrain. In lower elevations of the roadway, the realignment work is relatively straightforward where topographic constraints are minor and obstacles to widening are controlled by right-of-way. The most challenging activities are on the east end of the road between Mile Posts (MP) 0 and 3.0 where it climbs to a mountain pass at elevation 900 feet at MP 2.1 and descends to Chinkleyes Creek at MP 3.0. Reconnaissance work suggested that this section would require significant rock cuts in steep terrain to achieve a wide, stable condition with ample rockfall catchment. Existing data was limited with one prior reconnaissance visit in the early 2000s by the DOT&PF and anecdotal information regarding rockfall occurrences and slope failures from users.

In order to make reasonable assumptions regarding rock slope configurations for improvements and provide data needed for subsequent rock slope design, a significant amount of rock structure data was needed with limited time obtain it. During summer, industrial truck traffic on the roadway makes it unsafe for rock mapping crews to spend meaningful time at any given location. When the season is over, the area shuts down and support facilities in Pile Bay are closed immediately. Since lodging and support services are not available outside of the operations season, crews need to base in Iliamna and travel to Pile Bay daily. However, fall weather in this part of Alaska is poor, making traversing Iliamna Lake from Iliamna by boat and/or helicopter unreliable. In addition, since the road is not maintained, the time window between season shutdown and winter conditions make the window for work very short. Performing the work in the spring is not practical due to the amount of snowfall that the area receives and avalanche hazards during the spring snow shedding cycles in the mountainous section. Seasonal challenges are further complicated by access challenges to exposed rock along the alignment because of steep natural hillsides which make rope-supported access difficult and time consuming.

Field Data Collection

A geologist and engineer from Shannon & Wilson, Inc. conducted field reconnaissance and data collection along the road in October 2024. The aim of the effort was to conduct rock structure mapping at rock cuts along Williamsport Road, particularly between Mile Posts 0.0 and 3.0. While conducting the field work, the team observed ground conditions, vegetation conditions, exposed rock conditions, and looked for evidence of past rockfall or slope instability. The site was accessed via the road, using a truck, and by helicopter.

At rock exposures, the team collected rock type information as well as discontinuity orientation and characteristic information. A total of 15 rock cuts were visited and hand mapped. Five of these rock cuts were mapped via drone photogrammetry, where we developed a 3D mesh model and performed digital rock structure mapping from the model. A total of 62 measurements were collected via hand mapping and a total of 111 measurements were collected from 3D mesh models. Hand mapped locations were differentiated from drone locations based on rock exposure size, accessibility, and obscured visibility due to snowfall while observing the site.

Photogrammetry was collected in the field at rock exposures using a DJI Air3 quadcopter UAV. The UAV photos collect satellite information for camera position and use on-board instrumentation to know the orientation, height, and angles of collected photos. The rock exposures selected for photogrammetry included rock faces that were difficult to observe from the road surface due to size, overhang, or vegetation. The drone was flown by hand during photo collection, based on the size of the exposed rock the drone collected on average 300 to 700 photos per rock exposure. Slope stations recorded using this approach were typically between 100 to 300 feet long as high as 100 feet above the road. In general, photo collection in the field was performed without difficulty with the exception of high winds. The drone used was not able to be used in winds over 30 miles per hour which made drone flights not possible during one day of hand mapping. Drone imagery collected in the field was downloaded onto an external hard drive and reviewed visually each day to confirm photo quality and preserve the data. Due to the large size of the data collected, uploading the information to a remote server for further data preservation was not possible.

Data Processing and Analyses

Overlapping oblique photographs of the rock face were collected and stitched together using Pix4D to create a three-dimensional point cloud model for the rock face. Processing the photos through Pix4D required between a day of automatic processing to a week of hand selecting locations for the program to render a mesh. The meshes created by Pix4D were processed into CloudCompare models. In CloudCompare, we were able to view the three dimensional rock face image and identify discontinuities and determine the planar orientations of selected structural features. The result was a collection of structure orientations that could be checked against and incorporated into the hand mapping data. It is important to note that other rock structure information is not obtainable through the photogrammetry analyses and the discontinuity data are intended to complement the hand-collected information.

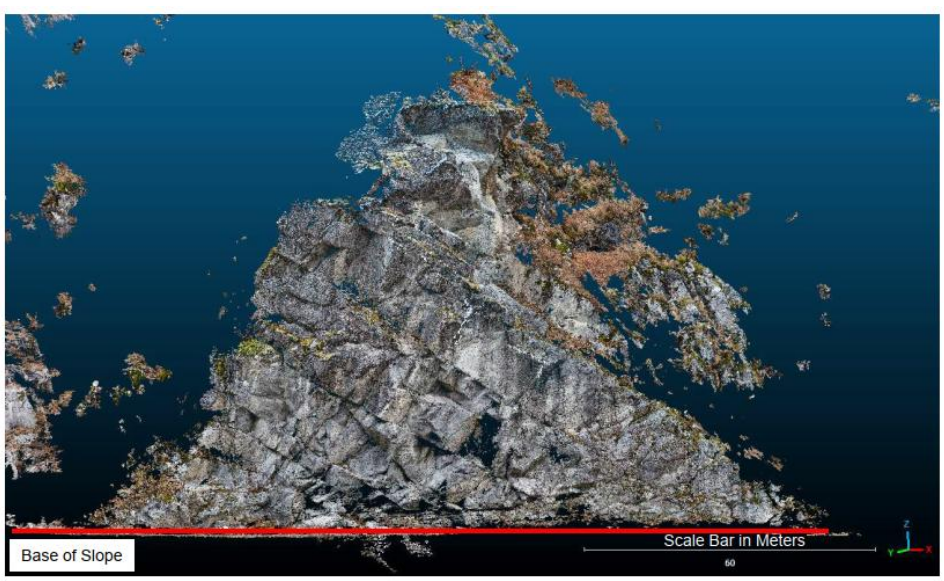

Figure 3. Example of point cloud generated by Pix4D. Red line marks the toe of the slope, the scale bar in the lower right corner is 60 approximately 195 feet (60 meters).

Challenges encountered during creation of the meshes in Pix4D were caused by the uniformity of the rock surface coloring. Low angle sunlight during some of the flights on sunny days cast shadows on the rock face and some photos and Pix4D could not automatically identify identical locations on the rock face in adjacent photos. Additionally, snowfall during one day of the fieldwork resulted in a similar effect, also resulting in difficulty for Pix4D to stitch adjacent photos. To work through these issues we manually selected locations on the rock surfaces to assist it in interpreting and stitching the photographic data.

Kinematic Analyses

Measurements taken by hand and measured digitally from photogrammetry were used to create Stereoplots and facilitate kinematic analyses. In general, controlling features within the rockmass were found to be moderate to steeply dipping joint sets. These joints were observed to be largely responsible for apparent planar shear failures across the site. Some of the steeply dipping joints indicated that toppling failures could be possible within certain rock cuts. Other lower angle and randomly oriented joint sets were identified that present the potential for wedge failures. In general, these structures appeared to be independent of lithology, which is generally uniform across the site. The figure below presents two stereoplots, the plot on the left includes the full data set collected during fieldwork inclusive of hand-measured structures and those measured from the 3-D meshes created through photogrammetry. The plot on the right includes only hand-collected structure orientation measurements. The plots are also annotated to show the interpreted joint sets and their orientations based on the full data set.

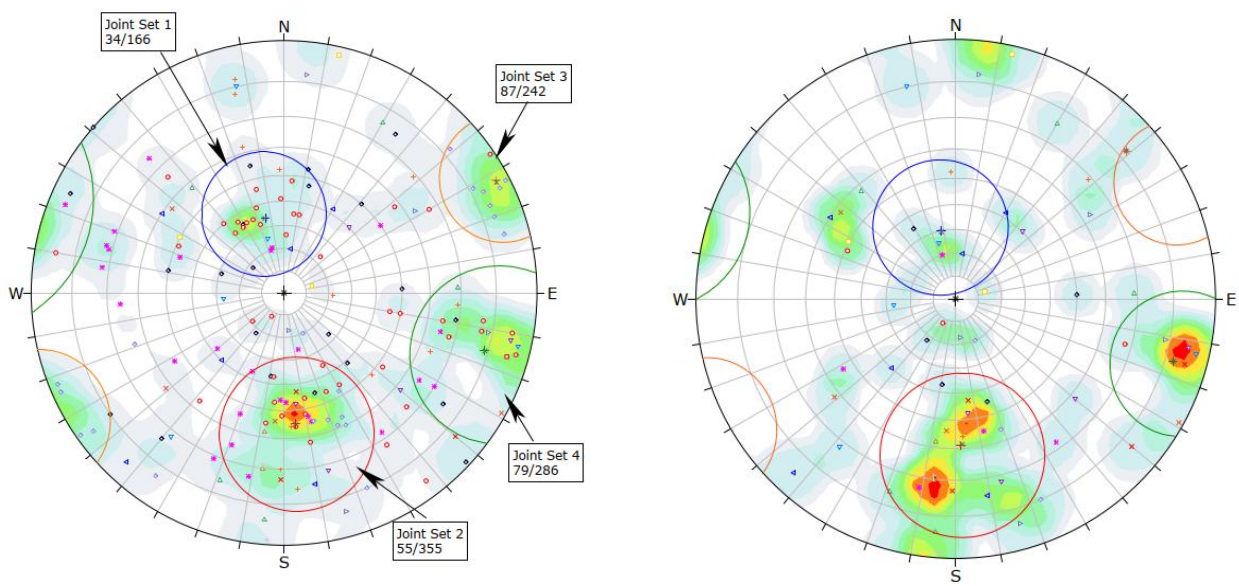

Figure 4. Stereoplot of all collected structure data (left) and only hand-collected data (right)

Comparing the two stereo plots in Figure 4 illustrates that the use of drones to collect supplemental structure data provides a clearer picture of the structure distribution in the exposed rock faces. Inclusion of the drone data suggests the presence of a second steeply dipping

structure dipping to the northeast that otherwise would likely have not been identified if only hand/ground based methods were used for data collection. It also provides clarity regarding which sets are more dominant and a more focused definition of the range of orientation variability within each joint set.

To perform our kinematic analyses, the site was split into two segments for kinematic analyses. The North Segment (MP 2.1 to 3.0) includes north facing rock cuts generally located between Chinkelyes Creek to the top of the pass. The South Segment (MP 2.1 to 0.0) includes south facing rock cuts between the top of the pass and Williamsport. The average slope orientations of these rock cuts were estimated and a generalized slope orientation was adopted for each kinematic analysis. The slope orientation in the North Segment rock cuts was 75/360 in dip/dip direction (degrees) and the South Segment rock cuts was 78/205 degrees. Joint sets were identified for all collected data (both North and South Segment rock cut data) given the apparent uniformity of the structure orientation observed. Joint sets identified from data and used in kinematic analyses are presented in the exhibits below. Note that Joint Set 3 is exclusively observed in the North Segment of road and Joint Set 1 is exclusively observed in the South Segment of road.

Kinematic analyses for cut slopes in the North Segment indicated that these rock cuts have potential to form planar shear and wedge failures, which were formed from the moderate to steeply dipping joint sets. There appeared to be less potential for toppling failures in these cuts. In the South Segment, kinematic analyses indicated that wedge and toppling failures are possible. We believe that planar shear failures are possible in the South Segment, but are less likely than the other forms of failures. In general, most of the joint sets that formed failures in the southern rock cuts were moderately dipping.

Based on our observations as well as anecdotal evidence on past performance, we understand that the rock slopes above the road have produced numerous rockfall events. These events include materials of variable size and volume, including instances where enough material has fallen on the roadway to fail the embankment below. Such an occurrence was observed in September 2004 at MP 1. Photos from this event show rock debris covering the roadway ranging in size from less than 1 foot in diameter to roughly 3 to 4 feet in diameter. It is unclear if this failure was the result of rock being released from the cut or the natural exposed slopes above the road.

Soil Slopes

Based on our more detailed site work, we identified an unanticipated slope condition that would present challenges during design and construction. Despite the apparent dominance of shallow bedrock between MP 0 and 3, there are numerous areas along the roadway where potential soil instabilities exist. Active areas include debris fans that are accumulation zones for active rockfall areas high above the roadway. Many of these areas have been cut into to create the road and are thus oversteepened. Other isolated areas of till soils are also present and exposed in several cuts above the roadway that could create similar failures, though likely lower in volume and severity compared to the rockfall accumulation zones. In addition, it was discovered that the section of the road between MP 1.9 and 1.1 is constructed on a dormant, overgrown talus slope.

The slope above the roadway likely experienced significant raveling up to several hundred feet upslope above the roadway during and immediately after construction and has since become overgrown and dormant. This feature was discovered during a helicopter flight through the pass where a subtle change in slope vegetation above the road could be observed at the apparent crest of the top of the raveling feature above the road. As such, minor disturbances in terms of loading or reshaping, could trigger progressive failures or instabilities that may be difficult to control.

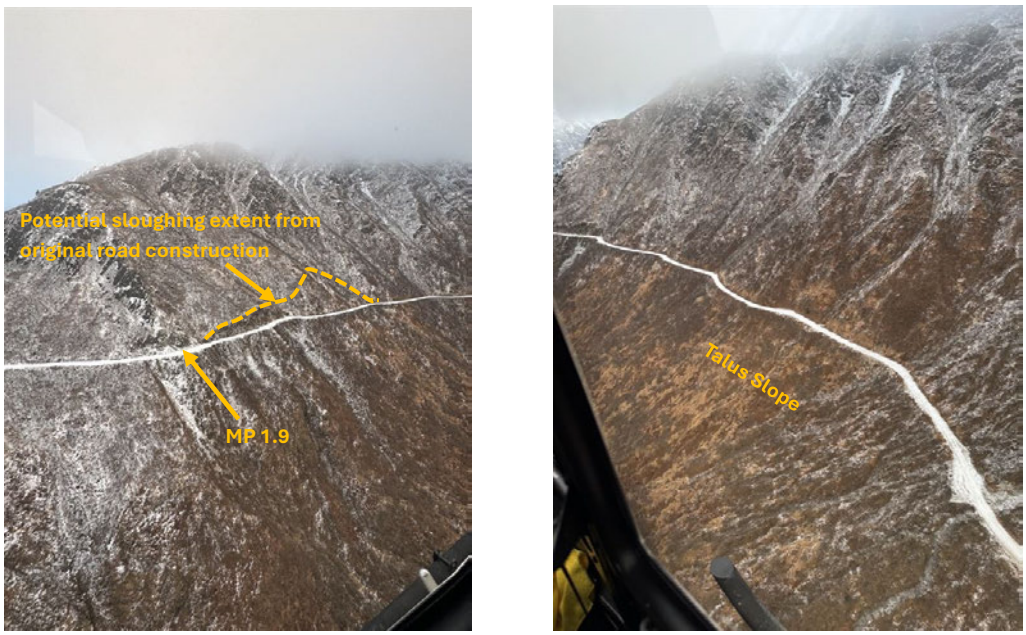

Figure 5. Oblique aerial images of Williamsport Road showing portions of talus slope

Construction Materials

Identification of construction materials along the roadway will be a key element in construction as importing sand, gravel, and rock for construction to the site would be cost prohibitive. We used numerous methods to evaluate potential material sources including review of DEMs, aerial imagery, and site photos to analyze the terrain and topography and drawing upon observations of surface conditions during reconnaissance efforts.

We reviewed sites that have previously been used for material sources for material type and potential for expansion. We looked for potential new soil borrow sites with similar terrain, topography, and vegetation to developed sites. Once identified, we estimated extents and changes in vegetation and topography. Sites that were located at higher elevations than the valley floor were presumed to have groundwater at greater depths than locations in the valley floor.

Considerations for rock material sites included potential slope instabilities, ease of development, and planned future work. Many of the sites that were mapped for our effort associated with road improvements were considered for rock material. Areas on more gentle slopes were considered for potential soil sources over those on steep slopes for both ease of development and for slope stability hazards. Finally, because cut sections will likely be necessary in areas where the

roadway has been identified for widening or straightening, the material from these cuts was identified as possible rock sources.

As a result of our evaluation, we identified eight potential sources along the alignment (four soil and four rock sources) ranging in potential approximate cut volume of 30,000 cubic yards (cy) to 680,000 cy. In order to develop borrow sources, additional explorations will be needed to confirm material types (and their properties) available and provide information that will help establish the source development methods and sequencing. Engineering analyses will be needed to establish excavation parameters as well as temporary and permanent cut slope configurations during and after material extraction, respectively. Further characterization will also confirm assumptions regarding overburden thicknesses and defining actual borrow source limits to establish a better understanding of the actual material volumes available. Laboratory testing on samples collected from potential borrow sources should include gradation and durability testing.

Additional explorations to prove up borrow sources will consist of performing test pit explorations to collect samples from soil sources and collection of samples from rock sources. Excavations in soil sources will allow evaluation of soil type distribution and evaluation of organic overburden thickness. While drilling explorations would be preferable for this effort to characterize deeper conditions, access and cost conditions make this approach impractical for early characterization, but may be used in subsequent planning phases if promising, potentially thick soil deposits are identified.

Causeway and Barge Landing

Access challenges to the existing barge landing at the natural beach near the east end of Williamsport Road are associated with expansive and shallow mud flats that are only inundated at extreme high tides. Extending a new causeway out onto the mudflats would allow more reliable access for barges and fishing vessels. The causeway will need to extend neary 3,600 feet from the existing west end of the road to access a new barge landing, haul-out ramp, and mooring bulkhead.

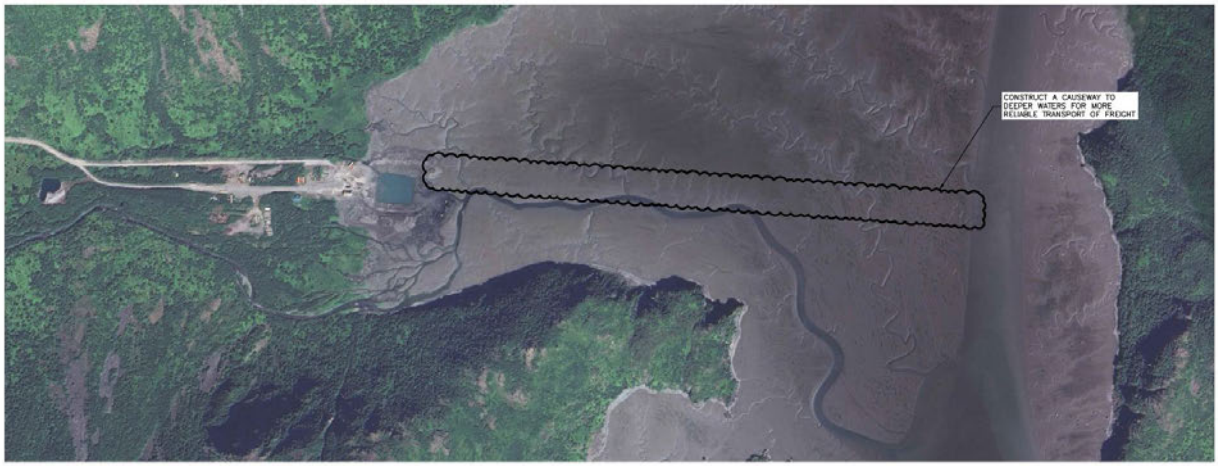

Figure 6. Approximate alignment of proposed causeway into Iliamna Bay (project drawing)

Existing Information

What is currently known about the mudflats and underlying soils is largely from prior exploration efforts by the USACE. The offshore project area at Williamsport is primarily underlain by estuarine deposits consisting of soft clay, silt, and fine sand that form the extensive tidal flats east of the end of Williamsport Road. These fine-grained sediments generally become thicker offshore and contain various amounts of organic material. Based on prior studies, classifications within the offshore area are predominantly lean clay (CL), silt (ML), and silty sand (SM), although gravel, cobbles, and occasional boulders were encountered locally within the deposits.

Existing subsurface information consists of five borings performed along an approximate causeway route extending east from the end of Williamsport Road. Information from these borings, as well as anecdotal reports from operators of the road, suggest that the upper portion of the offshore sediments is soft (MPT N-values typically less than 3), within the upper 5 to 10 feet below mudline. Below this depth, soil strength increases to a dense state and borings within the tidal flat area encountered thick sequences of clay and silt with interbedded sand layers. These conditions indicate that fine-grained estuarine deposits dominate the offshore conditions in the area and have been confirmed by dredging in the basin area at the haul-out location on the end of Williamsport Road. Prior work suggests that strength testing in the form of consolidated undrained (CU) and unconsolidated undrained (UU) tests were performed on undisturbed sediment samples, but the results of the testing are not presented in the available reports. Depths of the offshore borings were limited to a maximum of approximately 30 feet below mudline and deeper conditions are inferred through offshore geophysical explorations. These explorations confirm the presence of the shallow soft sediment horizons. Beneath this layer, the subsurface consists of denser sand, gravel, cobble, and boulder-bearing deposits interpreted to be glacial and alluvial in origin. Seismic reflection data indicated that bedrock is located 120 to 180 feet beneath the seafloor and locally as deep as 200 feet within Iliamna Bay.

Additional Characterization

While the existing information provides a reasonable understanding of the conditions that can be used to prepare preliminary design plans, some key additional information will be needed to support further design phases. Immediate future plans for explorations include performing a new offshore geophysical survey to confirm sediment, soil, and bedrock layering revealed by past studies and provide data in areas that were not included in the prior study. Eventually, offshore drilling explorations will be needed to further characterize the strength and consolidation characteristics of the near-surface soils that will eventually support the new causeway and landing embankment fills. Such information will allow more accurate material quantity estimation and evaluation of slope stability analyses to establish embankment fill slopes. Borings will also allow for the development of foundation of pile-supported structures such as mooring dolphins and bulkheads. Performing offshore borings in this area will be difficult due to extreme tidal fluctuations and the remote nature of the site. As such, the project layout and conceptual design will need to be well vetted and advanced to a degree that allows a high confidence in component (and therefore proposed boring) locations prior to mobilization.

CLOSURE

The field investigations completed during this phase of the project improved the understanding of geologic conditions along Williamsport Road and identified several factors that will influence future design efforts. With the addition of UAV photogrammetry the quantity of structure measurements collected provided more information of the dominant joint sets when compared to hand mapping alone. Field reconnaissance during this early stage also identified previously unrecognized conditions that will have significant project impacts that would not have been identified through desktop research alone, including active soil slope instabilities, debris accumulation areas, and sections of roadway constructed on dormant talus deposits that will require consideration during roadway improvements.

The information collected during this field effort provides a base for planning future subsurface investigations and advancing preliminary design of roadway improvements, borrow source development, and the proposed causeway and barge landing. The geologic characterization and information collected will be used for future design activities including establishing preliminary cut slope configurations, identify areas requiring slope stabilization, and prioritize future exploration locations. The work confirmed that combining conventional geologic hand mapping with UAV-based photogrammetry is an effective approach for collecting structural data in steep, remote terrain where access is limited, the rock slopes are considered large, and field seasons are short. This approach allowed a more representative characterization of rock structure while maximizing the value of limited field time and may be applicable to similar transportation projects in remote areas of Alaska.

REFERENCES

Historic Roads of Alaska, Driving the History of the Last Frontier. Prepared by: Alaska Department of Natural resources, Office of History and Archaeology and Interpretation and Education, Alaska State Parks. 2017.

Geology of Ala/ska Map Viewer. USGS. https://alaska.usgs.gov/science/geology/state_map/interactive_map/AKgeologic_map.html

Detterman, R.L., and Reed, B.L *Stratigraphy, Structure and Economic Geology of the Iliamna Quadrangle, Alaska.* U.S. Geological Survey. 1980.

25. The Famous "Billings Rims" and the Stagecoach Trail – Integrating 3D Geologic Modeling, Limit Equilibrium Slope Stability, and Discrete Element Rockfall Analyses

David Crotsley, PG, CPG
Geotechnical Team Lead
HDR Engineering, Inc.
1670 Broadway, Suite 3400
Denver, CO 80202
(717) 615-7898
david.crotsley@hdrinc.com

Bret Watkins, PG
Senior Geologist
HDR Engineering, Inc.
4645 Village Square Drive, Suite F
Paducah, KY 42001
(270) 538-1530
bret.watkins@hdrinc.com

Prepared for the 75th Highway Geology Symposium, September, 2026

Disclaimer

Statements and views presented in this paper are strictly those of the author(s), and do not necessarily reflect positions held by their affiliations, the Highway Geology Symposium (HGS), or others acknowledged above. The mention of trade names for commercial products does not imply the approval or endorsement by HGS.

Copyright Notice

Copyright © 2026 Highway Geology Symposium (HGS)

All Rights Reserved. Printed in the United States of America. No part of this publication may be reproduced or copied in any form or by any means – graphic, electronic, or mechanical, including photocopying, taping, or information storage and retrieval systems – without prior written permission of the HGS. This excludes the original author(s).

ABSTRACT

This case study presents the geotechnical and geologic design framework for the Stagecoach Trail corridor in Billings, Montana, a setting dominated by the "Billings Rims"—steep, jointed sandstone escarpments with a history of both frequent nuisance rockfall and episodic, high-magnitude block releases. Three preliminary trail alignments were advanced through a risk-informed, cost-benefit screening that explicitly accounted for differential exposure to rockfall sources, constructability within constrained benches, and long-term maintenance liabilities.

Using high resolution UAV photogrammetric data in conjunction with 3D geologic mapping, we developed a model of the site to resolve key stratigraphic contacts, persistent joint sets, and colluvium thickness variations along the slopes. The model underpinned a 3D limit-equilibrium slope stability analyses to evaluate slope stability, fill geometry, and potential rockfall catchment areas. Rockfall hazard was then characterized through 2D renderings as well as discrete element modeling utilizing ANSYS ROCKY, to evaluate the impacts of surface irregularities. Combining the use of geosynthetically stabilized earth slopes, localized rock stabilization and routing the trail to minimize exposure to pedestrians, the greenway trail will provide a critical link for Billings residents providing a safer connection from the Rims to the valley.

INTRODUCTION

The city of Billings, Montana, occupies a unique geologic setting defined by dramatic sandstone escarpments commonly known as the Billings Rims. These cliffs form a prominent topographic boundary separating upland residential development from the Yellowstone River Valley and represent one of the city's defining geologic features. While visually striking, the Rims also present persistent geologic hazards associated with rockfall, erosion, and slope instability.

The proposed Stagecoach Trail is intended to connect existing trail systems above and below the Rims, providing a critical recreational and transportation link for residents. Development of the trail requires construction within a steep and geologically active corridor where rockfall hazards, shallow bedrock, and constrained topography significantly influence design decisions. Traditional geotechnical investigations alone were insufficient to characterize the geologic hazards present; therefore, a multidisciplinary approach incorporating geologic mapping, rock slope engineering, and numerical modeling was adopted.

This paper presents the integrated methodology used to evaluate geologic hazards, develop a risk-informed trail alignment, and support the engineering design of the Stagecoach Trail corridor. Refer to Figure 1 for the project location.

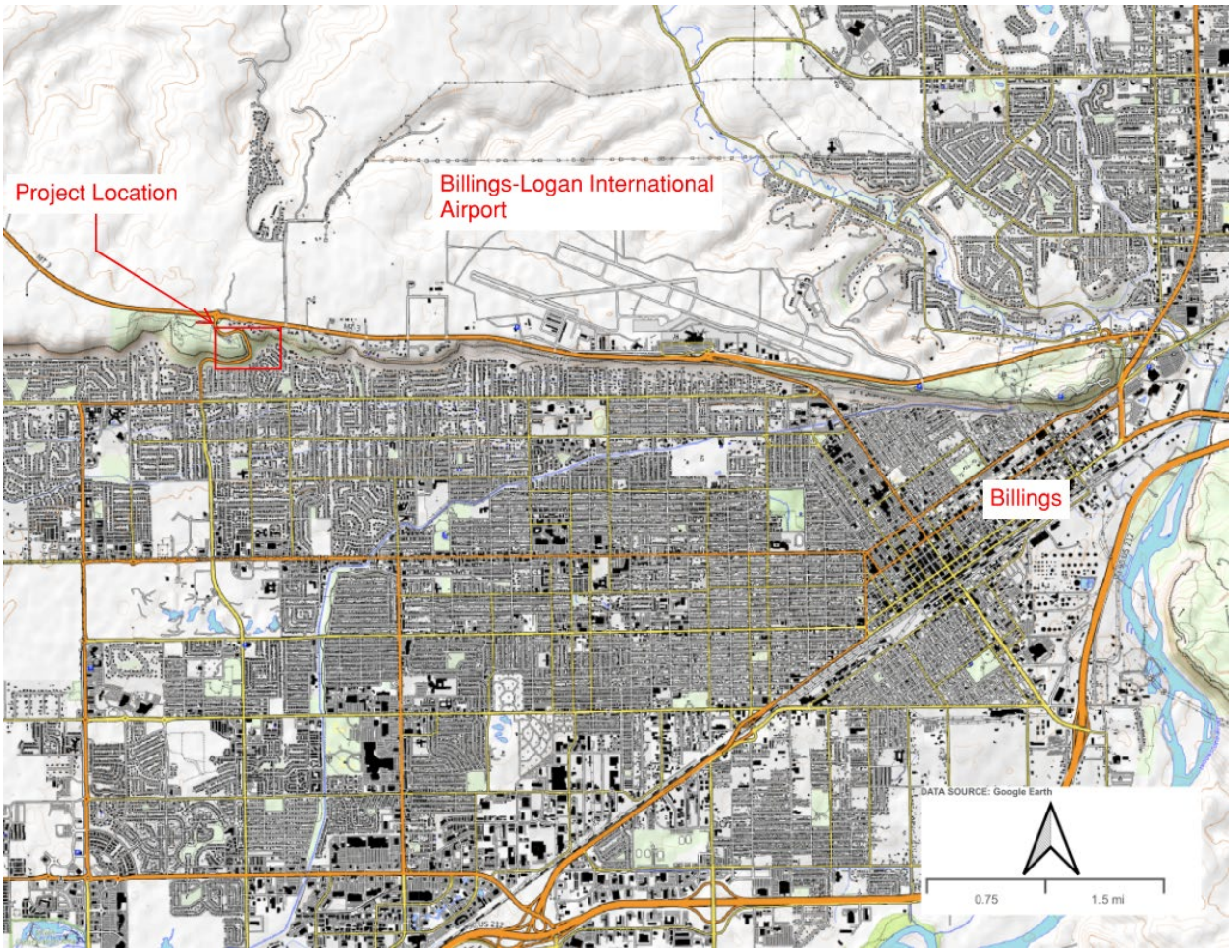

Figure 1 – Project Location Map

PROJECT DEVELOPMENT AND ALIGNMENT SCREENING

Three trail alignments were considered during preliminary project development. Alignment 1 generally follows the Zimmerman Trail Road corridor before ascending through an existing drainage gully. Alignment 2 traverses beneath a south-facing sandstone cliff line, while Alignment 3 remains lower on the slope and generally parallels portions of Zimmerman Trail Road.

Evaluation criteria included:

- Rockfall exposure
- Drainage considerations
- Earthwork requirements
- Constructability
- Long-term maintenance
- Public safety

- Retaining structure requirements

Preliminary screening indicated that Alignment 1 provided significant advantages because it incorporated existing topography and natural drainage features to reduce rockfall exposure while maintaining reasonable constructability. Alignment 2 presented the highest rockfall risk because significant portions of the trail would be located directly beneath active rockfall source areas. Alignment 3 reduced rockfall exposure but introduced additional grading and constructability challenges. Refer to Figure 2 for the Site Map.

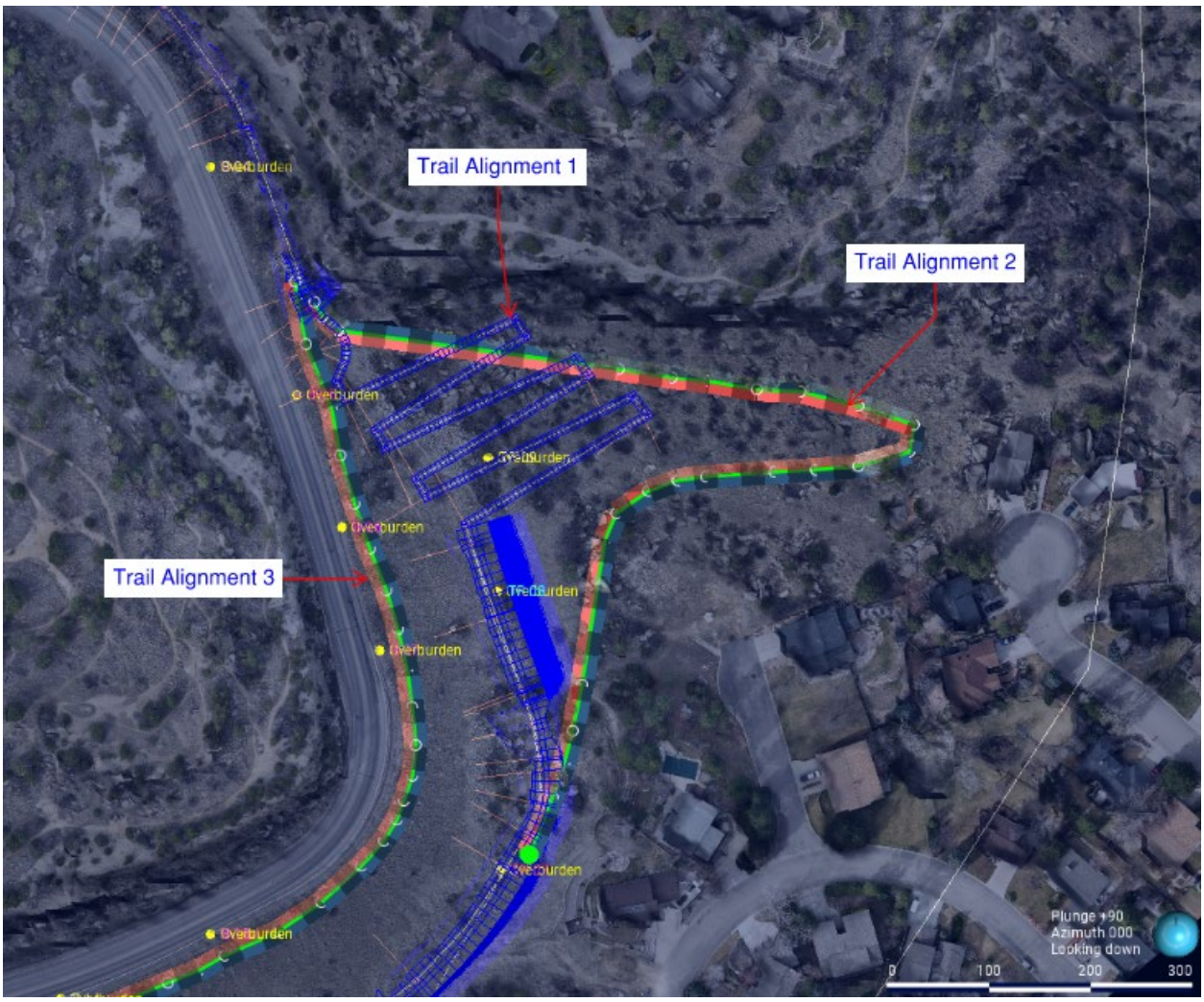

Figure 2 – Site Map

The alignment evaluation established the framework for subsequent geologic and geotechnical investigations by focusing analyses on both geologic hazards and engineering feasibility.

SITE GEOLOGY, EXPLORATIONS AND LABORATORY TESTING

Site Geology

The project site is situated within the Eagle and Telegraph Creek Formations. The more competent sandstone cliffs belong to the Eagle formation and the lower slope-forming colluvium and shales belong to the Telegraph Creek formation. The United States Geologic Survey (USGS, 1899) describes the two formations as below.

> *Eagle Formation: Basal part consists of thinly laminated sandstones stained light brown by lignitic material and containing concretions and nodular masses of iron ore. These grade up into very pure white sandstone, which forms bluffs 75 to 100 feet high along the Missouri River. Upper part of formation consists of less shaly sandstones with interbedded lignite seams. Total thickness 200 to 235 feet. Overlain by 2,000 feet of marine beds, designated as Montana formation. Underlain by Colorado formation, 1,850 feet thick. [Age is Late Cretaceous.]Named from type exposures along the Missouri River about mouth of Eagle Creek [4 0 mi below Fort Benton], Choteau Co., MT.*
>
> *Telegraph Creek formation. Yellow sandy shale parted in middle by a thin bed of concretionary sandstone, which caps an escarpment. Less prominent layers of concretionary sandstone occur in upper half of formation. Thickness 320 feet. Underlies Virgelle sandstone member of Eagle sandstone, and overlies Niobrara shale. Fossils predominantly Montana types. They include several species found in Eagle sandstone, mingled with forms usually found in Niobrara shale, of latest Colorado age.*

Rockfall History

The Billings Rimrocks have experienced a recurring pattern of rockfalls that have periodically damaged homes built below the sandstone cliffs. Documented incidents include a major boulder strike on a Granite Avenue home in 2011, as well as two separate events in 2018 when falling rocks damaged a residence on 37th Street West and a garage on Mountain View Boulevard. These events highlighted the ongoing rockfall hazard posed by the naturally weathering Rimrocks and raised concerns about development within potential rockfall runout areas.

The most significant recent event occurred in September 2019 on Laredo Place, when a massive boulder detached from the Rimrocks and struck a home, reportedly displacing the structure from its foundation. The incident prompted extensive geologic investigations, slope-stability assessments, and rockfall mitigation efforts by the City of Billings. Contractors removed additional unstable blocks from the cliff face, cleared fallen debris, and repaired roadway damage before reopening the area in January 2020. The event also led to lawsuits and forensic geotechnical evaluations, making it one of the most extensively investigated rockfall events in the recent history of the Billings Rims.

Site Explorations

Field investigations were completed during April 2025 and confirmed active rockfall conditions throughout the study area. Large detached sandstone blocks were observed below the cliff line, and numerous discontinuity-controlled failure features were identified along the highwall.

Rock mass quality varied considerably along the escarpment. Western portions of the cliff contained increased calcite cementation and dissolution features that promote frequent raveling

and smaller block failures. Eastern portions of the cliff generally consisted of more competent sandstone capable of generating larger and higher-energy rockfall events.

Field observations further demonstrated that natural drainage gullies act as rockfall traps in portions of the western corridor, whereas central and eastern cliff sections allow blocks to reach the lower slopes with relatively little natural attenuation.

UAV-Based Structural Mapping and Kinematics

High-resolution UAV imagery collected by IMEG Corporation was processed into a photogrammetric point cloud and evaluated using Maptek PointStudio. Structural discontinuities were identified through a combination of automated plane extraction and geological interpretation. These data were supplemented by field measurements collected during site reconnaissance.

Kinematic analyses were performed using Rocscience DIPS and assumed a sandstone friction angle of 32 degrees. Failure modes evaluated included planar sliding, wedge sliding, direct toppling, and flexural toppling.

Results indicated that:

- Flexural toppling represented approximately 45 percent of potential failures on south-facing slopes.
- Direct toppling represented approximately 11 percent of potential failures on south-facing slopes.
- Wedge failures represented approximately 23 percent of potential failures on southwest-facing slopes.
- Planar failures were relatively uncommon throughout the study area.

These results were consistent with field observations and demonstrated that rockfall generation is largely controlled by interactions between near-vertical joint sets and sub-horizontal bedding planes within the Eagle Formation sandstone.

The kinematic analyses served as a critical link between structural geology observations and subsequent rockfall hazard assessments by identifying the dominant mechanisms responsible for block release.

THREE-DIMENSIONAL GEOLOGIC MODELING

Basis of Model

Previous subsurface investigations at the project area have found that the subsurface generally consists of shallow clayey and silty sands to bedrock. Bedrock depths range from 0 to 19 feet bgs and consist of either shale or sandstone sedimentary rock. Based on the consistency of the encountered materials throughout the boring program, it is reasonable to assume that the thin clayey and silty sand layers overlying bedrock at the project site are relatively consistent in material gradation and strength. Therefore, one of the most critical elements in design with regard to this area is the top of rock elevation.

A 3D geologic model of the project site was generated based on previous subsurface investigations performed by Terracon (Boreholes and Test Pits) and measurements of top of rock taken in the field by experienced HDR geologists during the site visit. The primary intent of the model is to capture the top of rock surface at the project area. Because of the distance between subsurface explorations and field measurements, it can be expected that accuracy will decay with distance from discrete measurement points. However, the project site of interest is relatively consistent with many clear exposed outcrops which allows a trained model of top of rock to be generated with moderate accuracy.

Geologic modeling for this project site was performed using Seequent Leapfrog Version 2025.2.1.

Geologic Model Data Inputs

Seventeen (17) boreholes and ten (10) test pits were available from previous Terracon subsurface investigations at the project site. The locations of these were described earlier in Figure 3. Because of the consistency of the subsurface soils and rock encountered in the boring program, these layers were grouped into “Soil” and “Rock” layers within the geologic model. The topography and orthoimagery for this project site was incorporated by using UAV survey data from IMEG. A view of the boreholes with topography is shown in Figure 3 to illustrate how the model data inputs are developed.

Where outcrops are plainly visible within the 3D topography and orthoimagery, as well as where HDR Geologists encountered top of rock locations within the field, data points for top of rock were incorporated as polylines and 3D points, as shown in Figure 4.

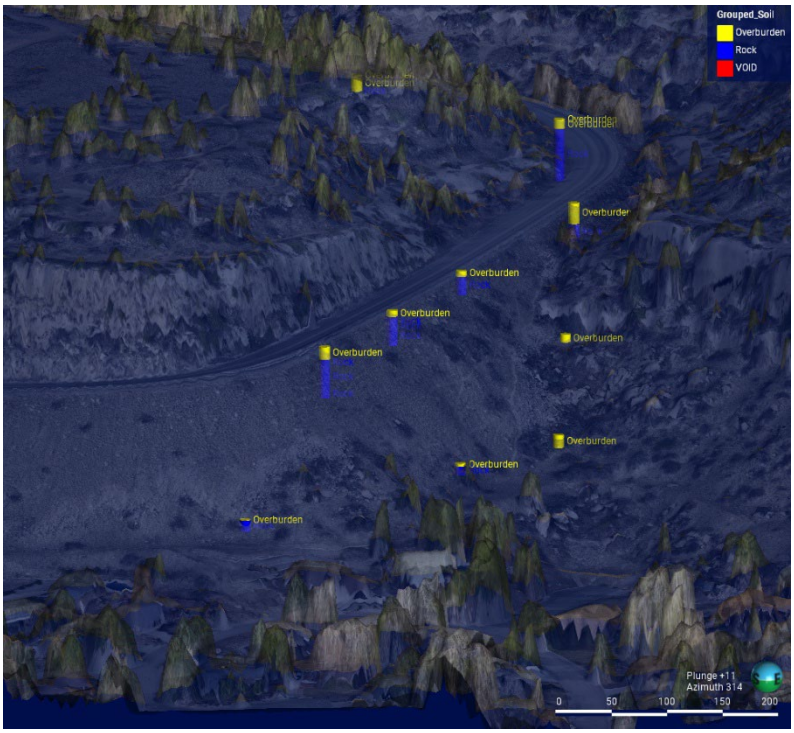

Figure 3: 3D model of boreholes

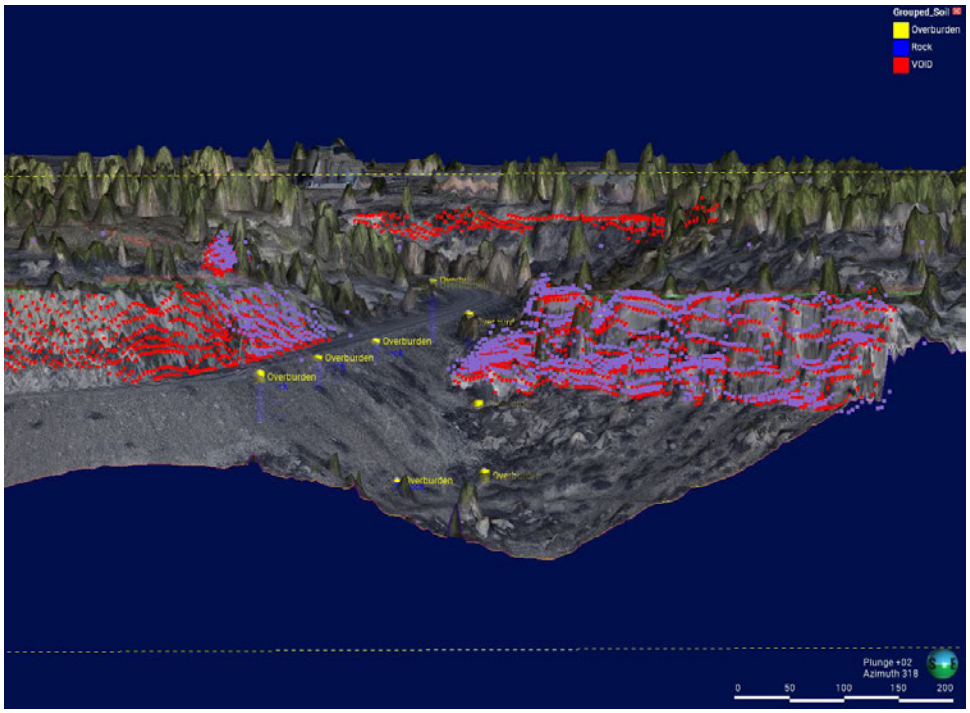

Figure 4: Top of rock data inputs on topography

ROCKFALL HAZARD CHARACTERIZATION

Rockfall hazards were evaluated using ANSYS ROCKY and Rocscience RocFall2. A preliminary 3D risk analysis was performed in ROCKY to evaluate the proposed alignments, then upon determining the alignment with the lowest risk profile, detailed analyses were subsequently performed using two-dimensional RocFall2 models. Four critical sections were selected where trail alignments intersected areas of elevated rockfall potential. These locations represented the highest anticipated interaction between potential rockfall trajectories and proposed trail alignments. Figure 5 below shows a view of the 3D rockfall analysis.

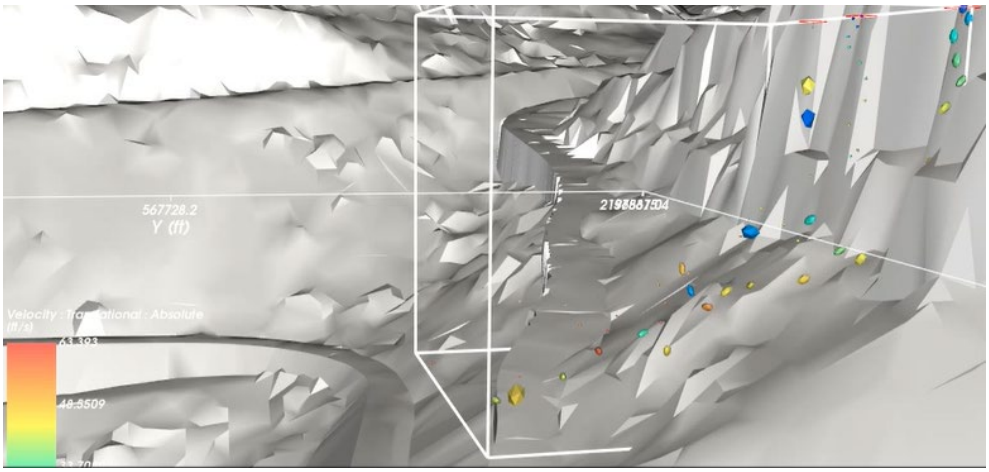

Figure 5: View of 3D rockfall analysis

Rockfall simulations incorporated field-derived material properties and representative block geometries ranging from approximately 700 pounds to greater than 10,000 pounds. Seven representative block shapes were modeled. Each block type was simulated 100 times, generating approximately 700 simulated rockfall trajectories at each section. Initial release conditions were conservatively assigned across mapped source areas along the cliff face.

The analyses demonstrated that trails located directly beneath the south-facing highwall experience the greatest exposure to rockfall impacts. Simulated trajectories routinely intersected Alignment 2, indicating that substantial mitigation measures would be required to achieve acceptable safety levels.

Conversely, Alignments 1 and 3 generally remained outside primary rockfall runout zones and benefited from favorable topography and increased offset distances from active source areas.

The modeling results confirmed that natural terrain features substantially influence rockfall behavior and can serve as effective mitigation features when incorporated into project design.

RETAINING WALL AND EMBANKMENT DESIGN

The proposed trail is anticipated to be supported by various heights and angles of fill slopes and retaining walls. These fill slopes range from 2:1 to 1:1 and in some areas approach 40 feet in height. The five anticipated retaining walls are expected to feature max heights around 20 feet and to be tiered to gain elevation for the trail. The following sections discuss the engineering design and analyses performed to support the proposed trail earthwork and retaining walls.

Global Stability

Global stability was evaluated with RocScience SLIDE2. The program uses limit equilibrium techniques to search for the critical failure surface that produces the minimum factor of safety. The factor of safety is defined as the sum of the resisting forces divided by the sum of the driving forces. Because the subsurface materials are predominantly cohesionless and drainage improvements are incorporated into the design, drained conditions are expected to govern long-term performance. The minimum required factors of safety for slope stability based on standard engineering practice and local guidelines are provided in Table 1 below.

Table 1 – Minimum Required Factors of Safety

Loading Case	Minimum Factor of Safety
Drained (Long Term, Near Structure)	1.5
Drained (Long Term, Earthwork)	1.3
Seismic (Drained Case w/ a_h=0.05g)	1.1

A live load surcharge of 90 psf was applied as an external load to model the pedestrian live load acting along the trail.

The adopted design strengths used in the stability analyses were developed based on the results of the historic laboratory test data and general engineering experience. A summary of the design strength parameters is presented in Table 2.

Table 2 – Design Shear Strengths

Material	Soil Strength Type	Unit Weight	Drained Strength		Unconfined Compressive Strength (UCS)	GSI	m_i	D
		γ_{total} (pcf)	c (psf)	Φ (°)	(psf)			
Rock Embankment	Mohr-Coulomb	135	0	40				
Controlled Fill	Mohr-Coulomb	120	0	30				
Overburden	Mohr-Coulomb	110	0	30				
Sandstone		135	0		5000000	50	16	0
Retaining Wall Fill	Mohr-Coulomb	120	0	32				
Retaining Wall	Infinite Strength	135	0					
RSS Fill	Mohr-Coulomb	100	0	40				

Slope stability was analyzed for the critical sections along each earthwork section and along critical wall heights for each wall. Bishop Simplified, GLE Morgenstern-Price and Spencer methods were utilized and the most critical Factor of Safety (FS) was selected. The results of the slope stability analyses are presented in Table 3.

Table 3 – Summary of Slope Stability Analyses

Section	Associated Structure or Earthwork	Computed Factor of Safety		Comment
		Drained (*Min.= 1.3/1.5)	Seismic (Min.= 1.1)	
39+00 1:1 RSS	Reinforced Soil Slope below Zimmerman Trail Road	1.3	1.2	Pass
41+25 1:1 RSS	Reinforced Soil Slope below Zimmerman Trail Road	1.3	1.2	Pass
42+25 1:1.5 RSS	Reinforced Soil Slope below Zimmerman Trail Road	1.5	1.4	Pass
44+75 1:1 RSS	Reinforced Soil Slope below Tiered MSE Walls	1.7	1.6	Pass
47+00	Tiered MSE Walls	1.5	1.3	Pass
51+00	Tiered MSE Walls	2.0	1.8	Pass
64+50	1.5:1 Steepened Rock Embankment Slope	1.3	1.1	Pass
55+50	Rock Cut Slope	7.3	6.8	Pass

*Minimum of 1.3 Factor of Safety for earthwork slopes far from a permanent structure, minimum of 1.5 Factor of Safety for earthwork slopes near permanent structures

The results of the stability analyses demonstrated that the earthwork slopes and structures meet or exceed the minimum required factors of safety for each design case. Therefore, the proposed design is valid and stable globally.

MSE Wall and RSS External Stability

RocScience RSWall analyses were performed for representative wall and RSS segments. Proposed MSE walls and RSS Slopes were analyzed using the LRFD Methodology, described in AASHTO 2024, for several potential failure modes (external stability, reinforcement stability, internal stability, base sliding, eccentricity, overturning and bearing).

Assumptions regarding the MSE wall components for these analyses are as follows:

- Reinforced Soil (sand)
  - Unit Weight of 120 pcf
  - Friction Angle of 34°
- Retained Soil (sand)
  - Unit Weight of 120 pcf
  - Friction Angle of 30°

- Foundation Soil for Long Term
  - Unit Weight of 120 pcf
  - Friction Angle of 30°
- Groundwater conditions are assumed dry
- Traffic live load surcharge of 90 psf
- Seismic design horizontal peak ground acceleration of 0.05g

Assumptions regarding the RSWall Components for these analyses are as follows:

- Reinforced Soil (sand)
  - Unit Weight of 100 pcf
  - Friction Angle of 40°
- Retained Soil (sand)
  - Unit Weight of 120 pcf
  - Friction Angle of 30°
- Foundation Soil for Long Term
  - Unit Weight of 120 pcf
  - Friction Angle of 30°
- Groundwater conditions are assumed dry
- Traffic live load surcharge of 90 psf
- Seismic design horizontal peak ground acceleration of 0.05g.

The potential failure modes were evaluated using RSWall (2025) and the AASHTO LRFD 2024 design guidelines were followed. The load (γ) and resistance (φ) factors presented in Table 4 below were applied in this evaluation:

Table 4 – Summary of Load and Resistance Factors for MSE Walls

Design Condition	External Stability Load Factors (γ)	
	Static	Static and Seismic
Vertical Earth Pressure for Sliding/Eccentricity	1	1
Vertical Earth Pressure for Bearing Capacity	1.35	1.35
Active Lateral Earth Pressure or Active Lateral Earth Pressure during Earthquake	1.5	1.5
Earthquake Loads	1	1
Live Load Surcharge	1.75	1.75
Dead Load Surcharge	1.5	1.5
	External Stability Resistance Factors (φ)	
Sliding at Reinforced Soil/Foundation Soil Interface	1	1
Bearing Capacity	0.65	0.65

The results of the RSWall analyses are shown below in Table 5.

Table 5 – Summary of RSWall Results

Case	Associated Structure	Lowest CDR*	Controlling Condition
RSS Case 1	Reinforced Soil Slope below Tiered MSE Walls	6.25	Bearing
Wall 1	MSE Wall 1	1.2	Bearing
Wall 2	MSE Wall 2	1.09	Base Sliding
Wall 3	MSE Wall 3	1.15	Base Sliding
Wall 4	MSE Wall 4	1.22	Base Sliding
Wall 5	MSE Wall 5	1.06	Base Sliding
RSS Case 1 (Optimized)	Optimized Reinforcement Layout for Reinforced Soil Slope below Tiered MSE Walls	6.25	Bearing

*Capacity Demand Ratio; minimum required CDR is 1.0

The results of the RSWall Analyses indicate that the proposed MSE walls and RSS Slopes are stable. Final MSE Wall design is the responsibility of the wall designer. This evaluation demonstrates the feasibility of MSE wall construction at the site; final design remains the responsibility of the wall system designer.

Keys to Success

The Stagecoach Trail design brought a unique challenge of a tight construction area, steep vertical gain, and unique geology rolled into one. Incorporating a preliminary 3D rockfall analysis helped to inform the design team of the options and cost implications for the selection of the alignment, developing the 3D Geologic model then streamlined the global stability and retaining wall design analyses to expedite the project and maintain design quality. The integration of these techniques supported a successful design both from a technical standpoint, as well as constructability and cost.

REFERENCES

AASHTO. (2024). *LRFD Bridge Design Specifications.* AASHTO.

Marinos, P., & Hoek, E. (2000). *GSI: A Geologically Friendly Tool for Rock Mass Strength Estimation.* Melbourne, Australia: ISRM International Symposium.

MDT. (2025). *Standard Specifications for Road and Bridge Construction.* MDT.

Terracon Consultants, Inc. (2017). *Geotechnical and Materials Engineering Report.* Billings.

USGS. (1899). *Geologic Atlas of the United States Folio GF-55.* Fort Benton, Montana: United States Geologic Survey.

26. PhotoMonitoring for Transportation Infrastructure in Geohazard Environments: Operational and Economic Advantages for Asset Owners

Marco Fiorio

NHAZCA S.r.l.

Via V. Bachelet 12, 00185 Rome, Italy

+39 06 95065820

Marco.Fiorio@nhazca.com

Michele Gaeta

NHAZCA S.r.l.

Via V. Bachelet 12, 00185 Rome, Italy

+39 06 95065820

Michele.Gaeta@nhazca.com

Tony Simmonds

Re-Monitor Inc.

+1 472 244 8575

T.simmonds@re-monitor.com

Paolo Mazzanti

Department of Earth Sciences & CERI Research Centre, Sapienza University of Rome

NHAZCA S.r.l

+39 06 95065820

Paolo.Mazzanti@nhazca.com

Prepared for the 75th Highway Geology Symposium, September 2026

Acknowledgements

The authors acknowledge WSDOT personnel involved in the SR14 Milepost 69 pilot application and the NHAZCA/Re-Monitor technical team involved in IRIS and PhotoMonitoring development. This acknowledgement does not imply agency endorsement of the interpretations presented in this paper.

Disclaimer

Statements and views presented in this paper are strictly those of the author(s), and do not necessarily reflect positions held by their affiliations, the Highway Geology Symposium (HGS), or others acknowledged above. The mention of trade names for commercial products does not imply the approval or endorsement by HGS.

Copyright Notice

Copyright © 2026 Highway Geology Symposium (HGS)

All Rights Reserved. Printed in the United States of America. No part of this publication may be reproduced or copied in any form or by any means - graphic, electronic, or mechanical, including photocopying, taping, or information storage and retrieval systems - without prior written permission of the HGS. This excludes the original author(s).

ABSTRACT

Transportation agencies in the United States require monitoring approaches that operate continuously, automatically, and safely to support decisions for high-value assets exposed to geohazards such as rockfalls, debris flows, erosion, creep, post-wildfire instability, and construction-related ground movement. This paper presents PhotoMonitoring as a scalable, contactless technology for geohazard monitoring, emphasizing its operational and economic advantages for highway and road infrastructure owners. In a typical workflow, high-resolution images acquired at user-defined intervals are transferred to a processing environment and analyzed using computer-vision algorithms for image preprocessing, co-registration, change detection, and Digital Image Correlation-based displacement analysis. The result is a high-frequency record of site evolution with full-field change and displacement maps, rather than sparse, periodic point observations alone. Compared with conventional inspection and instrumentation approaches, PhotoMonitoring can reduce field exposure, limit manual intervention, improve temporal density, and support earlier recognition of evolving deformation or detachment patterns. The workflow is illustrated through a 2025 application to an unstable rock slope along State Route 14 in Washington, where repeat UAV imagery and image-based change detection were used to assess rockfall-related change before and after a wildfire-triggered period of elevated hazard concern.

INTRODUCTION

Transportation agencies across the country manage extensive networks of roads, bridges, retaining structures, slopes, tunnels, culverts, and drainage assets whose serviceability depends on both structural condition and the stability of surrounding ground. Many of these assets are high-value and their operational stability is critical because a single closure can disrupt regional mobility, emergency access, freight movement, tourism, and local economies. They are also exposed to geohazards whose behavior can change rapidly: rockfall after freeze-thaw cycles or wildfire, debris flows during short-duration rainfall, slope creep under seasonal groundwater changes, erosion during floods, and instability induced by construction or maintenance activities are just some examples of hazards that can severely impact on the operability of the assets.

Traditional monitoring practice in the industry relies on periodic inspection, site visits after triggering events, geotechnical mapping, targeted instrumentation, and campaign-based survey or remote sensing. These methods remain essential, but they leave important gaps. Manual inspections may not capture short-lived precursors or nighttime events. Point instruments provide high-precision measurements only where installed. Survey campaigns can provide excellent spatial information but are usually too infrequent for operational decision-making after fast-changing events. For transportation owners, the practical monitoring problem is therefore not only accuracy, but also temporal density, spatial coverage, safety, cost, and the ability to deliver interpretable results fast enough to decision makers in order to support them in traffic-management, design of maintenance plans and in implementing emergency mitigating actions.

Recent infrastructure and geohazard events illustrate why monitoring strategies need to evolve. The 2007 I-35W bridge collapse in Minneapolis killed 13 people and led the National Transportation Safety Board (NTSB) to identify a design error in gusset plates, with contributing issues related to bridge rating, inspection, and oversight [1]. The Florida International University pedestrian bridge collapsed tragically in 2018 during construction killing six peoples who were driving their cars along the road underneath the structure; the NTSB report emphasized design and peer-review failures but also documented that significant cracking and distress had been observed before collapse [2]. These bridge cases are not geohazard examples, but they are relevant to asset owners because they show the risk of relying on intermittent interpretation of condition evidence when deterioration or instability is evolving.

The geohazard context is equally clear. Landslides occur throughout the United States and can damage transportation corridors, utilities, and communities [3]. The tragically notorious 2014 Oso landslide in Washington crossed State Route 530 and caused 43 fatalities, demonstrating the severe consequences that slope failures can have for both public safety and highway connectivity [4]. In Colorado, post-wildfire debris flows and sediment-laden runoff repeatedly affected Interstate 70 in Glenwood Canyon after the Grizzly Creek Fire, requiring closures, emergency response, and repair activities along one of the state’s most important corridors [5]. Internationally, the widely known 2018 collapse of the Morandi Bridge in Genoa, Italy, which resulted in 43 fatalities, highlighted the consequences of undetected corrosion in the

steel tendons embedded within the bridge's prestressed-concrete stay cables and reinforced the importance of long-term condition assessment, maintenance planning, and reliable monitoring of critical infrastructure [6].

The lesson common to these examples is not that a single monitoring technology can prevent complex failures. Rather, the lesson is that transportation agencies benefit from monitoring systems that make evolving conditions visible earlier, at lower operational cost, and with a documented time history that can be reviewed by engineers. PhotoMonitoring addresses this need by converting repeat imagery into quantitative measurements of change and displacement. Because cameras are relatively inexpensive, widely available, remotely deployable, and compatible with high-frequency acquisition, image-based monitoring can provide a scalable layer between occasional inspection and more expensive campaign-based survey.

PHOTOMONITORING TECHNOLOGY

PhotoMonitoring is an image-based monitoring approach that uses repeat photographs or image sequences to detect and measure changes and displacements affecting ground, rock slopes, structures, and construction work [7, 8]. The term has been coined by NHAZCA to define the method as the use of digital image-processing algorithms applied to optical imagery, producing two complementary outputs: change detection, which identifies the appearance or disappearance of material or shifts in surface conditions, and Digital Image Correlation (DIC), which tracks continuous surface displacements by following natural texture patterns over time. Modern imaging platforms, including satellites, UAVs, and terrestrial cameras, enable frequent, high-resolution acquisitions that make PhotoMonitoring a flexible, scalable, and increasingly widespread technique for remotely tracking ground deformation, landslides, and infrastructure–terrain interactions.

The core value of PhotoMonitoring lies in the dual nature of imagery: each image contains both measurement information and visual documentation. A single sequence can support qualitative review, change detection, displacement estimation, event inventory, and communication with nonspecialist decision makers. This is particularly useful for transportation agencies, where geohazard management requires rapid coordination among geotechnical staff, maintenance crews, emergency managers, and traffic operations. Maps of detected change, before-after image pairs, and displacement time series are often more intuitive than raw sensor streams alone.

Technically, PhotoMonitoring leverages the fact that a digital image is a matrix of numerical pixel values. Advanced image processing algorithms identify and track distinctive features such as textures, brightness variations, grains, pores, microcracks, and use them to reconstruct deformation. Unlike traditional surveying systems that rely on prisms or adhesive markers, PhotoMonitoring exploits the natural micro texture of surfaces to track dense grids of

control points, eliminating the logistics of installing physical targets and enabling continuous, high-density coverage.

Operational workflows follow a repeatable sequence: image acquisition (via fixed cameras or UAV surveys), data transfer, preprocessing, radiometric and photometric normalization, automated co-registration to remove camera or viewpoint shifts, and then change detection or displacement analysis. The WSDOT high-risk-slope materials describe the same structure implemented in IRIS: preprocessing, co-registration, structural-similarity change detection, multi-baseline persistence validation, connected-component clustering, configurable thresholds and confidence levels, GSD-based spatial-resolution checks, and DIC-based displacement analysis [9].

Accurate displacement measurement depends on several foundational choices: sensor type, acquisition platform, landslide characteristics, and environmental conditions. Image resolution is central and multifaceted. Geometric resolution determines the pixel density and enables detection of subpixel movements, down to 1/20 of a pixel under ideal conditions. Radiometric resolution governs sensitivity to subtle reflectance changes, while spectral resolution determines the ability to differentiate materials or surface types. Temporal resolution controls how frequently the same area is imaged, directly affecting the ability to track evolving phenomena. Sensor geometry also matters; displacement is measured within the image plane (in both its vertical and horizontal components), so the sensor should be positioned as perpendicular as possible to the expected direction of movement. Environmental factors such as lighting, vegetation, shadows, and weather can degrade image quality and are addressed through specialized processing workflows.

The technical maturity of the approach is supported by recent landslide-monitoring publications on peer reviewed journals. Molinari et al. documented the March 2025 Poggio Baldi landslide (Italy) sequence using a multi-sensor monitoring system in which IRIS-based image analysis combined co-registration, SSIM change detection, and DIC to reconstruct event evolution, and concluded that low-budget image-based monitoring systems are applicable to early-warning contexts [7]. Stefanini et al. reported the first systematic national-scale application of PhotoMonitoring for landslide surveillance in Italy: 13 landslide sites, 15 cameras, more than 150,000 images, 1,235 detected gravitational-event clusters, and validation against robotic total-station data with correlation coefficients from 0.831 to 0.999, with a mean of 0.966 [8].

IRIS PROCESSING WORKFLOW

IRIS is the web-based processing and visualization environment used by NHAZCA and Re-Monitor to operationalize PhotoMonitoring workflows. Its 2D imagery workflow supports both batch analyses of historical datasets and real-time monitoring projects that watch for newly acquired images. In a typical deployment, imagery is streamed from local storage, FTP/SFTP folders, cloud object storage, or camera feeds. Source folders are associated with a workspace, and each project stores acquisition metadata, schedule configuration, processing parameters, event status, and output artifacts.

The workflow begins with image acquisition and transfer. A fixed camera can acquire images automatically at a defined interval and transmit them through cellular, wired, or wireless communications. Aerial images acquired with a UAV campaign can be bulk loaded into IRIS platform right after flight completion. IRIS extracts or receives timestamps from filenames, metadata, or manual assignment, then generates event schedules by pairing images according to the monitoring objective. Change detection can use time-based pairing or recent-image validation. Displacement can use single-master, sliding-pair, or redundancy-based strategies depending on whether the user needs direct displacement from a baseline, incremental movement, or a globally consistent long-duration time series.

Each scheduled event is processed through a controlled pipeline. The pipeline loads master and slave images, applies optional preprocessing, coregisters the image pair, applies optional post-co-registration correction, computes change or displacement products, stores outputs, and updates event status. Results can be reviewed in browser-based viewers. Change-detection projects show before-after imagery, structural similarity maps, detected objects, validation status, labels, object sizes, and analytics such as counts, total changed area, largest object area, and spatial concentration. Displacement projects show vector fields, magnitude maps, component maps, AOI-based time series, and exports.

The architecture is designed for operational traceability. Schedules, events, image pairs, detected objects, displacement grids, displacement summaries, alerts, and worker states are stored in a database rather than only as loose files. Processing parameters are attached to projects and events so that an analyst can understand which configuration generated a result. Remote storage and object uploads are handled through storage services, and project outputs can be made available through browser viewers or PDF reports. This matters for transportation work because geohazard decisions often need an auditable trail: what image was processed, what threshold was applied, what result was delivered, and when.

IRIS also supports alert rules after a project has stable metrics. Change-detection alerts can be configured on object count, total changed area, maximum object area, or change intensity. Displacement alerts can be configured on cumulative displacement, incremental displacement, or velocity over all points or selected masks. Inactivity alerts can indicate when a camera or data

source stops sending new images. Alerts do not eliminate engineering review, but they provide a mechanism for prioritizing attention when many sites are monitored simultaneously.

TECHNICAL METHODS

Image preprocessing is used to reduce non-geotechnical differences before analysis. Typical controls include radiometric linearization, color constancy, local color correction, photometric normalization, denoising, band selection, contrast enhancement, and image-quality filtering. Contrast Limited Adaptive Histogram Equalization (CLAHE) can improve local contrast for feature tracking and displacement estimation [10]. Non-local means denoising can reduce random image noise while preserving edges [11]. Reference filtering can reject images affected by fog, rain, darkness, smoke, obstruction, poor exposure, or other acquisition problems before they enter a monitoring sequence. Suitable statistically based methods are employed to discard new images that significantly deviate from the validated image content in the database.

Co-registration is a critical step because small camera or UAV-viewpoint differences can create false changes. IRIS supports several matching approaches. Kanade-Lucas-Tomasi (KLT) tracking uses feature points and image pyramids to estimate motion between images [12, 13]. Dense Inverse Search (DIS) optical flow can support dense or elastic alignment where deformation is smooth or feature-based matching is unstable [14]. LAMMA-style multiscale template matching is used for robust local correlation under complex outdoor conditions. LightGlue-based matching is available for certain local tile-alignment workflows. RANSAC is used to estimate robust geometric transforms from matched correspondences while rejecting outliers [15]. Transformation models can include translation, affine, projective, elastic, or tile-affine blending, with masks used to constrain matching to stable areas where needed.

Change detection is performed by comparing a coregistered image pair and computing a structural change map. The primary change map is based on a modified implementation of the Structural Similarity Index Measure (SSIM), applied to the luminance channel, with configurable window size and component weights [16]. SSIM is useful because it compares local image structure rather than only pixel-by-pixel intensity differences. The resulting map highlights areas where image structure changed between the baseline and target image. After thresholding, IRIS then applies clusterization through connected component analysis in order to transform the raw change map into distinct clusters representing localized changes (Figure 1). An interpretable object inventory of changes within the monitored scenario is then created and stored for later access. Proper validation logic such as persistence thresholds, short-pair thresholds, merge distances, minimum object areas, and analysis masks are employed to reject outliers and false positives while ensuring the detection of real changes in the scene. Finally, an AI based classification stage is carried out to perform automatic labelling of all the changes detected within the field of view.

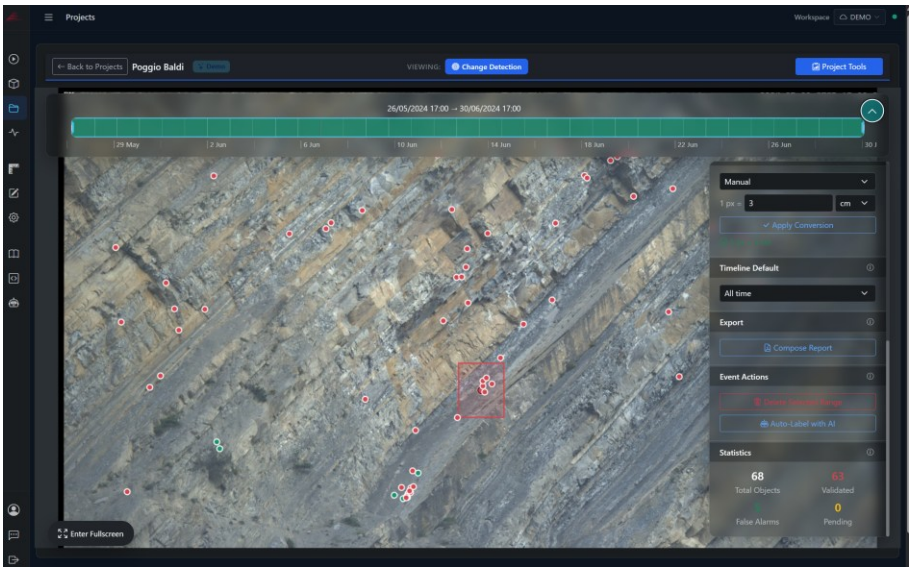

Figure 1: IRIS pixel-level change detection results for a high-unstable rock slope located in Italy, Poggio Baldi landslide. Each red dot represents a rock fall occurrence that was detected within the monitoring period (May-June 2024)

Displacement analysis estimates motion vectors over a regular image grid (Figure 2). Sparse KLT is suitable for fast measurement of small to moderate movements in textured scenes. Phase correlation is suitable for precise sub-pixel shifts within local windows and can use apodization, pyramid levels, and sub-pixel refinement. DIS optical flow is suitable for larger smooth deformation fields. LAMMA-style correlation is suitable for complex motion, large search ranges, or illumination variation. The displacement result contains grid coordinates, horizontal and vertical image displacement, quality indicators, and optional quality metrics such as peak ratio and signal-to-noise ratio. The knowledge of camera parameters such as sensor resolution, focal lens and the distance of the monitored target can be exploited to convert image displacement from pixel units to engineering units through the so-called ground sample distance (GSD). IRIS incorporates a friendly, easy to use tool (Figure 3), that allows users to quickly compute the resulting GSD given a specific camera setup and a distance to the target. A new, AI-based, monocular depth estimation algorithm is under development to determine the depth map of the scenario without the necessity to rely on a 3D model. This will allow agencies to quickly compute per-pixel ground resolution for monitored scenarios which can differ significantly from pixel to pixel in the case of strongly three-dimensional scenes.

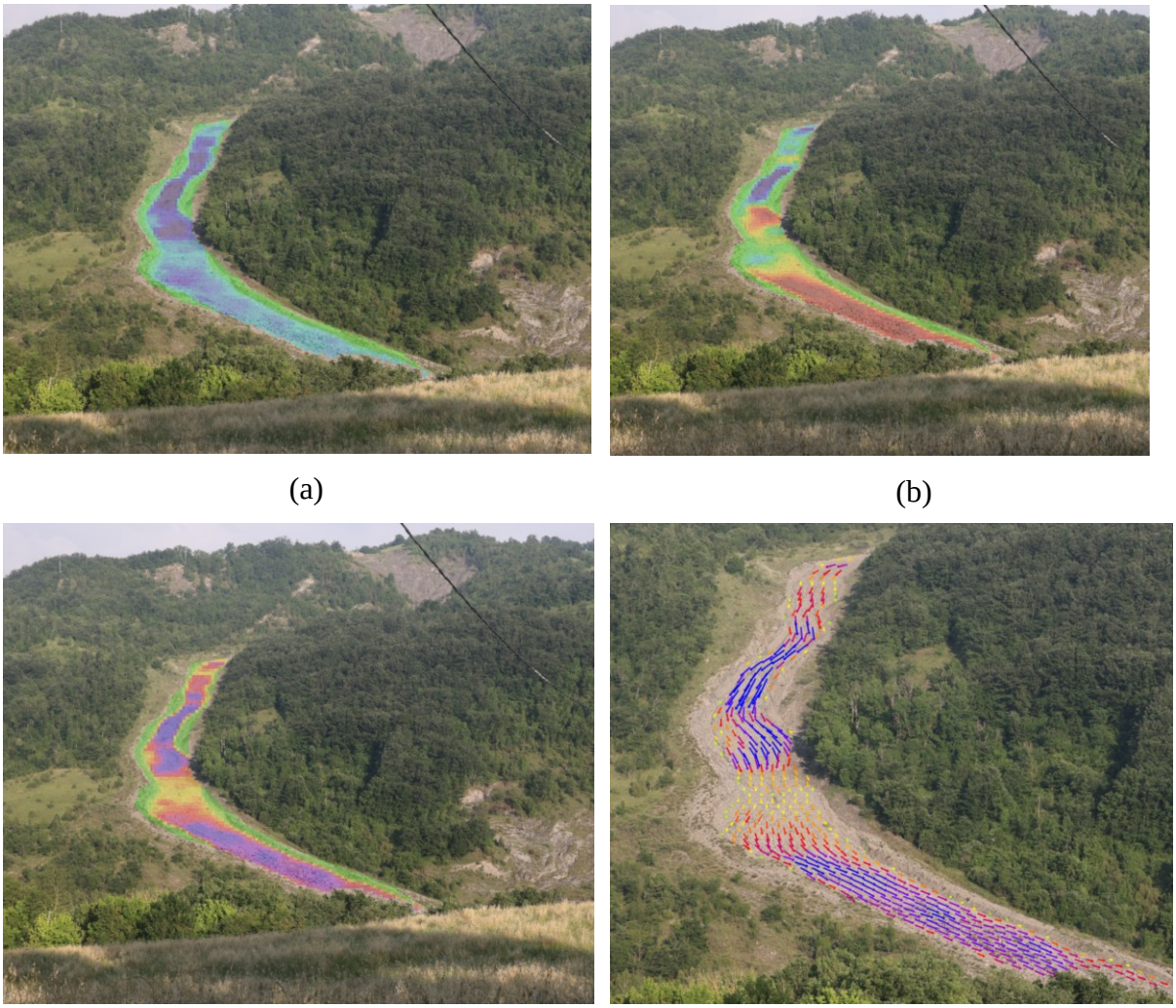

(a) (b)

(c) (d)

Figure 2: Displacement analysis results on the Biricuccola landslide (Italy) dataset, over the course of a one-month monitoring period in June 2024; the diagrams show 4 dense maps of displacements: (a) vertical component; (b) horizontal component; (c) magnitude; (d) quiver plot.

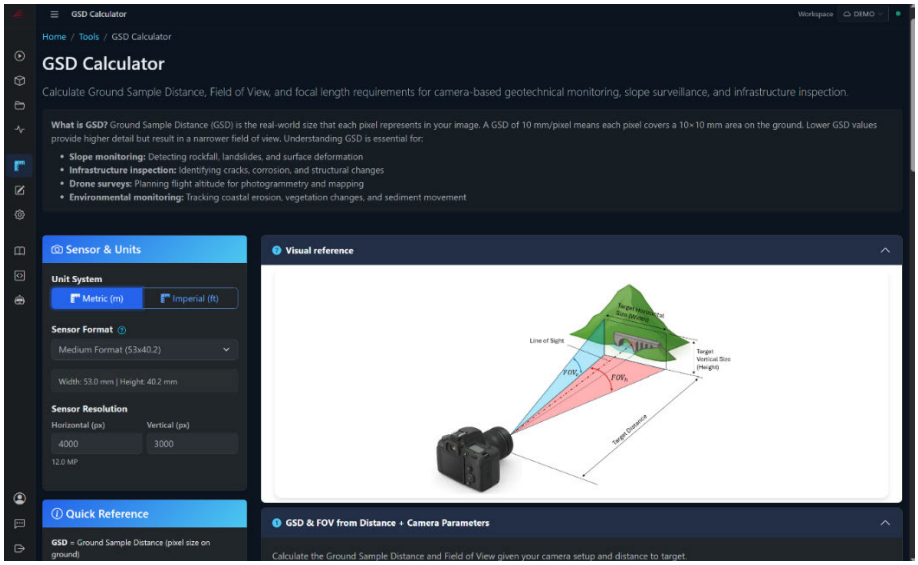

Figure 3: IRIS ground sample distance calculator.

Validation and QA/QC are treated as part of the measurement, not as an afterthought. Co-registration quality gates can warn or fail events when alignment is poor. Analysis masks can exclude sky, roads, water, vegetation, or traffic. Vegetation and shadow masks can suppress transient artifacts. Displacement validation can reject weak matches using match quality, peak ratio, signal-to-noise ratio, and median filtering. Change-detection validators can distinguish persistent changes from temporary shadows, vehicles, workers, or weather-related artifacts. The analyst remains responsible for tuning thresholds and reviewing results, but the pipeline provides a repeatable and documented basis for that review.

Although this paper focuses on image-based PhotoMonitoring, the same operational environment can support three-dimensional change detection from LiDAR or photogrammetric point clouds. M3C2 computes signed distances between point clouds along local surface normals with uncertainty-aware interpretation [17]. VoxFall-type workflows can segment discrete detachment or accumulation volumes. These 3D products are complementary to high frequency 2D imagery: 2D PhotoMonitoring can screen frequently and cheaply, while 3D surveys can provide volumetric measurements at lower temporal frequency or after significant events.

OPERATIONAL COMPARISON WITH CONVENTIONAL METHODS

PhotoMonitoring should be evaluated against the operational decision it supports. A robotic total station may be appropriate where a few reflectors can represent the critical deformation mode. A crackmeter or extensometer may be appropriate where a known discontinuity controls risk. LiDAR may be appropriate where volumetric change is required.

Field inspection remains necessary for geological interpretation and mitigation design. The role of PhotoMonitoring is to add low-cost temporal density and full-field visual coverage, especially where installing dense instrumentation is unsafe or uneconomic. Table 1 summarizes a comparison between PhotoMonitoring and other industry standard geohazard monitoring approaches, highlighting Typical strengths and shortcomings of each technology.

Approach	Typical Strength	Typical Limitation	Role in Highway Geohazard Management
Field inspection	Expert interpretation and direct observation	Intermittent, exposes staff to hazard	Essential for diagnosis and mitigation design
Point instrumentation	High precision at known critical locations	Sparse spatial coverage	Best for known cracks, blocks, or deformation zones
LiDAR/UAS survey	Dense spatial or 3D information	Campaign-based and higher processing burden	Best for volumetric change and detailed mapping
PhotoMonitoring	High-frequency, full-field, remotely reviewable imagery	Requires line of sight, image quality, and robust alignment. Monitoring stops at night unless infrared cameras are used.	Scalable screening and operational monitoring layer

Table 1: Operational comparison of geohazard monitoring approaches

CASE STUDY: STATE ROUTE 14 MILEPOST 69, WASHINGTON

In 2025, Re-Monitor and NHAZCA supported an application of image-based change detection for an unstable rock slope along State Route 14 in Washington, between approximately Milepost 68 and Milepost 69.5 with a monitored area of approximately 365,000 ft2 (Figure 4). The objective was to evaluate repeat-image processing for rockfall-related change detection and to provide rapid, interpretable information for a highway corridor affected by rock-slope hazards.

(a) (b)

Figure 4: Location (a) and extent (b) of the monitored site at SR14, MP69 WA (USA)

The initial dataset was acquired on March 10, 2025, using a DJI UAV flown on a pre-defined flight plan with RTK-corrected GNSS positioning and vertical sweep imaging of the rock face. This baseline survey was used to verify image quality and confirm suitability for Re-monitor's proprietary rockfall change-detection workflow. Based on the dataset review, Re-monitor provided WSDOT with acquisition guidance to improve repeatability between surveys and to maximize cross-epoch alignment and processing reliability. A second acquisition was carried out on March 25, 2025. Following the collection of the dataset, Re-Monitor immediately began to develop and test a dedicated co-registration algorithm to precisely align the March 10 and March 25 datasets. This was necessary because, due to different camera poses in the two flights, and due to inherent GPS precision limitation, corresponding images taken from two different aerial surveys showed a systematic shift in vertical and (to a lesser extent horizontal) directions as shown in Figure 5 (a)-(b). The results of the co-registration algorithms can be seen by comparing Figure 5 (c) and Figure 5 (d) showing precise alignment.

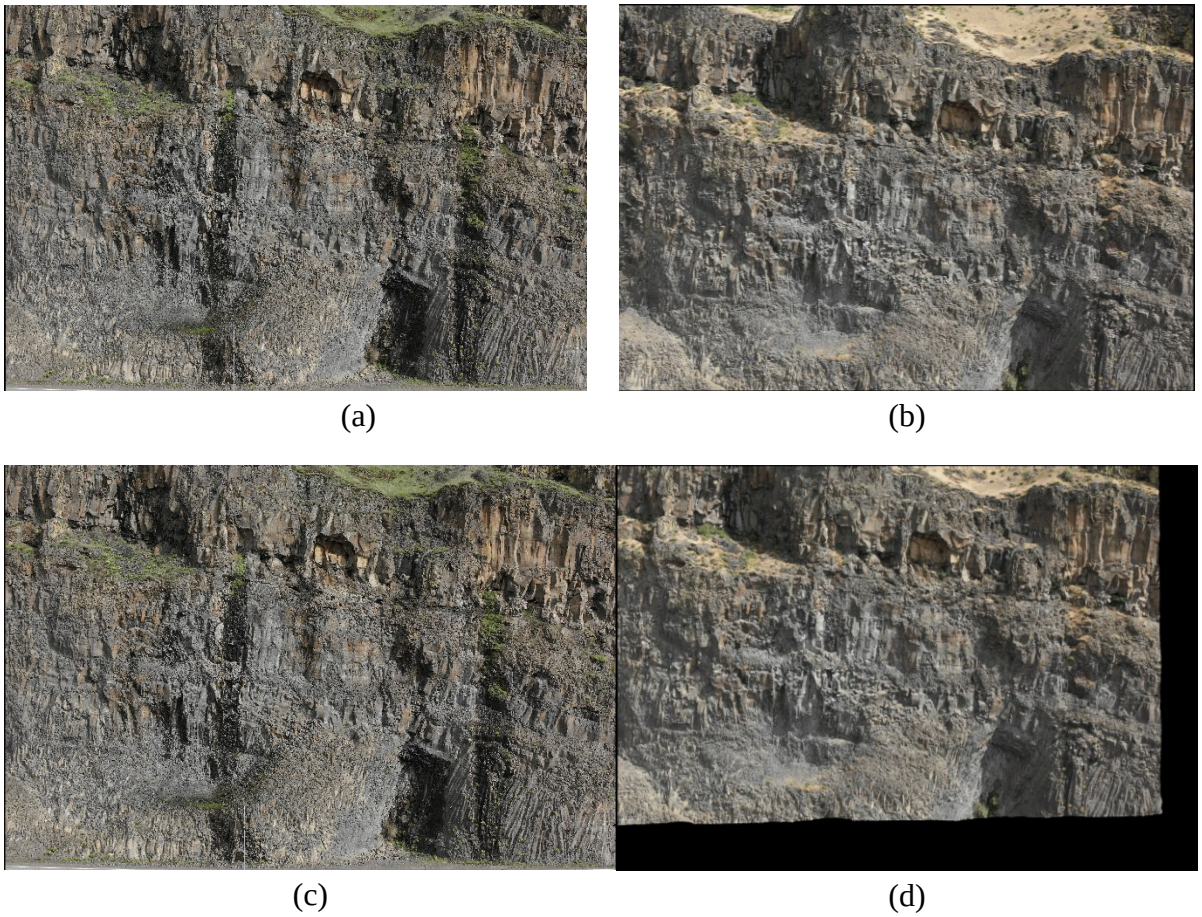

Figure 5: Effectiveness of IRIS co-registration algorithm tested on a dataset of SR14, MP69, WA. Primary images (a-c); Secondary image raw (b); Secondary image coregistered (d);

Additional UAV acquisitions in April were used to refine the co-registration approach and site-specific change-detection parameters. A May 20, 2025, dataset was then compared against the March 25 survey, and a rockfall-related change was detected using a structural similarity change map (Figure 6). This part of the project demonstrated the importance of robust image alignment for UAV-based monitoring: even with RTK positioning and repeated flight planning, image-to-image shifts can dominate the signal if not corrected before analysis.

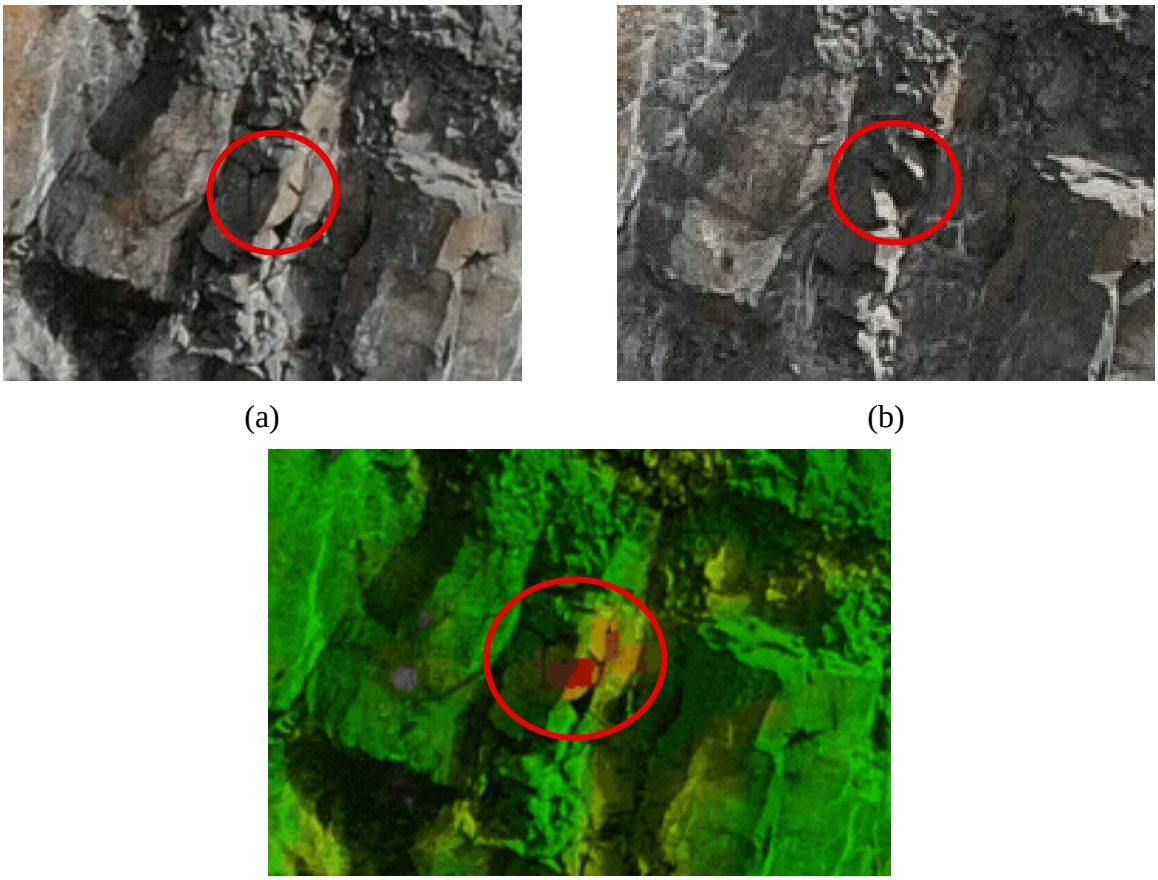

(a) (b)

(c)

Figure 6: Example of rock fall detection in the SR14, MP69 dataset: (a) March 25, 2025, dataset, pre-event; (b) May 20, 2025, dataset, post-event; (c) Structural Similarity index result map with red highlights on detected change.

The operational value of the workflow became more evident during a post-wildfire period. A wildfire began on July 18, 2025, producing elevated rockfall concern and an extended highway closure. WSDOT contacted Re-Monitor representatives on July 21, 2025, to request urgent analysis of the Milepost 69 rock slope. An emergency UAV flight was conducted on July 22, 2025, but the dataset was severely degraded by active smoke, strong winds, strong lighting differences, and the fact that the UAV did not follow the same flight plan. The images could not support meaningful quantitative results. A follow-up flight was scheduled and completed on July 26, 2025.

Processing began immediately after the July 26 imagery was shared. Preliminary change-detection results were delivered through a tailored web platform by July 28, 2025, and final results were delivered by July 30, 2025. The output provided WSDOT personnel with quantifiable information on the extent of changes in the monitored area. The case illustrates a realistic operational condition: emergency data are not always usable, repeatability matters, and a monitoring service must include both technical algorithms and acquisition feedback. It also

shows how a web-delivered PhotoMonitoring workflow can provide rapid post-event information without requiring repeated personnel access to an unstable rock face.

DISCUSSION

For transportation agencies, the most important benefit of PhotoMonitoring is not a single algorithmic output; it is the creation of a continuous, reviewable record of site behavior. High-frequency image acquisition can capture the timing of rockfall, debris deposition, slope movement, water-flow changes, construction disturbance, or maintenance activity. The same dataset can support engineering interpretation, public-agency documentation, contractor coordination, and post-event review. When multiple sites are monitored, automated screening and alerts can help prioritize limited geotechnical staff time.

PhotoMonitoring is particularly relevant to post-wildfire corridors. Wildfire can remove vegetation, alter soil and rock-slope response, increase runoff efficiency, and expose transportation corridors to rockfall and debris-flow hazards. The highest-risk periods may occur during short rainfall windows when field access is dangerous and agencies need rapid information. A fixed-camera system can provide near-real-time observation during those windows, while repeat UAV surveys can document broader slopes after storms or closures. The ability to compare images before and after a trigger event is valuable even when the final decision still depends on field inspection.

The technology is also relevant to risk management because it supports scalable triage. Not every rock slope can justify a dense network of contact instruments, radar, LiDAR, and full-time observation. However, many slopes can justify a camera, a communications link, and automated change screening. Sites that show repeated change or accelerating displacement can then be escalated to more detailed geotechnical investigation or higher-cost instrumentation. Conversely, sites showing no significant change over a defined period can be documented and reviewed with less field exposure.

The main technical constraints are known and manageable. Cameras require line of sight and must be installed where the expected ground sample distance is compatible with the monitoring objective. Outdoor imagery is affected by shadows, rain, snow, fog, smoke, vegetation, and traffic. UAV surveys require repeatable flight geometry and sufficient image quality. Algorithms require masks, validation thresholds, and QA/QC review to avoid false positives. These constraints should be stated clearly in procurement and monitoring plans. The system is most effective when acquisition design, processing configuration, and decision thresholds are developed together rather than treated as independent tasks.

The SR14 MP69 application demonstrates the practical nature of these constraints. The July 22 post-wildfire flight was not suitable for quantitative analysis, and the correct response was not to force an unreliable result, but to identify the problem, adjust acquisition, and process

the July 26 follow-up data. This is an important point for academic and operational users: automated monitoring must include mechanisms for rejecting poor data and documenting uncertainty. A false sense of precision is more dangerous than a clearly stated data-quality limitation.

CONCLUSIONS

PhotoMonitoring provides transportation agencies with a cost-effective and scalable remote-sensing layer for geohazard monitoring. By combining repeat imagery, automated preprocessing, robust co-registration, SSIM-based change detection, displacement analysis, validation, web visualization, and alerts, the method can transform cameras and repeat UAV surveys into operational monitoring tools. Its advantages are strongest where agencies need frequent observations, broad spatial coverage, reduced field exposure, and rapid review of high-risk assets.

The method is not a substitute for geotechnical engineering judgment, field inspection, or high-precision instrumentation where those are required. Instead, it fills a practical gap between sparse manual observation and expensive dense instrumentation. It can support highway rockfall monitoring, post-wildfire debris-flow and rock-slope response, construction-related deformation monitoring, tunnel convergence documentation, and long-term risk management for unstable slopes.

The SR14 MP69 application shows how image-based change detection can be used in a U.S. highway setting to process repeat UAV imagery, detect rockfall-related change, and deliver rapid post-wildfire results through a web platform. As transportation agencies face increasing pressure to manage aging infrastructure, climate-amplified geohazards, and limited inspection resources, PhotoMonitoring offers a practical approach for increasing temporal awareness and improving the evidentiary basis for asset-management decisions.

REFERENCES

[1] "Collapse of I-35W Highway Bridge, Minneapolis, Minnesota, August 1, 2007," National Transportation Safety Board, Washington, D.C., 2008.

[2] "Pedestrian Bridge Collapse Over SW 8th Street, Miami, Florida, March 15, 2018," National Transportation Safety Board, Washington, D.C., 2019.

[3] "Landslide Hazards Program," 2026. [Online]. Available: https://www.usgs.gov/programs/landslide-hazards. [Accessed 10 7 2026].

[4] "The 22 March 2014 Oso Landslide, Snohomish County, Washington," Geotechnical Extreme Events Reconnaissance Association, 2014.

[5] "I-70 Glenwood Canyon Safety Closures and post-wildfire debris-flow response materials," 2021. [Online]. Available: https://www.codot.gov. [Accessed 10 7 2026].

[6] "Relazione della Commissione Ispettiva Ministeriale sul crollo del viadotto Polcevera," Ministry of Infrastructure and Transport, Rome, Italy, 2018.

[7] A. Molinari, C. A. Stefanini, A. Cosentino, G. Mastrantoni, G. M. Marmoni, G. Santicchia, I. Farmakis and P. Mazzanti, "Multi-sensor anatomy of the March 2025 landslide sequence in Poggio Baldi (Northern Apennines, Italy)," *Landslides*, 2026.

[8] C. A. Stefanini, G. M. Marmoni, A. Molinari, G. Santicchia, A. Cosentino and P. Mazzanti, "Systematic Application of PhotoMonitoring for Landslide Surveillance in Italy: First Results from the Geosciences IR Project," *Italian Journal of Engineering Geology and Environment*, no. Special Issue 1, pp. 227-237, 2026.

[9] "Statement of Qualifications - Packet A, Enhanced Monitoring on High-Risk Unstable Slopes," Submitted to Washington State Department of Transportation, 2026.

[10] K. Zuiderveld, "Contrast Limited Adaptive Histogram Equalization," in *Graphics Gems IV*, San Diego, California, Academic Press, 1994, pp. 474-485.

[11] A. Buades, B. Coll and J. M. Morel, "A Non-Local Algorithm for Image Denoising," in *Proceedings of the IEEE Conference on Computer Vision and Pattern Recognition*, 2005.

[12] B. D. Lucas and T. Kanade, "An Iterative Image Registration Technique with an Application to Stereo Vision," in *Proceedings of Imaging Understanding Workshop*, 1981.

[13] J. Shi and C. Tomasi, "Good Features to Track," in *Proceedings of the IEEE Conference on Computer Vision and Pattern Recognition*, 1994.

[14] T. Kroeger, R. Timofte, D. Dai and L. Van Gool, "Fast Optical Flow Using Dense Inverse Search," in *Proceedings of the European Conference on Computer Vision*, 2016.

[15] M. A. Fischler and R. C. Bolles, "Random Sample Consensus: A Paradigm for Model Fitting with Applications to Image Analysis and Automated Cartography," *Communications of the ACM*, vol. 24, no. 6, pp. 381-395, 1981.

[16] Z. Wang, A. C. Bovik, H. R. Sheikh and E. P. Simoncelli, "Image Quality Assessment: From Error Visibility to Structural Similarity," *IEEE Transactions on Image Processing*, vol. 13, no. 4, pp. 600-612, 2004.

[17] D. Lague, N. Brodu and J. Leroux, "Accurate 3D Comparison of Complex Topography with Terrestrial Laser Scanner: Application to the Rangitikei Canyon, New Zealand," *ISPRS Journal of Photogrammetry and Remote Sensing*, vol. 82, pp. 10-26, 2013.

[18] "IRIS 2D Analysis Operator Manual, Version 2.0," NHAZCA S.r.l., 2026.

[19] "Statement of Qualifications - Packet B, Change Detection Analysis for Geohazard Monitoring," Submitted to Washington State Department of Transportation, 2026.

[20] B. D. Lucas and T. Kanade, "An Iterative Image Registration Technique with an Application to Stereo Vision," in *Proceedings of the 7th International Joint Conference on Artificial Intelligence*, Vancouver, Canada, 1981.

27. ReMi® Seismic Surveys for Non-Intrusive ASCE 7-22 Compliant Site Class, Rippability, Fault Location, and Design

John N. Louie
Terēan
450 Sinclair St.
Reno, NV 89503
(775) 674-9525
jlouie@terean.com

Alison Starr
Terēan
450 Sinclair St.
Reno, NV 89503
(775) 233-0845
astarr@terean.com

Bill Honjas
Terēan
450 Sinclair St.
Reno, NV 89503
(775) 391-7222
bhonjas@terean.com

Prepared for the 75th Highway Geology Symposium, September, 2026

Acknowledgements

The authors would like to thank the following individuals and entities for contributing the examples shown in: Fig. 3 – Salvador Lazcano Díaz del Castillo of Suelo-Estructura; Fig. 4 – Steve Wells of Landmark Testing; Fig. 5 – Justin Stratton of Southwest Geotechnical; Fig. 6 – Achievement Engineering; Fig. 7 – Crawford Incorporated; and Fig. 8 – Christian Kropf of Truckee Meadows Water Authority.

Disclaimer

Statements and views presented in this paper are strictly those of the author(s), and do not necessarily reflect positions held by their affiliations, the Highway Geology Symposium (HGS), or others acknowledged above. The mention of trade names for commercial products does not imply the approval or endorsement by HGS.

Copyright Notice

Copyright © 2026 Highway Geology Symposium (HGS)

All Rights Reserved. Printed in the United States of America. No part of this publication may be reproduced or copied in any form or by any means – graphic, electronic, or mechanical, including photocopying, taping, or information storage and retrieval systems – without prior written permission of the HGS. This excludes the original author(s).

ABSTRACT

ASCE/SEI Standard 7-22, Chapter 20 describes new standards for determining seismic site class that encourage geophysical surveying rather than cone penetrometer or standard penetration testing. Invasive methods can fail to achieve compliance because of refusal or difficulty for intrusive methods to access sites. For non-intrusive geophysical surveying to achieve code compliance it is important for geotechnical engineers to employ geophysical survey methods effective at determining Vs30. Without Vs30 measurements, taking the default seismic site class may lead to over-design of infrastructure, inflated construction costs and extended project timelines.

Code allowance of seismic surface-wave-arrays offers engineers the opportunity to perform one geophysical survey yielding Vs30 and site class along with a more comprehensive site investigation including assessments of landslide and liquefaction potential, rippability, depth to bedrock, fault location, and even P-wave velocity and Poisson's ratio. ASCE 7-22 compliant surface-wave surveys, when acquired, processed, and interpreted with Terēan ReMi® systems and software, will provide this full range of results while saving projects cost and time. Most sites require less than one hour to complete. Many case histories at scales from 15 ft to 3000 ft (5 m to 1000 m) serve to demonstrate these rapid and comprehensive results. Simpler geophysical surveys with more comprehensive results allow engineers to more efficiently complete geotechnical assessments, speeding infrastructure improvements.

INTRODUCTION

ASCE/SEI Standard 7-22, Chapter 20 (*1*) described new standards for determining seismic site class. Incorporated into the International Building Code (IBC) in 2024, this model code has so far been adopted by 49 U.S. states and the District of Columbia (*2*). Among many other changes from prior standards, ASCE 7-22 Chapter 20 calls for direct geophysical measurement of the shear-wave velocity property of rocks and soils at a building site, to a depth of 100 feet (30 meters). The standard limits the value of cone penetrometer or standard penetration testing for determining the seismic site class designation.

Vs30 and site class

The velocity profile from the surface to 100 ft (30 m) depth is averaged according to the equations in Chapter 20 to a site-specific shear-wave seismic velocity average referred as "Vs100" or "Vs30", depending on whether a project is using feet or meters, respectively. Here we will use "Vs30 "for compatibility with much of the academic literature. The value of the measured Vs30 determines the seismic site class designation according to Table 20.2-1 in Chapter 20 (*1, p. 226*). Site class designations range from a relatively safe class A for "hard rock" with a Vs30 exceeding 5000 ft/sec (1524 m/sec), through classes B, BC, C, CD, D, DE, E, to the softest and most hazardous class F for a Vs30 of less than 500 ft/sec (152 m/sec). The site-specific class designation guides appropriate earthquake-resistant building design.

Geophysical methods for measuring the shear-wave velocity property of rocks and soils can be classed as invasive or non-invasive. Invasive methods such as seismic cone penetrometer (SCPT) profiles require a borehole or tool pushing to a depth of 100 ft (30 m). Invasive methods can fail to achieve compliance because of refusal above 100 ft depth, or difficulty for heavy drill or penetrometer machinery to access sites.

The non-invasive geophysical methods for determining Vs30 do not require subsurface access. Instead, they use arrays of seismic sensors on the ground surface to time the passage of seismic waves horizontally across the site. Among geotechnical practitioners conducting seismic site assessments for ASCE 7-22 compliance, the two most popular of the non-invasive survey methods are multichannel analysis of surface waves (MASW), and Terēan ReMi® technology. Both MASW and ReMi use linear arrays of seismic sensors at least 200 ft (60 m) long to assure constraint of shear-wave velocities to depths exceeding 100 ft (30 m). As well, linear-array surveys must include sources of seismic energy known to be located along the line of the array, to assure ASCE 7-22 compliance.

Without such Vs30 measurements at every building site, the ASCE 7-22 guidelines (*1*) put new restrictions on how site class may be assessed. In most localities, a builder can accept a default site class of D without doing a compliant Vs30 measurement. Class D assumes that earthquake shaking will be substantially amplified relative to a site of average strength- a soft, deep soil that must be mitigated by designing large and strong foundations as well as strengthening the entire building structure. Taking the default seismic site class may lead to over-design of infrastructure, inflated construction costs and extended project timelines. A related problem arises when invasive methods hit refusal above 100 ft (30 m) depth. Without measured

shear-wave velocity all the way to 100 ft (30 m) depth, the Vs30 must be computed by extending the velocity of the soft layer just above refusal to the full 100 ft (30 m) depth. This procedure usually results in a Vs30 estimate substantially lower in value and more hazardous than the actual measured Vs30 (since the 100 ft [30 m] average would include the strong refusing layer).

Terēan ReMi® technology

Terēan's ReMi seismic survey technology inherits and improves on the refraction microtremor research by Louie since 1998. First published in 2001 (*3*), refraction microtremor is included in the 2022 *Consortium of Organizations for Strong Motion Observation Systems (COSMOS) International Guidelines for Applying Noninvasive Geophysical Techniques to Characterize Seismic Site Conditions* (*4*). The Guidelines paper sets out pitfalls and best practices in refraction microtremor surveying, as well as recent developments in refraction microtremor applications. This paper provides an update to the Guidelines paper, based on broadening uptake of Terēan ReMi® technology since 2022, with new case histories.

For more than 20 years, refraction microtremor surveys have proven to reliably yield measurements of subsurface shear-wave velocity to depths exceeding 300 ft (100 m). The U.S. Geological Survey (USGS) conducted a blind test where they recorded refraction microtremor and multichannel analysis of surface waves (MASW) surveys across boreholes in Santa Clara Valley, Calif. (*5*). All results of blind analysis by the USGS as well as by practitioners of both methods showed effective agreement with the suspension logger Vs results from deep boreholes (Figure 1). The bore logs show wide swings from very rapid variations in Vs that cannot be corroborated. By time-averaging (slowness averaging) in depth through the velocities shown in the invasive logs produces a close match to the non-invasive surface survey velocities. The refraction microtremor analyses incorporated dispersion data from low-frequency (<5 Hz) ambient seismic vibrations as well as active sources of seismic energy at higher frequencies, achieving velocity resolution to greater depth than some of the MASW analyses (*5*).

In 2003 an early Vs transect conducted refraction microtremor surveys at more than 200 sites following the San Gabriel River 60 km from the mountains, across the Los Angeles Basin urban area, to the ocean (*6*). Figure 2 compares the three of the 60 measured sites that are within 600 m distance of the ROSRINE Pico Rivera suspension shear-wave velocity log. The nearest (<200 m) of the velocity profiles to the well, in green, shows a close match to the log velocities. The variation between the profiles, due to variations in ground properties, is greater than the mismatch between the nearest refraction microtremor profile, and the well log.

Building-code compliance

Terēan's ReMi® technology greatly expands the capabilities of refraction microtremor surveys. More than 80 licensees are actively employing the technology today around the globe. The large majority of these licensees employ ReMi to rapidly measure Vs30 for compliance with ASCE 7-22 (*1*) and thus local building codes. The California Geological Survey (CGS) among many other agencies accepts ReMi determinations of Vs30 and seismic site class in permitting the design of critical facilities such as schools and hospitals. However, CGS and other agencies enforce strict compliance standards for ReMi measurements as well as other determinations.

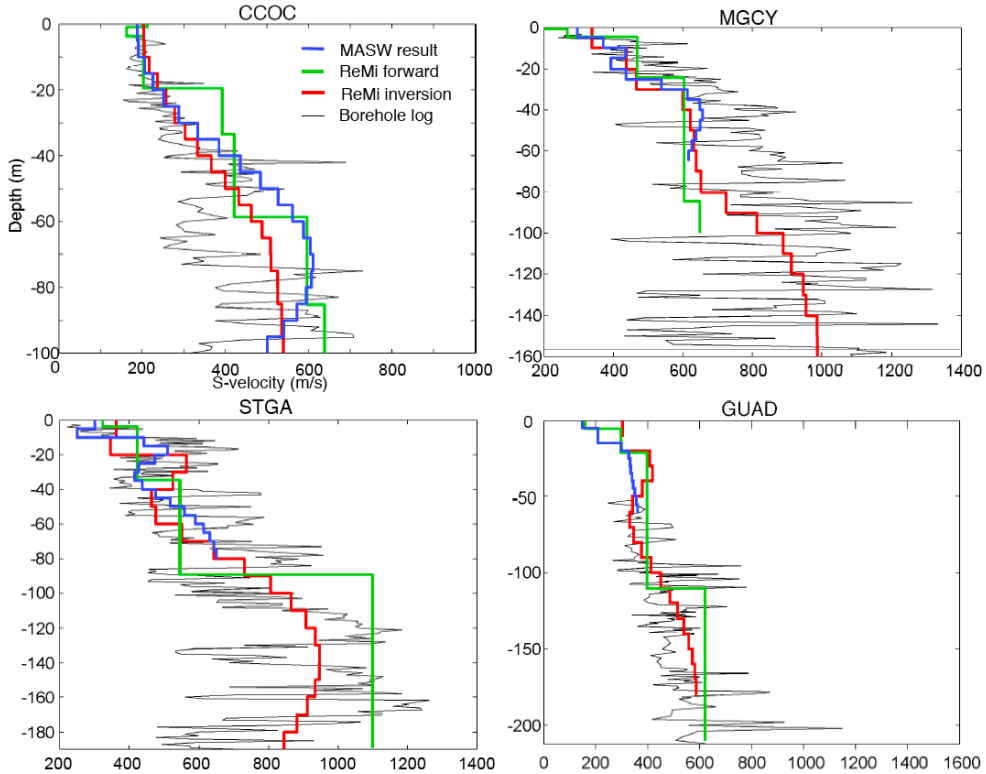

Figure 1 – Blind comparison of refraction microtremor profiles to MASW and logs (*5*)

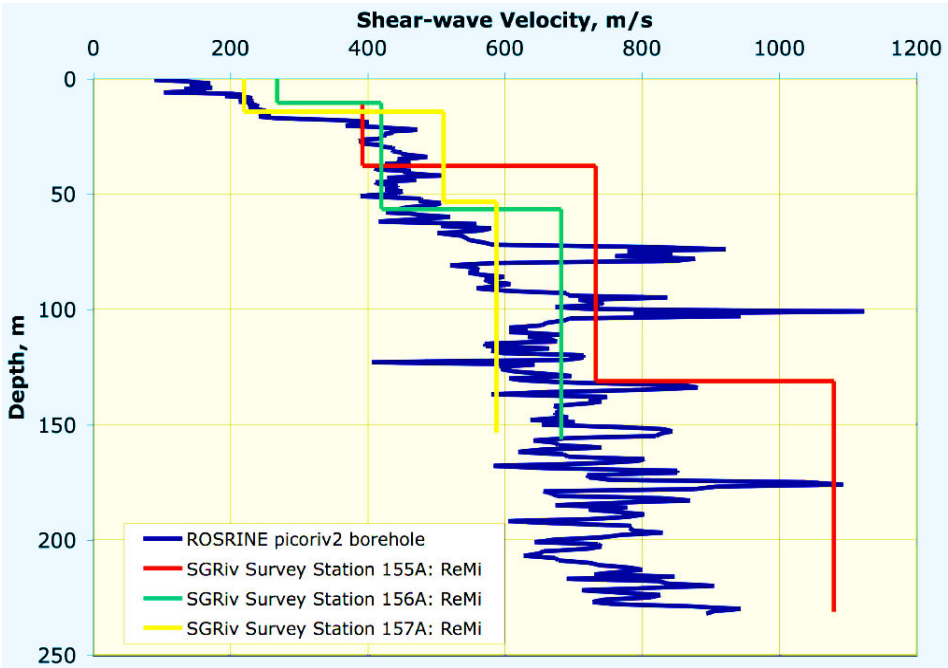

Figure 2 – Blind comparison of refraction microtremor profiles to a deep Vs log (*6*)

Terēan has worked extensively with CGS and others to ensure our technologies enable high-quality, building-code compliant results. To this end, we advocate that the following language be inserted into the specifications on measurement of shear-wave velocity within the 2026 National Earthquake Hazards Reduction Program (NEHRP) Provisions, developed by the Federal Emergency Management Agency and the Building Seismic Safety Council:

"Field measurements to develop a shear wave velocity profile should be performed using reliable techniques at the site or from measurements in similar soils in the site vicinity. Methods based on a single-direction linear array of surface instruments must include active sources of seismic energy located on the line of the array for the derivation of shear wave velocity profiles."

This language will effectively bring forward into the NEHRP Provisions some of the critical survey specifications recently listed by Louie and others (*4*). Clear guidance to practitioners is important in assuring effective compliance with building codes adopted from ASCE model codes (*1*), incorporating the NEHRP Provisions. Terēan provides our licensees with tools such as ReMi QAQC™ software, which evaluates data quality together with survey parameters live as practitioners collect array data, so they leave every site assured that they have high-quality, compliant results.

COMMON ADDITIONAL USES OF ReMi® SEISMIC SURVEYS

Terēan clients are actively using ReMi® surveys and solutions for much more than measuring Vs100 (Vs30 meters) for determining seismic site class. In the process of deriving Vs100, ReMi efficiently determines shear-wave velocity profiles from the surface to target depths of interest. Each profile determined is located at the midpoint of the array or sub-array of seismic sensors. Consistent with the *Guidelines* paper (*4*), each profile has a location accuracy equivalent to the sensor spacing along the array. The depth of features within each profile is constrained to an accuracy of 10% of their depth.

Most Terēan clients are deploying their sensor arrays in a manner that allows *tomography*, that is, determining a full two-dimensional subsurface cross section of the shear-wave velocity properties below at least the center half of the array length. These Vs sections are the result of Terēan ReMi 2dS™ software and services. The 2dS sections show layers of rock and soil and the boundaries between geotechnical units in the subsurface. Since the shear-wave velocity property of rocks is closely related primarily to bulk static and linear rigidity (G_{max}), with effectively secondary correction for density variations, ReMi 2dS™ sections identify geotechnical units on the basis of their bulk stiffness.

Depth to bedrock

For one example out of many, Suelo-Estructura, an engineering firm in Guadalajara, Jalisco, Mexico used ReMi 2dS™ software to determine the depth and thickness of layers and bedrock topography. The site was in the Mexico City vicinity, expected to be thick soil over weathered basalt flows. A deployment of 24 seismic sensors spaced at 16 ft (5 m) for less than a half hour was needed to record the array data. Figure 3 shows the cross section produced after

data analysis in 2dS. The section shows shear-wave velocities over about 200 ft (60 m) distance and to 100 ft (30 m) depth.

The section shows four main geotechnical units and their variations in thickness. At the surface are soft soils having Vs less than 850 ft/s (260 m/s) in purple. Underlying the soil is an interval of more compacted sediment 33-50 ft (10-15 m) thick with an intermediate Vs of 850-1200 ft/s (260-360 m/s) in blue. Below is a transition in stiffness 15-33 ft (5-10 m) thick from a Vs of 1200 ft/s (360 m/s) to the weathered basalt with a Vs above 1800 ft/s (550 m/s) in green and yellow. The basalt layer, which forms the local engineering bedrock in orange and red, is found at depths below the surface of 72-92 ft (22-28 m). Determining such variations in subsurface bedrock topography are required for rippability, determining overburden removal costs, and placement of engineered structures.

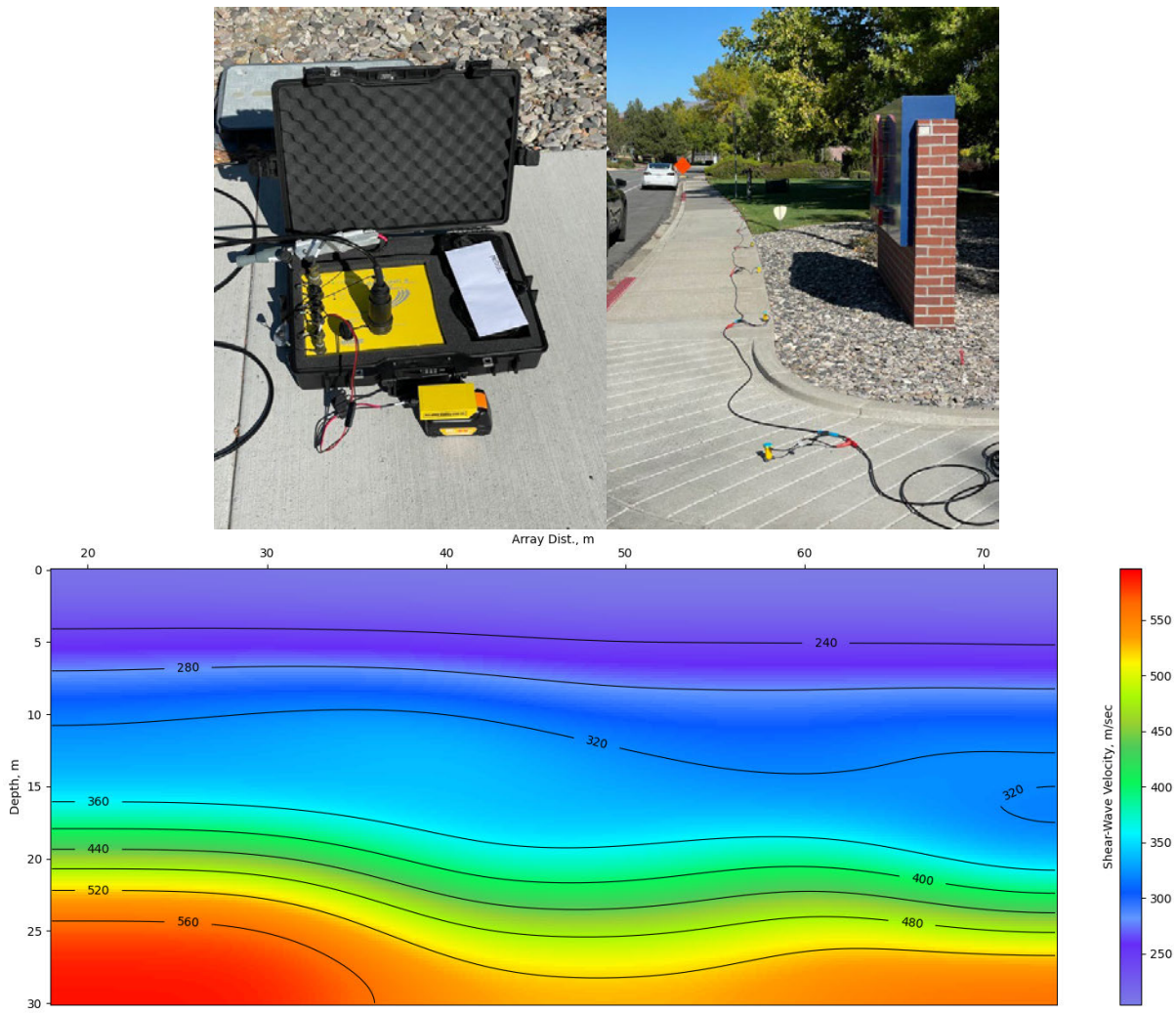

Figure 3 – (above) Photos of a ReMi®DAQ system deployed at an urban field site. (below) ReMi 2dS™ section measured by Suelo-Estructura near Mexico City (no V.E.).

Rippability

For just one of many examples, Landmark Testing conducted a ReMi 2dS™ survey to prepare for the design and construction of an accessible trail at Snow Canyon State Park in southwest Utah. Figure 4 shows the resulting 2dS section. Terēan 2dS™ software and solutions include proprietary technology that allows practitioners to determine rippability of subsurface materials using shear-wave velocities. One concern was that the 20 ft (6 m) topographic ledge would prove to be hard rock resistant to ripping and could have to be blasted to create a level, accessible trail.

The original Caterpillar Handbook of Ripping (*7*) gives rock and soil rippability as a function of seismic P- or compressional-wave velocity only. Review of ASCE-published literature on the relations between shear-wave and P-wave velocities allowed creation of rippability ranges based on Vs. In this case, the result reveals the subsurface materials to be rippable to marginally rippable in the upper 30 ft (10 m), having shear-wave velocities below 3000 ft/s (900 m/s). The topographic ledge proved to be weathered and fractured to a degree that permitted ripping. This result was verified during the trail construction process.

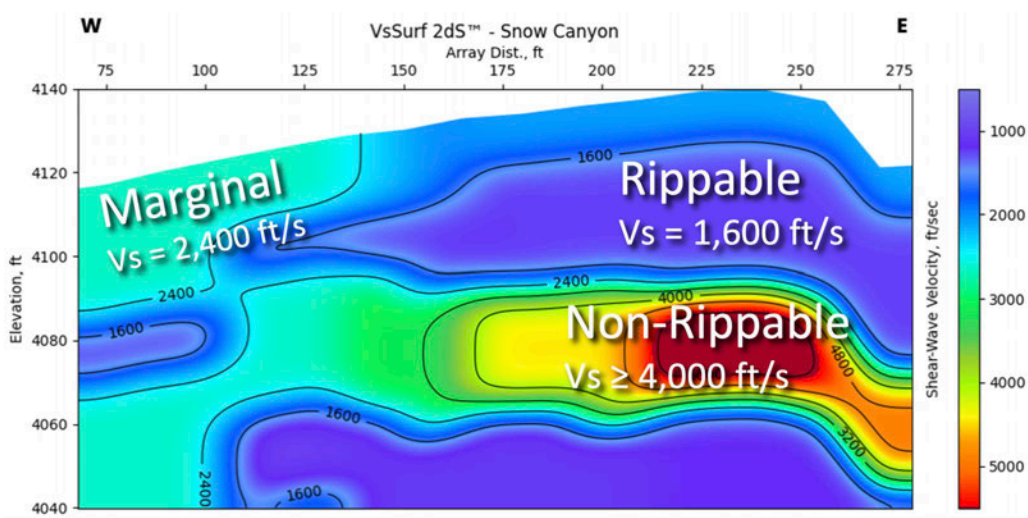

Figure 4 – ReMi 2dS™ section for Utah trail-construction rippability assessment (no V.E.)

Earthquake-fault location

Many Terēan licensees are conducting ReMi 2dS™ surveys for the purpose of locating earthquake fault lines. 2dS sections mapping subsurface changes in Vs can identify vertical offsets and discontinuities that occur in geological and geotechnical units in the presence of tectonic faulting processes. Such discontinuities, once recognized and located, can then assist the efficient planning of further paleoseismic investigations such as boring and trenching. Paleoseismic investigation is required to confirm all faulting parameters such as activity, recency, offset rate, date of last earthquake, and slip direction.

Normal and reverse faulting result in consistent vertical stratigraphic offsets across fault traces that 2dS sections can track. The dip of candidate faults, at least within the section imaged, is a frequent result of 2dS surveys. Multiple 2dS lines crossing a fault can allow interpretation of

fault strike in three dimensions. Stratigraphic offsets due to normal or reverse faulting should increase with depth, or stay the same, down into the section.

Strike-slip faults, on the other hand, may lead to less consistent offsets, or no vertical offsets at all. Locating a strike slip fault trace with ReMi 2dS™ requires recognizing such features as flower structures, low-velocity shattered zones, or offsets of channels or alluvial fan lobes in three dimensions. Such recognition tends to be most likely when profiling for more precise locations of fault traces long recognized and well-characterized nearby. In this way, ReMi 2dS™ surveys extend paleoseismic knowledge outward away from the (usually) relatively sparse sites of intensive investigations.

A multifamily housing developer commissioned Southwest Geotechnical to locate faults across a building site in the Las Vegas Metro Area of Nevada. Minor Quaternary fault traces appear across the site in long-standing maps and databases, such as from the U.S. Geological Survey (9). Southwest deployed six arrays of seismic sensors 760 ft (230 m) long, across the suspected fault traces. Array layout, recording, and pickup took Southwest's crew less than 90 minutes per line.

Figure 5 shows the 2dS section of shear-wave velocity structure resulting from one of the six lines. The longer arrays allowed the section to show structure and stratigraphy to a depth of 120 ft (37 m). Calcified, caliche-cemented soils form the stiff layers colored red, yellow, and green, with shear-wave velocities above 1200 ft/s (360 m/s). The lower-velocity, softer layers are in blue: artificial fill at the surface on the left side, and a clay layer consistently underlying the caliche. Near the center of the section, the stratigraphic package of the caliche layer with its underlying clay is consistently and vertically offset in a normal sense by 30 ft (9 m), down to the northwest. The 2dS section allowed location of the discontinuity, possibly the fault trace at the surface, to an accuracy of 33 ft (10 m). In this case, the likely fault proved to be, within the confines of this accuracy, just where prior mapping (*8*) had put it.

Some of the six lines suggested definite and consistent discontinuities that are likely the mapped faults but at locations displaced by 100 ft (30 m) from the mapped trace (*8*). Other lines produced sections that showed anastomosing and inconsistently layered caliche and do not suggest faulting. Southwest Geotechnical followed up with targeted drilling to confirm fault locations more accurately than 33 ft (10 m). The developer is using this information to plan building on the site, with the required setbacks from the possibly active normal faults.

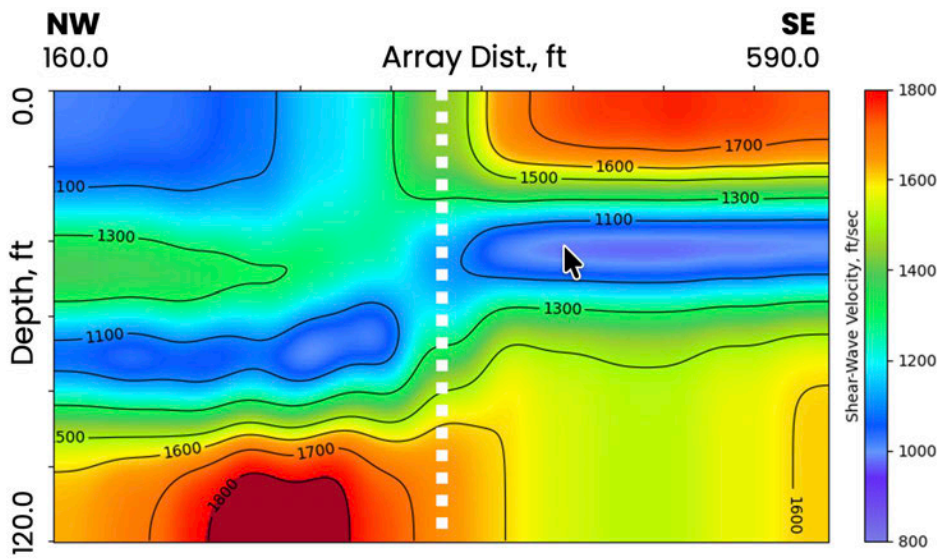

Figure 5 – ReMi 2dS™ section showing a minor fault in Las Vegas, Nevada (V.E.=2x)

Terēan assisted Achievement Engineering to locate the Calaveras fault in Pleasanton, California. The Calaveras fault is a long and very active strike-slip fault that is one of the few principal components of the Pacific-North America plate boundary in Northern California (*9*). The owner of a plot of land across the mapped fault trace wanted to develop additional housing on the plot. However, keeping new buildings out of the full 100 ft (30 m) width of the Alquist-Priolo default exclusion zone under California law would leave too little room for further development. The owner engaged Achievement to pinpoint the fault more accurately. Alameda County would allow building within the Alquist-Priolo zone, so long as the fault could be accurately located.

Achievement deployed three ReMi 2dS™ arrays, each 230 ft (70 m) long of industry-standard ReMiDAQ® recording of 24 seismic sensors. The ReMiDAQ® solution has Terēan's ReMi QAQC™ software built in, assuring rapid recording of high-quality array data. Each array took only 30 min to deploy, record for 15 minutes, and pick up. On-line active-source hammer blows were included, for full code compliance. Figure 6 shows one of the sections. The clear lateral discontinuities locate this major strike-slip fault with an accuracy of 10-15 ft (3-5 m). Alameda County was the permitting authority for this development, and they allowed planning and construction to proceed, given the fault location at this level of precision. Further paleoseismic study at this site, if undertaken for research purposes, could be efficiently targeted at this site as a result.

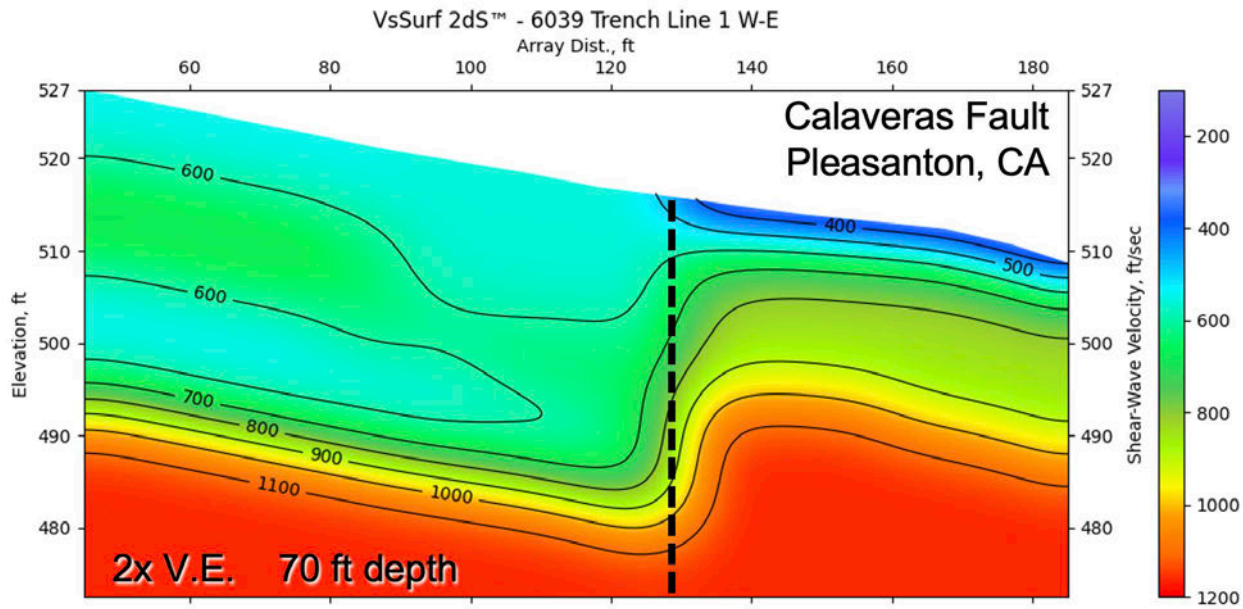

Figure 6 – ReMi 2dS™ section across the Calaveras fault (V.E.=2x)

Crawford Inc. is assisting Caltrans with the planning of a wildlife overpass at a key location in northeastern California where wildlife cross US Highway 395 to access water and forage around Honey Lake from their summer ranges in the Sierra Nevada. At this location, the highway runs for many miles right alongside the strike-slip Honey Lake fault zone (9). Although the Honey Lake fault zone is not on the plate boundary, it is a regionally significant fault, forming the boundary between the tectonically coherent Sierra Nevada block and the volcanics of the Cascade Range.

Crawford ran three ReMi 2dS™ arrays at the location of the proposed wildlife crossing, two oriented to cross the Honey Lake fault zone and one parallel to it. Figure 7 shows the Vs section resulting from one of the fault-crossing lines. At this location the fault is divided into several near-parallel strands creating a fault zone about 100 ft (30 m) wide. The strands are part of a left-stepping en-echelon structure, which on a right-lateral fault creates a push-up and a classic shutter ridge. Figure 7 finds the push-up to be the result of a positive flower structure on the NE side of the section. On the SW side of the section there may be a sag, the surface expression of a negative flower structure. A few feet of topographic relief express the sag and the push-up, from left to right. More prominent is the expression of perhaps 10 ft (3 m) of sag and push-up in the depths of the fast and slow units below. There are “pinches” in the upper stiff layer in red, that may correlate with three traces of the fault in the section. Since this is mainly a strike-slip fault, the vertical offsets do not have to consistent from depth to the surface. The central strand dividing the two flower structures comes to the surface at the location of a fault scarp Crawford identified from a Lidar survey, marked with a red arrow on Figure 7.

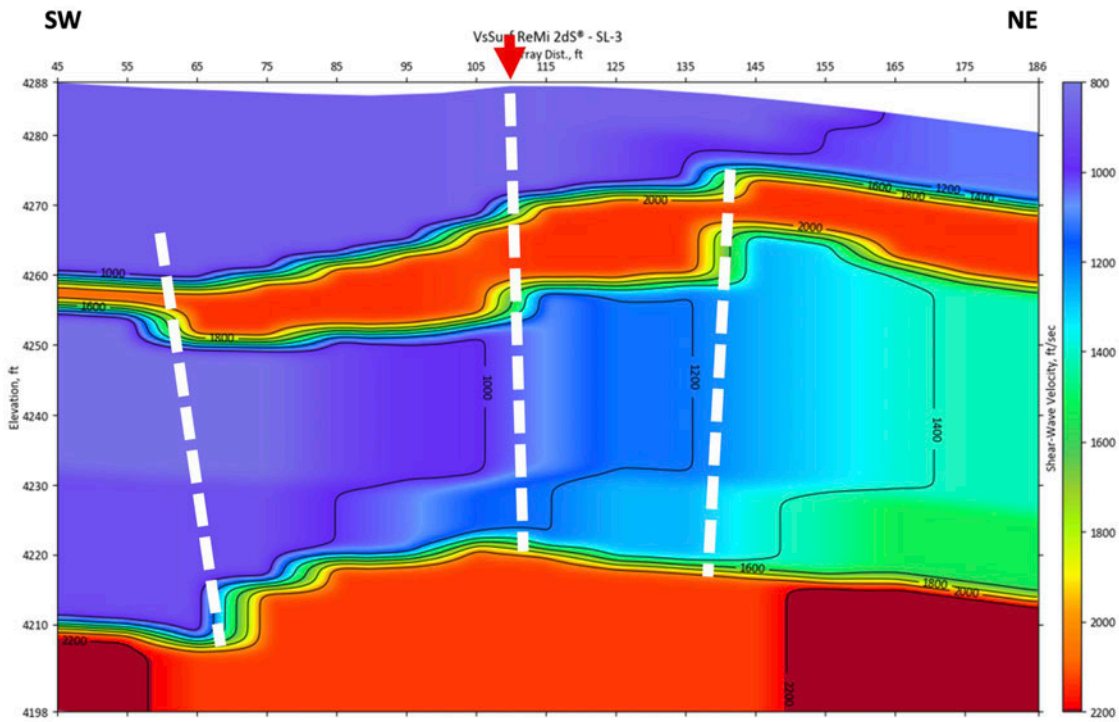

Figure 7 – ReMi 2dS™ section locating the Honey Lake fault zone (no V.E.)

Water resources

The basic ability of Terēan ReMi 2dS™ sections to define subsurface structure and stratigraphy is finding wide application in resource exploration. Several mining companies and both public and private water-supply companies are currently assessing their resources with ReMi 2dS™ surveys at dozens of localities. The mining companies find value in the ability to efficiently assess fault structure at depths up to 5000 ft (1500 m) using arrays up to 13,000 ft (4000 m) long. Such long arrays can take 4-8 hours to deploy, record, and pick up.

Water-supply agencies find value in how the 2dS sections can find changes in aquifer thickness and therefore its water production and storage capacity. In clastic sediments lacking much clay, there is a clear correlation between increasing porosity and lower shear-wave velocity. The agency delivering water to much of Reno, Nevada, Truckee Meadows Water Authority (TMWA), manages both surface and groundwater resources in much of the region. Using a Terēan ReMiNODE™ system, TMWA is collecting long-array data at the locations of several water-production wells that are due for re-drilling and refurbishment. Terēan assists TMWA by processing the array data into 2dS sections and working with their hydrogeologists on interpreting the sections.

Figure 8 shows the section resulting from a survey in urban south Reno, centered on a 30-year-old well due for refurbishment. The survey layout and recording took less than 6 hours. Correlating the Vs units in the section to the log and production data from the existing well allows the section to extend the identification of hydrostratigraphic units away from the well. The main production aquifer is the lower blue unit (D). The section suggests the aquifer may be thicker and the resource more accessible on the west side of the section. TMWA can input these

aquifer parameters into groundwater-flow as well as economic models to investigate the cost/benefit ratio of obtaining a new diversion permit and drilling a new well outside the currently permitted area.

A further point of interest on Figure 8 is where the section crosses a few of the very numerous traces of the active Mount Rose fault zone in the USGS database (8), at the orange arrows. This fault zone has both strike slip and normal slip. No significant discontinuities are visible below these locations in the boundaries of the more recent shallow units (A), (B), or (C). Given the 10%-of-depth vertical resolution criterion, it appears that even if these fault strands had been active in the Quaternary, there was not enough motion on any of them to produce as much as 10 ft (3 m) of vertical displacement. Earthquake geologists can consider these limits as they seek to characterize this complex fault system.

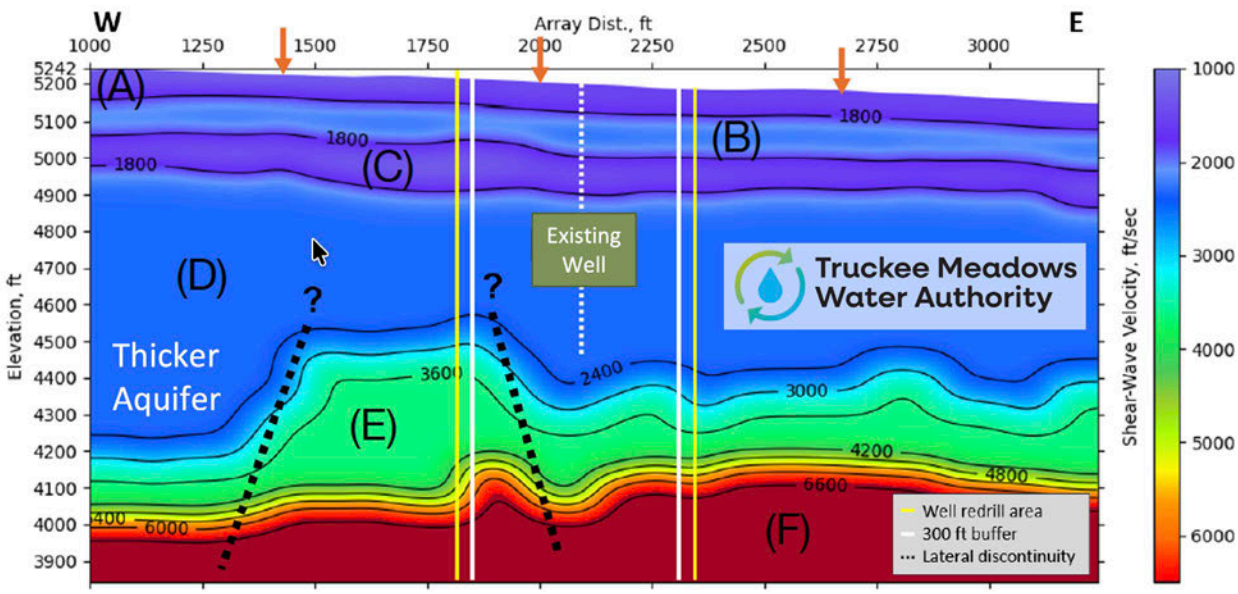

Figure 8 – ReMi 2dS™ locating changes in deep aquifer thickness (no V.E.)

CONCLUSIONS

Terēan ReMi® solutions are proving very effective for clients doing several types of work:

- Geotechnical and civil engineers assessing Vs30 and seismic site class;
- Engineering designers, drillers, and engineers assessing depth to bedrock;
- Excavators and engineers assessing rippability;
- Engineers and geologists locating fault traces; and
- Water resources agencies and hydrogeologists assessing aquifer thickness.

REFERENCES:

1. American Society of Civil Engineers. *Minimum design loads and associated criteria for buildings and other structures* (ASCE/SEI 7-22), Reston, Virginia, 2022. ISBN 978-0-78441-578-8.

2. MeltPlan. *International Building Code (IBC): Chapters, Requirements & How to Use It*. https://www.meltplan.com/buildingcodes/ibc. Accessed July 12, 2026.

3. Louie, J. N. Faster, better: shear-wave velocity to 100 meters depth from refraction microtremor arrays. *Bulletin of the Seismological Society of America* vol. 91 (2), 2001, pp. 347-364.

4. Louie, J. N., A. Pancha, and B. Kissane. Guidelines and pitfalls of refraction microtremor surveys. *Journal of Seismology* vol. 26, 2022, pp. 567–582, https://doi.org/10.1007/s10950-021-10020-5, open access.

5. Stephenson, W. J., J. N. Louie, S. Pullammanappallil, R. A. Williams, and J. K. Odum. Blind shear-wave velocity comparison of ReMi and MASW results with boreholes to 200 m in Santa Clara Valley: Implications for earthquake ground motion assessment. *Bulletin of the Seismological Society of America* vol. 95 (6), 2005, pp. 2506-2516.

6. Thelen, W. A., M. Clark, C. T. Lopez, C. Loughner, H. Park, J. B. Scott, S. B. Smith, B. Greschke, and J. N. Louie. A transect of 200 shallow shear velocity profiles across the Los Angeles Basin. *Bulletin of the Seismological Society of America* 96 (3), 2006, pp. 1055-1067, doi: 10.1785/0120040093.

7. Caterpillar Inc. *Handbook of Ripping*. 12th Edition, February 2000, Peoria, Illinois, 32 pp.

8. U.S. Geological Survey and Nevada Bureau of Mines and Geology. *Quaternary fault and fold database for the United States.* https://www.usgs.gov/natural-hazards/earthquake-hazards/faults, accessed July 14, 2025.

9. U.S. Geological Survey and California Geological Survey. *Quaternary fault and fold database for the United States.* https://www.usgs.gov/natural-hazards/earthquake-hazards/faults, accessed July 14, 2025.

28. Combined Geotechnical and Geophysical Data Collection for Pile Design at the Ankau Bridge in Yakutat, Alaska

Chloe Bjerklie, EIT
DOWL
5015 Business Park Blvd
Anchorage, Alaska 99503
cbjerklie@dowl.com

Matt Blakeslee CPG
DOWL
5015 Business Park Blvd
Anchorage, Alaska 99503
mblakeslee@dowl.com

Prepared for the 75th Highway Geology Symposium, September, 2026

Acknowledgements

The authors would like to thank the individuals/entities for their contributions in the work described:

DJ&A, P.C.
Esther Babcock, Ph.D. – Logic Geophysics & Analytics, Inc.
Samuel Christie, PE – DOWL, LLC
Discovery Drilling, Inc.

Disclaimer

Statements and views presented in this paper are strictly those of the author(s), and do not necessarily reflect positions held by their affiliations, the Highway Geology Symposium (HGS), or others acknowledged above. The mention of trade names for commercial products does not imply the approval or endorsement by HGS.

Copyright Notice

Copyright © 2026 Highway Geology Symposium (HGS)

All Rights Reserved. Printed in the United States of America. No part of this publication may be reproduced or copied in any form or by any means – graphic, electronic, or mechanical, including photocopying, taping, or information storage and retrieval systems – without prior written permission of the HGS. This excludes the original author(s).

ABSTRACT

The Ankau Bridge crosses the Ankau Slough in Yakutat, Alaska and provides access to recreational and culturally significant areas to the remote, coastal community. Constructed in 1961, the timber bridge has experienced significant deterioration due to the harsh tidal inlet marine environment. The bridge was recently assigned a Poor condition rating under the National Bridge Inventory during its last inspection in 2022, prompting the need for a replacement bridge. DOWL was tasked to perform a geotechnical investigation and develop pile foundation recommendations for the replacement structure.

Site conditions presented significant logistical challenges for conventional subsurface data collection within the channel along the proposed bridge alignment. The shallow depth of the Ankau Slough, strong tidal currents, and limited structural capacity of the existing bridge prevented the safe deployment of a barge for offshore drilling or drilling from the bridge deck. To address the limitations, a combined geotechnical and geophysical investigation was implemented to limit conventional borings to the abutments. Geophysical surveys consisting of seismic and electrical resistivity profiles were conducted along the shoreline and within the channel to fill the data gaps between the two abutments.

Correlation between the geophysical profiles and boring data at the abutments allowed for interpretation of subsurface conditions across the channel where direct drilling was not feasible. The combined dataset proved to be successful in providing sufficient information to support pile design and highlights the importance of adapting investigation strategies to address access limitations and complex conditions common to remote, Alaskan communities.

INTRODUCTION

Geotechnical data collection in Alaska presents unique challenges compared to much of the United States. Many projects are located in remote areas, and mobilizing equipment, such as drill rigs, frequently requires transportation by ferry, barge, aircraft, or a combination of these methods, resulting in significantly higher costs and constraining the duration and extent of field investigations. Additionally, dynamic environments create challenges, particularly in coastal and riverine environments, where tides, shallow water, seasonal weather, and limited transportation infrastructure can further restrict exploration activities.

In recent years these logistical constraints have encouraged the increasing use of geophysical methods to supplement conventional geotechnical investigations. Rather than replacing direct sampling, geophysical techniques provide continuous subsurface information between borings, allowing practitioners to better characterize geologic conditions while reducing the number of intrusive investigations required. When integrated with traditional geotechnical data, geophysical surveys can improve the efficiency of site characterization, optimize drilling programs, and reduce overall project costs, particularly in remote regions where mobilization expenses are substantial.

PROJECT BACKGROUND

The Ankau Bridge spans Ankau Slough in Yakutat, Alaska, and provides access to recreational and culturally significant areas used by the local community. Constructed in 1961, the approximately 500-foot-long timber bridge (Figure 1) has experienced significant deterioration from decades of exposure to the tidal inlet marine environment. During its most recent inspection in 2022, the bridge received a Poor condition rating under the National Bridge Inventory, prompting the development of a replacement. DOWL was retained by DJ&A to perform the geotechnical investigation and develop foundation recommendations and assist with the design of the proposed bridge replacement.

Figure 1: Ankau Bridge in Yakutat, Alaska

A conventional subsurface exploration program was initially planned to characterize conditions along the proposed bridge alignment. However, site conditions presented significant logistical challenges that limited the feasibility of traditional drilling methods. The shallow depth of Ankau Slough and strong tidal currents prevented efficient deployment of a barge-mounted drill rig within the channel. At the same time, the deteriorated condition and limited load-carrying capacity of the existing bridge restricted drilling operations from the bridge deck. Additionally, the bridge is listed on the historical register, making it very challenging to alter in any way. These constraints prevented direct collection of geotechnical data at many locations beneath the proposed structure and created a substantial data gap within the channel.

To address these limitations, the investigation strategy was modified to incorporate both geotechnical and geophysical methods. Conventional borings were completed at the bridge abutments where access was feasible at the channel level, while geophysical surveys consisting of seismic and electrical resistivity profiling were conducted along the shoreline and within the channel. The geophysical surveys provided continuous subsurface coverage between boring locations and across areas where direct drilling could not be safely performed.

Figure 2: The Aknau Slough at low tide

The geotechnical borings served as calibration points for interpretation of the geophysical data. Correlation between observed soil conditions at the abutments and geophysical signatures enabled development of a subsurface model extending across the channel. This integrated dataset provided sufficient information to evaluate subsurface stratigraphy, assess foundation conditions, and develop pile foundation recommendations for the replacement bridge.

This paper presents the investigation approach used for the Ankau Bridge Replacement project and discusses how geophysical data were utilized to supplement limited geotechnical exploration. The project demonstrates the value of integrating geophysical and geotechnical datasets to overcome access limitations and reduce subsurface uncertainty, a challenge that is frequently encountered during transportation projects in remote Alaska communities.

GEOPHYSICAL INVESTIGATION

To complete the geophysical investigation, DOWL retained Logic Geophysics & Analytics LLC (Logic) of Anchorage, Alaska. Logic conducted a combination of land-based and

marine geophysical surveys, as three of the five survey lines were located partially or entirely within the channel (Figure 3). The investigation included shear-wave velocity and electrical resistivity methods. For the marine seismic surveys, Logic deployed 230-foot weighted hydrophone strings consisting of 24 receivers spaced at 10-foot intervals and towed them along the channel bottom by boat. Electrical resistivity data were collected using conventional electrodes for the land-based surveys and graphite electrodes for the marine surveys.

Seismic Surveys

Shear-wave velocity (Vs) surveys were completed to characterize subsurface conditions between and beyond geotechnical borings, particularly in areas where conventional drilling could not be performed. The surveys provided continuous subsurface profiles that supplemented the geotechnical investigation by identifying changes in stratigraphy and the relative stiffness of soil and rock materials.

Figure 3: Hydrophones getting strung out across the channel by boat

Because portions of the survey alignment extended into the channel, the investigation used a combination of marine and land-based passive surface-wave methods (linear microtremor analysis). These methods measure naturally occurring ambient vibrations generated by sources such as tidal action, waves, distant earthquakes, and vehicle or marine traffic. Hydrophones were deployed within the channel, and geophones were used on land to collect continuous seismic data along survey lines parallel and perpendicular to the bridge.

The recorded data were processed to develop two-dimensional Vs profiles. These profiles were used to interpret subsurface stratigraphy and extrapolate material properties between geotechnical borings using correlations with boring logs and laboratory test results.

Electrical Resistivity Surveys

Electrical Resistivity Tomography (ERT) surveys were also conducted to supplement the geotechnical investigation by providing continuous information on the electrical properties of subsurface materials. Variations in electrical resistivity can be correlated with changes in soil type, grain size, porosity, moisture content, degree of saturation, weathering, and bedrock conditions.

The ERT surveys were conducted by injecting direct current into the ground through a pair of electrodes and measuring the resulting electrical potential at additional electrodes along

each survey line. Measurements were collected using multiple electrode spacings to investigate progressively greater depths. The recorded data were processed by Logic through an inversion algorithm to produce two-dimensional resistivity models that represent the interpreted distribution of subsurface electrical properties.

The resulting resistivity profiles were interpreted in conjunction with Vs profiles and geotechnical borings to identify subsurface stratigraphy and geologic boundaries relevant to project design.

GEOTECHNICIAL INVESTIGATION

A subsurface investigation was performed within the proposed bridge footprint and abutment areas using ten test borings advanced to depths ranging from 10 to 100 feet below ground surface (bgs).

Borings were advanced using track-mounted drill rig fitted with wash rotary tooling, a conventional geotechnical exploration method suitable for overburden soils and weak to moderately cemented rock. The method uses a rotating drill bit and circulating drilling fluid to loosen and remove cuttings, stabilize the borehole, and facilitate advancement through coarse-grained and variable subsurface materials. Soil samples were collected at regular depth intervals using split-spoon samplers, and penetration testing was performed to evaluate the relative density and consistency of subsurface soils. Due to the presence of coarse-grained deposits and challenges with sample recovery, both standard and modified penetration testing methods were utilized.

Figure 4: Drill rig advancing a boring at the north abutment

Recovered soil samples were visually classified and preserved for laboratory testing. Laboratory analyses included particle-size distribution and grain-size characterization to support interpretation of engineering soil properties. Groundwater levels were not measured because the drilling method precluded reliable observations, and groundwater monitoring installations were not completed due to the tidally influenced conditions at the site.

The full geotechnical and geophysical data collection plan relative to the existing bridge is shown in Figure 5.

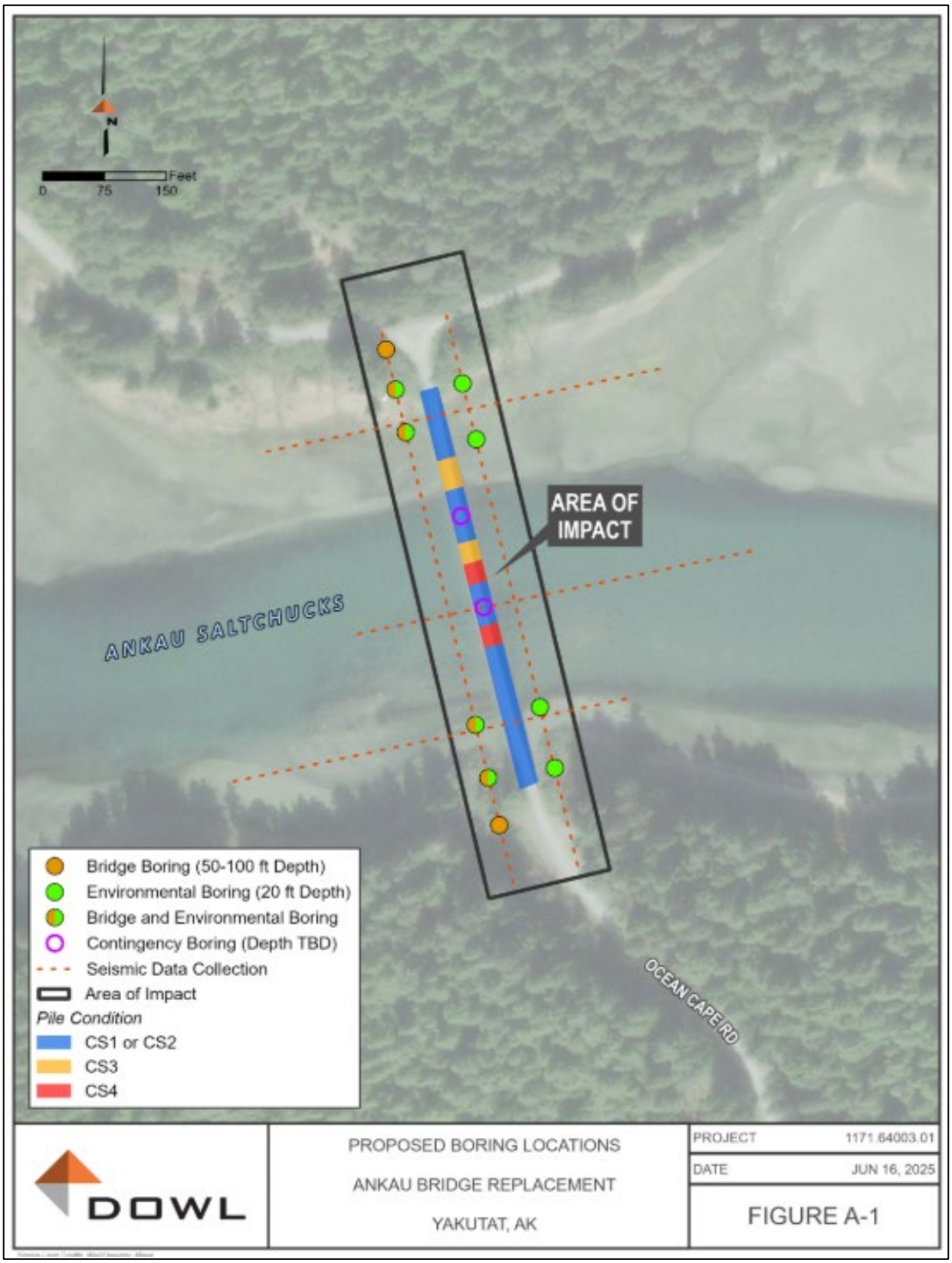

Figure 5: Geotechnical and Geophysical Data Collection Plan

RESULTS & SUBSURFACE CONDTIONS

Underlying the shallow topsoil layer, subsurface conditions interpreted from the Vs profiles (Figure 6) and confirmed by selected geotechnical borings were generally consistent across the alignment and with published geologic mapping for the Yakutat region. For the purposes of this project, the subsurface was divided into three generalized geologic units: (1) reworked glacial till, (2) normally consolidated glacial till, and (3) over-consolidated glacial till. These units are based on field observations, laboratory testing, and interpretation of the geophysical data and represent the generalized subsurface conditions along the proposed bridge alignment (Figure 7).

Reworked Glacial Till

The Vs profiles indicate that reworked glacial till is the predominant near-surface unit, extending from the ground surface to elevations of approximately –35 to –45 feet. The unit reaches up to about 45 feet thick beneath the channel and thins to approximately 10 to 25 feet near the abutments.

The deposit consists primarily of sand and gravel with variable silt and likely represents a combination of reworked glacial till and localized fluvial infill within kettle features. Glacial erratics and boulders may occur throughout. The unit was characterized as loose to medium dense near the surface, becoming medium dense with depth, with moderate strength, low to moderate compressibility, moderate permeability, and moderate sensitivity to moisture-content changes.

Normally Consolidated Glacial Till

Normally consolidated glacial till underlies the reworked deposit and extends from approximately –35 to –45 feet down to –65 to –75 feet elevation. The unit is generally 20 to 35 feet thick and is thickest beneath the center of the alignment.

The deposit consists of interbedded glacial till and moderately to well-sorted sand and gravel deposited during glacial advance and meltwater processes. Glacial erratics and boulders may be encountered throughout. The material was characterized as medium dense to very dense with moderate to high strength, low compressibility, high permeability, and low sensitivity to moisture-content changes.

Over-Consolidated Glacial Till

Over-consolidated glacial till is identified by a distinct increase in Vs and forms the deepest unit interpreted along the alignment. The top of the unit occurs at approximately –65 to –75 feet elevation and extends beyond the depth of the geophysical survey.

The deposit consists of dense to very dense, matrix-supported till composed of sand, silt, gravel, cobbles, and occasional boulders. The material exhibits high strength, very low compressibility, very low permeability, and minimal sensitivity to moisture-content changes.

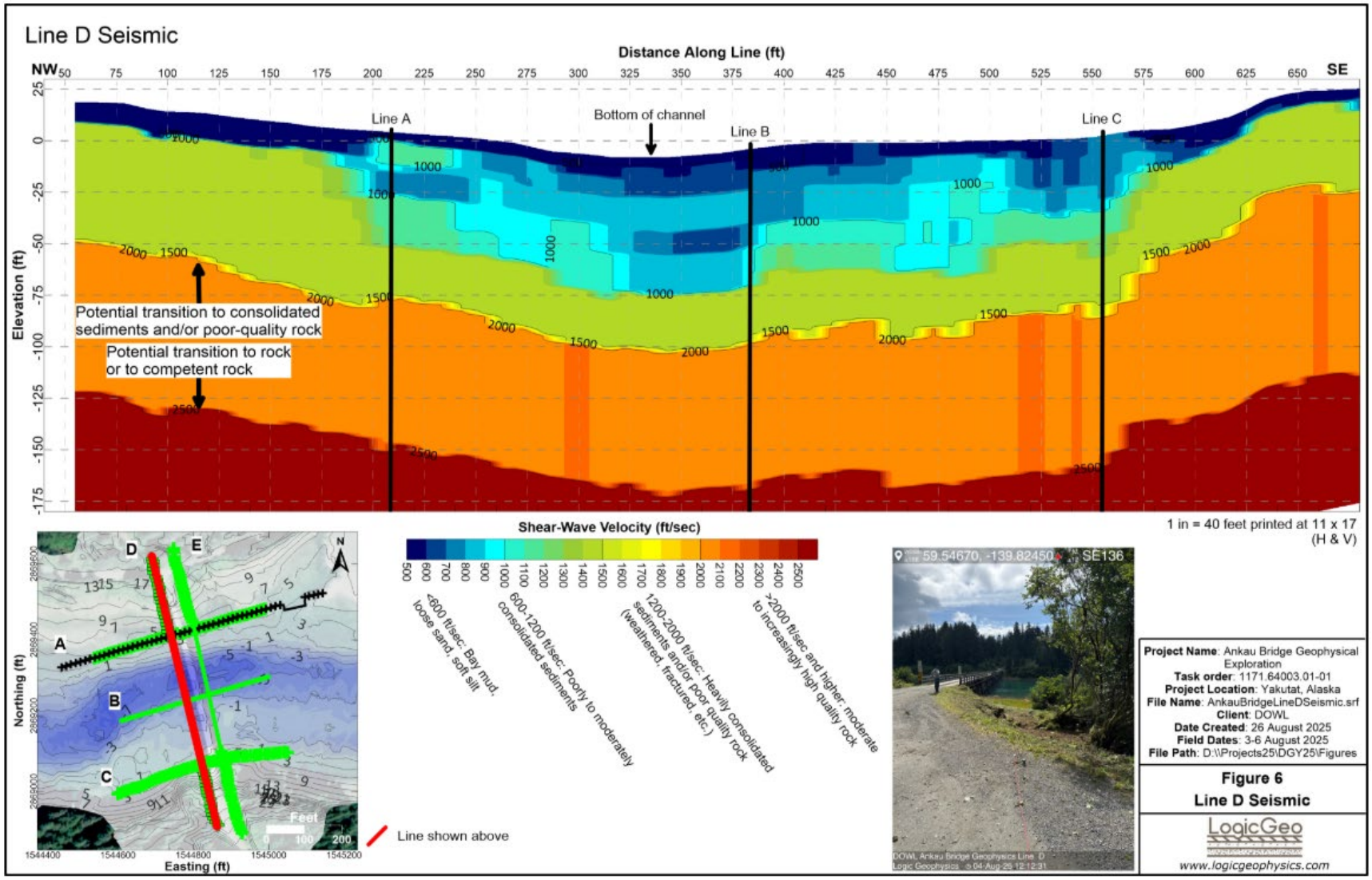

Figure 6: Vs profile parallel to the existing bridge, combination land-based and marine profile

Figure 7: Interpreted generalized cross section using geotechnical boring and geophysical profiles

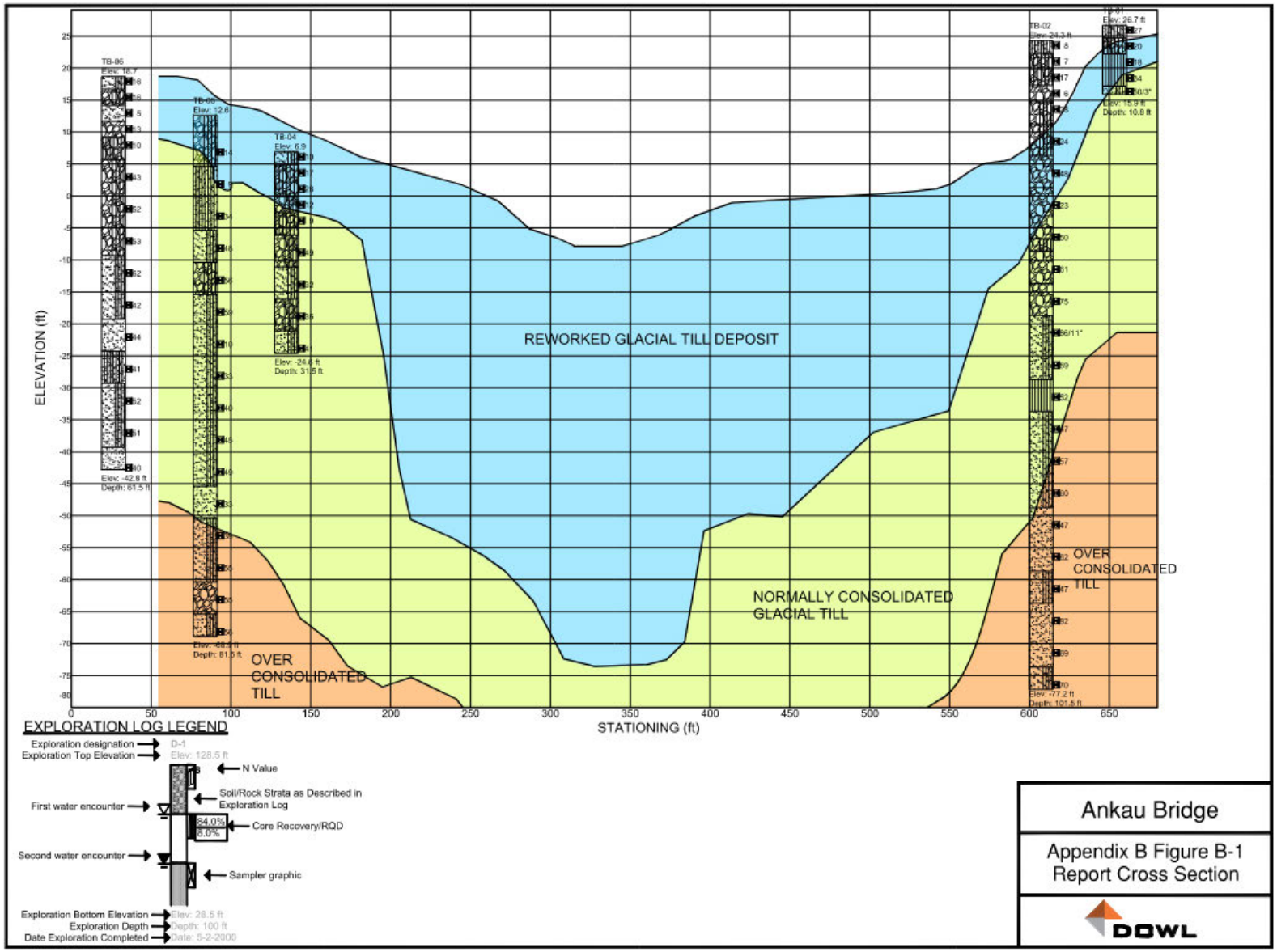

ENGINEERING ANALYSIS & APPLICATIONS

Geotechnical borings completed at each abutment were correlated to the results of the geophysical investigation by extracting one-dimensional Vs profiles from the seismic survey results at locations corresponding to, or in close proximity to, the geotechnical borings. One-dimensional profiles were also extracted at multiple locations within the channel and correlation between the subsurface conditions observed in the borings and the interpreted seismic data provided characterization of site stratigraphy and soil properties within the channel. The resulting Vs profiles were subsequently used to support geotechnical engineering analyses, including pile capacity evaluations and liquefaction assessments.

Seismic Design & Liquefaction Analysis

One of the primary objectives of the seismic survey, beyond site characterization of the channel, was the determination of the site's seismic classification. Because potentially liquefiable soils were identified at the site, the site was classified as Site Class F. Given the identified liquefaction hazards, Vs profiles derived from the seismic survey were analyzed using LiqSVs software to evaluate the potential extent and severity of liquefaction across the site. This approach was particularly important within the channel area, where standard penetration test (SPT) blow count data were not available. The availability of Vs profiles at both the abutments and within the channel provided a consistent basis for evaluating liquefaction potential throughout the project corridor, allowing for a more uniform and comprehensive assessment of subsurface conditions.

The design seismic loading used for liquefaction triggering analyses was based on a moment magnitude (Mw) of 7.4 and a peak ground acceleration (PGA) of 0.62g. The PGA corresponds to the mapped seismic acceleration coefficient for Site Class D obtained from the AASHTO hazard maps. Site Class D was selected for defining the input ground motion because the mapped acceleration coefficient is determined prior to the application of site-specific site class adjustments and therefore provides a consistent basis for liquefaction triggering evaluations. Liquefaction susceptibility was assessed using the Vs-based procedure developed by Kayen et al. (2013). Results of the analysis indicate the presence of a laterally continuous liquefiable layer within the channel, extending from approximately 34 to 64 feet bgs between Stations 315 and 390 (Figure 8). This identified liquefiable zone represents the primary area of concern for seismic ground deformation and potential impacts on foundation performance.

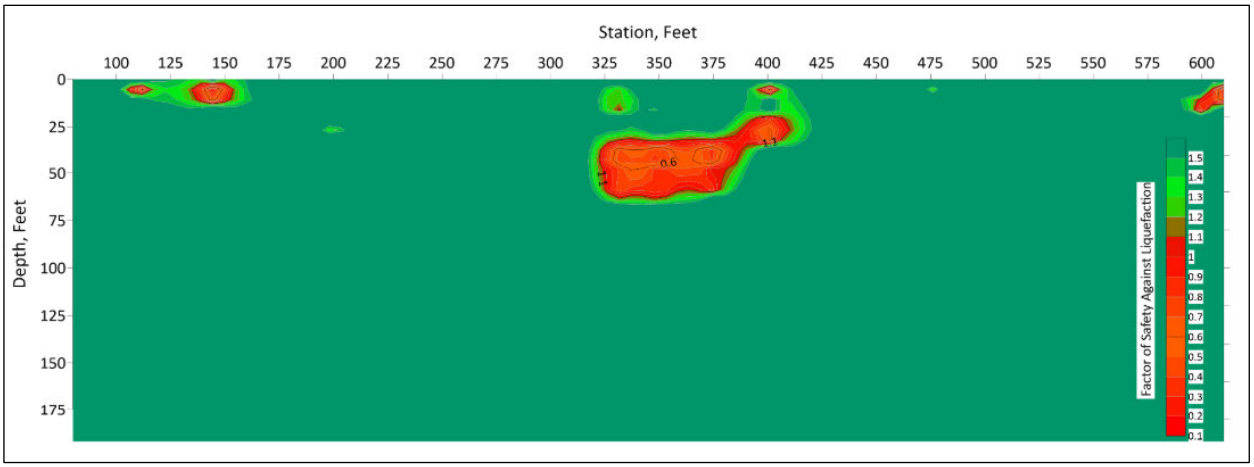

Figure 8: Liquefaction analysis results. The channel is located between stations 225 and 550

Pile Design

Deep driven steel pipe piles were selected as the preferred foundation system due to the combined effects of liquefaction susceptibility within the channel deposits and the potential for significant scour associated with strong tidal currents.

For axial pile capacity evaluations, the interpreted subsurface profile was simplified into representative geotechnical units reflecting the estimated density, strength, and gradation characteristics of the underlying soils. Pile design parameters were developed from the available boring data, Vs interpretations, and engineering correlations. Multiple published correlations between Vs and SPT blow counts were evaluated to identify the correlation that provided the best agreement with SPT values measured in the abutment borings. The correlation developed by Rollins et al. (1998), presented below, was selected for the analysis.

$$N_{60} = \left(\frac{v_s}{63.0}\right)^{\frac{1}{0.43}}$$

The correlated SPT values were subsequently used to estimate additional engineering properties, including soil unit weight and friction angle, through established empirical relationships. These derived parameters were combined with the interpreted subsurface stratigraphy to develop representative soil profiles for foundation design. The resulting geotechnical model was then used to evaluate the axial capacity of driven steel pipe piles at both the abutment and channel foundation locations. The integration of parameters derived from geotechnical borings and Vs-based correlations provided a consistent basis for pile capacity analyses across the project site.

Pile capacities were evaluated using procedures consistent with the American Petroleum Institute (API) methodology for driven piles in granular soils. This approach was selected because granular soils, consisting primarily of sand, gravel, and glacial till, predominate across the site and no cohesive strata of engineering significance were identified. Accordingly, drained soil behavior and effective stress parameters were assumed for long-term axial capacity analyses. The Vs-based interpretation of dense till deposits was used to identify the primary bearing strata supporting pile foundations. Axial capacities were calculated by considering both shaft resistance and end-bearing resistance developed within these competent units. Adjustments were made as

necessary to account for local variations observed between the geotechnical borings and geophysical survey results, resulting in a subsurface model that provided a consistent basis for foundation design across the project site.

CONCLUSION

The integration of geophysical methods with conventional geotechnical exploration provided a more comprehensive characterization of subsurface conditions than could have been achieved through drilling alone. Vs profiling and electrical resistivity tomography allowed continuous interpretation of subsurface stratigraphy between borings, identified lateral changes in geologic units, and characterized areas that were inaccessible or impractical for conventional drilling within the marine environment. By reducing uncertainty in subsurface conditions, these methods can improve geologic interpretations, optimize exploration programs, and reduce overall investigation costs.

For the Ankau Bridge Replacement Project, the combined geophysical and geotechnical datasets were used to develop a continuous subsurface model that supported foundation design across the bridge alignment. The Vs profiles were instrumental in identifying the depth and continuity of dense glacial till that forms the primary bearing stratum for the proposed driven steel pipe piles. These interpretations were incorporated into the development of generalized soil profiles used for axial pile capacity analyses, lateral pile resistance modeling, settlement evaluations, downdrag assessments, and preliminary pile tip recommendations. The geophysical data also increased confidence in extending geotechnical interpretations between borings, particularly beneath the channel where direct subsurface information was limited.

The integrated subsurface model also established the basis for the project's seismic evaluation. Preliminary analyses indicate that liquefaction is expected within the channel deposits during the design-level earthquake, while the underlying dense glacial till will provide competent support for the deep foundation system. As design progresses, a site-specific seismic response analysis will further evaluate ground motions, liquefaction effects, and associated seismic demands on the bridge foundations. This project demonstrates how integrating geophysical and geotechnical investigations can improve both the technical quality and efficiency of transportation infrastructure design, particularly in remote and challenging Alaskan environments.

REFERENCES:

- Federal Government Reports
  1. Kortum, Z., Luco, N., and Rezaeian, S., *Gridded earthquake ground motions for the 2023 AASHTO Design Specifications: U.S. Geological Survey data release*, 2022. https://doi.org/10.5066/P9EACMIX.
- Journal
  1. Kayen, Robert, et al. *Shear-Wave Velocity–Based Probabilistic and Deterministic Assessment of Seismic Soil Liquefaction Potential*. Journal of Geotechnical and Geoenvironmental Engineering, vol. 139, no. 3, 2013, pp. 407-419. ttps://doi.org/10.1061/(ASCE)GT.1943-5606.0000743.
  2. Rollins, K. M., Evans M. D., Diehl N. B., and Daily, W. D., *Shear modulus and damping relationships for gravels*, J. Geotech. Geoenviro. Eng., 1998. 124(5):396–405.
- University Report
  1. Wair, B. R., DeJong, J. T., and Shantz, T. *Guidelines for Estimation of Shear Wave Velocity Profiles.* Pacific Earthquake Research Center, University of California, PEER Report 2012/08, 2012.

29. Monitoring While Drilling in Glacial Deposits

Bruma Souza, Ph.D.
Weston & Sampson
55 Walkers Brook Drive, Suite 100
Reading, MA 01867
(781) 758-5199
souza.bruma@wseinc.com

Jean Benoît, Ph.D.
Department of Civil and Environmental Engineering, University of New Hampshire
33 Academic Way
Durham, NH 01824
(603) 978-5429
jean.benoit@unh.edu

Prepared for the 75th Highway Geology Symposium, September, 2026

Acknowledgements

The support for this research by the New Hampshire Department of Transportation Bureau of Materials and Research is greatly appreciated. Special thanks to Krystle Pelham, John Woodward, Ryan Boisvert, Christian Buerkle, Benjamin LaPointe, Adam Carr, Bradley Roberts, David Gaylord and Deirdre Nash for their time, interest, support, and collaboration. Thank you also to Michael Rodgers (MWD One) and Michel Lariau (Jean Lutz) for their input and assistance in preparing our equipment for testing.

Disclaimer

Statements and views presented in this paper are strictly those of the author(s), and do not necessarily reflect positions held by their affiliations, the Highway Geology Symposium (HGS), or others acknowledged above. The mention of trade names for commercial products does not imply the approval or endorsement by HGS.

Copyright Notice

Copyright © 2026 Highway Geology Symposium (HGS)

All Rights Reserved. Printed in the United States of America. No part of this publication may be reproduced or copied in any form or by any means – graphic, electronic, or mechanical, including photocopying, taping, or information storage and retrieval systems – without prior written permission of the HGS. This excludes the original author(s).

ABSTRACT

The latest Monitoring While Drilling (MWD) systems consist of several sensors mounted on conventional drill rigs to monitor various aspects of borehole drilling, whether drilling soil overburden or bedrock as well as coring in rock. These sensors record the advance rate, rotation rate, downthrust (pressure and force), torque, water/mud flow, water/mud pressure, vibration, among other parameters as a function of depth and time. These measurements are obtained in real-time by an automated system without interfering with routine drilling operations. The New Hampshire Department of Transportation (NHDOT) recently installed and implemented an MWD system on two drill rigs to support subsurface investigations. The equipment installed to date and the test procedures were gradually adapted and improved during an extensive field campaign across 14 sites, primarily involving glacial deposits commonly encountered in the region. MWD measurements were used to evaluate changes in ground stratigraphy and bedrock cores, and were compared with field logs and results from conventional geotechnical testing, such as the Standard Penetration Test (SPT), as well as Rock Quality Designation (RQD) for bedrock coring. This paper introduces the Monitoring While Drilling system used in this experimental campaign and discusses the results and data processing from drilling at one site in Londonderry, NH. The instrumentation is particularly helpful in delineating changes in stratigraphy and serves as a useful tool to bridge geotechnical data gaps in sites where results from SPT or other conventional tests are limited or sparse. MWD technology and approaches to data assessment are increasingly being developed in the United States and have strong potential to evolve into a reliable, standardized geotechnical test. To achieve this, correlations should be evaluated across a broader range of geological materials, and drilling techniques should be assessed and optimized to promote efficient drilling. Establishing procedures that produce high-quality parameters is essential to ensure that MWD measurements reflect the ground response and support reliable data interpretation.

INTRODUCTION

The Standard Penetration Test (ASTM D1586) is the most widely used in situ test in the United States for characterizing soil stratigraphy and penetration resistance in geotechnical investigations. Although the SPT has demonstrated reliability and broad applicability worldwide for more than a century, the method has limitations that can introduce uncertainty in a geotechnical profile. These limitations may include poor soil recovery, particularly in clean sands and gravelly soils, and the influence of gravel or larger-sized fragments on recorded blow counts. SPT testing can also be time-consuming, labor-intensive, and difficult or impractical in certain geologic conditions, such as dense gravelly soils, bouldery deposits, and bedrock. Because SPT sampling is typically performed at 5- to 10-foot intervals, stratigraphic changes between sampling intervals may not always be identified. The cone penetration test (CPT) is commonly used as an alternative method for rapid and continuous soil profiling; however, CPT advancement may be limited in very dense or stiff soils and in deposits containing large particles, such as gravel, cobbles, or boulders. In these conditions, the penetration resistance may exceed the capacity of standard geotechnical drilling equipment, often requiring specialized rigs to complete the investigation.

In response to these limitations and to help bridge gaps in geotechnical engineering, an emerging in situ test known as Monitoring While Drilling (MWD) has been increasingly promoted by departments of transportation as a useful tool to assess ground stratigraphy through a routine operation in almost every geotechnical project: drilling of boreholes. Every day in the U.S., subsurface investigations use various boring machines and penetration rigs to advance boreholes for applications including, but not limited to, stratigraphic profiling, collecting undisturbed samples, installing monitoring wells, and installing various instrumentation types, across numerous subsurface conditions for geotechnical purposes alone. It is conceivable that, in drilling activities for purposes other than geotechnical profiling (e.g., drilling for monitoring wells or instrumentation installation), little useful information is often obtained regarding ground geology and penetration resistance across several boreholes.

Monitoring While Drilling is an in-situ test that records the ground response from the imposed drilling method. This technique requires installing multiple sensors on a drill rig to record key aspects of drilling in real time. The use of MWD originated in the oil industry in the 1950s, where the need to measure penetration rates and tool performance guided research efforts to reduce the high costs of drilling wells thousands of feet deep. The application of MWD in geotechnical engineering started in the late 1970s with analog recorders and a limited number of sensors (1). As technology improved, digital recorders and more sophisticated and reliable sensors were introduced, leading to the development of empirical relationships between drilling parameters and geotechnical profiles and properties as later discussed in this paper (2-6).

The test is currently standardized by the European standard ISO 22476-15:2016 (7). However, information on testing procedures and recommendations for data reduction are still limited and imprecise in these standards. As a result, the current version of ISO 22476-15 (7) cannot be used as a guide for implementing MWD. The latest MWD systems can record parameters including drilling advance rate, rotation rate, downthrust, torque, drilling fluid flow and pressure, as well as vibration without interfering with normal drilling operations. When combined with other

geotechnical test methods, such as the SPT or the CPT, MWD profiles present a high potential to accurately represent subsurface conditions (8).

Two MWD systems were recently implemented by the NHDOT on two of their drill rigs. Equipment setup, test procedures, and data collection methods were iteratively refined throughout an experimental campaign spanning 14 sites, where SPT and/or CPT data were also collected. Initial results demonstrated that MWD data can provide valuable insights into subsurface variability, offering a continuous representation of drilling conditions, including in geological materials that experienced refusal during SPT or CPT testing (9-10).

This paper introduces the latest MWD equipment, presents a summary of recommended field correlations for data analysis, and summarizes the main lessons learned during this experimental campaign applied to data interpretation. Results and data interpretation from one test site are discussed, encompassing one profile of soil drilling and one profile of rock coring. MWD results were compared to SPT and RQD results. Lessons learned during this experimental campaign demonstrate the emerging potential of MWD in geotechnical projects and highlight the importance of efficient, high-quality drilling to obtain meaningful measurements for data interpretation, as discussed in later sections.

MWD EQUIPMENT

Table 1 lists the various parameters measured during the field experimental campaign discussed in this paper, along with their units according to the European standard and the draft American Association of State Highway and Transportation Officials (AASHTO) standard on MWD (11), as well as their corresponding conversions. All test instrumentation was installed on a CME-45C track-mounted mechanical drill rig used in routine NHDOT operations, shown in Figure 1.

A Jean Lutz system (DIALOG System Version 6.6.12) was selected in this research project as it was compatible with MWD equipment already in use at the University of New Hampshire. Although the system was designed to record all parameters listed in Table 1, the test equipment presents a major limitation for measuring torque, since it was initially designed for hydraulic drill rigs. As a result, a separate instrumented rod from MWD One was used to measure torque and downthrust force, as later described in this section. For a more detailed discussion of the sensors, system verifications, and gradual improvements undertaken during this experimental campaign, the reader is referred to Souza et al. (10).

Junction box, data logger, and PI box

The sensors in the system are wired and directly connected to a junction box (Figure 1a). The output from the various sensors is relayed to a data logger (Figure 1b), which is a rugged, weatherproof tablet computer. The logger controls all testing phases, considering the various calibration factors for each sensor. Measurements from all wired sensors are directly stored in the data logger. In contrast, measurements from the wireless torque sensor are initially gathered by a PI Box (Figure 1c), which communicates directly with the data logger in Figure 1b. The raw data files are exported through a USB port in the data logger. Data processing can be performed using the manufacturer's software, Excel, or MATLAB.

Table 1 – List of drilling parameters and their respective units.

Drilling parameter	Units		
	Default software	Draft AASHTO standard and conversion factor	European standards and conversion factor
Depth (d)	m	0.3048 ft	m
Drilling rate (u)	m/h	0.01667 in/min	m/h
Thrust pressure (Pe)	bar	14.50 psi	0.1 MPa
Thrust force (Fe)	N	0.225 lbs	0.001 kN
Rotation rate (Vr)	RPM	RPM	RPM
Torque (T)	N-m	8.85 lbs-in	0.001 kN-m
Vibration frequency (f)	Hz	Hz	Hz
Vibration acceleration (G)	m/s²	0.3048 ft/s²	m/s²
Drilling fluid pressure (P)	bar	14.50 psi	0.1 MPa
Drilling fluid flow rate (Qi)	L/min	3.78 GPM	L/min

Figure 1. MWD equipment installed on a track-mounted CME-45C drill rig.

The data logger screen can be wirelessly transmitted to any computer, enabling real-time remote monitoring or assisting with troubleshooting field issues. Each drilling parameter is measured internally by the system over time at a sampling frequency of 8 kHz. For data visualization and

processing, the user can select the depth recording step, which graphs to display, and which tabulated data to record. By default, the equipment recommends a 2 cm (0.8 inch) recording step, in which all data sampled within a single depth increment are averaged and displayed as a function of depth rather than time. Therefore, while the data is internally sampled at a fixed frequency (regular time increments), the output data will be generated at regular depth increments (irregular time increments).

Depth and advance rate

The drilled depth is measured using a linear displacement sensor (Figure 1i) mounted on the drill rig mast. It consists of a pulley assembly fixed on the drill mast and connected to the drill head. As the drilling depth advances, the internal potentiometer varies the output voltage calibrated to a length measurement. The internal system clock in the data logger records the measurement time and calculates the penetration rate. In this research, the recorder monitors all movements of the drill string but records data only at new advancing depths, allowing the driller to move up and down the borehole to flush cuttings without interfering with the measurements. However, data on all aspects of drilling are recorded internally over time and can be accessed by the user if necessary.

Downthrust pressure

The downthrust pressure, or crowd, imposed by the driller can be visually monitored using the standard pressure gauge installed on the drill rig and by the MWD system via a pressure transducer (Figure 1d) installed in the hydraulic pressure line near the rig gauge on the control panel. The installation requires a T-connector to tap into the hydraulic line.

The downthrust recorded using the pressure transducer must be corrected for the idling or baseline rig pressure and converted to force by taking into account the area of the piston cylinders (6.8 in.^{2} for the CME 45C used by the NHDOT) and to take into account the weight of the drill string as the borehole is advanced into the subsurface (e.g., 29 lbs for each 5-ft NWJ rod), as shown in Equation 1.

$$Pe=\{(Pe_{measured}-Pe_{baseline})*6.8\ in^2+(depth*29\ lbs\ /\ 5\ ft)\}\ /A_{drill\ bit} \quad (1)$$

where: Pe = corrected downthrust pressure (psi), $Pe_{measured}$ = downthrust pressure from the pressure transducer (psi) = gauge pressure, $Pe_{baseline}$ = baseline reading before the beginning of the test (psi), $A_{drill\ bit}$ = area of the drill bit used (in^2), $depth$ = current depth measurement for the given downthrust pressure (ft).

It is important to note that Pe in Equation 1 represents the net downthrust pressure. When a holdback pressure is applied, subtract the holdback pressure from the downthrust pressure to obtain the net pressure, Pe (net = downthrust – holdback).

Rotation rate

The rotation rate is measured using a proximity sensor mounted on a plate near a set of evenly spaced welded studs on the rotating shaft. The proximity sensor detects each stud (Figure 1g) as it passes in front of it and calculates the rotation rate in RPM based on the number of studs per unit time. For the CME 45C rig, 8 studs were used for each rotation. The number of welded studs is entered directly into the data logger by the user, and the measurement accuracy can be easily verified by visually counting the number of rotations over a known time (e.g., one minute) or by directly measuring it with a tachometer.

Torque and downthrust force

A wireless sensor was required to measure torque directly at the top of the drill string, as torque cannot be measured on mechanical drill rigs using hydraulic pressure transducers. The instrumented rod is shown in Figure 1f(I) and consists of a 2 ft long AWJ rod manufactured by MWD One, with torque rosettes and T-element strain gauges placed every 90° around the device's circumference to measure the downthrust. A wireless data transmitter communicates with both the auxiliary and main junction boxes. The system was calibrated to operate in conjunction with the JL system to measure torque and downthrust force (12). The instrumented drill rod directly measures the actual applied force and thus does not require subtracting any applied holdback force or include the weight of the rods.

Vibration

The vibration experienced by the drill rig while advancing in different geological materials is quantified using an accelerometer mounted near the top of the drill string, as shown in Figure 1f(II). The vibration sensor measures two variables: the vibration, expressed as a function of the gravitational constant ($g = 9.81$ m/s² = 32.2 ft/s²), and the vibration frequency, measured in Hertz (Hz). Although measurements using the vibration sensor will vary depending on its installation location on the drill rig, there is significant potential to use both frequency and acceleration as indicators of strata changes and the presence of rock fragments and gravel in soils.

Drilling fluid flow and pressure

Drilling fluid to assist drilling operations has traditionally been water for most boreholes drilled by the NHDOT. The inflow is measured with an electromagnetic flowmeter attached downstream of the drill rig pump, as shown in Figure 1h. The flowmeter records flow via electronic pulses and can therefore handle mud or water used as a drill fluid. The driller directly controls the inflow with a valve to ensure efficient removal of cuttings and reduce wear on the drill bit when coring rock. However, without the MWD instrumentation, precise flow-rate information is unavailable. In addition to the inflow, a second flowmeter can be installed at the outflow to measure the fluid lost in the subsurface (fluid lost = inflow – outflow). Measuring the net flow is especially useful in detecting cavities, fractures, or very porous geological material.

While the operator controls the injection flow, the injection pressure is measured using a pressure transducer attached via a T-connector along the drilling fluid pressure line located downstream of the water pump.

REVIEW OF MWD PARAMETER EVALUATION

In an MWD test, the resistance of a given geological material to drilling is often assessed in terms of compound parameters. These parameters consist of empirical relationships, indices, or energies that combine two or more drilling parameters. Although changes in drilling parameters often indicate changes in subsurface conditions, compound parameters attempt to normalize the effect of conditions imposed by the driller (e.g., rotation rate and downthrust). Such a normalization effort is indispensable for evaluating large data sets and establishing comparisons between different sites, even if the same test operator performed all tests. Unit consistency is imperative in using these expressions.

Several of the legacy relationships recommended by the MWD standards under development and often used in MWD data reduction were developed between the late 1950s and the 1980s, and were initially applicable to very deep wells drilled in rock using rotary drilling with roller bits. The reader is referred to Benoît et al. (1) for an in-depth discussion of these relationships and recommendations on compound parameter selection for data analysis.

Some compound parameters require the downforce (Fe) or crowd to estimate drilling energy. Using the MWD setup described in this paper, Fe can be obtained as described below. Souza et al. (10) present a comparison of net downthrust force measurements from the hydraulic sensor and measurements from the instrumented drill rod. It was demonstrated that the instrumented drill rod sensor placed directly at the top of the drill string yields more accurate, direct thrust measurements than the wired sensor using the hydraulic thrust pressure line, providing more instantaneous depth details with the rod on top of the drill string. For this reason, using downthrust measurements from the instrumented rod is recommended for compound parameter calculation and interpretation.

- Hydraulic pressure transducer

  The corrected downthrust pressure from the hydraulic pressure transducer can be divided by the drill bit's cross-sectional area to determine the net downforce. It is important to note that Pe represents the net downthrust pressure, i.e., the downthrust pressure when no holdback pressure is applied. When a holdback pressure is applied, subtract the holdback pressure from the downthrust pressure to obtain the net pressure, Pe (net = downthrust – holdback). This operation is not necessary when using the instrumented rod, as it directly measures the actual applied force.

- Instrumented drill rod

  The net downthrust force (Fe) is obtained directly from the instrumented drill rod. Some correlations may use the net downthrust pressure (Pe) instead. Fe can be converted to pressure by dividing by the drill bit's cross-sectional area.

Simon (2-3) and Somerton (4) contributed to the early development of compound parameters for quantifying the resistance of geological materials to drilling. Somerton (4) proposed an empirical

relationship (Equation 2), derived from a limited number of laboratory-scale rotary experiments in rock and concrete, to evaluate the advance rate as a function of downthrust and rotation rate.

$$S=\sqrt{1.5}\sqrt{\frac{V_R}{V_A}}\frac{F_e}{D^{1.5}} \quad (2)$$

where V_A = rate of penetration (in./min), D = bit diameter (in.), V_R = rate of rotation (rpm), F_e = effective weight on the bit (lbs), S = rock strength parameter (psi), also referred to as Somerton Index by others in the literature.

Somerton (4) noted that the expression shown in Equation 2 was not intended for general application and was sensitive to bit wear, particularly through empirical coefficients. He also reported that drilling resistance correlated better with triaxial strength than with unconfined compressive strength, which is more representative of in situ stress conditions.

In contrast, Simon (2-3) developed a more generalized formulation applicable across drilling methods. His expression was later shown to encompass Somerton's more limited formulation of rotary drilling as a special case. Benoît et al. (1) recommend using Equation 3, based on Simon (3), which includes the measured torque.

$$S = \frac{5.2\,\pi C_R V_R}{V_A\,D^2} \quad (3)$$

where V_A = rate of penetration (in./min), D = bit diameter (in.), V_R = rate of rotation (rpm), C_R = torque (in.-lbs), S = drilling resistance (psi)

Girard (13) modified the expression by Somerton (4), previously shown in Equation 2, to the formulation shown in Equation 4, resulting in a drilling resistance in units of lbs/in.$^{0.5}$.

$$S=\sqrt{\frac{V_R}{V_A}}Fe \quad (4)$$

In this particular case, if we define V_R in in./min (V_{Rm}) instead of RPM and divide the net downthrust force on the bit by the area of the borehole, this modified Girard expression leads to a drilling resistance in units of psi, which is compatible with previous expressions introduced by Somerton and Simon. Equation 5 shows the modified Girard expression.

$$S=\sqrt{\frac{V_R}{V_A}}\frac{Fe}{A} \quad (5)$$

Assessments by Benoît et al. (1) suggest that Simon's relationship, as shown in Equation 3, may provide more detail for stratigraphic interpretation. Torque provides a more direct measure of ground response and can help delineate stratigraphic changes. Although the Somerton index captures meaningful variation with depth, it is derived from thrust, a driller-controlled input, whereas torque is a reactive parameter governed by subsurface conditions. As such, interpreting formation behavior based solely on thrust (without corresponding torque data) can be misleading.

The energy to drill boreholes can also be estimated using Equation 6 developed by Teale (5).

$$e=\frac{Fe}{A_{drill\ bit}}+\frac{2*\pi*V_R*C_R}{A_{drill\ bit}*V_A} \quad (6)$$

where e = specific drilling energy (psi), Pe = net downthrust pressure (psi), V_R = rotation rate (rpm), C_R = torque (in.-lbs.), $A_{drill\ bit}$ = drill bit area (in.^{2}), V_A = advance rate (in./min).

Assessments by Souza et al. (9) and Rodgers et al. (14) demonstrate that, when plotted continuously with depth, specific energy can identify changes in the energy required to remove material, thereby helping delineate stratigraphic transitions. The specific drilling energy was shown to correlate with SPT N-values and CPT tip resistance, thus being a pertinent parameter for comparison with standardized geotechnical methods. It is noted, however, that for comparisons with SPT, N-values should not be capped once the refusal criteria are met.

Rodgers et al. (14) emphasize the importance of drilling efficiently and obtaining quality parameters for representative and reliable ground assessments. Drilling efficiency depends not only on the applied mechanical energy but also on how effectively that energy is converted into productive cutting, crushing, or shearing of the geological material. Proper flushing and removal of drill cuttings are therefore essential, as accumulated drill cuttings inside the borehole promote regrinding, increase friction and torque, and may thus artificially elevate the specific energy.

Drawing on the three drilling phases originally conceptualized by Teale (5) represented in Figure 3, Rodgers et al. (14) describe Phase 1 as an inefficient condition in which insufficient downthrust force prevents adequate bit engagement; the bit tends to slide or grind against the formation, and much of the measured energy is dissipated through friction rather than material removal. Phase 2 represents the optimal drilling condition, characterized by sufficient but not excessive crowd, stable penetration per rotation, effective bit indentation, and efficient cuttings removal. Under these conditions, the drilling response is governed primarily by the resistance of the geological material, producing more representative and repeatable MWD parameters, improved core recovery, and stronger correlations between specific energy and conventional strength measurements. In contrast, Phase 3 occurs when excessive downthrust or inadequate flushing causes cuttings to accumulate beneath the bit, leading to regrinding, elevated torque and energy demand, tool wear, sample disturbance, and unreliable strength estimates. Rodgers et al. (14) therefore argue that MWD should be conducted as close as possible to Phase 2, since efficient drilling minimizes equipment- and procedure-related influences and allows recorded parameters to better reflect actual subsurface conditions. This is critical for obtaining high-quality, design-relevant assessments rather than measurements dominated by drilling inefficiencies.

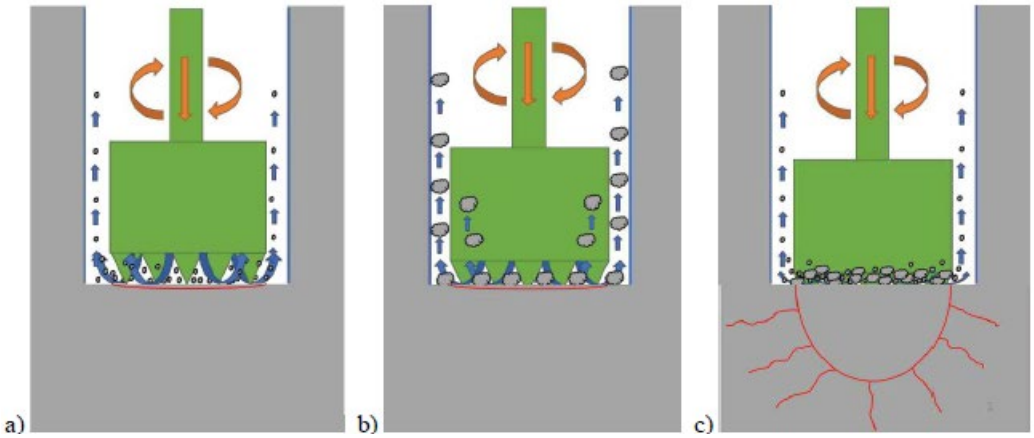

Figure 3 – The three phases of non-percussive rotary drilling after Rodgers et al. (14). a) Inefficient Phase 1, b) optimized Phase 2, and c) destructive Phase 3.

IN SITU TESTS

MWD testing was conducted at 14 sites across New Hampshire, as shown in Figure 3. The experimental program was divided into two phases. Phase 1 focused on sensor verification, system calibration and refinement, operator familiarization, and the development of testing procedures. The sensor installations, system adjustments, drill-bit selection, data-logging improvements, procedural modifications, and testing recommendations developed throughout the campaign are summarized by Souza et al. (10). Data collected during Phase 2 were then used for stratigraphic interpretation and evaluation of compound drilling parameters.

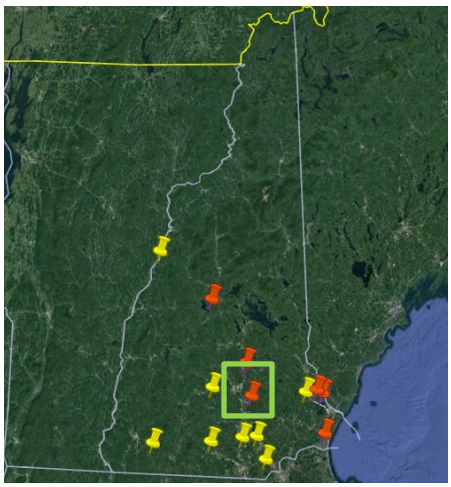

Figure 2 – NHDOT MWD testing site locations in New Hampshire. Phase 1 sites are shown in yellow, and Phase 2 sites are shown in red. Londonderry site highlighted in green.

This paper presents data processing and interpretation based on lessons learned during Phases 1 and 2 of the experimental campaign. The results discussed herein were collected at a site in Londonderry, NH, highlighted in green in Figure 2. Regional geologic mapping indicates

Pleistocene glacial till deposits overlying bedrock of the Berwick Formation, consisting of biotite-quartz-feldspar granofels or schist.

RESULTS AND DISCUSSION

The Londonderry boreholes used for this assessment consisted of approximately 16 ft of soil overburden drilling, drilled with a tricone roller bit, and about 10 ft of rock coring, drilled with a coring bit on a double-tube core barrel. Results and lessons learned are discussed in the following sections.

This paper is structured to guide the reader through the main patterns observed in MWD data before presenting the complete profiles. The objective is to provide a practical framework for recognizing and interpreting common trends, similar to a guided training exercise. Souza et al. (10) describe key features observed in MWD profiles during drilling through overburden soils and discuss how these features may be used to identify changes in subsurface stratigraphy.

During the initial assessment, parameters directly controlled by the driller, including thrust, rotational speed, and fluid inflow, were maintained as constant as practicable within each borehole. Variations in responsive parameters, such as the advance rate, torque, and drilling fluid pressure, were then evaluated as the borehole advanced through different strata. This approach was adopted to better isolate the influence of ground conditions on both the recorded parameters and the calculated compound parameters.

The selected operating conditions were not intended to represent the most efficient drilling approach for every material encountered. Rather, they provided a controlled basis for evaluating how changes in drilling response relate to stratigraphy. Understanding the influence of operator-controlled parameters remains essential for defining optimized drilling procedures and obtaining meaningful, repeatable, and comparable MWD measurements.

Soil Overburden Drilling

Lessons Learned on Data Interpretation

Before presenting the MWD profiles, the following general trends are introduced as a guide for identifying potential stratigraphic changes during drilling through overburden soils. These trends should be interpreted collectively and in relation to the operating conditions, since changes in driller-controlled parameters may influence the recorded response.

- **Penetration rate:** Low penetration rates are generally associated with dense or stiff, more resistant materials, such as gravel, cobbles, boulders, or bedrock. Abrupt decreases or increases in penetration rate may therefore indicate transitions to harder or softer strata, respectively. However, inadequate removal of cuttings and changes in drilling fluid composition may also affect the penetration rate and lead to misleading interpretations of drilling resistance (15).

- **Downthrust and rotation:** In more resistant materials, the driller may increase downthrust or rotation to increase the penetration rate. Because an increase in downthrust or rotation often produces a corresponding increase in penetration rate, changes to responsive parameters should be interpreted with caution whenever the operating settings are adjusted.

- **Drilling fluid pressure:** At a constant flow rate, lower fluid pressures generally suggest granular, permeable, or fractured materials. Conversely, higher pressures may indicate cohesive and less permeable soils, where restricted fluid movement and clogging around the drill bit can cause pressure buildup.

- **Compound parameters:** Changes in downthrust and other operating parameters may be reflected in calculated compound parameters despite their normalizing effect. Despite this influence, increases in SPT N-values or refusal in adjacent soil profiles were generally accompanied by higher drilling resistance and specific energy values at similar depths when corresponding materials were encountered. These parameters may therefore assist in identifying changes in layer resistance or relative density/consistency, provided that variations in drilling conditions are also considered.

- **Fluid system response:** Although fluid pressure is not included directly in compound parameter calculations, it is useful for identifying fluid loss, blockages, and specific geological features. Voids, fractures, and permeable zones are generally associated with pressure decreases, whereas pressure increases may indicate clogging in cohesive materials, particularly if flow and/or advance rates are inadequate or too rapid.

Interpreting a Soil Drilling Profile

The features listed in the previous section can be used to help identify changes in the ground stratigraphy. Figure 4 shows the drilling parameters for the borehole in soils and the respective compound parameters discussed in previous sections. To plot all four drilling-resistance profiles on a common scale and facilitate comparison, the Simon and Teale values were divided by 10 for the soil profile. For the rock profile, the Simon values were divided by 100, the Teale values by 50, and the modified Girard values by 2.

The key difference between the relationships developed by Somerton (4) and Simon (3) lies in the parameters they considered: Somerton accounted for thrust force but not torque, while Simon incorporated torque but did not consider thrust force. In contrast, Teale's specific drilling energy equation includes both thrust and torque.

When downthrust and rotation are maintained approximately constant, changes in penetration rate reflect variations in ground resistance: decreases in advance rates may reflect denser or more gravelly soils. As noted by Benoît et al. (1), Figure 3 suggests that Simon's equation provides more stratigraphic detail, showing more peaks and valleys – indicating that this compound parameter may be more helpful in delineating changes in ground stratigraphy.

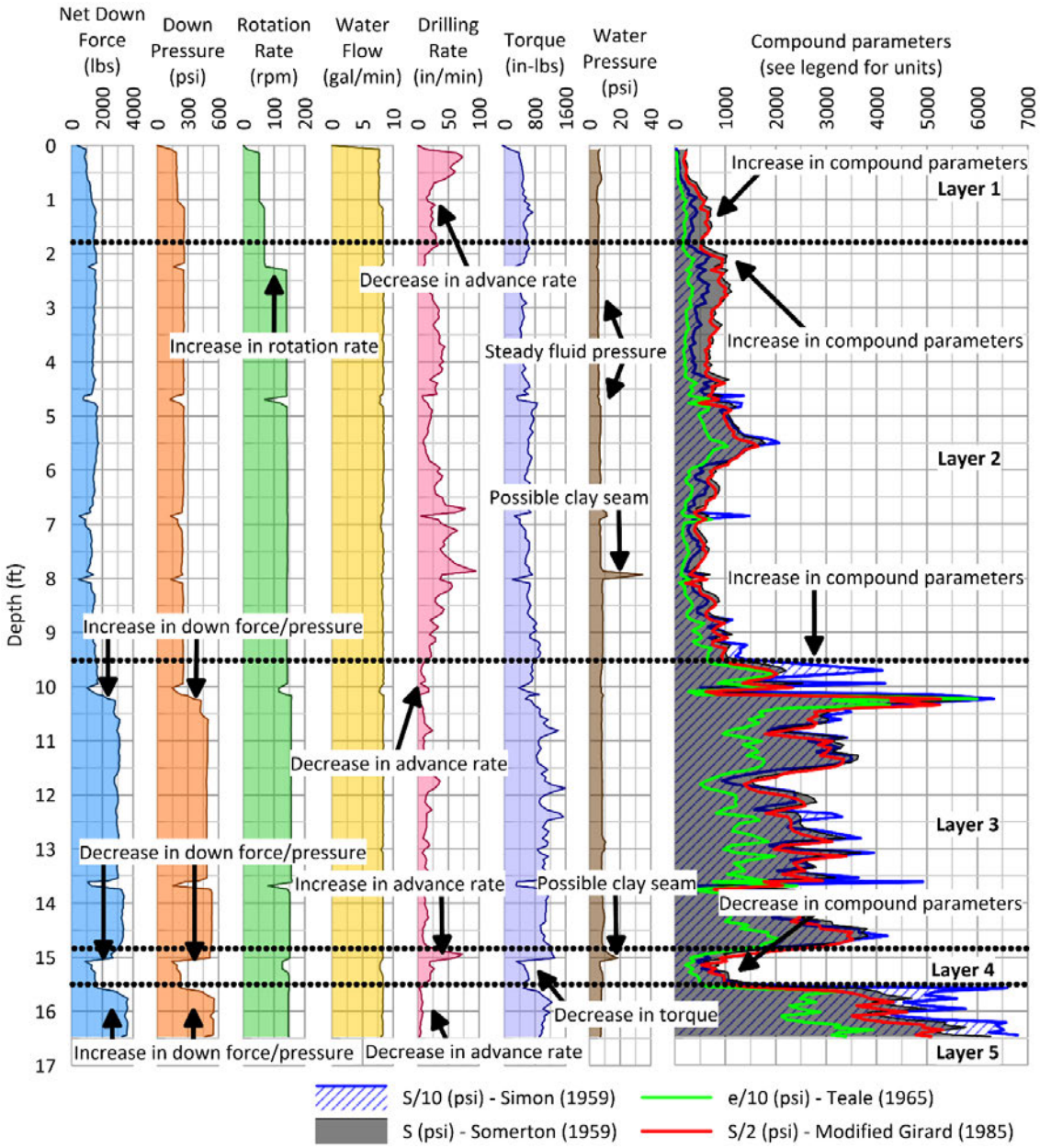

Figure 3 – Soil overburden drilling MWD profile in Londonderry, NH.

The figure summarizes the main features used to interpret the MWD profile. Based on qualitative changes in the recorded and compound parameters, five major strata can be distinguished. *Layer 1*, at the ground surface, is likely associated with fill and shows an apparent increase in density or drilling resistance below approximately 1 ft. This transition is reflected by a decrease in penetration rate, an increase in the compound parameters, and a small increase in net force. However, distinguishing artificial fill from native soil requires visual inspection and cannot be established from MWD measurements alone.

Layer 2 extends from approximately 2 to 9.5 ft and exhibits a relatively consistent range of compound parameters. An increase near the top of the layer coincides with the operator nearly doubling the rotational speed and should therefore not be attributed solely to a change in ground

conditions. Fluid pressure remains generally stable throughout this interval and across most of the profile, suggesting predominantly granular material or adequate flushing where cohesive soils may be present. A localized pressure spike at approximately 8 ft may indicate a thin clayey or silty seam.

Layer 3 extends from approximately 10 to 15 ft. An increase in the compound parameters begins near 10 ft, before the downthrust is nearly doubled at approximately 10.5 ft, suggesting an increase in relative density or ground resistance. The greater variability in the profiles may also indicate a higher gravel content. Despite the increase in downthrust, the penetration rate decreases, further supporting the interpretation of a denser or more resistant stratum.

Layer 4, between approximately 15 and 15.5 ft, shows lower apparent resistance than Layer 3. This is reflected by decreases in the compound parameters, downthrust, and torque, together with an increase in penetration rate. A localized increase in fluid pressure may indicate the presence of a clay seam.

Layer 5 begins below approximately 15.5 ft and is characterized by increases in downthrust and compound parameters. Although the penetration rate also increases, the greater applied downthrust required to advance through this interval, together with the higher compound values, suggests a denser or more resistant material.

Interpretation of MWD profiles should be supported by observations of drill cuttings and, where available, adjacent borehole data. At the current stage of MWD development, the measured profiles are more effective for identifying relative changes in drilling response than for independently classifying soil type. Visual examination of cuttings improves stratigraphic interpretation, helps distinguish local geological variability from apparent differences between adjacent boreholes, and provides a basis for comparing MWD responses with SPT logs. In this case, the cuttings indicated that the profile was predominantly granular, which is consistent with the generally stable fluid-pressure response. Effective flushing is therefore important not only for maintaining drilling efficiency and data quality, but also for recovering cuttings that support geological interpretation.

Figure 4 presents the same MWD profile together with SPT blow counts and stratigraphic information from an adjacent borehole. Blow counts are reported for each 6 in. increment to facilitate comparison with the recorded and compound MWD parameters, along with sample recovery and the corresponding SPT N-values. Overall, the SPT results support several of the trends discussed in Figure 3. Gravel encountered between approximately 4 and 6 ft and throughout the glacial till corresponds to local increases in drilling resistance, while increases in water pressure and penetration rate near 8 and 15 ft are consistent with clay seams. Similarly, the increase in compound parameters beginning at approximately 9.5 ft agrees with the higher N-values measured in the adjacent borehole, supporting the interpretation of a denser and more resistant layer.

Some differences between the profiles are expected due to the variability of glacial deposits. For example, a boulder logged between 12.8 and 13.9 ft in the SPT borehole was not encountered in the MWD borehole. Weathered rock was also encountered slightly shallower in the MWD

borehole, at approximately 15 ft. In addition, SPT recovery in these deposits was generally below 100% and often near 50%, which limits the precision of the stratigraphic log. The comparison therefore shows that MWD can complement discrete SPT information by providing a continuous profile of changes in drilling response, while interpretation remains stronger when supported by cuttings and nearby borehole data.

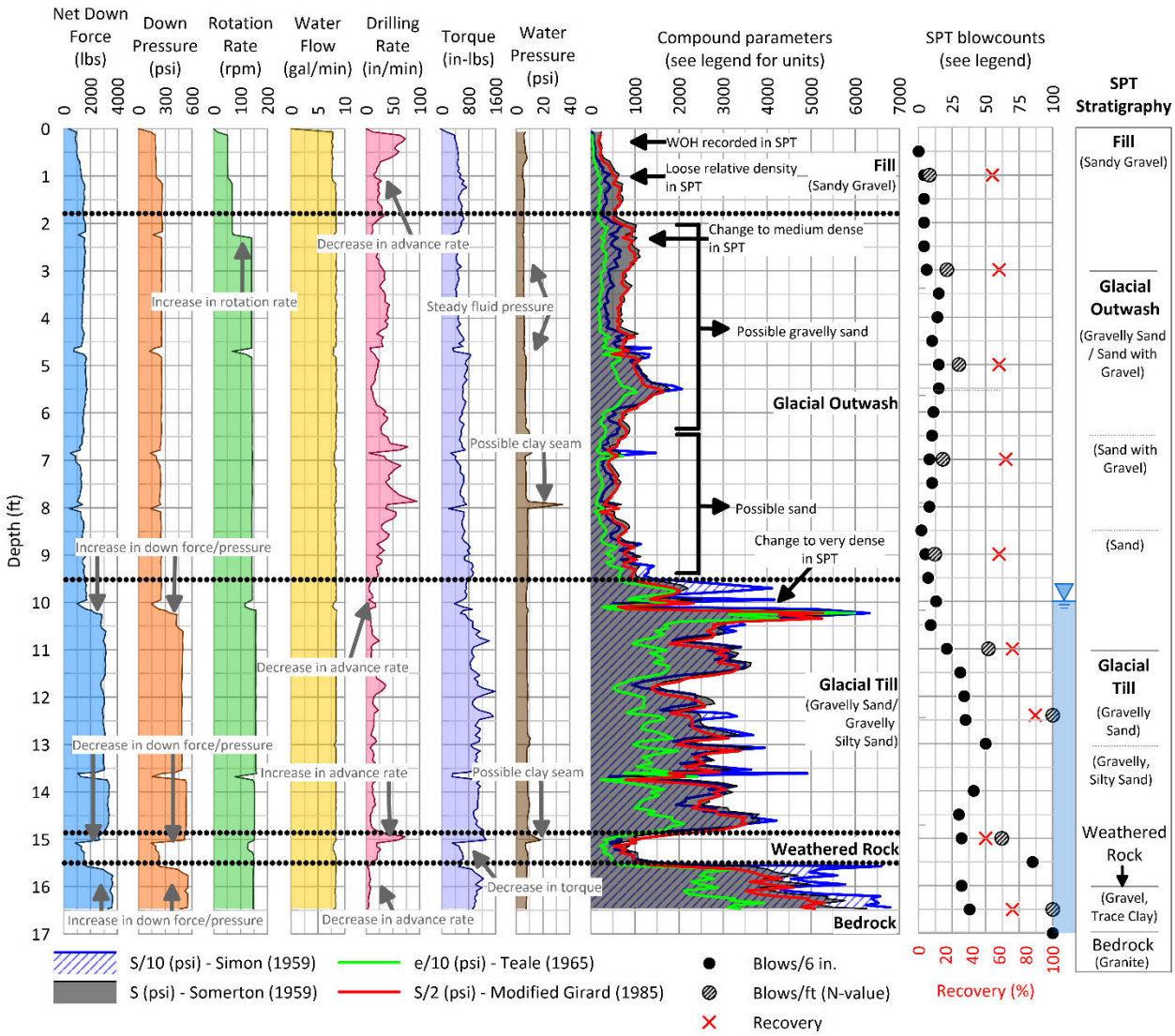

Figure 4 – MWD profile shown in Figure 3 compared to adjacent SPT.

Rock Coring

Lessons Learned on Data Interpretation

Benoît et al. (1) identify several MWD trends that may assist in assessing rock conditions during coring. These indicators should be interpreted collectively and in relation to changes in driller-controlled parameters, including downthrust, rotational speed, and injection flow.

- **Higher penetration rates and torque** may indicate fractured rock or interbedded soil seams.

- **Concurrent increases in fluid pressure and penetration rate** may indicate a cohesive seam, such as clay gouge within a fractured zone.

- **Lower and relatively stable penetration rates and torque** are generally associated with more intact rock.

- **Abrupt changes in torque or drilling resistance** may mark transitions between fractured and more competent rock.

- **Torque-based parameters may improve delineation of rock profile changes**, since torque represents a response to the material encountered rather than a parameter directly controlled by the driller.

Interpreting a Rock Core Profile

Figure 5 presents the MWD parameters for two core runs in granitic rock, together with photographs of the recovered cores. Core recovery was approximately 80%, while the low RQD values indicate substantial fracturing in both runs. The cores were also examined to distinguish natural fractures from those induced during drilling.

In Run 1, the interval between approximately 26.5 and 27.8 ft was highly fractured and contained clay remnants along joint surfaces. This condition is consistent with the simultaneous increases in fluid pressure, torque, and penetration rate recorded over the same interval. Most of the material loss in this run also occurred within this fractured zone. In contrast, the rock between approximately 28 and 30.5 ft was more intact and contained fewer fractures. In Run 2, clay gouge observed between approximately 33.2 and 34 ft corresponded to increased fluid pressure and penetration rate, together with lower torque. Below this interval, the rock appeared more competent, although a short section was not recovered. Such losses may occur near the end of a core run where localized fracturing allows material to fall from the core barrel.

It should be noted that for the drilling resistance methods that require the area (A) or the diameter (D) of the borehole, an equivalent diameter should be calculated using the area of the donut of the coring drill bit used for advancing the core barrel instead of the area or diameter of the borehole.

The drilling resistances in the rock coring profile shown in Figure 5 suggest that the use of torque may provide some assistance in delineating changes in stratigraphy. In this case, the Somerton index also provides good variations with depth; however, thrust is a driller-controlled parameter, while torque is a result of ground response. Therefore, incorporating thrust without accounting for the measured torque can be misleading.

The results presented in this paper seem to suggest that the expression by Simon (3) can reliably provide the level of stratigraphic detail necessary to build a geotechnical model of the

subsurface. As more MWD work is carried out, these expressions may be modified to account for drill bit wear and type. None of the expressions discussed in this paper include the effect of mud/water flow and pressure, which are key parameters to drilling in both soils and rock. It should also be noted that the recorded torque values are highly dependent on the type of drill bit. For example, for the same size, a tricone roller bit will require less torque than a drag bit.

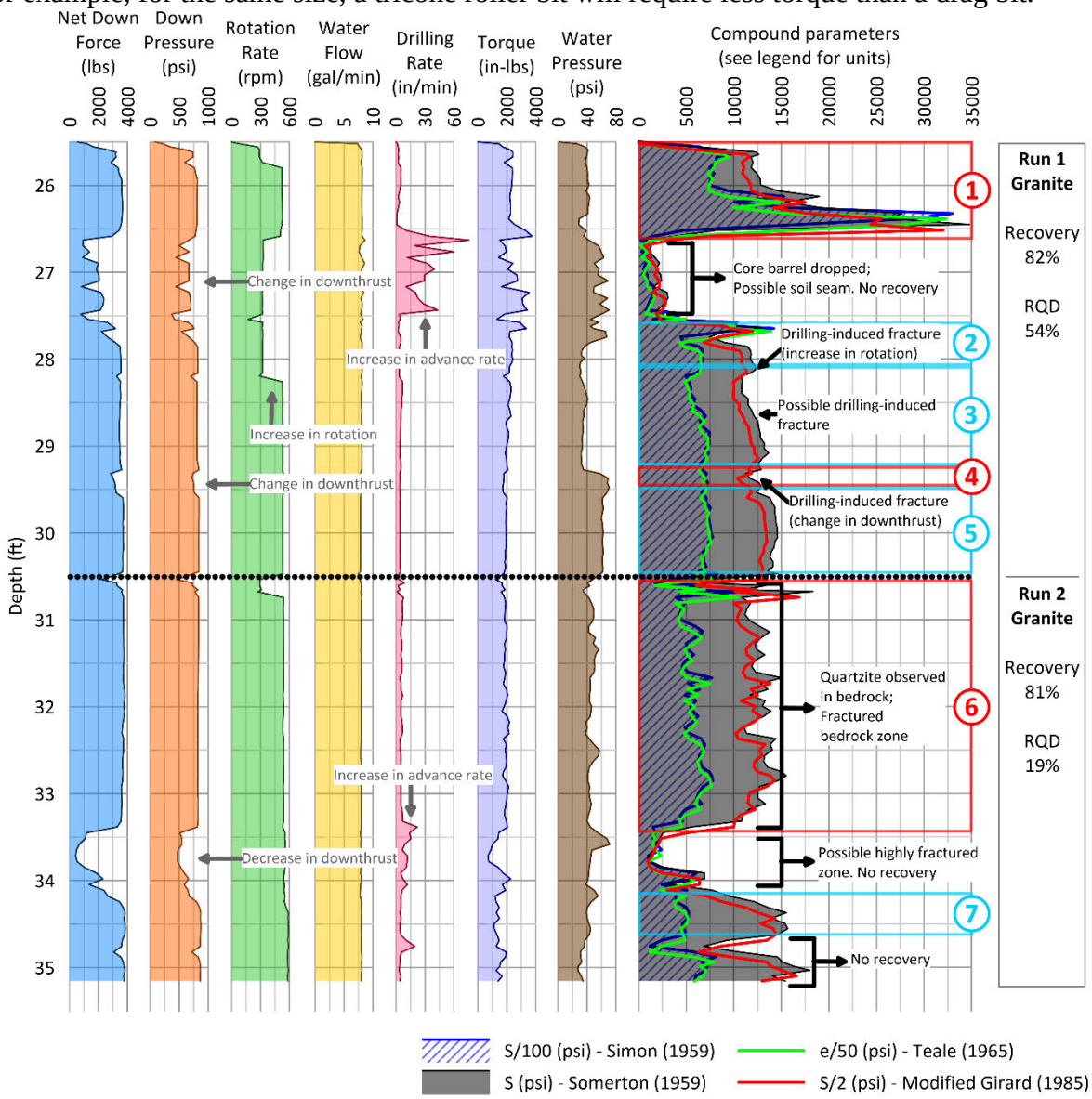

Run 1 (25.5' - 30.5'): Hard, slightly weathered, slightly fractured, medium grained, light greenish gray GRANITE. Low to moderate angle fractures with serpentinite and clay coatings. Dropped from 26.5' to 27.5'.

Run 2 (30.5' - 35.2'): Hard, moderately weathered, medium to coarse grained, light greenish gray GRANITE. Low to moderate angle fractures with clay coatings. 0 to 3' layer of gray quartzite.

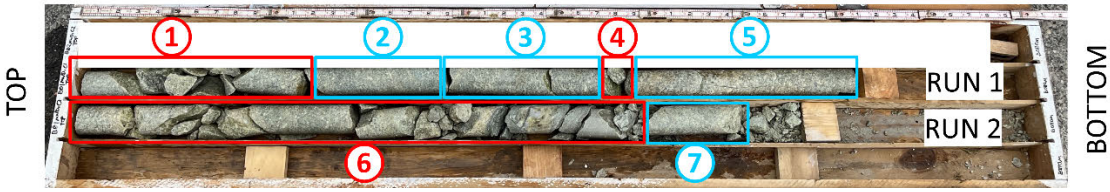

Figure 5 – Rock coring MWD profile in Londonderry, NH.

CONCLUSION

Monitoring While Drilling can contribute significantly to geotechnical subsurface characterization, particularly in materials that may be difficult to assess using conventional SPT or CPT explorations, such as gravelly soils, boulders, and bedrock. MWD provides continuous information with depth and can help bridge gaps where conventional testing is limited by poor recovery, refusal, or discrete sampling intervals.

This paper introduced the MWD equipment installed on NHDOT drill rigs, discussed compound parameters used to identify changes in stratigraphy, and presented examples from soil overburden drilling and rock coring at a site in Londonderry, NH. The results show that changes in advance rate, torque, drilling fluid pressure, and compound parameters can help delineate changes in ground resistance and rock condition. The Simon expression provided useful stratigraphic detail, particularly because it incorporates torque, which reflects the response of the material encountered. The instrumented drill rod, which directly measures force and torque at the top of the drill string, is strongly recommended for compound parameter calculation.

Compound parameters should not be interpreted independently of the recorded drilling parameters or changes in drilling conditions. Downthrust, rotation rate, drill bit type and condition, flushing, and cuttings removal can influence both measured and calculated parameters. MWD interpretation should therefore be supported by visual inspection of drill cuttings, recovered cores, and adjacent borehole information whenever available. Variations between nearby profiles should also be expected, particularly in heterogeneous glacial deposits. Efficient flushing is important not only for drilling efficiency and data quality, but also for recovering cuttings that support geological interpretation.

MWD technology has strong potential to develop into a reliable, standardized geotechnical test in the United States. Continued testing across different geological materials, drill bits, and drilling conditions is needed to improve interpretation, evaluate correlations with ground resistance, and move from qualitative stratigraphic assessment toward more quantitative applications. Establishing procedures that promote efficient drilling and produce high-quality parameters is essential to ensure that MWD measurements reflect the ground response and support reliable geotechnical interpretation.

ONGOING WORK

The NHDOT recently acquired a track-mounted CME-55 fully equipped with MWD instrumentation. In addition, the instrumented drill rod used to measure torque and downthrust was upgraded to include triaxial accelerometers, allowing vibration to be recorded at the top of the drill string. Rodgers et al. (12) demonstrated that vibration measurements can improve MWD interpretation by capturing how different geomaterials absorb, transmit, or reflect mechanical energy through the drill string. Collecting these measurements directly above the drill string is expected to provide more reliable and meaningful vibration data across varying geological materials and to support improved stratigraphic interpretation.

MWD data collection is ongoing, with current efforts focused on refining experimental procedures, improving drilling efficiency, and strengthening interpretation of subsurface stratigraphy from MWD profiles. As the database expands, the objective is to move beyond qualitative interpretation and develop more quantitative applications of MWD, including improved estimates of ground resistance in addition to stratigraphic delineation.

REFERENCES:

1. Benoît, J., Souza, B., and Reiffsteck, P. (2025). Simon to Somerton: A review of MWD drilling resistance. *Proceedings of the First International Conference on MWD*.
2. Simon, R. (1956). Theory of rock drilling. *Proceedings of the Sixth Annual Drilling and Blasting Symposium*, University of Minnesota.
3. Simon, R. (1959). Discussion of paper by Simon (1959). *AIME Petroleum Transactions*, 216, 361-363.
4. Somerton, W. H. (1959). A laboratory study of rock breakage by rotary drilling. *AIME Petroleum Transactions*, 216, 92-97.
5. Teale, R. (1965). The concept of specific energy in rock drilling. *International Journal of Rock Mechanics and Mining Sciences & Geomechanics Abstracts*, 2, 57-73.
6. Pfister, P. Drilling Parameter Recording in Soil Engineering. *Ground Engineering*, vol. 18 (3), 1985, pp. 16–21.
7. ISO 22476-15 (2016). *Geotechnical investigation and testing - Field testing - Part 15: Measuring while drilling*, 22 p.
8. Reiffsteck, P., Benoît, J., Bourdeau, C., and Desanneaux, G. (2018). Enhancing geotechnical investigations using drilling parameters. *Journal of Geotechnical and Geoenvironmental Engineering*, 144(3).
9. Souza, B., Benoît, J., and Pelham, K. (2024). Subsurface Characterization of Coastal Deposits Using Measurement While Drilling. *Proceedings of the 7th International Conference on Geotechnical and Geophysical Site Characterization.*
10. Souza, B., Benoît, J., and Pelham, K. (2025). Implementation and use of a Measurement While Drilling system: Lessons learned and future challenges. *Proceedings of the First International Conference on MWD*.
11. AASHTO (2025). *Measurement-While-Drilling (MWD) for Geotechnical Site Characterization.* Draft standard specification, Technical Subcommittee: Geotechnical Exploration, Instrumentation, Stabilization and Field Testing.
12. Rodgers, M., McVay, M., Horhota, D., Hernando, J., and Paris, J. (2020). Measuring while drilling in Florida limestone for geotechnical site investigation. *Canadian Geotechnical Journal*, 55(8), 1154-1167.
13. Girard, H. (1985). *Contribution à l'exploitation des paramètres de forage en génie civil*. Thesis, University of Bordeaux, France.
14. Rodgers, M. B., Kelch, W. W., and Jameson, D. (2025). The role of drilling efficiency in geotechnical measuring while drilling. *Proceedings of the First International Conference on MWD*.
15. Bingham, M. G. (1965). A new approach to interpreting rock drillability. *Oil and Gas Journal*, 93 p.

30. Risk-Based Blasting Specifications for Highway Rock Excavation: Mitigating Project Risk Through Proper Specification Development

Dr. Anthony Konya
DetX
304 N Broadway
Coweta, OK 74429
anthony@idc-pbs.com

Juliette Okel
DetX
304 N Broadway
Coweta, OK 74429
j.okel@detxglobal.com

ABSTRACT

Blasting specifications for highway rock excavation must balance measurable project outcomes with sufficient contractor flexibility to respond to changing geologic conditions. Performance-dominant specifications can leave scope, acceptance, and documentation requirements undefined, while overly prescriptive specifications can impose unsuitable blast designs and shift design responsibility toward the owner. This paper presents a risk-based hybrid framework that defines measurable performance requirements, establishes limited technical guardrails against recognizable high-risk designs, requires verification before critical evidence disappears, and provides a controlled process for adapting the blasting program as field information becomes available. The framework addresses blast-control zones, effective charge diameter, burden, stiffness ratio, perimeter loading, flyrock control, cooperating charge, test blasting, monitoring, drill and loading records, bid normalization, and variance procedures. The objective is to make the minimum acceptable blasting program visible before bid while preserving contractor responsibility for blast design and creating a verifiable, adaptable, and comparable basis for procurement.

INTRODUCTION

Rock blasting is one of the few highway construction activities in which a single, seconds-long operation can permanently alter the excavation, damage the remaining rock mass, affect nearby infrastructure, and eliminate much of the physical evidence needed to determine what occurred. Despite these consequences, blasting specifications are often treated as a minor subsection of rock excavation rather than as a primary engineering and risk-allocation document. They may require "controlled blasting," a stable final slope, and compliance with vibration limits without defining the minimum technical program necessary to achieve those results. The project therefore begins with a desired outcome but no common definition of the work required to produce it.

This deficiency creates risk before drilling begins. When the specification leaves critical requirements undefined, each bidder fills those gaps with its own assumptions. One contractor may price blasting at $4 per cubic yard based on large production holes, limited perimeter control, minimal monitoring, and basic documentation. Another may price the same quantity at $40 per cubic yard after including smaller holes, precision perimeter blasting, face profiling, test blasts, traffic protection, specialist review, monitoring, and complete drill and loading records. The price difference does not, by itself, establish which contractor is more competent. It demonstrates that the contractors are bidding fundamentally different blasting programs under the same pay item. The technically stronger bidder may be excluded as noncompetitive, while the lower bidder is rewarded for omitting controls that the owner may later discover were necessary.

An equally problematic specification can arise at the opposite extreme. A specification that dictates the complete hole pattern, loading configuration, initiation sequence, or explosive product may prevent the contractor from responding appropriately to the geology exposed during construction. Rock structure, weathering, groundwater, weak seams, voids, and changes in relief can make an owner-prescribed design unsuitable. Excessive prescription can therefore reduce engineering flexibility, produce inefficient or damaging results, and blur responsibility when the mandated design fails. The central specification problem is consequently not a simple choice between performance and prescription. It is determining which outcomes the owner must define, which design extremes must be prohibited, and which decisions should remain with the contractor.

Blasting makes this allocation particularly important because the work cannot be meaningfully inspected or reconstructed after firing without contemporaneous records. Actual burden, hole condition, charge distribution, decks, stemming, primer locations, and initiation timing are no longer directly observable once the blast occurs. If surveyed layouts, drill logs, as-loaded records, timing files, video, and monitoring data were not created before firing, the cause of backbreak, excessive overbreak, flyrock, poor fragmentation, vibration, or air overpressure may never be established with confidence. Poor performance can then be attributed broadly to "unexpected geology," while the owner has insufficient evidence to evaluate that explanation and the contractor has insufficient evidence to defend its work. A technical problem becomes a contractual dispute because the specification failed to preserve the information needed to manage it.

The appropriate solution is not simply a longer or more restrictive specification. It is a risk-based hybrid specification that begins with measurable performance requirements, adds limited prescriptive guardrails against recognizable high-risk designs, requires verification before critical evidence disappears, and establishes a controlled process for adapting the blasting program as field information becomes available. Federal Highway Administration guidance expressly recognizes specifications that combine performance and prescriptive elements with measurable thresholds, contractor quality control, owner verification, and defined payment provisions. *(1)* FHWA FP-24 applies this structure through performance requirements, geometry limits, qualified personnel, blast plans, test blasts, monitoring, documentation, and stop-and-revise provisions. *(2)* Unified Facilities Guide Specifications used in federal military construction similarly preserve contractor responsibility for blast design within project-specific restrictions and documentation requirements. *(3)* A 2025 U.S. Army Corps of Engineers bulletin documenting flyrock, cratering, rifling, overexcavation, and fractured foundations demonstrates that deficiencies in blasting design, specification development, and oversight remain consequential institutional risks. *(4)* The same principles apply to Department of War infrastructure programs and private projects near utilities, hospitals, dams, industrial facilities, and other sensitive receptors.

This paper presents a framework for developing these risk-based hybrid specifications. The process begins by defining project outcomes, failure modes, receptors, and blast-control zones. It then establishes technically compatible design envelopes for the limited variables most closely connected to project risk, including effective charge diameter, burden, stiffness ratio, perimeter loading, flyrock control, and maximum cooperating charge. Finally, it connects those requirements to test blasting, drill-log verification, monitoring, reporting, bid normalization, and a documented process for revising the program. The objective is not to design the contractor's blasts, but to ensure that every bidder prices a technically acceptable minimum program and that each blast remains verifiable, adaptable, and accountable.

THE SPECIFICATION PROBLEM

Performance and Prescriptive Extremes

Blasting specifications generally fall along a continuum between performance requirements and prescriptive requirements. Performance specifications are typically the simplest to develop because the owner identifies the required result and leaves the contractor responsible for selecting the means and methods necessary to achieve it. A performance-dominant specification may establish final line and grade, excavation tolerances, slope condition, fragmentation, flyrock containment, ground-vibration limits, and air-overpressure limits while preserving contractor control over drilling equipment, explosives, blast geometry, loading configuration, initiation timing, and sequence. The general concept of these specifications is to give the contractor flexibility to design the program, with the intention of creating competition and allowing the most effective, lowest-cost contractor to win the work.

The simplicity of a performance specification can, however, be deceptive. A requirement is not enforceable merely because it describes a desirable outcome. Terms such as "stable slope," "controlled blasting," "minimal overbreak," or "acceptable fragmentation" have little contractual value unless the specification also defines how the result will be measured, when it will be evaluated, who will determine acceptance, what records must be provided, and what corrective

action will be required. This is typically the major cause for concern in blasting, as the terminology is difficult to properly measure and is normally poorly defined. Furthermore, the difficult technical nature of blasting, the constant interface of the technical application with the rock mass, and the impossibility of reconstructing the blast after it is detonated often lead to arguments not over the performance; but over whether the performance could have been improved or was dictated by geologic conditions. This often presents owners with either attempting to manage a contentious relationship with the contractor and, in the worst extremes defend a rock mass that they possess little data on in court; or the owners end up with substantial price overruns on the project due to 'geologic claims.'

For example, a requirement to produce a stable rock slope may improperly combine several different responsibilities: controlling blast-induced damage, excavating within the specified tolerance, identifying unfavorable geologic conditions, and designing permanent stabilization. Unless these responsibilities are separated, the requirement is neither consistently biddable nor objectively enforceable. Thus, a performance specification may be simple to issue while becoming exceptionally difficult to administer after work begins.

A prescriptive specification occupies the opposite end of the continuum. It may dictate hole diameter, burden, spacing, subdrill, stemming length, explosive type, charge concentration, decking, delay sequence, perimeter-hole location, or even the complete blast pattern. This approach can be extremely troublesome because the owner must effectively design the blasting system before the excavation exposes the conditions under which that system will be used. Blasting variables are interdependent: changing hole diameter affects burden and spacing; burden affects confinement and relief; explosive diameter and distribution affect energy concentration; and bench height affects whether the resulting geometry provides an effective stiffness ratio. A prescribed detail that appears reasonable in isolation may therefore make the overall blast less effective or less safe.

The difficulty becomes greater where discontinuities, weathering, groundwater, weak seams, voids, or abrupt changes in rock quality are encountered. A pattern developed from limited preconstruction information can become unsuitable as excavation advances, yet the contractor may remain obligated to follow it. The prescription can restrict the contractor from making technically appropriate adjustments while simultaneously shifting responsibility toward the owner when the imposed design produces poor fragmentation, excessive backbreak, flyrock, incomplete floor breakage, or other undesirable results. Prescriptive requirements are not inherently inappropriate; they are valuable when a particular variable has a direct and well-understood relationship to a critical risk. The problem arises when the owner attempts to prescribe the entire blasting system without sufficient project-specific engineering or an effective process for revising the requirements as conditions change.

A risk-based hybrid specification avoids both extremes. It begins with measurable performance requirements, then adds only those prescriptive limits needed to exclude methods or operating ranges that create unacceptable project risk. It also establishes the submittals, records, test blasts, hold points, monitoring, acceptance procedures, and revision triggers necessary to verify performance and adapt the blasting program. The resulting specification does not design each blast for the contractor. Instead, it defines the permitted operating envelope, preserves contractor

responsibility for blast design, and prevents price competition from being based on the omission of essential controls. Table 1 summarizes the principal distinctions among the three approaches.

Table 1. Specification approaches and principal risk exposures

Approach	Primary Strength	Principal Exposure	Appropriate Use
Performance-dominant	Generally the simplest to develop and preserves contractor control over means, methods, and innovation.	Apparent simplicity can conceal undefined scope, subjective acceptance, incomparable bids, inadequate records, and weak enforcement.	Work for which required outcomes can be measured objectively and supported by effective qualification, verification, and acceptance procedures.
Prescriptive-dominant	Gives the owner direct control over selected design variables, equipment, or operating methods.	Can be extremely difficult to engineer correctly, freeze assumptions that do not match field conditions, restrict necessary adjustments, and shift responsibility toward the owner.	Narrow, proven requirements supported by project-specific engineering or controls necessary to address a defined safety, regulatory, or infrastructure risk.
Risk-based hybrid	Combines measurable outcomes with targeted operating limits, evidence requirements, and controlled adaptation.	Requires deliberate prebid risk analysis, clearly defined decision authority, and competent field administration.	Consequential or geologically variable blasting where bids must represent comparable levels of control and critical evidence disappears after firing.

Ambiguity, Adverse Selection, and Claims

Ambiguity in a blasting specification is not merely an editorial weakness. It prevents the owner and bidders from reaching a common understanding of the work being purchased. A requirement may sound technically appropriate while still failing to define a measurable quantity, an acceptable result, or the party responsible for achieving it. When that occurs, contractors do not bid the same blasting program. Each bidder prices its own interpretation of the requirement, and the resulting bids cannot be compared solely on unit price.

As an example, the commonly used requirement to perform “controlled blasting” with “closely spaced” and “lightly loaded” holes illustrates the problem. Controlled blasting is not a single method. The term may refer to conventional presplitting, precision presplitting, trim blasting, cushion blasting, line drilling, a reduced-charge buffer row, an air-decked production blast, or some combination of these techniques. Each method has a different purpose, sequence, cost, and relationship to the final excavation surface. Presplitting is normally fired before the adjacent production blast to establish a fracture plane, while trim or cushion blasting removes material remaining along the final wall after production blasting. A buffer row may reduce the energy reaching the perimeter, but it does not necessarily create or protect the final wall in the same manner as a properly designed presplit.

The modifiers “closely spaced” and “lightly loaded” provide no meaningful clarification. Closely spaced perimeter holes could mean 18, 24, 36, or 48 inches, and each spacing produces a different drilling quantity and cost. Light loading is equally indefinite. It may refer to the total explosive weight per hole, the maximum instantaneous charge, the explosive weight per foot of borehole, the relationship between explosive diameter and hole diameter, or the distribution of energy throughout the charged length. A specification cannot adequately describe perimeter loading without considering effective explosive diameter, linear charge concentration, explosive density and energy, coupling or decoupling, charge distribution, decking, stemming, hole deviation, and the initiation sequence relative to adjacent rows. Two holes containing the same total explosive weight can produce substantially different results if one uses a concentrated bottom charge and the other uses a continuous, distributed, decoupled charge.

This form of ambiguity is especially prevalent in performance specifications. Performance requirements are relatively simple to develop because the owner can state that the completed excavation must have a “stable slope,” “minimal backbreak,” “acceptable fragmentation,” or “no damage beyond the excavation line.” The difficulty is that these phrases describe preferences rather than enforceable performance unless the specification establishes objective definitions and acceptance procedures. A stable slope requirement must distinguish blast-induced damage from instability caused by the natural orientation and condition of the rock mass. It must also separate the contractor’s responsibility for excavation and scaling from the designer’s responsibility for permanent reinforcement, drainage, rockfall protection, or other stabilization measures.

Similarly, “minimal backbreak” is meaningless unless the contract identifies the theoretical excavation line, the permitted tolerance, the method and frequency of measurement, and the treatment of isolated geologic fallout. Fragmentation cannot be evaluated consistently unless the specification defines the size criteria, sampling area, measurement method, and disposition of oversize material. A flyrock requirement must establish the controlled area, protected areas, traffic restrictions, and whether the criterion prohibits material from leaving the blast area or merely from leaving the established exclusion zone. Environmental criteria require defined monitoring locations, instrument standards, reporting procedures, and actions to be taken when a threshold is approached or exceeded. Without these provisions, the owner may know what it generally wants but has not defined what the contractor must price or what the inspector must accept.

Ambiguity can also exist in responsibility and procedure even when numerical limits are provided. A specification may require a blasting plan without identifying its minimum contents, review period, revision requirements, or the effect of the owner’s review. It may require test blasts without defining their purpose, acceptance criteria, or whether unsuccessful test blasts are payable. It may authorize the engineer to require changes without distinguishing between a contractor correction necessary to achieve the specified performance and an owner-directed change to the original scope. These omissions become consequential when work is delayed, a blast fails to meet expectations, or the owner directs a more expensive method.

The commercial result is adverse selection. In a properly structured procurement, competition should favor the contractor capable of delivering the required work at the lowest responsible cost. Under an ambiguous specification, competition instead favors the bidder willing to assume the narrowest scope, overlook the greatest amount of risk, or rely on obtaining additional compensation after award. The contractor that recognizes the technical difficulty may include perimeter drilling, reduced-diameter explosives, distributed loading, buffer rows, blast monitoring, survey control, detailed records, and specialist field review. Another bidder may assume a larger production pattern, minimal perimeter treatment, fewer records, and corrective action only if specifically directed. The second contractor can submit a substantially lower price because it is not pricing the same program and is inherently pushing the risk back on ownership, normally unknowingly to the owner group.

For example, one bidder may interpret “controlled blasting” as perimeter holes drilled on 36-inch spacing with a concentrated charge, while another assumes 24-inch spacing, distributed decoupled loading, a reduced-charge buffer row, hole surveys, test sections, and documented adjustment after each blast. The second contractor’s price may be significantly higher even though its production rate and overhead are competitive. The price difference reflects the amount of control included in the work rather than the efficiency of the contractor. Nothing in the ambiguous specification allows the owner to distinguish between these explanations. The procurement therefore risks selecting a contractor based on its tolerance for unpriced risk rather than its technical capability or actual cost efficiency.

This does not mean that the highest bid represents the best blasting program or that every low bidder intends to underperform. The problem is that the specification provides no reliable means of determining what each bidder included. Competent contractors are forced either to price the program they believe the owner will eventually demand and risk losing the work, or to reduce their assumed scope to remain competitive. Over time, this procurement structure discourages technically rigorous bidders from competing and rewards contractors that treat undefined requirements as future negotiation opportunities. The apparent savings at award may therefore represent deferred project risk rather than an actual reduction in cost.

Claims arise when the owner's unstated expectation encounters the contractor's priced interpretation. If the lower-cost program produces excessive backbreak or a damaged final wall, the owner may direct the contractor to reduce hole spacing, change explosives, add a buffer row, conduct test blasts, or provide additional monitoring. The owner may characterize these measures as necessary to comply with the original requirement for controlled blasting. The contractor may respond that the directed measures were not contained in the bid documents and constitute a compensable change. If the owner withholds payment or requires corrective work, the disagreement can expand into claims for additional drilling, explosives, delay, standby time, scaling, stabilization, rehandling, or loss of productivity.

These issues are also why typical ownership complains about the risk of blasting – they normally do not mean risk in terms of flyrock or ground vibration, which can be technically controlled in a variety of manners. Instead, the risk arises from an inability to properly define the blasting program in a way that a technically sufficient contractor can properly bid and be awarded the work under the mechanism of low price.

Blasting makes these disputes particularly difficult because much of the physical evidence is destroyed or obscured when the blast is fired. The original burden, drill-hole condition, groundwater, charge placement, stemming condition, hole deviation, and initiation performance cannot be fully reconstructed afterward. Without contemporaneous drill logs, loading records, timing data, surveys, photographs, video, vibration records, and post-blast mapping, the parties may be unable to determine whether the result was caused by geology, an unsuitable design, poor execution, or an owner-imposed constraint. The claim then becomes a contest between competing narratives rather than an engineering evaluation supported by evidence.

Excessive prescription creates the opposite claims problem. When the owner dictates the complete hole pattern, loading configuration, or timing sequence, the contractor may argue that poor results were caused by the owner's imposed design. If field conditions differ from the assumptions underlying that design, the contractor may also seek compensation for changed conditions, lost productivity, or directed revisions. The owner is then placed in the position of defending a blast design that it may never have intended to assume. Ambiguous performance requirements and excessive prescription therefore reach the same undesirable endpoint through different paths: the parties dispute what was required, who controlled the relevant decision, and who must bear the resulting cost.

A risk-based hybrid specification addresses this problem by making the minimum acceptable blasting program visible before bid. Performance requirements define the results to be achieved and the methods by which those results will be evaluated. Targeted prescriptive limits exclude specific practices or operating ranges that present unacceptable risk. Submittal requirements, test blasts, hold points, monitoring, records, and revision triggers establish how performance will be demonstrated and how the program will adapt to field conditions. A defined variance procedure permits technically justified changes without informally transferring responsibility between the parties.

The objective is not to make every contractor use an identical blast design or to guarantee identical results. The objective is to ensure that every bidder prices a comparable minimum level of technical control, documentation, and risk management. When the required performance, prohibited extremes, evidence requirements, and decision process are visible before award, competition can return to contractor efficiency and technical judgment rather than being driven by omissions, optimistic assumptions, or future claims.

A RISK-BASED HYBRID FRAMEWORK

The framework has four layers: performance; guardrails excluding unacceptable designs; verification of planned through observed conditions; and adaptation through tests, action levels, hold points, and variances. Procurement clauses disclose information, quantities, review periods, and payment.

Start with Outcomes and Control Zones

Development starts with the finished facility and consequences, not a preferred pattern. Outcomes include slope geometry, overbreak, rockfall condition, fragmentation, subgrade protection, containment, and receptor compliance. Blasting cannot guarantee long-term stability; geotechnical design separately addresses structure, kinematics, drainage, and stabilization.

Divide work into control zones. A remote cut does not require the program appropriate beside a building, bridge, pipeline, traffic, or historic structure. Zoning considers geometry, rock structure, weathering, water, voids, receptor vulnerability, public exposure, access, and delay. For each zone identify the failure, consequence, measurable outcome, limited preventive variable, evidence, and response. Table 2 illustrates the conversion.

Table 2. Example conversion of blast risks into hybrid controls			
Risk	**Performance Requirement**	**Guardrail or Reference Envelope**	**Evidence and Response**
Flyrock	No rock beyond the controlled blast area.	Face profile, stemming/charge limits, stiffness ratio, clearance, and containment where warranted.	Checklist and video; stop, investigate, and revise after loss of control.
Final-slope damage	Stable line within stated profile and damage tolerances.	Controlled spacing/load, alignment, buffer row, descriptions on type of blasting, maximum charge allowances, and trial section.	Survey and mapping; revise when damage persists.
Vibration / air overpressure	Meet receptor-specific limits.	Cooperating-charge and delay controls, instruments, site-specific modelling, review of blast plans incorporating predictions, and conservative prediction.	Retain waveforms; use an action level below the limit.
Toe / coarse fragmentation	Excavatable muck and compliant floor.	Burden, stiffness, subdrill, and powder-factor envelopes; tests.	Inspect muckpile/floor; revise geometry, timing, or energy.
Geologic anomaly	No uncontrolled venting or localized overload, maintain accurate drill logs, require blast plans to be submitted based on local rock/structure.	Drill logs and defined decking/stemming responses for seams or voids.	Record actual loading; hold until treatment is documented.

Use the Minimum Necessary Guardrails

A guardrail removes an extreme without becoming a design. Examples include maximum diameter for a short lift; minimum burden and stemming; maximum perimeter spacing and linear charge; alignment tolerance; and provisional cooperating charge near a receptor. Values must be compatible because independent limits can create an impossible design space. It is important to notice the limiting factors in these; the specifications do not define what the burden or spacing must be, but it defines what minimums and maximums are able to be applied. This prevents the owner from prescribing the specification, while also allowing for technically sufficient work to be bid to achieve the actual intended performance.

Distinguish hard maxima, initial envelopes subject to demonstration, and action levels below contract limits. Provide a variance path requiring engineering justification and representative demonstration rather than prohibiting alternatives or accepting undocumented deviations.

TECHNICAL GUARDRAILS

A hybrid blasting specification is not a short performance statement supplemented with a few preferred construction practices. A properly developed hybrid specification is typically 30 to 50 pages in length because it must establish the technical guardrails within which the contractor

will design and execute the work. That length does not mean that the owner has designed every blast. It reflects the need to define the required performance, exclude unacceptable operating extremes, establish how compliance will be demonstrated, and prescribe the decisions that must occur when field performance departs from the expected range.

Technical guardrails are project-specific boundaries placed on variables that have a strong and reasonably predictable relationship to a significant project risk. They may address personnel qualifications, drilling accuracy, maximum borehole or explosive diameter, lift height, burden and spacing ranges, perimeter-control methods, stemming, decking, maximum charge weight per delay, initiation systems, test blasts, vibration and air-overpressure monitoring, flyrock protection, traffic control, blast records, acceptance, and corrective-action triggers. The specification becomes longer because each guardrail must identify what is being controlled, how it will be measured, what documentation is required, and what happens if the limit cannot be maintained.

The guardrails should be developed during design, before bidding begins and before a contractor selects production equipment. The owner first defines the required result and then identifies the credible ways in which the blasting program could fail to achieve it. The specification developer traces each consequential failure mode to the limited number of design or execution variables that most strongly influence it. A guardrail is justified where constraining one of those variables materially reduces the probability or consequence of failure and where compliance can be objectively verified. The controlling logic should therefore remain traceable from hazard, to failure mechanism, to controllable variable, to numerical limit, to verification and response.

This process is fundamentally different from inserting familiar blasting clauses into every project. A diameter limit that is appropriate for a short highway excavation may be unnecessarily restrictive for a high production bench. A vibration limit that protects a residential structure may not address a sensitive utility, fresh concrete, or operating industrial equipment. Similarly, a presplit requirement may be appropriate for a final rock cut but provide little value in an excavation that will be covered by a retaining structure. Guardrails must respond to the actual project risk rather than to an owner's general preference for a particular blasting method.

The relationship among lift height, burden, and explosive diameter provides a useful example. Short highway benches create a recurring risk because contractors equipped for large production blasting may attempt to use large-diameter, fully coupled blast holes in lifts that are too short to provide an effective relationship between height and burden. The large diameter permits a large burden, but the resulting block of rock is short and thick. It has limited ability to flex and move toward the free face, and blast movement tends to become more vertical. A charge-diameter guardrail can prevent this mismatch without requiring the owner to prescribe the complete burden, spacing, loading, and timing design.

The geometric relationship can be evaluated using stiffness ratio:

$$SR = \frac{H}{B}$$

where *SR* is stiffness ratio, *H* is the effective lift height, and *B* is burden, expressed in consistent units. Some references calculate stiffness ratio using total hole depth. For highway excavation, effective lift height is generally the more useful convention because subdrilling extends the hole below the planned floor but does not increase the height of rock above grade that can flex and move toward the face. The specification must expressly state which convention applies.

For preliminary evaluation in a simplistic form, burden may be estimated from effective charge diameter:

$$B = k_d D_e$$

where D_e is the effective continuous explosive-charge diameter and k_d is an empirical burden-to-charge-diameter factor. Bureau of Reclamation guidance reports that practical burden ratios vary with rock properties, explosive density, and loading conditions, with preliminary values commonly beginning near 25 to 30. *(6)* This relationship is a screening tool rather than a final blast-design equation and typical programs will use more intensive equations, such as the Kona Independent Variable Design Burden Equation. Rock structure, explosive energy, confinement, relief, hole deviation, groundwater, timing, and test-blast performance remain material design considerations.

Combining the two relationships gives:

$$SR = \frac{H}{k_d D_e}$$

and, where the specification establishes a minimum stiffness ratio:

$$D_{e,allowable} \leq \frac{H}{k_d SR_{min}}$$

FHWA guidance associates low stiffness ratios with poor fragmentation and increased potential for toe, backbreak, ground vibration, air overpressure, cratering, and flyrock. *(7)* At a low stiffness ratio, the burden is large relative to the lift height, producing a short, thick block that resists bending and forward displacement. More explosive energy may be consumed crushing rock around the borehole, breaking the floor and crest, or moving material vertically rather than displacing the burden toward the free face.

As stiffness ratio increases, the rock mass becomes more slender relative to the burden and can flex and displace more effectively. Ratios near 3 and 4 are commonly described as good and excellent preliminary conditions, respectively, although they are not universal acceptance criteria. Beyond approximately 4, additional increases generally provide diminishing fragmentation benefits. Extremely high ratios can introduce other problems, including greater sensitivity to hole

deviation, charge separation, initiation cutoff, and geologic variation over the length of the hole. The objective is therefore not to maximize stiffness ratio without limit, but to prevent the short, thick blast geometry associated with disproportionately poor performance.

An illustrative hybrid specification may impose the following maximum effective explosive-product diameters:

Table 3. Illustrative explosive-diameter guardrail and calculated stiffness ratios

Actual Effective Lift Height	Maximum Effective Continuous Explosive Diameter	Representative Height	Preliminary Burden at k_d = 25 to 30	Calculated Stiffness-Ratio Range
Up to and including 10 ft	1.25 in	10 ft	2.60 to 3.13 ft	3.20 to 3.84
Greater than 10 ft through 20 ft	1.50 in	15 ft	3.13 to 3.75 ft	4.00 to 4.80
Greater than 20 ft	2.00 in	25 ft	4.17 to 5.00 ft	5.00 to 6.00

The boundaries in Table 3 are stated expressly to avoid creating a new ambiguity at a 10- or 20-foot lift. The values are an illustrative starting envelope based on the authors' experience and are not a universal safe-design table. The appropriate limits must be evaluated against the project geology, required final-wall condition, available products, nearby receptors, drilling tolerances, and expected contractor equipment.

The calculations demonstrate how the guardrail operates. For a 10-foot lift, *H* is 120 inches. A 1.25-inch charge and a burden factor of 25 produce an estimated burden of 31.25 inches and a stiffness ratio of:

$$SR = \frac{120}{31.25} = 3.84$$

At a burden factor of 30, the estimated burden is 37.5 inches and the stiffness ratio becomes:

$$SR = \frac{120}{37.5} = 3.20$$

The 1.25-inch product therefore produces a preliminary stiffness-ratio range of approximately 3.20 to 3.84 at a 10-foot lift. This places the geometry within a range generally associated with effective forward movement and fragmentation while still leaving the contractor responsible for selecting the actual burden, spacing, loading distribution, stemming, and timing.

For a representative 15-foot lift, *H* is 180 inches. A 1.50-inch product produces estimated burdens of 37.5 to 45 inches. The corresponding stiffness ratios are:

$$SR = \frac{180}{45} = 4.00 \quad ; \quad SR = \frac{180}{37.5} = 4.80$$

For a representative 25-foot lift, H is 300 inches. A 2-inch product produces estimated burdens of 50 to 60 inches and stiffness ratios of:

$$SR = \frac{300}{60} = 5.00 \quad ; \quad SR = \frac{300}{50} = 6.00$$

The higher calculated ratios do not require the contractor to use the maximum permitted product diameter or the preliminary burden relationship. They instead show that the diameter cap is not likely to produce an excessively low stiffness ratio at the representative lift height. The contractor may select a different burden and loading arrangement where supported by the geology, explosive characteristics, test-blast results, and other specification limits.

The contrast with an uncontrolled design is substantial. If a contractor uses a 5-inch fully coupled bulk charge in a 10-foot lift, the preliminary burden becomes 125 to 150 inches, or approximately 10.4 to 12.5 feet. The resulting stiffness ratio is only:

$$SR = \frac{10}{12.5} = 0.80 \quad ; \quad SR = \frac{10}{10.4} = 0.96$$

This geometry places a burden approximately equal to or greater than the entire lift height. The bench has little opportunity to flex and move forward, and the potential for upward heave, cratering, flyrock, air overpressure, excessive vibration, coarse fragmentation, toe, and backbreak increases. The contractor may have selected the larger diameter because it reduces drilling footage and unit cost, but the apparent economy transfers a substantial performance and safety risk to the project. This, in turn, is transferred to the owner due to the difficulty of reconstructing a blast after-the-fact and the difficulty in defending against geologic change claims with lack of sufficient information. The diameter guardrail removes that extreme from the bidding strategy before award and allows an even field for contractors to bid similar risk scopes.

The specification must also define effective charge diameter carefully. Pumped or augered bulk explosive should normally be treated as fully coupled, making its effective diameter approximately equal to the loaded borehole diameter. An untamped packaged explosive may retain its nominal cartridge diameter, while a cartridge that is slit, tamped, compressed, or otherwise expanded may approach the borehole diameter. Charge diameter must be evaluated with borehole diameter, explosive density and energy, linear charge concentration, coupling, charge distribution, decking, stemming, and actual lift height. A nominal product label alone is insufficient to characterize the energy applied to the rock.

This example demonstrates the purpose of a technical guardrail. The owner does not dictate the final burden, spacing, explosive product, loading configuration, or delay sequence. Instead, the owner identifies a predictable high-risk mismatch - large-diameter production blasting in short highway lifts - and removes that mismatch from the allowable design space. Every bidder must then price equipment, products, and production rates capable of operating within the same minimum technical envelope. The contractor retains meaningful design freedom, but competition can no longer be based on an approach that exposes the project to an unacceptable probability of poor blast performance.

A well-developed hybrid specification contains multiple guardrails constructed in this manner. Each begins with a defined project risk, controls only the variables necessary to reduce that risk, requires evidence sufficient to verify compliance, and preserves a procedure for adjustment as the excavation reveals actual conditions. The resulting 30- to 50-page specification is longer than a basic performance specification because it does the engineering work necessary to prevent foreseeable failure before bidding, rather than attempting to correct the contractor's program after the blast has already been fired, and helps prevent low-bid’s due to unacknowledged risk transference back to the owner.

VERIFICATION AND ADAPTIVE CONTROL

Long-Term and Daily Submittals

A blasting program should be accompanied by two separate sets of blasting submittals, the first set is the master blasting submittals which are submitted prior to the project beginning. These submittals are the in-depth technical, monitoring, and safety plans that the blasting program will follow and cannot be deviated from unless approved by the ownership. The ownership is then responsible for reviewing and ensuring that the documents comply with the project specifications. A proportional master plan defines zones, representative designs, products, equipment, qualifications, monitoring, testing, forms, and variances. Safety planning covers guarding, communications, lightning, misfires, storage, fire, and emergencies; monitoring planning covers receptors, instruments, limits, action levels, modeling, reporting, and surveys.

The second set of documents is the daily blasting documents, these are typically the blast plan, submitted ahead of drilling for each blast detailing the exact contractor-developed prescriptive details for the individual blasting. Then following a blast, the document is modified to be the blast report, detailing how the blast was completed and any deviations from the plan. The owner is responsible for reviewing to ensure that the program follows the project specifications and the master blasting documents. Owner review does not relieve contractor responsibility or cure defective owner criteria. Figure 1 matters because the next blast can still change and this program design ensures it generally follows the correct principles but is flexible enough to accommodate variations in geology or the project setting.

Figure 1. Closed-loop hybrid specification process

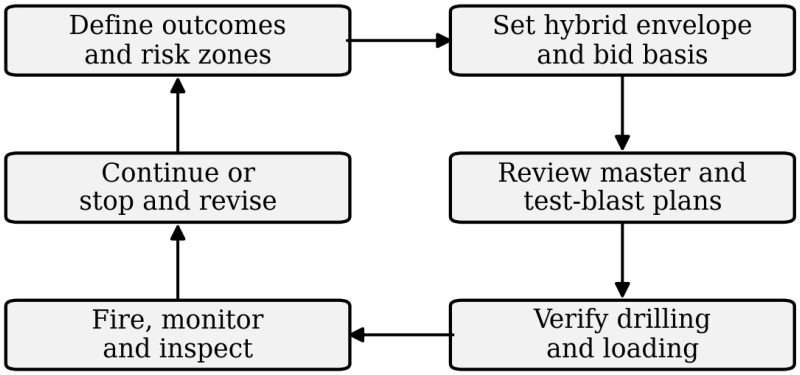

Measured results update the next approved design within the contract envelope.

LIMITATIONS

A hybrid specification cannot compensate for inadequate investigation, unsafe slope design, unqualified execution, or slow owner decisions. Incorrect guardrails can worsen risk, so requirements scale with consequence: a remote cut need not receive a hundred-page plan, while modest rock volume beside a hospital should not receive a one-page clause.

This practice-based framework explains how ambiguity, missing evidence, and delayed correction can be reduced. Without comparable data, it does not claim to eliminate overruns, changes, claims, or poor performance. Geology, delivery, staffing, and capability remain confounding factors.

Hybrid specification is not entirely new; public documents have long combined outcomes, limits, submittals, tests, and acceptance. The contribution is deliberate organization around failure modes, bid comparability, evidence, and adaptation; not restriction for its own sake.

CONCLUSIONS

Highway blasting risk begins before drilling when bidders assume different scopes and prices are compared without exposing them. Broad performance language permits inadequate programs; complete prescription replaces field engineering with owner assumptions that may not survive the geology.

A risk-based hybrid specification defines outcomes, uses limited guardrails, preserves contractor design authority, and captures actionable evidence. Tests, hold points, and variances make it adaptive. The stiffness example excludes oversized geometry without dictating the pattern; the logic also applies to perimeter loading, burden, stemming, cooperating charge, alignment, and logs. Each limit must be compatible, measurable, and adjustable on evidence.

Hybrid specifications do not remove geology, guarantee performance, eliminate changes, or immunize either party. They reduce risk by making the minimum program visible before bid, verifiable before evidence disappears, and correctable before one poor blast becomes repeated practice.

REFERENCES

1. Federal Highway Administration. *Types of Specifying*. United States Department of Transportation, Washington, D.C., updated May 23, 2022. https://www.fhwa.dot.gov/construction/specrevattach1.cfm. Accessed Aug. 15, 2026.

2. Federal Highway Administration. *Standard Specifications for Construction of Roads and Bridges on Federal Highway Projects, FP-24*. United States Department of Transportation, Washington, D.C., 2024.

3. United States Army Corps of Engineers, Naval Facilities Engineering Systems Command, and Air Force Civil Engineer Center. *Blasting—Surface*. Unified Facilities Guide Specification 31 23 06.00, Feb. 2021, Change 1, Nov. 2021. United States Department of Defense, Washington, D.C.

4. United States Army Corps of Engineers. *Engineering Oversight of Blasting Operations for Rock Excavation or Rock Production*. Engineering and Construction Bulletin 2025-2. United States Department of the Army, Washington, D.C., Mar. 6, 2025.

5. Sheahan, J., A. Zdinak, and J. DiMaggio. *Assuring Quality in Geotechnical Reporting Documents*. Report FHWA-HIF-17-016, Geotechnical Engineering Circular No. 14. Federal Highway Administration, United States Department of Transportation, Washington, D.C., Aug. 2016.

6. United States Bureau of Reclamation. *Engineering Geology Field Manual, 2nd ed., Volume II, Chapter 19, Blast Design*. United States Department of the Interior, Denver, Colo., 2001.

7. Konya, C. J. and E. J. Walter. *Rock Blasting and Overbreak Control*. Report FHWA-HI-92-001, National Highway Institute Course No. 13211. Federal Highway Administration, United States Department of Transportation, Washington, D.C., 1991.

8. Siskind, D. E., M. S. Stagg, J. W. Kopp, and C. H. Dowding. *Structure Response and Damage Produced by Ground Vibration from Surface Mine Blasting*. Report of Investigations 8507. United States Bureau of Mines, Washington, D.C., 1980, 74 pp.

9. Siskind, D. E., V. J. Stachura, M. S. Stagg, and J. W. Kopp. *Structure Response and Damage Produced by Airblast from Surface Mining*. Report of Investigations 8485. United States Bureau of Mines, Washington, D.C., 1980, 111 pp.

31. Developing a Database of Rockfall-Vehicle Impacts to Evaluate Human Vulnerability Along Transportation Routes

Autumn L. Helfrich
U.S. Geological Survey, Landslide Hazards Program
350 North Akron Road, Moffett Field, CA 94035
650-439-2818
ahelfrich@usgs.gov

Brian D. Collins
U.S. Geological Survey, Landslide Hazards Program
350 North Akron Road, Moffett Field, CA 94035
650-439-2466
bcollins@usgs.gov

Prepared for the 75th Highway Geology Symposium, September 2026

Acknowledgements

The authors would like to thank Karimah Comstock for their contributions with data compilation and research, and Eric Bilderback (USGS) and Skye Corbett (USGS) who provided helpful reviews in the preparation of this paper.

Disclaimer

Statements and views presented in this paper are strictly those of the author(s) and do not reflect positions held by the Highway Geology Symposium (HGS) or others acknowledged above. The mention of trade names for commercial products does not imply the approval or endorsement by HGS. Further, any use of trade, firm, or product names is for descriptive purposes only and does not imply endorsement by the U.S. Government.

Copyright Notice

As a product of the U.S. Government, this work is in the public domain in the United States.

ABSTRACT

Rockfall poses a widespread hazard along roads below steep slopes and affects the safety of roadway users. When vehicles are impacted by falling rock, occupants may sustain major injuries or be killed. However, low- or no-consequence rockfall impacts also occur and these are particularly important when evaluating the statistical vulnerability of people in vehicles struck by falling rock. Here, we examine more than 50 case studies from publicly available data sources (e.g., published literature, news reports) that document rockfalls with a confirmed vehicle impact. Using these resources, we record detailed site conditions (e.g., sourced from a roadcut or cliff, cause), rockfall metrics (e.g., volume, fall height), and vehicle characteristics (e.g., type, occupancy, travel direction) and compile that information into a database. These data provide a mechanism to evaluate relationships between hazard and risk through testing and development of vulnerability metrics. For example, from the site-specific event rockfall geometry characteristics (block size and fall height), the calculation of the potential energy of impacting blocks can be determined and compared with reported vulnerability outcomes. Additional statistical analysis can then be used to quantify the risk to people travelling along roadways and assess the likelihood of outcomes given site and vehicle characteristics. To develop statistically rigorous relationships, additional case studies are needed to develop an expanded database. Thus, this work highlights the benefit of preserving both the source area characteristics and the resultant human vulnerability outcomes in the wake of rockfall incidents to inform future risk assessments. These data and associated analyses can be used to assist transportation and land management agencies with risk assessment and decision making along rockfall-prone transportation corridors.

INTRODUCTION

Rockfalls are a common hazard along roadways in steep, mountainous terrain and can pose risk to people and infrastructure transiting these corridors (*1, 2*). Sourced from cliffs high above or from roadcuts directly adjacent to roadways, the impact of a rockfall on a vehicle may have devastating consequences, including fatalities. However, not all rockfall events result in impacts to vehicles, and not all rockfall impacts to vehicles result in harm to humans. In some cases, the support offered by a vehicle's fuselage may offer protection against injury if the impacting rock is either small or traveling at low velocity. On the other hand, falling blocks of rock can also be sufficiently large or moving with such high velocity to preclude any chance of human survival from direct impact. These extremes describe the range of human vulnerability from rockfalls impacts to vehicles which forms an important input for quantitative rockfall risk assessment.

Risk assessment methodologies are often applied to transportation corridors susceptible to rockfall in order to identify the most consequential hazards and to allocate sometimes limited resources for risk reduction (*3, 4*). As such, risk assessment, as it applies to rockfall, is the integrated result of a hazard analysis, a consequence analysis, and the associated risk calculations that link these contributing factors. Quantitatively, rockfall risk assessment is often expressed in terms of expected or possible consequences (C):

$$C = H \times (E \times V)$$

where H is the hazard, E is the value of the element at risk, and V is the vulnerability of the element to experience damage (*5*). Rockfall hazard is the probability that a rockfall may occur and reach an element, and thus is a function of source zone susceptibility, runout zone geometry, and the temporal occurrence probability that blocks of various volumes initially become detached from the cliff. These factors can be evaluated qualitatively or quantitatively, and at local or global scales depending on the extent of available data (*6, 7*). The term (E × V) can be regarded as the total vulnerability in that it applies V as a proportion of E. For example, if four people (E) are in a vehicle impacted by a rockfall but the vehicle protects 75% of the occupants (V), then the total vulnerability for the hazard event would be one person. However, herein we refer to vulnerability (V) exclusively as the proportion of elements exposed to a hazard. Whereas it may be straightforward to quantify the number of people occupying a vehicle through existing traffic data, the ability of a vehicle to protect (or expose) occupants from hazards is a much more difficult parameter to pinpoint. Vehicles vary in size, shape, height, and material and little research is available that offers insight into how V might vary between vehicles, or even what value should be used (e.g., *8, 9*). In a conservative quantitative risk assessment (i.e., that aims to assess the maximum possible risk), vulnerability may be assumed as "1" thereby indicating that any rockfall impact causes the maximum damage (fatalities). Our work aims to fill this knowledge gap through compilation and analysis of an empirical database documenting rockfall impacts to vehicles on roadways. The goal is to better define the relationship between rockfall vehicle impacts and human injuries and fatalities, thereby providing quantitative values of vulnerability for use in risk assessments. Analyzing these data ensures that theoretical vulnerability estimates and assumptions properly represent real-world observations (e.g., at what rate do rockfall-vehicle impacts actually result in fatal outcomes and how well do vehicles

protect people from impacts?). Importantly, we note that our study is only focused on rockfall impacts to vehicles and not vice versa. That is, we do not quantify vulnerability of human occupants for incidents where moving vehicles impact stationary rocks on a roadway from a previous rockfall, although we recognize the importance of this hazard component within the complete framework of rockfall risk assessment.

METHODS

We collected rockfall vehicle impact event data from a variety of published sources including media reports, news stories, video broadcasts, academic literature, and rockfall inventories (*10*). In some cases, we obtained additional event details directly from colleagues who, through their roles in transportation corridor management, could provide near-first-hand accounts. Because our study focus was specifically on rockfall impacts, we did not inventory nor assess vehicle impacts resulting from hazard events primarily characterized as floods, avalanches, debris flows, debris slides, or other types of landslides, as the vulnerability metrics from, for example, a debris flow that moves an entire vehicle, is likely to be considerably different from that caused by a single block impacting the same vehicle. We also focused our investigation solely on impacts to vehicles that were transiting or stationary on roadways. Although we documented several case studies involving passenger trains, we excluded these from our analysis due to the inherently different structural systems provided by train chassis compared to motor vehicles. We did make one exception to this: we included an event involving a passenger transport cabin running on a railway system due to the cabin's similarity to that of a typical car.

Our database is admittedly not fully representative of global rockfall-vehicle impact vulnerability and rather, is massively biased towards rockfall event reporting conducted in the English language via internet-search parameters as well as availability and access to published rockfall resources in the United States. However, our internet research did include and identify events in countries whose language is other than English through searches for rockfall-equivalent wording (e.g., in French – "chute de pierres") and subsequent translation of identified reports. Given the similarity of rockfall events and vehicles in many parts of the world, we expect the geographical biasing to have limited effect on vulnerability statistics extracted from the data.

Parameters extracted from rockfall events (Table 1) include those related to the overall logistics of the event (e.g., location, date, time), the rockfall characteristics (e.g., source area type, rockfall fall height and volume), vehicle characteristics (e.g., type of vehicle, number of occupants), and outcomes (e.g., number of fatalities and/or injuries). To be included in the event database, at a minimum, the following information was required: the general location, the type of vehicle involved, and confirmatory details about the source material (rock) and failure style (fall). Because the focus of our study is on impact events, we treat rockfalls that impacted multiple vehicles as independent events. Events found in aggregated crash data or internet-based reporting systems were often limited to summary statistics, specific time frames, or were access-restricted to internal agencies and could therefore not be included. Rockall events impacting vehicles in addition to those reported here have undoubtedly occurred prior to and during the period of data collection, but these events likely remain unreported in published or unpublished formats due to the small size of the rockfall events, absence of substantial damage to vehicles,

lack of injury to the persons involved, or are restricted for privacy or legal reasons due to personal information or provisional status.

Time and Location Parameters

We typically obtained event dates and times directly from the media sources reporting the rockfall incidents. Some analysis was required when reporting only indicated general timing details such as “a rockfall occurred last Tuesday” but these were overall easily rectified through the dates included in the media report themselves. In all cases, we used the local date and time for reporting (i.e., with no correction to UTC where applicable). Identifying the exact location of a rockfall vehicle impact (and especially the rockfall source area) was considerably more challenging. Whereas the country, province, and city were generally easily identified, more specific details were sometimes lacking. However, we were able to obtain the exact latitude and longitude of impact on the roadway for approximately 80% of the events using existing reporting (e.g., near a particular distance marker on a highway) and other similar details and resources. These included the extensive use of Google’s StreetView functionality within the Google Earth and Google Maps platforms to match rockfall locations with landmarks visible in event photographs often provided in media reports. We note, however, that this workflow was not always possible due to the lack of data availability for roads in many parts of the world.

Table 1 - Parameters extracted for rockfall vehicle impact database.

Time and Location	Rockfall Characteristics	Vehicle Characteristics	Outcome Details
Date	Source area type (roadcut vs. cliff)	Vehicle type	Fatalities
Approximate Time	Fall Height	Occupancy	Injuries
Country	Rockfall volume impacting vehicle	Maximum occupancy of vehicle	
Province or City	Total rockfall volume	Direction of driving (‘slope side’ versus ‘away side’)	
Latitude/ Longitude (of impact)	Probable cause (triggering mechanism)	Vehicle moving or stationary	
		Area of impact on vehicle	

Rockfall Characteristics

When the exact location of the vehicle impact and/or source area were known, we were able to identify important site characteristic details including the source area type (natural cliff or engineered roadcut) and the fall height of the rockfall. For some events, media reports provided direct measurement of the fall height (e.g., “a boulder fell 100 meters” (330 feet)). In other cases, the exact fall height could be calculated through differencing of the known impact location with the source area identified in photos. We typically conducted this calculation through elevations provided within the Google Earth platform; we estimate potential error in these measurements at between 3 and 30 feet (1 and 10 meters) depending on the size of the source area. However, for most events, only a minimum and maximum estimate of the fall height could be estimated from the lowest point above the roadbed that a rock could have detached from or from the highest point of the cliff band adjacent to the road – these sometimes had considerably large bounds on the order of several hundred feet (hundreds of meters).

We extracted two forms of volume estimates from available data: the volume impacting the vehicle and the total volume for the entire rockfall event. Estimates of these volumes were often challenging to identify due to a lack of reported detail (e.g., “boulder”, “debris”, “rock”) or in some cases, only a relative documented metric (e.g., “a boulder the size of a small car”). In many cases, we extracted sufficient detail directly from reports to obtain an approximate volume assessment using some basic assumptions (spherical volume, rock density of 165 lb/ft^3 (2,650 kg/m^3)) when either the length (e.g., “one-and-a-half-meter-tall” (5 ft)), or mass (e.g., “20-tonne rock” (22 ton)) was reported. However, when a volume estimate was not directly stated, we conducted additional research using available photographs or videos. For example, some media reports featured photographs of both the vehicle and the rockfall debris, and we estimated a rockfall volume range using a reference scale from objects with known dimensions (e.g., a car tire, a road lane width) in the photo. In other cases, we estimated the volume of impacting rock based on cues from the apparent damage to a vehicle side panel, rear light, or windshield without the rock mass itself pictured. Due to the wide potential range of these data, we identified the best estimate (average), as well as the minimum and maximum likely volumes for each parameter. In some cases, these volume reports are the same which indicates that the volume impacting the vehicle represents the total volume of the rockfall.

We also characterized volumes in relative terms, using terminology defined by Wieczorek et al. (*11*), spanning “extremely small” to “extremely large” (Table 2). These provide useful metrics for comparing events with widely varying degrees of certainty on their more exact volumes. In some cases, the best quantitative volume estimate of an event is provided by the relative size category; for these, the minimum and maximum volume bounds reflect the bounds of the referenced relative volume range (e.g., average of 3 yd^3 (2 m^3), with minimum of 0.7 yd^3 (0.5 m^3), and maximum of 7 yd^3 (5 m^3)). If more information was available to further constrain the volume estimate, we reported these narrower ranges.

Table 2 – Volume-range and relative-size categories of rockfalls after Wieczorek et al. (*11*).

Relative Size	Volume Range (yd^3)[1]	Average Volume (yd^3)[1]
Extremely small	0–0.7 (0–0.5 m^3)	0.3 (0.2 m^3)
Very small	0.7–7 (0.5–5 m^3)	3 (2 m^3)
Small	7–70 (5–50 m^3)	30 (20 m^3)
Medium	70–700 (50–500 m^3)	300 (200 m^3)
Large	700–7,000 (500–5,000 m^3)	3,000 (2,000 m^3)
Very large	7,000–70,000 (5,000–50,000 m^3)	30,000 (20,000 m^3)
Extremely large	70,000–700,000 (50,000–500,000 m^3)	300,000 (200,000 m^3)

[1] The presented rockfall volume scale was originally published in metric units. It has been converted to U.S. customary units with rounding to preserve the number of significant digits in each category.

Finally, we made our best assessment of the probable cause of the rockfall event (often termed the ‘triggering conditions’, e.g., rainfall, earthquake) based on information provided in available reports. Whereas this information is not necessarily important for the relationship between rockfall and resultant human vulnerability within a vehicle, it does provide helpful contextual information for each event.

Vehicle Characteristics

Media reports and associated photos proved useful for assessing the vehicle characteristics involved in the rockfall impact events. We documented the type of vehicle (car, SUV, truck, etc.) as well as the make and model when available or identifiable in photos. These details allowed an assessment of the maximum occupancy of the vehicle involved in the impact (i.e., the total number of seats) and therefore the maximum number of potential human exposures. Details on the occupancy of the vehicle at the time of impact were typically available in most reports, although sometimes extracted from recorded videos of the event from dashboard cameras located in adjacent cars. Some parameters could be filled logically using available narrative details, such as which side the vehicle was travelling with respect to the rockfall source area (e.g., ‘slope side’ or ‘away side’). For example, if a traveler whose vehicle was struck stated in the report that they were driving from one town to another, it was possible to determine which side of the road they were driving on at the time of impact. For cases where a vehicle was on a single lane roadway, these were considered to be transiting on the ‘slope side’. In most cases, media reports stated directly whether the vehicle was moving or stationary at the time of impact. For reports that were not explicit, we assumed that the vehicle was moving. Finally, we extracted details on the location of rockfall impact (e.g., hood, roof, windshield), typically through inspection of media photographs.

Outcomes

Media reports generally provided direct information on the numbers of fatalities and injuries (if any) from each rockfall event. When a vehicle was not occupied at the time of the rockfall, but the occupant was less than 1-minute from being in the vehicle, an estimate of whether the rockfall would have resulted in an injury or fatality was assumed. This estimation applies to two of the case studies.

Reference Information

To establish a reproducible database of the rockfall impact events, we documented all websites, webpages, citations, and other sources with the date the corresponding data were viewed. Additionally, we archived all photographs used in the data compilation and documented their sources.

RESULTS

Our rockfall vehicle impact database includes a total of 53 rockfalls (Figure 1), with a total of 140 exposed individuals in 57 different vehicles impacted between 1931 and 2026 (Table 3). Of the rockfalls reported in this database, 18 events resulted in at least one fatality and 33 events led to at least one person in a vehicle sustaining an injury. The database is designed to allow for potential future expansion should new data be identified and incorporated into ongoing analyses. Here, we present some preliminary results for select parameters from the database. We note that when statistics are reported, they reflect only the number of events (i.e., “n = ##”) for which the parameter of interest was available.

Geographic Distribution

Our database includes events from 16 countries, with the greatest number of events (24; 42%) recorded within the United States. Other countries with several documented events include France (8; 14%) and India (7; 12%); all other countries are represented by only one or two events each.

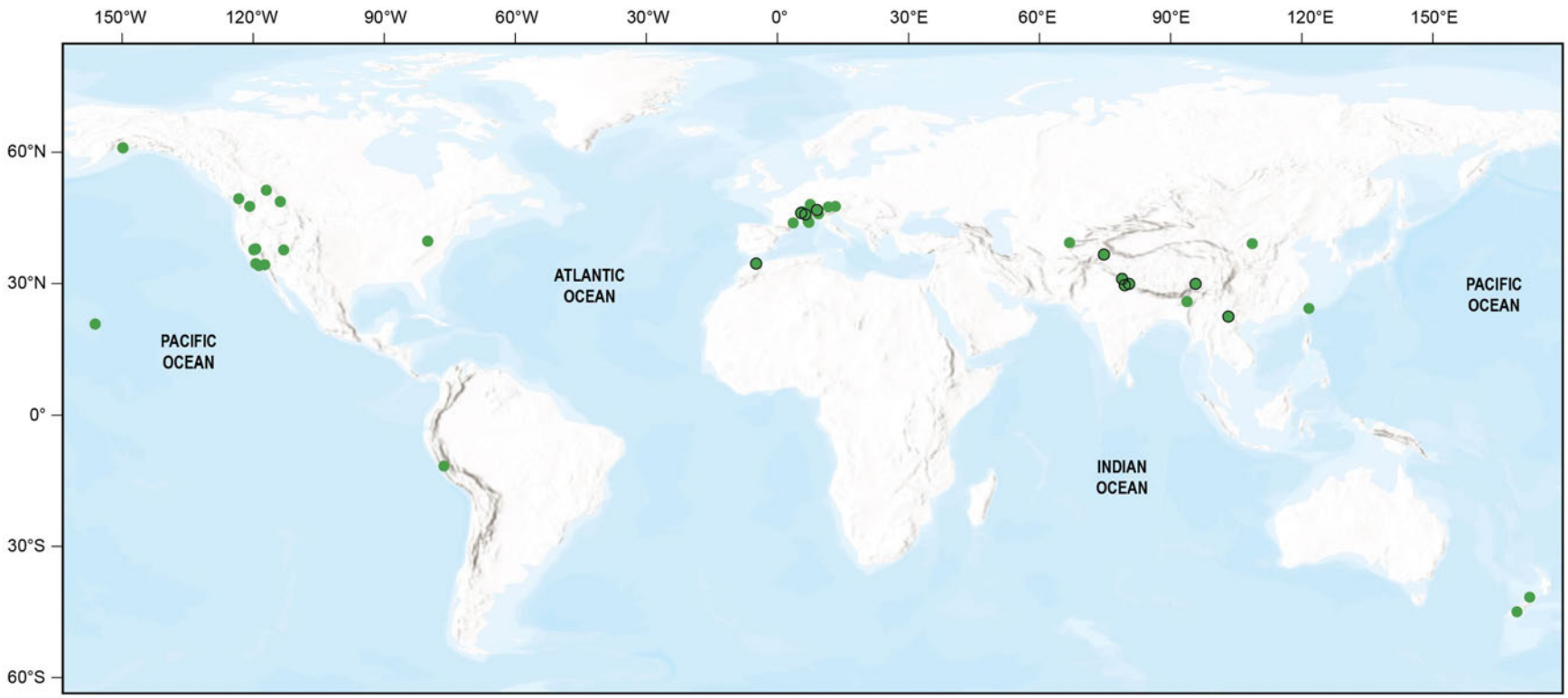

Figure 1 – Spatial distribution of 53 rockfall events resulting in impacts to 57 vehicles. Points shown in green represent known locations; points shown as hollow black circles are only known to the extent of the city or province, and the point has been positioned near the center of that city or province. Basemap from Esri.

Table 3 – Rockfall vehicle impact case studies.

Event ID[1]	City / Province	Event ID[1]	City / Province
1931_1226_USA	Yosemite N.P., California	2022_1111_Canada	West Vancouver, British Columbia
1996_0623_USA	Glacier N.P., Montana	2022_1209_Italy	Lecco Province
2000_1110_USA	Yosemite N.P., California	2022_1227_USA	Yosemite N.P., California
2002_0718_USA	Yosemite N.P., California	2023_0109_USA	Malibu, California
2006_0805_Switzerland	Duvin, Graubünden	2023_0408_Pakistan	Khyber Village of Gojal Valley, Hunza District
2009_0826_USA	Yosemite N.P., California	2023_0504_USA	Maui, Hawaii
2012_0125_France	Arly Gorge	2023_0704_India_1	Nagaland
2012_0301_France	Tenay	2023_0704_India_2	Nagaland
2012_0731_Germany	Breisach am Rhein	2023_0704_India_3	Nagaland
2012_1101_USA	Yosemite N.P., California	2023_1008_India	Pithoragarh District, Uttarakhand
2014_0527_USA	Yosemite N.P., California	2023_1210_France	Alpes-Marîtimes
2014_1120_USA	Yosemite N.P., California	2024_0225_Austria	Tennengau, Salzburgerland
2017_0522_India	Kakdighat, Almora	2024_0302_Peru_1	San Mateo de Huanchor, Huarochiri Province
2017_0928_USA	Yosemite N.P., California	2024_0302_Peru_2	San Mateo de Huanchor, Huarochiri Province
2018_0309_Switzerland	Vuorz, Graubünden	2024_0402_Morocco	Taounate Province
2018_0514_France	Saint-Jean-la-Rivière, Alpes-Maritimes	2024_0403_Taiwan	Hualien County
2018_0603_Vietnam	Lai Châu	2024_0503_France	Côte de Jeurre
2018_1003_China	Bome County, Tibet	2024_0531_India	Gangotri, Uttarkashi District
2018_1130_USA	Seward Highway, Alaska	2024_0705_India	Dimapur, Nagaland
2019_0125_USA	Seward Highway, Alaska	2024_1004_New Zealand	Cromwell Gorge
2019_0812_USA	Glacier N.P., Montana	2024_1018_USA	San Bernardino, California
2019_1113_New Zealand	Tasman District	2024_1027_USA	Maui, Hawaii
2020_0117_France	Haute-Savoie, Auvergne-Rhône-Alpes	2024_1106_Uzbekistan	Kitab District, Kashkadrya
2020_0126_Austria	Achenkirch Municipality	2025_0121_France	Causee-de-la-Selle
2020_0210_USA_1	Morgantown, West Virginia	2025_0905_USA	Colorado N.M., Colorado
2020_0210_USA_2	Morgantown, West Virginia	2025_1114_USA	Ojai, California
2020_1002_France	Labalme-sur-Cerdon	2025_1125_USA	Leavenworth, Washington
2022_0304_Canada	Golden, British Columbia	2026_0413_USA	Seward Highway, Alaska
2022_1008_USA	Cedar City, Utah		

[1] Format is YYYY_MMDD_Country

Rockfall Site Characteristics and Volumes

The majority of documented rockfall-vehicle impact events for which source area type information was available (n = 54) were initiated from cliffs (63%) compared to roadcuts (37%). This information is critical for assessing overall risk from natural versus engineered components of roadways and may be subject to varying levels of engineering, environmental, and safety standards depending on the location. Impacting rockfall volumes (Figure 2) ranged from extremely small (0.001 yd^3; 0.001 m^3) to medium (130 yd^3; 100 m^3) using the classifications of Wieczorek et al. (*11*). Total volumes involved in the events spanned a larger range (Figure 3) from softball sized rocks (0.003 yd^3; 0.002 m^3) to considerably larger volumes (16,000 yd^3; 12,000 m^3). The volume distribution is skewed towards the smaller volume classes for both impacting and total event volume (consistent with published studies; *12*) but still show the sizeable range over which impacting rockfalls occur.

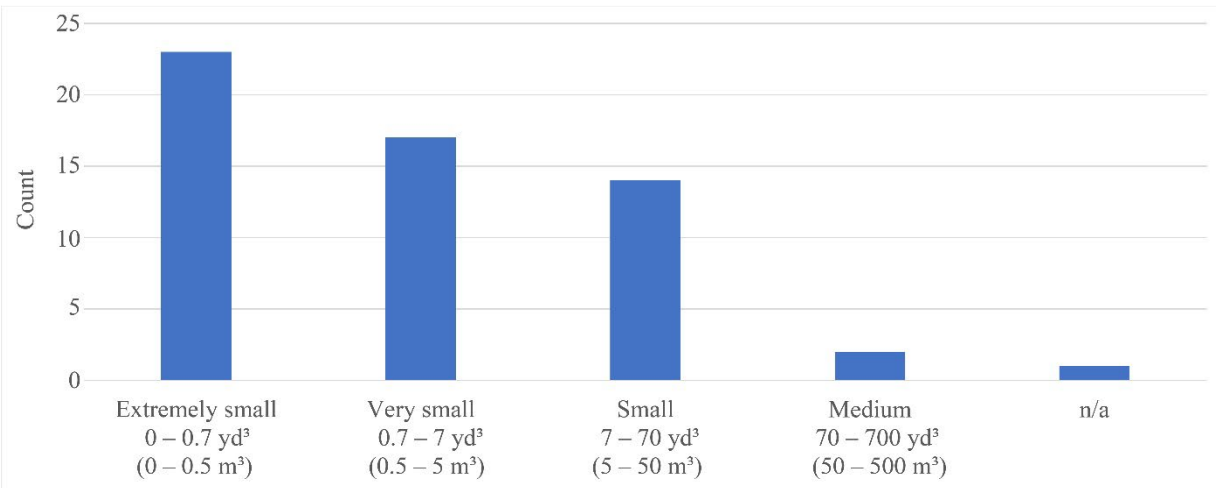

Figure 2 – Number of rockfall events by impacting volume class (n=57). Range of values for each volume class are shown using the classifications of Wieczorek et al. (*11*).

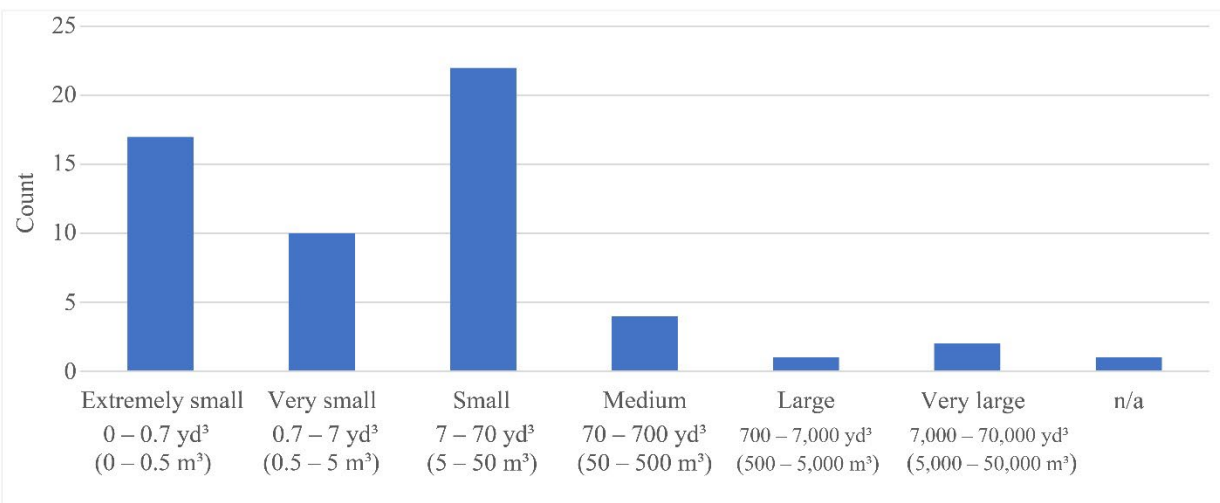

Figure 3 – Number of rockfall events by total volume class (n=57). Range of values for each volume class are shown using the classifications of Wieczorek et al. (*11*).

Vehicle Type and Motion Characteristics

Passenger cars (53%) and SUVs (24%) account for the majority of vehicle types in the database (Figure 4). This is likely consistent with the types of vehicles typically transiting roadways in the countries where rockfalls have been documented. The physical vulnerability of different vehicles and the resulting outcomes for people within those vehicles may be influenced by the type of vehicle struck by a rockfall. For example, a pickup truck or SUV is likely to be higher off the ground and potentially constructed of sturdier structural components if the vehicle has been made to carry heavy loads. On the other hand, the total vulnerability of a particular vehicle is also dependent on the number of seats that a vehicle provides and thus an SUV may have larger total occupancy compared to a car. These details must be considered when drawing conclusions with these data.

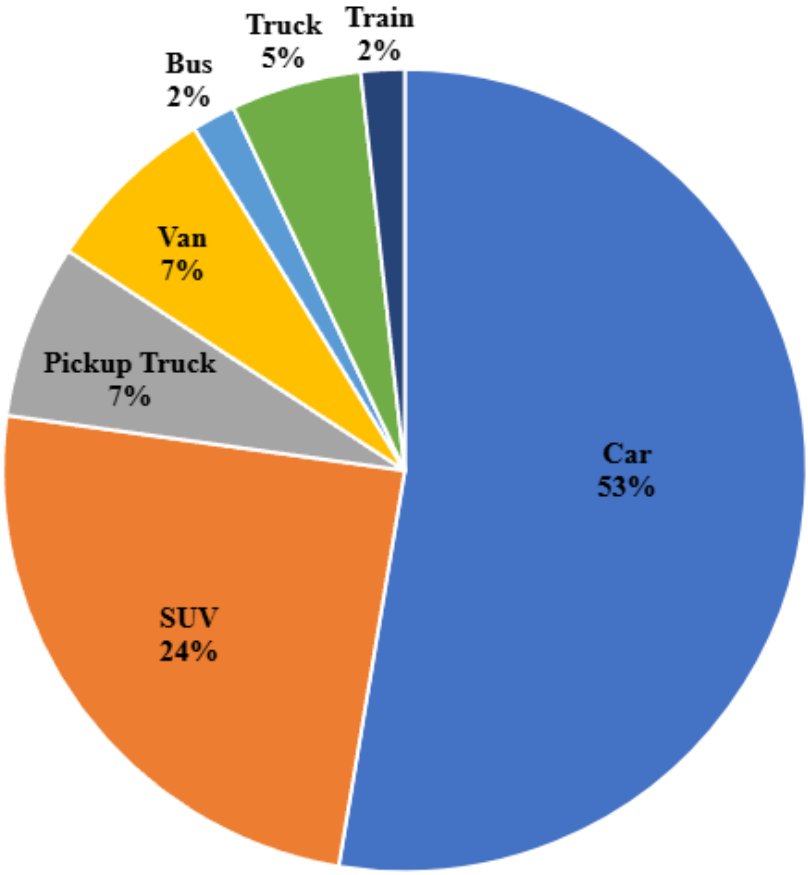

Figure 4 - Rockfall vehicle impact event by vehicle type (n=57).

Most rockfall impacts occurred when vehicles were in motion (85%) compared to those that were stationary (15%) for which data are available (n = 55). This aligns with expectations given the transitory purpose of roadways. Similarly, most rockfall impacts for which data are available (n = 43) also occurred on the side of the road closest to the cliff or roadcut (i.e., the ‘slope side’, 67%) compared to the ‘away side’ (33%). This also matches expectations with regard to rockfall trajectories – we expect that vertically falling rock blocks from cliffs or roadcuts that are directly adjacent to a roadway to impact the lane closest to the rockfall source.

Impact Area

Rockfalls identified in our database caused disparate sized impacts to vehicles depending on the size of transiting blocks and the total volume of the event. For this analysis, we excluded three events for which the impact area was unknown (thus, n = 54). In some cases, extremely small blocks passed through only the windshield of a vehicle creating a distinct hole, whereas in other events a boulder crushed the entirety of a car. The area of a vehicle that a falling block of rock makes impact can broadly be categorized into the following categories: 'entire', 'hood', 'windshield', 'roof', 'trunk', 'side', and 'trailer'. Whereas many rockfall events impacted more than one of these locations, for simplicity, we assigned the events into the category which formed the most predominant location of impact (Figure 5). Overall, most impacts captured in the data occurred on the hood (26%), roof (26%), or windshield (20%) which matches expectations based on the likely vertical trajectories of many rockfalls. We note that additional analysis is possible with these data but is not conducted here due to their preliminary nature.

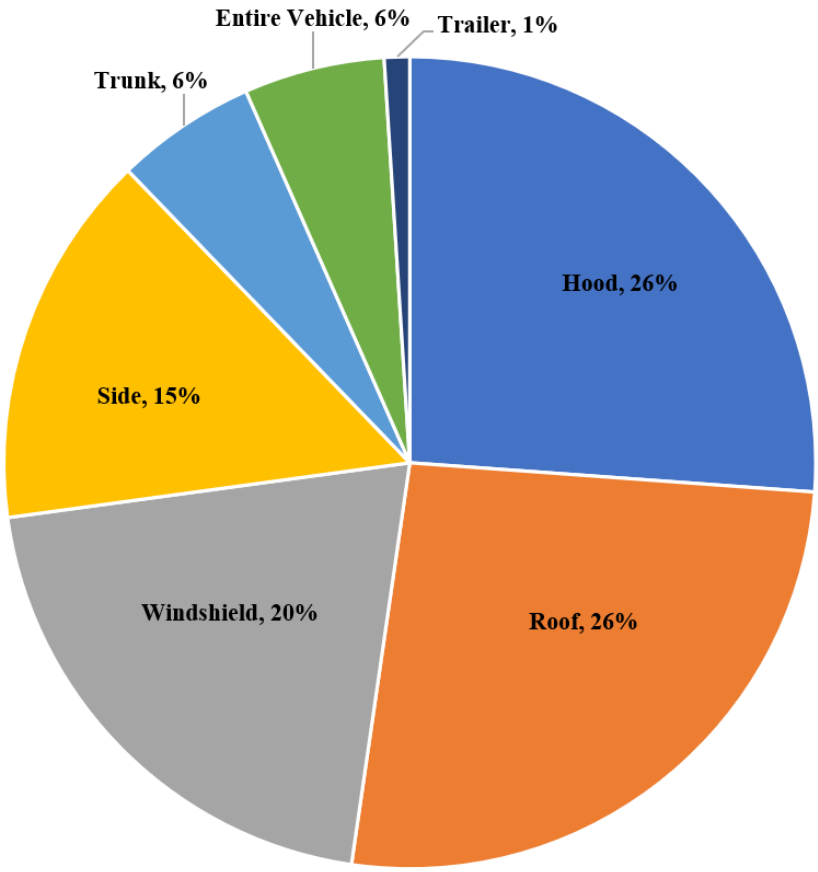

Figure 5 – Rockfall vehicle impact event by impact location (n=54).

Injuries and Fatalities

Although only preliminary in nature, we investigated some simple correlations between several rockfall and vehicle characteristic parameters, and resulting fatalities and injuries. These are presented as examples of the types of analyses that could be conducted with the data and have not been assessed for statistical significance. For three parameters (source area type, direction of driving, and vehicle motion), we calculated the percentage of incidents for each parameter that led to at least one fatality or at least one injury (Figure 6). For incidents that caused both fatalities and injuries to separate occupants, we treat these only as fatalities so as to not duplicate the statistical input of these events. For these analyses, we excluded a single event (thus, n = 56) from the database where the rockfall impacted only the trailer portion of a semi-truck given that this impact was unlikely to lead to direct human fatality or injury.

The results show that fatalities are more likely to occur from rockfalls sourced from cliffs (33% of the time) compared to roadcuts (15%). Injuries are similarly more likely with cliff-sourced rockfalls compared to roadcuts, but to a lesser degree (36% versus 30%). We hypothesize that this conclusion may be related to the higher potential energy of rockfalls from cliffs given their likely greater height (and thus potentially larger fall height). Exploration of this relationship awaits further study.

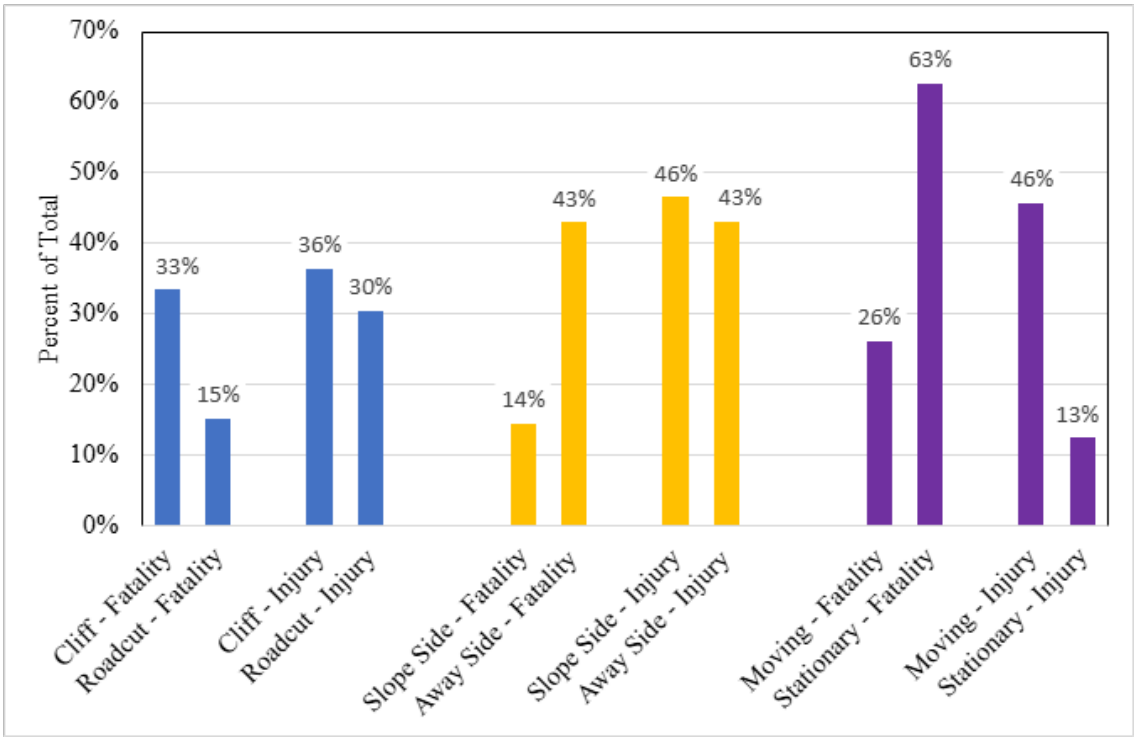

Figure 6 - Statistical analysis of fatalities and injuries resulting from three parameters related to rockfall and vehicle location characteristics. Values show the percentage of occurrences in which a rockfall caused a fatality or injury from each of the cases (e.g., cliff versus roadcut). For rockfall source location, n_{cliff} = 33, $n_{roadcut}$ = 20. For direction of driving, $n_{slope\ side}$ = 28, $n_{away\ side}$ = 14. For vehicle motion, n_{moving} = 46, $n_{stationary}$ = 8.

Our investigation of similar relationships for the direction of travel of the vehicle compared to human fatalities and/or injuries did not lead to a consistent or intuitive conclusion. We expected that the 'slope side' travel lane (i.e., the lane closest to the cliff or roadcut) would have led to a larger percentage of fatalities and injuries compared to the 'away side' (that on the 'outboard lane'). However, instead we found that fatalities were fewer for impacts on the slope side (14%) compared to the away side (43%). For injuries, the pattern was reversed, although also more similar, with slope side impacts leading to injuries 46% of the time compared to 43% for roadcuts. Although preliminary in nature and potentially affected by reporting bias due to the limited events in the database, these data, taken directly from worldwide case studies, might refute the view that the lane closest to a roadcut contains higher risk. This could be potentially due to asymmetric rock block distributions deposited across the lanes with only smaller blocks impacting vehicles closer to rockfall sources, or from some other unquantified setting or physical process.

The final metric we investigated compared the likelihood of human impacts based on if the vehicle was moving or stationary at the time of the rockfall event. The data show that stationary vehicles were more likely to result in a fatal outcome (63% of the time) compared to vehicles that were in motion (26%). However, the data for injuries provided the opposite conclusion with stationary impacts only leading to injuries 13% of the time compared to moving vehicles (46%). This discrepancy and overall metric may need additional data to tease out whether or not an actual causative relationship exists between these factors.

DISCUSSION AND CONCLUSIONS

We compiled rockfall-vehicle impact data from publicly available resources and published literature for a total of 57 events occurring on roadways in 16 countries with global extent. In these events, 33 people were killed and 67 people were injured by rockfall processes that directly impacted vehicles transiting a roadway. Although the results and correlations presented are preliminary due to the limited number of recorded events and available parameters, they provide useful information with respect to human vulnerability to rockfall on roadways. With plans to continue this effort, it will be necessary to determine what combined parameters describe a falling block with sufficient energy to puncture or otherwise damage a vehicle to the extent that it causes bodily injury or leads to fatalities of the occupants. Impact energy is largely governed by the block mass and fall height (along with attenuation characteristics of rock blocks as they fall and transit down a slope). However, in our preliminary database, these parameters carry large uncertainties. We are therefore seeking additional, well-constrained, rockfall vehicle impact case studies to conduct additional analysis, especially those that contain information on the impacting rock block volume and fall height as well as the attributes that define human vulnerability (e.g., passenger location, vehicle impact location, type of vehicle) in the wake of rockfall incidents. As we expand the database, we stress the importance of preserving and recording these parameters in future rockfall impact events.

The development of this database can support the calculation of statistically significant measures of human vulnerability to suffer non-fatal injuries or fatalities due to rockfall hazards while travelling in vehicles on roadways. It is expected that this may, in turn, provide critical

information for an empirically based update of the vulnerability parameter used in quantitative rockfall risk assessments and assist transportation professionals, engineers, and scientists with risk assessment planning along rockfall-prone transportation corridors.

REFERENCES

1. Budetta, P. Assessment of rockfall risk along roads. *Natural Hazards and Earth System Science*, vol. 4, 2004, pp. 71–81, https://doi.org/10.5194/nhess-4-71-2004, 2004.

2. Mignelli, C., Peila, D., Lo Russo, S., Ratto, S.M., Broccolato, M. Analysis of rockfall risk on mountainside roads: evaluation of the effect of protection devices. *Natural Hazards*, vol. 73, 2014, pp. 23–35, https://doi.org/10.1007/s11069-013-0737-4.

3. Bunce, C.M., Cruden, D.M., and Morgenstern, N.R. Assessment of the hazard from rock fall on a highway. *Canadian Geotechnical Journal*, vol. 34, 1997, pp. 344–356, https://doi.org/10.1139/t97-009.

4. Mavrouli, O., Corominas, J., Ibarbia, I., Alonso, N., Jugo, I., Ruiz, J., Luzuriaga, S., and Navarro, J. A. Integrated risk assessment due to slope instabilities in the roadway network of Gipuzkoa, Basque Country. *Natural Hazards and Earth System Science*, vol. 19, 2019, pp. 399–419, https://doi.org/10.5194/nhess-19-399-2019.

5. Turner, A.K. Rockfall risk assessment and risk management, chap. 5 *in* Rockfall: Characterization and Control, Turner, A.K. and Schuster, R.L. eds. Transportation Research Board, Washington D.C., 2012, 658 p.

6. Guzzetti, F., Reichenbach, P. and Ghigi, S. Rockfall hazard and risk assessment along a transportation corridor in the Nera Valley, central Italy. *Environmental Management*, vol. 34, 2004, pp. 191–208, https://doi.org/10.1007/s00267-003-0021-6.

7. Michoud, C., Derron, M.-H., Horton, P., Jaboyedoff, M., Baillifard, F.-J., Loye, A., Nicolet, P., Pedrazzini, A., and Queyrel, A. Rockfall hazard and risk assessments along roads at a regional scale: example in Swiss Alps. *Natural Hazards and Earth System Science*, vol. 12, 2012, pp. 615–629, https://doi.org/10.5194/nhess-12-615-2012.

8. Richards, D.C. *Relationship between speed and risk of fatal injury: pedestrians and car occupants.* Road Safety Web Publication No. 16. United Kingdom Department of Transport, 2010, 41 p.

9. Prochowski, L., Ziubiński, M., Dziewiecki, K., and Szwajkowski, P. Impact energy and the risk of injury to motorcar occupants in the front-to-side vehicle collision. *Nonlinear Dynamics*, vol. 110, 2022, pp. 3333–3354, https://doi.org/10.1007/s11071-022-07779-8.

10. Stock, G.M., Collins, B.D., Santaniello, D.J., Zimmer, V.L., Wieczorek, G.F., and Snyder, J.B. *Historical rock falls in Yosemite National Park, California (1857–2011)*, U.S. Geological Survey Data Series 746, 17 p. and data files, 2013, https://pubs.usgs.gov/ds/746/.

11. Wieczorek, G.F., Snyder, J., Alger, C., and Issacson, K. *Rock falls in Yosemite Valley, California.* U.S. Geological Survey Open-File Report 92-387, Report, v. 40, 1992, https://doi.org/10.3133/ofr92387.

12. Corominas, J., Mavrouli, O., & Ruiz-Carulla, R. Magnitude and frequency relations: are there geological constraints to the rockfall size?. *Landslides*, vol. 15, 2018, pp. 829–845. https://doi.org/10.1007/s10346-017-0910-z.

32. The Interrelationships of the Characteristic and Dilatant Friction Angles and Tangent Poisson's Ratio

Gary Norris
Emeritus Professor
University of Nevada Reno
1664 N. Virginia St, MS258
Reno, NV 89557
(775) 331-5582

norris@unr.edu

Prepared for the 75th Highway Geology Symposium, September, 2026

ABSTRACT

The characteristic friction angle (ϕ_c) has been used to develop a volumetric strain (ε_v) versus axial strain (ε_1) curve that closely matches the recorded volume change curve from the drained compressive triaxial test. Such characterization is provided in the paper, "The Characteristic Friction Angle, Its Determination and Use" (Norris, 2019) from the 70th Highway Geology Symposium. It is shown here in addition that the ratio of mobilized to characteristic friction angles (ϕ_m/ϕ_c), the tangent Poisson's ratio (ν_{tan}) and the mobilized angle of dilatancy (ψ) are each sole functions of the slope ($d\varepsilon_v / d\varepsilon_1$) on the volume change curve and, therefore, they are explicitly related to each other. The variation of such relationships is demonstrated via the data of a frictionless cap and base triaxial test.

INTRODUCTION

It is the intent here to show that the ratio of mobilized to characteristic friction angles (ϕ_m/ϕ_c), the tangent Poisson's ratio (ν_{tan}) and the angle of dilatancy (ψ) are each exclusively related to different variations of the variable, $d\varepsilon_v/d\varepsilon_1$, the slope on the volume change curve (ε_v vs ε_1) and, therefore, explicitly related to each other.

BACKGROUND

In the drained triaxial compression test, undertaken at constant confining pressure (σ_3), the deviator stress (σ_d) is usually plotted versus the axial strain (ε_1). The deviator stress, normalized by its peak or failing value (σ_{df}), is the stress level (SL). Accordingly, the change in the deviator stress with increasing axial strain of the cohesionless sample could as easily be characterized in terms of the mobilized secant friction angle (ϕ_m), i.e.

$$\phi_m = \sin^{-1} [SL\ A / (SL\ A + 2)] \qquad (1)$$

where

$$A = \tan^2 (45 + \phi/2) - 1 = 2 \sin \phi / (1 - \sin \phi) \quad \phi = \text{peak friction angle} \qquad (2)$$

Thus, the vertical axis of the stress-strain curve of Fig. 1 can be converted to its mobilized friction angle. Concurrent with the stress-strain response, the volumetric strain, the change in volume divided by the original sample volume ($\varepsilon_v = \Delta V / V_o$) is also recorded. Such response is portrayed versus ε_1 in Fig. 1 along with the stress-strain or mobilized friction angle-strain curve.

Of note are the characteristic friction angle (ϕ_c) and the constant volume or critical state friction angle (ϕ_{cv}). As shown, the characteristic friction angle occurs when the volumetric strain reaches its maximum compressive value, where the slope, $d\varepsilon_v/d\varepsilon_1$, is instantaneously zero. By contrast, the constant volume friction angle corresponds to where the volume change curve flattens out ($d\varepsilon_v/d\varepsilon_1 = 0$) and constant volume is achieved. This constant volume friction angle is also termed the critical state friction angle.

Figure 2 shows how the characteristic friction angle is envisioned and how it changes with density as expressed in terms of porosity (volume of voids / total volume) or void ratio, e (volume of voids / volume of solids). The peak friction angle (ϕ) less the volumetric dilatant component of strength at failure ($\Delta\phi_f$) corresponds to the difference in dilation, $(d\varepsilon_v/d\varepsilon_1)_f$ - ($d\varepsilon_v/d\varepsilon_1 = 0$) that occurs on the volume change curve. But this is the difference in friction angle between ϕ (for which $(d\varepsilon_v/d\varepsilon_1)_f$ occurs) and ϕ_c (where $d\varepsilon_v/d\varepsilon_1 = 0$). At the loosest state (at the critical void ratio), the peak, the characteristic (ϕ_c) and constant volume (ϕ_{CV}) friction angles all become one and the same.

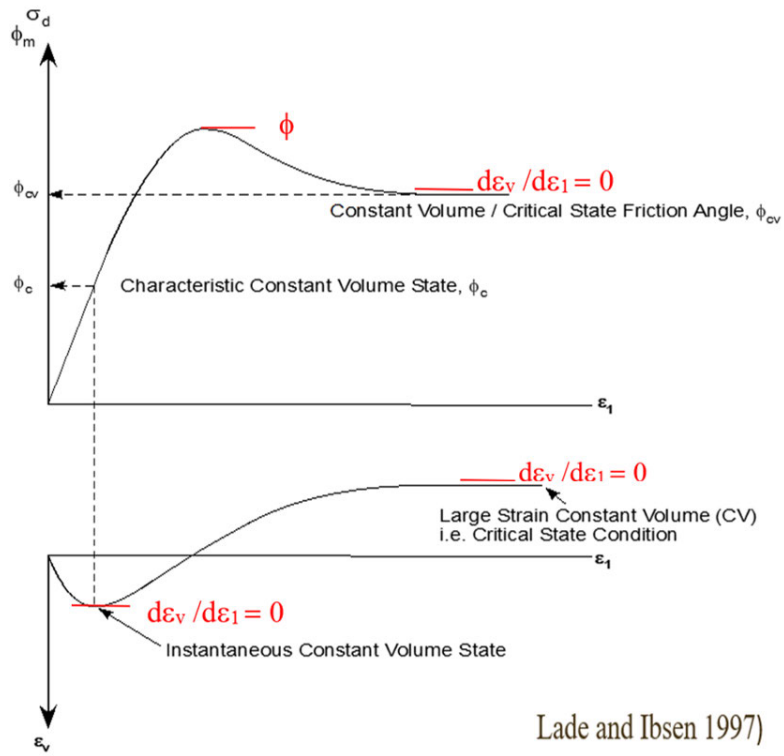

Figure 1 - Assessment of Characteristic (ϕ_c) and Constant Volume (ϕ_{cv}) Friction Angles of Sand (after Lade and Ibsen 1997)

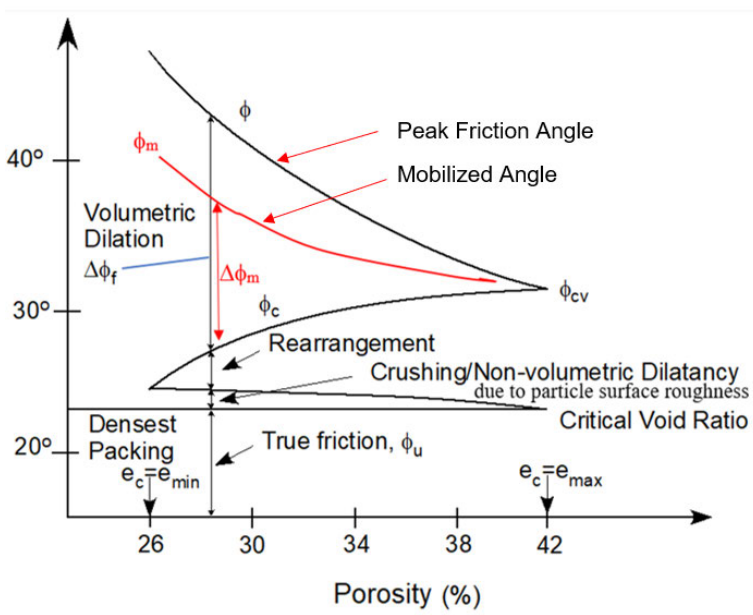

Figure 2 - Components of Friction Angle (Modified from Mitchell 1993, after Rowe 1962)

While the peak friction angle, ϕ, corresponds to SL = 1, another curve, ϕ_m, at a lower SL is also shown in Fig. 2. The difference between ϕ_m and ϕ_c, is $\Delta\phi_m$, the difference due to $d\varepsilon_v/d\varepsilon_1$ at ϕ_m and $d\varepsilon_v/d\varepsilon_1 = 0$, or just $(d\varepsilon_v/d\varepsilon_1)_m$.

The fundamental equation introduced at Portland's 2019 Highway Geology Symposium,

$$d\varepsilon_v/d\varepsilon_1 = 1 - \phi_m / \phi_c \tag{3a}$$

can be used to yield $\Delta\phi_m$. From Eq. 3a,

$$\phi_m / \phi_c = 1 - d\varepsilon_v/d\varepsilon_1 \tag{3b}$$

$$\phi_m = \phi_c (1- d\varepsilon_v/d\varepsilon_1) \tag{3c}$$

and

$$\Delta\phi_m = \phi_m - \phi_c \tag{3d}$$

$$\Delta\phi_m = \phi_c (1- d\varepsilon_v/d\varepsilon_1) - \phi_c \tag{3e}$$

so that

$$\Delta\phi_m = (- d\varepsilon_v/d\varepsilon_1)\, \phi_c \tag{3f}$$

In other words, $\Delta\phi_m$, is equal to the negative of the slope on the volume change curve times ϕ_c.

The use of this relationship is shown in Fig. 3 where at any axial strain, $\Delta\phi_m$ is given by Eq. 3f which associates the increase in ϕ above ϕ_c to the corresponding slope on the volume change curve. Be aware that Eq. 3 applies up to ϕ (the peak value). The angle ϕ_{cv} should replace ϕ_c in Eq. 3 for ϕ_m on the post peak side of of ϕ, because $d\varepsilon_v/d\varepsilon_1$ is thereby taken relative to ϕ_{cv} (corresponding to $d\varepsilon_v/d\varepsilon_1 = 0$). This is a subject for another time.

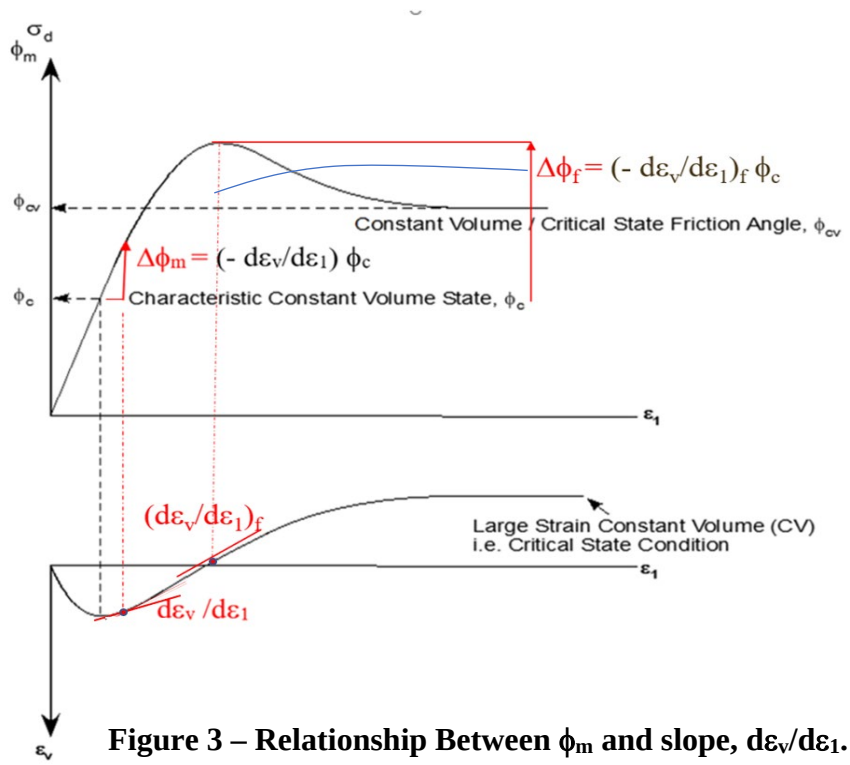

Figure 3 – Relationship Between ϕ_m and slope, $d\varepsilon_v/d\varepsilon_1$.

THE EXPLICIT RELATIONSHIPS OF THE TANGENT POISSON'S RATIO TO THE SLOPE ON THE VOLUME CHANGE CURVE AND THE RATIO OF MOBILIZED TO CHARACTERISTIC FRICTION ANGLE

In the triaxial test, the incremental volumetric strain ($d\varepsilon_v$) is related to the incremental axial ($d\varepsilon_1$) and lateral ($d\varepsilon_3$) strains as follows:

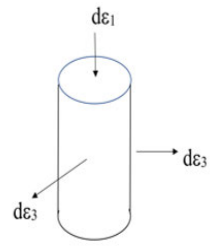

$$d\varepsilon_v = d\varepsilon_1 + 2d\varepsilon_3 \quad (4)$$

The derived negative of incremental lateral strain is therefore

$$-\, d\varepsilon_3 = ½\, (d\varepsilon_1 - d\varepsilon_v) \quad (5)$$

The tangent Poisson's ratios in the triaxial compression test is then

$$\nu_{tan} = -\frac{d\varepsilon_3}{d\varepsilon_1} = \frac{1}{2}\frac{(d\varepsilon_1 - d\varepsilon_v)}{d\varepsilon_1} = \frac{1}{2}\left(1 - \frac{d\varepsilon_v}{d\varepsilon_1}\right) \quad (6)$$

Substituting for $d\varepsilon_v/d\varepsilon_1$ from Eq. 3a in Eq. 6,

$$\nu_{tan} = ½\, (\phi_m / \phi_c) \quad (7a)$$

THE EXPLICIT RELATIONSHIPS OF THE ANGLE OF DILATANCY TO THE SLOPE ON THE VOLUME CHANGE CURVE AND THE MOBILIZED AND CHARACTERISTIC FRICTION ANGLES

A different angle, one that relates incremental volumetric strain to the incremental maximum shear strain causing it, $d\varepsilon_V/d\gamma_{max}$, is the angle of dilatancy, ψ. Figure 4 shows the Mohr circle of incremental strains for the triaxial compression test, for both ψ less than (compressive) and greater than zero (positive dilative) volume change. As shown, it is tan ψ that is equal to $(d\varepsilon_V/2)/(d\gamma_{max}/2) = d\varepsilon_V/d\gamma_{max}$, i.e.

$$\tan \psi = -\, d\varepsilon_V/d\gamma_{max} \quad (8)$$

Recall from Eqs. 4 and 5 the introduction of the incremental strains, $d\varepsilon_V$ and $d\varepsilon_1$. Note that the (expansive) $2\, d\varepsilon_3/2$ arrow of Fig. 4 is shown acting in the opposite direction of the (compressive) $d\varepsilon_1/2$ arrow. Substituting that $-\, d\varepsilon_3 = ½\, (d\varepsilon_1 - d\varepsilon_v)$ from Eq. 5 for $-\, d\varepsilon_3$ in $d\gamma_{max} = d\varepsilon_1 - d\varepsilon_3$ of Eq. 8, it can be shown that

$$\tan \psi = -\, 2\, d\varepsilon_v /d\varepsilon_1 \,/\, (3 - d\varepsilon_V/ d\varepsilon_1) \quad (9)$$

If then, one substitutes $d\varepsilon_v /d\varepsilon_1 = 1 - \phi_m/\phi_c$ from Eq. 3a into Eq. 9,

$$\tan \psi = -\, 2\, (1 - \phi_m/\phi_c)/[3 - (1 - \phi_m/\phi_c)] \quad (10a)$$

$$= -\, (2\phi_c - 2\phi_m) \,/\, (2\phi_c + \phi_m)$$

$$\tan \psi = (\phi_m - \phi_c) / (1/2\, \phi_m + \phi_c) \tag{10b}$$

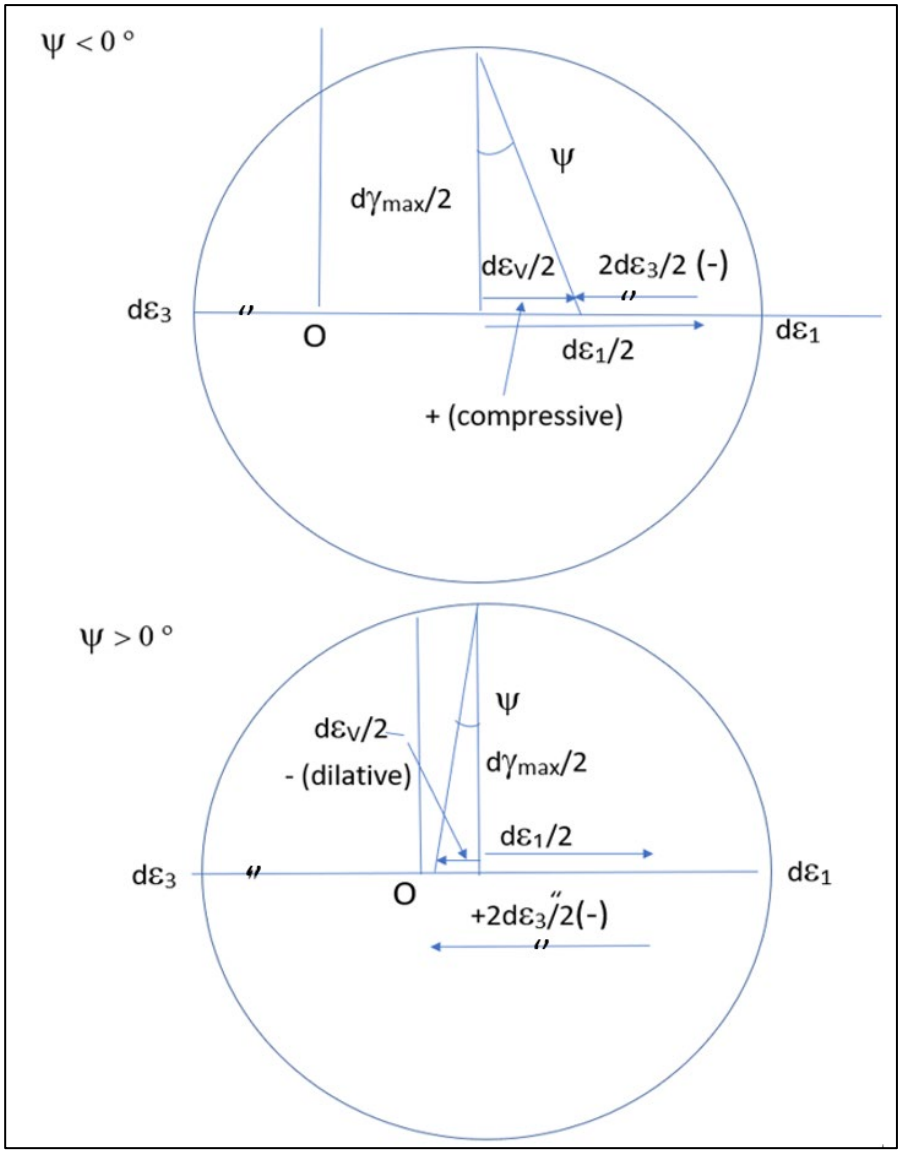

Figure 4 - Mohr Circles of Incremental Strain for the Triaxial Compression Test

THE EXPLICIT RELATIONSHIP OF THE ANGLE OF DILATANCY AND THE TANGENT POISSON'S RATIO

Dividing the numerator and denominator of the right hand side of Eq. 10b by ϕ_c,

$$\tan \psi = (\phi_m/\phi_c - 1) / (1/2\, \phi_m/\phi_c + 1) \tag{10c}$$

From Eq. 7a, $\phi_m/\phi_c = 2\nu_{tan}$ (7b)

Replacing ϕ_m/ϕ_c with $2\nu_{tan}$ in Eq. 10c,

$$\tan\psi = (2\,\nu_{tan} - 1)/(\nu_{tan} + 1) \quad (11a)$$

or its reverse,

$$\nu_{tan} = (1 + \tan\psi)/(2 - \tan\psi) \quad (11b)$$

SUMMARY OF INTERRELATIONSHIPS AND THEIR FURTHER EXTENSION

From the presentation so far, we have that

$$\phi_m/\phi_c = 1 - d\varepsilon_v/d\varepsilon_1 \quad (3b)$$

$$\nu_{tan} = -\frac{d\varepsilon_3}{d\varepsilon_1} = \frac{1}{2}\frac{(d\varepsilon_1 - d\varepsilon_v)}{d\varepsilon_1} = \frac{1}{2}\left(1 - \frac{d\varepsilon_v}{d\varepsilon_1}\right) \quad (6)$$

and $\tan\psi = -2\,d\varepsilon_v/d\varepsilon_1/(3 - d\varepsilon_V/d\varepsilon_1)$ (9)

all of which are sole functions of $d\varepsilon_v/d\varepsilon_1$. Following from Eq. 3a, it has been shown that

$$\nu_{tan} = ½\,(\phi_m/\phi_c) \quad (7a)$$

$$\tan\psi = (\phi_m - \phi_c)/(1/2\,\phi_m + \phi_c) \quad (10b)$$

$$\tan\psi = (2\,\nu_{tan} - 1)/(\nu_{tan} + 1) \quad (11a)$$

or $\nu_{tan} = (1 + \tan\psi)/(2 - \tan\psi)$ (11b)

Substituting $\sin^{-1}[SL\,A/(SL\,A + 2)]$ for ϕ_m from Eq. 1, i.e.

$$\phi_m = \sin^{-1}[SL\,A/(SL\,A + 2)] \quad (1)$$

in Eqs. 7a and 10b, it follows that

$$\nu_{tan} = \sin^{-1}[SL\,A/(SL\,A + 2)]/2\phi_c \quad (7c)$$

$$\tan\psi = (\sin^{-1}[SL\,A/(SL\,A + 2)] - \phi_c)/(\sin^{-1}[SL\,A/(SL\,A + 2)] + \phi_c) \quad (10d)$$

In other words, ϕ_m, ν_{tan} and tan ψ can be characterized/plotted as functions of SL, the developing deviator stress, σ_d, divided by the deviator stress at failure, σ_{df}. In turn, if the relationship of ε versus SL were known, e.g.

$$\varepsilon = SL\, e^{\,Coef\ SL} \times \varepsilon_{50} / \lambda \qquad x = 6.38/\, e^{\,0.5\ Coef} \tag{12}$$

as given by Norris and Yang (2025), the various parameters might be characterized/plotted versus the increasing axial strain as well.

DILATANT AND CHARACTERISTIC FRICTION ANGLES AND TANGENT POISSON'S RATIO VARIATIONS FROM A TYPICAL DRAINED TRIAXIAL COMPRESSION TEST

Figure 5 shows data exhibiting the evaluation of ϕ_c, ψ and ν_{tan} for one of 144 frictionless cap and base triaxial compression tests on seven sands from different geologic environments. (See the 70th HGS Norris, 2019 paper for the characteristics of the sands tested.) Note that the recorded test data (ε_1, ε_v and σ_d) appears in columns B, C and D. Column E, SL, is σ_d of column D divided by the maximum value of column D (σ_{df}). Column F is the mobilized friction angle, ϕ_m, of Eq. 1 ($\phi_m = \sin^{-1}$ [SL A / (SL A + 2)]) based on the SL values of column E. Column G is $\phi_{m,area} = \int \varphi_m d\varepsilon_1$ obtained from numerical integration involving columns F and B. Column H is ε_v based on Eq. 13,

$$\varepsilon_v = \varepsilon_1 - (1/\phi_c)\int \phi_m\, d\varepsilon_1 \tag{13}$$

which derives from $\varepsilon_v = \int (d\varepsilon_v / d\varepsilon_1)\, d\varepsilon_1$ with Eq. 3a ($d\varepsilon_v/d\varepsilon_1 = 1 - \phi_m / \phi_c$) used in place of ($d\varepsilon_v / d\varepsilon_1$). See the 70th HGS Norris, 2019 paper for details.

The recorded volume change curve of Test 62 (column C versus column B) is the blue line curve of Fig. 6, while the pink line curve is the calculated curve based on Eq. 13 (column H versus B) using a "best fit" value of ϕ_c reported in cell G7. The value in cell G7 is varied until the closest match of the calculated to the recorded curve is achieved.

Column I is $d\varepsilon_v / d\varepsilon_1$ obtained from a forward differencing of columns C and B. Columns K and L are ν_{tan} and tan ψ assessed from Eqs. 6 and 9. Column M of ψ follows from evaluation of column O. Column N. on the other hand, is ϕ_c assessed as a function of ϕ_m and $d\varepsilon_v/d\varepsilon_1$ as given by an additional form of Eq. 3, introduced here, i.e.

$$\phi_c = \phi_m / (1 - d\varepsilon_v/d\varepsilon_1) \tag{3g}$$

There is a plot below columns B through I of Fig. 5 of ϕ_c of column P versus ε_1 showing a fairly stable (mobilized) value of ϕ_c whose average (27.5°) fairly well matches the visually determined value of cell G7 used to generate the calculated/predicted pink line curve (column H versus B) of Fig. 6. Note that ϕ_c at failure (cell H7) differs from the best fit value which is why the calculated volume change curve deviates from the recorded curve of Fig. 6 near its end.

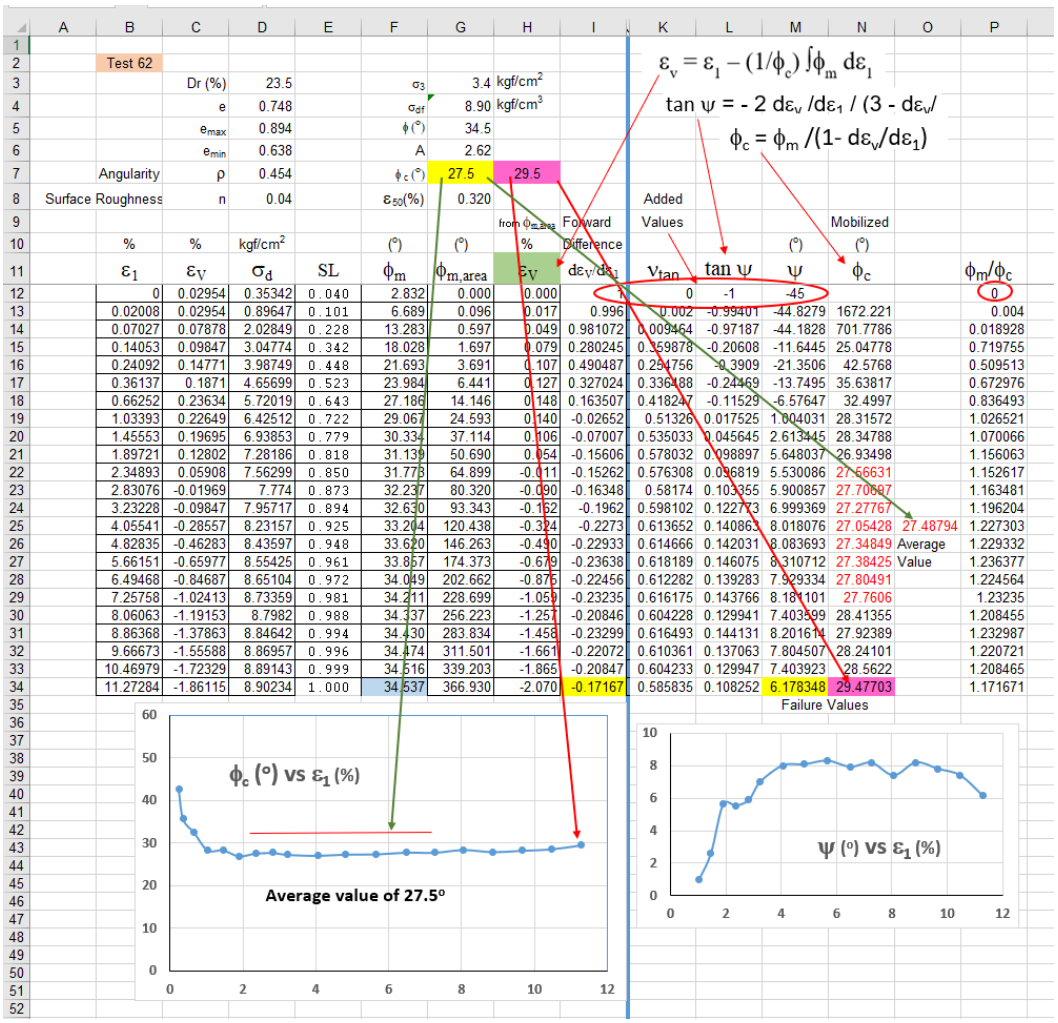

$$\varepsilon_v = \varepsilon_1 - (1/\phi_c)\int \phi_m \, d\varepsilon_1$$

$$\tan\psi = -2\, d\varepsilon_v / d\varepsilon_1 / (3 - d\varepsilon_v/$$

$$\phi_c = \phi_m / (1 - d\varepsilon_v/d\varepsilon_1)$$

	Test 62													
		Dr (%)	23.5		σ_3	3.4	kgf/cm^2							
		e	0.748		σ_{df}	8.90	kgf/cm^3							
		e_{max}	0.894		ϕ (°)	34.5								
		e_{min}	0.638		A	2.62								
	Angularity	ρ	0.454		ϕ_c (°)	27.5	29.5							
	Surface Roughness	n	0.04		ε_{50}(%)	0.320			Added					
							from $\phi_{m,area}$	Forward	Values			Mobilized		
	%	%	kgf/cm^2		(°)	(°)	%	Difference			(°)	(°)		
	ε_1	ε_V	σ_d	SL	ϕ_m	$\phi_{m,area}$	ε_V	$d\varepsilon_V/d\varepsilon_1$	ν_{tan}	tan ψ	ψ	ϕ_c		ϕ_m/ϕ_c
	0	0.02954	0.35342	0.040	2.832	0.000	0.000	1	0	-1	-45			0
	0.02008	0.02954	0.89647	0.101	6.689	0.096	0.017	0.996	0.002	-0.99401	-44.8279	1672.221		0.004
	0.07027	0.07878	2.02849	0.228	13.283	0.597	0.049	0.981072	0.009464	-0.97187	-44.1828	701.7786		0.018928
	0.14053	0.09847	3.04774	0.342	18.028	1.697	0.079	0.280245	0.359878	-0.20608	-11.6445	25.04778		0.719755
	0.24092	0.14771	3.98749	0.448	21.693	3.691	0.107	0.490487	0.294756	-0.3909	-21.3506	42.5768		0.509513
	0.36137	0.1871	4.65699	0.523	23.984	6.441	0.127	0.327024	0.336488	-0.24469	-13.7495	35.63817		0.672976
	0.66252	0.23634	5.72019	0.643	27.186	14.146	0.148	0.163507	0.418247	-0.11529	-6.57647	32.4997		0.836493
	1.03393	0.22649	6.42512	0.722	29.067	24.593	0.140	-0.02652	0.51326	0.017525	1.004031	28.31572		1.026521
	1.45553	0.19695	6.93853	0.779	30.334	37.114	0.106	-0.07007	0.535033	0.045645	2.613445	28.34788		1.070066
	1.89721	0.12802	7.28186	0.818	31.139	50.690	0.054	-0.15606	0.578032	0.098897	5.648037	26.93498		1.156063
	2.34893	0.05908	7.56299	0.850	31.773	64.899	-0.011	-0.15262	0.576308	0.096819	5.530086	27.56631		1.152617
	2.83076	-0.01969	7.774	0.873	32.237	80.320	-0.090	-0.16348	0.58174	0.103355	5.900857	27.70697		1.163481
	3.23228	-0.09847	7.95717	0.894	32.630	93.343	-0.162	-0.1962	0.598102	0.122773	6.999369	27.27767		1.196204
	4.05541	-0.28557	8.23157	0.925	33.284	120.438	-0.324	-0.2273	0.613652	0.140863	8.018076	27.05428	27.48794	1.227303
	4.82835	-0.46283	8.43597	0.948	33.620	146.263	-0.490	-0.22933	0.614666	0.142031	8.083693	27.34849	Average	1.229332
	5.66151	-0.65977	8.55425	0.961	33.857	174.373	-0.679	-0.23638	0.618189	0.146075	8.310712	27.38425	Value	1.236377
	6.49468	-0.84687	8.65104	0.972	34.049	202.662	-0.875	-0.22456	0.612282	0.139283	7.929334	27.80491		1.224564
	7.25758	-1.02413	8.73359	0.981	34.211	228.699	-1.059	-0.23235	0.616175	0.143766	8.181101	27.7606		1.23235
	8.06063	-1.19153	8.7982	0.988	34.337	256.223	-1.257	-0.20846	0.604228	0.129941	7.403599	28.41355		1.208455
	8.86368	-1.37863	8.84642	0.994	34.430	283.834	-1.458	-0.23299	0.616493	0.144131	8.201614	27.92389		1.232987
	9.66673	-1.55588	8.86957	0.996	34.474	311.501	-1.661	-0.22072	0.610361	0.137063	7.804507	28.24101		1.220721
	10.46979	-1.72329	8.89143	0.999	34.516	339.203	-1.865	-0.20847	0.604233	0.129947	7.403923	28.5622		1.208465
	11.27284	-1.86115	8.90234	1.000	34.537	366.930	-2.070	-0.17167	0.585835	0.108252	6.178348	29.47703		1.171671
											Failure Values			

Figure 5 - Spreadsheet of Test 62 Data

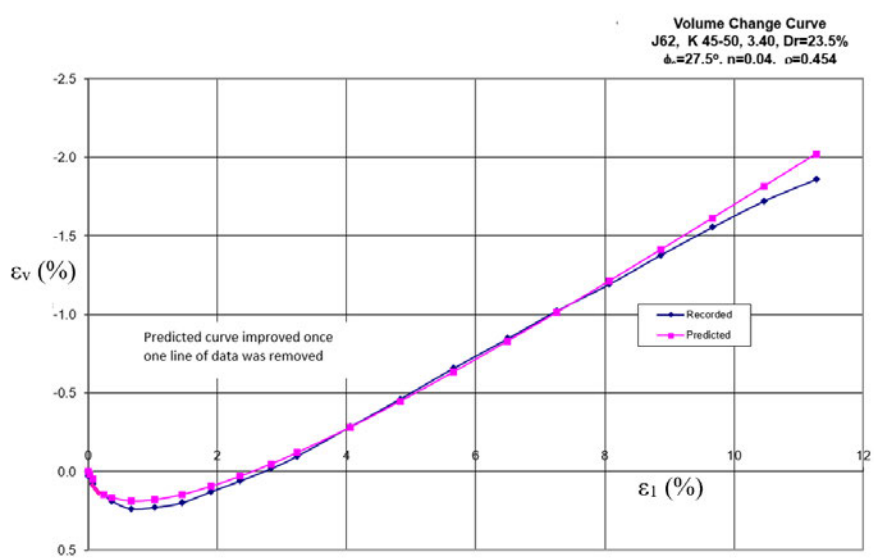

Figure 6 - Best Fit vs Recorded Volume Change Curves of Test 62

Figure 7 shows the variations of $d\varepsilon_v/d\varepsilon_1$ (column I), ν_{tan} (column K) and ψ (column M) versus ε_1 (column B) from the data sheet of Test 62. Figure 8, on the other hand, shows the explicit variations of ϕ_m/ϕ_c (column P), ν_{tan} (column K) and ψ (column M) versus $d\varepsilon_v/d\varepsilon_1$ (column I).

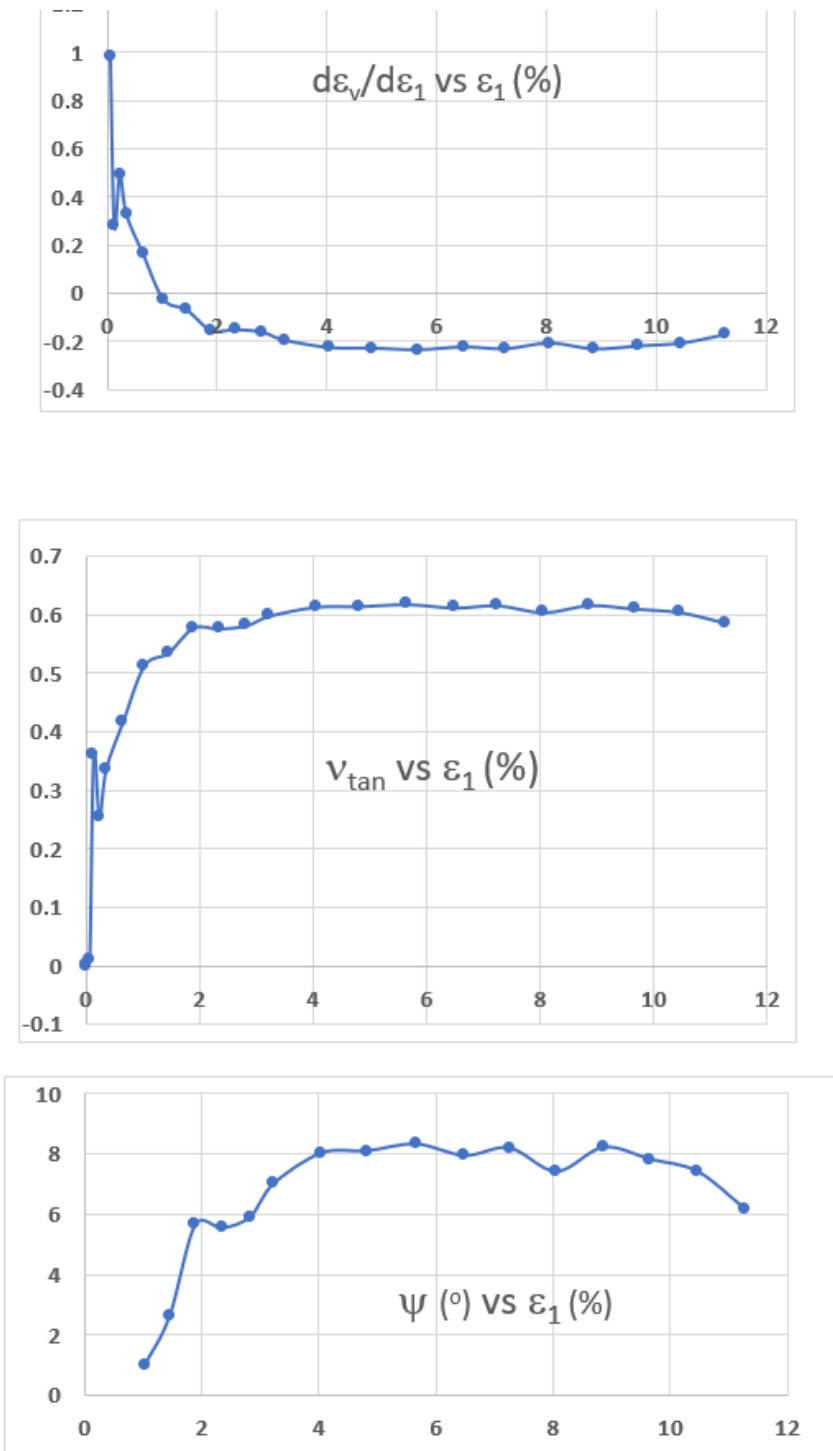

Figure 7 - The Variations of $d\varepsilon_v/d\varepsilon_1$, ν_{tan} and ψ (°) versus ε_1(%) of Test 62

Of particular note, the trendline equation for each of the curves of Fig. 8 yields an R^2 value of one, indicating the explicit nature of the variations.

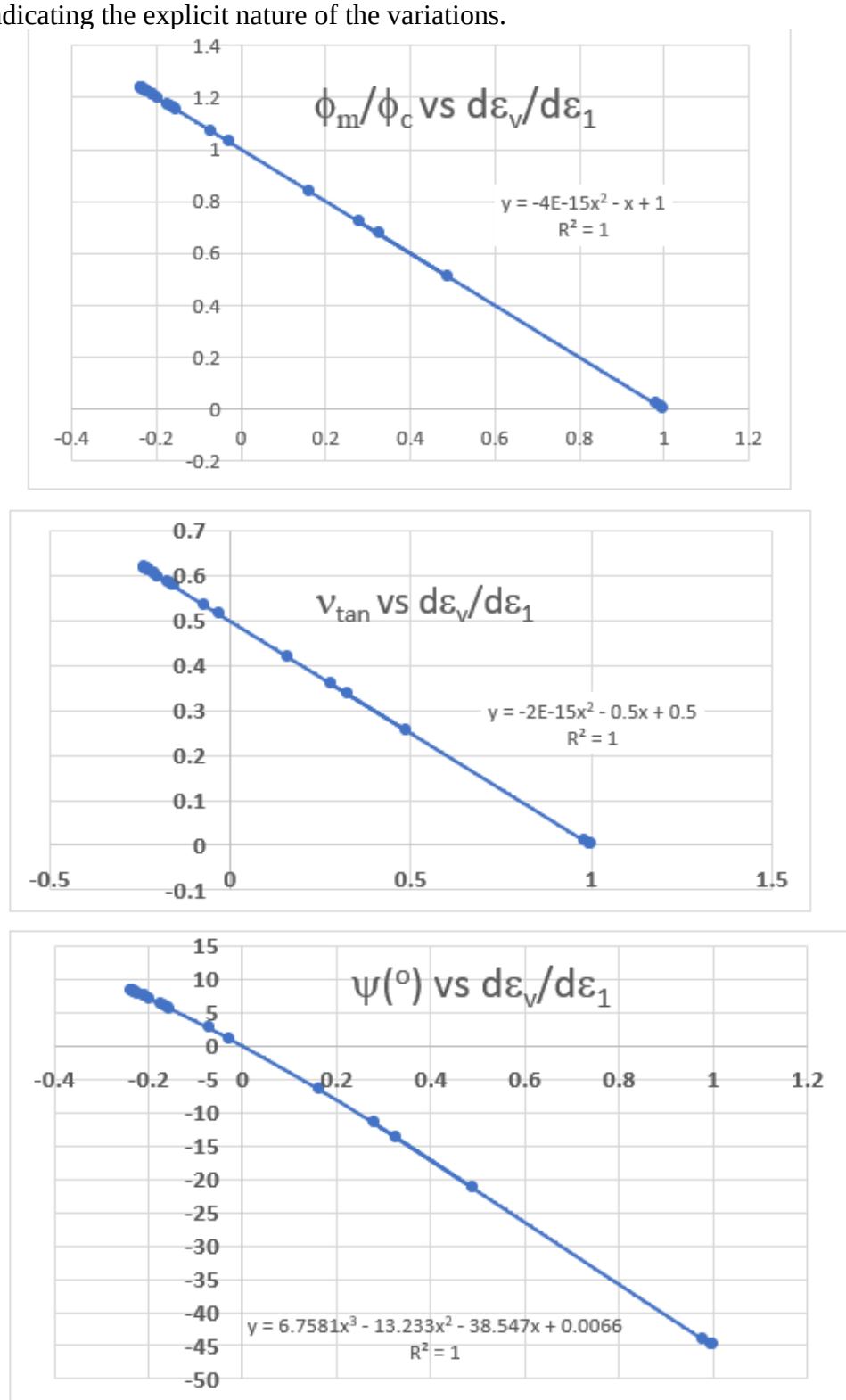

Figure 8 - The Variations of ϕ_m/ϕ_c, ν_{tan} and ψ (°) versus $d\varepsilon_v/d\varepsilon_1$ of Test 62

Figure 9 provides the explicit variations of ϕ_m/ϕ_c, ν_{tan} and ψ, one to another. As in Fig. 8, the trendline fit of the recorded data points yield equations of $R^2 = 1$.

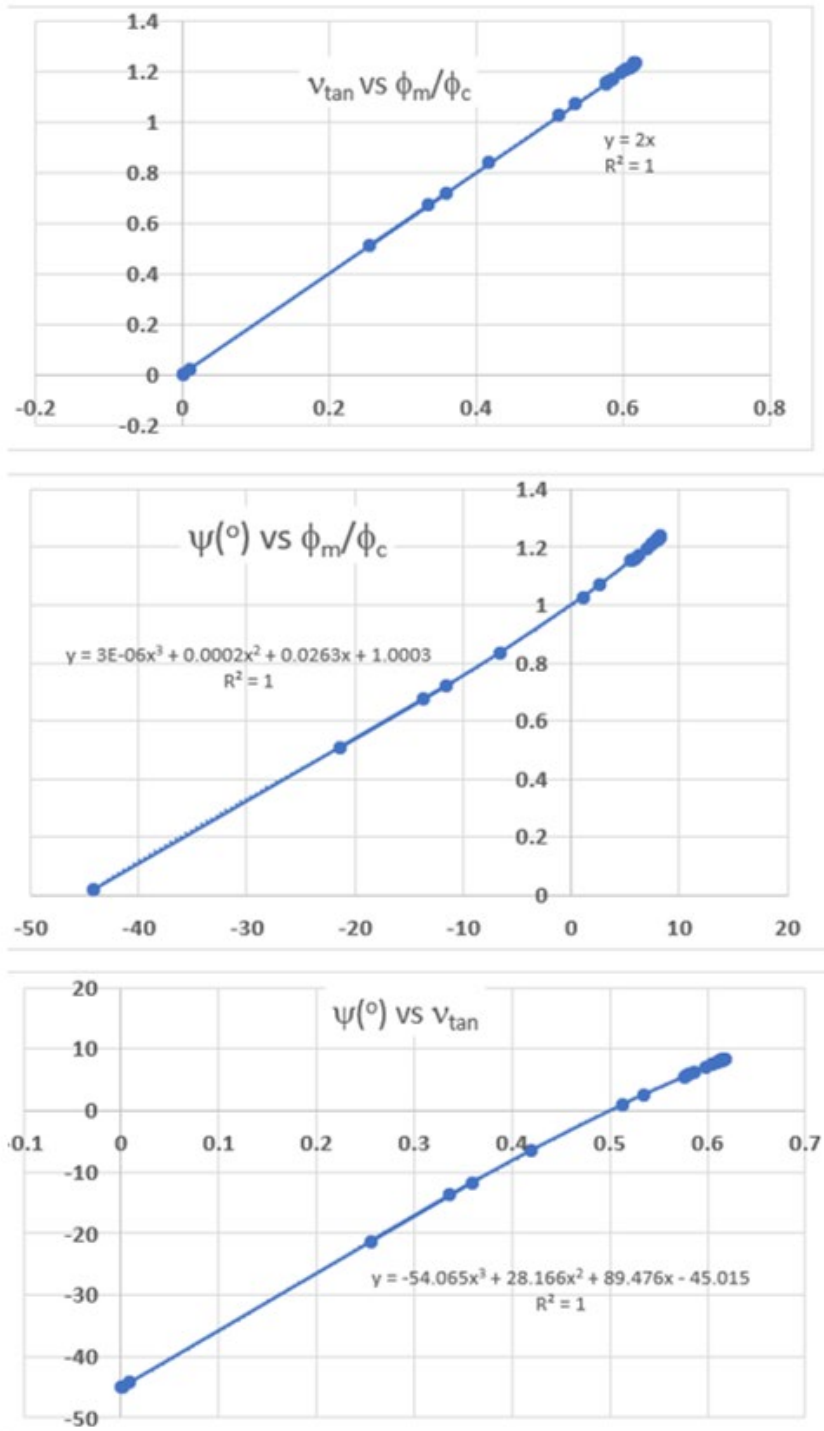

Figure 9 - The Interrelationships of ϕ_m/ϕ_c, ν_{tan} and ψ (°)

It is also worth pointing out that $\phi_m/\phi_c = 1$, $\nu_{tan} = 0.5$ and $\psi = 0$ when $d\varepsilon_v/d\varepsilon_1 = 0$; while $\psi = -45^o$ at $d\varepsilon_v/d\varepsilon_1 = 1$ (i.e. where SL and ε_1 are zero). These values are the same for all triaxial tests, not just Test 62.

DISCUSSION/CONCLUSIONS

From the right triangle of Fig. 4, it was demonstrated that $-d\varepsilon_v/d\gamma_{ma}$ is equal to tan ψ, a heretofore unrecognized relationship for the angle of dilatancy (ψ). Realize that the slope on the volume change curve ($d\varepsilon_v/d\varepsilon_1$), the angle of dilatancy (ψ) and the tangent Poisson's ratio (ν_{tan}) are not constant but vary with axial strain (ε_1), as shown for example, in Fig. 7. More importantly, the mobilized to characteristic friction angle (ϕ_m/ϕ_c), ν_{tan} and ψ vary explicitly with $d\varepsilon_v/d\varepsilon_1$ (Fig. 8). From each of the relationships of ϕ_m/ϕ_c, ψ and ν_{tan} to $d\varepsilon_v/d\varepsilon_1$, the explicit interrelationships to each other have been demonstrated (Fig. 9). The variations in ϕ_m, $d\varepsilon_v/d\varepsilon_1$, ν_{tan} and ψ with stress level (SL), based on a known value of ϕ_c, have also been derived.

From the recorded values of ε_1, ε_v and σ_d from the data sheet of a typical triaxial test (Test 62) it was shown how SL, ϕ_m, ε_v from a best fit ϕ_c, $d\varepsilon_v/d\varepsilon_1$, ν_{tan}, ψ and the mobilized ϕ_c are evaluated.

Finally, while the development of the volume change curve based on the best fit characteristic friction angle was originally presented in the 70th HGS paper, its evaluation was demonstrated in the spreadsheet of Test 62 data shown here (Fig. 5). That curve was then compared to the recorded curve (Fig. 6).

REFERENCES

Lade, P.V. and Ibsen L.B. A (1997). Study of the Phase Transformation and the Characteristic Lines of Sand Behavior. *International Symposium on Deformation and Progressive Failure in Geomechanics*. Asoaka and Adachi, Eds., Pergamon Press, Nagoya, Japan, pp 353-358.

Mitchell, J.K. (1993). Fundamentals of Soil Behavior. Second Edition, John Wiley & Sons, Inc., N.Y., pp. 61-64 and p. 372.

Norris, G. (2019). The Characteristic Friction Angle, Its Determination and Use. *Proceedings of 70th Highway Geology Symposium*, Portland, Oregon. Paper 14, 16 pp.

Norris, G. and H. Yang. (2025). A Nonlinear Stress-Strain Relationship for Soil and Rock. *ICE Geotechnical Engineering Journal*, Vol. 178, Issue 2, pp 247-256.

Rowe, P.W. (1962). Theoretical Meaning and Values of Deformation Parameters for Soil, The Strain Behavior of Soils, London: Foulis, pp. 143-194.

33. Developing the Triaxial Test Responses of Soil from Available Correlations and a Nonlinear Exponential Equation

Sherif Elfass
Associate Research Professor
University of Nevada Reno
1664 N. Virginia St, MS258
Reno, NV 89557
(775) 784-6664
elfass@unr.edu

Gary Norris
Emeritus Professor
University of Nevada Reno
1664 N. Virginia St, MS258
Reno, NV 89557
(775) 331-5582
norris@unr.edu

AND

Horng-Jyh Yang (Tigra)
Geotechnical Engineer
Geo-Environmental Branch
Naval Facilities Engineering Systems Command (Mid-Atlantic)
9324 Virginia Avenue Norfolk, VA 23511
(757 994-5849
horng-jyh.yang.civ@us.navy.mil

Prepared for the 75th Highway Geology Symposium, September, 2026

ABSTRACT

A nonlinear exponential stress-strain equation has been used to closely match the shear modulus reduction curves of Seed and Idriss (1970) for sandy soils and Vucetic and Dobry (1991) curves for clays over the strain range, $1x10^{-6}$ to 0.01, and the Duncan and Chang (1970) response over the moderate to large strain range (0.003 to soil failure). From the methodology to be presented here, along with cited correlations, and with a very few input parameters, the reader will be able to generate the following drained triaxial compression test responses for a cohesionless soil: the deviator stress (σ_d) versus axial strain (ε_1), the mobilized secant friction angle (ϕ_m) versus axial strain, the volumetric strain (ε_v) versus axial strain, the secant (ν_{sec}) and tangent (ν_{tan}) Poisson's ratios versus axial strain, the mobilized characteristic (ϕ_c) and dilatant friction (ψ) angles versus axial strain, and the secant Young's (E) and shear (G) modulus versus axial (ε_1) and shear (γ) strain responses, respectively, as well as the modulus ratios (E/E_i and G/G_o) versus strain. Cross plots of parameters related to axial strain can then be established as well. For the undrained behavior of saturated clay, the responses that can be generated are: the deviator stress versus axial strain, the secant Young's modulus versus axial strain, the shear modulus versus shear strain, as well as the modulus ratios (E/E_i and G/G_o) versus strain.

INTRODUCTION

An exponential relationship is presented here that covers the range in strain from $1x10^{-6}$ to soil failure. It was developed from the characterization of the triaxial test stress-strain behavior of lubricated or "frictionless" cap and base tests on samples with a height to diameter ratio of one that expanded cylindrically (with axial deformation measured over the central half of the sample) across a range in confining pressure (0.425 to 3.40 kgf/cm^2) on natural sands exhibiting a wide range in particle size, shape and surface roughness (Norris 2019). The relationship has been applied in the analysis of laterally loaded pile response (Ashour et al. 1998 and 2004) in sands and clays. Likewise, it has been used in the load-settlement-bearing capacity analysis of shallow foundations (Elfass, et al. 2007, Elsayed et al. 2011 and Nimeri et al. 2017, Norris 2024).

The equation (Norris 2024, Norris and Yang 2025) is reviewed here as part of its application using available correlations to develop a variety of triaxial test responses: the deviator stress (σ_d) versus axial strain (ε_1), the mobilized secant friction angle (ϕ_m) versus axial strain, the volumetric strain (ε_v) versus axial strain, the secant (ν_{sec}) and tangent (ν_{tan}) Poisson's ratios versus axial strain, the mobilized characteristic friction (ϕ_c) and dilatant friction (ψ) angles versus axial strain, and the secant Young's (E) and shear (G) modulus versus axial and shear strain (γ) responses, respectively, as well as the modulus ratios (E/E_i and G/G_o) versus strain for cohesionless (ϕ) and c-ϕ soil. For the undrained behavior of saturated clay, the responses that can be generated are: the deviator stress versus axial strain, the secant Young's modulus versus axial strain, the shear modulus versus shear strain, as well as the modulus ratios (E/E_i and G/G_o) versus strain.

THE EXPONENTIAL EQUATION

The axial strain, ε, in the frictionless cap and base triaxial test, conducted at constant confining

pressure, as a function of stress level, SL, applicable over the entire range of strain, $1x10^{-6}$ to failure, ε_f, or from SL = 0 to 1, can be expressed in exponential form as

$$\varepsilon = SL\ e^{3.707SL}\ \varepsilon_{50} / \lambda \qquad (1a)$$

where $$SL = \sigma_d / \sigma_{df} \qquad (1b)$$

Stress level, SL, is the current deviator stress, σ_d, divided by the deviatoric stress at failure, σ_{df}, and parameter Lambda, λ, is itself a function of SL, i.e.

$$\lambda = 3.19 \qquad \text{for } SL \leq 0.5 \qquad (1c)$$

$$\lambda = -7.1219\ SL^2 + 7.0592\ SL + 1.4403 \qquad \text{for } SL > 0.5 \qquad (1d)$$

The strain, ε_{50}, is the strain at SL = 0.5, or $\sigma_d = \sigma_{d,50} = ½\sigma_{df}$.

The ε_{50} value in Eq. 1a for cohesionless soil is a function of confining pressure,

$$\varepsilon_{50} = (\sigma_3 / \sigma_{3\ ref})^{\ n}\ \varepsilon_{50\ ref} \qquad n = 0.2 \qquad (1e)$$

corresponding to $\varepsilon_{50\ ref}$ at the reference pressure, $\sigma_{3\ ref}$. For saturated clay in undrained response, ε_{50} is independent of σ_3, or n = 0. Figures 2a and 2b, that appear after Fig. 1 are introduced to provide tentative $\varepsilon_{50\ ref}$ values for cohesionless and cohesive soils.

Alternatively, the exponential equation can be rewritten as

$$\varepsilon / \varepsilon_{50} = SL\ e^{3.707SL} / \lambda \qquad (2)$$

i.e., normalized strain ($\varepsilon/\varepsilon_{50}$) as a function of normalized stress (SL) as shown in Fig. 1 for a purely frictional (ϕ) or a c-ϕ soil (where c is the Mohr-Coulomb cohesion intercept). The corresponding mobilized friction angle, ϕ_m, is

$$\phi_m = \sin^{-1} [SL\ A / (SL\ A + 2)] \qquad (3a)$$

where $$A = 2 \sin \phi/(1-\sin \phi) \qquad \phi = \text{peak secant friction angle} \qquad (3b)$$

The mobilized friction angle divided by the peak value (ϕ_m/ϕ) versus normalized strain for a specific ϕ is also shown in Fig. 1.

Note that for a c-ϕ soil, σ_3 is taken from an offset (or new) origin, c/tan ϕ lower than the original origin, on the horizontal or normal stress axis. Accordingly, a c-ϕ soil is converted to a purely frictional (ϕ) soil for analysis.

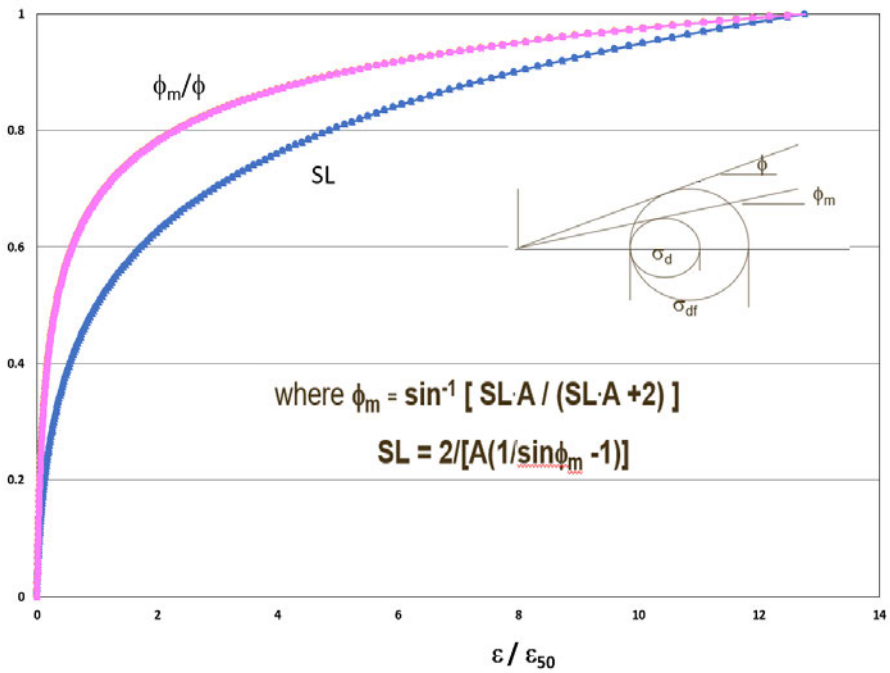

Fig. 1 SL and ϕ_m/ϕ (for ϕ = 35.9º) vs $\varepsilon/\varepsilon_{50}$

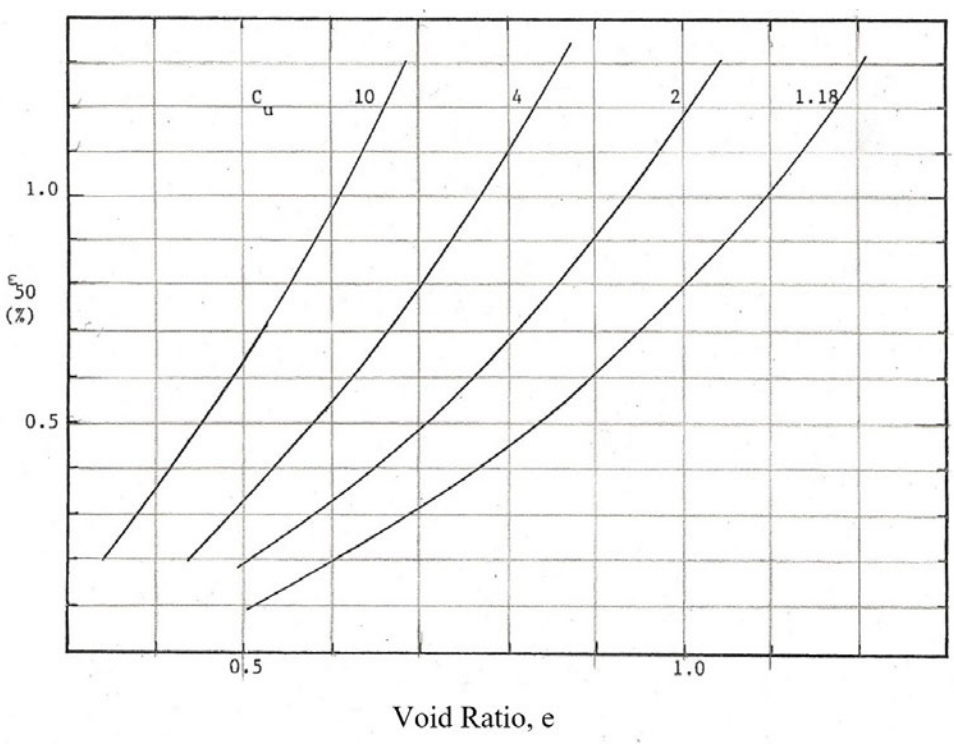

Fig. 2a ε_{50} (%) versus Void Ratio, e, at Confining Pressure, σ_3, of 0.425 kgf/cm^2

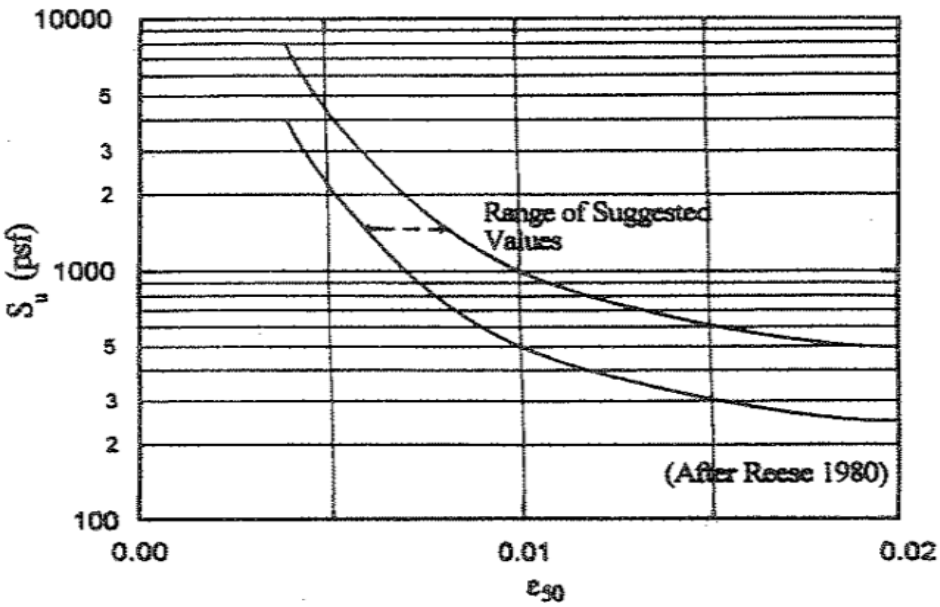

Fig. 2b Undrained Shear Strength, S_u (lb/ft^2), versus ε_{50}

The deviator stress (σ_d) versus axial strain (ε_1) curve derives from Fig. 1 where SL on the vertical axis is multiplied by the deviator stress at failure, σ_{df}, where

$$\sigma_{df} = A\ \sigma_3 \tag{3c}$$

(σ_3 is the constant held confining pressure); and $\varepsilon / \varepsilon_{50}$ on the horizontal axis is multiplied by ε_{50}.

If Eq. 1a is rewritten with σ_d/σ_{df} replacing the first SL

$$\varepsilon = \left(\frac{\sigma_d}{\sigma_{df}}\right) e^{3.707\ SL\ \frac{\varepsilon_{50}}{\lambda}} \qquad \text{(1a with 1b)}$$

the rearranged equation yields the secant Young's modulus, E,

$$E = \frac{\sigma_d}{\varepsilon} = \sigma_{df}\ e^{-3.707\ SL\ \frac{\lambda}{\varepsilon_{50}}} \tag{4a}$$

the secant line to the point on the stress strain curve of the current σ_d and ε. Substituting that $\sigma_{df} = A\ \sigma_3$ (Eq. 3c) for ϕ soil, E becomes

$$E = A\ \sigma_3\ e^{-3.707\ SL\ \frac{\lambda}{\varepsilon_{50}}} \tag{4b}$$

At SL = 0, $$E = E_i = 3.19\ \frac{A\ \sigma_3}{\varepsilon_{50}} \tag{4c}$$

such that Eq. 4b divided by Eq. 4c yields the Young's modulus ratio,

$$\frac{E}{E_i} = e^{-3.707\ SL\ \left(\frac{\lambda}{3.19}\right)} \tag{4d}$$

At SL = 0.5, λ = 3.19, E = E_{50} whereby

$$E_i = 6.38\ E_{50} \tag{4e}$$

The secant shear modulus, G, corresponding to the Young's modulus is

$$G = \frac{E}{2(1+\nu)} \tag{5a}$$

for which the initial modulus at SL = $1x10^{-6}$, G_o, becomes

$$G_o = \frac{E_i}{2(1+\nu_i)} \tag{5b}$$

The corresponding shear strain, γ, is

$$\gamma = \varepsilon\ (1 + \nu) \tag{6}$$

For the undrained response of saturated clay, the strength, σ_{df}, should be replaced by 2 S_u (i.e., 2 c) and the secant Poisson's ratio taken as 0.5 throughout, corresponding to no volume change. Likewise, E_{50} = ½ σ_{df} /ε_{50} = S_u/ε_{50} Everything else remains the same.

STRENGTH AND STRAIN PARAMETERS FROM AVAILABLE CORRELATIONS

The ε_{50} of sand for whatever confining pressure (σ_3) is contemplated can be obtained based on Eq. 1e where $\varepsilon_{50,ref}$ is the value from Fig. 2a at σ_{3ref} of 0.425 kgf/cm^2. On the other hand, the value of ε_{50} for clay can be taken as an average line midheight in the range of Fig. 3 (Fig. 2b but with axes reversed) as given in two parts,

$$\varepsilon_{50} = 4.4838\ S_u^{-0.927} \qquad \text{for } S_u \text{ in lb/ft}^2 < 850 \tag{7a}$$

$$\varepsilon_{50} = 0.1788\ S_u^{-0.446} \qquad > 850 \tag{7b}$$

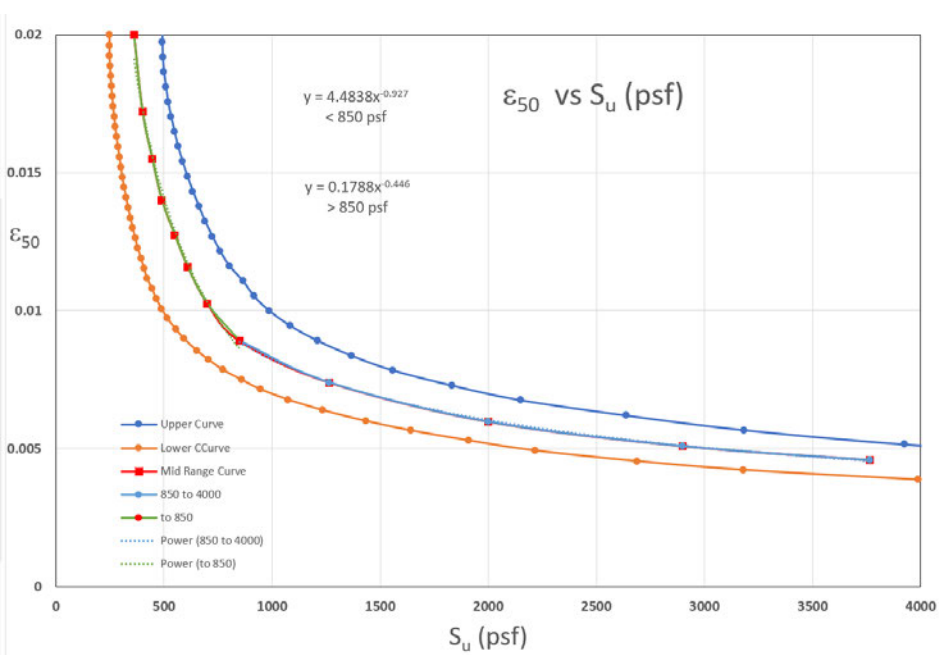

Fig. 3 Reese Curve of Fig. 2b with Reversed Axes

The ε_{50} is independent of confining pressure while undrained strength, S_u, may be approximated as $S_u = 0.2\ \sigma_{vo}'$ (7c)
after Ladd and Foott (1974) (or an alternate σ_{vo}' expression of choice) where σ_{vo}' is the vertical effective stress in the field for whatever depth is of interest. The σ_3 of the triaxial test is taken to be σ_{vo}'.

For sands, the drained friction angle can be approximated from a number of available correlations or for uniform quartz sands from Eq. 8a (Norris 2025),

$$\phi_{n=0} = (0.159\ Dr - 19.893)\ \rho^2 - (0.1198\ Dr - 2.3477)\ \rho + (0.0987\ Dr + 38.17) \qquad (8a)$$

where $\phi_{n=0}$ is the secant friction angle in degrees, a function of relative density (Dr) in %, and particle shape characterized by the sand's roundness value (ρ). See Fig. 4.

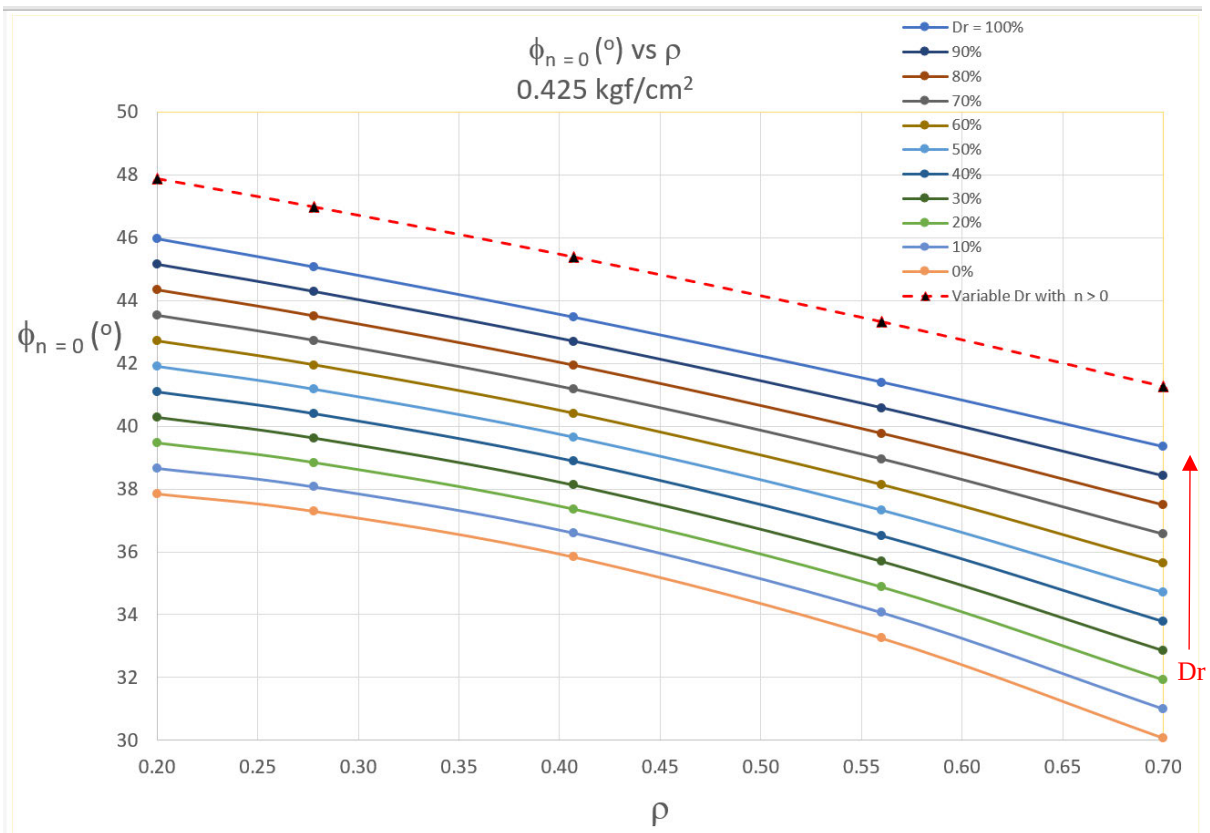

Fig. 4 Variation in $\phi_{n=0}$ with ρ for Different Dr Based on Eq. 8 for 0.425kgf/cm^2 Confining Pressure

Equation 8a is for particles of zero surface roughness (n) at the confining pressure (σ_3) of 0.425 kgf/cm^2. The friction angle with surface roughness ranging from 0 (for river channel sand) to 0.04 (for desert or coastal dune sand) can be assessed as

$$\phi = \phi_{n=0} /(1-n) \qquad (8b)$$

The dashed line at the top of Fig. 4 is the Dr = 100% $\phi_{n=0}$ line with a value of surface roughness of n = 0.04 applied to $\phi_{n=0}$ via Eq. 8b.

This friction angle, established for the confining pressure (σ_3) of 0.425 kgf/cm^2 pressure is taken to be 2.5 degrees lower at the pressure of 1.20 kgf/cm^2 and 4.5 degrees less at the pressure, 3.40 kgf/cm^2. (This corresponds to a log cycle change in secant friction angle, $\Delta\phi$, of 5 degrees with confining pressure.) The development for such evaluation is presented in the paper by Norris (2025) along with the comparator chart employed to assess particle roundness (ρ).

At this point, armed with values of σ_3, ε_{50} and ϕ for sand and σ_3 (say = σ_{vo}') and S_u for clay, the plot of σ_d versus ε_1 (and ϕ_m versus ε_1, for cohesionless material) can be established for a specified variation in SL from say 3x10^{-4} to 1. Likewise, the secant Young's modulus, E, and the modulus ratio E/E_i versus ε_1 and shear modulus, G, and modulus ratio G/Go versus γ can be plotted.

The Poisson's ratio (ν) for G in Eqs. 5 and 6 for undrained saturated clay response is 0.5 while the variation in secant Poisson's ratio with ε_1 for ϕ soil is still to be discussed. The evaluation of both the volumetric strain and the secant Poisson's ratio of cohesionless soil requires knowledge of the characteristic friction angle (Norris 2019) that is discussed in the following section.

THE CHARACTERISTIC FRICTION ANGLE AND THE CONSTRUCTION OF A CALCULATED VOLUME CHANGE CURVE

The characteristic friction angle is that mobilized friction angle, ϕ_m, where the volume change curve, ε_v vs ε_1, reaches its maximum compressive value (ε_v) and the tangent slope on the volume change curve, $d\varepsilon_v/d\varepsilon_1$, is zero. As shown in Fig. 5 from Norris (2019), the characteristic friction angle becomes an integral factor in linking volume change behavior to developing deviatoric stress as expressed in terms of the mobilized friction angle and given by the expression,

$$d\varepsilon_v/d\varepsilon_1 = 1 - \phi_m/\phi_c \qquad (9)$$

The integration of Eq. 10a, i.e.

$$\varepsilon_v = \int (d\varepsilon_v / d\varepsilon_1) d\varepsilon_1 \qquad (10a)$$

substituting $1 - \phi_m/\phi_c$ for $d\varepsilon_v/d\varepsilon_1$ from Eq. 9, leads to the volumetric strain as given in Eq. 10b,

$$\varepsilon_v = \varepsilon_1 - \frac{1}{\phi_c}\int \phi_m d\varepsilon_1 \qquad (10b)$$

Accordingly, the volumetric strain, ε_v, at any ε_1 is the offset from a 1:1 line of ε_v versus ε_1, equal to the area under the ϕ_m versus ε_1 curve, divided by ϕ_c, up to the value of ε_1 in question. Figure 6 shows the capability of matching the recorded volume change curve of a triaxial test based on Eq, 10b and the choice of a best fit characteristic friction angle. Note that the circled point in Fig. 6 represents the characteristic friction point (maximum value of compressive volumetric strain, where the tangent slope, $d\varepsilon_v/d\varepsilon_1 = 0$). But the (mobilized) characteristic friction angle varies

somewhat with the mobilized friction angle and the slope ($d\varepsilon_v/d\varepsilon_1$) on the volume change curve. Rearranging Eq. 9,

$$\phi_c = \phi_m / (1 - d\varepsilon_v/d\varepsilon_1) \tag{11}$$

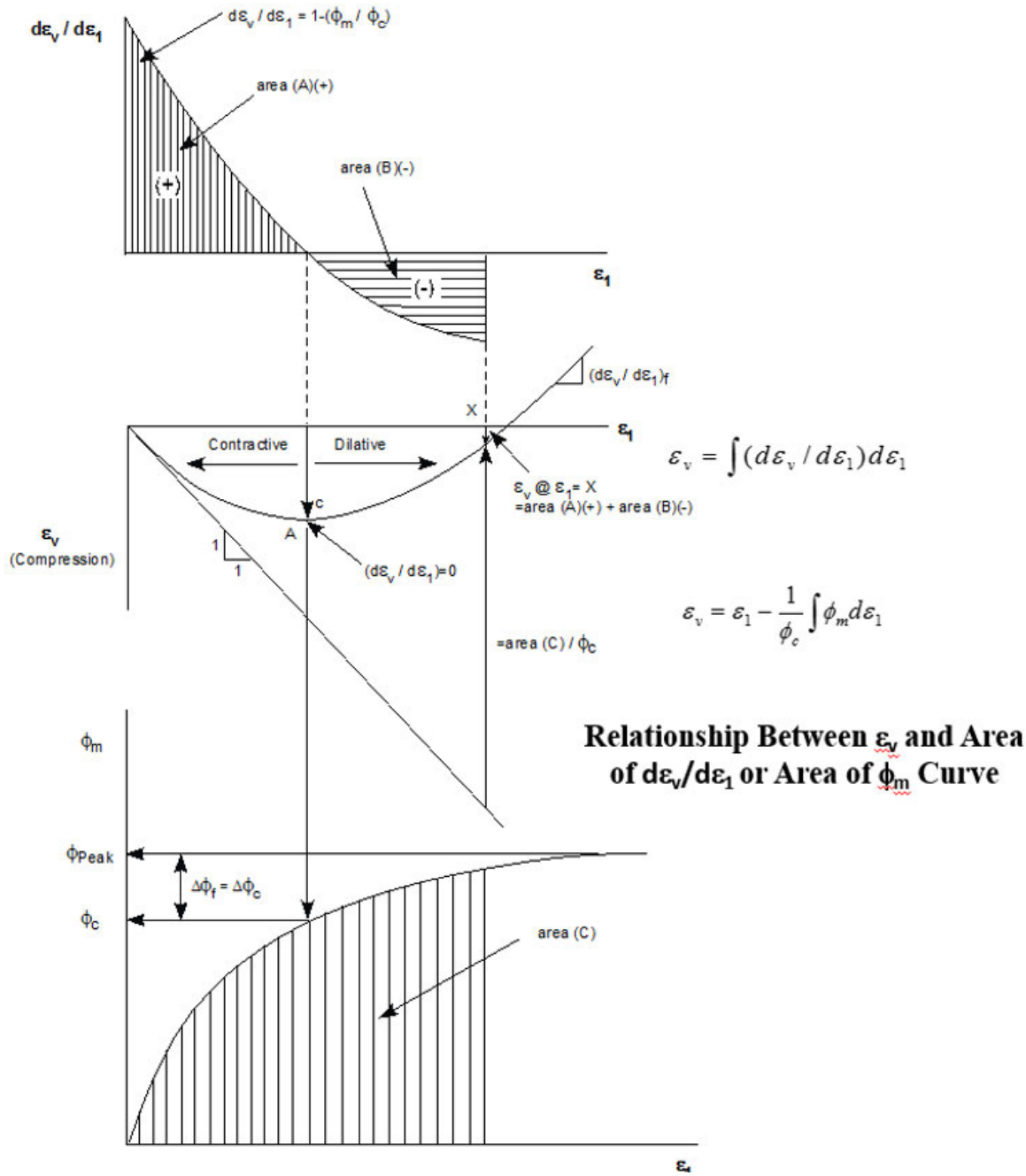

Fig. 5 Relationship Linking Mobilized Friction ϕ_m vs ε_1 and Volumetric Strain, ε_v:

$d\varepsilon_v/d\varepsilon_1 = 1 - \phi_m/\phi_c$

It is noted here that the mobilized value of ϕ_c in Eq. 11 at the characteristic point of Fig. 6 may differ slightly from the best fit value used in Eq. 10b that is needed to achieve the best match of the assessed to the recorded volume change curve.

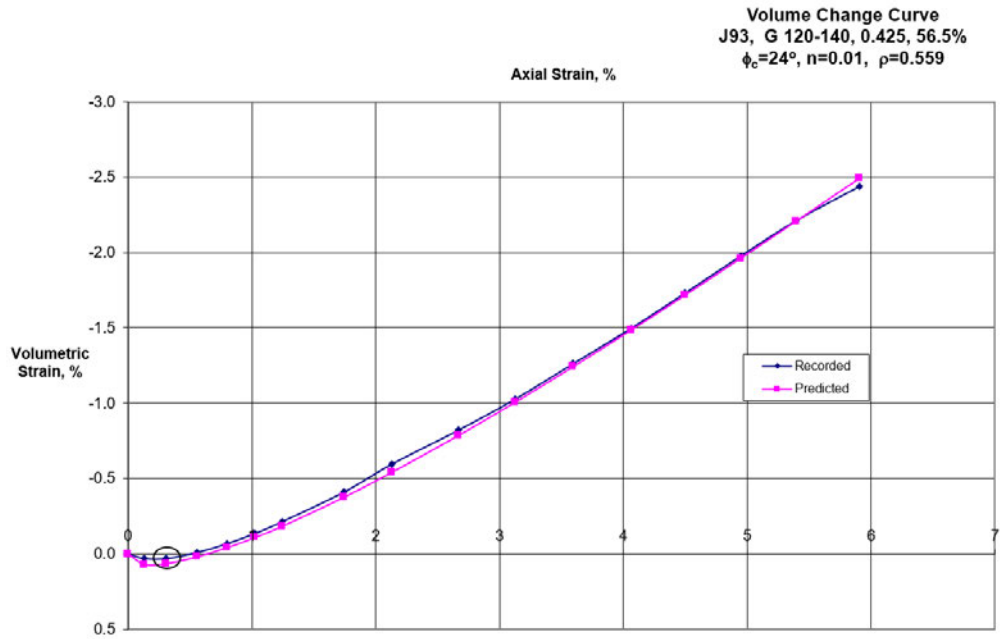

.

Fig. 6 Volume Change Curve of Test 93

As far as the availability of a correlation that might yield a value of ϕ_c, it is from the same study that produced Fig. 4, but extended, that the variation in characteristic friction angle with relative density, Dr, and roundness, ρ, is found to be

$$\phi_c = (0.0005\ Dr^2 - 0.1471\ Dr + 29\ 315)\ \rho^{-0.196} \qquad (12)$$

with ϕ_c in degrees for Dr in %. Figure 7 was generated using Eq. 12. Unlike the peak secant friction angle (ϕ) of Eqs. 8a and 8b, ϕ_c is independent of confining pressure and surface roughness.

The reader should note that while ϕ increases with Dr in Fig. 4, ϕ_c decreases with Dr in Fig. 7. For a given roundness value, ρ, at some value of Dr, ϕ and ϕ_c will become equal and that common friction angle will also be the constant volume/critical state friction angle for confining pressure 0.425 kgf/cm^2. While Fig. 4 will change for confining pressures 1.20 and 3.40 kgf/cm^2, Fig. 7 will not. Their meeting can be established from Eqs. 8a and 8b and Eq. 12 with Eq. 8a modified for the confining pressure of interest.

With the establishment of the characteristic friction angle, evaluation of the volume change curve (via numerical integration of Eq. 10 b) can be achieved. Separate from that, the secant friction angle can also be used to obtain tangent and secant Poisson's ratio relationships, as explained next.

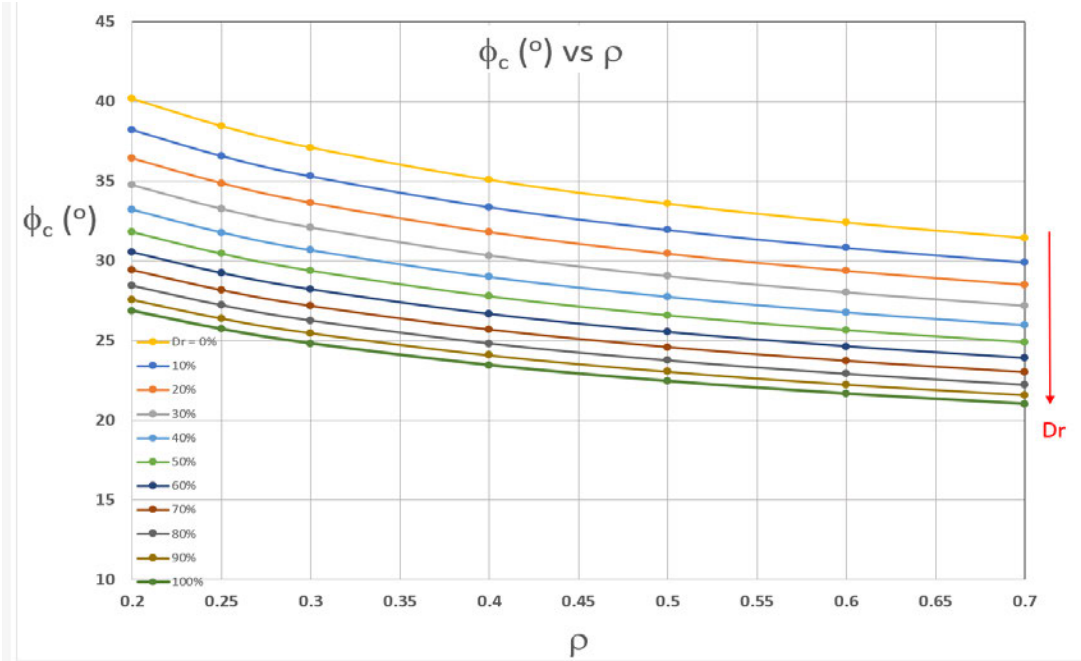

Fig. 7 Variation of the Characteristic Friction Angle, ϕ_c, with Shape (Roundness, ρ) and Relative Density, Dr

THE SECANT AND TANGENT POISSON'S RATIOS

In the triaxial test, the relationship between incremental volumetric ($d\varepsilon_v$), axial ($d\varepsilon_1$) and lateral ($d\varepsilon_3$) strains is

$$d\varepsilon_v = d\varepsilon_1 + 2\, d\varepsilon_3 \tag{13a}$$

whereby $$-\, d\varepsilon_3 = ½\, (d\varepsilon_1 - d\varepsilon_v) \tag{13b}$$

and $$-\, d\varepsilon_3 / d\varepsilon_1 = ½\, (1 - d\varepsilon_v / d\varepsilon_1) \tag{13c}$$

From Eq. 9, $$d\varepsilon_v/d\varepsilon_1 = 1 - \phi_m / \phi_c \tag{9a}$$

such that $$\phi_m / \phi_c = 1 - d\varepsilon_v/d\varepsilon_1 \tag{9b}$$

Given the equality of $(1 - d\varepsilon_v/d\varepsilon_1)$ on the right-hand side of Eqs. 9 and 13c,

$$-\, d\varepsilon_3 / d\varepsilon_1 = ½\, \phi_m / \phi_c \tag{14a}$$

or $$\nu_{tan} = -\, d\varepsilon_3 / d\varepsilon_1 = ½\, \phi_m / \phi_c \tag{14b}$$

Likewise, $$\nu_{sec} = -\, \varepsilon_3 / \varepsilon_1 = ½\, (\varepsilon_1 - \varepsilon_v) / \varepsilon_1 \tag{15a}$$

$$\nu_{sec} = ½\, (1 - \varepsilon_v / \varepsilon_1) \tag{15b}$$

$$\nu_{sec} = ½ (1 - \varepsilon_v / \varepsilon_1) = ½ \{1 – [(\varepsilon_1 – \int \phi_m \, d\varepsilon_1) / \phi_c)] / \varepsilon_1]\} \quad (15c)$$

$$\nu_{sec} = (½ / \phi_c) \int \phi_m \, d\varepsilon_1) / \varepsilon_1 = (½ / \phi_c) \, \phi_{m,area} / \varepsilon_1 \quad (15d)$$

where $\phi_{m,area}$ is the area under the ϕ_m versus ε_1 curve (area C in Fig. 5) up to the ε_1 in question.

For undrained loading of saturated clay where $d\varepsilon_v$ and ε_v are zero (no volume change), both ν_{tan} and ν_{sec} are one-half.

THE SHEAR MODULUS AND SHEAR MODULUS RATIO OF COHESIONLESS SOIL

With ν_{sec} from Eq. 15d for cohesionless (ϕ) soils, and γ of Eq. 6, γ as a function of ν_{sec} can then be evaluated. This makes the evaluation of G (Eq. 5a) and G_o (Eq. 5b), as well as G/G_o, possible, for whichever case of loading, A or B in Fig. 8 is envisioned. Note that case B represents simple shear loading as evaluated from triaxial test response.

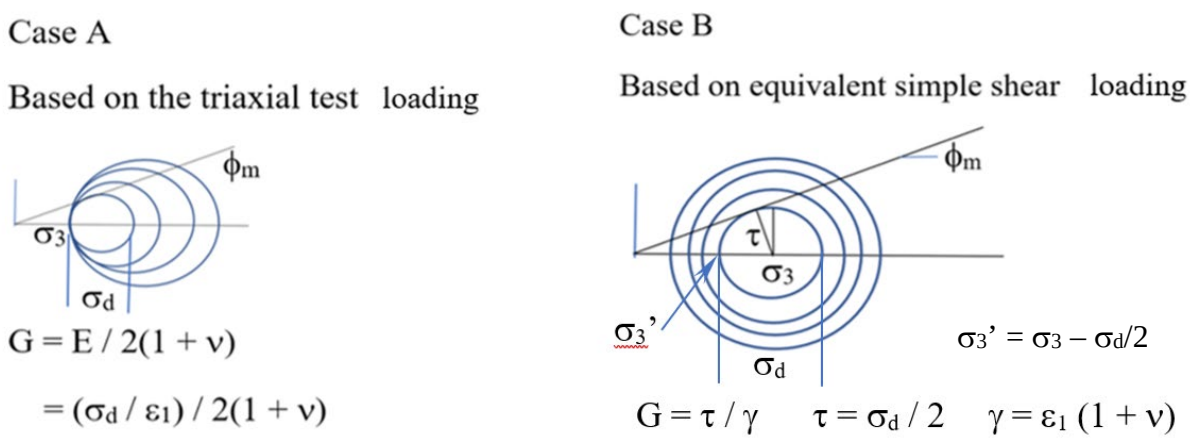

Fig. 8 Evaluation of Shear Modulus, G, for Triaxial or Simple Shear Loading

Case A type loading was used to simulate the Seed and Idriss (1970) and Vucetic Dobry (1991) G/Go curves of the Norris (2024) and the Norris and Yang (2025) papers.

For undrained loading of saturated clay, where there is no volume change, S_u (=½ σ_{df}) and the stress-strain responses are independent of confining pressure, such that σ_3' in case B yields the same result for G as σ_3 in case A.

ARRANGEMENT OF THE ORDER OF COMPUTATIONS IN A SPREADSHEET

Consider first, the arrangement of columns of a spreadsheet and the equations to use for the case of undrained loading of saturated clay, a S_u strength soil. It is a much easier solution than for the cohesionless ϕ soil (or a c-ϕ soil with displaced origin, as an equivalent ϕ soil) that will follow. Figure 9 shows the setup for the S_u soil solution. Given S_u in column C, σ_{df}, ε_{50}, E_{50}, E_i and Go

(for ν = 0.5) shown in column D are then assessed sequentially based on the equations given next to these parameters in column E, with their values appearing in column F. For a S_u = 1000 lbs/ft^2

	A	B	C	D	E	F	G	H	I	J	K
1						Coef	3.707				
2						x	1.00				
3		S_u (psf)	500	σ_{df}	= 2 S_u	1000	psf	S_u			
4			.	ε_{50}	A or B	0.014116		< 850 psf	ε_{50} = 4.4838 $S_u^{-0.927}$		0.014116
5				E_{50}	= S_u / ε_{50}	35422	psf	>850 psf	ε_{50} = **0.1788** $S_u^{-0.446}$		0.011185
6				E_i	= 6.38 E_{50}	225990	psf				
7				ν	= 0.5	2(1 + ν) =	3				
8				G_o	=E_i / 2(1+ν)	75330	psf				
9											
10		Eqs	1c & 1d	1a	SL σ_{df}	σ_d / ε_1	E/E_i	6	5a	= E/E_i	
11		SL	λ	ε_1	σ_d	E	E/E_i	γ	G	G/G_o	
12		0.00035	3.19	1.55E-06	0.35	225697.2	0.998703	2.32613E-06	75232.4	0.998703	
13		0.001	3.19	4.44E-06	1	225154	0.9963	6.66211E-06	75051.34	0.9963	
14		0.002	3.19	8.92E-06	2	224320.9	0.992613	1.33737E-05	74773.64	0.992613	
15		0.005	3.19	2.25E-05	5	221840.1	0.981636	3.38081E-05	73946.69	0.981636	
16		0.01	3.19	4.59E-05	10	217766.1	0.963609	6.88812E-05	72588.71	0.963609	
17		0.02	3.19	9.53E-05	20	209841.3	0.928542	0.000142965	69947.11	0.928542	
18		0.03	3.19	0.000148	30	202204.9	0.894751	0.000222546	67401.65	0.894751	
19		0.04	3.19	0.000205	40	194846.4	0.86219	0.000307935	64948.81	0.86219	
20		0.05	3.19	0.000266	50	187755.7	0.830813	0.000399455	62585.24	0.830813	
21		0.06	3.19	0.000332	60	180923	0.800579	0.000497449	60307.68	0.800579	
22		0.07	3.19	0.000402	70	174339	0.771445	0.000602275	58113	0.771445	
23		0.08	3.19	0.000476	80	167994.6	0.743371	0.000714309	55998.19	0.743371	

Fig. 9 Spreadsheet for a S_u Strength Soil

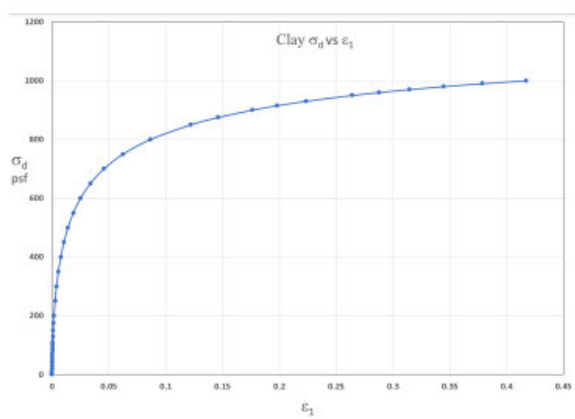

Fig. 10a Clay's Stress-Strain Curve

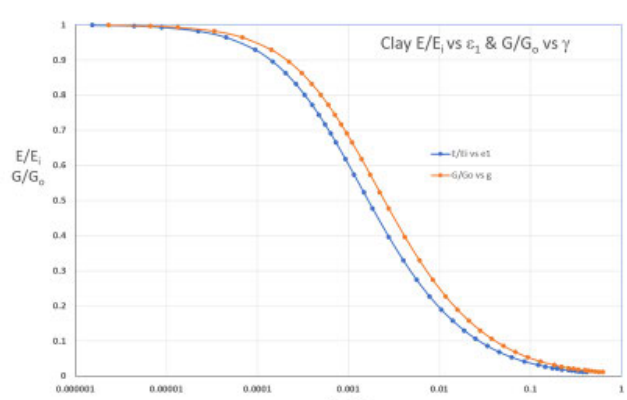

Fig. 10b Clay's Young's and Shear Modulus Reduction Curves

and values of SL that the user specifies in column B, successive computations of λ, ε_1, σ_d, E, E/E_i, γ, G and G/G_o in columns below Row 11 follow, based on the equations or operations indicated in Row 10. Note that for $\nu = 0.5$, G/G_o and E/E_i values are identical though they are plotted versus different strains, ε_1 and γ. Figure 10 shows the stress-strain curve and the modulus reduction curves established from the clay spreadsheet of Fig. 9.

The separate spreadsheets for a ϕ soil for cases A and B loading are shown in Figs. 11 and 12. Figure 11 is the spreadsheet for case A based on the given values of σ_3, ϕ, ϕ_c and ε_{50} in column C. From that A, σ_{df}, E_{50}, E_i and G_o are calculated based on the formulas shown in column E yielding values shown in column G. As with the spreadsheet of Fig. 9, a column of specified SL values leads to successive computations based on the equations in row 10 above the line of headings of row 11.

	A	B	C	D	E	F	G	H	I	J	K	L	M	N	O
1															
2		σ_3 (kgf/cm^2)	1												
3		ϕ (deg)	36	A	$= 2\sin\phi/(1-\sin\phi)$		2.85								
4				σ_{df}	$= \sigma_3$ A		2.85								
5		ε_{50}	0.005	E_{50}	$= 1/2\sigma_{df}/\varepsilon_{50}$		285								
6				E_i	$= 6.38\ E_{50}$		1819								
7		ϕ_c (deg)	28	G_o	$= E_i/2(1+\nu_i)$	$\nu_i = 0$	909.7								
8															
9							Numerical						Case A		
10		Eqs	1c & 1d	1a	reversed 1b	3a	Integration	10b	9a	10a	15d	4a	5a		6
11		SL	λ	ε_1	σ_d (kgf/cm2)	ϕ_m	$\int\phi_m d\varepsilon_1$	ε_v	$d\varepsilon_v/d\varepsilon_1$	ε_v	ν_{sec}	E (kgf/cm^2)	G (kgf/cm^2)	G/G_o	γ
33		0.35	3.19	0.002008	0.998144	19.44614	0.027905	0.001011	0.305495	0.001011	0.248185	497	199	0.21890	0.002506
34		0.4	3.19	0.002762	1.140736	21.29725	0.043268	0.001217	0.239384	0.001217	0.279747	413	161	0.17738	0.003535
35		0.45	3.19	0.00374	1.283328	23.00814	0.064933	0.001421	0.178281	0.001421	0.310038	343	131	0.14396	0.004899
36		0.5	3.19	0.005002	1.42592	24.59587	0.094965	0.00161	0.121576	0.00161	0.339049	285	106	0.11701	0.006697
37		0.55	3.168485	0.006667	1.568512	26.07468	0.137162	0.001769	0.068761	0.001769	0.367369	235	86	0.09456	0.009116
38		0.6	3.111936	0.008914	1.711104	27.45661	0.197286	0.001868	0.019407	0.001868	0.395239	192	69	0.07562	0.012436
39		0.65	3.019777	0.011977	1.853696	28.75189	0.283394	0.001856	-0.026853	0.001856	0.422514	155	54	0.05980	0.017038
40		0.7	2.892009	0.016211	1.996288	29.96928	0.407706	0.00165	-0.070331	0.00165	0.449096	123	42	0.04670	0.023492
41		0.75	2.728631	0.022158	2.13888	31.11634	0.589338	0.00111	-0.111298	0.00111	0.474944	96.5	32.7	0.03597	0.032682
42		0.8	2.529644	0.030686	2.281472	32.19964	0.859321	-3.76E-06	-0.149987	-3.76E-06	0.500061	74.3	24.8	0.02724	0.046031
43		0.85	2.295047	0.043255	2.424064	33.22491	1.270476	-0.002119	-0.186604	-0.002119	0.524495	56.0	18.4	0.02020	0.065942
44		0.9	2.024841	0.062482	2.566656	34.19719	1.918651	-0.006041	-0.221328	-0.006041	0.54834	41.1	13.3	0.01458	0.096744
45		0.925	1.876384	0.076028	2.637952	34.66486	2.385045	-0.009152	-0.238031	-0.009152	0.560188	34.7	11.1	0.01222	0.118618
46		0.95	1.719025	0.093507	2.709248	35.12091	2.994932	-0.013455	-0.254318	-0.013455	0.571945	29.0	9.2	0.01013	0.146988
47		0.975	1.552764	0.11656	2.780544	35.5658	3.80971	-0.019501	-0.270207	-0.019501	0.583651	23.9	7.5	0.00828	0.184591
48		1	1.3776	0.147835	2.85184	36	4.928801	-0.028194	-0.285714	-0.028194	0.595356	19.3	6.0	0.00665	0.235849

Fig. 11 Spreadsheet for Case A of a ϕ Soil

The equations employed in successive columns of the spreadsheet of Fig. 12 for a given column of σ_{dx} values are as follows:

$$\sigma_3' = \sigma_3 - \tau = \sigma_3 - \sigma_{dx}/2 \tag{16a}$$

$$\phi_m = \sin^{-1}[(\sigma_{dx}/2)/\sigma_3] \tag{16b}$$

$$\sigma_{df} = \sigma_3' A \tag{16c}$$

$$SL = 2 / A(1/ \sin \phi_m - 1) \tag{16d}$$

$$\sigma_d = SL\ \sigma_{df} \tag{16e}$$

$$\varepsilon_{50} = \varepsilon_{50\ ref} (\sigma_3' / \sigma_{3\ ref}')^{0.2} \tag{16f}$$

$$\varepsilon_1 = SL\ e^{3.707\ SL}\ \varepsilon_{50} / \lambda \quad \text{for } SL \leq 0.5 \tag{16g}$$

$$\varepsilon_1 = SL\ e^{Coef\ SL} \times \varepsilon_{50} / \lambda \quad \text{for } SL > 0.5 \tag{16h}$$

$$E = \sigma_d / \varepsilon_1 \tag{16i}$$

$$\nu_{sec} = (½ / \phi_c) \int \phi_m\, d\varepsilon_1 / \varepsilon_1 \tag{16j}$$

$$\gamma = \varepsilon_1 (1 + \nu_{sec}) \tag{16k}$$

$$G = \tau/\gamma \qquad \text{or} \qquad = E / 2(1 + \nu_{sec}) \tag{16l}$$

	A	B	C	D	E	F	G	H	I	J	K	L	M	N	O	P	Q
1																	
2	σ_3 (kgf/cm^2)	1.20	2458	psf													
3	ϕ (deg)	36	A	= 2sinϕ/(1-sinϕ)		2.85	Corf	2.00	For SL > 0.5								
4			σ_{df}	= σ_3 A		3.42	x	2.35									
5	$\varepsilon_{50,0.425}$	0.00408	ε_{50}	=$\varepsilon_{50,0.425}(\sigma_3/0.425)^{0.2}$		0.005021											
6			E_{50}	= 1/2$\sigma_{df}/\varepsilon_{50}$		341											
7	ϕ_c (deg)	28	E_i	= 6.38 E_{50}	ν_i = 0	2174											
8			G_o	= E_i/2(1+ν_i)		1087.0											
9																	
10						SL σ_{df}											E/2(1+v)
11	σ_{dx} (kgf/cm2)	σ_3'(kgf/cm^2)	ϕ_{mB}	σ_{df}	SL_B	σ_d	τ	λ	ε_{50}	ε_1	E (kgf/cm^2)	$\int\phi_m d\varepsilon_1$	ε_v	ν_{sec}	γ	G (kgf/cm^2)	G/G_o
12	0.0027378	1.20	0.065359	3.418304	0.000801	0.002738	0.001369	3.19	0.00502	1.26E-06	2165.671	4.13E-08	1.26E-06	0.000584	1.26E-06	1082	0.995588
13	0.0034222	1.20	0.081699	3.417328	0.001001	0.003422	0.001711	3.19	0.00502	1.58E-06	2163.568	6.47E-08	1.58E-06	0.00073	1.58E-06	1081	0.994475
14	0.0068444	1.20	0.163399	3.412448	0.002006	0.006844	0.003422	3.19	0.005018	3.18E-06	2153.065	2.6E-07	3.17E-06	0.001463	3.18E-06	1075	0.988924
15	0.017111	1.19	0.408499	3.397809	0.005036	0.017111	0.008556	3.19	0.005014	8.06E-06	2121.705	1.66E-06	8.01E-06	0.00367	8.09E-06	1057	0.972377
16	0.0342221	1.18	0.81702	3.37341	0.010145	0.034222	0.017111	3.19	0.005007	1.65E-05	2069.934	6.85E-06	1.63E-05	0.007395	1.67E-05	1027	0.945142
17	0.0684442	1.17	1.634206	3.324612	0.020587	0.068444	0.034222	3.19	0.004992	3.48E-05	1968.259	2.92E-05	3.37E-05	0.014996	3.53E-05	970	0.891987
18	0.1026662	1.15	2.451724	3.275814	0.031341	0.102666	0.051333	3.19	0.004978	5.49E-05	1869.1	7.04E-05	5.24E-05	0.02288	5.62E-05	914	0.840521
19	0.1368883	1.13	3.269742	3.227016	0.042419	0.136888	0.068444	3.19	0.004963	7.72E-05	1772.482	0.000134	7.24E-05	0.031024	7.96E-05	860	0.790776
20	0.1711104	1.11	4.088429	3.178218	0.053838	0.17111	0.085555	3.19	0.004948	0.000102	1678.434	0.000225	9.39E-05	0.039431	0.000106	807	0.742761
21	0.2053325	1.10	4.907952	3.12942	0.065614	0.205332	0.102666	3.19	0.004932	0.000129	1586.979	0.000349	0.000117	0.048103	0.000136	757	0.696478
22	0.2395546	1.08	5.728483	3.080622	0.077762	0.239555	0.119777	3.19	0.004917	0.00016	1498.143	0.000511	0.000142	0.057047	0.000169	709	0.651928
23	0.2737766	1.06	6.550195	3.031824	0.090301	0.273777	0.136888	3.19	0.004901	0.000194	1411.947	0.00072	0.000168	0.066267	0.000207	662	0.609106
24	0.3079987	1.05	7.373262	2.983026	0.10325	0.307999	0.153999	3.19	0.004885	0.000232	1328.413	0.000984	0.000197	0.07577	0.000249	617	0.568008
25	0.3422208	1.03	8.197862	2.934229	0.116631	0.342221	0.17111	3.19	0.004869	0.000274	1247.56	0.001314	0.000227	0.085561	0.000298	575	0.528625
26	0.3764429	1.01	9.024176	2.885431	0.130463	0.376443	0.188221	3.19	0.004853	0.000322	1169.405	0.001724	0.00026	0.095646	0.000353	534	0.490948
27	0.444887	0.98	10.68268	2.787835	0.159582	0.444887	0.222444	3.19	0.00482	0.000436	1021.249	0.002845	0.000334	0.11661	0.000486	457	0.420698
28	0.5133312	0.94	12.3503	2.690239	0.190813	0.513331	0.256666	3.19	0.004785	0.000581	884.0387	0.004515	0.000419	0.138851	0.000661	388	0.357063
29	0.5988864	0.90	14.45006	2.568244	0.233189	0.598886	0.299443	3.19	0.004741	0.000823	727.9882	0.007758	0.000546	0.168395	0.000961	312	0.286599
30	0.6844416	0.86	16.56985	2.446249	0.279792	0.684442	0.342221	3.19	0.004695	0.001162	589.0986	0.013019	0.000697	0.200091	0.001394	245	0.225795
31	0.855552	0.77	20.88418	2.202259	0.388488	0.855552	0.427776	3.19	0.004598	0.002364	361.9839	0.035522	0.001095	0.268382	0.002998	143	0.131274
32	1.0266624	0.69	25.3265	1.95827	0.52427	1.026662	0.513331	3.183708	0.004491	0.004953	207.2871	0.09535	0.001548	0.343777	0.006656	77	0.070955
33	1.1977728	0.60	29.93862	1.71428	0.698703	1.197773	0.598886	2.895773	0.004373	0.010016	119.5805	0.23527	0.001614	0.419435	0.014218	42	0.038751
34	1.266217	0.57	31.84279	1.616684	0.783219	1.266217	0.633108	2.6004	0.004322	0.014633	86.52898	0.377892	0.001137	0.461141	0.021382	30	0.02724
35	1.300439	0.55	32.80964	1.567886	0.829422	1.300439	0.65022	2.39591	0.004296	0.018335	70.92703	0.497546	0.000565	0.484581	0.02722	24	0.021976
36	1.3346611	0.53	33.78712	1.519088	0.878594	1.334661	0.667331	2.144883	0.004268	0.023786	56.1112	0.679059	-0.00047	0.509798	0.035912	19	0.017095
37	1.3688832	0.52	34.77589	1.47029	0.931029	1.368883	0.684442	1.839248	0.004241	0.032432	42.20825	0.975445	-0.00241	0.537088	0.04985	14	0.012631
38	1.3859942	0.51	35.27473	1.445891	0.958574	1.385994	0.692997	1.663004	0.004227	0.038891	35.63782	1.201689	-0.00403	0.551765	0.06035	11	0.010564
39	1.4106848	0.49	36.00001	1.410684	1	1.410685	0.705342	1.377598	0.004206	0.052946	26.64364	1.702583	-0.00786	0.574227	0.08335	8	0.007785

Fig. 12 Spreadsheet for Case B of a ϕ Soil

Note the introduction of a Coef different from 3.707 in Eq. 16h. A lower value than 3.707 applies if a standard triaxial test stress-strain curve is to be simulated, where end restraint at the cap and base of the sample causes deviation from that that of the frictionless cap and base test [Norris (2024) and the Norris and Yang (2025)].

Based on the data appearing in the columns of Figs. 11 and 12, various plots can be generated:

σ_d vs ε_1

ϕ_m vs ε_1

ε_v vs ε_1

ν_{sec} vs ε_1

E and E/E_i vs ε_1

G and G/G_o vs γ

as shown in Figs. 13 – 15.

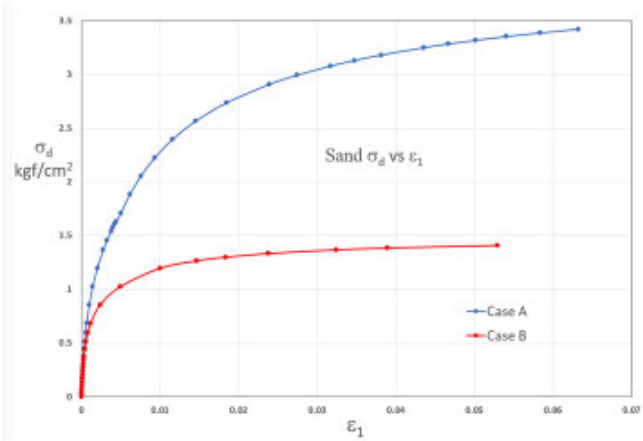

Fig. 13a Sand Stress-Strain Curve

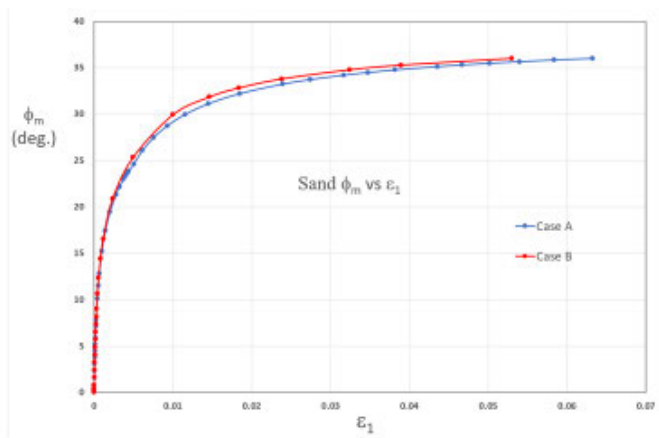

Fig. 13b Sand ϕ_m vs ε_1 Curve

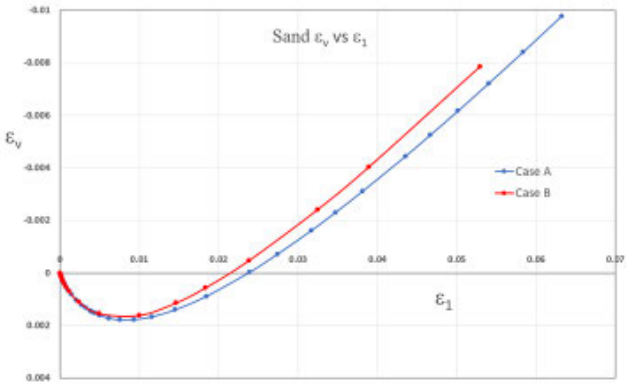

Fig. 14a Sand Volume Change Curve

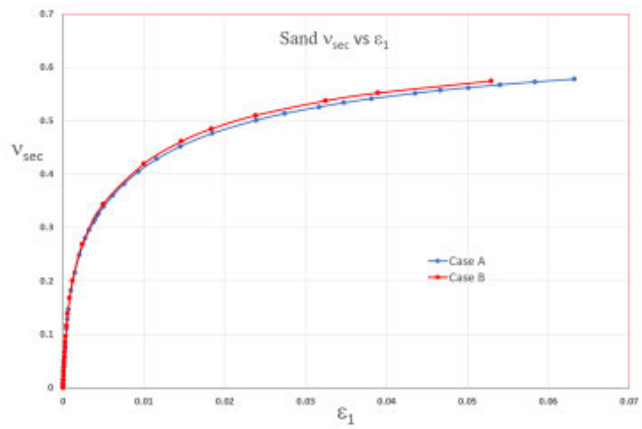

Fig. 14b Sand νsec vs ε_1 Curve

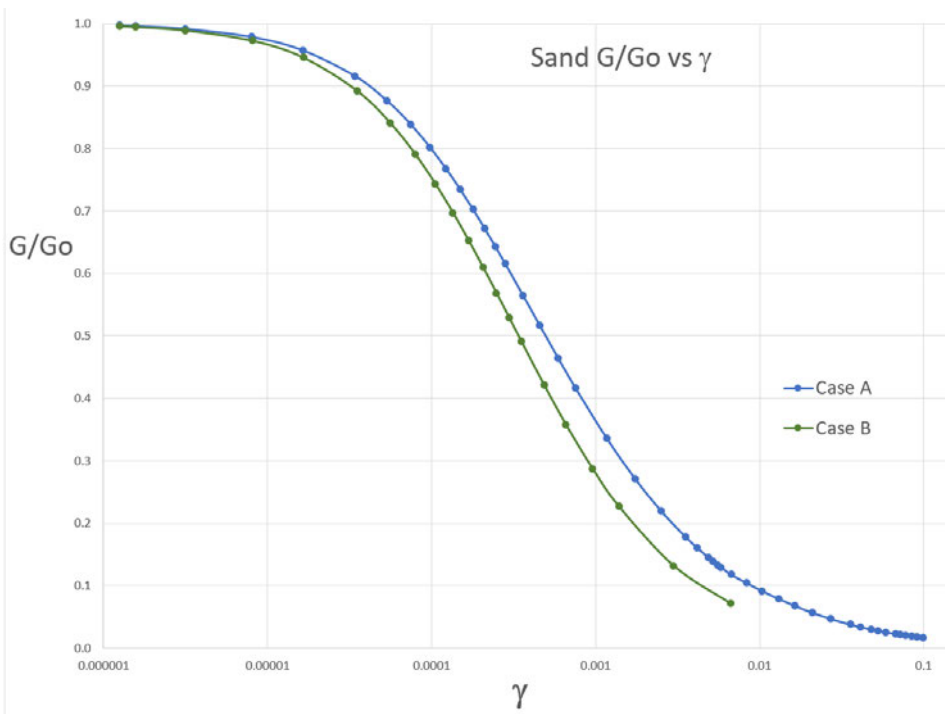

Fig. 15 Shear Modulus Reduction Curves for a ϕ Soil

Not shown are additional columns of parameters that might be added; i.e., the tangent Poisson's ratio, the mobilized characteristic friction angle and the developing angle of dilatancy, ψ as assessed as follows:

ν_{tan} from Eq. 14b

ϕ_c from a rearranged Eq. 9b

and $\tan \psi = -d\varepsilon_v / d\gamma_{max}$ (17a)

where $d\gamma_{max} = (d\varepsilon_1 - d\varepsilon_3) = d\varepsilon_1 + ½ (d\varepsilon_1 - d\varepsilon_v)$ (17b)

which lead to the relationships (Norris 2024):

$$\tan \psi = (2\, \nu_{tan} - 1)/ (\nu_{tan} + 1) \quad (18a)$$

$$\tan \psi = (\phi_m - \phi_c)/ (½\, \phi_m + \phi_c) \quad (18b)$$

Of particular interest with respect to the above is when $\nu_{tan} = ½$, $\psi = 0$ and, in turn, $d\varepsilon_v/d\varepsilon_1 = 0$.

DISCUSSION / CONCLUSIONS

The current presentation has provided the methodology and equations along with certain correlations for input parameters for the development of a wide range of triaxial test responses for both cohesionless (ϕ) and cohesive (S_u) soils. The basic exponential equation (1a or 2) was derived from the study of 144 frictionless cap and base tests representing a wide range in uniform particle size fractions of varying particle shape and surface roughness of quartz sands taken from nature. (See Norris 2019 for details.)

References

Ashour, M., Norris, G. and Pilling, P. (2004*) Lateral Behavior of Pile Groups in Layered Soil*, Journal of Geotechnical and Geoenvironmental Engineering, ASCE, Vol. 130, No. 6, pp. 580–592.

Ashour, M., Norris, G., and Pilling, P. (1998). *Lateral Loading of a Pile in Layered Soil Using the Strain Wedge Model,* Journal of Geotechnical and Geoenvironmental Engineering, ASCE, Vol. 124, No. 4, pp. 303-315.

Duncan, J. and Chang, C. (1970) *Nonlinear Analysis of Stress and Strain in Soils.* Journal of the Soil Mechanics and Foundation Division, ASCE, Vol. 96, No. 5, pp. 1629-1654.

Elfass, S., Norris, G., and Vimalaraj, P. (2007) *A Simple Bearing Capacity Equation.* GeoDenver 2007, ASCE, New Peaks in Geotechnics. In: Advances in Shallow Foundations, GSP, Vol. 171, pp 1–10.

Elsayed, A., Elfass, S., Norris, G. and Vimalaraj P. (2011) *A New Approach for Non-Linear Load-Settlement Assessment of Shallow Foundations*, Geo-Frontiers Congress 2011-Advances in Geotechnical Engineering, Dallas, Texas, March 13-16, 2011.

Ladd, C. and Foott, R. (1974) *New Design Procedure for Stability of Soft Clays*, Journal of Geotechnical and Geoenvironmental Engineering, Vol. 100, No. GT7, pp 763-786.

Nimeri, M., Elfass, S. and Norris, G. (2017) *Load–settlement Response of Shallow Foundations Resting on Granular Soil*, Innovative Infrastructure Solutions, Vol. 2, No. 33.

Norris, G. (2019) *The Characteristic Friction Angle, Its Determination and Use*. Proc. 70th Highway Geology Symposium, Portland, Oregon. Paper 14, 16 pp.

Norris, G. (2024) *Recent Applicable UNR Geotechnical Research*. Proc of 73rd Highway Geology Symposium, Lawrence, Kansas. Paper 14, 30 pp.

Norris, G. (2025). *The Influence of Particle Shape and Surface Roughness on the Friction Angle of Quartz Sands.* Proceedings of 74th Highway Geology Symposium, Morgantown, West Virginia. 22 pp.

Norris, G. and H. Yang. (2025) *A Nonlinear Stress-Strain Relationship for Soil and Rock*. *ICE* Geotechnical Engineering Journal, Vol. 178, Issue 2, pp 247-256.

Seed, H. and Idriss I. (1970) *Soil Moduli and Damping Factors for Dynamic Response Analyses*, Report EERC 70-10, Earthquake Engineering Research Center, University of California, Berkeley.

Vucetic, M. and Dobry, R. (1991) *Effect of Soil Plasticity on Cyclic Response*, Journal of Geotechnical Engineering, Vol. 117, No. 1, pp 89-10.

34. I-80 Mine Subsidence: Geologic Characterization and Emergency Stabilization, Wharton, New Jersey

Christina M. Comuso
New Jersey Department of Transportation
1035 Parkway Ave.
Ewing NJ, 08618
856-357-1141
christina.comuso@dot.nj.gov

Brian T. Felber, P.E.
HNTB Corporation
9 Entin Road, Suite 202
Parsippany, NJ 07054
973-800-5502
bfelber@hntb.com

Matthew D. Riegel, P.E.
HNTB Corporation
9 Entin Road, Suite 202
Parsippany, NJ 07054
973-632-7541
mdriegel@hntb.com

Prepared for the 75th Highway Geology Symposium, September 2026

Acknowledgements

The authors would like to thank the following individuals/entities for their contributions in the work described:

Mohab A. Hussein Ph.D., PE, PMP, DBIA – NJDOT, project team leader, paper review
Amanda McElwain – NJDOT, project team member, paper review
Kimberly Sharp – NJDOT, project team member
NJDOT Operations
Joseph Juzwin, PE – HNTB Corporation, project team member, paper review
John Schuring, Ph.D., PE – HNTB Corporation, project team member, paper review
John Szturo, PG – HNTB Corporation, project team member, paper review
Ray Sandiford, PE – HNTB Corporation, project team member
Jerry DiMaggio, PE – HNTB Corporation, project team member
Jeff Reid, PG – Hager Richter Geoscience
Rob Garfield, PG – Hager Richter Geoscience
Lucian Spiteri, PE – Keller – North America
James Meyers, PE – Keller – North America
Brian LoVerdi – Keller – North America
IEW Construction Group, Inc. – Prime Contractor
Yu and Associates, Inc. – Field Inspection Support
Collier Geophysics, LLC – Geophysical Support
MFS Engineers and Surveyors, DPC – Survey and LiDAR Change Detection
Geo-Instruments, Inc. – SAA and MPBX installation and reporting
Specto Technologies, LLC – Data Collection Hub for Biaxial Tiltmeters
Ameritech Slope Constructors, Inc. – Mesh Procurement and Transport

Disclaimer

Statements and views presented in this paper are strictly those of the author(s), and do not necessarily reflect positions held by their affiliations, the Highway Geology Symposium (HGS), or others acknowledged above. The mention of trade names for commercial products does not imply the approval or endorsement by HGS.

Copyright Notice

Copyright © 2026 Highway Geology Symposium (HGS)

All Rights Reserved. Printed in the United States of America. No part of this publication may be reproduced or copied in any form or by any means – graphic, electronic, or mechanical, including photocopying, taping, or information storage and retrieval systems – without prior written permission of the HGS. This excludes the original author(s).

ABSTRACT

This case history examines the engineering geology and rapid site characterization efforts that guided the emergency response to a series of mine subsidence events beneath Interstate 80 at Mile Marker 34 in Wharton, New Jersey. The affected highway segment was located above the Mt. Pleasant Mine, which was in operation from 1786 to 1896, and experienced three collapses within a 200-foot stretch between December 2024 and March 2025, forcing full closure of both travel directions on one of the most heavily traveled corridors in the United States.

The project required rapid characterization of the mine geometry and assessment of risks to public safety and critical transportation operations. The subsurface evaluation integrated ground penetrating radar, microgravity, multichannel analysis of surface waves, downhole sonar, borehole televiewers, and targeted drilling, along with review of historic mine documents to delineate the mine stope and identify contributing mechanisms.

To reopen the corridor the response team completed the rapid design and construction of a micropile-supported concrete slab system spanning the mine feature. A comprehensive instrumentation program, including Shape Acceleration Arrays, multipoint borehole extensometers, tiltmeters, and seismographs, provided real-time data during construction and continues to support long-term monitoring.

This case history highlights the critical role of engineering geology, geophysics, and rapid site characterization in mitigating geologic hazards that threaten major transportation infrastructure.

Introduction

Interstate 80 (I-80) is a major transportation corridor in northern New Jersey carrying approximately 114,036 vehicles per day through Morris County. The highway traverses the historic Dover Mining District, a region extensively mined for magnetite iron ore from the 18th through early 20th centuries. New Jersey has roughly 588 known abandoned mines, as shown on Figure 1.

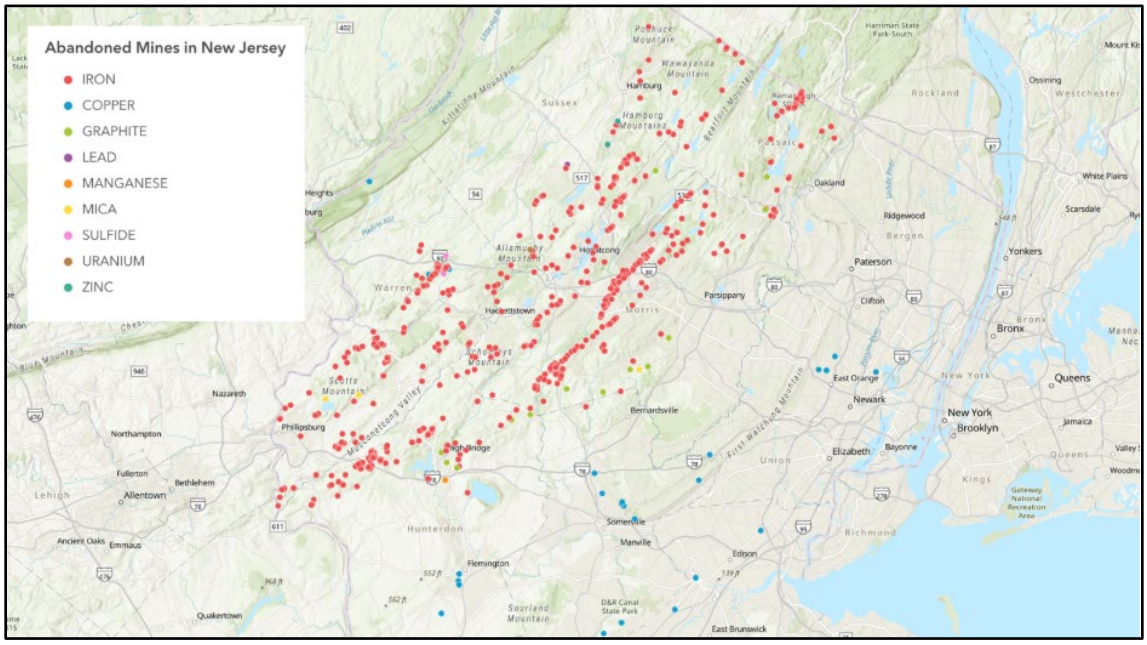

Figure 1 – NJDEP Known Abandoned Mines in New Jersey

Abandoned underground mine workings present long-term geologic hazards where voids, shafts, or partially failed structures can lead to progressive ground instability. This paper documents a sequence of mine subsidence events beneath I-80 and the engineering geology and geotechnical response implemented to restore service and mitigate long-term risks.

Project Location

The project is located at Mile Marker 34 in the Borough of Wharton, Morris County, New Jersey, immediately west of the I-80 bridge over Route 15, as shown on Figure 2. The site lies within the New Jersey Highlands physiographic province and directly overlies the Mt. Pleasant Mine, part of the Dover Mining District. The impacted facility is critical for shipping, commerce, and defense considering I-80 provides access to New York City, Port Newark, and Picatinny Arsenal.

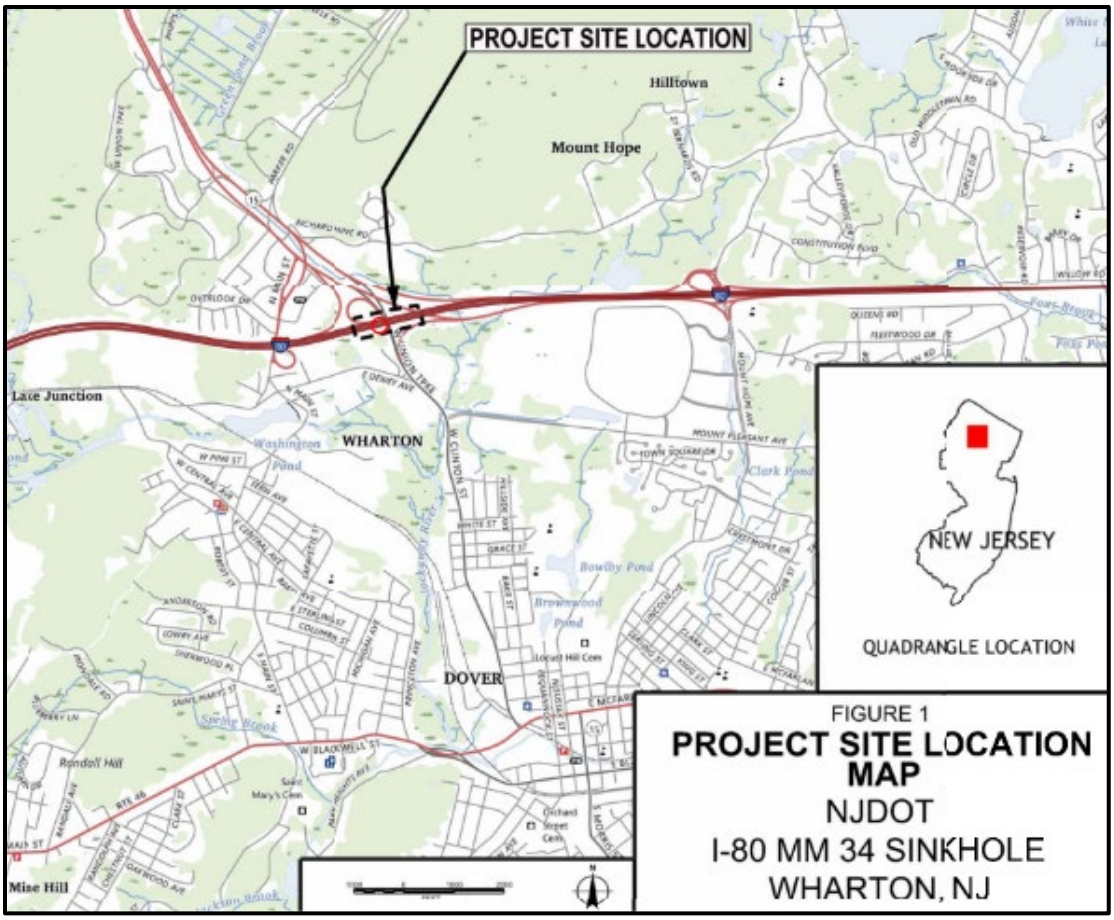

Figure 2 – Project location map showing I-80 at Mile Marker 34

Sequence of Events

Three mine subsidence events developed within a 200-foot segment of I-80 in the span of three months:

- December 26, 2024 – Mine Subsidence Location 1 formed in the eastbound shoulder and lane (~20 ft × 25 ft × 21 ft deep) closing traffic to I-80 EB, with repairs completed and traffic restored in 4 days
- February 10, 2025 – Mine Subsidence Location 2 formed ~70 ft northeast in the center lane (~11ft x11ft x 4 ft deep) closing I-80 EB
- March 19, 2025 – Mine Subsidence Location 3 (~15 ft x 15 ft x 30 ft deep) formed in the median closing I-80 WB, and was filled with concrete
- Traffic was restored in the following phases:
    - May 21, 2025 – I-80 EB right 2 lanes and shoulder
    - May 30, 2025 – I-80 WB right 2 lanes and shoulder
    - June 14, 2025 – I-80 EB all lanes
    - June 21, 2025 – I-80 WB all lanes

Photo of Mine Subsidence Location 1

Photo of Mine Subsidence Location 2

Photo of Mine Subsidence Location 3

Figure 3 – Mine Subsidence Location Photos

Geology

The project area is located within the New Jersey Highlands, a subdivision of the Reading Prong of the New England Physiographic Province. This region is distinguished by discontinuous, rounded ridges separated by deep, narrow valleys, resulting in rugged topography controlled by both bedrock structure and lithologic variability (Ref. 15). The northeast-trending ridges reflect the structural grain of the underlying crystalline metamorphic and igneous rocks, which formed approximately 1 billion years ago during the Mesoproterozoic Grenville Orogeny. Subsequent episodes of fluvial and glacial erosion exposed these rocks in their present form.

The site lies within the terminal moraine of the Wisconsin glacial stage, which spans a width of approximately 2 to 3 miles in this area, see Figure 4 (Ref. 16). Surficial deposits are primarily Late Wisconsinan in age, reflecting the retreat of the ice sheet around 20,000 years before present (Ref. 14). The broader landscape in northern New Jersey records three major glaciations, the Pre-Illinoian, Illinoian, and Late Wisconsinan, listed from oldest to youngest.

Each of these glacial events contributed to the complex distribution of glacial sediments in the northern portion of the state.

Regionally, the site is situated within the historic Dover Mining District, one of the earliest iron-producing regions in the United States. Magnetite has been mined in the district since the early 18th century, occurring within Pre-Cambrian meta-sedimentary rocks, magnetite-bearing units, and intrusive igneous rocks. Bedrock underlying the project site consists primarily of quartz–oligoclase gneiss from the Losee Metamorphic Suite, as shown in Figure 5 (Ref. 12). This medium- to coarse-grained, light greenish-gray gneiss contains variable proportions of hornblende, augite, biotite, and magnetite. Magnetite mineralization occurs as individual grains or aggregates 0.04 to 0.20 inches in diameter, and as veinlets, layers, or massive homogeneous bodies (Ref. 17). These ore deposits are interpreted as high-temperature metasomatic replacement bodies formed during the Early Proterozoic. At larger scales, the magnetite bodies are typically lath-shaped, extending up to 2 miles in length with average thicknesses of 10 to 20 feet, dipping at angles greater than 45° and striking 10° to 40° NE.

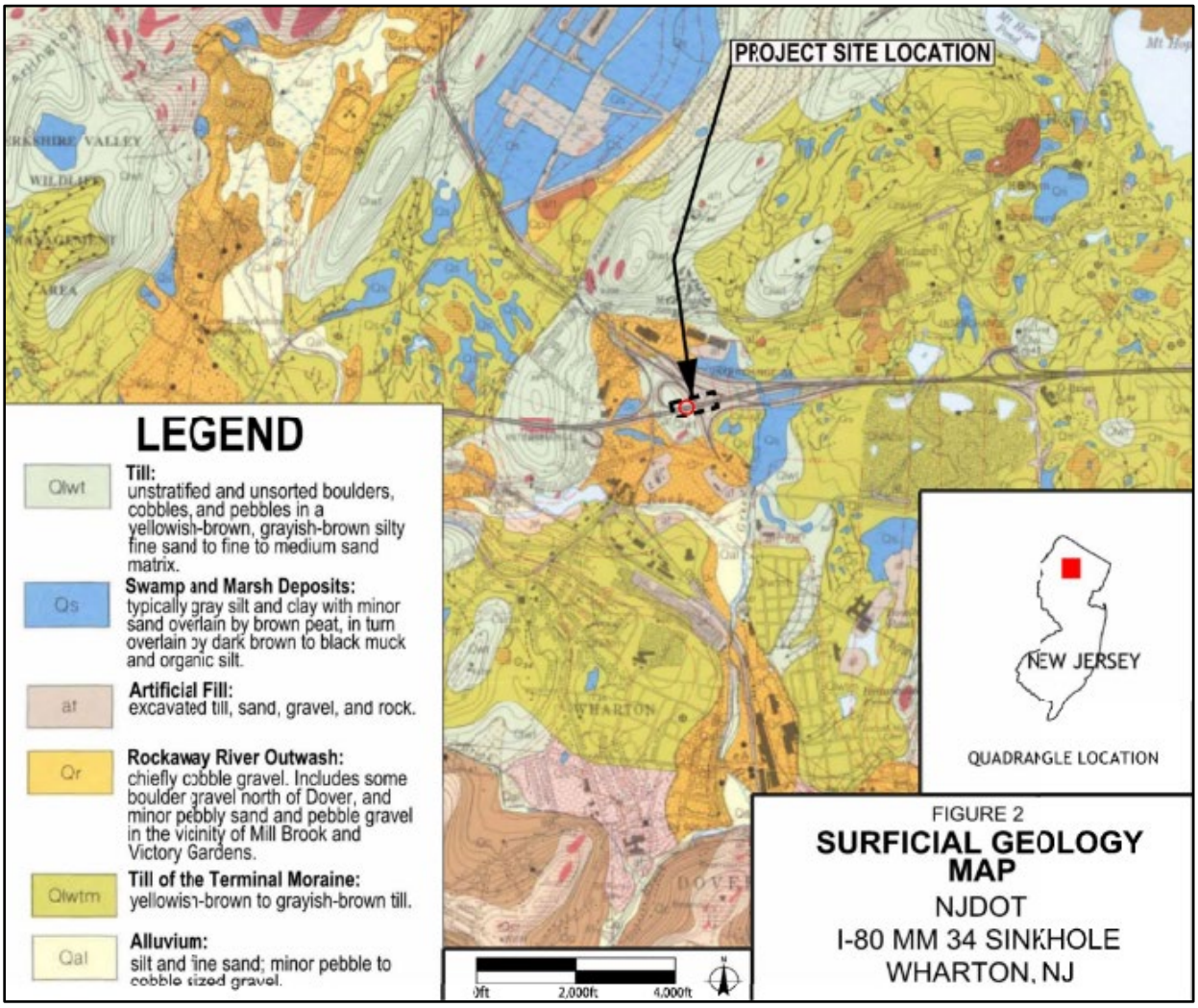

Figure 4 – Surficial Geology

Overlying the bedrock is a dense to very dense layer of glacial till deposited during the advance and retreat of the glacier. The till consists of an unstratified and unsorted mixture of boulders, cobbles, pebbles, and a silty sand matrix. The till material is typically dense to very dense. As the site is located near the glacial terminus, residuum or saprolite (decomposed rock) also occurs at the bedrock/overburden contact at some locations. The saprolite retains a faint rocklike structure, but is friable and noncompact, with the appearance of sand and silt.

Most of the project site is covered by urban fill associated with the construction of Interstate 80 in the late 1950s. The fill material is primarily sand, but may also contain boulders, clay, wood, brick, cinders, ash, and other debris. Within the project limits, fill thickness reaches up to approximately 30 feet near the west abutments of I-80 over Route 15, decreasing westward with increasing bedrock elevation.

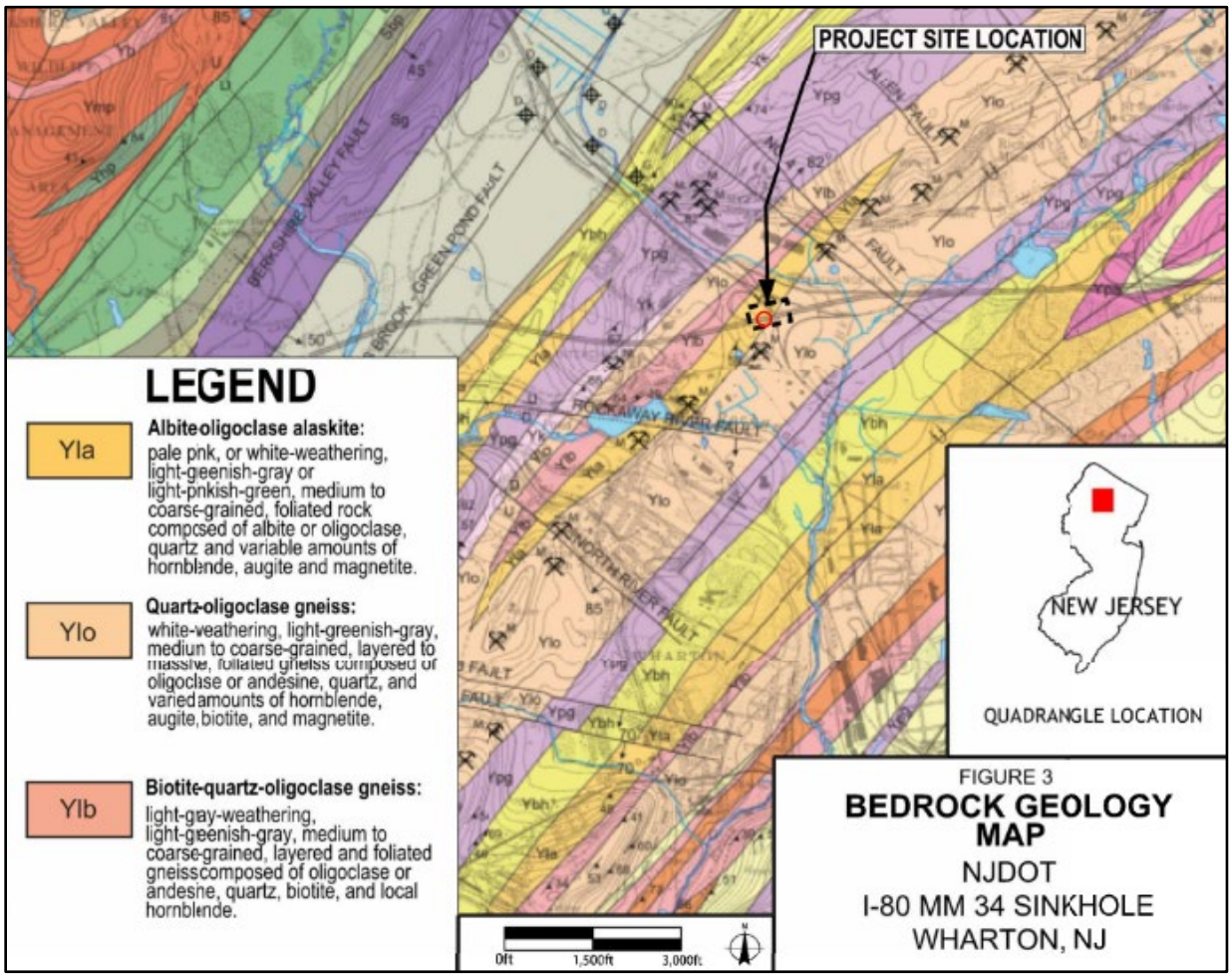

Figure 5 – Bedrock Geology

Mine Characterization

The Mt. Pleasant Mine, opened in 1786 and is one of the earliest and most economically significant iron mines in New Jersey. Operations occurred continuously until its closure in 1896. Over its lifetime, the mine produced an estimated 400,000 tons of magnetite ore (Ref. 18).

Assays performed in 1880 showed a high metallic iron content ranging from 64.9 to 67.0 percent (Ref. 3), underscoring its importance within the Dover Mining District. At the time of its closure, the mine extended approximately 2,300 feet along strike and reached depths of about 700 feet along the dip (roughly 590 feet vertically), although workings beneath the present I-80 corridor occupy a much smaller portion of the overall mine footprint.

Mining at Mt. Pleasant was largely confined to the “Main vein”, which averaged 6 to 8 feet in width, striking approximately N43°E and dipping 57°SE. Ore occurred in steep, narrow shoots within the Losee Gneiss Metamorphic Suite. Several east striking, steep north dipping transverse faults described in early reports (Ref. 3) were confirmed during modern subsurface investigations. The high strength of the surrounding bedrock permitted the use of open stoping and adit stoping mining methods, leaving substantial portions of the rock roof self-supporting. Timber, masonry, and unmined rock pillars supplemented roof stability, some of which were discovered during recent subsurface investigations. Historical illustrations of comparable district mines depict steep, slot like stopes, inclined access shafts, and systematic pillar placement and are shown on Figures 6 and 7. These features are consistent with the interpreted geometry at Mt. Pleasant. The 1883 New Jersey Geological Survey Annual Report also noted abundant offsets and cross faults functioning as natural pillars between ore shoots.

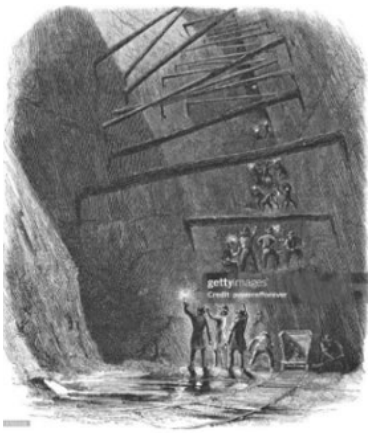

a. Mining in steps up the slot-like stope, Hibernia Mine, Rockaway Township (Getty images)

b. Ore cart riding down an inclined shaft that follows the stope, Hibernia Mine, Rockaway Township (iStock)

c. Ore collection at the base of the stope, Mount Byram mine, Mine Hill (Getty images).

Figure 6: Renderings of Typical Mining Practices in the Dover Mining District

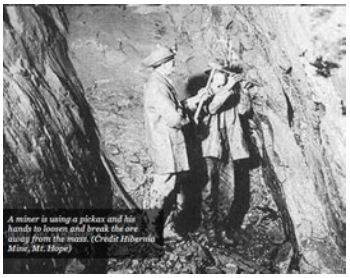

Figure 7: Historic Photos of Typical Mining Practices in the Dover Mining District (Credit Hibernia Mine, Mt. Hope)

Historic documentation of the underground workings is sparse, therefore reconstruction of the mine's geometry relied heavily on historical publications, small scale regional plans, subsurface investigations, and comparison with nearby mines. Little to no updated interior mine maps exist, and the workings are fully inundated below the water table. Records indicate backfilling was not standard practice in the Dover District, so the Mt. Pleasant workings are presumed to remain largely open except for internal pillars, localized collapses, and piles of low-grade ore or waste rock.

As part of this investigation, field reconnaissance was conducted to identify any visible mine openings, closures, topographic irregularities, mining debris or subsidence related features. All observed features were GPS-logged.

This field data was then integrated with the 1958 Sims Map, 1868 and 1888 iron mine maps, LiDAR hill shade imagery, a 1930 aerial photo, and 2013 ground improvement plans for the nearby Avalon development, which is situated on the Bullfrog Mine to the southwest. The parallel trends of the Bullfrog and Mt. Pleasant mines provided additional geometric control.

Using these correlated features, the Mt. Pleasant Mine trace from the Sims Map was georeferenced onto modern imagery, aligning surficial pond geometry and mapped faults. A projection with an accuracy of about ±20 ft, shows Mine Subsidence Locations 1–3 plotting parallel to the mine trend but slightly northwest of it, consistent with the southeast dip of the stope. The 1958 Sims vertical longitudinal projection and plan view are included as Figure 8 and highlight the estimated elevations and plan layout of the mine.

A review of historic I-80 as-built plans revealed a "top rim of old mine hole" within the present eastbound roadway, accompanied by stone foundations and drainage features indicative of historic hoisting and dewatering. Subsequent subsurface investigations encountered a concrete cap within this feature, likely an early attempt to seal the shaft, though recent ground subsidence suggests the cap is no longer effective. Additional records from the New Jersey Department of Labor's mining archive further corroborated the mine's geometry and location.

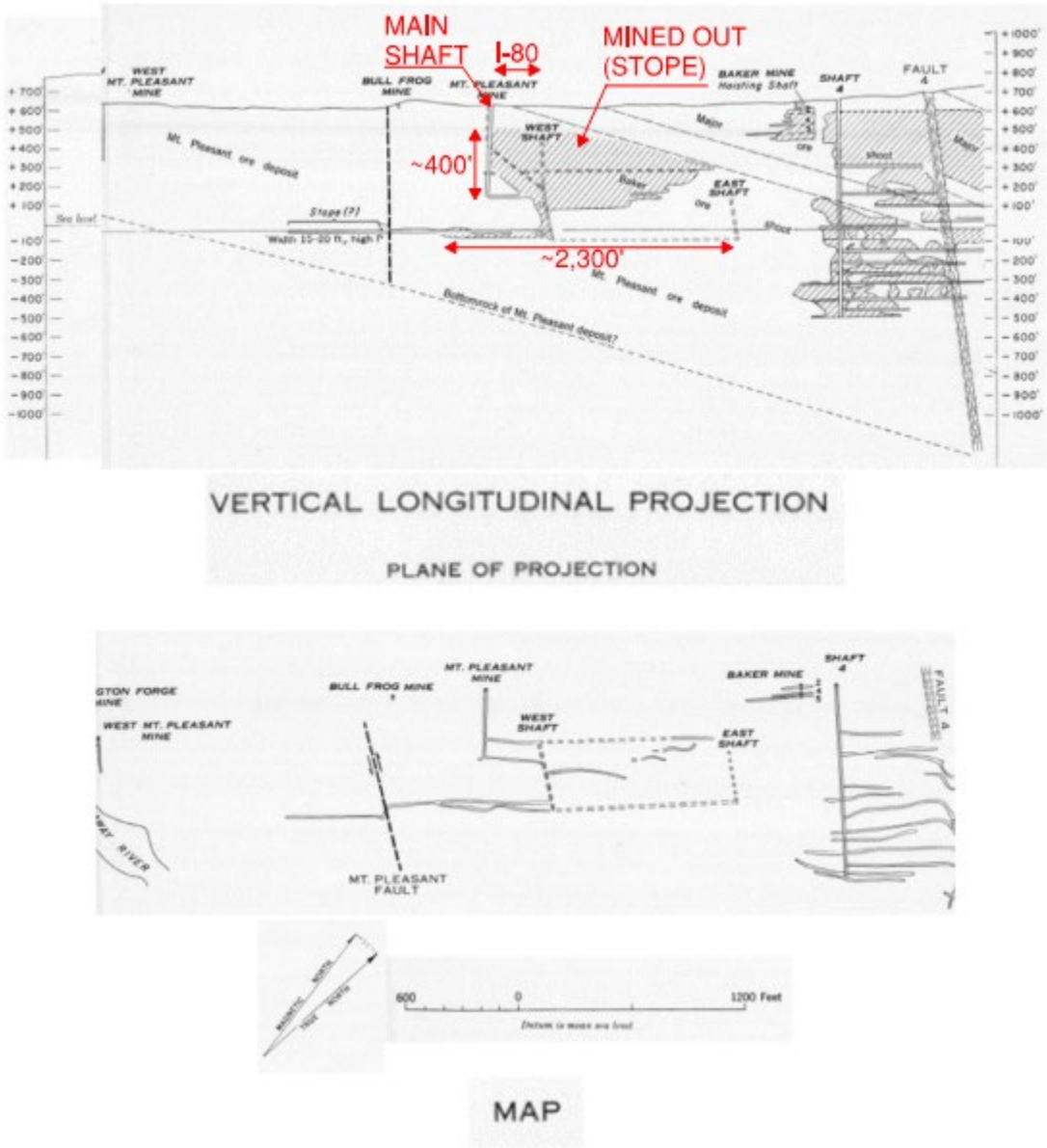

Figure 8: Annotated Projected Elevation of Mt. Pleasant Mine (Ref. 18)

Subsurface Exploration

In December 2024, numerous existing soil borings were available from an NJDOT Interchange Improvements Project in the design phase. Six of these borings were located within or directly adjacent to Mine Subsidence Location 1.

On February 10, 2025, a soil boring drilling contractor mobilized to the site to drill borings in the vicinity of the reported depression located roughly 70 feet northeast of Mine

Subsidence Location 1. During drilling there was loss of drilling fluid and upon drilling to a depth of 16 feet, the driller, helper, and mud-tub suddenly dropped approximately 4 feet, as the pavement failed, and Mine Subsidence Location 2 was exposed to the surface. The boring work was suspended, and a safety exclusion zone was implemented around the open surface void.

Keller - North America of Rockaway, NJ was contracted by IEW, Inc, NJDOT's prime emergency contractor to advance 5.5-inch diameter unsampled probe holes which were logged for penetration rate, spring compression, soil cuttings, water, and driller commentary. The probe holes were used to locate voids and top of rock. The probe holes also served as a compaction grouting mitigation as described herein, and showed instances of voids and underground mine features which would play a significant role in boring location layout development. This work was performed on steel road plates with the drill operator using a remote control for improved site safety. Probe holes were advanced following mine subsidence location 2, to obtain data rapidly in advance of the soil borings.

A subsurface exploration program consisting of 35 borings was performed by HNTB serving as the lead consulting engineer between March and April 2025 by multiple drilling companies. The Standard Penetration Test (SPT) in-situ testing was performed at each boring, in general accordance with ASTM D1586. Rock cores were obtained in general accordance with ASTM D2113. The depth of borings ranged from 16 feet to 172 feet. The objective of the exploration was to locate voids, top of rock, and mine stope alignment and depth.

Due to the occurrence of mine subsidence events in the project area, it was crucial to limit the use of water in the drilling area which necessitated the use of thick bentonite drilling mud to advance casing as far as possible into the soil/rock. The drilling was complicated by cobble and boulder obstructions, and the inclined stope floor, which resulted in several casings and drill rod strings being abandoned in place after bending or shearing. The subsurface exploration also confirmed some natural pillars of magnetite remained within the stope, which is consistent with the literature. A brick pillar or bulkhead was encountered at one location, refer to Figure 9.

Geophysics

Multiple geophysical methods were utilized to help characterize any subsurface anomalies that may be present within the project area. This was done to further investigate the existing voids as well as identify any additional areas that would warrant investigation and ground improvement measures. The geophysical methods used include Ground Penetrating Radar (GPR), Multichannel Analysis of Surface Waves (MASW), Microgravity, Downhole Video and Sonar, and borehole Acoustic and Optical Televiewers (ATV/OTV).

GPR analysis was performed by Hager-Richter Geoscience (HRGS) and Advanced Infrastructure Design (AID). HRGS conducted their survey in February 2025 along all I-80 EB and WB lanes, as well as the median. AID also conducted their survey in February 2025, specifically along all lanes of I-80 Westbound approximately 500 feet before and after the

overpass over Rt. 15. While GPR is limited in its penetration depth for subsurface analysis (about 4 feet), some anomalies were identified by both companies, and they were investigated as part of the HNTB boring program. Anomalies were identified at the 12-inch RCP which traverses below I-80 WB. These shallow anomalies were investigated using pavement core and Dynamic Cone Penetrometers (DCPTs) on February 23, 2025 and then further investigated with soil borings in March 2025, following the development of Mine Subsidence Location 3. Shallow voids were not validated with the DCPT's and soil borings.

HRGS performed microgravity geophysical surveys in 12 feet roadway longitudinal x 10 feet roadway transverse grid patterns typically. The gravimeter measures relative changes in the Earth's gravitational field, to map mass or density changes, which aids in identifying voids. I-80 EB data was collected on February 11, 2025. Median data was not collected due to soft, uneven ground conditions. I-80 WB data was collected on February 21, 2025 by HRGS. The gravimeter is very sensitive to temperature and vibration from traffic or construction which made scheduling and performing this survey challenging.

A reduction in mass was identified at the southeast quadrant of the site, which is likely associated with the fact that rock depth increases to the east and also potentially due to edge effects from the adjacent abutment and Rt 15 SB underpass. Another reduction in mass was evident in the contours near the Mt. Pleasant Mine projection. Unfortunately, the microgravity method does not provide information on depth to rock or depth to voids.

MASW uses surface waves, carried out with a user generated seismic source such as a hammer or weight drop, to map variations in the shear wave velocity of the subsurface materials along the subject area. MASW analysis was conducted by HRGS and Collier Geophysics. HRGS performed MASW lines on February 13, 2025, along the I-80 Eastbound lanes and on February 18, 2025 along lines crossing south to north on each side of the bridge over Route 15. Collier Geophysics performing MASW lines on February 18, 2025, along the I-80 WB lanes. HRGS performed additional MASW passes on the WB roadway on March 23, 2025, following Mine Subsidence Location 3. All data was presented as 2D subsurface cross sections along the lines showing shear wave velocity down to depths of 30-60ft. Areas of concern were outlined by both companies, correlating with voids encountered during the HNTB compaction grouting program and areas of lower mass identified by the Microgravity.

A borehole geophysical logging program consisting of Optical Televiewer (OTV) and Acoustic Televiewer (ATV) logging was performed upon completion of some boreholes. The testing was done for HNTB between March 2025 and April 2025 by HRGS.

The vertical datum used to report the results was the depths measured below the ground surface at the location of each borehole. The depths of bedrock structures are reported as the average depths of the top and bottom intersections of the bedrock structures and the borehole walls. The orientations of bedrock structures (fractures, bedding, foliation, veins, and other

planar geologic features) are reported as the dip azimuth (dip direction) and dip angle (dip) of each structure. The OTV and ATV dip azimuth data is referenced to true north using a magnetic declination of 13° west and the bedrock structure dip angle data are reported from horizontal. The presence of magnetite rendered the dip direction data unreliable, but the dip angles were able to be interpreted by HRGS. The ATV and OTV were helpful for identifying voids and mine features.

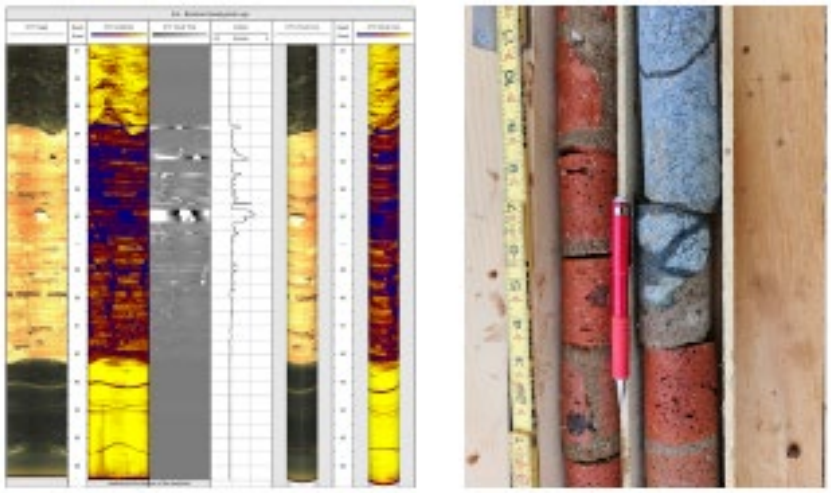

Figure 9 – ATV/OTV Log through Brick Pillar and Core

Colog, Inc. of Golden, Colorado performed downhole video to identify voids and sonar to determine the approximate size and shape of water filled void mine features. Other methods such as electrical resistivity were not performed or viable due to the presence of magnetite.

Mine Subsidence Location 1 Repair

The initial mine subsidence event was repaired using a reverse / inverted filter comprised of granular fill, geosynthetics, steel mesh, and reinforced concrete, as illustrated in Figure 10 below. This approach allowed for rapid restoration of traffic to I-80 Eastbound within 4 days.

Most materials were readily available from an adjacent quarry or locally; however, the steel mesh required a rapid overnight delivery from North Carolina. Concrete curing time and time for asphalt to cool before subsequent lifts were placed and traffic restored were some schedule critical items. Throughout all ensuing adjacent mine subsidence events, no evidence of displacement to this temporary repair was identified, however, this area was ultimately within the subsequent micropile supported slab mitigation limits. Micogravity geophysical surveys were performed before pavement was placed, in an effort to locate voids in the area surrounding the repair. Monitoring and additional investigation were recommended, with a plan to develop long-term mitigation as part of an interchange improvements project, which was already in design for this site.

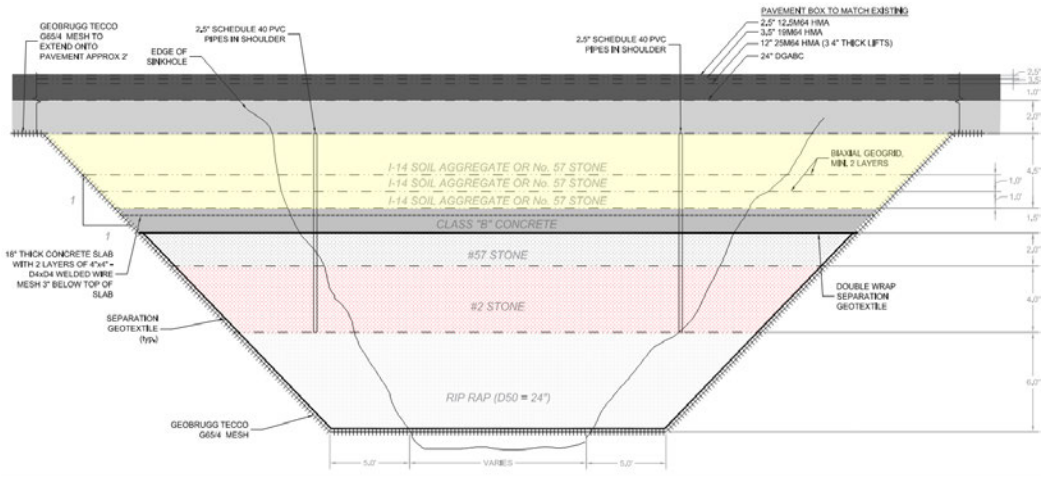

Figure 10: Mine Subsidence Location 1 Repair Detail

Ground Improvement

Compaction grouting was used to densify overburden soils and fill voids for improved site safety. In addition, the compaction grouting provided early insight into the top of rock elevation, void locations based on drilling rod drops and grout takes, mine stope and shaft location, alignment, depth, and inclination. The compaction grouting method implemented consisted of drilling a 5.5 inch OD casing to a depth of approximately 3 feet into top of rock, filling the casing with low mobility grout with a 2 – 4 inch slump and 500 psi 28-day compressive strength. Each initial compaction grouting location followed the spacing of the microgravity survey grid in attempt to correlate ground density and grout volumes. In areas with increased grout volumes supplemental grout holes were added until cutoff criteria were met, refer to Figure 11. The casing was retracted in 2-foot stages and pressure was applied, with each stage terminating when a 100 cf volume, 500 psi pressure, or heave cutoff criteria was achieved.

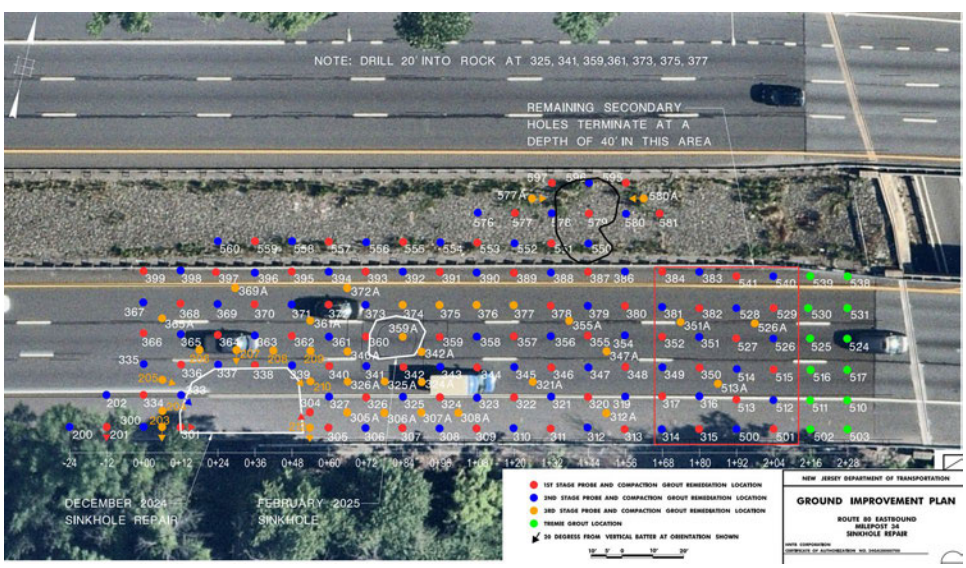

Figure 11 – Compaction grouting plan relative to mine alignment.

Micropile Supported Slab

Following the occurrence of Mine Subsidence Location 3 and the I-80 WB closure, the project team and stakeholders agreed to advance a long-term repair for both the EB and WB roadways, which consisted of a micropile supported slab spanning 30 feet over the mine feature. Micropiles were the preferred foundation element type due to their ability to be advanced through obstructions and into rock, ability to resist large loads, and due to their low vibration production during installation.

The micropiles were designed in accordance with AASHTO LRFD Bridge Design Specifications (Ref. 1) and the NJDOT Bridges and Structures Design Manual (Ref. 10). Supplemental design guidance was obtained from FHWA Micropile Design and Construction Reference Manual (Ref. 8). A 3D Bentley Leapfrog model was developed showing the ground elevation, top of rock elevation, voids, stope, and compaction grout volumes per stage, to aid in establishing micropile supported slab extents.

The slab consists of a single row of micropiles on each side of the mine adit (bench at the top of the stope). The micropile supported slab was flanked on each side by a three row micropile supported mat foundation. A total of 146 micropiles were installed. In the north-south direction the micropile supported slab extended from the south edge of I-80 to the north edge of I-80 and was skewed approximately 38.8 degrees across the roadway to align more closely with the trend of the stope. The micropile and slab layout are shown on Figure 12.

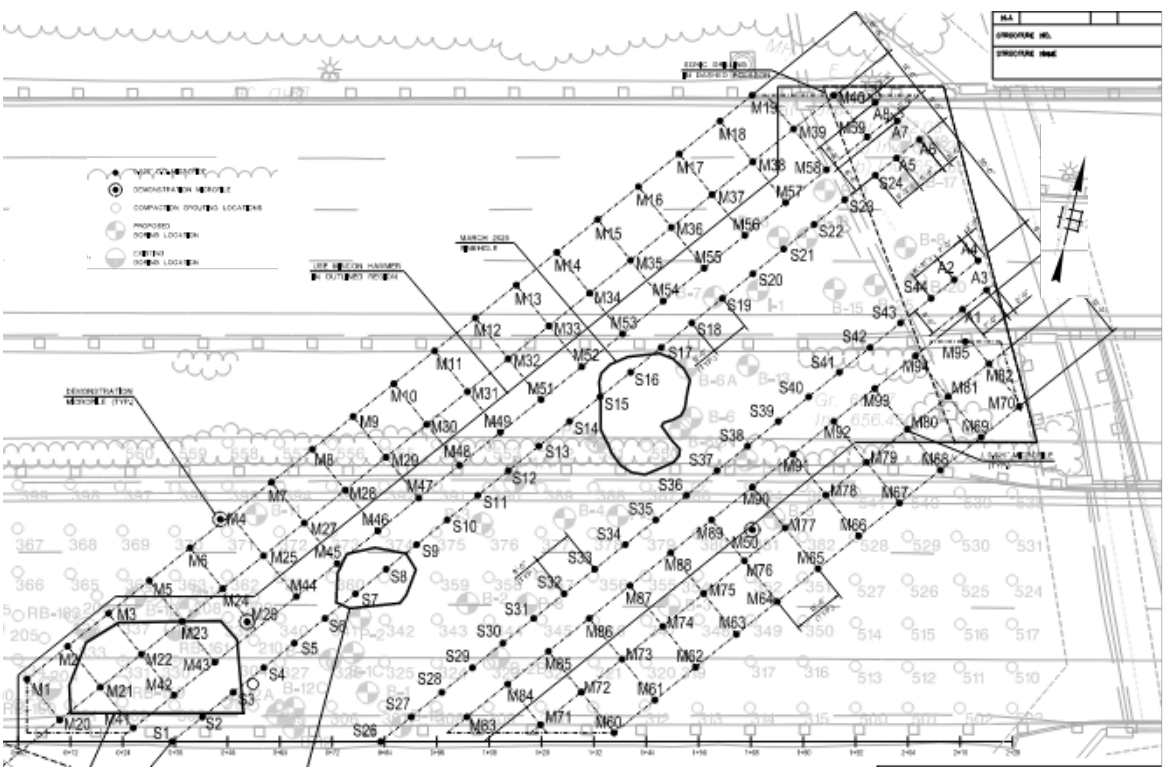

Figure 12 – Micropile Layout

Factored axial compressive strength limit state load combinations per micropile ranged from 43 kips to 425 kips. Negligible axial tensile strength limit state load demands were calculated for a single micropile, A1, with a maximum uplift demand of 47 kips, which did not control the design. The micropiles were grouped into three design sections based on the factored axial compressive demands of 250 kips, 300 kips, and 425 kips.

The micropile design considered a sacrificial steel corrosion loss of 0.002 inches per year for the 75-year service life, or 0.15 inches to the casing's outside surface based on FHWA GEC No. 12 (Ref. 6, Volume I, Page 192), for buried pile foundations. Uncoated (black) reinforcing bars were installed due to material availability, and considering the grout cover provided a single level of corrosion protection.

The micropiles were tremie grouted using Type A construction methods, and bonded in the gneiss bedrock. A presumptive nominal unit grout-to-ground bond of 22 ksf was estimated based on AASHTO LRFD Bridge Design Specifications Table C10.9.3.5.2-1 and used in the design. The factored geotechnical (grout-to-ground) bond resistance for compression and tension was determined with a resistance factor of 0.55 since verification load testing was not performed. Proof load testing was, however, performed on more than 5 percent of piles. End bearing was not included in the axial compressive resistance. Load transfer over a plunge length was not considered with bond lengths ranging from 10 to 20 feet.

The micropiles were designed structurally for axial compression, combined axial compression and flexure, and axial tension. Combined axial compression and flexure calculations assumed the 9.625" OD x 0.545" wall API N80, casing was reduced to half its thickness to account for the threaded connections Combined axial and flexure were evaluated using the Richards & Rothbauer Method and the AASHTO/FHWA Method.

The 28-day compressive strength of the grout was 5 ksi. A single #18 or #24 ASTM A615 Grade 75 threaded bar was installed in each micropile. The micropiles are designed to resist buckling for an unbraced length of up to 20'.

A minimum of 5 percent of micropiles were proof load tested in accordance with ASTM D3689. Axial tension test methods were deemed acceptable given their ease of execution and slightly more conservative results. The tests were performed to verify the nominal unit grout-to-ground bond resistance for the full compression load demand. The proof load tests were performed to 0.7 times the nominal resistance required. Grout cubes and grout specific gravities using a mud balance were also obtained.

Some notable construction related challenges, included:

1. Safe access to the micropile locations due to reoccurring mine subsidence occurrences, which was mitigated with a working platform that used the outer micropiles for temporary support as the micropiles closer to the mine feature were installed

2. Drilling through cobble and boulder obstructions in the fill and till, which was mitigated by use of Mincon, Numa, and Sonic drilling methods
3. Drilling through sloping voids, which resulted in a tendency for the casing to walk and in several instances shear off
4. Minimizing vibration adjacent to the existing bridge founded on spread footings, which was mitigated using Numa and sonic drilling methods.

Monitoring

A long-term instrumentation and monitoring program was implemented to monitor deformations below the micropile supported slab using Shape Acceleration Array (SAA), Multipoint Borehole Extensometers (MPBX), and LiDAR stations. Biaxial tiltmeters and seismographs were installed to monitor existing structures.

Prior to implementing the long-term monitoring, daily LiDAR survey and comparisons of surface measurements to detect change were performed. The primary objective of the LiDAR monitoring was for site safety and to provide advanced detection of any potential subsequent mine subsidence locations. This approach became challenging to interpret as the site construction activities resulted in local changes in ground elevation from excavation, materials on site, and other obstructions affected the LiDAR survey results.

On February 11, 2025, the day after Mine Subsidence Location 2 opened, two biaxial tiltmeters were installed on the west abutments of the I-80 over Rt. 15 structures, with one on the EB bridge and one on the WB bridge. The primary objective of the tiltmeters was to remotely and continuously monitoring changes in rotation at the existing bridge abutments.

During construction three triaxial geophone anchor seismographs were used to measure construction borne vibration, with automated alerts set to trigger for any peak particle velocities which exceed the USBM safe levels of blasting vibration (Ref. 20), which defines tolerable Peak Particle Velocities (PPV) in inches per second (ips) dependent on the vibration frequency in hertz (Hz). The seismographs were initially located with one outside the zone of influence of construction to obtain baseline vibration levels from the I-80 WB traffic, near the south edge of I-80 pavement, and one approximately 50’ south of I-80, but subsequently relocated based on the current work area. It should be noted that the nearest residential structure is more than 200’ from vibration producing construction activities, but the existing I-80 over Rt. 15 bridges fall within the zone of influence. Vibration producing activities primarily included drilling compaction grout holes using Straight 5” Down the Hole Hammers (DTHH) or winged Overburden Drilling Systems (ODS) and drilling micropiles using 8” down the hole hammers, Numa ring system, and sonic drilling methods. Vibration levels typically produced by this type of equipment are PPV of roughly 0.09 ips at 25 feet from the source (Ref. 9).

The SAA was installed in 2.7 inch OD ABS inclinometer casing roughly 0.5 to 1.5 ft below the bottom of slab elevation, at the northeast extent and southwest extent, respectively. The 200ft long alignment of the SAA is approximately centered over the trend of the stope to top of rock intersection. The purpose of the SAA is to monitor deformation immediately below the micropile supported slab to identify the location of future potential soil migration and ground subsidence development. A pully system was constructed such that the SAA can be removed from the inclinometer casing for maintenance or allow for independent readings with a horizontal inclinometer. The SAA is connected to a data logger which has power supply and communicates with the GeoCloud Website. The SAA is an SAAX, intended for horizontal installation applications to monitor vertical settlement, and was manufactured by Measurand and installed by Geo Instruments.

The MPBX were installed in 12 locations, with three or four extensometers per borehole. The MPBX are intended to measure settlement at various depths at various points to obtain more advanced information related to soil migration and sinkhole development. The MPBX were manufactured and installed by Geo Instruments, and have an approximately 4 inch maximum range.

Two LiDAR stations to monitor surficial settlement have been ordered and are anticipated to be installed in the median of Rt. 15 north of I-80 and to the west of the project site at near the Huff mine, which experienced a mine subsidence event in 2008.

Monitoring has indicated stable performance with no significant deformation trends.

Potential Causes and Contributing Factors

Soil raveling into mine voids was identified as the primary mechanism for mine subsidence. Other potential contributing triggering mechanisms may include an April 2024 Magnitude 4.8 Earthquake located less than 40 miles from the I-80 site, a Fall 2024 drought, and a stormwater drainage pipe which was discharging into a swale located at the Mine Subsidence Location 1.

The mine was closed in 1896 and construction of this segment of I-80 was completed in 1958. The top rim of old mine hole was called out on the plans for I-80, but no details were provided for how the abandoned mine was mitigated for the I-80 construction. It was not customary for abandoned mine owners in this region to backfill or cap mines at the time of closure, such that the mine likely remains with a water filled stope.

Some boulders and concrete were identified during the subsurface exploration, at the top of rock elevation at the shaft location, indicating a cap was constructed. Water filled voids were encountered at the location and elevation anticipated for the stope.

Conclusions

The mine subsidence events beneath I-80 MP 34 demonstrate how historic mining districts can significantly affect modern infrastructure and highlight the need for strong coordination between local stakeholders, government agencies, technical experts, and first responders. The rapid characterization of the Mt. Pleasant Mine became essential after three mine subsidence events occurred within a 200-foot stretch between December 2024 and March 2025, causing wide disruptions to traffic and local communities along one of New Jersey's busiest corridors.

The work performed at I-80 MP 34 reinforces the importance of understanding and integrating legacy mining information, geotechnical characterization, and infrastructure planning, to help anticipate potential hazards, shorten response times, and support resilient designs and decision making. Subsurface exploration proved critical for understanding subsurface conditions and delineating depth to top of bedrock. Ground penetrating radar, microgravity, MASW, downhole sonar, borehole televiewers, probe investigative drilling, along with the historic mine records provided clarification on the mine workings, which aided in the rapid design and construction of a micropile supported slab mitigation. Compaction grouting also played an important role by stabilizing loose overburden soils and reducing ongoing soil migration into the mine workings. Introduction of water and air during drilling has the potential to impact sensitive mine features and sites. Sonic drilling was used where the risk of mine subsidence was greater and helped minimize further deterioration of the subsurface conditions during construction. Realtime monitoring using shape acceleration arrays, borehole extensometers, LiDAR, tiltmeters, and seismographs supported safety for construction and long-term risk management throughout the project area.

Key takeaways and lessons learned from the I-80 mine subsidence project include the necessity of interdisciplinary coordination, the value of accessible historic mine documents, the importance of rapid collaboration during emergencies, and the need for ongoing instrumentation to manage residual hazards. Even though there are approximately 588 abandoned mines across New Jersey, the limits of many mine workings remain poorly understood and documentation is often limited, incomplete, or difficult to find. The I-80 project sheds light on the importance for governing agencies to proactively identify, document, and track potential mine hazards in areas where abandoned mines are present and may cause significant impact to the transportation system and local communities. Lastly, this project emphasizes the broader need to eliminate silos and promote sharing of data and expertise across various disciplines. This effort is vital when identifying risks within historic mining districts and for protecting critical infrastructure from potential mine subsidence hazards.

References

1. AASHTO. LRFD Bridge Design Specifications. 10th Ed. 2024.
2. AASHTO. Standard Specifications for Highway Bridges. 17th ed. 2002.
3. Bayley, W.S. Iron Mines and Mining in New Jersey: New Jersey Geological Survey, Final Report Series. 1910
4. Burmister, D.M. Suggested Methods of Test for Identification of Soils. American Society for Testing Materials. 1958.
5. FHWA. Geotechnical Engineering Circular No. 5 – Geotechnical Site Characterization. April 2017.
6. FHWA. Geotechnical Engineering Circular No. 12 – Design and Construction of Driven Pile Foundations. September 2016.
7. FHWA. Geotechnical Engineering Circular No. 13 – Ground Modification Methods Reference Manual. April 2017.
8. FHWA. Micropile Design and Construction Reference Manual. December 2005.
9. FTA. Transit Noise and Vibration Impact Assessment. September 2018.
10. NJDOT. Design Manual for Bridges and Structures. 6th Ed. October 7, 2016.
11. NJDOT. Straight Line Diagrams. 2025. https://njsld.org/NJDOT/SLD/SheetViewer/00000080__/32/4
12. NJGS. Bedrock Geologic Map of the Dover Quadrangle, Morris and Sussex Counties, New Jersey. 2012. https://dep.nj.gov/wp-content/uploads/njgws/maps/ofmap/ofm91.pdf
13. NJGS. Geologic History and Virtual Field Trip of the New Jersey Highlands. https://nj.gov/dep/njgs/enviroed/freedwn/HighlandsVFT.pdf
14. NJGS. Glacial Sediment and the Ice Age in New Jersey. 1998. www.state.nj.us/dep/njgs/enviroed/infocirc/glacial.pdf
15. NJGS. Physiographic Provinces of New Jersey. 2006. https://www.nj.gov/dep/njgs/enviroed/infocirc/provinces.pdf
16. NJGS. Surficial Geology of the Dover Quadrangle, New Jersey. 1989. https://dep.nj.gov/wp-content/uploads/njgws/maps/gmseries/gms89-2.pdf
17. Puffer, John H. Precambrian Rocks of the New Jersey Highlands. Department of Geological Sciences, Rutgers University Newark, New Jersey, 1980. NYSGA Field Guide No. 2. 1
18. Sims, P.K. Geology and Magnetite Deposits of Dover District, Morris County, New Jersey: U.S. Geological Survey Professional Paper. 1958
19. Stoffer, P. Geology of the New York City Region A Guide to Geology Field-Trips in the NYC Region. 2019. https://gotbooks.miracosta.edu/gonp/nyc/
20. USBM RI8507. Structure Response and Damage Produced by Ground Vibration from Surface Mine Blasting. 1980.

35. Overview of Landslide Management Programs for Linear Pipeline Infrastructure Corridors

Chris Markley, P.G.
Geosyntec Consultants
10 Corporate Drive, Suite 1600, Bedford, NH 03110
Christopher.Markley@geosyntec.com
(605) 280-4060

Bailey Theriault, P.G.
Geosyntec Consultants
10 Corporate Drive, Suite 1600, Bedford, NH 03110
Bailey.Theriault@Geosyntec.com
(315) 730-6263

Prepared for the 75th Highway Geology Symposium, September 2026

Disclaimer

Statements and views presented in this paper are strictly those of the author(s), and do not necessarily reflect positions held by their affiliations, the Highway Geology Symposium (HGS), or others acknowledged above. The mention of trade names for commercial products does not imply the approval or endorsement by HGS.

Copyright

Copyright © 2026 Highway Geology Symposium (HGS)

All Rights Reserved. Printed in the United States of America. No part of this publication may be reproduced or copied in any form or by any means – graphic, electronic, or mechanical, including photocopying, taping, or information storage and retrieval systems – without prior written permission of the HGS. This excludes the original author(s).

ABSTRACT

Landslides can pose significant risks to linear infrastructure like highways, railroads, and pipelines. To minimize the impacts of landslide hazards on infrastructure, landslides should be proactively identified, characterized, and if necessary, mitigated and monitored. This paper outlines a systematic approach to identify and manage landslide hazards in the pipeline industry, where operators may be managing thousands of landslide hazards located along tens of thousands of miles of pipeline. Where long distances of buried pipelines are constructed in areas of high landslide incidence, a landslide management program needs a consistent approach for data collection and analysis, where it is essential to identify threats early and prioritize responses based on the severity of each hazard. Once an initial landslide inventory is established and threats are assessed, a landslide management program needs to continue to evaluate and identify changing landslide conditions and associated threats that may increase or decrease over time. It is essential to recognize new and emerging identification and monitoring techniques and to use complementary technologies to balance strengths and weaknesses of each monitoring method. This paper will discuss a three-level approach for landslide assessment, detailing the processes implemented to identify and evaluate landslide threats, as well as the long-term monitoring approaches used at a system-wide scale, including the use of repeat LiDAR surveys (i.e., LiDAR Change Detection Analysis), interferometric synthetic aperture radar (InSAR) data, aerial and drone patrol/reconnaissance, and ground patrol. Case studies will be presented from the Appalachian Basin, including how the three-level assessment approach was broadly applied along approximately 164 miles of pipeline in West Virginia, and how the understanding of the threat of a specific landslide in West Virigina to pipeline integrity evolved through observations made during successive assessments over the course of 10 years.

INTRODUCTION

A landslide is typically defined as the "movement of a mass of rock, debris, or earth down a slope," and encompasses geologic processes such as debris or mud flows, rotational slides (slumps), translational slides, earth flows, rock falls, or debris slides (*1*, *2*). Landslides can damage pipelines in several ways, including bending the pipe, compressing and tensioning the pipe, undermining and exposing the pipe, leaving the pipe unsupported, or by directly striking the pipe during rapid movements such as debris flows or rockfalls.

Pipeline construction and operation in landslide-prone areas, along with fewer preferred routing options, have led to an increase in landslide-related issues during and after pipeline construction. Human activities can further increase the likelihood of landslide development and movement. Landslides can be dynamic in nature and can continue to change through time, and the development of new landslides along a pipeline can add risk to pipeline integrity, which can adversely affect public safety, the environment, or the safe operation of a pipeline. As a result, there is a growing need to identify, characterize, and closely monitor landslide hazards throughout both the construction and operating life of each pipeline system. It is essential to recognize new and emerging identification and monitoring techniques and to use complementary technologies to balance strengths and weaknesses of each monitoring method.

Prior to the publication of the Framework for Geohazard Management by the Interstate Natural Gas Association of America (INGAA) in 2023, a generally accepted framework for managing landslides and their impact on the integrity of pipelines did not exist. The three assessment levels discussed below were developed over many years but were detailed most recently and comprehensively in the Framework for Geohazard Management (*3*).

THE LANDSLIDE MANAGEMENT PLAN AND THE THREE-LEVEL APPROACH FOR LANDSLIDE ASSESSMENT

The Three-Level approach for landslide assessment and management is based on the systematic procedure of identifying, characterizing, assessing, and mitigating/monitoring landslides. The process begins with an initial regional, desktop assessment (Level 1 Assessment), progressing to more focused assessments of landslide hazard areas and specific hazard sites (Level 2 Assessment), leading to a highly detailed, site-specific assessment of the landslide hazard (Level 3). The landslide hazard classification should be reassessed throughout each level of assessment, as more information is collected, and more is known about each landslide. Through each successive level of assessment, the level of detail of the landslide hazard characterization increases, while typically the number of landslide hazards requiring additional assessment decreases with each level (Figure 1).

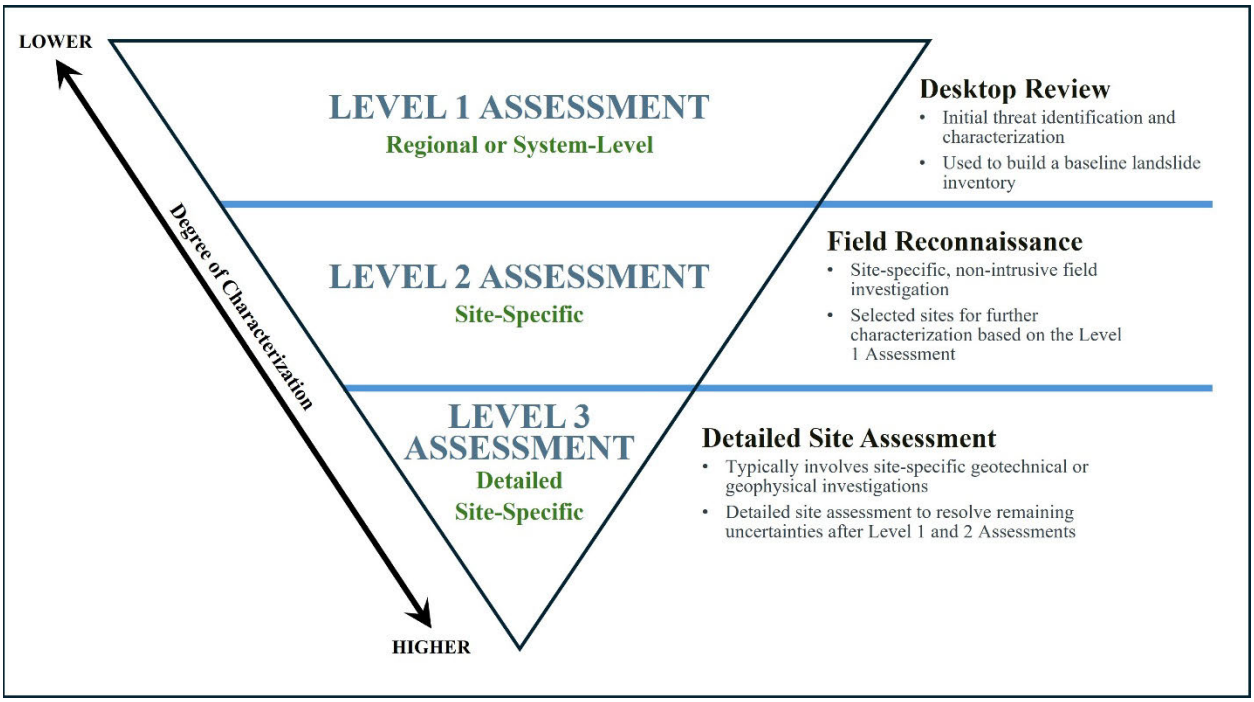

Figure 1: The Three-Level Framework for Landslide Assessment. The figure is modified from the INGAA Foundation: Recommended Practice for Pipeline Integrity Management of Landslide Hazards (*4*)

It is important to develop a framework and classification system for the landslide hazard management program prior to the initiation of the Three-Level Assessment program. The landslide hazard classification system should be based on the apparent threat to a pipeline from a landslide. The landslide hazard classes are related to and should help drive the appropriate responses.

The data management system should be established using a GIS (Geographic information system)-based approach that can evolve throughout the lifespan of the landslide management program. A GIS-based approach provides the basic working tools to identify, map, and document landslide hazards and allows data from other sources and subsequent assessments to be integrated into the system. The data management system is used throughout all three assessment levels but is established during the Level 1 Assessment with the development of a landslide inventory.

Level 1 Assessment

A Level 1 Assessment is intended to establish a baseline landslide inventory through a desktop-based evaluation to identify landslide hazards along existing pipeline rights-of-way (ROWs), or along a proposed pipeline alignment. In addition to identifying individual landslides of concern, the Level 1 Assessment provides pipeline operators with a system-wide understanding of landslide concentration, versus areas with little or no landslide activity. A Level 1 Assessment helps to prioritize follow-up evaluations and resource allocation toward areas with the greatest potential threat to the pipeline.

Typical data sources reviewed during a Level 1 Assessment include the following:

- Publicly available data (e.g., topographic, geologic, and soils maps; reports or published datasets on the incidence of locally occurring landslides);
- Owner-specific data (e.g., records of known landslide locations, available monitoring information, whether site-specific or system-wide; and as-built drawings or construction reports documenting landslides); and,
- Remote-sensing data (e.g., public and/or project-specific Light Detection and Ranging (LiDAR) data, aerial photography, Interferometric Synthetic Aperture Radar (InSAR) data).

An absence of publicly available or owner-specific landslide-related information does not equate to an absence of landslides, only that no hazards have been identified to date. While various datasets can prove useful during a Level 1 Assessment, high-resolution LiDAR data are particularly useful in areas where dense vegetation obscures direct observation of the ground conditions, and where a clear view of the ground is difficult through other traditional methods (e.g., from the ground or air, or from aerial photographs) (Figure 2).

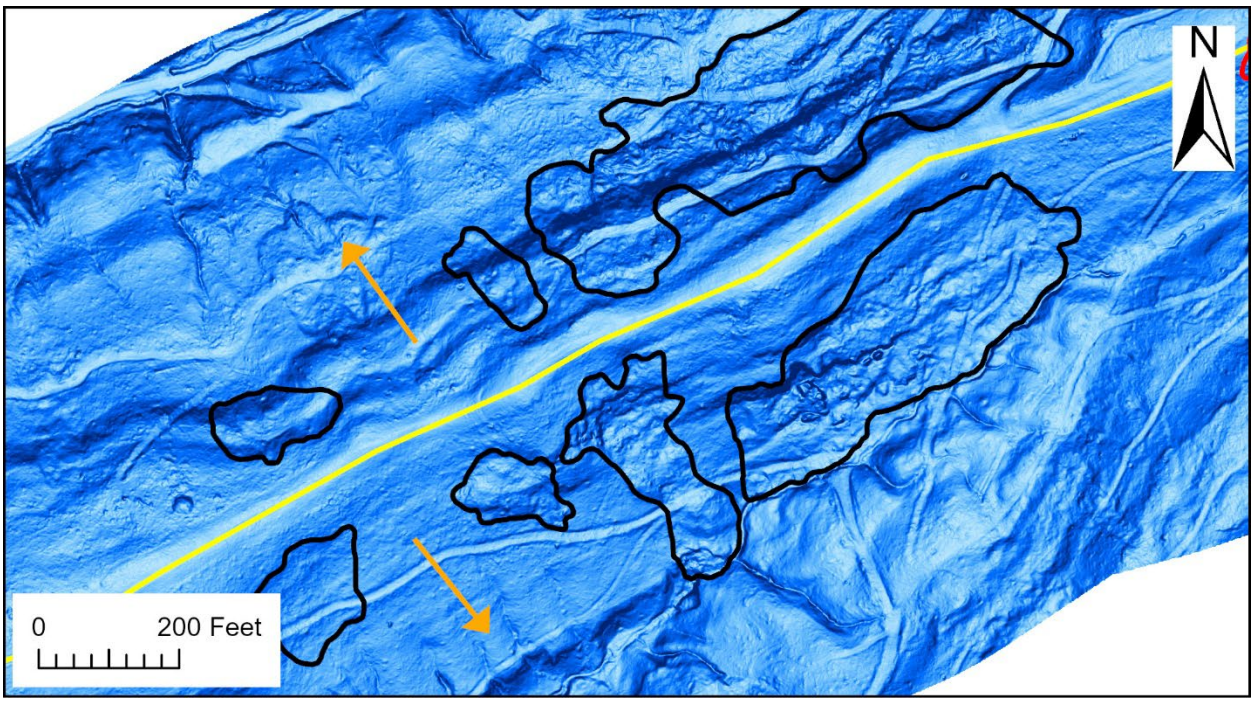

Figure 2: High-resolution LiDAR imagery (displayed as percent slope in blue-scale) of a pipeline (yellow line), slope direction (orange arrows) and identified landslides (outlined in black). The pipeline is located on a ridge top.

Hazard classifications assigned during a Level 1 Assessment are used to identify landslides of concern that may require more detailed evaluation (e.g., in a Level 2 Assessment), while lower-threat features do not require more detailed evaluation but remain in the overall landslide inventory so they can be reevaluated if the site conditions change.

Level 2 Assessment

A Level 2 Assessment is a site-specific, nonintrusive field evaluation of the higher-priority landslide hazards identified during the Level 1 Assessment. The landslides and potential landslides evaluated during a Level 2 Assessment represent a subset of the overall Level 1 inventory, typically consisting of features interpreted to pose a greater potential threat to the pipeline. A Level 2 Assessment generally includes geomorphic and geologic reconnaissance without subsurface exploration, drilling, or excavation. A Level 2 Assessment is intended to verify whether the features identified during the Level 1 Assessment are landslides and, for confirmed landslides, to better define their location and potential effect(s) on the pipeline.

Level 2 Assessments should be performed by an individual or field team experienced in geomorphic landslide identification and characterization. The field assessment should document the geomorphic and geologic conditions observed during the field visit, including conditions both within and outside of the pipeline ROW to develop a more complete understanding of the slope at the time of the site inspection. The presence, location, and condition of key landslide features should be documented and assessed to accurately determine the possible effects of the landslide on the pipeline (Figure 3).

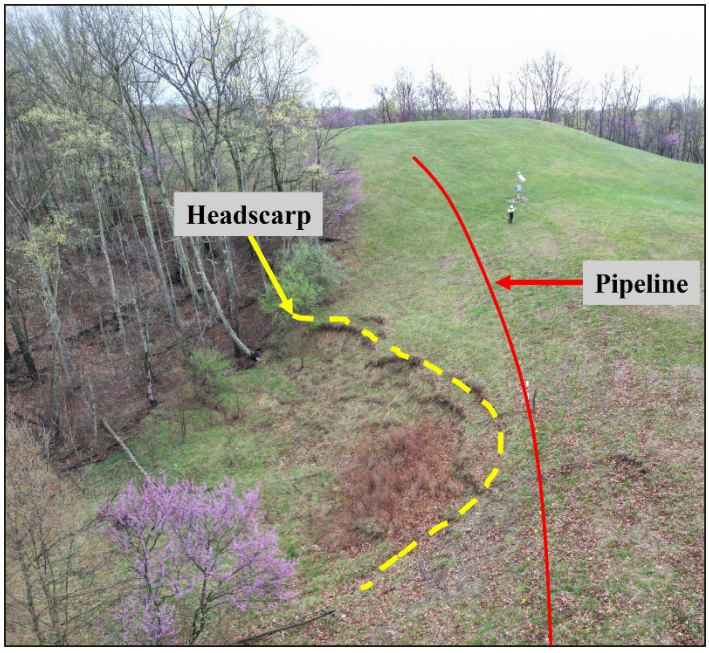

Figure 3: Aerial photo from a Level 2 Assessment where the relationship between the location of the landslide and the pipeline are confirmed.

Data obtained during the Level 2 Assessment field assessment should be used to confirm or revise the preliminary landslide hazard mapping, landslide characterization, and threat classifications assigned during Level 1 Assessment. For new pipelines, data collected during the Level 2 Assessment may inform construction best practices. The findings from a Level 2 Assessment can be used to determine whether mitigation or monitoring is warranted, or whether additional subsurface investigation is needed to adequately define the potential threat to the

pipeline (i.e., Level 3 Assessment). Most landslides do not require additional assessment beyond Level 2; therefore, only a small percentage of the total landslides typically proceed to Level 3.

Level 3 Assessment

A Level 3 Assessment is the most detailed, site-specific level of assessment, and is usually completed for only a small subset of sites identified during prior Level 1 and Level 2 Assessments. The objective of a Level 3 Assessment is to address any remaining uncertainties after completion of Level 2 and to collect the information needed to decide what actions, such as mitigation or monitoring, should be taken.

The methods used to conduct a Level 3 Assessment are tailored to the specific landslide and may include detailed surface mapping, geophysical surveys, subsurface investigations such as drilling or test pits, and the possible installation of monitoring instruments such as inclinometers or strain gauges (Figure 4).

Figure 4: Excavated section of pipeline for the purpose of installing strain gauges.

Information gathered during a Level 3 Assessment should be combined with the results of Level 1 and Level 2 to improve the overall understanding of the landslide and its potential threat to the pipeline. The Level 3 findings should be used to verify or adjust the landslide characterization and threat level established during Levels 1 and 2. The landslide inventory created during Level 1 Assessment and revised during Level 2 should also be updated again to reflect the information gathered during the Level 3 Assessment. If further action is required, the information gathered during the Level 3 Assessment is used to support the development of mitigation and monitoring plans, or response plans in the event of catastrophic pipeline failure due to landslide movement.

Periodic Reassessment

An important facet in the maintenance of the landslide inventory is periodic reassessment of available data. The purpose of the reassessment is to re-evaluate landslide hazards using the information gathered during all three levels of assessment, coupled with current data to update the site characterization. The reassessment can be completed after a set period of time (i.e., every 5 years), or may be completed earlier, if large amounts of new data become available.

A reassessment of the data may lead to the identification of hazards that formed over the period between assessments and have been undetected through other monitoring methods (i.e., aerial reconnaissance). The reassessment may determine if the magnitude of the hazard at each site has increased or decreased since the last assessment.

Continuing Systemwide Monitoring

Even as a landslide management program matures, systemwide monitoring is necessary to identify emerging threats along the pipeline, especially in areas of high landslide concentration. Systemwide monitoring methods allow for data to be collected over large areas during a relatively short period of time. Such techniques are typically considered a cost-effective way to monitor landslides, as a larger region can be monitored at a lower cost than site-specific monitoring of each specific landslide within the same area. With systemwide monitoring, the areas between known hazards can be reviewed for emerging hazard conditions.

It is important to incorporate new and developing identification and monitoring techniques and to use complementary technologies to balance strengths and weaknesses of each monitoring method. Several commonly used types of systemwide monitoring include:

- LiDAR Change Detection - Repeated acquisition and comparison of LiDAR data over the same area can be used to identify areas of active landslide movement over time.
- Aerial Reconnaissance – Experienced, trained geologists or geotechnical professionals view the ground surface from a helicopter or fixed-wing aircraft. The purpose of the reconnaissance is to focus solely on landslide threat assessment. Aerial reconnaissance can be conducted quickly and may be necessary following a significant event that may trigger landslides (e.g., an intense storm).
- InSAR Data – InSAR data are collected by satellites, which scan the ground and allow for detection and monitoring of changes in the ground surface over large areas. InSAR data can be useful in identifying larger areas of movement; however, smaller landslide movement may be missed due to the resolution of the data.
- Inertial Measurement Unit (IMU) Bending Strain Data - IMU data collected during an in-line inspection (ILI) of a pipeline identify areas of bending strain along a pipeline segment by an external force, such as a landslide. Bending strain data can be used in Level 1 Assessments to identify locations that might be affected by landslide movement, and in later levels of assessment for monitoring along pipeline systems and segments when two or more IMU data sets are compared.

CASE STUDIES

The Appalachian Plateau physiographic region is characterized by rugged, hilly terrain, heavily dissected by streams and tributaries. The bedrock geology comprises mostly flat-bedded alternating sequences of sedimentary units that include sandstone, siltstone, claystone, shale, limestone, and coal. In West Virginia's portion of the Appalachian Plateau, a combination of natural geologic, geographic, and climatic conditions contributes to the prevalence of landslides. Landslides in West Virginia are generally triggered by saturated soil and the lack of drainage systems to remove surface water and groundwater. Additionally, landslides may be triggered by human activity during construction (e.g., excavations).

Case Study #1 – Confidential Pipeline, West Virginia, US

For an existing pipeline system located in West Virginia, the three-level approach was followed to develop a landslide inventory along approximately 164 miles of pipeline ROW. The Level 1 Assessment began in 2015 with desktop review of high-resolution project-specific LiDAR data, during which landslides were initially identified, delineated, and characterized. Upon completion of the Level 1 Assessment, 607 possible landslides were identified within 100 feet of the pipeline alignment (a mapping corridor of 200 feet). Of those 607 possible landslides, 174 progressed to Level 2 Assessment. Based on the Level 2 Assessment results, site-specific monitoring was implemented at 74 sites (Level 3), including installation of strain gauges, monitoring points, or a combination of the two (Table 1).

To supplement the site-specific program, a regional monitoring program was developed that included the following components: (1) Annual LiDAR Change Detection Analysis conducted along the entire 164 miles of pipeline. (2) IMU data collected and reviewed at a 4- to 7-year interval. (3) Aerial reconnaissance of the ROW was conducted at regular intervals via helicopter, where the pilot was instructed to notify the local pipeline operator if any emergent landslide hazards were observed.

Table 1: Assessment Results by Level

2015/2016 Initial Assessments	
# of Landslides Identified During the Level 1 Assessment	607
# of Landslides Evaluated During a Level 2 Assessment	174
# of Landslides That Progressed to Level 3	74
Subsequent Assessments	
# of New Landslides Identified After Initial Level 1 & 2 Assessments	120
# of New Landslides Evaluated During a Level 2 Assessment	42
# of New Landslides That Progressed to Level 3	13
Landslide Totals to Date	
# of Total Landslides Identified Along the Pipeline	727
# of Total Landslides Evaluated During a Level 2 Assessment	216
# of Total Landslides That Progressed to Level 3	87

Since the initial Level 1 and Level 2 Assessments, an additional 120 landslides have been identified along the West Virginia pipeline, mostly through the annual LiDAR Change Detection Analysis program or from review of IMU data. Of the 120 new landslides, 42 were evaluated during a Level 2 Assessment, 13 of which progressed to Level 3.

The results presented in Table 1 highlight the need for continued assessments after the initial round of assessments have been completed. Although many landslides were identified during the assessments conducted in 2015 and 2016, subsequent assessments identified new, emerging threats that would have otherwise gone undetected if not for ongoing monitoring.

Case Study #2 – Confidential Pipeline Project, West Virginia, US

At a location in southwestern West Virgina, one landslide complex has progressed through each assessment level, and continues to require monitoring. The following section outlines how the hazard was identified and how the hazard characterization has changed over time, based on data collected during each Assessment.

Level 1 Assessment – 2015 – The initial regional-scale Level 1 Assessment for the pipelines located in West Virginia was conducted in 2015 using publicly available aerial imagery and high-resolution LiDAR data collected by the pipeline operator. The landslide complex was identified on an east-northeast facing slope of a mountain composed of the interbedded shale, siltstone, and sandstone units that make up the Conemaugh Group (5) (Figure 5A). While reviewing the LiDAR data, the mapper noted a “Possible landslide complex, encompassing the entire western slope, and spanning the ROW traveling axial across the alignment. Possible landslide deformation observed on the ROW across the GIS pipeline centerline; ROW is possibly deformed and ROW margins are difficult to discern. Small trees or shrubs can be seen growing in the ROW in aerial photography (Google Earth: 4/13/2011).”

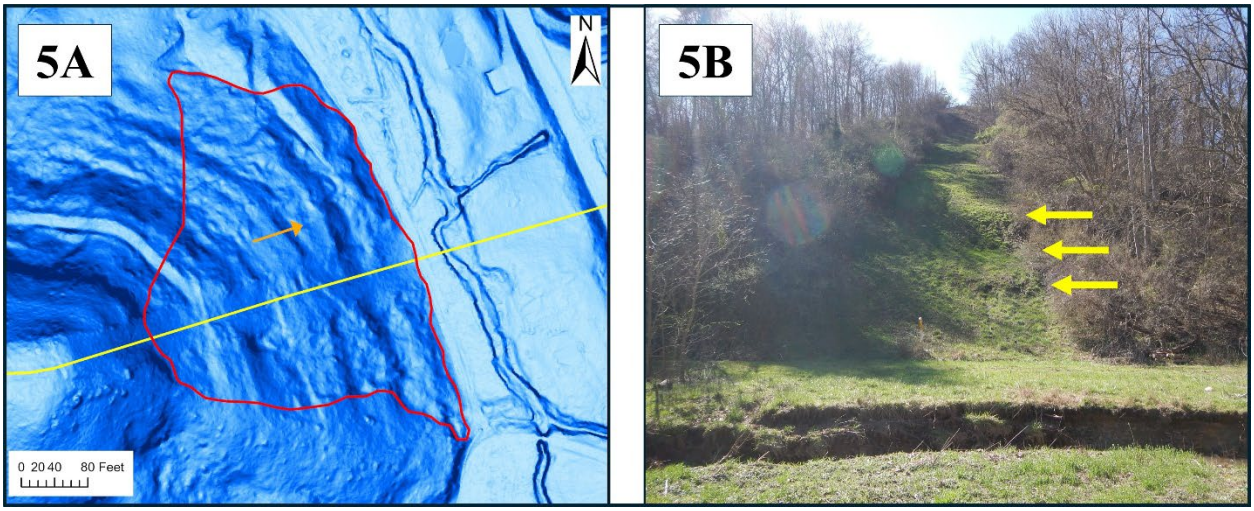

Figure 5A: High-resolution LiDAR imagery (displayed as percent slope in blue-scale) from 2015 of the relationship of a pipeline (yellow line) to a landslide complex (outlined in red) identified during the Level 1 Assessment. The orange arrow represents the slope direction. Figure 5B: Photo of the landslide complex looking upslope along the pipeline ROW, taken during the 2016 Level 2 Assessment. The yellow arrows point to the area of well-defined hummocks noted during the assessment.

Level 2 Assessment – 2016 – Due to the disturbance observed within the ROW during the Level 1 Assessment, a site assessment of the landslide complex was included in a larger field campaign. During the site assessment, the major attributes noted by the field team included two areas of post-construction, recent landslide movement located within the ROW (Figure 5B). One area of recent activity was located near the base of the slope and consisted of well-defined hummocks that measured up to 2 feet high over the location of the pipeline. The second area was located mid-slope and consisted of an internal failure with an internal scarp, hummocks, and toe which measured up to 2 feet high, all of which crossed the location of the pipeline. The landslide morphology observed outside of the ROW appeared older than that within the ROW. The minimum depth to the center of the pipeline was measured to be approximately 4 feet deep.

Level 3 Assessment – 2017 – The presence of the recent landslide morphology observed during the Level 2 Assessment within the ROW necessitated further monitoring of the landslide complex. To determine the rate and direction of ground movement, in 2017, seven survey monuments were installed within the ROW along the length of the landslide complex; four survey monuments located south of the pipeline and three survey monuments located north of the pipeline. The survey monuments were set to be monitored quarterly, where any recorded movement over a set threshold would require a follow-up site assessment.

Due to the high concentration of landslide related activity in West Virginia, a decision was made to implement systemwide monitoring, which mainly consisted of 1) annual collection of LiDAR data for LiDAR Change Detection Analysis, and 2) collection and review of IMU data over a 4-to-7-year period.

Between 2017 and 2021, the LiDAR Change Detection Analysis recorded no evidence of active ground movement within the landslide complex. Measurements of the survey monuments also showed no movement during the same time span.

LiDAR Change Detection Analysis – 2022 – During the LiDAR Change Detection Analysis, where data from 2022 were compared against data from 2021, possible landslide movement was detected within the landslide complex (Figure 6A & 6B). The mapper noted "Recent movement within [the landslide complex] and across the pipeline centerline. The LiDAR change signature appears to cross the location of the pipeline within the ROW."

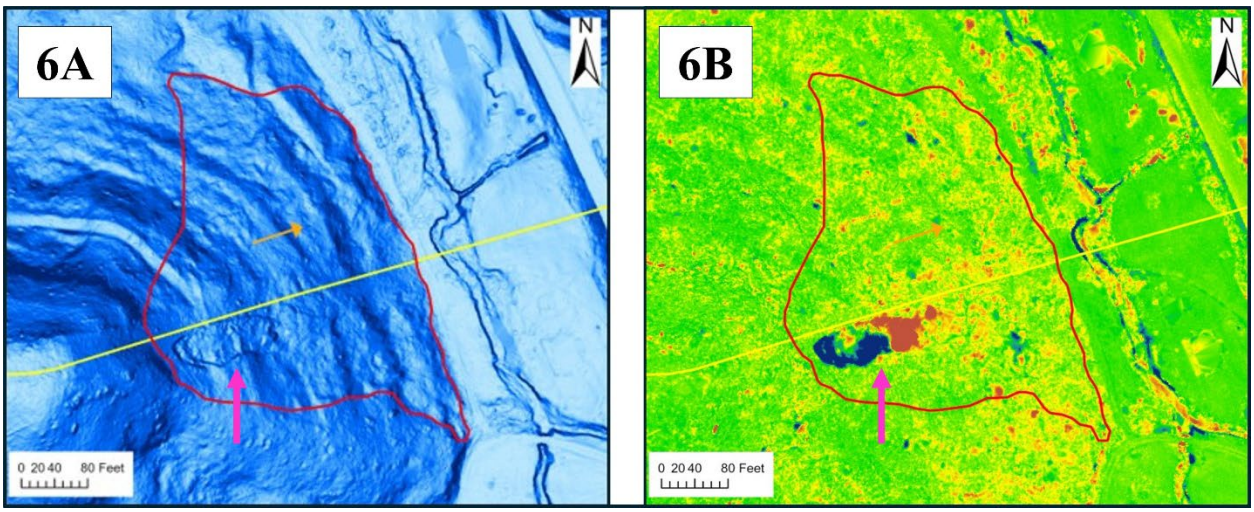

Figure 6A: High-resolution LiDAR imagery acquired in 2022 of the same landslide complex in West Virginia. Figure 6B: LiDAR Change Detection Heat Map produced by comparing the 2021 and 2022 LiDAR data. The cool colors (i.e. blues) represent areas of net loss and warm colors (i.e. orange to red) represent areas of net gain. Yellow green represents areas with little or no change. The pink arrows highlight the area of active movement.

Repeat Level 2 Assessment – 2023 – Due to the disturbance observed within the landslide complex during the LiDAR Change Detection Analysis, a follow-up site assessment was scheduled to determine the magnitude of the failure within the ROW. During the follow-up site assessment, the field team noted that a recent internal failure occurred within the ROW and that the size of the internal landslide morphology measured up to 4 feet high and crossed the location of the pipeline (Figure 7). Based on the size of the recent failure, and the depth to the center of the pipeline, it was determined that the base of the recent failure was located below the depth of the pipeline; therefore, continued landslide movement may have an adverse effect to pipeline integrity.

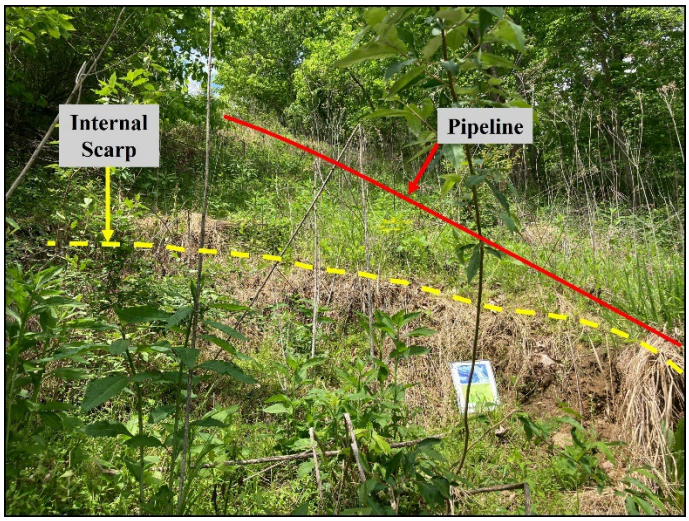

Figure 7: Photo looking upslope at the internal scarp observed within the ROW during the repeat Level 2 Assessment. The morphology observed during the 2023 site visit corresponded to the area of change identified during the 2022 LiDAR Change Detection Analysis.

Additional Level 3 Assessment – 2025 – Due to the added threat to the integrity of the pipeline imposed by the 2023 internal movement, the decision was made to install four sets of strain gauges on the pipeline along the length of the landslide complex. During installation of the strain gauges, the pipeline is excavated and the entire ROW is typically disturbed, which effectively erases any landslide morphology within the ROW. After installation, the slope within the ROW is regraded and reseeded (Figure 8A).

Figure 8A: Photo looking upslope at the recently regraded ROW located within the landslide complex. The slope was regraded after installation of strain gauges in 2025. Figure 8B: Looking upslope at the debris flow, which occurred after the slope regrading of Figure 8A.

Repeat Level 2 Assessment – 2026 – Early in the spring of 2026, the local pipeline operators noticed a recent failure within the pipeline ROW which necessitated a repeat Level 2

Assessment. During the 2026 site assessment, the field team noted that a recent failure of the material within the ROW resulted in a debris flow located on the lower portion of the slope (Figure 8B). The failure appeared to be localized in the ROW fill material and did not appear to be indicative of larger, deep-seated landslide movement.

Following the 2026 assessment, the plan for the landslide complex, is to continue to monitor the slope through the systemwide monitoring program. If any changes are observed, another round of assessments will occur. If the installed strain gauges detect any changes in the strain on the pipe, the hazard classification of the landslide complex will immediately be upgraded, and the site will likely be scheduled for mitigation.

CONCLUSION

In regions with high landslide incidence, there is an increasing need to recognize, understand, and closely manage landslides, prior to, during, and post-construction of pipelines. The three-level approach to landslide assessment provides a cost-effective method to systematically identify, characterize, evaluate, and if necessary, mitigate and monitor landslides that may have the potential to affect a pipeline.

The approach begins with a regional-scale assessment and identifies high hazard landslide targets during subsequent levels of assessment. Mitigation and/or monitoring efforts can then be focused only on sites deemed necessary. The three-level approach allows a landslide management program to evolve through time, monitoring known hazards at a systemwide or site-specific level, while identifying new hazards as they emerge.

REFERENCES

1. Cruden, D.M. A simple definition of a landslide. *International Association of Engineering Geology*, No. 43, 1991, p. 27-29.
2. Cruden, D.M. and Varnes, D.J. *Chapter 3, Landslide Types and Processes, in Turner, K.A., and Schuster, R.L., eds., Landslides – Investigation and Mitigation*. Special Report 247. Transportation Research Board, National Research Council, National Academy Press. 1996. p. 36-75.
3. Wang, Y., Fleck, P., McKenzie-Johnson, A., Theriault, B., West, D., Framework for Geohazard Management. INGAA Foundation. March 2023.
4. McKenzie-Johnson, A., Theriault, B., Wang, Y., Fleck, P., Ebrahimi, A., Liu, B., West, D. Recommended Practice for Pipeline Integrity Management of Landslide Hazards. INGAA Foundation. April 2023.
5. Horton, J.D., San Juan, C.A., and Stoeser, D.B., 2017, *The State Geologic Map Compilation (SGMC) geodatabase of the conterminous United States (ver. 1.1, August 2017)*: U.S. Geological Survey Data Series 1052, 46 p., https://doi.org/10.3133/ds1052. Data accessed 6/17/2026.

36. TWO DIMENSIONAL SEISMIC SITE RESPONSE ANALYSIS FOR A NEW BRIDGE IN A SUBDUCTION ZONE ENVIRONMENT

Zia Zafir, PhD, PE, GE,
Kleinfelder
3130 Kilgore Road Suite 200
Rancho Cordova, CA 95670
(916)825-5683
zzafir@kleinfelder.com

Prepared for the Highway Geology Symposium, September, 2026

Acknowledgments

The author would like to thank the following individuals for their contributions to this project.

Xing Zheng – Caltrans
James Gingery – Keller
Anoosh Shamsabadi – HDR
Hubert Law – Earth Mechanics, Inc.

Disclaimer

Statements and views presented in this paper are strictly those of the author(s), and do not necessarily reflect positions held by their affiliations, the Highway Geology Symposium (HGS), or others acknowledged above. The mention of trade names for commercial products does not imply the approval or endorsement by HGS.

Copyright Notice

Copyright © 2026 Highway Geology Symposium (HGS)

All Rights Reserved. Printed in the United States of America. No part of this publication may be reproduced or copied in any form or by any means – graphic, electronic, or mechanical, including photocopying, taping, or information storage and retrieval systems – without prior written permission of the HGS. This excludes the original author(s).

ABSTRACT

Smith River Bridge replacement project involves construction of a new about 1,000-foot-long four-span hunched box girder bridge with a continuous deck isolated by triple frictional pendulum (TFP) bearings. The bridge will replace an existing bridge supported by two abutments and 17 piers. The site is located in northwest California near Crescent City in an active seismic region. The seismic environment around the project area is dominated by the Cascadia Subduction Zone (CSZ). Although some shallow crustal faults are located near the bridge site, the seismic hazards for this bridge are governed by the CSZ. Based on the available subsurface information, geotechnical/geologic conditions vary significantly along the length of the bridge, ranging from shallow metamorphic bedrock north of the river, to deep alluvium consisting of saturated sand, silt, gravel and cobbles south of the river. Depth of alluvium at the south side extends to about 130 to 150 feet below the ground surface. In order to perform three-dimensional (3D) soil-structure-interaction analysis of the bridge and foundation systems, three-component time histories at 10-foot vertical intervals along the foundation length at each pier and abutment location are needed. Due to the variation in geotechnical/geologic conditions along the longitudinal direction of the bridge, a two-dimensional (2D) seismic site response analysis is required to develop three-component time histories. The 2D seismic site response analyses were performed using a computer program QUAD4M. Response spectrum at the bedrock level was developed using recommended procedures by California Department of Transportation (Caltrans) and using probabilistic and deterministic seismic hazard analysis (PSHA and DSHA). Seven sets (each set containing two orthogonal horizontal motions and one vertical motion) of spectrally matched time histories representing subduction zone environment were developed and used in the 2D seismic site response. In addition, a computer program (DEEPSOIL) was used to perform one-dimensional (1D) seismic site response analyses to model site response in the transverse direction of the bridge. Results of QUAD4M were calibrated against the DEEPSOIL results in the transverse direction of the bridge. This presentation will present the results of ground motion hazard analyses, deaggregation analyses, selection and spectrally matching seven sets of time histories, and results of 1D and 2D site response analysis. Results of seismic site response show significant variation in site response along the longitudinal direction which can’t be captured in a 1D site response analysis.

INTRODUCTION

This paper presents the results of our site-specific seismic hazard and site response analyses for the Smith River (Dr. Fine) Bridge replacement project in Del Norte County, California. The Smith River (Dr. Fine) Bridge replacement project involves construction of a new 1,000-foot-long, four-span box girder bridge with a continuous deck isolated by triple frictional pendulum (TFP) bearings. The bridge will replace an existing bridge supported by two abutments and 17 piers. The bridge is located on Highway 101 in northwest California near Crescent City in an active seismic region. Figure 1 shows the location of the bridge and it also shows the boring locations. This paper reflects current knowledge regarding seismic hazard around the project area. The subsurface soil conditions used in this study were obtained from geotechnical investigations performed by Caltrans at the project site.

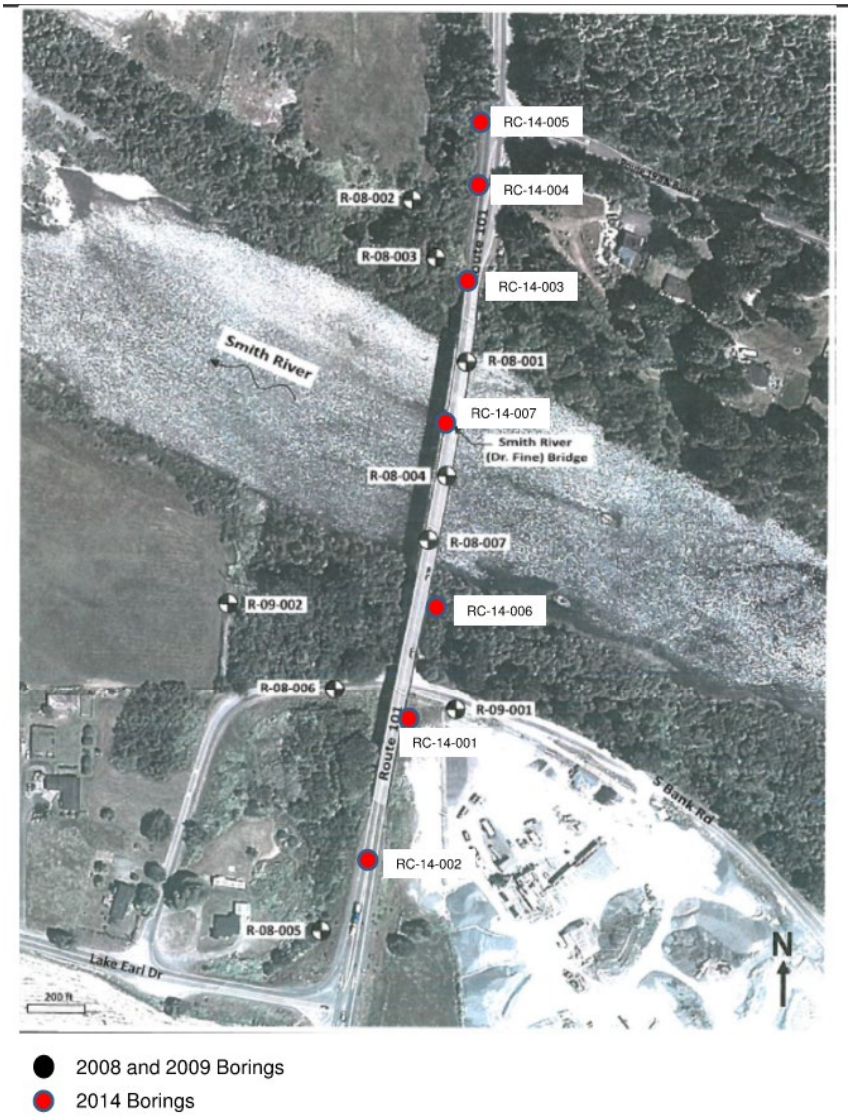

Figure 1: Project and boring location map

ANALYSIS METHODOLOGY

The purpose of this seismic hazard analysis is to develop site-specific ground motion criteria in terms of peak ground accelerations and response spectral accelerations for the subject site by using a seismic source model (proximity to active faults, major historical earthquakes, and regional seismicity) and subsurface soil conditions at the site. The response spectrum is a graphical representation relating the maximum response of a single degree of freedom, elastic damped oscillator with different fundamental periods to dynamic loads. A site-specific spectrum for any given return period represents uniform-risk earthquake ground motions consistent with the seismic source model and the local site response. In addition to free-field spectrum, a kinematic spectrum is also developed. The final ground surface spectrum is developed using the results of site response and kinematic analyses. Since the site is underlain by sloping bedrock with depths to bedrock changing significantly across the bridge, a two-dimensional (2D) site response analysis is needed along the longitudinal direction of the bridge. One-dimensional site response analysis in the transverse direction is appropriate for this project. Specifically, our scope of services included the following:

- Literature review of available geologic and seismic setting of the area and developing a site-specific seismic source model.
- Estimating the shear wave velocity profile for the subsurface using information from soil borings and suspension logging performed by Caltrans.
- Estimating the average shear wave velocity at an Elevation of -120 feet, which is the bottom of the site response model.
- Performing site-specific probabilistic seismic hazard analyses (PSHA) to develop Uniform Hazard Spectrum (UHS) at the bottom of the site response model for ground motions having 5% probability of exceedance in 50 years (return period of about 975 years). This is the target “outcrop” spectrum for spectral matching of time histories.
- Selecting seven sets of time histories based on the site conditions, controlling fault magnitude, distance, and mechanism.
- Spectrally matching seed time histories with the target “outcrop” UHS for site response analyses using computer programs DEEPSOIL and QUAD4M.
- Developing an idealized soil profile and associated soil parameters based on the results of field investigations for DEEPSOIL and QUAD4M analyses.
- Perform equivalent linear 1D site response analyses using computer program DEEPSOIL in the transverse direction.
- Perform equivalent-linear 2D site response analyses using computer program QUAD4M in the longitudinal direction.

- Perform kinematic analysis to develop kinematic response spectra at abutments and bents.

- Obtain results from 1D and 2D site response analyses in terms of longitudinal, transverse, and vertical time histories for acceleration, velocity and displacement and their response spectra at 10-foot vertical intervals along the pile/shaft length at each abutment and bent.

- Development of site-specific, uniform-hazard horizontal response spectra at ground surface for the design earthquake for 5 percent damping using the results 1D, 2D and kinematic response.

SUBSURFACE CONDITIONS AND GROUNDWATER

Caltrans performed borings and geophysical tests at this site. Borings were performed in 2008, 2009 and 2014. At this time, Logs of Test Borings (LOTB) for this project have not been prepared and we obtained pertinent information from the rough drafted boring logs. In addition, shear wave velocity measurements were performed at two locations (RC 14-001 and RC 14-003) using suspension logging techniques. Based on the data obtained from boring logs, the bridge alignment is underlain by fill materials overlying younger alluvium consisting of sands and gravels with minor cobbles in turn underlain by cobbles and boulders with sand and gravel matrix overlying bedrock consisting of greywacke and shale. Depth to bedrock varies from about 130 to 150 feet at the south abutment to about 40 feet at the north abutment. Shear wave velocities used in our analyses are presented in Figure 2. An idealized profile with boring logs and shear wave velocity measurements are presented on Figure 3. Groundwater is within 15 feet below the ground surface.

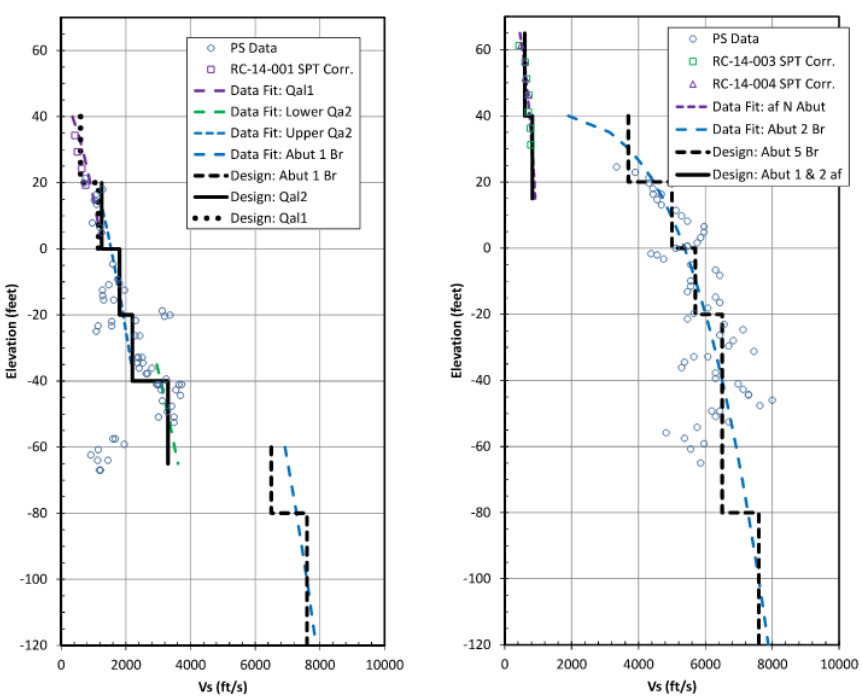

Figure 2: Shear Wave Velocity Profile, Left (RC 14-001), Right (RC 14-003)

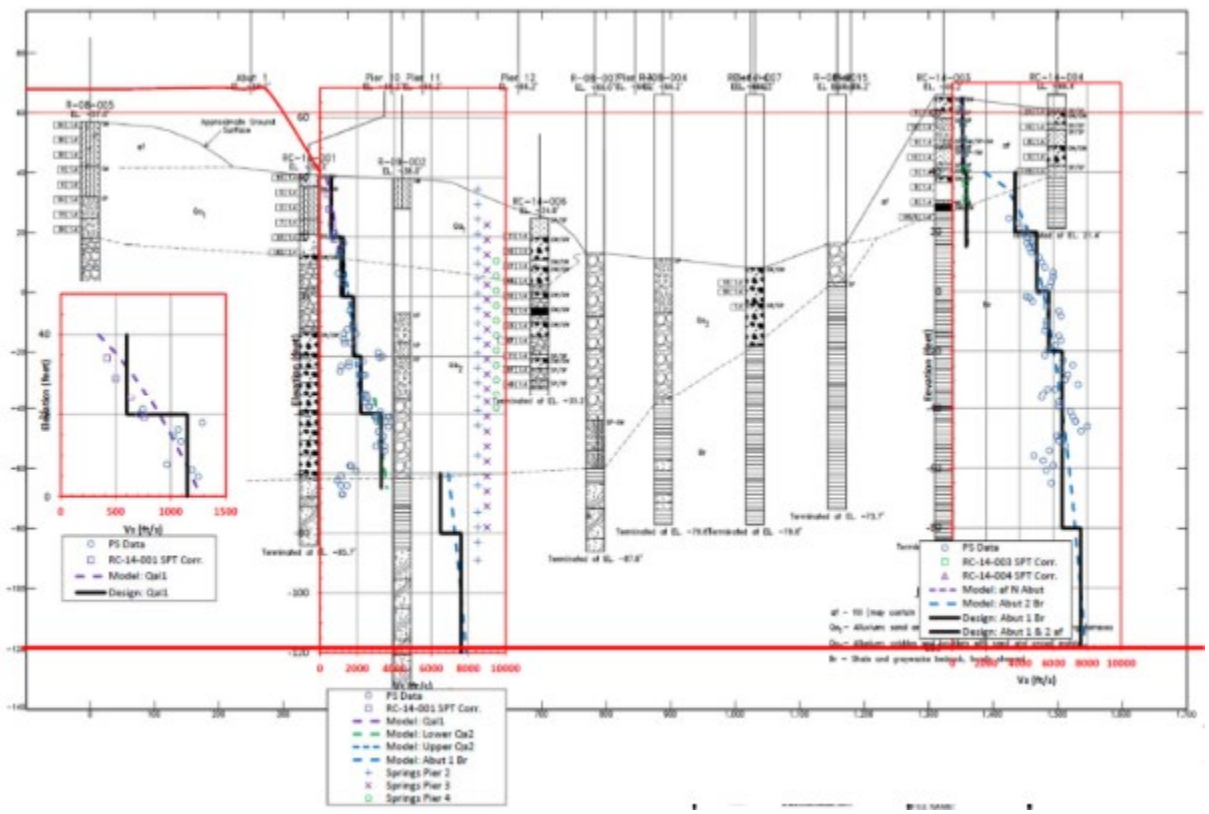

Figure 3: Idealized Soil Profile

SEISMIC HAZARD ANALYSIS

The purpose of our seismic hazard analysis is to establish a target rock spectrum at the bedrock level. Based on the results presented in Figure 3, V_S values are in excess of 7,600 feet/sec (2,300 m/s) at an elevation of -120 feet which corresponds to the bedrock level for our model. However, as can be seen from Figure 3, that there is a lot of scatter in the Vs data and as such using 2,300 m/s in our ground motion hazard analysis may not represent a realistic scenario. In addition, many of the NGA Ground Motion Prediction Equations (GMPE) are limited to maximum V_{S30} values from 1,200 to 1,500 m/s. Based on the uncertainty in the V_S value at the bedrock level, we have used a V_{S30} value of 1,000 m/s to estimate spectral accelerations at the bedrock level.

Probabilistic seismic hazard analyses were used to estimate the peak and spectral ground accelerations for the rock outcrop for ground motions having 5% probability of exceedance in 50 years (return period of about 975 years) as discussed above. This analysis involves the selection of an appropriate predictive relationship to estimate the ground motion parameters, and, through probabilistic methods, determination of peak and spectral accelerations. Petersen et al. (2014) seismic source model was used.

We also compared the probabilistic values with the deterministic values. There are several opinions about the magnitude and distance to be used in a deterministic analysis. USGS

uses several different postulations of the location of CSZ. In addition, it has been proposed that for engineering purposes, the scenario of a series of M8.3 events happening on the CSZ is more appropriate for the design purposes. Due to uncertainty about location and magnitude, Caltrans used a magnitude of 8.3 at a distance of about 31 km for this site for CSZ. Using the same values, the probabilistic values are higher than the deterministic values. Therefore, the controlling spectrum is the probabilistic spectrum.

Ground Motion Models (GMM)

Recently five Next Generation of Attenuation (NGA) West-2 GMMs were developed by the Pacific Earthquake Engineering Research (PEER) Center. These GMMs are Abrahamson, Silva, and Kamai (2014), Boore, Stewart, Seyhan, and Atkinson (2014), Campbell and Bozorgnia (2014), Chiou and Youngs (2014), and Idriss (2014). We have used four of the five GMMs with an exception of Idriss (2014) for our analyses. Idriss (2014) relationship is only applicable to sites with V_{S30} values between 450 and 900 m/s. An equal weight of 0.25 was assigned to each of the selected four GMPEs for shallow crustal earthquakes.

We have selected the model presented by Youngs et al. (1997) with a weight of 0.25, Atkinson and Boore (2003) Global Model with a weight of 0.25, and Zhao et al (2006) with a weight of 0.5 to characterize the Cascadia Subduction Zone events, which is consistent with Peterson et al. (2008).

All of these GMMs use an estimate of the average shear wave velocity of the soil profile in the analysis. As mentioned above, we have used V_{S30} of 1,000 m/s in our analysis. Spectral acceleration values were obtained by averaging the individual hazard results.

Target Outcrop Spectrum

As discussed earlier, the target response spectrum for the outcrop is developed by comparing probabilistic and deterministic spectra. Since probabilistic is higher than the deterministic, the target spectrum is controlled by probabilistic spectrum. Vertical spectrum was calculated using the Gulerce and Abrahamson (2011) method. Since the fundamental period of the proposed base isolation system for the bridge ranges between 5-6 seconds, we have developed outcrop spectra up to a period of 10 seconds.

The resulting outcrop horizontal and vertical spectra for 5 percent damping are presented on Figure 4. These outcrop spectra are the target spectra for our time history matching routine to develop spectral-matched time histories for site response analyses.

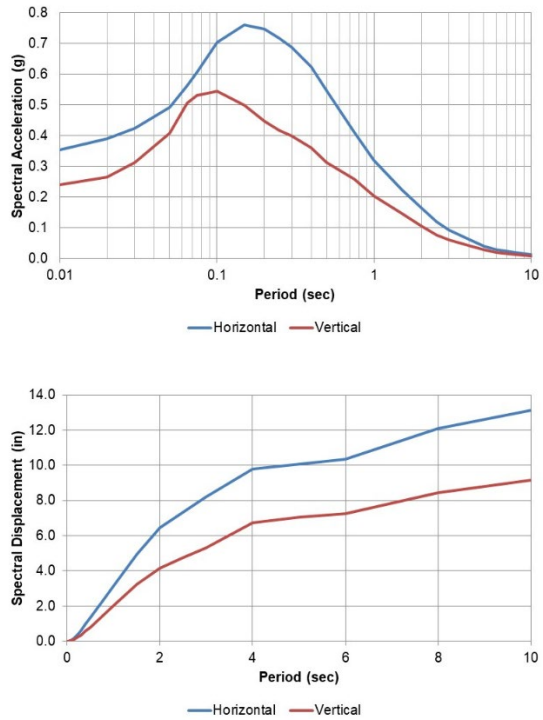

Figure 4: Site-Specific ARS Curves for Outcrop

Deaggregation Analysis

Since the target spectrum is controlled by the probabilistic spectrum, a deaggregation analysis was performed to estimate the pairs of controlling magnitude and distances for different spectral periods. Deaggregation analysis was performed to establish dominant earthquake magnitude and distance which would be key for selecting time histories. Based on the results of deaggregation analysis, the controlling seismic event is magnitude 8.3-9 associated with CSZ at a distance of about 15 to 35 km for all spectral periods. Although there are shallow crustal faults less than 15 km from the site, they don't control the hazard for this site.

Time Histories

Time histories of earthquake strong ground motions were evaluated for input into our DEEPSOIL and QUAD4M models to develop the site-specific, free field response spectrum for the existing subsurface conditions. A discussion of our time history selection process and spectral matching procedures follows.

Selection of Time Histories

We selected seven earthquake acceleration time histories for incorporation into our site response model. The time histories were chosen based on spectral shape, site conditions, moment magnitude, site distance, fault rupture mechanism and duration of strong shaking. Utilizing the criteria above, we reviewed the database at Pacific Earthquake Engineering Research (PEER) Center for NGA, the Consortium of Organizations for Strong Motion

Observation Systems (COSMOS), and California Integrated Seismic Network (CISN) and selected the strong motion records shown in Table 1. Since the seismicity of this site is controlled by CSZ for the periods of interest, selected time histories include subduction/reverse mechanisms.

Table 1: Selected Time Histories

Earthquake	Station	Lowest Usable Frequency	Mw	Dist. (km)	Mechanism
2010 Chile	Concepcion	NA	8.8	35	Subduction
2010 Chile	Matanzas	NA	8.8	38	Subduction
2011 Tohoku, Japan	IWT005	NA	9.0	50	Subduction
2011 Tohoku, Japan	IWT016	NA	9.0	56	Subduction
2003 Tokachi-Oki	HKD086	NA	8.0	117*	Subduction
1999 Chi-Chi	TCU088	0.1	7.6	18	Reverse Oblique
1999 Chi-Chi	CHY029	0.0375	7.6	11	Reverse Oblique

*Hypocentral Distance
NA = not available

Spectra-Matched Time Histories for Rock Outcrop Spectrum

Spectral matching of the selected time histories was performed using the computer program RSPMATCH (Atik and Abrahamson 2010) as implemented in the Spectral Matching module in EZ-FRISK (2016).

Figures 5 shows the Target Outcrop Spectrum, the original spectrum of the time history selected, and the spectrum after matching for one component of the 2010 Chile time history. Other time histories were matched similarly. These time histories were used in 1-D and 2-D site response analyses.

SITE RESPONSE ANALYSIS

For the longitudinal direction, the site response analyses were performed using the 2D, equivalent linear, time domain finite element computer program QUAD4M (Hudson et al. 1994). This program solves the equations of motion in the time domain and iterates to achieve compatibility between shear strain, shear moduli and damping according to specified modulus reduction and damping curves. QUAD4M incorporates a transmitting boundary (Lysmer and Kuhlemeyer 1969) at the base which allows for the absorption of outwardly propagating waves, that simulate the existence of an infinite half-space. The use of a 2D model for the longitudinal response allows the possibility of accounting for wave scattering, surface wave generation (for in-plane particle motion, i.e., Rayleigh waves), and basin edge effects. Horizontal and vertical input excitation were applied at the base of the QUAD4M model. From a wave propagation

standpoint, the horizontal and vertical input excitations correspond to SV (shear wave with in-plane motion) and P (compression) waves. QUAD4M cannot be used to model SH waves (shear waves with out of plane motion) which oscillate in the bridge-transverse direction; site response for this polarity of motion was performed using a 1D model as described below.

The 1D site response analyses in the bridge transverse direction were performed using the computer program Deepsoil Version 6.0 (Hashash 2015) in an equivalent linear mode. Deepsoil's equivalent linear analyses are performed in the frequency domain using procedures that are consistent with the well-known program SHAKE (Schnabel, et al. 1972). Soil non-linearity is accounted for using strain-dependent modulus degradation and damping curves. Similar to QUAD4M, the program iterates until compatible effective strain levels are obtained for each sub layer within the model. The 1D site response analyses were performed at the two abutments and 3 bents to cover the response along the bridge alignment in the transverse direction.

In addition, kinematic analyses were performed to assess the presence of piles on the site response. Results of all of these analyses are presented and discussed in the next section.

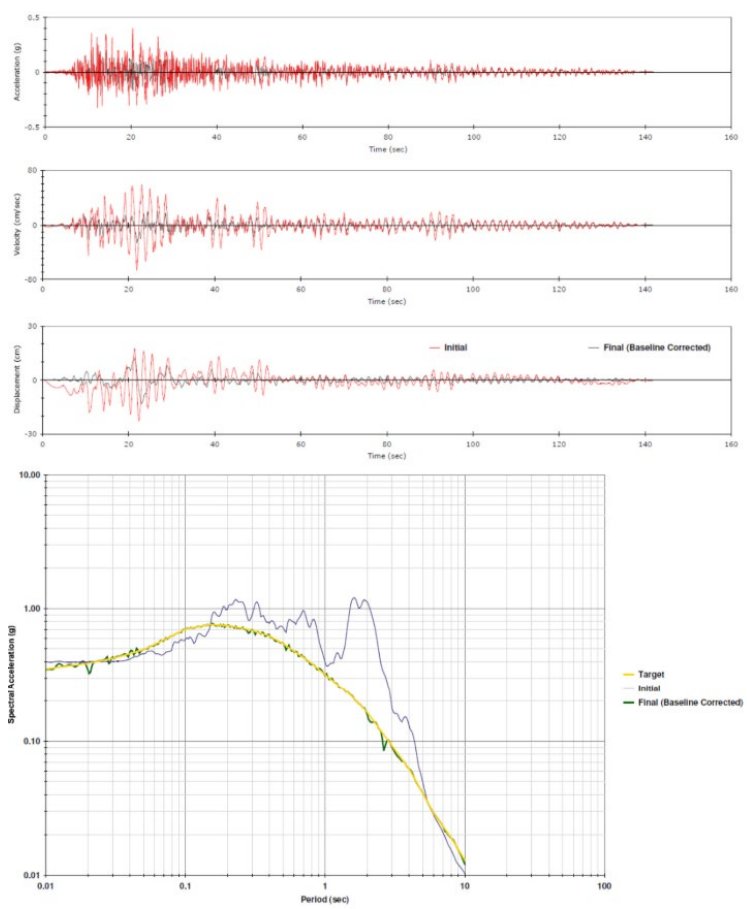

Figure 5: Time History and Spectra of Original and Matched Motions – 2010 Chile EQ – L

RESULTS AND DISCUSSIONS

Results in terms of longitudinal, transverse, and vertical time histories for acceleration, velocity and displacement and their response spectra at 10-foot vertical intervals along the pile/shaft length at each abutment and bent were obtained and provided to Caltrans. Figure 6 shows mean response spectra resulting from both 1D and 2D site response analyses. The 1D mean response spectra at Abutments 1 and 5 and at Bents 2, 3, and 4 are presented in Figure 6. The kinematic response spectrum is also presented.

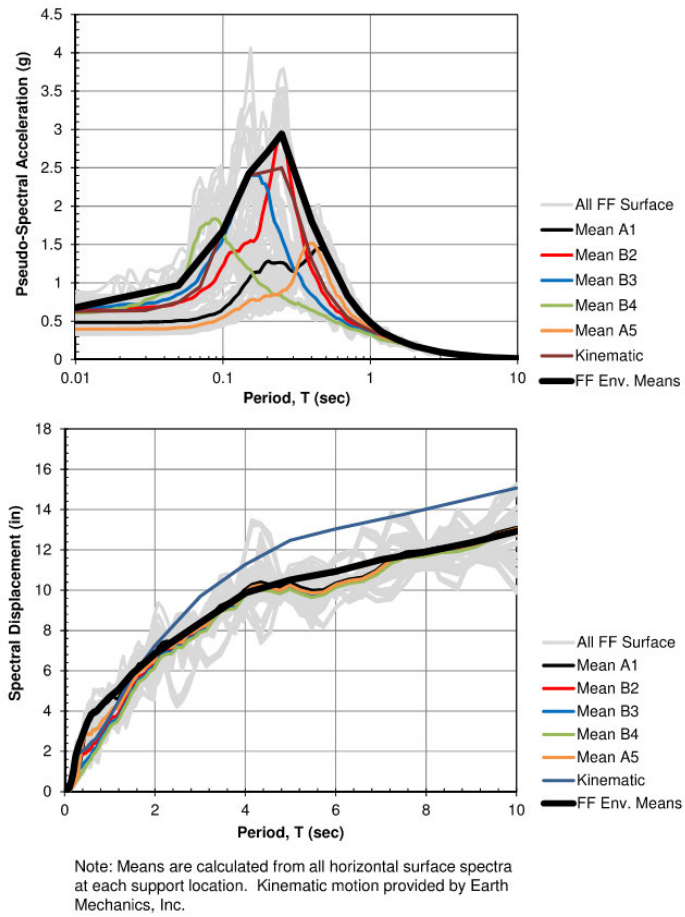

Figure 6: Summary of mean surface spectra with the envelope

Figure 7 shows all the 84th percentile spectra including the kinematic and the enveloping spectrum. The enveloping spectrum resulted from taking the envelop of mean spectrum at each abutment and bent locations instead of enveloping all surface response spectra. Figures 6 and 7 shows that different spectra are greater or smaller than each other at different periods. The enveloping 84th percentile spectrum was recommended for the design.

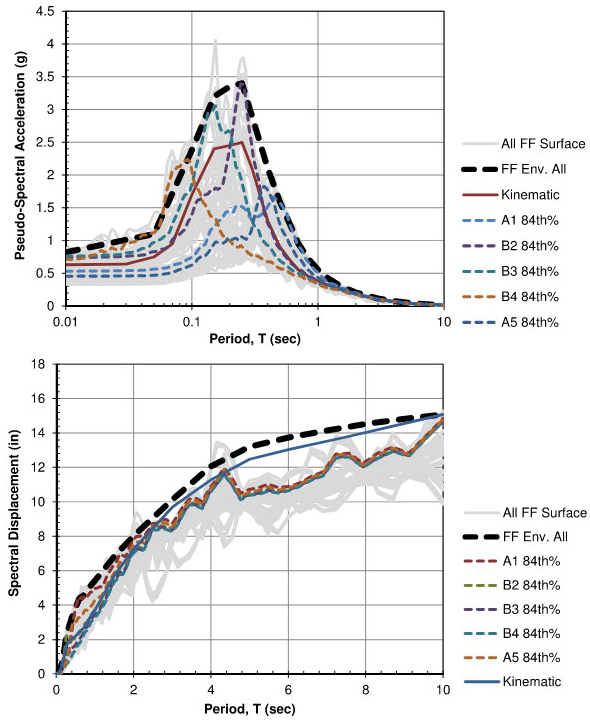

Note: 84th percentile values are calculated from all horizontal surface spectra at each support location. Free field envelope (FF Env. All) is an envelope of all the reslults except for a few oulying peaks. Kinematic motion provided by Earth Mechanics, Inc.

Figure 7: Summary of all surface 84th percentile spectra along with the enveloping spectrum.

CONCLUSIONS AND RECOMMENDATIONS

The site is underlain by a matrix of soils, gravel, cobbles, and boulders overlying bedrock. Depth to bedrock at the site varies from more than 150 feet at the south end to tens of feet at the north end. Shear wave velocity (V_S) measurement at the site involved suspension logging resulting in V_S measurements with high uncertainty. Because of this uncertainty, we pegged the rock V_S to 1,000 m/s. However, a sensitivity analysis of bedrock properties showed some increase in rock motion for different V_S values. The ground motion was developed for a return period of about 1,000 years as required by Caltrans. However, for some critical bridges in the state, Caltrans has used return period of 1,000 to 2,000 years. In addition, building codes use a return period of about 2,500 years for building designs. For a return period of 2,500 years, the spectrum is about two times the 1,000-year spectrum.

Recent studies by Stewart (2016) have also shown that site response procedures do not capture site amplification beyond the site period and typically result in unconservative values. We estimate that site period for this site is around 0.6-0.7 second. As a result of this, our 1-D and 2-D results, in the period range greater than 0.6-0.7 second, are unconservative. Therefore, we recommended that design response spectrum be adjusted beyond the site period to the free field surface response spectrum developed using GMHA. The results show that in some cases, performing 2D site response analysis is important and needed to capture the effects of site response during an earthquake.

REFERENCES

Abrahamson, N., Silva, W., and Kamai, R., 2014, Summary of the ASK14 Ground Motion Relation for Active Crustal Regions, Earthquake Spectra: August 2014, 30(3), 1025-1055.

Atik, L.A. and Abrahamson, N., 2010, An Improved Method for Nonstationary Spectral Matching, Earthquake Spectra: August 2010, 26(3), 601-617.

Atkinson, G.M. and Boore, D.M. (2003) Empirical Ground-Motion Relations for Subduction-Zone Earthquakes and Their Application to Cascadia and Other Regions. Bulletin of the Seismological Society of America, 93, 1703-1729.

Boore, D., Stewart, J., Seyhan, E., and Atkinson, G., 2014, NGA-West2 Equations for Predicting PGA, PGV, and 5% Damped PSA for Shallow Crustal Earthquakes, Earthquake Spectra: August 2014, 30(3), 1057-1085.

Campbell, K., and Bozorgnia, Y., 2014, NGA-West2 Ground Motion Model for the Average Horizontal Components of PGA, PGV, and 5% Damped Linear Acceleration Response Spectra, Earthquake Spectra: August 2014, 30(3), 1087-1115.

Chiou, B., and Youngs, R., 2014, Update of the Chiou and Youngs NGA Model for the Average Horizontal Component of Peak Ground Motion and Response Spectra, Earthquake Spectra: August 2014, 30(3), 1117-1153.

Cornell, C.A., 1968, Engineering Seismic Risk Analysis, Bulletin of the Seismological Society of America, Vol. 58, No. 5.

Cornell, C.A., 1971, Probabilistic Analysis of Damage to Structures Under Seismic Loads, Dynamic Waves in Civil Engineering, London.

DeepSoil, 2016, 1D Seismic Site Response Analysis Software, University of Illinois, Urbana Champaign.

Groholski, D., Hashash, Y., Kim, B., Musgrove, M., Harmon, J., and Stewart, J., 2016, Simplified Model for Small-Strain Nonlinearity and Strength in 1D Seismic Site Response Analysis, Journal of Geotechnical and Geoenvironmental Engineering.

Gulerce, Z. and Abrahamson, N. A. (2011), “Site-Specific Design Spectra for Vertical Ground Motion,” *Earthquake Spectra*, 27 (1), pp. 1023-1047.

Hudson, Martin B.; Beikae, Mohsen; Idriss, I. M. (1992); QUAD4M, a Computer Program to Evaluate the Seismic Response of Soil Structures Using Finite Element Procedures and Incorporating a Compliant Base, University of California, Davis

Idriss, I. M., 2014, An NGA-West2 Empirical Model for Estimating the Horizontal Spectral Values Generated by Shallow Crustal Earthquakes, Earthquake Spectra: August 2014, 30(3), 1155-1177.

Lysmer, J. and Kuhlemeyer, R. L. (1969), Finite Dynamic Model for Infinite Media, Journal of the Engineering Mechanics Division, American Society of Civil Engineers, p 860-877.

PEER, 2014, PEER NGA-West2 Database (PEER Report 2013/03), by: Timothy D. Ancheta, Robert B. Darragh, Jonathan P. Stewart, Emel Seyhan, Walter J. Silva, Brian S.J. Chiou, Katie E. Wooddell, Robert W. Graves, Albert R. Kottke, David M. Boore, Tadahiro Kishida, and Jennifer L. Donahue.

Petersen, M.D., Moschetti, M.P., Powers, P.M., Mueller, C.S., Haller, K.M., Frankel, A.D., Zeng, Yuehua, Rezaeian, Sanaz, Harmsen, S.C., Boyd, O.S., Field, Ned, Chen, Rui, Rukstales, K.S., Luco, Nico, Wheeler, R.L., Williams, R.A., and Olsen, A.H., 2014, Documentation for the 2014 Update of the United States National Seismic Hazard Maps, USGS Open-File Report 2014-1091, 243 p., https://dx.doi.org/10.3133/ofr20141091.

Risk Engineering, Inc., 2017, EZ-FRISK™ Online User's Manual, EZ-FRISK™ Version 8, Risk Engineering, Inc., Boulder, Colorado.

Youngs, R. R., S. -J. Chiou, W. J. Silva and J. R. Humphrey, 1997, Strong Ground Motion Attenuation Relationships for Subduction Zone Earthquakes, Seismological Research Letters, Vol. 68, No. 1, 58-73.

37. LiDAR-Based Delineation of Alluvial and High-Angle Fan Landforms for Hazard Recognition, Land-Use Planning, and Transportation Corridor Resilience

Jonathan R. Lovekin, P.G.
Colorado Geological Survey
1801 Moly Road
Golden, CO 80401
Phone: 303-384-2654
Email: jlovekin@mines.edu
Amy Crandall, P.E.
Colorado Geological Survey
1801 Moly Road
Golden, CO 80401
Phone: 303-384-2632
Email: acrandall@mines.edu

Acknowledgements

The authors gratefully acknowledge the Colorado Water Conservation Board for support of the alluvial- and high-angle-fan mapping effort and related post-wildfire resilience work.

The authors thank Dr. Wendy Zhou, Kassandra Lindsey, Emily Perman, Declan Knies, and F. Scott Fitzgerald for technical discussions and contributions related to data development, mapping context, project communication, and manuscript clarity.

Disclaimer

Statements and views presented in this paper are strictly those of the author(s), and do not necessarily reflect positions held by their affiliations, the Highway Geology Symposium (HGS), or others acknowledged above. The mention of trade names for commercial products does not imply the approval or endorsement by HGS.

Copyright Notice

Copyright © 2026 Highway Geology Symposium (HGS)

All Rights Reserved. Printed in the United States of America. No part of this publication may be reproduced or copied in any form or by any means – graphic, electronic, or mechanical, including photocopying, taping, or information storage and retrieval systems – without prior written permission of the HGS. This excludes the original author(s).

ABSTRACT

Repeated land-use reviews in western Colorado revealed a practical hazard-recognition problem: alluvial and high-angle fan landforms were not always consistently identified, mapped, or evaluated in existing hazard and geologic information. Although these depositional landforms influence where sediment-laden floods and debris flows intersect developed areas and transportation corridors, they were commonly generalized within broader surficial map units or obscured by development and channel modification. This paper describes the development of a statewide LiDAR-based inventory designed to improve recognition of these geomorphic receiving landforms and support screening-level geologic judgment in land-use, post-wildfire, and transportation-corridor settings.

Using 1-meter digital elevation models, terrain derivatives, slope criteria, geomorphic interpretation, quality-control review, and field verification, the Colorado Geological Survey delineated more than 8,854 alluvial and high-angle fan landforms across ten Colorado counties, with five additional counties currently undergoing quality assurance and quality control (QA/QC) review for planned production. The repeatable mapping workflow emphasizes apex position, basin and channel connectivity, fan morphology, landform preservation, and a two-axis confidence framework that independently evaluates confidence in landform identification and mapped boundary extent.

The importance of these receiving landforms became especially evident following the 2020 Grizzly Creek Fire and subsequent debris-flow impacts in Glenwood Canyon, where transportation consequences were governed not only by hazardous source basins but also by the depositional settings where sediment-laden flows emerged from confined channels and intersected Interstate 70 and other infrastructure (1). The inventory is intended as a screening-level susceptibility and exposure dataset rather than a probability model, runout model, or site-specific design tool. By systematically identifying geomorphic receiving landforms, it provides the missing geomorphic layer between source-basin hazard assessments and corridor-scale consequences, supporting hazard recognition, transportation screening, emergency planning, geotechnical asset management, and resilience-oriented decision support (2–4).

INTRODUCTION

Wildfire impacts do not end when the flames are extinguished. In steep mountain watersheds, post-fire storms can generate sediment-laden floods, debris floods, and debris flows that threaten highways, bridges, culverts, rail corridors, and other transportation infrastructure. Considerable progress has been made in identifying hazardous source basins and estimating post-fire debris-flow likelihood, volume, and rainfall-triggering conditions (5–7). For transportation agencies, however, an equally important question remains: where will those sediment-laden flows emerge from confined channels, spread across depositional landforms, and intersect critical infrastructure?

The importance of this distinction became especially apparent following the 2020 Grizzly Creek Fire and the subsequent debris-flow impacts in Glenwood Canyon, Colorado. Adjacent tributary basins experienced similar wildfire and storm conditions, yet their transportation consequences differed because of their geomorphic setting. Debris flows originated within steep source basins, but their impacts on Interstate 70 were strongly influenced by the receiving landforms where sediment accumulated before interacting with transportation infrastructure. These events demonstrated that transportation consequences are governed not solely by where hazards originate, but by the connected geomorphic system through which runoff and sediment are transferred (1).

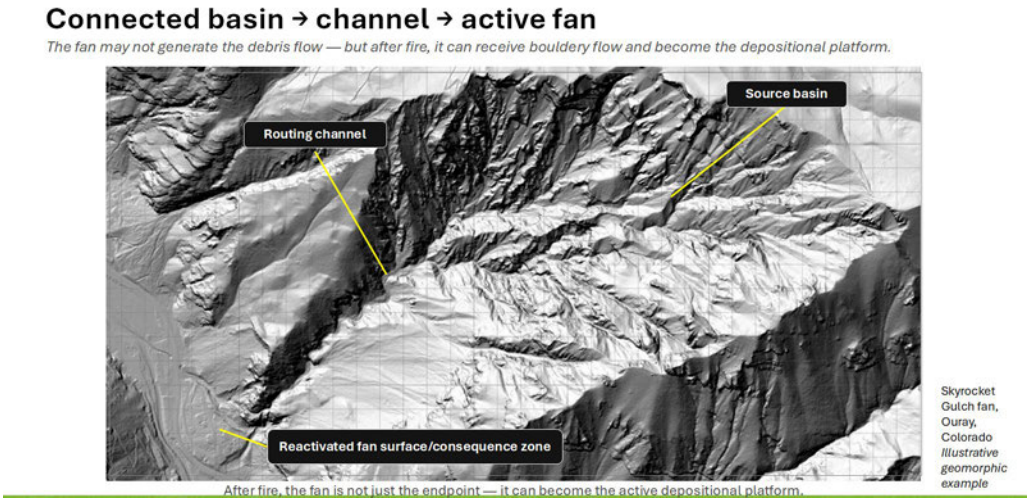

Figure 1. Conceptual Source Basin–Routing Channel–Receiving Fan Framework. Conceptual illustration of the connected geomorphic system that forms the basis for the LiDAR-Based Alluvial Fan (LAF) Inventory. Skyrocket Gulch near Ouray, Colorado, is shown as an illustrative example.

The LiDAR-based Alluvial Fan (LAF) Inventory originated from repeated Colorado Geological Survey land-use reviews conducted in western Colorado. Those reviews revealed that many alluvial and high-angle fan landforms were absent from existing geologic mapping, generalized within larger surficial map units, or partly obscured by transportation corridors, development, and channel modification. As a result, geomorphically similar landforms were not always recognized consistently despite having comparable hazard and transportation significance. These

recurring observations demonstrated the need for a systematic method to identify depositional receiving landforms consistently across Colorado.

To address this mapping gap, the Colorado Geological Survey developed the LAF Inventory, a statewide effort to systematically delineate both alluvial and high-angle fan landforms using 1-meter digital elevation models, terrain derivatives, slope criteria, geomorphic interpretation, quality-control review, and field verification. Rather than predicting when debris flows will occur, the inventory identifies where sediment-laden flows are most likely to spread, deposit, avulse, erode, or intersect transportation corridors after leaving confined mountain channels.

The mapping methodology emphasizes geomorphic connectivity between source basins, routing channels, and depositional receiving landforms. Candidate fan polygons are evaluated using apex position, basin connectivity, landform morphology, terrain derivatives, and supporting field evidence. Because transportation corridors frequently modify or obscure original depositional surfaces, mapped polygons are assigned two independent confidence measures: one reflecting confidence that the mapped feature represents an alluvial or high-angle fan landform, and a second reflecting confidence in the interpreted boundary extent. This two-axis confidence framework explicitly communicates mapping uncertainty while preserving the screening value of reconstructed landforms in modified transportation corridors.

Recent work within the Highway Geology Symposium community has increasingly emphasized corridor-scale geohazard management, geotechnical asset management, transportation resilience, and decision-support systems for infrastructure management. Oester (2) described the implementation of geotechnical asset management in Colorado, Post et al. (3) demonstrated corridor-scale geohazard management along Colorado State Highway 133, and Post and Wade (4) expanded this concept into integrated geohazard decision support for resilient transportation infrastructure. The LAF Inventory complements these efforts by providing the missing geomorphic receiving-landform layer that links source-basin hazard assessments with transportation consequences.

The resulting inventory represents a screening-level susceptibility and exposure dataset rather than a probability model, runout model, or engineering design product. Source-basin models estimate where hazardous flows may originate, while engineering analyses evaluate site-specific mitigation and design. The LAF Inventory identifies the depositional receiving landforms where transportation consequences are most likely to develop, providing a practical decision-support dataset that strengthens hazard recognition, corridor screening, emergency planning, transportation asset management, and resilience-oriented decision making.

PROJECT BACKGROUND

The LAF Inventory originated from repeated Colorado Geological Survey land-use reviews conducted throughout western Colorado. During those reviews, recurring questions arose about whether existing geologic mapping adequately identified alluvial fan landforms for hazard evaluation and land-use decision-making. Although many fan deposits had been mapped as generalized Quaternary units, the individual depositional landforms themselves were frequently absent, incompletely delineated, or difficult to recognize where highways, development, channel modification, or vegetation obscured their geomorphic expression.

These observations became particularly apparent during hazard reviews in Pitkin County, where planning staff questioned whether existing mapping provided sufficient detail to support consistent evaluation of alluvial-fan hazards. While the immediate question concerned individual development proposals, the broader implication was that similar landforms across Colorado were not being recognized consistently because available mapping products had been developed for different purposes and at different mapping scales. The recurring nature of these observations demonstrated that the issue extended beyond any individual county or development proposal. Existing statewide geologic maps remain essential for understanding regional geology, surficial materials, and geologic history, but they were generally not intended to systematically identify individual depositional fan landforms or evaluate their geomorphic connectivity to upstream drainage basins. Consequently, comparable landforms were sometimes interpreted differently during hazard evaluations despite exhibiting similar geomorphic characteristics.

These observations led to the development of the LAF Inventory as a systematic statewide effort to identify alluvial and high-angle fan landforms using consistent geomorphic criteria. Rather than replacing existing geologic mapping, the inventory provides an additional geomorphic dataset designed specifically to improve recognition of depositional receiving landforms during hazard screening, land-use review, and related geologic evaluations.

ALLUVIAL AND HIGH-ANGLE FANS AS RECEIVING LANDFORMS

Alluvial and high-angle fans are depositional landforms that develop where sediment-laden flow exits a confined mountain channel and spreads across a lower-gradient surface. These landforms evolve through repeated episodes of debris flows, debris floods, hyperconcentrated flows, and fluvial deposition, producing geomorphic receiving environments that commonly accumulate sediment over long periods.

Traditional post-fire hazard investigations have focused primarily on identifying where hazardous flows initiate by evaluating factors such as burn severity, rainfall intensity, watershed characteristics, and basin morphology (5–7). Those investigations have substantially improved understanding of debris-flow initiation and source-basin susceptibility. However, source-basin analyses alone do not identify where sediment-laden flows ultimately emerge from confined channels or where they are most likely to spread across depositional surfaces.

The LAF Inventory addresses this complementary geomorphic question by systematically identifying receiving landforms connected to upstream drainage basins. These mapped landforms do not predict the occurrence, probability, magnitude, or timing of future debris flows, nor do they represent runout modeling or engineering design. Instead, they identify geomorphic settings where sediment-laden flows have repeatedly deposited material and where future depositional processes may reasonably be expected to occur if sediment reaches the fan surface.

Systematic identification of receiving landforms also provides a consistent framework for evaluating geomorphic connectivity between source basins and downstream depositional environments. This emphasis on connected geomorphic systems forms the basis for the LiDAR mapping methodology described in the following section.

RECEIVING LANDFORMS AND TRANSPORTATION CONSEQUENCES

Throughout this paper, alluvial and high-angle fans are treated as receiving landforms within a connected geomorphic system. Their importance lies not simply in their morphology, but in their geomorphic connectivity to sediment-producing basins and in their potential to receive sediment-laden flows after those flows leave confined mountain channels. Consequently, hazard recognition depends not only on identifying depositional landforms, but also on understanding their relationship to upstream source basins and the downstream transportation and community assets they support.

From a screening perspective, geomorphic connectivity is therefore as important as the presence of landforms. A fan disconnected from an active source basin presents a fundamentally different hazard-screening problem than a fan directly below a steep watershed that can produce post-fire debris flows or sediment-laden floods. Likewise, a fan that crosses Interstate 70, a bridge approach, a culvert, a rail corridor, or an emergency-access route has greater practical significance than an otherwise similar landform without exposed infrastructure.

The LAF Inventory complements source-basin hazard assessments by identifying the depositional receiving landforms where transportation and land-use consequences are most likely to develop if an upstream hazard is realized. Rather than predicting when hazardous flows will occur, the inventory identifies where those flows are most likely to spread, deposit, avulse, or intersect developed corridors after leaving confined mountain channels.

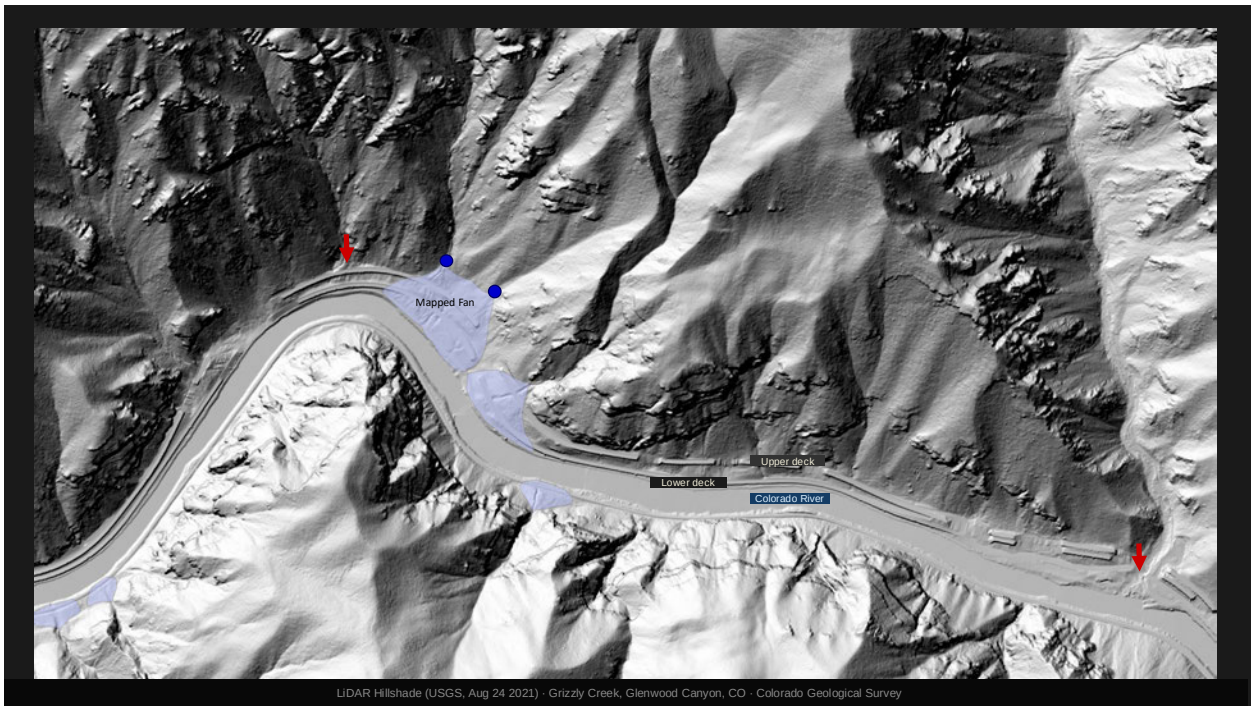

Figure 2. Mapped Alluvial Fan Landforms Along Interstate 70 in Glenwood Canyon.

The Glenwood Canyon corridor illustrates this relationship well. Numerous tributary drainages emerge from confined bedrock channels onto mapped alluvial and high-angle fan landforms

before intersecting Interstate 70 and the Colorado River. These depositional receiving landforms are not always readily apparent on conventional geologic mapping or aerial imagery, yet they strongly influence where sediment accumulates and where transportation consequences develop.

Figure 3. Contrasting Transportation Consequences in Adjacent Post-Fire Drainages.

Figure 3 illustrates this concept by comparing two adjacent tributary drainages that experienced similar wildfire and storm conditions but produced different transportation consequences because of their geomorphic setting. The drainage on the left lacks a mapped receiving fan because the canyon wall, the Colorado River, and the transportation corridor offer little opportunity for deposition before sediment reaches the highway. In contrast, the drainage on the right is connected to a mapped alluvial fan that provides a depositional surface where sediment spreads before intersecting Interstate 70. Although hazardous flows originate within the upstream basin, the receiving landform largely governs where corridor-scale consequences develop (1).

WHY A NEW INVENTORY WAS NEEDED

Conventional geologic mapping and LiDAR-based geomorphic mapping answer different, but complementary, questions.

Regional and detailed geologic maps correctly identify alluvium, colluvium, terraces, glacial deposits, and other surficial materials while providing the geologic framework needed for engineering, hydrogeologic, and scientific investigations. However, screening-level evaluation of post-fire hazards and sediment-routing processes requires a different level of geomorphic interpretation. Rather than asking *What surficial deposit is present?*, screening commonly requires answers to questions such as: *Where is the receiving fan? Which basin and channel feed it? Where is the depositional surface most likely to intersect transportation infrastructure?*

LiDAR-derived terrain models make these questions easier to answer by revealing subtle geomorphic features - including apexes, fan margins, slope breaks, abandoned distributary channels, and depositional surfaces - that may be difficult to recognize using conventional geologic mapping, aerial imagery, or field observations alone.

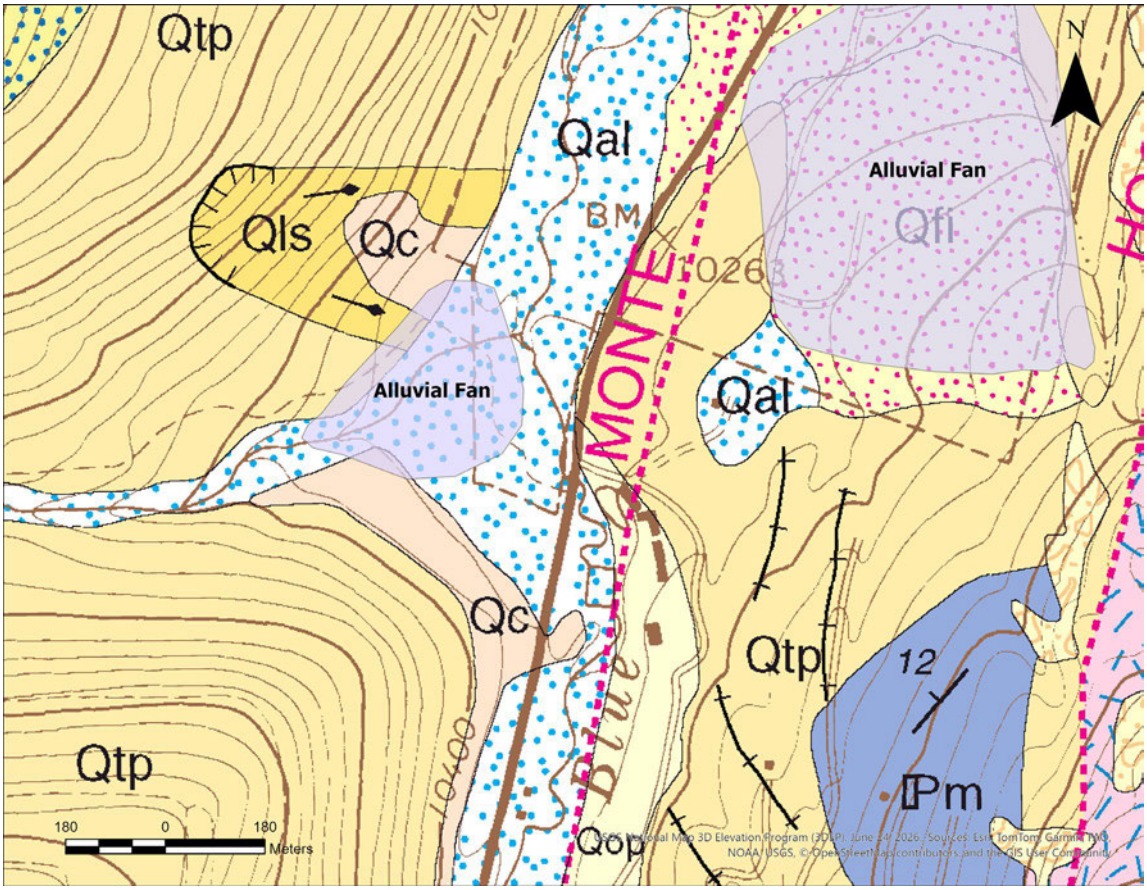

Figure 4. Conventional Surficial Geologic Mapping with LiDAR-Derived Alluvial Fan Delineation. (9)

Conventional geologic mapping identifies surficial deposits, whereas LiDAR-based geomorphic interpretation delineates individual alluvial fan landforms based on fan morphology, basin connectivity, and depositional receiving zones. The LiDAR-derived inventory complements, rather than replaces, conventional geologic mapping by providing the geomorphic framework needed for screening-level hazard recognition and transportation applications.

The distinction is therefore one of purpose rather than accuracy. Conventional geologic maps describe the distribution, origin, and relative age of surficial materials. The LAF Inventory identifies connected depositional landforms and their relationship to upstream drainage basins, providing a consistent geomorphic framework for screening-level hazard recognition. The following section describes the data sources and repeatable mapping methodology used to develop that inventory.

DATA SOURCES AND MAPPING WORKFLOW

The LAF Inventory workflow combines high-resolution LiDAR-derived terrain data with geomorphic interpretation, quality-control review, and field verification to systematically identify depositional receiving landforms across Colorado (8). Although developed to support hazard recognition and land-use review, the methodology is equally applicable to transportation corridor screening and other regional geologic investigations.

The mapping process was designed to be repeatable while preserving professional geologic judgment. Rather than relying on automated landform classification, the workflow applies consistent geomorphic criteria to guide interpretation across all mapped counties. LiDAR-derived terrain models provide the primary mapping base, while terrain derivatives, watershed characteristics, drainage connectivity, and geomorphic context are integrated during interpretation.

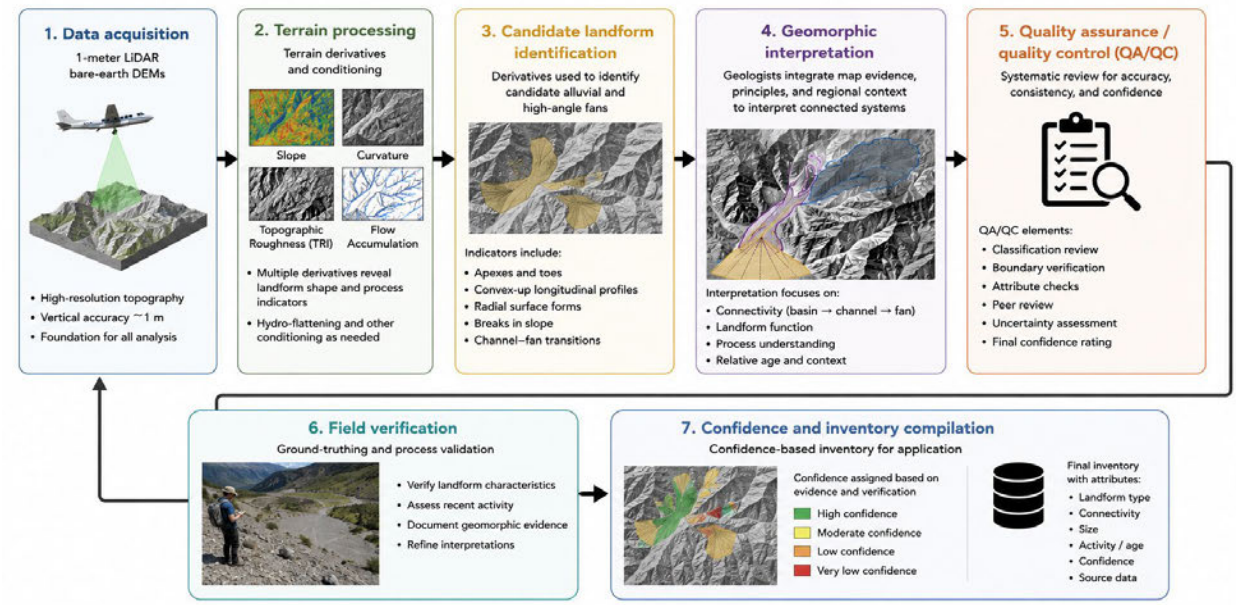

Figure 5. Repeatable LiDAR-based mapping workflow illustrating data acquisition, terrain processing, geomorphic interpretation, quality assurance, field verification, confidence assessment, and final inventory compilation.

Mapping begins by identifying candidate alluvial and high-angle fan landforms at basin mouths and locations where confined channels emerge onto lower-gradient terrain. Candidate polygons are then evaluated using multiple geomorphic criteria, including apex position, basin and channel connectivity, fan morphology, terrain derivatives, slope characteristics, and supporting geomorphic evidence. Polygon boundaries are interpreted manually using these complementary datasets rather than generated through automated classification alone.

Each mapped polygon undergoes quality-control review and, where practical, field verification. Quality assurance focuses on consistency of landform interpretation, polygon geometry, drainage connectivity, and mapped extent across the statewide inventory. Field observations are used to

verify geomorphic interpretation, refine mapped boundaries where necessary, and improve consistency between counties.

Because landform recognition and boundary interpretation involve different sources of uncertainty, each polygon is assigned two independent confidence measures. The first evaluates confidence that the mapped feature represents an alluvial or high-angle fan landform based on available geomorphic evidence. The second evaluates confidence in the interpreted polygon boundary, recognizing that development, transportation corridors, channel modification, vegetation, and erosion may partially obscure original depositional surfaces. Evaluating these components independently allows the inventory to communicate mapping uncertainty without reducing its usefulness for screening-level applications.

Application of this workflow produced a consistent statewide inventory of alluvial and high-angle fan landforms suitable for regional screening and comparison. The characteristics of the completed inventory are presented in the following Results section.

CLASSIFICATION CRITERIA

Slope is useful for classifying landforms, but geomorphic connectivity explains their significance within a hazard-screening framework. In this inventory, mapped polygons were classified as alluvial fans where the mean landform slope was less than or equal to 20 degrees and as high-angle fans where the mean landform slope exceeded 20 degrees. The 20-degree threshold provides a practical mapping classification rather than a strict geomorphic or process boundary.

Landform classification alone, however, was not sufficient for inventory development. Candidate landforms were also evaluated for geomorphic connectivity to upstream drainage basins. The primary screening question was whether the mapped depositional surface remained connected to a basin and channel system capable of delivering sediment-laden flows onto the fan. Mean slope describes the landform; basin–channel–fan connectivity explains its significance for screening-level hazard recognition.

Classification therefore relied on multiple complementary lines of geomorphic evidence rather than any single terrain metric or automated GIS classification. Mean slope, apex position, basin connectivity, landform morphology, terrain derivatives, and depositional setting were evaluated together to determine whether a candidate polygon represented an alluvial or high-angle fan appropriate for inclusion in the inventory (8).

MAPPING MODIFIED TRANSPORTATION CORRIDORS

Transportation corridors present one of the greatest challenges in delineating alluvial and high-angle fan landforms. Roads, fills, cuts, culverts, bridges, retaining walls, channel modifications, utilities, and urban development commonly obscure, modify, or remove portions of the original depositional surface. Consequently, mapped polygons represent the best-supported interpretation of the depositional landform rather than a precise representation of every preserved surface.

Modified fan boundaries were treated similarly to interpreted geologic contacts. Some boundaries were directly observed, some were approximate, and others were inferred where anthropogenic modification obscured the original geomorphic expression. Interpretation

incorporated multiple independent lines of evidence, including apex position, basin and channel connectivity, preserved lateral margins, slope breaks, radial contour patterns, distributary swales, historical imagery, cut-slope exposures, culvert and outfall relationships, and continuity with adjacent unmodified fan sectors.

The mapping process did not treat obscured ground as observed ground. Where transportation infrastructure concealed portions of a fan, the mapped extent reflected the degree of supporting evidence. Strong geomorphic evidence supported interpretation of reconstructed boundaries. Partial evidence resulted in lower confidence or inferred boundaries. Where evidence was insufficient to define a defensible depositional footprint, no polygon was mapped.

In modified transportation corridors, the most reliable interpretations commonly resulted from convergence of several independent observations rather than recognition of a single diagnostic landform. As a practical mapping criterion, polygons were retained only where the apex location, basin connectivity, and at least one additional geomorphic control were independently supported by LiDAR, imagery, historical information, or field observations. Where this threshold was not achieved, boundaries were classified as inferred or omitted from the final screening inventory.

Table 1. Evidence Framework for Delineating Alluvial and High-Angle Fan Landforms in Modified Transportation Corridors

Evidence Type	Primary Contribution	Common Failure Mode	Use in Confidence Assignment
LiDAR hillshade and DEM derivatives	Identify apexes, margins, slope breaks, swales, radial slope decay, and toe trimming.	Road benches, fills, berms, and retaining walls can mimic landform edges.	High when morphology is coherent; moderate when only partial remnants are preserved.
Basin-to-corridor connectivity	Confirms connection to an upstream source basin and channel.	Modern culverts or ditches may reflect engineered rerouting.	Separate apex/pathway confidence from distal-boundary confidence.
Current and historical imagery	Documents landform continuity, disturbance history, and pre-widening surfaces.	Vegetation, grading, misregistration, incomplete coverage.	Upgrade confidence where imagery agrees with LiDAR and field evidence.
Field observations and cut exposures	Checks sedimentology and geomorphic context.	Road fill or riprap mistaken for natural deposits.	Confirm, downgrade, or withhold mapped boundaries.
Do-not-map threshold	Prevents false precision.	Pressure to complete coverage.	Omit or flag low-confidence rather than present a speculative polygon.

Evidence used to delineate alluvial and high-angle fan landforms where transportation infrastructure has modified or obscured original depositional surfaces. Multiple independent lines of geomorphic evidence were evaluated before reconstructed polygons were retained in the statewide inventory.

QUALITY CONTROL AND CONFIDENCE

Quality control evaluated both GIS geometry and geomorphic interpretation. Candidate polygons were reviewed for apex position, basin connectivity, polygon geometry, drainage relationships, landform morphology, slope characteristics, classification consistency, and agreement with adjacent terrain. Review emphasized statewide consistency so that comparable landforms were interpreted using the same geomorphic criteria regardless of county.

Each polygon was evaluated using two independent confidence measures:

- Landform confidence, representing confidence that the mapped feature is an alluvial or high-angle fan based on available geomorphic evidence.

- Boundary confidence, representing confidence in the interpreted extent of the mapped landform, particularly where transportation corridors, development, or channel modification obscure original depositional surfaces.

Evaluating these confidence measures independently recognizes that identification of a landform and delineation of its boundaries involve different sources of uncertainty. In many modified transportation corridors, the presence of a fan is well supported while portions of its distal boundary remain interpretive. Separating these assessments communicates uncertainty more effectively than assigning a single confidence value to the entire polygon.

High-confidence polygons exhibit a clearly defined apex, direct basin connectivity, preserved fan morphology, identifiable lateral margins or slope breaks, and corroborating historical or field evidence. Moderate-confidence polygons retain strong geomorphic support but include one or more partially reconstructed boundaries. Low-confidence polygons possess suggestive geomorphic characteristics but insufficient evidence to delineate a defensible depositional footprint. In these situations, polygons were either retained as preliminary screening features with appropriately reduced confidence or omitted from the final inventory.

Surface-state attributes further distinguish preserved, partly modified, highly modified, and reconstructed landform extents, allowing users to understand both the confidence of interpretation and the degree of anthropogenic modification.

The resulting confidence framework is intended to communicate mapping uncertainty explicitly while preserving the value of the inventory as a screening-level geomorphic dataset. It does not imply the probability of future debris-flow occurrence, predict runout, or replace site-specific engineering investigations. Instead, it provides a transparent and repeatable method for documenting professional geomorphic interpretation within a statewide inventory.

RESULTS

The completed LAF Inventory currently includes 8,854 mapped alluvial and high-angle fan landforms distributed across ten Colorado counties, with five additional counties currently undergoing quality assurance and quality control (QA/QC) review for planned publication. Figure 6 illustrates the current geographic extent of the completed inventory and counties presently in progress.

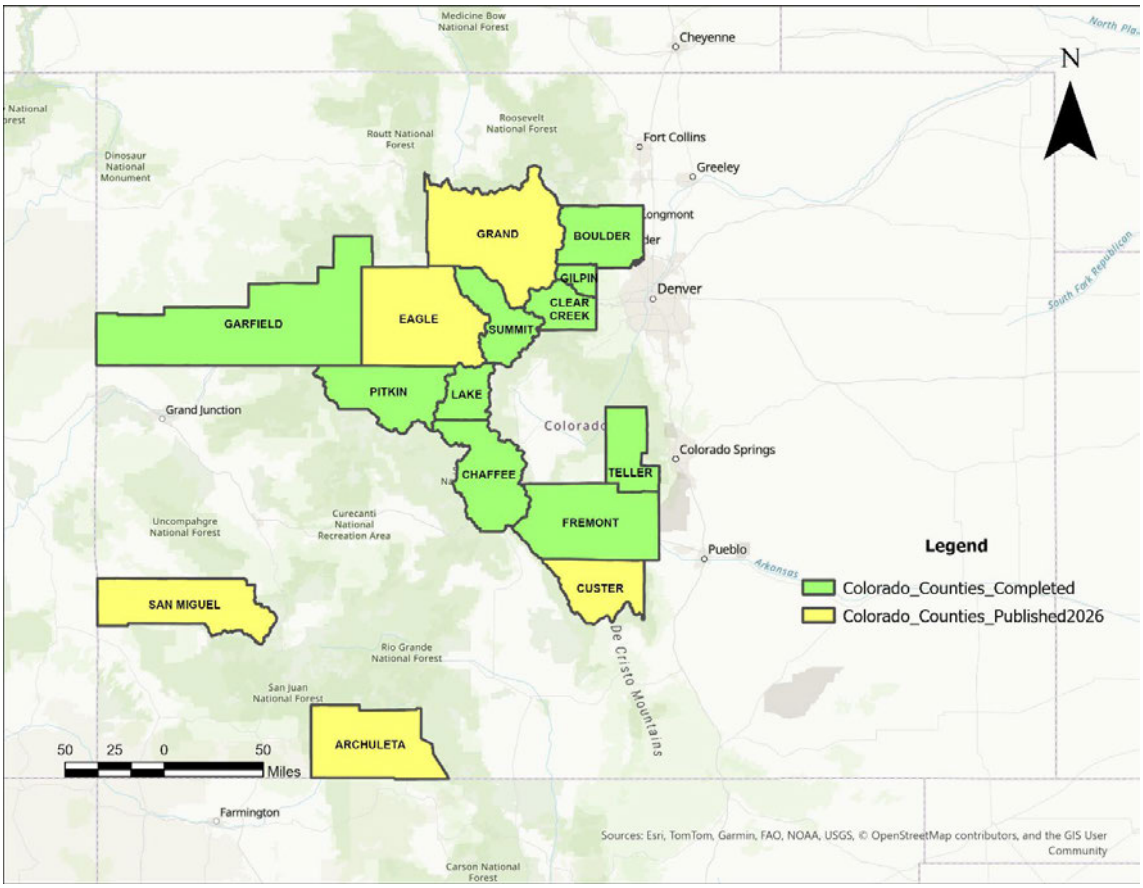

Figure 6. LiDAR-Based Alluvial Fan Inventory Coverage in Colorado. Current status of the Colorado Geological Survey's LiDAR-Based Alluvial Fan (LAF) mapping project. Green counties represent the ten completed inventory areas included in this study (Boulder, Chaffee, Clear Creek, Fremont, Garfield, Gilpin, Lake, Pitkin, Summit, and Teller). Yellow counties represent five additional inventory areas (Archuleta, Custer, Eagle, Grand, and San Miguel) that are currently in QA/QC review and planned for publication in 2026. County boundaries are shown for project context. Base map sources: Esri, TomTom, Garmin, FAO, NOAA, USGS, © OpenStreetMap contributors, and the GIS User Community.

The completed inventory is among the largest systematic compilations of alluvial and high-angle fan landforms currently available in Colorado. Although mapped landforms vary substantially in size, morphology, preservation, and degree of anthropogenic modification, application of a consistent statewide workflow produced a uniform inventory suitable for regional screening and comparison. Summary characteristics of the completed inventory are presented in Table 2.

Table 2. Summary of the Completed LiDAR-Based Alluvial and High-Angle Fan Inventory	
Inventory Characteristic	**Value**
Counties completed	10
Counties in progress	5
Total mapped fan landforms	8,854
Alluvial fans	7,093 (80.1%)
High-angle fans	1,761 (19.9%)
Mean mapped fan area	6.96 ac
Median mapped fan area	1.81 ac
Largest mapped fan	868.8 ac
Smallest mapped fan	0.005 ac

Summary statistics for the completed LiDAR-Based Alluvial Fan (LAF) Inventory across ten Colorado counties. Area statistics were calculated from polygon geometry. Records with invalid geometry were retained in inventory totals but excluded from area calculations.

While Table 2 summarizes the overall characteristics of the completed inventory, Table 3 quantifies the relationship between mapped alluvial and high-angle fan landforms and the Colorado Department of Transportation highway network. Spatial comparison with the highway network demonstrates the widespread occurrence of mapped receiving landforms adjacent to transportation corridors.

The inventory also documents that receiving landforms commonly intersect transportation infrastructure. Numerous highways, bridge approaches, culverts, maintenance facilities, rail corridors, and community access routes occupy mapped alluvial and high-angle fan landforms. These observations indicate that interactions between depositional receiving landforms and transportation infrastructure are widespread across Colorado rather than isolated to individual corridors.

Mapped alluvial and high-angle fan landforms occur throughout mountain regions of western and central Colorado and are commonly associated with tributary drainages that emerge from confined bedrock channels onto lower-gradient valley surfaces. Although individual landforms vary considerably in size, morphology, preservation, and degree of modification, application of a consistent statewide mapping methodology produced a uniform inventory suitable for regional screening and comparison among counties.

Table 3. Proximity of Mapped Alluvial and High-Angle Fan Landforms to Colorado Department of Transportation Highways				
CDOT Highway Class	**Fans Within 100 m (n)**	**Fans Within 100 m (%)**	**Fans Directly Crossed (n)**	**Fans Directly Crossed (%)**
Interstate	110	1.2	16	0.2
Principal Arterial	264	3.0	74	0.8
Minor Arterial	300	3.4	77	0.9
Collector	116	1.3	54	0.6
Any Highway (Overall)	779	8.8	219	2.5

Relationship between mapped alluvial and high-angle fan landforms and Colorado Department of Transportation functional-class highways. "Within 100 m" identifies mapped fan polygons located within a 100-m buffer of highway centerlines. "Directly Crossed" identifies fan polygons intersected by mapped highway centerlines. Highway functional classes are not mutually exclusive because individual fan landforms may intersect multiple roadway classes.

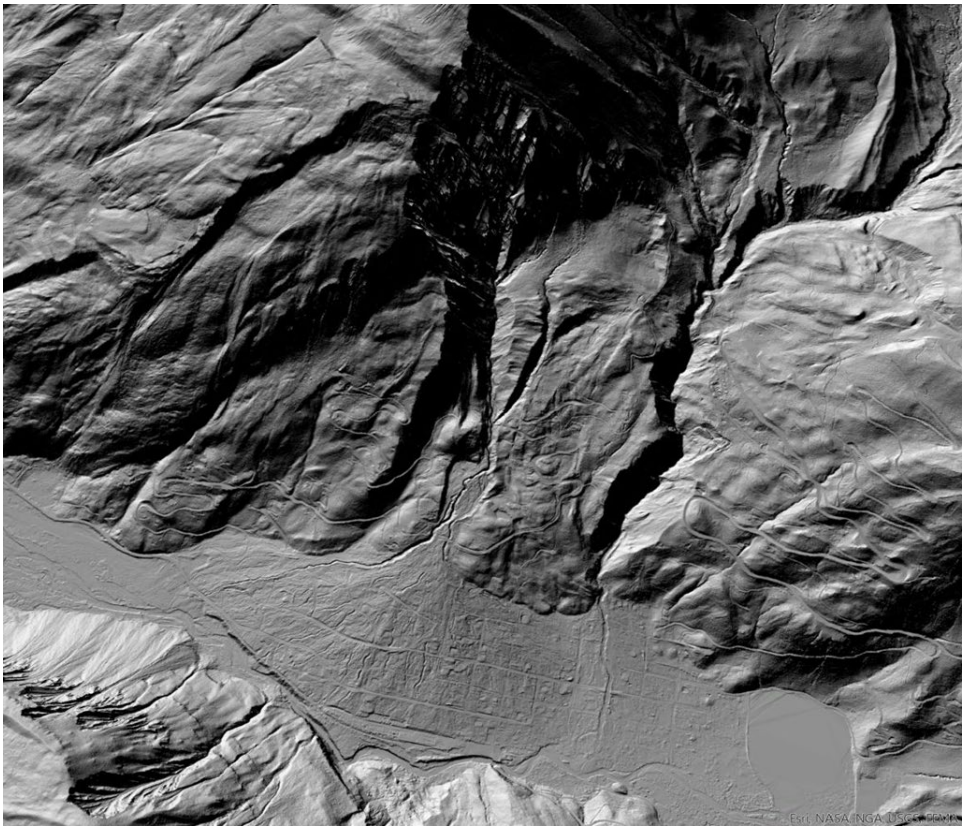

Figure 7. LiDAR-Based Recognition of Alluvial Fan Morphology in Marble, Colorado. Bare-earth LiDAR hillshade reveals the morphology and extent of the alluvial fan underlying the developed portion of Marble, Colorado. The example illustrates how LiDAR-based geomorphic interpretation can identify depositional receiving landforms beneath existing development, supporting regional hazard recognition, land-use review, and transportation corridor screening.

The Marble example illustrates how LiDAR-derived terrain models improve recognition of depositional landforms that have been modified by development while preserving sufficient geomorphic evidence to support consistent interpretation. Similar relationships between mapped fan landforms and transportation infrastructure were observed throughout the inventory, although the degree of preservation and anthropogenic modification varied among counties.

The statewide inventory establishes a consistent regional dataset describing the distribution and geomorphic characteristics of alluvial and high-angle fan landforms. The following section examines how this inventory can be applied as a screening-level decision-support resource for transportation planning, hazard recognition, emergency response, and related geologic applications.

APPLICATIONS FOR DECISION SUPPORT

The LAF Inventory extends beyond traditional geomorphic mapping by providing transportation agencies and land-use practitioners with a screening-level framework for recognizing depositional receiving environments that influence infrastructure exposure during post-fire debris flows, sediment-laden floods, and related geomorphic hazards. Although the inventory does not predict debris-flow occurrence or replace engineering analyses, it identifies where transportation assets occupy geomorphic settings that may concentrate sediment deposition and flood impacts.

Rather than replacing source-basin hazard models, rainfall-threshold analyses, or site-specific engineering investigations, the inventory complements them by identifying the connected receiving landforms where transportation and land-use consequences are most likely to develop. In this way, the inventory provides the missing geomorphic layer linking hazard initiation with downstream infrastructure consequences.

Land-Use Applications

For land-use review, the inventory improves early hazard recognition by helping reviewers identify whether proposed development occupies a depositional receiving landform and whether that landform remains connected to a basin capable of producing debris flows, debris floods, or sediment-laden floods. The inventory also helps determine when generalized mapping may be insufficient and when additional site-specific geologic evaluation is appropriate.

The inventory does not replace field investigation, professional judgment, or engineering studies. Instead, it supports more informed screening decisions by identifying locations where additional geologic investigation may be warranted before development proceeds.

Transportation Applications

For transportation agencies, the inventory functions as a receiving-landform layer within a broader corridor-scale decision-support framework.

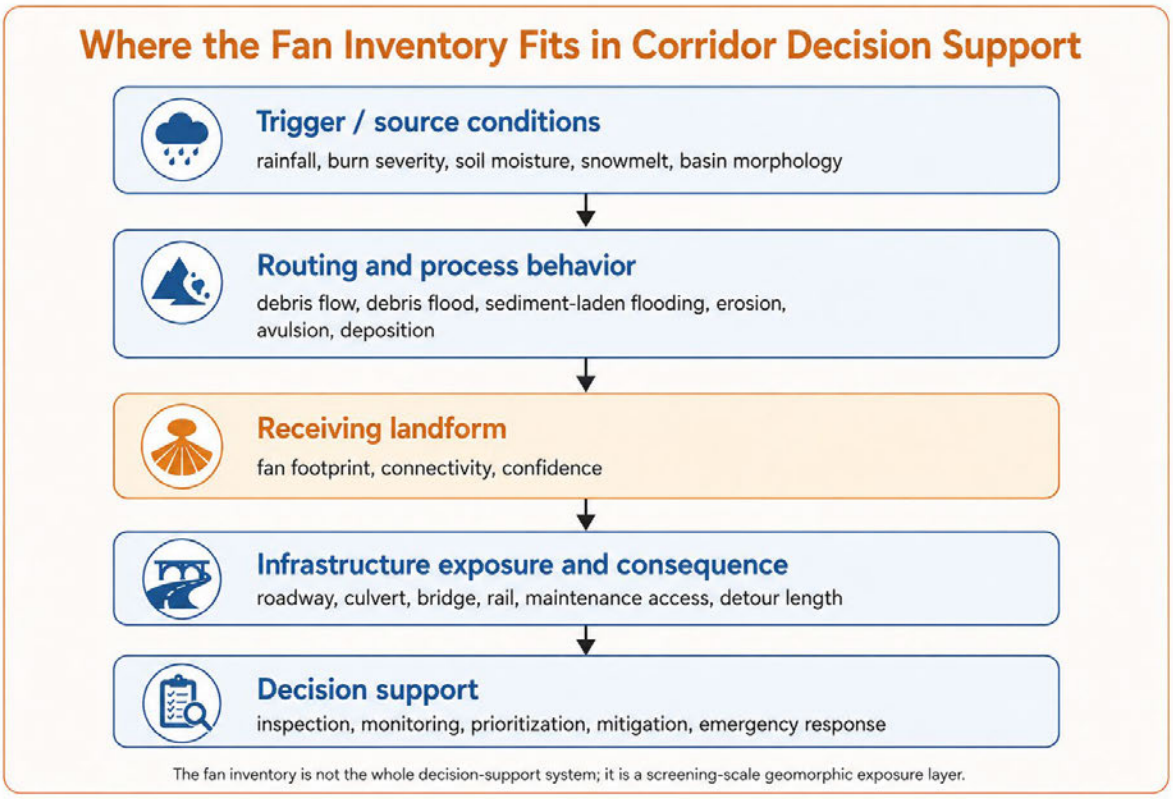

Figure 8. Conceptual decision-support framework illustrating how interpreted receiving-landform polygons complement source-basin analyses, infrastructure inventories, monitoring, and engineering evaluation. The LiDAR-based Alluvial Fan Inventory provides a screening-level geomorphic exposure layer rather than a probability model or engineering design tool.

Within this framework, fan polygons can be integrated with burned-basin mapping, rainfall thresholds, post-fire probability models, bridge and culvert inventories, roadway criticality, traffic volumes, emergency-access requirements, maintenance history, and other transportation datasets. The inventory helps identify locations where sediment-laden flows are geomorphically predisposed to emerge from confined channels and intersect transportation infrastructure.

In post-fire settings, the inventory supports rapid corridor screening and prioritization. During routine operations, it provides a consistent geomorphic framework for field investigations, maintenance planning, monitoring, and subsequent engineering evaluation. Dynamic information—including burn severity, rainfall forecasts, snowmelt, soil moisture, observed movement, and other monitoring data—can be combined with the mapped inventory to improve situational awareness and decision support while maintaining the central role of field verification and professional geologic judgment.

RELATIONSHIP TO RECENT HGS WORK

Recent Highway Geology Symposium contributions provide both the operational motivation and the broader decision-support context for this inventory. Debelak, Kidner, and colleagues

documented the Grizzly Creek Fire, subsequent debris-flow impacts to Interstate 70 in Glenwood Canyon, and the application of post-fire debris-flow modeling to emergency planning, mitigation, and recovery (1). Their work illustrates the practical transportation problem that motivates this study.

Post et al. presented a corridor-scale geohazard management approach for Colorado State Highway 133 (3), while Post and Wade subsequently described an integrated decision-support framework for resilient transportation infrastructure (4). The LiDAR-based Alluvial Fan Inventory complements these efforts by providing a geomorphic input layer that identifies the depositional receiving landforms where hazardous processes and transportation infrastructure intersect.

The inventory is not intended to function as a hazard model, probability model, or engineering design product. Rather, it provides a screening-level geomorphic exposure layer that strengthens corridor-scale geohazard management by improving recognition of receiving landforms and their relationship to transportation assets.

This work also extends Colorado's geotechnical asset management framework described by Oester (2). In that context, mapped alluvial and high-angle fan landforms become another geospatial layer that supports transportation resilience, infrastructure prioritization, and risk-informed decision-making. Dynamic datasets—including satellite observations, rainfall thresholds, soil-moisture monitoring, and future decision-support tools—are strengthened when interpreted within an accurate geomorphic framework.

LIMITATIONS

The LiDAR-based Alluvial Fan Inventory is a screening-level susceptibility and exposure dataset. It is not a probability model, debris-flow runout model, hydraulic model, or site-specific engineering design product. It does not estimate event frequency, triggering rainfall, flow depth, velocity, runout extent, or design loads, nor does it replace detailed geologic mapping, hydrologic or hydraulic analyses, debris-flow modeling, geotechnical investigation, or engineering design.

Mapping quality depends upon LiDAR resolution, vegetation cover, preservation of original landforms, anthropogenic modification, historical information, imagery, and field observations. In developed transportation corridors, portions of mapped boundaries may necessarily be interpreted beneath fills, pavement, channel modifications, or other infrastructure. These interpreted boundaries are intended for screening and prioritization rather than regulatory or engineering delineation.

The explicit treatment of mapping uncertainty is therefore a deliberate feature of the methodology rather than a limitation of the inventory. Professional geomorphic interpretation, supported by the two-axis confidence framework, provides users with a transparent understanding of both landform identification and mapped boundary confidence while preserving the usefulness of the inventory for screening-level applications.

CONCLUSIONS

This study presents a repeatable LiDAR-based methodology for systematically identifying and delineating alluvial and high-angle fan landforms across Colorado. The resulting statewide inventory currently includes more than 8,854 mapped alluvial and high-angle fan landforms distributed across ten completed Colorado counties, with five additional counties currently undergoing quality assurance and quality control (QA/QC) review for planned publication.

The principal scientific contribution is recognition of depositional receiving landforms as the missing geomorphic layer linking source-basin hazards to downstream transportation and land-use consequences. By emphasizing geomorphic connectivity rather than landform morphology alone, the inventory improves understanding of where sediment-laden flows are most likely to intersect infrastructure after leaving confined mountain channels.

A repeatable statewide mapping methodology, supported by quality-control review, field verification, and a two-axis confidence framework, provides a transparent approach for documenting professional geomorphic interpretation while explicitly communicating mapping uncertainty.

Although the inventory is not intended for event prediction or engineering design, it provides a practical decision-support resource that complements source-basin hazard assessments, transportation asset management, and future geohazard decision-support systems. Integration of receiving-landform inventories with watershed analyses, post-fire hazard models, monitoring networks, and emerging decision-support technologies offers a practical pathway toward more resilient transportation infrastructure and more informed geologic decision making.

REFERENCES

1. Debelak, A., Kidner, E., and Group, R. *Emergency Planning and Mitigation for Post-Fire Debris Flows in Glenwood Canyon, Colorado.* Proceedings of the 72nd Highway Geology Symposium, Tacoma, Washington, 2023, pp. 187–206.

2. Oester, N., Group, R., and Ortiz, T. *Implementation and Application of Geotechnical Asset Management in Colorado.* Proceedings of the 70th Highway Geology Symposium, Portland, Oregon, 2019, 12 pp.

3. Post, R., Pihl, R., Oester-Mapes, N., and Group, B. *Geohazard Management on Colorado SH 133 from Planning to Mitigation.* Proceedings of the 72nd Highway Geology Symposium, Tacoma, Washington, 2023, pp. 355–371.

4. Post, R., and Wade, W. *Geohazard Decision Support: Leveraging AI and Satellite Data for Infrastructure Resilience.* Proceedings of the 74th Highway Geology Symposium, Morgantown, West Virginia, 2025, 15 pp.

5. Cannon, S.H., Gartner, J.E., Wilson, R.C., Bowers, J.C., and Laber, J.L. *Storm Rainfall Conditions for Floods and Debris Flows from Recently Burned Areas in Southwestern Colorado*

and Southern California. Geomorphology, Vol. 96, Nos. 3–4, 2008, pp. 250–269. https://doi.org/10.1016/j.geomorph.2007.03.019.

6. Staley, D.M., Negri, J.A., Kean, J.W., Laber, J.L., Tillery, A.C., and Youberg, A.M. *Prediction of Spatially Explicit Rainfall Intensity-Duration Thresholds for Post-Fire Debris-Flow Generation in the Western United States. Geomorphology*, Vol. 278, 2017, pp. 149–162. https://doi.org/10.1016/j.geomorph.2016.10.019.

7. Kean, J.W., Staley, D.M., Lancaster, J.T., Rengers, F.K., Swanson, B.J., Coe, J.A., Hernandez, J., Sigman, A., Allstadt, K.E., and Lindsay, D.N. *Inundation, Flow Dynamics, and Damage in the 9 January 2018 Montecito Debris-Flow Event, California, USA: Opportunities and Challenges for Post-Wildfire Risk Assessment. Geosphere*, Vol. 15, No. 4, 2019, pp. 1140–1163. https://doi.org/10.1130/GES02048.1.

8. Lovekin, J.R., Crandall, A., Zhou, W., Perman, E.A., and Knies, D. *LiDAR-Based Delineation and Classification of Alluvial and High-Angle Fans for Regional Post-Wildfire Geohazard Assessment in Colorado, USA. GeoHazards*, Vol. 6, No. 3, Article 45, 2025. https://doi.org/10.3390/geohazards6030045.

9. Wallace, C.A., Keller, J.W., McCalpin, J.P., Bartos, P.J., Route, E.E., Jones, N.N., Gutierrez, F., Williams, C.L., and Morgan, M.L. *Geologic Map of the Breckenridge Quadrangle, Summit and Park Counties, Colorado.* Colorado Geological Survey Open-File Report OF-02-07, Denver, Colorado, 2003, scale 1:24,000. https://doi.org/10.58783/cgs.of0207.sfov6687.

38. A Framework for Corrosion and Asset Prioritization in Reinforced Soil Systems

Nelson Pearson, PE, MSCE
Civil Solutions Associates, Inc., dba Eastern Sierra Engineering (ESE)
4515 Towne Drive
Reno, NV 89521
775-8287220
npearson@esengr.com

Prepared for the 75th Highway Geology Symposium, September, 2026

Acknowledgements

The author gratefully acknowledges the unwavering support of his wife and family, whose encouragement made this work possible. Special thanks are extended to Dr. Raj Siddharthan for his mentorship, technical guidance, and leadership throughout the Nevada MSE wall corrosion investigations. The author also thanks his colleagues at Eastern Sierra Engineering for their continued support and commitment to technical excellence.

Disclaimer

Statements and views presented in this paper are strictly those of the author(s), and do not necessarily reflect positions held by their affiliations, the Highway Geology Symposium (HGS), or others acknowledged above. The mention of trade names for commercial products does not imply the approval or endorsement by HGS.

Copyright Notice

Copyright © 2026 Highway Geology Symposium (HGS)

All Rights Reserved. Printed in the United States of America. No part of this publication may be reproduced or copied in any form or by any means – graphic, electronic, or mechanical, including photocopying, taping, or information storage and retrieval systems – without prior written permission of the HGS. This excludes the original author(s).

ABSTRACT

Current design practice for metallic Mechanically Stabilized Earth (MSE) walls relies on electrochemical characterization of the reinforced backfill and empirical metal-loss models to estimate the long-term durability of the reinforcement. While these methods establish the corrosion assumptions used for design, they provide limited means of verifying that buried reinforcements continue to perform as intended throughout their service life. This paper presents a practical framework for extending corrosion verification beyond construction by integrating Linear Polarization Resistance (LPR) monitoring into transportation asset management.

The framework was developed through reanalysis of the Nevada Department of Transportation Phase II statewide corrosion monitoring program, including electrochemical characterization and 177 in-service corrosion measurements collected from representative metallic MSE walls. Measured corrosion rates were normalized using the Corrosion Severity Ratio (CSR), a dimensionless index that compares observed corrosion activity to the corresponding AASHTO design corrosion model. Site-level CSR rankings were then combined with normalized electrochemical conditions to establish a practical approach for prioritizing corrosion monitoring, inspection, and maintenance activities.

The statewide results generally support the current corrosion design methodology, with most monitored reinforcements exhibiting corrosion activity consistent with the underlying design assumptions. Localized CSR exceedances were observed, particularly at sites with unfavorable electrochemical conditions; however, isolated elevated corrosion rates alone do not indicate unacceptable long-term deterioration. Rather, the principal value of corrosion monitoring lies in establishing long-term trends in reinforcement performance that validate design assumptions and provide transportation agencies with objective condition data for risk-informed, condition-based management of metallic-reinforced soil infrastructure.

1. INTRODUCTION

Mechanically Stabilized Earth (MSE) walls have become one of the most widely used retaining systems in transportation infrastructure, providing a cost-effective and reliable solution for supporting bridge abutments, roadway widening, grade separations, and embankments. Their ability to retain steep earth masses under diverse loading conditions results from the interaction between buried metallic reinforcements, select backfill, and facing elements, creating a composite structural system in which the reinforcements provide the tensile resistance necessary to stabilize the soil mass. The long-term performance of these structures depends on the ability of the metallic reinforcements to maintain sufficient tensile capacity throughout their intended service life.

Corrosion, or metal loss, of buried metallic reinforcements is a naturally occurring, irreversible electrochemical process that progressively reduces reinforcement cross-sectional area and tensile capacity. Current MSE wall design practice addresses this deterioration by establishing electrochemical acceptance criteria for reinforced backfill materials and accounting for anticipated metal loss by including sacrificial steel thickness in the reinforcement design. While these measures are intended to provide the required service life, they rely on predicted corrosion behavior derived from electrochemical characterization of the reinforced backfill performed during design and construction. Following construction, the actual corrosion performance of the buried reinforcements is rarely validated, and the extent to which measured in-service corrosion remains consistent with the design assumptions is generally unknown.

Following construction, the buried reinforcements become largely inaccessible without intrusive investigation, preventing direct assessment of their condition. Consequently, condition assessments are generally limited to observations of the exposed wall face, while maintenance decisions rely primarily on construction records, electrochemical acceptance testing performed during construction, published corrosion models, and assumed service lives. Although electrochemical laboratory testing characterizes the corrosive potential of the backfill, it does not quantify the corrosion activity occurring on the reinforcement itself.

Previous investigations of Nevada MSE walls demonstrated that actual in-service corrosion conditions can differ significantly from design assumptions. Unexpected discoveries of advanced corrosion at the I-515/Flamingo Road and I-15/Cheyenne Boulevard interchanges highlighted the limitations of relying solely on construction acceptance testing and service-life predictions and emphasized the need for direct condition assessment of buried reinforcements. These investigations ultimately established the technical basis for expanding corrosion monitoring from a design-verification tool to a condition-based asset-management practice.

Building upon these investigations, this paper presents a practical framework for integrating electrochemical soil characterization and Linear Polarization Resistance (LPR) monitoring into transportation asset management. By combining electrochemical characterization with direct measurements of in situ corrosion activity, the framework extends corrosion evaluation beyond design verification to support the long-term management of metallic MSE wall infrastructure. The purpose of this paper is to demonstrate how corrosion monitoring can be incorporated into a transportation asset management program by using the Corrosion Severity Ratio (CSR) as a normalized measure of reinforcement condition to rank corrosion severity and prioritize monitoring, inspection, and maintenance activities.

2. BACKGROUND

This section summarizes the engineering principles underlying corrosion of metallic MSE wall reinforcements and establishes the technical basis for the proposed asset management framework. Topics include MSE wall behavior, underground corrosion mechanisms, electrochemical characterization of reinforced backfill, corrosion monitoring using Linear Polarization Resistance (LPR), the development of Nevada's corrosion monitoring program, and the role of corrosion condition assessment in transportation asset management.

2.1. Mechanically Stabilized Earth Walls

Mechanically Stabilized Earth (MSE) walls represent one of the most significant advancements in modern geotechnical engineering by enabling soil, a material with limited tensile capacity, to function as a structural element through reinforcement. A typical MSE wall consists of facing panels, select reinforced backfill, metallic reinforcing elements, and retained soil. The interaction between the backfill and the reinforcements, together with the connection between the reinforcements and the facing panels, creates a composite system capable of retaining steep earth masses while supporting a wide variety of static and dynamic loading conditions. Their constructability, economy, and long-term performance have made MSE walls a preferred retaining structure for transportation agencies throughout the United States.

Mechanically Stabilized Earth walls function by reinforcing the retained soil mass so that it behaves as a coherent composite structure rather than an unreinforced granular material. External loading induces tensile forces within the metallic reinforcements as relative movement develops across potential internal failure surfaces. These tensile forces are transferred through soil-reinforcement interaction, providing the internal stability required to maintain equilibrium of the reinforced soil mass. Corrosion progressively reduces the effective cross-sectional area of the reinforcement, thereby reducing its available tensile capacity. Continued section loss decreases the structural reliability of the reinforcement system and ultimately reduces the factor of safety against internal failure, making corrosion one of the principal long-term durability considerations for metallic MSE wall design.

The long-term performance of an MSE wall depends on the reinforcing elements' ability to maintain the tensile resistance required to stabilize the reinforced soil mass. Current design methodologies for metallic MSE wall reinforcements aim to preserve this tensile capacity throughout the intended service life by limiting corrosion-induced loss of section. The long-term performance of an MSE wall depends on the reinforcing elements maintaining the tensile resistance required to stabilize the reinforced soil mass throughout the intended service life. Current design methodologies address corrosion by specifying electrochemical acceptance criteria for reinforced backfill and providing sacrificial steel thickness based on published metal-loss models. Collectively, these measures establish the corrosion assumptions upon which the design service life is based. Their effectiveness, however, ultimately depends on whether those assumptions remain representative of actual in-service performance throughout the structure's service life

2.2. Underground Corrosion of Metallic Reinforcement

Underground corrosion of metallic reinforcement is an unavoidable electrochemical process that occurs naturally in buried infrastructure. The corrosion process requires three fundamental components: an electrolyte capable of transmitting ionic current, an electrical potential to drive ion transfer, and oxygen or another oxidizing species to sustain electrochemical reactions. Within MSE walls, these conditions are inherently present. Microscopic imperfections along the reinforcement surface provide electrical potential, oxygen is readily available within

the free-draining reinforced backfill, and soil moisture containing dissolved salts functions as the electrolyte. Consequently, corrosion cannot be eliminated in metallic MSE wall systems; engineering practice instead seeks to manage the rate at which it occurs.

Corrosion initiates when localized anodic and cathodic regions develop on the reinforcement surface. Iron atoms at anodic locations oxidize and dissolve into the surrounding soil as ferrous ions, while electrons released during this reaction migrate through the steel to cathodic regions. Simultaneously, ionic current flows through the surrounding soil moisture, completing the electrochemical circuit. This continuous transfer of ions progressively reduces the cross-sectional area of reinforcement, decreasing its available tensile capacity and, ultimately, the internal stability of the reinforced soil system.

From a geotechnical perspective, the surrounding backfill serves as the electrolyte within the corrosion cell. While eliminating the naturally occurring electrical potential or oxygen within an MSE wall is generally impractical, the electrolytic capacity of the reinforced backfill can be managed through material selection and specification. Consequently, current design practice characterizes the electrochemical properties of the backfill, including soil resistivity, pH, soluble chlorides, soluble sulfates, and oxidation-reduction potential, to establish an electrochemical environment assumed to produce corrosion behavior consistent with the design methodology. Following construction, however, the extent to which actual in-service corrosion performance remains consistent with these assumptions is rarely validated.

2.3. Electrochemical Characterization of Reinforced Backfill

Electrochemical characterization of reinforced backfill forms the foundation of current MSE wall corrosion design practice. Laboratory testing is used to characterize the electrochemical environment surrounding the buried reinforcements and establish the corrosion assumptions underlying the empirical metal-loss models used for design. The measured electrochemical properties quantify the backfill's electrolytic potential, allowing designers to determine the appropriate sacrificial steel thickness necessary to ensure the reinforcements retain adequate tensile capacity throughout the intended design service life. The resulting data are then compared with AASHTO and agency acceptance criteria to determine whether a backfill source is suitable for reinforced-soil applications.

Current practice evaluates five principal electrochemical properties: minimum soil resistivity, pH, soluble chlorides, soluble sulfates, and organic content. Collectively, these parameters characterize the electrolyte surrounding the reinforcement. It is important to recognize that neither an individual parameter nor the combined acceptance criteria can directly predict long-term corrosion behavior. Instead, the combined criteria are intended to establish a reinforced backfill environment that can reasonably be assumed to exhibit moderately aggressive corrosion characteristics, thereby supporting the application of empirical metal-loss models and the determination of sacrificial steel thickness required to achieve the intended design service life.

The electrochemical acceptance criteria were developed as practical engineering limits rather than absolute corrosion thresholds. Their purpose is to establish a reasonably consistent electrochemical environment while maintaining sufficient flexibility in aggregate source selection to avoid unnecessary restrictions on material availability, constructability, and project cost. The resulting specifications represent a practical balance between long-term durability, predictable corrosion behavior, and economical construction.

Among these properties, minimum soil resistivity is generally regarded as the best overall indicator of the corrosivity of reinforced backfill. Determined in accordance with AASHTO T

288, the test measures the electrical resistivity of a representative soil specimen over a range of moisture contents until the minimum resistivity is achieved. The specimen is progressively wetted, with resistivity measured at each increment, until additional moisture no longer reduces electrical resistance. Resistivity serves as an indirect measure of the concentration of readily dissolved ionic species in the pore fluid and, consequently, of the soil electrolyte's ability to sustain ionic current. Lower resistivity values correspond to greater ionic conductivity and, in general, to more aggressive corrosion conditions and accelerated metal loss, making minimum soil resistivity the single best indicator of reinforced backfill corrosivity.

The use of minimum laboratory resistivity introduces an inherent disconnect between laboratory characterization and long-term field performance. The specified value represents the maximum electrolytic potential of the backfill under standardized laboratory conditions, typically occurring at or near saturation, whereas the reinforcement is exposed to continually changing moisture conditions throughout its service life. Seasonal precipitation, drainage performance, groundwater fluctuations, and climatic conditions continually alter the electrolytic potential of the reinforced backfill and the corrosion environment surrounding the reinforcement. Consequently, the laboratory value represents a standardized index of potential corrosivity rather than a direct measurement of the electrochemical conditions experienced by the reinforcement in service. This distinction becomes increasingly important when laboratory characterization is used to estimate the deterioration of reinforcement over design lives of 75 years or more.

The remaining electrochemical parameters refine the assessment of the corrosion environment. Soil pH influences the stability of galvanized coatings and the corrosion behavior of steel. Soluble chlorides increase the concentration of dissolved ions in the pore fluid, thereby increasing electrolyte conductivity and promoting localized corrosion by disrupting protective corrosion products. Soluble sulfates contribute to the electrolyte's chemical aggressiveness and may accelerate deterioration under favorable environmental conditions. Organic content serves primarily as a screening parameter, as excessive organic matter can alter soil chemistry and promote biologically mediated corrosion. Together, these parameters provide a practical engineering framework for characterizing the electrochemical environment and establishing reinforced backfill with sufficiently predictable corrosion behavior to support service-life design.

Electrochemical characterization has remained the foundation of MSE wall corrosion design for more than three decades. However, these laboratory tests evaluate only the corrosive potential of the backfill, not the corrosion activity occurring on the reinforcement itself. They cannot account for temporal changes in moisture content, environmental conditions, or site-specific corrosion behavior throughout the structure's service life. Consequently, electrochemical characterization establishes the corrosion assumptions used during design but does not validate the actual corrosion performance of buried reinforcements throughout their service life. This distinction underscores the need for long-term corrosion monitoring capable of directly measuring in situ corrosion activity, validating the assumptions underlying the design methodology, and providing the condition information needed to support transportation asset management.

2.4. Corrosion Monitoring

Corrosion monitoring represents the logical extension of electrochemical characterization from design into long-term asset management. Current MSE wall design relies on laboratory characterization of reinforced backfill and empirical metal-loss models to establish the corrosion assumptions used for design. While these approaches provide the basis for determining sacrificial steel thickness and intended service life, they do not evaluate actual corrosion

performance after construction. Corrosion monitoring provides the means to assess in situ corrosion conditions by directly measuring reinforcement performance under field conditions, allowing transportation agencies to validate the corrosion assumptions established during design and determine whether actual in-service corrosion behavior remains consistent with those assumptions.

Several techniques are available for monitoring corrosion of buried metallic infrastructure, including visual excavation, sacrificial coupons, electrical resistance probes, and electrochemical monitoring. Among these methods, Linear Polarization Resistance (LPR) has become one of the most practical techniques for evaluating metallic MSE wall reinforcements as it provides rapid, non-destructive measurements of corrosion activity without requiring removal of the reinforcement. Developed specifically for transportation applications, LPR has been recommended by the FHWA for evaluating the long-term performance of metallic MSE wall reinforcements.

Linear Polarization Resistance measures the polarization resistance of the electrochemical corrosion cell by applying a small electrical perturbation to the reinforcement and measuring the resulting current response. The measured polarization resistance is converted to corrosion current using the Stern-Geary relationship, allowing the instantaneous corrosion rate of the reinforcement to be determined. Unlike the electrochemical characterization of reinforced backfill, which evaluates the environment surrounding the reinforcement, LPR directly quantifies corrosion activity on the reinforcement under actual in-service conditions.

It is important to recognize that LPR measures instantaneous corrosion activity rather than cumulative metal loss. Individual measurements provide a snapshot of corrosion behavior at the time of testing, while repeated measurements establish long-term corrosion trends and allow direct comparison with the assumptions underlying the corrosion design methodology. When integrated with electrochemical characterization, LPR provides transportation agencies with the information needed to validate corrosion design assumptions, evaluate the long-term performance of buried reinforcements, and support condition-based management of metallic MSE wall infrastructure.

2.5. Previous Nevada Corrosion Investigations

Over the past two decades, the Nevada Department of Transportation (NDOT) has conducted a series of corrosion investigations that progressively advanced the understanding of corrosion performance in metallic Mechanically Stabilized Earth (MSE) wall reinforcements. Collectively, these investigations transformed corrosion evaluation from isolated forensic investigations into a comprehensive statewide corrosion monitoring program and established the technical foundation for incorporating corrosion monitoring into transportation asset management.

This progression began with the unexpected discovery of advanced corrosion within a metallic MSE wall during rehabilitation activities. Comprehensive forensic investigations included direct metal-loss measurements, electrochemical characterization of the reinforced backfill, Linear Polarization Resistance (LPR) monitoring, and metallurgical evaluation of the reinforcing steel. The investigation concluded that the reinforced backfill exhibited substantially greater corrosivity than anticipated, resulting in deterioration of the reinforcement that exceeded the assumptions used during design. More importantly, the investigation demonstrated that advanced corrosion could develop with little or no visible distress at the wall face, highlighting the limitations of relying solely on construction acceptance testing, empirical metal-loss models, and visual inspections to assess the long-term condition of buried reinforcements.

The unexpected discovery of corrosion prompted the NDOT Phase I corrosion investigation, which reexamined the electrochemical characterization procedures historically used to accept reinforced backfill. Statistical comparison demonstrated that Nevada Test Method T235 consistently overestimated the minimum soil resistivity relative to AASHTO T 288, resulting in an underestimation of the corrosivity of reinforced backfill. A correlation was subsequently developed to relate historical test results to current AASHTO requirements, allowing historical construction records to be reevaluated using a consistent electrochemical basis. Application of the revised methodology identified additional MSE wall sites exhibiting electrochemical conditions warranting further investigation and established the technical basis for expanding statewide corrosion monitoring.

Building upon the Phase I recommendations, the NDOT Phase II investigation expanded electrochemical characterization and in situ corrosion monitoring to representative metallic MSE wall sites throughout Nevada. Electrochemical testing substantially increased the statewide database describing reinforced backfill characteristics, while extensive LPR monitoring provided direct measurements of in-service corrosion activity across a broad range of site conditions. The investigation demonstrated that electrochemical characterization and corrosion monitoring provide complementary information. Electrochemical characterization establishes the corrosion assumptions used during design, whereas LPR monitoring evaluates actual reinforcement performance under field conditions and provides a means to validate those assumptions throughout the structure's service life. The Phase II investigation also demonstrated that measured corrosion rates varied among sites exhibiting similar electrochemical characteristics, reinforcing the importance of direct field monitoring for evaluating long-term corrosion performance.

Collectively, these investigations represent the evolution of NDOT's corrosion program from identifying unexpected corrosion to refining corrosion design practice to validating long-term reinforcement performance. The present study builds upon this progression by demonstrating how corrosion monitoring can be incorporated into transportation asset management through the Corrosion Severity Ratio (CSR). By normalizing measured corrosion activity relative to the design assumptions, CSR provides a practical measure of the condition of reinforcement that can be used to classify corrosion severity, prioritize monitoring and inspection activities, and support long-term management of metallic MSE wall infrastructure.

2.6. Asset Management of Reinforced Soil Structures

Transportation agencies throughout the United States manage an aging inventory of MSE walls that represent substantial public investments and serve critical roles within the transportation network. Many of these structures were designed for service lives approaching or exceeding 75 years and are now entering stages where corrosion-related deterioration becomes an increasingly important consideration. Previous Nevada investigations demonstrated that buried metallic reinforcements can experience structurally damaging corrosion while exhibiting little or no visible distress at the wall face. Consequently, effective management of metallic MSE walls requires condition information beyond routine visual inspection.

Transportation asset management has evolved from age-based maintenance strategies to condition-based decision-making, in which engineering decisions are guided by measured infrastructure performance rather than by assumed deterioration. For buried metallic reinforcements, this presents a unique challenge, as the primary structural components become inaccessible following construction. With expanding infrastructure inventories, increasing

maintenance demands, and finite public resources, agencies must prioritize limited funding toward the structures exhibiting the greatest need.

The quality of these decisions is fundamentally dependent upon the quality of the information used to support them. The engineering principle of *"garbage in equals garbage out"* applies equally to transportation asset management. Regardless of the sophistication of deterioration models or lifecycle cost analyses, inaccurate or incomplete condition information inevitably produces ineffective maintenance strategies, inaccurate budget forecasts, and inefficient allocation of public resources. Electrochemical characterization and empirical metal-loss models establish the corrosion assumptions used during design; however, they do not quantify the actual condition of buried reinforcements throughout their service life.

Corrosion monitoring addresses this uncertainty by directly evaluating the in situ performance of reinforcement and validating the assumptions underlying the corrosion design methodology. Early identification of elevated corrosion activity enables agencies to increase monitoring, conduct targeted investigations, improve drainage, or implement planned rehabilitation before deterioration progresses to the point that costly emergency repairs are required. This proactive approach improves budget planning, maximizes limited maintenance funding, and minimizes impacts to the traveling public.

To incorporate measured corrosion performance into transportation asset management, a consistent measure of reinforcement condition is required. The Corrosion Severity Ratio (CSR) provides this normalization by comparing measured corrosion activity with the corrosion assumptions established during design. By accounting for differences in reinforcement type, age, and expected corrosion behavior, CSR provides a common measure of corrosion severity that can be compared across an inventory of MSE walls. Site-level CSR values provide a practical basis for classifying corrosion severity and prioritizing monitoring, inspection, maintenance, and rehabilitation activities, allowing transportation agencies to maximize limited resources while supporting the long-term stewardship of metallic MSE wall infrastructure.

3. METHODS

The Nevada Department of Transportation (NDOT) Phase II MSE wall corrosion database was reanalyzed to develop a practical framework for incorporating corrosion monitoring into transportation asset management. The methodology uses the Corrosion Severity Ratio (CSR) as a normalized measure of the corrosion condition to classify corrosion severity relative to the assumptions established during design. Rather than predicting corrosion rates, the methodology provides a consistent basis for comparing corrosion performance among MSE wall sites and prioritizing monitoring, inspection, maintenance, and rehabilitation activities.

3.1. Data Compilation and Preparation

The analysis utilized the electrochemical characterization and Linear Polarization Resistance (LPR) monitoring data collected during the NDOT Phase II MSE wall corrosion investigation. No additional field investigations or laboratory testing were performed. The Phase II investigation included seven MSE wall sites representing a range of construction eras, reinforcement types, and environmental conditions. Electrochemical characterization included minimum soil resistivity, soluble sulfate concentration, soluble chloride concentration, and pH. Corresponding LPR measurements provided direct observations of in-situ corrosion activity. Only observations containing both electrochemical characterization data and corresponding LPR measurements were included in the analysis.

Historical minimum soil resistivity values obtained using Nevada Test Method T235 were converted to equivalent AASHTO T 288 values using the Phase I correlation. All electrochemical and corrosion data were reviewed for consistency of units and reporting. Measured corrosion rates were converted to the Corrosion Severity Ratio (CSR) using the methodology established during the Phase II investigation

$$CSR = \frac{CR_{measured}}{CR_{design}} \quad (1)$$

where $CR_{measured}$ is the instantaneous corrosion rate determined from the LPR measurements and CR_{design} is the corresponding corrosion rate defined by the applicable AASHTO metal-loss model for the reinforcement type and corrosion stage.
This normalization yields a dimensionless measure of corrosion performance that enables direct comparison among reinforcement elements across different ages, reinforcement types, coating conditions, and corrosion environments. Values of CSR ≤ 1.0 indicate corrosion performance consistent with the design assumptions, whereas CSR > 1.0 indicates measured corrosion conditions that exceed those assumptions.

By normalizing measured corrosion activity to the applicable design corrosion rate, CSR serves as an indicator of corrosion condition for comparing corrosion severity across an inventory of MSE walls. Within the proposed framework, CSR provides a consistent basis for classifying corrosion severity, ranking sites according to reinforcement condition, and supporting transportation asset management decisions related to monitoring, inspection, maintenance, and rehabilitation.

3.2. Corrosion Condition Assessment Framework

Current MSE wall design assumes that reinforced backfill satisfying established electrochemical acceptance criteria will provide corrosion performance consistent with the metal-loss models used to determine sacrificial steel thickness and design service life. The proposed framework extends this design methodology by incorporating long-term corrosion monitoring to validate these assumptions through direct measurements of in-situ reinforcement performance.

Within the proposed framework, the Corrosion Severity Ratio (CSR) serves as the indicator of corrosion condition for transportation asset management. By comparing measured corrosion activity with the corresponding corrosion rate assumed during design, CSR provides a normalized measure of the condition of reinforcement that permits direct comparison among reinforcement elements representing different construction eras, reinforcement types, coating conditions, and corrosion stages. The development and calculation of CSR are presented in the following section.

Corrosion condition assessment represents one component of the broader asset management process. Asset prioritization integrates corrosion conditions with the electrochemical conditions that influence corrosion and the asset's operational characteristics. Conceptually, this relationship may be expressed as

$$\text{Asset Priority} = f(\text{Corrosion Severity, Electrochemical Severity, Asset Characteristics}) \quad (2)$$

where CSR represents the measured corrosion condition, Electrochemical Conditions represent the measured characteristics of the reinforced backfill, including minimum soil resistivity,

soluble sulfate concentration, soluble chloride concentration, and pH, and Asset Characteristics include engineering, operational, and agency-specific considerations such as structure age, location, structural criticality, functional classification, inspection history, maintenance history, traffic importance, available funding, and other agency priorities.

This framework distinguishes corrosion condition assessment from asset prioritization. Corrosion monitoring validates the assumptions established during design, CSR translates measured corrosion activity into a normalized condition indicator, and the broader asset management process integrates corrosion condition with electrochemical conditions and asset characteristics to support monitoring, inspection, maintenance, and rehabilitation decisions.

4. RESULTS

This study evaluates the corrosion assumptions underlying current MSE wall design by comparing the electrochemical conditions of reinforced backfill with measured in-service corrosion performance. The results are presented in three stages. First, the electrochemical conditions defining the corrosion environment are summarized. Next, the measured corrosion activity obtained through Linear Polarization Resistance (LPR) monitoring is presented. Finally, the Corrosion Severity Ratio (CSR) is used to normalize the measured corrosion rates relative to the design assumptions, providing a consistent corrosion condition indicator for comparison among the monitored MSE wall sites

4.1. Electrochemical Conditions of Reinforced Backfill

Electrochemical characterization was performed on reinforced backfill samples collected as part of the Nevada Department of Transportation (NDOT) corrosion monitoring program. Building upon the investigations completed during Phase I, the statewide program progressively expanded the electrochemical database to include representative MSE wall sites spanning a range of construction eras, reinforcement types, and environmental conditions throughout Nevada, ultimately comprising more than 130 electrochemical measurements collected from seven such sites. The expanded dataset validated the Phase I screening methodology by demonstrating that the sites identified for further investigation exhibited electrochemical conditions consistent with elevated corrosion potential under current reinforced backfill acceptance criteria, providing the technical basis for the Phase II corrosion monitoring program. Summary statistics for the statewide dataset are presented in Table 1.

Table 1: Summary Statistics for Electrochemical Properties of Nevada MSE Walls Included in the Corrosion Monitoring Program

	Soluble Chlorides [ppm]	**Soluble Sulfates [ppm]**	**Minimum Soil Resistivity [Ω-cm]**	**pH**	**Organic Content [%]**
Minimum	0	0	267	6.6	0.1
Maximum	2700	1700	9709	11.8	3.1
Mean	118	247	2440	8.8	0.5
Median	11	160	2297	9.0	0.3
Skewness	5.3	2.4	1.5	-0.1	2.4
Standard Deviation	371	307	1707	0.7	0.6
n	111	111	130	131	72

The measured electrochemical conditions exhibited substantial variability across the monitored sites. Minimum soil resistivity ranged from 267 to 9,709 Ω-cm, with a mean of 2,440 Ω-cm and a median of 2,297 Ω-cm. Soluble chloride concentrations ranged from 0 to 2,700 ppm, while soluble sulfate concentrations ranged from 0 to 1,700 ppm. Soil pH ranged from 6.6 to 11.8 with a median of 9.0, and organic content ranged from 0.1 to 3.1 percent. Soluble chloride and sulfate concentrations exhibited pronounced positive skewness, whereas soil pH remained comparatively uniform throughout the dataset.

Comparison with the current reinforced backfill acceptance criteria is presented in Table 2. Minimum soil resistivity exhibited the highest rate of exceedance, with 86 of 130 observations (66%) below the current acceptance criterion of 3,000 Ω-cm. Soluble sulfate concentrations exceeded the acceptance criterion in 9 of 111 observations (35%), followed by organic content (14%) and soluble chlorides (12%). Only one pH measurement (1%) fell outside the acceptable range.

Table 2: Electrochemical Property Exceedance Relative to Current Reinforced Backfill Acceptance Criteria

Parameter	Acceptance Criteria	Observations Exceeding Criteria	Percent
Soluble Chlorides [ppm]	≤100	13 of 111	12%
Soluble Sulfates [ppm]	≤200	39 of 111	35%
Minimum Soil Resistivity [Ω-cm]	≥3000	86 of 130	66%
pH	5.0–10.0	1 of 131	1%
Organic Content [%]	≤1.0	14 of 72	14%

Note: Acceptance criteria are based on current reinforced backfill electrochemical requirements. Percentages are calculated using the number of available observations for each parameter.

Collectively, these results demonstrate that the monitored MSE walls span a broad range of electrochemical conditions representative of metallic-reinforced soil systems throughout Nevada. These data establish the corrosion environment underlying the design assumptions and provide the reference against which measured in-service corrosion performance is evaluated in the following sections.

4.2. Linear Polarization Resistance Instantaneous Corrosion Rate

Linear Polarization Resistance (LPR) monitoring provides direct measurements of instantaneous corrosion activity occurring on buried metallic reinforcements under actual field conditions. Unlike electrochemical characterization, which establishes the electrochemical conditions and corrosion assumptions used during design, LPR quantifies the in-service corrosion performance of the reinforcement itself. The Phase II corrosion monitoring program included measurements from in-service galvanized reinforcements, galvanized steel coupons, and plain steel coupons distributed among seven representative MSE wall sites. Summary statistics for the measured corrosion rates are presented in Table 3. Collectively, the LPR monitoring program produced 177 direct measurements of in-service corrosion activity, representing one of the most comprehensive corrosion-monitoring datasets currently available for metallic MSE wall reinforcements.

Measured corrosion rates exhibited substantial variability among the monitored sites and reinforcement types. Mean corrosion rates ranged from less than 1 µm/yr for several in-service galvanized reinforcements to more than 20 µm/yr at one monitored site, while maximum

measured corrosion rates exceeded 60 µm/yr. Corrosion rates measured on plain steel coupons were generally higher than those on galvanized reinforcement, reflecting the protective effect of zinc coatings. Considerable variability was also observed within individual sites, indicating that corrosion activity is not uniform even within a common reinforced backfill environment.

Table 3: Summary Statistics for LPR Corrosion Rates by Site and Element Type

Site	Element Type	n	Mean LPR [µm/yr]	Median LPR [µm/yr]	Minimum LPR [µm/yr]	Maximum LPR [µm/yr]	Standard Deviation [µm/yr]
Alt. US 50 / Alt. US 95	IGR	4	2.6	0.7	0.5	8.3	3.8
US 395 / Huffaker Lane	IGR	3	0.7	0.5	0.4	1.3	0.5
I-15 / Cheyenne Blvd.	IGR	10	20.4	12.5	0.6	56.4	20.5
	GSC	20	1.1	0.5	0.2	5.9	1.3
	PSC	20	4.1	1.3	0.3	20.6	5.9
I-15 / Lamb Blvd.	GSC	6	6.4	5.5	3	13.5	3.9
	PSC	6	6.5	4.2	0.8	18.6	6.8
I-515 / Charleston Blvd.	GSC	6	4.2	3.5	0.5	10.7	3.7
	PSC	6	7.2	7	2.5	12.4	3.6
I-515 / Las Vegas Blvd.	IGR	2	1.3	1.3	1.1	1.6	0.3
	GSC	3	0.5	0.3	0.3	0.8	0.3
	PSC	3	4.5	4.3	2.8	6.4	1.8
SR 160 / Jones Rd.	IGR	10	1	0.9	0	2.3	0.8
	GSC	28	1.6	0.9	0	6.6	1.8
	PCS	26	5.4	3.4	0	26.5	6.3
I-515 / Flamingo Rd.	IGR	8	2.2	2.6	0	3.3	1.3
	PSC	60	5.5	4.4	0	60.2	8.3

Note: IGR – In-service Galvanized Reinforcement; GSC – Galvanized Steel Coupon; PCS – Plain Steel Coupon

Figure 1 illustrates the distribution of measured corrosion rates for the in-service galvanized reinforcements. Corrosion activity varied considerably among the monitored sites, with the I-15/Cheyenne Boulevard site exhibiting the broadest distribution and highest measured corrosion rates. The remaining sites generally exhibited narrower distributions centered at comparatively lower corrosion rates. The observed variability demonstrates that corrosion performance differs substantially among structures and provides the basis for comparing measured reinforcement performance throughout the statewide monitoring program.

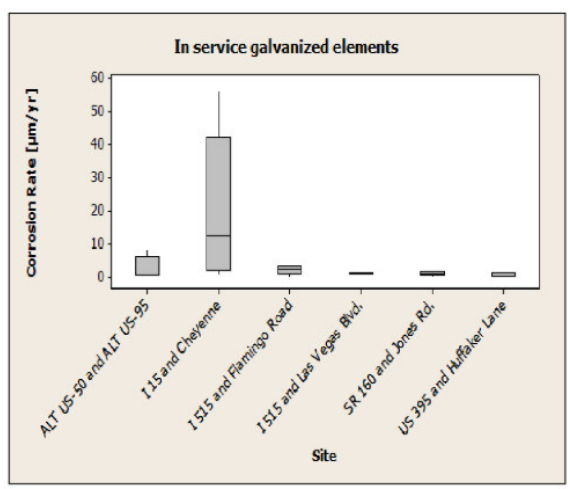

***Figure 1**: Distribution of measured LPR corrosion rates for in-service galvanized reinforcements by monitored site (adapted from the NDOT Phase II Corrosion Investigation)*

4.3. Corrosion Severity Ratio

Direct comparison of measured LPR corrosion rates among MSE walls is complicated by differences in reinforcement type, galvanization, age, and corrosion stage. The Corrosion Severity Ratio (CSR) normalizes measured corrosion activity relative to the corresponding empirical AASHTO metal-loss model used during design, expressing reinforcement performance as a ratio of measured corrosion to the corrosion assumptions underlying the design methodology. This normalization produces a dimensionless measure of reinforcement condition that permits direct comparison among structures regardless of reinforcement type, construction era, or corrosion stage.

Summary statistics for CSR by reinforcement element type are presented in Table 4. Although the measured LPR corrosion rates varied substantially among in-service galvanized reinforcements (IGR), galvanized steel coupons (GSC), and plain steel coupons (PSC), normalization using CSR largely removes these differences by expressing corrosion activity relative to the applicable design corrosion model. The resulting CSR values therefore represent a common measure of corrosion condition independent of reinforcement type.

Table 4: Corrosive Severity Ratio (CSR) by element type derived from Phase II data.

Element Type	Min. CSR	Mean CSR	Median CSR*	Max. CSR	Standard Deviation	n
In-service Galvanized Reinforcement (IGR)	0.00	1.65	0.20	14.10	3.34	37
Galvanized Steel Coupons (GSC)	0.00	0.10	0.10	0.90	0.20	75
Plain Steel Coupons (PSC)	0.00	0.29	0.10	5.00	0.52	132

While the coupon measurements provide a controlled means of evaluating corrosion performance, the in-service galvanized reinforcements provide the most direct measure of the condition of the structural reinforcement. Summary statistics for the in-service reinforcement CSR values are presented in Table 5. Among the monitored sites, the I-15/Cheyenne Boulevard interchange exhibited the highest normalized corrosion severity, with a mean CSR of 5.1 and individual observations as high as 14.1. The remaining monitored sites exhibited mean CSR values below 1.0, indicating corrosion activity generally consistent with or below the design assumptions.

Table 5: Summary of site-specific Corrosion Severity descriptive station derived from Phase II data

Site	n	Mean CSR	Median CSR	Min. CSR	Max. CSR	Standard Deviation
Alt. US 50 / Alt. US 95	4	0.6	0.2	0.1	2.1	1
US 395 / Huffaker Lane	3	0.1	0	0	0.1	0
I-15 / Cheyenne Blvd.	10	5.1	3.1	0.2	14.1	5.1
I-515 / Flamingo Rd.	8	0.5	0.7	0	0.8	0.3
I-515 / Las Vegas Blvd.	2	0.1	0.1	0.1	0.1	0
SR 160 / Jones Rd.	10	0.3	0.2	0	0.6	0.2

The normalized in-service CSR values demonstrate that corrosion condition varies substantially among monitored structures despite differences in reinforcement age and type. By expressing measured corrosion activity relative to the corrosion assumptions established during design, CSR provides a standardized condition indicator suitable for comparing reinforcement

condition across an inventory of MSE walls. The following section extends this approach by integrating the Phase II observations into a statewide corrosion condition assessment to support site-level comparison and asset prioritization.

4.4. Site-Level Corrosion Severity Ranking

Transportation agencies manage MSE walls as assets rather than individual reinforcement elements. Accordingly, the observation-level results were synthesized at the site level using the proposed asset management framework.

This study evaluates the first two components of this relationship. The Corrosion Severity Ratio (CSR) represents measured reinforcement performance relative to the AASHTO design corrosion model, while the electrochemical conditions characterize the corrosive environment surrounding the reinforcement. Asset characteristics, including structural importance, inspection history, maintenance history, traffic impacts, and available funding, are agency-specific considerations and are beyond the scope of this study.

To facilitate comparison among sites, each electrochemical parameter was normalized relative to its corresponding reinforced-backfill acceptance criterion. Similar to CSR, a normalized value of 1.0 represents the applicable acceptance criterion, values less than 1.0 indicate compliance with the criterion, and values greater than 1.0 indicate an exceedance. The parameter-specific normalization relationships were defined as

$$ESR_{\rho} = \frac{3000}{\rho}$$
$$ESR_{Cl} = \frac{Cl}{100}$$
$$ESR_{SO_4} = \frac{SO_4}{200}$$
$$ESR_{pH} = \max\left(\frac{5.0}{pH}, \frac{pH}{10.0}\right)$$

where $\rho$is the minimum soil resistivity [Ω-cm], and $Cl$and $SO_4$are the soluble chloride and sulfate concentrations [ppm], respectively. The resistivity relationship is inverted: lower resistivity corresponds to a higher corrosion potential.

The normalized electrochemical values were used to develop independent Electrochemical Severity Rankings for minimum soil resistivity, soluble chlorides, soluble sulfates, and pH. The parameters were intentionally evaluated independently because each represents a distinct characteristic of the corrosion environment, and combining them into a single index could obscure significant exceedances in individual electrochemical properties. These rankings were then compared with the site-level Corrosion Severity Ranking derived from the CSR analysis.

The resulting rankings provide complementary measures of reinforcement condition. The Corrosion Severity Ranking identifies sites exhibiting elevated measured corrosion activity, whereas the Electrochemical Severity Ranking identifies sites with backfill conditions more conducive to continued corrosion. Together, these rankings provide the condition assessment inputs to the proposed asset management framework while allowing transportation agencies to incorporate asset-specific characteristics when establishing inspection, maintenance, and rehabilitation priorities.

Table 6: Site Level Corrosive Severity Ranking

Site	Corrosion Severity Rank	Resistivity Rank	Chloride Rank	Sulfate Rank	pH Rank
I-15 / Cheyenne Blvd.	1	2	3	1	5
I-515 / Flamingo Rd.	2	1	5	2	4
Alt. US 50 / Alt. US 95	3	4	2	4	2
I-515 / Charleston Blvd.	4	3	4	3	6
I-15 / Lamb Blvd.	5	6	1	5	3
US 395 / Huffaker Lane	6	5	6	6	1
I-515 / Las Vegas Blvd.	7	7	7	7	7

Note: Corrosion Severity Rank is based on the site-level Corrosion Severity Ratio (CSR). Electrochemical Severity Rankings are based on the normalized electrochemical relationships for minimum soil resistivity, soluble chlorides, soluble sulfates, and pH. Rank 1 represents the most severe condition for each category

The site-level rankings demonstrate that measured corrosion severity and electrochemical severity are related but not surrogate indicators of long-term reinforcement performance. Sites with failing electrochemical conditions exhibited the greatest frequency, magnitude, and variability of CSR exceedances; however, isolated CSR values exceeding 1.0 were also observed at sites satisfying the electrochemical acceptance criteria. These observations indicate that the current electrochemical acceptance criteria and associated AASHTO corrosion models provide a robust basis for service-life design, but also demonstrate that instantaneous metal-loss rates may exceed those assumed during design, even where the electrochemical acceptance criteria are satisfied. LPR measures the instantaneous rate of metal loss; consequently, a single elevated CSR value cannot differentiate a transient increase in metal-loss rate from a sustained aggressive metal-loss process.

5. DISCUSSION

The results demonstrate that corrosion design and corrosion monitoring provide complementary assessments of long-term MSE wall performance. Electrochemical characterization verifies that reinforced backfill satisfies the environmental assumptions established during design, whereas Linear Polarization Resistance (LPR) monitoring evaluates whether in-service reinforcement performance remains consistent with the corresponding metal-loss assumptions. By normalizing measured corrosion activity relative to the AASHTO design corrosion models, the Corrosion Severity Ratio (CSR) provides a practical framework for validating design assumptions and incorporating corrosion monitoring into transportation asset management. The following discussion examines the implications of these findings for design verification, long-term reinforcement performance, and condition-based asset management.

5.1. Validation of Current Design Methodology

Current MSE wall corrosion design assumes that reinforced backfill satisfying established electrochemical acceptance criteria will exhibit corrosion behavior consistent with the AASHTO metal-loss models used to determine sacrificial steel thickness and design service life. The results generally support this assumption. Most monitored reinforcement elements exhibited corrosion activity consistent with the underlying design assumptions, indicating that the current electrochemical acceptance criteria and associated corrosion models provide a robust basis for service-life design.

Localized CSR exceedances were observed throughout the statewide monitoring program; however, the greatest frequency, magnitude, and variability occurred at sites where one or more electrochemical acceptance criteria were not satisfied. These observations demonstrate that the current design methodology provides a reliable framework for long-term corrosion design while reinforcing the importance of compliance with established electrochemical acceptance criteria.

Corrosion design and corrosion monitoring serve complementary engineering functions. The design methodology establishes the expected long-term metal loss rate, whereas corrosion monitoring evaluates the actual in-service performance of the reinforcement. Accordingly, the objective of corrosion monitoring is not to replace the current design methodology but to periodically validate the assumptions underlying the design service life.

5.2. Instantaneous Corrosion Severity Versus Long-Term Reinforcement Performance

Linear Polarization Resistance (LPR) monitoring provides a direct measurement of the instantaneous rate of metal loss occurring at the time of testing. Unlike the empirical AASHTO metal-loss models, which represent the long-term corrosion behavior assumed during design, LPR captures the electrochemical response of the reinforcement under the prevailing field conditions. Consequently, instantaneous corrosion severity is inherently variable and reflects the combined influence of moisture content, electrolyte chemistry, oxygen availability, temperature, and other environmental conditions existing at the time of measurement. The variability observed throughout the statewide monitoring program is therefore consistent with the fundamental behavior of buried metallic reinforcement rather than an indication of deficiencies in the current design methodology.

This distinction is fundamental to interpreting corrosion severity. Sites with failing electrochemical conditions exhibited the greatest frequency, magnitude, and variability of elevated CSR values; however, instantaneous corrosion severity ranged from negligible to highly aggressive. Likewise, isolated CSR exceedances were observed at sites satisfying the electrochemical acceptance criteria. These observations demonstrate that a single LPR measurement provides only a snapshot of corrosion severity and cannot determine whether elevated metal-loss rates represent a transient response to short-term environmental conditions or the onset of a sustained aggressive metal-loss process.

Direct interpretation of measured metal-loss rates is further complicated by differences in reinforcement type, galvanization, age, and corrosion stage. A corrosion rate that is acceptable for one reinforcement system may represent accelerated deterioration for another. Consequently, measured metal-loss rates alone provide limited value for comparing corrosion severity across a statewide inventory of MSE walls.

The Corrosion Severity Ratio (CSR) addresses this limitation by normalizing the measured instantaneous metal-loss rate relative to the corresponding AASHTO design corrosion rate. Rather than evaluating corrosion rate alone, CSR quantifies corrosion severity relative to the assumptions established during design. A CSR less than 1.0 indicates corrosion severity below the design assumptions, a value near 1.0 indicates corrosion severity generally consistent with the anticipated long-term deterioration rate, and values exceeding 1.0 indicate corrosion severity greater than assumed by the design methodology. This normalization transforms instantaneous corrosion measurements into a simple, dimensionless measure of corrosion severity. By expressing reinforcement performance relative to the design assumptions, CSR provides an intuitive engineering metric that facilitates straightforward interpretation and comparison across an inventory of metallic MSE walls.

The engineering significance of CSR lies not in its intuitive interpretation but in its application over time. A single elevated CSR value indicates accelerated metal loss due to reinforcement; however, it cannot distinguish a transient increase in corrosion severity from a sustained aggressive metal-loss process. Repeated CSR measurements establish corrosion severity trends that validate the long-term assumptions underlying the AASHTO corrosion models and distinguish short-term fluctuations from persistent deterioration capable of producing significant structural metal loss. In this manner, corrosion monitoring evolves from a point-in-time assessment of corrosion severity to a long-term evaluation of reinforcement performance, providing transportation agencies with a practical means of validating design assumptions throughout the service life of metallic MSE wall infrastructure

5.3 Implications for Transportation Asset Management

The observations presented herein demonstrate that the principal value of corrosion monitoring lies not in a single measurement but in establishing long-term trends in reinforcement performance. While an isolated LPR measurement provides an assessment of instantaneous corrosion severity, it cannot determine whether elevated metal-loss rates represent a transient response to changing environmental conditions or a sustained aggressive metal-loss process. Repeated CSR measurements can establish corrosion severity trends that validate the long-term metal-loss assumptions incorporated into the AASHTO design methodology while providing agencies with greater confidence in assessing long-term reinforcement performance.

Despite advances in corrosion monitoring, an important knowledge gap remains. Current practice provides limited guidance regarding the relationship between corrosion severity measured at discrete reinforcement elements and the structural condition of the MSE wall as a whole. Likewise, the extent to which localized deterioration of reinforcement or the loss of individual reinforcement elements affects overall wall performance remains poorly understood. Consequently, an elevated CSR indicates corrosion severity that requires additional evaluation but does not independently establish a structural deficiency or the need for rehabilitation.

This uncertainty is compounded by the inaccessibility of the primary structural components. Unlike many transportation structures, the condition of buried metallic reinforcements cannot be reliably evaluated through routine visual inspection. As demonstrated by the Nevada investigations, significant reinforcement deterioration may occur with little or no visible distress at the wall face. Without historical corrosion monitoring data, transportation agencies have limited information to determine whether observed corrosion severity is localized or widespread, and whether it is transient or progressive. The prudent engineering response is therefore to assume that the condition may represent unacceptable deterioration, frequently resulting in additional investigation or emergency rehabilitation.

Long-term corrosion monitoring reduces this uncertainty by providing the temporal context necessary to distinguish transient corrosion events from sustained aggressive metal-loss processes. Rather than reacting to isolated corrosion measurements, agencies can evaluate deterioration trends and identify structures exhibiting persistent deterioration of reinforcement before significant structural metal loss develops. This condition-based approach provides objective engineering information to support inspection, maintenance, rehabilitation, and capital planning decisions.

Ultimately, the value of long-term corrosion monitoring extends beyond corrosion assessment to transportation asset management. Integrating corrosion severity trends with electrochemical characterization provides agencies with objective condition data that

complements traditional inspection programs and validates long-term design assumptions. By identifying sustained deterioration before emergency intervention becomes necessary, transportation agencies can prioritize limited resources, improve budget predictability, optimize life-cycle expenditures, and transition from reactive emergency repairs to proactive, condition-based asset management.

6. CONCLUSION

Current MSE wall corrosion design relies on two fundamental assumptions. The first is that construction materials testing verifies that the reinforced backfill satisfies established electrochemical acceptance criteria, thereby providing an environment consistent with the corrosion assumptions underlying the design methodology. The second is that reinforcements within this verified environment will experience the long-term metal-loss rates assumed during design. While current construction quality assurance practices validate the electrochemical properties of the reinforced backfill, they do not validate the corresponding long-term corrosion performance of the buried reinforcement after construction.

The results presented herein demonstrate that corrosion monitoring provides a practical extension of this design verification process throughout the structure's service life. Electrochemical characterization verifies the corrosive environment during construction, whereas Linear Polarization Resistance (LPR) monitoring directly evaluates the in-service corrosion performance of the reinforcement. By comparing measured corrosion activity with design corrosion models, the Corrosion Severity Ratio (CSR) provides a normalized measure of reinforcement performance relative to the design assumptions.

The statewide monitoring results generally support the current design methodology, with most monitored reinforcement exhibiting corrosion activity consistent with the underlying metal-loss models. Localized CSR exceedances were observed, particularly at sites with unfavorable electrochemical conditions; however, isolated elevated corrosion rates alone do not necessarily indicate unacceptable long-term deterioration. Instead, they highlight the need for periodic corrosion monitoring to determine whether elevated corrosion severity is transient or a sustained departure from the metal-loss assumptions underlying the design methodology. The principal value of corrosion monitoring, therefore, lies in establishing long-term reinforcement performance trends that validate the service-life assumptions used during design and provide transportation agencies with greater confidence in the long-term performance of metallic MSE wall infrastructure.

Viewed in this context, corrosion monitoring represents the operational continuation of the corrosion verification process initiated during construction. Construction materials testing verifies that the reinforced backfill satisfies the environmental assumptions required for design, while periodic corrosion monitoring verifies that the reinforcement continues to perform in a manner consistent with the service-life assumptions upon which the structure was designed. Together, these complementary processes provide transportation agencies with objective information for condition-based asset management, allowing monitoring, inspection, maintenance, and rehabilitation activities to be prioritized based on measured reinforcement performance rather than assumed deterioration alone.

7. REFERENCES

American Association of State Highway and Transportation Officials (AASHTO). *LRFD Bridge Design Specifications.* 4th Edition. American Association of State Highway and Transportation Officials, Washington, D.C., 2007.

American Association of State Highway and Transportation Officials (AASHTO). *Standard Method of Test for Determining Minimum Laboratory Resistivity of Soil (AASHTO T 288).* American Association of State Highway and Transportation Officials, Washington, D.C.

American Association of State Highway and Transportation Officials (AASHTO). *Standard Specifications for Highway Bridges.* 17th Edition. American Association of State Highway and Transportation Officials, Washington, D.C., 2002.

Association of Metallically Stabilized Earth (AMSE). *Reduced Zinc Loss Rate for Design of MSE Structures.* McLean, Virginia, 2006.

ASM International. *ASM Handbook, Volume 13A: Corrosion—Fundamentals, Testing, and Protection.* ASM International, Materials Park, Ohio.

Berg, R.R., Christopher, B.R., and Samtani, N.C. *Design of Mechanically Stabilized Earth Walls and Reinforced Soil Slopes.* FHWA-NHI-10-024/025. Federal Highway Administration, Washington, D.C., 2009.

Darbin, M., Jailloux, J.M., and Montuelle, J. *Durability of Reinforced Earth Structures: The Results of a Long-Term Study Conducted on Galvanized Steel.* Proceedings of the Institution of Civil Engineers, Part 1: Design and Construction, Vol. 84, 1988.

Decker, J.B., Rollins, K.M., and Ellsworth, J.C. *Corrosion Rate Evaluation and Prediction for Piles Based on Long-Term Field Performance.* Journal of Geotechnical and Geoenvironmental Engineering, Vol. 134, No. 3, pp. 341–351, 2008.

Elias, V. *Corrosion/Degradation of Soil Reinforcements for Mechanically Stabilized Earth Walls and Reinforced Soil Slopes.* FHWA-NHI-00-044. Federal Highway Administration, Washington, D.C., 2000.

Elias, V. *Durability/Corrosion of Soil Reinforced Structures.* FHWA-RD-89-186. Federal Highway Administration, Washington, D.C., 1990.

Elias, V., Christopher, B.R., and Berg, R.R. *Mechanically Stabilized Earth Walls and Reinforced Soil Slopes Design and Construction Guidelines.* FHWA-NHI-00-043. Federal Highway Administration, Washington, D.C., 2001.

Elias, V., Fishman, K.L., Christopher, B.R., and Berg, R.R. *Corrosion/Degradation of Soil Reinforcements for Mechanically Stabilized Earth Walls and Reinforced Soil Slopes.* FHWA-NHI-09-087. Federal Highway Administration, Washington, D.C., 2009.

Fishman, K.L. *Consultant's Report: Corrosion Evaluation of MSE Walls I-515/Flamingo Road, Las Vegas, Nevada.* McMahon & Mann Consulting Engineers, P.C., May 2005.

Fishman, K.L. *Investigation of Corrosion in Metallic Mechanically Stabilized Earth Walls – Phase I.* Nevada Department of Transportation, Carson City, Nevada.

Fishman, K.L., and Withiam, J.L. *LRFD Metal Loss and Service-Life Reduction Factors for Metal-Reinforced Systems.* NCHRP Report 675. Transportation Research Board, Washington, D.C., 2011.

Jones, D.A. *Principles and Prevention of Corrosion.* 2nd Edition. Prentice Hall, Upper Saddle River, New Jersey.

Nevada Department of Transportation. *Nevada Test Method T235: Minimum Resistivity of Soil.*

Nevada Department of Transportation. *Standard Specifications for Road and Bridge Construction.* Carson City, Nevada.

Padilla, F., Ghods, P., and Alfantazi, A. *Practical Model for Three-Stage Corrosion Behavior of Galvanized Steel Reinforcements in Soil. Corrosion*, Vol. 69, No. 5, 2013.

Pearson, N., Siddharthan, R.V., and Luke, B. *Assessment of In-Situ Conditions at Nevada Mechanically Stabilized Earth Wall Sites Using Electrochemical Soil Characteristics and Linear Polarization Resistance.* Final Research Report. University of Nevada, Reno, prepared for the Nevada Department of Transportation, Reno, Nevada.

Polarization Resistance Monitor PR-4500. *Operation Manual.* Version 2.0. CC Technologies Systems, Inc., Dublin, Ohio, 1999.

Raeburn, C.L., Monkul, M.M., and Piles, M.R. *Evaluation of Corrosion of Metallic Reinforcements and Connections in MSE Retaining Walls.* FHWA-OR-RD-08-10. Oregon Department of Transportation and Federal Highway Administration, Salem, Oregon, 2008.

Romanoff, M. *Underground Corrosion.* National Bureau of Standards Circular 579. U.S. Government Printing Office, Washington, D.C., 1957.

Scully, J.C. *The Fundamentals of Corrosion.* 3rd Edition. Pergamon Press, Oxford, England.

Stern, M., and Geary, A.L. "Electrochemical Polarization: I. A Theoretical Analysis of the Shape of Polarization Curves." *Journal of the Electrochemical Society*, Vol. 104, No. 1, 1957.

39. Applications of Smart Rock Technology to Evaluate Rockfall Hazards

Bruma Souza, Ph.D.
Weston & Sampson
55 Walkers Brook Drive, Suite 100
Reading, MA 01867
(781) 758-5199
souza.bruma@wseinc.com

Jean Benoît, Ph.D.
Department of Civil and Environmental Engineering, University of New Hampshire
33 Academic Way
Durham, NH 03824
(603) 978-5429
jean.benoit@unh.edu

Marion Bost, Ph.D.
Cerema
25 Avenue François Mitterrand
Bron, France 69500
+33 06 65 78 84 68
marion.bost@cerema.fr

Prepared for the 75th Highway Geology Symposium, September, 2026

Acknowledgements

The authors would like to thank the New Hampshire Department of Transportation and the French Region AURA for the financial support of these research projects.

Thank you to the technical team of the RRO Laboratory at University Gustave Eiffel for their support in this experimental campaign: Patrick Joffrin, Christophe Pruvost, and Nicolas Vermorel.

Thank you to Noah MacAdam at the University of New Hampshire Technical Service Center for his support in this experimental campaign.

Thank you to Artur Apostolov for his support in improving the latest Smart Rock sensors.

Thank you to Dr. Philippe Reiffsteck for his time and collaboration during these experimental campaigns, especially in Measurement While Drilling technology.

Disclaimer

Statements and views presented in this paper are strictly those of the author(s), and do not necessarily reflect positions held by their affiliations, the Highway Geology Symposium (HGS), or others acknowledged above. The mention of trade names for commercial products does not imply the approval or endorsement by HGS.

Copyright Notice

Copyright © 2026 Highway Geology Symposium (HGS)

All Rights Reserved. Printed in the United States of America. No part of this publication may be reproduced or copied in any form or by any means – graphic, electronic, or mechanical, including photocopying, taping, or information storage and retrieval systems – without prior written permission of the HGS. This excludes the original author(s).

ABSTRACT

Rockfall events pose a risk of irreversible damage to motorists on transportation corridors and other infrastructure in many states across the country. Rockfall hazard assessment for transportation corridors commonly relies on trajectory modeling approaches that use empirically selected input parameters, commonly based on a limited understanding of rockfall movement on different ground material types. This limitation is partly due to the difficulty of obtaining field measurements that fully capture the movement of a falling block. To help address this limitation, Smart Rock (SR) sensors have proven useful for geotechnical instrumentation of these natural hazards. The latest SRs consist of 3D-printed capsules equipped with triaxial dual accelerometers, a triaxial gyroscope, and an altimeter that measure rockfall motion from the perspective of the falling block. This paper introduces the latest sensors, discusses SR data outputs, and summarizes the main methods and applications of the Smart Rock technology over a five-year experimental research program. Data collected from more than 400 controlled and in situ tests using instrumented blocks of different mass across sites in the northeastern U.S. and France were evaluated alongside camera measurements and ground characterization methods. Results demonstrate that SR instrumentation provides new information on rockfall movement and its interaction with the ground that cannot be captured through conventional methods. Measurements from the falling rock perspective can be used to support the selection of model input parameters and provide insights to improve the accuracy of existing simulation software.

INTRODUCTION

Rockfalls occur when individual blocks detach from a slope or rock face and move downslope through free fall, rebound, rolling, or sliding. Although rockfalls generally involve smaller volumes than landslides or rock avalanches, they can pose significant risks to people and infrastructure, such as buildings, roads, and railways (1). Mitigation is particularly challenging in mountainous areas, where difficult access may limit the removal of unstable blocks or installation of protective structures (2).

Rockfall risk assessments require estimates of block trajectories, bounce heights, runout distances, kinetic energies, and impact forces. These estimates help identify susceptible areas and support the design of catchment ditches, barriers, and other protective structures (3-4). Early design methods relied primarily on field observations and empirical relationships between slope geometry and expected block motion (5-6). Numerical simulation software is now commonly used to estimate rockfall behavior using simplified representations of the slope, ground materials, and block-ground interactions (1).

The behavior of a falling block is difficult to predict as it depends on block shape and size, its velocity and rotation before impact, and the properties of different ground surfaces (2,5). Rockfall motion is three-dimensional and combines translation and rotation over terrain that may vary considerably in composition and topography. Although video systems can measure block trajectories and velocities, they generally provide limited information on rotation, acceleration, and the response of the block during impact (7).

To address these limitations, the University of New Hampshire developed Smart Rock (SR) sensors that are embedded within test blocks to measure acceleration and rotation from the falling block perspective (8-11). A five-year laboratory and field research program recently demonstrated the potential of SR sensors to characterize block motion and complex impact events that are difficult to capture using conventional methods (12-13). This paper introduces the latest SR sensors, describes their main data outputs, and summarizes the main experimental methods and applications developed during this research.

SMART ROCK SENSORS

Video recording and event back-analysis have improved the study of rockfall motion but provide limited information on block-ground interactions and block rotation as it falls (7,14). In this context, small Inertial Measurement Units (IMUs), equipped with triaxial accelerometers and gyroscopes, have increasingly been embedded in test blocks to measure rotation and impact response under different test conditions.

The latest Smart Rock sensor, shown in Figure 1, consists of a 3D-printed capsule containing two triaxial accelerometers, a triaxial gyroscope, and an altimeter. The high-g, ±400 g accelerometer measures the high accelerations generated during impacts and rebounds, while the low-g, ±16 g accelerometer provides higher resolution at lower acceleration levels. The low-range accelerometer also helps identify whether the block is in free fall (approximately 0 g) or at rest (approximately 1 g). The ±4,000 degrees-per-second (dps) gyroscope simultaneously

measures rotation rates about three axes. The altimeter tracks changes in elevation and provides complementary trajectory information, particularly when video recording is unavailable.

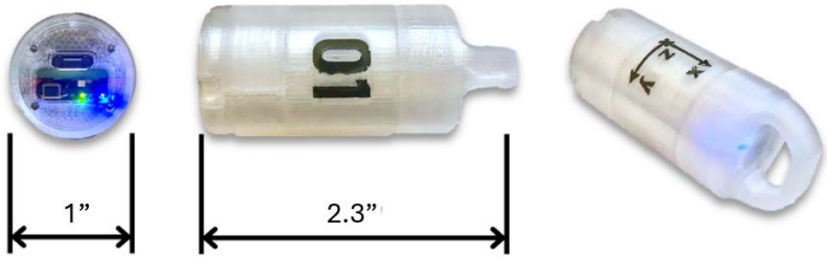

Figure 1 – Latest generation of UNH Smart Rock sensors.

A SR can be prepared for testing in less than one minute. Data are normally recorded at 100 Hz or at up to 500 Hz when the altimeter is disabled. A translucent cap allows the operator to confirm the sensor status through visible indicator lights. Measurements are automatically saved as a .csv file on a micro-SD card and are available for processing immediately after each test. The sensor is rechargeable through a standard micro-USB connection.

Smart Rock sensors were embedded in test blocks with varying masses, sizes, and geometries to investigate rockfall motion under both controlled and field conditions. Over the five-year research program, acceleration, rotation and altimetry data were collected from the falling block’s perspective with the main objectives of:

- Characterizing block motion during and after impact on ground surfaces of soft, medium, and hard deformability.
- Measuring impact duration under controlled and field conditions.
- Assessing ground deformability using accelerometer data.
- Quantifying the contribution of block rotation to overall motion.
- Characterizing field-scale rockfall motion without camera systems.
- Obtaining approximate changes in block position during impact using altimeter data.

SENSOR OUTPUT INTERPRETATION

Field testing was conducted through two experimental campaigns, as discussed in this paper. The first campaign evaluated the use of Smart Rocks to identify the different modes of motion of falling blocks (free fall, bouncing, rolling, sliding) using sensor data (12). Approximately 80 tests were completed using natural blocks weighing between 6.6 and 66 kg on rock cuts of different heights and slopes in New Hampshire. Results demonstrated that acceleration and rotational velocity measured from the falling block perspective could be used to distinguish the types of rockfall movement without the need for video recording systems.

One test site was a 49.5-ft-high granodiorite rock cut in Warner, New Hampshire, with an average inclination of 70° to 85°. A 3.5- to 5-m-wide catchment ditch containing granular soil was located at the base of the slope. Eight rockfall tests were performed at this site. Figure 2 presents one of these tests using a 40.3-lbs natural block.

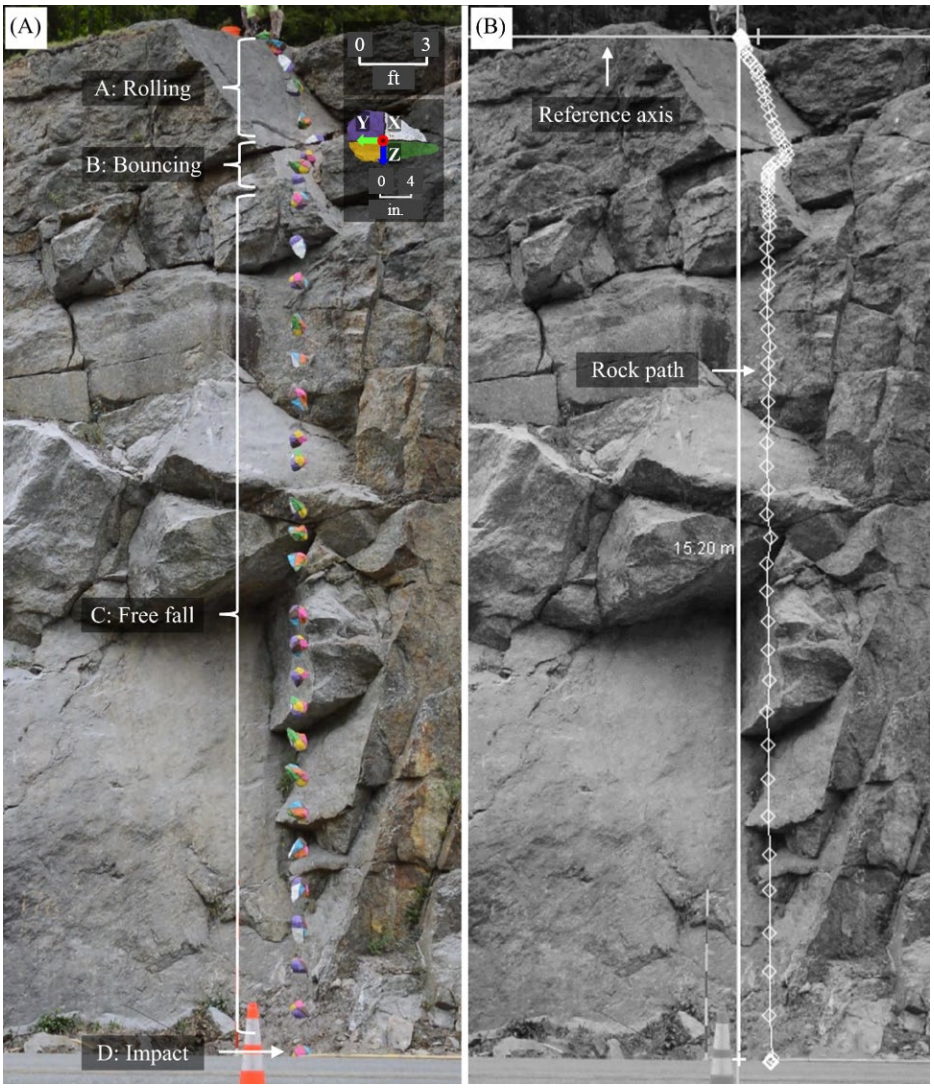

Figure 2 – Field rockfall trajectory in Warner, NH: (a) combination of video frames and (b) tracker software.

Figure 3 shows the Smart Rock outputs for the test shown in Figure 2. The letters A through D in Figures 2 and 3 indicate the different rockfall stages, matched through both SR and video recording times.

Inertial accelerometers do not measure applied forces directly; they measure acceleration relative to gravity. A sensor at rest, aligned with gravity, records a resultant acceleration of 1 g; in free fall, it records approximately 0 g. During rockfall, the sensor simultaneously experiences translation and rotation about three axes, however, the sensor orientation as the block falls downslope is generally unknown. Therefore, patterns in the resultant acceleration and rotational velocity outputs were used to identify the following modes of motion:

- **At rest:** Constant resultant acceleration of approximately 1 g and negligible rotational velocity.
- **Impact or rebound:** A sharp acceleration peak, generally recorded by the high-g accelerometer, accompanied by a change in rotational velocity.

- **Free fall:** Resultant acceleration of approximately 0 g and nearly constant resultant rotational velocity.
- **Rolling:** Increasing or decreasing rotational velocity accompanied by relatively small acceleration peaks.
- **Sliding:** Small acceleration peaks accompanied by little or no rotation.

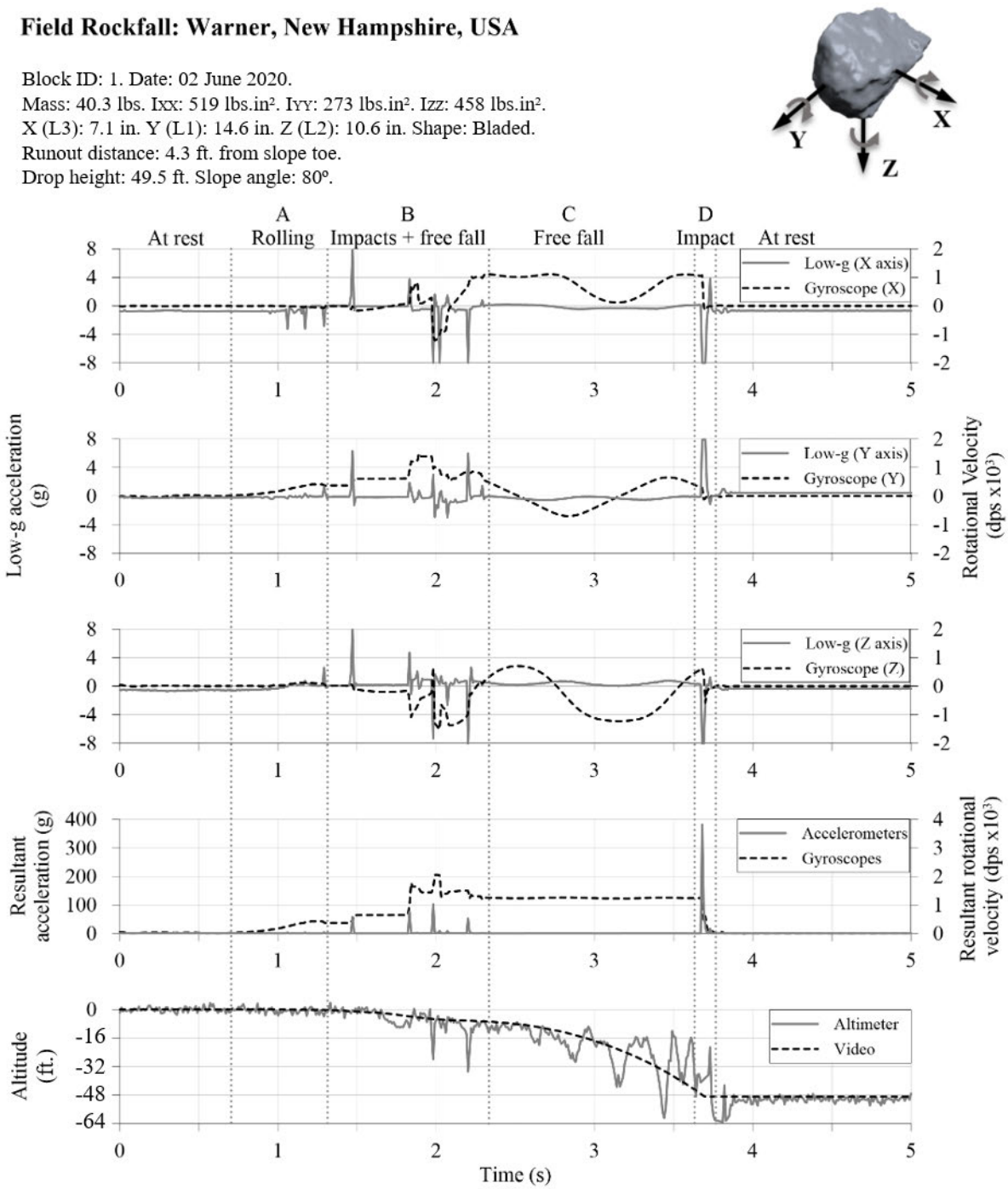

Figure 3 – Smart Rock sensor output for field rockfall test in Warner/NH.

In the example shown, the block initially rolled along the upper portion of the slope (A), producing increasing rotational velocity and acceleration peaks below 4 g. It then rebounded four times against the rock face (B), as indicated by larger acceleration peaks and changes in rotation following each impact. The block then fell freely for approximately 2 s (C), during which it recorded approximately 0 g and rotated about all three axes. The nearly constant resultant rotational velocity during this stage is consistent with the absence of external forces acting on the block in free fall (4). At approximately 3.7 s, the block impacted the catchment ditch and immediately came to rest (D). The measured runout distance from the slope toe was 1.3 m.

Acceleration and rotational velocity measurements from the three sensor axes were combined into resultant values. Using the measurements from both low and high-g accelerometers, the block recorded resultant accelerations of approximately 50 to 100 g during rebounds against the rock face and a maximum of 382 g during its final impact with the catchment ditch. Based on a block mass of 40.3 lbs, these accelerations correspond to estimated impact forces of approximately 1 to 2 tons-force and 7.5 tons-force, respectively. These estimates describe the magnitude, but not the direction, of the impact force. Maximum and average rotational velocities were 2,053 and 947 degrees per second, respectively.

The initial experimental campaign established the basis for interpreting Smart Rock outputs and using acceleration and rotational velocity measurements to characterize rockfall motion. The resulting conclusions and lessons learned guided the design of the subsequent controlled and field experimental campaigns presented in the following sections.

TESTS PERFORMED UNDER CONTROLLED CONDITIONS

Ground conditions strongly influence whether, after impact, a falling block experiences rebound, rolling, sliding, or comes to rest. Most available experimental data describe impacts on a limited range of materials and test conditions. The absence of a consistent methodology for evaluating rockfall behavior upon impact on different ground surfaces makes it difficult to obtain and select representative input parameters for rockfall models.

A controlled experimental program was developed to investigate the interaction between the falling block and the ground using a consistent, repeatable testing procedure (13). A total of 310 drop tests were performed using concrete blocks ranging in mass from 2.2 to 236 lbs. The blocks were released from heights between 1 and 33 ft. onto surfaces inclined from 0° to 60°. These conditions produced impact velocities between approximately 14.5 and 47.5 ft./s, representing a range commonly encountered during rockfall events. Six impact surfaces were evaluated: sand, gravel, sandy gravel, concrete, rough rock, and smooth rock. Together, these materials represented soft, medium, and hard ground conditions.

Each block had an orifice at its center of gravity for the Smart Rock sensor. The sensors were secured inside the block using a custom-printed cap or a steel plate, as shown in Figure 4. Blocks were released vertically with minimal initial rotation, and each test condition was repeated three times. Figure 5 shows the experimental setups to vertically release the test blocks at the University of New Hampshire and University Gustave Eiffel’s rockfall testing station (France).

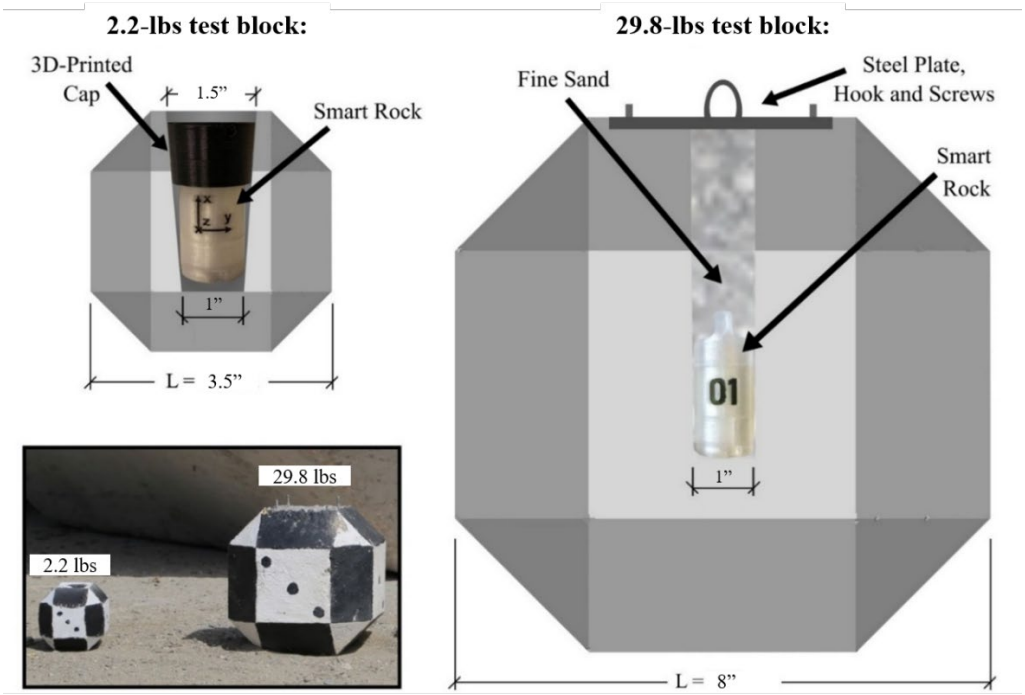

Figure 4 – Test block configurations. The 2.2 and 29.8 lbs weights consider the weight of the block, sensor, and additional materials to confine the SR (cap/plate, hook, and screws).

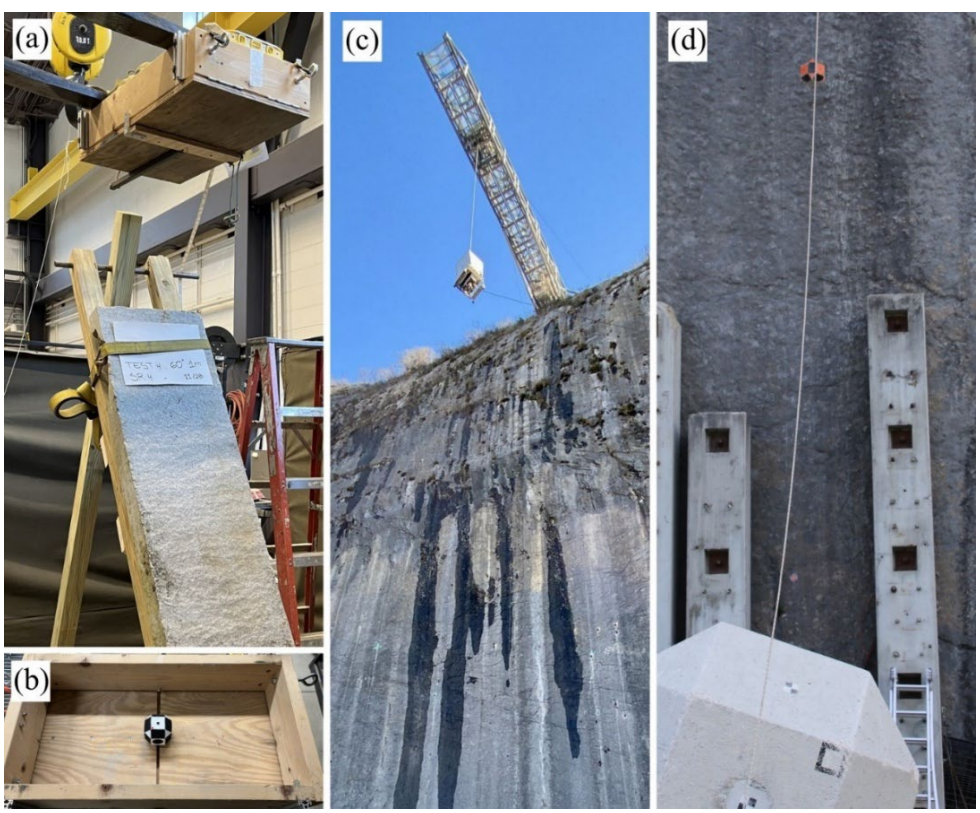

Figure 5 – (a) UNH small-scale setup on rough granite, positioned at 60°, and (b) close-up of rock dropper. (c) Crane at the UGE rockfall test station and (d) test setup on concrete at 20°: 29.8 lbs block, 16 ft. drop.

Smart Rock measurements were synchronized with high-speed cameras positioned in front of and beside the test area, as represented in Figure 6. This combined approach provided information not normally available from video observations alone. The combined camera views provided the three-dimensional block trajectory, including displacement, penetration, and translational velocity. Smart Rock measurements allowed the impact phase to be studied directly.

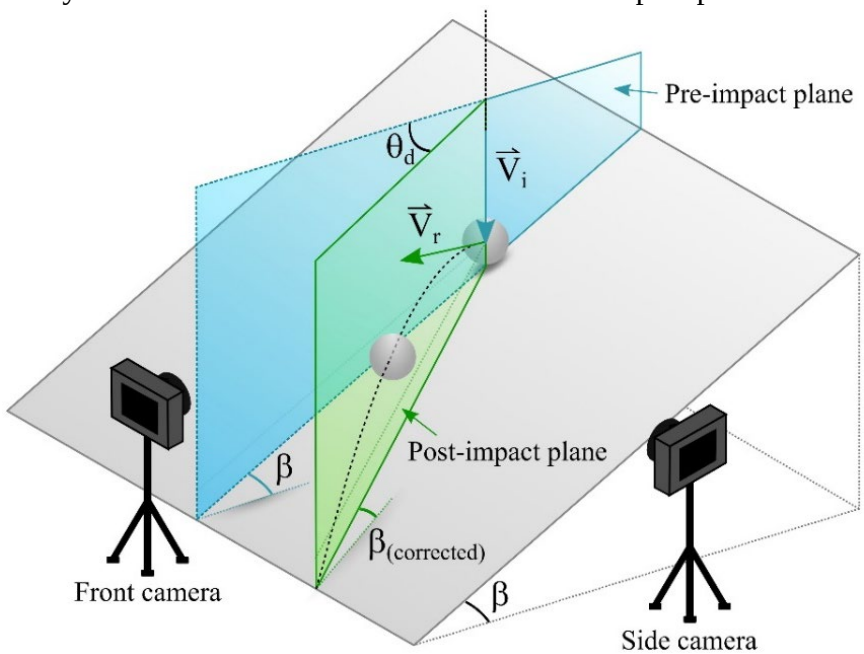

Figure 6 – Schematic of tests performed under controlled conditions on an inclined plane and frontal and lateral camera views of one drop test on sand.

The acceleration measurements identified the exact time of ground contact, the magnitude and duration of impact, and subsequent rebounds. The gyroscope showed how rotation developed during impact and whether the block transitioned into rebound, rolling, or sliding. One example test is shown in Figure 7, where the 29.8-lbs block was released from a drop height of 16 ft. onto sandy gravel soil prepared at a slope of 20º.

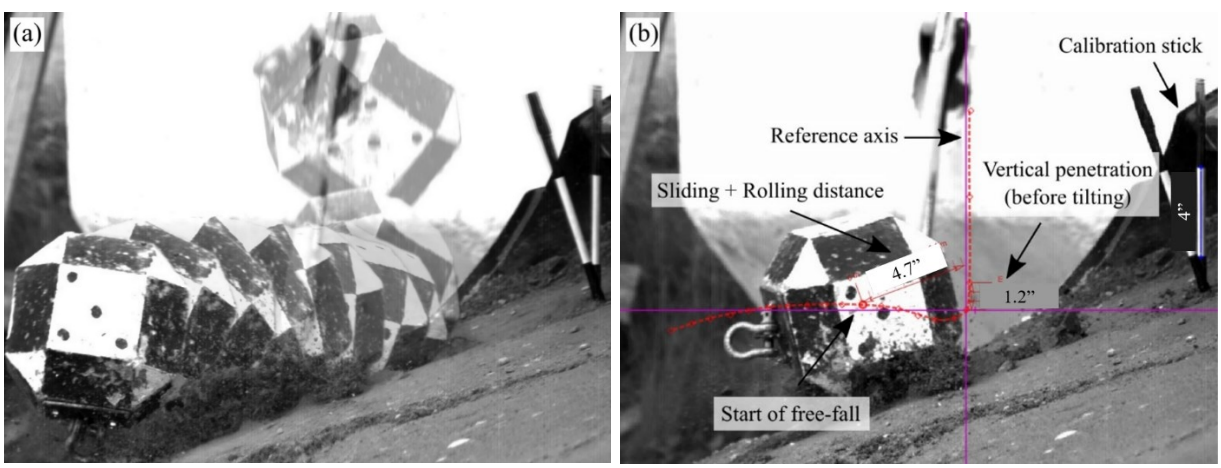

Figure 7 – (a) Block trajectory through combined video frames, and (b) block trajectory using Tracker software.

Figure 8 presents in black the SR resultant accelerations measured in six representative tests performed under different boundary conditions, including changes in material, block mass, and drop height. Before release, the stationary block recorded approximately 1 g and negligible rotation. During free fall, the resultant acceleration approached 0 g as observed in previous experiments, while impact produced a sharp acceleration peak and an increase in rotational velocity. These patterns were used to determine impact duration, estimate impact forces, and distinguish the modes of motion occurring immediately after contact for different material types.

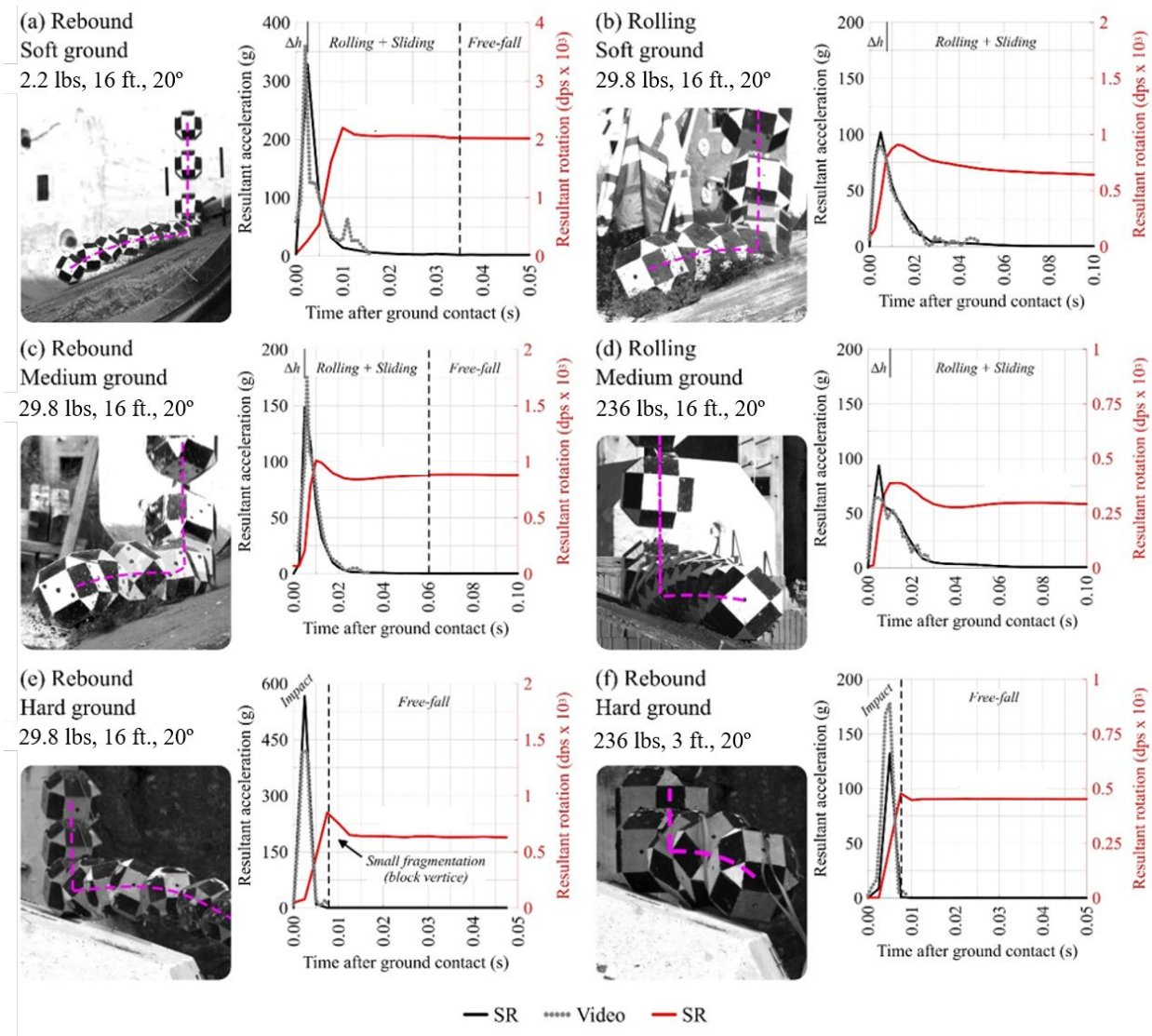

Figure 8 – Rockfall trajectories under controlled conditions and their respective resultant acceleration and rotational velocity curves obtained through SR and video measurements.

The tests under controlled conditions also demonstrated an application of the Smart Rock for ground characterization, by normalizing impact duration data by the block height. The resulting values formed distinguishable ranges for soft, medium, and hard surfaces. This provides a

practical method for evaluating the impacted ground using measurements collected by the falling block itself, rather than relying only on visual material descriptions.

Independent ground characterization was conducted to evaluate and validate this approach. A lightweight deflectometer measured surface deformability, while a portable Measurement While Drilling device (PMWD, Figure 9a) and a lightweight dynamic cone penetrometer (LDCP, Figure 9b) evaluated resistance to penetration and subsurface variability. Several characterization tests (67 in total) were completed in surfaces prepared under controlled conditions. Agreement between the PMWD, LDCP, and Smart Rock results supported the use of normalized impact duration as an indicator of ground type.

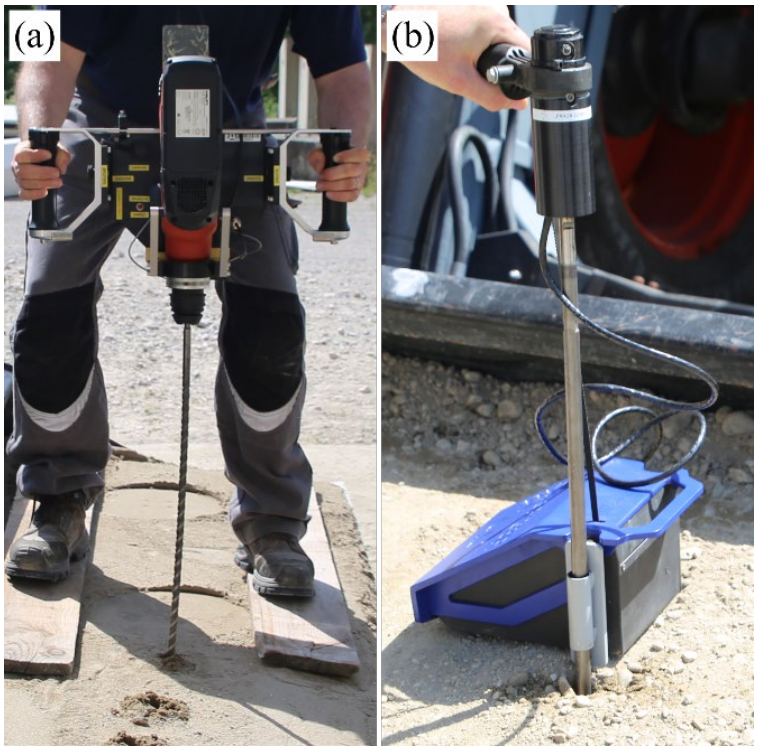

Figure 9 – Characterization tests under controlled conditions: (a) PMWD on sand and (b) LDCP on sandy gravel.

The Smart Rock measurements further showed the importance of block rotation. Rotational kinetic energy represented up to 40% of the post-impact translational kinetic energy under some test conditions. Since block rotation is difficult to quantify through conventional video analysis, direct measurements from the embedded sensor provide valuable information for evaluating energy transfer and calibrating models. Overall, the controlled testing program provided a database correlating block motion, impact response, and ground deformability across a broad range of boundary conditions.

A few studies have also assessed the contribution of rotation in controlled lab tests or field tests, mostly using camera systems. They also showed that block rotation can account for a significant portion of the kinetic energy (KE). Using high-speed camera measurements and video-based trajectory reconstruction, Chau et al. (15) reported rotational energy contributions up to 40% of

the translational kinetic energy after impact for plaster spheres impacting hard surfaces. Another study by Wang et al. (16), using infrared camera tracking of nearly spherical limestone blocks impacting concrete slabs, measured ratios of rotational KE after impact divided by the total incident KE of up to 15% for 2.2 lbs blocks and 5% for 22 lbs blocks. On deformable materials, Heidenreich (17) used video analysis of impacts on sand and found that rotational energy contributed, on average, about 20% of the translational KE after impact and approximately 5% of the incident KE, suggesting that rotational effects are also relevant when ground penetration occurs.

TESTS PERFORMED IN FIELD CONDITIONS

The controlled experiments established relationships between Smart Rock measurements, block motion, and ground deformability. A second field campaign was conducted to evaluate whether these relationships could be applied to natural slopes, where terrain geometry, vegetation, and subsurface conditions vary (13).

Figure 10 – Field tests in Enfield and Franklin, NH.

Twelve additional field experiments were performed at two sites in New Hampshire, shown in Figure 10. Concrete blocks weighing 29.8 lbs and containing two Smart Rock sensors were released from known locations with minimal initial velocity. The sites were selected to represent ground surfaces with different degrees of deformability. PMWD and LDCP tests were completed along the test slopes to independently characterize subsurface resistance and classify the terrain as soft, medium, or hard.

One of the sites, in Enfield, NH, consisted of a 590-ft.-long and 150-ft high grassy slope, the lower part of the Whaleback ski resort as shown in Figure 11. The upper slope had an average inclination of approximately 20°, while the lower portion flattened to less than 5°. Subsurface profiles indicated that the upper slope consisted predominantly of looser granular soil ("soft" ground), whereas the lower slope contained a denser and more variable material with gravel, pebbles, and cobbles ("medium" ground).

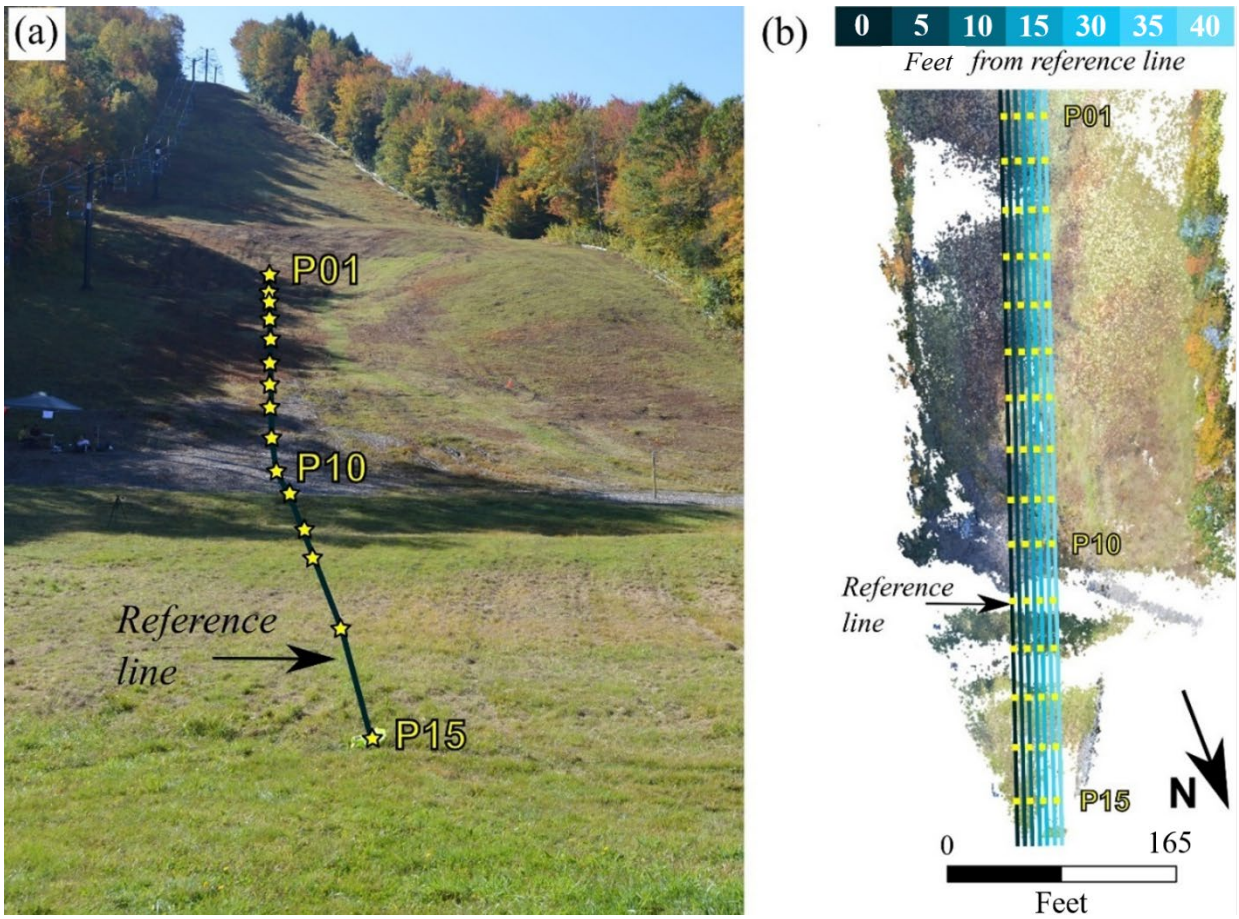

Figure 11 – (a) Test slope in Enfield/NH, USA. The spaces between each pair of stars measure 33 ft. along the slope surface. (b) Distribution of test locations along the slope profile.

A total of 6 instrumented tests were performed at the Enfield site. The blocks generally moved through repeated sequences of rebound and free fall, with short periods of rolling near the beginning and end of their trajectories. The Smart Rock records allowed each impact to be identified without the need for video verification. At this site, impact durations were measured

from 590 acceleration peaks. The trajectory from one of the tests is shown in Figure 11. Altimeter measurements were matched with the slope profile, obtained through photogrammetry, to estimate the location of each impact, and the normalized impact durations were used to classify the impacted surface as soft, medium, or hard based on results from the controlled tests.

The Smart Rock results showed predominantly soft impacts along the upper slope and a transition toward medium impacts downslope, as shown in Figure 12. This pattern was consistent with the independent PMWD and LDCP profiles. Isolated, hard impacts were generally associated with shallow cobbles or exposed rock rather than a continuous hard-ground layer. This distinction is relevant as a falling block responds to the material at its specific point or area of contact, which may differ from the general description assigned to a larger slope segment.

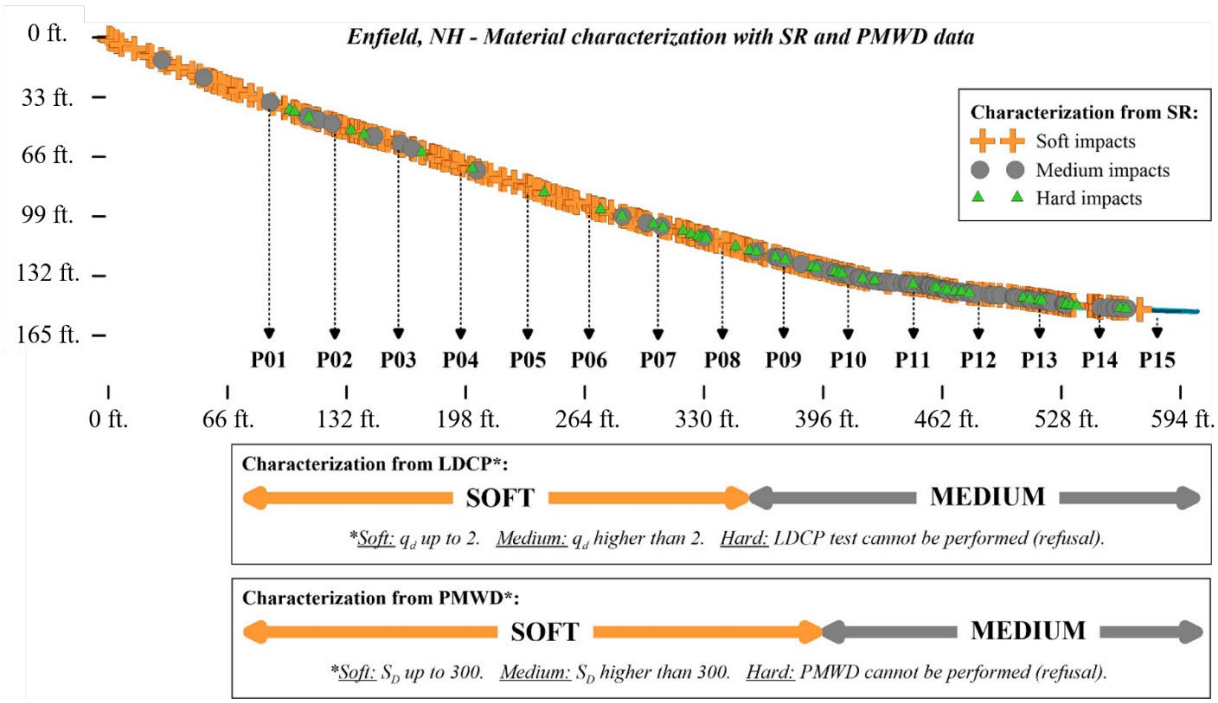

Figure 12 – Material characterization in Enfield, NH, based on SR data and in situ characterization testing with LDCP and PMWD.

Across both field sites, acceleration data from more than 700 impacts were evaluated. The agreement between Smart Rock classifications and conventional ground characterization demonstrated that impact measurements can provide information about spatial changes in ground conditions along a rockfall trajectory. The altimeter also provided approximate impact locations when a slope profile was available. These applications are particularly useful on long or inaccessible slopes, where installing cameras or conducting detailed subsurface investigations may be impractical or not possible.

MODEL COMPARISONS

Rockfall models are widely used to estimate trajectories, bounce heights, kinetic energies, and runout distances. However, their predictions depend strongly on how the ground and block-

ground interaction are represented. Smart Rock data provides a direct means of evaluating these assumptions and selecting model inputs based on measured block behavior.

Three two-dimensional rockfall programs, PlatRock, PROPAG, and RocFall, were evaluated using lumped-mass and rigid-body approaches (12,13). Although three-dimensional models are increasingly available, two-dimensional approaches remain widely used and often form the basis of more advanced simulations. The selected programs also allowed the influence of block shape and different impact formulations to be evaluated.

The comparison was completed in two stages. First, the controlled drop tests using the 29.8-lbs block were simulated using default parameters recommended by each program as shown in Figure 13. These tests provided the most complete experimental dataset across soft, medium, and hard ground. Model predictions were compared with measured translational and rotational energies, modes of motion, and apparent coefficients of restitution, which describe the fraction of velocity retained after impact. This comparison showed how each program represented a single impact under known conditions and provided initial ranges of calibrated input parameters.

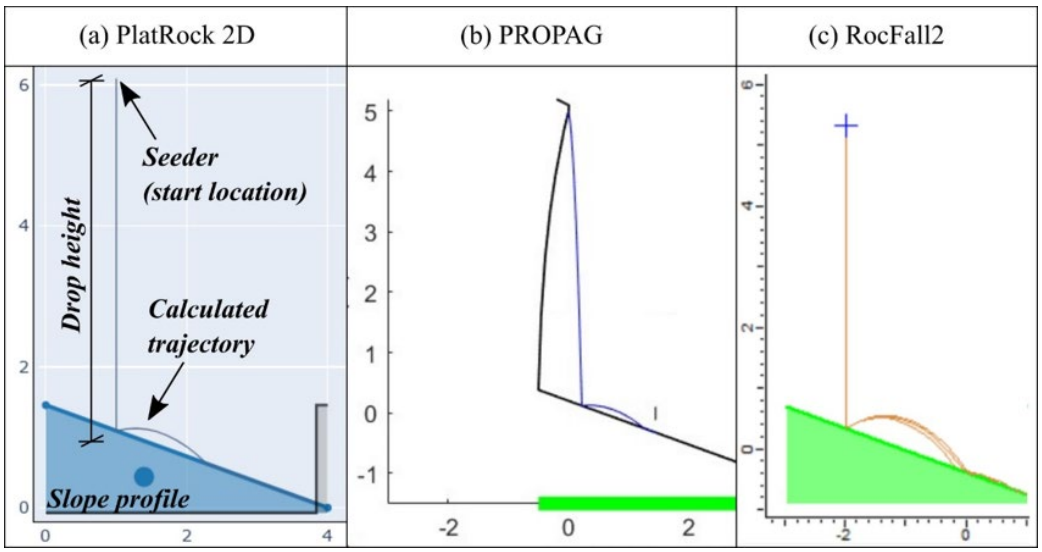

Figure 13 - Sample software trajectory outputs – medium ground, 20° slope, 16 ft. drop.

In the second stage, the Enfield and Franklin field experiments were simulated using slope profiles generated from photogrammetry. Ground materials were assigned using the Smart Rock, PMWD, and LDCP classifications. Simulations were first performed with default material parameters and then repeated using parameters calibrated from the controlled tests. Predicted runout distances and rotational behavior were compared with the field measurements. Figure 14 presents the modeled trajectories for both lumped mass (a) and rigid body (b) modeling approaches in RocFall at the Franklin site. The modeled trajectories are compared to the field endpoint locations in blue.

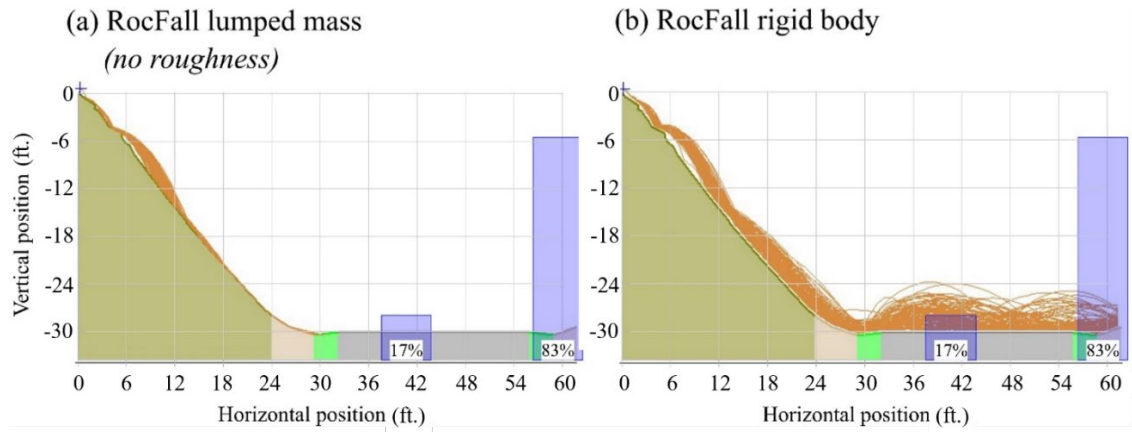

Figure 14 – RocFall modeled trajectories using default input parameters. (a) Lumped mass without roughness and (b) rigid body model. The bar charts represent the endpoint distribution of the field tests.

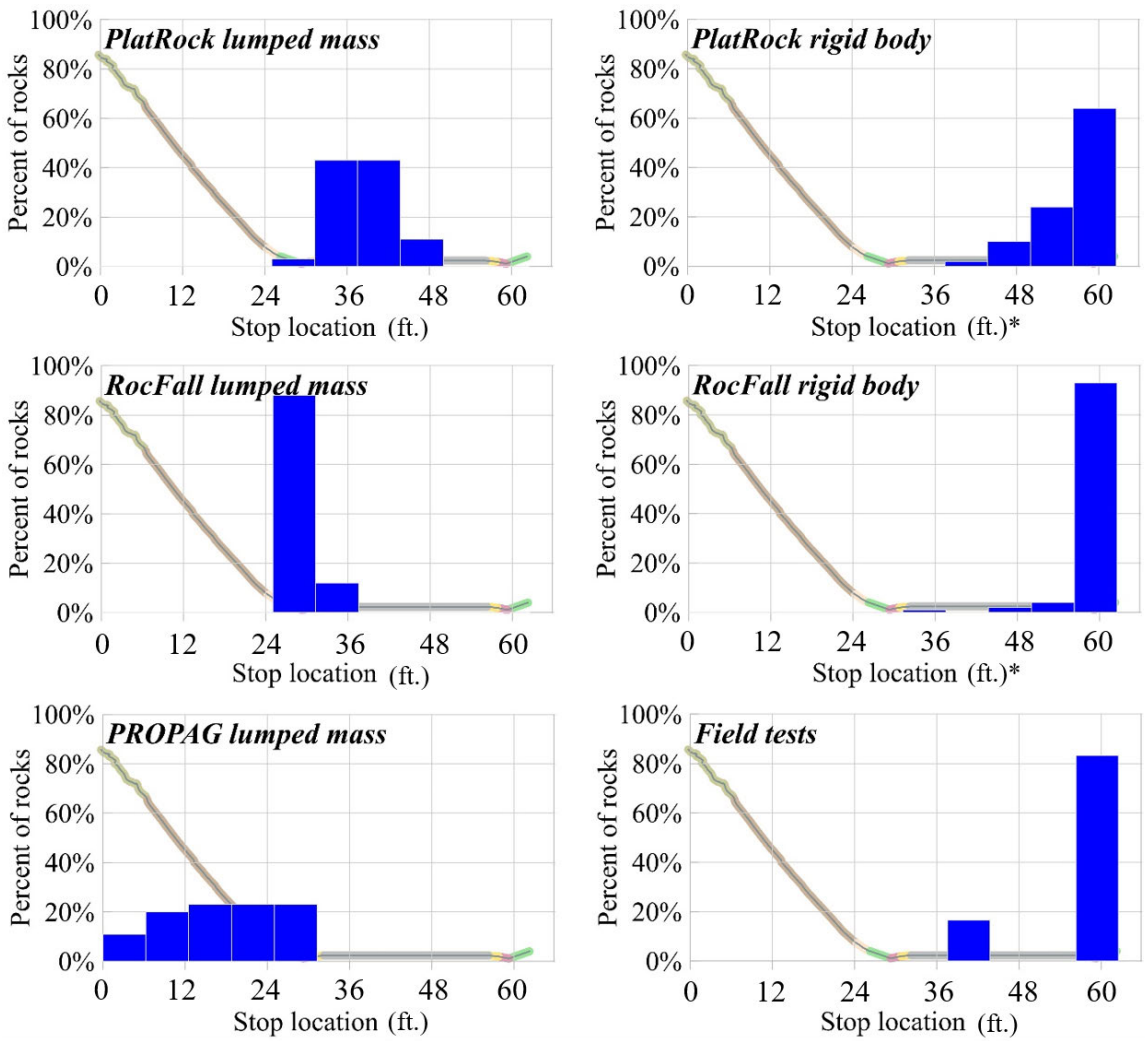

Figure 15 – Summary of block runout for rockfall models and field tests in Franklin, NH. * Please note that runouts at x = 60 ft. in the models do not always imply that the block fully stopped.

Figure 15 compares the measured runout for each rockfall model and the field measurements at the Franklin site. The PROPAG software only performs predictions using lumped mass models. The runout distances measured in the field were plotted in the last graph for comparison with the numerical results. It can be observed that, while rigid body models reached the runout locations for the field experiments, most lumped mass models stopped in the first catchment ditch the start of the road.

The comparisons highlighted limitations of conventional modeling approaches. Most models treat impact as instantaneous and do not represent penetration into deformable ground. Lumped-mass models typically reproduce impact as a rebound from a single contact point, which can reasonably describe some impacts on hard surfaces but is less representative of the prolonged and irregular interactions often observed on soft and medium ground. These models also do not calculate block rotation directly because block geometry is not explicitly represented.

Rigid-body approaches include block shape and rotation, but still require simplified descriptions of the impact surface and energy transfer. Consequently, the selection of input parameters remains challenging, particularly for deformable or spatially variable ground. The controlled and field measurements showed that the same general material description may produce different block responses depending on impact velocity, slope angle, block geometry, and local subsurface conditions.

The main application of the Smart Rock in this assessment was therefore not limited to checking whether a model reproduced a specific trajectory. The technology provided measurements for identifying why simulations differed from observed behavior and for selecting inputs based on experimental data. Combining sensor measurements with portable ground characterization offers a practical framework for calibrating models and improving rockfall hazard estimates at sites where default material parameters may not be representative.

CONCLUSIONS

This paper presented the development and application of Smart Rock technology for evaluating rockfall hazards from the perspective of the falling block. More than 400 experiments were conducted during the research program, including an initial field campaign with natural blocks, 310 controlled drop tests, and 12 additional field tests designed to validate the controlled findings.

These tests demonstrated that Smart Rocks can be used to measure aspects of rockfall motion that are difficult to obtain using cameras or field observations alone. Acceleration and rotational velocity records were used to identify free fall, impact, rebound, rolling, sliding, and rest. The measurements also provided impact timing, impact duration, peak acceleration, rotational behavior, and approximate changes in elevation.

Under controlled conditions, SRs allowed a more in-depth study of the impact phase, in addition to pre- and post-impact motion that is normally assessed by high-speed video systems. When combined with high-speed video, the measurements produced a comprehensive dataset describing translational and rotational energy transfer across soft, medium, and hard ground. The

results demonstrated that rotation can represent a significant portion of post-impact energy and should be considered when evaluating rockfall motion and protective systems. These tests also provided ranges of rotational energy contribution for different ground types and test conditions.

The Smart Rock also provided a new application for characterizing impacted ground. Impact duration normalized by block height was used to distinguish broad ranges of soft, medium, and hard surfaces. Field validation using more than 700 impact records showed agreement with independent PMWD and LDCP measurements. This approach may be especially useful on inaccessible slopes, where conventional investigations and continuous camera coverage are difficult.

Finally, the controlled and field measurements provided an experimental basis for evaluating rockfall simulation programs. Comparisons with PlatRock, PROPAG, and RocFall demonstrated how assumptions related to impact duration, ground penetration, block shape, and rotation influence model predictions. Smart Rock data can therefore support model calibration, help a more objective input parameter selection, and help identify block-ground contact conditions that may require improved representation.

These applications demonstrate that Smart Rock technology can connect experimental testing, field characterization, and numerical modeling. Future studies can extend this approach to larger blocks, additional block geometries, and more varied slope and ground conditions. The technology may also be used to evaluate protective structures directly by measuring the acceleration, rotation, and energy changes experienced by an instrumented block during impact.

REFERENCES:

1. Volkwein, A., K. Schellenberg, V. Labiouse, F. Agliardi, F. Berger, et al. Rockfall Characterisation and Structural Protection—A Review. *Natural Hazards and Earth System Sciences*, Vol. 11, 2011, pp. 2617–2651. doi: ffhal-00653458.
2. Pfeiffer, T. J., and T. D. Bowen. Computer Simulation of Rockfalls. *Environmental & Engineering Geoscience*, Vol. XXVI, No. 1, 1989, pp. 135–146. https://doi.org/10.2113/gseegeosci.xxvi.1.135.
3. Turner, A. K., and J. D. Duffy. Modeling and Prediction of Rockfall. In *Rockfall Characterization and Control*, A. K. Turner and R. L. Schuster, eds., Transportation Research Board, Washington, D.C., 2012, pp. 334–406.
4. Wyllie, D. C. *Rock Fall Engineering*. CRC Press, Taylor & Francis Group, New York, 2015.
5. Ritchie, A. M. *Evaluation of Rockfall and Its Control*. Washington State Highway Commission, 1963.
6. Pierson, L. A. *The Rockfall Hazard Rating System*. Report FHWA-OR-GT-92-05, Engineering Geology Group, Oregon State Highway Division, and Federal Highway Administration, 1991. https://rosap.ntl.bts.gov/view/dot/22762.

7. Glover, J. M. H. *Rock-Shape and Its Role in Rockfall Dynamics*. Doctoral thesis, Durham University, 2015.

8. Harding, M. J. *Design and Development of a Debris Flow Tracking "Smart Rock"*. Master's thesis, University of New Hampshire, 2011.

9. Gullison, M. A. *Analysis of "Smart Rock" Data from Debris Flow Experimentation*. Master's thesis, University of New Hampshire, 2013.

10. Harding, M. J., B. K. Fussell, M. A. Gullison, J. Benoît, and P. De Alba. Design and Testing of a Debris Flow "Smart Rock." *Geotechnical Testing Journal*, Vol. 37, No. 5, 2014. https://doi.org/10.1520/GTJ20130172.

11. Apostolov, A. *Development and Testing of Motion Tracking "Smart Rock" Devices for Geotechnical Applications*. Master's thesis, University of New Hampshire, 2016.

12. Souza, B. M. M. *Use of Smart Rocks to Improve Rock Slope Design*. Master's thesis, University of New Hampshire, 2021.

13. Souza, B. M. M. *Evaluation of Rockfall Trajectories Using Smart Rocks and Measurement While Drilling*. Doctoral dissertation, University of New Hampshire, 2024.

14. Caviezel, A., and W. Gerber. Brief Communication: Measuring Rock Decelerations and Rotation Changes During Short-Duration Ground Impacts. *Natural Hazards and Earth System Sciences*, Vol. 18, No. 11, 2018, pp. 3145–3151. https://doi.org/10.5194/nhess-18-3145-2018.

15. Chau, K. T., Wong, R. H. C., and Wu, J. J. Coefficient of restitution and rotational motions of rockfall impacts. *International Journal of Rock Mechanics and Mining Sciences*, Vol. 39, No. 1, 2002, pp. 69–77. https://doi.org/10.1016/s1365-1609(02)00016-3.

16. Wang, Y., Jiang, W., Cheng, S., Song, P., and Mao, C. Effects of the impact angle on the coefficient of restitution in rockfall analysis based on a medium-scale laboratory test. *Natural Hazards and Earth System Sciences*, Vol. 18, No. 11, 2018, pp. 3045–3061. https://doi.org/10.5194/nhess-18-3045-2018.

17. Heidenreich, B. *Small- and half-scale experimental studies of rockfall impacts on sandy slopes (Thèse No. 3059)*. Doctoral Dissertation, Faculté Environnement Naturel, Architectural et Construit, École Polytechnique Fédérale de Lausanne, 2004.

DIMENSIONING
PLATFORM
Plan
Calculate
Report
NEW
THE FIRST SITE VISIT
IS NOW VIRTUAL.
Use premium photogrammetry and 3D geodata to dimension protection systems, run calculations and generate project reports.
ONE PLATFORM. ONE WORKFLOW.
Scan the QR code.
Sign up and start
dimensioning.
geobrugg.com/dimensioning
BRUGG
Geobrugg
Safety is our nature

GSI GeoStabilization International®
ACCESS LIMITED
ROADGUARD
JDC JENSEN DRILLING COMPANY
A GeoStabilization International Company

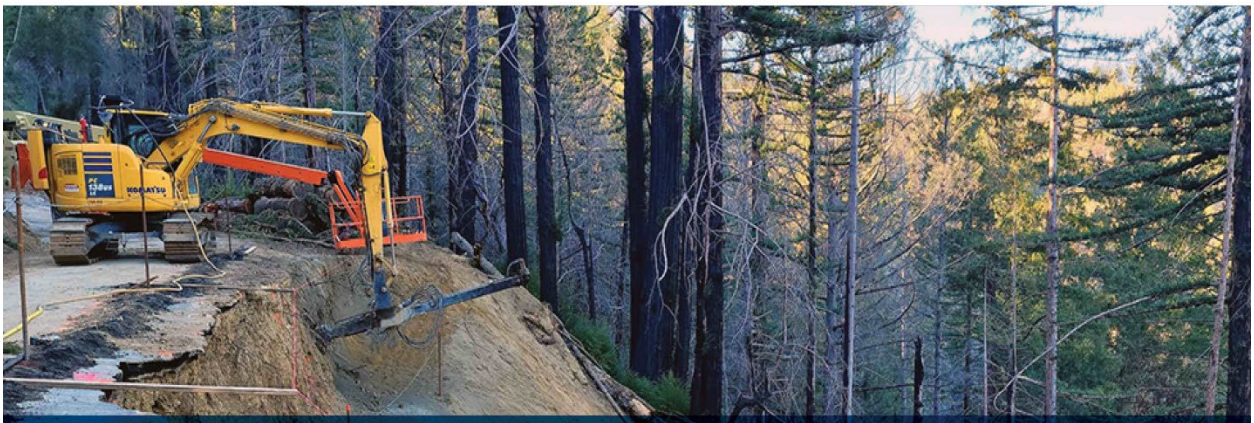

Rapid Stabilization Response

Specialty In-House Engineering & Project Management

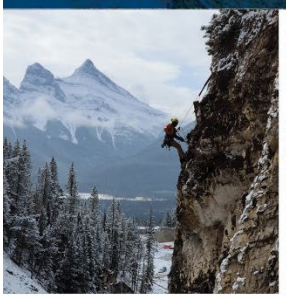
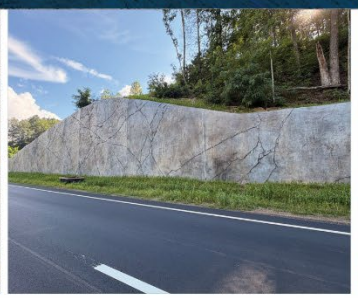

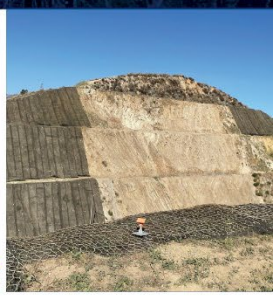

OUR SERVICES

- Slope Stabilization
- Roadway Failure Repair
- Rockfall Mitigation
- Retaining Wall Repair
- Debris Removal
- Horizontal Drains
- River & Stream Channel Restoration
- Difficult Access Drilling
- Slope Excavation & Scaling
- Micropile Foundations
- Temporary Shoring
- Shotcrete & Aesthetic Finish
- Bridge Abutment/ Foundations
- Ground Improvement Drilling & Pressure Grouting
- Guardrail Services

www.geostabilization.com | www.accesslimited.com |www.roadguard.com
855.942.1550

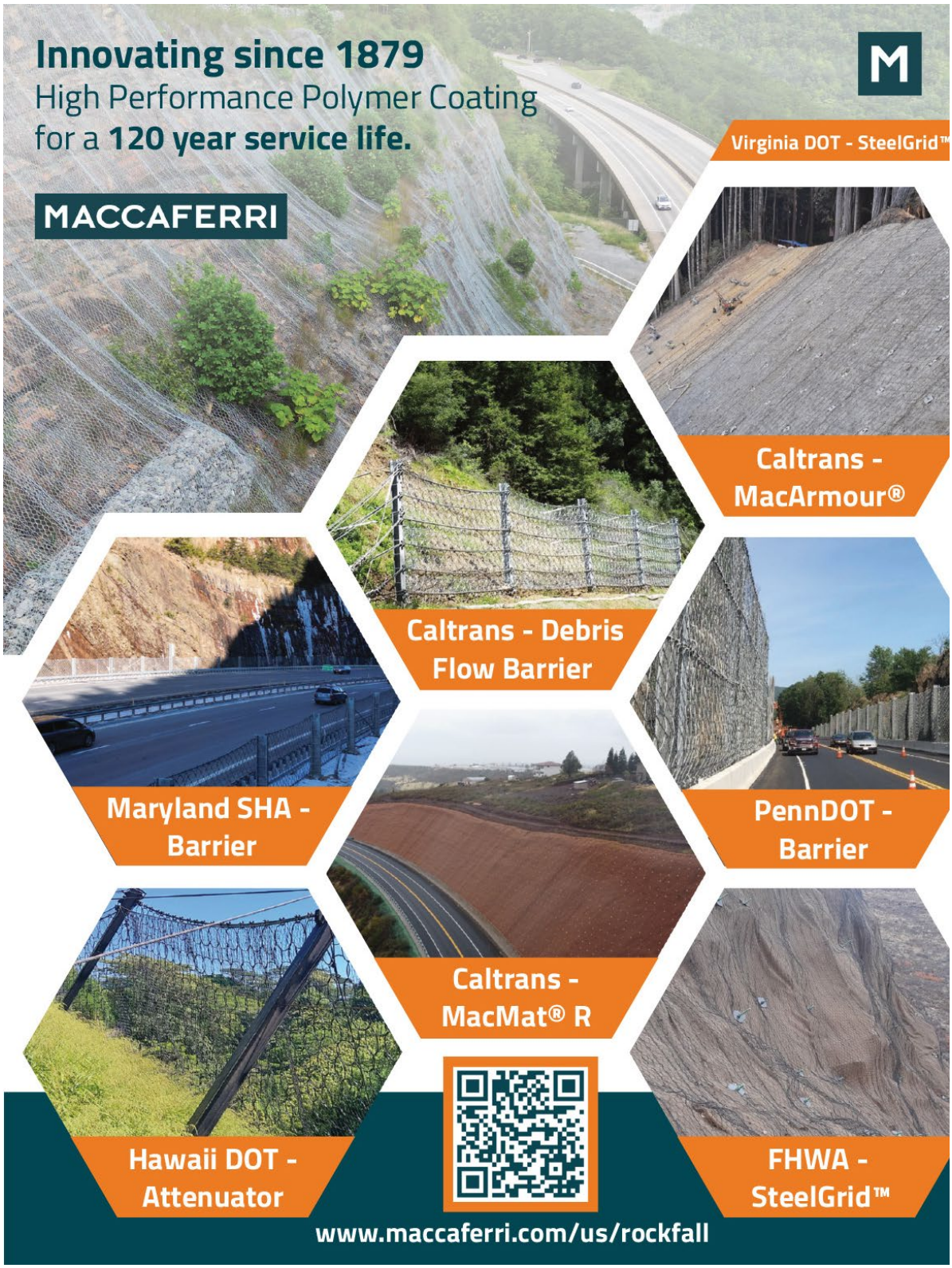
Innovating since 1879
High Performance Polymer Coating
for a 120 year service life.
MACCAFERRI
M
Virginia DOT - SteelGrid™
Caltrans - MacArmour®
Caltrans - Debris Flow Barrier
Maryland SHA - Barrier
PennDOT - Barrier
Caltrans - MacMat® R
Hawaii DOT - Attenuator
FHWA - SteelGrid™
www.maccaferri.com/us/rockfall

Thank You for Attending the

75th Annual Highway Geology Symposium.

See You Next Year in Pennsylvania!